



ERZURUM TECHNICAL UNIVERSITY

2010

FACULTY of ENGINEERING and ARCHITECTURE

**International Conference on Advances in
Engineering, Architecture,
Science and Technology
(ICA-EAST 2021)**

**December 15-17, 2021
in Erzurum, Turkey**

**PROCEEDINGS
BOOK**

ISBN: 978-605-74839-1-1

1st INTERNATIONAL CONFERENCE ON ADVANCES IN ENGINEERING, ARCHITECTURE, SCIENCE AND TECHNOLOGY

DECEMBER 15-17, 2021 in Erzurum, TURKEY

Organizer of the Conference

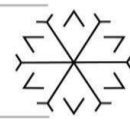
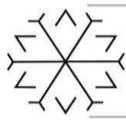
Faculty of Engineering and Architecture at Erzurum Technical University

Editors

Prof. Dr. Ali Fatih YETİM

Assoc. Prof. Dr. Salih AKPINAR

Res. Asst. Uğur KILIÇ



HONORARY CONFERENCE CHAIR

Prof. Dr. Bülent ÇAKMAK

GENERAL CHAIR

Prof. Dr. Ali Fatih YETİM

CONFERENCE CHAIR

Assoc. Prof. Dr. Salih AKPINAR

ORGANIZING COMMITTEE

Assoc. Prof. Dr. Nur Hüseyin KAPLAN

Assoc. Prof. Dr. Muhammed Yasin ÇODUR

Assoc. Prof. Dr. Mahyar MAALI

Assoc. Prof. Dr. Tuba YETİM

Asst. Prof. Dr. Türkay KOTAN

Asst. Prof. Dr. İbrahim ATES

Asst. Prof. Dr. Onur ÇOMAKLI

Asst. Prof. Dr. Burak Kaan ÇIRPICI

Asst. Prof. Dr. Çağlar DUMAN

Asst. Prof. Dr. Merve YILDIRIM

Asst. Prof. Dr. Yaşar DAŞDEMİR

Asst. Prof. Dr. Mahmut TUTAM

Asst. Prof. Dr. Merve KAYACI ÇODUR

Asst. Prof. Dr. Ömer Halil ÇAVUŞOĞLU

Asst. Prof. Dr. Işıl KARABEY AKSAKALLI

Dr. Rumeysa BAYAR

Dr. Çağrı ULUDÜZ

Res. Asst. Emre MANDEV

Res. Asst. Resul ŞAHİN

Res. Asst. Burak GEDİK

Res. Asst. Kadir Diler ALEMDAR

Res. Asst. Yasin Demir

Res. Asst. Ali Kıvanç Şahin

Res. Asst. Ömer Faruk Yıldırım

Res. Asst. Nadide ÇAĞLAYAN

Res. Asst. Ömer Faruk ÇAPAROĞLU

Res. Asst. Elif AYIK

Res. Asst. Güven Balta

Res. Asst. Şeyma KOCADAĞIŞTAN

Res. Asst. Yelda Gamze YALÇINER

Res. Asst. Uğur KILIÇ

SECRETARY

Res. Asst. Yasin Demir

Res. Asst. Elif AYIK

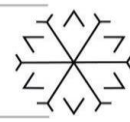
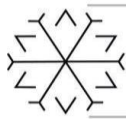
Res. Asst. Ömer Faruk ÇAPAROĞLU

Res. Asst. Yelda Gamze YALÇINER

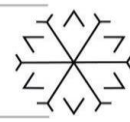
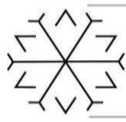
SCIENTIFIC COMMITTEE

Prof. Dr. İrfan KAYMAZ, Erzurum Technical University

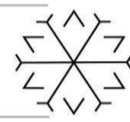
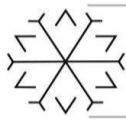
Prof. Dr. Birol SOYSAL, Erzurum Technical University



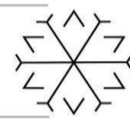
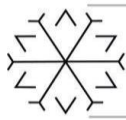
Prof. Dr. Mehmet Akif CEVİZ, Erzurum Technical University
Prof. Dr. Abdulkadir Cüneyt AYDIN, Atatürk University
Prof. Dr. Adnan DERDİYOK, Sakarya University
Prof. Dr. Ahmet Ferhat BİNGÖL, Atatürk University
Prof. Dr. Alaeddin ARPACI, İstanbul Technical University
Prof. Dr. Andrey Ronzhin
Prof. Dr. Ayhan ÇELİK, Atatürk University
Prof. Dr. Bedir TEKİNERDOĞAN, Wageningen University
Prof. Dr. Olja Cokorilo, University of Belgrade
Prof. Dr. Bülent ÇAVUŞOĞLU, Atatürk University
Prof. Dr. Cafer ÇELİK, Atatürk University
Prof. Dr. Hakan GÖKDAĞ, Bursa Technical University
Prof. Dr. Halil İbrahim Okumuş, Karadeniz Technical University
Prof. Dr. Handan Türkoğlu, İstanbul Technical University
Prof. Dr. Hossein Showkati, Urmia University
Prof. Dr. İhsan EFEOĞLU, Atatürk University
Prof. Dr. İnci Deniz Ilgın
Prof. Dr. İrfan KARAGÖZ, Uludağ University
Prof. Dr. İrfan KURTBAŞ, Hitit University
Prof. Dr. İsmail Hakkı ALTAŞ, Karadeniz Technical University
Prof. Dr. İsmail Hakkı Çavdar, Karadeniz Technical University
Prof. Dr. Jasmina Pašagić Škrinjar, University of Zagreb
Prof. Dr. Masoud Hajjalilue Bonab, University of Tabriz
Prof. Dr. Mehmet ERTUĞRUL, Atatürk University
Prof. Dr. Mehmet Hamit ÖZYAZICIOĞLU, Atatürk University
Prof. Dr. Mehmet İhsan KARAMANGİL, Uludağ University
Prof. Dr. Mehmet Önder EFE, Hacettepe University
Prof. Dr. Meltem Eti Proto, Sapienza University of Rome & Rome University of Fine Arts
Prof. Dr. Murat Ekinci, Karadeniz Technical University
Prof. Dr. Mustafa AKTAŞ, Ondokuz Mayıs University
Prof. Dr. Ömer Delialioğlu, Middle East Technical University
Prof. Dr. Ömer GÜNDOĞDU, Atatürk University
Prof. Dr. Ratko Đuričić, University of East Sarajevo
Prof. Dr. Salim KAHVECİ, Karadeniz Technical University
Prof. Dr. Serpil EROL, Gazi University
Prof. Dr. Suat ÖZDEMİR, Hacettepe University
Prof. Dr. Süleyman TOSUN, Hacettepe University
Prof. Dr. Şeref Sağıroğlu, Gazi University
Prof. Dr. Temel Kayıkçıoğlu, Karadeniz Technical University
Prof. Dr. Tevhit KARACALI, Atatürk University
Prof. Dr. Turgay Tugay BİLGİN, Bursa Technical University
Prof. Dr. Yong C. WANG, University of Manchester
Prof. Dr. Mehmet Çopur, Bursa Technical University
Prof. Dr. Osman Nuri Şara, Bursa Technical University
Prof. Dr. Ömer Laçın, Atatürk University
Prof. Dr. Özlem Korkut, Atatürk University



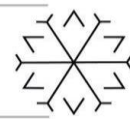
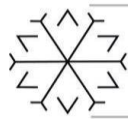
Prof.Dr. Sinan Yapıcı, Malatya İnönü University
Prof. Dr. Kadir TÜRK, Karadeniz Technical University
Assoc. Prof. Dr. Nur Hüseyin KAPLAN, Erzurum Technical University
Assoc. Prof. Dr. Ahmet DUMLU, Erzurum Technical University
Assoc. Prof. Dr. Kağan Koray AYTEN, Erzurum Technical University
Assoc. Prof. Dr. Tuba YETİM, Erzurum Technical University
Assoc. Prof. Dr. Fatih TOSUNOĞLU, Erzurum Technical University
Assoc. Prof. Dr. Ahmet Burak CAN, Hacettepe University
Assoc. Prof. Dr. Aleksandar Stevanovic, University of Pittsburgh
Assoc. Prof. Dr. Aleksandra BOGDANOVIC, Ss. Cyril and Methodius University
Assoc. Prof. Dr. Ali İnan, Adana Alparslan Turkes Science and Technology University
Assoc. Prof. Dr. Ali Sinan Dike, Adana Alparslan Turkes Science and Technology University
Assoc. Prof. Dr. Barış ERDİL, Van Yüzüncü Yıl University
Assoc. Prof. Dr. Borna Abramovic, University of Zagreb
Assoc. Prof. Dr. Burak Erkayman, Atatürk University
Assoc. Prof. Dr. Fatma Zehra ÇAKICI, Atatürk University
Assoc. Prof. Dr. Danielle Sinnet, University of West of England
Assoc. Prof. Dr. Elif Kılıç Delice, Atatürk University
Assoc. Prof. Dr. Emre Özkop, Karadeniz Technical University
Assoc. Prof. Dr. Emre ÖZYURT, Gümüşhane University
Assoc. Prof. Dr. Fatih KABURCUK, Sivas Cumhuriyet University
Assoc. Prof. Dr. Fatih Mehmet ÖZKAL, Atatürk University
Assoc. Prof. Dr. H. Tonguç Tokol, Marmara University
Assoc. Prof. Dr. Hacı Süleyman GÖKÇE, Bayburt University
Assoc. Prof. Dr. İbrahim Yücel ÖZBEK, Atatürk University
Assoc. Prof. Dr. İlhan ÇELİK, Samsun University
Assoc. Prof. Dr. İlker TEKİN, Karabuk University
Assoc. Prof. Dr. Jülide Erkmén, Kars Kafkas University
Assoc. Prof. Dr. Marinko Maslarić, University of Novi Sad
Assoc. Prof. Dr. Marko Subotić, University of East Sarajevo
Assoc. Prof. Dr. Marta STOJMANOVSKA, Ss. Cyril and Methodius University
Assoc. Prof. Dr. Mehmet Emin Erendor, Türkiye Manas University
Assoc. Prof. Dr. Momcilo Dobrodolac, University of Belgrade
Assoc. Prof. Dr. Murat Beken, Bolu İzzet Baysal University
Assoc. Prof. Dr. Musa ARTAR, Bayburt University
Assoc. Prof. Dr. Mustafa YILMAZ, Atatürk University
Assoc. Prof. Dr. Muteber Erbay, Karadeniz Technical University
Assoc. Prof. Dr. Müge Göker Paktaş, Marmara University
Assoc. Prof. Dr. Neslihan Alemdar, Marmara University
Assoc. Prof. Dr. Önder Aydemir, Karadeniz Technical University
Assoc. Prof. Dr. Özge Kerkez Kuyumcu, Marmara University
Assoc. Prof. Dr. Ramazan ÖZÇELİK, Akdeniz University
Assoc. Prof. Dr. Sabri BIÇAKÇI, Balıkesir University
Assoc. Prof. Dr. Serdar SELAMET, Bogazici University
Assoc. Prof. Dr. Serkan ŞENOCAK, Atatürk University
Assoc. Prof. Dr. Sevil Şen Akagündüz, Hacettepe University



Assoc. Prof. Dr. Temel VAROL, Karadeniz Technical University
Assoc. Prof. Dr. Tuğrul Çavdar, Karadeniz Technical University
Assoc. Prof. Dr. Aslı ÇEKMİŞ KANAN, İstanbul Teknik Üniversitesi
Assoc. Prof. Dr. Can UZUN, Altınbaş Üniversitesi
Assoc. Prof. Dr. Gökçe HACIOĞLU, Karadeniz Teknik Üniversitesi
Asst. Prof. Dr. Ali Ünlütürk, Erzurum Technical University
Asst. Prof. Dr. Babak KARIMI, Erzurum Technical University
Asst. Prof. Dr. Hilal KOÇ POLAT, Erzurum Technical University
Asst. Prof. Dr. Mahmut TUTAM, Erzurum Technical University
Asst. Prof. Dr. Merve KAYACI ÇODUR, Erzurum Technical University
Asst. Prof. Dr. Merve YILDIRIM, Erzurum Technical University
Asst. Prof. Dr. Mete ÖZBALTAN, Erzurum Technical University
Asst. Prof. Dr. Ömer Halil ÇAVUŞOĞLU, Erzurum Technical University
Asst. Prof. Dr. Turgay DUMAN, Erzurum Technical University
Asst. Prof. Dr. Saffet Gökçen ŞEN
Asst. Prof. Dr. Meltem GÖR BÖLEN
Asst. Prof. Dr. Adil YÜCEL, İstanbul Technical University
Asst. Prof. Dr. Ahmed Riedh Al-Hamaoy, Al-Nahrain University
Asst. Prof. Dr. ALİ CELEN, Erzincan University
Asst. Prof. Dr. Atinc Yılmaz, Beykent University
Asst. Prof. Dr. Aylin Aras, Bursa Technical University
Asst. Prof. Dr. Serkan Sipahi, Atatürk University
Asst. Prof. Dr. Dimitrios Tsolis, University of Patras
Asst. Prof. Dr. Elif Özmetin, Balıkesir University
Asst. Prof. Dr. Erbil Kavcı, Kars Kafkas University
Asst. Prof. Dr. Erdal ÖNER, Bayburt University
Asst. Prof. Dr. Erdem Aksakal, Atatürk University
Asst. Prof. Dr. Fuat AKAL, Hacettepe University
Asst. Prof. Dr. Furat Ibrahim Hussein, University of Baghdad
Asst. Prof. Dr. Hamid Yılmaz, Bayburt University
Asst. Prof. Dr. M. Fatih ÇORAPSIZ, Atatürk University
Asst. Prof. Dr. Marina Zanne, University of Ljubljana
Asst. Prof. Dr. MEHRZAD MOHABBI, Bingöl University
Asst. Prof. Dr. Mohammad Ali Sahraei, Girne American University
Asst. Prof. Dr. Pelin ANGIN, Middle East Technical University
Asst. Prof. Dr. Tuba Eroğlu AZAK, Milli Savunma University
Asst. Prof. Dr. Tuba Sarı, Bursa Technical University
Asst. Prof. Dr. Yaşar Andelip Erdoğan, Marmara University
Asst. Prof. Dr. Yeşim OK, Atatürk University
Asst. Prof. Dr. Željko Stević, University of East Sarajevo
Asst. Prof. Dr. Željko Stević, University of East Sarajevo
Asst. Prof. Dr. Zeynep Neşe KURT ALBAYRAK, Atatürk University
Asst. Prof. Dr. Işıl KARABEY AKSAKALLI, Erzurum Technical University
Dr. Çağrı ULUDÜZ, Erzurum Technical University
Dr. Rumeysa BAYAR, Erzurum Technical University
Dr. Abbas Al-Refai, The University of Jordan

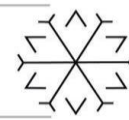
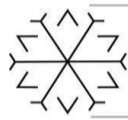


Dr. Abdolhossein Naghizadeh, University of Free State
Dr. Ammar Al-Bazi, Coventry University
Dr. Anton Saveliev
Dr. Dario Babic, University of Zagreb
Dr. Felix Okonta, University of Johannesburg
Dr. Haitao Liao, University of Arkansas
Dr. Ian Mackie, University of Sussex
Dr. Jingming Liu, Hebei University of Technology
Dr. Liliana Delgado Hidalgo, Universidad del Valle
Dr. Mohammad A. Shbool, The University of Jordan
Dr. Ondrej Stopka, Institute of Technology and Business
Dr. Rahim Dehkharghani, University of Bonab
Dr. Rouzbeh DABIRI, Islamic Azad University of Tabriz
Dr. Tone Lerher, University of Maribor
Dr. Orkan Zeynel GÜZELCİ, University of Porto
Dr. Mehmet Hakan DURAK, Erzurum Technical University
Dr. Volkan KIZILOĞLU, Erzurum Technical University

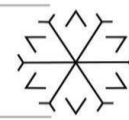
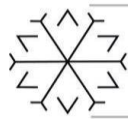


CONTENTS

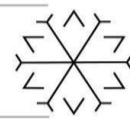
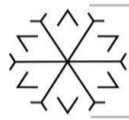
Smoother Sliding Mode Tracking Control of Quadrotor UAV by Using Saturation Function	1
Design and Control of One-DOF Helicopter System	10
Predicting the Result of Penalty Kick using Statistical and Match Day Features	15
Advanced Cyberbullying Identification with Bidirectional Encoder Representations from Transformers	22
Design and Simulation of Soft-Switched PWM Full-Bridge DC-DC Converter with Snubber Cell and No Additional Control	23
An Advanced Visible Light Communication Technique: Li-Fi (Light Fidelity)	32
ECC Implementation on FPGA with Fast and Pipelined Arithmetic Units	39
Development of a Fuzzy Logic Based Control Algorithm for Charge-Discharge of a Battery System	48
Epileptic Seizure Detection Based on EEG Data Using Discrete Wavelet Transform	57
LED Selection Algorithm for Indoor Li-Fi Systems	63
Characterization of ZnO Thin Films Deposited by SILAR and Spin Coating Methods	70
Investigation of Multisection Mode Locked 980 nm and 1550 nm Diode Lasers	75
Mathematical Analysis and Control of Six Degrees of Freedom Flight Simulators	82
Design and Implementation of Band Pass Filter based PI Controlled Shunt Active Power Filter to Fulfill IEEE-519 Harmonic Distortion Limits.....	90
Effect of Ultrashort Laser Pulse Shape on the Dipole Spectrum of a Single Electron.....	97
Mel-Spectrograms and Data Augmentation for Spoken Digit Classification	101
Comparison of Cognitive Workload and Resting States in Different Brain Lobes and EEG Frequency Bands	109
Performance Comparison of IEEE 802.11p Wave and IEEE 802.11 MAC Protocols Based on AODV Routing Protocol	119
Calculation of Electric Motor Values for Wind Turbines Electromagnetic Field Effect	125
Single Phase 5-Level NPC Multilevel Inverter Using Level-Shifted Sinusoidal PWM	130
A Software Based Simulation for Adaptive Optics System of Eastern Anatolia Observatory.....	138
Causal Learning versus Machine Learning	142
Three-Dimensional Modelling and Simulation of Porous silicon based PEM Fuel Cells using COMSOL Multiphysics	143
Investigation of Factors Affecting Radar Systems with Fuzzy Logic Method	144
Design of Flexible Antennas for Mobile Communication and 5G Application	150
Resource Allocation in Non-Orthogonal Multiple Access	154
A Decision Based Fusion Method for Brain Lesion Images	161
Design and Comparison of MPPT Under Shading Conditions With Different Algorithms for Photovoltaic Systems	163
A High Directivity 2.8GHz Microstrip Directional Coupler Design by using Grey Wolf Optimizer for Radio Telescope Systems	169
Nonlinear Controller Design of DC-DC Buck Converter and Real Time Application	170
A Performance Metric Proposal to Evaluate Effectiveness of Demand Side Management in Smart Grids	179
Effects of Grid Integration of Electric Vehicles and Charging Stations	180
Printed Circuit Board Surface Defect Detection using YOLOv4 algorithm.....	181
Analyzing Pattern for Huge Databases	189
Investigation of The Initialization Contour Effect In The Chan-Vese Method.....	195
IoT Enabled Technologies: Associated Issues and Challenges	201
Comparison of Copy-Move Image Forgery Detection Techniques	210
A Study on Detection of Forest Fire	219
Creating Cloud GIS Based Geographical Indication Tourism Web and Mobile Apps	223
A Novel Most Probable Path Computation of Stochastic Hidden Systems with Updated Parameters by using a 1-Step Optimization Discrete Control Algorithm	228
Covid-19 Detection with Deep Learning Methods from X-Ray Images	229
Can Machines Talk? Turkish Voice Assistant and Chatbot Design with Artificial Intelligence in Erzurum Technical University.....	230
Sentiment analysis in Persian using discourse and external semantic information.....	237
BCI-based Game Design Promoting Our Cultural Heritage.....	245
Voice Spoofing Countermeasure to Detect Replay Attacks Using Spectral Features and BiLSTM.....	246
An Overview of Ransomware Attacks and Mitigation Techniques.....	254



Deep Computerized System for Lung Based Diagnostic Problems In Ct Scans.....	260
A Performance Monitoring System with the Capability of Detecting Anomalies for Corporate Business Intelligence Reporting Systems...	261
Sentiment Analysis of Turkish Tweets on Covid-19 Using Word Embedding vectors and Bidirectional Long Short Term Memory Networks	270
Recognition of Electronic Circuit Components Using a Modern Convolutional Object Detector.....	271
Detection of Distributed Denial of Service (DDoS) Attacks with Machine Learning Methods	279
Wi-Fi Fingerprint-based Indoor Localization in Different Environments	280
Using Deep Learning Models for Classification Hyperspectral Data.....	281
A New Mathematical Model for Private Car Sharing	282
Two-Step Method Based on Local Search for Two-Dimensional Two-stage Cutting Stock Problem.....	283
A Discrete Differential Evolution Algorithm for Unidirectional Loop Layout Problem.....	291
Improving Warehouse Operations by Radio Frequency Identification (RFID) Technology	292
Prediction of COVID-19 Death Rates with Artificial Neural Network Under Different Time Series Models Based on Moving Averages...	303
The Method of Modulated Fourier Series Expansion Applied to Hourly Electricity Consumption	310
Jetty Optimization and An Application.....	318
Review On: Construction Waste Minimization by Adopting Different Techniques	319
Types Of Construction Waste, Their Contributions To The economy And Sustainability Of The Project.....	326
Modeling of COVID-19 Pandemic with Artificial Neural Network: A Case Study for Turkey and the USA.....	333
Effect of Elastic Foundation on The Vibration of Non-Homogeneous Orthotropic Shell Geometry.....	334
Deep Learning Based Intelligent Traffic Volume Measurement.....	343
Parametric Analysis of a Box Girder Highway Bridge for Different Lead Rubber Bearing Properties Using API	350
The Influence of The Horizontal Friction on The Internal Forces of The Slab on Ground Affected by Shrinkage	359
Impacts Of Climate Change On Water Resources Of Turkey	366
X-Ray Impermeability of Concretes Containing Celestite Aggregate Produced With Calcium Aluminate Cement	373
Effect of Low Content of Hemp Fibre on Flexural Behavior of Mortar.....	379
Leveraging Clean and Advanced Technologies to Increase Health System Resilience in Conflict Areas	384
Dynamic Analysis of a Framed Machine Foundation with Vibration Isolation Materials.....	385
Some Mechanical Properties of Polymer Modified Concrete	386
Effect of Antifreeze Additives on The Properties of Mortars Containing Silica Fume Exposed to Frost in Fresh State	394
Optimization of urban bus stops for increasing the use of public transportation	405
Ultimate Drift Ratio Limit of Steel Plate Shear Walls	415
Numerical Analysis of the Impact of Polypropylene Fiber on the Shear Strength of Hollow-Core Slabs.....	423
Numerical Analysis on Spiral Heat Exchanger; Effects of Using Nanofluid and Ball Turbulators	434
Geopolymers in Soil Stabilization from Past to Present.....	443
Modal Analysis of Industrial Steel Stacks with Soil-Structure Interaction.....	448
Numerical Investigation of the Solute Dispersion Phenomenon Based on the Advection–Diffusion Equation.....	449
The Effect of Using Various Reinforcement Mesh on Fire Performance of Composite Flooring System.....	455
Clays and Polymer/Clay Nanocomposites and Their Application in Engineering.....	464
Experimental Behaviour of Screw Beam-to-Column Connections in Cold-Formed Steel Under Cyclic Loading - A review	470
Sustainable Aviation Fuels: Policy and Production.....	478
Carbon Negative Buildings.....	479
Workability of Concrete Having Hybrid Natural Fibers of Different Lengths for Easy Pouring.....	483
Review On Potential Of Waste Materials As Fire-Resistant Materials	489
Potential Of Used-Diesel-Engine-Oil As An Admixture In Cement Composites: A Detailed Review	497
An Overview on Different Corrugated Sheets from Manufacturing to Housing Element	503
Determination of Changes in Precipitation and Snowpack Using Innovative Trend Analysis in Sinirbaşı Basin	508
Numerical Analysis of Embankment Slopes Reinforced by Different Methods Using Plaxis 2D Program	509
The Examination of The Effect Of Rock Salt On The Setting Time Of The Grout By Utilizing The Taguchi Method	510
Evaluation of The Importance of Geomorphic Indices on River Basins Located on Different Slopes, Case Study: Sivas Province, Koyulhisar, Turkey	511



A View of Historic Structures Survived in 1859 Erzurum Earthquake	520
An Application of Cold Weather Concreting in Erzurum	521
Titanium-Zinc as an Architectural Material: ETU Campus Gate Project	522
A Model for Visualization of Customer's Attention That Occurs on the Furniture by Using Eye-Tracking Technology and Determination Its Effect on New Product Design.....	531
Erzurum Surp Minas Church	537
Evaluation of the Components of Design Thinking in Terms of Design Education	543
Understanding the Meanings of Sustainability: Historical Roots, Current Perspectives, Future Directions	549
Rural Studies in A Disaster Region – Obruk Plateau	556
Urban Regeneration: Construction of Factor model.....	562
Using Digital Technology in Architectural Design Education and Its Effect on Creativity	571
Impact of Climate Change on Building Energy Consumption	572
Study on Adsorption Performance of MIL-101 (Cr) for Ibuprofen Uptake from Aqueous Media	577
Mechanochemical Synthesis and Characterization of Mn-B Phases	578
Investigation of Photocatalytic Activity of Calcium Aluminate Spinel Ceramics Synthesized by Microwave Assisted Combustion Method.....	579
Cannabis Production And State Policy In Turkey	585
Bio-Catalytic Conversion of CO ₂ to Solid Carbonate.....	592
Determination of Geographical Origin in Alcoholic Beverages Using Vibrational Spectroscopy and Chemometrics	593
Determination of some quality parameters of cheese by portable FT-NIR combined with PLSR.....	594
Investigation Of Properties Of Renewable Films Prepared With Aloe Vera Gel	595
An Experimental and Simulation Analysis of A Single-Cylinder Diesel Engine Fuelled by C ₂ Alcohol and Nano-Sized Materials	596
Comparison of Experimental and Simulation Results for Alcohol and Nanofuels in CI Engines	606
Frameless PMSM Position Control in Pan-Tilt System with 2-Axes	616
Investigation of Tribological Properties of Ultra High Molecular Weight Polyethylene (UHMWPE) Bearings.....	625
Design and development of an industrial conveyor line with computerized control	633
Tuned gyrostabilizer for control of vibrations in Two-wheeled Robot.....	634
Energy and carbon dioxide savings analysis for a single-family dwelling in Muğla region.....	635
Synthesis and Characterization of Magnetic Metal Organic Framework (MOF) for Methyl Orange Removal from Aqueous Solutions	642
Parametric Analysis of Photovoltaic Module.....	643
Numerical Analyses Of The Effect Of Reflector Emissivity At Radiant Tube Heaters.....	651
Quantification of hemodynamic parameters of fetal hearts using computational fluid dynamics.....	652
Development of An Image Processing Tool for IVUS Images-Based Patient-Specific CFD Simulations	653
Long-Term Stability Analysis of Surface-Modified Nanofluids	654
Investigation of The Effects of Different Corrosion Grades on Bending Strength of S235 Box Profiles	655
Conformity in Theoretical and Experimental Analyses, Performance of Heat pumps	656
Investigation of The Static Strength of Porcelain Fused to Metal Dental Crowns with Surface Protrusions Produced by Selective Laser Melting by Finite Element	657
Studies on Adhesivly Bonded Layers under cyclic loading	658
An Experimental Study of Erosion Corrosion Behavior for Passive Metals	659
Comparison of Electrochemical Corrosion Performances Using Variable Scan Rates on Surfaces with Different Layer Thicknesses.....	660
Effects of Connector Placement on The Biomechanical Performance of Spinal Implants Under Tension and Compression Loads	661
Triboperformance of Quenched and Single and Double Tempered AISI 4140 Steel	662
Wave Dispersion Characteristics Of Nanorods with Uniform Porosity	669
The Use of a Low-Cost Laser Scanning Range Finder Sensor to Estimate the Volume of an Object	670
Chemical Properties of Metal Materials Used in Columns from the Hellenistic, Roman and Byzantine Periods in Stratonikeia and Lagina	675
The Electrochemical Behavior of Cp-Ti Coated by Ti-doped Al ₂ O ₃ and Ni-doped Al ₂ O ₃	676
Determination of Cutting Parameters for Peripheral Milling of S355J Sheet Metal with Aggressive-High-Performance Machining Method.....	677
Mechanical and Tribological Properties of SLMed Silver Coated Copper Powder Material	682
The Effects of Selective Laser Melting Process Parameters on Thermal Conductivity of 316L Stainless Steel.....	691
Use of Phase-Changing Materials in Building Wall Blocks.....	698



Crack Path Prediction in Functionally Graded Materials Using a Local Criteria	706
Influence of the geometrical discontinuity on the mixed mode Crack Propagation in Functionally Graded Materials	707

Smoother Sliding Mode Tracking Control of Quadrotor UAV by Using Saturation Function

Nurullah ÖZKAN ^{1*}[0000-0003-0532-3362] and Hacı Mehmet GÜZEY ²[0000-0002-2215-9536]

¹nozkan@sivas.edu.tr, Department of Aeronautical Engineering, Sivas Science and Technology
University

²mehmet.guzey@sivas.edu.tr, Department of Electrical - Electronics Engineering, Sivas Science and
Technology University

Abstract

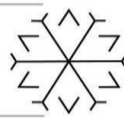
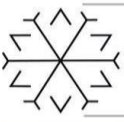
In this paper, trajectory tracking control of quadrotor unmanned aerial vehicle is designed by using a second-order sliding mode controller with saturation function. Sliding mode controller (SMC) is chosen because of the well-handled property of SMC on the systems with uncertain and have under-actuated dynamics like quadrotor UAV. With the help of SMC, trajectory tracking error is handled perfectly on simulations. Firstly, the controllers are designed with known dynamics of the quadrotor and simulation results are obtained with the respect to that. Later the controllers are designed with unknown dynamics of the quadrotor and simulation results are obtained with the respect to that. Designing the controllers of the unknown dynamical system sign function and saturation function is used to compensate for the unknown dynamics. The controller inputs designed with saturation function show that the smoothness of the sliding mode controller inputs is increased. That is the desired results especially studying on sliding mode controller. Simulation results are compared and the proposed controller is proved the effectiveness of tracking control of quadrotor UAV.

Keywords. Quadrotor UAV, Sliding Mode Controller, Saturation Function

1. Introduction

Nowadays, the robotic systems have become one of the most promising fields because of the rapid increase in the technology and accessibility of these technologies. Unmanned Aerial Vehicles (UAVs) are one of the sub groups of these robotic systems. In the group of UAVs, there are four sections, one of them is rotary wing. Quadrotor is part of rotary wing section (Singhal, 2018). Quadrotor is used in many fields from military applications like border security, surveillance to civilian applications like agricultural purposes, delivery of goods and fighting for wildfires (Hassanalian and Abdelke, 2017). Design and controllability of the quadrotor is relatively easier therefore in many papers and project, quadrotor is used to prove the control algorithms, many techniques and applications (Mahony, Kumar and Corke, 2012; Kushleyev, Mellinger and Powers, 2013; Halcı, Gazi and Cihan, 2019; Toks, 2019; Nguyen *et al.*, 2020; Bingöl and Güzey, 2021)

There are many algorithms available in control design of the quadrotors. Mainly, the controllers can be categorized in two categories: linear controllers and non-linear controllers. In order to be able to control Quadrotor by using linear control techniques, some approximations like small angle approximation (Chen and Wang, 2013) are used. The mostly used one of the linear controllers, as of in many systems in industry, is the Proportional Integral Derivative (PID) controller (Li, 2011). Linear Quadratic Regulator (LQR) is one of linear controllers and it also an optimal controller is used in literature. The control algorithm controls the linear dynamic of the quadrotor by minimalizing the specific cost function which is chosen for application (Foehn, Scaramuzza and Motivation, 2018). Feedback linearization is a non-linear controller is used in quadrotor control. In feedback linearization controller design, non-linear dynamics of the quadrotor is transformed the equivalent linear dynamics and these dynamics are used in controller design (Voos, 2009). Backstepping control is also non-linear controller that used in control design of the quadrotor (Bouabdallah and Siegwart, 2007). In backstepping control design, controller is divided into steps. Subsystems are stabilized recursively in each step. Sliding Mode Controller (SMC) is another non-linear control algorithm used in quadrotor control. In literature, SMC is used for robustness property especially on unwanted effects like parameter variations, model uncertainties and disturbances (Shtessel and Landrum, 2012). In quadrotor



controller, system dynamics are into divided under-actuated and fully-actuated subsystems for designing SMC controller (Xiong and Zhang, 2016). The main problem of the SMC is the chattering effect which is because of discontinuous control inputs. As a result of this problem, application of SMC in real world systems is challenging and can be dangerous (Levant, 2010).

In this paper, decreasing high chattering of the SMC inputs and obtaining smoother inputs using saturation function is targeted. The saturation function limits the chattering as a function of a given threshold. Using the smoother SMC, tracking controller is designed for quadrotor. The paper is organized as following. In section 2, quadrotor model is discussed broadly, while smoother sliding mode tracking controller is designed in section 3. In the fourth section, the simulation results for the quadrotor are provided to show the applicability of the designed controller for a given trajectory and some concluding remarks are given in section 5.

2. The Quadrotor Dynamical Model

The Quadrotor has a rotor on each arm to control four basic movements that allow it to reach the desired position and attitude. Four input signals are defined for these four movements of the quadrotor. Detailed exploitation of the dynamic model of quadrotor can be found in a number of papers therefore it won't discussed in here. To get further information of the dynamical model of the quadrotor, one can found in (Voos, 2006). In modelling of the dynamical model of the UAV we use an inertial frame (c_{i1}, c_{i2}, c_{i3}) which is fixed to earth and body frame (c_{b1}, c_{b2}, c_{b3}) which is fixed to quadrotor. Its origin is in the center of mass of the quadrotor. It can be seen in Fig.1. The attitude of the quadrotor UAV is given as (Φ, θ, ψ) which are Euler angles representing, roll, pitch and yaw angles respectively which shown in Fig 1. (x, y, z) is the position of the quadrotor in inertial frame.

The first input is u_1 , which increases or decreases the speed of all propellers in the same proportion. Vertical movement of the quadrotor in z-axis is controlled with u_1 input. The second input signal, u_2 , increases or decreases the speed of the left propeller, while simultaneously reducing or increasing the speed of the right propeller by the same amount, causing a torque along the x-axis of the body. Thus, roll movement is obtained along the x axis. The third input u_3 , in the same logic as u_2 , simultaneously changes the speed of the propellers of the front and aft rotors, resulting in pitching motion along the y-axis. The fourth input u_4 , reduces or increases the speeds of the left and right propellers simultaneously, while increasing or decreasing the speeds of the aft and front propellers. Thus, the yaw movement defined as the quadrotor rotating around its own axis is obtained. They defined as below:

$$\begin{aligned} u_1 &= (F_1 + F_2 + F_3 + F_4), \quad u_2 = (-F_2 + F_3) \\ u_3 &= (-F_1 + F_4), \quad u_4 = \frac{d(-F_1 + F_2 + F_3 - F_4)}{b} \end{aligned} \quad (1)$$

$F_i = bw_i^2$ ($i = 1, 2, 3, 4$) are thrust forces that rotors (in our model there are four rotors) generated. b is the lift coefficient, d is the force to moment scaling factor and w_i is the speed of the rotor $i = 1, 2, 3, 4$.

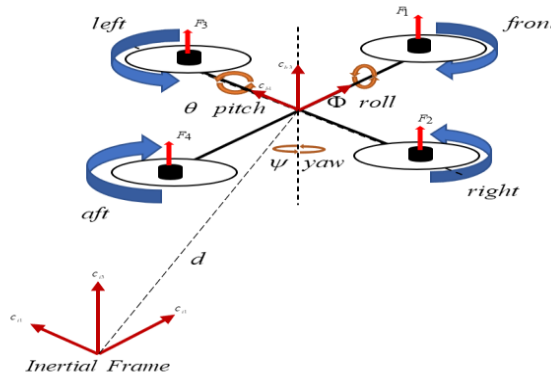
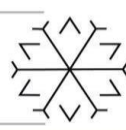


Figure 1. Configuration of the quadrotor.



As discussed above, obtaining of the dynamic model of the quadrotor is not given in here. One, who would like to look at the obtaining of the dynamic model, can go to reference papers to find detailed explanations. The dynamics of quadrotor are given as below (2) – (7):

$$\ddot{x} = \frac{1}{m} (\cos \Phi \sin \theta \cos \psi + \sin \Phi \sin \psi) u_1 - \frac{K_1 \dot{x}}{m} \quad (2)$$

$$\ddot{y} = \frac{1}{m} (\cos \Phi \sin \theta \sin \psi - \sin \Phi \cos \psi) u_1 - \frac{K_2 \dot{y}}{m} \quad (3)$$

$$\ddot{z} = \frac{1}{m} (\cos \Phi \cos \theta) u_1 - g - \frac{K_3 \dot{z}}{m} \quad (4)$$

$$\ddot{\Phi} = \dot{\theta} \dot{\psi} \frac{I_y - I_z}{I_x} - \frac{J_r}{I_x} \Omega_r \dot{\theta} + \frac{l}{I_x} u_2 - \frac{K_4 l}{I_x} \Phi \quad (5)$$

$$\ddot{\theta} = \dot{\psi} \dot{\Phi} \frac{I_z - I_x}{I_y} + \frac{J_r}{I_y} \Omega_r \dot{\Phi} + \frac{l}{I_y} u_3 - \frac{K_5 l}{I_y} \dot{\theta} \quad (6)$$

$$\ddot{\psi} = \dot{\Phi} \dot{\theta} \frac{I_x - I_y}{I_z} + \frac{1}{I_z} u_4 - \frac{K_6}{I_z} \dot{\psi} \quad (7)$$

where m is the quadrotor's total mass; g is gravity force; l is the distance between the center of the quadrotor and the propellers; I_x, I_y, I_z are the inertias with respect to axes; J_r is the inertia of the propeller; K_i ($i=1, 2, \dots, 6$) are the drag coefficients.

3. Controller Design

In this work, a sliding mode controller by using saturation function is designed for a quadrotor for trajectory tracking. In order to design the controller of the quadrotor dynamic equations are subjected to the following transformation.

$$f_1 = -g - \frac{K_3 \dot{z}}{m}, \quad g_1 = \frac{\cos \Phi \cos \theta}{m} \quad (8)$$

$$f_2 = \frac{(\cos \Phi \sin \theta \sin \psi - \sin \Phi \cos \psi) u_1}{m} - \frac{K_2 \dot{y}}{m}, \quad g_2 = 0 \quad (9)$$

$$f_3 = \frac{(\dot{\theta} \dot{\psi} (I_y - I_z) - J_r \dot{\theta} \Omega - K_4 l \dot{\Phi})}{I_x}, \quad g_3 = \frac{l}{I_x} \quad (10)$$

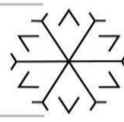
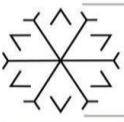
$$f_4 = \frac{(\cos \Phi \sin \theta \cos \psi + \sin \Phi \sin \psi) u_1}{m} - \frac{K_1 \dot{x}}{m}, \quad g_4 = 0 \quad (11)$$

$$f_5 = \frac{(\dot{\psi} \dot{\Phi} (I_z - I_x) + J_r \dot{\Phi} - K_5 l \dot{\theta})}{I_y}, \quad g_5 = \frac{l}{I_y} \quad (12)$$

$$f_6 = \frac{(\dot{\Phi} \dot{\theta} (I_x - I_y) - K_6 \dot{\psi})}{I_z}, \quad g_6 = \frac{1}{I_z} \quad (13)$$

Above equations (8) – (13) can be written as below (14) – (16):

$$\ddot{x} = f_4 + g_4 u_3, \quad \ddot{y} = f_2 + g_2 u_2, \quad \ddot{z} = f_1 + g_1 u_1 \quad (14)$$



$$\ddot{\phi} = f_3 + g_3 u_2, \quad \ddot{\theta} = f_5 + g_5 u_3, \quad \ddot{\psi} = f_6 + g_6 u_4 \quad (15)$$

The controller coefficients which are designed and proved in (Zheng, Xiong and Luo, 2014) k_{ij} ($i, j = 1, 2, 3, 4$) are as below (16):

$$k_{21} = \frac{-m}{u_1 \cos \psi} (a_{11} a_{12} + a_{21} a_{31} + a_{31} a_{11}), k_{22} = \frac{-m}{u_1 \cos \psi} (a_{11} a_{21} a_{31}), k_{23} = k_{33} = 1, k_{24} = a_{11} + a_{21} + a_{31} \quad (16)$$

$$k_{31} = \frac{m}{u_1 \cos \phi \cos \psi} (a_{11} a_{22} + a_{22} a_{32} + a_{32} a_{12}), k_{32} = \frac{m}{u_1 \cos \phi \cos \psi} (a_{12} a_{22} a_{32}), k_{34} = a_{11} + a_{22} + a_{32}$$

where a_{ij} ($i = 1, 2, 3$ and $j = 1, 2$) are corresponding desired eigen values as explained in (Zheng, Xiong and Luo, 2014). Then, the sliding manifolds of dynamics are given as below (17) – (20):

$$s_1 = k_{11} (\dot{z}^d - \dot{z}) + k_{12} (z^d - z) \quad (17)$$

$$s_2 = k_{21} (\dot{y}^d - \dot{y}) + k_{22} (y^d - y) + k_{23} (\dot{\Phi}^d - \dot{\Phi}) + k_{24} (\Phi^d - \Phi) \quad (18)$$

$$s_3 = k_{31} (\dot{x}^d - \dot{x}) + k_{32} (x^d - x) + k_{33} (\dot{\theta}^d - \dot{\theta}) + k_{34} (\theta^d - \theta) \quad (19)$$

$$s_4 = k_{41} (\dot{\psi}^d - \dot{\psi}) + k_{42} (\psi^d - \psi) \quad (20)$$

where $k_{11} = 1$, $k_{12} > 0$, $k_{41} = 1$, $k_{42} > 0$, $k_{13} = k_{14} = k_{43} = k_{44} = 0$. x^d, y^d, z^d are the desired trajectory. Φ^d, θ^d, ψ^d are desired Euler angles which defines our desired attitude. Time derivative of the surfaces are as below (21) – (24):

$$\dot{s}_1 = k_{11} (\ddot{z}^d - \ddot{z}) + k_{12} (\dot{z}^d - \dot{z}) = k_{11} (\ddot{z}^d - (f_1 + g_1 u_1)) + k_{12} (\dot{z}^d - \dot{z}) \quad (21)$$

$$\dot{s}_2 = k_{21} (\ddot{y}^d - \ddot{y}) + k_{22} (\dot{y}^d - \dot{y}) + k_{23} (\ddot{\Phi}^d - \ddot{\Phi}) + k_{24} (\dot{\Phi}^d - \dot{\Phi}) \quad (22)$$

$$= k_{21} (\ddot{y}^d - (f_2 + g_2 u_2)) + k_{22} (\dot{y}^d - \dot{y}) + k_{23} (\ddot{\Phi}^d - (f_3 + g_3 u_2)) + k_{24} (\dot{\Phi}^d - \dot{\Phi})$$

$$\dot{s}_3 = k_{31} (\ddot{x}^d - \ddot{x}) + k_{32} (\dot{x}^d - \dot{x}) + k_{33} (\ddot{\theta}^d - \ddot{\theta}) + k_{34} (\dot{\theta}^d - \dot{\theta}) \quad (23)$$

$$= k_{31} (\ddot{x}^d - (f_4 + g_4 u_3)) + k_{32} (\dot{x}^d - \dot{x}) + k_{33} (\ddot{\theta}^d - (f_5 + g_5 u_3)) + k_{34} (\dot{\theta}^d - \dot{\theta})$$

$$\dot{s}_4 = k_{41} (\ddot{\psi}^d - (f_6 + g_6 u_4)) + k_{42} (\dot{\psi}^d - \dot{\psi}) \quad (24)$$

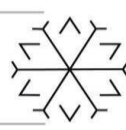
In order to make the stabilization of the sliding mode surfaces simpler we transform the time derivative of the surfaces like $\dot{s}_i = F_{ki} + F_{ui} + G_i u_i$ ($i = 1, 2, 3, 4$). In controller design, our purpose is to design robust controller to the quadrotor for the part that we don't know exactly its dynamics. Therefore, we add two parts, F_{ki} ($i = 1, 2, 3, 4$) for known part of the dynamics and F_{ui} ($i = 1, 2, 3, 4$) for unknown part of the dynamics. Our sliding mode controller is designed to compensate the unknown part of the dynamics. The equations are shown as below (25) - (38):

$$\dot{s}_1 = F_{k1} + F_{u1} + G_1 u_1 \quad (25)$$

$$F_{k1} = k_{11} \ddot{z}^d + k_{12} (\dot{z}^d - \dot{z}), \quad F_{u1} = -k_{11} f_1, \quad G_1 = k_{11} g_1$$

$$\dot{s}_2 = F_{k2} + F_{u2} + G_2 u_2 \quad (26)$$

$$F_{k2} = k_{21} \ddot{y}^d + k_{22} (\dot{y}^d - \dot{y}) + k_{23} \ddot{\Phi}^d + k_{24} (\dot{\Phi}^d - \dot{\Phi}), \quad F_{u2} = -k_{21} f_2 - k_{23} f_3, \quad G_2 = k_{21} g_2 + k_{23} g_3$$



$$\begin{aligned}\dot{s}_3 &= F_{3k} + F_{3u} + G_3 u_3 \\ F_{3k} &= k_{31} \ddot{x}^d + k_{32} (\dot{x}^d - \dot{x}) + k_{33} \ddot{\theta}^d + k_{34} (\dot{\theta}^d - \dot{\theta}), \quad F_{3u} = -k_{31} f_4 - k_{33} f_5, \quad G_3 = k_{31} g_4 + k_{33} g_5\end{aligned}\quad (27)$$

$$\begin{aligned}\dot{s}_4 &= F_{k4} + F_{u4} + G_4 u_4 \\ F_{k4} &= k_{41} \ddot{\psi}^d + k_{42} (\dot{\psi}^d - \dot{\psi}), \quad F_{u4} = -k_{41} f_6, \quad G_4 = k_{41} g_6\end{aligned}\quad (158)$$

To stabilize the sliding surfaces, following Theorem is provided.

Theorem: Given the derivative of sliding surface, (25)-(28), let the controllers given as below (29):

$$u_i = \frac{1}{G_i} (-F_{ki} - \eta_i \text{sat}(s_i)) \quad (i = 1, 2, 3, 4) \quad (29)$$

$\eta_i > 0$ ($i = 1, 2, 3, 4$) is constant controller design parameter. Saturation function defined as below:

$$\text{sat}(s_i) = \begin{cases} \text{sign}(s_i) & \text{if } |s_i| \geq \text{Threshold} \\ s_i & \text{if } |s_i| < \text{Threshold} \end{cases} \quad (30)$$

where $\text{Threshold} > 0$ is a design parameter. Then, the surfaces, s_i ($i = 1, 2, 3, 4$) are bounded stable and the bound can be reduced by choosing smaller threshold. Proof of that is explained in equation (31).

Proof:

First, define the Lyapunov candidate function as below (35):

$$L_i = \frac{1}{2} s_i^2 \quad (31)$$

and take the derivative of (31) to get

$$\dot{L}_i = s_i \dot{s}_i = s_i (F_{ki} + F_{ui} + G_i u_i) \quad (32)$$

Use the controller signals (29), in equations (25)-(28).

Case 1: $|s_i| \geq \text{Threshold}$

If threshold greater or equal to absolute of the sliding surface $\text{sat}(s_i)$ will be equal to $\text{sign}(s_i)$.

$$\begin{aligned}\dot{L}_i &= s_i (F_{ki} + F_{ui} + G_i u_i) \\ &= s_i \left(F_{ki} + F_{ui} + G_i \frac{1}{G_i} (-F_{ki} - \eta_i \text{sat}(s_i)) \right) \\ &= s_i F_{ui} - s_i \eta_i \text{sign}(s_i) = s_i F_{ui} - \eta_i |s_i|\end{aligned}\quad (33)$$

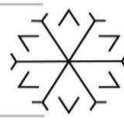
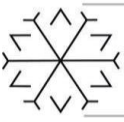
For the definition of the Lyapunov stability \dot{L}_i should be less than zero. To make it happen mathematically we can do equation (33) as below (34):

$$|s_i| |F_{ui}| - \eta_i |s_i| \geq s_i F_{ui} - \eta_i |s_i| = \dot{L}_i \quad (34)$$

From above equation (38) it can be seen that left-hand side is greater or equal to right-hand side and which is equal to \dot{L}_i .

$$\dot{L}_i \leq |s_i| |F_{ui}| - \eta_i |s_i| \quad (35)$$

If one proves that $(|s_i| |F_{ui}| - \eta_i |s_i|) < 0$ one can also prove that $\dot{L}_i < 0$. Then, the proof is obtained for Lyapunov stability theory when absolute value of the F_{ui} less than η_i . It can be seen that in equation (36) as below.



$$\begin{aligned} |s_i|(|F_{ui}| - \eta_i) &< 0 \\ |F_{ui}| &< \eta_i \end{aligned} \quad (36)$$

Hence, all the sliding surfaces are asymptotical stable when threshold is greater or equal to absolute of the sliding surface. Control inputs u_i , depending upon case 1 is as below (37):

$$u_i = \frac{1}{G_i}(-F_{ki} - \eta_i \text{sign}(s_i)) \quad (i = 1, 2, 3, 4) \quad (37)$$

Case 2: $|s_i| < \text{Threshold}$

If threshold less than absolute of the sliding surface $\text{sat}(s_i)$ will be equal to s_i .

$$\begin{aligned} \dot{L}_i &= s_i(F_{ki} + F_{ui} + G_i u_i) \\ &= s_i \left(F_{ki} + F_{ui} + G_i \frac{1}{G_i}(-F_{ki} - \eta_i \text{sat}(s_i)) \right) \\ &= s_i F_{ui} - s_i^2 \eta_i \end{aligned} \quad (38)$$

For the definition of the Lyapunov stability \dot{L}_i should be less than zero. To make it happen mathematically we can do equation (39) as below:

$$|s_i|(|F_{ui}| - \eta_i |s_i|) \geq s_i F_{ui} - \eta_i s_i^2 = \dot{L}_i \quad (169)$$

From above equation (39) it can be seen that left-hand side is bigger or equal to right-hand side and which is equal to \dot{L}_i .

$$\dot{L}_i \leq |s_i|(|F_{ui}| - \eta_i |s_i|) \quad (40)$$

If one proves that $|s_i|(|F_{ui}| - \eta_i |s_i|) < 0$ one can also prove that $\dot{L}_i < 0$. Then, the proof is obtained for Lyapunov stability theory when absolute value of the F_i is less then $\eta_i |s_i|$. It can be seen that in equation (41) as below.

$$\begin{aligned} |s_i|(|F_{ui}| - \eta_i |s_i|) &< 0 \\ |F_{ui}| &< \eta_i |s_i| \end{aligned} \quad (41)$$

Hence, all the sliding surfaces are asymptotical stable when threshold is less than absolute of the sliding surface. Control inputs u_i , depending upon case 2, is as below (42):

$$u_i = \frac{1}{G_i}(-F_{ki} - \eta_i s_i) \quad (i = 1, 2, 3, 4) \quad (42)$$

For both, case 1 and case 2, if controller signals (29) are inserted inside of (25)-(28). The Lyapunov stability conditions are met and all the sliding surfaces are asymptotically stable.

4. Simulation Result

In order to show the result of the smoothness of the sliding mode controller designed with using saturation function on the quadrotor some desired trajectory is given. Its mathematical equation can be found as below:

$$\begin{aligned} x^d &= \sin(c_1 t), \quad y^d = \cos(c_2 t), \quad z^d = c_3 t \\ c_1 &= 0.5, \quad c_2 = 0.5, \quad c_3 = 1 \end{aligned}$$

c_1, c_2 and c_3 are the parameters which are used to define the given trajectory. Desired attitude of the quadrotor is given as $\phi^d = 0, \theta^d = 0$ and $\psi^d = 0$. The initial position and the attitude of the quadrotor are given as below:

$$\begin{aligned} x(0) = 0, \quad y(0) = 0, \quad z(0) = 0, \quad \dot{x}(0) = 0, \quad \dot{y}(0) = 0, \quad \dot{z}(0) = 0 \\ \phi(0) = 0, \quad \theta(0) = 0, \quad \psi(0) = 0, \quad \dot{\phi}(0) = 0, \quad \dot{\theta}(0) = 0, \quad \dot{\psi}(0) = 0 \end{aligned}$$

The model parameters of the quadrotor are given as below (Zheng, Xiong and Luo, 2014):

$$\begin{aligned} g = 9.81 \text{ m/s}^2, \quad m = 1.1 \text{ kg}, \quad l = 0.21 \text{ m} \\ I_x = I_y = 1.22 \text{ Ns}^2 / \text{rad}, \quad I_z = 2.2 \text{ Ns}^2 / \text{rad}, \quad J_r = 0.2 \text{ Ns}^2 / \text{rad} \\ K_1 = K_2 = K_3 = 0.1 \text{ Ns/m}, \quad K_4 = K_5 = K_6 = 0.12 \text{ Ns/m} \end{aligned}$$

$$k_{11} = k_{12} = 0.1, \quad k_{41} = k_{42} = 1,$$

The controller parameters are chosen as: $\eta_1 = \eta_2 = \eta_3 = \eta_4 = 200$

$$a_{11} = a_{21} = a_{31} = a_{21} = a_{22} = a_{32} = 2$$

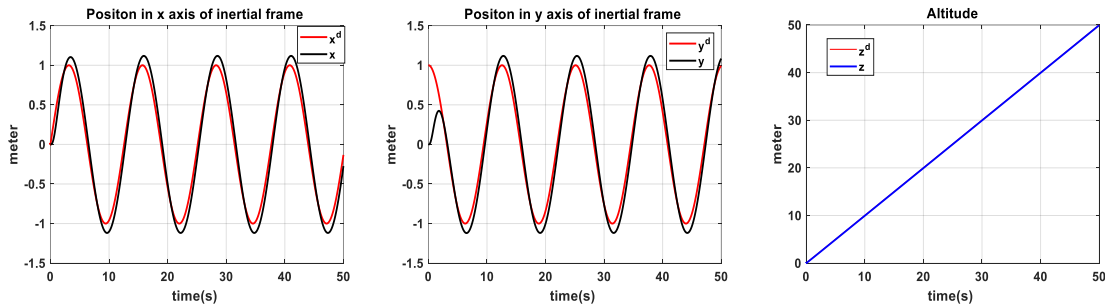


Figure 2. x, y and z component of the desired trajectory and x, y and z of the quadrotor

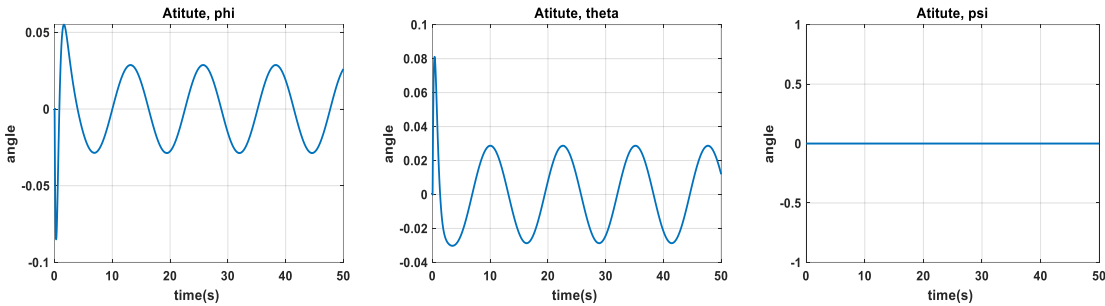


Figure 3. Attitude of the quadrotor while tracking trajectory

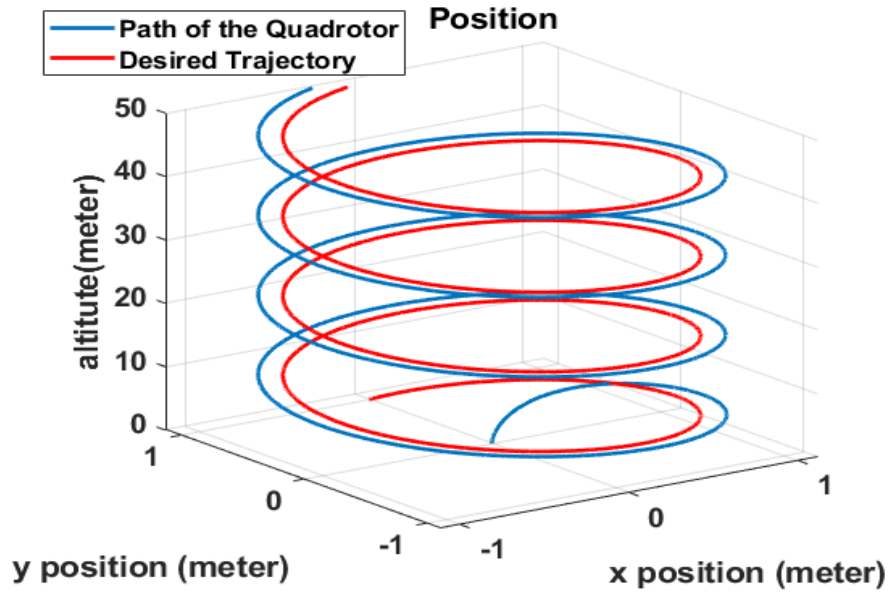
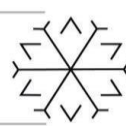


Figure 4. Desired trajectory and the path of the quadrotor

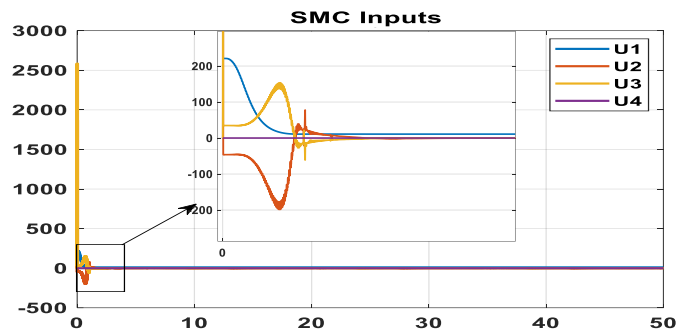


Figure 5. Sliding mode control inputs for threshold 0.5

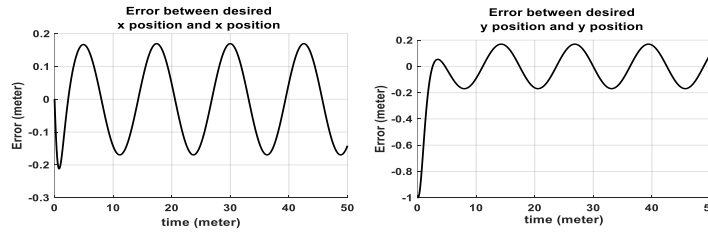


Figure 6. Error between x and y component of desired trajectory and x and y position of the quadrotor for threshold 0.5

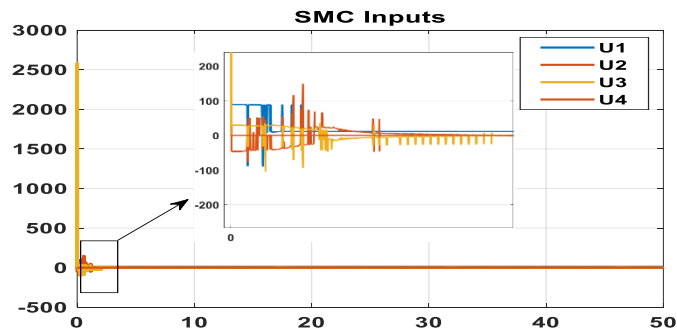
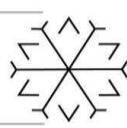


Figure 7. Sliding mode control inputs for threshold 0.005



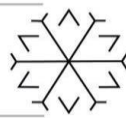
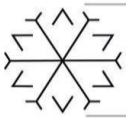
Position components (x, y, z) of the quadrotor while tracking the trajectory (x^d, y^d, z^d) are shown in Fig 2 and complete trajectory in inertial frame and the path of the quadrotor is shown in Fig 4. In simulation results, there is some error between trajectory and the path of the quadrotor. The reason of the error is the saturation function. Although the saturation function gives error it is good point of tracking performance. The error is almost negligible. It is maximum 20 cm in metric scale. The attitude of the quadrotor is shown in Fig 3. The yaw angle is always zero because that is our desired yaw angle. Small changes in phi and theta angles is because of the trajectory. From Fig 2 and Fig 3, it can be seen that all states asymptotically converge the desired values that come from desired trajectory with some error. The reason of this error is saturation function as discussed above. The sliding mode controller inputs are shown in Figure 5 for threshold 0.5. The error can be seen in Fig 6 up to threshold 0.5 for saturation function. It can be seen that for smaller threshold which is 0.005, the controller inputs have more chattering.

5. Conclusions

In the paper, a smoother sliding mode tracking controller for the quadrotor was developed. Decreasing of high chattering of the SMC inputs and obtaining smoother inputs with using saturation function was obtained. Although chattering was decreased, some error was occurred while tracking of the given trajectory. From tracking point of view, trajectory was not followed perfectly however applicability point of view, the tracking error was almost negligible and it can be tolerated. Additionally, the controller inputs were smoother and that was good for real time applications. In the simulations, two different cases were considered: control performance with lower threshold and higher threshold. Controller with lower saturation threshold slightly reduced the tracking error whereas the chattering on the control signal increased significantly when compared to the controller with higher saturation threshold.

5. References

- Bingöl, Ö. and Güzey, H. M. (2021) 'Neuro sliding mode control of quadrotor UAVs carrying suspended payload'. doi: 10.1080/01691864.2020.1870557.
- Bouabdallah, S. and Siegwart, R. (2007) 'Full Control of a Quadrotor', (1), pp. 153–158.
- Chen, L. and Wang, G. (2013) *Attitude Stabilization for a Quadrotor Helicopter Using a PD Controller* *, *IFAC Proceedings Volumes*. IFAC. doi: 10.3182/20130902-3-CN-3020.00163.
- Foehn, P., Scaramuzza, D. and Motivation, A. (2018) 'Onboard State Dependent LQR for Agile Quadrotors', pp. 6566–6572.
- Hacı, B., Gazi, V. and Cihan, O. (2019) 'Modelling and Coordination of a Swarm of Quadrotors Using Lagrange Dynamics and Potential Functions', pp. 963–970.
- Hassanalian, M. and Abdelke, A. (2017) 'Progress in Aerospace Sciences Classifications, applications, and design challenges of drones: A review', (April). doi: 10.1016/j.paerosci.2017.04.003.
- Kushleyev, A., Mellinger, D. and Powers, C. (2013) 'Towards a swarm of agile micro quadrotors', pp. 287–300. doi: 10.1007/s10514-013-9349-9.
- Levant, A. (2010) 'Chattering Analysis', 55(6), pp. 1380–1389.
- Li, J. (2011) 'Dynamic Analysis and PID Control for a Quadrotor', pp. 573–578.
- Mahony, R., Kumar, V. and Corke, P. (2012) 'Multirotor Aerial Vehicles: Modeling, Estimation, and Control of Quadrotor', (September).
- Nguyen, H. T. *et al.* (2020) 'EAI Endorsed Transactions Control Algorithms for UAVs: A Comprehensive Survey', 7(23), pp. 1–11. doi: 10.4108/eai.18-5-2020.164586.
- Shtessel, Y. B. and Landrum, B. (2012) 'Quadrotor vehicle control via sliding mode controller driven by sliding mode disturbance observer', 349, pp. 658–684. doi: 10.1016/j.jfranklin.2011.06.031.
- Singhal, G. (2018) 'Unmanned Aerial Vehicle Classification, Applications and Challenges: A Unmanned



Aerial Vehicle classification , Applications and challenges: A Review', (November). doi: 10.20944/preprints201811.0601.v1.

Toks, M. A. (2019) 'Decentralized Formation Control of a Swarm of Quadrotor Helicopters', *2019 IEEE 15th International Conference on Control and Automation (ICCA)*, pp. 1006–1013.

Voos, H. (2006) 'Nonlinear sState-dependent riccati equation control of a quadrotor UAV', *Proceedings of the IEEE International Conference on Control Applications*, pp. 2547–2552. doi: 10.1109/CACSD-CCA-ISIC.2006.4777039.

Voos, H. (2009) 'Nonlinear control of a quadrotor micro-uav using feedback-linearization', *IEEE 2009 International Conference on Mechatronics, ICM 2009*, (April), pp. 3–8. doi: 10.1109/ICMECH.2009.4957154.

Xiong, J. and Zhang, G. (2016) 'Sliding Mode Control for a Quadrotor UAV with Parameter Uncertainties', pp. 207–212.

Zheng, E., Xiong, J. and Luo, J. (2014) 'Second order sliding mode control for a quadrotor UAV', *ISA Transactions*, 53(4), pp. 1350–1356. doi: 10.1016/j.isatra.2014.03.010.

Design and Control of One-DOF Helicopter System

Mehmet Akif Macit ^{1*}[0000-0001-9450-2391] and Ali Unluturk ²[0000-0001-9722-1587]

¹macitakif@gmail.com, Department of Electrical-Electronics Engineering, Faculty of Engineering and Architecture, Erzurum Technical University, Erzurum

²ali.unluturk@erzurum.edu.tr, Department of Electrical-Electronics Engineering, Faculty of Engineering and Architecture, Erzurum Technical University, Erzurum

Abstract

In this study, a One-Degree of Freedom (One-DOF) helicopter system that can move vertically up and down in the x-axis direction has been designed. A single rotor Brushless Direct Current (BLDC) motor, which is widely used in unmanned aerial vehicles, has been mounted on this One-DOF helicopter. It is aimed to enable it to fly by adding a single bladed propeller to the brushless direct current motor. There is a GY-88 10 DOF Inertial Measurement Unit (IMU) on the One-DOF helicopter system. On the GY-88 10 DOF IMU Module, it includes MPU 6050 motion sensor (3-axis gyroscope and 3-axis acceleration sensor), HMC5883L (3-axis magnetometer) module and BMP085 barometer pressure sensor on a single board for a complete orientation and heading measurement. Stable tilt angle measurement has been performed by combining 3-axis gyroscope and 3-axis acceleration sensors data with the developed Kalman Filter (KF) software. Closed-loop controller algorithms such as Proportional (P), Proportional Integral (PI) and Proportional Integral Derivative (PID) have been developed for the control of the vertical take-off and landing One-DOF helicopter system. The performances of these developed classical controllers have been evaluated in detail in the experimental results section.

Keywords: One-DOF Helicopter, BLDC Motor, PID Controller, Kalman Filter, IMU.

1. Introduction

Unmanned Aerial Vehicles (UAVs) attract the attention of the scientific community, the private sector and hobby researchers thanks to their flexible maneuvering capabilities. Today, small-sized hobby-purpose unmanned aerial vehicles, which are light, economical and capable of fast forward flight by hovering in the air in narrow spaces, are easily accessible (Bristeau et al., 2011). Also, different types of UAVs have been designed recently in order to respond to the needs of people in an efficient, economical and reliable way. For example, different flying car models continue to be developed for urban air transportation, urban passenger transportation, health sector, cargo transportation and logistics support activities in the military. The use of unmanned aerial vehicles in civilian applications, especially in the military field, has become widespread and has gained an important place. In addition to these, UAVs are the most important and practical tools for on-site response, especially in natural disasters and emergencies.

The complex dynamic model and non-linear structure of these aircraft, it makes the work of researchers very difficult (Jafar et al., 2016). Unmanned aerial vehicles such as helicopters are nonlinear systems. Therefore, it is unstable and difficult to model (Humaidi and Hasan, 2019). There is also no systematic and general adaptive controller design procedure that can be applied to all nonlinear systems such as UAVs. Therefore, the properties and operating procedures of nonlinear systems are usually converted into a linear and specific system. Then, this linear structure is analyzed and the system is controlled by using controllers such as classical P, PI, PD and PID. PID controllers are widely used because of their simple structure (Kim, 2012). The most preferred controller type in robotic applications is PID (Mane et al., 2013; Rithirun et al., 2021). Unmanned aerial vehicles also have higher system tolerance due to their usage areas. Therefore, it is necessary to match the properties and operating procedures of the nonlinear system with a linear and specific system. After the analysis of the structure, efficiency can be obtained by using PI, PD and PID controller.

In this paper, we introduce a control methodology to stabilize the One-DOF arm around the balance point, and also in which degree it is desired, without any model, and then in next attempts we will present how to control the One-DOF helicopter by P, PI and PID type controller.

The rest of this paper has been organized as follows. In Section II, hardware structure and software of One-DOF helicopter have been introduced. In Section III, controller performances has been experimentally tested for different scenarios. Finally, some concluding remarks have been presented in Section IV.

2. Hardware Structure and Software

Firstly, the first prototype model of the One-DOF helicopter system was obtained with SolidWorks, the computer aided 3D solid modeling and design software of which Erzurum Technical University has a license server (Erzurum Technical University, 2021). A real-time mechanical arm system that can move up and down in the x-axis direction according to the model dimensions obtained from the SolidWorks software was built. Equipment of the One-DOF helicopter system: 2200kv BLDC motor (The model number of the BLDC is 1xA2212/6T), Electronic Speed Control (ESC) unit, 3S Lithium Polymer (Li-Po) battery, GY-88 10 DOF IMU sensor board and Arduino UNO microprocessor. Arduino UNO is a portable embedded device that allows users to design and control robotic or mechatronic systems. The block diagram in Figure 1 shows the hardware structure of the One-DOF helicopter in detail.

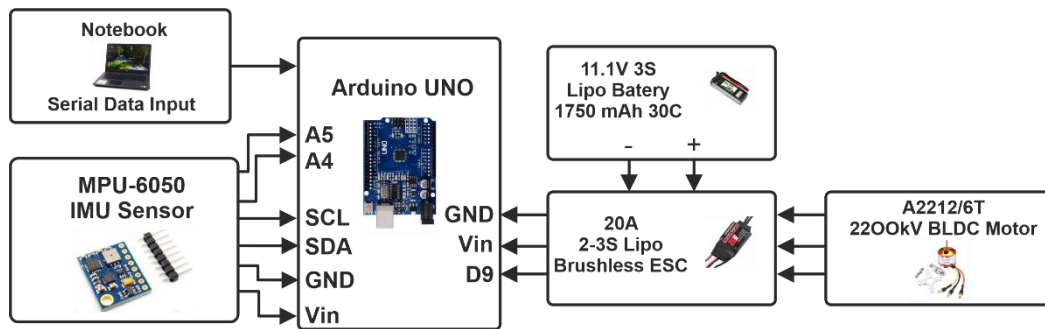


Figure 1. Hardware structure of One-DOF helicopter

There is a BLDC motor on the 1-DOF helicopter. Technical parameter of the BLDC motor is given in Table 1 (ABRA 2021).

Table 1. Parameter of the BLDC motor

MODEL	KV (rpm/V)	Voltage (V)	Prop	Load Current (A)	Power (W)	Pull (g)	Efficiency (g/W)	Li-Po Cell	Weight (g)
A2212	930	11.1	1060	9.8	109	660	6.1	2-4S	52
	1000		1047	15.6	173	885	5.1		
	1400		9050	19.0	210	910	4.3		
	1800		8060	20.8	231	805	3.5		
	2200		6030	21.5	239	732	3.1	2-3S	
	2450		6030	25.2	280	815	2.9		

As can be seen from Table 1, the BLDC motor rotates at 2200 rpm per volt. The rated voltage of the motor is 11.1V. The load current is 15.6 A, the shaft power of the motor is 173W. It has an efficiency of 5.1g/W. BLDC motor can be powered by 2-4S li-po battery.

The mechanical structure of the One-DOF helicopter system consists of a base and two vertical plates. The base plate is 180 mm wide and 400 mm long. The vertical plates have a length of 250 mm and a height of 350 mm, with a support plate between them. There is a cylindrical structure to which the main rod is connected by bearings between the two plates. The main bar has a width of 50 mm and a length of 650 mm. The elements that make up the system are placed on this bar. The SolidWorks drawing of One-DOF helicopter is shown in Figure 2a. The main parts of the realized One-DOF helicopter can be seen in Figure 2b.

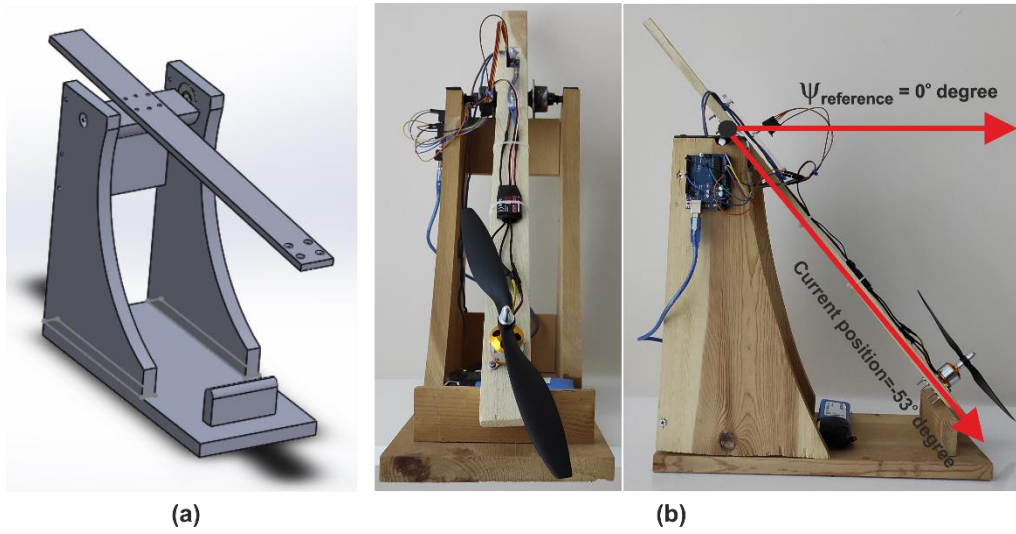


Figure 2a) Solidworks model of One-DOF helicopter 2b) Realized One-DOF helicopter

3. Experimental Results

Classical P, PI and PID controller structures have been applied in the stability control of the One-DOF helicopter system. A low cost IMU (GY-88) sensor is used to keep the system at the desired reference point. The IMU is widely used to determine motion, orientation, and altitude. In IMU control applications, it provides information about the dynamics of the system and provides feedback to the controller. This IMU contains sensor gyroscope and acceleration sensors. The tilt angle was obtained by combining the data obtained from the gyroscope and acceleration sensor with the KF software. The tilt angle value of the One-DOF helicopter system is approximately -53° degrees when in the current position at rest. PID controller structures were tried in the stability control of the One-DOF helicopter. The realized PID controller parameter coefficients K_p , K_i and K_d were determined experimentally. The PID controller structure is given in Figure 3.

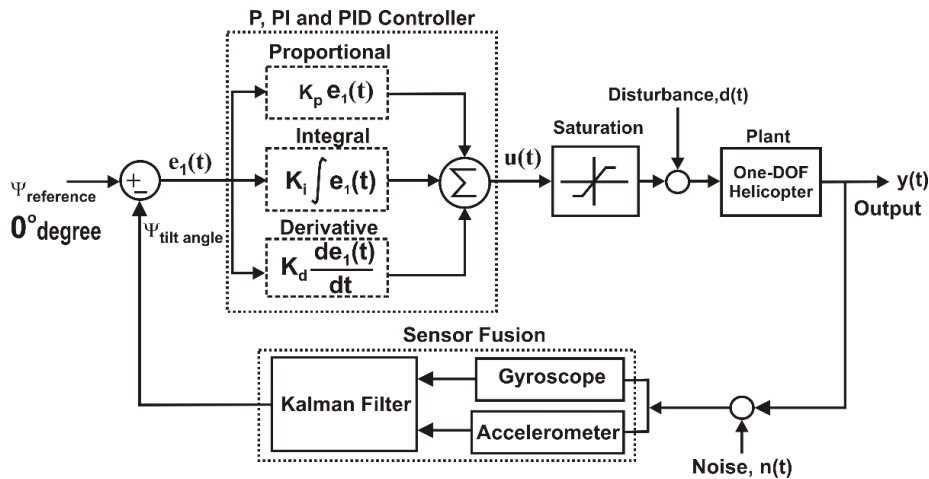


Figure 3. PID controller structure of One-DOF helicopter

The system was first checked with the proportional control method. Different proportional gain ($K_p = 0.57, K_p = 1.14, K_p = 1.71$) values applied to the system. The tilt angle change is shown in Figure 4. As can be seen in Figure 4, the reference point of the One-DOF helicopter could not be reached to 0° degrees at different proportional controller gain values. As a result, the control of the system cannot be performed only with a proportional controller.

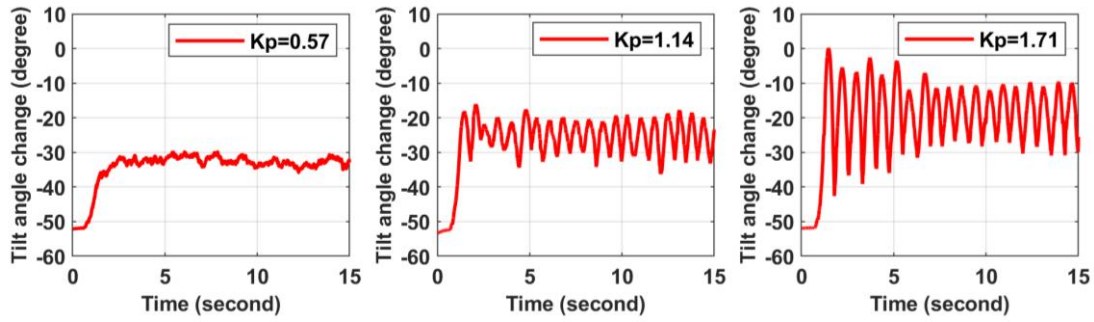
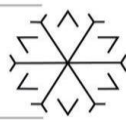
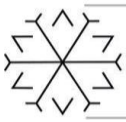


Figure 4. Different proportional controller gains of One-DOF helicopter

Secondly, proportional-integral controller was tested on the One-DOF system. Figure 5 shows the graph obtained for different PI ($K_p = 0.17$ $K_i = 0.0016$, $K_p = 0.37$ $K_i = 0.01$, $K_p = 0.5$ $K_i = 0.0015$) controller gain values. As can be seen from the figure, the system tends to go to the reference point by excessive oscillation. Excessive oscillations are not a desirable situation in the control of systems.

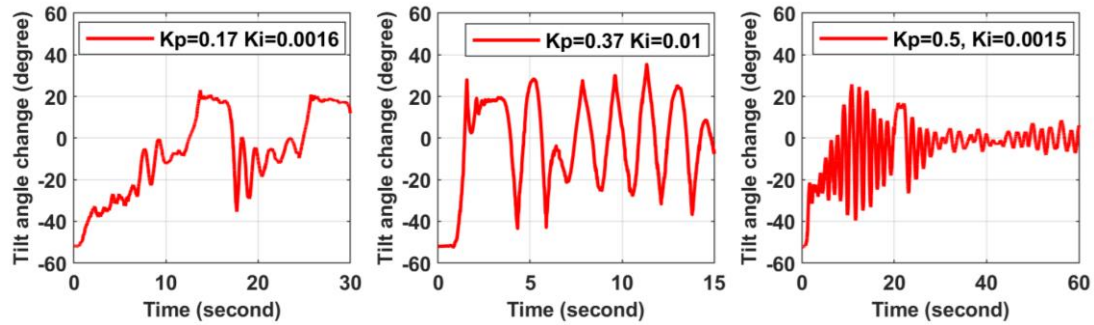


Figure 5. Different proportional-integral controller gains of One-DOF helicopter

Finally, the proportional-integral-derivative controller structure was tested on the One-DOF system. Figure 6 shows the graph obtained for different PID controller gain values. As can be seen from the figure, the system went to the reference point in a more stable way. The stable state of the system was obtained with the realized $K_p = 0.57$, $K_i = 0.0017$ and $K_d = 0.016$ PID gain parameters.

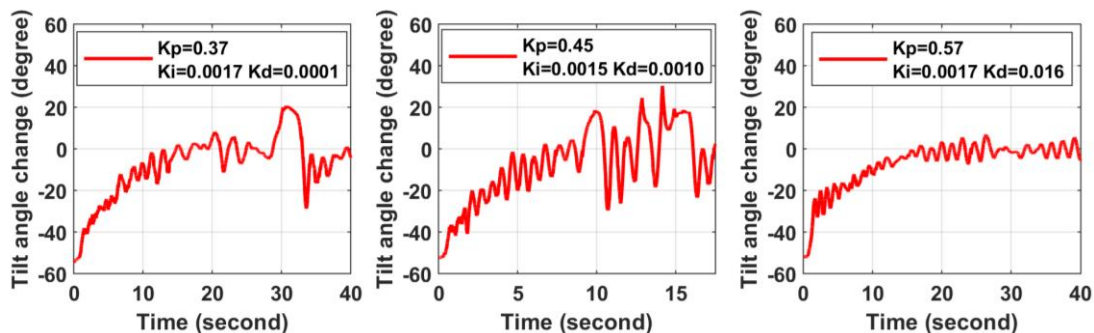
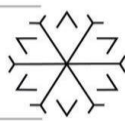


Figure 6. Different proportional-integral-derivative controller gains of One-DOF helicopter

4. Conclusion

In this study, performances of classical P, PI and PID based controllers developed for stable control of One-DOF helicopter around balance point are presented. All real-time system responses have been received and stabilization has been achieved taking into account sensor feedback. As a result of the real-time experimental results, it has



been seen that the One-DOF helicopter fails the balance point control at different proportional controller gain values $K_p=0.17$, $K_p=1.14$, $K_p=1.71$. In the tested PI controller gain parameters ($K_p=0.17$, $K_i=0.0016$, $K_p=0.37$, $K_i=0.01$, $K_p=0.5$, $K_i=0.0015$), excessive oscillations occurred in the transient state transition during the placement of the One-DOF helicopter to the reference point. In the PID controller, on the other hand, the balance stability is not good in some parameters ($K_p=0.37$, $K_i=0.0017$, $K_d=0.0001$ and $K_p=0.45$, $K_i=0.0015$ and $K_d=0.0010$). However, with the PID gain parameters $K_p=0.57$, $K_i=0.0017$ and $K_d=0.016$, the stable state of the system was obtained. In this PID parameter, the transient and steady state response of the system is quite successful. In future studies, it is aimed to implement advanced controller structures on the system.

References

- ABRA (2021). "A2212/6T 2200KV Brushless DC Motor for RC Quadcopters Planes Boats Vehicles and DIY Kits". Web Adress: <https://abra-electronics.com/quadcopters/motors/mot-qc-02.html>, Date of Access: 01.12.2021.
- Bristeau, P., Callou, F., Vissière, D., & Petit, N., (2011). "The Navigation and Control technology inside the AR. Drone micro UAV". 18th IFAC world congress, 18(1), 1477-1484, Milano, Italy.
- Erzurum Technical University, (2021). "Lisanslı Yazılımlar", Web Adress: <https://destek.erzurum.edu.tr/kb/faq.php?id=12>, Date of Access: 03.12.2021, Erzurum, Turkey.
- Humaidi, A. J., & Hasan, A. F., (2019). "Particle swarm optimization-based adaptive super-twisting sliding mode control design for 2-degree-of-freedom helicopter". *Measurement and Control*, Vol. 52(9-10), 1403-1419.
- Jafar, A., Ahmad, S. M. & Ahmed N. (2016). "Mathematical modeling and control law design for 1DOF Quadcopter flight dynamics," 2016 International Conference on Computing, Electronic and Electrical Engineering (ICE Cube), pp. 79-84, IEEE, Quetta, Pakistan.
- Kim, D. H., (2012). "Design and tuning approach of 3-DOF emotion intelligent PID (3-DOF-PID) controller". In 2012 Sixth UKSim/AMSS European Symposium on Computer Modeling and Simulation, pp. 74-77, IEEE, Malta.
- Mane, R., Mahapatro, K. A. & Gundecha, A. D., (2019). "Single Degree of Freedom Helicopter Model: Laboratory Setup Design". 2019 International Conference on Advances in Computing, Communication and Control (ICAC3), IEEE, Mumbai, India.
- Rithirun, C., Charean, A., & Sawaengsinkasikit, W. (2021). "Comparison Between PID Control and Fuzzy PID Control on Invert Pendulum System". In 2021 9th International Electrical Engineering Congress (iEECON), pp. 337-340, IEEE, Pattaya, Thailand.

Predicting the Result of Penalty Kick using Statistical and Match Day Features

Ural Akincioglu ¹[0000-0001-9875-510X] and Onder Aydemir ²[0000-0002-1177-8518]

¹ uralakincioglu@ktu.edu.tr, Electronics and Communications Engineering, Of Faculty of Technology,
Karadeniz Technical University

² onderaydemir@ktu.edu.tr, Department of Electrical and Electronics Engineering, Faculty of
Engineering, Karadeniz Technical University

Abstract

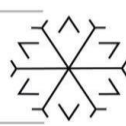
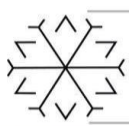
In football, the penalty kick is a very hotly anticipated position that no one knows beforehand how it will end up. Nevertheless, some statistical and match-day features might help to estimate the result of the penalty kick. In this study, we extracted 12 features from penalty positions and match days and used k -nearest neighbor classifier in order to predict how it will end up. The most suitable feature combination was selected to achieve the highest classification accuracy (CA) performance. Moreover, we ran the proposed method a hundred times to show its robustness and to avoid the random selection of training and testing sets. The proposed method was tested with 110 penalty kicks from the Turkish Super League. We concluded that the result of a penalty kick can be predicted with a maximum CA rate of 75.95%.

Keywords. Football, machine learning, penalty kick

1. Introduction

Football has become an increasingly important part of daily life in society throughout the history (Erdogan, 2008). Although it seems like 22 men run for a ball in football, it has become a big industry in the last 25 years (Kuyucu, 2014). Football, which is an event followed by people all over the world independent of economic status, has an important area of employment that has become a huge industry and football is never just football (Kuper, 1994; Onturk et al, 2019). To be successful in this game, teams make investments with large budgets such as player transfers, manager/coaching team agreements, youth team expenditures and training facility/stadium constructions or maintenance costs of existing ones. One of the main purposes of these investments is to win a cup as a champion. To achieve this aim, it is necessary to score more goal(s) than the opponent. It can be clearly said that the closest position to the goal is the penalty kick. Therefore, being successful in penalty position is very effective in reaching the aim.

Penalty kicks have been analyzed from various perspectives in literature. Timmis et al. (2018) recorded the data from 12 participants while taking penalties wearing an eye-tracking device. They found significant differences in quiet eye (QE) between successful and unsuccessful penalty kicks. As a result of their research, it was reported that the QE period was important for penalty kicks to be successful. Unsuccessful penalties had shorter QE periods and earlier QE offsets. Moreover, unsuccessful penalty kicks were taken more centrally, and the goalkeeper saved the ball more easily. In another study, Wood and Wilson (2010) recorded eye-tracking data of 18 experienced football players across different anxiety states and goalkeeper movements while taking five penalty kicks. The results showed that moving goalkeepers were more and much more effective in high-anxiety situations than stationary ones in penalty kicks. In another penalty kick-based study, Piras and Vickers (2011) collected gaze data and motor behavior of the goalkeepers, penalty takers' motor behaviors and information about the ball while in the air with a mobile eye tracker device and an external camera. Goalkeepers saved more instep (28%) than inside (12%) foot kicks. However, some differences were detected in fixation frequency, location, duration, or transitions that could be attributed to the type of penalty kick. Fixation transitions (or the frequency of gaze shifts between locations) were significantly higher on goals than on saves. During the last phase of the ball kicking action, the QE was on the visual pivot and was longer throughout the saves than goals. Moreover, goal probability increased when the last fixation on the ball was longer than 1.1 milliseconds (ms).



In another approach, Almeida et al. (2016) collected penalty kick data from Internet web sites and TV broadcasts. They aimed to investigate the primary and reaction effects of situational (competition phase, match location, match status and match period), individual (preferred foot of penalty taker's, position, and age difference between goalkeeper and penalty taker's), and performance factors (shot direction and goalkeeper's action). The data consist of penalties from the Europa League and Champions League (from the seasons 2010-2011 to 2014-2015). A total of 536 penalty data were considered and divided into three groups: goals, saved shots or missed shots. They used multinomial logistic regression analysis to determine the effects of factors on penalty outcomes. The logistic regression model showed that probability of penalty kicks being saved significantly increased in the middle of the match (between the 30th and 60th minutes). Additionally, they were saved when the shots were directed to the lower zones of the goal, especially to the lower center-right zone of the goal (according to the goalkeeper's perspective). Moreover, the possibility of missing a penalty significantly increased if the shot was directed to the high zones of the goal. Based on their findings, penalty takers should shoot to the upper corners of the goal, and goalkeepers should wait more to dive to the correct side of the ball. Although the performance factors were the most determinative for the penalty outcome, situational factors such as match period could also impact the success of penalty kicks.

To the best of our knowledge, this is the first work attempting to estimate the result of penalty kicks as a goal or not. To do so, we considered 12 different features (penalty taker's position, penalty taker's nationality, league week, penalty taker's preferred foot, home/away status, the league position of penalty taking team, penalty minute, match starting time, match score before taking penalty kick, shot direction of penalty kick, type of kicking the ball, and style of approaching the ball) extracted from match videos and some sports web-sites. To find the most effective features, we tested all possible feature subsets with different classification methods, including k -nearest neighbor (k -NN), decision tree (DT), and support vector machines (SVM). The obtained results showed that the result of a penalty kick might be estimated with a classification accuracy (CA) rate of 70.98% on average by k -NN.

2. Material and Methods

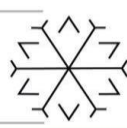
2.1. Data Set Description

The data set consists of a total of 110 penalties, half of which were goals. All penalties were from the Turkish Super League seasons (6 penalties from the 2018-2019 season, 29 penalties from the 2019-2020 season, 59 penalties from the 2020-2021 season, and 16 penalties from the 2021-2022 season). The penalty information was taken from Transfermarkt (Transfermarkt 2021), and analyses were carried out by watching the videos of these penalties from beIN Sports (beIN Sports 2021).

As a result of the analyses, 12 different attributes were selected as features. These features are, penalty taker's position, penalty taker's nationality, league week, home/away status, the league position of penalty taking team, preferred foot, penalty minute, match starting time, match score before taking penalty kick, shot direction of penalty kick, type of kicking the ball, and style of approaching the ball respectively. The features and groups are listed in Table 1.

While determining the position and nationality of the player who took the penalty, the player information in Transfermarkt was used. Football players were grouped into 3 different groups (defender, midfielder, and striker) according to their positions. According to their nationality, the football players were grouped into 3 different continent groups: European, African-Asian, and American.

Information on whether the team taking the penalty was the home team or the away team, the match starting time, the match score before taking a penalty kick, the penalty minute, and the league position of the penalty taking team were obtained from Transfermarkt. In the match-starting time feature, two different groups were created, before and after 6 pm. The match score before taking the penalty kick feature was defined as the goal difference. If the team which took a penalty was winning, the goal difference was set to plus goal difference, and if it was losing, the goal difference was set to the minus goal difference. If the match was drawn at the time of penalty, the goal difference was set to zero. Penalty minutes were divided into six groups. These groups were obtained by dividing 90 minutes into 6 equal parts ($0 < 1^{\text{st}}$ Group ≤ 15 , $15 < 2^{\text{nd}}$ Group ≤ 30 , $30 < 3^{\text{rd}}$ Group ≤ 45 , $45 < 4^{\text{th}}$ Group ≤ 60 , $60 < 5^{\text{th}}$ Group ≤ 75 , $75 < 6^{\text{th}}$ Group ≤ 90). Additional times in the first and second halves were grouped as 45th and 90th minutes. League position of the penalty taking team feature was obtained by the league table of the previous week. This feature was set to zero during the first week of the league. Due to the pandemic, different numbers of teams have competed in the super league in the last 3 years, so the number of weeks in the league has also changed (2018-2019, 2019-2020 seasons 34 weeks, 2020-2021 season 42 weeks, 2021-2022 season 38 weeks).



The league week feature was obtained by dividing the number of week in which the penalty was taken by the total number of weeks of the season.

Table 1: Features and Groups

Feature	Groups
Penalty Taker's Position (F1)	1-Defence, 2-Midfielder, 3-Forward
Penalty Taker's Nationality (F2)	1-European, 2-Asian-African, 3-American
League Week (F3)	2021-2022 Season 38 Weeks in Total 2020-2021 Season 42 Weeks in Total 2019-2020 Season 34 Weeks in Total 2018-2019 Season 34 Weeks in Total
Home/Away Status (F4)	1-Home, 2-Away
League Position of Penalty Taking Team (F5)	Penalty Taking Teams League Position in the Previous Week
Preferred Foot (F6)	1-Right, 2-Left
Penalty Minute (F7)	(0<1 st Group <=15, 15<2 nd Group<=30, 30<3 rd Group<=45, 45<4 th Group<=60, 60<5 th Group<=75, 75<6 th Group<=90)
Match Starting Time (F8)	1-Before 6 pm, 2-After 6 pm
Match Score Before Taking Penalty Kick (F9)	Goal Difference
Shot Direction of Penalty Kick (F10)	1-right lower, 2-right medium, 3-right upper, 4-center lower, 5-center medium, 6-center upper, 7-left lower, 8-left medium, 9-left upper
Type of Kicking the Ball (F11)	1-Inside, 2-Instep
Style of Approaching the Ball (F12)	1-Walk, 2-Run

Penalty taker's preferred foot, type of kicking the ball, style of approaching the ball and shot direction of penalty kick features were obtained by watching these penalties from beIN Sports. Preferred foot feature was divided into 2 groups: right and left foot. Style of approaching the ball feature was determined based on whether the football player approached the ball by walking or running, and groups were realized according to these two situations. The type of kicking the ball feature was determined as to whether the football player kicked the ball with the inside or instep foot and groups were realized according to these two situations. As shown in Figure 1, there are 9 different features for the shot direction of penalty kick (according to the goalkeeper, 1-right lower, 2-right medium, 3-right upper, 4-center lower, 5-center medium, 6-center upper, 7-left lower, 8-left medium, 9-left upper). If the goalkeeper in the center of the goal (without opening his arms) could save the ball without moving to the right or left in any way, the direction was defined as the center of the goal, and if he could catch the ball by moving to the right or left, the direction was defined as the right or left of the goal, respectively. From the goalkeeper's knee to the ground was set to lower, from above of the goalkeeper's knee to middle of the goal was set to medium and above middle of the goal was set to upper.

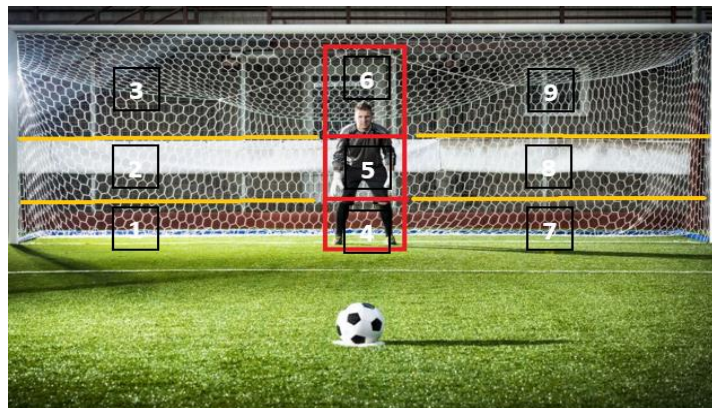
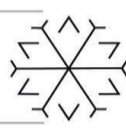
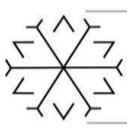


Figure 1: Shot Direction of Penalty Kick



The data set was randomly divided into training and testing sets. The training set consisted of 56 data, 28 of which were goals and 28 of which were not. The data in the training set were used to train the system. The test set consists of a total of 54 data, 27 of which were goals and 27 were not. The test set was used to test the system accuracy after the system was trained with the training set.

2.2. Classification and Feature Selection Procedures

SVM is an efficient and easy classification method used to analyze data in classification and regression analyses (Aydemir, 2020). In this algorithm, the classes are separated by drawing a boundary line. This was accomplished by finding a hyper-plane in the feature space. Thus, by increasing the distance between the hyperplane and the nearest data point from each class, we minimized the empirical classification errors. A better training performance can be achieved by shifting the hyperplane through the regularization parameter C and sigma parameters. Class determination, which uses the input vector, weight vector, and deviation, can be calculated by the following equation:

$$y = \begin{cases} \text{Class 1 if } w^T \cdot x + b < 0 \\ \text{Class 2 if } w^T \cdot x + b \geq 0 \end{cases} \quad (1)$$

where y is class information, x is the input vector, w is the weight vector, and b is the deviation.

The k-NN is a popular, easy, and helpful algorithm, which successfully classifies binary and multi-class problems. In the classification step, all the training trials are required to define the label of a test trial on the set of A labeled examples and predefined B classes. The k- NN algorithm calculates the distances between the testing trial and all training trials to detect its nearest neighbors. k-NN uses a majority vote to define the class label of the testing trial set on the k nearest neighbor(s). Euclidean distance function is used for to calculate the metric distance between two data points. The distance of a test trial from a training trial can be calculated using the following equation:

$$D = \sqrt{(X - X_1)^2 + (Y - Y_1)^2} \quad (2)$$

where D is distance, X, and Y are the coordinates of a training trial, and X_1, Y_1 are the coordinates of a testing trial.

Decision tree algorithm is a supervised learning algorithm. Decision tree algorithm can be used for regression and classification problems. Decision tree is an easy method for classification. Each node in the decision tree is labeled with an input feature. Information from the node labeled with the input feature is labeled with each of the target feature probabilities, creating new subnodes. The probabilities of the class or classes are labeled on each leaf of the decision tree. This indicates that the data set is classified by the tree to a particular class or probability distribution.

CA was used to evaluate the performance of the three classifiers. We calculated the CA by dividing the correctly classified penalty goal situation trials by the total number of considered trials for the classification and multiplying this by 100 to obtain the percentage. CA can be calculated using the following equation:

$$\text{Classification Accuracy} = \frac{\text{Correctly Classified Trials}}{\text{Total Number of Trials}} \times 100 \quad (3)$$

We tested all possible feature subsets, which included 4096 subsets, to determine the most effective feature combination. It is worthwhile mentioning that the most effective feature combination is the subset of considered 12 features, which provided the highest CA in the training set. To demonstrate the robustness of the method and avoid random selection problems in the sub-training and test sets, the feature selection procedure was applied one hundred times. Therefore, we calculated the mean CA and standard deviation of this accuracy for each classification node. A flowchart of the proposed method is shown in Figure 2.

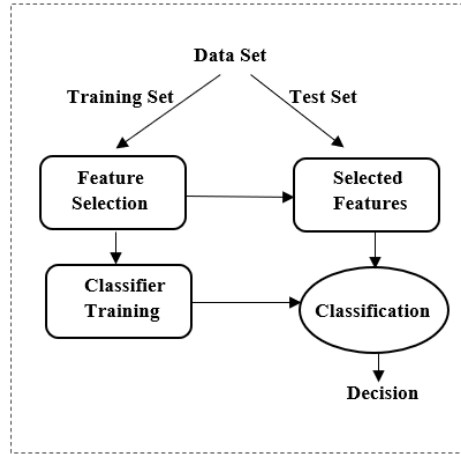
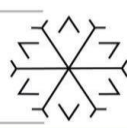


Figure 2: Flowchart of The Proposed Method

3. Results

In this study, we predicted the result of a penalty kick using 12 features extracted from match videos and match days. In Figure 3, the *k*-NN feature selection frequency of 100 runs is shown in the training sets. It is clearly seen from Figure 3 that, F3 feature was selected 80 times, which was the highest number. In contrast, F5 feature was included in the best subset combination only 9 times. The highest CA among 100 runs was achieved as 75.95% with the combination of F2+F3+F9+F11.

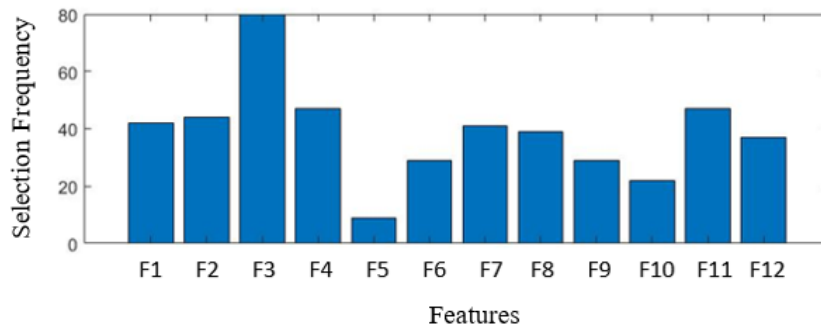


Figure 3: Feature Selection Frequency of *k*-NN

We also tested the proposed method using the DT and SVM classifiers. Based on the DT classifier, the feature selection frequency values of 100 runs in training sets are given in Figure 4. As seen from Figure 4, F4 and F11 features were the most frequently selected features by being selected 46 times each. On the other hand, F5 feature was included in the best subset combination only 17 times. The highest CA among 100 runs was achieved as 70.37% with the combination of F2+F4+F6+F11+F12.

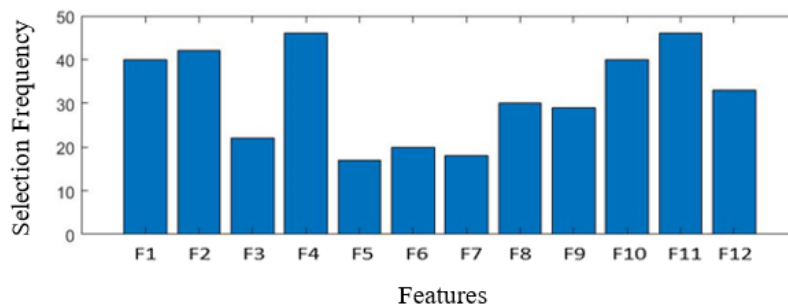
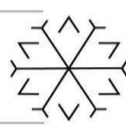
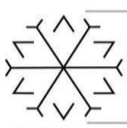


Figure 4: Feature Selection Frequency of DT



In Figure 5, the SVM feature selection frequency of 100 runs is shown in the training sets. It is seen from figure 5 that, the F3 feature was the most frequently used feature with a selection record of 65 times. Contrary to this, F2 feature was included in the best subset combination only 17 times. The highest CA for 100 runs was achieved as 70.37% with the combination of F3+F4+F6+F8+F9+F10.

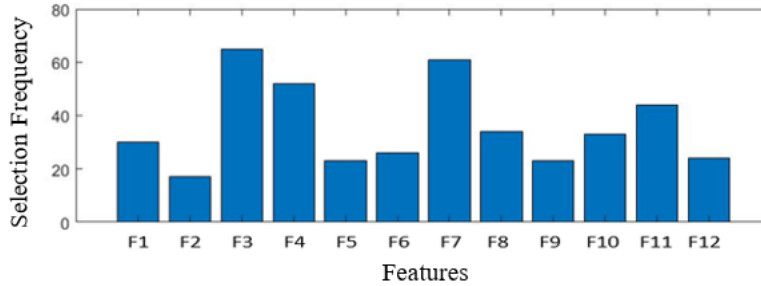


Figure 5: Feature Selection Frequency of SVM

We also calculated the average CA and their standard deviation (STD) values for each classifier over 100 runs. According to the results in Table 2, 70.98%, 65.11%, 64.96% CAs and ± 2.16 , ± 2.32 , ± 2.72 STDs were achieved for k -NN, DT, and SVM, respectively. The CA values were given in percentages. It can be said that the small values of the STDs demonstrated the robustness of the proposed method.

Table 2: Average CA and STD Results

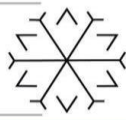
Classification Method	CA	STD
k -NN	70.98	± 2.16
DT	65.11	± 2.32
SVM	64.96	± 2.72

4. Conclusion

In this study, we used 12 statistical and match day features to predict the result of a penalty kick. The proposed algorithm was tested using k -NN, DT, and SVM classifiers. Furthermore, we ran the proposed method a hundred times to show its robustness and to avoid the random selection of training and testing sets. The k -NN, DT, and SVM achieved CA rates of 70.98%, 65.11%, and 64.96% on average, respectively. Additionally, the lower standard deviation values proved the robustness of the proposed method. It can be said that k -NN is the most suitable classifier for predicting the result of a penalty kick. Moreover, the results also showed that F3 feature was the most important attribute among the considered 12 features. As a future work, we plan to use some additional information including electromyogram and eye-tracking signals to increase the predicting rate of a penalty kick.

References

- Almeida, C., Volossovitch, A. And Duarte, R., 2016. Penalty kick outcomes in UEFA club competitions (2010-2015): The roles of situational, individual and performance factors. *International Journal of Performance Analysis in Sport*, 2(16), pp.508-522.
- Aydemir, O., 2020. A new performance evaluation metric for classifiers: polygon areametric. *Journal of Classification*, 1(38), pp.16-26.
- beIN Sports, viewed 11 Nov 2021, <https://beinsports.com.tr/>.
- Erdogan, I., 2008, Futbol ve Futbolu İnceleme Üzerine, *İletişim Kuram ve Araştırma Dergisi*, 26, pp.1-58.
- Kuper, S., 1994, *Futbol Asla Sadece Futbol Değildir*, İthaki, İstanbul.



Kuyucu, M., 2014, Futbol Endüstrisinde Sosyal Medya Pazarlama Uygulamaları, *The Journal of Academic Social Sciences*, 7(7), pp.161-175.

Onturk, Y., Karacabey, K. and Ozbar, N., 2019, Günümüzde Spor Denilince İlk Akla Neden Futbol Gelir? Sorusu Üzerine Bir Araştırma, *Ankara Üniversitesi Beden Eğitimi ve Spor Yüksekokulu SPORMETRE Beden Eğitimi ve Spor Bilimleri Dergisi*, 17(2), pp.1-12.

Piras, A. And Vickers, J., 2011. The effect of fixation transitions on quiet eye duration and performance in the soccer penalty kick: instep versus inside kicks. *Cognitive Processing*, 3(12), pp.245-255.

Timmis, M., Piras, A. and van Paridon, K., 2018. Keep Your Eye on the Ball; the Impact of an Anticipatory Fixation During Successful and Unsuccessful Soccer Penalty Kicks. *Frontiers in Psychology*, 9.

Transfermarkt, viewed 11 Nov 2021, <https://www.transfermarkt.com/>.

Wood, G. And Wilson M., 2010. A moving goalkeeper distracts penalty takers and impairs shooting accuracy. *Journal of Sports Sciences*, 9(28), pp.937-946.

Advanced Cyberbullying Identification with Bidirectional Encoder Representations from Transformers

Mehmet Bozuyula ¹*[0000-0002-7485-6106]

¹mbozuyula05@posta.pau.edu.tr, Pamukkale University, Department of Electrical and Electronics Engineering

Abstract

The interaction between social media users increases rapidly with massive data generation. These data are analyzed on several perspectives such as sentiment analysis, fake news identification and cyberbullying analysis. Cyberbullying, being a main security issue, is the source of many cybercrimes and there is a constant need to design automated cyberbullying identification systems. There are many studies conducted on cyberbullying analysis for the English language. However Turkish language related cyberbullying detection methods are infrequent. Furthermore, Turkish is an agglutinative language which requires pre-processing steps to obtain a reliable identification model. In this context, traditional machine learning models for Turkish natural language problems needs some pre-processing such as tokenization, stemming, stop-word removal, feature selection etc. to attain an efficient model. In other words, pre-processing steps should be tested with an optimization scheme to obtain a reliable model. This tedious pipeline is recently remedied with neural transformers such as Bidirectional Encoder Representations from Transformers (BERT). In other words, newly proposed transformer models does not require the mentioned language processing steps. In this study, we compared traditional machine learning algorithms such as Naïve Bayes Multinomial (90.6%), Logistic Regression (85.5%), Support Vector Machine (88.8%), Random Forests (85.5%) and newly developed Turkish language transformer (BERTurk, 99.7%) for cyberbullying identification problem. We compared the experimental results on top of accuracy values and we obtained best accuracy of conventional machine learning model as Naïve Bayes Multinomial (90.6%) and BERTurk (99.7%) as for neural transformers. From this result, we may propose that the new transformer models do not require heavy pre-processing steps and they may generate efficient models.

Keywords. Cyberbullying, machine learning, bidirectional encoder representations from transformers, BERTurk

Design and Simulation of Soft-Switched PWM Full-Bridge DC-DC Converter with Snubber Cell and No Additional Control

Gorkem Ozkur¹ [0000-0002-6265-8452] and Huseyin Yesilyurt² [0000-0002-8969-1893]

¹gozkur12@gmail.com, Department of Electrical and Electronics Engineering, Izmir Katip Celebi University, Izmir, Turkey

²huseyin.yesilyurt@ikc.edu.tr, Department of Electrical and Electronics Engineering, Izmir Katip Celebi University, Izmir, Turkey

Abstract

In this paper, a soft-switched PWM full bridge DC-DC converter with snubber cell and no additional control design is proposed. The active snubber cell in the proposed converter has a modular structure and does not need an additional control signal. The converter has all the advantages of PWM control, plus all semiconductors operate under soft switching and there is no voltage stress on any switch element. The methods used in the operating modes analysis and design considerations of the proposed converter are explained in detail. Theoretical analyzes of the proposed full-bridge DC-DC converter verified by a simulation circuit with 33 kHz switching frequency, 100 V output voltage, 80 A output current.

Keywords. DC-DC Converter, PWM Full Bridge, Snubber Cell, Soft Switching, Zero Voltage – Zero Current Switching

1. Introduction

Pulse Width Mode (PWM) converters and their derivatives have attracted great attention in the field of power electronics since the 20th century with their analysis, operational principles, controls and designs. Today, they still play a key role in power processing, as well as advances in switching techniques and magnetic devices (Wu, 2016). PWM controlled DC-DC converters are widely used in industry due to their advantages such as high-power density, fast transition response and easy control (Ruan, 2014).

Full Bridge (FB) PWM DC-DC converters are frequently preferred in medium to high power applications due to their advantages such as isolation, easy control and low primary current. FB PWM DC-DC converters have many applications such as battery charging systems, power factor regulator, renewable energy systems, telecommunication equipment and welding machines (Saygun, Beser & Unlu, 2017).

By increasing the switching frequency in PWM converters, the power density can be increased and the transition response can be accelerated, but with the increase of the switching frequency, the switching losses also increase and the following disadvantages occur:

- Low power density,
- High EMI and RF noises,
- Use of bigger heat sinks and increased cost,
- Disruption of control and communication signals.

The effect of these negativities can be minimized by applying the Soft Switching (SS) methods (Ching & Chan, 2008). With the soft switching technique, it can reduce switching losses, diode reverse recovery losses, switching voltage and current voltages on converter components (Anyalebechi & Ogboh, 2019).

Phase Shift (PS) control methods are generally applied to provide SS in FB converters, but transmission losses are high in PS methods due to high circulation current. The ZVS PSFB converters allows switching devices to operate at reduced switching losses and stress while increasing energy conversion efficiency (Ibrahim, Yahaya, Saad, and Ahmed, 2016).

Also, PSFB converters have a more complex control system compared to traditional PWM converters (Bai, Nie & Mi, 2010). Pre-designed SS PWM converters (Z. Chen, Y. Chen & Q. Chen, 2019), (Tran, Yu, Vu & Choi, 2016) seem to require the use of additional control signals.

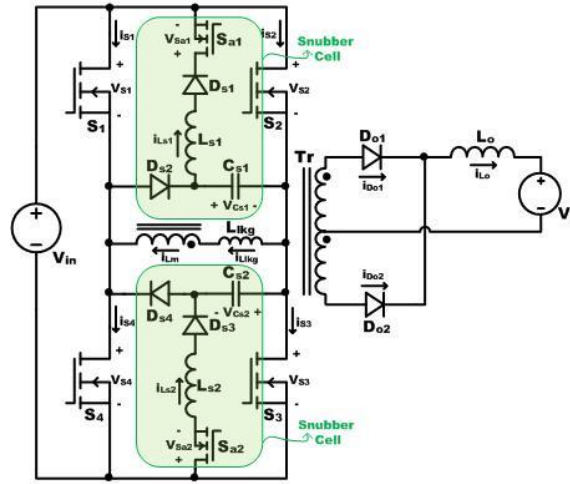


Figure 1. Proposed SS PWM FB DC-DC Converter.

In this study, FB PWM DC-DC converter design with snubber cell and no additional control is proposed. The circuit diagram of the proposed FB PWM DC-DC converter is given in Figure 1. The modular active snubber cell shown in Figure 1 was previously applied to the Half Bridge (HB) PWM DC-DC converter (Bodur, Yesilyurt, Akboy & Ting, 2020). However, HB converters are generally used at medium power levels. At higher power levels, FB converters are preferred because of their advantages such as low primary current and easy applicability. The proposed SS FB PWM DC-DC converter is easier to implement than conventional SS methods, as it contains an active modular snubber cell and does not require additional control signals.

In addition, the proposed FB converter is suitable for battery charging systems. In battery charging systems, since the output voltage never drops to 0 even when the battery is discharged, in current control mode, the converter generally operates at a high charge rate. In high fill rate operation, the snubber inductance L_s can be selected with a large value. Thus, more efficient operation of the offered converter is ensured. Choosing L_s large makes snubber operation better and reduces the resonant current, thus reducing conduction losses (Feizi & Beiranvand, 2020).

2. Operating Principles and Analysis of Proposed Converter

The following equations have been used while performing the proposed converter analysis.

- i. S_1, S_2, S_3 and S_4 are the main switches of the converter, S_{a1} and S_{a2} are the auxiliary switches of the converter.
- ii. D_1 and D_2 are the main diodes of the converter, $D_{s1}, D_{s2}, D_{s3}, D_{s4}$ are auxiliary diodes and D_{o1} and D_{o2} are output diodes.
- iii. C_{s1} and C_{s2} are snubber capacitors and the equation $C_{s1} = C_{s2} = C_s$ applies.
- iv. L_{s1} and L_{s2} are snubber inductances, L_o is the output inductance and the equation $L_{s1} = L_{s2} = L_s$ applies.
- v. T_r is the power transformer, n is the turns ratio, L_m is the magnetizing inductance of the transformer and L_{lkg} is the leakage inductance of the transformer. The value of L_m is very large and the equation $i_{Lm} = 0$ is valid.
- vi. Resonant circuits and semiconductor power elements are ideal.
- vii. The input voltage and output current of the circuit are constant over a switching period.

The circuit operating occurs in a total of 12 modes. The analyzes of the operating modes are made for the case where the gate signals are applied to the switches S_1 and S_3 . The similar modes occur for the other half-period. The operation waveforms of the designed circuit are given in Figure 2.

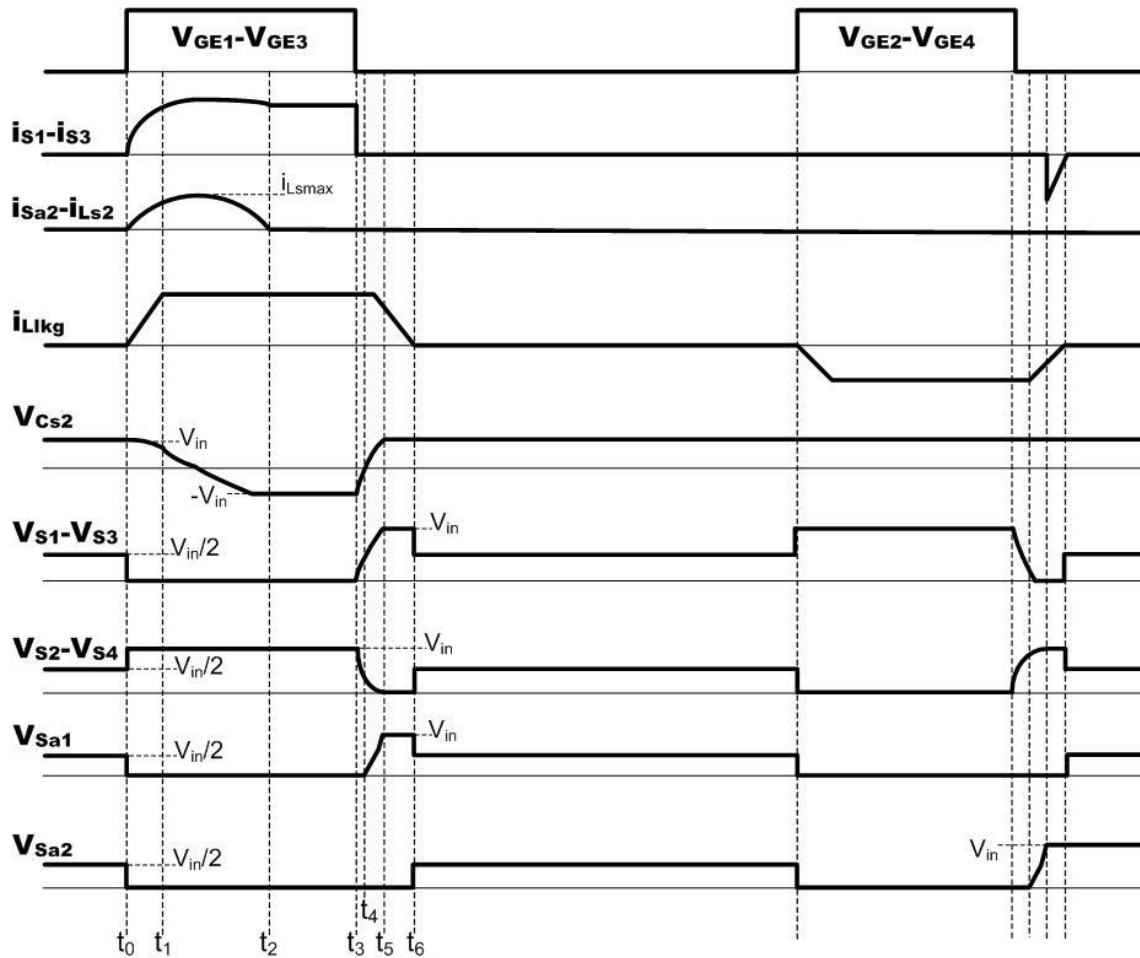
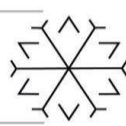
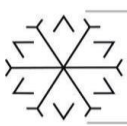


Figure 2. Operation waveforms of the proposed converter.

Freewheeling Mode

D_{o1} and D_{o2} are in conduction and all other semiconductor elements used in the circuit are in cutoff. In the freewheeling mode, the main switches voltages $v_{s1} - v_{s4}$ and auxiliary switches voltages v_{sa1} and v_{sa2} are equal to $V_{in}/2$ and the voltages of the snubber capacitors v_{Cs1} and v_{Cs2} are equal to V_{in} . Switch currents $i_{s1} - i_{s4}$, snubber inductance currents i_{sa1} , i_{sa2} and leakage inductance current i_{llkg} are equal to zero.

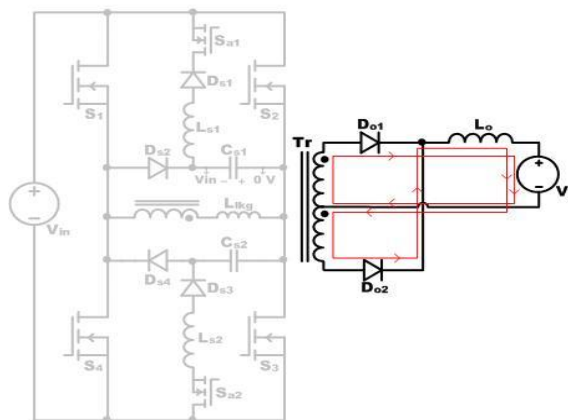


Figure 3. Freewheeling Mode.

Mode 1 ($t_0 - t_1$)

The signals of the switches S_1 , S_3 and the signal of the auxiliary switch S_{a2} start to be applied at the moment $t = t_0$ and these switches transmit simultaneously. S_1 , S_3 and S_{a2} turn on with zero current switching (ZCS). Voltage V_{in} is applied on L_{lkg} and leakage inductance current i_{lkg} starts to increase linearly. At the same time, resonance begins to occur between C_{s2} and L_{s2} . In this interval, D_{o1} and D_{o2} are on and $i_{D_{o1}}$ is increasing while $i_{D_{o2}}$ is decreasing.

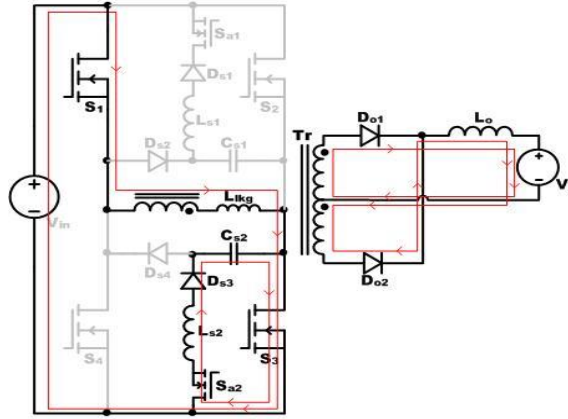


Figure 4. Mode 1.

Mode 2 ($t_1 - t_2$)

At the time of $t = t_1$, $i_{D_{o1}}$ becomes equal to I_{L_o} , therefore D_{o2} goes to cutoff and this mode starts. In this mode, S_1 , S_3 and S_{a2} are on and the resonance between L_{s2} and C_{s2} continues. Also, $i_{L_{s2}}$ reaches its maximum value $i_{L_{s2}(max)}$, then it drops to 0. $v_{C_{s2}}$ changes its direction and reaches $-V_{in}$. S_{a2} turns off with zero current switching (ZVZCS), and diode D_{s3} turns off with ZVS. Simultaneously, S_{a2} and D_{s3} turns off at $t = t_2$ and this mode ends.

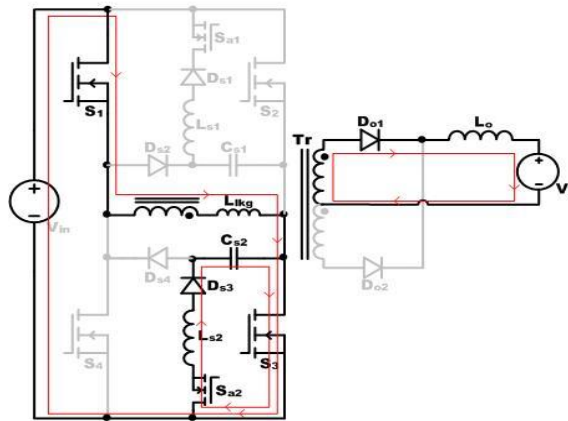


Figure 5. Mode 2.

Mode 3 ($t_2 - t_3$)

This mode is the same as the normal PWM FB converter mode. S_1 , S_3 and D_{o1} are in conduction. The power drawn from the source is transferred to the output via the transformer. Since the L_o is large enough, it works as a current source and a constant current I_{L_o}/n passes over the L_{lkg} . In this mode, $v_{C_{s2}}$ is equal to $-V_{in}$.

This mode ends when the signals of the S_1 , S_3 and S_{a2} are turn off at the time $t = t_3$.

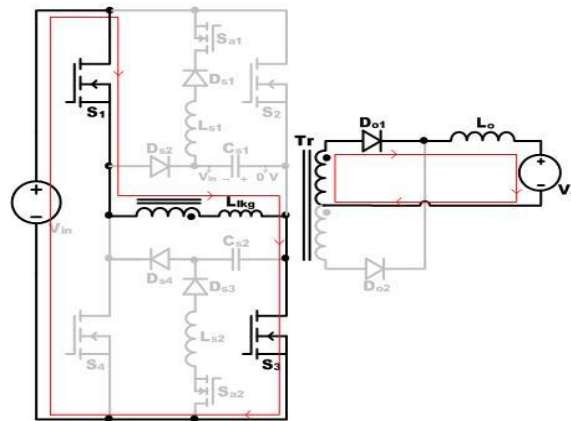


Figure 6. Mode 3.

Mode 4 ($t_3 - t_4$)

In this mode, C_{s2} starts to charge with a constant current I_{L_o}/n . In this way, S_1 and S_3 turn off with ZVS. Also, D_{s4} turns on with ZVZCS. At $t = t_4$, $v_{C_{s2}}$ is equal to 0 V, therefore D_{o2} turns on and this mode ends.

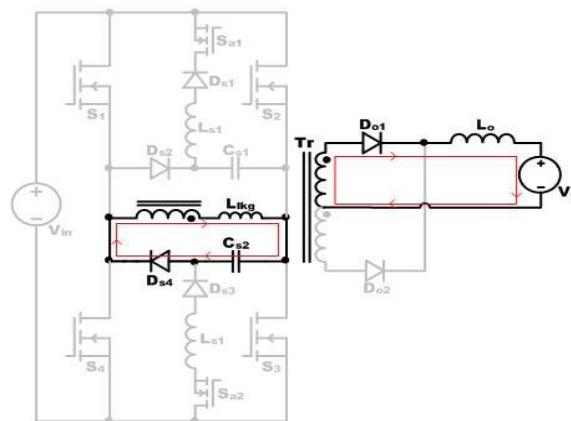


Figure 7. Mode 4.

Mode 5 ($t_4 - t_5$)

D_{o2} turns on and this mode begins. In this mode, there is a resonance between L_{lkg} and C_{s2} . L_{lkg} transfers its energy to C_{s2} , so while $i_{L_{lkg}}$ is decreasing and $v_{C_{s2}}$ is increasing. At $t = t_5$, $v_{C_{s2}}$ equals to V_{in} and the reverse parallel diode of switches S_1 and S_2 turns on and this mode ends.

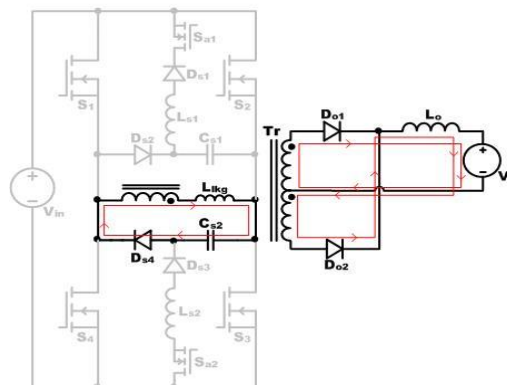


Figure 8. Mode 5.

Mode 6 ($t_5 - t_6$)

In this mode there is a constant voltage $-V_{in}$ on L_{lkg} and the current $i_{L_{lkg}}$ decreases linearly. At time $t = t_6$, $i_{L_{lkg}}$ equal to 0 A and this mode ends.

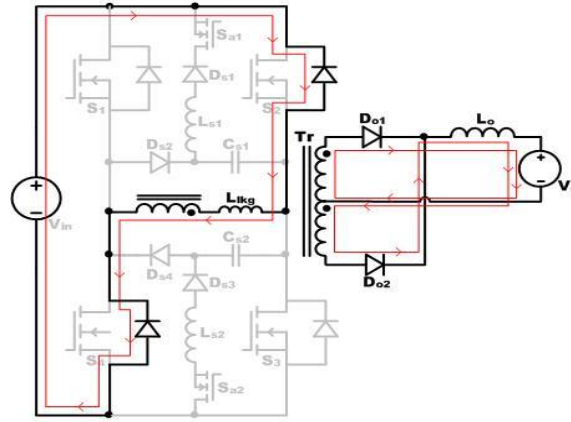


Figure 9. Mode 6.

3. Design Considerations

3.1. Determination of C_s

The snubber capacitor C_s reduces the EMC level by slowing the rising edge of the switch voltage of S_1 to allow the switches to turn off under ZVS. Fall time (t_f) of discrete IGBTs are usually below 100 ns. Choosing a large snubber capacitor causes the v_{s1} voltage to rise slowly at the moment of turning off the switch and has a positive effect on the EMC results. However, choosing C_s too large will increase the current stress and losses on the key elements and negatively affect the efficiency. It has been seen that the increase of v_{s1} around 300 ns at the maximum output current has a very positive effect on the EMC tests (Bodur, Yesilyurt & Ozel, 2013).

Switch voltage S_1 rises in stage 4 and stage 5, in stage 4 the output current is reflected as I_{Omax}/n to the primary, and in stage 5 there is resonance between L_{lk} and C_{s2} . In these two cases, the capacitor C_{s2} is considered to be linearly charged with constant current I_{Omax}/n , and the following equation is used for C_s selection.

$$C_s \geq \frac{I_{Omax} t_f}{n V_{in}} \quad (1)$$

3.2 Determination of L_s

While choosing L_s , it should be done according to the minimum duty value (λ_{min}) that V_{Cs2} can change direction. If L_s is selected small, the current stresses of the semiconductors will increase, while if it is selected large, the capacitor voltages at λ_{min} value will not change direction and soft switching will be disrupted.

T denotes the switching period and the choice of L_s is determined by the following equation.

$$\pi \sqrt{L_s C_s} \leq \lambda_{min} T \quad (2)$$

3.3 Determination of L_{lk}

The value of L_{lk} should be determined by taking into account the state of charge of the capacitor. When L_{lk} transferring its energy to C_{s2} in stage 5, the value of V_{Cs2} should increase from 0 to V_{in} . For this reason, the selection should be made according to the following equation for this case.

$$\frac{1}{2} L_{kg} \left(\frac{I_{omin}}{n} \right)^2 \geq \frac{1}{2} C_s (V_{in})^2 \quad (3)$$

4. Simulation Results

The simulation of the proposed soft-switched PWM full-bridge DC-DC converter with snubber cell and no additional control has been made. Figure 10 shows the simulation schematic and Table 1 shows the basic parameters of the converter and the selected values.

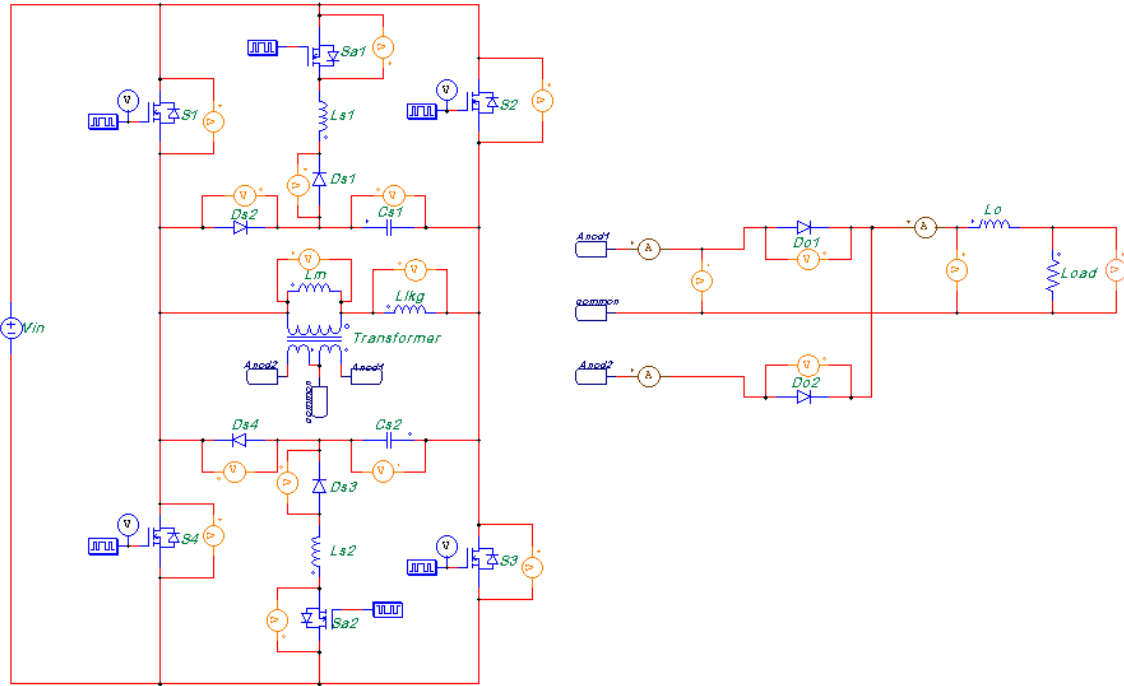


Figure 10. Simulation schematic of proposed converter.

Table 1. Parameters of the proposed converter

Parameters	Values
V_{in}	540 V
V_o	100 V
T_r transformation ratio	8:5:5 (n=1.6)
Switching frequency	33 kHz
Output Current Range	30 A – 100 A
C_s	35 nF
L_s	30 μ H
L_{kg}	30 μ H

As mentioned in the operation modes, it is expected that the S_1 switch will turn on with ZCS at the beginning of stage 1 and turn off with ZVS at the end of stage 2. Auxiliary switch S_{a2} is expected to turn on with ZVZCS at the beginning of stage 1 and turn off with ZCS at the end of stage 2. As seen in Figure 11, both switches work as expected and soft switching is provided at expected moments.

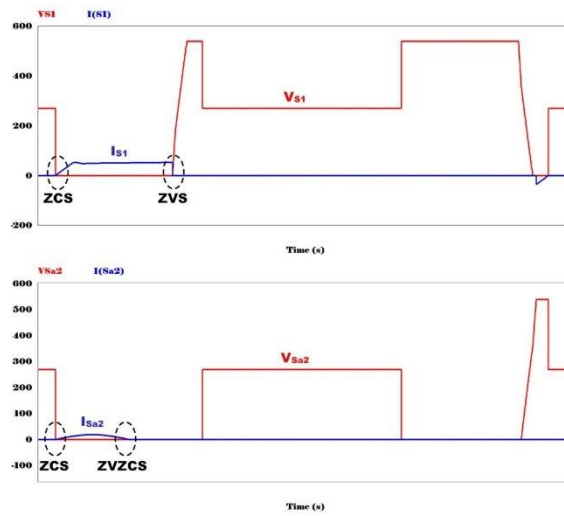


Figure 11. Simulation waveforms of S_1 and S_{a2} .

In Figure 12, the V_{Cs2} signal is shared and it is clearly seen that the C_{s2} capacitor charges and discharges at the expected moments, as explained in the operation modes.

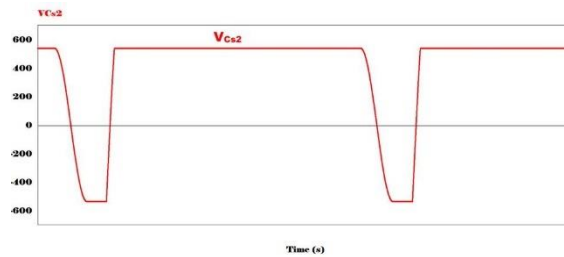


Figure 12. Simulation waveform of C_{s2} .

The D_{s3} auxiliary diode is expected to turn off with ZVS at the end of stage 2 and the D_{s4} auxiliary diode is expected to turn on with ZVZCS at the beginning of stage 4. As can be seen in Figure 13, both diodes provide soft switching at the expected moments.

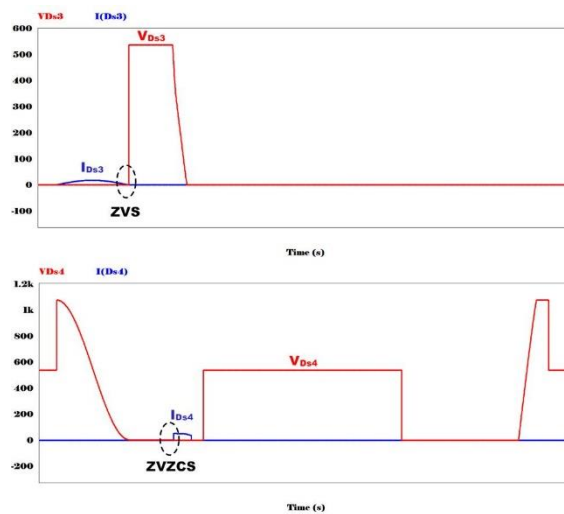
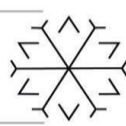
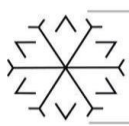


Figure 13. Simulation waveforms of D_{s3} and D_{s4} .



5. Conclusion

In this study, a soft-switched PWM full bridge DC-DC converter with snubber cell and no additional control design is proposed. The proposed soft-switched converter is very advantageous thanks to its features such as easy applicability and no need for additional control signals. Theoretical analyzes and operating stages of the presented PWM converter were explained in detail and supported by relevant visuals. Afterwards, the theoretical analyzes of the converter were verified with a simulation circuit with 33 kHz switching frequency, 100 V output voltage and 80 A output current values. After the simulation, it was observed that the main switches turned on with ZCS and turned off with ZVS, and the auxiliary switches turned on with ZCS and turned off with ZVZCS. Also, it was observed that D_{s3} diode turns off with ZVS and D_{s4} diode turns on with ZVZCS.

6. References

- Anyalebechi, A & Ogboh, V 2019, "A Novel Soft Switching PWM Dc-Dc Converter", vol. 13, pp. 66-76
- Bai, H., Nie, Z and Mi, C.C 2010, "Experimental Comparison of Traditional Phase-Shift, Dual-Phase-Shift, and Model-Based Control of Isolated Bidirectional DC-DC Converters," in IEEE Transactions on Power Electronics, vol. 25, no. 6, pp. 1444-1449.
- Bodur, H., Yesilyurt, H., Akboy, E., & Ting, N. S., (2020). A novel active snubber cell for soft-switched isolated PWM half-bridge converter. *Electrical Engineering*, vol. 102, pp. 1821-1830.
- Bodur, H., Yesilyurt H and Ozel, H 2013, "An improved lossless passive snubber cell for PFC boost converter," 2013 3rd International Conference on Electric Power and Energy Conversion Systems, pp. 1-6.
- Ching, T. W. and Chan, K. U. 2008 "Review of soft-switching techniques for high-frequency switched-mode power converters," 2008 IEEE Vehicle Power and Propulsion Conference, pp. 1-6.
- Chen, Z., Chen, Y and Chen, Q 2019, "Isolated Series-Capacitor-Based Full-Bridge Converter with Reduced Circulating Losses and Wide Soft Switching Range," in IEEE Journal of Emerging and Selected Topics in Power Electronics, vol. 7, no. 2, pp. 1272-1285.
- Feizi, M and Beiranvand, R 2020, "An Improved Phase-Shifted Full-Bridge Converter with Extended ZVS Operation Range for EV Battery Charger Applications," 2020 11th Power Electronics, Drive Systems, and Technologies Conference (PEDSTC), pp. 1-6.
- Ibrahim, O., Yahaya, N.Z., Saad N. and Ahmed, K. Y. 2016 "Design and simulation of phase-shifted full bridge converter for hybrid energy systems," 2016 6th International Conference on Intelligent and Advanced Systems (ICIAS), pp. 1-6, doi: 10.1109/ICIAS.2016.7824043.
- Ruan, X 2014, Design and Simulation of ZVZCS Phase-Shifted Full Bridge PWM Converter. doi/book/10.1002/9781118702215
- Tran, D., Yu, S., Vu, & Choi, H.W 2016, "A novel soft-switching full bridge converter," 2016 IEEE 8th International Power Electronics and Motion Control Conference (IPEMC-ECCE Asia), pp. 3226-3229.
- Saygun, A, Beser, E & Unlu, M 2017, "COMPARATIVE STUDY OF SOFT SWITCHING METHODS USED IN DC-DC CONVERTER", *Journal of Naval Sciences and Engineering*, 13 (1) , pp. 1-22.
- Wu, T 2016, "Decoding and Synthesizing Transformerless PWM Converters", in IEEE Transactions on Power Electronics, vol. 31, no. 9, pp. 6293-6304.

An Advanced Visible Light Communication Technique: Li-Fi (Light Fidelity)

Büşra AYDIN¹*[0000-0002-5465-5446] and Çağlar DUMAN²[0000-0002-1845-8605]

¹ busra.aydin26@erzurum.edu.tr, Erzurum Technical University

² caglarduman@erzurum.edu.tr, Erzurum Technical University

Abstract

Light Fidelity (Li-Fi) in which light emitting diodes (LEDs) are used for data transfer is a promising alternative to Wireless Fidelity (Wi-Fi). Li-Fi systems use the visible light wavelength range (380-750 nm) of the electromagnetic spectrum. Therefore, lighting and data transmission can be carried out at the same time. In this paper, we made fundamental analysis of an indoor Li-Fi system using LED arrays by lighting and data transmission simulations. The simulation results showed that the examined Li-Fi system offers illumination and data transmission in accordance with the standards.

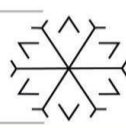
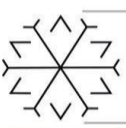
Keywords. Light fidelity, visible light communication, signal to noise ratio

1. Introduction

Today there is a high demand for wireless mobile communication systems. However, as a result of this high demand, the available Radio Frequency (RF) bandwidth may be insufficient. For this reason, researchers have investigated regions of the electromagnetic spectrum that can be alternatives to the RF spectrum. Promising results have been obtained in studies using visible light wavelengths (Ergül et al., 2015). One of these studies is visible light communication (VLC). VLC gained its real fame with the introduction of Li-Fi in 2011. Li-Fi is an advanced technic of VLC, it transmits data with LEDs, which have become spread in lighting systems, nowadays. Therefore, lighting systems offer suitable infrastructure for Li-Fi systems (Haas et al., 2015). Thanks to fast switchability feature of the LEDs and wide spectrum of the visible light, transmission of large amount data is possible at high speeds. Li-Fi has potential for enormous cost savings and reduction of carbon footprint thanks to integration of lighting and communication missions. However, Li-Fi is still an emerging technology and it is not widely spread because of problems like short range and obstacle handling (Sarkar et al., 2015). There are various studies aiming to improve the performance of the VLC and Li-Fi systems in the literature.

In 2010, a simulation for indoor visible light communication is performed with MATLAB and Simulink by Nguyen et al. The illumination distributions and the root mean square delay propagation are analyzed. Lee et al. (2011) analyzed the indoor multipath reflections characteristics. Additionally, they concluded that VLC offers greater bandwidth than infrared communication. VLC gained popularity with Li-Fi, which was also announced by Harald Haas in 2011. Haas is the named inventor of this technology, which is introduced in his talk on TED global visible light communication (Haas et al., 2015). In 2015, carrierless amplitude phase modulation (CAP) is proposed by Haigh et al. for Li-Fi. CAP is computationally complex but high spectral efficiency is achieved in the band-limited Li-Fi channel. On the other hand, Çoğalan (2015) proposed a new multi-user transmission method in Li-Fi systems by using a compound eye transmitter and the non-negative feature of the transmitted signal. A power allocation approach based on the LED selection algorithm is proposed in same study. A study conducted in 2019, an optical cellular network configuration model is proposed. Evaluations are made depended on data rate and bit error rate (BER) performance. In addition, various modulation schemes have been applied for system improvements. In this study, 100 Gbps data transmission rate has been reached (Gismalla et al., 2019). In 2020, GaN-based micro light emitting diode (μ LED) array and orthogonal frequency division multiplexing (OFDM) are used and a high-speed VLC system for long distance applications is experimentally demonstrated. At 0.3, 2, 5, 10, 15 and 20 m distances, 11.74, 11.72, 10.11, 6.58, 2.84 and 1.61 Gbps speeds are achieved, respectively (Xie et al., 2020). In the study made by Nor (2021), hybrid systems to be created using millimeter wave communication (mmWave), Wi-Fi and Li-Fi and the performances of these systems are examined. It has been reported that the designed system performs better than traditional designs in terms of efficiency and user satisfaction.

The paper is organized as follows. In Section 2, theoretical calculations of lighting and transmission functions are described in detail. Simulation methods and the obtained results are discussed in Section 3. Finally, the paper is concluded in Section 4.



2. Li-Fi System Model

2.1. Basic Properties of LED Lights

Li-Fi systems are expected to provide lighting in accordance with standards in addition to data transmission. The illumination of an indoor can be obtained by the calculations described in this section. E_0 is direct illumination in room. As can be seen from equation (1), if LED arrays are used, E_0 is obtained from sum of direct illuminances (Mamus et al., 2016).

$$E_0 = \sum_{i=1}^{n_s} I(0) \cos^m(\phi_i) \cos(\psi) / d_{0i}^2 \quad (1)$$

In equation (1), $I(\phi)$ is the luminous intensity, ϕ is irradiance angle and $I(0)$ is center luminous intensity for a LED. Luminous intensity is a value based on ϕ because of the LEDs have the Lambertian radiation pattern. In equation (1), n_s represent number of LEDs, ψ is incidence angle and d_{0i} is distance between i -th LED and detector. Also, m is the order of Lambertian emission and it is calculated with the semi-angle at half illuminance of LED $\phi_{1/2}$ as in equation (2) (Gfeller and Bapst, 1979; Kahn and Barry, 1997; Komine and Nakagawa, 2004).

$$m = -\ln 2 / \ln(\cos \phi_{1/2}) \quad (2)$$

Illumination must be range of 300 lx to 1500 lx for offices according to standards of International Organization for Standardization (ISO) (Mamus et al., 2016).

2.2. Received Power from LED Lights

The optical power transmitted by the LEDs can reach a point on the receiver or on a reflective surface. The reflective surface acting as a point light source. The optical power can reach to the detector after single or multiple reflections. The total optical power has two basic components based on direct line-of-sight optical channel DC gain ($H(0)$) and reflection optical channel gain on the reflected path ($dH(0)_{ref}$). $H(0)$ is expressed as in (3). It should not be forgotten, the receiver cannot detect the light when the angle of incidence ψ is greater than the receiver field of view (FOV) angle Ψ_c (Gfeller and Bapst, 1979; Kahn and Barry, 1997).

$$H(0) = \begin{cases} \frac{(m+1)A}{2\pi d_0^2} \cos^m(\phi) T_s(\psi) g(\psi) \cos(\psi), & 0 \leq \psi \leq \Psi_c \\ 0, & \psi \geq \Psi_c \end{cases} \quad (3)$$

In (3) $g(\psi)$, A and $T_s(\psi)$ are optical concentrator gain, physical area of the detector and gain of the optical filter, respectively. $g(\psi)$ is calculated as in (4) where, n is the refractive index of the photodetector lens (Gfeller and Bapst, 1979; Kahn and Barry, 1997; Komine and Nakagawa, 2004).

$$g(\psi) = \begin{cases} \frac{n^2}{\sin^2 \Psi_c}, & 0 \leq \psi \leq \Psi_c \\ 0, & \psi \geq \Psi_c \end{cases} \quad (4)$$

$dH(0)_{ref}$ can be obtained from (5) (Komine and Nakagawa, 2004).

$$dH_{ref}(0) = \begin{cases} \frac{(m+1)A}{2\pi d_1^2 d_2^2} \rho dA_{wall} \cos^m(\phi_1) \cos(\theta_1) \cos(\theta_2) T_s(\psi) g(\psi) \cos(\phi_2), & 0 \leq \psi \leq \Psi_c \\ 0, & \psi \geq \Psi_c. \end{cases} \quad (5)$$

In (5), ρ is reflection factor. Geometry used in equation (5) is as in Figure 1 (Komine and Nakagawa, 2004; Albayrak and Türk, 2017).

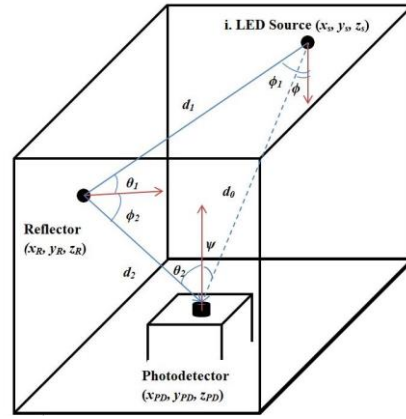
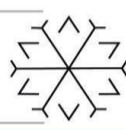


Figure 1: Propagation model of the incident beam.

The total received power (P_r) is as in equation (6).

$$P_r = \sum^{LEDs} \left\{ P_i H(0) + \int_{wall} P_i dH_{ref}(0) \right\}, \quad (6)$$

where P_i is optical power transmitted by a LED.

2.3. Signal to Noise Ratio

Ratio of signal power (S) to noise power (N) is called Signal to Noise Ratio (SNR). SNR is a parameter determining the quality of the communication system (Komine and Nakagawa, 2004). Shaaban et al. (2019) proposed a calculation method for SNR analysis. In this method thermal noise and inter symbol interference (ISI) noise are neglected. Therefore, noise components consist of shot noise and amplifier noise. S calculation is expressed as in (7).

$$S = \gamma^2 P_r^2 \quad (7)$$

where γ is photodetector conversion efficiency. Sum of the shot noise σ_{shot}^2 and the amplifier noise σ_{am}^2 gives the variance N as shown in equation (8).

$$N = \sigma_{shot}^2 + \sigma_{am}^2 \quad (8)$$

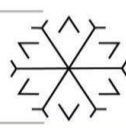
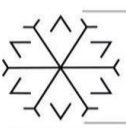
σ_{shot}^2 is obtained from equations (9) and (10).

$$\sigma_{shot}^2 = 2q\gamma(P_r + P_n)B_n \quad (9)$$

$$B_n = I_2^2 R_b \quad (10)$$

In these equations, q , B_n and P_n represent the electronic charge, the equivalent noise bandwidth and the noise power of the ambient light, respectively. Additionally, I_2 is noise bandwidth factor; it is function of the transmitter pulse shape and equalized pulse shape only, and is independent of bit rate. For example, $I_2 = 0.562$ for a rectangular transmitter pulse shape and a full raised-cosine equalized pulse shape (Kahn and Barry, 1997). R_b is data transmission rate of the system. Depended on amplifier noise density (i_{am}) and amplifier bandwidth (B_a), variance of the amplifier noise is expressed as in equation (11) (Shaaban et al., 2019).

$$\sigma_{am}^2 = i_{am} B_a \quad (11)$$



3. Simulation Method and Results

In order to perform basic lighting and data transmission analyzes of Li-Fi systems, the indoor visible light communication system model shown in Figure 2 is used. The visible light communication system is simulated using MATLAB with parameters given in Table 1.

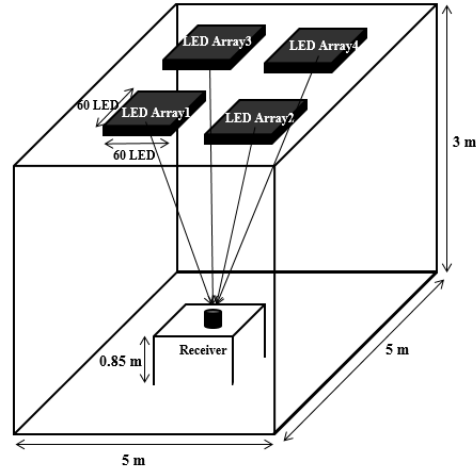


Figure 2: Model of indoor visible light wireless communication system.

Table 1: Parameters used for simulation.

Parameters	Symbol	Value
Optical power transmitted by a LED	P_t	20 mW
Power angle at half-light	$\phi_{1/2}$	70
Light intensity	$I(0)$	0.73 cd
Number of LEDs in a LED array	-	3600 (60 × 60)
Distance between LEDs	-	0.01 m
Size of LED luminaire	-	0.59 × 0.59
FOV	ψ_c	60°
Photodetector physical area	A	1.0 cm ²
Optical filter gain	$T(\psi)$	1.0
The refractive index of the photodetector lens	n	1.5
Reflection coefficient of the wall	ρ	0.8
The noise power of the ambient light	P_n	19.272 μW
Noise bandwidth factor	I_2	0.562
The data transmission rate	R_b	100 Mbps
The amplifier noise density	i_{am}	5 pA/√Hz

The direct illumination in the room is calculated between 313.52 lx and 1211.49 lx as in Figure 3. These values are in the range of 300 lx to 1500 lx, which ISO has determined as required lighting for offices.

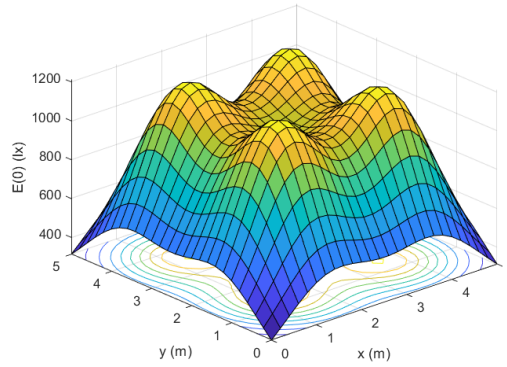
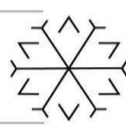


Figure 3: Direct illumination distribution.

The optical signals reach to the receiver through two paths as direct and reflected. The received power distribution in the room is obtained as in Figure 4. The direct received optical power (P_d) is calculated between -2.83 dBm and 3.97 dBm.

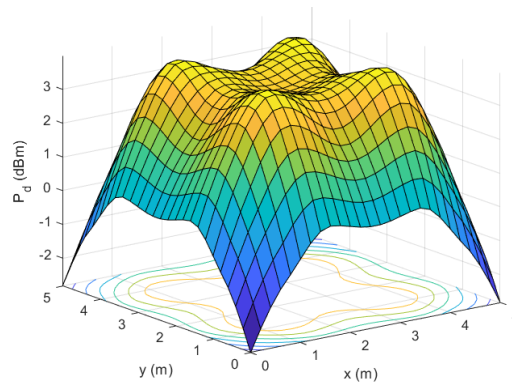


Figure 4: The distribution of direct received optical power.

The optical power distribution formed because of reflected light from the walls is obtained as in Figure 5. The highest value of received optical power from reflected path (P_{ref}) is obtained as -3.64 dBm.

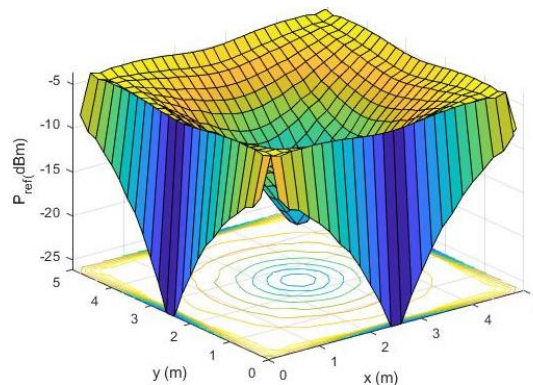


Figure 5: The distribution of received optical power from reflected path.

The sum of the optical power components taken from the direct and reflected paths gives the total received optical power. The total received optical power (P_r) distribution is obtained between -2.83 dBm and 4.22 dBm. Distribution of the total received optical power is obtained as in Figure 6.

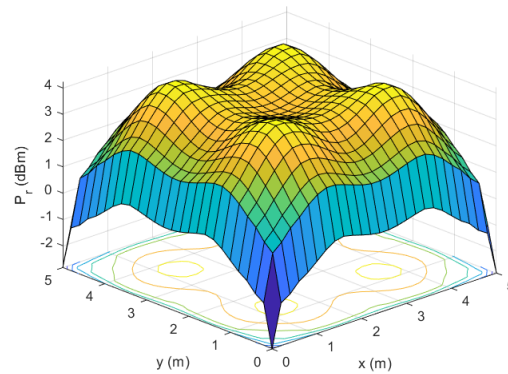


Figure 6: The distribution of total received optical power.

Distribution of the SNR without inter symbol interference effect is obtained as in Figure 7. The SNR values are calculated between 61.59 dB and 74.44 dB. All simulation results are compatible with other studies in the literature (Komine et al., 2004; Shaaban et al., 2019).

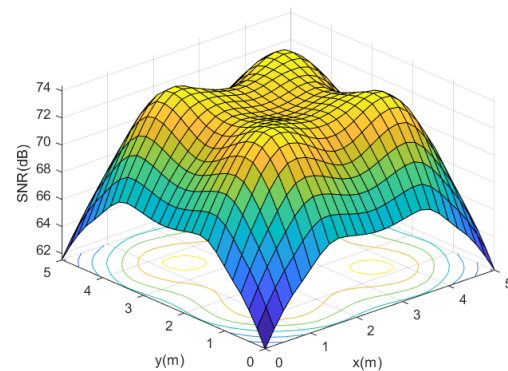


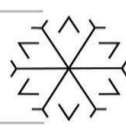
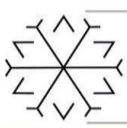
Figure 7: The distribution of SNR.

4. Conclusion

Li-Fi is a low-cost, environmentalist and high-speed data transmission technology. In order to benefit from the full potential of Li-Fi, problems such as obstacle handling and short distance should be solved. In this study, basic lighting and data transmission analyzes of an indoor Li-Fi system are performed with MATLAB simulations. Lighting in room is calculated in the range of 313.52 lx to 1211.49 lx which is sufficient lighting for the office according to the standards. On the other hand, the use of LED arrays has increased obtained optical power. In addition, the first reflections are calculated and the constructive effect of the reflections on the received optical power is observed. SNR, which is a measure of system quality, is calculated between 61.59 dB and 74.44 dB. These values are sufficient for uninterrupted communication, but inter symbol interference should not be neglected for a more realistic calculation. Also, by using different optical modulation techniques and/or advanced LED and photodetector technologies, high speed and long-range communication will be possible.

References

- Albayrak, C. and Türk, K. (2017) 'Rate adaptive system for visible light communications', 40th International Conference on Telecommunications and Signal Processing (TSP), 5 - 7 July, 200-203, Barcelona, Spain.
- Cogalan, T., Haas, H. and Panayirci, E. (2015) 'Power control-based multi-user Li-Fi using a compound eye transmitter', 2015 IEEE Global Communications Conference (GLOBECOM), 1-6.
- Ergul, O., Dinc, E. and Akan, O. B. (2015) 'Communicate to illuminate: State-of-the-art and research challenges for visible light communications', Physical Communication, 17, 72-85.
- Haas, H., Yin, L., Wang, Y. and Chen, C. (2015) 'What is lifi?', Journal of lightwave technology, 34(6), 1533-1544.
- Haigh, P. A., Le, S. T., Zvanovec, S., Ghassemlooy, Z., Luo, P., Xu, T. and Canyelles-Pericas, P. (2015) 'Multi-band carrier-less amplitude and phase modulation for bandlimited visible light communications systems', IEEE Wireless Communications, 22(2), 46-53.



- Gismalla, M. S. , Abdullah, M. F., Mabrouk, W. A., Das, B. and Niass, M. I. (2019) 'Data Rate and BER Analysis for Optical Attocells Configuration Model in Visible Light Communication', 2019 International Conference on Information Science and communication Technology (ICISCT).
- Gfeller, F. R. and Bapst, U. (1979) 'Wireless in-house data communication via diffuse infrared radiation', Proceedings of the IEEE, 67(11), 1474-1486.
- Kahn, J. M. and Barry, J. R. (1997) 'Wireless infrared communications', Proceedings of the IEEE, 85(2), 265-298.
- Komine, T. and Nakagawa, M. (2004) 'Fundamental analysis for visible-light communication system using LED lights', IEEE Transactions on Consumer Electronics, 50(1),100-107.
- Lee, K., Park, H. and Barry, J. R. (2011) 'Indoor channel characteristics for visible light communications', IEEE Communications Letters, 15(2), 217-219.
- Mamus, A., Yesilkaya, A. and Panayirci, E. (2016) 'Kapalı Ortam Görünür Isık Kanallarının Modellenmesi ve Denkleştirilmesi', EMO Bilimsel Dergi , 5 (9) , 18-29.
- Nguyen, H. Q., Choi, J.-H., Kang, M., Ghassemlooy, Z., Kim, D. H., Lim, S.-K. and Lee, C. G. (2010) 'A MATLAB-based simulation program for indoor visible light communication system', 2010 7th International Symposium on Communication Systems, Networks and Digital Signal Processing, 21-23 July, Newcastle Upon Tyne, UK.
- Nor, A. M. (2021) 'Access point selection in beyond 5G hybrid mmWave/Wi-Fi/Li-Fi', Physical Communication, 46.
- Sarkar, A., Agarwal, S. and Nath, A. (2015) 'Li-Fi technology: data transmission through visible light', International Journal of Advance Research in Computer Science and Management Studies, 3(6).
- Shaaban, R., Ranganathan, P. and Faruque, S. (2019) 'Visible Light Communication Security Vulnerabilities in Multiuser Network: Power Distribution and Signal to Noise Ratio Analysis', Perspectives on Asian Tourism, 1–13.
- Xie, E., Bian, R., He, X., Islim, M. S., Chen, C., McKendry, J. J. and Dawson, M. D. (2020) 'Over 10 Gbps VLC for long-distance applications using a GaN-based series-biased micro-LED array'. IEEE Photonics Technology Letters, 32(9), 499-502.

ECC Implementation on FPGA with Fast and Pipelined Arithmetic Units

Sukru Uzun^{1*}, Mehmet Akif Akkaya², Serdar Suer Erdem, Furkan Cayci

Department of Electronic Engineering, Gebze Technical University (GTU), Turkey

¹sukruuzun@gtu.edu.tr,

²akifakkaya@gtu.edu.tr,

²serdem@gtu.edu.tr,

²furkan.cayci@gtu.edu.tr,

Abstract

In the last decade, Elliptic Curve Cryptosystems (ECC) has been increasing in popularity due to their smaller bit sizes and convenience of modular reduction compared to other public-key cryptosystems like RSA. Since mid 80s, ECC has been studied widely in academia and explored in the industry to be used as an efficient public-key cryptography option. Many software and hardware implementations have been developed to implement most compact and efficient design. However, there are still potential improvements to accelerate computations in FPGAs. Even though, ASIC is mostly the fastest way to implement any cryptographic algorithm in any field, due to their price, FPGAs are still widely preferred in practice especially for prototyping.

In this work, we present an enhanced design of multiplication and pipelined ECC computation schedule in order to increase throughput of scalar multiplication. Despite the fact that, there are two major prime fields of ECC that are $GF(p)$ and $GF(2^m)$, our work covers only $GF(p)$ which is one of the most common one and also suggested by National Institute of Standards and Technology (NIST). P256 (256-bit key length) is one of the most popular curves in $GF(p)$ prime field because of its key size and security correlation. Our design performs both point multiplication and addition within 0.2 ms and runs at 90 MHz.

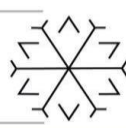
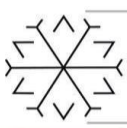
Mhz frequency for P256.Keywords. Elliptic Curve Cryptosystem, Big Integer Arithmetic, Fast Multiplication, FPGA, High-Performance

1. Introduction

Elliptic Curve Cryptography (ECC) (Koblitz, 1987) is a public-key cryptographic system which lets the user obtain equivalent security with less key sizes compared to a well known public-key crypto algorithm, RSA (Lenstra, Verheul, 2001). Without compromising security aspects, acquiring high throughput, low resource usage and low power consumption have become of great importance. Since improving the performance of ECC is essential, several methods have been proposed to speed up the computation of the ECC. One of these techniques are utilizing Mersenne primes which come with easiness of the modular reduction operation, as recommended by the National Institute of Standards and Technology (NIST) (National Institute of Standards and Technology, 2013). We use the P256 curve though which is mostly used and equivalent to RSA 3072 key size.

Scalar multiplication ($Q = kP$) which includes point additions and doublings is a fundamental process in ECC. In order to calculate point Q, Point P is added to itself ($k - 1$) times on the same curve. Points P and Q are public points, while scalar k is a private scalar number. Given the values of P and Q, it is computationally challenging to obtain the value of k because of the Discrete Logarithm Problem (DLP) (McCurley, 1990).

In order to accelerate these units various works have been studied. The basis of accelerating these operations depends on fast multiplication. In (Marzouqi, Al-Qutayri, Salah, Schinianakis, Stouraitis, 2016), an extensive pipelining technique for Karatsuba-Ofman method is employed for high throughput. Another fast method for multiplication is Toom-Cook (Ding, Li, Gu, 2019). This method is considerably fast but its resource usage is high. In (Mehrabi, Doche, Jolfaei, 2020), (Asif, Hossain, Kong, Abdul, 2018), (Matutino, Araujo, Sousa, Chaves, 2017), RNS based point multiplication has been studied to fasten common arithmetic operations for P256 prime. (Guillermin 2010) is also implemented using RNS based arithmetic units, moreover it has been designed



by using Montgomery ladder. Then parallelism and pipelining lead to high performance. In addition to these implementations there are some designs which contain Digital Signal Processing (DSP) units to enhance multiplication and addition as well. (Mcivor, Mcloone, Mccanny, 2006), (Guneysu, Paar, 2008), (Varchola, Guneysu, Mischke, Microecc, 2011), (Ananyi, Alrimeih, Rakhmatov, 2009), (Alrimeih, Rakhmatov, 2014) and (Wu, 2015) are example of using DSP in their designs. Most of them are committed to a single NIST prime field. In industrial applications, generally only one NIST prime field is used where a prime field of ECC is required.

In this paper, we describe the design and implementation of a GF (p) prime field of ECC. The design is built to support the NIST P256 curve. Other curves, which have smaller key sizes, are also supported by only changing the modular reduction module. We mainly focus on multiplication, scheduling and pipelining. We implemented an efficient schedule using two multiplications, one addition, three modular reduction and one modular inversion units. The main drawback is the number of DSP units therefore we have tried to optimize it to maintain portability. Schedule and pipelining can be adjusted for targets which have different resource requirements.

The remainder of this paper is organized as follows. Section II presents the overall ECC and its mathematical background. Section III details the design of the main arithmetic blocks including the addition/subtraction, multiplication, modular reduction and modular inverse units. Pipelining and scheduling are described in Section IV. Implementation results and comparisons with other designs can be found in Section V and Section VI concludes with some results.

2. Elliptic Curve Cryptography

In the following section, mathematical background of ECC will be introduced briefly, relevant to this work. Elliptic Curves are versatile mathematical objects that we can utilize them to make encryption, decryption digital signature and key exchange. These are all fundamental processes in cryptography and this is why it is called a cryptosystem. Note that only GF (p) will be subject of this work since GF (2^m) is deprecated by NIST due to their limited adoption (Chen, Moody, Regenscheid, Randall, 2019).

ECC constructions rely on group theory to guarantee the security of the system. An elliptic curve over prime field GF (p) is represented by (x, y) coordinates. These coordinates should satisfy the following equation which is called Weierstrass equation.

$$y^2 = x^3 + ax^2 + b \quad (1)$$

where $a, b \in GF(p)$ and $4a^3 + 27b^2 \neq 0$ and p be a prime with $p > 3$. We can obtain (x, y) points by making some arithmetic computations based on the group of points defined on this curve. There are basically two types of arithmetic operations which are addition $R = P + Q$ and doubling $R = 2P, P = Q$. The fundamental process in ECC is scalar multiplication ($Q = kP$) and it can be calculated by Algorithm 1 or by simply adding repeated points (i.e. $P + P + \dots + P$) for k-times.

In affine coordinates, point addition and point doubling computations are very rough because of division operation. According to affine formulas, modular inversion has to be used after every addition or doubling. However, in projective coordinates, we only operate modular inversion once per scalar multiplication. In contrast, there are some burdens which are additional add-sub and multiplication operations. It is still much more worthwhile to compute in projective coordinates. The Weierstrass equation has some changes in projective coordinates which is described in the equation 2.

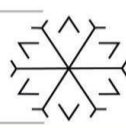
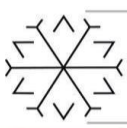
$$Y^2Z = X^3Z + a_4XZ^2 + a_6b \quad (2)$$

The point (X_1, Y_1, Z_1) on equation 2 corresponds to the affine point $(X_1/Z_1, Y_1/Z_1)$ when $Z_1 \neq 0$.

– Addition

In order to compute point addition in affine coordinates, $1 + 2M + 6S$ is required. On the other hand, $15M + 7S$ is needed to compute in projective coordinates.

$$\begin{aligned} A &= Y_2Z_1 - Y_1Z_2, \quad B = X_2Z_1 - X_1Z_2, \quad C \\ &= A^2Z_1Z_2 - B^3 - 2B^2X_1Z_2, \end{aligned}$$



$$\begin{aligned} X_3 &= BC, & Z_3 &= B^3Z_1Z_2, \\ Y_3 &= A(B^2X_1Z_2 - C) - B^3Y_1Z_2 \end{aligned} \quad (3)$$

- Doubling

In point doubling, the number of multiplication is more than point addition, however add-sub operations are less. In affine coordinates, by doing $I + 6M + 4S$ operations point doubling should be done. And $18M + 4S$ for the other.

$$\begin{aligned} A &= a_4Z_1^2 - 3X_1^2, & B &= Y_1Z_1, C \\ &= X_1Y_1B, & D &= A^2 - 8C \\ X_3 &= 2BD, & Z_3 &= 8B^3, \\ Y_3 &= A(4C - D) - 8Y_1^2B^2 \end{aligned} \quad (4)$$

Please note that, number of arithmetic operations, which mentioned above, are calculated with two input arithmetic units. Parameter multiplication by simple integers is also counted.

3. Proposed Design for Modular Arithmetic

Figure 1 illustrates the proposed circuit design used for ECC modular arithmetic operations. It has the following four units: Addition and subtraction, multiplication, modular reduction, and modular inversion.

Addition and subtraction unit, multiplication unit, and modular reduction unit are used for modular multiplication. The latencies of these three units are important because ECC scalar point multiplication needs a large number of modular multiplications. Multiplication is slower than addition and subtraction. Moreover, it is even slower than the modular reduction for the P256 curve because the reduction is performed modulo the special prime $2^{256} - 2^{224} + 2^{192} + 2^{96} - 1$. Thus, hardware resources are mainly used to improve the speed of the multiplier unit so that this unit has a similar latency with the other two units.

Algorithm 1 Scalar Multiplication

```

1: Input: P (X, Y), A(X1, Y1), B(X2, Y2), int(k)
2: Output: Q = k.P, Q(0, 0)
3: for i = 0 : l - 1 do
4:   A = P + Q
5:   B = 2P
6:   if k(i) = 1 then
7:     Q = A
8:   end if
9:   P = B
10:  k = k >> 1
11: end for

```

In Fig. 1, the memory unit is composed of BRAMs and flip-flops. In order to reduce area usage and increase max. frequency, we tried to avoid multiplexers so that BRAM is the sensible solution for that matter. Every arithmetic module has its own BRAM cell with fixed size. Their sizes are determined by Fig. 5 and Fig. 6. Each module has its own information about, how many different data will be used for each process. Address controller's main purpose is to direct corresponding data to the arithmetic unit. It's only responsibility is adjusting the BRAM address. Therefore, we do not have to use a multiplexer for data but we do for addresses whose width is much smaller than data width.

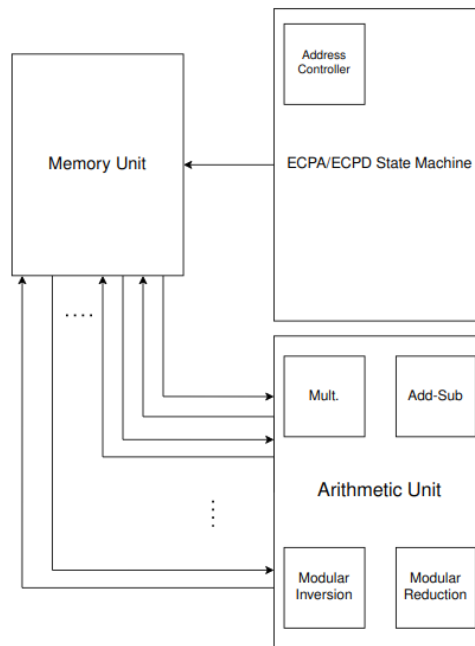


Fig. 1 Hardware Implementation of ECC Core

Addition-Subtraction

Addition and subtraction operations are easy to implement compared to other units. Thanks to summing operations and carry chain units in most advanced FPGA, these two operations require less complexity. We implement both arithmetic operations in one IP (Intellectual Property). As mentioned before, the multiplication unit is responsible for the latency mainly. Thus, addition and subtraction units are optimized for area complexity rather than time complexity. And, its latency is similar to the multiplication unit. The design of this unit is scalable to enable use of the unit for other prime fields.

Multiplication

Multiplication of large integers is a commonly used operation in many cryptographic algorithms. Performing this operation in embedded systems is a computationally challenging task. As mentioned, there are some multiplication architectures for hardware platforms however, they do not provide sufficient performance for large-size multiplication operations. Our design uses DSP48E1 slices available on Xilinx 7 Series FPGAs.

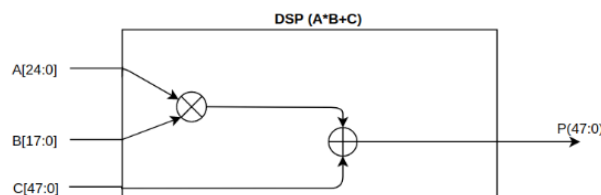


Fig. 2 Accumulator of DSP slice

To perform a 256x256 multiplication using these slices, we developed a special architecture. In this architecture, the first input is divided into 24 bit and the second input is divided into 17 bit parts. Then, the 24x17 bit partial products are calculated by the DSP slices. The partial products are combined by using 48 bit C ports of the DSP slices.

$$A = A(255 : 232) \dots A(47 : 24) \parallel A(23 : 0)$$

$$B = B(255 : 239) \dots B(33 : 17) \parallel B(16 : 0) \tag{5}$$

Figure 3 illustrates the straightforward implementation of 256x256 bit product from the smaller 24x17 partial products. The partial products are computed and combined by 11x16=176 DSP slices. As seen, the partial products should be appropriately shifted before adding together.

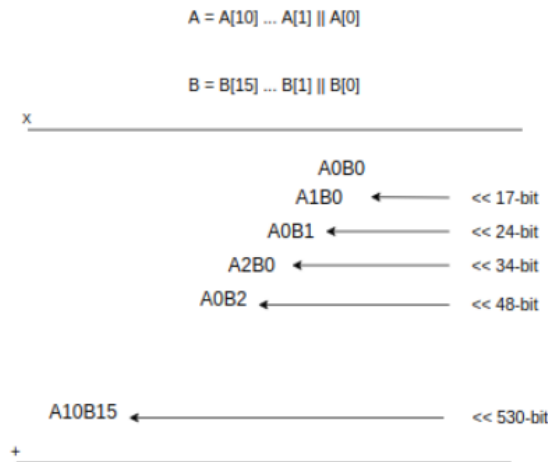


Fig. 3 Straightforward 256x256 bit multiplication with 24x17 bit DSP slices

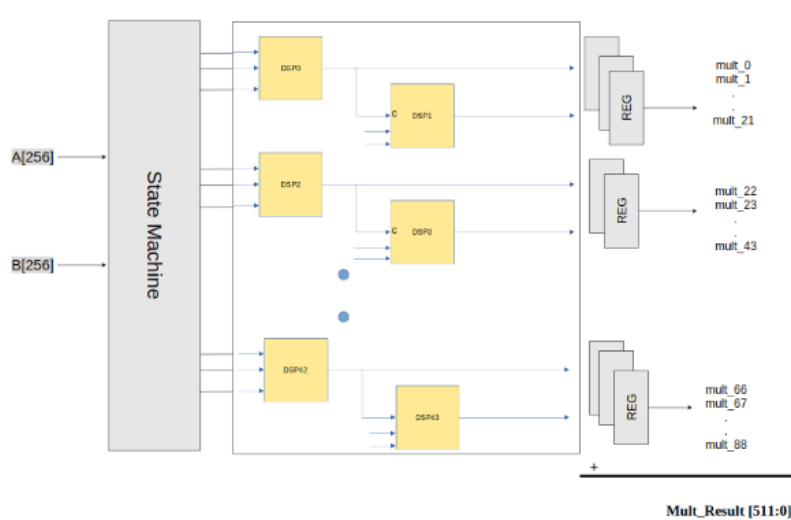


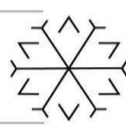
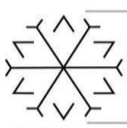
Fig. 4 Proposed 256x256 bit multiplication by using 24x17 bit DSP slices

Unfortunately, the straightforward implementation in Figure 3 has a very large critical path. Thus, we propose the architecture in Figure 4 to compute and accumulate the partial products of 256x256 bit multiplication. A state machine was written and a maximum of two DSP is connected at once. The intermediate results are registered and then they are added in 3 steps. The design uses 44 DSP slices and produces 256x256 bit multiplication in 5 clocks.

Modular Reduction

Algorithm 2 presents the modular reduction for the prime field used in the P256 curve. As seen, four addition, four subtraction and two scaling are required. The result should be in the range of $-4p < x < 5p$. x is defined in algorithm 2.

We also design the modular reduction unit so that its latency is the same as the 256x256 multiplication unit. Therefore we could minimize the resource usage. Reduction unit is based on a well-known model which is called Wallace tree. Modular reduction unit with the Wallace tree is shown in Fig. 2. This figure represents only one cell of the reduction module. For the P256 curve, there are eight cells.



Modular Inverse

Modular inverse has the largest latency in all units. Fortunately, we need only one modular inverse per scalar multiplication. Although it is used once, its latency is crucial for the system throughput.

As mentioned before, modular inverse is needed for the conversion from projective coordinates (X_1, Y_1, Z_1) to affine coordinates (X, Y) as follows.

$$X = X_1(Z^{-1} \bmod P \ 256), Y = Y_1(Z^{-1} \bmod P \ 256) \tag{6}$$

Binary extended euclidean method is implemented to accelerate modular inversion. There are special studies (Hossain, Kong, 2015) which just focus on this unit, to improve its performance. In our work, we derive it from this paper (Savas, Koc, 2000). The whole algorithm can be obtained there. Comparing modular inversion studies, ours has good results in terms of resource usage and latency among others.

Algorithm 2 Modular reduction specified for the NIST curve P256

- 1: Input: 512 bit nonnegative integer $x = (x_{15}, \dots, x_2, x_1, x_0)$ in base 2^{32} .
 - 2: Output: $x \bmod 2^{256} - 2^{224} + 2^{192} - 1$
 - 3: Concatenate 32-bit partials to 256-bit integer
 - $Z_1 = (x_7, x_6, x_5, x_4, x_3, x_2, x_1, x_0),$
 - $Z_2 = (x_{15}, x_{14}, x_{13}, x_{12}, x_{11}, 0, 0, 0),$
 - $Z_3 = (0, x_{15}, x_{14}, x_{13}, x_{12}, 0, 0, 0),$
 - $Z_4 = (x_{15}, x_{14}, 0, 0, 0, x_{10}, x_9, x_8),$
 - $Z_5 = (x_8, x_{13}, x_{15}, x_{14}, x_{13}, x_{11}, x_{10}, x_9),$
 - $Z_6 = (x_{10}, x_8, 0, 0, 0, x_{13}, x_{12}, x_{11}),$
 - $Z_7 = (x_{11}, x_9, 0, 0, x_{15}, x_{14}, x_{13}, x_{12}),$
 - $Z_8 = (x_{12}, 0, x_{10}, x_9, x_8, x_{15}, x_{14}, x_{13}),$
 - $Z_9 = (x_{13}, 0, x_{11}, x_{10}, x_9, 0, x_{15}, x_{14})$
 - 4: Compute $x = z_1 + 2z_2 + 2z_3 + z_4 + z_5 - z_6 - z_7 - z_8 - z_9 \bmod 2^{256} - 2^{224} + 2^{192} - 1$
-

4. Pipeline and Scheduling

Our design uses pipelining to reduce latency. Figure 5 shows the pipelining of point addition and Figure 6 shows the pipelining of point multiplication. As seen in Figure 4, the multiplication unit pipeline has two levels of DSPs.

Note that, we use two multiplications, one addition and three modular reductions in the arithmetic unit. Multiplication unit is our bottleneck because of the number of DSPs so that we determine other unit numbers in regard to it. For instance, if we could use 4 multiplications, we would increase the number of addition and modular reduction units. It is all up to the hardware platform which will be used. We decided to use a reasonable amount of DSPs for other platforms as well.

This pipeline method is implemented and adjusted by state machines on the hardware side. These number of states may be reduced, yet Fig. 5 and Fig. 6 are the best options according to our study. Modular inversion unit is not added to these tabs because it is used once for per scalar multiplication, it is not needed for intermediate processes in projective coordinate.

	1	2	3	4	5	6	7	8	9	10	11	12	13	14	15	16	17	18
1. Mult	M1=X2.Z1	M3=Y2.Z1	M5=Z1.Z2		M7=C.C	M9=A.A	M11=M7.C	M13=M5.M9	M15=M7.M8				X3=B.C		M16=S1.A			
2. Mult	M2=X1.Z2	M4=Y1.Z2	M6=Z1.M2		M8=M4.C	M10=M5.C	M12=M6.M7	M14=M7.M2	Z3=M7.M10									
1. Add-Sub			C=M1-M2	A=M3-M4					A1=M11+M12		B=M13-A1		S1=M14-B				Y3=M16-M15	
1. Reduction		M1	M3	M5		M7	M9	M11	M13	M15				X3		M16		Y3
2. Reduction		M2	M4	M6		M8	M10	M12	M14	Z3								
3. Reduction				C	A					A1		B		S1				

Fig. 5 Pipelined point addition schedule

	1	2	3	4	5	6	7	8	9	10	11	12	13	14	15	16
1. Mult	M1=X.X	B=Y.Z	M4=a.M2	C=M3.B	M7=YY	M9=8.C	Z3=M8.M6	M12=M10.M7	M14=2.B		X3=M14.D		M15=A.S1			
2. Mult	M2=Z.Z	M3=X.Y	M5=3.M1	M6=B.B	M8=8.B	M10=8.M6	M11=AA	M13=4.C								
1. Add-Sub					A=M4+M5				D=M11-M9		S1=M13-D				Y3=M15-M12	
1. Reduction		M1	B	M4	C	M7	M9	Z3	M12	M14		X3		M15		
2. Reduction		M2	M3	M5	M6	M8	M10	M11	M13							
3. Reduction						A				D		S1				Y3

Fig. 6 Pipelined point doubling schedule

5. Implementation

Our implementation is performed on Xilinx Virtex-7 FPGA platform. We also use the Xilinx Vivado 2018.3 program to synthesize our design. The proposed architecture runs at 90 MHz and consumes 7.2k slices, 88 DSP48 blocks (18x24-bit multipliers) and 8 BRAM blocks. Most of these values and detailed comparison with other studies are marked in Table 1.

Table 1. Comparison of scalar multiplication over P256

	Ref.	Hardware	Area (Slice)	DSP	Freq (MHz)	Latency (ms)
	Ours	Virtex-7	7.2k	88	90	0.2
	(Guneyesu, Paar, 2008)	XCV4FX12	1.7k	32	490	0.495
	(Wu, Wang, 2019)	XC7VX330t-3	8.4k	32	310	0.526
	(Marzouqi, Al-Qutayri, Salah, 2013)	XC5VLX50	10.2k	0	66.7	6.63
	(Feng, Li, 2017)	Stratix II	14.2k ¹	64	86.9	0.16
	(Mehrabi, Doche, Jolfaei, 2020)	Virtex-7	14k	560	125	0.25
	(Choi, Lee, Kim, Kim, 2018)	Virtex-6	18.6k	0	121.6	0.3
	(Ding, Li, Gu, 2019)	Virtex-6	7.6k [*]	48	291	0.054
	(Awaludin, Larasati, Kim, 2021)	Virtex-7	7.3k	136	204	0.158

^{*} Slices are estimated as LUT/4.

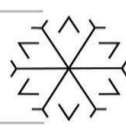
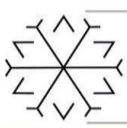
¹ In terms of ALM

In our design, we have focused on multiplications like most others. In our design, we focused on the P256 prime field which is one of the most used fields in industry and optimized multiplication. Therefore it supports 256x256 multiplication and below. Using modular multiplication or addition (Mehrabi, Doche, Jolfaei, 2020), (Alrimeih, Rakhmatov, 2014), (Awaludin, Larasati, Kim, 2021) is an option for these designs, however we decided to reduce the latency by scheduling. On the other hand, there are some studies (Guneyesu, Paar, 2008) which do not use modular reduction. Instead reduce values while doing addition or multiplication. In order to do that, lots of BRAM blocks have been used to keep modular values. Most of these studies (Mcivor, Mcloone, Mccanny, 2006), (Guneyesu, Paar, 2008), (Ananyi, Alrimeih, Rakhmatov, 2009), (Ding, Li, Gu, 2019), (Marzouqi, Al-Qutayri, Salah, 2013) present their design as a processor. By using these mostly repeated operations, making a simple processor might be the best idea of all. One of the other advantages of processors is, they usually support various prime fields. Basically, our design can be considered as a processor with three instructions which are point addition, point doubling and modular inversion. However, it is much more primitive than proposed processor architectures.

To sum up, we compared our implementation results and see that it has considerable place among other studies. As mentioned, we utilized scheduling and pipelining to find the best result of the scalar multiplication by using the predetermined units. The main difference with other works is our multiplication performance and scheduling tables.

6. Conclusion

We presented a novel ECC implementation for the P256 prime field with their arithmetic units for accelerating computationally expensive atomic blocks of modular operations over a restricted set of prime fields GF (p). Specifically, we focus on acceleration of multiplication. Due to point addition and doubling containing lots of multiplication in projective coordinates. Our design supports only NIST-recommended P256 prime. However, different prime fields can be supported implementing respective modular reduction



units. Our Xilinx Virtex-7 FPGA implementation, which runs at 90 MHz and consumes 7.2k-88/DSP-Slice, takes 0.2 ms to perform a typical scalar multiplication.

In our future work, we will focus on extending the proposed hardware architecture to implement other safe NIST prime fields (Lange, 1999) and want to focus on side-channel attacks and their countermeasure implementations.

References

Alrimeih, H., Rakhmatov, D. (2014) Fast and flexible hardware support for ecc over multiple standard prime fields. *IEEE Transactions on Very Large Scale Integration (VLSI) Systems* 22(12), 2661–2674. <https://doi.org/10.1109/TVLSI.2013.2294649>

Ananyi, K., Alrimeih, H., Rakhmatov, D. (2009) Flexible hardware processor for elliptic curve cryptography over nist prime fields. *IEEE Transactions on Very Large Scale Integration (VLSI) Systems* 17(8), 1099–1112. <https://doi.org/10.1109/TVLSI.2009.2019415>

Asif, S., Hossain, M.S., Kong, Y., Abdul, W. (2018) A fully rns based ecc processor. *Integration* 61, 138–149. <https://doi.org/https://doi.org/10.1016/j.vlsi.2017.11.010>, <https://www.sciencedirect.com/science/article/pii/S0167926017304467>

Awaludin, A.M., Larasati, H.T., Kim, H. (2021) High-speed and unified ecc processor for generic weierstrass curves over $gf(p)$ on fpga. *Sensors* 21(4). <https://doi.org/10.3390/s21041451>, <https://www.mdpi.com/1424-8220/21/4/1451>

Chen, L., Moody, D., Regenscheid, A., Randall, K. (2019) Recommendations for discrete logarithm-based cryptography: Elliptic curve domain parameters. Tech. Rep., National Institute of Standards and Technology

Choi, P., Lee, M.K., Kim, J.H., Kim, D.K. (2018) Low-complexity elliptic curve cryptography processor based on configurable partial modular reduction over nist prime fields. *IEEE Transactions on Circuits and Systems II: Express Briefs* 65(11), 1703–1707. <https://doi.org/10.1109/TCSII.2017.2756680>

Ding, J., Li, S., Gu, Z. (2019) High-speed ecc processor over nist prime fields applied with toom-cook multiplication. *IEEE Transactions on Circuits and Systems I: Regular Papers* 66(3), 1003–1016. <https://doi.org/10.1109/TCSI.2018.2878598>

Feng, X., Li, S. (2017) A high-speed and spa-resistant implementation of ecc point multiplication over $gf(p)$. In: 2017 IEEE Trustcom/BigDataSE/ICCESS. pp. 255–260. <https://doi.org/10.1109/Trustcom/BigDataSE/ICCESS.2017.245>

Guillermin, N. (2010) A high speed coprocessor for elliptic curve scalar multiplications over fp. *International Workshop on Cryptographic Hardware and Embedded Software* 6225, 48–64

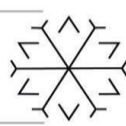
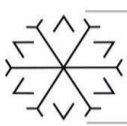
Guneysu, T., Paar, C. (2008) Ultra high performance ecc over nist primes on commercial fpgas. *Cryptographic Hardware and Embedded Systems – CHES* 5154

Hossain, M.S., Kong, Y. (2015) High-performance fpga implementation of modular inversion over f_{256} for elliptic curve cryptography. In: 2015 IEEE International Conference on Data Science and Data Intensive Systems. pp. 169–174. <https://doi.org/10.1109/DSDIS.2015.47>

Koblitz, N. (1987) Elliptic curve cryptosystems. *Mathematics of Computation* 48(177), 203–209

Lange, T. (1999): Safecurves: choosing safe curves for elliptic-curve cryptography daniel j. bernstein university of illinois at chicago & Lenstra, A., Verheul, E. (2001) Selecting Cryptographic Key Sizes. *Journal of Cryptology* 14(4), 255–293

Marzouqi, H., Al-Qutayri, M., Salah, K. (2013) An fpga implementation of nist 256 prime field ecc processor. In: 2013 IEEE 20th International Conference on Electronics, Circuits, and Systems (ICECS). pp. 493–496. <https://doi.org/10.1109/ICECS.2013.6815461>



- Marzouqi, H., Al-Qutayri, M., Salah, K., Schinianakis, D., Stouraitis, T. (2016) A high-speed FPGA implementation of an RSD-based ECC processor. *IEEE Trans. VLSI Syst* 21(1), 151–164
- Matutino, P.M., Araujo, J., Sousa, L., Chaves, R. (2017) Pipelined fpga coprocessor for elliptic curve cryptography based on residue number system. In: 2017 International Conference on Embedded Computer Systems: Architectures, Modeling, and Simulation (SAMOS). pp. 261–268. <https://doi.org/10.1109/SAMOS.2017.8344638>
- McCurley, K.S. (1990) The discrete logarithm problem. In: *Proc. of Symp. in Applied Math.* vol. 42, pp. 49–74. USA
- Mcivor, C., Mcloone, M., Mccanny, J. (2006) Hardware elliptic curve cryptographic processor over $gf(p)$. *IEEE Transactions on Circuits and Systems I: Regular Papers* 53(9), 1946–1957. <https://doi.org/10.1109/TCSI.2006.880184>,
- Mehrabi, M.A., Doche, C., Jolfaei, A. (2020) Elliptic curve cryptography point multiplication core for hardware security module. *IEEE Transactions on Computers* 69(11), 1707–1718. <https://doi.org/10.1109/TC.2020.3013266>
- National Institute of Standards and Technology (2013), Gaithersburg, MD, USA: FIPS 186-4–Digital Signature Standard (DSS), <https://doi.org/10.6028/NIST.FIPS.186-4>
- Savas, E., Koc, C.K. (2000) The montgomery modular inverse-revisited. *IEEE transactions on computers* 49(7), 763–766
- Varchola, M., Guneyasu, T., Mischke, O.: Microecc (2011) A lightweight reconfigurable elliptic curve crypto processor. In: 2011 International Conference on Reconfigurable Computing and FPGAs. pp. 204–210. <https://doi.org/10.1109/ReConFig.2011.61>
- Wu, T. (2015) Elliptic curve $gf(p)$ point multiplier by dual arithmetic cores. In: 2015 IEEE 11th International Conference on ASIC (ASICON). pp. 1–4. <https://doi.org/10.1109/ASICON.2015.7516997>
- Wu, T., Wang, R. (2019) Fast unified elliptic curve point multiplication for nist prime curves on fpgas. *Journal of Cryptographic Engineering* 9(4), 401–410

Development of a Fuzzy Logic Based Control Algorithm for Charge-Discharge of a Battery System

Cem MORKOÇ ¹*[0000-0002-1688-5259] and Uğur YÜZGEÇ ²[0000-0002-5364-6265]

¹cem.morkoc@bilecik.edu.tr, Bilecik Seyh Edebali University, Graduate Institute of Education, Energy Systems Engineering, Bilecik, Turkey

²ugur.yuzgec@bilecik.edu.tr, Bilecik Seyh Edebali University, Faculty of Engineering, Computer Engineering, Bilecik, Turkey

Abstract

In this study, a fuzzy logic controller-based battery charge-discharge control algorithm has been developed to obtain power from a simulation model of an energy system continuously and stably. The current and voltage of the DC busbar, as well as the battery unit, are continuously monitored and used as input data for the algorithm's fuzzy logic controller. And the output of the fuzzy logic controller used as duty ratio for the DC-DC buck boost converter's switching elements. Thus, charge-discharge control of a battery unit to be used as an energy storage unit in an energy system is provided with a developed fuzzy logic-based controller. Also, with the developed simulation model, suitable codes for the TMS320F28335 Digital Signal Processor (DSP) were produced with the embedded code generation method to be used in real world applications.

Keywords. Battery charger, energy storage systems, embedded code generation, the fuzzy logic controller

1. Introduction

These days when we have almost completed the first quarter of the 21st century, many different methods can be used to meet the ever-increasing energy needs. Although the method used to produce energy changes, energy storage systems are needed to ensure the continuity and stability of the energy obtained. When the relevant literature is examined, it is rarely possible to find applications, where the energy obtained, is used directly. However, this way of use greatly reduces the continuity and stability of the energy obtained, especially when it comes to renewable energy sources, which are increasing their popularity today.

For such reasons, it is of great importance to constantly monitor the energy obtained from renewable or fossil-based sources and to store excess energy in cases where there is more energy production than needed to use it in a way to fill the gap in cases where there is less production than needed. For this purpose, many applications have been developed for energy storage systems and the control of these systems. When these applications are examined, it is seen that they are carried out using PI or PID controllers for reasons such as being easier to understand and apply. However, for these controllers, which have a simple structure, the fact that the controller parameters are determined by trial and error also complicates the system design process (Karuppiah, Karthikumar ve Arunbalj, 2018; Haque ve Razzak, 2021; Kumar *vd.*, 2021).

Instead, it may be appropriate to use controllers such as Fuzzy Logic Controller, which can respond quickly to variable system parameters and have adaptive features, to overcome such constraints. Considering all these situations, fuzzy logic controllers are preferred in applications where energy storage system control is desired. In this study, charge-discharge control of a simulated energy storage system is provided by a developed fuzzy logic controller-based algorithm.

In the first section of this article, the general structure of the energy system and the charging and discharging methods of the battery unit, which will be used as an energy storage unit in this system, are discussed. In the second section, the simulation model developed for this energy system and its units is presented. In the third section, the fuzzy logic controller-based algorithm developed for the charging and discharging of the battery unit is presented. In the last section, the obtained results are shared.

2. System Structure

2.1. Battery Charge – Discharge System

As can be seen in Figure 1, the system consists of the battery unit, the load unit, DC-DC buck-boost converter unit and the fuzzy logic-based charge-discharge control algorithm. The battery unit used as energy storage while in the charge state or source while in the discharge state. DC-DC buck-boost converter unit responsible for transferring the power from the DC busbar to the battery unit by decreasing while in the charge state, and transferring the power from the battery to the DC busbar by increasing the power while in the discharge state. The fuzzy logic-based charge-discharge control algorithm unit generates the switching signals required for this converter.

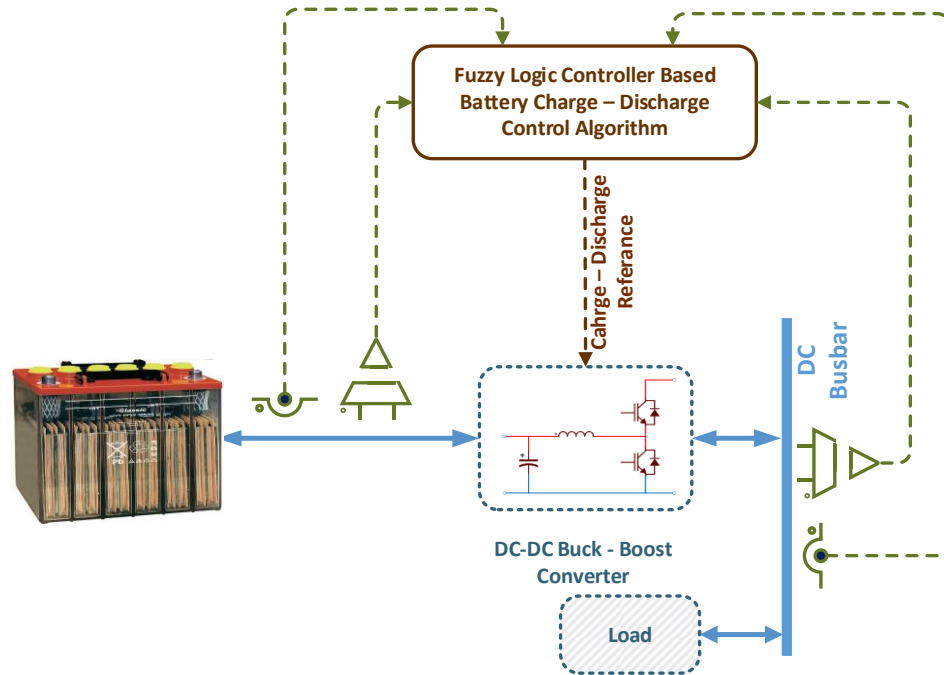


Figure 1. Battery Charge-Discharge System General Schematic.

For a battery, charging is a conversion process that converts electrical energy into chemical energy to be stored in the battery cell. When the relevant literature is examined, it is seen that the Constant Potential Charge method stands out as a battery charging method (Mahmuddin, Yusran ve Klara, 2017). Although the number of stages in the Constant Potential Charge method differs in different approaches, it is the three-stage approach that is mostly used.

Constant Current Charging is the first phase where high constant current charging is applied so that most of the battery charging can be carried out. The constant current applied at this stage is determined as the highest possible current value that will not cause the battery to be damaged by overheating or reduce its lifespan. The current value at which a typical 12V battery can be charged in the constant current phase is determined as $C/10$. Here C is the capacity value of the battery expressed in Ah.

Constant Voltage Charge is the second stage in which a constant voltage charge is applied until the battery charge current drops to approximately $C/50$ to $C/100$ so that the battery can reach a fully charged (100%) state. While the battery voltage remains constant at the determined value (voltage level reached in the previous stage), this stage where the battery current gradually decreases towards full charge is also called the absorption stage.

The third and final stage is the Floating Charge stage, also called the trickle charge. At this stage, a constant voltage is applied to the battery, whose charge state has already reached 100%, in a way that will maintain its 100% state of charge and prevent self-discharge. When the charging process is completed, the voltage at the battery terminals becomes slightly less than the voltage reached during the constant voltage charging Stage (Husnayain, 2017).

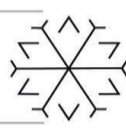
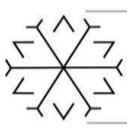


Figure 2 shows the charge graph of a battery charged with the three-stage constant potential charging method.

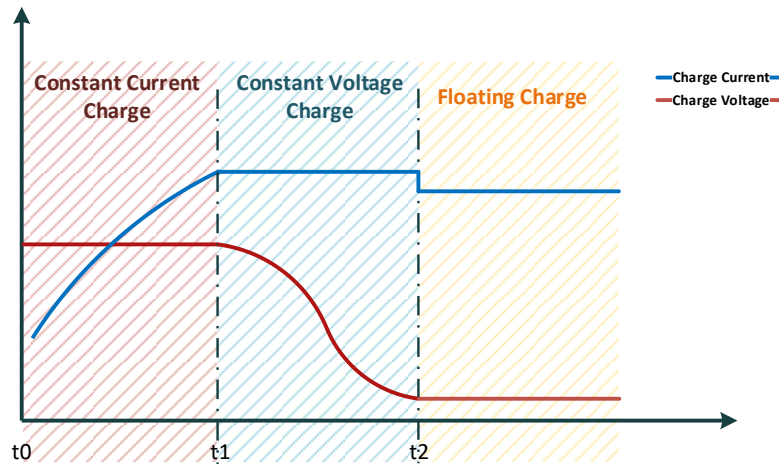


Figure 2. Three Stage Battery Charge (Bhatt, Hurley ve Wölfle, 2005; Armstrong, Glavin ve Hurley, 2008)

The flow chart of the developed fuzzy logic controller-based battery charge-discharge control algorithm is shown in Figure 3. First of all, it is decided whether the battery should be in charge or discharge states.

When the battery is in charge state;

If the battery voltage is below the reference voltage value determined for constant voltage charging, it is charged with the current value determined for constant current charging until it reaches this value (Constant Current Charge).

When the battery voltage reaches the reference voltage value determined for the constant voltage charging, the battery is switched to the constant voltage charging stage so that this voltage value is constant. At this stage, while the voltage at the battery terminals remains constant, the battery charging current gradually decreases (Constant Voltage Charge).

When this current value falls below a determined value, the floating charge stage is started. At this stage, it is ensured that the battery voltage remains constant at the specified reference voltage value so that the battery remains fully charged (Floating Charge).

In charging mode, the DC-DC buck-boost converter operates in buck mode from DC busbar to the battery.

When the battery is in discharge state;

Since the power demanded by the load cannot be met, this missing power is tried to be completed by the discharge of the battery. The developed algorithm generates the switching signals and sends them to the switching elements to transfer the required amount of power to the load. Here, the discharge process is carried out in accordance with the references determined to protect the battery from deep discharge or going out of the discharge current limits.

In discharge mode, the DC-DC buck-boost converter operates in boost mode from the battery to the DC busbar.

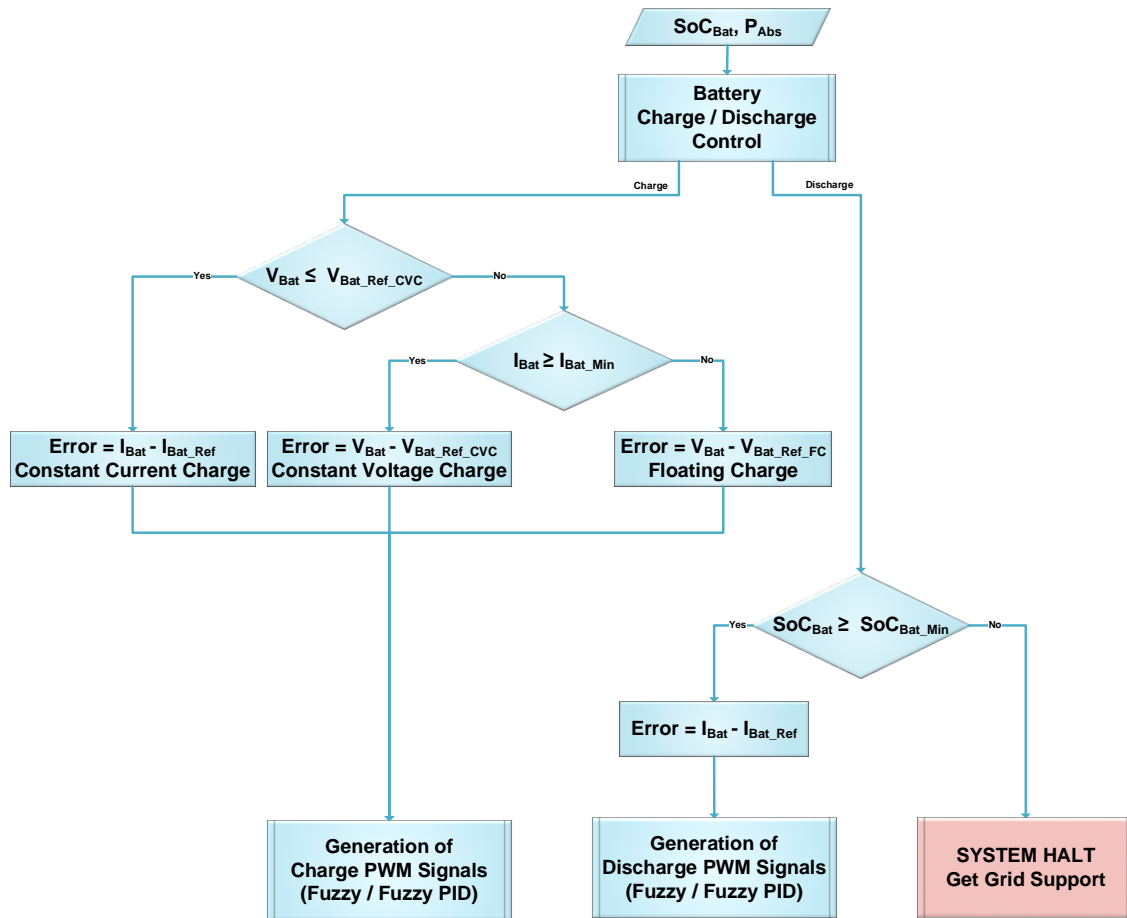
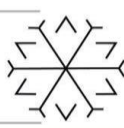
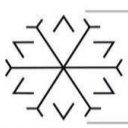


Figure 3. Flowchart of The Proposed Fuzzy Logic Controller Based Battery Charge – Discharge Control Algorithm.

2.2. Simulation Model

The battery unit has been simulated on the PSIM program by using the catalog values given in Table 1. In the same direction, a simulation model was created in the PSIM program for a typical DC-DC buck-boost converter shown in Figure 4. The developed battery charge-discharge control algorithm is written in the Simplified C block in the PSIM program using the C programming language. The load unit is modeled with a resistor. The system simulation model created is shown in Figure 5. In this simulation model, the battery unit and DSP environment are represented by blue and yellow regions, respectively.

Table 1. Yuasa NPW45-12 Industrial VRLA Battery Catalog Data

Nominal voltage (V)	12
10-hr rate Capacity to 10.8V at 20°C (Ah)	6.6
Float charge voltage at 20°C (V)/Cell	2.275 (±1%)
Capacity loss per month at 20°C (% approx.)	3
Cyclic (or Boost) charge Voltage at 20°C (V)/Cell	2.42 (±3%)
Float charge current limit (A)	No limit
Cyclic (or Boost) charge current limit (A)	2.125
Measured at 1 kHz (mΩ)	24

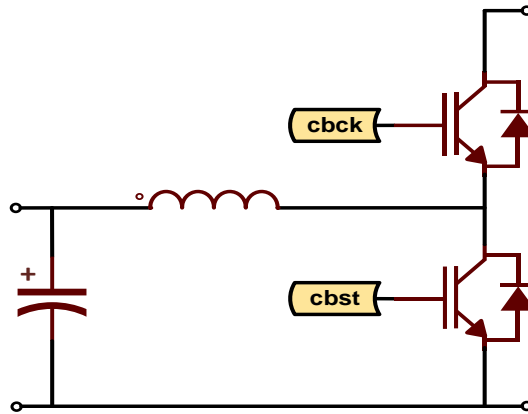


Figure 4. DC-DC Buck-Boost Converter

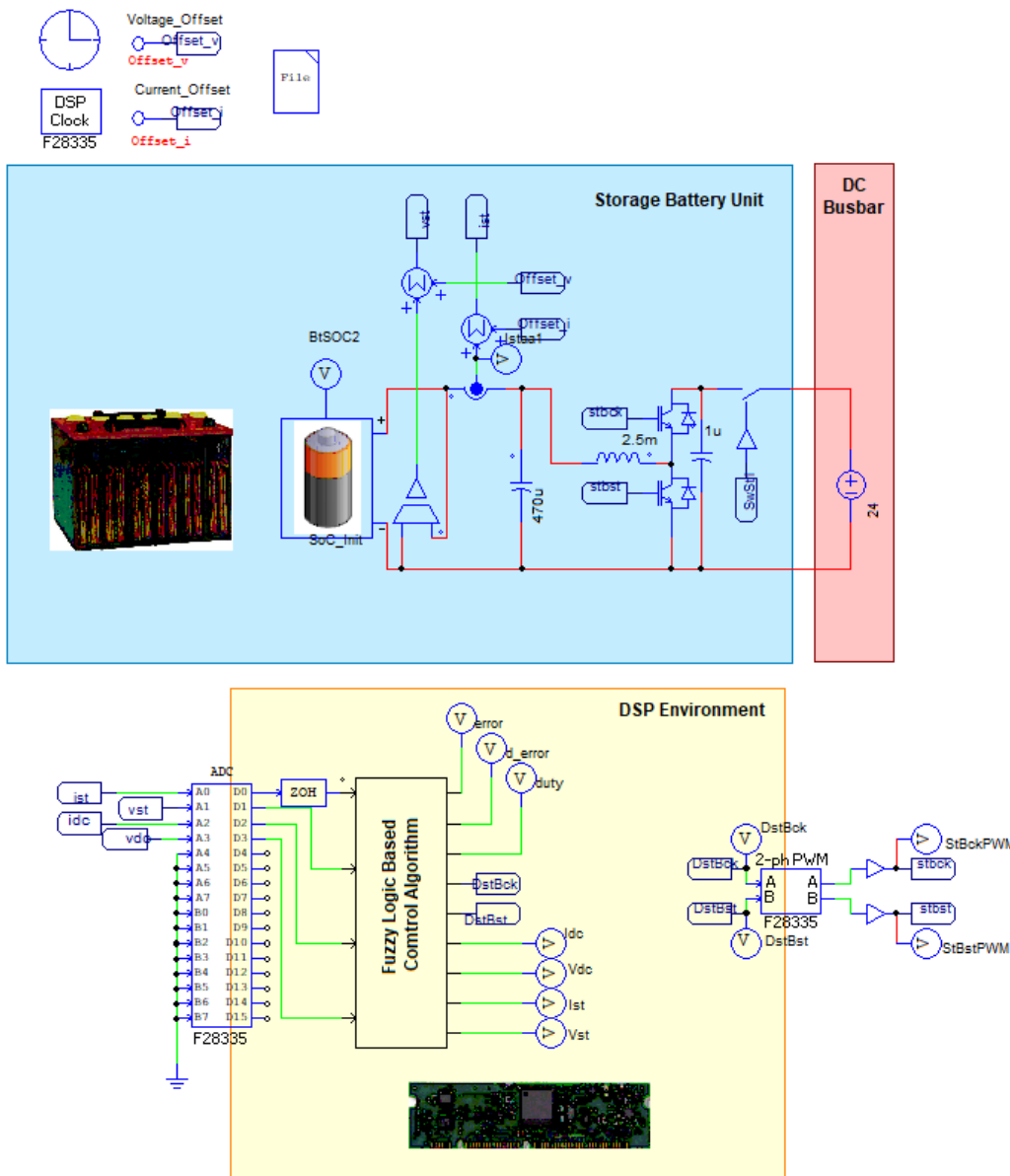
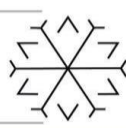


Figure 5. The Simulation Model of The Battery Charge – Discharge Control System



In this simulation model, the battery block has three outputs that represent the positive and negative terminals and State of Charge (SoC) value of the battery. The SoC can be defined as the ratio of the difference between the capacity discharged from a battery since the last fully charged battery's state of charge (full SoC) and the nominal capacity to the nominal capacity, given in Equation 1 (Sauer *vd.*, 1999). Here, C_N is the nominal capacity and Q_b is the charge balance which is a term meaning capacity expended per unit time. The SoC data of the batteries, which will assume the task of storing the energy while in the charge state and providing backup energy while in the discharge state, is very valuable for the system to continue its operation healthily and stably.

$$SoC = \frac{C_N - Q_b}{C_N} \tag{1}$$

A resistor is used to represent the loads to be connected to the system. In addition, the current and voltage values at the output of the battery and on the DC busbar, which are very important for the developed algorithm, were determined using the relevant sensors. The DSP environment has also been simulated so that the microcontroller embedded codes can be automatically generated. To process the measured analog values by DSP, an analog to digital converter (ADC) block, to generate DC-DC buck-boost converter switching signals according to the determined duty ratio value a pulse width modulation (PWM) block, and to write the developed algorithm in C language a Simplified C block was used.

2.3. Fuzzy Logic Controller Based Battery Charge – Discharge Control Algorithm

The voltage and current values on the battery and the DC busbar are measured with sensors and converted into digital data with the ADC block. One or more of the values such as maximum charging voltage or current, maximum discharge current given in the catalog values of the battery (preferred according to being in charge or discharge state) are determined as reference values. The power between the terminals of the battery and the DC busbar are calculated. The error and the change of error, which are the input values of the designed two inputs and one output fuzzy logic controller, are determined. Here, the error is determined as the difference between the battery voltage or current and the reference voltage or current. The change of error was determined as the difference between the current error value and the previous error value. Subsequently, these entries were fuzzified using the Mamdani method by using membership functions in the fuzzify step (Haj-Ali ve Ying, 2002). Seven triangular type membership functions determined for each entry were created as given in Figure 6, and these functions were defined in a matrix in C language. Membership function was selected between -1 and 1 for error entry, while a smaller range of -0.1 to 0.1 was selected for change of error. In the rule base step, it is calculated which rule in the rule base corresponds to the fuzzy values obtained in the previous step. The rule base used is shown in Figure 7. Thus, active rules and the activity levels of these rules were determined.

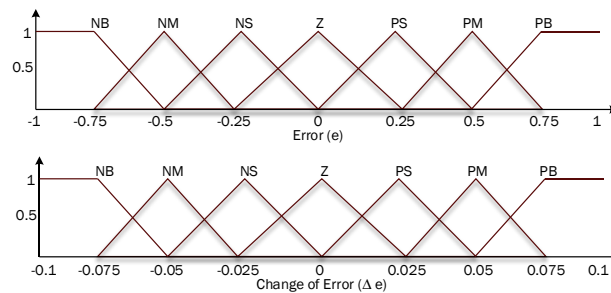


Figure 6. Input Membership Functions For Error and Change of Error.

E	NB	NM	NS	Z	PS	PM	PB
NB	0	7	14	21	28	35	42
NM	1	8	15	22	29	36	43
NS	2	9	16	23	30	37	44
Z	3	10	17	24	31	38	45
PS	4	11	18	25	32	39	46
PM	5	12	19	26	33	40	47
PB	6	13	20	27	34	41	48

Figure 7. Rule Base of Fuzzy Logic Controller Model.

In the defuzzification step, the defuzzification process was carried out using Equation 2 by using the center of gravity method. As can be seen from Figure 8, seven triangular membership functions for output have been selected so that their value range is 0.1 to 0.7. Since the duty ratio to be obtained at the output of this step takes a value below 0.1 or above 0.7, it will affect the switching process negatively, so a range has been determined so that these values will not be exceeded. The defuzzified value obtained is sent to the PWM block of the microcontroller to generate the switching signals of the DC-DC buck-boost converter. The error and the change of error values, as well as the current, voltage and power values of the battery and the DC busbar, are saved as previous values for the next cycle. Then the algorithm returns to the beginning. Thus, the algorithm recalculates the duty ratio according to the new voltage, current, and power values.

$$Defuzzified\ Output = \frac{\sum \mu_o(i).i}{\sum \mu_o(i)} \quad (2)$$

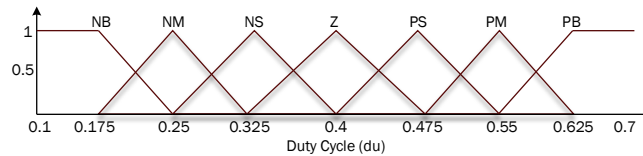


Figure 8. Output Membership Functions for Duty Cycle.

3. Simulation Results

The developed algorithm was run on the simulation model and the results are shown in Figures 9 – 11. Figure 9 shows the current, voltage and battery state of charge graphs obtained for the 3-stage charging system when the energy storage unit is in charge state. Accordingly, in the first graph, the red curve represents the battery current, the blue and pink curves represent the battery charging current references, and the green curve represents the stage of the 3-stage charging system of the charging process. In the second graph, the red curve represents the battery voltage and the blue curve represents the battery charge voltage reference. In the third graph, the battery state of charge value is seen.

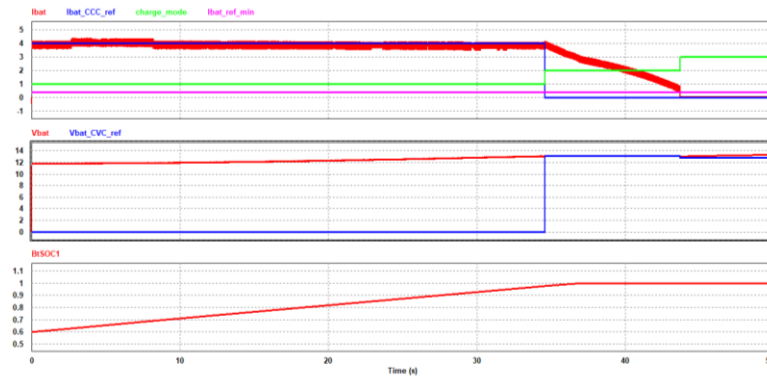


Figure 9. Simulation Results - 3 Stage Charge.

When the results are examined, it is seen that approximately the first 35 seconds of the 50-second simulation period is the 1st stage in the charging system, that is, the constant current charging stage, the next 10 seconds are the 2nd stage, that is, the constant voltage charging stage, and the remaining time is the 3rd stage, the floating charge stage. In the constant current charging phase, it is desired to charge the battery with the specified reference charging current, which is determined as 4A. It is seen that the battery is charged with a slight oscillation of around 4A. At this stage, while the battery voltage reference is zero, the battery voltage increases rapidly, and in this direction, the battery state of charge value approaches 1 from the initial value of 0.6. When the battery voltage reaches the determined reference value, which is determined as 13.1V, in approximately 35 seconds, the constant voltage charging phase is started. The state of charge value, which is very close to 1 in the previous stage, reaches 1 at this stage. At the same time, the battery continues to be charged with the specified reference voltage, which is determined as 13.1V, until the voltage drops to the minimum current reference value, which is determined as 0.4A. When the battery charging current drops to reference value, the battery is fully charged. The battery is kept in the floating charge stage with a value slightly below the voltage it reached in the previous stage, which is determined as 12.8V, in order to maintain this situation without allowing it to self-discharge. At this stage, the battery can be kept stable in a way that it will maintain the fully charged state it has reached even for very long periods of time.

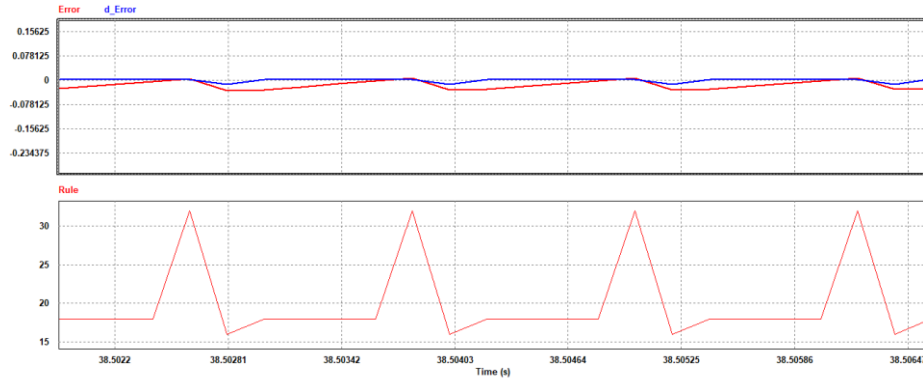


Figure 10. Simulation Results - Error, Change of Error and Rules of Fuzzy Logic Controller

In Figure 10, for a very short moment of the simulation around 38.5 seconds; In the first graph, the red curve represents the error and the blue curve represents the change of the error, while the second graph shows the change in the active rules of the fuzzy logic controller.

Figure 11 shows the voltage, current, the active rules of the fuzzy logic controller and battery state of charge graphs obtained when the energy storage unit is in discharge state. Accordingly, in the first graph, the red curve represents the DC busbar voltage; the blue curve represents the battery discharging voltage reference. In the second graph, the red curve represents the battery current and the blue curve represents the battery voltage. In the third graph, the change in the active rules of the fuzzy logic controller is seen. In the fourth graph, the battery state of charge value is seen.

For the discharge simulation, the initial state of charge of the battery is set as 0.8. In this direction, there is a voltage of around 12.5V at the battery terminals. Firstly, a voltage of 24V is demanded in the DC busbar and the fuzzy logic controller discharge algorithm increases the voltage at the battery terminals to this value. The reference DC busbar voltage is then reduced to 20V and increased back to 26V. As desired, it is seen that the DC busbar voltage follows the reference voltage values given, by the voltage transferred from the battery by boosting it. During the entire discharge process, it is observed that the battery current constantly changes in negative values to create a voltage at the demanded values in the DC busbar. The negative values of the battery current and as well as the decrease in the battery state of charge are due to the discharge of the battery.

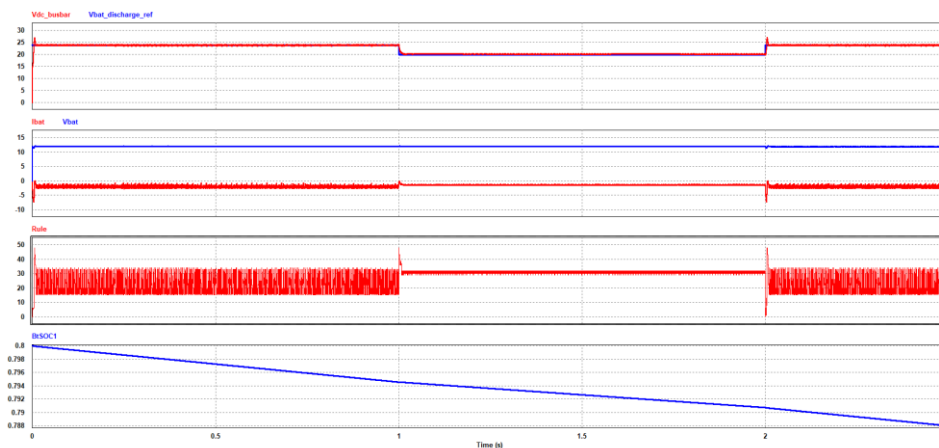
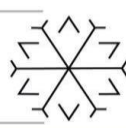
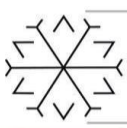


Figure 11. Simulation Results - Discharge

4. Conclusion

The performance of the proposed fuzzy logic controller-based battery charge-discharge control algorithm is monitored. When the results obtained are examined, it is seen that while the battery is in the charging mode, the charging process is completed in accordance with the 3-stage battery charging method, and the discharge process can be performed within the appropriate limits in the discharge mode. In the constant current charging phase, which is the first phase of the 3-stage battery charging method, a 4 Ampere charging current reference was determined and the battery could be charged with small oscillations around this



current value; In the second stage, the constant voltage charging stage, a 13.1 Volt charge voltage reference was determined and it was observed that the battery could reach full charge with this voltage value, and a voltage reference of 12.8 Volts was determined in the floating charge stage, which is the last stage, and it was observed that the battery maintains its full state with this reference.

In the discharge mode, voltage reference values of 24, 20 and 26 Volts are given for the DC busbar, respectively. The voltage obtained by discharging the battery within the discharge current limits was transferred to the DC busbar by boosting, thus ensuring that the DC busbar voltage is at reference values.

As a result, the usability of a fuzzy logic-based control algorithm instead of classical control algorithms, which are inadequate and nonlinear system parameters in storage unit included energy system applications, has been confirmed.

References

- Armstrong, S., Glavin, M. E. ve Hurley, W. G. (2008) "Comparison of battery charging algorithms for stand alone photovoltaic systems", *PESC Record - IEEE Annual Power Electronics Specialists Conference*, ss. 1469–1475. doi: 10.1109/PESC.2008.4592143.
- Bhatt, M., Hurley, W. G. ve Wölfle, W. H. (2005) "A new approach to intermittent charging of valve-regulated lead-acid batteries in standby applications", *IEEE Transactions on Industrial Electronics*, 52(5), ss. 1337–1342. doi: 10.1109/TIE.2005.855665.
- Haj-Ali, A. ve Ying, H. (2002) "Structure analysis of Mamdani fuzzy PID controllers with nonlinear input fuzzy sets", *Annual Conference of the North American Fuzzy Information Processing Society - NAFIPS*, 2002-January, ss. 19–21. doi: 10.1109/NAFIPS.2002.1018023.
- Haque, M. R. ve Razzak, M. A. (2021) "A buck converter-based battery charging controller for electric vehicles using modified PI control system", *2021 IEEE International IOT, Electronics and Mechatronics Conference, IEMTRONICS 2021 - Proceedings*, (3), ss. 7–10. doi: 10.1109/IEMTRONICS52119.2021.9422646.
- Husnayain, F. (2017) *Profile of 12-V Voltage-Regulated Lead-Acid Battery*. The University of Manchester. Available at: https://www.research.manchester.ac.uk/portal/files/61846817/FULL_TEXT.PDF.
- Karuppiah, M., Karthikumar, K. ve Arunbalj, A. (2018) "A transformerless buck-boost converter with PID controller (closed loop controller)", *Proceedings of the 2017 IEEE International Conference on Intelligent Techniques in Control, Optimization and Signal Processing, INCOS 2017*, 2018-February, ss. 1–7. doi: 10.1109/ITCOSP.2017.8303145.
- Kumar, K. K. vd. (2021) "Design and Development of Closed Loop PI Controlled solar integrated modified A source dc to dc Boosting Topology for standalone battery charging system", *Proceedings of the 6th International Conference on Communication and Electronics Systems, ICCES 2021*. IEEE, ss. 117–122. doi: 10.1109/ICCES51350.2021.9488941.
- Mahmuddin, F., Yusran, A. M. ve Klara, S. (2017) "On the use of an Arduino-based controller to control the charging process of a wind turbine", *AIP Conference Proceedings*, 1814(December). doi: 10.1063/1.4976284.
- Sauer, D. U. vd. (1999) "State of charge - What do we really speak about?", *The 21st International Telecommunications Energy Conference*, (February 2016).

Epileptic Seizure Detection based on EEG Data Using Discrete Wavelet Transform

Hakan BİÇER ¹*[0000-0002-0184-9597] and Semih ERGİN ²*[0000-0002-7470-8488]

¹hakanbicer9608@gmail.com, Eskisehir Osmangazi University, Faculty of Engineering, Institute of Science and Technology, Eskisehir, Turkey

²sergin@ogu.edu.tr, Eskisehir Osmangazi University, Faculty of Engineering, Department of Electric-Electronics, Eskisehir, Turkey

Abstract

Over the years, epileptic seizure detection has been a crucial issue among researchers. Numerous research papers have been published in order to detect and identify epileptic seizures by analyzing scalp electroencephalography (EEG) which measures the electrical brain activity. The main purpose of this study was classifying EEG signal as seizure or non-seizure, which can help doctors to identify and recognise seizures beforehand. Dataset used in this study is MIT Physionet Scalp EEG Database. Firstly, High-pass Butterworth filter with 0.5 Hz cutoff frequency was used, which filters the signal digitally and clears noise and artefacts. After filtering process, Discrete Wavelet Transform (DWT) which decomposes the signal into detail and approximation coefficients was used, which in turn makes analyzing signal more accurate. DWT provides both frequency and time domain features at the same time which results in better accuracy. 5 detailed bands, from d2 to d7 encompassing the frequency bands from 0.5 Hz to 64 Hz, were used for feature extraction due to providing high accuracy. After obtaining the coefficients, features, e.g., energy, min, max, mean, variance, skewness, kurtosis, standard deviation were extracted using coefficients which belong to different frequency bands. Furthermore, 2-second, 4-second, 8-second, 12-second, 16-second and 20-second epochs were used to compare the effect of epoch size in accuracy. In order to classify data, Support Vector Machine (SVM), Logistic Regression and Random Forest classifiers were applied using statistical features of the coefficients. The results were quite satisfying with an accuracy of more than 90% for both epochs and all classifiers.

Keywords. Discrete wavelet transform, EEG, Logistic Regression, Random Forest, Seizure detection, SVM

1. Introduction

A wide range of people worldwide suffer from epilepsy, which is characterized by recurrent seizures caused by abnormal activities in the brain (Fisher et al., 2014). Electroencephalography (EEG) is a technology that keeps the record of electrical activities in the brain with multiple signal channels, which is significant for seizure detection, spike detection etc. (Chen et al., 2017). EEG recordings are usually quite long and continuous signals. Seizures occur at uncertain times, which means it might appear at any time (Shoeb and Guttag, 2010; Siddiqui et al., 2020) and therefore, there have been an immense amount of research to develop and improve algorithms and applications for detecting seizure and facilitating the work done by doctors. There are some research areas, such as detecting epileptic and healthy signal, ictal (on seizure) vs. inter-ictal for seizure onset detection, which are generally considered as EEG signal classification problem. (Chen et al., 2017). Since seizure detection is the most prevalent classification problem, the main objective of this work was to classify EEG data as healthy or epileptic.

EEG is a continuous, non-stationary and complex signal which makes it challenging to analyze. Thus, it is sensible to divide large continuous data into segments (epochs), use frequency-domain to analyze EEG signal segments and extract some meaningful information about it. Dividing continuous data into epochs is called window-based method which is crucial for extracting important features from non-stationary signals, assuming that they are stationary (Barlow, 1985). 2-second, 4-second, 8-second, 12-second, 16-second and 20-second segments were utilized in this study.

Discrete Wavelet Transform (DWT) is one the most successful method among the other methods like Fourier Transform (FT) and Fast Fourier Transform (FFT). It represents the signal more appropriately in all frequency bands (Chen et al., 2017). Since DWT has generally triumphed over those methods in the literature in terms of accuracy, it was chosen to analyze the EEG data. Mother wavelet and decomposition level were chosen as 'coif3' and 7, respectively, because results of this combination are the optimal for CHB-MIT database according to Chen et al. (2017).

Features were extracted from each frequency subband in all 23 channels. Determining features is still vague issue and dramatically affects overall success of the algorithm. 8 features (Energy, Max, Min, Mean, Std, Skewness, Kurtosis, Variance) were used in this study for the best combination of computational cost and accuracy, since they are the most discriminative features as stated in Chen et al. (2017). After the extraction of features, segments with-seizure and without-seizure were trained with SVM, Logistic Regression and Random Forest. Results which were obtained from SVM, Logistic Regression and Random Forest were more than 89.2%, 89.4% and 95.7%, respectively, for all epochs.

2. Methods

EEG signal acquisition, pre-processing, feature extraction and classification stages are imperative for pattern recognition of epileptic seizure detection.

2.1. EEG Database

MIT Physionet Scalp EEG Database, which was gathered at Children Hospital Boston, Massachusetts Institute of Technology (CHB-MIT), was used in this study. This database is published in 2010 and open access on a physionet server. It is comprised of the number of seizure and non-seizure EEG recordings from pediatric patient of the CHB (Goldberger et al., 2000). The dataset comprises 24 cases, and each case contains multiple seizure and non-seizure recording files in European data format (.edf). Seizure start and end time are annotated clearly. In this study, raw data (.mat files which can be found in PhysioBankATM) were used. The sampling rate of EEG signals is 256 Hz. Mostly, there are 23 channels in each file; however, there are some dummy (named “-”), ECG and VNS signals in some files which were excluded in this study.

There are numerous research papers using this database in the literature. Chen *et al.* (2017) conducted a comprehensive research using DWT and comparing its key parameters. They evaluated their model in both CHB-MIT and UBonn (Andrzejak et al., 2001) dataset. Alickovic, Kevric and Subasi (2018) used this dataset to compare the performance of three different signal processing methods in epileptic seizure detection. Similarly, Thodoroff, Pineau and Lim (2021) implemented deep learning and offered a recurrent convolutional architecture. This architecture uses spectral, temporal and spatial features of a seizure.

In this work, seizures lasting more than 20 seconds were extracted from the files with seizure. And every seizure data was split into 2-second EEG epochs as in (Shoeb and Guttig, 2010). In order to keep data balanced, 16 and 4 second segments were extracted from every file without seizure for training and testing, respectively. They were also split into 2-second, 4-second, 8-second, 12-second, 16-second and 20-second epochs. Consequently, 23 channels and different size of epochs were used from 24 cases in total.

2.2. Preprocessing

The preprocessing stage's primary goal is to improve and boost the system performance by removing noise from raw EEG signals. Thus, the High-Pass filter and the noise removal process were employed. In order to do that, redundant channels like “ECG” and “VNS” were discarded and 2nd order IIR High-Pass Butterworth filter with the cutoff frequency at 0.5 Hz was used. The frequency response of IIR filter can be seen in Figure 1.

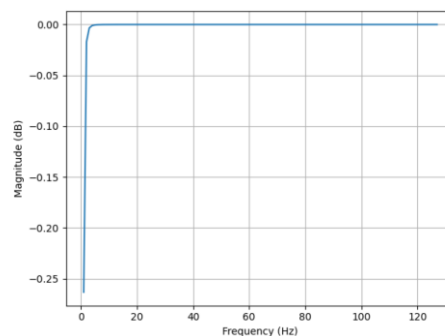
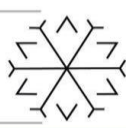


Figure 1: Frequency response of IIR filter.

2.3. Feature Extraction

Discrete Wavelet Transform plays an important role in extracting significant information about continuous data. Fast Fourier Transform provides only spectral information in frequency domain, while losing information in time



domain. However, DWT provides information about both frequency and location in time domain with high resolution, which makes it a type of time-frequency analysis. Therefore, DWT represents continuous signals more accurately and has less information loss. That is the reason why it is used in this study before extracting features.

There are two parameters that should be defined: mother wavelet and decomposition level. Different combination of parameters results in various detection outcome. Selecting decomposition level is more important and has more effect on the result than choosing mother wavelet. According to Chen et al. (2017), the optimal combination is to use 'coif3' as a mother wavelet and 7 as a decomposition level for the CHB-MIT dataset.

Each decomposition level represents specific frequency bands and has some wavelet coefficients as shown in Figure 1.

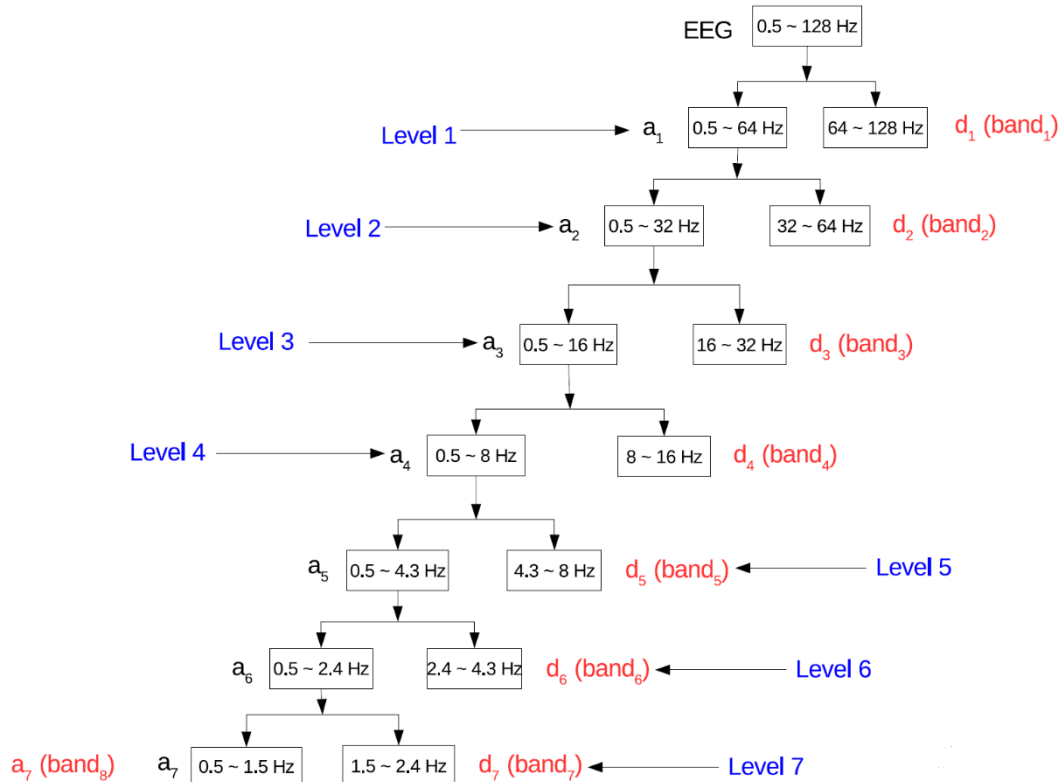


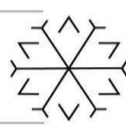
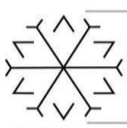
Figure 2: Structure of 7-level wavelet decomposition of CHB-MIT Dataset (Chen *et al.*, 2017).

Since sampling rate is 256 Hz, the frequency band includes from -128 Hz to 128 Hz. For real signals, negative part should be neglected (Lehman, 2014). As a result, frequency band starts from 128 Hz as can be seen above, and then decomposed into different frequency bands. There are 7 decomposition levels here, which means that 7 detailed and 7 approximation coefficients are obtained. All detailed and 1 approximation coefficients can be used for feature extraction. However, some frequency bands lead to a loss in accuracy. Thus, 5 detailed bands, from d2 to d7 encompassing the frequency bands from 0.5 Hz to 64 Hz, were used for feature extraction due to providing high accuracy in Chen et al. (2017).

According to Chen et al. (2017), the most discriminative features which provide the highest accuracy are energy, max, min, mean, standard deviation, normalized standard deviation and skewness. In this study, all these features were used except normalized standard deviation. Instead, kurtosis and variance were added as extra features. Hence, 8 features were extracted from 6 frequency bands each, which in turn resulted in 48 features in total for one channel. For 23 channels, 1104 features were used for representing one epoch. Namely, each feature vector dimension is 1104 for all epoch sizes.

2.4. Classification

Feature vectors were classified as “seizure” and “non-seizure” using linear SVM, Logistic Regression and Random Forest Classifiers. They are both supervised learning algorithm which uses labels of training dataset to learn pattern and create a model. 8322 of 2-second and 6266 of 4-second feature vectors, that were trained in total, with dimension of 1104 were given to SVM, Logistic Regression and Random Forest algorithms in order to create



models. After creation of models, 2142 of 2-second and 1600 of 4-second data were tested on each model. Likewise, the number of data trained and tested changes depending on epoch sizes. It should be noted that feature dimension can be decreased to reduce computational burden. However, this can lead to accuracy loss. Similarly, training data can be increased to increase accuracy, but this would add more burden on the algorithm, leading to more computational cost. In other words, every combination and act have an effect on algorithm. Therefore, it is attempted to keep everything balanced and optimal according to Chen et al. (2017).

3. Results

Results demonstrates that Random Forest classifier outperformed Logistic Regression and SVM in general in terms of accuracy for all epoch sizes. Even though the performance of Random Forest was better than Logistic Regression and SVM, it can be said that all classifiers are good enough to be used for epileptic seizure detection.

On the other hand, 2-second epochs are more discriminative when it comes to the signals with seizure. This is the most crucial result obtained from this study. However, epochs which have longer duration like 20 seconds are far more distinctive for normal signals and provide better overall accuracy. 2-second epochs and Random Forest combination is the best in terms of detecting seizures with 95.2% of overall accuracy. Besides, frequency bands and features extracted from filtered signals work well and successfully. Overall, feature extraction method based on bandpass filter and classifiers, especially Random Forest, showed that this proposed system can be successfully utilized as a detector of epileptic seizure. Results that can be seen in Table 1.

Table 1: Summary of classification results for three classifiers.

Window Length	SVM			Logistic Regression			Random Forest		
	Accuracy	Recall	Precision	Accuracy	Recall	Precision	Accuracy	Recall	Precision
2 sec	89.2	86.0	92.5	89.4	85	94	95.2	93.0	97.5
4 sec	92.3	86.3	91.8	92.1	84.7	96.2	95.6	89.9	97.8
8 sec	94.8	86.8	89.8	95.9	86.1	98.8	95.2	81.5	96.5
12 sec	95.0	81.3	88.0	96	83.7	98.5	95.9	77.5	97.6
16 sec	96.1	81.7	87.8	96.3	81.7	98.6	97.0	76.6	100.0
20 sec	97.0	81.3	90.4	96.6	78.1	99.1	96.7	71.9	97.9

It should be noted that adjustment and tuning of classifiers play a vital role in accuracy. Therefore, tuning parameters should be selected wisely.

These results outperformed outcomes of the study carried on by Chen *et al.* (2017) which used the similar method. They found 92.30% overall accuracy, whereas it is more than 92.30% using SVM in all window lengths except for 2-sec. Especially, Random Forest classifier accuracy results are far more better than that study (Chen *et al.*, 2017).

4. Discussion

The aim of this study was to distinguish epileptic seizures from non-seizures in EEG data effectively and accurately and investigate the effect of the size of epochs. All classifiers were trained using different size of epochs. The most discriminative 8 features were extracted from all bands and channels. It can easily be seen that the classifiers, feature combinations and size of segments affect the success and the duration of the method.

Firstly, choosing epochs duration is uncertain and controversial issue. Duration of segments should be selected as minimum as possible to obtain a stationary signal. However, small segments will lead to increase in computational complexity, whereas long segments bring about decrease in accuracy. Thus, it should be selected to keep computational complexity and accuracy balanced.

On the other hand, choosing mother wavelet, decomposition levels and features like max, min, etc. plays an important role in accuracy. As it is mentioned before, decomposition level has more influence on accuracy than mother wavelet (Chen et al., 2017). Different combinations can be tried to see effects of those settings. However, it is suggested that using “coif” and “sym” is optimal choice as a mother wavelet (Chen et al., 2017). In addition, decomposition level should comprise all conventional human EEG rhythms (i.e., δ (< 4 Hz), θ ($4 - 7$ Hz), α ($8 -$



15Hz), β (16 – 31Hz) and γ (> 31Hz)) for better performance. Features extracted from all bands affect the model, significantly. Therefore, optimal features in terms of accuracy should be determined carefully.

It should be noted that optimal settings can be varied depending on not only dataset but also patient. That is, different datasets and patients can result in difference in accuracy. For this reason, rigorous approaches that can be robust in any dataset and patient should be developed. Method developed in this paper can be utilized in other datasets and can be compared in terms of robustness as a future work.

5. Conclusion

Detecting epileptic seizures manually from very long scalp EEG recordings is demanding and challenging for doctors. In this work, DWT based method was proven that it is possible to detect seizures automatically and effectively. Automatic seizure detection can be done successfully with more than 90% of accuracy depending on the classifier, which in turn makes us rely on computer-aided systems and lowers the burden on doctors. This work might help doctors to discriminate and detect seizures in a very short time. Therefore, it should be improved in further studies in terms of speed, computational complexity and accuracy.

References

Alickovic, E., Kevric, J. and Subasi, A., 2018. Performance evaluation of empirical mode decomposition, discrete wavelet transform, and wavelet packed decomposition for automated epileptic seizure detection and prediction. *Biomedical Signal Processing and Control*, 39, pp.94-102.

Andrzejak RG, Lehnertz K, Mormann F, Rieke C, David P, Elger CE. Indications of nonlinear deterministic and finite-dimensional structures in time series of brain electrical activity: Dependence on recording region and brain state. *Physical Review E*. 2001 November; 64(6):1–8. doi: 10.1103/PhysRevE.64.061907 PMID: 11736210

Barlow, J. S. (1985). Methods of analysis of nonstationary EEGs, with emphasis on segmentation techniques: a comparative review. *Journal of clinical neurophysiology: official publication of the American Electroencephalographic Society*, 2(3), 267-304.

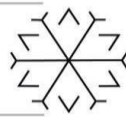
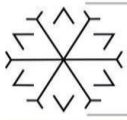
Chen, D., Wan, S., Xiang, J., & Bao, F. S. (2017). A high-performance seizure detection algorithm based on Discrete Wavelet Transform (DWT) and EEG. *PloS one*, 12(3), e0173138. <https://doi.org/10.1371/journal.pone.0173138>.

Fisher, R. S., Acevedo, C., Arzimanoglou, A., Bogacz, A., Cross, J. H., Elger, C. E., Engel, J., Jr, Forsgren, L., French, J. A., Glynn, M., Hesdorffer, D. C., Lee, B. I., Mathern, G. W., Moshé, S. L., Perucca, E., Scheffer, I. E., Tomson, T., Watanabe, M., & Wiebe, S. (2014). ILAE official report: a practical clinical definition of epilepsy. *Epilepsia*, 55(4), 475–482. <https://doi.org/10.1111/epi.12550>.

Goldberger, A. L., Amaral, L. A., Glass, L., Hausdorff, J. M., Ivanov, P. C., Mark, R. G., Mietus, J. E., Moody, G. B., Peng, C. K., & Stanley, H. E. (2000). PhysioBank, PhysioToolkit, and PhysioNet: components of a new research resource for complex physiologic signals. *Circulation*, 101(23), E215–E220. <https://doi.org/10.1161/01.cir.101.23.e215>.

Lehmann, Lutz. (2014). Re: How can we calculate the frequency band of a DWT filter? Retrieved from: <https://www.researchgate.net/post/How-can-we-calculate-the-frequency-band-of-a-DWT-filter/5387b60cd039b1f2448b467a/citation/download>.

Shoeb, A. H., & Guttag, J. V. (2010). Application of machine learning to epileptic seizure detection. In *Proceedings of the 27th International Conference on Machine Learning (ICML-10)* (pp. 975-982).



Siddiqui, M. K., Morales-Menendez, R., Huang, X., & Hussain, N. (2020). A review of epileptic seizure detection using machine learning classifiers. *Brain Informatics*, 7(1), 1-18.

Thodoroff, P., Pineau, J. and Lim, A., 2021. Learning Robust Features using Deep Learning for Automatic Seizure Detection. [online] arXiv.org. Available at: <<https://arxiv.org/abs/1608.00220>> [Accessed 30 November 2021].

LED Selection Algorithm for Indoor Li-Fi Systems

Ahmet Fetullah YILMAZ ¹[0000-0002-8816-1380] and Çağlar DUMAN ²[0000-0002-1845-8605]

¹afyilmaz@gelisim.edu.tr, Istanbul Gelisim University

²caglarduman@erzurum.edu.tr, Erzurum Technical University

Abstract

Light Fidelity (Li-Fi) is a wireless visible light communication technique in which data is transmitted by light emitting diodes (LEDs). However, this technology is still in the development stage and there are some problems that need to be overcome. One of these problems is disruptive effect of inter-symbol interference (ISI) at high speeds. Optical signals reaching a receiver from different paths cause ISI and increase in ISI decreases SNR. In this study, we presented an LED selection algorithm for indoor Li-Fi Systems in order to reduce ISI effect.

Keywords. Light fidelity, valid ratio, inter-symbol interference

1. Introduction

Li-Fi is a technology that transmitting data by LEDs switched at a speed cannot detect by human eye. It is a visible light communication method that provides two directional and highspeed data transmission (Sharma and Sanganal, 2014). As an alternative to Wi-Fi modems, Li-Fi systems contain LEDs equipped with transceiver (Raj et al., 2018). With the developments of lighting technology, LEDs are becoming widespread and Li-Fi technology can be easily integrated to indoors without need for an additional equipment (Johri, 2016).

Due to the wavelength range used by Li-Fi systems, high-speed data transmission is possible and there is no interference with the devices working at RF wavelengths (Sarkar et al., 2015). It is considered that Li-Fi may have an important place in the wireless communication industry in the near future (Kumar et al., 2021).

In the case of multiple users in Li-Fi systems, studies based on evolutionary algorithm have been carried out to offer the best SNR value for each user (Wang et al., 2017; Ren et al., 2021). To increase the computational efficiency of these systems, the hyper-heuristic evolutionary algorithm has good results (Sharma et al., 2018). It has been shown that interference between multiple users can be improved using joint LED selection and precoding (Yang et al., 2021). A recent study has shown that by using machine learning, the complexity of selecting the appropriate LEDs can be reduced and acceptable amount of bit error rate (BER) performance can be achieved (Zhang et al., 2021).

In this study, an LED selection algorithm reducing the ISI effect in a Li-Fi system is described. The ISI caused by same optical signals reaching a user from various paths is considered but the ISI caused by different optical signals sending to different users is not considered. With emerging of new high-speed LEDs in the future, ISI-induced noise will be more increased and therefore the SNR will decrease further. In Section 2, the indoor Li-Fi systems and basic parameters used for communication LEDs selection are described. In section 3, obtained simulation results and designed LED choosing algorithm are presented and in last section, these results are discussed.

2. Indoor Li-Fi Model and LED Selection

A room model with dimensions of 5.0 m × 5.0 m × 3.0 m is used for LED selection algorithm calculations. The layout of the LED arrays is given in Figure 1. The LED arrays are placed at height of 2.5 m from the ground and a user terminal at height of 0.85 m from the ground is defined.

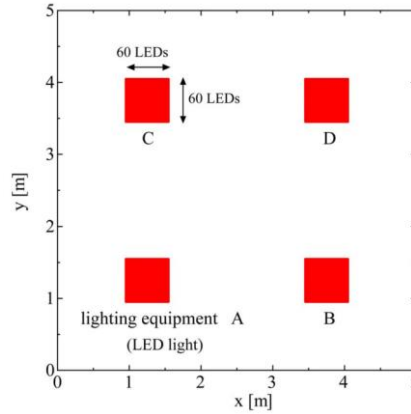


Figure 1: The layout of the LED arrays.

A matrix representing all LEDs is defined. Since there are 4 LED arrays in the room, each LED array is expressed as $K_{11}, K_{12}, K_{21}, K_{22}$ sub matrices. By combining these matrices, a K matrix is obtained that defines all LEDs. K matrix is shown in Equation (1). In K matrix, $k_{(x,y)}$ elements are taken as 1 for communication LEDs and $k_{(x,y)}$ elements are taken as 0 for rest of the LEDs.

$$K = \begin{bmatrix} K_{11} & K_{12} \\ K_{21} & K_{22} \end{bmatrix} = \begin{bmatrix} \begin{bmatrix} k_{95,95} & \cdots & k_{95,154} \\ \vdots & \ddots & \vdots \\ k_{154,95} & \cdots & k_{154,154} \end{bmatrix} & \begin{bmatrix} k_{95,345} & \cdots & k_{95,404} \\ \vdots & \ddots & \vdots \\ k_{154,345} & \cdots & k_{154,404} \end{bmatrix} \\ \begin{bmatrix} k_{345,95} & \cdots & k_{345,154} \\ \vdots & \ddots & \vdots \\ k_{404,95} & \cdots & k_{404,154} \end{bmatrix} & \begin{bmatrix} k_{345,345} & \cdots & k_{345,404} \\ \vdots & \ddots & \vdots \\ k_{404,345} & \cdots & k_{404,404} \end{bmatrix} \end{bmatrix} \quad (1)$$

Figure 2 shows an On-Off-Keying (OOK) modulated signal with a T period. Here each optical signal from the LEDs is divided to positive and negative components.

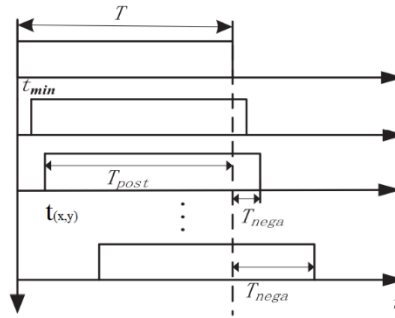


Figure 2: Arrival times of signals from communication LEDs (Ren et al., 2021)

The negative and positive components of the transmitted signals are calculated as in Equations (2) and (3). The positive component part of the message signal creates the signal power (P_s) and the negative component creates the ISI power (P_{ISI}). As seen from the figure, optical signal components reaching the receiver after the end of the first signal, are the negative components. The negative optical signal components can be interfered with next optical signals, this phenomenon is called inter-symbol interference (Ren et al., 2021).

$$T_{(x,y)nega} = t_{x,y} - t_0 \quad (2)$$

$$T_{(x,y)post} = T - T_{(x,y)nega} \quad (3)$$

where $t_{(x,y)}$ and t_0 show the times of the optical signals arrive to the receiver and the time of first optical signal arrive to the receiver, respectively.

By using the positive and negative components, a parameter named valid ratio (VR) can be determined. VR is defined as the ratio of the positive component of the optical signal to the negative component of the optical signal. SNR of the communication system changes depend on VR . For very small and big VR values, the SNR value is



small so there is an optimal value for VR . A threshold value for valid ratio (Th_{VR}) can be defined and a LED selection algorithm based on Th_{VR} can be used to increase the SNR by decreasing ISI. Elements of the K matrix in Equation (1) are updated by using Equation (4). Accordingly, if VR value obtained for a LED is greater than the determined Th_{VR} value, related $k_{(x,y)}$ is selected as 1 and related $k_{(x,y)}$ is 0 for other cases. The LEDs corresponding to the value which $k_{(x,y)}$ is 1 are used for communication with the user and the others are used for lighting purposes or for another user.

$$k_{(x,y)} = \begin{cases} 1, & \frac{T_{(x,y)post}}{T_{(x,y)nega}} > Th_{VR} \\ 0, & \text{others} \end{cases} \quad (4)$$

If Th_{VR} value is chosen small, number of the communication LEDs increase, resulting higher ISI. Increase in ISI causes a decrease in SNR. When Th_{VR} value is large, number of communication LEDs decrease and this cause a decrease in signal power, too. A decrease in signal power and an increase in ISI have similar effect on SNR. Therefore, there is an appropriate Th_{VR} value for each user depending on its location to keep the SNR value as high as possible.

3. Simulation Results

MATLAB 2020b is used to investigate SNR based on receiver location and communication LED number. SNR calculations are carried out as described in Aydın (2021). As stated in the study, with the increase of ISI power, the shot noise increases and therefore the SNR decreases. In the simulations, users are considered at the center of the room, at the corner of the room, and at directly under an LED array, respectively. The parameters used in the simulations are presented in Table 1.

Table 1: Parameters used in simulations.

Parameters	Values
Optical power transmitted by a LED	20 mW
Semi angle at half-power	70
Light intensity	0.73 cd
Number of LEDs (nxn)	3600(60x60)
Distance between LEDs	0.01 m
Size of LED light	0.59x0.59
Open loop gain	10
Fixed capacitance of photodetector per unit area	112 pF/cm ²
FET channel noise factor	1.5
FET transconductance	30mS
Absolute temperature	298K
Background current	5100 μ A
Data rate	500 Mbps
Noise bandwidth factors	$I_2=0.562; I_3=0.0868$
Photodetector conversion efficiency	0.53 A/W
FOV angle	60°
Photodetector physical space	1.0 cm ²
Optical filter gain	1.0
The refractive index of the photodetector lens	1.5
Reflection coefficient of a wall	0.8

Figure 3 shows SNR values for the different number of LEDs at different receiver locations while the data rate is 500Mbit/s. It has been observed that the SNR value from 10x10 LEDs to 60x60 LEDs does not show extreme changes for the user just below a luminaire. For other users, the SNR value has experienced changes according to the number of communication LEDs. As can be seen from the figure, the SNR depends on the user's location and the number of communication LEDs. Also, number of communication LEDs should be an optimum value to obtain higher value depend on location of a user.

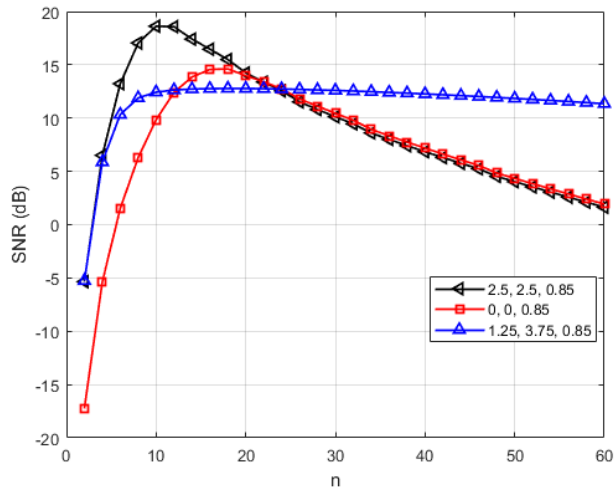
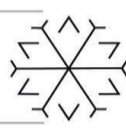
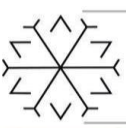


Figure 3: SNR calculation based on LED numbers

The LED selection algorithm shown in Table 2 is applied to obtain best SNR value for the users at different places in the room.

Table 2: LED Selection Algorithm.

Calculate reaching time of optical signal coming from each LED to the receiver.

Sort these values from smallest to largest and delete repeated values.

$n=0$;

For each reaching time

 % Initialization

$Snr0=0$;

$Th_{VR}=1$;

 Get the new K matrix from Equation (4) according to Th_{VR} .

 Calculate SNR.

$Snr1=SNR$;

While ($Snr1>Snr0$)

$Th_{VR}=Th_{VR}+1$;

$Snr0=Snr1$;

 Get the new K matrix from Equation (4) according to Th_{VR} .

 Calculate SNR.

$Snr1=SNR$;

end

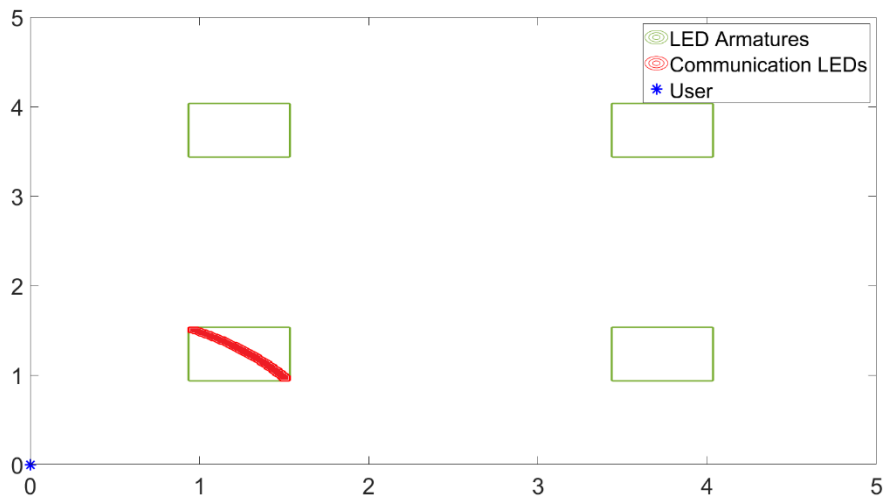
$Snr(n)=Snr0$;

$n=n+1$;

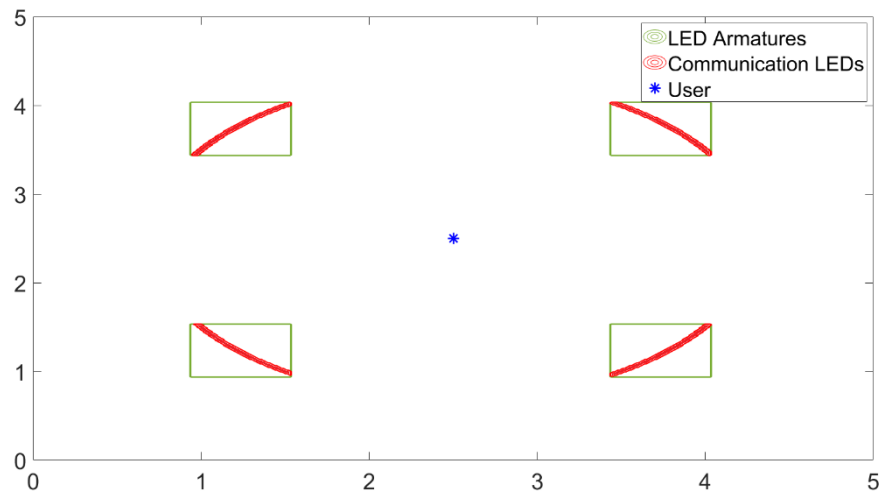
end

Find K matrix obtained for maximum value of $Snr(n)$ to determine communication LEDs.

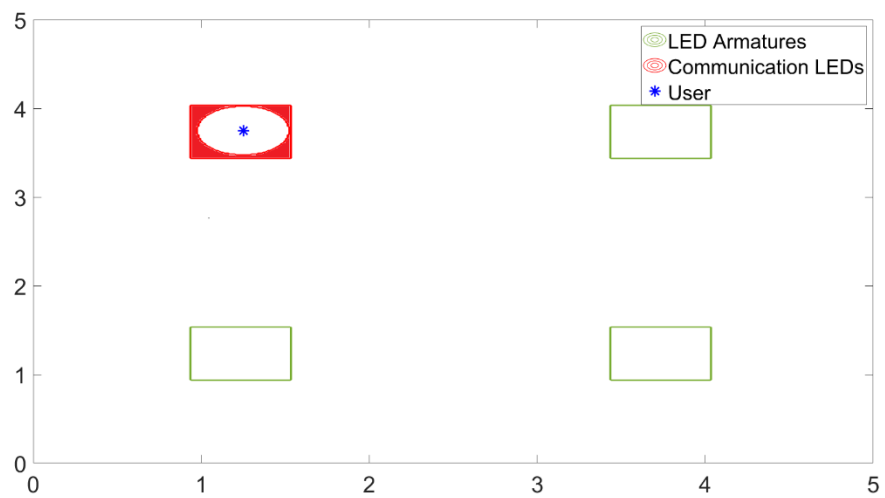
Positions of the communication LEDs are shown in Figure 4. The communication LEDs are selected as explained in Table 2. In the figure, the communication LEDs, the LED armatures and the position of the users are shown with red, green and blue colors, respectively.



(a)



(b)



(c)

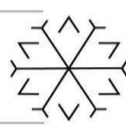
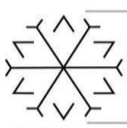


Figure 4: Selected LEDs for communication for (a) (0, 0, 0.85), (b) (2.5, 2.5, 0.85) (c) (1.25, 3.75, 0.85) coordinates.

In Table 3, the numbers of communication LEDs selected depending on the user locations and obtained SNR values are presented. It has been observed that just increasing number of communication LEDs does not mean achieving higher SNR value. Best SNR value for a user can be obtained by selection of appropriate communication LEDs at optimum number according to position of the user. Also, for all the user locations it is observed that the obtained SNR values are above 13.6 dB, which is required SNR value for uninterrupted communication (Komine at al., 2004).

Table 3. Number of communication LEDs and obtained SNR values depending on user location.

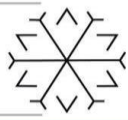
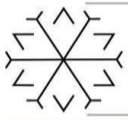
Location	Number of LEDs	SNR (dB)
0, 0, 0.85	612	23.8987
2.5, 2.5, 0.85	1306	30.7660
1.25, 3.75, 0.85	1239	39.6052

4. Conclusion

In this paper, a LED selection algorithm is applied to improve SNR in a Li-Fi system. The communication LEDs are selected according to location of the user. Other LEDs of the armateurs can be used for lighting or for communication with another user. In the simulations, 13.6 dB, which is required for uninterrupted communication is exceeded for various user positions. The results show that, obtained SNR values are increased with increasing number of communication LEDs for some cases. In addition, dependent on location of the user, bigger SNR value can be achieved with lower number of communication LEDs.

References

- Aydın, B 2021, 'LED Dizileri Kullanılarak Yüksek Hızlı Li-Fi Sistem Tasarımı', MA thesis, Erzurum Technical University, Erzurum.
- Johri, R. (2016) Li-Fi, complementary to Wi-Fi. In. International Conference on Computation of Power, Energy Information and Commuincation (ICCPEIC). IEEE. 015-019.
- Komine, T., and Nakagawa, M. (2004). Fundamental analysis for visible-light communication system using LED lights. IEEE transactions on Consumer Electronics, 50(1), 100-107.
- Komine, T., Lee, J. H., Haruyama, S. and Nakagawa, M. 2009. Adaptive equalization system for visible light wireless communication utilizing multiple white LED lighting equipment. IEEE Transactions on Wireless Communications, 8(6), 2892-2900.
- Kumar, J. D., Priyadharsini, K., Srinithi, K., Sampriha, R. V., & Babu, C. G. (2021, March). An Experimental Analysis of Lifi and Deployment on Localization Based Services & Smart Building. In 2021 International Conference on Emerging Smart Computing and Informatics (ESCI) (pp. 92-97). IEEE.
- Raj, B. D., Rakesh, B., Avinash, N., Balakrishnan, K. and Basavaraju, S. (2018). Visible Spectrum using Optical Communication. Perspectives in Communication, Embedded-systems and Signal-processing-PiCES 2018, 2(7), 153-156.
- Ren, J., Zhu, Y., Zhang, Y., and Li, D. (2021). Optimization of multi-receiver SNRs for indoor visible light communication based on modified evolutionary algorithm. Optik, 228, 166158.
- Sarkar, A., Agarwal, S., and Nath, A. (2015). Li-Fi technology: data transmission through visible light. International Journal of Advance Research in Computer Science and Management Studies, 3(6).
- Sharma, R. R. and Sanganal, A. (2014). Li-Fi Technology: Transmission of data through light. International Journal of Computer Technology and Applications. 5(1), 150.



Sharma, R., Kumari, A. C., Aggarwal, M., & Ahuja, S. (2018). Optimal LED deployment for mobile indoor visible light communication system: Performance analysis. *AEU-International Journal of Electronics and Communications*, 83, 427-432.

Wang, L., Wang, C., Chi, X., Zhao, L., & Dong, X. (2017). Optimizing SNR for indoor visible light communication via selecting communicating LEDs. *Optics communications*, 387, 174-181.

Yang, Y., Yang, Y., Chen, M., Feng, C., Xia, H., Cui, S., & Poor, H. V. (2021). Joint LED Selection and Precoding Optimization for Multiple-User Multiple-Cell VLC Systems. *IEEE Internet of Things Journal*.

Zhang, F., Wang, F., Zhang, J., & Zuo, T. (2021). SVM aided LEDs selection for generalized spatial modulation of indoor VLC systems. *Optics Communications*, 127161.

Characterization of ZnO Thin Films Deposited by SILAR and Spin Coating Methods

Melih ÖZDEN ¹*[0000-0002-6383-1464] and Çağlar DUMAN ²[0000-0002-1845-8605]

¹melih.ozden@erzincan.edu.tr, Erzincan Binali Yıldırım University

²caglarduman@erzurum.edu.tr, Erzurum Technical University

Abstract

In this study, zinc oxide (ZnO) thin films are deposited on a silicon substrate by using Successive Ionic Layer Adsorption and Reaction (SILAR) and spin coating methods. Scanning electron microscopy (SEM) and X-ray diffraction (XRD) measurements are made to examine the surface morphologies and crystal structures of the obtained samples, respectively, and photoluminescence (PL) measurements are taken to investigate optical properties of the films. From the SEM measurements, it is observed that the surfaces are homogeneous and ZnO nano-rods are formed on the surfaces and the presence of ZnO peaks is confirmed from the XRD measurements. From the PL measurements, it is observed that the samples can emit light around 380 nm. The measurements reveal that the thin films deposited by spin coating method have better characteristics than deposited by SILAR method.

Keywords. Zinc oxide, SILAR, spin coating

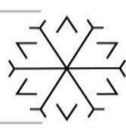
1. Introduction

ZnO is a Group II-VI semiconductor. Due to its internal defects, it naturally deposits as n-type and has a hexagonal crystal structure. It has a direct bandgap of around 3.4 eV at room temperature and a powerful excitonic binding energy of the order of 60 meV (Willander *et al.*, 2009; Mondal, Kanta and Mitra, 2012). Because of these properties, it is understood that efficient radiation based on exciton can be obtained from ZnO at room temperature. In addition, it is an important advantage that it is a material resistant to particle radiation damage (Look, 2001). Due to these properties, they are used in many electronic and optical applications such as solar cells, transparent conductive films, chemical sensors, varistors, light-emitting diodes, UV photodetectors, laser diodes, and gas sensors (Güney and Duman, 2016).

Various methods are used for growth of ZnO thin films, such as SILAR, chemical vapor deposition (CVD), chemical bath deposition (CBD), pulsed laser deposition (PLD), molecular beam epitaxy (MBE), electrochemical deposition (ECD) and spin coating. ZnO naturally deposits as n-type by deviating from stoichiometry due to defects such as oxygen vacancies and zinc slits in its internal structure (Özgür *et al.*, 2005).

Taner *et al.*, in 2011 have been investigated effect of number of SILAR cycles on characteristics of ZnO thin films deposited on glass. At the end of 10, 15, 20, 25 SILAR cycles, four different samples have been obtained. It is observed that the crystal structure with random orientation of ZnO improved with the increased number of the SILAR cycles. The variation of bandgap due to the structural changes, and the cauliflower shapes forming on the surface become clearer as the SILAR cycle number increased. The effects of the selected substrate for ZnO thin film deposition are examined. For this reason, ZnO thin films are deposited on copper, silicon, and glass substrate by using SILAR method. From the XRD measurements, they found that (101), (103), and (002) preferential orientations predominate for copper, silicon, and glass, respectively. The SEM results showed that the ZnO grains deposited on the copper substrate have hexagonal structure, the ones deposited on the silicon substrate have the form of spindles, and the ones deposited on the glass substrate have the shape of small flowers and prisms (Raidou *et al.*, 2014).

Spin speed used for spin coating effect the thicknesses of ZnO thin films. For this aim, ZnO thin films coated on the glass substrate at 1000, 2000, 3000, 4000, 5000, and 6000 rpm are investigated. It is shown that the film thickness decreases with increasing spin speed. Also, transmittance and bandgap measurement values obtained at 2000 and 3000 rpm are closest to bulk ZnO (Ajadi, Agboola and Adedokun, 2016). Also, by increasing annealing temperature of spin coated ZnO thin films, the bandgap values decrease and the surface roughnesses increase (Sanjeev and Kekuda, 2015).



In this study, ZnO thin films are deposited by SILAR and spin coating methods. These methods are preferred because they are economical and easily accessible. In both methods, ZnO thin films are deposited by combining the prepared chemical solutions and the substrate materials under suitable conditions. In SILAR method, the substrate is dipped in the prepared chemical solutions many times. In the spin coating method, the chemical solution dropped on the substrate spreads homogeneously on the substrate as a result of rapid rotation of the substrate, and a thin film layer is obtained. In the study, silicon is preferred as the substrate for easy adaptation of the produced thin films to various electronic circuits. Surface morphologies and crystal structures of ZnO thin films are investigated by scanning electron microscopy (SEM) and X-ray diffraction method (XRD), respectively. Examination of the optical properties of thin films is carried out by photoluminescence spectroscopy (PL).

2. Material and Method

2.1. Successive Ionic Adsorption and Reaction (SILAR)

SILAR method, which is one of the chemical methods that can be used in thin film deposition, takes its name from the initials of the term 'Successive Ionic Layer Adsorption and Reaction'. This method is suggested by Ristov et al. in 1985 for the first time and named as SILAR by Nicolau in the same year. SILAR method can be used to deposit binary and triple compounds of elements in different groups of the periodic table (Akaltun, 2006). SILAR method consists of 3 main parts as shown in Figure 1.

- Preparation of solutions containing suitable ions,
- Dip of the substrate into solutions thus deposition on the substrate and
- Repeating this process as many times as desired.

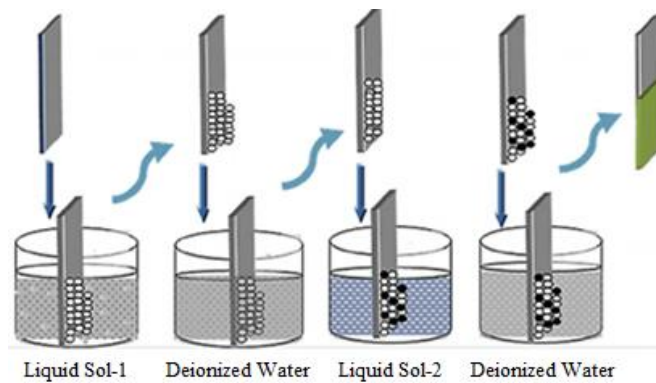
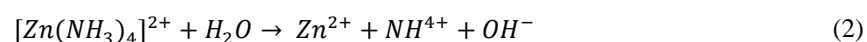
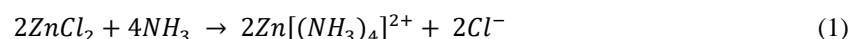


Figure 1: Schematic diagram of SILAR method

SILAR method is suitable for deposition on large surfaces. It is preferred because of its applicability, simplicity and low cost. Qualified thin films can be obtained with SILAR method by optimizing the preparation conditions of the liquid solutions, the concentration, pH value, reaction and rinsing time (Astam, 2006).

In this study, 682 mg of zinc chloride ($ZnCl_2$) is added to 50 ml of deionized water to obtain 0.1 M precursor solution. The pH of the solution is adjusted to 10 by adding 6 ml of ammonia. The resulting solution is mixed for 5 minutes and transferred to a beaker. A SILAR round is completed by keeping the substrates in zinc chloride solution for 30 seconds, in the air for 15 seconds and deionized water at $90^\circ C$ for 15 seconds. The processes are repeated 80 times. The chemical reactions that occur during the deposit of ZnO structures with SILAR method are as shown in Equation (1) to (4) (Güney and Ertarğın, 2015).



2.2. Spin Coating

The spin coating method is discovered by Ebelmen in 1846 and in 1939, Geffcken demonstrated that a thin film can be deposited on a SiO₂ substrate by this method. This method is extensively studied by Schott Glass in the 1950s. This method is widely used due to its simplicity, low cost, and easy accessibility. Also, thin films of varying thickness from nanometers to micrometers can be deposited by using this method (Brook, 1989).

In this method, the solution chosen depending on the thin film to be deposited is dripped onto the substrate and the substrate is spun at a speed depending on the desired thin film thickness. The solution spreads homogeneously on the substrate with the effect of centrifugal force and excess solution is removed over the substrate. In this way, the same film thickness is created at every point of the substrate (Özdemir, 2013). Figure 2 shows the stages of the spin coating method.

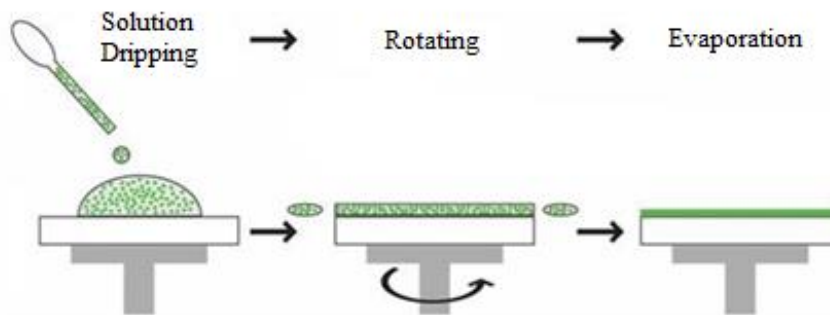


Figure 2: Spin coating method schematic diagram

Spin coating method starts with preparation of 0.5 M precursor solution. It is obtained by adding 5.48775 g of zinc acetate dihydrate ($Zn(CH_3COO)_2 \cdot 2H_2O$) to 50 ml of 2-methoxy ethanol ($C_3H_8O_2$). To obtain 0.5 M secondary solution, 1.512 ml of monoethanolamine (C_2H_7NO) is mixed with 50 ml of 2-methoxy ethanol ($C_3H_8O_2$). A homogeneous solution is formed by combining these two solutions in a beaker and mixing at 60°C for 2 hours. The prepared solution is dripped onto the silicon substrate and the substrate is spun at 3000 rpm for 30 seconds. Then the sample is baked at 250°C for 10 minutes. These processes are repeated 10 times and the sample is annealed at 450°C for 30 minutes as final step.

3. Characterization of ZnO Thin Films

The XRD measurements of the samples are presented in Figure 3. When the figures are examined, it is understood that the marked peaks are compatible with the ZnO peaks in the literature (Kodigala, 2011). There are ZnO peaks for the samples deposited by both methods as labeled in the figure. It is noteworthy that the number of peaks is less in the spin coating method compared to SILAR method.

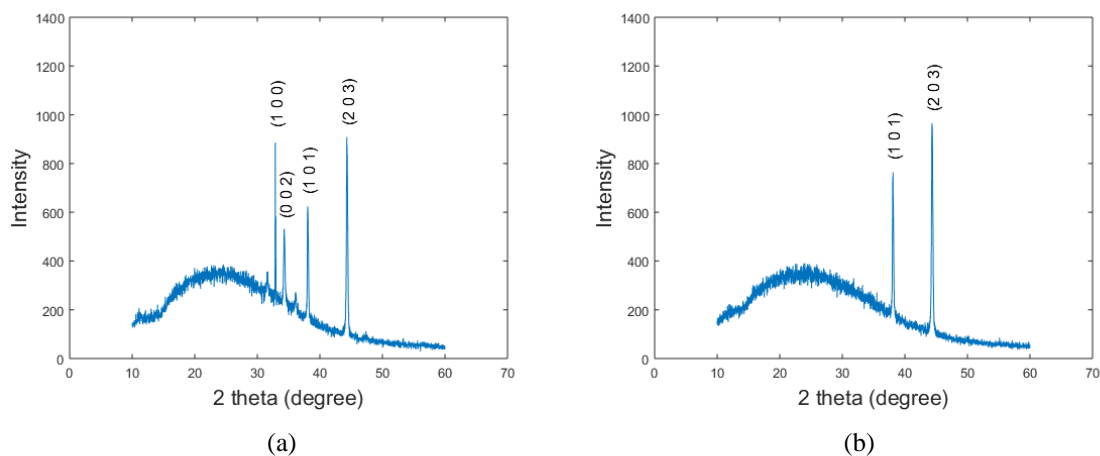


Figure 3: XRD results of the samples deposited by a) SILAR method and b) spin coating method.



Figure 4 shows SEM images of the samples. In both figures, nanostructures draw attention. Especially with SILAR method, nano flower shaped structures are formed. Size of the ZnO particles deposited by using the spin coating method is smaller than size of the ZnO particles deposited by using SILAR method. Also, it is clear from the figure, the spin coating method is better than SILAR in terms of homogeneity.

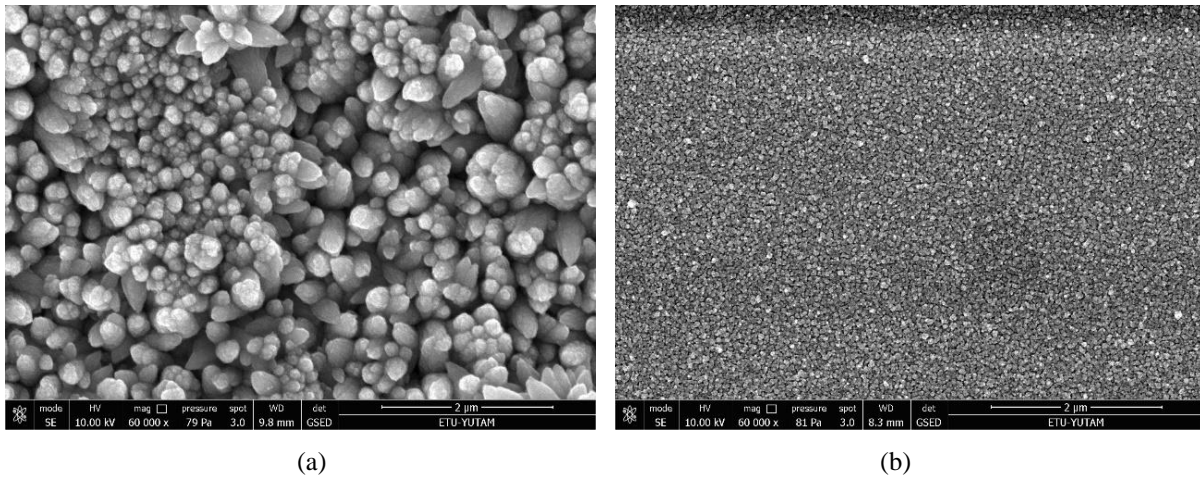


Figure 4: SEM images of the sample deposit by using a) SILAR method, b) spin coating method.

Figure 5 shows the PL measurement results of the samples. The samples are excited by a laser lasing at 650 nm. In the figure, the radiations of both samples in the UV region and the visible region draw attention. The radiation in the visible region originates from crystal defects (oxygen vacancies and zinc slits) in the internal structure of ZnO. These PL peaks can be reduced with more careful selection of the deposition parameters. The radiation around 380 nm is result of the direct bandgap of ZnO, which is around 3.26eV. The sample deposited with the spin coating method has a higher PL density around 380 nm than the sample deposited with SILAR method.

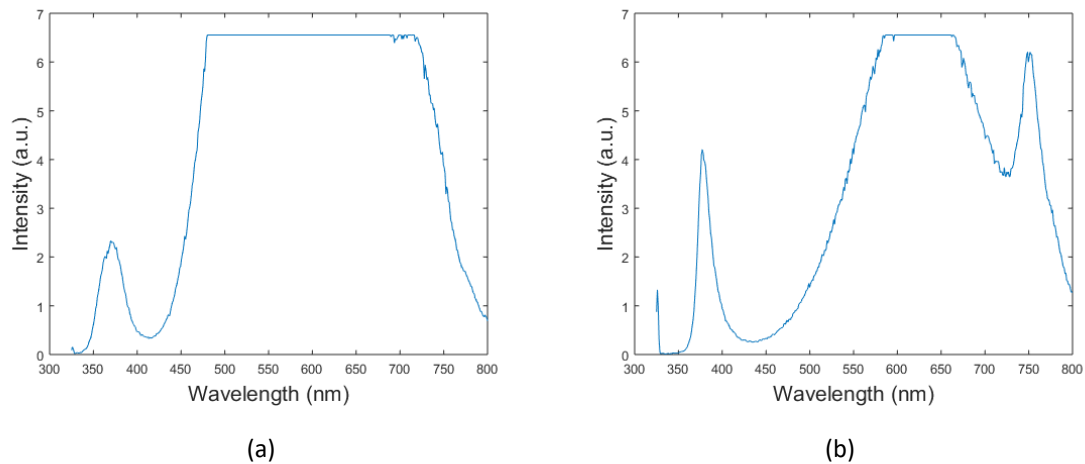
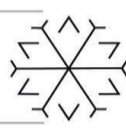
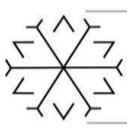


Figure 5: PL measurement results of the sample deposit by a) SILAR method and b) spin coating method

4. Conclusion

Within the scope of the study, ZnO thin films are coated on silicon substrates using SILAR and spin coating methods. XRD, SEM, and PL measurements of the obtained thin films are examined. Both methods can be used for ZnO thin film deposition. XRD measurement results indicate that there are ZnO peaks on the samples obtained by both methods and the number of preferential orientations in the sample grown by the spin coating method is less. The SEM measurements show the presence of nano flower shaped structures on the sample obtained with the SILAR method. The SEM measurements also show that more homogeneous films are obtained by using spin coating method. The PL results show that both samples emit around 380 nm and the emission of the sample obtained with spin coating method is more powerful. In summary, characterization results indicate that better quality ZnO thin films can be deposited with spin coating method.



Acknowledgements

This work is supported by Erzurum Technical University BAP Program (Project No: ETÜ BAP 2017/24)

References

- Ajadi, D.A., Agboola, S.M. and Adedokun, O. (2016) 'Effect of Spin Coating Speed on Some Optical Properties of ZnO Thin Films', *Journal of Materials Science and Chemical Engineering*, 04(05), pp. 1–6. doi:10.4236/msce.2016.45001.
- Akaltun, Y. (2006) *CdSe, ZnSe ve Cd_xZn_{1-x}Se Yarıiletken İnce Filmlerinin SILAR Tekniği ile Büyütülmesi Yapısal, Optik ve Elektriksel Özelliklerinin İncelenmesi*. Doktora Tezi. Atatürk Üniversitesi.
- Astam, A. (2006) *InSe İnce Filmlerin SILAR Yöntemiyle Büyütülmesi ve Karakterizasyonu*. Yüksek Lisans Tezi. Atatürk Üniversitesi.
- Brook, R. (1989) 'Sol-gel technology for thin films, fibers, preforms, electronics and specialty shapes. Edited by L. C. Klein. Noyes Publications, New Jersey, USA 1988. xxi, 407 pp., bound, US\$72.- ISBN 0-8155-1154-X', *Advanced Materials*, 1(8–9), pp. 309–309. doi:10.1002/adma.19890010816.
- Güney, H. and Duman, Ç. (2016) 'Influence of Te and Se doping on ZnO films growth by SILAR method', in. *International Conference On Advances In Natural and Applied Sciences ICANAS 2016*, Antalya, Turkey, p. 020122. doi:10.1063/1.4945948.
- Güney, H. and Ertarğın, M.E. (2015) 'Effective annealing of ZnO thin films grown by three different SILAR processes', *Eastern Anatolian Journal of Science*, 1(1), pp. 20–24.
- Kodigala, S.R. (2011) *Cu(In_{1-x}Ga_x)Se₂ Based Thin Film Solar Cells*. Academic Press.
- Look, D.C. (2001) 'Recent advances in ZnO materials and devices', *Materials Science and Engineering: B*, 80(1–3), pp. 383–387. doi:10.1016/S0921-5107(00)00604-8.
- Mondal, S., Kanta, K.P. and Mitra, P. (2012) 'Preparation of ZnO film on p-Si and I-V characteristics of p-Si/n-ZnO', *Materials Research*, 16(1), pp. 94–99. doi:10.1590/S1516-14392012005000149.
- Özdemir, T. (2013) *Investigation of optical model of the irradiated ZnO : Al thin films by neutrons*. Master's Thesis. İstanbul Technical University.
- Özgür, Ü. *et al.* (2005) 'A comprehensive review of ZnO materials and devices', *Journal of Applied Physics*, 98(4), p. 041301. doi:10.1063/1.1992666.
- Raidou, A. *et al.* (2014) 'Effect of substrate on ZnO thin films grown by SILAR method', in *2014 International Renewable and Sustainable Energy Conference (IRSEC)*. *2014 International Renewable and Sustainable Energy Conference (IRSEC)*, pp. 695–700. doi:10.1109/IRSEC.2014.7059829.
- Sanjeev, S. and Kekuda, D. (2015) 'Effect of Annealing Temperature on the Structural and Optical Properties of Zinc Oxide (ZnO) Thin Films Prepared by Spin Coating Process', *IOP Conference Series: Materials Science and Engineering*, 73, p. 012149. doi:10.1088/1757-899X/73/1/012149.
- Willander, M. *et al.* (2009) 'Zinc oxide nanorod based photonic devices: recent progress in growth, light emitting diodes and lasers', *Nanotechnology*, 20(33), p. 332001. doi:10.1088/0957-4484/20/33/332001.

Investigation of Multisection Mode Locked 980 nm and 1550 nm Diode Lasers

Rukiye Aksakal¹[0000-0002-2708-2937], Kamer Ozge Arslan²[0000-0002-0999-3710] and Bulent Cakmak³[0000-0002-9939-4809]

¹ rukiyeaksakal@atauni.edu.tr, Department of Electrical Electronical Engineering, Ataturk University

² ozge.arslan@erzurum.edu.tr, High Technology Research and Development Center, Erzurum Technical University

³ bulent.cakmak@erzurum.edu.tr, Department of Electrical Electronical Engineering, Erzurum Technical University

Abstract

The variations of the power versus time, the carrier density versus time and the pulse widths of the 980 nm InGaAs/GaAs and 1550 nm AlGaInAs/InP passively mode locked semiconductor lasers consisting two gain sections and one absorption section are comparatively modelled using traveling wave equations. Pulse width of the both semiconductor lasers is the same, which is 1.57 ps. Additionally, 980 nm lasers exhibited better performance in terms of higher power, which is calculated to be 1200 mW. Finally, the pulse width was calculated for different lengths of the absorption section. It is observed that as the length of the absorption section increases, the power also increases. However, if the length of the absorption section is reduced, it is necessary to increase the current applied to the gain section to increase the power.

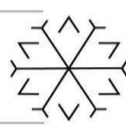
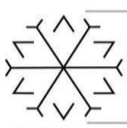
Keywords. Laser, semiconductor, mode-locked, modelling

1. Introduction

Lasers have managed to take their place among the indispensable technologies of the 21st century due to their frequent use in fields such as industry, medicine, defense, communication, etc. (Kaushal and Kaddoum, 2017). The aim of laser production is to obtain laser beams with high power and a single wavelength (monochromatic) (Arslan et al., 2021; Patil and Dhami, 2008). In this context, semiconductor lasers have emerged as the most widely used laser type among laser types. Mode-locked lasers, which are one of the ultra-short pulsed and high-power laser production techniques in semiconductor laser technologies, are of great importance (Derickson et al., 1992; Ma et al., 2019). The basic factor in mode locking is that all modes formed in the laser cavity are in phase. In this technique, the frequency range between the modes is desired to be equal and therefore the gain or loss of the laser cavity is modulated. Thus, time-spaced pulses are produced whose repetition rate is equal to the round-trip time in the cavity (Ippen, 1994; Kuntz et al., 2007). For mode-locked laser operation, passive mode-locked lasers are preferred because they are easier to construct and successful in producing ultra-short pulses. In the passive mode locking technique, the gain section of the laser is forward-biased with current, while the absorption part is biased with the reverse voltage (Javaloyes et al., 2013). Multisection mode-locked lasers are often preferred because they provide higher output power than single-section lasers. In our previous work, we reported a comparison of passive-mode locked semiconductor lasers with one and two gain section (Aksakal et al., 2020). According to the results obtained, it was observed that the passive mode locked lasers with two gain sections have higher output power and shorter pulse duration. In this study, wavelength dependent output power and pulse duration of a passive mode locked semiconductor laser with two gain sections are investigated. In addition, output power variations were obtained depending on the length of the absorption section and the current.

2. Theoretical Analyses

2.1. Travelling Wave Equations



Mode locking is described as the propagation of an optical pulse through a waveguide medium (Zatni et al., 2004). Both position and time-dependent modelling techniques are needed for the analysis of these propagation ultrashort optical pulses. Travelling wave equation in which optical mode in a cavity is combination of forward and backward propagation waves, can be described as (Williams et al., 2004).

$$\frac{1}{v_g} \frac{\partial F(t,z)}{\partial t} + \frac{\partial F(t,z)}{\partial z} = (g - i\delta - \alpha_i)F(t,z) + i\kappa R(t,z) + s_f(z,t) \quad (1)$$

$$\frac{1}{v_g} \frac{\partial R(t,z)}{\partial t} - \frac{\partial R(t,z)}{\partial z} = (g - i\delta - \alpha_i)R(t,z) + i\kappa F(t,z) + s_r(z,t) \quad (2)$$

Where F and R are the slowly varying complex envelope amplitudes for the forward and reverse optical fields (Zatni et al., 2004). In these equations v_g , g , α_i , δ , κ and $s_{r,f}$ are the group velocity of optical pulse, the local gain, the local loss, the detuning factor, the coupling parameter and the spontaneous emission noise, respectively. These equations take into account only waves in propagation direction and neglect waves in other directions (Williams et al., 2004). Gain and absorbance dependent on carrier and photon densities at gain and absorber sections of the laser are given by

$$g(N) = \frac{\Gamma g_G [n_t - N(t,z)]}{2(1 + \varepsilon_g P(t,z))} \quad (3)$$

$$g(N) = \frac{\Gamma g_A [N(t,z) - n_t]}{2(1 + \varepsilon_A P(t,z))} \quad (4)$$

where Γ is the confinement factor, $g_{G/A}$ is the differential gain constant, n_t is the transparent carrier density, $\varepsilon_{G/A}$ is the gain compression factor and P is the photon density.

Carrier rate equations for gain and absorption sections are given by,

$$\frac{\partial N(t,z)}{\partial t} = \frac{I}{eV} - \frac{N(t,z)}{\tau_G} - \frac{2v_g P(t,z)g}{\Gamma} \quad (5)$$

$$\frac{\partial N(t,z)}{\partial t} = -\frac{N(t,z)}{\tau_A} + \frac{2v_g P(t,z)g}{\Gamma} \quad (6)$$

where I is the laser driving current, e is the electron charge, V is the active layer volume, $\tau_{G/A}$ is the carrier lifetime at the gain and absorber sections. The carrier lifetime at the gain section is,

$$\tau_G = (A + BN(t,z) + CN(t,z)^2)^{-1} \quad (7)$$

where A is the recombination coefficients, C is the Auger recombination coefficient (Adams et al., 1987; Avrutin et al., 2000; Zatni et al., 2004; Zhang et al., 1994; Williams et al., 2004).

Table 1. Constants and laser parameters used for modelling

Parameter	Symbol	Value
Spontaneous emission factor	\mathcal{Q}_{sp}	10^{-3}
Length of gain1 section	L_{G1}	80 μ m
Length of gain2 section	L_{G2}	180 μ m
Length of absorber section	$L_{Absorber}$	45 μ m
Active-region width	w	5 μ m
Active-layer thickness	d	0.2 μ m



Confinement factor	ρ	0.3
Effective mode index	$\bar{\mu}$	3.4
Group refractive index	Γ_g	4
Linewidth enhancement factor	β_c	5
Facet loss	$\langle \alpha_m \rangle$	45 cm^{-1}
Internal loss	$\langle \alpha_{int} \rangle$	40 cm^{-1}
Gain constant	a	$2.5 \times 10^{16} \text{ cm}^2$
Carrier density at transparency	n_o	10^{18} cm^{-3}
Nonradiative recombination rate	A_{nr}	10^8 s^{-1}
Radiative recombination coefficient	B	$10^{-10} \text{ cm}^3/\text{s}$
Auger recombination coefficient	C	$3 \times 10^{-29} \text{ cm}^6/\text{s}$
Wavelengths	λ	980 nm and 1550 nm

Constants and laser parameters used in the calculations are given in Table 1. In our study, laser configuration are used in the calculations, as shown in Figure.1.

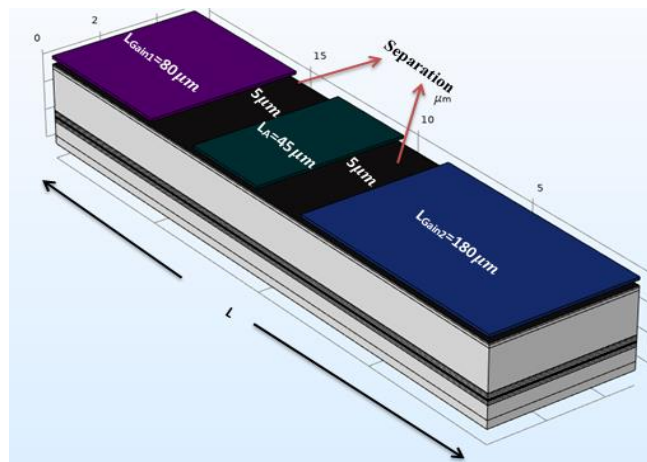


Figure 1: Configuration of a passively mode locked semiconductor laser used in the modelling, $L_{G1}=80\mu\text{m}$, $L_{G2}=180\mu\text{m}$ and $L_{\text{Absorber}}=45\mu\text{m}$

3. Modelling Results of Diode Lasers

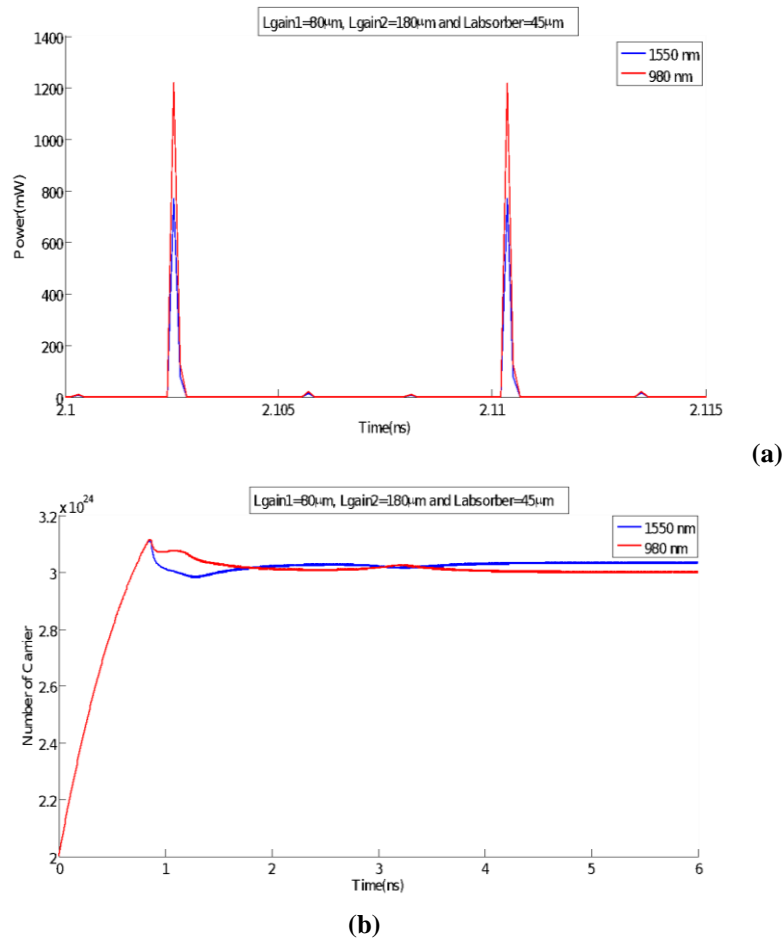
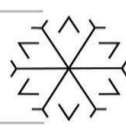
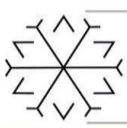


Figure 2: Modelling of passively mode locked semiconductor laser two gain sections for $L_{\text{gain1}}=80\mu\text{m}$, $L_{\text{gain2}}=180\mu\text{m}$ and $L_{\text{absorber}}=45\mu\text{m}$: a) Variation of power versus time for 1550 nm wavelength (blue solid line) and 980 nm wavelength (red dashed line), b) the number of carriers versus time for 1550 nm wavelength (blue solid line) and 980 nm wavelength (red dashed line)

In the modelling, the current is 120 mA while the reverse bias voltage is -0.5V and the length of the absorber section is 45 μm . Variations of the power versus time and the number of carriers versus time for 980 nm and 1550 nm at the passively mode locked semiconductor laser consisting of two gain sections with one absorption section are comparatively obtained. As seen Figure 2(a), pulse width of the 980 nm and 1550 nm semiconductor lasers is equal and 1.57 ps.

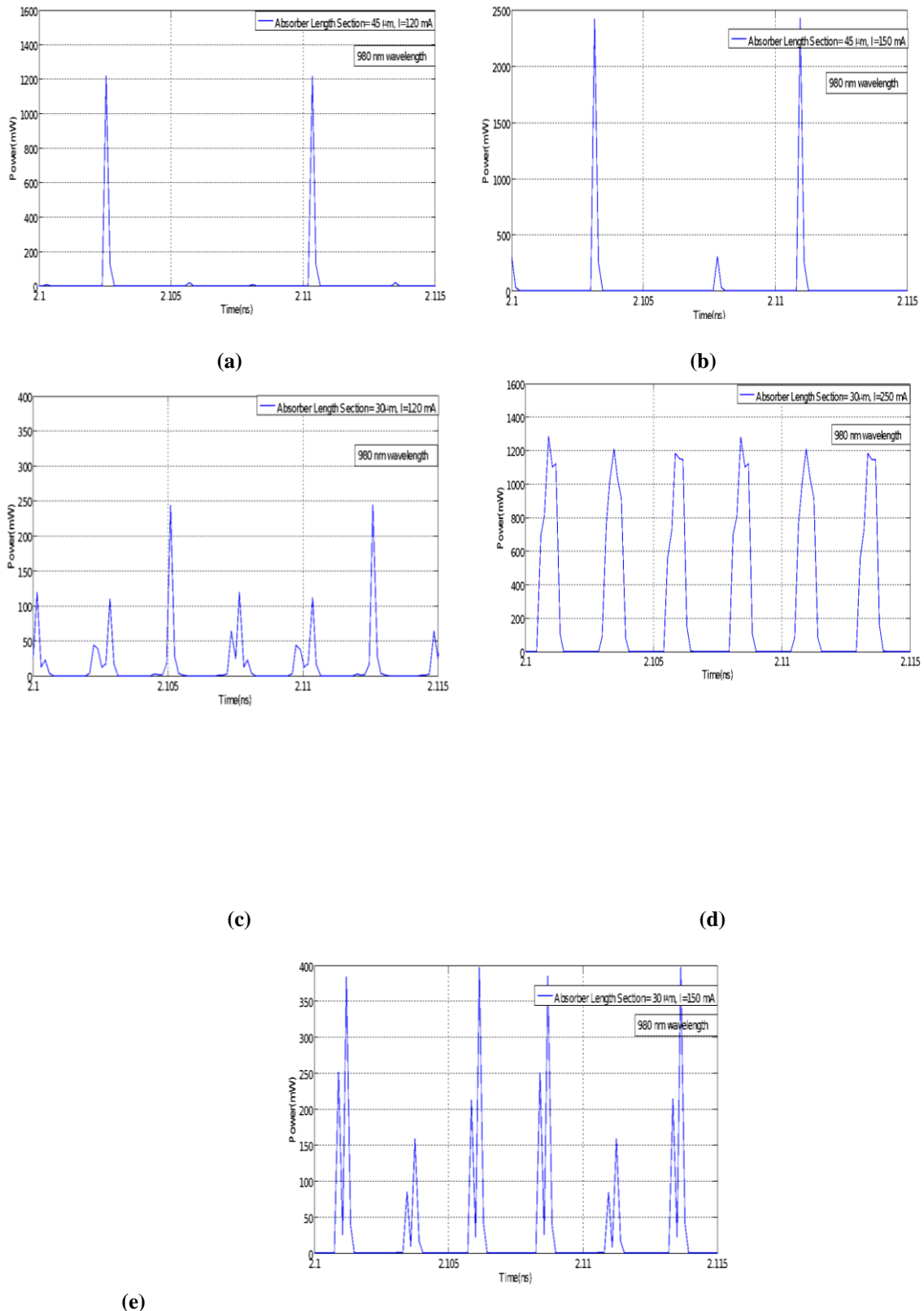
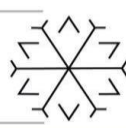
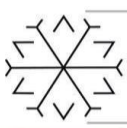


Figure 3: Variation of the power versus time for different length of absorber section and for $L_{gain1}=80 \mu\text{m}$, $L_{gain2}=180 \mu\text{m}$ and 980 nm wavelength: a) $L_{Absorber}=45 \mu\text{m}$, $I=120\text{mA}$ b) $L_{Absorber}=45 \mu\text{m}$, $I=150\text{mA}$ c) $L_{Absorber}=30 \mu\text{m}$, $I=120\text{mA}$ d) $L_{Absorber}=30 \mu\text{m}$, $I=150\text{mA}$ e) $L_{Absorber}=30 \mu\text{m}$, $I=250\text{mA}$

Figure 3(a) and (c) demonstrate the variations of the power versus time for different absorber lengths. The pulse width is obtained to be 1.57 ps while the length of the absorption section is 45 μm and the current is 120 mA (Figure 3(a)). As shown in Figure 3(c), the pulse width is calculated to be 82.6 ps while the current is increased to



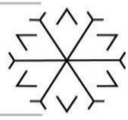
120 mA and the length of the absorption section is kept at 30 μm . The lengths of the gain and absorber sections are $L_{\text{gain1}}=80 \mu\text{m}$, $L_{\text{gain2}}=180 \mu\text{m}$ in all cases. It is observed that as the length of the absorption section increases while the current is kept constant, the power decreases and the pulse width increases in which higher order modes accompany with the variation of the power. Figure 3(b) demonstrates that the pulse width is calculated to be 1.78 ps when the length of the absorption section is 45 μm and the current is 150 mA but side modes occur. Figure 3(e) demonstrates that the pulse width is calculated to be 2.3 ps when the length of the absorption section is 30 μm and the current is 250 mA. In this case, higher order modes that deteriorate the power are eliminated. It is noted that if we want to reduce the length of the absorption section, as shown in Figure 3(c), (d) and (e), the current must be increased even more. When the length of the absorption section is reduced, in Figure 3(a) and (e), the power increases by increasing the current, as well as increasing the pulse width.

4. Conclusion

In this study, modelling of passively mode locked semiconductor lasers with 980 nm InGaAs/GaAs and 1550 nm AlGaInAs/InP has been carried out. The lasers with two gain sections and one absorber section are comparatively modelled using traveling wave equations. In the modelling, the variations of the power versus time, the carrier density versus time and the pulse widths of the 980 nm and 1550 nm wavelength semiconductor lasers are comparatively obtained. Pulse width of the laser output for 980 nm InGaAs/GaAs and 1550 nm AlGaInAs/InP lasers is obtained to be equal. Additionally, the power output at the wavelength of 980 nm is also higher. The pulse width was also calculated for different lengths of the absorption section. As a result, it has been reported that the power increases as the length of the absorption section increases. If we want to keep the absorption section shorter and also increase the power output, the current applied to the gain section must be increased.

References

- Adams, M. J., Steventon, A. G., Delvin, W. J. and Henning, I. D. (1987) Semiconductor lasers for long wavelength optical-fibre communications systems. England: Short Run Press Ltd.
- Aksakal, R., Duman, C. and Cakmak, B. (2020) Numerical investigation of 1550 nm passively mode-locked diode lasers with different gain and absorber configurations. *Laser Physics*, 30.
- Arslan, K. O., Aksakal, R. and Cakmak, B. (2021) Comparative results of 980 nm InGaAs/GaAs and 1550 nm AlGaInAs/InP diode lasers. *Mater. Today Proc.*, 46(16), pp.7015-7020.
- Avrutin, E. A., Marsh, J. H. and Portnoi, E. L. (2000) Monolithic and multi-gigahertz mode-locked semiconductor lasers: constructions, experiments, models and applications. *IEEE Proc. Optoelectron.*, 147, p.p. 251–278.
- Derickson, D. J., Helkey, R. J., Mar, A., Karin, J. R., Wasserbauer, J. G. and Bowers, J. E. (1992) Short pulse generation using multisegment mode-locked semiconductor lasers. *IEEE J. Quantum Electron.*, 28(10), pp. 2186–2202.
- Ippen, E. P. (1994) Principles of passive mode locking. *Appl. Phys. B Laser Opt.*, 58(3), pp. 159–170.
- Javaloyes, J., Balle, S., Avrutin, E. A., Tandoi, G., Stolarz, P., Sorel, M., Ironside, C.N. and Marsh, J. (2013) Dynamics of semiconductor passively mode-locked lasers: Experiment and theory. *International Conference on Transparent Optical Network*, p.p 1-4.
- Kaushal, H. and Kaddoum, G. (2017) Applications of lasers for tactical military operations. *IEEE Access*, 5, pp. 20736–20753.
- Kuntz, B. M., Fiol, G., Laemmlin, M., Meuer, C. and Bimberg, D. (2007) High-speed mode-locked quantum-dot lasers and optical amplifiers. *Proceedings of the IEEE*, 95(9), pp. 1767–1778.
- Ma, J., Qin, Z., Xie, G., Qian, L. and Tang, D. (2019) Review of mid-infrared mode-locked laser sources in the 2.0 μm -3.5 μm spectral region. *Appl. Phys. Rev.*, 6(2), pp. 0–29.
- Patil, U. and Dhami, L. (2008) Overview of lasers. *Indian J. Plast. Surg.*, 41(3), pp. 193–203.
- Williams, K. A., Thompson, M. G. and White, I. H. (2004) Long-wavelength monolithic mode-locked diode lasers. *New J. Phys.*, 6(1), pp. 1–30.
- Zatni, A., Khatip, D., Bour, M., Bihan, J. L. B. and Elhaziti, M. (2004) Analysis of the spectral stability of the



phase shift DFB laser (3PS-DFB). *Ann. Telecommun.*, 3, pp. 1031–1044.

Zhang, L. M., Yu, S. F., Nowell, M. C., Marcenac, D. D., Carroll, J. E. and Plumb, R. G. S. (1994) Dynamic analysis of radiation and side-mode suppression in a second-order DFB laser using time-domain large-signal traveling wave model. *IEEE J. Quantum. Electron.*, 30 pp. 1389–1395.

Mathematical Analysis and Control of Six Degrees of Freedom Flight Simulators

Merve KURT ^{*[0000-0002-2181-5386]} and Ahmet DUMLU ^[0000-0002-2181-5386]

Department of Electrical & Electronics Engineering, Erzurum Technical University, 25700, Erzurum, Turkey

merve.kurt025@gmail.com, ahmetdumlu@erzurum.edu.tr

Abstract

In this paper; information was given about the mechanical designs of six-degree-of-freedom flight simulators used for training purposes in the aviation industry, and all the detailed mathematical analyzes required for the control of the systems were carried out in detail. First of all, kinematic analyzes of the simulator have been made, and then the dynamic model of the linear motors used as actuators in the system has been obtained by using Newton's laws. All the outputs obtained as a result of the mathematical analyzes were used in the real-time trajectory control of the system. Thanks to the kinematics, control and data communication sub-functions prepared in Matlab-Simulink, the performance outputs of the system were examined in detail. According to the outputs obtained from the real-time trajectory control experiments, it has been shown that the mathematical analyzes for the system are correct and the trajectory tracking performance of the system can be increased, especially by determining the PID controller parameters depending on system modelling.

Keywords. Parallel manipulator, flight simulator, kinematic analysis, Model based PID control

1. Introduction

Flight simulators are preferred for pilot flight training in today's aviation industry. In order to train experienced pilot candidates, before the real flight, training is given with the help of a simulator in a virtual environment. Thanks to this simulator, the pilot candidate is provided to feel the translational and rotational movements of a real airplane at the closest level. In addition, a flight environment close to reality is created with a computer software so that the pilot candidate can perceive these movements. In order for this event to be close to reality, there is a parallel structure mounted on the underside of the simulator as shown in Figure 1 (Havelsan, 2021). This parallel structure is called the Stewart platform (Merlet., 2006). Thanks to this parallel structure, first proposed by Stewart in 1965, 3 translational and 3 rotational motions in free space can be achieved.



Figure-1: Flight simulator (Havelsan 2021)

For the aircraft cabin shown in Figure 1 to perform realistic translational and rotational movements, linear motors placed parallel to each other under the cabin must be well controlled. These motors must be able to respond quickly for reference input signals and must be robust against possible noise. There are many control methods developed for such systems in the literature. The backstepping controller controller was employed to control the flight



simulator (Liu and Wang., 2010). A sliding mode controller was designed to by (Liang-yu and Wu., 2011). M. Becerra-Vargas implemented a H-Infinity controller for for similar flight simulators. (M. Becerra-Vargas., 2015).

It is seen that all the articles listed above are a simulation study. In other words, none of these studies have been tested on a real simulator system. In this study, a real-time PID control method based on kinematic analysis has been developed. First of all, kinematic analyzes of the simulator have been made, and then the dynamic model of the linear motors used as actuators in the system has been obtained by using Kirchhoff and Newton's laws. All the findings obtained as a result of the mathematical analyzes have been used in the real-time trajectory control of the system. The real-time execution and outputs prove that the given kinematic based PID control technique progressively increases the system's controller efficiency.

2. General Mechanical Structure of Flight Simulator

The Stewart platform mechanism used in flight simulators has a special parallel structure. Structurally, the Stewart platform design consists of an top or mobile table and a fixed base plate. These two platforms in the system are connected to each other by six legs with universal joints. In addition, there are actuators that can change the length of the legs in the system. The Stewart platform mechanism has six controllable degrees of freedom.

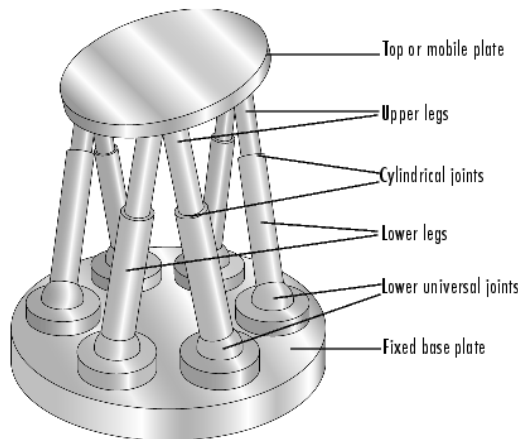


Figure-2: Structure of flight simulator

3. Mathematical Analysis of Flight Simulator

In this section, the necessary mathematical analyzes will be performed to successfully perform the trajectory control of the flight simulator. First of all, the kinematic analysis of the system will be performed. Then, dynamic analysis of linear motors used in the system will be made.

3.1. Kinematic Analysis of Flight Simulator

The main purpose in kinematic analysis is to determine the leg length values that can bring the aircraft cabin to the desired position. In order to perform the this analysis of the system the coordinate system defined by A(x, y, z) is placed on the fixed platform and the coordinate system defined by B(u, v, w) is placed on the moving platform , as shown in Figure-3.

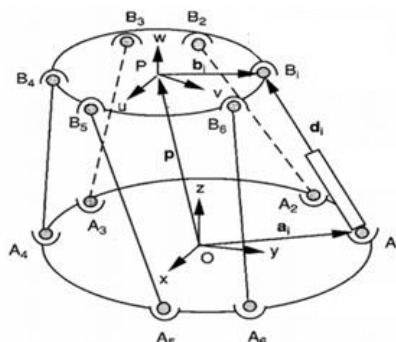
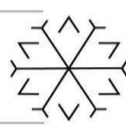


Figure-3: Schematic demonstration of the Stewart platform



The vectors a_i and b_i shown in the Figure-3 are the radius vectors of the fixed and mobile platforms, respectively. Each of these vectors is defined according to its own coordinate system as in Equation 1 and 1.

$$a_i = [a_{ix} \ a_{iy} \ a_{iz}]^T \quad (1)$$

$$Bb_i = [b_{iu} \ b_{iv} \ b_{iw}]^T \quad (2)$$

As it is known, in order to express any vector defined in the B coordinate system in the A coordinate system, the rotation matrix expressed in Equation 3 must be used.

$$R_A^B = [u_x \ v_x \ w_x \ u_y \ v_y \ w_y \ u_z \ v_z \ w_z] \quad (3)$$

The vector elements u, v and w expressed in Equation-3 represent the unit vector components extending along the moving platform. According to the schematic representation given in figure-3, a closed loop vector equation for the i leg of the system can be written as follows.

$$\underline{A_i B_i} = p + AR_B Bb_i - a_i \quad (4)$$

In this case, the length of the i leg can be obtained by the scalar product of the vector $\underline{A_i B_i}$ as follows.

$$d_i^2 = [p + AR_B Bb_i - a_i]^T [p + AR_B Bb_i - a_i] \quad (5)$$

$$d_i^2 = p^T p + [Bb_i]^T [Bb_i] + a_i^T a_i + 2p^T [AR_B Bb_i] - 2p^T a_i - 2[AR_B Bb_i]^T a_i \quad (6)$$

$$d_i = \sqrt{p^T p + [Bb_i]^T [Bb_i] + a_i^T a_i + 2p^T [AR_B Bb_i] - 2p^T a_i - 2[AR_B Bb_i]^T a_i} \quad (7)$$

According to this result, when certain position and orientation values of the moving platform are given, the actuator length (leg length) that will bring the moving platform to these position and orientation values can be easily found with the help of Equation-7.

3.2. Dynamic Analysis of Linear Motors

In order to control the simulators, the linear motors used in the system must be moved precisely. In order to precisely control the six linear models used in the system, the dynamic model of these motors must be obtained correctly. The mechanism of a linear dc motor is shown in the figure 4 (Mao and Hung., 2016). The mathematical equation of the motor consisting of ball screw drive system is expressed as follows.

$$K_t K_e \dot{\theta}_1 = -R_m \tau_e + K_t u \quad (8)$$

$$J \ddot{\theta}_1 + B \dot{\theta}_1 + K \theta_1 = \tau_e + KRx \quad (9)$$

$$M \ddot{x} + D \dot{x} + Kx + F_L = \frac{KR N_1}{N_2} \theta_1 \quad (10)$$

In Equation (8-10), K_t and K_e are the torque and motor back-electromotive force constants respectively. R_m is the motor resistance, τ_e is the motor torque and u is the input voltage. J , B and K are the inertia moment, viscous damping coefficient and equivalent stiffness of the DC linear motor respectively. As shown in Figure 4, θ_1 and θ_2 are the rotational angle of gear 1 and 2, And finally, R is the ratio of linear to rotational motion, K is the stiffness of the ball screw, M is the mass, L is the ball screw lead, F_L is the load disturbance and D is the viscous damper coefficient. Here, the relationship between R and L is denoted by $R = \frac{L}{2\pi}$.

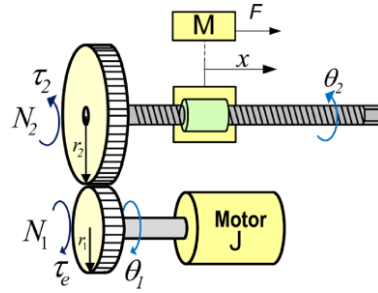


Figure-4: The Mechanism of Linear DC motor (Mao and Hung., 2016).

4. Trajectory Tracking Control Technique of Flight Simulator

Figure 5 shows the block diagram required for trajectory control of a flight simulator. First of all, the reference trajectory defined for the flight simulator in cartesian space is substituted in the kinematic equation defined in Equation 7 and appropriate leg length values are calculated. These calculated leg lengths are accepted as reference values for linear motors. Then, these values are compared with the current positions of the linear motors. Thus, the error values expressed as $e(t)$ in Equation 11 are obtained. The values of K_p , K_i and K_d parameters, which will directly affect the PID controller performance, are determined by using the dynamic model of the system expressed by Equation 10. After determining the appropriate parameters, the obtained control signal $u(t)$ is applied to linear motors.

$$u(t) = K_p e(t) + K_i \int e(t) dt + K_d \frac{de(t)}{dt} \tag{11}$$

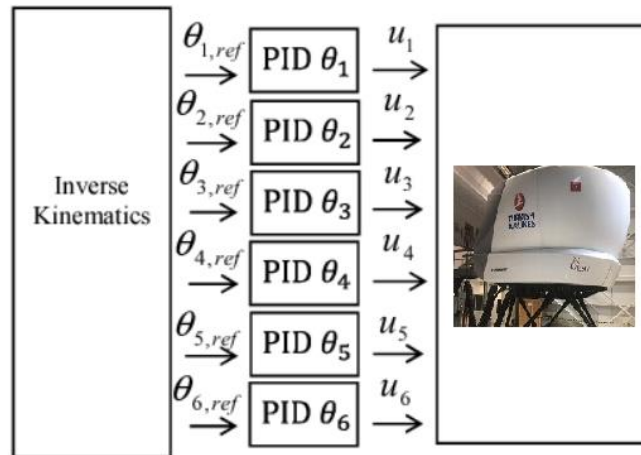


Figure-5: Block diagram of the control system

5. Experimental Results

The image of the prototype flight simulator used in this study is given in Figure 5. The system has 6 linear actuators. In addition, there are 12 universal joints and 3 specially designed roller bearings as mechanical parts. The system has 6 linear actuators. These actuators are connected to the upper and lower platforms by means of 12 universal joints. Both base and upper platform plates are made of plexiglass. The flight simulator has a load carrying capacity of up to 180N. System control is performed by the MyRIO microprocessor manufactured by National Instruments.

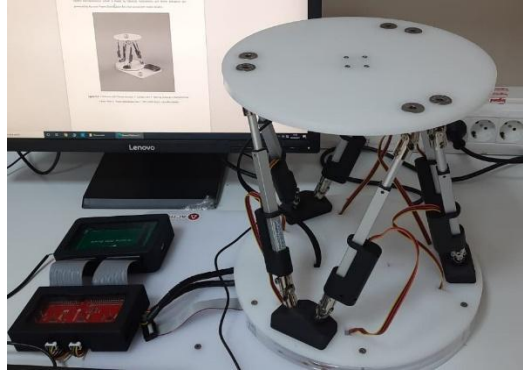
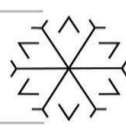
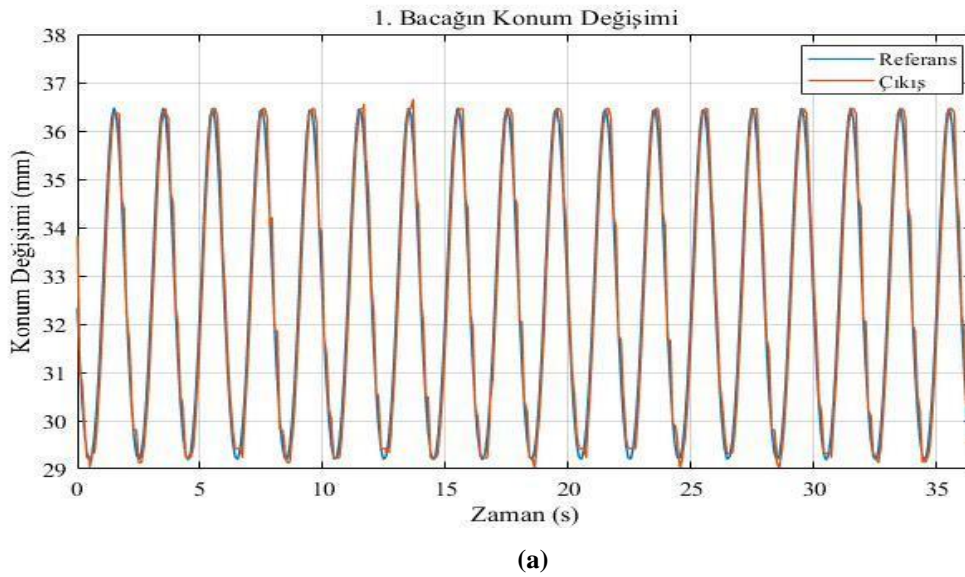


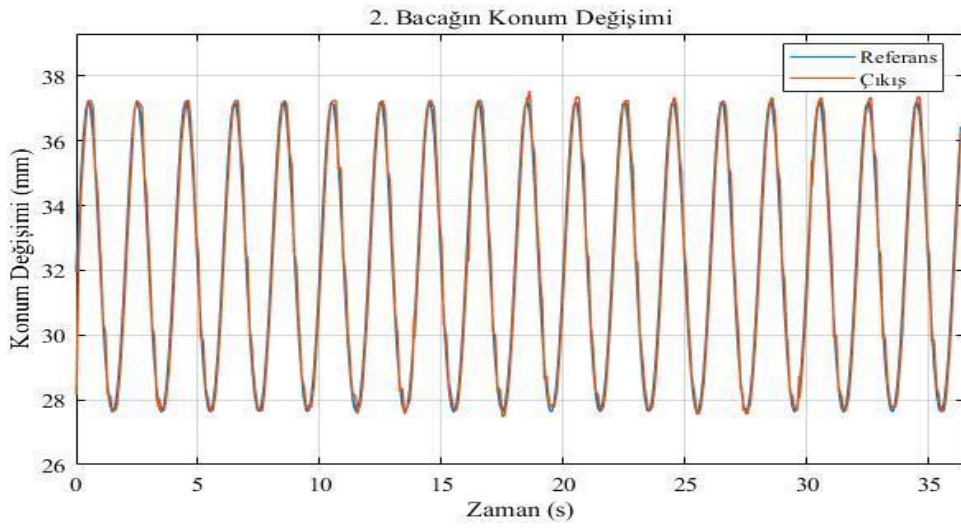
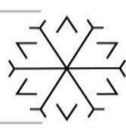
Figure-5: The image of the prototype flight simulator

In this study, the controller has been created on SIMULINK. The MyRIO microprocessor has been run to perform real-time executions. The sampling time for the setup has been adjusted to 0.01 sec. In order to determine the controller performance, the reference trajectory defined by Equation 12 has been defined to the flight simulator.

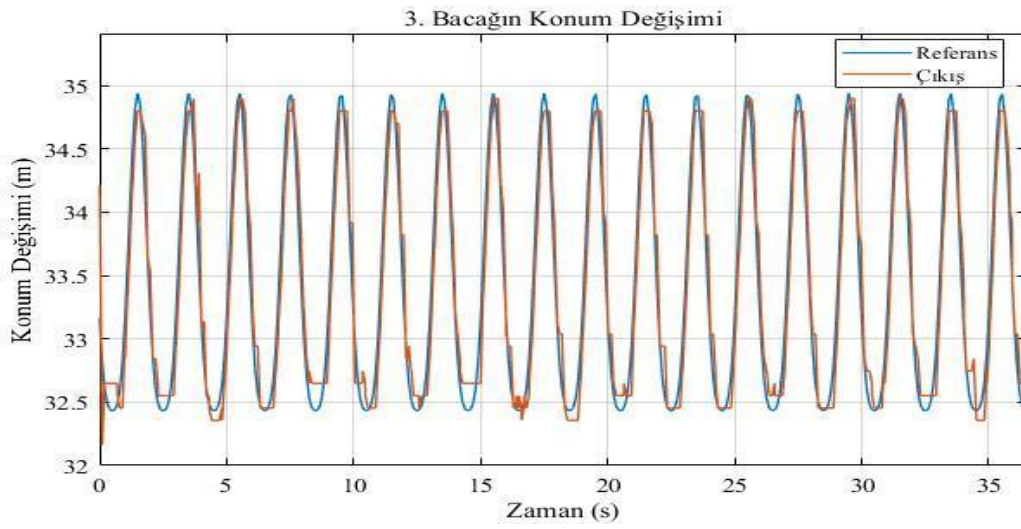
$$x(t) = 15\sin(2 * \pi * (5/10) * t), y(t) = 0, z(t) = 200 \quad (12)$$

The reference signal changes calculated for 6 motors against the defined trajectory and the experimentally obtained motor output signal changes are shown in Figure 5-10. As seen from Figures, the proposed model based PID control provides a pretty fast and effective output during the real-time execution, in addition to this, performing an acceptable small overshoot on the trajectory and precise tracking performance.

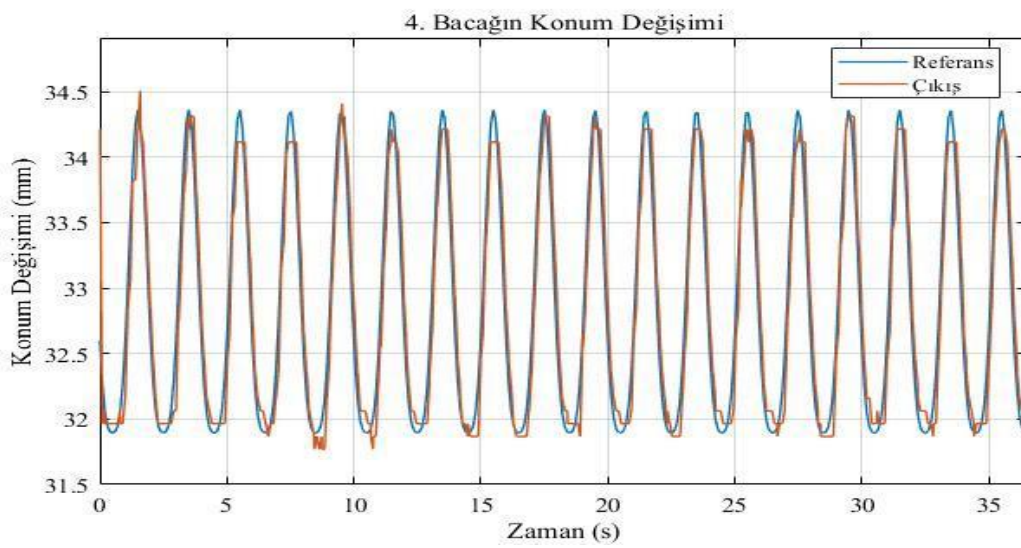




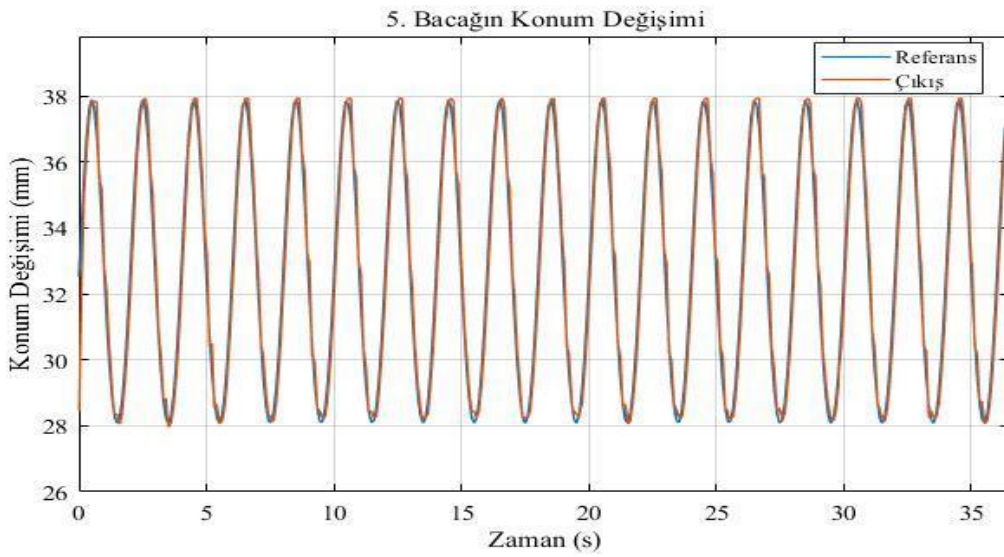
(b)



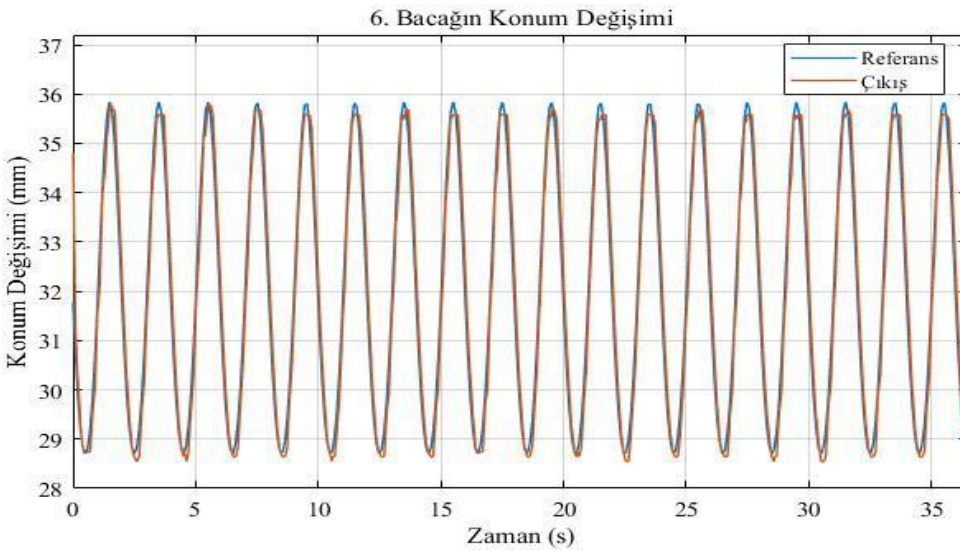
(c)



(d)



(e)



(f)

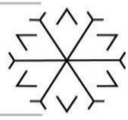
Figure-2: Actuator leg position changes

6. Conclusion

In this study, the mathematical analyzes required for the control of flight simulators are presented in detail. Thanks to the correct modeling of the system dynamics, a PID controller with appropriate parameters has been designed. The main contribution of this study to the literature is to share all kinematic analyzes of flight simulators, which are frequently used in the aviation industry, and to position the system correctly in real time. The main contribution of this study to the literature is to share all the mathematical analyzes of flight simulators, which are frequently used in the aviation industry, and to create the PID controller structure necessary to position the system correctly in real time. All these analyzes will be able to provide new contributions to the literature by using different types of controllers.

References

Havelsan2021, <https://www.havelsan.com.tr/sektorler/egitim-ve-simulasyon/sivil-havacilik/havelsan-ucus-simulatorleri>



M. Becerra-Vargas, "Comparison of robust control techniques for use in flight simulator motion bases," 2015 12th International Conference on Informatics in Control, Automation and Robotics (ICINCO), 2015, pp. 344-348.

Merlet, J.P. (2006). *Parallel Robots* (Second Edition). Springer, Dordrecht, Netherlands, 261-312.

Mao W-L, Hung C-W. Adaptive neural network-based synchronized control of dual-axis linear actuators. *Advances in Mechanical Engineering*. July 2016. doi:10.1177/1687814016654603

S. Liang-yu and W. Wu, "Flight simulator servo system friction compensation based on variable structure control," 2011 IEEE 3rd International Conference on Communication Software and Networks, 2011, pp. 645-648, doi: 10.1109/ICCSN.2011.6014652.

Z. Liu and J. Wang, "Research on adaptive friction compensation for flight motion simulator based robust backstepping controller," *Proceedings of the 29th Chinese Control Conference*, 2010, pp. 3333-3338.

Design and Implementation of Band Pass Filter based PI Controlled Shunt Active Power Filter to Fulfill IEEE-519 Harmonic Distortion Limits

Doğan ÇELİK¹*[0000-0002-8348-130X] and Mehmet Emin MERAL²[0000-0003-0841-4630]

¹dogancelik@yyu.edu.tr, Department of Electrical and Electronics Engineering, Van Yuzuncu Yıl University, Turkey

²emeral@yyu.edu.tr, Department of Electrical and Electronics Engineering, Van Yuzuncu Yıl University, Turkey

Abstract

Nonlinear electronic devices and increasing applications of power electronic equipment induce large-scale harmonic current/voltage distortions in power systems, which influence the efficiency and reliable operation of the entire system. A shunt active power filter (SAPF) can be taken into consideration as a useful technical solution to mitigate harmonics as well as reactive power compensation in the modern power distribution system. Therefore, the design and implementation of reliable power filters that diminish current and voltage harmonics to fulfill IEEE-519 harmonic distortion limits and the power quality requirements is a substantial requirement of modern power systems. In this paper, the design and implementation of the bandpass filter (BPF) based proportional-integral (PI) controlled SAPF is presented to regulate total harmonic distortion (THD) well within IEEE-519 and IEC 61000 standards. The presented BPF based PI control method provides better harmonic rejection capability compared with the low pass filter required by the instantaneous p-q theories. Constant DC-link voltage control is also achieved during susceptible load changes. The presented method can be implemented in both single and three phase power systems. The various results are conducted to confirm the advantages and effectiveness of the presented BPF based current controller for the SAPF in comparison with the other representative control methods.

Keywords. Active power filter, Bandpass filter, IEEE-519 standard, Nonlinear loads, Power electronic

1. Introduction

The electrical power distribution system is one of the most undefended systems to the power quality issues such as voltage/current harmonic distortion levels as a result of the common use of nonlinear electronic devices and increasing applications of power electronic equipment. The main sources of harmonics are nonlinear electronic switching devices including energy-efficient lighting, variable frequency drives and computer power supplies (VFDs), power electronic equipment VFDs, Arcing devices, rectifiers, electronically commutated (EC) motors and EV chargers, etc. Table 1 highlights the characteristics of harmonics under specific loads type. Many countries have enforced their standards to meet voltage and current harmonic distortion limits. IEEE standard 519-2014 for voltage and current harmonic distortion limits are presented in Table 2 and 3 (IEEE 519 Working Group 1992; Das 2015; Eroğlu et al. 2021; Kanjiya, Khadkikar & Zeineldin 2014). Shunt active power filters (SAPFs) are commonly paid regard as a useful technical solution to dampen the voltage and current harmonics as well as reactive power compensation in the modern power system (Zhang et al. 2015).

To avoid and dampen the propagation of the voltage and current harmonics, recently several approaches have been addressed. There are many control methods applicable to the APFs such as instantaneous reactive power theory, hysteresis controls, model predictive control, feedforward control, dead-beat, proportional-integral (PI), nonlinear control, neural network technique (Pradhan & Mishra 2018; Fei & Chu 2019; Son, Kim & Cho 2017; Fang, Fei & Wang 2020; Hou et al. 2019; Zhou, Yuan & Dong 2020; Javadi, Woodward & Al-Haddad 2017). The commonly used control method is the instantaneous power theory for harmonic current compensation (Harirchi & Simoes 2018). Low-pass filters (LPF) are usually utilized to separate fundamental components of load currents, but they lead to phase delays. Another disadvantage of traditional instantaneous power theory is that it has poor performance under unbalanced grid conditions. Jayasankar & Vinatha (2020) have discussed a self-tuning filter based instantaneous power theory to overcome the limitations of the LPF. Gong, Sou & Lam (2021) have designed



a vector PI current controller is designed and analyzed for the LC-coupling hybrid APF, which operates with minimum DC-link voltage.

This paper aims to design and implement bandpass filter (BPF) based PI controlled SAPF to isolate and dampen voltage and current harmonic distortion well within IEEE-519 and IEC 61000 standards. The constant DC-link voltage is achieved under load change. The performance of the presented control method is tested under several test cases such as nonlinear loads (NLLs), load change and highly inductive NLL. Simulation results on PSCAD/EMTDC environment are reported to indicate the availability of theoretical analyses.

Table 1: The characteristics harmonics for various load types.

Source	Individual harmonics
Transformer energization	2, 3, 4
Arcing devices	2, 3, 4, 5, 7...
EC motor	5, 7, 11, 13, 17, 19...
Fluorescent/LED lights	3, 5, 7, 9, 11, 13...
Switch-mode power supply	3, 5, 7, 9, 11, 13...
6-pulse drive/rectifier	5, 7, 11, 13, 17, 19...
12-pulse drive/rectifier	11, 13, 23, 25...
18-pulse drive	17, 19, 35, 37...
24-pulse drive	23, 25, 47, 49...

Table 2: IEEE Std 519-2014 Voltage distortion limits

PCC Voltage	Individual harmonic (%)	THD (%)
$v_{pcc} \leq 1.0 \text{ kV}$	5.0	8.0
$1 \text{ kV} < v_{pcc} \leq 69 \text{ kV}$	3.0	5.0
$69 \text{ kV} < v_{pcc} \leq 161 \text{ kV}$	1.5	2.5
$161 \text{ kV} < v_{pcc}$	1.0	1.5-2.0

Table 3: IEEE Std 519-2014 for current distortion limits

$v_{pcc} < 69 \text{ kV}$	Individual harmonic order					TDD
	$3 \leq h < 11$	$11 \leq h < 17$	$17 \leq h < 23$	$23 \leq h < 35$	$35 \leq h \leq 50$	
$\frac{I_{SC}}{I_L}$						
< 20	4.0	2.0	1.5	0.6	0.3	5.0
$20 < 50$	7.0	3.5	2.5	1.0	0.5	8.0
$50 < 100$	10.0	4.5	4.0	1.5	0.7	12.0
$100 < 1000$	12.0	5.5	5.0	2.0	1.0	15.0
> 1000	15.0	7.0	6.0	2.5	1.4	20.0

2. Configuration of Power System with NLLs and SAPF

The main role of a SAPF is to dampen the harmonic injection to the utility grid by compensating the harmonic currents. The circuit configuration of the power system with NLLs and SAPF is shown in Figure. 1. The SAPF is tied to the utility grid through interfacing inductor and resistor (L_f and R_f) at the point of common coupling (PCC). An interfacing inductor is utilized to eliminate the effect of oscillations in the current. L_g and R_g denote the equivalent inductor and resistor of grid impedance, respectively. The current harmonic source is NLLs, which are diode bridge rectifiers with inductor and resistor (L_{dc} and R_{dc}) at the DC-side. v_{dc} and C_{dc} is the DC-link voltage and capacitance of the SAPF, respectively.

3. BPF based PI Controlled SAPF Structure

The block diagram of the BPF based PI controller is shown in Figure 2. The PI controller is used for DC-link voltage control. The obtained errors between DC-link voltage (v_{dc}) and reference voltage (v_{dc}^*) are multiplied with the phase angle of the PCC voltage to generate grid reference current.

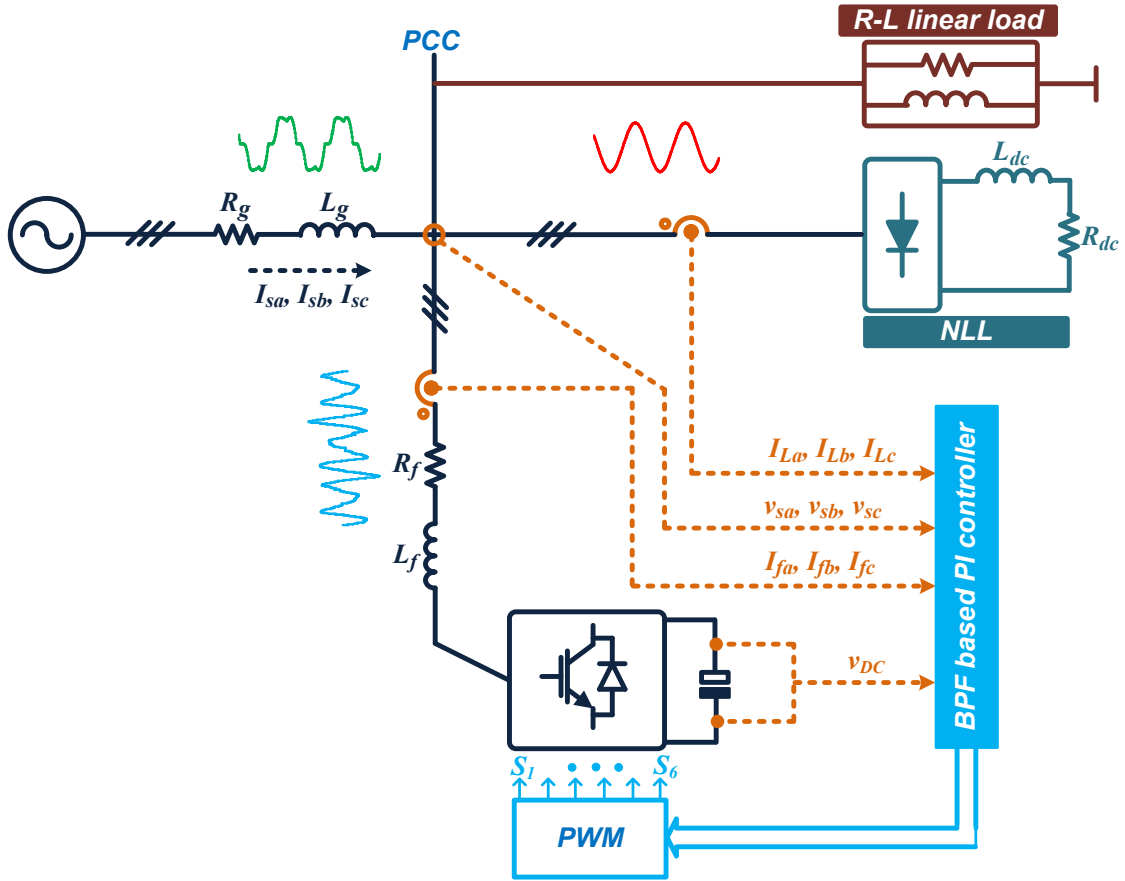


Figure 1: Circuit configuration of power system with NLLs and SAPF

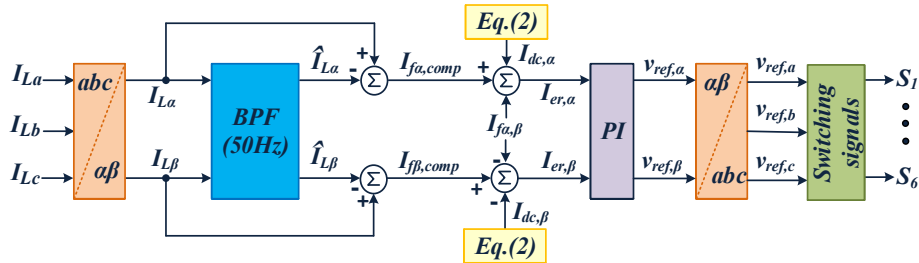


Figure 2: Block diagram of the BPF based PI controller.

Extracted load currents ($\hat{I}_{L\alpha}$ and $\hat{I}_{L\beta}$) from BPF and measured load currents are used to obtain the compensating current components ($I_{f\alpha,comp}$ and $I_{f\beta,comp}$) as follows.

$$I_{f\alpha,comp} = I_{L\alpha} - \hat{I}_{L\alpha} \quad I_{f\beta,comp} = I_{L\beta} - \hat{I}_{L\beta} \quad (1)$$

The obtained error between measured DC-link voltage and reference voltage is multiplied with the phase angle of the PCC to determine the active currents to be compensated by the SAPF.

$$\begin{aligned} I_{dc,\alpha} &= (v_{dc}^* - v_{dc}) \left(k_{p,1} + \frac{k_{i,1}}{s} \right) \sin \sin (\omega t + \varphi) \quad I_{dc,\beta} \\ &= (-v_{dc}^* + v_{dc}) \left(k_{p,1} + \frac{k_{i,1}}{s} \right) \cos \cos (\omega t + \varphi) \end{aligned} \quad (2)$$

where φ is the phase angle of the PCC voltage. The DC-link capacitor voltage of the SAPF is tracking the reference value with the proper PI control by providing an essential active power supply from the utility grid to meet the losses in it (Chilipi et al. 2018; Dubey, Mishra & Kumar 2021). The current tracking errors are written by (3).

$$I_{er,\alpha} = I_{f\alpha,comp} - I_{dc,\alpha} - I_{f\alpha} \quad I_{er,\beta} = I_{f\beta,comp} - I_{dc,\beta} - I_{f\beta} \quad (3)$$

The reference voltages are obtained with currents errors and PI control.

$$v_{ref,\alpha} = I_{er,\alpha} \left(k_{p,2} + \frac{k_{i,2}}{s} \right) \quad v_{ref,\beta} = I_{er,\beta} \left(k_{p,2} + \frac{k_{i,2}}{s} \right) \quad (4)$$

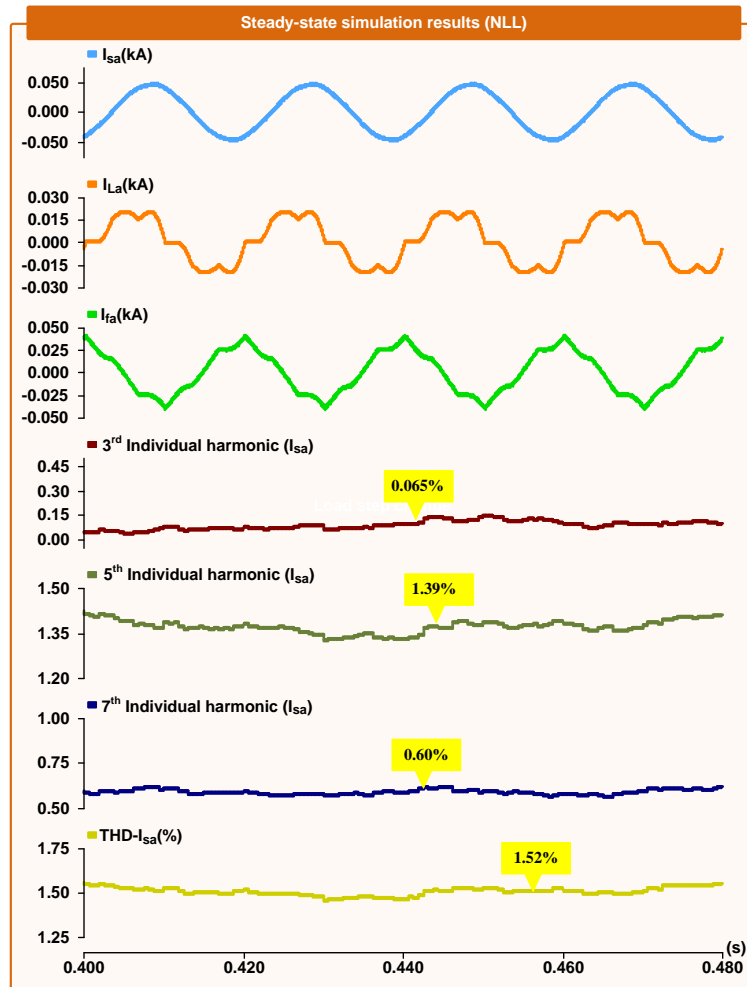


Figure 3: Steady-state simulation results: source current, load current compensation current, individual harmonics (3rd, 5th and 7th) and THD (from top to bottom)

4. Results

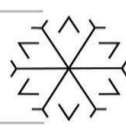
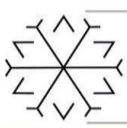
In order to confirm the application of the BPF based PI control presented in the SAPF topology; simulations result based on PSCAD/EMTDC software are addressed in this section. The parameters used in the simulation are given in Table 4.

Figure 3 depicts the steady-state performance of SAPF under NLL. The waveforms of the load current, compensation current, individual harmonics and THD of phase A are shown in Figure 3. Although the load current is extremely distorted with a THD of almost 20.65%, the harmonics of the currents are efficiently eliminated and a sinusoidal grid or source current is obtained with a small THD of 1.50%.

Table 4: Parameters for SAPF topology

Parameters	Value
Grid voltage	380V _{L-L,rms}
DC-link capacitance	1100uF
DC-link reference voltage	650V
RL filter inductance	5mH, 5mohm
Grid frequency	50Hz

The dynamic performance of the BPF based PI control is evaluated under highly inductive NLL and load variations at the same time. The compensating current drawn by the SAPF diminishes as the load diminishes. At the bottom of Figure 4, the control of the DC-link is achieved under load decrease. It can be observed that the measured



voltage tracks the reference value (v_{dc}^*) corresponds to 650V (0.65 p.u.) quite well. The THD values and individual harmonic content are quite low after current harmonic compensation with the BPF based PI controller.

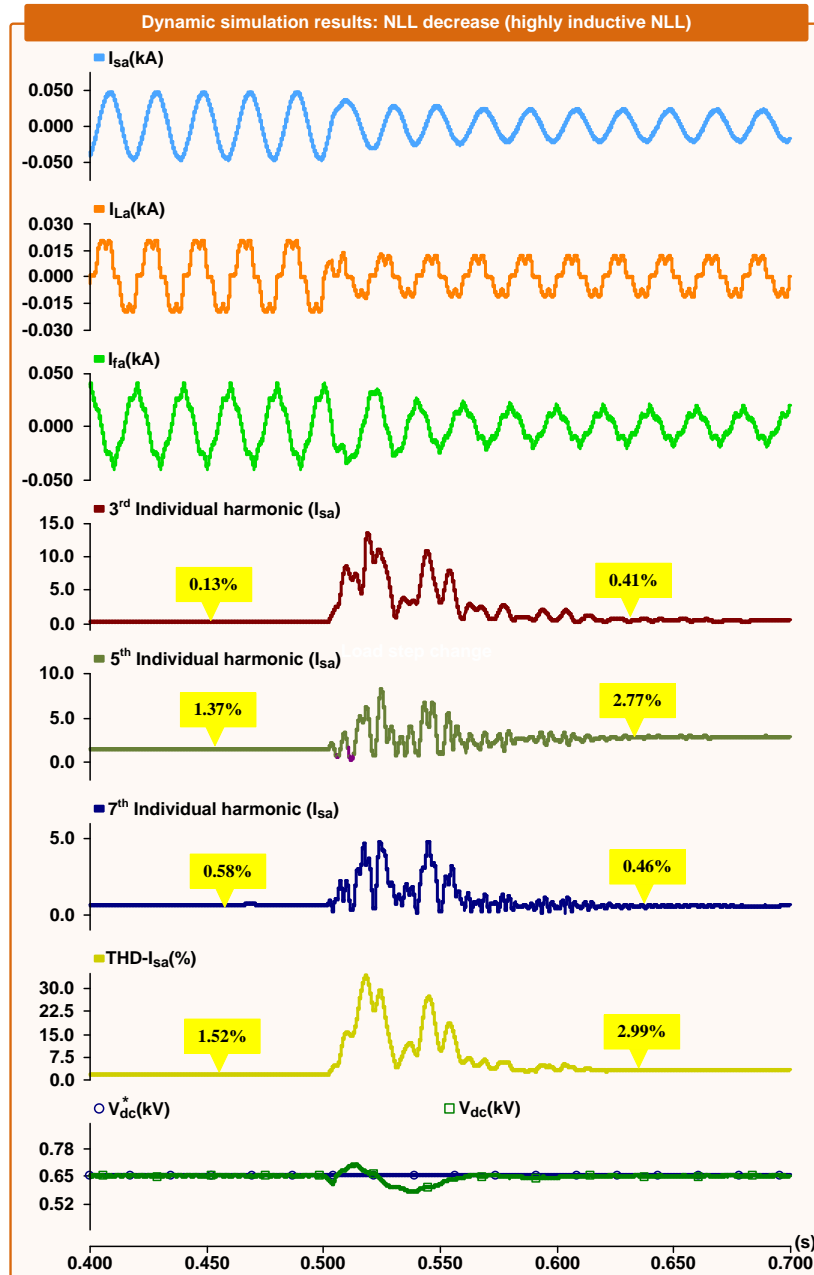


Figure 4: Dynamic simulation results under load decrease: source current, load current compensation current, individual harmonics (3rd, 5th and 7th), THD and DC-link voltage (from top to bottom).

The THD values are decreased from 20.45% and 28.34 to 1.52% and 2.99%, respectively after harmonic currents injected by the SAPF are compensated (see Figure 4) under load change and highly inductive NLL. In addition, the individual harmonic contents are analysed and mitigated.

The system performance is also assessed under dynamic load increase as shown in Figure 5. At 0.5s, The THD values of source currents fall from 20.65% to 1.50%. The results show that the DC-link voltage is maintained as constant under step load change. The THD and individual harmonics acquired is well below the IEEE-519 standard.

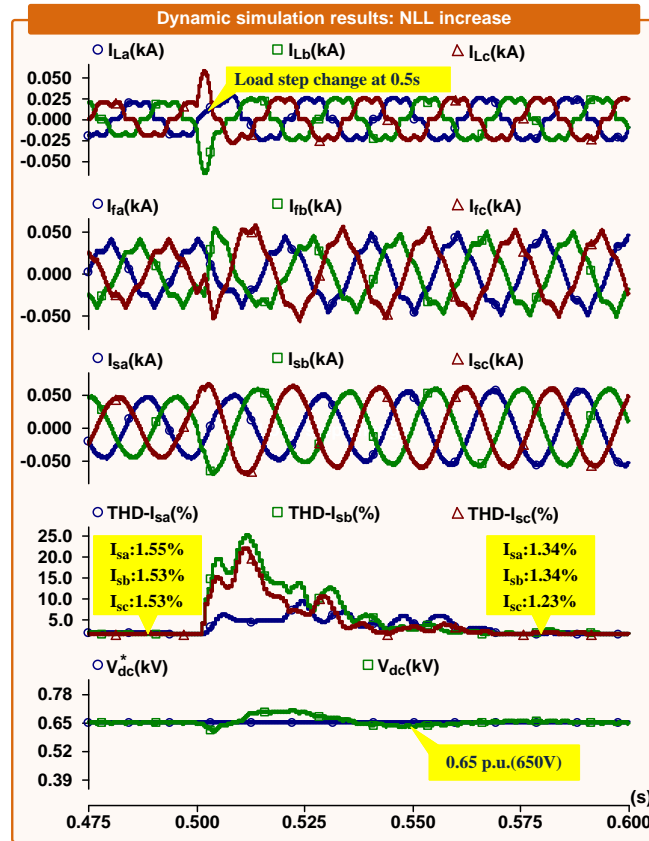
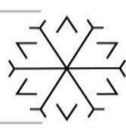


Figure 5: Dynamic simulation results under load increase: load currents, compensation currents, source currents, THD of phase currents and DC-link voltage (from top to bottom).

5. Conclusions

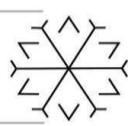
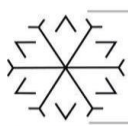
In this paper, a BPF based PI control applied to a SAPF is presented. The grid or source currents have been obtained as a sinusoidal shape with the elimination of harmonic components under extensive case studies developed with PSCAD/EMTDC software. The presented control method provides an improvement in THD values (almost 1.72%) to meet IEEE-519 and IEC-61000 standards. The DC-link voltage has been maintained and tracked at the reference value under load step changes. The results have been shown that mitigating harmonic currents at the grid side overcome power quality issues, successfully. Simulation results indicate that BPF based PI control is a good choice for APF applications.

Acknowledgements

The authors are grateful to Van Yuzuncu Yil University Scientific Research Projects Coordination Unit (Van, Turkey) for financial support of this study (Project number: FYD-2021-9636)

References

- Chilipi, R, Al Sayari, N, Al Hosani, K, Fasil, M & Beig, AR 2018 "Third order sinusoidal integrator (TOSSI)-based control algorithm for shunt active power filter under distorted and unbalanced voltage conditions," *International Journal of Electrical Power & Energy Systems*, vol. 96, pp. 152-162.
- Das, JC 2015 "Power system harmonics and passive filter designs" *John Wiley & Sons*.
- Dubey, AK, Mishra, JP & Kumar, A 2021 "Modified CCF based shunt active power filter operation with dead-band elimination for effective harmonic and unbalance compensation in 3-phase 3-wire system," *IEEE Transactions on Power Delivery*, Early Access, pp. 1-12.



- Eroğlu, H, Cuce, E, Cuce, PM, Gul, F, Iskenderoğlu, A 2021, "Harmonic problems in renewable and sustainable energy systems: A comprehensive review", *Sustainable Energy Technologies and Assessments*, vol. 48, 101566.
- Fang, Y, Fei, J, & Wang, T 2020 "Adaptive backstepping fuzzy neural controller based on fuzzy sliding mode of active power filter," *IEEE Access*, vol. 8, pp. 96027-96035.
- Fei, J & Chu, Y 2019, "Double hidden layer output feedback neural adaptive global sliding mode control of active power filter," *IEEE Transactions Power Electronics*, vol. 35, no. 3, pp. 3069-3084.
- Gong, C, Sou, WK & Lam, CS 2021 "Design and analysis of vector proportional–integral current controller for LC-coupling hybrid active power filter with minimum DC-link voltage," *IEEE Transactions Power Electronics*, vol. 36, no. 8, pp. 9041-9056.
- Harirchi, F & Simoes, MG 2018, "Enhanced instantaneous power theory decomposition for power quality smart converter applications" *IEEE Transactions Power Electronics*, vol. 33, no. 11, pp. 9344-9359.
- Hou, S, Fei, J, Chu, Y & Chen, C 2019, "Experimental investigation of adaptive fuzzy global sliding mode control of single-phase shunt active power filters," *IEEE Access*, vol. 7, pp. 64442-64449.
- IEEE 519 Working Group 1992, "IEEE recommended practices and requirements for harmonic control in electrical power systems" IEEE STD, 519-1992.
- Javadi, A, Woodward, L & Al-Haddad, K 2017, "Real-time implementation of a three-phase THSeAF based on a VSC and a P+ R controller to improve the power quality of weak distribution systems," *IEEE Transactions Power Electronics*, vol. 33, no. 3, pp. 2073-2082.
- Jayasankar, VN & Vinatha, U 2020, "Backstepping controller with dual self-tuning filter for single-phase shunt active power filters under distorted grid voltage condition" *IEEE Transactions Industrial Applications*, vol. 56, no. 6, pp. 7176-7184.
- Kanjiya, P, Khadkikar, V & Zeineldin, HH 2014, "Optimal control of shunt active power filter to meet IEEE Std. 519 current harmonic constraints under nonideal supply condition", *IEEE Transactions on Industrial Electronics*, vol. 62, no. 2, pp. 724-734.
- Pradhan, M, Mishra, MK 2018, "Dual p-q theory based energy-optimized dynamic voltage restorer for power quality improvement in a distribution system", *IEEE Transactions on Industrial Electronics*, vol. 66, no. 4, pp. 2946-2955.
- Son, G, Kim, HJ & Cho, BH, 2017 "Improved modulated carrier control with on-time doubler for a single-phase shunt active power filter," *IEEE Transactions Power Electronics*, vol. 33, no. 2, 1715-1723.
- Zhang, Y, Dai, K, Chen, X, Kang, Y & Dai, Z 2018, "Stability analysis of SAPF by viewing DFT as cluster of BPF for selective harmonic suppression and resonance damping", *IEEE Transactions on Industry Applications*, vol. 55, no. 2, pp. 1598-1607.
- Zhou, J Yuan, Y & Dong, H 2020, "Adaptive DC-Link Voltage Control for Shunt Active Power Filters Based on Model Predictive Control," *IEEE Access*, vol. 8, pp. 208348-208357.

Effect of Ultrashort Laser Pulse Shape on the Dipole Spectrum of a Single Electron

Muhammed Sayrac ^{1*}[0000-0003-4373-6897]

¹muhammedsayrac@cumhuriyet.edu.tr, Department of Nanotechnology Engineering, Sivas Cumhuriyet University, Sivas, Turkey

Abstract

In this study, the effects of ultrashort laser pulse shape for the laser-matter interaction have been considered. Three different pulse shapes, Gaussian, Super-Gaussian, and Cosine-Squared, are used to calculate the dipole spectrum of the single atom by considering the Lewenstein model. The ultrashort laser pulse shapes are presented, and it has been found that the super-Gaussian laser pulse, which has a spiky and strong tail, has been more effective in transferring energy to the electron. The electron is excited and gains kinetic energy under the ultrashort laser pulse. The laser pulse-electron interaction affects the ground state wave function and the returning electron wave packet. The optimum dipole spectrum, which is extended to higher photon energies, has been obtained under the Super-Gaussian pulse shape.

Keywords. Ultrashort Pulse shapes, Intense Laser Field, Electron Dipole Spectrum, Gaussian, Electron Propagation

1. Introduction

Laser-matter interaction brings out the nonlinear phenomena. Electron propagation under the intense and short laser pulse has been the subject of great interest for experimental and theoretical research. Attempts have been made to achieve ultrahigh technological devices using high-intensity ultrashort laser pulses [1]. The ionized electron wave packet is controlled by the driving laser field. The dipole spectrum of a single atom is evaluated by the electric field of the driving pulse.

The spectral distribution of an electron depends on several parameters, namely the ionization potential of the target atom, driving laser wavelength, the intensity of the laser field, and the pulse shape. These parameters steer the electron during the propagation. The electron accelerated under the laser field, and gain kinetic energy. Then, the electron recombines with the parent atom, and the emission of its gained energy is released.

In this paper, the dipole spectrum of a single electron is obtained for different pulse shapes by using the Lewenstein model. An ultrashort laser pulse excites the electron to gain energy that directly affects the interference of the ground state wave function and the returning electron wave packet. The paper is organized as follows. Section 2 gives the expression of the pulse shapes and the dipole moment. Section 3 is devoted to the simulation results where the effects of laser pulse shapes and dipole spectrum are examined. Finally, the summary of the whole analysis is presented in the last section.

2. Theory

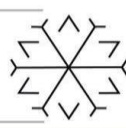
In this study, we consider different pulse shapes to obtain the dipole spectrum of a single atom. The pulse shapes are assumed to be an ultrashort pulse, and the spectrum is broad. Gaussian pulse shape, Super-Gaussian pulse shape, and Cosine-squared pulse shape are used as a driving field to compute the dipole spectrum of a single electron. The pulse envelope for the pulse shape is given below [2].

$$E \approx e^{-(t/\tau)^2} \rightarrow \text{Gaussian}$$

$$E \approx e^{-(t/\tau)^4} \rightarrow \text{Super - Gaussian}$$

$$E \approx \text{Cos}\left(\frac{t}{\tau}\right)^2 \rightarrow \text{Cosine - Squared}$$

here t is the time axis in atomic units, and τ is the full width at half-maximum (FWHM) pulse duration. In the case of the driving field being an ultrashort pulse, the driving field has many frequency components, i.e. the spectrum is broad.



The Gaussian pulse shape is described with a Gaussian function. On the other hand, the Super-Gaussian pulse shape has a spiky appearance with heavy tails. The Cosine-Squared pulse is the square of the cosine function. The pulse shapes simulated by using Eq. 1 are presented in Fig. 1.

By considering the different pulse shapes, the Single Atom Dipole Response of an electron is simulated by using the Lewenstein method [3]. The dipole moment is given in Ref. [4].

$$d(t) = -ie_x \int_0^{\infty} d\tau \left(\frac{\pi}{\varepsilon + i\tau/2} \right)^{3/2} E \cos(t - \tau) D_x(\rho_s(t, \tau) - A_x(t - \tau)) \times \exp(-iS_s(t, \tau)) D_x^*(\rho_s(t, \tau) - A_x(t)) + c.c.$$

where the probability amplitude for the driving field is $D_x^*(\rho_s(t, \tau) - A_x(t))$. A coupling the ground state to the vacuum continuum state is $D_x(\rho_s(t, \tau) - A_x(t - \tau))$. The phase of the electron acquired during propagation is $\exp(-iS_s(t, \tau))$. S_s is the quasiclassical action corresponding to the electron trajectory [5].

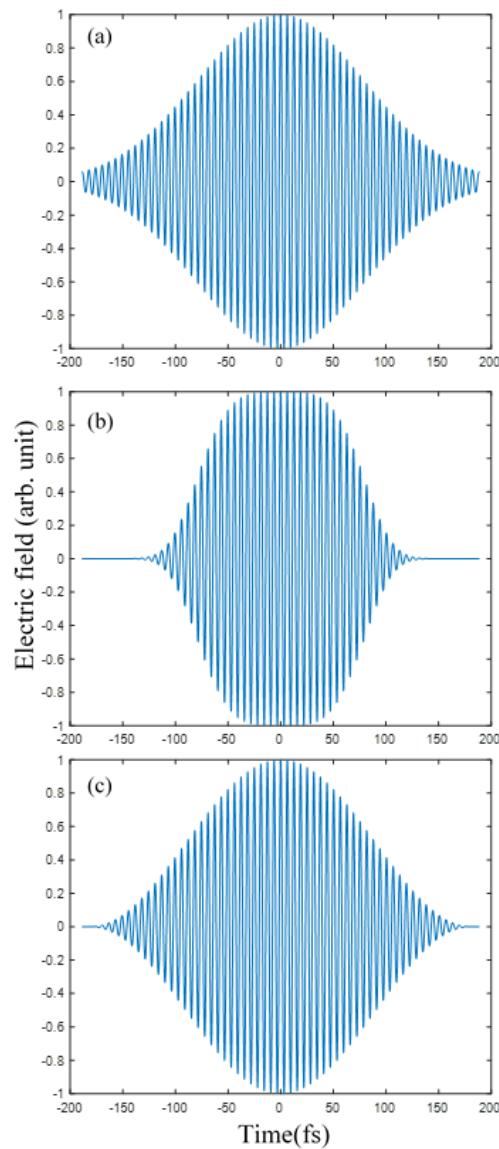
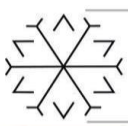


Figure 1: The simulated driving pulse shapes of (a) Gaussian, (b) Super-Gaussian, and (c) Cosine-Squared.



3. Results

The dipole response of a single atom is simulated by considering different driving pulse shapes with 70fs FWHM pulse duration, the central wavelength of 1000nm, and the intensity of $10^{14}\text{W}/\text{cm}^2$. The simulated driving pulse shapes are presented in Fig. 1.

For the different driving pulse shape described in Eq. 1, the dipole spectrum of a single atom is calculated by considering the contribution of short and long electron trajectories. Most of the laser field is considered to have Gaussian distribution. The dipole spectrum is simulated for each described pulse shape presented in Fig.1. The frequency conversion of the initial driving radiation of 1000nm (corresponding photon energy of 1.24eV) is achieved up to about 80eV photon energy (corresponding wavelength of about 15nm). Figure 2 is for the simulation results taking into account the Gaussian pulse shape, where the extension of the radiation up to 75eV is obtained.

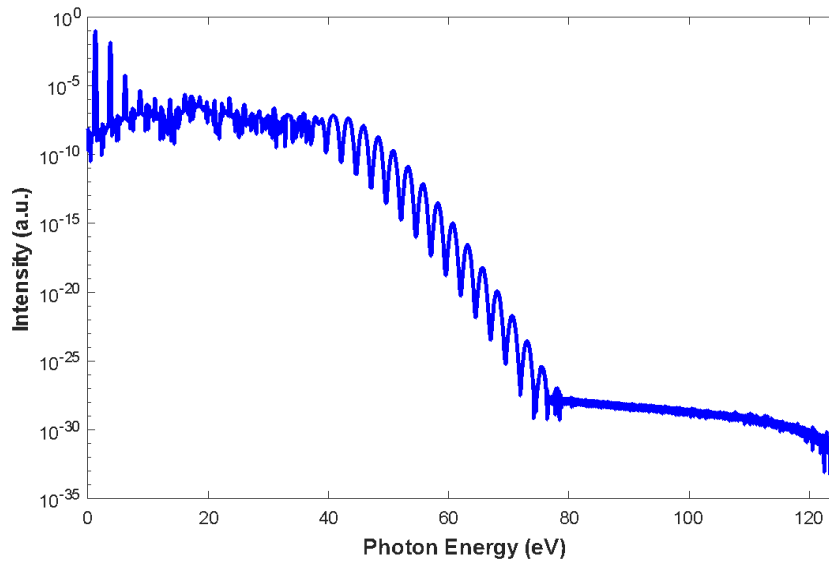


Figure 2: The electron dipole spectrum by using Gaussian pulse shape.

Moreover, the Super-Gaussian pulse shape has stronger wings compared to the Gaussian pulse, Fig. 1. The electron dipole spectrum under the super-Gaussian pulse shape is simulated, and the generated photon energy up to $>80\text{eV}$ is well resolved. The reason for the high photon energy is because of the strong spiky peak and strong wing of the Super Gaussian pulse shape.

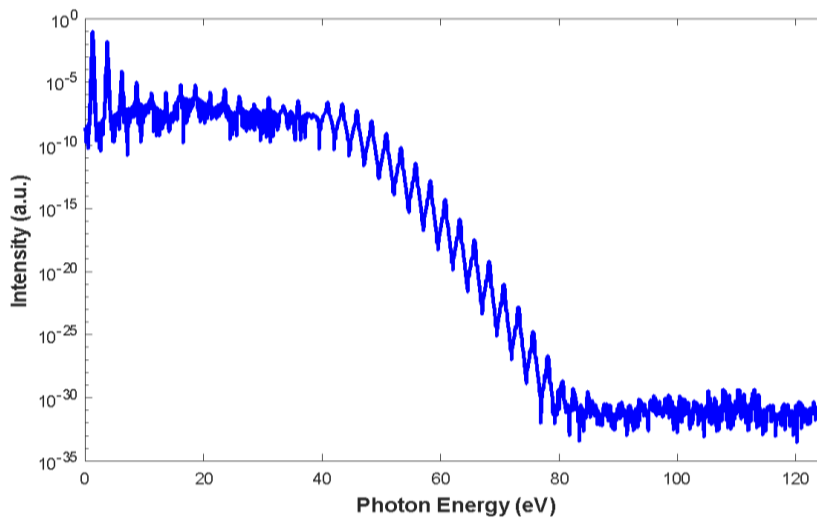
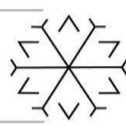
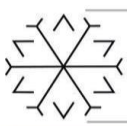


Figure 3: The electron dipole spectrum by using a Super-Gaussian pulse shape.



Finally, the Cosine-Squared pulse shape distribution is used for the simulation input parameter. The square term brings a slightly strong tail on the Cosine-Squared pulse shape. The calculated dipole spectrum up to 80eV photon energy is achieved in Fig. 4.

Overall, the photon energy of the generated radiation due to electron-laser interaction is obtained in an energy range from 75eV to >80eV, which is comparable to the photon energy of the fundamental field. The frequency conversion is significant for producing optical pulses with high photon energy for practical applications, which require high spatial and temporal resolution.

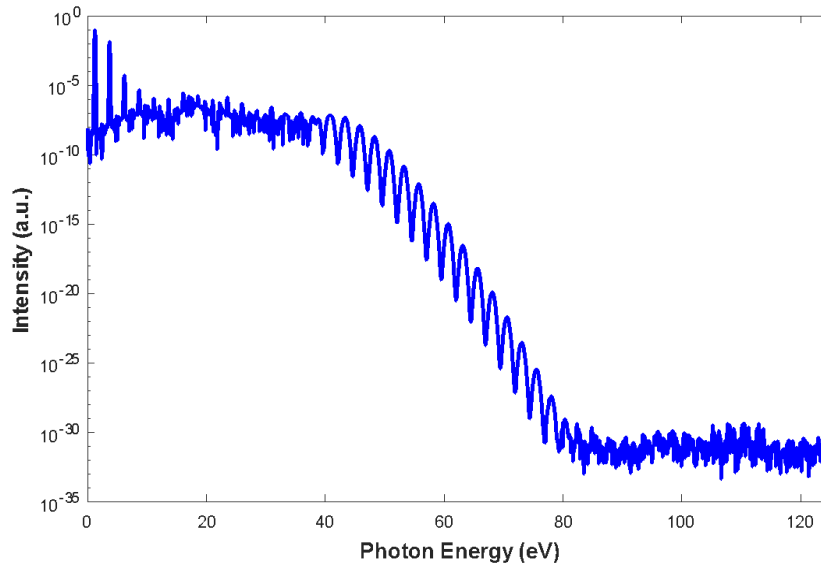


Figure 4: The electron dipole spectrum by using Cosine-Squared pulse shape.

4. Conclusion

In this work, the different pulse shape is considered for obtaining dipole spectrum, which gives the emitted radiation after the laser-matter interaction. The laser-matter interaction results in electron ionization and propagation under the effect of the laser field. The shape of the laser field directly affects the propagation of the free electron in the continuum.

Overall, the electron trajectories after the ionization are mainly affected by the driving laser field. The shape of the pulse controls the electron excursion time and results in different spectral distributions. The sharpness and strong wings of the pulse shape accelerate the electron, and the electron gains more kinetic energy. This results in the strong recombination, i.e. overlapping ground state wave function with the returning electron wave packet.

The simulation study can be useful for pre-experimental studies to determine how ultrashort pulse shape affects the electron behavior under the intense laser field, i.e. propagation, ionization, and recombination of an electron, or interference of electron wave packet with the ground-state electron wave packet.

References

- [1] M. Fouladi, H. Akou, "Effect of ultrafast laser pulse shape on the electron-plane wave interaction in vacuum," *JOSA B*, 36 603-609, 2019.
- [2] R.P. Encyclopedia, Gaussain Pulses - *RP Photonics Encyclopedia*, 2021.
- [3] M. Lewenstein, P. Balcou, M.Y. Ivanov, A. L'Huillier, P.B. Corkum, "Theory of high-harmonic generation by low-frequency laser fields," *Phys. Rev. A*, 49 2117-2132, 1994.
- [4] P. Antoine, A. L'Huillier, M. Lewenstein, P. Salières, B. Carré, "Theory of high-order harmonic generation by an elliptically polarized laser field," *Phys. Rev. A*, 53 1725-1745, 1996.
- [5] S. Bhardwaj, "Limits of Long Wavelength High Harmonic Generation," Department of Electrical Engineering and Computer Science, Massachusetts Institute of Technology, Department of Electrical Engineering, and Computer Science., 2010.

Mel-Spectrograms and Data Augmentation for Spoken Digit Classification

Mohamad Melad Ali ASHAMES¹ [0000-0002-2837-1343] and Semih ERGİN² [0000-0002-7470-8488]

^{1,2} Eskişehir Osmangazi University, Electrical, and Electronics Engineering Department,
Meselik Campus, 26480, Eskişehir/Turkey

¹muhashames@gmail.com,

²sergin@ogu.edu.tr

Abstract

A spectrogram is a visual representation of a time-domain signal's strength or "loudness" at various frequencies. It's an algorithm commonly used in audio spectral analysis and other fields. In this study, spectrograms were obtained and then mapped onto the Mel-Scale for the task of spoken digit analysis and classification. Gaussian noise was added to the audio data for the sake of data augmentation. Features were extracted from Mel-Spectrograms using a 7-layer Convolutional Neural Network (CNN), while the classification of these features was realized using two different classifiers: fully connected neural networks and Support Vector Machines (SVMs).

Keywords. Spectrogram, Mel-Scale, spoken digit, speech recognition, CNN, SVM.

1. Introduction

Speech recognition is a capability that enables a program to process human speech into a written or visualized format. In this study, we focused on the problem of English spoken digits identification. Nowadays spoken digit identification is an important task since it is used in various fields such as banking, social security, customer services, etc. In such fields we find ourselves obligated to list out the digits one by one over the phone to ensure that second parties can successfully access our information. English spoken digit recognition was performed in several studies. Bazzi and Katabi (2000) investigated the use of SVMs for English spoken digit recognition. Feature vectors were extracted from the Mel-Frequency cepstral coefficients of the speech signal and then reduced using principal component analysis (PCA). Becker et al. (2018) explored the efficiency of layer-wise relevance propagation (LRP) to identify relevant features for two neural network architectures that process either waveform or spectrogram representations of English spoken digits datasets. The results confirm that the networks are highly reliant on features marked as relevant by LRP. In a later study, Sharan used wavelet transform in forming the time-frequency representation (Sharan, 2020). The time-frequency representation is resized using bicubic interpolation to obtain scalograms which were used for recognizing spoken digits using CNN. The next sections of this paper will handle the use of Mel-Spectrograms, CNN, and SVM for English spoken digit processing and classification.

2. Materials and Method

There are many ways to represent audio data, like, waveform, Chroma features, Mel Frequency Cepstral Coefficients (MFCCs), Spectrograms, Mel-Spectrograms, and many more. In this study, the Mel-Spectrograms are used. Spectrograms that are scaled to the Mel-Scale have a closer representation of the human audio perception than other representations on the frequency scale. Thus, the Mel Spectrogram images of the spoken digits are extracted to be used as input to the CNN model.

2.1. Data

In this study, the Speech Commands dataset was used. It is a dataset for limited-vocabulary speech recognition by Google Brain (Warden, 2018). The data consists of audio files of spoken digits (from zero to nine)

and some other spoken words that were not used. Each digit has 2352-2377 audio files (Wav format). The length of each audio file is 1 second. Raw data were trimmed so that every digit has 2352 audio files each. A total of 23520 files were used in this study. Also, white (Gaussian) noise was added to each file which doubled the number of audio files (see section 2.4).

2.2. Spectrogram

The spectrogram is an important representation of audio data because human hearing is based on a kind of real-time spectrogram encoded by the cochlea of the inner ear (O'Shaughnessy, 1987). The spectrogram can be defined as an intensity graph (usually on a log scale, such as dB) of the Short-Time Fourier Transform (STFT) magnitude. Spectrograms are two-dimensional graphs, with a third dimension represented by colors. Time runs from left (past) to right (present) along the horizontal axis. The vertical axis represents frequency, which can also be thought of as pitch or tone, with the lowest frequencies at the bottom and the highest frequencies at the top. As it can be seen in Figure 1, the amplitude (or loudness) of a particular frequency at a particular time is represented by the third dimension, which is color, with dark blue corresponding to low amplitudes and brighter colors up through red corresponding to progressively stronger (or louder) amplitudes.

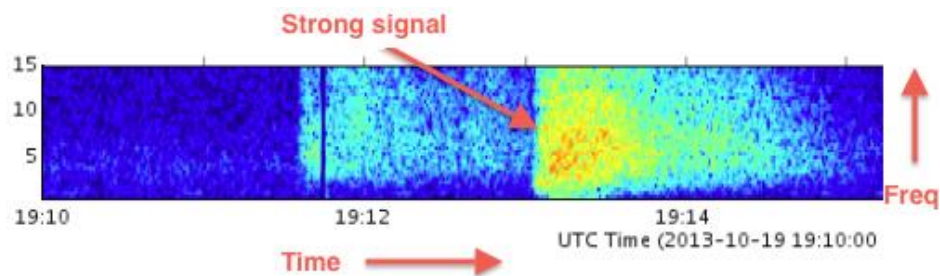


Fig. 1 Spectrogram dimensions: frequency, time, and color (Anonymous, 2021).

Sound is an analog signal, to obtain the spectrograms of sound signals they must be digitalized. Hence, each signal was sampled with a rate of 22050 samples per second. Figure 2 presents a waveform of a spoken digit belonging to the class (seven) where all the samples are shown, while Figure 3 only shows the samples between 0 and 100.

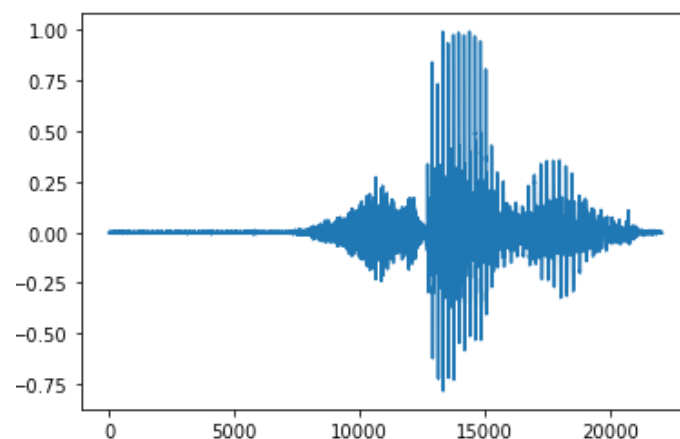


Fig. 2 waveform of a spoken digit belonging to the class (seven) samples with a rate of 22050 samples/second.

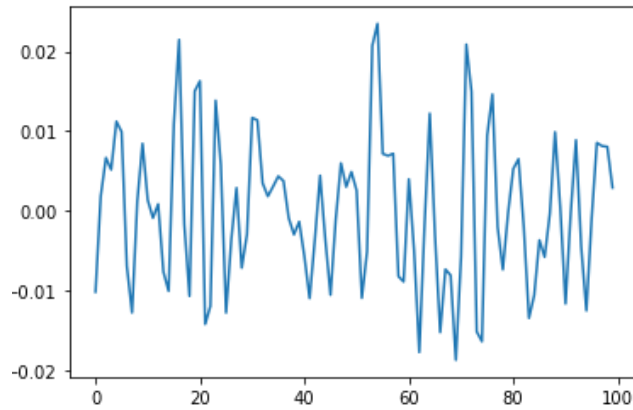


Fig. 3 A segment of 100 samples of the waveform in figure 2.

To generate a spectrogram, a time-domain signal is divided into shorter segments of equal length. Then, the fast Fourier transform (FFT) is applied to each segment (This is called Short-Time Fourier Transform). The term fast Fourier transform (FFT) refers to an efficient implementation of the discrete Fourier transform (DFT) for highly composite transform lengths. The STFT is simply a sequence of FFTs of windowed signal segments, where the windows are usually allowed to overlap in time, typically by 25-50%. The window length, as can be seen in Figure 4, determines the number of FFTs used to create the spectrogram. Plotting the spectrum of this sequence of stacked FFT segments creates the spectrogram.

To obtain the spectrograms, each spoken digit audio signal was divided into short time windows (segments) of 2048 samples (which corresponds to a physical duration of 93 milliseconds at a sample rate of 22050 Hz), making hops of size 512 samples each time to sample the next window, this way a %25 overlap is achieved.

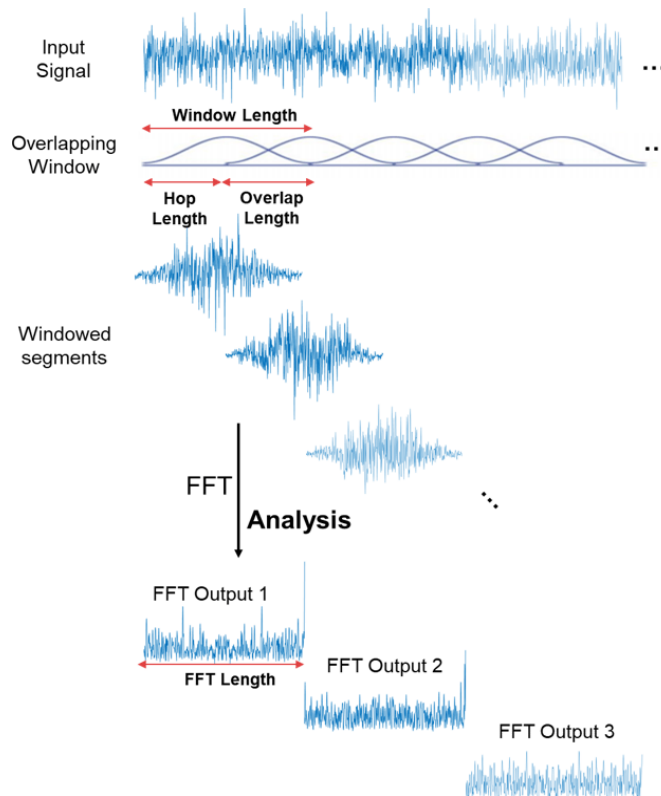


Fig. 4 Applying FFT on several windows of a particular number of samples (Anonymous, 2019).

Then, the FFT was applied to each window. Figure 5 shows a window of 2048 samples from the same waveform in figure 2.

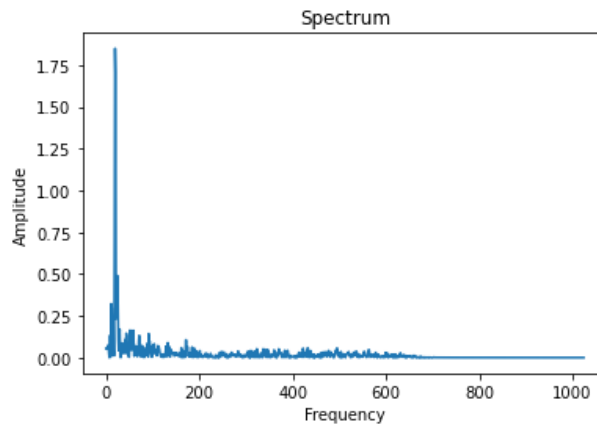


Fig. 5 A window of 2048 samples

Plotting the segments, we obtain the image in Figure 6(a). Here the y-axis is in Hertz (Hz). To obtain a spectrogram, we transform the y-axis (frequency) to log scale, and the “color” axis (amplitude) to decibels, as can be seen in Figure 6(b) where the spectrogram of the same signal above is illustrated.

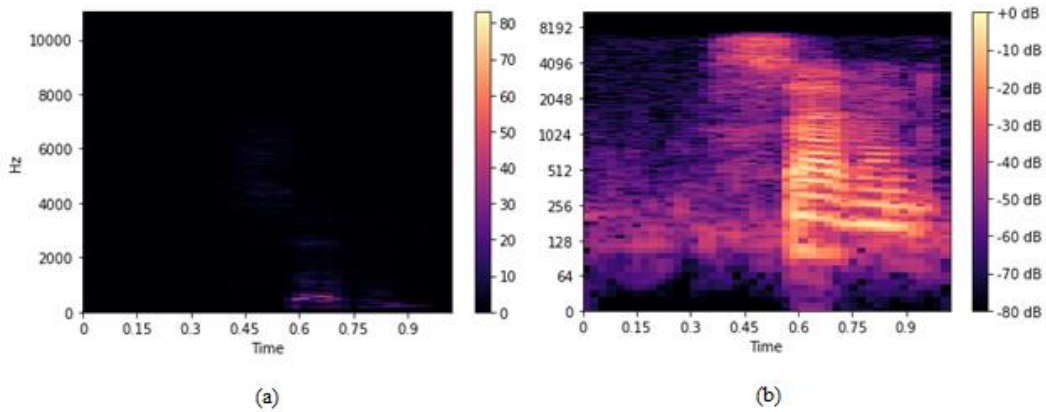


Fig. 6 (a) Representation of the matrix obtained from the FFT stack, (b) spectrogram of the same signal.

2.3. The Mel-Spectrogram

Humans are better at detecting differences in lower frequencies than higher frequencies. In more detail, a human can easily tell the difference between 500 and 1000 Hz but is hardly able to tell a difference between 10,000 and 10,500 Hz, even though the distance between the two pairs is the same. The Mel-Scale mimics humans’ perception of sound. Sounds of equal distance on the Mel-Scale are perceived to be of equal distance to humans. The transformation from the Hertz scale to the Mel Scale is computed by Eqs. (1).

$$M = 1127 \times \log(1 + f/700) \tag{1}$$

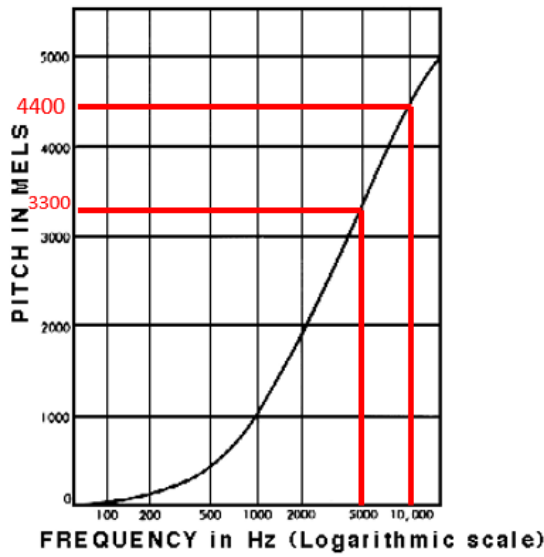


Fig. 7 The relationship between Hertz and Mels (Perera and Luening, 1975).

A Mel Spectrogram is a spectrogram where the frequencies are converted to the Mel-Scale (a Spectrogram with the Mel-Scale as its y-axis). Figure 7. Shows the relationship between Hertz and Mels. To generate a Mel-Scale, we separated the frequency spectrum into 128 evenly spaced frequencies (not by distance on the frequency dimension, but distance as it is heard by the human ear). Then we mapped the y-axis (frequency) of the obtained spectrograms onto the Mel-Scale to form the Mel-Spectrograms. A result Mel-Spectrogram of the same signal processed above can be seen in Figure 8.

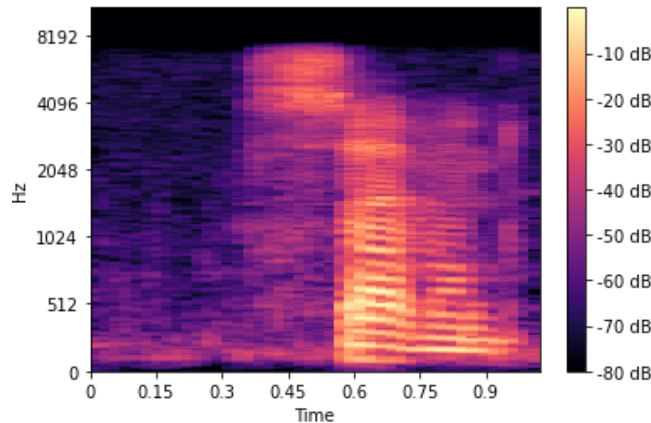


Fig. 8 Spectrogram of an audio file belonging to the class (seven)

2.4. Audio Augmentation

Since a 7-layer CNN model is used for extracting features from the obtained Mel-Spectrograms, the more input data the better. This helps with generalizing the model and preventing overfitting by providing more diverse features. To augment the audio data, Gaussian (white) noise was added to each spoken digit's audio file, resulting in a total of 47040 audio files when added to the original data (4704 for each class). Then, the Mel-Spectrogram of each noisy spoken digit audio file is created and added to the dataset of noiseless Mel-Spectrograms. Figure 9 (a) shows a Mel-Spectrogram of a spoken digit of the class (seven), and a Mel-Spectrogram belonging to its noisy version (b).

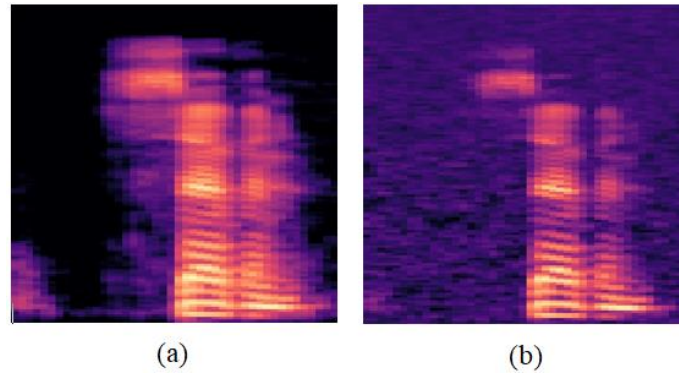


Fig. 9 Mel-Spectrogram of a spoken digit of the class “seven” (a), Mel-Spectrogram belonging to its noisy version (b).

2.5. Feature Extraction and Classification

To extract features from the Mel-Spectrograms, a 7-layer CNN architecture is designed. The input layer’s size is $377 \times 387 \times 3$, which is the size of the created Mel-Spectrograms. The architecture consists of 6 convolutional layers with 3×3 kernels. The padding parameter is fixed to “1” at each convolutional layer. Every convolutional layer is followed by a batch normalization layer, a ReLU activation function, and a max-pooling layer except for the last convolutional layer which is followed by only a batch normalization and a ReLU layer. Max pooling layers have kernels of 2×2 size and a stride value of 2. The seventh layer is a fully connected layer for classification followed by a SoftMax function. The fully connected layer is then replaced with an SVM classifier, and the classification accuracy of both classifiers is compared.

2.6. Training Procedure

The dataset is partitioned into training, test, and validation sets by a rate of 0.7, 0.2, and 0.1, respectively. The training parameters in table 1 were held the same through the three experiments discussed in section 3.

Table 1. Training parameters

Training Parameters & Results	Value
Training Set Size	70%
Validation Set Size	10%
Test Set Size	20%
Mini Patch Size	10
Optimizer	SGDM
Hardware	6 GB GPU NVIDIA 1660TI
Learning Rate	Constant 0.0001
Number of Epoch	20

3. Results

Three different experiments were carried out. In the first experiment, only Mel-Spectrograms of the original dataset were used as input data, while in the second experiment only Mel-Spectrograms of noisy data were used. In the third experiment, an augmented dataset containing Mel-Spectrograms of both original and noisy data was used as the input of the CNN model. The validation accuracy and elapsed time of the training procedure belonging to each experiment can be seen in table 2. The classification results of both fully connected and SVM classifiers can also be seen in Tables 3 and 4, respectively.



Table 2. Training Results.

Parameter	Original Data	Noisy Data	Augmented Data
Validation Accuracy	94.51%	92.2%	95.11%
Elapsed Time	34 min & 14 sec	34 min & 45 sec	69 min & 43 sec

Table 3. Test Results using 7-layer CNN.

Metric	Original Data	Noisy Data	Augmented Data
Accuracy (ACC)	94.6%	91.8%	95.3%
Specificity (SP)	100%	100%	99.6%
Sensitivity (SN)	99.3%	99.5%	99.5%
Positive Prediction Value (PPV)	1	1	0.996
Negative Prediction Value (NPV)	0.993	0.995	0.995
False Positive Rate (FPR)	0	0	0.003
False Negative Rate (FNR)	0.006	0.004	0.004
False Discovery Rate (FDR)	0	0	0.003
False Omission Rate (FOR)	0.006	0.004	0.004

Table 4. Test Results using 6-layer CNN model with an SVM classifier.

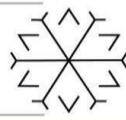
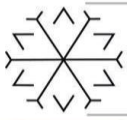
Metric	Original Data	Noisy Data	Augmented Data
Accuracy (ACC)	93.5%	90.3%	94.3%
Specificity (SP)	98.9%	99.4%	99.2%
Sensitivity (SN)	98.1%	98.7%	99.4%

4. Conclusion

The proposed spoken digit classification approach had been proven to be as successful as leading studies in the literature with an accuracy of 95.3% with the fully connected network as a classifier. The reached results show the efficiency of using Mel-Spectrogram features for speech recognition and classification. It was also proved that audio data augmentation help generalizes the CNN model and increase the overall classification accuracy. It is recommended to use the latest version of the used Speech Commands dataset which contains more data. In most cases, more input data boosts the classification accuracy and model generalizability. In addition, using Transfer Learning can also boost the reached results.

References

- Bazzi, I. and Katabi, D., 2000. Using support vector machines for spoken digit recognition. In Sixth International Conference on Spoken Language Processing.
- Becker, S., Ackermann, M., Lapuschkin, S., Müller, K.R. and Samek, W., 2018. Interpreting and explaining deep neural networks for classification of audio signals. arXiv preprint arXiv:1807.03418.
- Mathworks (2019) Short-time FFT. Available at: <https://www.mathworks.com/help/dsp/ref/dsp.stft.html> (Accessed: 01 December 2021).



O'Shaughnessy, D., 1987. *Speech Communication, Human and Machine* Addison Wesley. Reading MA.

Perera, R. and Luening, O., 1975. *The development and practice of electronic music*. Prentice Hall.

Sharan, R.V., 2020, December. Spoken digit recognition using wavelet scalogram and convolutional neural networks. In *2020 IEEE Recent Advances in Intelligent Computational Systems (RAICS)* (pp. 101-105). IEEE.

The Pacific Northwest Seismic Network (PNSN) (2021) What is a Spectrogram?. Available at: <https://pnsn.org/spectrograms/what-is-a-spectrogram/> (Accessed: 01 December 2021).

Warden, P., 2018. *Speech commands: A dataset for limited-vocabulary speech recognition*. arXiv preprint arXiv:1804.03209.

Comparison of Cognitive Workload and Resting States in Different Brain Lobes and EEG Frequency Bands

Sevde Gul Korkmaz ^{1*}[0000-0001-6043-1353], Onur Erdem Korkmaz ²[0000-0001-6336-6147]

and Onder Aydemir ³[0000-0002-1177-8518]

¹sevdedoner@gmail.com, Department of Electrical and Electronics Engineering, Karadeniz Technical University, Trabzon, Turkey

²onurerdem.korkmaz@atauni.edu.tr, Ispir Hamza Polat Vocational College, Atatürk University, Erzurum, Turkey

³onderaydemir@ktu.edu.tr, Department of Electrical and Electronics Engineering, Karadeniz Technical University, Trabzon, Turkey

Abstract

Cognitive fatigue can be defined as a decrease in cognitive resources that develops over time upon continuous cognitive demands. Cognitive fatigue is caused by many factors and has many negative consequences. It can have important results in daily and business life. For this, it is critical to be able to detect cognitive fatigue. Many methods are used to detect cognitive fatigue. Detecting cognitive fatigue with EEG offers both low cost and high reliability. In this study, experiments were conducted with 8 participants, 5 men and 3 women, to detect cognitive fatigue using EEG signals. For this purpose, five minutes of EEG data were taken during rest and when the questions were solved. When the graphical results were examined, it was seen that the frontal region electrodes were better than the other region electrodes in separating both blocks. Additionally, beta and gamma bands give better results than other bands in separating cognitive workload and resting blocks, regardless of the channel.

Keywords. Cognitive fatigue, EEG, Frequency Bands, Brain Lobe, Analyzer

1. Introduction

Today, fatigue is defined as a general concept. Fatigue encompasses many factors and has many consequences. Cognitive fatigue is also a type of fatigue. It affects performance in daily life. Cognitive fatigue is a psycho-biological condition resulting from prolonged activities. Its effects and consequences can reach dreadful dimensions.

Cognitive fatigue shows its effects in many areas of daily life. It is considered a temporary state in the physical sense. However, it has dreadful and dangerous consequences. It has been reported that cognitive fatigue increases the margin of error during any task and is a symptom of common neurological disorders in adults [1]. In addition to these, cognitive fatigue has been accepted as an important determinant of performance in the field of sports and exercise [2]. Therefore, the detection of cognitive fatigue is important in many areas.

Many methods are used to detect cognitive fatigue. These; electrodermal activity, evaluation of parameters of heart rate variability, electroencephalography (EEG), magnetoencephalography (MEG), electrocardiography (ECG), functional magnetic resonance imaging (fMRI) and oculography. Among these methods, brain-based studies have given more reliable results [3]. In Table 1 given below, brain-based methods used in the detection of cognitive fatigue are compared. Here, detecting cognitive fatigue with EEG offers both low cost and high reliability. In this sense, the detection of cognitive fatigue with EEG provides an advantage.

EEG is low-amplitude bioelectric signals detected by electrodes from the scalp surface. The amplitude of the EEG signals is the expectation of 1–400 μ V peak to peak. They have a wide frequency band. Frequency ranges represent different activities. They are studied as waves defined in five different frequency bands with different properties. These; delta, theta, alpha, beta and gamma.

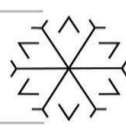
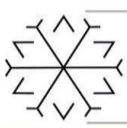


Table 1: Comparison of Brain-Based Methods Used to Detect Cognitive Fatigue [3].

	Image/ Data Quality	Temporal Resolution	Spatial Resolution	Reliability
MRI	High	Low	Very High	High
fMRI	High	Low	Very High	High
MEG	Medium	Very High	Low	Low
EEG	Medium	Very High	Medium	High

Analysis of the EEG signal has been shown to be an effective method that can be used to determine cognitive fatigue of shifts in the alpha, beta and theta power [4]. In an experiment by Dehais et al. the mental fatigue of the 32-channel EEG system and the electrophysiological effects of mental loading were measured. Two experiments were conducted on the simulator under real flight conditions and they revealed that the emergence of cognitive fatigue is related to alpha, theta and beta band strengths. The classification accuracy reached 76.9% and 89.1% in distinguishing mental fatigue [5]. In another study, Trejo et al. experimented with 16 people with EEG signals they received greater than 30 channels. They found close to evidence for the 3-state fatigue model by applying Bayesian analysis on the received signals [6,7]. In another study, Papakostas conducted a 76-session cognitive experiment by administering the Wisconsin Card Sorting Test and its modified version to 19 male and female subjects. By using the EEG signals recorded during the experiment, the classification was performed using the Support Vector Machine algorithm and an accuracy of 67% was obtained [8].

When the studies in the literature were examined, no study was found (as examined) that visually compared the resting and cognitive workload between both EEG bands and brain lobes. In this study, theta, alpha, beta and gamma bands are discussed in the detection of cognitive fatigue with EEG. Using these bands, resting and cognitive workload activities were visually compared in the frontal, occipital, parietal and central lobes of the brain.

2. Materials and Methods

The proposed methods are composed of four main steps and block diagram is shown in Figure 1. Here, firstly the proposed paradigm is presented to the subject on a LED display. Corresponding brain electrical activities are recorded simultaneously with EEG cap to monitor the brain response of the subject to the stimulus. After the EEG data recording, noise is removed from the EEG data during the preprocessing phase. Finally, band power was calculated by dividing the EEG data into blocks where resting and cognitive workload.

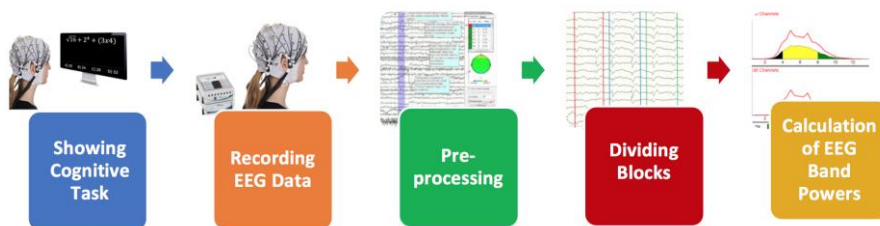


Figure 1: Block-diagram of proposed system

2.1. Paradigm

The paradigm consists of two blocks. In the first block, the participant resting by looking at the '+' symbol on the computer screen for five minutes. In the second block, the participant listened to the news while mentally solving the questions displayed on the computer screen for five minutes. At the end of the experiment, questions about the news were asked. For this reason, they were asked to listen carefully to the news recording while solving the questions. Multiple-choice and mind-solving questions were asked. The difficulty levels of the questions were adjusted as equal as possible. A-B-C-D options were determined and labels were attached to the A-S-D-F keys on the keyboard and these options were brought side by side for less artifact.

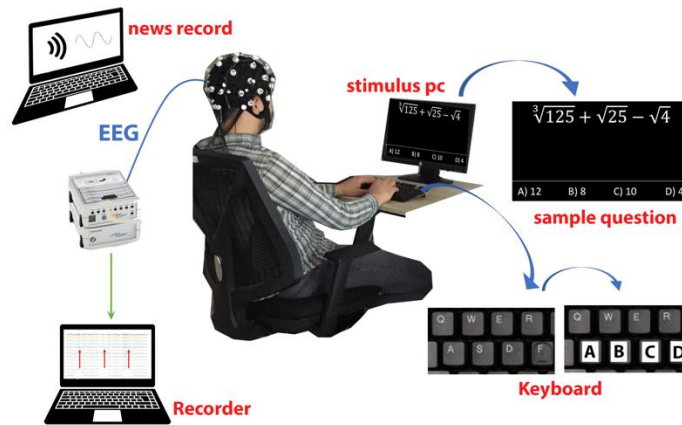


Figure 2: The paradigm of the proposed method.

2.2. EEG Recording

The data collection process was approved by the Health Sciences Institute Ethics Board of Ataturk University and all participants signed the Consent Form, verified the board, before the start of EEG recording session. In the study, stimuli were demonstrated using a 1920 x 1080 resolution-LED display. The experiments were conducted while the participants were sitting on a comfortable sofa positioned 1 m from the screen. Simultaneous EEG recording is taken while performing both blocks (resting and cognitive workload block).

Experiments were conducted with a total of 8 participants, 5 men (mean age 30 ± 6.05) and 3 women (mean age 30 ± 5.29), to detect cognitive fatigue. In experiment, EEG signals were captured using ActiChamp device by Brain Product. During the experiment, unipolar EEG recording was performed by placing the electrodes according to the international 10/20 system and all electrode impedance values were maintained below 5 K Ω during data collection. The 'Fz' channel was used as the reference electrode and the sampling frequency for EEG recording was set to 250 Hz.

2.3. EEG Signal Processing

Analysis was performed using the Brain Vision Analyzer 2.0.1 package program (Brainproducts Gilching, Germany). Signal processing is composed of two steps as pre-processing and band power calculation. In the pre-processing step, EEG data, captured from 31 channels, are first passed through a band-pass filter set to 4-8 Hz for theta, 8-12 Hz for alpha, 12-30 Hz for beta and 30-100 Hz for gamma [9–10]. Then, raw data inspection (RDI) was performed. The RDI transform allows you to check the raw EEG data for physical artifacts. When the gradient criterion is applied, the absolute difference between two sampling points should not exceed the specified value. In the gradient criteria maximal allowed voltage step was determined 50 $\mu\text{V}/\text{ms}$. When the max-min criterion is applied, the difference between the maximum and minimum in a segment should not exceed the specified value. The maximal difference of values in 200 ms intervals (segment) was determined 200 μV . Finally when the amplitude criterion is applied, the amplitude must not violate specified max - min values. Maximal and minimal allowed amplitude value was determined 200 μV and -200 μV respectively. EEG points providing these values were marked as bad before and after 200ms and were excluded from the analysis [11].

Before the band power calculation block, all EEG data divided into bands were divided into resting and cognitive workload blocks. The EEG signal is a mixture of neural oscillations. A signal can be expressed as a combination of different sine waves, each with its own frequency, amplitude and phase. The previous statement is the definition of Fourier analysis and entails the decomposition of the EEG signals into its constituent frequency components. Fourier transformation is a tool for analyzing stationary signals (the morphology of the signal does not change over time). EEG signals are non-stationary by nature. Treating it as a semi-stationary signal, the parts of the signal of interest to be analyzed are extracted. The semi-stationary data segment is extracted and Fast Fourier Transform (FFT) applied to each segment. The FFT is essentially a simple Discrete Fourier Transform algorithm [12]. The explanation of the FFT algorithm is shown in Figure 3.

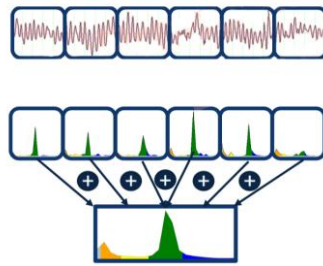


Figure 3: The FFT algorithm [12]

$$X(f) = \int_{-\infty}^{\infty} x(t) \cdot \psi(t, f) dt \tag{1}$$

$$\psi(t, f) = e^{i2\pi ft} = \cos(2\pi ft) + i \cdot \sin(2\pi ft) \tag{2}$$

$$X(f) = \int_{-\infty}^{\infty} x(t) \cdot [\cos(2\pi ft) - i \cdot \sin(2\pi ft)] dt \tag{3}$$

Where $x(t)$ is EEG signal, f is the frequency and $X(f)$ is Fourier coefficients.

$$A(f) = \sqrt{\text{Re}(f)^2 + \text{Im}(f)^2} = |X(f)| \tag{4}$$

$$A(f)^2 = [X(f)]^2 \tag{5}$$

where $A(f)$ is spectral amplitude and $A(f)^2$ is spectral power.

Each block was divided into 2 second segments, the spectral power of each segment was calculated and averaged for each channel. The spectral power calculation steps are shown in Figure 4. The steps shown for the resting block were performed within the cognitive load block.

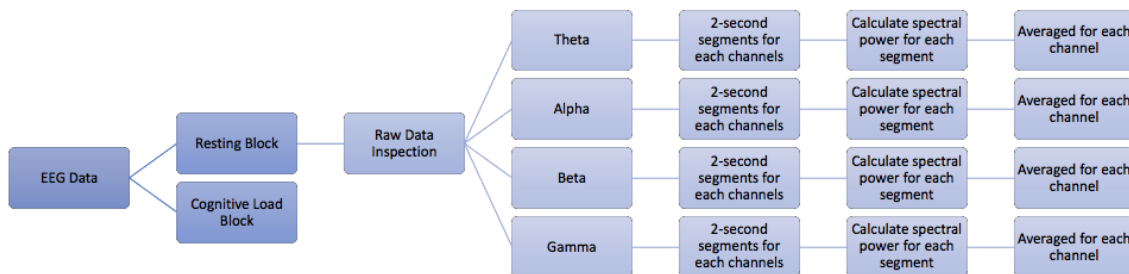


Figure 4: Spectral power calculation steps

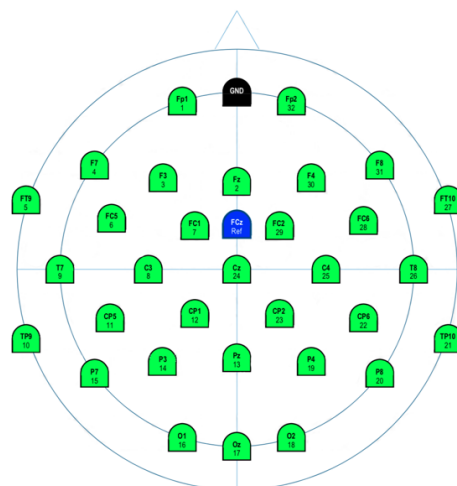
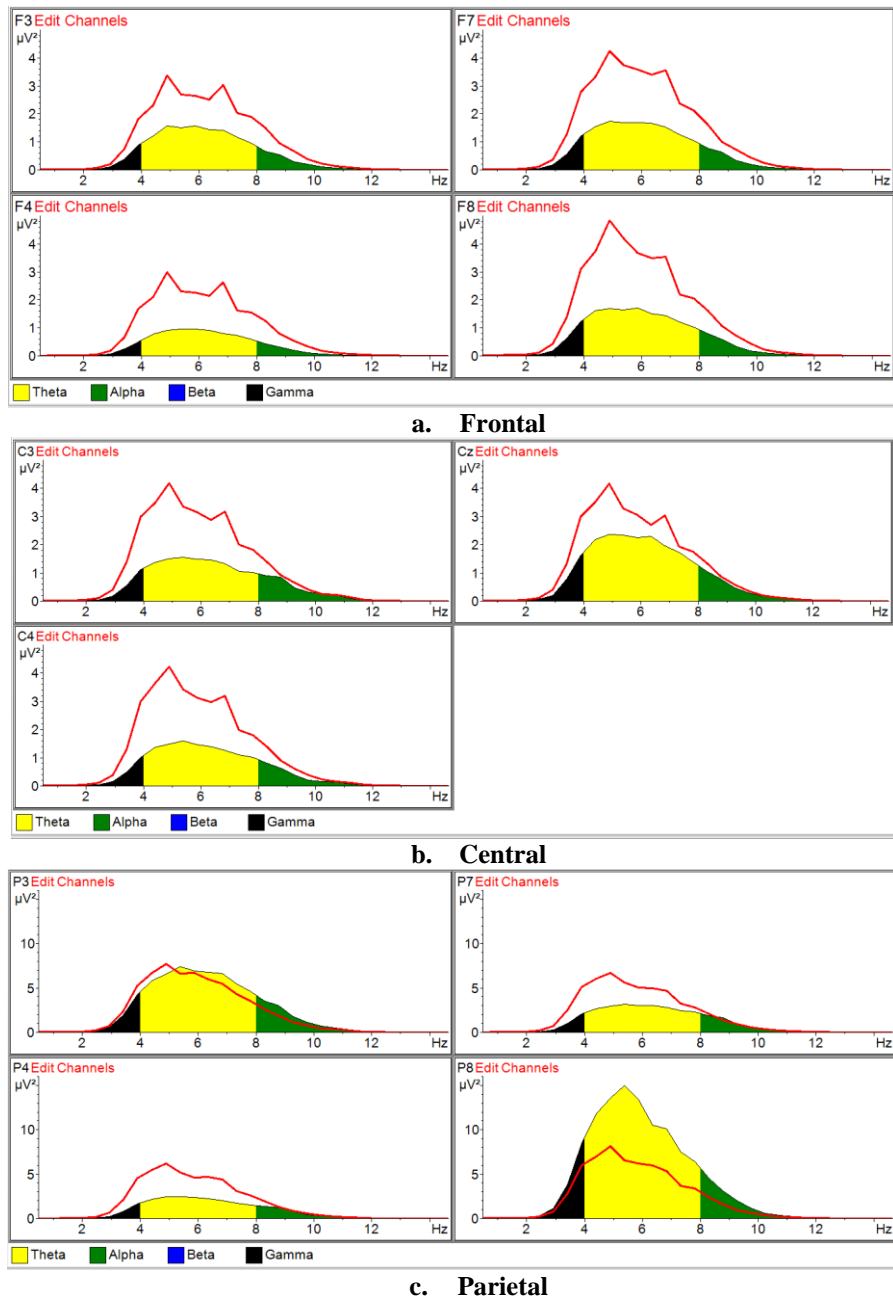


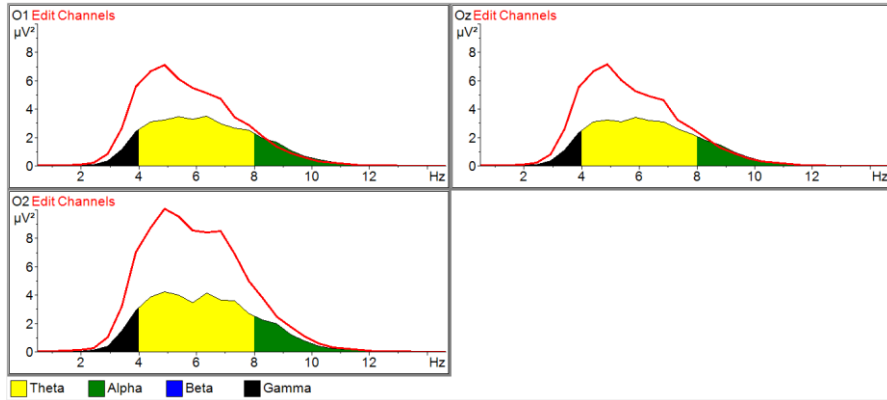
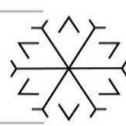
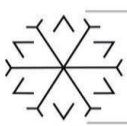
Figure 5: EEG electrodes placed according to the international 10–20 system



3. Results

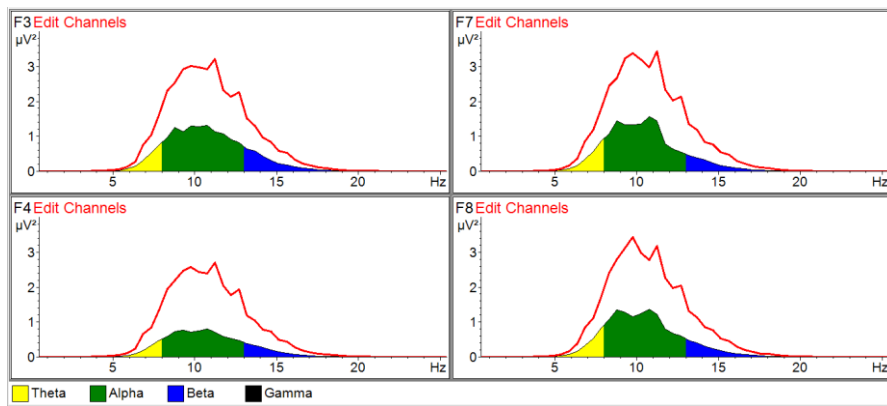
Electrodes in different parts of the brain were used while calculating the spectral power of the resting and cognitive workload blocks. F3-F4-F7 and F8 electrodes were used for the frontal region, C3-Cz and C4 for the central region, P3-P4-P7 and P8 for the parietal region and O1-Oz and O2 electrodes for the occipital region (Figure 5). Comparative results for both blocks are shown in different bands and different brain regions. Since a mental operation is performed in the cognitive workload block, the spectral power value of this block is higher than resting block. When Figures 6, 7, 8 and 9 are examined, it is seen that the frontal region electrodes are more effective in comparing cognitive workload and resting plots. When part 'a' of each figure is examined, it is seen that the spectral power (area) of the rest block is less than the spectral power (red line) of the cognitive workload block. Additionally, beta and gamma bands seem to be more effective than other bands in separating the two blocks, regardless of the channels. (Figure 8–9).



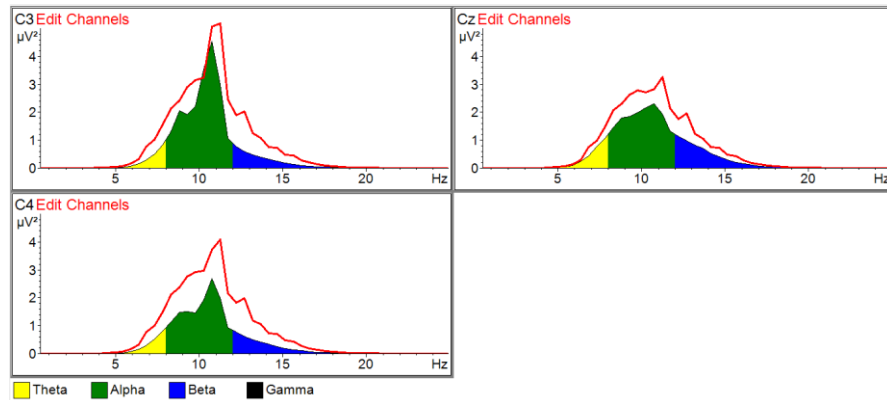


d. Occipital

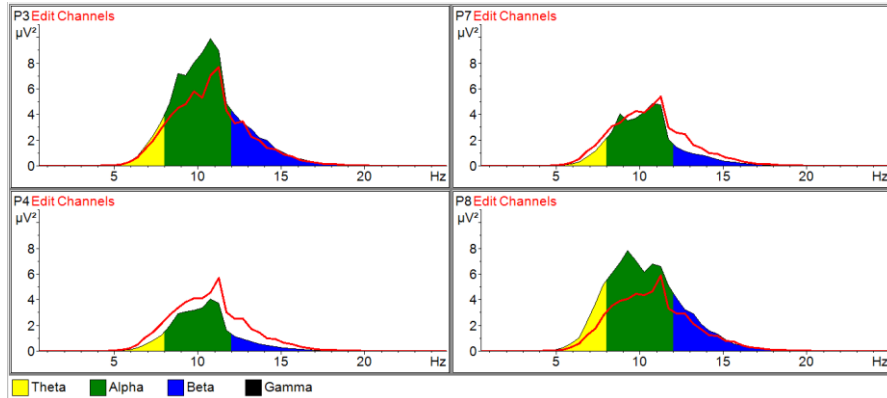
Figure 6: Spectral power comparison of different brain lobes for theta band in resting (area) and cognitive load block (red line).



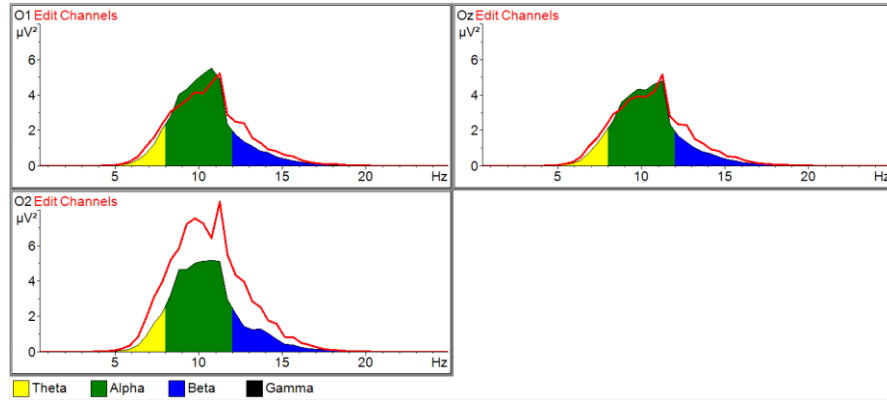
a. Frontal



b. Central

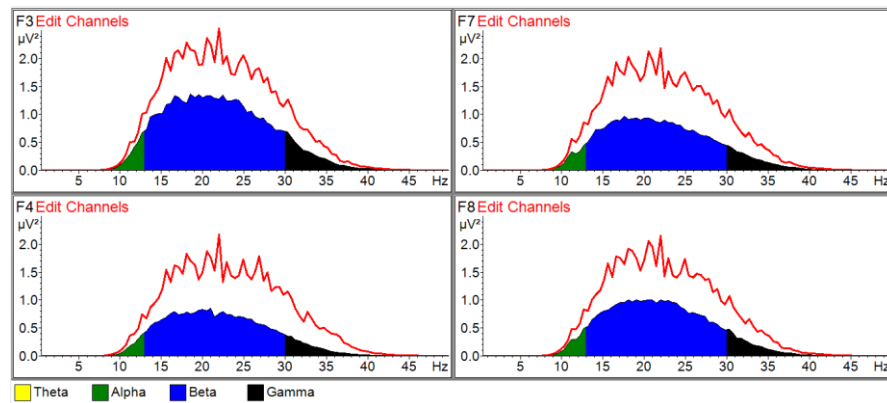


c. Parietal

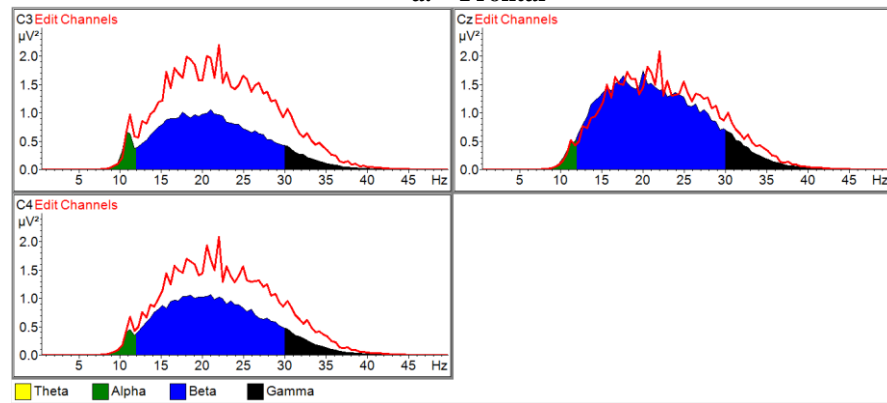


d. Occipital

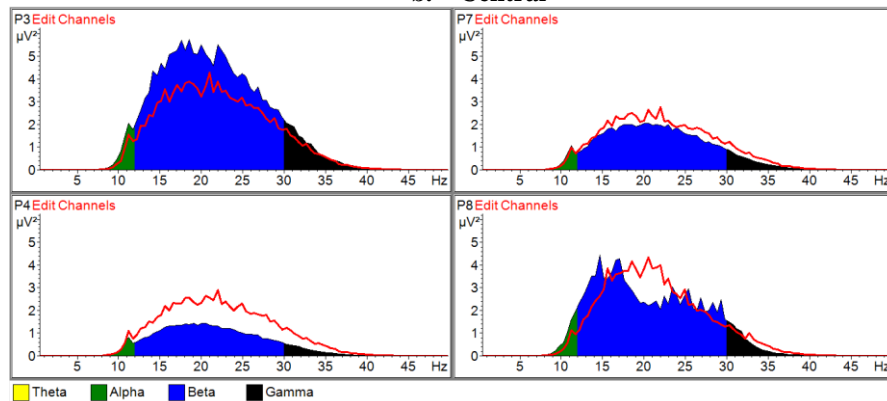
Figure 7: Spectral power comparison of different brain lobes for alpha band in resting (area) and cognitive load block (red line).



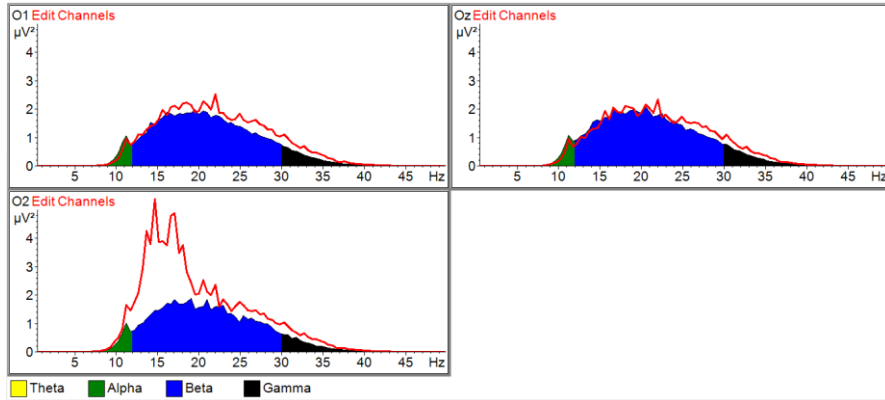
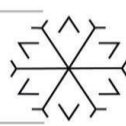
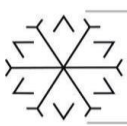
a. Frontal



b. Central

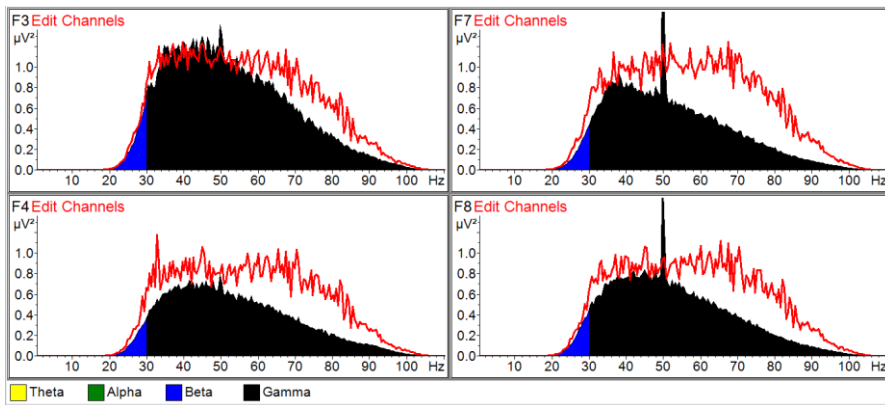


c. Parietal

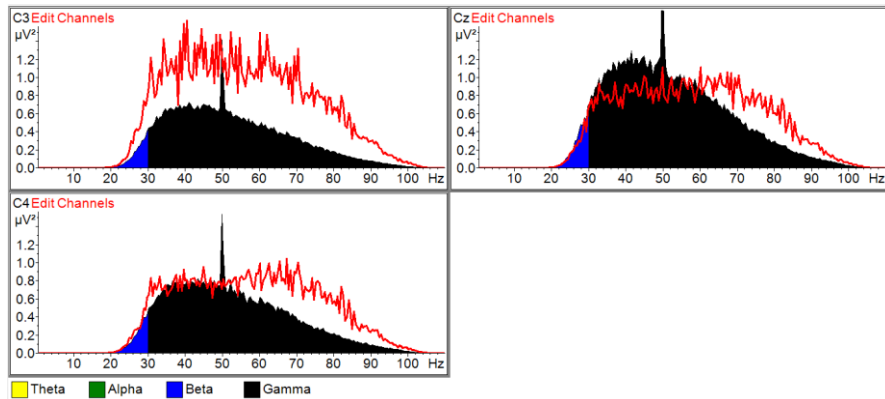


d. Occipital

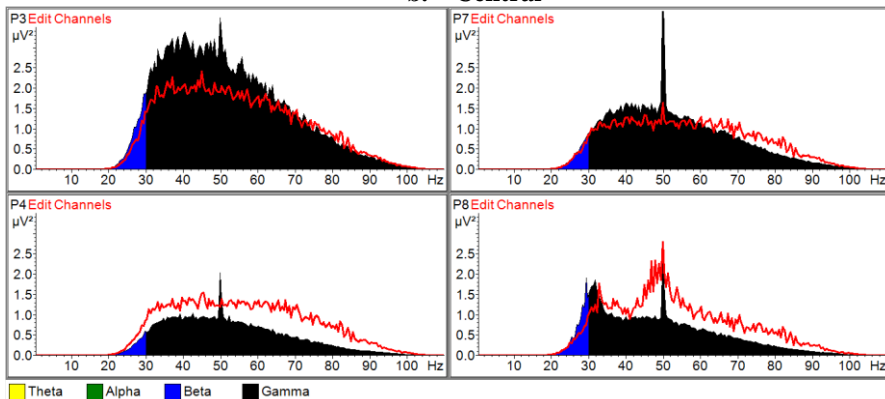
Figure 8: Spectral power comparison of different brain lobes for beta band in resting (area) and cognitive load block (red line).



a. Frontal



b. Central



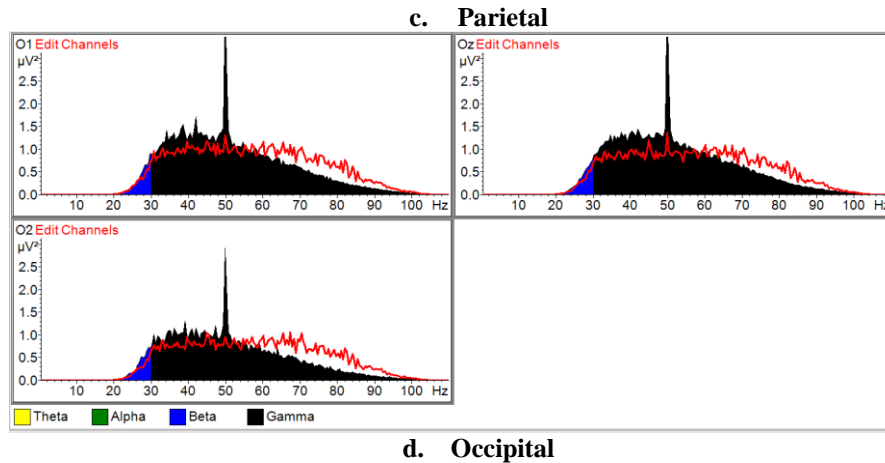


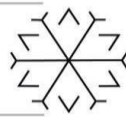
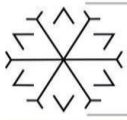
Figure 9: Spectral power comparison of different brain lobes for gamma band in resting (area) and cognitive load block (red line).

4. Conclusion

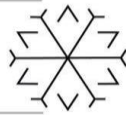
Detection of cognitive fatigue is important for issues such as preventing accidents and learning more efficient. Therefore, this study employed graphical EEG data to analyze cognitive fatigue status, thereby enabling persons, to understand whether cognitively tired. In this study, we propose a new assessment for cognitive workload using our dataset. The method we proposed showed the graphical difference in EEG data in cognitive workload and resting blocks, both in EEG band and in different lobes. According to the results, frontal region electrodes (F3-F4-F7-F8) are more effective in separating cognitive workload from resting using EEG signals. Since beta and gamma components are formed in EEG signals during cognitive processing, perception, learning, problem solving and thinking, it will be useful to use these two bands to distinguish between the two blocks. The results showed that the optimum difference achieved when beta and gamma band are used simultaneously. However, the influence that each band on the distinguish differs. Of the features, the gamma value causes the most significant changes for graphical assesment. The results indicate that the EEG signals of cognitive workload block are easier to identify compared to those of resting block; this is because the EEG signals of resting block contain additional information. In our future work, a classification algorithm will be developed to separate both blocks with the preliminary information we have obtained from here. According to these preliminary results, results will be obtained using frontal region electrodes and beta-gamma bands in the classification study.

References

- [1]. Chaudhuri, Abhijit, and Peter O. Behan. "Fatigue in neurological disorders." *The lancet* 363.9413 (2004): 978-988.
- [2]. Weinberg, R. S., and D. Gould. "Introduction to psychological skills training." *Foundations of sport and exercise psychology* (2003).
- [3]. Kamrani, Ehsan. On-chip integrated functional near infra-red spectroscopy (fNIRS) photoreceiver for portable brain imaging. Diss. École Polytechnique de Montréal, 2014.
- [4]. Dehais, Frédéric, et al. "Monitoring pilot's cognitive fatigue with engagement features in simulated and actual flight conditions using an hybrid fNIRS-EEG passive BCI." *2018 IEEE International Conference on Systems, Man, and Cybernetics (SMC)*. IEEE, 2018.
- [5]. Dehais, Frédéric, et al. "A Neuroergonomics Approach to Measure Pilot's Cognitive Incapacitation in the Real World with EEG." (2020): 1-9.
- [6]. Johansson, Birgitta, et al. "A self-assessment questionnaire for mental fatigue and related symptoms after neurological disorders and injuries." *Brain Injury* 24.1 (2010): 2-12.
- [7]. Ekim, A., Aydemir, Ö and Demir, M. "Bilişsel Yorgunluğun EEG İşaretleri ile Sınıflandırılması, TıpTekno 2020."



- [8]. Papakostas, Michalis, Akilesh Rajavenkatanarayanan, and Fillia Makedon. "CogBeacon: A Multi-Modal Dataset and Data-Collection Platform for Modeling Cognitive Fatigue." *Technologies* 7.2 (2019): 46.
- [9]. Abdul-Latif, A. A., Cosic, I., Kumar, D. K., Polus, B., & Da Costa, C. (2004, December). Power changes of EEG signals associated with muscle fatigue: the root mean square analysis of EEG bands. In *Proceedings of the 2004 Intelligent Sensors, Sensor Networks and Information Processing Conference, 2004.* (pp. 531-534). IEEE.
- [10]. Bhardwaj, H., Tomar, P., Sakalle, A., & Ibrahim, W. (2021). EEG-Based Personality Prediction Using Fast Fourier Transform and DeepLSTM Model. *Computational Intelligence and Neuroscience*, 2021.
- [11]. Brain Products GmbH. *BrainVision Analyzer 2 User Manual* <https://www.brainproducts.com/downloads.php?kid=2> (2019).
- [12]. Brain Products GmbH webinar <https://www.gotostage.com/channel/brainproducts>



Performance Comparison of IEEE 802.11p WAVE and IEEE 802.11 MAC Protocols Based on AODV Routing Protocol

Nurgunes Onal ¹[0000-0002-7198-2481] and Bulent Cavusoglu ²[0000-0002-8974-8191]

¹nurgunes.onal@atauni.edu.tr, Department of Electrical & Electronic Engineering Ataturk University
Erzurum, Turkey

²bcavusoglu@atauni.edu.tr, Department of Electrical & Electronic Engineering Ataturk University
Erzurum, Turkey

Abstract

The vehicle technology with the communication networks reduces traffic congestion, accidents and ensure the safety of people in daily life traffic. The Vehicular Ad hoc Network (VANET) provides applications that enables vehicles to communicate each other directly. VANET requires a reliable and faster communication since it has high mobility and rapid change of topology. In this paper, we present the comparison of IEEE 802.11a, 802.11b, 802.11p, 802.11ac, 802.11n MAC protocols by choosing the routing protocol as AODV (Ad hoc On-Demand Distance Vector Routing) in vehicle networks. SUMO (Simulation of Urban Mobility) is used to create traffic model and the comparison of the IEEE protocols used is evaluated using NS-3 (Network Simulator). In this paper, Average Routing Goodput, Mac/Phy Overhead and End-to-End Delay are considered as evaluation parameters. Performance evaluations shows that IEEE 802.11a and 802.11p protocols give better performance results than other protocols used in terms of Average Routing Goodput, Mac/Phy Overhead and End-to-End Delay metrics.

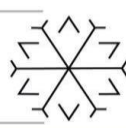
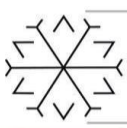
Keywords. VANET, MAC Protocols, 802.11p, AODV, NS3

1. Introduction

Vehicular Ad Hoc Network (VANET) is a connected vehicle technology for moving vehicles based on wireless communication. When a vehicle communicate with other vehicle, it is called as Vehicle to Vehicle (V2V) communication and when a vehicle communicate with infrastructure such as Road Side Unit (RSU), it is called as Vehicle to Infrastructure (V2I) communication. In this paper, we use a V2V communication architecture to build a simulation with NS-3. Due to the high mobility and fast changing topology, it is important which communication technologies are used for the vehicle communication. These communication technologies aim to improve road safety, traffic efficiency, driver and passenger comfort. They can be grouped into three categories based on their range such as long range, mid-range and short-range communication. Cellular systems (2G/3G/4G/5G) and WiMAX are used for long range communication. Wi-Fi and DSRC/WAVE are technologies used for mid-range communication. As for short range communication, Infrared, Bluetooth and ZigBee are used (Anwer and Guy, 2014). This paper focuses on the comparison of 802.11a, 802.11b, 802.11ac, 802.11n and 802.11p MAC protocols using AODV routing protocol in vehicle networks for mid-range communication. The remaining paper is organized as follows: Section-2 overviews of 802.11 MAC protocols and 802.11p WAVE, Section-3 briefly describes the AODV routing protocol, Section-4 explains performance evaluation metrics, Section-5 and Section-6 respectively give simulation scenario and analysis of results. Finally, Section -7 concludes the paper.

2. Overview of IEEE 802.11 Mac Protocols and 802.11p WAVE

The VANET uses an Ad Hoc based wireless network that is applied to vehicles. Wireless Fidelity (Wi-Fi) are commonly used to build adhoc networks due to their adjustability and mobility, allowing users to connect to the network at any time and from any location. Wi-Fi consist of several MAC protocols including 802.11a, 802.11b, 802.11n, 802.11p and 802.11ac. These protocols are used to provide wireless connectivity for V2V and V2I communications. 802.11a works in the 5 GHz frequency band and provides a data rate of 54 Mbps. 802.11b works in the 2.4GHz frequency band and achieves maximum 11Mbps data rate. 802.11n works both the 2.4GHz and 5GHz frequency and the maximum data rate of 802.11n is 600 Mbps. 802.11n is compatible with 802.11a and 802.11b protocols (Anwer and Guy, 2014). 802.11ac is



based on 802.11n. It operates in 5 GHz frequency band and provides a data rate of 6,93 Gbps (Yulandi *et al.*, 2017).

Wireless access in vehicle environments (WAVE), commonly known as IEEE 802.11p, is a standard developed for reliable communication between vehicles or vehicles-road side units. WAVE is an updated version of 802.11a standard, and it provides some useful outcomes when applying for vehicular communication with an operating 10 MHz bandwidth and frequency of 5.9 GHz (Sarvade and Kulkarni, 2017). This is half the bandwidth that is used in 802.11a. This enables the receiver to handle better with the radio channel characteristics in vehicular communication, such as signal reflections from nearby vehicles or residences (Grafling, Mahonen and Riihijarvi, 2010). The difference between IEEE 802.11a and IEEE 802.11p is given in Table 1.

Table 1: Difference Between IEEE 802.11a and IEEE 802.11p.

Parameters	IEEE 802.11a	IEEE 802.11p
Maximum Data Rate (Mbps)	Up to 54	Up to 27
Modulation	OFDM	OFDM
BandWidth (MHz)	20	10
Frequencies (GHz)	5	5.9
Range (m)	100	300

3. AODV Routing Protocol

Routing is the process by which nodes in a vehicular network exchange information about the topology and connection state with one another in order to find the optimum path (Erritali and El Ouahidi, 2013). In AODV (Ad hoc On-Demand Distance Vector Routing), routes are only established on demand, and only those that are in use are kept. The source node transmits a route request packet (RREQ) to all of its neighbors, who subsequently broadcast the RREQ to their neighbors, and so on, until it reaches the destination or any intermediate node with new knowledge about the route to the requested destination. (Amina and Mohamed, 2018). Each node that receives a packet keeps the address of the neighbor node to which the packet was sent and ensures that the return path is established.

4. Performance Evaluation Metrics

4.1. Average Routing Goodput

Average Routing Goodput is the ratio of the cumulative received bytes for the routing protocol over the total simulation time as given in (1).

$$\text{Average Routing Goodput} = \text{Cumulative Received Bytes} / \text{Total Simulation Time} \quad (1)$$

The higher the value of the goodput, the more data is successfully routed over the network.

4.2. Mac/Phy Overhead

Overhead in the network stems from packets relating to just route updates. These packets include no information about the actual message (Deepak and Rajkumar, 2018). Total physical bytes (Total phy bytes) represent the total amount of data actually transmitted at physical layer for each vehicle. Total application bytes (total app bytes) represents the sum of Basic Safety Message (BSM) transmitted bytes and cumulative transmitted bytes from routing protocol (Wang *et al.*, 2019). Mac/Phy overhead is the ratio given by (2).

$$\text{Mac/Phy Overhead} = (\text{Total phy bytes} - \text{total app bytes}) / \text{total phy bytes} \quad (2)$$

Since the network bandwidth is shared by both types of packets (routing and actual message), the smaller the rate, the better the performance.



4.3. End to End Delay

End-to-End Delay is the entire amount of time it takes for a packet to delivered from the source node to the destination node.

5. Simulation Scenario

For the experimental setup, the simulation is run on Ubuntu 20.04 operating system, SUMO version 1.9.2 as a road traffic simulator, NS-2 Mobility Trace Exporter for generation of movements file and NS-3.29 for network simulation. Figure 1 shows the generate scenario using SUMO. As shown in Figure 1, we use a real-world urban map downloaded from Open Street Map for a part of Erzurum city Turkey. The urban area of Erzurum with the highest traffic density is selected for the simulation area with coordinates 39.911638-41.272437. Figure 2 shows the movement of vehicles.

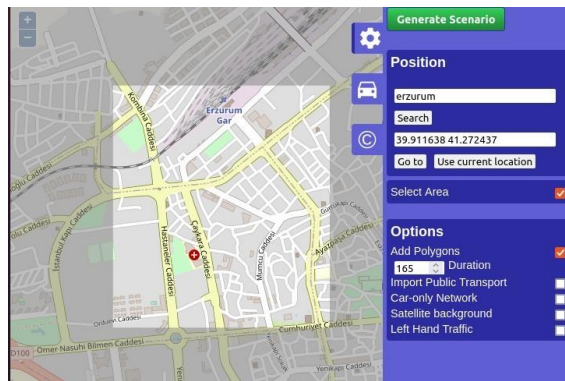


Figure 1: Generate Scenario Using SUMO

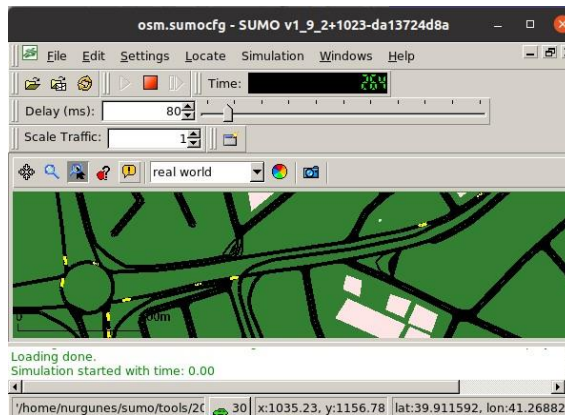
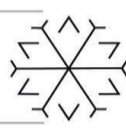
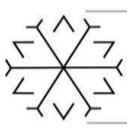


Figure 2: Movement of Vehicles

The simulation was set up to evaluate the comparison of 802.11a, 802.11b, 802.11n, 802.11p and 802.11ac MAC protocols on the basis of AODV routing protocol under varying node densities (25, 50, 100, 150, 200). Table 2 shows the details of the simulation setup.

Table 2: Simulation Setup.

Parameters	Specifications
Operating System	Ubuntu 20.04 LTS
Simulator	NS-3.29
Traffic Simulator Tool	SUMO
Topology	Real Map



Routing Protocol	AODV
Package Size	200 Bytes
Number of Nodes	25, 50, 100, 150, 200
Nod Speed	20 m/s
Scenario	V2V
MAC Protocol	802.11a, 802.11b, 802.11n, 802.11p, 802.11ac
Transmission Power	20 dBm
Transmission Range	145m
Mobility Model	Random Waypoint
Propagation Model	Two Ray Ground

Table 2 (Continued): Simulation Setup

6. Simulation Analysis

The simulation analyzes is evaluated according to the Average Routing Goodput, Mac/Phy Overhead and End-to-End Delay performance metrics as given below. The parameters have been plotted using GNU Plot.

6.1. Average Routing Goodput

Figure 3 shows IEEE 802.11p MAC standard performs better in terms of Average Routing Goodput with small number of nodes. As the number of nodes increases, Average Routing Goodput of AODV protocol gradually decreases on the basis of 802.11p. IEEE 802.11a standard shows better performance in terms of Average Routing Goodput with increasing number of nodes. When it comes to 802.11n standard, the Average Routing Goodput gives poor performance all number of nodes.

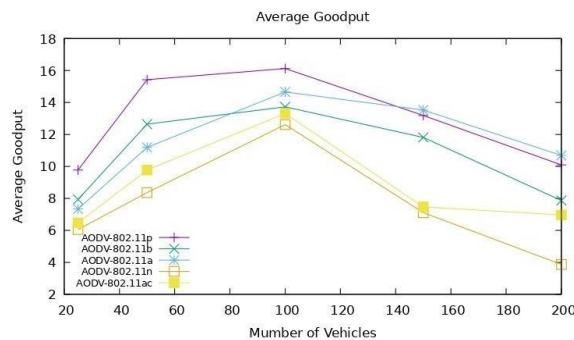


Figure 3: Average Routing Goodput vs. Number of Nodes

6.2. Mac/Phy Overhead

Figure 4 shows the comparison of Mac/Phy Overhead among IEEE 802.11 MAC protocols. We can observe that 802.11a and 802.11 p Mac protocols provide better results than the other protocols. The 802.11ac has highest Mac/Phy Overhead.

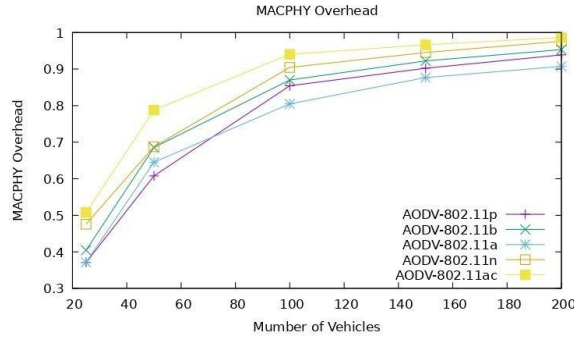
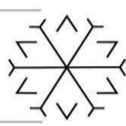


Figure 4: Mac/Phy Overhad vs. Number of Nodes

6.3. End to End Delay

Figure 5 shows 802.11p and 802.11a protocols give lowest End-to-End Delay in all density of nodes. As the number of nodes increases, the End-to-End Delay of 802.11 p increases slightly compared to 802.11a. 802.11n and 802.11ac protocols gives higher End-to-End Delay than other protocols.

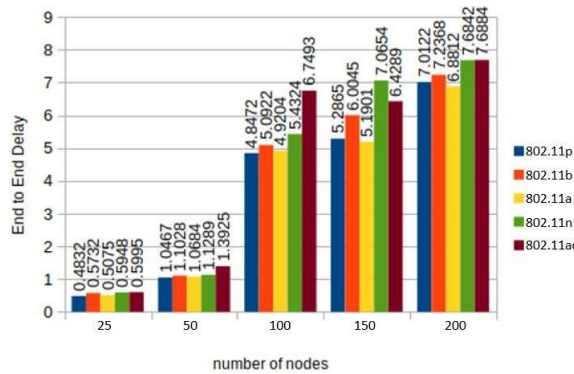


Figure 5: End-to-End Delay vs. Number of Nodes

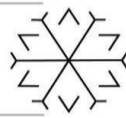
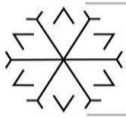
7. Conclusion

In this paper, we have evaluated the performance of 802.11p, 802.11b, 802.11a, 802.11n and 802.11ac MAC protocols in a VANET network by using performance evaluation metrics like Average Routing Goodput, Mac/Phy Overhead and End-to-End Delay. These protocols are applied with varying number of network sizes with a constant node speed. For the Average Routing Goodput, IEEE 802.11a MAC standard has better result for V2V communications compared to the other protocols in high number of nodes but 802.11p performs very close performance to 802.11a in high number of nodes. Performance evaluation shows that 802.11p standard is already better in terms of Average Routing Goodput in low density of nodes. The poorest Average Routing Goodput belongs to 802.11n standard. Compared to other protocols, 802.11a and 802.11p protocols also give the better results according to the Mac/Phy Overhead performance metric. We observe that the 802.11a and 802.11p protocols have lowest End-to-End Delay. The 802.11b standard, on the other hand, did not give as good results as 802.11a and 802.11p, nor as poor as 802.11n and 802.11ac in all performance measurement metrics. As a conclusion, 802.11a and 802.11p protocols are more suitable for both safety and non-safety applications due to their high Average Routing Goodputs and low End-to-End Delays according to our results.

References

Anwer, M.S. & Guy, C. (2014). A Survey of VANET technologies. *Journal of Emerging Trends in Computing and Information Sciences*, 5(9), (pp.661–671).

Yulandi et al., 2017. Comparison of different WLAN standard on propagation performance in V2V named data networking. *2017 IEEE Asia Pacific Conference on Wireless and Mobile (APWiMob)*.



Sarvade, V.P. & Kulkarni, S.A. (2017). Performance analysis of IEEE 802.11ac for vehicular networks using realistic traffic scenarios. *2017 International Conference on Advances in Computing, Communications and Informatics (ICACCI)*.

Grafling, S., Mahonen, P. & Riihijarvi, J. (2010). Performance evaluation of IEEE 1609 wave and IEEE 802.11p for vehicular communications. *2010 Second International Conference on Ubiquitous and Future Networks (ICUFN)*.

Erritali, M. & El Ouahidi, B. (2013). Performance evaluation of ad hoc routing protocols in VANETs. *Third International Symposium on Automatic Amazigh Processing (SITACAM' 13)*, 3(2), (pp.33–40).

Amina, B. & Mohamed, E. (2018). Performance evaluation of VANETs routing protocols using sumo and NS3. *2018 IEEE 5th International Congress on Information Science and Technology (CiSt)*.

Deepak & Rajkumar. (2018). Performance comparison of routing protocols in VANETs using network simulator-NS3. *International Journal of Research in Electronics and Computer Engineering (IJRECE 2018)*, 6(2), (pp.2097–2104).

Wang, T. et al. (2019). Enabling bidirectional traffic mobility for its simulation in smart city environments. *Future Generation Computer Systems*, 92, (pp.342–356).

Calculation of Electric Motor Values for Wind Turbines Electromagnetic Field Effect

Selçuk Alparslan AVCI ¹*[0000-0003-4918-5272]

¹selcukavci@karabuk.edu.tr, Department of Electrical-Electronics Engineering, Faculty of Engineering
Karabuk University

Abstract

A wind turbine is a system that converts the kinetic energy in the wind into mechanical energy and then converts the mechanical energy into electrical energy. A wind turbine generally consists of tower, blades, rotor, gearbox, generator (alternator), electrical-electronic materials. The kinetic energy of the wind is converted into mechanical energy in the rotor. The rotational movement of the rotor shaft is accelerated and transferred to the generator in the body. The electrical energy obtained from the generator is stored by batteries or delivered directly to the receivers. To understand how wind turbines work, two important aerodynamic forces must be well known. These are drag and lift forces. Drag force is a force that occurs on an object in the direction of flow. For example, when the maximum drag force that can occur on a flat plate is when the air flow is 90⁰ perpendicular to the object; The minimum drag force occurs when the air flow is parallel to the surface of the object. Lift force is a force that occurs perpendicular to the flow direction. Since this force causes the aircraft to take off from the ground, it is called the lift force. In this paper, the values of the electric motors in the turbine have been calculated in order to find the electromagnetic effect emitted by the wind turbine, which is one of the renewable energy sources.

Keywords. Wind turbine, electromagnetic propagation, electric machines

1. Introduction

Countries that have a say in the world economy makes significant investments in energy resources and make great efforts to increase the use of they are doing become an indispensable part of our lives energy during its production, transportation and consumption causes environmental pollution (Taghinezhad, Alimardani, Mosazadeh and Masdari, 2019). Renewable energy resources do not pollute the environment and have a long life is great for meeting energy needs is an advantage. Most of the renewable energy sources One of the advantageous ones is wind energy. Wind; solar energy reaching earthIt is a force of nature that emerges as a result (Heier, 1998). Sun the temperature difference on the earth due to its energy cause pressure changes (Chen, Arnalte and McCormick, 2000). This winds occur as a result of changes. According to the Wind Energy Potential Atlas (REPA) theoretical wind energy potential in Turkey is 48,000 MW. Existing electricity grid infrastructure can be connected to the electricity grid wind energy potential is at the level of 10,000 MW calculated (Bardal and Sætran, 2017). Wind in Turkey until 2020 reaching 20,000 MW in installed power is predicted.

2. Development of wind turbines

As seen in Figure 1, the wind in the world energy is increasing rapidly. to wind energy This increasing trend, especially those working on energy become an area of interest for R&D companies and researchers. has arrived. Studies have shown that wind their potential to be converted into energy in the country, benefits, cost analysis and most importantly blade design and efficiency of wind turbine. It is about increasing with material technique.

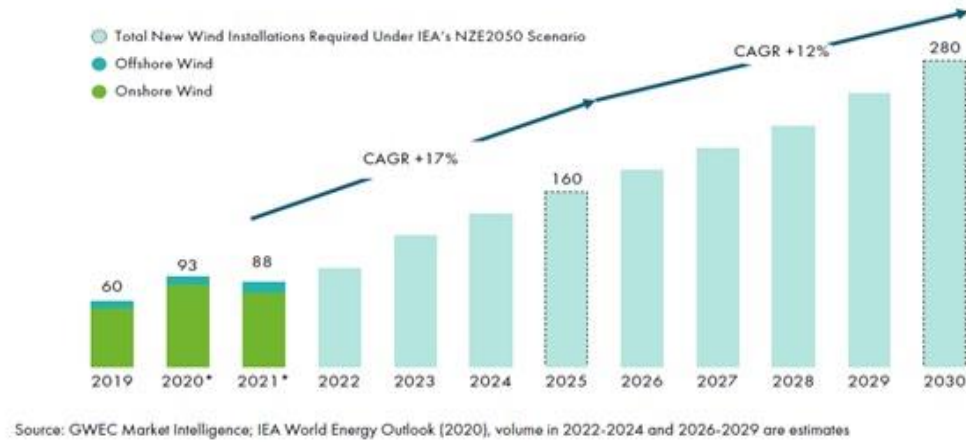
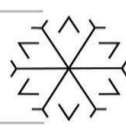


Figure 1: Estimated Wind Energy Capacity of the World in the Next Years.

2.1. Wind Power Calculation

Wind power is a measure of possible wind energy (Allaei, Tarnowski and Andreopoulos, 2015). Wind power is a function of the cube of wind speed. If the wind speed doubles, the energy in the wind increases by a factor of eight. Small changes in wind speed cause large changes in wind energy. For example, the amount of energy that can be produced by a wind of 22.6 m/s is twice the energy that can be produced by a wind of 20 m/s. ($20^3 = 8000$, $22.6^3 = 11543$). Small wind speed errors that can be made with site selection or measurement errors can cause big errors in a wind turbine investment. Therefore, before purchasing a wind turbine, an accurate and continuous wind study should be done (Han, Yan, Han and He, 2015). To be economically viable, a wind turbine should have an annual average wind speed of at least 5.4 m/s (12 mph) at the location where it will be installed.

$$W = rAv^3 \quad (1)$$

W: power, r: air density, A: wing area v: wind speed

$$W = 0.625Av^3 \quad (2)$$

$$A = \pi R^2 \quad (3)$$

R: rotor radius (m)

3. Turbine Design

While designing the turbine, first of all, data should be obtained by using the simulation program. Then, turbine design should be done according to the results obtained (Çadirci and Ermiş, 1992). Ansys commercial software is used in this design. It is designed according to the values given in figure 2.



DOMAIN: Turbine Rest	
Type	Immersed Solid
Location	WIND TURBINE REST VOLUME
Settings	
Domain Motion	Stationary
DOMAIN: Turbine Rotor	
Type	Immersed Solid
Location	ROTOR VOLUME
Settings	
Domain Motion	Rotating
Angular Velocity	-1 [rev s ⁻¹]
Axis Definition	Two Points
Rotation Axis From	0 [m], 0 [m], 15.34 [m]
Rotation Axis To	1 [m], 0 [m], 15.34 [m]
DOMAIN: Wind Tunnel	
Type	Fluid
Location	BODY
Materials	
Water	
Fluid Definition	Material Library
Morphology	Continuous Fluid
Settings	
Buoyancy Model	Non Buoyant
Domain Motion	Stationary
Reference Pressure	1 [atm]
Turbulence Model	k epsilon
Turbulent Wall Functions	Scalable

Domain	Boundaries	
Turbine Rest	BOUNDARY: Turbine Rest Default	
	Type	Wall
	Location	Primitive 2D B 2
Turbine Rotor	Settings	
	BOUNDARY: Turbine Rotor Default	
	Type	Wall
Wind Tunnel	Location	Primitive 2D C
	Settings	
	BOUNDARY: Inlet	
	Type	Inlet
	Location	Domain Inlet
	Settings	
	Flow Regime	Subsonic
	Mass and Momentum	Average Static Pressure
	Pressure Profile Blend	0.05
	Relative Pressure	0 [Pa]
	Pressure Averaging	Average Over Whole Outlet
	Settings	
Domain Motion	Rotating	
Angular Velocity	-1 [rev s ⁻¹]	
Axis Definition	Two Points	
Rotation Axis From	0 [m], 0 [m], 15.34 [m]	
Rotation Axis To	1 [m], 0 [m], 15.34 [m]	
BOUNDARY: Wind Tunnel Default		
Type	Wall	
Location	Domain Bottom, Domain Top	
Settings		
Mass and Momentum	No Slip Wall	
Wall Roughness	Smooth Wall	
BOUNDARY: Sides		
Type	Wall	
Location	Domain Side 1, Domain Side 2	

Figure 2: Desing Data.

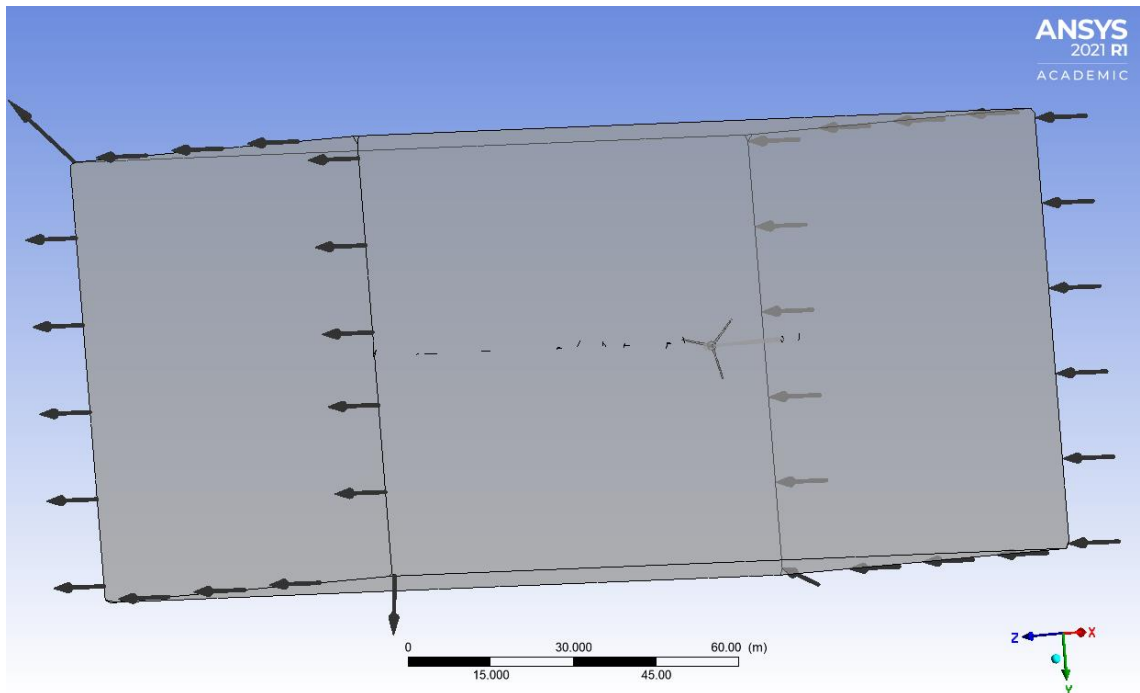


Figure 3: Model of Simulation.

3D representation of the design made in figure 3 is made. It consists of 2 parts as the wind turbine and the boundary layer. Measurements is made by sending the wind from a region of the boundary layer. In figure 4, voltage and power values are shown depending on time. It is observed that the initial values is higher. In figure 5, apart from the initial values, it is observed that the kinetic energy values is higher.

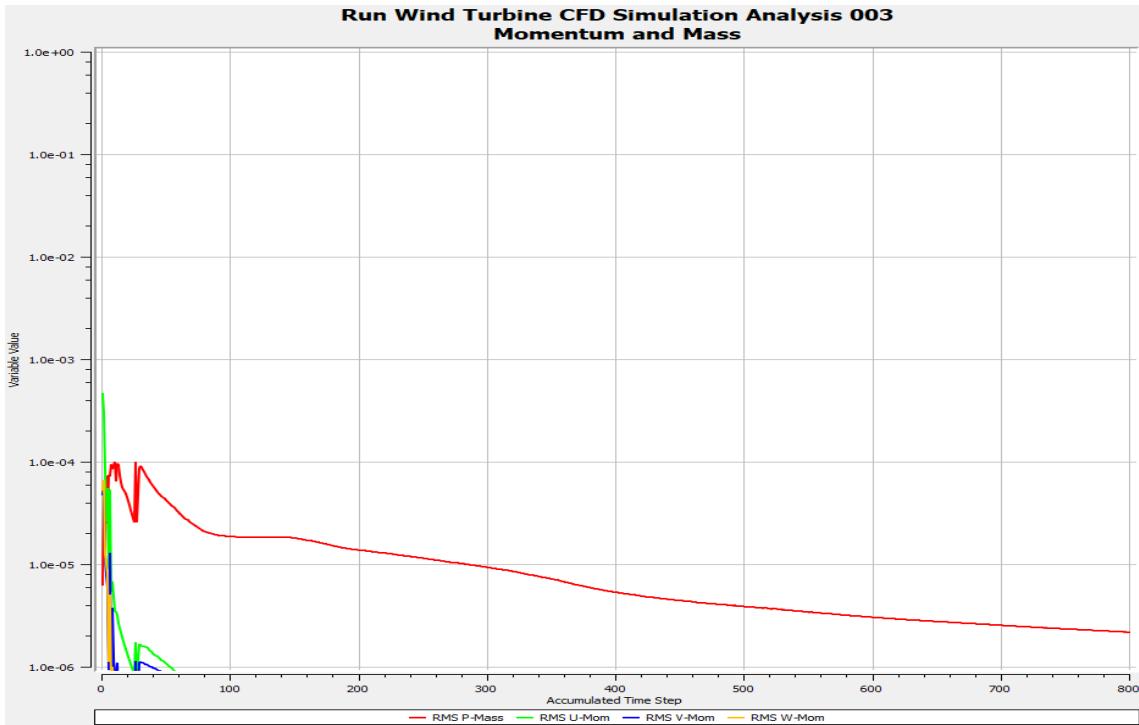
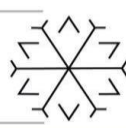
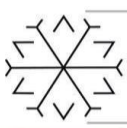


Figure 4: Results value

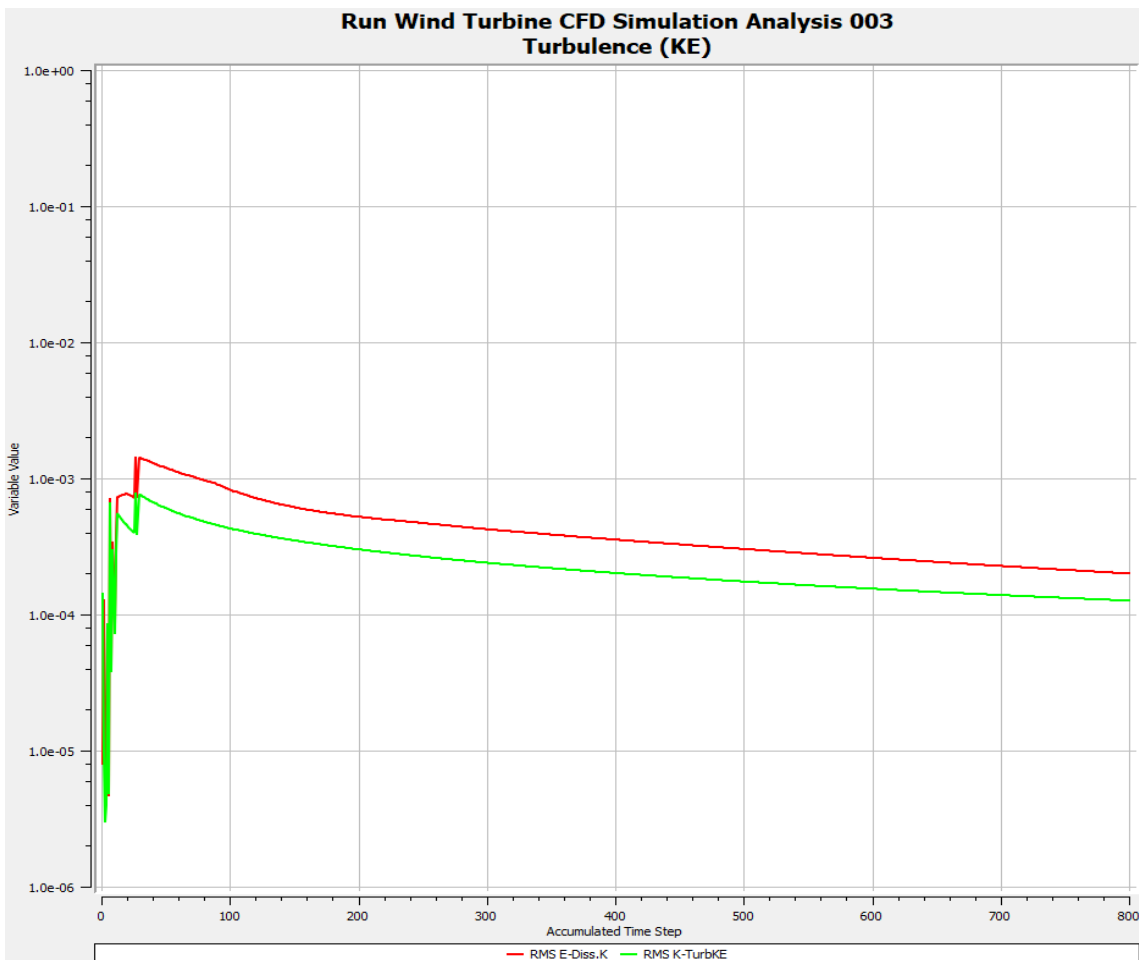


Figure 5: Results value



4. Conclusion

The high wind potential in Turkey and the government mechanisms to use renewable energy. It is foreseen that larger and more powerful turbines will be installed in the coming years. More improvement and development of transportation and installation processes along with large wind turbines in this direction required. As a result, the energy produced in wind turbines is one of the renewable energy sources. There are issues whose effects on human health need to be investigated. One of them is the effect of electromagnetic radiation emitted by the electric motors in the turbine on human health. Therefore, electromagnetic effects can be found according to the motor values. In order to minimize the electromagnetic effect, efficient and lowest powered motors should be selected.

References

- Taghinezhad, J., Alimardani, R., Mosazadeh, H. and Masdari, M., 2019. Ducted Wind Turbines A Review. *Int. J. Futur. Revolut. Comput. Sci. Commun. Eng.*, vol. 5, no. 4, pp. 19-25.
- Heier S., 1998. *Grid Integrtrion of Wind Energy Conversion System* 2nd edition, John Wiley and Sons Ltd. pp.106-116, 54-65, 230-245.
- Chen Z., Arnalte S.G. and McCormick M., 2000. A Fuzzy Logic Controlled Power Electronic System for Variable Speed Wind Energy Conversion System. *IEEE Conference*, pp.114-119.
- Bardal, L. M. and Sætran, L. R., 2017. Influence of turbulence intensity on wind turbine power curves. *Energy Procedia*, vol. 137, pp. 553-558.
- Allaei, D., Tarnowski, D. and Andreopoulos, Y., 2015, December. INVELOX with multiple wind turbine generator systems. *Energy*, vol. 93, pp. 1030-1040.
- Han, W., Yan, P., Han, W. and He, Y., 2015. Design of wind turbines with shroud and lobed ejectors for efficient utilization of low-grade wind energy. *Energy*, vol. 89, pp. 687-701.
- Çadirci, I., and Ermiş, M., 1992. Double-Output Induction Generator Operating at Subsynchronous and Supersynchronous Speeds: Steady-State Performance Optimisation and Wind Energ Recovery. *IEEE Proceedings-B*, vol.139, pp.429-442.

Single Phase 5-Level NPC Multilevel Inverter Using Level-Shifted Sinusoidal PWM

Turgay Duman ^[0000-0002-9132-9885]

turgay.duman@erzurum.edu.tr, Erzurum Technical University

Abstract

Multilevel inverters have become popular for medium and high-power applications because of having advantages over conventional inverters such as higher voltage levels, low THD, lower $\frac{dv}{dt}$ per switch and etc. Multilevel inverters often require isolated separate dc sources, making them suitable for use in renewable energy systems such as PV systems. There are three main types of multilevel inverters: diode clamped, flying capacitor, and cascaded H-bridge multilevel inverter. Three-level diode clamped inverter as known as neutral point clamped (NPC) inverter is a popular multilevel topology used in medium voltage applications because of its ability to synthesize voltage levels higher than its component switches' voltage rating. In this paper, a single phase 5-level NPC multilevel inverter generated from a combination of two 3-level NPC inverters is analysed. The level-shifted SPWM (LS-SPWM) is used to generate required gate signals for each switch. The simulation of the overall system is carried out in MATLAB/Simulink[®], and the obtained simulation results are presented.

Keywords. level-shifted SPWM, multilevel inverters, neutral point clamped, 5-level NPC.

1. Introduction

The use of multilevel inverters (MLIs) has been increasing in the power industry over the recent years. Multilevel inverters have several advantages including low total harmonic distortion because of multilevel output waveforms, lower dv/dt ratio per switch since the voltage is distributed in more number of switches. The multilevel inverters theory was first introduced by (Richard H. Baker and Bannister, 1974). A few examples of different types of multilevel inverters are the cascaded H-bridge (CHB), flying capacitor, and neutral point clamped (NPC) inverter. The three level inverter topology consisting of Neutral-point Clamped (NPC) inverter was studied by (Nabae, Takahashi and Akagi, 1981). Later, the flying capacitor converter (FCC) topology was introduced by (Meynard and Foch, 1992). The NPC and FCC topologies use a single DC source, a new topology enabling the usage of separate DC sources called cascaded H-bridge (CHB) topology was presented in (Tolbert, Peng and Habetler, 1998).

The pulse with modulation (PWM) is widely used in multilevel inverters to provide switching signals. The PWM methods can be categorized according to switching frequency as shown in Figure 1. The common used modulation techniques are carrier-based sinusoidal PWM (SPWM), space vector PWM, and selective harmonic elimination (SHE). A brief summary of multilevel inverter circuit topologies, their controls, and applications was given by (Rodriguez, Lai and Peng, 2002).

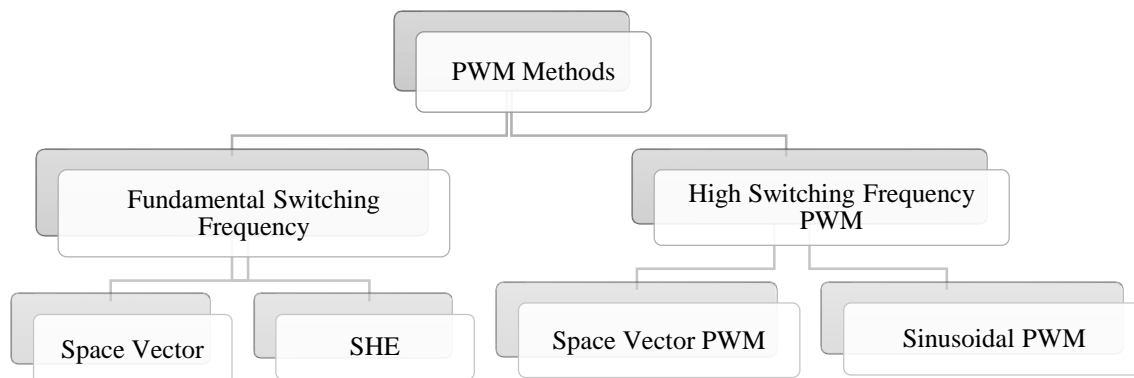


Figure 1: Classification of PWM methods



NPC multi-level inverter can be divided into two groups, three-level NPC and five-level NPC, according to the number of levels of the waveform produced at the output. The three-level neutral-point clamped (3L-NPC) converter is made up of two typical two-level VSCs layered one on top of the other with slight modifications. The higher converter's negative bar and the lower converter's positive bar are linked to produce the output phase, while the original output terminals are coupled to form a neutral point "o" through two clamping diodes. The five-level NPC inverter is basically a combination of two three-level NPC legs which each leg consists of four switches and two diodes, and the output is taken from midpoint of left leg and right leg (Du *et al.*, 2018). The circuit diagrams of 3L-NPC and 5L-NPC multilevel inverters are illustrated in Figure 2.

The DC-link voltage (V_{dc}) is divided in half at the neutral point. Therefore, only half of the total DC-link voltage must be blocked by each power device. When compared to a two-level converter, the operating voltage and power rating of the 3L-NPC converter may be doubled using the same semiconductor technology. The neutral point of 3L-NPC generates zero voltage level along with $-\frac{V_{dc}}{2}$ and $+\frac{V_{dc}}{2}$ at the output. However, the 5L-NPC-MLI generates five-level waveform at the output as $-V_{dc}, -\frac{V_{dc}}{2}, 0, +\frac{V_{dc}}{2}, V_{dc}$. Therefore, lower $\frac{dv}{dt}$ and harmonic content in the output voltage and current waveforms can be achieved along with producing more voltage. The switch states of 5L-NPC MLI and voltage levels are depicted in Table 1.

One of the major drawbacks of the 5L-NPC-MLI is the capacitor voltage balancing in neutral-point besides using more number of switches. In literature, several modulation schemes and control techniques have been presented to address this problem regarding with the neutral-point voltage balancing (Saeedifard, Iravani and Pou, 2007; Khajehoddin, Bakhshai and Jain, 2008; Guan and Li, 2017; Moonem, Duman and Krishnaswami, 2017; Wang *et al.*, 2021). Among these proposed topologies, the carrier-based PWM schemes are the most common used ones because of their simplicity and ease of implementation. Therefore, level-shifted sinusoidal pulse-width modulation (LS-SPWM) method has been chosen to produce required switching signals in this study.

This paper presents the design, modulation and control of 5L-NPC multilevel inverter. This paper is structured as follows. Section II discusses the level shifted SPWM (LS-SPWM) along with modulation index for 5L-NPC inverter. The obtained simulation results with THD analysis of 5L-NPC are given in Section III, and conclusion part is given in Section IV.

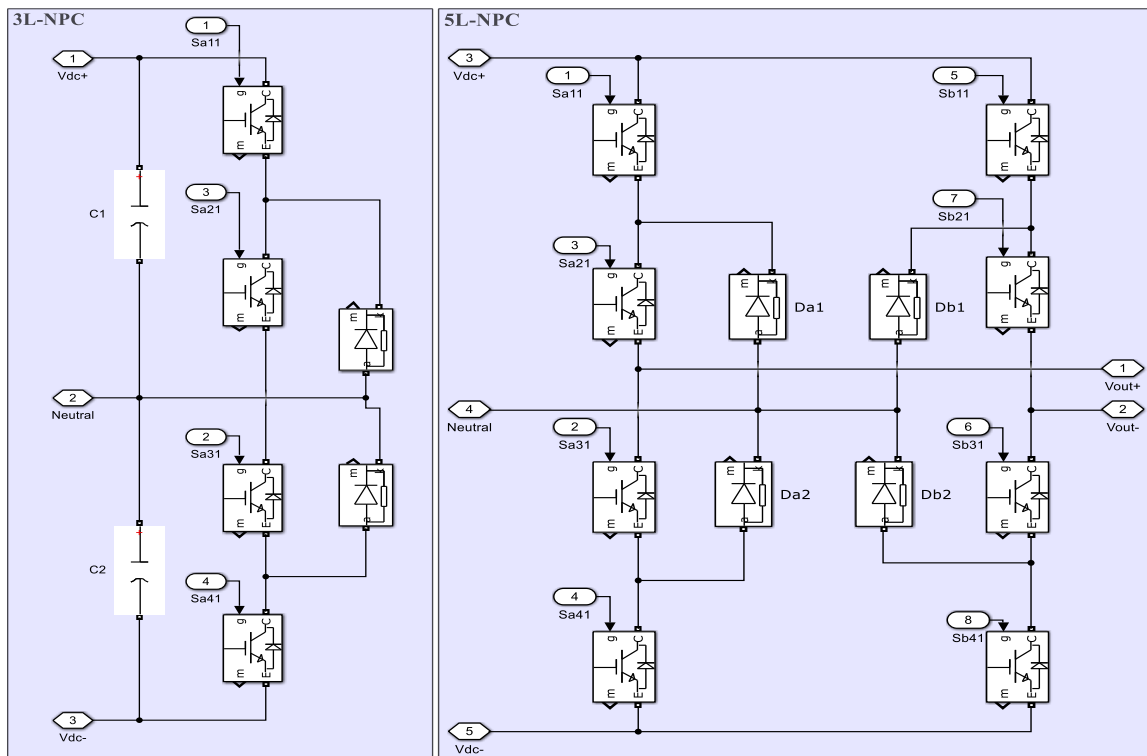


Figure 2: Circuit diagrams of 3L-NPC and 5L-NPC multilevel inverters.

Table 1: Switch states of 5L-NPC MLI and voltage levels.

	S_{a11}	S_{a21}	S_{a31}	S_{a41}	S_{b11}	S_{b21}	S_{b31}	S_{b41}
V_{dc}	ON	ON	OFF	OFF	OFF	OFF	ON	ON
$\frac{V_{dc}}{2}$	ON	ON	OFF	OFF	OFF	ON	ON	OFF
	OFF	ON	OFF	ON	OFF	OFF	ON	ON
0	ON	ON	OFF	OFF	ON	ON	OFF	OFF
	OFF	ON	ON	OFF	OFF	ON	ON	OFF
	OFF	OFF	ON	ON	OFF	OFF	ON	ON
$-\frac{V_{dc}}{2}$	OFF	ON	ON	OFF	ON	ON	OFF	OFF
	OFF	OFF	ON	ON	OFF	ON	ON	OFF
$-V_{dc}$	OFF	OFF	ON	ON	ON	ON	OFF	OFF

2. LS-SPWM and Modulation Index

LS-SPWM method is based on amplitude shift between triangular carrier waveforms having higher switching frequency and a sinusoidal waveform having frequency of 50 or 60 Hz. To generate the PWM signals for each switch, the reference sinusoidal waveform is compared with level shifted triangular carrier waveforms. There are different types of LS-SPWM depending on the phase relation between adjacent carriers. These variations are described as: (i) phase disposition (PD), where all carrier signals are identical but vertically phase shifted as shown in Figure 3(a); (ii) phase opposition disposition (POD), where the upper triangular carriers are in phase and the lower triangular carriers are phase shifted 180° to upper ones as shown in Figure 3(b); and (iii) alternate phase opposition disposition (APOD), where all the triangular carriers are alternately placed in phase opposition as shown in Figure 3(c) (Wu, Bin; Narimani, 2017). Among aforementioned techniques, phase disposition (PD) is implemented to generate required carrier signals for LS-SPWM since it generates the lowest THD at the output voltage waveform.

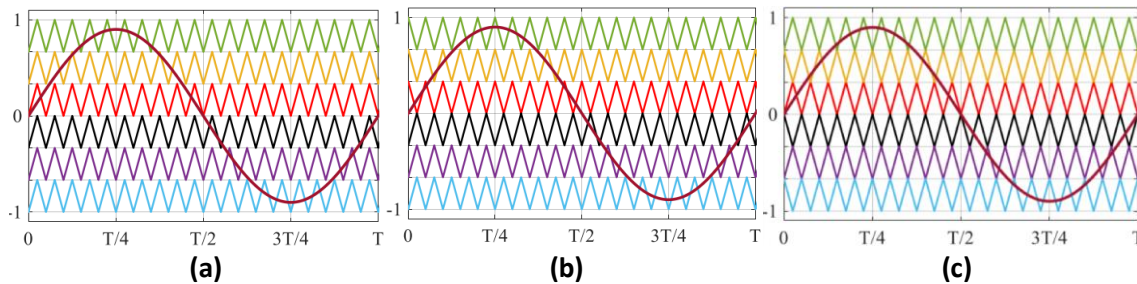


Figure 3: (a) PD-PWM, (b) POD-PWM, and (c) APOD-PWM.

There are four switches on each leg where the upper and lower switches are complementary to each other. For example, $S_{a11} - S_{a31}$ and $S_{a21} - S_{a41}$ are the complementary switches for leg-a, and the same rule also applies for leg-b. There are two triangle carrier signals which are level shifted and two sinusoidal reference signals which are phase shifted 180° in LS-SPWM. To generate switch signals for the leg-a, the sinusoidal reference signal with 0° phase is compared to two carrier waveforms. On the other hand, the same two triangular carrier waveforms are compared to another sinusoidal waveform which has a 180° phase shift to achieve the switch signals for the leg-b.

The simulink model of the LS-SPWM method, and the phase-shifted modulation signals along with level-shifted carrier signals are illustrated in Figure 4 and Figure 5, respectively. The switching frequency was chosen 750 Hz. for better representation of modulation and carrier signals as shown in Figure 5. The resulting PWM output signals using this technique for left leg and right leg are shown in Figure 6.

Modulation index (m) is the amplitude ratio between the reference sinusoidal signal and the amplitude of the carrier triangular signal as illustrated in (1).

$$m = V_{ref}/V_{carrier} \quad (1)$$

There is a direct relationship between modulation index and the output inverter voltage. This index can be varied between 0 to 1 to control the inverter output. To get the maximum output it should be equal to 1. At the lower modulation index the amplitude of the reference signal is smaller than the amplitude of the carrier



signal which causes a drop at the inverter output voltage. It should be noted that the modulation index can be further increased by suitably adding a third harmonic in reference signals, which is very common in industrial applications of multilevel inverter, and a higher voltage value can be obtained at the output. The modulation index can be increased to 1.15 by adding a third harmonic waveform with a peak value of 0.16 as shown in Figure 7. However, third harmonic injection was not applied in this paper and the modulation index was chosen as 0.96 to stay in the linear modulation mode.

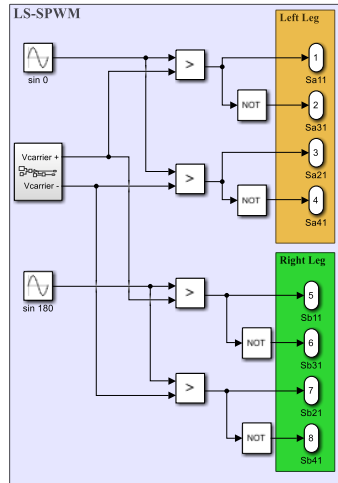


Figure 4: Schematic diagram of LS-SPWM in Simulink

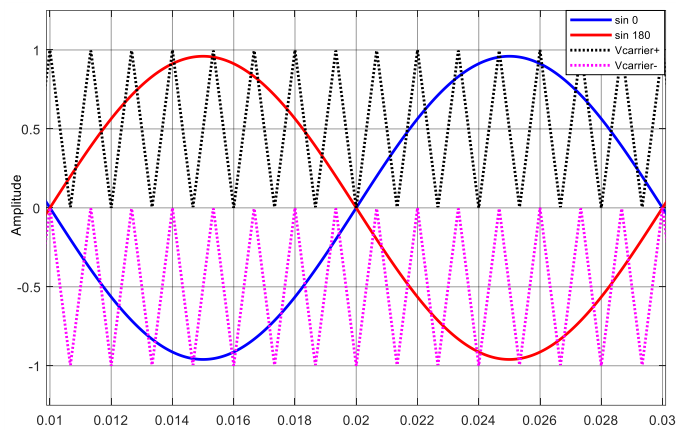


Figure 5: Modulation signals and level-shifted carrier signals

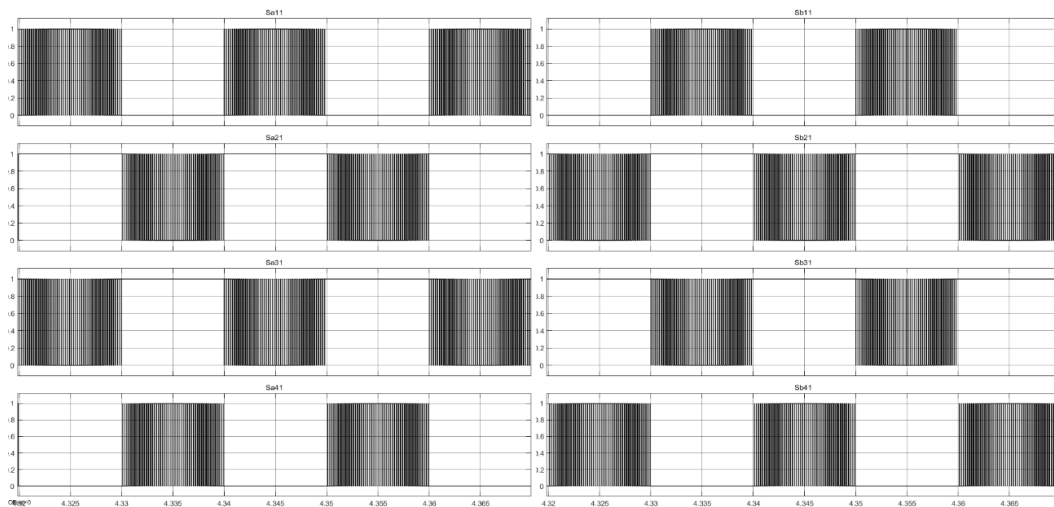


Figure 6: PWM output signals for left leg and right leg.

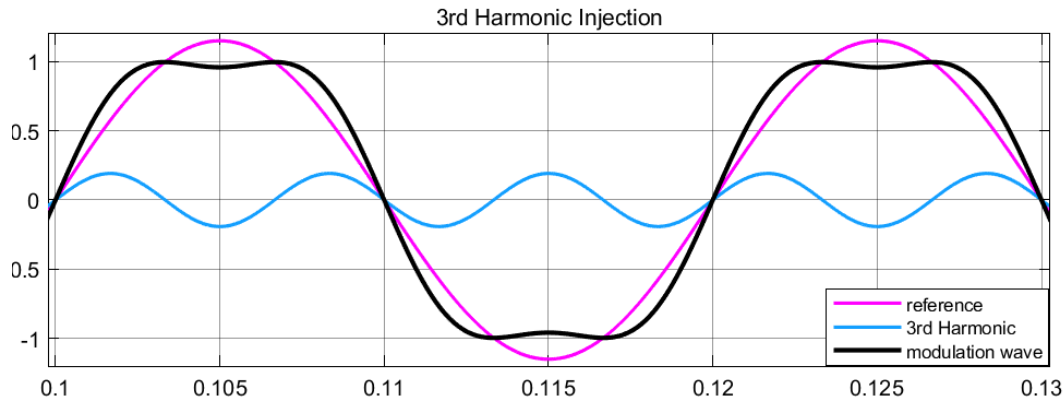
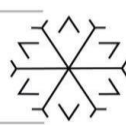
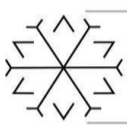


Figure 7: Modulation waveform with injection of sinusoidal third harmonic

3. Simulation Results

The simulation of 5-level NPC-MLI along with LS-SPWM has been carried out in MATLAB/Simulink[®]. The input dc voltage value was chosen as 1.6 kV since power IGBTs are available up to voltage rating of 3.3 kV and more.

Figure 8 depicts schematic diagram of the overall system. There is an R-L filter used to filter out the output voltage waveform. The required resistor and inductor values can be smaller for the output filter since five-level voltage waveform was generated at the aoutput. The five-level voltage waveform along with filtered current and voltage waveforms are illustrated in Figure 9. The total harmonic distortion analysis can be done using FFT analysis tool in powergui. Figure 10 shows THD display of filtered output voltage based on the fundamental. There are only 2-3 volts difference between top and bottom capacitors voltages as illustrated in Figure 11.

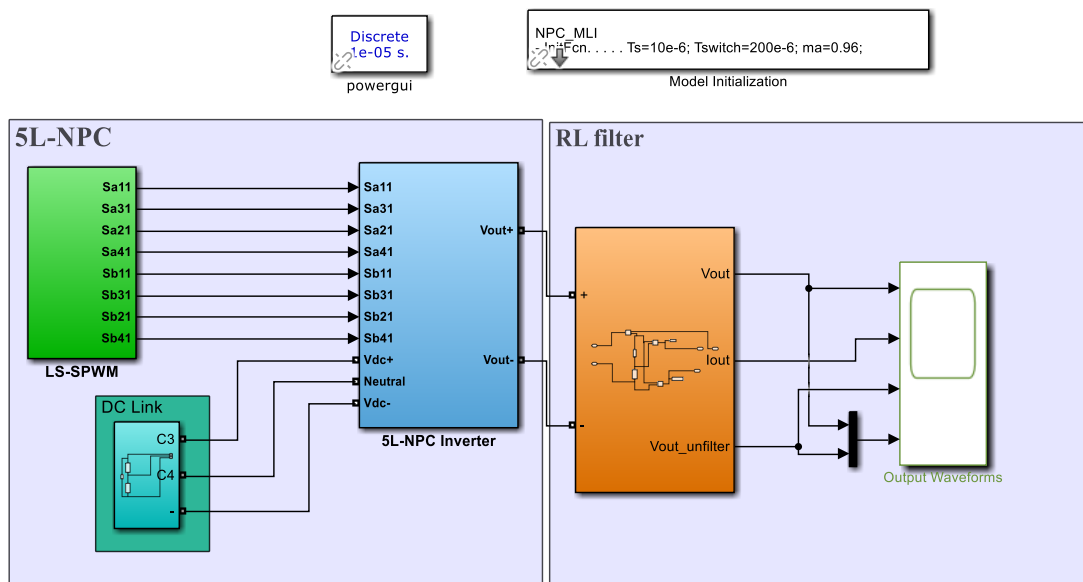


Figure 8: Schematic diagram of the overall system in Simulink.

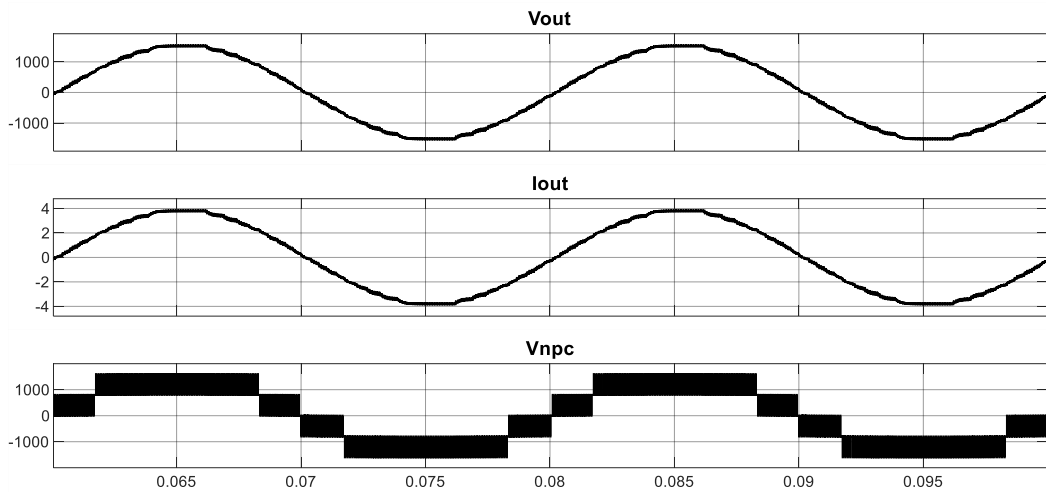


Figure 9: Voltage and current output waveforms.

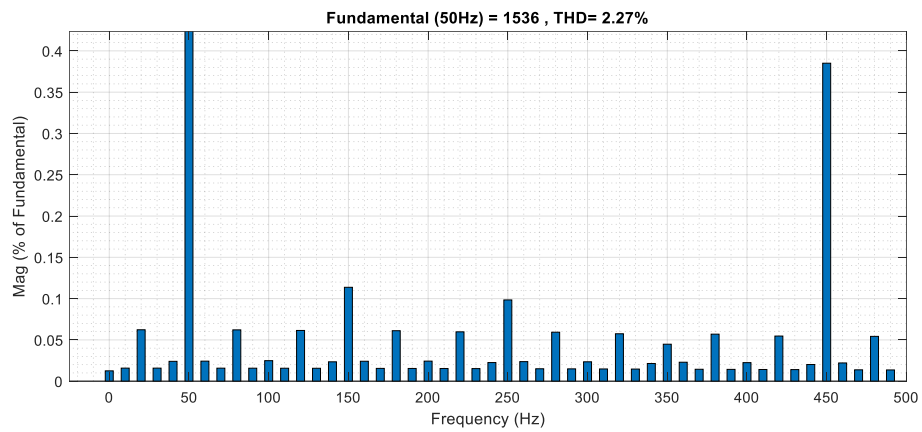


Figure 10: THD of filtered output voltage.

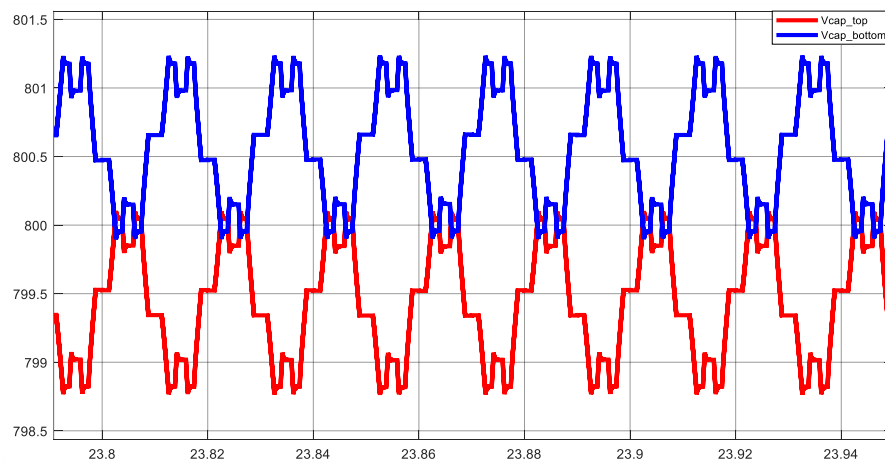
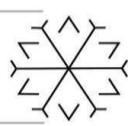
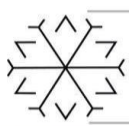


Figure 11: DC-link capacitor voltages



4. Conclusion

Multilevel inverter topologies are gaining popularity over traditional voltage source inverters thanks to recent advances on power electronics and semiconductor technologies. Multilevel inverters usually require separated dc sources, so renewable energy systems such as photovoltaic power systems can be used to obtain the required input dc voltage. There are different types of multilevel inverters used in medium or high-power applications, and 5L-NPC-MLI is one of them. In this study, single phase 5L-NPC-MLI has been modelled along with LS-SPWM used to generate required signals for switches in MATLAB/Simulink[®]. The 5L-NPC-MLI generates five-level waveforms at the output so that lower dv/dt and harmonic content can be achieved in the output voltage and current waveforms, reducing switching losses and THD. The simulation results showed that there is a negligible voltage difference between dc-link capacitors. However, in case of any capacitor voltage unbalance, the voltage balancing methods proposed in the literature can be used to balance the capacitor voltages.

References

Du, S. *et al.* (2018) *Modular Multilevel Converters: Analysis, Control and Applications*. doi: 10.1002/9781119367291.

Guan, Y. and Li, L. (2017) 'DC-link capacitor voltage balancing in five-level neutral point clamped Inverters using space vector modulation', in *IECON 2017 - 43rd Annual Conference of the IEEE Industrial Electronics Society*, pp. 1037–1042. doi: 10.1109/IECON.2017.8216178.

Khajehoddin, S. A., Bakhshai, A. and Jain, P. K. (2008) 'A Simple Voltage Balancing Scheme for m-Level Diode-Clamped Multilevel Converters Based on a Generalized Current Flow Model', *IEEE Transactions on Power Electronics*, 23(5), pp. 2248–2259. doi: 10.1109/TPEL.2008.2001892.

Meynard, T. A. and Foch, H. (1992) 'Multi-level conversion: high voltage choppers and voltage-source inverters', in *PESC '92 Record. 23rd Annual IEEE Power Electronics Specialists Conference*, pp. 397–403 vol.1. doi: 10.1109/PESC.1992.254717.

Moonem, M. A., Duman, T. and Krishnaswami, H. (2017) 'Capacitor voltage balancing in a neutral-point clamped multilevel dc-dc dual active bridge converter', in *2017 IEEE 8th International Symposium on Power Electronics for Distributed Generation Systems (PEDG)*, pp. 1–7. doi: 10.1109/PEDG.2017.7972484.

Nabae, A., Takahashi, I. and Akagi, H. (1981) 'A New Neutral-Point-Clamped PWM Inverter', *IEEE Transactions on Industry Applications*, IA-17(5), pp. 518–523. doi: 10.1109/TIA.1981.4503992.

Richard H. Baker and Bannister, L. H. (1974) 'ELECTRIC POWER CONVERTER'.

Rodriguez, J., Lai, J.-S. and Peng, F. Z. (2002) 'Multilevel inverters: a survey of topologies, controls, and applications', *IEEE Transactions on Industrial Electronics*, 49(4), pp. 724–738. doi: 10.1109/TIE.2002.801052.

Saeedifard, M., Iravani, R. and Pou, J. (2007) 'Analysis and Control of DC-Capacitor-Voltage-Drift Phenomenon of a Passive Front-End Five-Level Converter', *IEEE Transactions on Industrial Electronics*, 54(6), pp. 3255–3266. doi:



10.1109/TIE.2007.905967.

Tolbert, L. M., Peng, F. Z. and Habetler, T. G. (1998) 'Multilevel inverters for electric vehicle applications', in *Power Electronics in Transportation (Cat. No.98TH8349)*, pp. 79–84. doi: 10.1109/PET.1998.731062.

Wang, K. *et al.* (2021) 'Neutral-Point Voltage Balancing Method for Five-Level NPC Inverters Based on Carrier-Overlapped PWM', *IEEE Transactions on Power Electronics*, 36(2), pp. 1428–1440. doi: 10.1109/TPEL.2020.3006960.

Wu, Bin; Narimani, M. (2017) *High-power converters and AC drives*. Wiley & Sons.

A Software Based Simulation for Adaptive Optics System of Eastern Anatolia Observatory

Furkan Güvenir^{1*}[0000-0001-8966-2411], Cahit Yeşilyaprak^{1,2}[0000-0003-1894-7190] and Birol Soysal³[0000-0003-3945-5427]

¹fguvenir@gmail.com, Atatürk University Astrophysics Research and Application Center (ATASAM)

^{1,2}cahity@atauni.edu.tr, Atatürk University Astrophysics Research and Application Center (ATASAM),
Atatürk University Faculty of Science Dept of Astronomy and Space Sciences

³birol.soysal@erzurum.edu.tr, Erzurum Technical University Faculty of Engineering and Architecture
Dept of Electrical Electronics Engineering

Abstract

In this work, software-based simulation is described to show that software-based simulation is a way to carry out performance analysis of the Adaptive Optics (AO) system of the Eastern Anatolia Observatory (DAG for Turkish acronym) telescope. AO system is a focal plane instrument which compensates negative effects of the atmosphere. Observation time of the telescope is precious and it is beneficial in terms of project management to characterize AO system using simulation before testing AO system on site. Simulation to evaluate performance analysis of DAG AO system was created by defining the optical structure of the DAG telescope, defining the atmospheric parameters and establishing the DAG AO system structure. Developed software-based simulation gives well approximated performance values which DAG AO system will show under different conditions.

Keywords. Eastern Anatolia Observatory, adaptive optics, simulation, telescope

1. Introduction

Telescope, which is the basic equipment used by observational astronomy, gives chance to humanity in order to increase knowledge about the universe since 1600s. With the development of the telescope technology, the dimensions and the resolution of the telescopes are increasing. After 1990, it became possible to observe faint objects with modern telescopes as a result of the development in the telescope and telescope instruments. Thanks to these developments, with the studies made using modern telescopes many groundbreaking scientific studies such as exoplanet discoveries and the discovery of the existence of black holes have been successfully completed. While the lens diameter of Galileo's telescope was a few centimeters, modern telescopes have primary mirrors with diameters up to 10 meters. The increase in the size of the telescopes has necessitated the development of new technologies in many varying fields (Kitchin 2007).

Ground-based telescopes are exposed to the disturbing effects of the atmosphere. Although appropriate observation locations on Earth are chosen for telescope installation, the disturbing effects of the atmosphere limit the performance of the telescopes. Atmospheric turbulence causes aberration in wavefront which lead to deflection of the light reaching the telescope. Aberrated wavefronts reaching telescope cause aberrations in the image to be obtained by the telescope. Dealing with the disturbing effects of the atmosphere is important for the quality of the image the telescope will obtain. In order to eliminate the atmospheric effects, the design ideas of the AO system were presented to the literature by H. Babcock in 1953 (Babcock 1953). AO is a telescope instrument that aims to achieve the ideal performance of the telescope by eliminating the disturbing effects of the atmosphere and has been used in modern telescopes after 1990.

Turbulence effects are eliminated thanks to three main components in the AO system. These are wavefront sensor (WFS) that measures the deviations in the wavefront, deformable mirror (DM) that corrects the distorted wavefront by changing the shape of its surface, and the real-time controller that calculates the commands necessary for the DM to create a smooth wavefront using the information collected by the WFS.

The AO system eliminates atmospheric effects in real time and improves the spatial resolution of the images to be obtained by the telescope. This allows the telescope to approach the resolution limit that it will reach without atmospheric effects. In other words, there is a possibility that telescope can reach diffraction limit by the help of AO system. With the AO system, it has become possible to separate two independent but



close point sources. Thus, modern telescopes, whose light-gathering power increases due to the increase in the size of the primary mirror, can observe the fainter objects with high resolution. The existence of the AO system is crucial to modern telescopes. The performance of the AO system is of great importance in the image quality of the telescope. The representative structure of the AO system is shown in Figure 1.

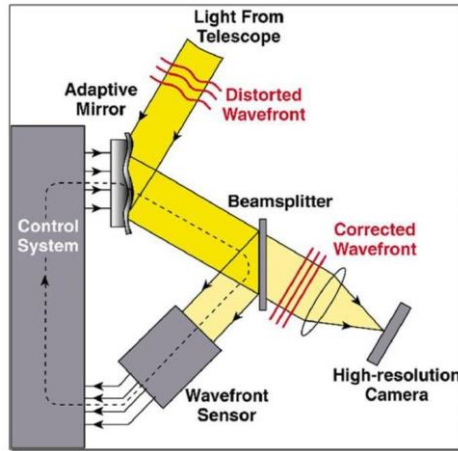


Figure 1: Basic schematic of adaptive optics (Max 2001).

The AO system is a system specially designed for each telescope, taking into account the characteristics of the telescope and the atmosphere of the location where the telescope will be located. It is necessary to analyze the performance of the AO system and measure the performance values it shows under different conditions. Performance analysis of the AO system should be carried out by means of software-based simulations, laboratory tests and tests in the focal plane of the telescope. It is important for the designed AO system to work in harmony with the telescope and to know its response in different scenarios for the selection of observations suitable for the conditions. Observation time of the telescope is precious and it is good to shorten the duration of the commissioning. Therefore, in order to characterize AO system and shorten the time of commissioning it is advised to develop a software-based simulation for AO system of the telescope.

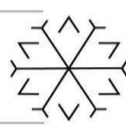
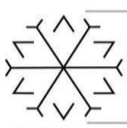
DAG is being built on the Karakaya hills at an altitude of 3170 meters in Erzurum. The telescope, which has a primary mirror with a diameter of four meters, will be put into service with the infrastructure and equipment that will meet the requirements of modern astronomy. The DAG telescope, with its AO system, aims to bring Turkey to a competitive position in the world in space observation.



Figure 2: Eastern Anatolia Observatory and its telescope.

2. Method for Developing a Software-based Simulation

It is aimed to evaluate the performance of the DAG AO system with the developed simulation software. By developing a software-based simulation it is expected to reach the performance values that the DAG AO system will show under different conditions. Moreover, a software-based simulation will shorten the AO test times to be made in the DAG telescope and laboratory environment. The most eye-catching outcome of having a simulation is to provide the data set that will contain broad observation scenarios.



2.1. PAOLA

PAOLA (Performance of Adaptive Optics for Large Apertures, PAOLA) infrastructure was used in the software of the simulation (Jolissaint 2010). In PAOLA, synthetic approach method is used instead of Monte-Carlo modeling used by many other simulation infrastructures. Synthetic modeling provides some advantages over Monte-Carlo modeling. The most important advantage of synthetic modeling is the short computation time. Basically, the core of the method is based on an analytic expression for the residual phase spatial power spectrum (PSD, which is a statistical quantity), and its relationship with the long exposure (or time average) optical transfer function (OTF), from which the AO system Point Spread Function (PSF) can be obtained. Figure 3 shows PAOLA toolbox flow chart.

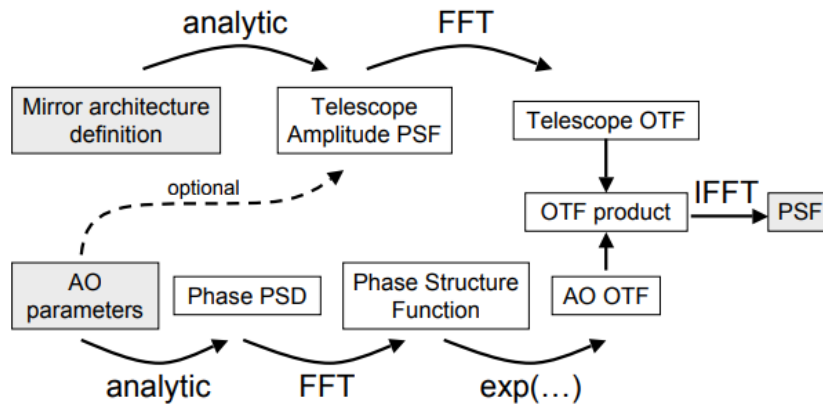


Figure 3: PAOLA toolbox flow chart (Jolissaint 2006).

2.2. DAG AO system simulation

PAOLA-based simulation software was developed to analyze the performance of the DAG AO system. The equipment in the DAG AO system is defined in the simulation. The performance of the AO system was evaluated under the influence of the DAG telescope optics and the atmosphere, and the images on the scientific camera of the DAG were obtained. The performance of the DAG AO system was evaluated by analyzing the images. The simulation software of the DAG AO system can be divided into five main parts.

- The first section is the section where static errors in the system are defined.
- In the second part of the simulation, first of all, the DAG telescope is defined. Then, the atmospheric features of Karakaya hill, where the DAG telescope is located, are defined. Finally, the components of the DAG AO system are defined. After the telescope, atmosphere and AO system are defined, PSF can be obtained from the system with the observation parameters.
- The solution of the Non-Common Path Aberrations (NCPA) problem is developed by applying phase diversity.
- Photon noise is added to the system. Thus, PSF is obtained by creating realistic observation data.
- The image obtained by the telescope is observed on DAG's scientific camera. The read noise of the DIRAC is also taken into account. Thus, the image to be produced by the DAG telescope is obtained by considering the photon noise and the detector reading noise.

3. Results

Through the developed simulation, performance analysis of the DAG AO system can be carried out at different atmospheric seeing angles, different guide star magnitudes and different observation wavelengths. The performance analysis of the DAG AO system under different conditions was calculated utilizing the Strehl ratio values. When natural guide star magnitude is 12 and the imaging wavelength is 1,65 micrometers, the Strehl ratio is 75.44% taking seeing angle as 1.0 arcseconds. Figure 4 is a simulation output showing how DAG telescope can image Neptune with and without adaptive optics correction. While the image in left column is the result of the DAG telescope image without AO correction, the Neptune image in the right column is the result of the DAG AO system correction.

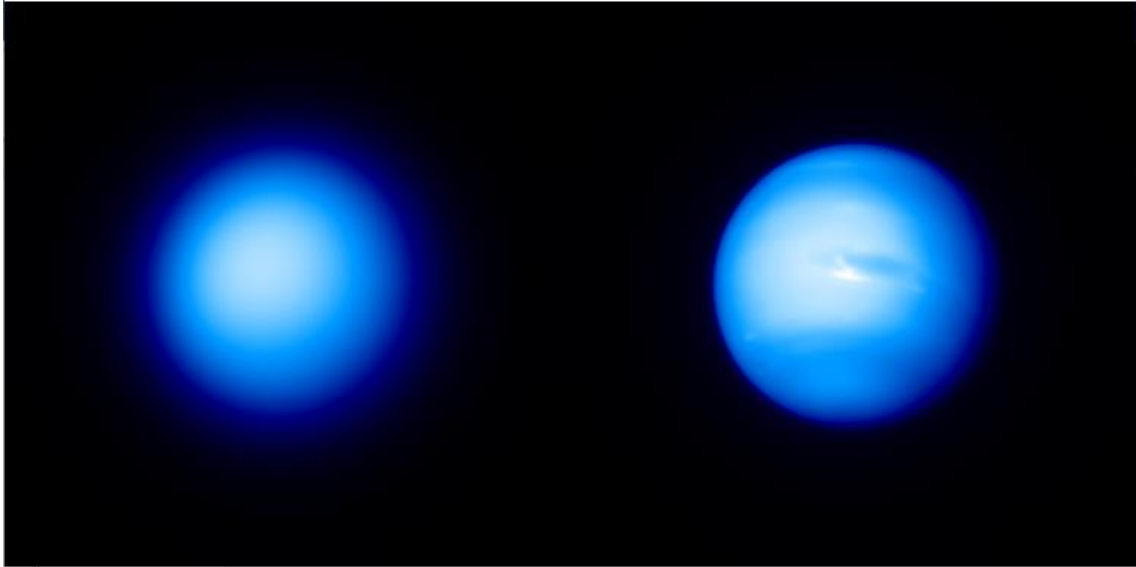


Figure 4: Neptune simulation when AO system of DAG is off and on.

4. Conclusion

Ground-based telescopes are affected negatively due to the disturbing effects of the atmosphere. AO is a technique to eliminate negative effects of the atmosphere. Performance of AO has high importance; therefore, it is essential to evaluate performance of AO under different conditions. In order to evaluate the performance of the AO system of the DAG telescope under different conditions, a software-based simulation was developed. Strehl ratio is the output which is used as criteria to evaluate the performance of the AO system in the simulation. Utilizing the developed software-based simulation it is possible to measure AO performance under varying atmospheric seeing angles, natural guide star magnitudes and observation wavelengths. Simulation results showed that AO system significantly eliminated the negative effects of the atmosphere.

Acknowledgements

Authors would like to thank Republic of Turkey; Atatürk University, Erzurum/Turkey (DAG and ODA Projects No: 2011K120230 and 2016K121140); Atatürk University Astrophysics Research and Application Center (ATASAM), Erzurum/Turkey.

References

- Babcock, H. W, 1953, 'The possibility of compensating astronomical seeing', Publications of the Astronomical Society of the Pacific, 65 (386), 229-236.
- Jolissaint, L, 2010, 'Synthetic modeling of astronomical closed loop adaptive optics', arXiv preprint arXiv:1009.1581.
- Jolissaint, L, Véran, J-P, and Conan, R, 2006, 'Analytical modeling of adaptive optics: foundations of the phase spatial power spectrum approach' JOSA A, 23 (2), 382-394.
- Kitchin, C. R, & Andersen, G 2007, *The telescope: Its history, technology, and future*, Princeton University Press.
- Max, C, 2001, 'Introduction to adaptive optics and its history', American Astronomical Society 197th Meeting. NSF Center for Adaptive Optics University of California at Santa Cruz

Causal Learning versus Machine Learning

Saffet Gökçen Şen ^[0000-0002-0748-5165]

saffet.sen@erzurum.edu.tr, Department of Electrical and Electronic Engineering, Erzurum Technical University.

Abstract

Causal learning is a kind of learning which depends on a causal model and a set of data. The causal model is constructed according to the laws of logic, the scientific knowledge accumulation, daily life experience or the expert knowledge. The causal model tells the story behind the available data. In other words, the causal model explains the causal mechanisms that generate the available data. A feature of the model can be a function of only a noise term or a function of some other features and a noise term. The noise terms are used to model effects of unconsidered or unobserved factors. The function expressing a feature in terms of some other features and a noise term represents an autonomous mechanism inside the causal model. An autonomous mechanism is not affected by the changes in other mechanisms or a change in an autonomous mechanism does not influence other mechanisms. The autonomy in causal models is important since it enables the definition of interventions and counterfactuals. A diagram can be obtained from the definition of a causal model. This diagram can be constructed by drawing an arrow from each cause of a feature to the feature. The diagram is also called the graph of the causal model. If this graph is acyclic and the noise terms are jointly independent, then the causal model is said to be Markovian. In a Markovian causal model, a feature is conditionally independent of its ancestors in the graph given its parents. The graph of a Markovian causal model is a directed acyclic graph (DAG). DAGs are indispensable tools to the study of causal models. The features of the causal model become the nodes of the DAG. The edges of the DAG represent the autonomous mechanisms relating features to their parents. A set of data stands for a probability distribution of the features. Different models can generate the same set of data and the related probability distribution. Hence, the problem of identifiability emerges. The identifiability issue will be persistent irrespective of the amount of data. Which model is to be used to represent the available data? Identifiability is a problem of machine learning which relies on only the available data. Machine learning can make calculations about statistical quantities which are defined using only the available data. On the other hand, causal models deal with causal quantities which are defined using a causal model. The causal effect of a feature on another feature is a causal quantity. The identification problem of the causal effect is a solved issue in causal learning. If two causal models have the same probability distribution and the same DAGs, then the causal effects derived from these two causal models will be the same. Another pitfall of machine learning is that it is based on statistical associations among features. Such a basis is prone to errors, instabilities due to spurious correlations among features. In causal learning, it is possible to determine the causal effect of a feature on another feature using only the observational data which is the available data. There is no need for real life experiments. Interventions and counterfactuals are two important concepts from causal learning. Detailed information about these concepts and more can be obtained from (Pearl,2009). Causal learning should be the preferred type of learning for achieving stability and reliability in data related operations like predictions and policy decisions.

Keywords. Causal learning, causal model, causal effect, identifiability, machine learning.

References

Pearl, J 2009, *Causality Models, Reasoning, and Inference*, Cambridge University Press.

Three-Dimensional Modelling and Simulation of Porous silicon based PEM Fuel Cells using COMSOL Multiphysics

Ufuk ALPER ¹[0000-0001-9144-00092] and Meltem GÖR BÖLEN ²[0000-0002-5340-6026]

¹ufkalpr@erzurum.edu.tr

²meltem.gor@erzurum.edu.tr, Erzurum Technical University

Abstract

Proton Exchange Membrane Fuel Cell (PEMFC) has emerged as one of the most promising energy technologies in recent years. In terms of technological advancement and device performance, three-dimensional modeling is critical. The features and type of membrane, gas diffusion layer (GDL), catalyst, and operating factors such as operating pressure, cell operating temperature, relative humidity, mass flow rate of feed gases, channel geometries, stack design and active area, all affect the performance of a PEMFC. Recent research into the elements that determine the durability and performance of PEMFCs has found that the performance of the fuel cell strongly depends on the performance of the type of membrane used and the active area. Therefore, proton exchange membranes made of Nafion are the most popular. It is, however, unstable at high temperatures. On the other hand, proton transmission can also be enabled by nanoporous silicon, which has nano-sized holes. Besides, the pores act as diffusion barriers within big fuel molecules and are stable at high temperatures, which is a critical performance feature, thus porous silicon can be used as a membrane in PEMFC. In this paper, a three-dimensional PEMFC model has been developed and is used to investigate the effects of active area on nafion filled porous silicon membrane based PEMFC performance. Under the specified inlet operating conditions, three active area (0.28 cm², 0.36 cm² and 0.44 cm²) were studied for the PEMFC. The numerical results showed that the performance of a fuel cell is better at high active area than at low. Accordingly, the PEMFC has the highest cell potential at 0.44 cm², especially in the high current density region. Finally, the numerical results of the proposed three-dimensional model are compared with the available experimental data and that represent good accordance. All the following results are generated with a constant cell voltage of 0.4V.

Keywords. PEMFC, Porous silicon, COMSOL

Acknowledgement

This work was supported by TUBITAK.

References

- Jourdani, M., Mounir, H., & Marjani, A. (2017). Three-Dimensional PEM Fuel Cells Modeling using COMSOL Multiphysics. *The International Journal of Multiphysics*, 11(4), 427-442.
- Gold, S., Chu, K., Lu, C., Shannon, M.A., Masel, R.I. 2004. Acid loaded porous silicon as a proton exchange membrane for micro fuel cells. *Journal of Power Sources* 135, 198-203. USA.
- Sezgin, B., Caglayan, D. G., Devrim, Y., Steenberg, T., & Eroglu, I. (2016). Modeling and sensitivity analysis of high temperature PEM fuel cells by using Comsol Multiphysics. *International journal of hydrogen energy*, 41(23), 10001-10009.
- Hipple, S. (2007). Using Comsol to Model the Cathode of a PEM Fuel Cell. *Instructor*.
- Girimurugan, R., Aravinth, S. P., Aravinthasamy, M., & Gowthaman, P. (2015). Performance Analysis of High Temperature PEM Fuel Cell with Single Flow Channel Configuration. *Int J Innov Res Creative Technol*, 1, 7-10.
- Wang, M., Wang, X., Wu, S., Tan, Z., Liu, L., & Guo, X. (2011, February). Nano porous silicon membrane with channels for micro direct methanol fuel cells. In *Nano/Micro Engineered and Molecular Systems (NEMS), 2011 IEEE International Conference on* (pp. 968-971). IEEE.
- Xia, L., Zhang, C., Hu, M., Jiang, S., Chin, C. S., Gao, Z., & Liao, Q. (2018). Investigation of parameter effects on the performance of high-temperature PEM fuel cell. *International Journal of Hydrogen Energy*, 43(52), 23441-23449.

Investigation of Factors Affecting Radar Systems with Fuzzy Logic Method

Betül Yapalıklan ^{1*}[0000-0000-0000-00000] Ibrahim Isik ^{2*}[0000-0003-1355-9420] and Mehmet Bilal Er ³[0000-0002-2074-1776]

¹btlyplkn@gmail.com, Department of Electrical Electronics Engineering, Inonu University, Malatya, Turkey

²ibrahim.isik@inonu.edu.tr, Department of Electrical Electronics Engineering, Inonu University, Malatya, Turkey

³bilal.er@harran.edu.tr, Department of Computer Engineering, Harran University, Sanliurfa, Turkey

Abstract

The factors such as weather forecast radars and mountainous around the military systems under the receiver and the transmitter antennas affecting this systems. The presence of hydrometers in weather conditions during the measurement, wind intensity, radar proximity of wind farms are among the factors that prevent to obtain accurate results from radar systems. In this context, a detailed literature review was made to solve the problems with the method of fuzzy logic and neuro-fuzzy systems, which we believe to be influenced by the discipline of making accurate predictions for reducing those affecting radar systems, and suggestions were made on how to solve these problems.

Keywords. radar systems; fuzzy logic; wind turbine

1. Introduction

Radar systems can be used in the military fields for the determination of weather conditions. Radar systems have basically two different methods. In first method, the transmitting and receiving antennas are located in different places. There are two signals, which are the signal sent from the receiver and the reflected signal, which is formed by detecting the signal sent from the receiver and reflected from the target in the transmitter. By comparing the difference between these two signals, the target point is determined. One or both of the receiving and transmitting antennas can be mobile or fixed. In second method, the transmitting antenna is used for the broadcasting systems such as the gsm operators, which refers to as illuminators, and only the receiving antenna is used as a fixed. Compared to the first method, this method is advantageous in that it reduces the cost of the receiving antenna and prevents the receiver antenna from becoming an open target, especially in military target detection, by using currently broadcasting illuminators and in target detection with 2 channels as sent and reflected signals in signal processing. If the factors affecting the accurate target detection in both the first and second methods while detecting the target of the radars are listed, the target here includes not only the military area, but also the determination of the weather conditions, all the factors affecting the antennas, being mobile, the illuminator being active, These factors are perceiving stationary objects in the environment as if they are moving with the effect of Doppler, windy, stormy weather conditions or having hydrometeors in the air. In Equation (1), the bistatic radar system equation used in such systems is given (İleri, 2021).

$$(R_R R_T)_{max} = \left(\frac{P_T G_T G_R \lambda^2 \sigma_B F_T^2 F_R^2}{(4\pi)^3 K T_s B W_n L_T L_R SNR_{min}} \right)^2, \quad (1)$$

where, P_T is transmitted power, G_T transmit antenna gain, G_R receive antenna gain, λ signal wavelength, σ_B target bicidal radar cross section, F_T Tx to target spread factor, F_R Rx to target spread factor, k Boltzman constant, T_s receiver system temperature, BW_n noise bandwidth at receiver, L_T transmit system losses, L_R receiver system losses, R_T distance between transmitter and target, R_R distance between receiver and target, SNR expresses signal to noise ratio (İleri, 2021).



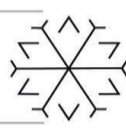
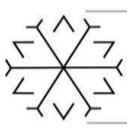
In the fuzzy logic method, the elements belonging to the sets are called membership elements. Contrary to classical logic, the probability of membership elements to be found in any of the sets is ranked as having the highest probability of 1 and at least 0 probability. For example, a hue of 0.5 green is formed by a mixture of 0.5 yellow and 0.5 blue hues. It is called as light green; 0.25 green color; It consists of a mixture of 0.75 yellow and 0.25 blue, which gives the definition of light green. As can be seen, the fuzzy logic method shows the potential of the logic method, which is closest to the human brain, in artificial intelligence applications, by presenting a system that gives intermediate colors and their tones rather than clear color definitions (Ve *et al.*, 2012).

Radar systems are affected by raindrops, causing false measurements PIA (path-integrated attenuations) (Delrieu *et al.*, 1999). In one of the studies examined, an experiment was conducted with the receiving and transmitting antennas on the mountain and 7 rain sensors placed at intervals between these antennas to measure the rain. It was obtained that the effect of rain was reduced as a result of filtering. The experiment was carried out on a mountain called Saint Jean le Vieux. Scatter formulas are used here (Delrieu *et al.*, 1999). Sensitivity according to drop size in terms of eliminating attenuation by establishing a consistent relationship between equivalent reflectance factor (Z_e), attenuation coefficient (k), and rain rate, as a solution to incorrect measurements in radar systems measuring at x band and c band wavelengths due to the attenuation effect of raindrops. In this approach, firstly, based on the attenuation equation, the relationship between the coefficients was formulated with DSD (Drop Size Distribution) modeling, then a real rain rate profile was selected in order to analyze this situation, and a reflection profile was hypothetically derived by using the relations between the coefficients used in the formulas, and the data obtained was, used in data processing. The first of the methods used in data processing is the direct application of the Z-R relationship, called the ZR method. The second is that the Z-R transformation is achieved by the method known as the HB method. After data processing, the values obtained with the real values are compared using the Nash criterion, which is called the verification procedure. Although all these methods are applied according to the x band, it has been observed that they are applicable in the c band (Delrieu, Hucke and Creutin, 1999).

Radar systems have also been observed that natural events such as rain, snow, ash cloud, volcanic particle density are used to measure the density of falling to the ground (Falconi and Marzano, 2019). It has been determined that there are different interpretations among the pilots in the interpretation of the weather radar screens, and a research has been carried out on the cause of this situation. As a result of the 4-day tests completed by the pilots, when the test results of the same screen image were compared, it was observed that the results were different from each other. In this situation, it has been observed that while the correct interpretations are taken from the radar system in direct proportion to the experience of the pilots, despite possible false images, it has been observed that those who are relatively inexperienced reach more false results than the experienced ones. It remains a mystery whether, it is depending on the order of the images on the radar display screen or the pilots are predicting turbulence (Wiggins, 2014).

Radar devices can detect events called ground echoes, which are reflected from the slopes of the mountains, from the sea surface, or as a result of echoes from buildings, as heavy precipitation. In order to prevent this situation, the fuzzy logic sets, which is called as fuzzy logic sets, found according to the Abeyess probability distribution, which uses the variables of the fuzzifier, rules, inference engine and fuzzifier, eliminating the ambiguities and reducing the echo. The correct image was obtained for the c-band radar system by removing the AP (precipitation in the radar image caused by the ground echo) with the obtained images (Rico-Ramirez and Cluckie, 2008) in this study.

A team consisting of pilots and people who worked in the US military who did not want their identities to be disclosed was formed and this team was interviewed to determine the effect of wind turbines on radar systems. In the interview, it has been determined that the number of wind turbines and the proximity of the wind turbine to the radar systems have significant effects on radar systems. The damage to be caused by wrong measurements is especially for the US military, since the enemy soldiers can easily infiltrate from the place where the wind farms are installed in the event of a possible war, illegal methods such as smuggling and drugs can enter and exit the country from these areas without being noticed, and the height of the wind turbine occupies the landing and exit level of an aircraft. It has been revealed that the trainings can be held in a very limited area in the USA, and that, although there should be no electromagnetic pollution for electromagnetic test systems, accurate test results cannot be obtained due to electromagnetic pollution caused by wind turbines (Auld, McHenry and Whale, 2014). In order to solve these problems, between the radar upgrade and the radar and the wind farm, it is aimed to reduce ghosting (the effect of wind turbine on radar) by entering distance, reduce ghosting with software upgrades, and improve radar detection by processing data of the area covered by space-filling radars and the wind farm with a secondary radar.



Although each proposed solution provides advantages and disadvantages according to its place, it has been determined that improvements in radar detection are provided (Auld, McHenry and Whale, 2014). The fourier transforms of the signals of the wind turbine clutter called WTC (Wind turbine clutter) are taken and the fourier turns of the overlapping signals are subtracted from the total signal, and the required non-distorted signal is obtained. An algorithm for WTC reduction has been developed with various formulas by examining the time and frequency domains (Uysal, Selesnick and Isom, 2016). It is aimed that the efficiency obtained from wind energy will be 20% by 2030, although realizing this provides many advantages, it also brings many disadvantages, one of these disadvantages is WTC caused by wind turbines.

In another study, an algorithm is developed to eliminate WTC for the core and flash in the structure of a single wind turbine. While creating this algorithm, CPA (phase alignment), spectral flatness, spectral moment, HWR and spectral delta deviation were used. By using the obtained data in a statistical study, an algorithm that obtained more accurate results with the increase of WTC was obtained (Hood, Torres and Palmer, 2010). Z_{dr} (Use of differential reflectance) is used to distinguish between rain and ice, classification using linear depolarization, while LDR is used to determine the graupel region with Z_{dr} and horizontal polarization, using specific differential propagation phase (KDP) and copolar correlation coefficient, also difference reflectance (ZDP) (Liu and Chandrasekar, 2000). In this study, fuzzy logic was used to determine the factors such as rain, ice, ice in storm, snow that occur as a result of weather events. Fuzzy logic provides a broad definition by establishing a specific rule in which various parameters are included, instead of a restricted probability distribution such as 1 and 0. Neuro-fuzzy systems are more efficient than fuzzy logic. The advantage of this system is that while a single rule is used in fuzzy logic, more than one rule is determined in neuro-fuzzy logic, allowing much more efficient definitions (Liu and Chandrasekar, 2000). Wide usage areas of laser systems such as military, medical, vehicle tracking, armament, how this system is open to development, advantages and disadvantages are examined in detail (Affan Ahmed, Mohsin and Zubair Ali, 2020). The application of fuzzy logic systems in wind description has been efficient in reducing wind turbine effects (Bianco and Wilczak, 2002).

2. The Proposed Methods

Although there are different approaches and solutions to eliminate the problems of precipitation, shadowing and ground echo caused by factors such as weather conditions and terrain conditions that affect the correct detection of radar systems, each solution for each problem has been aimed to solve only one problem. For example, when examining weather conditions, a separate solution is sought to eliminate the confusion caused by the effects of events such as raindrops, snowflakes, and hail in the radar system, while a separate solution is sought for wind farms that affect the radar, and a separate solution for attenuation due to the mountainous terrain. A separate solution has been found for its reflections. However, if the radar system is both rainy, close to the wind turbine, in a mountainous region, and in a residential area close to the sea, where ground reverberation can be at high levels, the distortions caused by ground reverberation will be at the highest level. As it can be seen, in such a case, it is quite difficult to find out what the cause of the deterioration is and which source should be used to solve the problem. The use of fuzzy logic and neuro-fuzzy logic methods in studies that try to solve the degradation caused by hydrometeors, which are the result of natural events, and ground reverberation together, and the use of the estimation of the atmospheric boundary layer affecting radar systems with the wind-based fuzzy logic method.

In a different study, combined these two studies and by adding elements that affect other radar systems on top of it, it is provided the motivation to make solutions with fuzzy logic and neuro-fuzzy logic. As shown in Figure 1, the graphs obtained from the solution of the rain event with the fuzzy system show that the wrong measurement caused by the rain was eliminated. Figure 1 shows the graphical results obtained as a result of an experiment to eliminate the rotation of the mountain consisting of rain measurement sensors, receiving and transmitting antennas placed on the Saint Jean mountain and the decrease in the signal received after rain on the mountain (Delrieu *et al.*, 1999). Figure 1 shows the Range-Time graph, Figure 1.A shows the apparent distance-based rain reflection profile between Mount Saint Jean and the radar antenna. In Figure 1.B, the graph drawn with a continuous line in the mountain return time graph, and the average apparent rain reflection rate caused by the roughness and rotations in the mountain structure are shown in the graph in a time-dependent manner. While the function drawn with the solid line in the graph is the rain reflection ratio, the part expressed with the dashed line shows the estimation of the rain-induced attenuation ratio (PIA). Figure 1.C is the graph of the function calculated by doubling the strength of the signal received from the receiving antenna, and Figure 1.D shows the average rain rate obtained in line with the data received by the installed rain gauges. Paying attention, the point where the signal strength is the lowest in Figure 1.B gives us the point where the rain is most intense in Figure 1.D. The correlation between



Figure 1.B and Figure 1.D shows an inverse ratio between rain and radar measurement (Delrieu *et al.*, 1999).

In Figure 2, when the blur method is used in estimation of mixing depth, the efficiency obtained compared to the standard method is visibly noticeable from the radar screen image results. It is important to correctly determine the convective boundary layer of the atmosphere in order to accurately predict the weather. However, the solution of this boundary layer determination problem remains up-to-date. It shows that correct results are obtained in atmospheric depth estimation based on wind as one of the membership elements for solving the problem. In this method, fuzzy logic was first used to find the SNR, then fuzzy logic was applied over the SNR again and the depth estimation was obtained with the FSFD (fuzzy spectral-fuzzy depth) method. The depth estimation obtained using fuzzy logic is shown in Figure 2.A, and the depth estimation graph obtained using fuzzy logic in Figure 2.B. In both graphs, the black dots show the depth estimation obtained by the SNR method, and the dots indicated by the triangle show the result obtained from the RASS (Radio Acoustic Sounding System), which gives more accurate results compared to the SNR method. The fact that the black dots in Figure 2.A converge to the triangles in Figure 2.B, which we know to give more accurate results, shows us that the fuzzy logic method provides accurate results (Bianco and Wilczak, 2002).

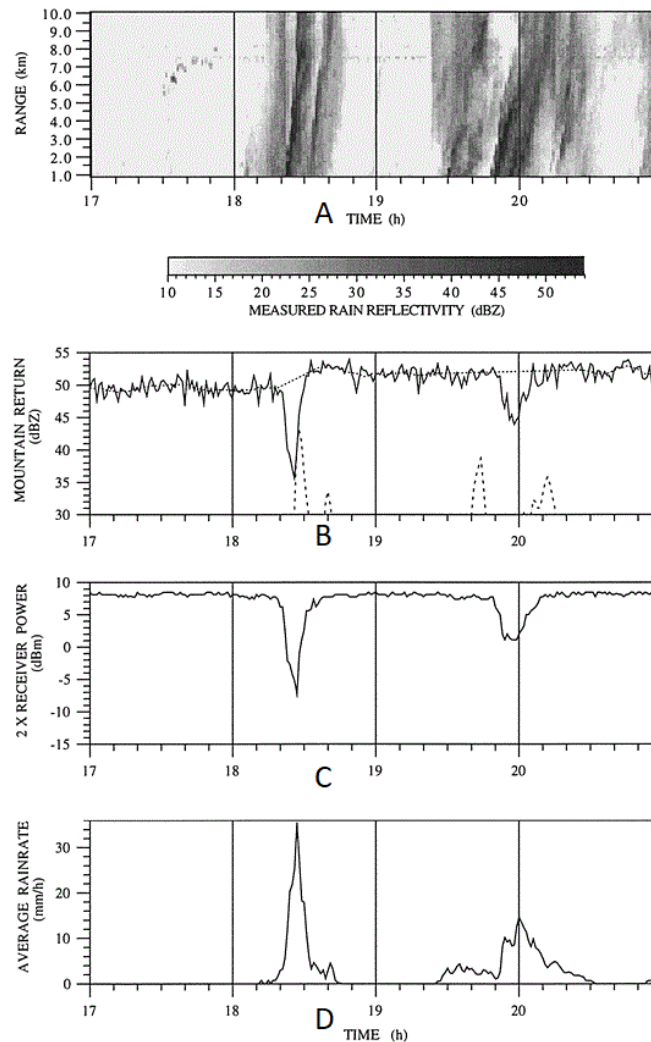


Figure 1: Solution of mean rain rate with fuzzy deman (Delrieu *et al.*, 1999).

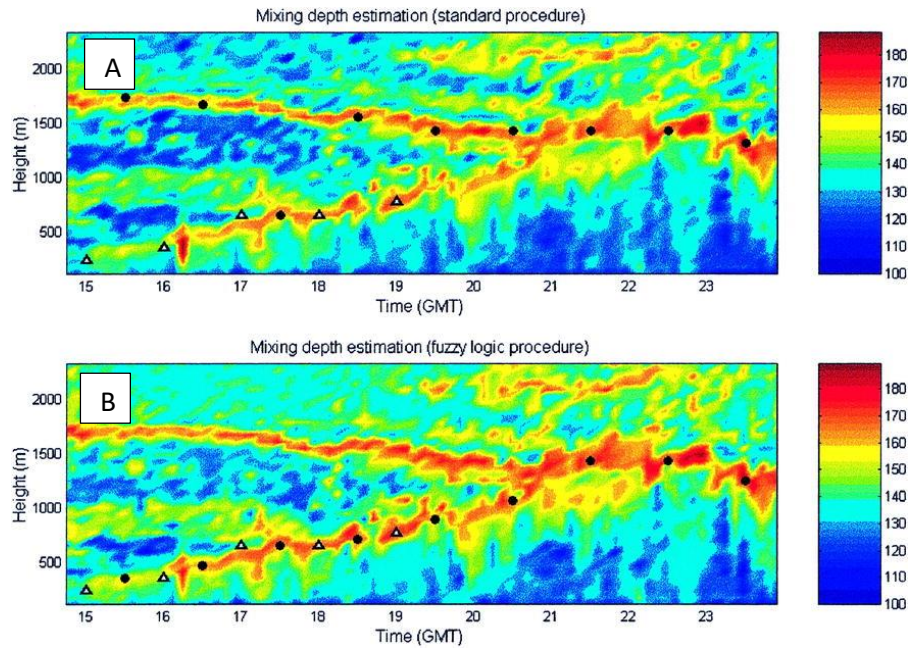
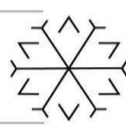
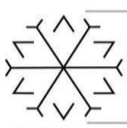


Figure 2: The use of fuzzy logic based on wind in atmospheric depth estimation (Bianco and Wilczak, 2002).

Two pulse signals are sent simultaneously, vertically and horizontally, to determine the water droplets, which are the raw material of hydrometeor types such as rain and snow formed as a result of precipitation. The ratio of these pulses from the vertical signal to the horizontal signal gives the differential reflection coefficient Z_{dr} . Since droplet size is an important variable in distinguishing hydrometeor types, Z_{dr} is a useful variable in differentiating hydrometeor types. In Equation (3), the equation of the reflection coefficient of rain is given.

$$f_{rain_zdr}(Z_{DR}) = \frac{1}{1 + \left[\frac{Z_{DR} - 2.25}{1.83} \right]^2}^{16.22} \quad (3)$$

With the fuzzy logic system for the reflection coefficient Z_{DR} , drizzle, rain, dry and low density snow, dry and high density crystals, wet and melting snow, dry graupel, wet graupel, small hail, large hail, rain and hail. The membership function can be solved as the reflection coefficient with the blurring method, which has a mixture effect. In the determination of hydrometeor type, the beginnings and endings of hydrometeors appearing in similar ready-made natural conditions, sometimes more than one hydrometeor type can be seen at the same time or the transitions are very fast made it difficult to predict the data type. As a solution to this, membership functions were determined using fuzzy method and neuro-fuzzy method (Liu and Chandrasekar, 2000). The algorithm of the system that is intended to be built, taking into account the studies carried out, is shown in Figure 3. In the studies, it was tried to find different solutions one by one for the factors affecting the radar system. However, it is thought that it would be more appropriate to collectively solve all the variables affecting the radar system by first applying the fuzzy logic for each problem and obtaining the system input variables with correct results, then applying a fuzzy logic method again for the results to affect each other. The disadvantage in other systems was that effective results were not obtained as fuzzy logic in solving each problem and each problem was evaluated separately. The advantage in the proposed system is that both the fuzzy system is applied one by one to solve each problem and it is a system that will make accurate radar estimation for the effects of these effects on each other.

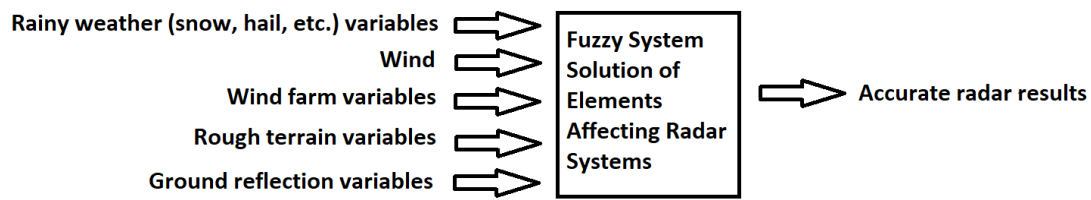


Figure 3: The intended implementation.

3. Conclusion

In this study, the factors affecting the radar systems and the present solutions were examined, the use of fuzzy logic systems as a solution method, and the graphics of the results obtained from the studies in this field were examined. It has been shown with a system algorithm that the fuzzy logic method gives accurate results, and the use of a fuzzy logic system that covers all these effects for the improvement of the radar system and will provide more accurate results. In future studies, it is aimed to simulate this system and test it on a real radar data.

References

- Affan Ahmed, S., Mohsin, M. and Zubair Ali, S. M. (2020) 'Survey and technological analysis of laser and its defense applications', *Defence Technology*, (xxxx). doi: 10.1016/j.dt.2020.02.012.
- Auld, T., McHenry, M. P. and Whale, J. (2014) 'Options to mitigate utility-scale wind turbine impacts on defence capability, air supremacy, and missile detection', *Renewable Energy*, 63, pp. 255–262. doi: 10.1016/J.RENENE.2013.09.017.
- Bianco, L. and Wilczak, J. M. (2002) 'Convective boundary layer depth: Improved measurement by Doppler radar wind profiler using fuzzy logic methods', *Journal of Atmospheric and Oceanic Technology*, 19(11), pp. 1745–1758. doi: 10.1175/1520-0426(2002)019<1745:CBLDIM>2.0.CO;2.
- Delrieu, G. et al. (1999) 'Rain measurement in hilly terrain with X-band weather radar systems: Accuracy of path-integrated attenuation estimates derived from mountain returns', *Journal of Atmospheric and Oceanic Technology*, 16(4), pp. 405–416. doi: 10.1175/1520-0426(1999)016<0405:RMIHTW>2.0.CO;2.
- Delrieu, G., Huc, L. and Creutin, J. D. (1999) 'Attenuation in rain for X- and C-band weather radar systems: Sensitivity with respect to the drop size distribution', *Journal of Applied Meteorology*, 38(1), pp. 57–68. doi: 10.1175/1520-0450(1999)038<0057:AIRFXA>2.0.CO;2.
- Falconi, M. T. and Marzano, F. S. (2019) 'Weather radar data processing and atmospheric applications: An overview of tools for monitoring clouds and detecting wind shear', *IEEE Signal Processing Magazine*, 36(4), pp. 85–97. doi: 10.1109/MSP.2019.2890934.
- Hood, K., Torres, S. and Palmer, R. (2010) 'Automatic detection of wind turbine clutter for weather radars', *Journal of Atmospheric and Oceanic Technology*, 27(11), pp. 1868–1880. doi: 10.1175/2010JTECHA1437.1.
- Liu, H. and Chandrasekar, V. (2000) 'Classification of hydrometeors based on polarimetric radar measurements: Development of fuzzy logic and neuro-fuzzy systems, and in situ verification', *Journal of Atmospheric and Oceanic Technology*, 17(2), pp. 140–164. doi: 10.1175/1520-0426(2000)017<0140:COHBOP>2.0.CO;2.
- 'Radar ile Yerdeki Hareketli Hedeflerin Tespiti Kadir İleri Doktora Tezi Elektrik - Elektronik Mühendisliği Tez Danışmanı Prof. Dr. Necmi Serkan TEZEL' (2021).
- Rico-Ramirez, M. A. and Cluckie, I. D. (2008) 'Classification of ground clutter and anomalous propagation using dual-polarization weather radar', *IEEE Transactions on Geoscience and Remote Sensing*, 46(7), pp. 1892–1904. doi: 10.1109/TGRS.2008.916979.
- Uysal, F., Selesnick, I. and Isom, B. M. (2016) 'Mitigation of wind turbine clutter for weather radar by signal separation', *IEEE Transactions on Geoscience and Remote Sensing*, 54(5), pp. 2925–2934. doi: 10.1109/TGRS.2015.2508380.
- Ve, F. et al. (2012) 'Dicle Üniversitesi Sosyal Bilimler Enstitüsü'.
- Wiggins, M. W. (2014) 'Differences in situation assessments and prospective diagnoses of simulated weather radar returns amongst experienced pilots', *International Journal of Industrial Ergonomics*, 44(1), pp. 18–23. doi: 10.1016/j.ergon.2013.08.006.

Design of Flexible Antennas for Mobile Communication and 5G Application

Hilal KOÇ POLAT ¹[0000-0003-2382-1736], M. Dilruba GEYİKOĞLU ²[0000-0003-2399-4741]

and Bülent ÇAVUŞOĞLU ³[0000-0002-8974-8191]

¹hilal.koc@erzurum.edu.tr, Erzurum Technical University

²miracg@atauni.edu.tr, Ataturk University

³bcavusoglu@atauni.edu.tr, Ataturk University

Abstract

In this paper, two different silver microstrip patch antennas operated at 22 GHz and 32 GHz are presented for mobile and 5G applications, respectively. The proposed antennas are designed in CST Microwave Studio software and bended on a cylindrical structure for a flexibility test in the simulation environment. These antennas are fabricated by using silver paste on capton polyimide substrate with screen printing technique. These antennas are bended on the cylindrical structures for a flexibility test in the CST simulation environment. The measurement results of fabricated antennas demonstrate fitness of the design to mobile and 5G applications.

Keywords. 5G; capton polyimide; CST Microwave Studio; flexible microstrip antenna; screen printing method.

1. Introduction

Mobile communication technology is one of the important fields of the research in communication systems. The mobile network demands new communication systems to increase its capacity. The available spectrum used in the mobile communication systems is below 6 GHz (Yu et al., 2017). The new systems with more bandwidth, reliability and interference-free transmission require the use of frequency bands above 6 GHz in order to meet data rates because the frequency spectrum between 9 kHz and 6 GHz is almost occupied for the existence mobile communication. In fact, the frequency range between 30 GHz and 300 GHz is considered as a candidate for the 5G systems (Bae et al., 2014).

In this study, two different flexible silver microstrip patch antennas operated at 22 GHz and 32 GHz are designed for the communication system. Capton polyimide film with a low loss factor over a wide frequency ($\tan \delta = 0.002$) is chosen as an antenna substrate due to the good balance of physical, chemical and electrical properties. Moreover, Capton Polyimide is very robust with a very low profile (50.8 μm), a tensile strength of 165 MPa at 73 ° F, a dielectric strenght of 3500-7000 vol/mil and a temperature range of -65 to 150 ° C (Khaleel et al., 2013). A copper tape is used as an antenna ground. Thus, it is ensured that the SMA connector is attached to the fabricated antenna well.

2. Antenna Design and Fabrication

The antennas designed on the planar capton polyimide are shown in Figure 1. The capton polyimide is bended on the cylindrical structure which has different diameter in order to test flexibility in the CST simulation. The antenna operated 32 GHz are bended for the flexibility test on the cylindrical structures with a radius of curvature of 3.18mm, 4.77mm and 9.54mm for 90°, 60° and 30° bending, respectively. The antenna operated 22 GHz are bended for the flexibility test on the cylindrical structures with a radius of curvature of 6.36mm, 9.54mm and 19.08mm for 90°, 60° and 30° bending, respectively. The resonance frequencies of the antennas are evaluated under bending conditions. The resonance frequencies tend to slip or fall because there is a change in the effective electrical length of the radio frequency components (Khaleel et al., 2013). The antennas with 90° bending are shown in Figure 2.

The main text body must be written with regular (non-italics and non-bold) characters. All titles and headings in the paper must be bold and first letters should be written capital. Italic characters must be used only when necessary (Nouns in Latin, abbreviations, theories/definitions, quotations, etc.).

One space distance must be placed after the commas and full stops.

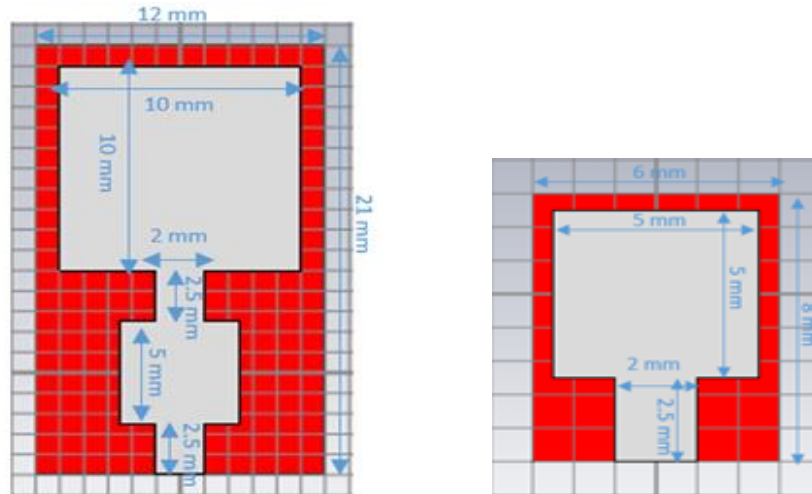
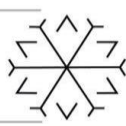


Figure 1: Geometry of the designed planar antennas at (a) 22 GHz and (b) 32 GHz.

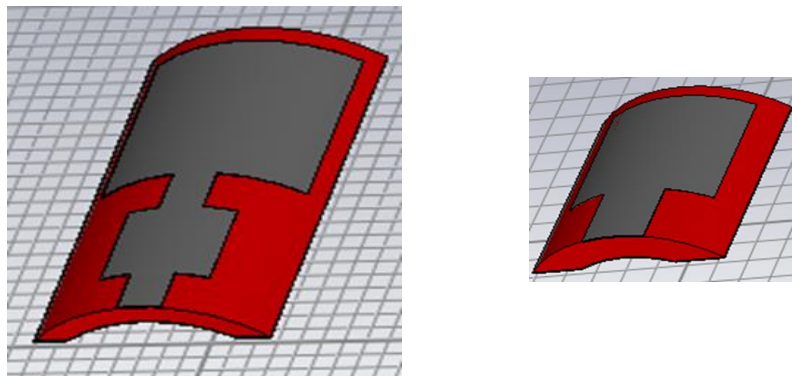


Figure 2: Bending planar antennas with 90°.

The proposed antennas are fabricated using screen printing technique. This technique used by electronic manufacturers is one of the high-efficiency and cost-effective techniques (Xiao et al., 2016). The pictures of the fabricated planar antennas are shown in Figure 3.

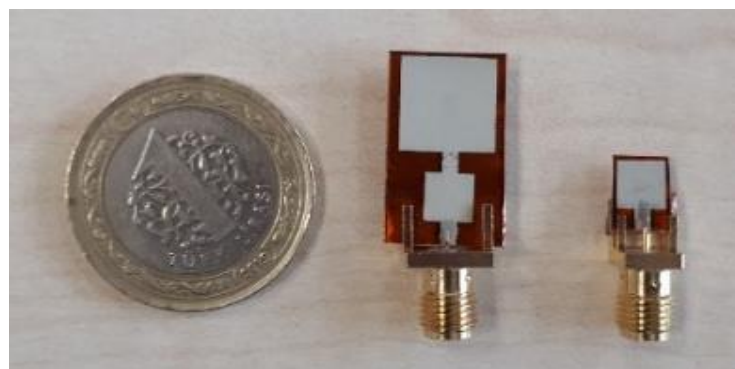
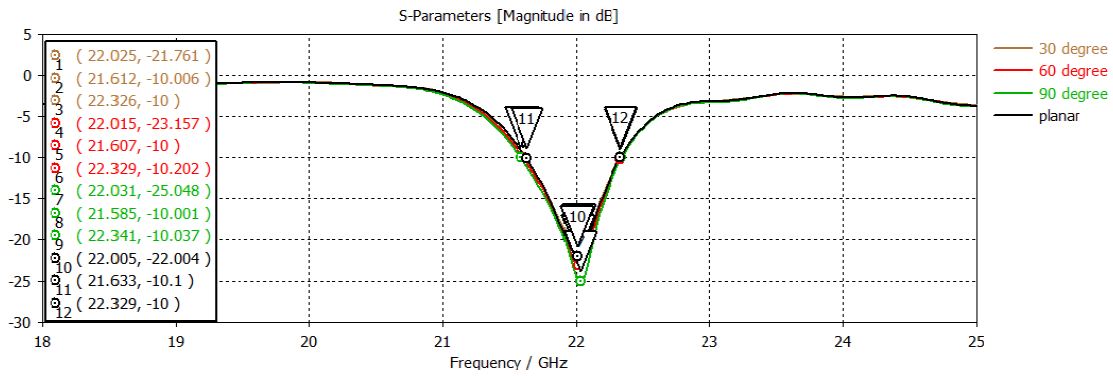
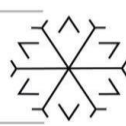
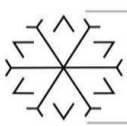


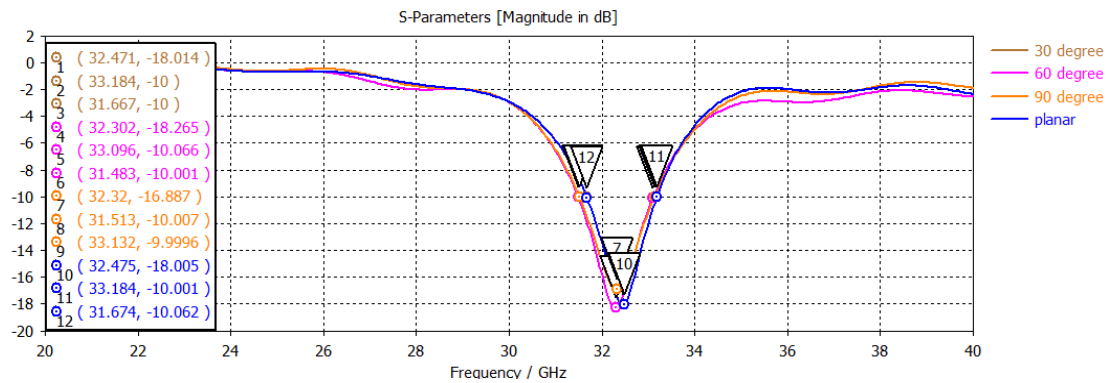
Figure 3: Picture of the fabricated planar antennas at 22 GHz and 32 GHz.

3. Comparison of Simulation and Measurement Result

The reflection coefficients of the antennas with the bended substrates are shown in Figure 4. The simulation and measurement results are shown Figure 5. The resonance frequency and bandwidth of the antennas obtained in simulation and measurement are presented in Table 1. It can be realized that the bandwidth is not significantly affected and the resonance frequency is slightly affected.

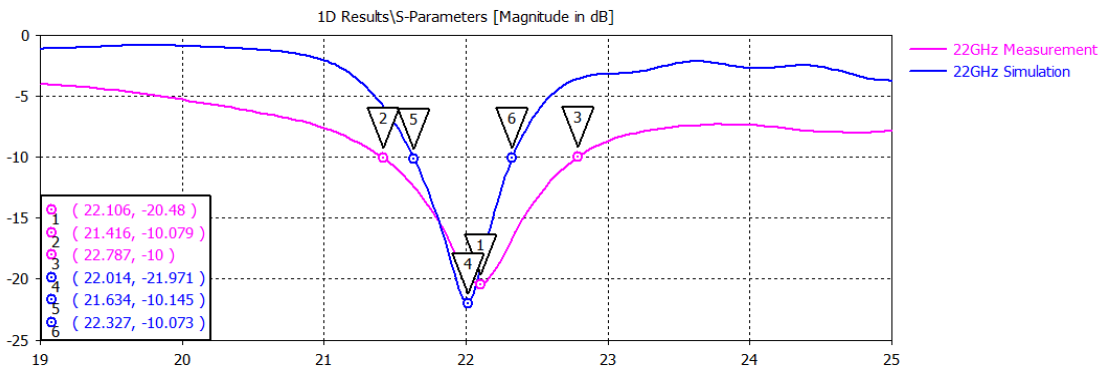


a)

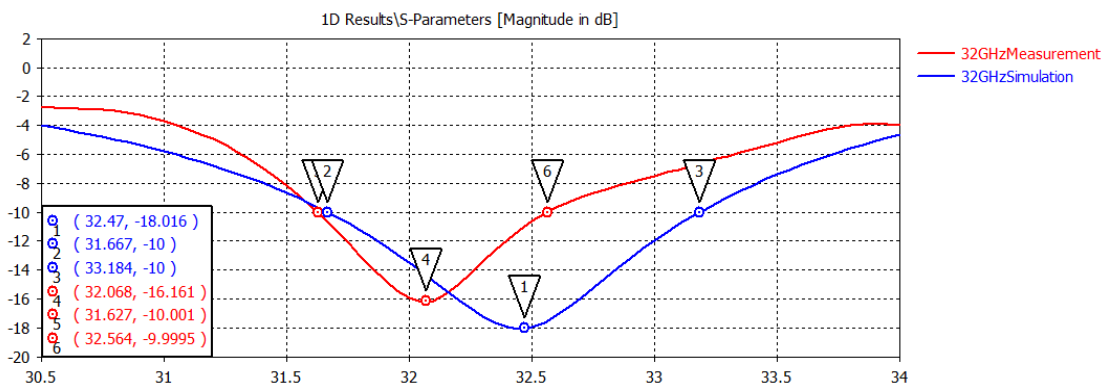


b)

Figure 4: Reflection coefficients of the designed bended antennas (a) 22 GHz and (b) 32 GHz.



a)



b)

Figure 5: Reflection coefficients of the simulated and measured planar antennas (a) 22 GHz and (b) 32 GHz.

**Table 1:** Comparison of Simulation and Measurement Result for 22 GHz and 32 GHz Antennas

	Antenna Geometry	22 GHz		32 GHz	
		Resonance Frequency (GHz)	Bandwidth (MHz)	Resonance Frequency (GHz)	Bandwidth (MHz)
Simulated	Planar	22.014	696	32.470	1517
	30 degree	22.025	729	32.471	1514
	60 degree	22.015	709	32.302	1621
	90 degree	22.031	757	32.32	1619
Fabricated	Planar	22.106	1388	32.068	930

4. Conclusion

In this study, two different flexible silver microstrip patch antenna are fabricated. One of the antennas is operated at 22 GHz SHF band allocated for mobile applications, the other is operated at 32 GHz EHF band for 5G application. The main design consideration is to provide an antenna geometry where a reconfigurable antenna can be obtained by following the same design and combining them by using the switches. When the geometry is analyzed carefully it can be seen that the 32 GHz antenna is used as microstrip feed part of the 22 GHz antenna and the design looks very similar in this manner. The main motivation of this paper is to introduce the idea of this type of reconfigurable antennas and to test them in terms of bending due to the fact that 5G technologies will require to have flexible antennas. It can easily be seen that this reconfigurable and bendable antenna design is really promising for future technologies. An appropriate microswitch design can be used to provide the switching between the two antennas and a dual band operating antenna can be obtained easily. This type of standard design opens the gate for possibility of computerized multi-band antenna operations by utilizing machine learning techniques. Future direction of this study will be towards this direction.

References

- BAE, J., CHOI, Y. S., KIM, J. S. & CHUNG, M. Y. Architecture and performance evaluation of MmWave based 5G mobile communication system. 2014 International Conference on Information and Communication Technology Convergence (ICTC), 2014. IEEE, 847-851.
- KHALEEL, H. R., AL-RIZZO, H. M., ABBOSH, A. I. & KISHK, A. 2013. Design, fabrication, and testing of flexible antennas. *Advancement in Microstrip Antennas with Recent Applications*, 363-383.
- XIAO, G. G., ZHANG, Z., LANG, S. & TAO, Y. Screen printing RF antennas. 2016 17th International Symposium on Antenna Technology and Applied Electromagnetics (ANTEM), 2016. IEEE, 1-2.
- YU, Z., YU, J., RAN, X. & ZHU, C. 2017. A novel Koch and Sierpinski combined fractal antenna for 2G/3G/4G/5G/WLAN/navigation applications. *Microwave and Optical Technology Letters*, 59, 2147-2155.

Resource Allocation in Non-Orthogonal Multiple Access

Caner KÜÇÜKYILMAZ ¹[0000-0002-0424-389X] and Gökçe HACIOĞLU ²[0000-0002-8478-4476]

¹ canerkyyy@gmail.com , Karadeniz Technical University

² gokcehacioglu@ktu.edu.tr , Karadeniz Technical University

Abstract

In the Non-Orthogonal Multiple Access (NOMA) system, Resource Allocation (RA) is analyzed under two headings: User Pairing (UP) and Power Allocation (PA). Resource allocation is a combination of UP and PA. With UP, the users in the cell are divided into more than one group and NOMA is applied separately for each group. In this study, resource allocation has been made in the power domain for pairs, each of which has two users. This study is based on the fact that the data rate that the users will obtain is higher than the data rate that they will obtain in the traditional Orthogonal Multiple Access (OMA) method. Within the scope of the study, it is aimed to group the users with an optimal match and to increase the total data rate of the system. In addition, NOMA power allocation is made by Particle Swarm Optimization (PSO) algorithm, which is one of the heuristic optimization algorithms. The performance of PSO used power domain NOMA method is compared with the performance of the classical OMA method. According to simulation results; the proposed PSO power domain NOMA method has higher data rate for each of two users in groups.

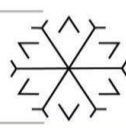
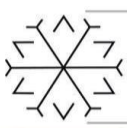
Keywords. Non-Orthogonal Multiple Access, User Pairing, Power Allocation, Resource Allocation, Particle Swarm Optimization

1. Introduction

In the modern world; Internet usage for education, shopping, social platform usage and similar purposes has been increasing rapidly. In addition, the need for more efficient sharing of bandwidth with the Internet of Things (IoT) and 5G system arises. With the increase in the number of devices and users, it is obvious that there will be a great increase in demand of resources. It is not possible to resolve the increase in resource demand with currently used multiple access methods. In addition, it is known that existing multiple access methods cannot meet other requirements of 5G system such as dense system capacity, high data rates, low latency, high reliability and accessibility, low device cost and energy efficient networks. Advanced technologies are required to meet these needs. Some potential candidates such as Multiple-Input Multiple-Output (MIMO) systems, Millimeter Wave Communication, Ultra-Dense Networking, and Non-Orthogonal Multiple Access (NOMA) may meet these requirements. NOMA stands out as the most potential candidate among these candidates with its spectral efficiency, low latency and allowing more connections.

While only one user can be assigned to a resource in traditional Orthogonal Multiple Access (OMA) methods, more users can be assigned to the same resource with Non-Orthogonal Multiple Access (NOMA) methods. Spectral efficiency increases as the resource is allocated to more users. In addition, the total data rate of the system is increased in this way. In traditional Orthogonal Multiple Access methods, the user may have to wait for a long time to access a resource. However, in the Non-Orthogonal Multiple Access method, two or more users are assigned to each resource block, reducing the time the user has to wait to access the resource (*Dai et al., 2015*).

Key advantages of Non-Orthogonal Multiple Access (*Maraqa et al., 2020*);



- High band efficiency (band efficiency increases as multiple users use the same time and frequency resource).
- User fairness: In traditional multiple access methods, the user with better channel conditions is more advantageous. In Noma, higher power and fairness are given to the user with difficult channel conditions.
- Allows high connectivity (especially with the internet of things, IoT being included in 5G, billions of smart devices must be connected. Noma allows this by placing more users on the resource).
- Compatibility (NOMA can be easily applied to existing multiple access methods).
- Low latency (latency is reduced because users are simultaneously served in the same time slot instead of a dedicated time slot).

NOMA can be basically studied under four headings. These are; Power Domain NOMA (PD-NOMA), Time Domain NOMA (TD-NOMA), Code Domain NOMA (CD-NOMA) and Frequency Domain NOMA (FD-NOMA) (*Dai et al., 2018; Sari et al., 2018; Sari et al., 2000*). The PD-NOMA was first introduced to increase the spectral efficiency of wireless networks by allowing multiple users to share both time and frequency resources simultaneously. The main idea in the NOMA method is that users' signals are transmitted at the same time and in the same frequency region with different power coefficients. In the transmitter, the signals of the users are transmitted by Superposition Coding (SC) method by superimposing different powers. SC is a technique of transmitting information from a single source to several receivers simultaneously. In other words, it allows the transmitter to transmit information of multiple users at the same time. In SC, the transmitter transmits by superimposing the signals of all users by multiplying each user's signal by the power factor determined for that user. In the receiver part, the signals are separated from each other by applying Successive Interference Cancellation (SIC) method (*Islam et al., 2016*). The SIC method is applied to eliminate the deliberately created interference with the SC method. The basic idea here is to decode the signals of the users sequentially. In order to perform the decoding process, the power coefficients allocated to the users must be known. When applying SIC, the user with the strongest channel decodes the signal of the user with the weakest channel, then subtracts that signal from the total signal. It decodes the signals of all users in order, from the weakest user to the strongest, until only its own signal remains. In this way, all interference in the signal is eliminated (*Islam et al., 2016*).

In downlink communication, NOMA method has approximately 30% more spectral efficiency than traditional OMA methods (*Benjebbour et al., 2013*). Because of the computational complexity caused by the interference of signals, the extra system load required for channel feedback coordination and error propagation, it is not possible to apply the NOMA method to all users in a common way. For this reason, the idea of applying the NOMA method separately for each user group was put forward by dividing the users in the system into groups (*Islam et al., 2018*). The division of users into groups is called User Pairing (UP), while the distribution of available power among users is called Power Allocation (PA). In the NOMA method, the combination of UP and PA is called Resource Allocation (RA). In RA, PA phase is usually treated as an independent problem, either after the UP phase or as a sub-step within the UP algorithm (*Kara et al., 2017*).

2. System Model

2.1. User Pairing

UP should ideally create minimal computational complexity while maintaining user fairness. It should also be aligned with the PA strategy to ensure high efficiency. There are a number of UP algorithms, depending on the desired performance, deployment environment, and application complexity (*Islam et al., 2018*). Some of these methods are Random Pairing, Extensive Search, Dynamic User Clustering, Matching Theory, and Optimal User Pairing (*Dai et al., 2018; Islam et al., 2018; Zhang et al., 2016; Parida and Das, 2014; Ali et al., 2016; Zhu et al., 2018*).

In the Optimal User Pairing method (*Zhu et al., 2018*), which is also used in this study, the difference in the channel gains of the users is taken into account. In this method, it is shown that the system will reach the total maximum data rate by matching the users with the largest channel gain differences. In the study, in which the channel gains of the users are considered as $g_1 \geq g_2 \geq g_3 \geq g_4$, a system with four users was initially considered. Here users are divided into two groups for all possible combinations. When these combinations are examined, it has been shown that the maximum system gain occurs when users are matched as $\{U_1, U_4\}$ and $\{U_2, U_3\}$. Then, it is shown for the case of $2k$ users in the system. This method is applicable when users are grouped in pairs. Not used if there are 2 or more users in a group.

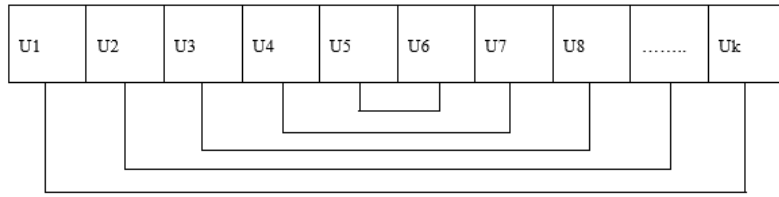


Figure 1. User pairing method.

2.2. Power Allocation

In the NOMA method, unlike the OMA method, PA has a more critical role as users are multiplexed in the power field. Generally, the PA for the NOMA system is determined by the users' channel conditions, Quality of Service (QoS) requirements, Channel State Information (CSI), total power constraint, and system target. However, incorrect use of the PA method leads to unfairness and an incorrect ratio distribution among users. It may also cause the SIC process to fail, resulting in system interruption. In addition to these criteria, different PA performance criteria can be mentioned. For example, criteria such as the number of users accepted for a resource block, total rate, user fairness, probability of outages, and total power consumption can be shown (Islam et al., 2018). There are different PA methods proposed for the NOMA system in the literature. These proposed methods are generally examined in two groups as Fixed Power Allocation and Dynamic Power Allocation.

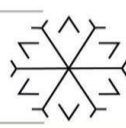
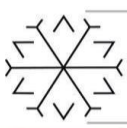
2.3. Particle Swarm Optimization

Optimization is the process of obtaining the optimal solution by setting certain constraints for the targeted purposes. The desire to reach the best result is always at the forefront in optimization. The constraints and assumptions determined for each optimization problem are variable and shaped according to the applied method. The problem to be solved is mathematically formulated under various constraints to maximize or minimize it. Optimization algorithms can be examined under two headings as Exact Methods and Approximate Methods (Yang, 2020). Exact Methods are algorithms that enable the solution of the problem to reach the global optimum result precisely. Linear Programming and Dynamic Programming algorithms are examples of Exact Methods. Approximate Methods, on the other hand, are algorithms where the solution of the problem does not fully reach the global optimum answer, but reaches a value as close as possible to the optimum answer. Despite this, the reason why it is preferred is that it can produce fast solutions. Approximate methods are preferred for problems involving many operations and complex solutions. Approximate methods are examined under two headings as Heuristic and Metaheuristic Algorithms. Heuristic algorithms focus on the problem and provide a solution for a single problem. Metaheuristic algorithms are generally used to generate solutions to problems.

The Particle Swarm Optimization (PSO) algorithm developed by Kennedy et al. is a Heuristic algorithm inspired by the behavior of fish and birds moving in flocks. The main idea in the creation of PSO is based on herd intelligence in animals. When animals that behave like a herd are examined, it has been seen that the behaviors they show randomly in situations such as feeding and protection help them to reach their goals more easily. PSO is based on approximating the position of individuals in the herd to the best positioned individual in the herd. Each particle uses its previous experience to adjust its position towards the best position in the swarm. Here, each individual looking for a solution is called a particle, and the collection of particles is called a swarm. During the solution search, the best state of a particle when it is closest to the solution is called the personal best, and the current state of the particle that is closest to the solution in the whole swarm and during the entire search is called the globalbest. The suitability function is used to understand the proximity of an individual to the solution. The main purpose of the suitability function is to determine how close it is to the true solution. Personalbest and globalbest values are updated according to the suitability function. The update continues until the desired result is achieved (Özsağlam and Çunkaş, 2008).

The PSO algorithm can be expressed as follows (Özsağlam and Çunkaş, 2008):

- A start swarm is generated with randomly generated starting positions and velocities.
- The suitability values of all particles in the swarm are calculated.
- The person best (pbest) from the current generation is found for each particle. The number of the best in the swarm is equal to the number of particles.



- The global best (*gbest*) is selected among the local bests in the current generation.
- Positions and velocities are refreshed as follows.

$$V_{i+1} = V_i + C1 \times rand1 * (pbest - xx) + C2 \times rand2 \times (gbest - xx) \quad (1)$$

In (1); *xx* is the particle value, *v* is the rate of change of the particle, *c* is the fixed value for scaling, and *rand* is the randomly generated value.

- Steps 2,3,4,5 are repeated until the stopping criterion is met.

3. Simulation Method and Results

NOMA Resource Allocation system is shown Figure 2 and simulated using MATLAB with parameters given in Table 1.

In MATLAB, the channel coefficient is created for each user, taking into account the distance of randomly generated users in the coordinate plane from the base station. Then, the users ranked according to these channel coefficients are divided into pairs according to the Optimal User Pairing algorithm. The NOMA method is applied separately for each group created. Here, the power coefficients allocated to the users and accordingly the data rates are found using the PSO algorithm. The algorithm works according to the criteria that the speed of each user is at least as much as the data rate they will obtain in OMA and that the sum of the power coefficients of the users is equal to one.

The simulations were made 30 times for each transmit power because of the users randomly located in each run of the simulations. The channel coefficient is obtained by the following equation.

$$h_i = x_i d_i^{-\beta} \quad (2)$$

In (2); *h_i* denotes channel coefficient, *d_i* denotes distance to base station of user *i*. The path loss exponent is denoted by *β* and it is equal to two. The parameter *x_i* is a complex random variable and its' amplitude has Rayleigh distribution. The results were obtained by taking average of the values that obtained 30 times.

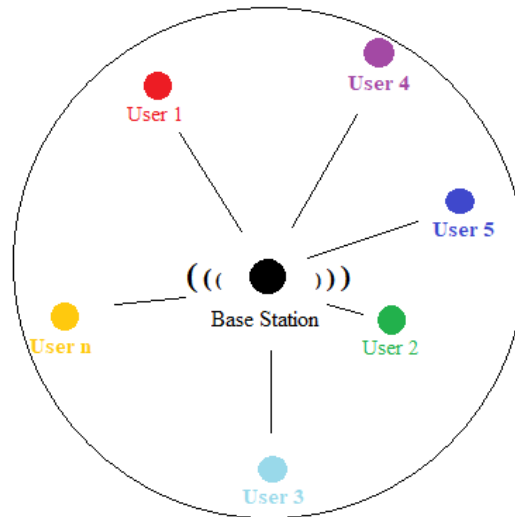


Figure 2. Randomly generated set of users' representations.

**Table 1.** Parameters used for MATLAB simulation.

Parameters	Value
Number of users	32
Macro base station coverage	300 m
Minimum distance of the user from the macro base station	10 m
Macro base station power in dbm	20 dbm
Bandwidth	1e6
Noise power density dbm/Hz	-174
Path Loss Exponent	2
PSO penalty coefficient	1e15
PSO particle count	25
PSO iteration number	150

The equations used to calculate the OMA and NOMA data rates of the users in the system are given below:

$$RNOMA = w \log_2 \left(1 + \frac{B_i P |h_i|^2}{P |h_i|^2 \sum_{k=i+1}^N + \sigma^2} \right) \quad (3)$$

In (3); w is the bandwidth, B_i is the power coefficient user i , P is the total power of Base Station, h_i is the channel gain, σ^2 is the variance of Additive White Gaussian Noise.

$$ROMA = \frac{w}{ks} \log_2 \left(1 + \frac{|h_i|^2 P}{\sigma^2 ks} \right) \quad (4)$$

In (4); w is the bandwidth, ks is the number of users, h is the channel gain, P is the total power of Base Station, σ^2 is the variance of Additive White Gaussian Noise.

Different performance metrics such as efficiency (accessible data rate), energy efficiency and fairness index are used to evaluate the performance of each wireless communication system. Fairness was taken into account in the proposed NOMA system. Fairness is used as the objective function in the PSO algorithm shown below.

$$F = \frac{(\sum_{i=1}^{ks} RNOMA_i)^2}{ks \sum_{i=1}^{ks} RNOMA_i^2} \quad (5)$$

In (5); $RNOMA_i$ denotes the data rate of user i for proposed Noma system. The proposed NOMA system aims to allocate as equal data rate as possible to paired users.

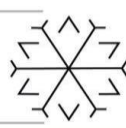
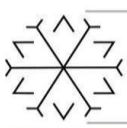


Figure 3. shows the data rates of paired users as an example. According to results the proposed system provides more data rate for each of two users in the pair for most of the transmit power. Because users' locations are randomly selected, the proposed NOMA system may have lower data rates for a user at some power levels. On the other hand, the total data rate of the proposed system is higher than the OMA system for each power level.

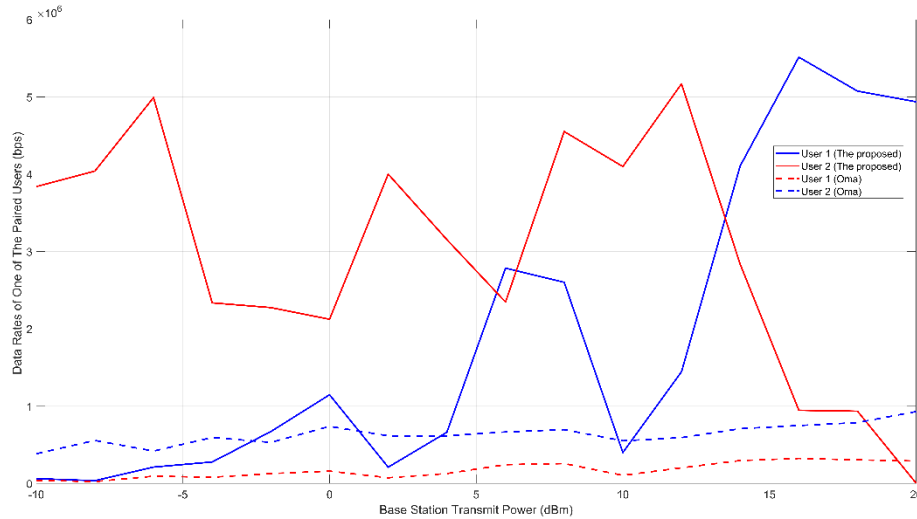


Figure 3. Data rates of the users in a pair

Figure 4. shows the total data rate of 32 users that randomly located in area has 300m radius. According to the results, the proposed PSO-NOMA system can have six times the data rate of the OMA system. On the other hand, the data rate of the NOMA system decreases as the transmit power rises above 12 dBm.

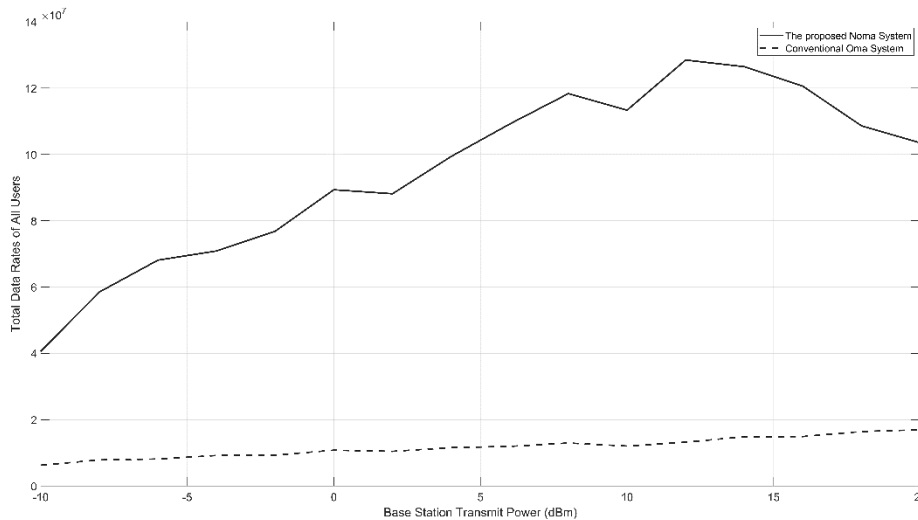


Figure 4. Total data rates of $k_s = 32$ users

4. Conclusion

For a PD-NOMA system, resources were allocated to users using the PSO algorithm, with the performance criterion being fairness among users. Users were randomly placed in an area with a radius of 300m. Because random locations were involved in each run of the simulations, the program was run 30 times for each transmission power. Thus, it is aimed to reach more realistic results. PD-NOMA was implemented between users paired under different groups. As a result of this study, it has been shown that PD-NOMA can have a data rate of 6 times higher than the traditional OMA system. It should be noted here that as the transmit power of the Base Station increases, the data rate gain of the NOMA system is affected due to the increase in interference. The use of OMA in some



pairs and the use of NOMA in some pairs may be considered in future studies. Different User Pairing algorithms can be used as the band needs to be used more efficiently to increase spectral efficiency.

References

- Ali, M.S., Tabassum, H. and Hossain, E., 2016. Dynamic user clustering and power allocation for uplink and downlink non-orthogonal multiple access (NOMA) systems. *IEEE access*, 4, pp.6325-6343.
- Benjebbour, A., Saito, Y., Kishiyama, Y., Li, A., Harada, A. and Nakamura, T., 2013, November. Concept and practical considerations of non-orthogonal multiple access (NOMA) for future radio access. In 2013 International Symposium on Intelligent Signal Processing and Communication Systems (pp. 770-774). IEEE.
- Dai, L., Wang, B., Ding, Z., Wang, Z., Chen, S. and Hanzo, L., 2018. A survey of non-orthogonal multiple access for 5G. *IEEE communications surveys & tutorials*, 20(3), pp.2294-2323.
- Dai, L., Wang, B., Yuan, Y., Han, S., Chih-Lin, I. and Wang, Z., 2015. Non-orthogonal multiple access for 5G: solutions, challenges, opportunities, and future research trends. *IEEE Communications Magazine*, 53(9), pp.74-81.
- Islam, S.R., Avazov, N., Dobre, O.A. and Kwak, K.S., 2016. Power-domain non-orthogonal multiple access (NOMA) in 5G systems: Potentials and challenges. *IEEE Communications Surveys & Tutorials*, 19(2), pp.721-742.
- Islam, S.R., Zeng, M., Dobre, O.A. and Kwak, K.S., 2018. Resource allocation for downlink NOMA systems: Key techniques and open issues. *IEEE Wireless Communications*, 25(2), pp.40-47.
- Kara, F., Gemici, Ö.F., Hökelek, İ. and Çirpan, H.A., 2017, May. Optimal power allocation for DL NOMA systems. In 2017 25th Signal Processing and Communications Applications Conference (SIU) (pp. 1-4). IEEE.
- Maraqa, O., Rajasekaran, A.S., Al-Ahmadi, S., Yanikomeroğlu, H. and Sait, S.M., 2020. A survey of rate-optimal power domain NOMA with enabling technologies of future wireless networks. *IEEE Communications Surveys & Tutorials*, 22(4), pp.2192-2235.
- ÖZSAĞLAM, M.Y. and ÇUNKAŞ, M., 2008. Optimizasyon problemlerinin çözümü için parçacık sürü optimizasyonu algoritması. *Politeknik Dergisi*, 11(4), pp.299-305.
- Sari, H., Maatouk, A., Caliskan, E., Assaad, M., Koca, M. and Gui, G., 2018, April. On the foundation of NOMA and its application to 5G cellular networks. In 2018 IEEE Wireless Communications and Networking Conference (WCNC) (pp. 1-6). IEEE.
- Sari, H., Vanhaverbeke, F. and Moeneclaey, M., 2000. Multiple access using two sets of orthogonal signal waveforms. *IEEE Communications Letters*, 4(1), pp.4-6.
- Parida, P. and Das, S.S., 2014, December. Power allocation in OFDM based NOMA systems: A DC programming approach. In 2014 IEEE Globecom Workshops (GC Wkshps) (pp. 1026-1031). IEEE.
- Yang, X.S. ed., 2020. *Nature-Inspired Computation and Swarm Intelligence: Algorithms, Theory and Applications*.
- Zhang, H., Zhang, D.K., Meng, W.X. and Li, C., 2016, May. User pairing algorithm with SIC in non-orthogonal multiple access system. In 2016 IEEE International Conference on Communications (ICC) (pp. 1-6). IEEE.
- Zhu, L., Zhang, J., Xiao, Z., Cao, X. and Wu, D.O., 2018. Optimal user pairing for downlink non-orthogonal multiple access (NOMA). *IEEE Wireless Communications Letters*, 8(2), pp.328-331.

A Decision Based Fusion Method for Brain Lesion Images

Elif Eda Takgil ¹[0000-0003-2102-8398] and Nur Hüseyin Kaplan ²[0000-0002-4740-3259]

¹ elif.takgil46@erzurum.edu.tr, Erzurum Technical University

² huseyin.kaplan@erzurum.edu.tr, Erzurum Technical University

Abstract

Image fusion has many application areas such as medical imaging, image processing, machine learning, and artificial intelligence. The process of image fusion is obtained new and improved images by combining images obtained from different sensors or images in different phases produce by the same sensor in a way that complements each other's missing aspects.

Medical image fusion is used in the diagnosis and evaluation of medical problems with the help of images created by medical imaging methods. Image fusion aims to applicability and improves imaging quality. Multiple medical image fusion algorithms and devices have shown remarkable success in improving diagnostic accuracy based on medical images.

This study is based on the fusion of brain lesion images obtained with an fMRI (Functional Magnetic Resonance Imaging) device and the evaluation of fusion results. For the detection of brain lesions, different phases from the fMRI device are fused with the Guided Filter Based Multifocal Image Fusion (GFDF) and Cross Bilateral Filter (CBF) Image Fusion methods via Focal Region Detection. These fused images are fed to a Convolutional Neural Network (CNN), which is designed and trained to assess the image quality. These input images are split into non-overlapping blocks and the method that gave the best result for each block is determined with the CNN model and a decision map was drawn. According to the decision map, an improved image is obtained, combining the best parts of the two methods that are fused. At the same time, all these methods are tested visually and quantitatively.

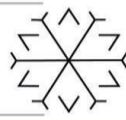
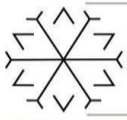
In this study, many of the classical and modern fusion methods are examined in detail. Fusion results of classical methods such as Intensity-Hue-Saturation Transform (IHS) and Principal Component Analysis (PCA) are compared with modern fusion methods CBF and GFDF (Kumar, 2015; Qiu et al., 2019). In this comparison, classical methods obtain lower achievement than modern methods. Therefore, CBF and GFDF are preferred as fusion methods in the study.

The neural network trained to evaluate the quality of the fusions consists of three layers. These are ResNet, Spatial pyramid pooling (SPP), and Fully-connected layer. The purpose of ResNet is to learn image properties from the input image to evaluate image quality. The SPP layer takes input images of any arbitrary size of the network architecture. Finally, a fully connected layer classifies the input image according to the learned information. It delivers outputs from the SPP layer to different levels of image quality. The dataset consisting of 982 images of the network is used for training and an accepted and validated data set for image quality analysis (Sheikh & Bovik, 2006). The network is trained with overlapping 100×100 -pixel sub-images extracted from the large images of the training dataset. For each large image, overlapping 100×100 -pixel subimages are sampled in 14 equal steps. Then obtained fusion images are given to this trained network with CBF and GFDF methods. The trained network segmented the input images and determined the method that give the best results in each part, and presented the improved image to us (Li et al., 2017).

As a result, more favorable images are obtained for expert interpretation from the fused images, and it is observed that using a decision map, which combines better parts of different fusion methods, has better quality than the input fusion images.

Keywords. CBF, GFDF, Image Fusion, Image Processing, CNN

References



- Kumar, B. S. (2015). Image fusion based on pixel significance using cross bilateral filter. *Signal, image and video processing*, 9(5), 1193-1204.
- Li, Y., Ye, X., & Li, Y. (2017). Image quality assessment using deep convolutional networks. *AIP Advances*, 7(12), 125324.
- Qiu, X., Li, M., Zhang, L., & Yuan, X. (2019). Guided filter-based multi-focus image fusion through focus region detection. *Signal Processing: Image Communication*, 72, 35-46.
- Sheikh, H. R., & Bovik, A. C. (2006). Image information and visual quality. *IEEE transactions on image processing*, 15(2), 430-444.

Design and Comparison of MPPT Under Shading Conditions With Different Algorithms for Photovoltaic Systems

Yasin Sezer¹ and M. Cengiz Taplamacıoğlu²

¹yasin.sezer@tubitak.gov.tr,

1 Department of Electrical and Electronics Engineering, Gazi University, Eti Mh. Yükseliş Sk. No: 5

Kat: 3 06570 Maltepe/ANKARA

²taplam@gazi.edu.tr,

2 Department of Electrical and Electronics Engineering, Gazi University, Eti Mh. Yükseliş Sk. No: 5

Kat: 3 06570 Maltepe/ANKARA

Abstract

The need for energy is increasing rapidly, especially last decade. Recently, the energy demand for humanity is mostly provided by fossil or nuclear sources, which are extremely dangerous for the environment, and also fossil sources are limited resources. As a result of this usage, the demand for clean and sustainable energy sources is increasing every day. Solar power energy production comes foremost among other renewable sources. Because of having some problems about efficient conversion of energy from solar energy to electrical energy and consistency of solar radiation, the usage of solar power technology needs to be researched and enhanced every day.

The change of solar irradiation and temperature have significant effects on solar panel's efficiency. To maximize efficiency, usage of maximum power point tracker is became a necessity. In the present study, a Photovoltaic (PV) system with Maximum Power Point Tracking using boost converter topology has been implemented and simulated in MATLAB / Simulink programme. Comparison of different MPPT algorithms such as perturb and observe (P&O), incremental conductance (INC), and particle swarm optimization (PSO) methods have been examined at different solar irradiation and for different temperatures. Important parameters, possible to be selection criteria for the PV systems, such as efficiency, response time and power oscillations have been examined and compared to each other is given in detail. Obtained results show that the PSO method has the highest efficiency, but INC and P&O methods adapt faster to the changing environmental conditions when compared to the PSO method.

Keywords. Maximum Power Point Tracking (MPPT), MPPT Algorithms, Photovoltaic (PV) Systems, PV MPPT Under Shading Conditions, PV Systems with Boost Converter

1. Introduction

Increasing demand for energy production causes rise of fossil fuel utilization and as a result, the carbon emission is increasing and damaging to the environment. Under these circumstances, humankind is in search of clean and sustainable energy sources for the bright future. As a consequence of that, renewable energy sources such as solar energy, wind, biomass, hydropower, ocean waves, tides, geothermal heat become more popular each passing day. Especially solar energy is one of the most important renewable energy source since it is clean, inexhaustible and abundant in most parts of the world. Also, thanks to the use of solar energy, the dependence on foreign countries can be eliminated.

The efficiency of photovoltaic arrays are highly dependent on solar irradiation input level and temperature. Direct usage of PV arrays without MPPT is an inefficient method since I-V and P-V characteristic curves of PV arrays are not linear and specify a unique maximum power point. To benefit from photovoltaic arrays with maximum efficiency, a maximum power point tracker is required (Attou, Massoum and Saidi, 2014).

MPPT can be defined as a system consisting of two basic components such as DC-DC converter and its controller. There are several methods and different algorithms such as artificial neural network (ANN), particle swarm optimization (PSO), genetic algorithm (GA), incremental conductance method (INC), perturbation and observation method (PO) and Cuckoo Search (CS) to control the switching element of the

converter (Baba, Liu and Chen, 2020). These techniques are different from each other with respect to complexity, cost, efficiency, response and robustness (Yahyaoui, 2018).

In this study, a maximum power point tracker using boost converter is proposed. Different control algorithms such as Perturb And Observation method (PO), incremental conductance (INC) and Particle Swarm Optimization (PSO) have been applied in the control block as the duty cycle of the DC/DC converter. 4x4x200 Watt PV array is used to obtain 3.2 kW active solar power, a boost converter is used for maximum power point tracking and a resistive load is modelled and simulated in MATLAB / Simulink. Algorithms on MPPT are compared to each other at different irradiance and temperature in terms of efficiency, power oscillations and response time.

2. Modelling of a Solar Cell Structure

The solar cell is a p-n semiconductor junction and fundamental element of a PV array. The equivalent circuit model of the solar cell is given in Figure 1.

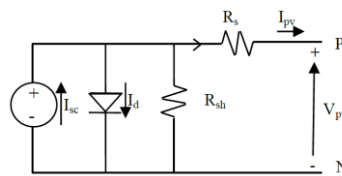


Figure 1: Equivalent circuit model of the solar cells (Attou, Massoum and Saidi, 2014)

The I-V characteristic of a solar array is given in Equation (1) :

$$I_{pv} = I_{sc} - I_o \left(\exp\left(\frac{q(V + R_s I)}{nKT}\right) - 1 \right) - \frac{V + R_s I}{R_{SH}} \quad (1)$$

The parameters of Equation (1) are defined as (Attou, Massoum and Saidi, 2014) :

- I_{pv} is output current of cell and V is the voltage across the cell terminals.
- R_s is the series resistance and R_{SH} is the shunt resistance of the photovoltaic panel.
- I_{sc} is the light-generated current and I_o is the reverse saturation current.
- n is the dimensionless factor or known as the ideality factor.
- K is the Boltzmann constant, T is the temperature in Kelvin and q is the electronic charge.

From Equation (1) it can be clearly understood that output characteristics of solar cells are not linear and highly dependent on radiation intensity, output load and temperature. Equation (1) is used for simulations to obtain I-V and P-V curves of solar cells. A typical I-V and P-V curve of a solar cell is given in Figure 2.

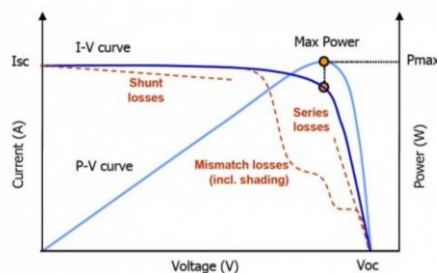
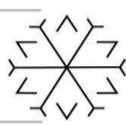
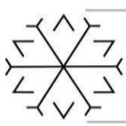


Figure 2: Typical I-V and P-V Curves of a solar cell (Hocaoglu et al., 2018)

3. Design of MPPT with Boost Converter and Overview of Algorithms

3.1. Circuit Schematic and Design Parameters

The circuit schema of MPPT with boost converter and Algorithm block is given in Figure 3. PV array panel parameters are also given in Table 1. In this area of study, to achieve 3.2 kW nominal panel output power, 4 series and 4 parallel connection is implemented. Accepted nominal panel output power is 1000 W / m² as the irradiance input and 25° C degree as the temperature of the PV array. A boost converter topology and algorithms for MPPT is used for maximum power point tracking. The output of the



algorithm block is implemented as duty cycle of the PWM signal applied to the gate of the switching element of the boost converter.

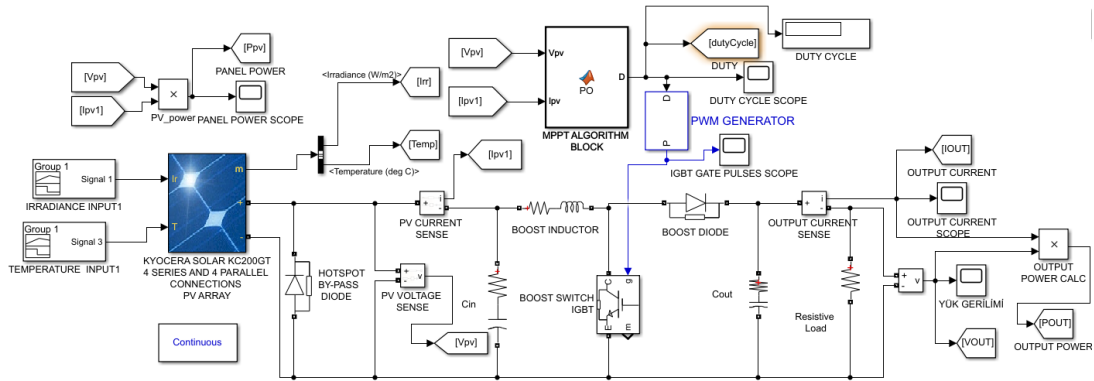


Figure 3: Circuit Schematic of MPPT with Boost Converter in MATLAB / Simulink

Table 1: PV Panel parameters used in Simulation (HIGH EFFICIENCY MULTI-CRYSTAL PHOTOVOLTAIC MODULE, 2007)

PANEL PARAMETERS KYOCERA SOLAR KC200GT			
Maximum Power of One Photovoltaic Module (Watt)	200.143	Voltage at Maximum Power V_{mp} (Volt)	26.3
Open Circuit Voltage of One Photovoltaic Module V_{oc} (Volt)	32.9	Current at Maximum Power I_{mp} (Ampere)	7.61
Short Circuit Current of One Photovoltaic Module I_{sc} (Ampere)	8.21		

3.2. Basic Principles of MPPT Algorithms

There are several types of MPPT algorithms and classifications according to tracking techniques (Baba, Liu and Chen, 2020). The main concern is evaluating whether the algorithm is an optimal one or not (Motahhir, El Ghzizal, Sebti and Derouich, 2018). MPPT algorithms can be classified based on tracking techniques (Baba, Liu and Chen, 2020). Classification of algorithms used in this work is given in Table 2. The detailed working principle flowchart of perturb and observation method, incremental conductance method and particle swarm optimization is given in Figure 4, Figure 5 and Figure 6 respectively.

Table 2: Classification of MPPT algorithms based on tracking techniques (Baba, Liu and Chen, 2020)

CLASSIFICATION OF MPPT ALGORITHMS BASED ON TRACKING TECHNIQUES		
Tracking Techniques with Mathematical Calculations	Tracking Techniques with Intelligent Prediction	Tracking Techniques with Trial and Error
Incremental Conductance Method	Particle Swarm Optimization	Perturb And Observation Method

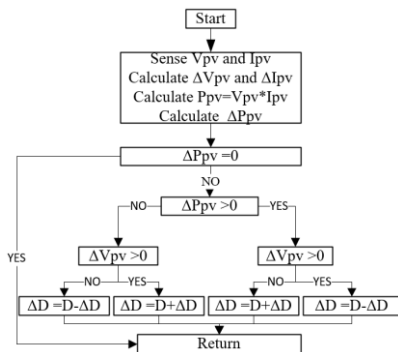


Figure 4: Flowchart of Perturb and Observe Method

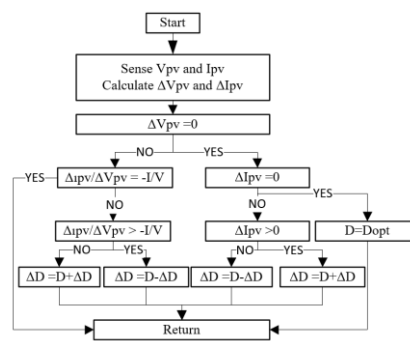


Figure 5: Flowchart of Incremental Conductance Method

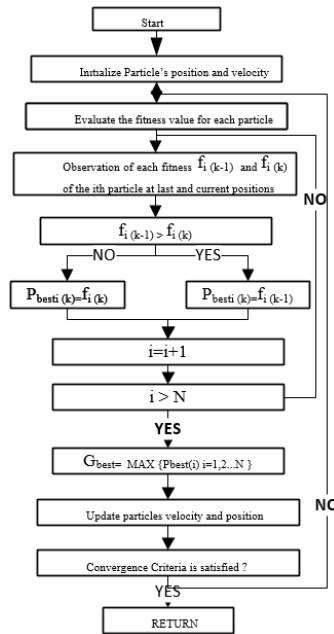


Figure 6: Flowchart of Particle Swarm Optimization Method

4. Simulation Results

Simulation results of MPPT algorithms perturb and observation method, incremental conductance method and particle swarm optimization used in this study are given in Figure 7, Figure 8 and Figure 9 respectively. Implemented irradiance and temperature inputs of PV array is given in Figure 10. Obtained circuit parameters are given in Table 3, Table 4 and Table 5.

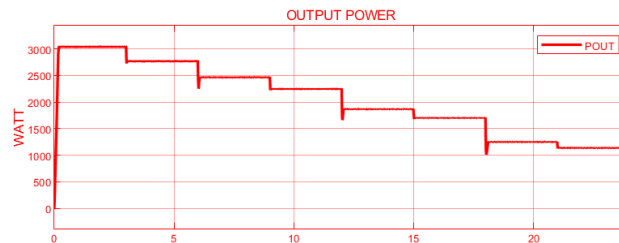


Figure 7: Output Power of MPPT with Perturb And Observation Algorithm

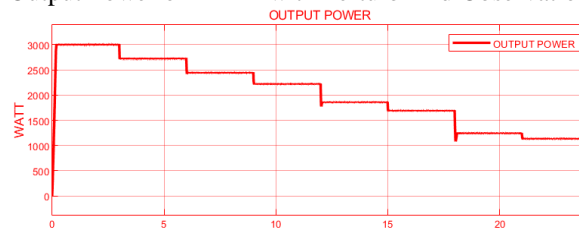


Figure 8: Output Power of MPPT with Incremental Conductance Algorithm

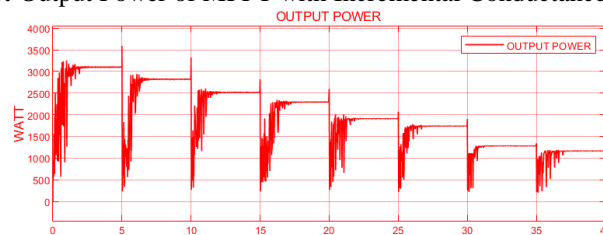


Figure 9: Output Power of MPPT with Particle Swarm Optimization

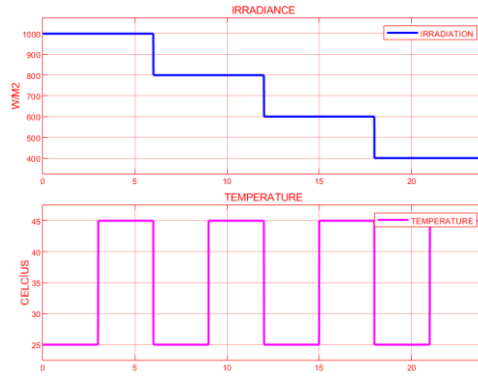
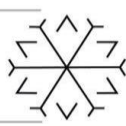


Figure 10: Applied Irradiance and Temperature input to the PV array

Table 3: Circuit Parameter Measurements with Perturb and Observation Method

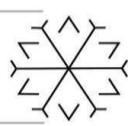
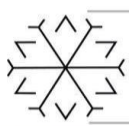
Algorithm	Irradiation (W / m2)	Temperature (Celsius)	Ppv (W)	Vpv (V)	Ipv (A)	Pout (W)	Vout (V)	Iout (A)	Efficiency %	Response Time (millisecond)
Perturb And Observation	1000	25° C	3202	105,290	30,4	3041	389,90	7,798	94,97189257	18
	1000	45° C	2924	95,74	30,5	2769	372,10	7,442	94,69904241	30
	800	25° C	2584	106,160	24,3	2464	351,10	7,022	95,35603715	70
	800	45° C	2360	97,19	24,3	2247	335,2	6,704	95,21186441	20
	600	25° C	1949	106,5	18,3	1867	305,5	6,11	95,79271421	100
	600	45° C	1774	96,57	18,4	1702	291,7	5,834	95,94137542	40
	400	25° C	1299	106,38	12,21	1249	249,9	4,998	96,1508853	120
	400	45° C	1184	96,49	12,27	1138	238,5	4,77	96,11486486	20

Table 4: Circuit Parameter Measurements with Incremental Conductance Method

Algorithm	Irradiation (W / m2)	Temperature (Celsius)	Ppv (W)	Vpv (V)	Ipv (A)	Pout (W)	Vout (V)	Iout (A)	Efficiency %	Response Time (millisecond)
Incremental Conductance	1000	25° C	3202	108,76	29,44	3003	387,5	7,75	93,78513429	18
	1000	45° C	2924	101,42	28,83	2727	369,3	7,386	93,2626539	10
	800	25° C	2584	109,77	23,54	2443	349,5	6,99	94,54334365	20
	800	45° C	2360	100,81	23,41	2221	333,2	6,664	94,11016949	10
	600	25° C	1949	108,39	17,98	1859	304,8	6,096	95,38224731	60
	600	45° C	1774	99,1	17,9	1691	290,7	5,814	95,32130778	10
	400	25° C	1299	105,18	12,35	1244	249,4	4,988	95,76597383	100
	400	45° C	1184	96,16	12,31	1134	238,1	4,762	95,77702703	25

Table 5: Circuit Parameter Measurements with Particle Swarm Optimization Method

Algorithm	Irradiation (W / m2)	Temperature (Celsius)	Ppv (W)	Vpv (V)	Ipv (A)	Pout (W)	Vout (V)	Iout (A)	Efficiency %	Response Time (millisecond)
Particle Swarm Optimization	1000	25° C	3202	105,2	30,4	3093	393,3	7,866	96,59587758	1800
	1000	45° C	2924	95,63	30,6	2818	375,3	7,506	96,374829	1500
	800	25° C	2584	105,9	24,4	2511	354,3	7,086	97,1749226	1500
	800	45° C	2360	96,29	24,5	2291	338,5	6,77	97,07627119	1725
	600	25° C	1948	106,3	18,3	1905	308,6	6,172	97,7926078	1800
	600	45° C	1778	96,9	18,4	1736	294,6	5,892	97,63779528	1600
	400	25° C	1298	106,1	12,2	1278	252,8	5,056	98,45916795	1175
	400	45° C	1184	96,23	12,3	1164	241,2	4,824	98,31081081	1850



5. Conclusions

In this study, a maximum power point tracker with boost converter is designed, and controlled by different algorithms which are perturb and observation (P&O), incremental conductance (INC) and particle swarm optimization (PSO) methods respectively. The methods are implemented under the same DC/DC converter parameters. The important circuit parameters such as panel power, panel voltage, panel current, output power, output voltage, output current, response time which is steady-state time of the output power, power oscillations in the neighborhood of steady-state output power and efficiency are obtained from MATLAB / Simulink simulation environment at varying weather conditions in terms of irradiance and temperature of PV array to observe the performance of algorithms. P&O and INC methods have the % 95,52 and %94.74 mean efficiency over the period of simulation. The efficiency of PO method is higher than INC method. INC method has the lowest efficiency among all methods but shows the fastest response and lowest power oscillations characteristics when compared to all the other methods. Therefore, INC method provides the smoothest power curve. That also means INC method adapts easier to the changing weather conditions when compared to other methods. The efficiency of intelligent prediction-based method PSO is obtained as %97,42. The mean response time of PSO is 1618.75 milliseconds. PSO shows the best efficiency performance but its response time is significantly slower than the other methods, which means adaptation to fast-changing environmental conditions may have some failures in this intelligent method. Also, its high power oscillations may cause considerable stresses on the PV array.

References

- Attou, A., Massoum, A. and Saidi, M., Mar. 2014. 'Photovoltaic Power Control Using MPPT and Boost Converter' *Balkan Journal of Electrical and Computer Engineering*, 2, no. 1, pp. 23-27.
- Baba, A.O., Liu, G. and Chen, X. (2020). Classification and Evaluation Review of Maximum Power Point Tracking Methods. *Sustainable Futures*, 2, p.100020.
- Yahyaoui, I., 2018. *Advances in renewable energies and power technologies*. 1st ed. Elsevier Science, pp.115-137.
- Hocaoglu, F., Serttas, F., Kurekci, M., Akarlan, E., Cinar, S., Dogan, R. and Yonetken, A., 2018. Comparison of experimentally obtained I-V curves of different PV modules. *2018 9th International Renewable Energy Congress (IREC)*.
- Motahhir, S., El Ghzizal, A., Sebti, S. and Derouich, A., 2018. Modeling of Photovoltaic System with Modified Incremental Conductance Algorithm for Fast Changes of Irradiance. *International Journal of Photoenergy*, 2018, pp.1-13.
- Energymatters.com.au. 2007. *HIGH EFFICIENCY MULTI-CRYSTAL PHOTOVOLTAIC MODULE*. [online] Available at: <<https://www.energymatters.com.au/images/kyocera/KC200GT.pdf>> [Accessed 27 November 2021].

A High Directivity 2.8GHz Microstrip Directional Coupler Design by using Grey Wolf Optimizer for Radio Telescope Systems

Bilge Şenel¹*^[0000-0003-3612-936X] and Fatih Ahmet Şenel²^[0000-0003-1918-7277]

¹bilgeturkel@sdu.edu.tr, Department of Electrical and Electronics Engineering, Faculty of Engineering, Süleyman Demirel University

²fatihsenel@sdu.edu.tr, Department of Computer Engineering, Faculty of Engineering, Süleyman Demirel University

* Corresponding Author

Abstract

In this study, a microstrip directional coupler is designed for solar radio monitoring systems. Solar radio monitoring is a special branch of radio astronomy that facilitates space weather forecasting and provides timely warnings about solar eruptive events that may affect human activities. 2.8 GHz solar radio flux is one of the most widely studied frequencies of solar radio activity. The solar radio flux at 2.8 GHz provides information about space, as well as some parameters of the solar wind. Because it has recently been shown that UV and X-ray flux data obtained from space are highly related to these data. Directional couplers take part in the RF block of solar radio flux monitoring systems. They are used to divide power at the desired ratio. Directional couplers could be designed different coupled line forms as coaxial lines, striplines, microstrip lines and broadside striplines. In this study we prefer microstrip coupled lines because of the advantages of printed circuit board and ease of design. The coupler schematic designed in the study comprises a coupled lines, matching lines and transmission lines with a characteristic impedance of 50Ω for SMA ports. There are five different structural parameters of the designed coupler. These structural parameters are the length of the coupled lines, the lengths of the matching circuit, the lengths of the transmission lines to be connected to the ports, the distance between the coupled lines and the widths of transmission lines. The following five parameters are generally used to characterize a directional coupler: coupling coefficient (S_{31}), directivity (it is obtained difference between (S_{41}) and (S_{31})), isolation (S_{41}), insertion loss (S_{21}) and input return loss (S_{11}) expressing the power reflected from the first port. The coupling factor is an indicator of the rate at which the input power is coupled to the output port. Directivity refers to the coupler's ability to isolate forward and reverse waves. Isolation shows how much power is transferred to port 4. The insertion loss shows the rate at which the input power is transferred to through port. An ideal coupler should have infinite directivity and isolation. Although directivity is a very important parameter for couplers, couplers based on microstrip lines suffer from poor directivity because of different even and odd mode phase velocities. In practice, directional couplers usually require directivity of 30dB or higher. But this directivity value is quite difficult to achieve, especially at high bandwidths. Along with high directivity, other performance parameters must also meet the required design requirements. In this study, the coupler design is considered as an optimization problem, and it is aimed to fulfill all the desired conditions as much as possible. The structural parameter lengths that need to be to get ideal S parameters have been optimized using the Grey Wolf Optimizer algorithm. This optimization process was carried out using the Python programming language. The EM simulation of the study was carried out with Ansys HFSS 18. Cheap and easy-to-find FR_4 substrate material has been preferred. The following methodology has been followed in the coupler design. Firstly, the design frequency and S_{31} were determined. For this study, S_{31} was determined to be 15dB. Secondly based on the determined coupling coefficient and frequency values, the lengths and width of the coupled lines and the distance between the two coupled lines were calculated. These calculated values were taken as the midpoints in determining the structural parameter range to be optimized. After this step, the optimum structural parameter values that will give the desired S parameters were optimized. Finally, the coupler was simulated with optimum lengths, width and distance. According to the simulation results, it has been seen that the S_{31} and S_{21} are better than 15dB&1dB respectively. Also, the directivity and S_{11} are higher than 30dB&40dB. It has been observed that the coupler with optimal structural parameters provides the desired targets and has a high performance.

Keywords. Radio telescopes, solar radio flux receiver, microstrip directional coupler, high directivity, Grey wolf optimizer.

Nonlinear Controller Design of DC-DC Buck Converter and Real Time Application

Tuğrulhan AKGÜL ¹[0000-0001-7274-5843], Armin Lotfi EGHLM ²[0000-0002-7670-3883] and Hacı Mehmet Güzey ³[0000-0002-2215-9536]

¹tugrulhan.akgul@erzurum.edu.tr, Department of Electrical and Electronic Engineering, Faculty of Engineering And Architecture, Erzurum Technical University, Erzurum/TURKEY

²armin.lotfi.eghlim@gmail.com, Department of Electrical and Electronic Engineering, Faculty of Engineering, Atatürk University, Erzurum/TURKEY

³mehmet.guzey@sivas.edu.tr, Department of Electrical and Electronic Engineering, Faculty of Engineering and Natural Sciences, Sivas University of Science and Technology, Sivas/TURKEY

Abstract

DC-DC (Direct Current-Direct Current) converters are widely used for different purposes such as DC motor control, maximum power point tracking in solar cell and switching power supplies. In recent years, studies on power electronics for converting uncontrolled voltage at the input of the converter to a desired voltage in output have been increased. In this study, a non-linear back-stepping controller for the DC-DC Buck converter is designed and tested in real time. The designed controller was observed using the MATLAB/Simulink toolbox and Quanser Q8-USB data acquisition device. In high power application, the effects of parasitic elements are not neglectible so in the model of Buck converter have been considered. The designed controller provides accurate performance in wide range of input voltage variation. The accuracy of the designed controller was observed with the real-time experiment.

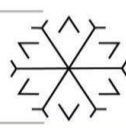
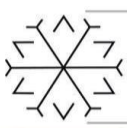
Keywords. DC-DC Converters, Nonlinear Control, Parasitic Elements

1. Introduction

DC-DC (Direct Current-Direct Current) converters are the important power electronic circuits used in a variety of electrical systems like electric cars, ships, airplanes, power supply of computers, renewable energy generation facilities such as solar power plants and wind power plants. They have been became part of DC power supply systems such as maximum power point tracking (MPPT) and turbine management (Ramash Kumar and Jeevananthan, 2010). Designed DC-DC power converters are very useful with low cost and high efficiency for essential applications such as solar cell storage systems and fuel cell-powered electric vehicles where 48V (Voltage) DC needs to be fixed (Kivrak, Power and Systems, 2016).

DC-DC converters can be defined as DC transformers where reactive components are filtered and transmitting DC voltage or current to the output load at a different level from the input source. However, they perform conversion by using electronic switching devices, not as electromagnetic devices like conventional transformers. Due to the electronic switching processes, this type of converters operate according to the periodic time. The average output voltage of DC-DC converters can be defined as a linear function of the switch duty ratio, and this output voltage varies from 1V for special VLSIs (very large-scale integrated circuits) to tens of kilovolts in X-ray lamps. For selecting the topology of DC-DC converters, not only with adjustable output voltages but also the power levels controlling, reducing voltage-current stresses of semiconductor switches and the using of magnetic components are considered.

In order to correct the power factor of AC networks, reducing harmonics and changing the input of the inverters, DC-DC converters are frequently used in the intermediate stages of rectifier and load. Another application of DC-DC converters for electrical grid systems is interfaces between AC networks and DC renewable energy sources such as photovoltaic arrays. Especially a multi-output DC-DC converter is preferred as a suitable solution in such industrial applications where one or more output voltage levels are needed (Rashid, 2001).



In other study, DC-DC Buck converter have been used for different purposes such as electric traction systems, various machine tools and DC power supplies. Because of utilizing transistor and diode as power switching elements, the converter has been introduced as nonlinear so regarded as time varying dynamic systems (Salimi, Soltani, Markadeh, *et al.*, 2013). Considering the linearization model, it is possible to use a linear controller for this circuit (Ramash Kumar and Jeevananthan, 2010). The linear controller is simple to implement and may cause instability in the system. It is more convenient to use the nonlinear technique to regulate the output voltage of the converter. Various nonlinear controller design such as back-stepping controllers (Salimi, Soltani and Markadeh, 2011), feedback linearization controllers (Hwu and Tau, 2005), feedback linearization controller for leader follower based approach (Guzey, H. M. *et al.*, 2018), adaptive back-stepping controllers (McIntyre, Schoen and Latham, 2013), sliding-mode controllers (Chen, 2012), passivity-based controllers are available in the literatures. The sliding mode controller is robust for uncertainties in the system dynamics while switching frequency, chattering and steady-state error variation can be listed as the disadvantages of this controller (Salimi, Soltani, Zakipour, *et al.*, 2013). In feedback linearization technique, there are dynamically overshoot-undershoot in the systems response with variation in input or reference voltage. The other type of nonlinear controller is adaptive back-stepping control, using the Lyapunov function and the uncertain dynamics parameters estimating in model and the control function are handled (Salimi, Soltani and Zakipour, 2011). In the passivity-based control (PBC), controller is developed efficiently by using the appropriate system model and using the best controller coefficients. It has an appropriate dynamic response to various changes in input and reference voltage and also in load resistance changes (Salimi and Eghlim, 2015).

In this study, a method based on back-stepping control approach is proposed for the control of DC-DC Buck converter. The nonlinear controller is designed by using the real model of the converter. The stability designed controller is guaranteed by considering the Lyapunov theorem. The effect of the parasitic elements (such as the equivalent series resistance (ESR) of the inductor, the ESR of the power switch and etc.) are considered State Space Averaged Model (SSAM). According to experimental results, it has been observed that the designed controlling method has effective transient responses with acceptable steady-state error and has accurate responses.

In the organization of this study, In the second chapter, the modelling of DC-DC Buck converter is mentioned. In the third chapter, SSAM representation with parasitic elements for the Buck converter is presented and in fourth chapter, a back-stepping controller is proposed. Laterly In the fifth chapter, controller designed results of the for DC-DC Buck converter are figured in MATLAB/Simulink Q8-USB environment. In the sixth chapter, the conclusion is stated.

2. DC-DC Buck Converter

Due to the power switch and doide elements in the DC-DC Buck converter circuit, there are two different circuit, first when the switch is ON and diode is OFF (ON-STATE), second when switch is OFF and diode is ON (OFF-STATE). By using the averaging technique and inserting all components affect like inductor, capacitor and parasitic elements, the state-space model of Buck converter are considered so by achieving exact model of converter, the transient and steady responses of designed controller is improved. By selecting the Lyapunov function, back-stepping controller for Buck converter designed and guaranteed the system stability.

Table 1: Symbols Used and Their Explanation.

Symbols and Descriptions		Symbols and Descriptions	
t	Time	i_L	Inductor current
f	Switching frequency	i_C	Capacitor current
kHz	Kilo Hertz	H	Henry
ms	Milliseconds	F	Farad
t_{on}	When the switch stays on	Ω	Ohm
t_{off}	When the switch is off	L	Inductor
T_s	Total period	C	Capacitor
μ	Switching function dependent on controller signal	R	Load resistor
D	Duty cycle rate	r_L	Equivalent series resistance of inductor
V_d, E	Source voltage	r_C	Equivalent series resistance of capacitor
V_o	Output voltage	r_S	Equivalent series resistance of the switch
V_{ref}	Reference voltage	r_D	Equivalent series resistance of diode
V_L	Inductor voltage	D	Diode
V_C	Capacitor voltage	S	Switch
v_d	Forward voltage of diode	k_1	Control coefficient of the controller
i_o	Output current	k_2	Control coefficient of the controller

2.1. Operating Buck Converters in Continuous Conduction Mode

The DC-DC Buck converter generates lower averaged output voltage due to varying voltage in Buck converter input.

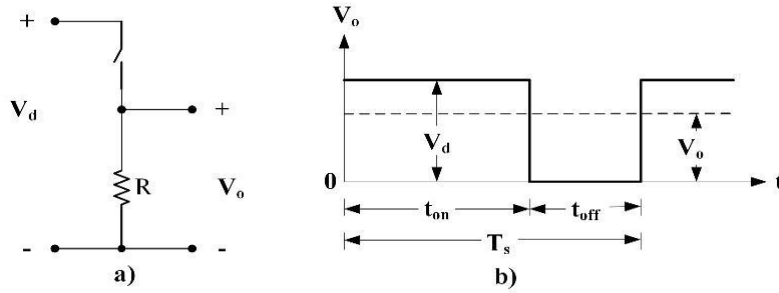


Figure 1: a) Simple Switched DC-DC Converter b) Output voltage of Buck converter (Mohan, Undeland and Robbins, 2003).

In Figure 1.a, basic Buck converter is shown by assuming the ideal switch, constant input voltage and pure resistive load. The output voltage waveform is shown in Figure 1.b so the averaged output voltage of Buck converter according to duty cycle of controller signal can be written as (1) (Mohan, Undeland and Robbins, 2003):

$$V_o = \frac{1}{T_s} \int_0^{T_s} v_o(t) dt = \frac{1}{T_s} \left(\int_0^{t_{on}} V_d dt + \int_{t_{on}}^{T_s} 0 dt \right) = \frac{t_{on}}{T_s} V_d = k V_d$$

Considering the above equation, the output voltage can be controlled by changing the duty cycle ratio. Output voltage ripple is resolved by a low-pass filter containing a capacitor and an inductor. The corner frequency of the low pass filter used in Buck converter is much lower than the switching frequency so the filter is eliminating ripple voltage in the output voltage of converter. In ON-STATE, energy flows from input power supply to the inductor, thus a voltage is appeared on the inductor and this voltage have linear correspond to inductor current. In OFF-STATE the switch is opened and stored energy in inductor flows to load through the diode.

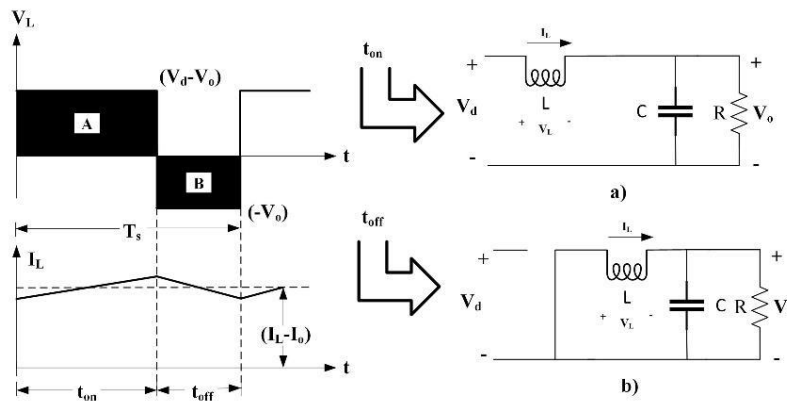


Figure 2: Illustrations of The Buck Converter in Continuous Conduction Mode (Mohan, Undeland and Robbins, 2003) a) ON-STATE b) OFF-STATE.

In continuous conduction mode, the waveform of inductor voltage is repeated until the next period and average voltage of the inductor must be equal zero.

$$\int_0^{T_s} v_L dt = \int_0^{t_{on}} v_L dt + \int_{t_{on}}^{T_s} v_L dt = 0$$

therefore it could be written as:

$$(V_d - V_o)t_{on} = V_o(T_s - t_{on}) \rightarrow \frac{V_o}{V_d} = \frac{t_{on}}{T_s} = D$$

In this case, the output voltage varies linearly with the duty cycle coefficient and does not depend on any of the other circuit parameters; Therefore, in continuous operation, Buck converter is similar to the DC transformer and could be controlled continuously by duty cycle of switching.

2.2. Effect of Parasitic Elements on Converters

In high power or low output voltage the Parasitic elements have significant effect on converter performance and its stability and also could insert nonlinear characteristic in output response.

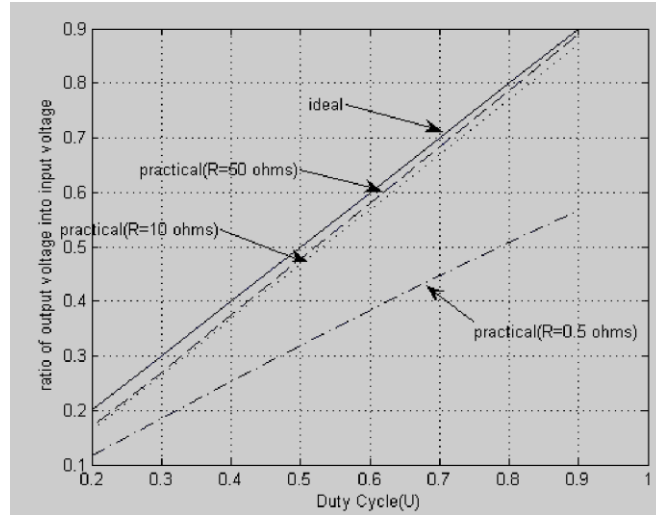


Figure 3: The Effect of Parasitic Elements on Converteres (Salimi and Eghlim, 2015).

In Figure 3, the curve was drawn based on inserting practical measurement, converter input voltage equals to 20V and 1mh inductor has 0.2Ω resistance, 40μF output capacitor and a 25KHz switching frequency is assumed (Salimi and Eghlim, 2015). Due to low switching performance, the dotted curve in the graph (R=0.5Ω) is impracticable.

3. Design of The State Space Average Model for DC-DC Buck Converter

In the presence of parasitic elements, the design of Buck converter is figured as follow:

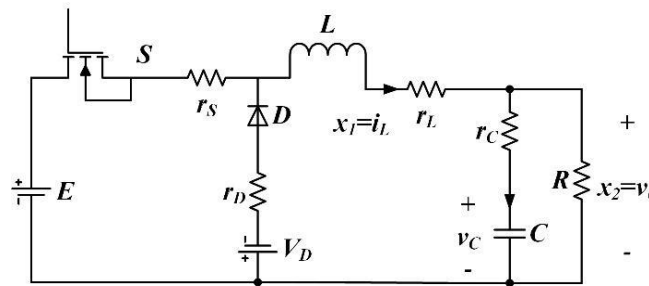


Figure 4: Basic Circuit of The Buck Converter with Parasitic Elements.

In high power-low voltage applications, the arasitic elements must be modeled as an equivalent series resistance (ESR). In the modeling, r_L, r_s, r_D, r_C are defined as the equivalent series resistances of the inductor, switching element, diode and capacitor, respectively. There is also another parasitic element that affects the characteristics of Buck converter, modeled as V_D and defined as the forward voltage of diode. The effect of the capacitor equivalent series resistance can be neglected with choosing the appropriate switching frequency, $\hat{t} > 5\tau$ (Salimi and Eghlim, 2015).

Buck converter has two state variables and are defined as follow:



$$x = \begin{bmatrix} i_L \\ v_C \end{bmatrix} = \begin{bmatrix} x_1 \\ x_2 \end{bmatrix}$$

So x_1 represents the inductor current and x_2 the capacitor voltage (converter output voltage). The Buck converter can be modeled in a continuous mode of operation (CCM) using the state space averaging technique (Rashid, 2001) and controller signal for converter is obtained by Pulse Width Modulation technique (PWM). According to this technique, T ($T=1/f$, f switching frequency) is switching time period and μ Duty cycle of controller signal ($0 \leq \mu < 1$). By Considering the circuit shown in Figure 5.a the switch is ON and the diode is OFF and in Figure 5.b switch is OFF and diode is ON.

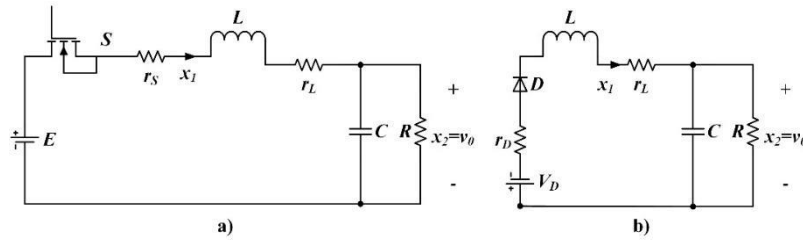


Figure 5: The State of The Buck Converter (Mohan, Undeland and Robbins, 2003) a) Switch is Closed and Diode is Open-circuit b) Switch is open-circuit and Diode is ON.

Depending on the circuit in Figure 5.a, the state space model can be defined as follow (5).

$$\begin{cases} \dot{x}_1 = -\frac{1}{L}(r_L + r_s)x_1 - \frac{1}{L}x_2 + \frac{1}{L}E \\ \dot{x}_2 = \frac{1}{C}x_1 - \frac{1}{RC}x_2 \end{cases}$$

In this state the current inductor increases linearly and stores a magnetic field in inductor core (Akgül, 2020).

Similarly, in Figure 5.b when the switch is OFF and the diode is ON ($\mu T_s \leq t \leq T_s$) stored energy in core of inductor is transferred to output by diode; and state-space model can be defined as the (6).

$$\begin{cases} \dot{x}_1 = -\frac{1}{L}(r_L + r_D)x_1 - \frac{1}{L}x_2 - \frac{1}{L}V_D \\ \dot{x}_2 = \frac{1}{C}x_1 - \frac{1}{RC}x_2 \end{cases}$$

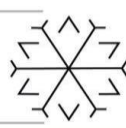
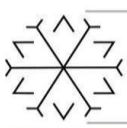
By using SSAM model technique, the Buck converter model can be define as below (In equation (7) the $\bar{\mu}$ is defined as $\bar{\mu} = 1 - \mu$):

$$\begin{cases} \dot{x}_1 = -\frac{1}{L}(r_L + \mu r_s + \bar{\mu} r_D)x_1 - \frac{1}{L}x_2 + \frac{1}{L}(\mu E + \bar{\mu} V_D) \\ \dot{x}_2 = \frac{1}{C}x_1 - \frac{1}{RC}x_2 \end{cases}$$

4. Design Back-Stepping Controller to DC-DC Buck Converter

For designing back-stepping controller, the feedback control law and Lyapunov function will be used and this controller could be used for any nonlinear systems. In this plant (Buck converter), there are switching elements like power FET-diode and this switches insert nonlinear properties to system responses. Therefore, the designed controller based on back-stepping is suitable for this plant. The state error vectors are used to design the controller, and the error vector is set to zero. The controller's goal in this study is to eliminate the output voltage error. The method that used for the control of the buck converter is described in two steps:

First Step: Calculating the required inductor current reference to obtain the desired output voltage



By defining capacitor voltage of Buck converter as x_2 and desired output voltage as x_2^d , the first error vector could be defined as:

$$e_2 = x_2 - x_2^d$$

So the time derivative of the output voltage error is:

$$\dot{e}_2 = \dot{x}_2 - \dot{x}_2^d \rightarrow \dot{e}_2 = \frac{1}{C}x_1 - \frac{1}{RC}x_2 - \dot{x}_2^d$$

Also inductor current of buck converter is named as x_1 , In this step of controller design virtual controller as inductor reference current will be proposed; The Lyapunov function by using voltage capacitor error e_2 can be defined as follow:

$$L_2 = \frac{1}{2}e_2^2$$

Therefore, time derivative of L_2 is:

$$\dot{L}_2 = e_2\dot{e}_2 \rightarrow \dot{L}_2 = e_2 \left[\frac{1}{C}x_1 - \frac{1}{RC}x_2 - \dot{x}_2^d \right]$$

By selecting x_1 as a virtual controller, the first controller could be defined as below and mentioned as inductor reference current:

$$x_1^d = C \left[\frac{1}{RC}x_2 + \dot{x}_2^d - k_2e_2 \right]$$

Choosing K_2 as a positive coefficient as inserting in equation (12), time derivative of Lyapunov function has negative value:

$$\dot{L}_2 = -k_2e_2^2$$

So the stability of virtual controller guaranteed and e_2 convert to zero and the output voltage of Buck converter reaches the desired value $x_2 \rightarrow x_2^d$.

Second Step: Controller input design

The difference between the inductor current x_1 and its reference value that obtained in (12), the second error vector could be defined as below:

$$e_1 = x_1 - x_1^d$$

To control the inductor current, let's consider the following Lyapunov function:

$$L_1 = \frac{1}{2}e_1^2$$

The time derivative of the Lyapunov function is obtained as (16).

$$\dot{L}_1 = e_1\dot{e}_1 \rightarrow \dot{L}_1 = e_1 \left[\dot{x}_1 - \dot{x}_1^d \right]$$

If \dot{x}_1 is taken from (12), expression (16) can be written as follows.

$$\dot{L}_1 = e_1 \left[-\frac{1}{L}(r_L + \mu r_s + \bar{\mu} r_D)x_1 - \frac{1}{L}x_2 + \frac{1}{L}(\mu E + \bar{\mu} V_D) - C \left(\frac{1}{RC}\dot{x}_2 + \ddot{x}_2^d - k_2\dot{e}_2 \right) \right]$$

As seen in Equation (17), Equation (18) is obtained when $(1-\mu)$ is written instead of $\bar{\mu}$ controller signal.



$$\dot{L}_1 = e_1 \left[-\frac{1}{L}(r_L + \mu r_S + (1-\mu)r_D)x_1 - \frac{1}{L}x_2 + \frac{1}{L}(\mu E + (1-\mu)V_D) - C \left(\frac{1}{RC}\dot{x}_2 + \ddot{x}_2^d - k_2\dot{e}_2 \right) \right]$$

And could be rewritten as (19).

$$\dot{L}_1 = e_1 \left[\left(-\frac{1}{L}(r_S - r_D)x_1 + \frac{1}{L}(E - V_D) \right) \mu - \frac{1}{L}(r_L + r_D)x_1 - \frac{1}{L}x_2 + \frac{1}{L}V_D - C \left(\frac{1}{RC}\dot{x}_2 + \ddot{x}_2^d - k_2\dot{e}_2 \right) \right]$$

By definitions as follows:

$$f = \left[-\frac{1}{L}(r_L + r_D)x_1 - \frac{1}{L}x_2 + \frac{1}{L}V_D - \frac{1}{R}\dot{x}_2 - C\ddot{x}_2^d + Ck_2\dot{e}_2 \right], g = \left[-\frac{1}{L}(r_S - r_D)x_1 + \frac{1}{L}(E - V_D) \right]$$

So time derivative Lyapunov function (19) could be written as:

$$\dot{L}_1 = e_1 [g\mu + f] \quad (21)$$

By selecting μ as controller:

$$\mu = (1/g) \times (-f - k_1 e_1) \quad (22)$$

Inserting (22) in (21), the derivative of the Lyapunov is written as:

$$\dot{L}_1 = -k_1 e_1^2$$

When k_1 coefficient is chosen as positive constant, time derivated of Lyapunov function is negative and its stability is guaranteed; e_1 in converted to zero so inductor current will be converted to desired value. Hence, the output voltage reaches the desired output voltage x_2^d . The controller signal in Equation (22) is clearly given below.

$$\mu = \left(1 / \left(-\frac{1}{L}(r_S - r_D)x_1 + \frac{1}{L}(E - V_D) \right) \right) \times \left[\frac{1}{L}(r_L + r_D)x_1 + \frac{1}{L}x_2 - \frac{1}{L}V_D + \frac{1}{R}\dot{x}_2 + C\ddot{x}_2^d - Ck_2\dot{e}_2 - k_1 e_1 \right]$$

The controller signal μ designed for Buck converter is derived as input PWM signal and produce that the appropriate gate trigering signal for power FET.

5. Application and Real-Time Results for DC-DC Buck Converter

In this section, a practical circuit has been created for the designed back-stepping controller and a real-time experiment has been made to follow the reference voltage. The nominal values of the controller and power circuit elements are presented in Table 2.

Table 2: Characteristics of The Buck Converter.

1	Input Power Supply	12 V	6	Static Resistance of Switch	0.1 Ω
2	Inductor Value	150 μ H	7	Dynamic Resistance of Diode	0.001 Ω
3	Output Capacitance Value	330 μ F	8	Diode Forward Voltage	0.7 V
4	Switching Frequency	7.8 kHz	9	k_1	19.1
5	Inductor ESR Value	0.1 Ω	10	k_2	3.9

5.1. Real Time Application of Buck Converter

In the experimental system (Figure 6), MATLAB/Simulink 2017a Toolbox and Quanser Q8-USB data acquisition device, the FET driver circuit and 12V power supply are used; IRF-460 (MOSFET) is used as power switch and 6A10ATC is used as power diode. IC-6N136 and ICL-7667 integrated circuit (IC) are used as optocoupler and FET driver perspectivly. ACS712-5A chip as current sensor is utilized to measure the inductor current and 12V-10A switching DC power supply is used as the input power source of the Buck converter.

The designed controller approach with considering the nominal values has been tested in Figure 6. Reference voltage $V_{ref} = 6V$ is selected. Output load resistor value is 20Ω . The result of designed back-stepping controller for DC-DC buck converter is shown in Figure 7 as real-time experiment.

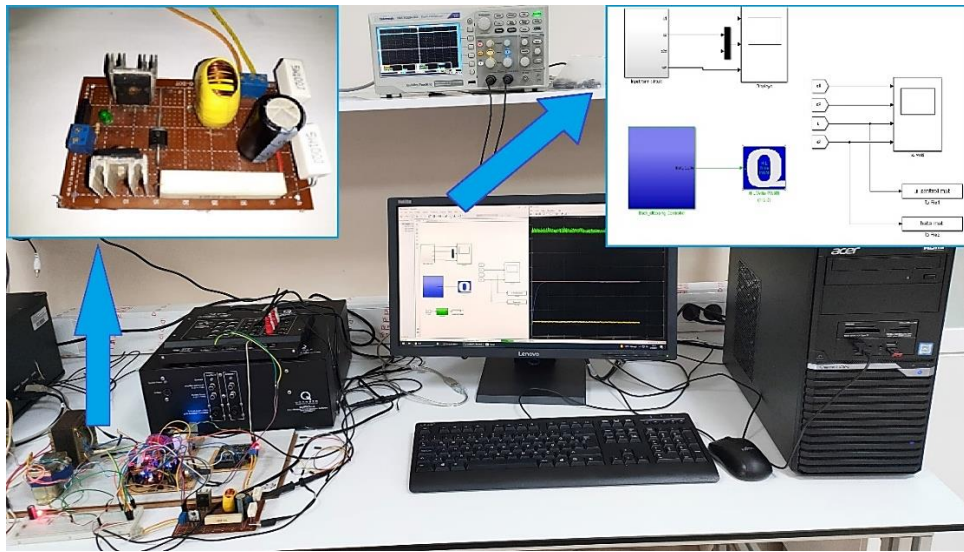


Figure 6: Experimental System of The Buck Converter.

Considering the nominal values that presented in Table 1, the output voltage of Buck converter, inductor current, the output error voltage of Buck converter and the graphs of the generated controller signal are presented. As seen in Figure 7, an appropriate controller signal (μ) is generated so output voltage error of Buck converter is converted to zero and the reference voltage is followed.

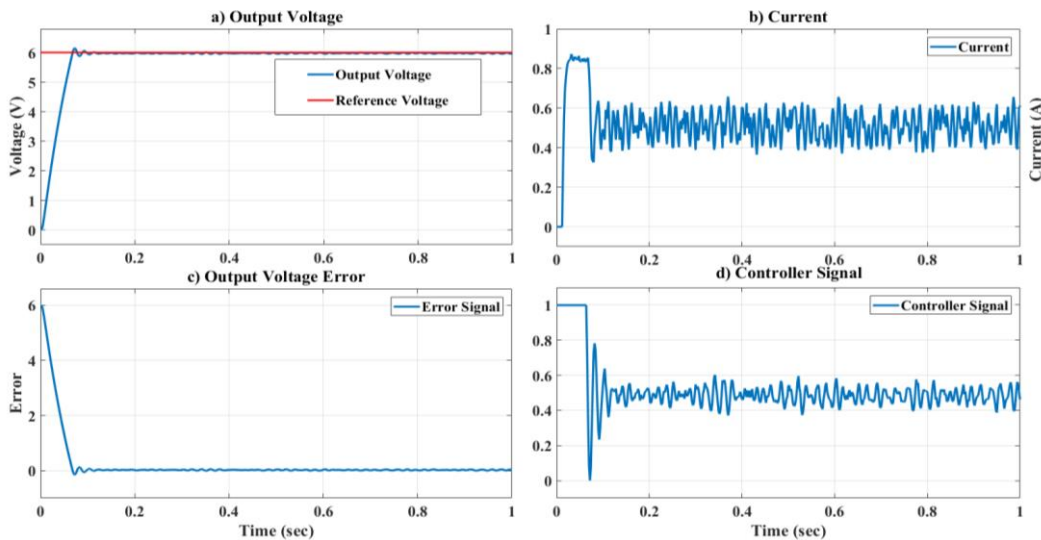


Figure 7: Graphs of The Real-Time Experiment for Designed Controller Approach.

As seen in Figure 7.a, the converter was controlled by a back-stepping controller and the reference voltage was followed at $T_s = 0.0840$ sec. The percent overshoot of the output voltage is measured as $OS = 2.4932\%$. At the same time, the rise time of the output voltage was measured as $T_r = 0.0500$ sec and the overshoot time as $T_p = 0.0720$ sec. The buck converter started to work by drawing about 1A current from the source. The graph of the inductor current is shown in Figure 7.b. Figure 7.c shows the output voltage error of the Buck converter. The experimental result is measured as Steady State Error = 0.0407 for the designed controller. Finally, the controller signal is presented as the input PWM unit in Figure 7.d.

6. Conclusion

The control of a DC-DC Buck converter using the state-space average model, which is generated by considering parasitic elements, is suggested in this paper using the back-stepping nonlinear control approach. Using the



MATLAB/Simulink toolbox and Quanser Q8-USB data acquisition device, the controller for the DC-DC Buck converter was developed in real time and evaluated. The converter with 12V DC input voltage and back-stepping controller transfers 6V voltage as output. It has been observed that when the real-time test setup designed for the Buck converter is operated, it follows the 6V reference voltage. The controller will have acceptable transient and steady-state responses if suitable K coefficients are chosen for it, according to the test results. The output voltage error of the back-stepping controller proposed for the DC-DC Buck converter has been confirmed to be quite low, and the output voltage converges to the desired voltage.

As a result, when controlled with the proposed back-stepping controller, the Buck converter, which is modeled by considering its parasitic elements, has acceptable dynamic and steady-state responses. The non-linear back-stepping controller, which is designed based on the exact model of the converter, can work at high power and low voltages with high performance. Among the planned studies is an evaluation of the control efficiency of various nonlinear controllers designed in the presence of disturbances that may affect the Buck converter.

References

- Akgül, T. (2020) 'Nonlinear Back-Stepping Controller Design Of DC-DC Buck Converter and Real Time Application', MA thesis, Erzurum Technical University, Erzurum.
- Chen, Z. (2012) 'PI and sliding mode control of a Cuk converter', *IEEE Transactions on Power Electronics*. IEEE, 27(8), pp. 3695–3703. doi: 10.1109/TPEL.2012.2183891.
- Guzey, H. M. *et al.* (2018) 'Optimal synchronizing speed control of multiple DC motors', *Proceedings of the 2018 International Conference on Optimization and Applications, ICOA 2018*, 0(2), pp. 1–5. doi: 10.1109/ICOA.2018.8370508.
- Hwu, K. I. and Tau, Y. T. (2005) 'A forward converter having an FPGA-based PID controller with parameters on-line tuned', *Proceedings of the International Conference on Power Electronics and Drive Systems*, 2, pp. 1239–1243. doi: 10.1109/peds.2005.1619877.
- Kivrak, S., Power, H. and Systems, G. (2016) 'Pwm Controlled Dc-Dc Boost Converter Design and Pwm Controlled Dc - Dc Boost Converter Design and', (October), pp. 4–13.
- McIntyre, M. L., Schoen, M. and Latham, J. (2013) 'Simplified adaptive backstepping control of buck DC:DC converter with unknown load', *2013 IEEE 14th Workshop on Control and Modeling for Power Electronics, COMPEL 2013*. IEEE, pp. 1–7. doi: 10.1109/COMPEL.2013.6626443.
- Mohan, N., Undeland, T. M. & Robbins, W. P., (2003) 'Power Electronics: Converters, Applications, and Desing' John Wiley & Sons, USA.
- Ramash Kumar, K. and Jeevananthan, S. (2010) 'Design of sliding mode control for negative output elementary super lift luo converter operated in continuous conduction mode', *2010 IEEE International Conference on Communication Control and Computing Technologies, ICCCT 2010*. IEEE, pp. 138–148. doi: 10.1109/ICCCCT.2010.5670542.
- Rashid, M. H. Editor in chief., (2001) 'Power Electronics Handbook' Academic Press, USA.
- Salimi, M., Soltani, J., Markadeh, G. A., *et al.* (2013) 'Indirect output voltage regulation of DC-DC buck/boost converter operating in continuous and discontinuous conduction modes using adaptive backstepping approach', *IET Power Electronics*, 6(4), pp. 732–741. doi: 10.1049/iet-pel.2012.0198.
- Salimi, M., Soltani, J., Zakipour, A., *et al.* (2013) 'Sliding mode control of the DC-DC flyback converter with zero steady-state error', *PEDSTC 2013 - 4th Annual International Power Electronics, Drive Systems and Technologies Conference*. IEEE, pp. 158–163. doi: 10.1109/PEDSTC.2013.6506695.
- Salimi, M. and Eghlim, A. L. (2015) 'Passivity-based control of the DC-DC buck converters in high-power applications', *IEEE Region 10 Annual International Conference, Proceedings/TENCON*. IEEE, 2015-Janua, pp. 1–6. doi: 10.1109/TENCON.2014.7022387.
- Salimi, M., Soltani, J. and Markadeh, G. A. (2011) 'A novel method on adaptive backstepping control of buck choppers', *2011 2nd Power Electronics, Drive Systems and Technologies Conference, PEDSTC 2011*. IEEE, pp. 562–567. doi: 10.1109/PEDSTC.2011.5742482.
- Salimi, M., Soltani, J. and Zakipour, A. (2011) 'Adaptive nonlinear control of DC-DC buck/boost converters with parasitic elements consideration', *Proceedings - 2011 2nd International Conference on Control, Instrumentation and Automation, ICCIA 2011*. IEEE, pp. 304–309.

A Performance Metric Proposal to Evaluate Effectiveness of Demand Side Management in Smart Grids

Recep Çakmak ^{1*}[0000-0002-6467-6240]

¹rcakmak@gumushane.edu.tr, Department of Electrical and Electronics Engineering, Gümüşhane University, Gümüşhane, Turkey

Abstract

Traditionally, in an electrical power system peak demand is considered an important parameter when compared to the average demand. So, the Peak to Average Ratio (PAR) metric is utilized in the power systems frequently when planning, operation, and assessment processes. The aim of the power system operators is to make a flatter demand (load) curve, which means that it has a lower PAR. Conventionally, in the electrical grid, which has bulk power plants that use conventional sources such as nuclear, coal, oil, natural gases or hydro, the power system operation executes through “the generation follows the load” concept. Due to environmental concerns, renewable energy-based electricity generation has been increasing. The increased share of the renewable energy systems in the electrical power system leads to more intermittent and variable power injection to the grid. A significantly increasing share of renewable sources of power generation is necessitated a revolution in the concept to ensure a balance between demand and generation. Therefore, in the 21st-century sustainable energy system “the load follows the generation” concept is embraced instead of “the generation follows the load” to engage more renewable energy-based power plants. It is expected that this concept change would have realized in smart grids through Demand-Side Management (DSM). DSM is one of the essential components of the smart grid and it provides to control the consumption at the customer side. Also, DSM is a cost-effective solution in the smart grids to decrease peak demand and to solve the problems which cause when generated power and consumed power are not matched at the power system. Although peak load reduction is important for the power systems by DSM reduce to need highly polluting peaker power plants and to decrease losses, maybe more important point is the provide matching between renewable generation and demand at peak generation times occurred by distributed renewable-based power plants. Because more renewable-based power plants should be constituted as much as possible to provide a sustainable power supply. However, renewable-based power plant penetration may lead to some power quality problems even a collapse in the grid. In this study, a performance metric has been proposed to use in the scheduling of time-shiftable loads through demand response programs for DSM in the smart grids. Also, this metric can be used to measure the effectiveness of the DSM. The proposed metric (AG2AC) calculates the rate of average Power Generation (P_G) at the Generation Period (T_G) to average Power Consumption (P_C) at T_G and it is defined by Equation 1. Besides the PAR, AG2AC can be used in load scheduling optimization problems as a fitness function to get optimal load scheduling.

$$AG2AC = \frac{\frac{1}{T_G} \sum_0^{T_G} P_G}{\frac{1}{T_G} \sum_0^{T_G} P_C} \quad (1)$$

Furthermore, PAR and AG2AC can be utilized together as a Combined Metric (CM) for multi-objective optimization problems by weighting coefficients α and β as shown in Equation 2.

$$CM = \alpha(PAR) + \beta(AG2AC) \quad (2)$$

To sum up, in this study, AG2AC and CM metrics are proposed and some of DSM results are evaluated by analyzing the load curves through the AG2AC. Also, this study suggests combining of AG2AC and PAR for multi-objective optimization problems. Future studies will be related to utilizing the proposed metric in the optimal load scheduling problems.

Keywords. Demand-Side Management, Demand Response, Performance Metric, Smart Grids.

Effects of Grid Integration of Electric Vehicles and Charging Stations

Ramazan Özcan ^{1*}[0000-0002-8251-275X] and Turgay Duman ²[0000-0002-9132-9885]

¹ramazan.ozcan48@erzurum.edu.tr, Erzurum Technical University

²turgay.duman@erzurum.edu.tr, Erzurum Technical University

Abstract

With the increasing world population and developing industry, the use of fossil fuels has increased to meet the increasing energy need. This increased consumption of fossil fuels has also brought about important environmental effects such as air pollution. Most of the fossil fuels consumed are used for transportation. Electric vehicles are considered the most appropriate solution to reduce fuel consumption and related air pollution in the transportation sector. Therefore, the production of electric vehicles is increasing day by day and some incentives are being made to spread their use. According to the Global EV Outlook 2021 report, over 10 million electric cars were on the world's roads in 2020 and other studies predict that by 2030, the number of electric vehicles worldwide may be between 120-250 million. For EVs to be a viable option for transportation, some issues need to be resolved, such as battery cost, efficient charging strategies, interoperability of charging stations and the impact of EV integration on the grid. It is predicted that serious effects on the grid such as voltage fluctuations and imbalance between phases may occur due to the deterioration of the supply-demand balance in the grid as a result of the widespread use of electric vehicles. Therefore, solving the problems that arise during the integration of electric vehicles and charging stations into the grid is crucial. Some factors such as charging scenarios, electric vehicle driving profiles, electricity grid, and demographic structure need to be taken into account when installing electric vehicle charging stations. In this study, the effects of electric vehicles and charging stations on the grid have been examined and the results have been presented.

Keywords. Electric Vehicles , Charging Stations, Effects on the Grid

Printed Circuit Board Surface Defect Detection using YOLOv4 algorithm

Işıl KARABEY AKSAKALLI ²[0000-0002-4156-9098], Uğur KILIÇ ^{1*}[0000-0003-4092-3785], and Barış ÖZYER ²[0000-0003-0117-6983]

¹isil.karabey@erzurum.edu.tr, Department of Computer Engineering, Erzurum Technical University

²ugur.kilic@erzurum.edu.tr, Department of Computer Engineering, Erzurum Technical University

³baris.ozyer@atauni.edu.tr, Department of Computer Engineering, Ataturk University

Abstract

Defect detection in the manufacture of printed circuit boards (PCB) is a crucial requirement for quality inspections. In the past, defect inspections in PCB production were performed ineffectively by human observation. Nowadays, machine vision systems are often used in circuit board surface defect detection thanks to the developments in deep learning methods. In this paper, we handled six basic manufacturing defects that frequently occur in small-sized electronic printed circuit boards manufactured with computer-aided design tools. We applied a deep learning model using the YOLOv4 algorithm, which is a machine vision-based method. We evaluated the model based on different thresholds and different numbers of images according to common manufacturing defects. The experimental results show that the created model has 97% mean average precision (mAP@0.5) at a 0.5 threshold value.

Keywords. PCB Defect, Automatic Optical Inspection, Vision-based Method, YOLOv4

1. Introduction

To operate electronic circuit elements without encountering any problems, the surface of printed circuit boards must be designed flawlessly. The layout and designs of the printed circuit boards are generated with computer-aided design tools. During production, incomplete or incorrectly processed assembly errors are frequently observed due to the increasing demand and production speed in the PCB production process. To test the accuracy of the generated printed circuit boards, companies usually assign a few operators for each station and make critical observations with the naked human eye. However, this process takes much longer to be detected by human power than a computer system. In addition, it is hard to see the defects on the PCB surfaces generated as a result of the electronic circuit elements with the naked eye since they are too small to identify. Alternatively, automatic defect detection systems such as In-Circuit Test (ICT), Function-Circuit Test (FCT), Automatic Optical Inspection (AOI) are used to detect PCB defects (Caliskan and Gurkan, 2021). In this study, the most common manufacturing defect types (open circuit, short, mouse bite, spurious copper, spur, and missing hole) in small-sized electronic printed circuit boards generated with computer-aided design tools are detected using a machine vision-based method named YOLOv4. Figure 1 shows defect types identified in this study.

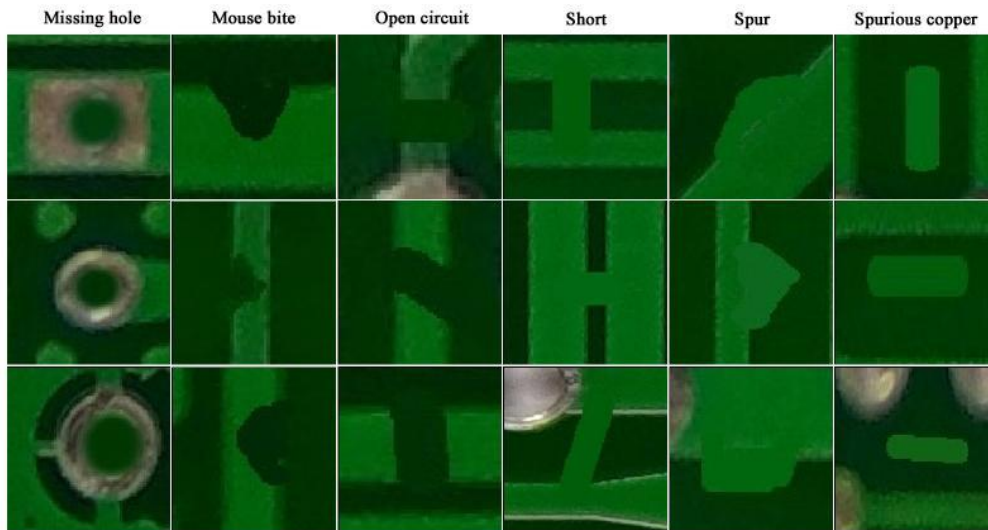


Figure 1: PCB surface defect types (Huang and Wei, 2019)

The remaining parts of the study are organized as follows. Related studies using deep learning methods to detect PCB defects are included in Section 2. In Section 3, the dataset, labeling, and training phases used for PCB defect detection are explained. Then the deep neural architecture of the YOLOv4 method is described. In Section 4, the experimental results of the created model are evaluated. Finally, the study is concluded in Section 5.

2. Related Work

PCB defect detection can be divided into three parts as direct inspection by a human operator, automatic defect inspection systems, and camera-based machine vision. Defect detection using human factors varies according to operators, and researchers focus more on machine vision-based defect inspection since PCB sizes are getting smaller with the development of technology. ICT is one of the automatic defect detection systems, and it measures the electrical properties of PCB components with an automated electrical test probe. On the other hand, FCT systems control all the intended functions of a PCB. However, since the hardware cost of these systems is relatively high, researchers focus on machine vision-based AOI algorithms instead of these systems. The AOI system detects defects with high-quality images using an industrial camera such as a CCD (charge-coupled device) or a Radiant vision camera equipped with a CMOS (complementary metal-oxide-semiconductor image sensor). The training phase performed by using various artificial neural networks for the PCB defects that can be encountered frequently in a real production environment is an important stage for the consistency of AOI systems (Kim et al., 2021).

To overcome unbalanced datasets that occur in the early production phase and do not contain all types of defects, Kim et al. (2021) performed image segmentation (image augmentation) to improve the model training performance. They proposed a skip-connected convolutional autoencoder for a PCB defect inspection system. The experimental results stated that the performance improvement process with a false pass rate below 1.7% and an accuracy of 98% by applying a simple unsupervised autoencoder model in 3900 imperfect and perfect images. Sezer and Altan (2021) proposed a deep learning model in which model parameters are estimated with a population-based optimization algorithm that imitates atomic motion to detect solder paste defects on PCBs in the early stages of the mass production process. Using AlexNet, which is among the CNN models, the 55% accuracy rate for six types of defect classes (correct soldering, incorrect soldering, missing soldering, excess soldering, short circuit, and undefined object) is increased to 99.28% with the proposed hybrid ASO (Atom search Optimization)-CNN algorithm. Jia and Liu (2021) indicated that traditional detection and recognition algorithms based on automatic optical inspection (AOI) cannot accurately detect PCB defects since these algorithms highly require visual cues. The authors proposed an ICCaNet deep convolutional neural network with a deeper structure and more complex parameters using the LeNet-5 structure to address these problems. The proposed deep neural network model is compared to popular CNN methods, and it is observed that the ICCaNet model achieved a 97.73% average accuracy rate. Lan et al. (2021) improved the advanced reasoning speed of the model by adding Batch normalization to the convolutional layer in the YOLOv3 object detection algorithm, and they shortened the training time required to detect PCB defects. They aimed to solve the low detection efficiency and high missed detection rate problems in PCB surface defect detection. In addition, they increased the detection performance of the model for small and medium-sized defects on the PCB by using the GIoU (Generalized Intersection over Union) performance metric and loss function instead of the unchanged objective function and evaluation metrics in the

YOLOv3 network. In the third step, they used the K-means++ clustering algorithm to optimize the appropriate anchor boxes in the PCB defect dataset they used. Finally, multi-scale training is applied to increase the robustness of the model to detect images at different resolutions. As a result of the validation of this method in the experimental environment, a mAP (mean average precision) value of 92.13% is obtained, and the detection rate is increased by 63f/s compared to the traditional YOLOv3 method.

3. Proposed Method

3.1. YOLOv4 Architecture

The YOLOv1 algorithm is firstly proposed by Redmon et al., (Redmon et al., 2016). YOLO is an object detection algorithm based on convolutional neural networks, and it is frequently used in real-time object detection applications since it has faster and more successful results than algorithms using other convolutional neural networks (CNN). Among various CNN algorithms, R-CNN (Girshick et al., 2014), Fast R-CNN (Girshick, 2015), and Faster R-CNN (Ren, 2015) are region-based CNN algorithms, and they perform object detection in two stages. In the first stage, object boundaries are detected. In the second stage, convolutional neural network classifiers are executed for the detected regions. Since the object detection process is performed in two stages, the processing time is prolonged. In the YOLO algorithm, the image is passed through the convolutional neural network in a single step and the output class of the predicted object and the bounding box coordinates of the object are obtained. The YOLO algorithm first divides the input image into $S \times S$ -sized grids. Each grid cell in the image is responsible for determining whether the object exists or not. Furthermore, the grid cell is responsible for determining the attribute information (x , y , w , h , confidence score, class) of the predicted object. The YOLOv4 algorithm was published by Bochkovskiy et al. (2020). Bochkovskiy et al. (2020) created a new version of the YOLO algorithm that can be trained quickly on a single graphics processing unit (GPU) and generates more accurate results. To obtain high accuracy in information retrieval, the effects of Bag-of-Freebies and Bag-of-Specials techniques are examined, and the most suitable ones for the algorithm are used. The general architecture of YOLOv4 is shown in Figure 2.

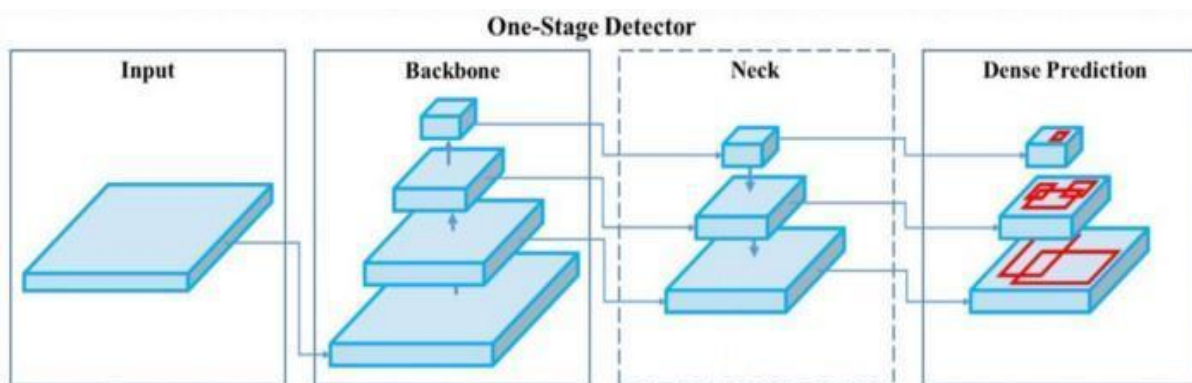


Figure 2: YOLOv4 Architecture (Wang et al., 2020)

YOLOv4 consists of an input image, backbone network, Neck and Head (Dense Prediction) parts. In the YOLOv4 model, the CSPDarknet53 (Wang et al., 2020) neural network is used as a backbone network. CSPDarknet53 performs splitting and merging operations on the feature map to provide more gradient flow from the network. YOLOv3 is used in the head of the YOLOv4 model. YOLOv4 has increased AP (average precision) by 10% and fps by 12% compared to the YOLOv3. In this study, the YOLOv4 algorithm, widely used in real-time object detection applications, is used for defects that may occur on PCB surfaces during the production phase.

3.2. Dataset

In this study, PCB surface data published by The Open Lab on Human-Robot Interaction of Peking University ("<http://robotics.pkusz.edu.cn/resources/dataset/>") is used to detect PCB defects. In the dataset, six different types of defects are defined for PCB surface: missing hole, mouse bite, open circuit, short, spur, and spurious copper. The type of defects, the number of images, and the total number of defects for each defect type are shown in Table 1. We split the dataset into 20% for testing, 20% for validation, and 60% for training data.



Table 1:PCB defect dataset

Type of defects	Number of images	Number of defects
Missing hole	115	497
Mouse bite	115	492
Open Circuit	116	482
Short	116	491
Spur	115	488
Spurious copper	116	503
Total	693	2953

3.3. Dataset Labeling

To label each defect in the dataset, we used the LabelImg program to determine the coordinates of PCB defects in the images in the data set. All images in the data set are individually labeled, and the coordinates of the PCB defects are recorded in YOLO format. When the YOLO format is used in the LabelImg program, the program creates a .txt file containing the class and coordinate information of the labeled object of each image file. In the labeling process, we aimed to increase the probability of the algorithm recognizing the defects by taking care not to exceed the boundaries of the defects in the images. A sample visual of the labeling process of images is given in Figure 3.

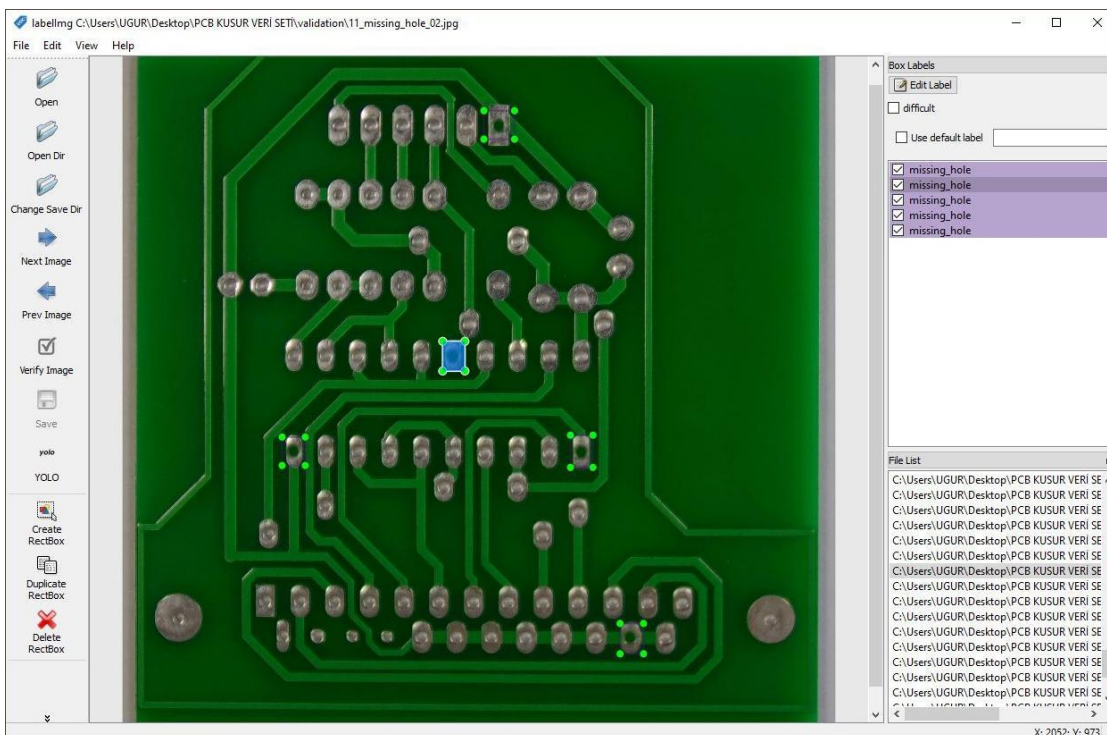
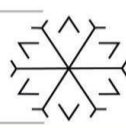
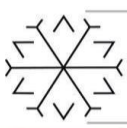


Figure 3: The process of labeling images

3.4. Training

The YOLO algorithm requires some parameters and files to train using the Darknet backbone. The configuration file contains the structure of the YOLO algorithm. It has some parameters that affect the speed, success and processing load of the network. For this reason, “yolov4-custom.cfg” from the Darknet library is used and edited



for the PCB defect dataset. In the configuration file, the number of classes and, accordingly, the value of the last layer of the existing network model has been changed. After the configuration file is set, the file with the extension ".names" with the class names and the file with the extension ".data" where the file paths of the training and test data are specified. Then the ".cfg", ".names", ".data" files required for the training are set, the training phase is started using the "yolov4.conv.137" file as the starting weights. The training process is carried out on the GPU on a computer with Intel(R) Core(TM) i5-7400 CPU 3.00 GHz processor, NVIDIA GeForce RTX 2080 8GB GPU. Model training is carried out in 52 hours as 12000 iterations. In Figure 4, the mean average precision (mAP) and loss function values of the training results are shown graphically. The loss function measures the error rate and performance of the trained model. The loss function calculates how much the prediction made by the model differs from the ground truth. So, the loss value should be low in a successful model. mAP is a metric used to measure the accuracy of object detection. The mAP value shows how much the bounding box of the detected object and the actual bounding box of the object overlap. A successful model should have a high mAP value.

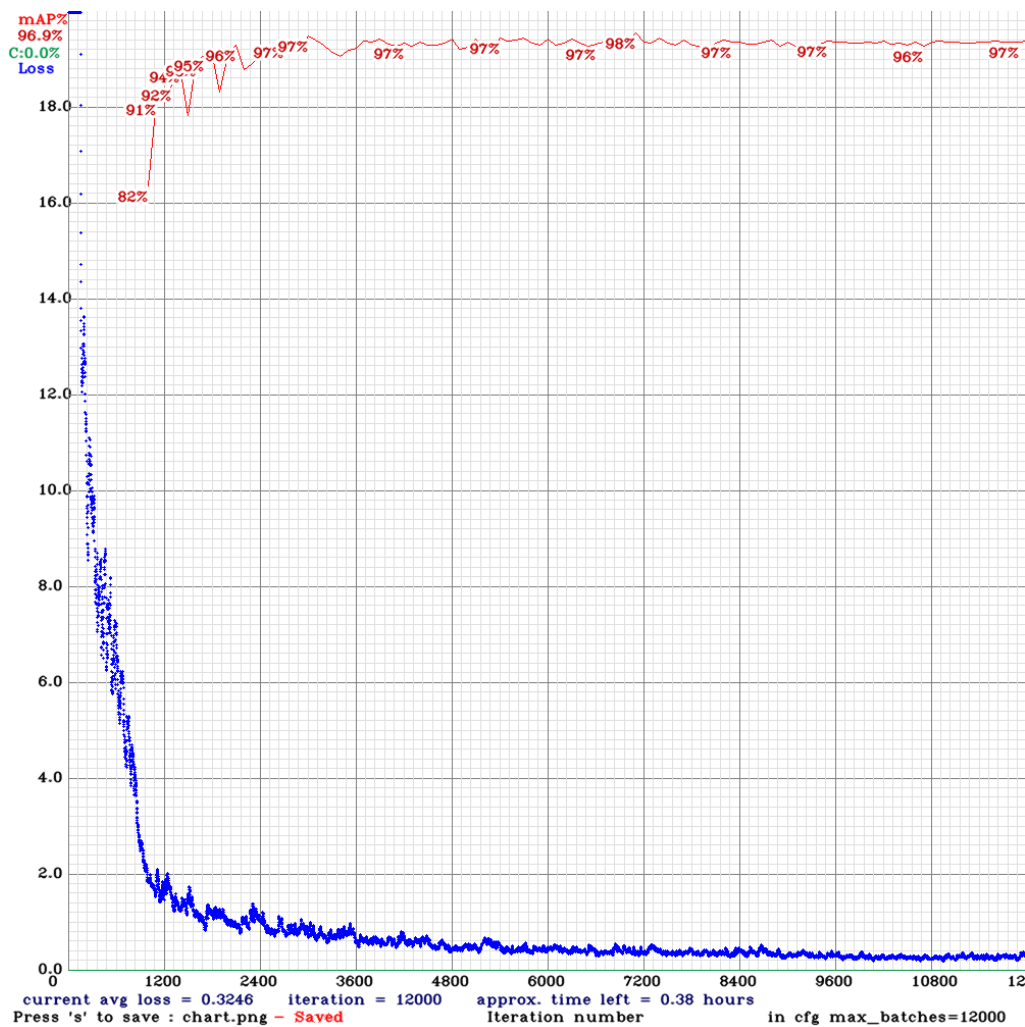


Figure 4: Evaluation of mAP and loss values (red curve: mAP value, blue curve: Loss function) by training iterations.

Figure 4 illustrates that the highest mAP value (98%) is obtained between 6000-7200 iterations during the training phase. In the experimental results section, the weight values with the highest mAP value are used in the experiments on the test set.

4. Experimental results

To evaluate the performance of the model created during the training phase, it is necessary to determine how many defects on the test images are detected correctly and how many faults are detected incorrectly. The IoU



(Intersection over Union) value is used as the threshold value in the evaluation process. IoU is an evaluation metric that measures the similarity between the detected defect's bounding box and the defect's actual bounding box. The IoU score ranges from 0 to 1; the closer the two boxes are, the higher the IoU score. $\text{IoU} \geq 0.5$ is used as general acceptance to convert the detection of a defect into classification. It means that if the IoU value of the detected defect is bigger and equal to 0.5, defect detection is classified as True Positive (TP). In comparison, if the IoU value is smaller and equal to 0.5, it means that this is a false detection and classified as False Positive (FP). When a defect is available in the image and the model cannot detect it, it is classified as False Negative (FN). Firstly, TP, FP, and FN values are obtained for different IoU values using the images in the test set. Then, precision, recall, and F1-score metrics are calculated using the obtained TP, FP, and FN values. The obtained value is given in Table 2.

Table 2: The performance evaluation on the test dataset according to different IoU threshold values

IoU Threshold	TP	FP	FN	Precision	Recall	F1 Score
10 %	574	24	17	0.96	0.97	0.97
20 %	570	18	21	0.97	0.96	0.97
30 %	566	17	25	0.97	0.96	0.96
40 %	564	16	27	0.97	0.95	0.96
50 %	564	15	27	0.97	0.95	0.96
60 %	564	14	27	0.98	0.95	0.96
70 %	562	13	29	0.98	0.95	0.96
80 %	559	12	32	0.98	0.95	0.96
90 %	550	8	41	0.99	0.93	0.96

When Table 2 is examined, it is seen that the created model has successful results on the test set. The $\text{mAP}@0.5$ value on the test set of the model is calculated as 97%. In Figure 5, identified sample defects applying the YOLOv4 algorithm for the six test set images.

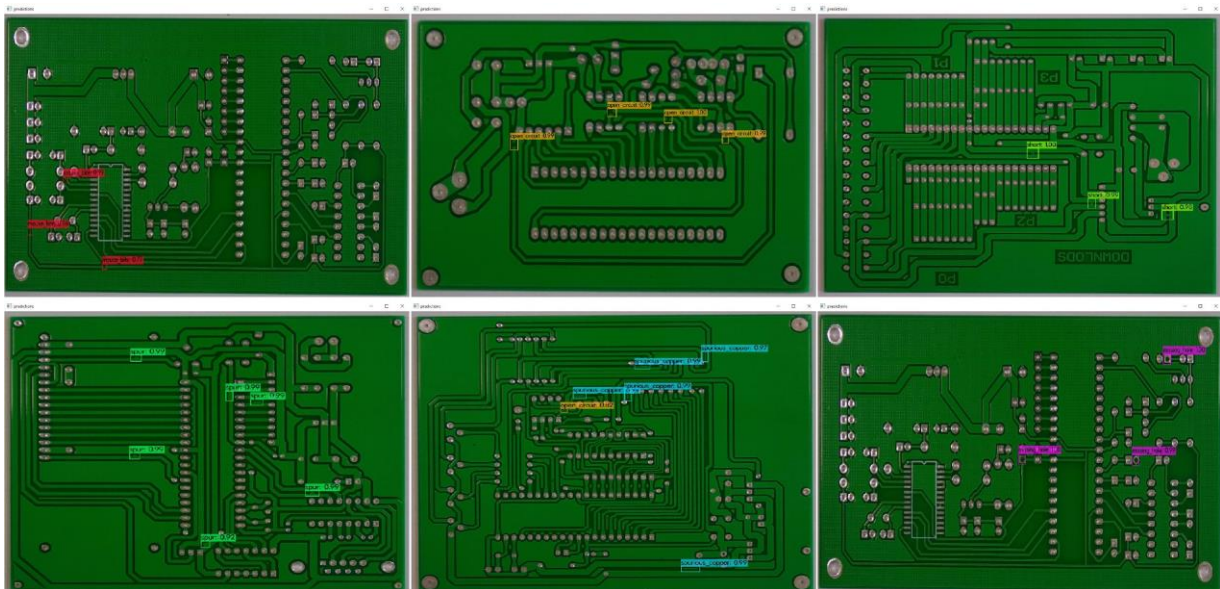
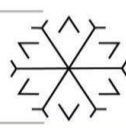
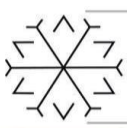


Figure 5: Experimental results of the model on the test dataset



The experimental results of the model according to defect types at 50% IoU threshold value are listed in Table 3. When Table 3 is examined, it is seen that the "spur" defect type decreases the success of the model, and spur defect appears to be more challenging to distinguish from other defects.

Table 3: Defect-based results of the model in the test set at 50% IoU threshold

Defect Type	TP	FP	Average Precision
Missing hole	101	1	99.74
Mouse bite	91	3	98.64
Open circuit	93	3	97.21
Short	97	1	98.33
Spur	85	5	89.81
Spurious copper	97	2	98.21

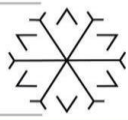
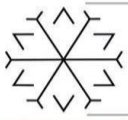
5. Conclusion

In this study, six fundamental manufacturing defects that frequently occur in small-sized electronic printed circuit boards produced with computer-aided design tools are detected with the model created using a machine vision-based algorithm named YOLOv4. The success of the model created from the experimental results is calculated to be 97% at mAP@0.5. It has been observed that spur defect decreases the success of the model. It is thought that the success of the model can be increased by increasing the number of images with Spur defects in the training set.

In future studies, PCB serial conveyor belt mechanisms will be established for new experimental studies. In addition, the training dataset will be expanded by capturing new PCB surface images, and PCB surface defects will be detected in a real-time environment using the serial conveyor band assembly.

References

- Caliskan, A. and Gurkan, G., 2021, August. Design and Realization of an Automatic Optical Inspection System for PCB Solder Joints. In 2021 International Conference on INnovations in Intelligent SysTems and Applications (INISTA) (pp. 1-6). IEEE.
- Huang, W. and Wei, P., 2019. A PCB dataset for defects detection and classification. arXiv preprint arXiv:1901.08204.
- Kim, J., Ko, J., Choi, H. and Kim, H., 2021. Printed circuit board defect detection using deep learning via a skip-connected convolutional autoencoder. *Sensors*, 21(15), p.4968.
- Sezer, A. and Altan, A., 2021, June. Optimization of deep learning model parameters in classification of solder paste defects. In 2021 3rd International Congress on Human-Computer Interaction, Optimization and Robotic Applications (HORA) (pp. 1-6). IEEE.
- Jia, X. and Liu, Z., 2021. Character Identification for Integrated Circuit Components on Printed Circuit Boards Using Deep Learning. *Journal of Electrical Engineering & Technology*, pp.1-16.
- Lan, Z., Hong, Y. and Li, Y., 2021, January. An improved YOLOv3 method for PCB surface defect detection. In 2021 IEEE International Conference on Power Electronics, Computer Applications (ICPECA) (pp. 1009-1015). IEEE.
- Redmon, J., Divvala, S., Girshick, R. and Farhadi, A., 2016. You only look once: Unified, real-time object detection. In *Proceedings of the IEEE conference on computer vision and pattern recognition* (pp. 779-788).
- Girshick, R., Donahue, J., Darrell, T. and Malik, J., 2014. Rich feature hierarchies for accurate object detection and semantic segmentation. In *Proceedings of the IEEE conference on computer vision and pattern recognition* (pp. 580-587).



Girshick, R., 2015. Fast r-cnn. In Proceedings of the IEEE international conference on computer vision (pp. 1440-1448).

Ren, S., He, K., Girshick, R. and Sun, J., 2015. Faster r-cnn: Towards real-time object detection with region proposal networks. Advances in neural information processing systems, 28, pp.91-99.

Bochkovskiy, A., Wang, C.Y. and Liao, H.Y.M., 2020. Yolov4: Optimal speed and accuracy of object detection. arXiv preprint arXiv:2004.10934.

Wang, C.Y., Liao, H.Y.M., Wu, Y.H., Chen, P.Y., Hsieh, J.W. and Yeh, I.H., 2020. CSPNet: A new backbone that can enhance learning capability of CNN. In Proceedings of the IEEE/CVF conference on computer vision and pattern recognition workshops (pp. 390-391).

Analyzing Pattern for Huge Databases

Nihirra Kakkar^{1*}

¹nihirracs@gmail.com, Brightlands School, India

Abstract

In today's scenario, size of database is growing at a tremendous speed and analyzing such data for various purposes is of utmost importance. In this paper, we have applied our methodology to datasets of different sizes and discussed the experiment results in analyzing the pros and cons of various models. We have given an implementation model for knowledge discovery from huge unlabeled temporal databases by employing a combination of HMM and K-means technique.

Keywords –pattern analysis, HMM, KMM, KM HMM, recursive model.

1. Introduction

With the huge growth of data (Chaiken et al., 2008), there has been a pressing issue to find tools and techniques to extract meaning information from this raw data and convert it into knowledge. For this, the data has to be analyzed by finding the patterns of the raw data and thereafter use these patterns to generate knowledgeable data. These can be achieved through data analyses, which involve simple queries, simple string matching, or mechanisms for displaying data (Kobayashi, et al., 1997). In general, unlabeled data is mined with the help of data clustering. Clustering (Kobayashi, et al., 1997, Hinneburg et al., 1998, Agrawal et al., 1998, Kaufman et al., 1990), as a robust tool of Knowledge Discovery, aims to find hidden patterns in datasets by “grouping data items together according to some criterion of closeness”.

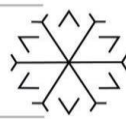
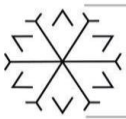
The functionality and effectiveness of KM HMM (Smyth et al., 1997, Babita et al., 2014, Babita et al., 2015) recursive model is first tested on one subset and its results are then backed up by different subsets of larger sizes. KM HMM (Smyth et al., 1997) stands for the model based clustering approach. It combines the power of K-means clustering with HMM, where K-means initializes the experiment by clustering the profiles. The resulting clusters are then used as an auto-labeling mechanism such that profiles that are grouped into the same cluster receive the same label.

The KM HMM model is able to group unlabeled data according to its underlying structure, i.e., patient's medical behaviors. The discovery is a data driven process which progresses through different hierarchical paths in unearthing the patterns in different age cohorts. Those patterns carry patient's medical information, and a proper interpretation could reveal some hidden but important knowledge such as a medical behavior pattern of aged diabetics or abnormal medical behavior pattern which could lead in fraud investigation. These are only few examples of application that can be achieved if some ground truth is made available.

We implement K-means clustering (Perrone et al., 2002) and Hidden Markov model (Kobayashi, et al., 1997) approach, referred as KM HMM (Babita et al., 2014, Babita et al., 2015) recursive model, on smaller subsets in order to obtain a first insight into the effectiveness of the approach (Babita et al., 2014), and to serve as a basis for comparisons when subjecting the same method to the entire set of data. Then, the findings are then combined to produce the best performing approach which is then applied to the entire set of data.

2. Literature Review

Several clustering algorithms are proposed by various researchers, like Partitioning clustering algorithms, such as K-means (Agrawal et al., 1998) and CLARA (Kaufman, et al., 1990) that assign objects into k clusters (predefined cluster number), that further iteratively reallocate objects to improve the quality of results



obtained from clustering. Although K-means is a popular clustering algorithm (Kobayashi, et al., 1997) which is easy-to-understand also but at the same time it is very sensitive to the selection of the initial centroids and has no general solution to find the optimal number of clusters for a given data set. Few authors have proposed Model-based clustering methods that are based on the assumption, that data is generated by mixture of underlying probability distributions and optimization with the help of models such as statistical approach, neural network approach and other AI approaches. The typical techniques in this category are Autoclas (Cheeseman et al., 1998), DENCLUE (Hinneburg et al., 1998) and COBWEB (Fisher et al., 1987) but they are facing a challenge of choosing a suitable one from the model based candidates. These clustering based approaches suffer from high computational cost, especially when the scale of data is very large. Another most commonly used model is HMM model, the Hidden Markov Model (HMM) which is based on statistical modeling. Encoding of temporal pattern has made this approach very popular. A number of variants of HMMs (Panuccio et al., 2002, Perrone et al., 2002, Smyth et al., 1997) exist like discrete HMM, continuous observation HMM, and input-output HMM, to name a few but they are also facing the challenge of heavy computational cost. To overcome these issues, we have proposed a recursive model which reduces the computational burden and to improve the quality of the model.

3. Proposed Model

In this section, our KM HMM approach is detailed through the application on one subset, then its functionality is further confirmed by applying the method on few other subsets. These preliminary experiments are important and necessary since they provide a vehicle to unfold the methodology. The step by step introduction of our method, the detailed discussions at the end of each step and the walk through of the sample profiles form the key in explaining the methodology.

3.1 Subset Selection

There are numerous ways in selecting reasonable subsets. What matters here is data quality: the selected subset has to be an unbiased representative of the data. We have divided the whole set of profiles into nine age cohorts, we decided to select one of the age cohorts to carry out our first experiment. Patients in age cohort 45-55 are well away from the female reproductive ages, and are still reasonably youthful as not to suffer from age related illnesses. Their profiles are not expected to be too complex to overly challenge the methodology. The data set is further downsized by constructing a rule-based selection e.g. particular illness based or gender.

The experiment and the results are presented here.

3.2 KM HMM Based Recursive Model:

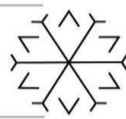
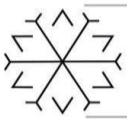
Using a fixed number of clusters for age cohort 45-55.

KM HMM (Smyth et al., 1997) combines the power of K-means clustering with HMM, such that profiles that are grouped into the same cluster receive the same label, whereas profiles in different clusters receive a different one. Thus, the profiles are labeled according to the cluster membership. While these labels do not carry any meaning (other than cluster membership), it allows the application of a supervised learning scheme such as HMM.

By creating a model (HMM) for each cluster, HMM learns to detect patterns in given time series data which best describe the data in a given cluster. The result is a set of HMMs, one for each cluster. The procedure can then be applied recursively to each of the pattern classes in order to further segment a dataset into ever smaller classes. In practice, our methodology is unfolded through the following two steps:

Step 1: K-means Clustering

The first step of the proposed pattern discovery methodology addresses the clustering of data. In our case, the data subjected to the experiments are patients' profiles. K-means (Perrone et al., 2002) clustering takes each profile as a 352 dimensional vector and calculates its distance towards centroids of each cluster, and



eventually assigns the profile to the cluster where the distance between the profile and the centroid reaches minimum.

Table1: Basic information for the K-Means Clustering algorithm.

Name of Cluster	Number of Profiles	Benefit Range in \$
Cluster 1	28,608	8.15-1181.85
Cluster 2	9,427	124.95-2303.65
Cluster 3	1,447	357.25-7894.00
Cluster 4	1,199	393.60-7159.40
Cluster 5	1,216	505.10-9070.65
Cluster 6	903	645.60-8232.35

K-means takes the initial parameters and performs data clustering. The cluster detected by K-means are then analyzed, and clusters smaller than 200 are discarded (by assigning the patterns to the remaining clusters). The application of K-means algorithm results in 6 clusters. The patterns in each cluster are then uniquely labeled as Cluster1, Cluster2, ..., Cluster6 respectively. The benefit here stands for the total benefit paid for a patient throughout the year where the profile is drawn against.

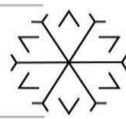
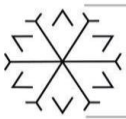
Step2: HMM Data Modeling and Recursive Mining

With HMM modeling (Kobayashi, et al., 1997), data is assessed according to contextual information embedded within the temporal sequence which we refer to as profiles. The process of estimating the values of these parameters is considered as the training of HMM models. For this experiment, a maximum 1,500 profiles are selected when the cluster size is over 2,000 (such as Cluster1 and Cluster2), otherwise 90% of the data from the cluster are subject to training (such as Cluster3 to Cluster6). Table 2 specifies the size of each training set.

Table2: Information of dataset in terms of its size in training hidden Markov model.

Cluster	Number of Profiles	Size of Training Set
Cluster 1	28,608	1,500
Cluster 2	9,427	1,500
Cluster 3	1,447	1,302
Cluster 4	1,199	1,079
Cluster 5	1,216	1,094
Cluster 6	903	812

For our experiments, we used the freely available, and well matured HMM software package known as HTK version 2.0. We customized the software package so as to allow the dealing with very large and gzip compressed databases. This was necessary since HMM is not normally suited to deal with data mining



tasks. One of the parameters that needs to be set when using the HTK 2.0 software package is the number of states in the HMM.

Following experiments are based on a left-right HMM with 3 states.

Table 3 provides the training results of the 6 HMMs in terms of mean and variance of each HMMs. However experiments on HMMs trained with more than one state were aborted due to lack of information.

Table 3: HMM training results: mean and variance of HMM

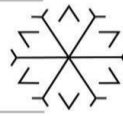
HMM Model	Mean Value	Variance Value
HMM1	6.128910e+00	5.203418e+02
HMM2	2.477937e+01	3.275482e+03
HMM3	4.600096e+01	1.269653e+04
HMM4	5.877817e+01	2.111918e+04
HMM5	6.670536e+01	2.268726e+04
HMM6	7.352632e+01	2.508250e+04

Class1 is the largest which attracts 27,740 profiles while Class5 is the smallest with only 186 profiles. It is observed that the K-means clustering algorithm and the hidden Markov model grouped the profiles differently. Upon closer inspection of the K-means clustering results when compared to the HMMs classification results, it can be stated that the HMM classification makes more sense. On a global scale the K-means clustering algorithm grouped the profiles as a whole profile, it works on the distance from the centroids to point of 352-dimensions. Hence at times it has grouped profiles which to the naked eyes appear to be quite different.

Table 4: Classification result by the HMM model with comparison to K-means Clustering

CLUSTER	CLASS 1	CLASS 2	CLASS 3	CLASS 4	CLASS 5	CLASS 6	TOTAL
CLUSTER 1	25,458	3,055	95	0	0	0	28,608
CLUSTER 2	2,274	6,005	1,003	82	10	53	9,427
CLUSTER 3	6	642	524	82	33	160	1,447
CLUSTER 4	1	246	501	123	56	272	1,199
CLUSTER 5	1	256	498	112	46	303	1,216
CLUSTER 6	0	92	377	95	41	298	903
CLUSTER 7	27,740	10,296	2,998	494	186	1,086	42,800

On the other hand, the hidden Markov model groups profiles together based on the time evolution of the profiles. The classification of profiles is the result of considering the context in which benefit is paid. For example, the hidden Markov model is able to assess whether a benefit paid is out-of-the-ordinary by considering the context within which the benefit was paid, this is an interesting observation given that the HMMs were trained on data labeled by K-means. This process should keep on continuing recursively till



further classification is possible. The process of Recursive mining allows the classes to be re-clustered into sub-clusters where the iterative mining will operate on each of the sub-clusters. The sub-clusters will then be modeled and iteratively mined by HMM so that new HMMs or patterns are discovered for each of the newly generated sub-clusters.

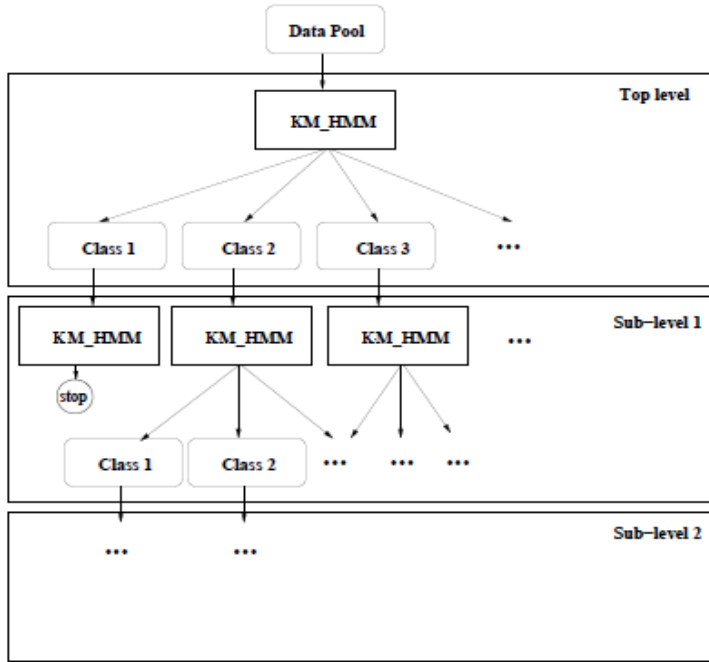


Figure 1: Recursive Refinement

The above figure shows the recursive process of our methodology. It demonstrates what has been done by the two processes of clustering and recursive mining: all the profiles in the data pool of a particular age group are subdivided and processed to get a further level with the help of clustering, modeling, and iterative mining as was described above.

All profiles of the above table of age cohort of 45-55 year are classified by the set of 63 HMMs generated for this cohort group. The classification is performed as follows: a profile is presented to all 63 HMMs, and the HMM which responds with the highest likelihood value wins. i.e., the profile is classified into the class represents by the winning HMM. Finally, at the end of this recursive modeling, we would like to re-visit the 36 profile which have been discussed in step 1 and step 2.

The 63 final HMMs are applied in classifying these 36 profiles in order to illustrate how these profiles are grouped at the end of the iterative training procedure. It is observed that the final HMMs provide a much finer classification to the profiles.

4. Conclusion

In this paper, we have implemented our analytical algorithm i.e. recursive KMM Model on a smaller subset and later on the complete set, in order to understand the effectiveness of KM HMM model. The distinctiveness of our model is the way the clustering KM HMM is applied on the dataset. Initially, to overcome the weakness of HMM on large datasets, we have applied the model iteratively. Also, in place of applying the model on entire dataset in one go by understanding all profiles of training set, we have done the mining iteratively in a controlled manner.

This helps to keep the training time in acceptable limits while keeping the model refined in each iteration. We analyzed through the implementation model of KM HMM recursive model that we are getting more refined data as compared to K-means model. Thus iterative process makes HMM available for modeling a large set

of data and maintains the known asset and the strength of HMMs. In our further study, we will take larger dataset and find the efficiency of this model and also compare it with other existing models.

5. References

- ,R.,Jenkins, B. and Larson, P. (2008)‘Easy and Efficient Parallel Processing of Massive Data Sets’ , *PVLDB*, 1(2):pp1265–1276.
- Kaufman, L. andRousseeuw, P. (1990) ‘Finding Groups in Data: an Introduction to Cluster Analysis’.
- Kobayashi, S. (1997) ‘Partly-hidden markov model and its application to gesture recognition’ *IEEE International Conference on Acoustics, Speech and Signal Processing*, Vol.4, pp 3081–3084.
- Hinneburg, A. and Keim, D. (1998)‘An Efficient Approach to Clustering in Large Multimedia Databases with Noise’*KDD*.
- Agrawal, R,Gehrke,J. and Raghavan, D. (1998)‘Automatic subspace clustering of high dimensional data for data mining applications’*ACM SIGMOD Conference*, pp.94-105 .
- Sheikholeslami, G. ,Chatterjee, S. and Zhang, A.(1998)‘Wave cluster: A multi-resolution clustering approach for very large spatial databases’ , *Very Large Databases Conference*, pp.428-439.
- Panuccio, A.Bicego, M. and Murino, V.(2002) ‘A hidden markov model-based approach to sequential data clustering’ *Joint IAPR International Workshops SSPR 2002 and SPR 2002*, pp 734–743.
- Perrone, M. and Connell, S.(2000)‘K-means clustering for hidden markov models’*7th International Workshop on Frontiers in Handwriting Recognition*, pp 229–238.
- Smyth, P.(1997) ‘Clustering sequences with Hidden Markov Models’ *Advances in Neural Information Processing Systems* Vol.9, pp648–654.
- Babita, S. and Rawat, P. (2014)‘An Approach to Analyze Pattern from Large Database of Healthcare’
- Babita, S. and Rawat, P. (2015)‘Analysing Patterns for Huge Databases’ *International Journal of Engineering and Innovative Technology (IJEIT)* Vol 4(1), pp 187-191.
- MacQueen, J. (1967)‘Some Methods for classification and Analysis of Multivariate Observations’ *5th Berkeley Symposium on Mathematical Statistics and Probability*, University of California Press, pp.281-297.
- Kaufman, L. and Rousseeuw, P. (1990)‘Finding Groups in Data: an Introduction to Cluster Analysis’ John While & Sons.
- Jiang, D. ,Tung, A. and Chen, G. (2010) ‘ Map-join-reduce: Towards Scalable and Efficient Data Analysis on Large Clusters’ *TKDE*, 23(9):1299–1311.
- Han, S., Chen, D. and Mok, A.(2008) ‘Online Scheduling Switch for Maintaining Data Freshness in Flexible Real-Time Systems’*RTSS*, pp. 115–124.
- Xiong, Y. and Yeung, D. (2002)‘Mixtures of arma models for model-based time series clustering’ *IEEE International Conference on Data Mining* pp 717–720.
- Cheeseman, P., Kelly, K., Self, M. and Freeman, D. (1998) ‘AutoClass: A bayesian classification system’, *5th International Conference on Machine Learning*, pp. 54-64
- Fisher, D.(1987) ‘Improving Inference through Conceptual Clustering’ *AAAI Conferences*, pp.461-465.

Investigation of The Initialization Contour Effect In The Chan-Vese Method

Nurullah OZTURK ¹[0000-0001-7766-6757] and Serkan OZTURK ²[0000-0002-0309-3420]

¹nurullah.ozturk@amasya.edu.tr, Amasya University, Gumushacikoy Hasan Duman Vocation School, Amasya, Turkey

²serkan@erciyes.edu.tr, Erciyes University, Department of Computer Engineering, Kayseri, Turkey

Abstract

Image segmentation is the process of separating the image into meaningful regions. The success of the segmentation process depends on proper initial contour selection and correct convergence of the contour. The location and size of the initialization contour can cause the method to be stuck at the local minimum, segmentation of the wrong regions, and increase the number of steps. Therefore, initialization contour selection is very effective in the success of the method. In this paper, effective initialization contour selection has been investigated for the region-based Chan-Vese method. Initialization contours of different sizes and positions have been applied on different types of images, and image segmentation successes have been examined. Experimental results have shown that multiple contour selection is an effective initial contour and eliminates the local minima problem for the Chan-Vese method.

Keywords. Image segmentation, Chan-Vese method, initialization contour

1. Introduction

Image segmentation is an important image processing method that divides the image into meaningful parts by grouping pixels with similar characteristics. The purpose of segmentation is to make the image more understandable for analysis by reducing the complexity of the image. Therefore, it is very important to perform segmentation with absolute accuracy. It is used for image analysis, target extraction, and recognition in image processing applications such as image segmentation, medical imaging, satellite imaging, and industrial vision systems. Various factors such as noise effect, light change, image quality, various types of patterns, variable dynamic topological structures, changes in the size and scale of the object can adversely affect the performance of the segmentation method and obtain different results. Therefore, since there has been no generally applicable segmentation method, segmentation has been performed according to the encountered situation. In the literature, many methods have been proposed for image segmentation (Kumar ve Srivastava, 2017; Liu et al., 2018; Haiping et al., 2020).

Kass et al. proposed the active contour method known as the snake model (Kass et al., 1987). This method is an energy-based and deformable segmentation model. Therefore, the active contour methods are widely used in many different fields. The active contour methods enable the region to be found and segmented by expanding or shrinking a closed contour near the object to be in accordance with the given constraints. In these methods, three forces cause deformation of the contour. The image energy provides the contour moving to areas such as lines and edges. The internal energy of the given contour controls whether the shape is round or has sharp lines. The external force of the contour is responsible for the convergence of the contour to the searched region. The sum of these forces has been expected to be less than the specified value. If it is not small, the contour is moved, and the energies are recalculated. Active contour methods are based on the energy minimization principle for the correct convergence. The Chan-Vese method is the most popular active contour method (Chan and Vese, 2001). The Chan-Vese method is a region-based method instead of the image gradient information in the segmentation process. It provides more successful segmentation in images with blurred edge information or noise.

Initialization contour selection is a common problem for the active contour segmentation methods. Because the given initialization contour can cause the method to get stuck in the local minimum, segmentation of wrong regions, or by increasing the number of steps of this method, to affect the performance negatively. In this paper, an effective contour selection study has been carried out by examining the performance of different initial contours on the Chan-Vese method.



The organization of the paper is as follows. Literature reviews are given in Section 2. In Section 3, the Chan-Vese method is described. The proposed method is explained in Section 4. The experimental results and analysis are demonstrated in Section 5. The conclusion is given in Section 6.

2. Related work

Many different methods have been proposed to overcome the initialization contour problem. Çataloluk and Çelebi proposed a hybrid segmentation method that used the gravitational search algorithm and Chan-Vese methods for the solution of the initial contour problem of the Chan-Vese method (Çataloluk and Çelebi, 2018). Liu and Peng suggested the local region-based Chan-Vese method to provide more successful segmentation for inhomogeneous images by reducing the dependency on the initial contour (Liu ve Peng, 2012). Wang et al. presented a method using the Chan-Vese method and the Sobel operator. In this study, images were segmented with both the Chan-Vese method and the Sobel operator, and an effective segmentation was achieved by combining the obtained results (Wang et al., 2018). Mandal et al. developed the new segmentation method using the Chan-Vese method and the particle swarm algorithm to solve the local minima and initialization contour of the Chan-Vese method for medical images (Mandal et al., 2014). Xu et al. proposed a new method using the Chan-veese method with global statistical information to overcome the sensitivity to the initial contour in the Chan-Vese method (Xu et al. 2017). Wang et al. suggested a new active contour method that used both local and global Gaussian distribution fitting energies to reduce sensitivity to the initialization contour (Wang et al., 2014). Wang et al. offered the local Chen-Vese model, which was based on techniques of curve evolution, local statistical function and level set method and was more successful in segmentation (Wang et al., 2010). Lan et al. proposed a hybrid segmentation method based on thresholding and the Chen-Vese method to improve the initialization contour problem (Lan et al., 2012). Jamaludin et al. presented a new segmentation method for improving the convergence speed of the Chan Vese method (Jamaludin et al., 2015).

In this paper, the segmentation effect of different initiation contours in the Chan-Vese method has been investigated. It has been aimed at determining the effective contour for the method by applying the initial contours of different sizes and features to images with different characteristics.

3. Chan-Vese method

The Chan-Vese method is the most widely used active contour method derived from the Mumford-Shah segmentation method (Chan and Vese, 2001). The method starts with a closed curve. This curve then finds the object boundaries to be segmented by expanding or contracting according to the constraints of the image. In the method, segmentation is done by minimizing the energy function and it uses the level set function to solve the energy function. The energy function of the Chan-Vese method is given in Eq. (1).

$$F(C, c_1, c_2) = \mu \cdot \text{Lenght}(C) + v \cdot \text{Area}(\text{in}(C)) + \lambda_1 \int_{\text{in}(C)} |I(x, y) - c_1(C)|^2 dx dy + \lambda_2 \int_{\text{out}(C)} |I(x, y) - c_2(C)|^2 dx dy \quad (1)$$

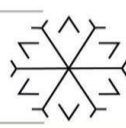
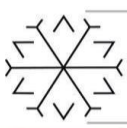
where I and C represent the given image and contour, respectively. c_1 and c_2 are the constants connected to C . c_1 is the average pixel intensity inside C , and c_2 is the average pixel intensity outside C . λ_1 and λ_2 are positive constants that provide the smoothness of the inner and outer boundary of C , respectively. μ controls the smoothness of the evolving C curve, while v penalizes the inner area of the boundary.

The level sets function is a two-dimensional $\phi(x, y)$ Lipschitz function and is applied to represent the boundary value. In the Lipschitz function, when $\phi(x, y) = 0$ it is on the C curve, $\phi(x, y) > 0$ means it is outside the C curve, and $\phi(x, y) < 0$ means it is inside the C curve (Chan and Vese, 2001).

The rearrangement of C according to the level set function in the Chan-Vese method is shown in Eq. (2).

$$F(c_1, c_2, \phi) = \mu \int_{\Omega} (\phi(x, y)) |\phi(x, y)| dx dy + v \int_{\Omega} H(\phi(x, y)) dx dy + \lambda_1 \int_{\Omega} |I(x, y) - c_1|^2 H(\phi(x, y)) dx dy + \lambda_2 \int_{\Omega} |I(x, y) - c_2|^2 (1 - H(\phi(x, y))) dx dy \quad (2)$$

In this energy function, H is the Heaviside function and δ is Dirac delta function. This function is used to ensure that the transitions of the C curve from zero to 1 and from 1 to zero are not abrupt. In this way, the stability of the method is ensured. The Heaviside function and Dirac delta function are given in Eq. (3).



$$H(\phi) = \frac{1}{2} \left[1 + \frac{2}{\pi} \arctan \left(\frac{\phi}{\varepsilon} \right) \right] \quad (\phi) = \frac{1}{\pi} \frac{\varepsilon}{\varepsilon^2 + \phi^2} \quad (3)$$

To minimize the energy function with respect to c_1 and c_2 , ϕ is fixed. Obtained c_1 and c_2 are given in Eq. (4).

$$c_1 = \frac{\int_{\Omega} I(x, y) H(\phi(x, y)) dx dy}{\int_{\Omega} H(\phi(x, y)) dx dy} \quad c_2 = \frac{\int_{\Omega} I(x, y) (1 - H(\phi(x, y))) dx dy}{\int_{\Omega} (1 - H(\phi(x, y))) dx dy} \quad (4)$$

The function used for energy minimization of the Chan-Vese equation (Eq.(2)) is given below.

$$\frac{\partial \phi}{\partial t} = (\phi) \left(-\lambda_1 (I - c_1)^2 + \lambda_2 (I - c_2)^2 + \mu \operatorname{div} \left(\frac{\nabla \phi}{|\nabla \phi|} \right) - v \right) \quad (5)$$

Chan-Vese performs multidimensional segmentation on images. However, the initialization contour has an important effect on the success of the method. It causes segmentation of the wrong regions in the image, increasing the run time and the number of steps of the method.

4. Proposed method

Effective initial contour selection has been investigated to eliminate the local minima problem of the Chan-Vese method and obtain efficient image segmentation. In the proposed study, different initial contours have been used such as small, large, and multiple. The basic steps of the proposed method are as follows:

1. Get the image I and the parameter values.
2. Select the initial contour C .
3. Calculate image intensities, c_1 and c_2 by using Eq. 4.
4. Calculate the energy minimization of the Chan-Vese by using Eq. 5.
5. Control the evolution of the contour. If it is not stable, repeat steps 3–5.
6. Calculate the fitness values and to evaluate the new initialization contour. Go to step 2.

In the proposed method, the Chan-Vese method has been applied by choosing different initial contours for each image. Then, the fitness values determined for the segmentations that were obtained have been calculated. Finally, by evaluating all the results obtained, effective contour selection for the Chan-Vese method has been decided.

5. Experimental results

In the Chan-Vese method, an effective initial contour determination has been carried out to eliminate the local minimum problem and obtain successful segmentation results. Matlab 2018b program has been used in the experimental application. Among the parameters in the Chan-Vese method, the values of λ_1 and λ_2 have been accepted as constant 1. While v value is 0, μ value is kept constant as 0.1. The Aircraft and Eagle images in Figure 1 and Figure 2 have been selected from the Berkeley library (Berkeley Database). The results obtained have been evaluated according to the number of steps (Iter), Dice (DC), and Jaccard (JC) coefficients to determine the effective initialization contour.

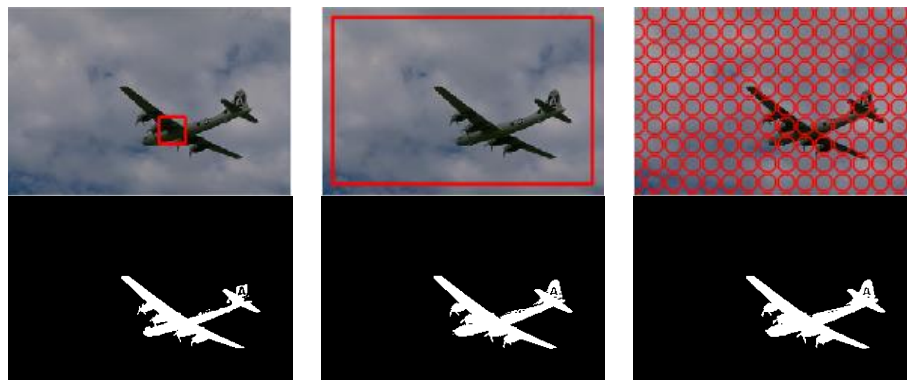


Figure 1: The effect of different initial contour in the Aircraft image.

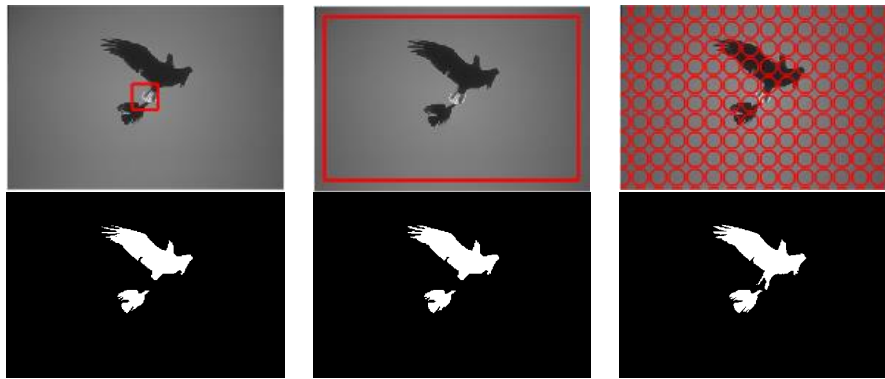


Figure 2: The effect of different initial contour in the Eagle image

In the Chan-Vese method, the effect of the initialization contour given on images with a single object, two objects, and multiple objects has been examined. The small initial contour is set above the object region. Because choosing the contour on a different region may cause the method to segment incorrect or unnecessary areas. In Figure 1, the selection of the small contour in the aircraft image has failed to define the upper part of the fuselage and the tail zone exactly. Large contour and multiple contour selections have been obtained similar results. In Figure 2, different contour selections have given close segmentation results in the eagle image. But the small contour has been applied in the rice image in Figure 3 could not detect all the rice grains. However, large contour and multiple contour applications have shown similar segmentation results.

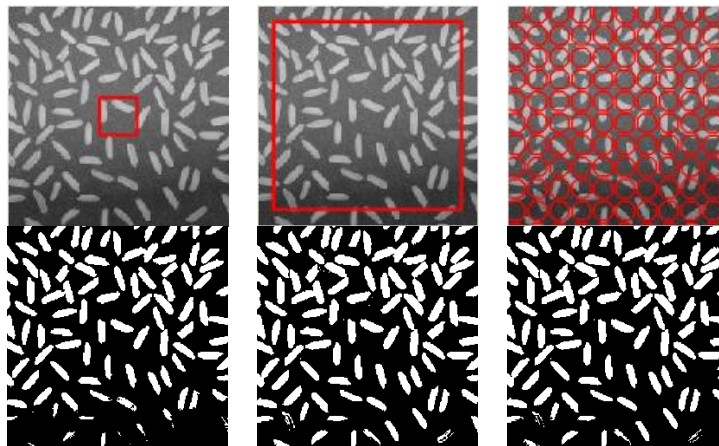


Figure 3: The effect of different initial contour in the rices image

Iteration (iter), Dice (DC), Jaccard (JC) indices have been used to evaluate the segmentation results objectively. Iteration has been used to evaluate the speed performance of the method. The Jaccard similarity index is used to calculate the similarity and difference between two sets of images as the obtained segmentation image and the reference image. JC is defined as follows.

$$JC(A, B) = \frac{|A \cap B|}{|A \cup B|} \quad (6)$$

where A represents the obtained image as a result of the applied contour, and B represents the reference image. The Dice measure is similar to the Jaccard index measurement. It is also used to evaluate the performance of the segmentation method. DC is defined as follow.

$$DC(A, B) = \frac{2 * |A \cap B|}{|A| + |B|} \quad (7)$$

The higher the JC and DC criteria values, the more successful the method is in image segmentation. Objective evaluation results are given in Table 1.

Table 1: Objective evaluation results.

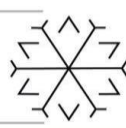
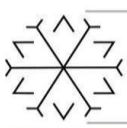


Image	Contour	Iter	JC	DC
Aircraft	Small	840	0.7785	0.8754
	Big	1270	0.8638	0.9269
	Multiple	1050	0.8849	0.9389
Eagle	Small	550	0.8303	0.9073
	Big	51	0.8528	0.9206
	Multiple	170	0.9300	0.9637
Rice	Small	5320	0.8243	0.9037
	Big	10000	0.8515	0.9256
	Multiple	1146	0.8602	0.9348

When Table 1 is evaluated as Iter, the success of the contour selection in the applied images varies. But in general, the multi-contour method is more successful for Iter. When DC and JC are evaluated, the multiple contour selection method achieves the highest success.

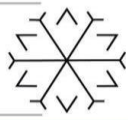
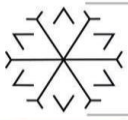
In general, multiple initialization contour selection has provided both the advantage of detecting details in the image of the small contour and the advantage of searching the entire image of the large contour, providing effective segmentation in the image.

6. Conclusions

In this study, an improvement has been made for effective initialization contour selection in the Chan-Vese method. Initialization contours of different sizes and positions are applied to images. For small contour selection, the contour must be set on the object region to be segmented. However, this method may fail to search the entire image surface. Large contour selection may cause unnecessary or wrong region segmentation in the image. However, it explores the whole image surface. Multiple contour selection is more effective in image segmentation due to the advantages of other methods. Experimental results show that multiple initial contour selection in the Chan-Vese method provides more successful and effective segmentation without being stuck to the local minima.

References

- Kumar N, Srivastava V. (2017) The Different of Digital Image segmentation Techniques: A Review. IJCTT, vol. 49, no. 2, pp. 76-82.
- Liu X, Deng Z, Yang Y. (2018) Recent progress in semantic image segmentation. Artificial Intelligence Review, pp. 1-18.
- Haiping Y, He F, Pan Y. (2020) A survey of level set method for image segmentation with intensity inhomogeneity. Multimedia Tools and Applications 79(39), pp. 28525-28549.
- Kass M, Witkin A, Terzopoutlos D. (1987) Snakes: Active contour models. International Journal of Computer Vision, pp: 321-331.
- Chan T, Vese L. (2001) Active contour without edges. IEEE Trans. Image Process. 10 (2) pp. 266-277.
- Çataloluk H, Çelebi F V. (2018) A novel hybrid model for two-phase image segmentation: GSA based Chan-Vese algorithm. Engineering Applications of Artificial Intelligence 73, pp. 22-30.
- Liu S, Peng Y. (2012) A local region-based Chan-Vese model for image segmentation. Pattern Recognition 45(7), pp.2769-2779.
- Zhibin W, Wang K, Yang F, Pan S, Han Y. (2018) Image segmentation of overlapping leaves based on Chan-Vese model and Sobel operator. Information processing in agriculture 5(1), pp.1-10.
- Mandal D, Chatterjee A, Maitra M. (2014) Robust medical image segmentation using particle swarm optimization aided level set based global fitting energy active contour approach. Eng. Appl. Artif. Intell. 35, pp. 199-214.



- Xu H., Jiang G., Yu M., and Luo T., (2017) A global and local active contour model based on dual algorithm for image segmentation, *Comput. Math. with Appl.*, vol. 74, no. 6, pp. 1471–1488.
- Wang, H., Huang, T. Z., Xu, Z., & Wang, Y. (2014). An active contour model and its algorithms with local and global Gaussian distribution fitting energies. *Information Sciences*, 263, 43-59.
- Wang, X. F., Huang, D. S., & Xu, H. (2010). An efficient local Chan–Vese model for image segmentation. *Pattern Recognition*, 43(3), 603-618.
- Lan, H., Zhang, L., & Wang, X. (2012). Initialization techniques for Chan-Vese model with thresholding. In *Applied Mechanics and Materials* (Vol. 198, pp. 227-232). Trans Tech Publications Ltd.
- Jamaludin, S., Zainal, N., & Zaki, W. M. D. W. (2015, November). Fast and accurate iris localization based on improved Chan-Vese active contour model. In *2015 IEEE 3rd International Conference on Smart Instrumentation, Measurement and Applications (ICSIMA)* (pp. 1-6). IEEE.
- The Berkeley Segmentation Dataset and Benchmark
<https://www2.eecs.berkeley.edu/Research/Projects/CS/vision/bsds/>. Accessed: 10 April 2021.

IoT Enabled Technologies: Associated Issues and Challenges

Vidhita Mittal^{1*}

¹emvidhitacs@gmail.com, Welham Girls' School, India

Abstract

Technologies are sprawling with additions to IoT. It has emerged as an area of unbelievable potential and growth of new infrastructure and technology. It becomes a boon for humanity with lot of advantages and is trying to empower the inanimate physical objects to act without any human intervention; its centric concepts like augmented reality, smart city, self-driven cars, smart environment, e-health care, etc. have a ubiquitous presence now. While these applications require higher data-rates, large bandwidth, increased capacity, low latency and high throughput. In light of these emerging concepts, this paper reviews the enabling technologies of IoT that makes possible to predict futuristic techniques. It also shed light on concerned issues and challenges faced by these enabling technologies with their perspective solutions. Furthermore, it focuses on art of current state and future research directions of IoT.

Keywords -Internet of Things (IoT),Wireless Sensor Network (WSN),Big Data Analytics, Cloud Computing

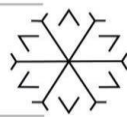
1. Introduction

TheInternet of Things or IoT has been originating a new revolutionary world from smart refrigerator to wearable technologies and from smart homes to smart conurbation soon (Eason et al., 2017). It is an emerging technology that facilitates modern human lives (Gatsis et al., 2017) by using internet to enables the communication based on IP between electronic devices and sensors. The objectives of IoT is not just allowing billions of devices communicate simultaneously but also taking business decision making and automating diverse processes. It also helps to overcome many challenges, through increased capacity and Artificial intelligence and enhancing a new web era.

The term IoT was devised by Kevin Ashton in 1999 with reference to the supply chain management (Ahmed et al., 2016). The concept of IoT means “smartness”, an ability to independently obtain and apply knowledge (Atzori et al., 2010). Consequently, IoT refers to the “things or devices and sensors” that are smart, uniquely addressable based on their communication protocols, and are adaptable and autonomous with inherent security. Atzori et al. (Gupta et al., 2017) have characterized IoT in three visions. The first one is Internet Oriented vision i.e. the vision focuses on connectivity between the things; second is things Oriented that means the vision focuses on generic objects; and the third one is Knowledge Oriented that elaborates the vision focuses on how to represent, store and organize information. IoT is enabled by several technologies including Wireless Sensor Networks, Cloud Computing, Big data analytics, Embedded Systems, security Protocols and architectures, communication protocols, fifth generation (5G) networks and Semantic Search engines. Using these technologies, the ‘smart environment’ concept has become boom but diverse as it covers transportation/logistics, healthcare, utilities, personal home/offices and much more. This paper focuses on providing an overview of technical details of each technology associated with IoT andtheir summarized key issues and challengesand the future research direction associated with these technologies presented in the recent research papers.

2. IoTEnabled Technologies

Enabling technologies for the Internet of Things are grouped into three categories i.e. technologies that enable “things” to attain contextual information, technologies that permit “things” to process contextual information, and (Ćolaković et al., 2017) technologies to improve safety and privacy of the network. The first two categories make functional building blocks of IoT i.e. “Intelligence” into “things”; it also made functional features of IoT that differentiate it from the usual Internet. While the third category is not a functional but rather a factual requirement, without which the penetration of the IoT would be severely



reduced (Minerva et al., 2015). The brief introduction of these enabling technologies that affords the users of IoT to use these extensive techniques is:

2.1 Wireless Sensor Network

The common vision of smart grid, smart homes, intelligent transportation and other infrastructure systems is usually associated with one single concept, the internet of things (IoT), where through the use of sensors, the entire physical infrastructure is closely coupled with information and communication technologies and intelligent monitoring and management can be achieved via the usage of networked embedded devices. With the rapid technological development of sensors, WSNs will become the key technology for IoT. A wireless sensor network (WSN) is the leading component of IoT that folds surrounding information and sends it to the main server for its execution. However, unlike traditional WSN, IoT-based WSN needs to be smarter (Buyya et al., 2009). Predominantly, IoT-based WSN does not only execute ordinary tasks, for instance, collecting environmental data, but also perform important functions with least or no human involvement. It is now combined with IoT in an innovative way to moving towards new technology.

2.2 Cloud Computing

The amount of big data that is generated by IoT, a lot of strain is put on the internet infrastructure. This has made users to look for an option that would reduce this load. The integration of cloud computing gives these opportunities to an IoT. The on-demand delivery of computing power, database storage, applications and IT resources facilitates multiple customers with the help of a multi-tenant cloud model. It enables organizations to provide high level abstraction like a virtual machine (VM) infrastructure at user premises instead of building a computing infrastructure. Where IoT generates huge amount of data, Cloud Computing helps to find travel path for this data. Cloud computing also helps to scale up the infrastructure of the enterprise, without setting up an additional hardware and infrastructure. In addition to this, cloud computing also enables better collaboration for users by facilitating to store as well as access data remotely. Thus has altered the way in which technologies can be accessed, managed and delivered and act as important utility services in the future (Ahmeda et al., 2017).

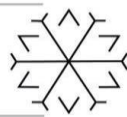
2.3 Big Data Analytics

As the large amount of data generated by IoT dealing with their storage and analytics facilitates data-driven decisions that can improve business-related outcomes. It has exponentially increased over the time and promise competitive advantages in Business. As a result, the demands of adapting data analytics to big data in IoT have increased as well, thereby changing the way that data are collected, stored, and analyzed. Big data and analytics have great potential for extracting meaningful information from the data produced by sensor devices (Pérez et al., 2015). The data that may be stored in many different platforms is used to filter aggregate and analyse by stream analytics (Beri et al., 2018) and make data integration process vital. The big data enabling technologies in the IoT context are related to ubiquitous wireless communication, machine learning, real-time analytics and data capturing elements, such as embedded systems and commodity sensors. Big data technologies can also be offer data storage and processing services in an IoT environment, while data analytics allow business people to make better decisions. IoT applications are the major sources of big data.

2.4 Embedded System

The invention of smart devices makes number of task for the person easier. These devices are created using embedded systems which isa microprocessor based hardware and software device that allow the sensor devices to work in a mutual manner to create an electronic system. Embedded systems also play an important role in Internet of Things (IoT) due to their unique characteristics and features such as real time computing, low power consumption, low maintenance and high availability. Hence, when it comes to designing of these embedded IoT systems, they need to be designed for specific functions, possessing qualities of a good product design like low power consumption, secured architecture, reliable processor, etc. that requires changing current embedded system design and architecture to suit real-time operations, smaller size of the unit and lowered power consumption and become cost efficient for IoT.

2.5 Security Protocol and Architecture



IoT is also termed as cyber-physical system for evaluating state information and performing automatic computation by combining networking infrastructure with smart devices. So, whenever we address a security paradigm in IoT a wider aspect of scenarios is considered by combining architectures, users, communications, technologies and applications. In an IoT infrastructure nodes are communicating and disseminating information for a short period of time, and sometimes only once in their lifetime. Therefore, it is challenging to predict, in advance, which node will interact to which node through which protocol or service through which they will attempt access. So, in highly scalable and dynamic system of IoT, the entity authentication is not only based on single identity but also based on group of identities i.e. 'attributes' that can help to reduce the overhead on the system by avoiding the need to store and specify policies based on the identity of each entity (Mehmood et al., 2013).

2.6 5G

IoT and 5G are new generation of technology. As the need of the hour is faster network with high capacity, 5G combined with IoT can serve connectivity needs. With the expansion of 5G spectrum, faster data transmission facilitates modern human growing needs. The throughput is expected to reach up to 20 gigabits per second while allowing shorter response times. It will be possible to transmit data in real time with the help of 5G. At the same time, the new technology brings an increase in the relative movement speed the connection quality will be much more stable up to a speed of 500 kilometers per hour, which will bring enormous benefits in future of IoT.

2.7 Semantic Search Engines

Semantic search technologies are those in which search engine searches the most accurate results in the large pool of data storage units independently by understanding. It is predicted that successful applications of semantics on computers and will create new technologies that use human-readable and structured machine data to assist both humans and machines. Semantic Web technology permits IoT devices to "understand" and process data using structured and machine readable descriptions of resources (Burhanuddin et al., 2010). Machine-interpretable data descriptions can also show where data originates from, how it can be related to its context, which provides the data, and what the various attributes of the data are. This framework guides how the semantically annotate and easily interpret information exchanged among IoT devices. The integration of semantic principles and their application are supposed to improve the edition processes of IoT devices in the near future.

3 ENABLING TECHNOLOGIES: ISSUES AND CHALLENGES

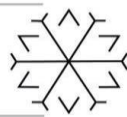
The involvement of IoT systems in all aspects of life made it complex and gave rise to several issues and challenges. These issues are also a challenge for the IoT developers in designing and adopting the advanced smart tech society. As technology is growing, challenges and need for advanced IoT system growing too. Hence, IoT developers need to take care of old issues; think about new issues arising and should provide solutions for them. Some of issues and challenges faced by involving enabling technologies of IoT are:

3.1 WSN

In an IoT environment Wireless sensor nodes are typically deployed for gathering sensitive information from unattended or hostile environments and prominently exposed for security attacks; thus strongly affecting the user privacy and the network performance. Consequently, an exploration of the major and minor security requirements is necessary in the Wireless Sensor Networks for managing issues and challenges in WSN (Dunlap et al., 2011). In order to allow WSN to become an intrinsic part of the IoT in a secure way, several security issues and challenges must be considered. These are:

3.1.1 Devices Heterogeneity: Connection of smart devices to other devices which are heterogenic in nature is major challenge while building IoT as they run on different platforms; they use different protocols to communicate.

3.1.2 Scalability: The scalability of the IoT plays a well-known challenge because every day new devices/objects are getting connected with the network. So, issues like addressing/naming conventions, service management, information management etc. has to be addressed.



3.1.3 Ubiquitous data exchange through wireless technologies: The wireless technologies are used to connect smart devices that involve issues like availability, network delays, congestion etc.

3.1.4 Energy-optimized solutions: As many devices are connected via networks, energy spent for data communication will be high. The challenge is to optimize the use of energy required for communication between different devices.

3.1.5 Localization and tracking capabilities: The smart objects must be identified and tracking of them is required to maintain the security.

3.1.6 Self-organization Capabilities: It is required that the smart objects should sense the environment and autonomously react to real world situations, without much human intervention.

3.1.7 Semantic interoperability and data management: IoT exchange data among different smart objects, it is required that there should be a standardized format for data exchange in order to ensure the interoperability among applications.

3.1.8 Embedded Security and privacy preserving mechanisms: In IoT, security and privacy are the major issues in order to get acceptance from users. IoT technology should be secure and privacy-preserving by design.

3.1.9 Ultra-large sensing device access: The installation of WSN sensing devices in the future will grow exponentially due to the needs for comprehensive monitoring in transportation, electricity, industry and other critical infrastructures and the number of the WSN devices will account for most of the scale. As a result, how to cope with a very large scale of WSN device access is an important challenge.

3.1.10 Massive heterogeneous data processing: With the large-scale application of WSN technology in the information and intelligence process of infrastructures, the amount of data produced by WSN sensors will grow from today's EB level to ZB level. Hence, the transmission and storage including timely treatment of mass data will be an unprecedented challenge.

3.2 Cloud Computing

Since the IoT suffers from limited processing power and storage, it must also contend with issues such as security, performance, reliability, privacy. The integration of the IoT with the Cloud is the best way to overcome most of these issues. The Cloud can even benefit from the IoT by expanding its limits with real world objects in a more dynamic and distributed way, and providing new services for billions of devices in different real life scenarios. There are many challenges which could potentially prevent the successful integration of the Cloud-based IoT paradigm. These challenges include:

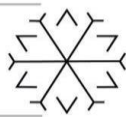
3.2.1 Security and privacy

Cloud-based IoT makes it possible to transport data from the real world to the Cloud but an important issue is how to provide appropriate authorization rules and policies to ensure that only authorized users can access sensitive data; this is crucial when it comes to preserving users' privacy, and particularly when data integrity must be guaranteed (Dar et al., 2016). Whenever serious IoT applications move into the Cloud, issues arise like lack of trust in the service provider, information regarding service level agreements (SLAs), and the physical location of data (Doukas et al., 2012), (Atlam et al., 2017). Sensitive information breaching issues also does not solve by public key cryptography because of the processing power constraints imposed by IoT objects (Dar et al., 2016). New challenges also require specific attention; for example, the distributed system is exposed to number of possible attacks, such as SQL injection, session riding, cross site scripting, and side-channel. Moreover, important vulnerabilities, including session hijacking and virtual machine escape are also problematic in the IoT trends (Dar et al., 2016), (Botta et al., 2014).

3.2.2 Heterogeneity

One particularly important challenge faced by the Cloud based IoT approach is related to the extensive heterogeneity of devices, platforms, operating systems, and services that exist and might be used for new or developed applications. Cloud platforms suffer from heterogeneity issues; for instance, Cloud services generally come with proprietary interfaces, thus allowing for resource integration based on specific providers (Doukas et al., 2012). In addition, the heterogeneity challenge can be exacerbated when end-users adopt multi-Cloud approaches, and thus services will depend on multiple providers to improve application performance and resilience (Aljawarneh et al., 2016).

3.3 Big Data



We know that cloud used to store big data generated by IoT devices; the related issues are storing this data during long period of time as well as need complex analysis for this (Aljawarneh et al., 2016). Handling such a huge amount of data produced is a big issue, as the application's performance is heavily based on the properties of this data management service. Finding a perfect data management solution which will allow the Cloud to manage massive amounts of data is still a big issue (Meddeb et al., 2016). Furthermore, data integrity is a vital element, not only because of its effect on the service's quality, but also because of security and privacy issues, the majority of which relate to outsourced data (Doukas et al., 2012), challenges faced by Big data analytics:

3.3.1 Exploiting the temporal usefulness of IoT

IoT data have a temporal aspect that can be useful in making real-time decisions, improving quality, and providing an excellent user experience. In IoT solutions, the insights from the IoT data are often either time consuming or not put into use immediately. This trend changes into a proactive one to make correlations, derive insights, and find seasonal, emerging, and diminishing patterns using IoT data (Desai et al., 2015). We should implement solutions that can handle data at the gateway level or device level from where the IoT data and processes are initially received.

3.3.2 Diversity Issue

The IoT paradigm has heterogeneous protocols, standards, and platforms. Although the IoT paradigm does not have a universal protocol, multiple protocols may co-exist because of the different requirements and their intended uses. Therefore, IoT systems may not be able to support multiple protocols in an extensible way. Intelligent gateway solutions (Rihan t al., 2016), must provide seamless integration and interoperability between various protocols.

3.3.3 Data management Issue

IoT data are valuable assets. With the exponential increase in the number of IoT devices, systems, and processes, new approaches, such as Data Lakes (Chrismishler et al. 2015), have emerged to handle big data. Data Lakes stores structured and unstructured data without any pre-conceived notion of how these data will be used afterward. This approach does not have applied scheme mapping or query languages and can store any data without restrictions. However, Data Lakes introduces few issues such as insertion of any data and loss of agility. To avoid such issues, different techniques has been imposed (Tanimoto et al., 2016).

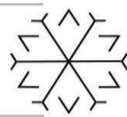
3.3.4 Security challenges

A major hindrance in the broad integration of IoT in industries lies in its security. Several challenges, such as the recent Dyn attack (Tawalbeh et al., 2017), underscore the importance of having secure IoT devices, platforms, and applications which otherwise can lead to major catastrophes, such as the successful execution of a massive DDOS attack. The IT professionals in these industries have their hands full with the security issues of BYOD (Alaba et al., 2017) and the implementation of on-site cloud infrastructures in their organizations. Therefore, IoT security issues only add to their worries.

3.4 .Embedded systems

When it comes to developing embedded IoT devices, the hardware design is viewed as a critical component for the success of the IoT product. In order to ensure the embedded IoT product meets the required function, consumes low power, and is secure and reliable, a lot of challenges are faced by the embedded IoT device manufacturers during the hardware designing phase of these devices. Below are a few hardware design challenges of the embedded IoT devices (Alaba et al., 2017).

- 3.4.1 Problems in ensuring smooth integration of new services
- 3.4.2 Difficulty in adapting to new environments
- 3.4.3 Frequent changes in hardware and software facilities
- 3.4.4 Issues in packaging and integration of small size chip with low weight and lesser power consumption
- 3.4.5 Carrying out energy awareness operations, etc.



3.4.6 The Security Crisis in Embedded System Design as different approaches has to be designed to secure all the components of embedded systems from prototype to deployment

3.4.7 High Power Dissipation of Embedded System Design for getting the best performance out of real-time applications and devices.

3.4.8 For ensuring a reliable product design, conducting in-depth testing, verification, and validation is another challenge.

3.4.9 Inadequate Functional Safety of Safety-Critical Embedded Systems as Embedded systems are considered as generalized control systems, which perform various control functions that require autonomy, reconfiguration, safety, fault-tolerance and need to eliminate all the unacceptable risks to meet functional safety requirements. These considerations highly influence their use in applications due to which, a number of timing and task-scheduling problems arise.

3.4.10 Apart from flexibility and security, embedded systems are tightly constrained by cost.

3.5 5G

The Consumer Technology Association (CTA) has reported that 5G will reach speeds of 10 Gbps, making it 100 times faster than 4G. But challenges of 5G are mentioned here:

3.5.1 Frequency bands

5G requires frequencies up to 300GHz, Some bands, better known as mmWaves, may carry far more capacity and deliver a 20-fold increase over LTE's fastest theoretical throughput. Wireless carriers still need to bid for the higher spectrum bands, as they build and roll out their respective 5G networks.

3.5.2 Deployment and coverage

5G antennas, can handle more users and data, but can only beam out over shorter distances, which means that antennas and base stations will be smaller in the 5G era, but we have to install more of them on buildings or homes to compensate for their shorter range. For this reason, it is likely that carriers will continue to use lower-frequency bands to cover wider areas until the 5G network matures.

3.5.3 Costs to build and buy

Building a network is expensive – carriers will raise the money to do it by increasing customer revenue. And it's not just building a layer on top of an existing network; it's laying the groundwork for something new altogether.

3.5.4 Device support

The concept behind the IoT is too predicated on a fast network that can tie devices and services together. People want to see how much the additional speed will enrich their lives with related issues and challenges.

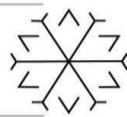
3.5.5 Security and privacy

Though 5G falls under the Authentication and Key Agreement (AKA), a system designed to establish trust between networks, it would currently be possible to track people nearby using their phones or even eavesdrop on live phone calls. With data speeds expected to be magnitudes faster than current levels, so too will connectivity increase.

3.6 SEMANTICS IN THE IOT

Challenges of IoT are related to the possibility to consider relevant issues of the physical world, ensuring technical interoperability from technologies to deliver information, and ensuring a possibility for the information to be understood and processed. The challenges identified from related work which are related to semantic technologies in the IoT are organized in the following groups:

3.6.1 Scalability and flexibility



Scalability is to become one of major research problems, the research in this area has to consider the following issues: automated (or semi-automated) annotation of available resources, semantic association discovery and analysis (resource connection or activation), and efficient solutions to create, analyze and explore linked IoT data of various resources (Alaba et al., 2017). Some studies in the IoT domain address the rising problem of ensuring IoT scalability (Barnaghi et al., 2012).

3.6.2 Standardization and Reusability

Standardization is a vital area of concern in any data engineering field as it infers stable quality levels over time and steadiness against unexpected faults. It is essential to define and follow a standard specification guide so that further enhancements can be added to existing solutions without significant effort (Tsai et al., 2014).

3.6.3 High level processing

Usually IoT data consumers, either humans or machines, are not interested in unit measurements but rather in high level contextual meaning of data. Such high-level abstractions should be machine interpretable for computers and human-understandable for humans,

3.6.4 Data quality

Some semantic description models such as the W3C SSN ontology offer attributes to describe qualitative aspects of data (Alaba et al., 2017). Analysis of such data quality reveals that these data often are not consistent. For machine-learning or knowledge-dependent application, such data is unacceptable. As data volume increases, inconsistency and redundancy become troubling issues. Inconsistent data detection for distributed networks becomes even more challenging.

3.6.5 Data confidentiality and privacy

Another challenge is helping a user to feel more comfortable and enabling intuitive browsing and uncover methods and approaches of utilizing user data for malicious means.

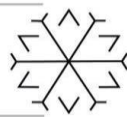
4. Future Research Direction

The IoT can best be described as a Complex Adaptive System (CAS) that will continue to evolve hence requiring novel and creative forms of software engineering, project management, as well as several other disciplines to grow it further and manage it the coming years. As more and more research studies are conducted, new dimensions to the IoT processes, technologies involved and the objects that can be connected continue to emerge, further finding way for much more application functionalities of IoT. The fact that IoT is so expansive and affects almost all areas of our lives, makes it important research topic for studies in various related fields such as information technology and computer science, economic development, water quality maintenance, well-being, industrialization etc. IoT is bringing up transformation in the traditional structure of the society into high tech structure through the concept of smart home, smart city, smart vehicles and many more. Rapidupgradations are being done with the help of related technologies such as machine learning, natural language processing to understand the need and use of technology at home. Various other technologies such as Cloud Computing technology, Wireless Sensor Network, etc. must be used with IoT servers to provide an efficient smart city while also considering the environment aspect of smart city. Therefore, energy efficient technologies and Green technologies should also be considered for the design and planning of smart city infrastructure. Thus new technologies must necessarily be coupled to existing models and should serve as axes for the creation of new models.

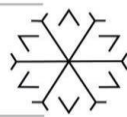
5. Conclusion

Recent advancements in IoT have drawn attention of researchers and developers worldwide. IoT developers and researchers are working together to extend the technology on large scale and to benefit the society to the highest possible level. However, improvements are possible only if we consider the various issues and shortcomings in the present technical approaches listed in the paper. In this paper, we presented several issues and challenges that IoT developer must take into account to develop an improved model. Also, important application areas of IoT are also discussed where IoT developers and researchers are engaged. As IoT is not only providing services but also has without a doubt a massive capability to be a tremendously transformative force, which will, and to some extent does already, positively impact millions of lives worldwide so need to be paid attention at each and every aspect of IoT.

6. References



- Eason, G. Noble, B. and Sneddon, I. (2017) 'On certain integrals of Lipschitz-Hankel type involving products of Bessel functions' *Phil. Trans. Roy. Soc. London*, Vol. A247, pp. 529–
- Gatsis, K. and Pappas, GJ. (2017) 'Wireless control for the IoT: power spectrum and security challenges' *IEEE/ACM second international conference on internet-of-things design and implementation (IoTDI)* Vol. 22(7) , pp.97–114.
- Ashton, K. (2009) 'Internet of Things' *RFID J*, Vol. 22(7), pp. 97–114.
- Ahmed, E. Yaqoob, I. Gani, A. and Guizani, M. (2016) 'Internet-ofThings-based smart environments: State of the art, taxonomy, and open research challenges' *IEEE Wireless Commun.*, Vol.23(50), pp. 10–16.
- Atzori, L. Iera, A. and Morabito, G. (2010) 'The Internet of Things: A survey' *Comput. Netw.*, Vol. 54(15), pp. 2787–2805.
- Gupta N, Gupta J.,2017, Internet of Things (IoT): a vision of any-time any-place for any-one. *Int Rob Auto J.*;2(6):234–240. DOI: 10.15406/iratj.2017.02.00041
- Rose, K. Eldridge, S. and Chapin, L. (2015) 'The Internet of Things: An Overview Understanding the Issues and Challenges of a More Connected World' *The Internet Society*.
- Čolaković, A. Hadžiali, M (2018), 'Internet of Things (IoT): A review of enabling technologies, challenges, and open research issues' doi.org/10.1016/j.comnet.2018.
- Minerva, R. Biru, A and Rotondi. D. (2015) 'Towards a Definition of the Internet of Things (IoT)', <http://iot.ieee.org/images/files/pdf/IEEE>.
- Buyya, R. Shin, C. Venugopal, S. and Brandic, I. (2009) 'Cloud computing and emerging IT platforms: Vision , hype , and reality for delivering computing as the 5th utility' *Futur. ener. Comput. Syst.*, pp. 599–616.
- Ahmeda, E., Yaqooba, I Hashema, I. Khanb, I., Imranc, I, Athanasios, V, Vasilakos, D. (2017), <http://dx.doi.org/10.1016/j.comnet.2017.06.013> 1389-1286/© Elsevier
- Pérez, J., Carrera, D. (2015) 'Performance characterization of the servioticity api: an iot-as-a-service data management platform' *Big Data Computing Service and Applications IEEE*, pp. 62–71
- Beri, R. (2018) 'Embedded System in IoT' *International Journal of Innovation & Research in Computer Science* Issue 5th , pp 2349-2783
- Pal, S. Hitchens, M. Varadharajan, V. (2018) 'Identity for the Internet of Things: Survey, Classification and Trends' *International Conference on Sensing Technology (ICST)*, pp. 45–51.
- Mehmood, A. and Baksh, A.(2013) 'Communication Technology that suits IoT: A critical Review' doi: 10.1007/978-3-642-41054-3.
- Hosenkhan, M. Pattanayak, B (2020) 'Security Issues in Internet of Things (IoT): A Comprehensive Review' *New Paradigm in Decision Science and Management; Springer*, pp. 359–369.
- Alam, S. Siddiqui, S. Ahmad, A. (2020), 'Internet of Things (IoT) Enabling Technologies, Requirements, and Security Challenges' *Advances in Data and Information Sciences*, Springer, pp. 119–126.
- Li, Y. Gao, M. Yang, L. Zhang, C. and Zhao, X. (2020), 'Design of and research on industrial measuring devices based on Internet of Things technology', *Ad. Hoc. Netw.*
- 'ZigBee – The Internet of Things' (2019), <http://www.vesternet.com/zigbee>
- Decuir, J. (2010) 'Bluetooth 4.0: Low Energy', <http://chapters.comsoc.org/vancouver/BTLER3.pdf> .
- Ee, G., Noordin, N, Ali, K. (2010) 'A Review of 6LoWPAN Routing Protocols', *Asia Pacific Advanced Network*.
- Sarma, C. Girão, J., (2009) 'Identities in the future internet of things. Wireless Personal Communications' Vol 49(3), pp 353–363
- '<http://www.savingtrust.dk/publications/concepts/destsconcept-for-energy-saving-devices-metering-equipment-andwireless-communication>
- Pfisterer, D. Pfisterer, K. Romer, D. Bimschas, O. Kleine, R. Mietz, C. Truong, H. Hasemann (2011) 'SPITFIRE: Toward a Semantic World'
- Boyd , D. and Crawford, K. 'Six Provocations for Big Data' *Computer and Information Science*, Vol. 123.



- Burhanuddin, M. Mohammed, A. Ismail, R. Basiro, H. 'A review on security challenges and features in WSN: IoT perspective', Vol 10(7)
- Balte, A. Kashid, A. and Pati, B. (2015) 'Security Issues in Internet of Things (IoT): A Survey' International Journal of Advanced Research in Computer Science and Software Engineering.
- Dunlap, J. (2011) 'From billing & technology convergence to ecosystem convergence: Why M2M matters to your business' *Technology for Service Providers*, Vol. 8(7), pp. 13.
- Feldman, S. (2012) 'Creating information synergy', IDC.
- Suciu, G. Vulpe, S. Halunga, O. Fratu, G., Todoran V. (2013) 'Smart Cities Built on Resilient Cloud Computing and Secure Internet of Things' *Control Systems and Computer Science (CSCS)*, pp. 513-518.
- Alenezi, A. Zulkipli, N. Atlam, H. and Wills, G. (2017) 'The Impact of Cloud Forensic Readiness on Security', *Cloud Computing and Services Science*, pp. 1-8.
- Dar, K. Taherkordi, A. and Eliassen, F. (2016) 'Enhancing Dependability of Cloud-Based IoT Services through Virtualization' *Internet-of-Things Design and Implementation (IoTDI)*, pp. 106-116
- Doukas, C. and Maglogiannis, I. (2012) 'Bringing IoT and cloud computing towards pervasive healthcare' *Innov. Mob. Internet Serv. Ubiquitous Comput. IMIS*, pp. 922-926
- Atlam, H. Alenezi, A. and Wills, G. (2017) 'An Overview of Risk Estimation Techniques in Risk-based Access Control for the Internet of Things' *Internet of Things, Big Data and Security*, pp. 1-8
- Botta, A. Donato, V. and Pescapé, A. (2014) "On the Integration of Cloud Computing and Internet of Things," 2014 International Conference on Future Internet of Things and Cloud, Barcelona, pp. 23-30
- Aljawarneh, S. Radhakrishna, V. and Janaki, V. (2016) 'A similarity measure for temporal pattern discovery in time series data generated by IoT' *International Conference on Engineering & MIS (ICEMIS)*, pp. 1-4,
- Desai, P. Sheth, A. and Anantharam, P. (2015) 'Semantic Gateway as a Service Architecture for IoT Interoperability', doi: 10.1109/MobServ.2015.51, pp. 313-319
- Meddeb, A. (2016), 'Internet of things standards: who stands out from the crowd?' *Communications Magazine*, Vol. 54(7), doi: 10.1109/MCOM.2016.7514162, pp. 40-47.
- Fang, H. (2015) 'Managing data lakes in big data era: What's a data lake and why has it become popular in data management ecosystem' *Cyber Technology in Automation, Control, and Intelligent Systems (CYBER)*, doi: 10.1109/CYBER.2015.7288049, pp. 820-824.
- Rihan (2016) 'Constance: an intelligent Lake system' *SIGMOD/PODS'16*
- Chrismishler, C. (2015) 'The future of Internet things : strategic finance', [http://refhub.elsevier.com/S1389-1286\(17\)30259-1/sbref0065](http://refhub.elsevier.com/S1389-1286(17)30259-1/sbref0065)
- Tanimoto, S. Yamada, M. Iwashita, and Kanai, A. (2016) 'Risk assessment of BYOD: Bring your own device' *IEEE 5th Global Conference on Consumer Electronics*, doi: 10.1109/GCCE.2016.7800494, pp. 1-4.
- Tawalbeh, L. Tawalbeh, H. (2017), 'Lightweight crypto and security' *Security and Privacy in Cyber-Physical Systems: Foundations, Principles, and Applications*; Wiley, pp. 243-261.
- Alaba, F. Othman, M. Hashem and Alotaibi, F. (2017), 'Internet of Things security: A survey' *Netw. Comput. Appl.*, Vol 88, pp 10-28.
- Rehman, A. Mehmood, K and Baksh, A. (2013), 'Communication Technology That Suits IoT – A Critical Review' *WSN4DC*, pp. 14-25
- Barnaghi, P. Wang, W. Henson, C. and Taylor, K.. (2012) 'Semantics for the Internet of Things' *Int. J. Semant. Web Inf. Syst.* Vol. 8(1), pp. 1-21.
- Gyrard, S. Datta, K Bonnet, C. and Boudaoud, K. (2014) 'Standardizing Generic Cross-Domain Applications in Internet of Things' *IEEE Globecom Work. GC Workshops*, pp. 589-594.
- Perera, C. Zaslavsky, A. Christen, P. and Georgakopoulos, D. (2014), 'Context Aware Computing for the Internet of Things: A Survey' *IEEE Commun. Surv. Tutorials*, Vol. 16(1), pp. 414-454.
- Weber, R. (2010) 'Internet of Things – New Security and Privacy Challenges' *Comput. Law Secur. Rev.* Vol. 26(1), pp. 23-30.
- Tsai, C. Lai, C. and Vasilakos, A. (2014) 'Future Internet of Things: Open Issues and Challenges' doi.org/10.1007/s11276-014-0731-0, Vol. 20, pp. 2201- 2217

Comparison of Copy-Move Image Forgery Detection Techniques

Moataz Z. Salim ¹[0000-0002-4806-8552], Remzi Yildirim ²[0000-0000-0000-00000], Ali J. Abboud ³[0000-0000-0000-00000]

¹mzshaa7@gmail.com, Ankara Yıldırım Beyazıt University, Turkey

²ryildirim@ybu.edu.tr, Ankara Yıldırım Beyazıt University, Turkey

³ali.j.abboud@gmail.com, University of Diyala, Iraq

Abstract

In the world of digital forgeries and especially image forgery, the Copy-Move forgery (CMF) is one of the most common forgeries, where a part (or parts) of the image is copied and pasted in the same digital image, and that is because the various simple tools used to do this work. In any event, such work is done to tamper or hide information in order to provide a fake identity for what the image is presenting. This kind of forgery can be hard to detect depending on the processing made on the copied part. Hence, many algorithms have been proposed to detect and localize the forgeries. However, most of the detection algorithms have similar structures, where they read an image and through different proposes and methods detect the forged part and localize it. In this paper, a discussion is presented on four different methods of detecting and localizing the forgeries on a dataset with random shaped copied regions, with a focus on the matching methods taking into consideration the F-Score, Precision, Recall and the execution time.

Keywords. Copy-Move, DCT, DWT, Feature Matching, Image Forgery.

1. Introduction

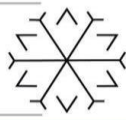
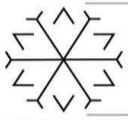
Image forgery is used in various fields such as multimedia security, journalism, and scientific publications (Qazi et al., 2013). Generally, image forgery can be classified to two main categories: Active techniques and Passive techniques (Saranya et al., 2019). Non-Blind/intrusive techniques are usually referred to as Active techniques and they need major processed data to be embedded in the original image during the initial processing of the photo. An example for such techniques will be digital signatures and digital watermarking. On the other hand, Passive techniques are the non-intrusive/blind techniques and they usually don't require or demand any prior information to include in the digital image. By such method, a digital image can be tampered by various ways such as scaling, rotating, blurring, copy-move, adding noise, resizing, image splicing, and a lot more.

Copy-move is one of the most popular methods for manipulating images (Redi et al., 2011). It can be done by copying a part from an image and pasting it into the same image with the purpose of hiding unwanted objects or reduplicating objects as shown in Figure 1. In copy-move forgery (CMF), the forged region still shares most of its original features, such as the color palette or pattern noise, with the rest of the image.



Figure 1: Example of CMF (CVIP, no date): original image (on the left); forged image (on the right).

Most of the copy-move forgery detection (CMFD) algorithms have a similar composition. Highly similar feature vectors are matched in pairs. The similarity of two features can be determined by different similarity criteria, such as Euclidean distance. It was spotted that for the effectiveness of CMFD algorithms, feature vectors have a fundamental role (Redi et al., 2011). Generally, there are two major differences between most of the proposed approaches; the type of the features that are used for matching image blocks, and the method of matching.



By combining the keypoint feature and the block-based feature, Pun et al. (Pun et al., 2015) proposed a method to discover copy-move forgery. When compared to existing contemporary copy-move forgery detection techniques, experimental results indicate that their proposed method achieves much better detection results for copy-move forgery images under a variety of challenging conditions, such as geometric transforms, JPEG compression, and downsampling (Meena and Tyagi, 2019). Wenchang et al. (Wenchang et al., 2016) proposed a new method for detecting copy-move forgery that combined a new idea called particle swarm optimization (PSO) with the SIFT keypoint. The authors used the best bin first (BBF) algorithm for feature matching in their study. The technique had a 99 percent precision, but it was unable to detect forgery when the duplicated region was very small (Meena and Tyagi, 2019).

In this paper, a discussion based on a comparison between four different matching algorithms is presented in order to study and understand the outcome of matching algorithms on the performance of copy-move detection techniques. The rest of the paper is organized as follows: Section 2 is some important key elements, Section 3 is an introduction to the methods, Section 4 and 5 are the experimental setup, results, and discussion.

2. Key Elements and Background

In this section, an introduction to the main methods and techniques that are used in the detecting algorithms and also for the comparison is presented. The reader can learn more about those methods by looking up the references listed in each subsection.

Feature extraction and similarity checking parts that match exactly are the critical steps in copy-move forgery detection.

2.1. Feature Extraction

2.1.1 Discrete Cosine Transform (DCT)

The DCT is a Fourier-related transform that expresses a finite sequence of data points in terms of a sum of cosine functions oscillating at different frequencies. It is similar to the Discrete Fourier Transform (DFT) but uses only real numbers. Transform coding in image processing is based on the proposition that pixels in an image have a certain level of correlation with their neighbors. As a result, transformation is defined as the process of mapping spatial (correlated) data into transformed (uncorrelated) coefficients, and DCT is used to try to decorrelate the image data (Yanping et al., 2011).

2.1.2 Discrete Wavelet Transform (DWT)

The DWT is a linear transform that separates a data vector into different frequency components by operating on a vector with a length that is an integer multiple of 2. DWT reduces the computational complexity by reducing image information and analyzing the relevant data (Loai et al., 2017).

2.1.3 Scale Invariant Feature Transform (SIFT)

SIFT proposes a method for extracting distinguishing invariant features from images that may be used to reliably match diverse viewpoints of an object or scene in a given image. The features are scale and rotation invariant, and they provide reliable matching across a wide range of affine transformations, distortions, changes in 3D viewpoint, noise addition, and illumination changes (Singh et al., 2014).

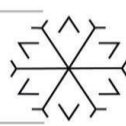
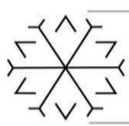
2.2. Similarity Checking

2.2.1 K-Means Clustering

Clustering is the grouping of patterns (typically expressed as a vector of measurements or a point in a multidimensional space) based on their similarity. Within each cluster, patterns are more similar than patterns from other clusters. For its simplicity, k-means is a popular clustering technique. The aim of k-means clustering is to divide n observations into k clusters and assign each data object to the cluster with the closest mean (Al-qershi et al., 2016).

2.2.2 Exact Match

This technique is used to locate image regions that are identical. Starting from the top left corner to the bottom right corner, a square block is moved over the image, extracting matrices and storing them in a two-dimensional array. The array's two indistinguishable rows correlate to two identical image segments. The rows are then lexicographically ordered, rather than being matched with other rows. As an outcome, rows with similar pixel values get closer together (Arora and Singh, 2019).



2.2.3 Robust Match

The approximation (robust) match detection technique is similar to the exact match detection technique, with the exception that it does not order and match the representation of the blocks, but their robust representation that consists of quantized Discrete Cosine Transform coefficients. (Fridrich et al., 2003).

3. The Proposed Methods In The Comparison

In this section, a brief introduction to the mechanisms of the algorithms is presented.

3.1 A Proposed Accelerated Image Copy-Move Forgery Detection

In the research paper by Fadl et al. (Fadl and Semary, 2014), the algorithm goes as follows, after taking an image and converting it to grayscale, it divides the image into small 8×8 overlapping blocks, and to extract the features, Discrete Cosine Transform (DCT) is used first to extract the coefficients and then they are reordered using Zigzag scanning and sorted in a matrix. Followed after that the K-Means technique for similarity checking purposes. After clustering, the blocks were lexicographically sorted and saved in a matrix. And finally, the correlation between each pair of the sorted blocks is calculated, which, and based on the formula given in (Fadl and Semary, 2014), can be used to detect the forged part.

3.2 Image forgery detection for high resolution images using SIFT and RANSAC algorithm

In the research paper by G. Ramu et al. (Ramu and Babu, 2017), the proposed method goes as follows, an input image is read and 4th level Discrete Wavelet Transform (DWT) is applied to it in order to get the coefficients. The calculated superpixel is applied in the SLIC algorithm to form the non-overlapping irregular blocks. A superpixel is a set of pixels that share similar characteristics (such as pixel intensity) while SLIC stands for Simple Linear Iterative Clustering which is an algorithm that produces superpixels by grouping pixels based on their color likeness and closeness in the image plane. Then the features are extracted by using SIFT algorithm and are matched by calculating Dot products among unit vectors (Ramu and Babu, 2017). And finally, the RANSAC algorithm is used to localize the forged regions, where it also eliminates the unwanted matches.

3.3 Exact Matching Method-Copy-Move Forgery Detection

In the (Jha. et al., 2020) research paper, the proposed method goes as follows, an input image is given and converted to grayscale, and then the image is resized to 128×128 pixels. Continued by implementing the Exact Match algorithm where the image is divided into overlapped blocks, and for each of the blocks, the features are extracted, which represent pixel values. Followed by Lexicographic sorting for the matrix, where it holds the extracted features. And finally, the matching process is done by searching sequential identical rows of the matrix and getting the particular block positions. And the method is implemented by (Tejas, 2018).

3.4 Detection of Copy-Move Forgery in Digital Images

In the (Fridrich et al., 2003) research paper, a method to detect copy-move forgeries is proposed, and implemented by (Gaye, 2019). The forgery detection works in the Robust Match method. Where a given image is scanned from the upper left corner to the lower right corner while sliding a $B \times B$ block. And for each block, the DCT transform is calculated, the DCT coefficients are quantized and stored as one row in a matrix. Then the rows of the matrix are lexicographically sorted, which represent the extracted features. And if two sequential rows of the sorted matrix A are detected, the algorithm stores the locations of the matching blocks in a separate list and increments a shift-vector counter. And after that, the shift vector between the two matching blocks is calculated.

Worth mentioning, of all four compared methods, this research paper is the oldest.

4. Experimental Setup

4.1 Image Dataset Preparation

The dataset is taken from The Computer Vision and Image Processing Group (CVIP), which belongs to the Department of Engineering (DI) at the University of Palermo (CVIP, no date). The dataset is converted from BMP images to JPG images with the size of 256×256 pixels. The dataset is selected precisely due to the forged regions (copied and pasted regions) being in different shapes and sizes which is unlike many other datasets with fixed rectangular, circular shapes, or any known shapes, this makes the detection process quite challenging which simulates real situations. For each image, the copied regions are pasted in varied locations to create a sense of spatial synchronization and homogeneity between them and their neighbors.

The dataset has a group of 50 images with a different one copied and pasted part, and another group of 20 images that for each of them, two different operations were performed, scaling and rotation. For each



image, 3 different angles were taken for rotation of the forged region. 30°, 60°, and 90° respectively. And with the same number of samples, 3 different levels of scale were taken for the forged region. 0.75, 1.25, and 1.75 respectively.

4.2 Metrics

The average execution time is calculated by the following formula:

$$AvgT = \frac{Executiontime}{Numberofsamples} \quad (1)$$

Precision is a metric that quantifies the number of exact positive predictions given, while Recall is a metric that quantifies the number of exact positive predictions made out of all positive predictions that could have been made (Jason, 2020). They can be calculated as follows:

$$P = \frac{Truepositive}{Truepositive+Falsepositive} \quad (2)$$

$$R = \frac{Truepositive}{Truepositive+Falsenegatives} \quad (3)$$

F-Measure serves to integrate Precision (P) and Recall (R) into a single metric that accounts for both properties (Jason, 2020). It can be calculated as follows:

$$F - Measure = \frac{2PR}{P+R} \quad (4)$$

5. Experimental Results And Discussion

The experiments were carried out on the Matlab R2017b, 12GB of RAM and processor of octa-core at 1.80GHz 1.99 GHz. The prepared dataset involves various images with different operations applied on the duplicated part to create the copy-move forgery, and the parameters were kept default for each program. The source codes were taken from public repositories, and all the rights belong to the owners. In this section, a discussion is given upon the results of each proposed method in the comparison. Table 1 and 2 show the Precision, Recall, F-Measure, and Execution time for the methods at the end of this section. For the ease of seeing the detailed comparison for each algorithm method, a sample output is shown for one general image (Figure 2-3).



Figure 2: Sample image used for the comparison (for the unprocessed forgeries).



Figure 3: Sample image used for the comparison (for the processed forgeries).

5.1 A Proposed Accelerated Image Copy-Move Forgery Detection

This proposed method took a noticeable time in executing compared to the other methods. The output shows the work of the Fast K-Means clustering where the matched regions are in the same color and the resulting image of the localized parts where the matched points (rectangular shaped) are in blue and red colors. It is easy to notice in Figure 4 the final result did not perform well in detecting the forged regions in terms of localizing the forged parts with no processed copied parts as compared to the original image. The average execution time for the unprocessed 50 samples of copy-move forgeries is:

AvgT = 92.79 seconds.

The algorithm performance was relatively the same in terms of execution time for the processed forgeries, and the output did not perform well in terms of localizing the forged regions, as shown in Figure 5. The average execution time for the processed 20 samples (for each sample, two states were taken: rotation and scaling) of copy-move forgeries is:

AvgT = 93.65 seconds.

It is worth mentioning that the algorithm performed better in detecting square or rectangular cut forgeries from the dataset.

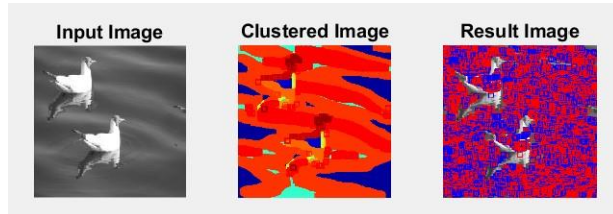


Figure 4: An output sample of the (Fadl and Semary, 2014) proposed algorithm.

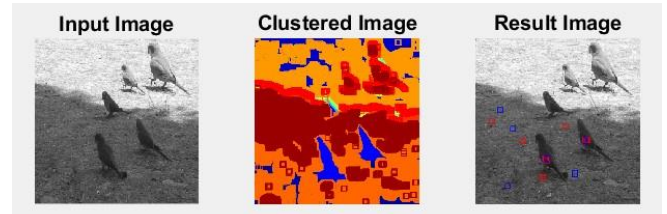


Figure 5: An output sample of the (Fadl and Semary, 2014) proposed algorithm. The sample forgery is processed by scaling it to 1.75.

The proposed method displays the resulting image by drawing the matched blocks on the grayscale image. The pros of this paper could be listed as it has a flexible algorithm structure that can be improved. A possible improvement for future work could be optimizing the comparison between the correlation and threshold to further likelihoods.

5.2 Image forgery detection for high resolution images using SIFT and RANSAC algorithm

The output shows beside the original image, the result of DWT where the HL, LH, and HH are shown, alongside the forgeries displayed in the cluster and the non-overlapping irregular blocks. Figure 6 shows a sample output of the sheer copied regions of the forgery. The average execution time for the unprocessed 50 samples of copy-move forgeries is:

AvgT = 7.18 seconds.

The algorithm performance was relatively the same in terms of execution time for the processed forgeries, and the output was just like the first experiment for pretty much all the samples of the processed forgeries, as shown in Figure 7. The average execution time for the processed 20 samples (for each sample, two states were taken: rotation and scaling) of copy-move forgeries is:

AvgT = 6.04 seconds.

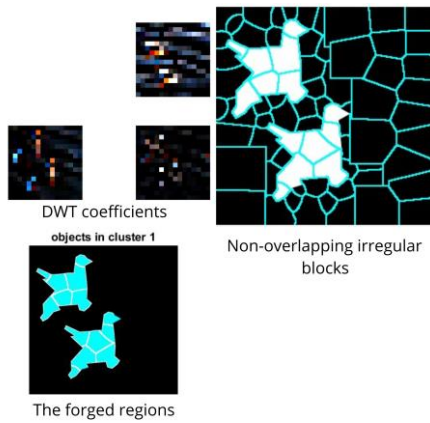
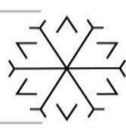


Figure 7: An output sample of the (Ramu and Babu, 2017) proposed algorithm.

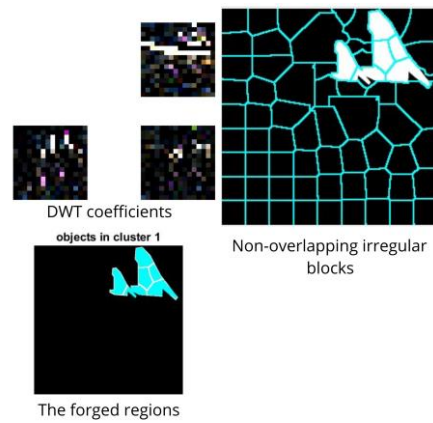


Figure 6: An output sample of the (Ramu and Babu, 2017) proposed algorithm. The sample forgery is processed by scaling it to 1.75.

The execution time was relatively quick compared to the other methods. The cons of this method can be stated as the algorithm shows the forged regions based on the mask rather than the predicted regions as an output. The RANSAC algorithm is one of the pros of this research paper for reducing the undesired matches. In the extraction of the superpixel, the Haar wavelet is used to find the superpixel size S . This can be applied in different approaches to ease the way of calculating S .

5.3 Exact Matching Method-Copy-Move Forgery Detection

The output of this method shows the original image, alongside the copied part. The proposed algorithm succeeded in detecting and localizing the forgeries for some of the samples in terms of checking the output by bare eyes to some extent with an acceptable measures of F-Measure. Figure 8 shows a sample of the output for a copy-move forgery. The average execution time for the unprocessed 50 samples of copy-move forgeries is:

$$\text{AvgT} = 24.06 \text{ seconds.}$$

The algorithm performance was comparatively the same in terms of execution time for the processed forgeries, and the output was just like the first experiment for not detecting some of the processed forgeries in terms of checking the output by bare eyes to some extent with an acceptable measures of F-Measure. Figure 9 gives a sample of the output. The average execution time for the processed 20 samples (for each sample, two states were taken: rotation and scaling) of copy-move forgeries is:

$$\text{AvgT} = 23.63 \text{ seconds.}$$

copy moved part

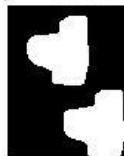
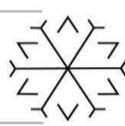
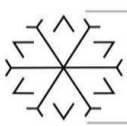


Figure 8: An output sample of the (Jha. et al., 2020) proposed algorithm.

copy moved part



Figure 9: An output sample of the (Jha. et al., 2020) proposed algorithm. The sample forgery is processed by scaling it to 1.75.



Although the research paper suggests a Robust Match method, it is easy to observe the presented output does not give the exact forged region for most of the samples taken compared to the original non-forged image, which can be listed under the cons of this method. The research paper gives an approach of the Robust Match that, as simple as the concept is, can be implemented for any copy-move detection algorithm. The average reduction in execution time is observed to be about 24% using this method (Jha. et al., 2020).

5.4 Detection of Copy-Move Forgery in Digital Images

The output of this method shows the original image alongside the detected forgery regions and the F-Measure, as shown in a sample in Figure 10. The average execution time for the unprocessed 50 samples of copy-move forgeries is:

$$\text{AvgT} = 22.58 \text{ seconds.}$$

The F-Measure value for the sample shown in Figure 8 is:

F-Measure = 0.87, which is considered good compared to the other samples.

The implementation of the proposed method failed to detect the forgery of the sample and most of the 20 samples. Figure 9 shows the sample output of the processed forgery, with a value of 0 of the F-Measure which indicates the failure of detecting the forgeries.

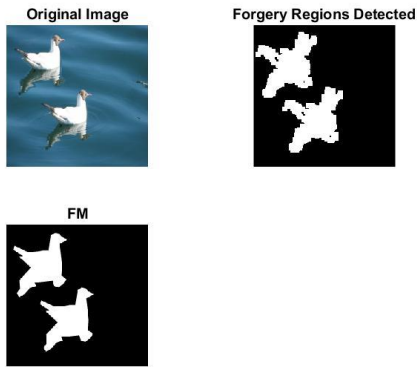


Figure 10: An output sample of the (Fridrich et al., 2003) proposed algorithm.

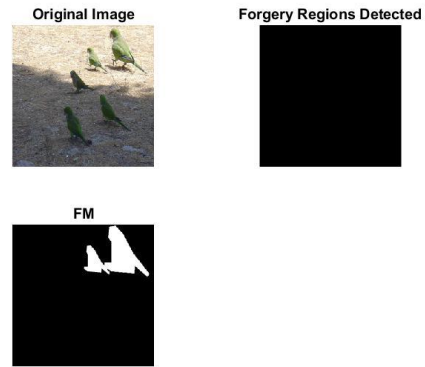


Figure 11: An output sample of the (Fridrich et al., 2003) proposed algorithm. The sample forgery is processed by scaling it to 1.75.

The algorithm works perfectly fine in detecting most of the simply copied regions, whilst it could not detect any forgeries of the processed ones, which can be listed on the top of the cons. This method is introduced to the comparison for the sake of variation of the techniques and methods, and it can be adjusted for further operations, such as changing the block size to a larger number to prevent false matches as stated in (Fridrich et al., 2003).

Table 1: A comparison showing the scores and measures between the four methods based on the sample shown in Figure 2.

	Method (Fadl and Semary, 2014)	Method (Ramu and Babu, 2017)	Method (Jha. et al., 2020)	Method (Fridrich et al., 2003)
Precision	NA	0.17	0.17	0.96
Recall	NA	0.14	0.42	0.8
F-Score	NA	0.16	0.24	0.87
Execution time	101.13 Seconds	7.34 Seconds	48.96 Seconds	22.62 Seconds



Table 2: A comparison showing the scores and measures between the four methods based on the sample shown in Figure 3 for the forgery region processed by scaling it to 1.75.

	Method (Fadl and Semary, 2014)	Method (Ramu and Babu, 2017)	Method (Jha. et al., 2020)	Method (Fridrich et al., 2003)
Precision	NA	0.08	0.06	0.5
Recall	NA	0.14	1	0.07
F-Score	NA	0.1	0.12	0.12
Execution time	91.31 Seconds	7.87 Seconds	49.05 Seconds	21.37 Seconds

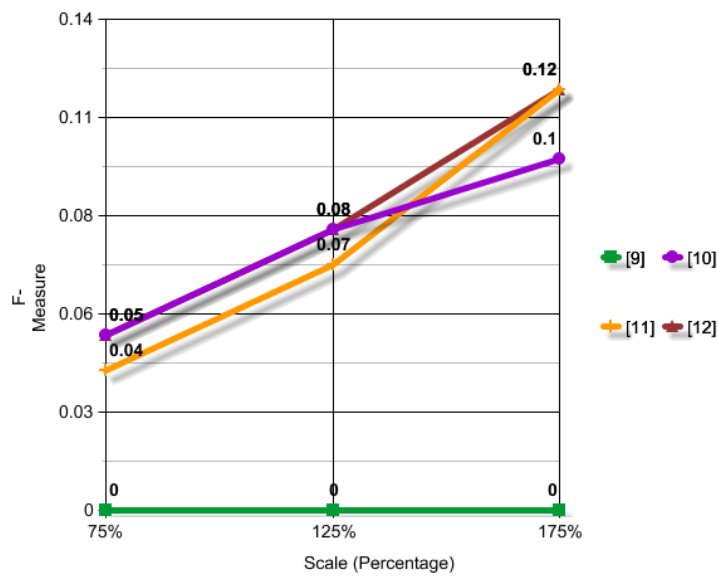


Figure 13: F-Measure values of detection of the four methods for the scaling of 75%, 125%, and 175%.

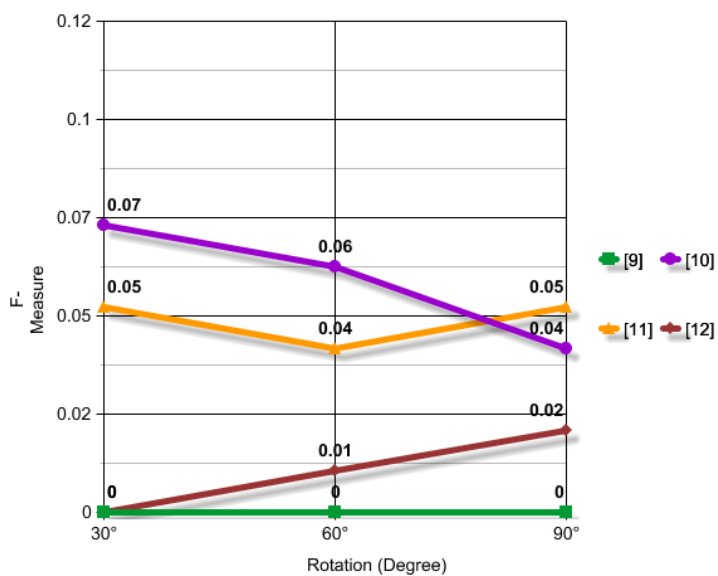
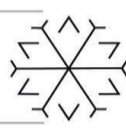
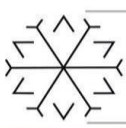


Figure 12: F-Measure values of detection of the four methods for the rotation of angles 30°, 60°, and 90°.



Figures 12 and 13 show how the F-Measure differs as the level of scaling increases and the angle of rotation increases. It can be seen that as the scaling increases, the F-Measure increases a bit accordingly with a slight difference at (Ramu and Babu, 2017). Whilst it appears the F-Measure decreases with the angle of rotation for (Ramu and Babu, 2017), besides slight increases for (Jha. et al., 2020) and (Fridrich et al., 2003). The experiments were made on the same sample image of Figure 3.

6. Conclusion

In this paper, an opinion is given on a comparison between four matching methods that have been used in copy-move forgery detection. The experimental results show diverse outcomes of the four methods with different experiments with different numbers of measurements and scores. Each proposed method has its pros and cons, varied with the Matching methods and Feature extraction techniques. And all of them could be adjusted for different purposes.

References

- Al-qershi, O, et al. (2016) 'Copy-Move Forgery Detection Using on Locality Sensitive Hashing and k-means Clustering'. 10.1007/978-981-10-0557-2_65.
- Arora, P. and Singh, D. (2019) 'Copy Move Image Forgery Detection with Exact Match Block Based Technique'. *Oriental journal of computer science and technology*. 12. 123-131. 10.13005/ojcast12.03.07.
- Computer Vision and Image Processing Group (CVIP), Department of Engineering (DI), University of Palermo. <http://www.diid.unipa.it/cvip/>.
- Fridrich, J. et al. (2003). 'Detection of Copy-Move Forgery in Digital Images'. *Int. J. Comput. Sci. Issues*. 3. 55-61.
- G. Ramu and S. Babu, (2017) 'Image forgery detection for high resolution images using SIFT and RANSAC algorithm', *2nd International Conference on Communication and Electronics Systems (ICCES)*, pp. 850-854, doi: 10.1109/CESYS.2017.8321205.
- Gaye Durmaz. (2019) <https://github.com/gayedurmazz/Copy-Move-Forgery-Detection>.
- Jason Brownlee, (2020), <https://machinelearningmastery.com/precision-recall-and-f-measure-for-imbalanced-classification/>.
- Jha, K. et al. (2020) 'DIGITAL IMAGE FORGERY DETECTION', *International Research Journal of Engineering and Technology (IRJET)*.
- Loai A, et al. (2017) 'Copy-Move Forgery Detection using Integrated DWT and SURF'. *Journal of Telecommunication, Electronic and Computer Engineering (JTEC)*, Article/1658.
- Meena K. and Tyagi V. (2019) 'Image Forgery Detection: Survey and Future Directions'. *Data, Engineering and Applications*. Springer, Singapore.
- Pun, C. et al. (2015) 'Oversegmentation and feature point matching'. *IEEE Trans. Inf. Forensics Secur.* 10, 1705–1716.
- Qazi T. et al. (2013) 'Survey on blind image forgery detection', *IET Image Process*; 7: 660-670.
- Redi JA, et al. (2011) 'Digital image forensics: a booklet for beginners'. *Multim Tools Appl* 51:133–162.
- S. Fadl and N. Semary. (2014) 'A proposed accelerated image copy-move forgery detection', *IEEE Visual Communications and Image Processing Conference*, pp. 253-257, doi: 10.1109/VCIP.2014.7051552.
- Saranya M. et al. (2019) 'Digital Image Forgery Detection', *International Journal of Recent Technology and Engineering (IJRTE)*, 2277-3878.
- Singh, K. et al. (2014) 'Fast and robust passive copy-move forgery detection using SURF and SIFT image features', *9th International Conference on Industrial and Information Systems (ICIIS)*, pp. 1-6, doi: 10.1109/ICIINFS.2014.7036519.
- Tejas K., (2018) <https://github.com/Tejas1415/Discreet-Cosine-Transform-DCT-Singular-Value-Decomposition-SVD-based-Copy-Move-Forgery-Detection>.
- Wenchang, S. et al. (2016) 'Improving image copy move forgery detection with particle swarm optimization techniques'. *China Commun.* 139–149.
- Yanping H. et al, (2011) 'Improved DCT-based detection of copy-move forgery in images', *Forensic Science International*, Volume 206, Issues 1–3, Pages 178-184, ISSN 0379-0738.

A Study on Detection of Forest Fire

Kemal Akyol^{1*}[0000-0002-2272-5243]

¹kakyol@kastamonu.edu.tr, Department of Computer Engineering, Kastamonu University, Kastamonu, Turkey.

Abstract

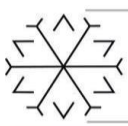
Forest fires cause great harm to people and nature. Fires, which threaten millions of hectares of forest land in the world each year, have enormous negative impacts on biodiversity. These negatives could be prevented by using expert decision support systems equipped with today's technology. The main aim of this study is to examine comparatively the performances of the Random Forest, Support Vector Machines, and Logistic Regression classifiers trained on the dataset including only three attributes to detect whether there is a forest fire. The dataset contains 1713 samples, including 386 fires and 1327 no fires. After the min-max normalization process, the performances of the classifiers were evaluated with the hold-out technique. Balanced accuracy, sensitivity, and specificity metrics were used to compare the performances of the models. It was seen that the Random Forest classifier offers more successful performance compared to others with 72.70% balanced accuracy in experiments.

Keywords. Forest fire, machine learning, random forest, performance evaluation.

1. Introduction

Animals and birds live in forests that provide oxygen. For this reason, it is essential to track and protect forests and forest assets (Cui, 2020). Fire is a global problem with a strong negative impact on biodiversity (González, González-Trujillo, Muñoz, & Armenteras, 2021). Forest fire is one of the main causes of the degradation of ecosystem and human life. Therefore, it is considered one of the pressing issues. The wildfire disaster is currently the subject of intense research around the world. Avoiding potential impacts and minimizing the occurrence of catastrophic events as much as possible requires the right strategies, modeling, and forecasting of severe conditions (Mohajane et al., 2021). As a result, with its extremely destructive power in forest ecosystems, fire threatens millions of hectares of forest land worldwide every year.

Very intense wildfires devour homes, wildlife, and form various adverse effects and increase global temperature (Ram Prasanna, Mathana, Ramya, & Nirmala, 2021). To minimize the losses caused by the fire, it is necessary to carry out studies based on the prediction system and remote sensing (Zheng et al., 2020). Mohajane et al. developed models that include a combination of frequency ratio and classifier algorithms by utilizing the altitude, slope, aspect, distance to roads, distance to residential areas, land use, and normalized difference vegetation index. The authors stated that their hybrid model could improve the performance of wildfire susceptibility studies and could be applied to other fields (Mohajane et al., 2021). Zheng et al. tested the performance of their proposed model based on the ant miner algorithm on historical fire data between 2000 and 2018 to determine the fire risk levels. The authors reported that their proposed model could be used to predict the fire risk of forested areas in cloud-rich regions (Zheng et al., 2020). Cui aimed to detect fire accidents in forests by utilizing the internet of things. The author monitored the forests and detected anomalies by using deep convolutional neural networks to overcome wildfire risks (Cui, 2020). Tang et al. handled forest fire susceptibility in Huichang County, China, due to frequent fire events. They determined the most successful classifier by applying optimized repeated random subsampling and analyzed the forest fire with the Support Vector Machines classifier, which they fine-tuned with a genetic algorithm (Tang, Machimura, Li, Liu, & Hong, 2020). Silva et al. discussed forest degradation caused by fire based on a combination of forest inventory and satellite remote sensing data in areas with bamboo in the eastern part of the Brazilian state of Acre (Silva et al., 2021). Çolak and Sunar examined fire risk using remote sensing technology. With this aim, they integrated pre-fire multi-time remote sensing data and ancillary data from the geographic information system to evaluate the spatial and temporal patterns of forest fire risk in the Mendere region of Izmir (Çolak & Sunar, 2020). Qadir et al. used geographic datasets on fire hotspots, topography, vegetation types, percentage of tree cover, ecoregion, and climate for bushfire risk in Nepal. They used geographic information system-based modeling approaches with multi-spectral satellite-derived data for future fire prediction in villages. In their study, the authors reported that 302



villages of the total of 3967 villages were potentially at high fire risk (Qadir, Talukdar, Uddin, Ahmad, & Goparaju, 2021).

In this study, experiments were carried out on the publicly available dataset with the hold-out technique to detect forest fires, and the performances of the classifiers were discussed.

The remaining parts of the study are as follows. Section 2 describes the dataset used in this study and the methodology applied. Experimental studies and results are presented and discussed in Section 3 in detail. Finally, the study concludes with the final remarks in Section 4.

2. Material and Method

2.1. Dataset

In this study, the public dataset composed by Sayad (Oulad SAYAD, 2018) was used. The dataset includes the remote sensing data obtained from multiple regions in central Canada. This dataset has 1713 samples including 386 samples for fire class and 1327 samples for non-fire class, and it is available on the Mendeley repository. There are three attributes; NDVI, LST, and Thermal Anomalies in the dataset. Table 1 presents the attributes in the dataset.

Table 1: Attributes and descriptions in the dataset

No	Attribute	Description
1	NDVI	Normalized Difference Vegetation Index
2	LST	Land Surface Temperature
3	Thermal Anomalies	Thermal Anomalies

2.2. Model Building

Random Forest (RF), Support Vector Machines (SVM), and Logistic Regression (LR) classifiers were used to detect forest fire. Before building the models, ‘fire’ and ‘no fire’ classes in the target attribute were converted to categorical values of 1 and 0, respectively, and then min-max normalization was applied to the dataset. Then, the performances of the classifiers trained on the training set were examined on the testing set in detail. The classifiers were used with their default parameters in the study. Figure 1 presents the overall block diagram of this study.

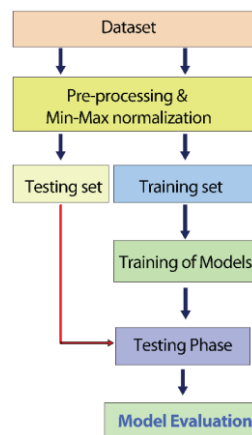
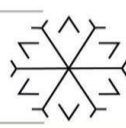
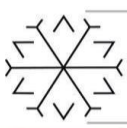


Figure 1: General block diagram of the study

The performances of the models are measured using the basic criteria of True Positive (TP), True Negative (TN), False Positive (FP) and False Negative (FN) in the confusion matrix for the dataset which has two-class. Here, TP and TN indicate the number of fire and no fire samples classified correctly, respectively while FN and FP denote the number of fire and non-fire samples classified incorrectly, respectively. The performances of the models were measured using the balanced accuracy (unweighted average recall), sensitivity and specificity metrics which are given in Equations 1 and 3, respectively. Sensitivity measures how accurately the models classify positive samples, and specificity measures how accurately they classify negative samples (Altman & Bland, 1994). In other words, the sensitivity and specificity metrics refer to



the ratio of correct classification of true positives and true negatives, respectively. Balanced accuracy (Brodersen, Soon Ong, Stephan, & Buhmann, 2010) is the average of the recall on the positive class and recall on the negative class. This metric gives the correct expectation for each class prediction when the class ratio is unbalanced in the dataset.

$$\text{Sensitivity} = \frac{TP}{TP+FN} \tag{1}$$

$$\text{Specificity} = \frac{TN}{TN+FP} \tag{2}$$

$$\text{Balanced accuracy} = \frac{\text{Sensitivity}}{2} + \frac{\text{Specificity}}{2} \tag{3}$$

2.3. Experimental Results and Discussion

Figure 2 demonstrates the confusion matrices obtained by the models for the testing set. Moreover, Table 2 summarizes the performances of the models via the balanced accuracy, sensitivity, and specificity metrics. According to the results, LR misclassified 9 and 70 samples from no fire and fire classes, respectively. SVM misclassified 6 and 69 samples from no fire and fire classes, respectively. RF misclassified 16 and 36 samples from no fire and fire classes, respectively. The sensitivity values presented by the models vary between 5.41% and 51.35%. RF, SVM, and LR presented 94.05%, 97.77%, and 96.65% specificities, respectively, and in this context, the specificities of the classifiers are quite high. Sensitivities of LR and SVM classifiers are not good with 5.41% and 6.76%, respectively. The sensitivity value of the Random Forest based model is well below of acceptable level with 51.35%. In addition, LR, SVM and RF classifiers offered balanced accuracy of 51.03%, 52.27% and 72.70% respectively. Overall, the training set used for training of the models in this study has an unbalanced distribution with 1058 samples labeled 0 and 312 samples labeled 1, and it is thought that the results obtained by the machine learning algorithms are not decent with this reason.

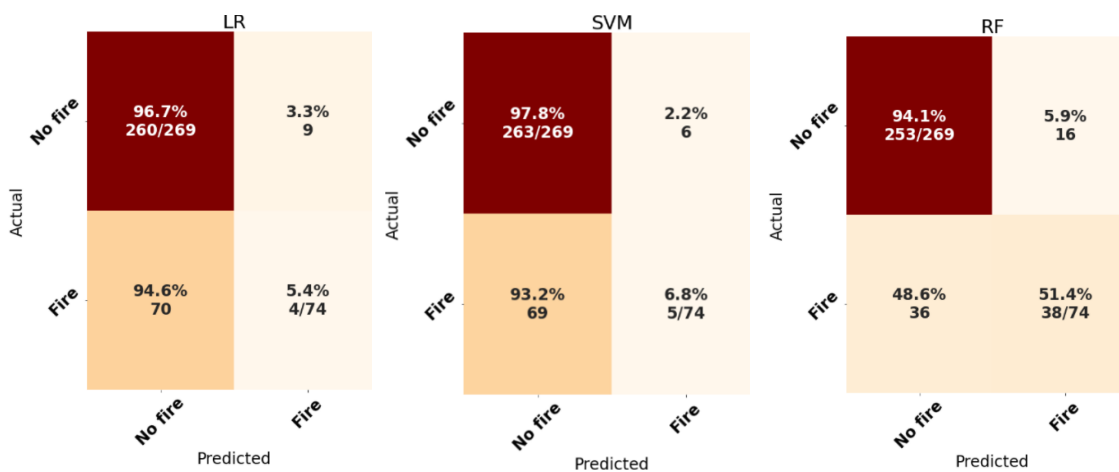


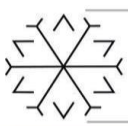
Figure 2: Confusion matrices of the classifiers on the testing set

Table 2: Experimental results on the test dataset

Classifiers	Balanced accuracy (%)	Sensitivity (%)	Specificity (%)
LR	51.03	5.41	96.65
SVM	52.27	6.76	97.77
RF	72.70	51.35	94.05

3. Conclusion

It is very important to track changes in nature to prevent fires in forests that produce oxygen, which is important for life. In this study, fire classification was made using remote sensing data fire published by Sayad from different areas with and without. According to the experimental results, the RF correctly classified 253 of 269 negative samples and 38 of 74 positive samples in the testing set. Although RF is more successful than other algorithms, the sensitivity value offered by this classifier is quite below the acceptable level. Furthermore, it is thought that the negative effects of the relatively few attributes, and



more important that the unbalanced data distribution which is the limitation of the dataset used in this study on machine learning.

Acknowledgements

Author would like to thank Oulad Sayad (Oulad SAYAD, 2018) for the publicly available wildfire dataset.

References

- Altman, D. G., & Bland, J. M. (1994). Diagnostic tests. 1: Sensitivity and specificity. *BMJ (Clinical Research Ed.)*, 308(6943), 1552. <https://doi.org/10.1136/BMJ.308.6943.1552>
- Brodersen, K. H., Soon Ong, C., Stephan, K. E., & Buhmann, J. M. (2010). The balanced accuracy and its posterior distribution. <https://doi.org/10.1109/ICPR.2010.764>
- Çolak, E., & Sunar, F. (2020). Evaluation of forest fire risk in the Mediterranean Turkish forests: A case study of Menderes region, Izmir. *International Journal of Disaster Risk Reduction*, 45, 101479. <https://doi.org/10.1016/j.ijdrr.2020.101479>
- Cui, F. (2020). Deployment and integration of smart sensors with IoT devices detecting fire disasters in huge forest environment. *Computer Communications*, 150, 818–827. <https://doi.org/10.1016/j.comcom.2019.11.051>
- González, T. M., González-Trujillo, J. D., Muñoz, A., & Armenteras, D. (2021). Differential effects of fire on the occupancy of small mammals in neotropical savanna-gallery forests. *Perspectives in Ecology and Conservation*, 19(2), 179–188. <https://doi.org/10.1016/j.pecon.2021.03.005>
- Mohajane, M., Costache, R., Karimi, F., Bao Pham, Q., Essahlaoui, A., Nguyen, H., ... Oudija, F. (2021). Application of remote sensing and machine learning algorithms for forest fire mapping in a Mediterranean area. *Ecological Indicators*, 129, 107869. <https://doi.org/10.1016/j.ecolind.2021.107869>
- Oulad SAYAD, Y. (2018). Forest Fire Data Set, 1. <https://doi.org/10.17632/XW3FFCG6YP.1>
- Qadir, A., Talukdar, N. R., Uddin, M. M., Ahmad, F., & Goparaju, L. (2021). Predicting forest fire using multispectral satellite measurements in Nepal. *Remote Sensing Applications: Society and Environment*, 23, 100539. <https://doi.org/10.1016/j.rsase.2021.100539>
- Ram Prasanna, K., Mathana, J. M., Ramya, T. A., & Nirmala, R. (2021). LoRa network based high performance forest fire detection system. *Materials Today: Proceedings*. <https://doi.org/10.1016/j.matpr.2021.05.656>
- Silva, S. S. da, Fearnside, P. M., Graça, P. M. L. de A., Numata, I., Melo, A. W. F. de, Ferreira, E. L., ... Lima, P. R. F. de. (2021). Increasing bamboo dominance in southwestern Amazon forests following intensification of drought-mediated fires. *Forest Ecology and Management*, 490, 119139. <https://doi.org/10.1016/j.foreco.2021.119139>
- Tang, X., Machimura, T., Li, J., Liu, W., & Hong, H. (2020). A novel optimized repeatedly random undersampling for selecting negative samples: A case study in an SVM-based forest fire susceptibility assessment. *Journal of Environmental Management*, 271, 111014. <https://doi.org/10.1016/J.JENVMAN.2020.111014>
- Zheng, Z., Gao, Y., Yang, Q., Zou, B., Xu, Y., Chen, Y., ... Wang, Z. (2020). Predicting forest fire risk based on mining rules with ant-miner algorithm in cloud-rich areas. *Ecological Indicators*, 118, 106772. <https://doi.org/10.1016/j.ecolind.2020.106772>

Creating Cloud GIS Based Geographical Indication Tourism Web and Mobile Apps

Şevket Bediroğlu^{1*}[0000-0002-7216-6910]

1: sbediroglu@gantep.edu.tr, Gaziantep University

Abstract

Geographic indication is an important and attractive asset for tourism activities. Geographic indication and gastronomy tourism are rapidly growing in recent years. Lack of studies on advertising these geo-indicated products cause some obscurity problems for citizens. At this point digital maps, internet and cloud based applications are essentials for letting citizens know about these products. At this study, gastro-tourism portal was created via integrating GIS files and related media files such as, photographs, videos etc. Javascript and HTML language was used during study. Arcmap and Arcgis Online programs were also used for GIS support. This portal and web app support decision-making process for tourist while accessing geographically indicated foods and other components. System also have some GIS based functionalities such as, navigation, routing, 3D view etc.

Keywords. Cloud Computing, Tourism, Geographic Indications, Gastronomy, Web Based GIS

1. Introduction

The presence of certain foods in certain regions reveals the existence of a strong relationship between culture and food. This situation created by the locality makes the food an important geographical marker in tourism marketing. This link between a region and gastronomy finds its response in tourism. Food becomes a tool in directing tourists to certain regions or countries (Richards, 2002; Kızıllırmak et al., 2016) Distinctive local food products can be a branded asset for a destination. The brand serves as a reliable signal of quality when the consumer lacks in expertise and time to access the quality of the food. (Han, 1989; Seal and Piramanayagam, 2018).

Geographical indication can shortly be described as the protection of a local product or value with certain regulations. Geographical indications are divided into two categories called "origin name" and "geographical indication" (Yıkımlı and Ünal, 2016). Geographical indication in gastronomy tourism is very important in order to attract the masses of tourists to the country and ensure the sustainability (Yıkımlı and Ünal, 2016). Local food and products have a highly important place in tourism activities. These goods must be registered with geographical indications in order to transfer them to future generations (Pamukçu et al., 2021). When geographical indication is associated with gastronomy tourism, it provides significant tourism income to the region by forming a destination element, for tourists, toward regions where goods are produced (Pamukçu et al., 2021).

Gaziantep has important and valuable resources for the development of gastronomy tourism. The city stands out with its rich culinary heritage. The region has unique product, food preparation and consumption patterns. Of the 44 geographical indications registered for Gaziantep, 40 of them are food and beverages (Karasavuran and Dirlik, 2019).

A map provides information on existence, the location of, and the distance between ground features, such as populated places and routes of travel and communication (Akinola, Odeyemi and Suru 2011; Eboy, 2017). The Geographic Information Systems (GIS) applications are recently used in the management of parks, facilities management, assessment of visual resources, and new areas identification for new tourism development initiatives (Wahab and Sconthodu, 2018). By using GIS, it becomes possible to integrate tourism information, visualize complex scenarios, present powerful ideas and derive effective solutions, otherwise not possible (Eboy, 2017). Lack of broad information based on the internet about tourism information, and lack of organized information about tourism facilities & destinations is main challenge (Zerihun 2017).

Cloud computing; It is the distribution of hardware and software systems from service provider data centers in the form of applications over the Internet (Armbrust et al., 2010; Bediroglu, 2013). One of the important characteristics of cloud computing is that it seamlessly integrates the computational resources distributed in the physical space and provides them to its users, so that the users are able to quickly access the required computational resources or



services at any time and at any location (Wang et al., 2018). In Cloud GIS, the time and monetary losses required for the initial setup and maintenance of the system can be avoided. This is very important because in a GIS project, the creation of basic components such as software licensing, application development, software and hardware in the initial setup of the system are processes that require high budgets. For such reasons, many companies do not use GIS even though they know that they need GIS-supported solutions. Thanks to the flexible structure of Spatial Cloud Computing, such problems will decrease to very low levels, especially the initial setup cost of the system.

Purpose of this study is creating gastro-tourism portal via integrating GIS files and related media files such as, photographs, videos etc. This portal and web app aim will support decision-making process for tourist while accessing geographically indicated foods and other components. For these purposes, Cloud GIS based web apps were created and published to internet. System presents an elastic and dynamic approach for tourist and service provider attractions. A user friendly design was preferred during mobile app creation. Last user can easily apply sophisticated GIS analysis with no effort and well knowledge of GIS principles.

2. Methodology

Methodology workflow is shown at Figure 1. First step is collecting GIS data about geographically indicated products having Gaziantep city origin, accessible at Gaziantep city. Second step is collecting media files related with these products. This process includes photographs, videos and texts. Then process continues with aggregating these datasets in integrated database. At this step user friendly gastronomy maps will be prepared using cartographic capabilities of GIS environment. In following stage cloud based web apps were created using Arcgis Online and Javascript language. Then the integrated dataset was moved to cloud data storage. In last stage, the operations were integrating social media platforms to created web app in manner of informing users about other users' comments about suggested gastro-point. Final step was publishing these apps and maps to internet. The preferred method in practice is to associate visual, written and all information with the location, unlike the classical only location-based map applications. In addition, the designed system makes it possible to perform comprehensive geographical analysis. Sophisticated geographical analyzes are carried out on the back (server) with the functions offered on the last user's side with a simple interface and understandable buttons, and the results are conveyed to the end user in a way they can understand.

Methodology Workflow

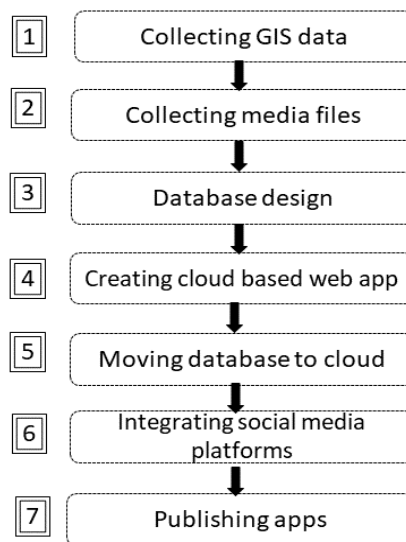
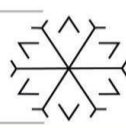
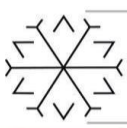


Figure 1: Methodology and workflow diagram

3. Case Study

3.1. Study area



Gaziantep city is chosen for study area. Reason for choosing Gaziantep is city's rich food diversity and having geographically indicated foods. City has 44 geo-indicated products. City is located at southeast side of Turkey; study area is shown at Figure 2.

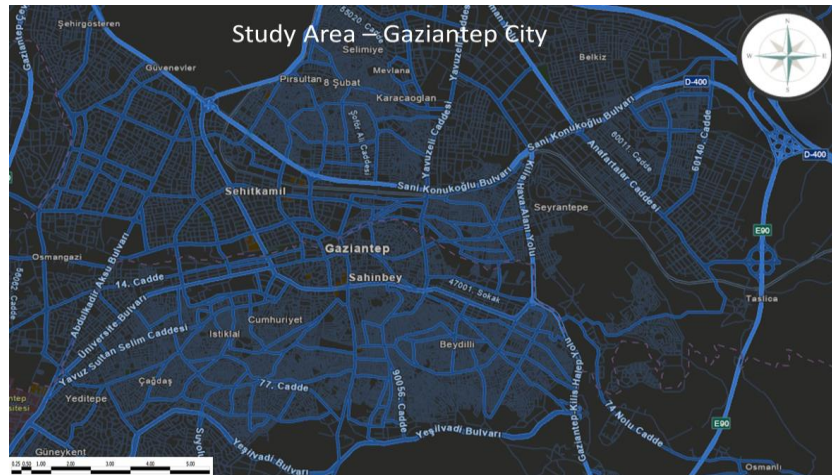


Figure 2: Study area / Gaziantep city

3.2. Data Preparation and Database Design

At first step, geo-indicated product list was prepared from city's chamber of commerce website and other official resources. City has 44 geo-indicated products and media files dealt with these products were prepared. Afterwards GIS dataset was collected from web sources and tourism maps using ArcMap 10.4 software. Figure 3 show raw GIS data preparation stages. WGS 84 projection system was preferred for data projection type.

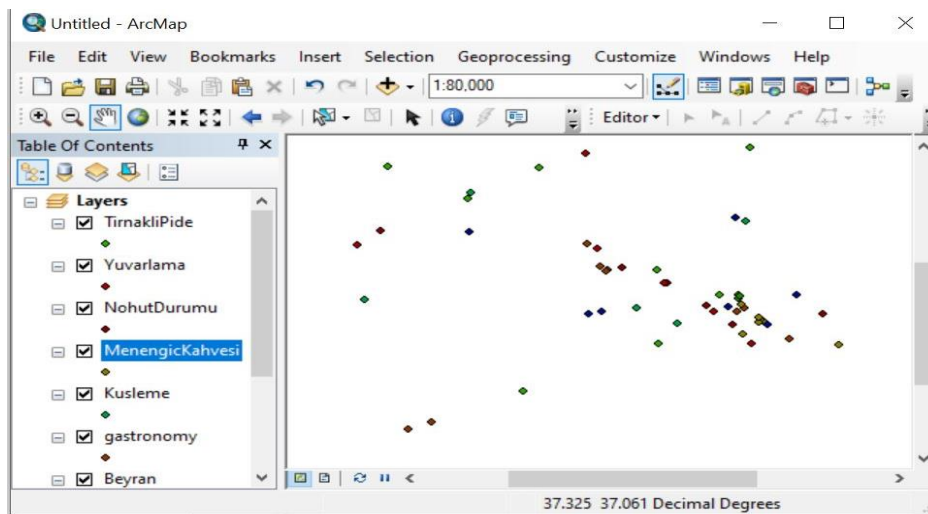


Figure 3: A view from raw GIS data preparation

Figure 4 shows designed web app using Arcgis Online cloud platform. With this application, users can access and query related locations of geo-indicated products. At this stage, Javascript and HTML languages have been used for creating apps. System has some tools such as navigation bar, 3d view bar, basemap change (satellite, osm, hybrid etc.) Functionalities and design elements of app is also changable. By this way, web and mobiles apps created may be done more user friendly for the next user requirements.

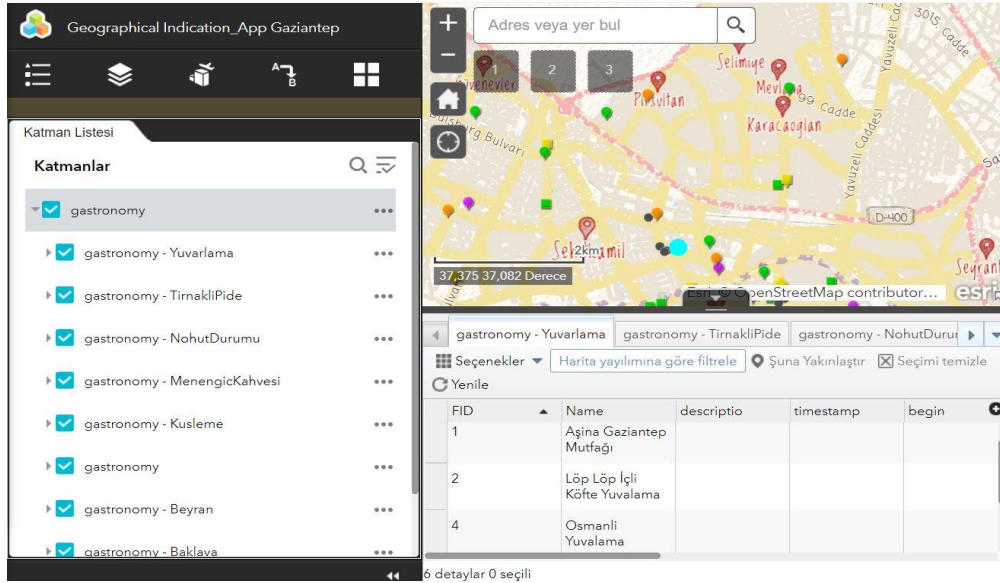


Figure 4: General view of web application and attribute query

Figure 5 shows mobile application design stages. Mobile app of geo-indicated locations also have same functions with web app. Mobile app is adaptive to various screen resolutions for specific purposes.

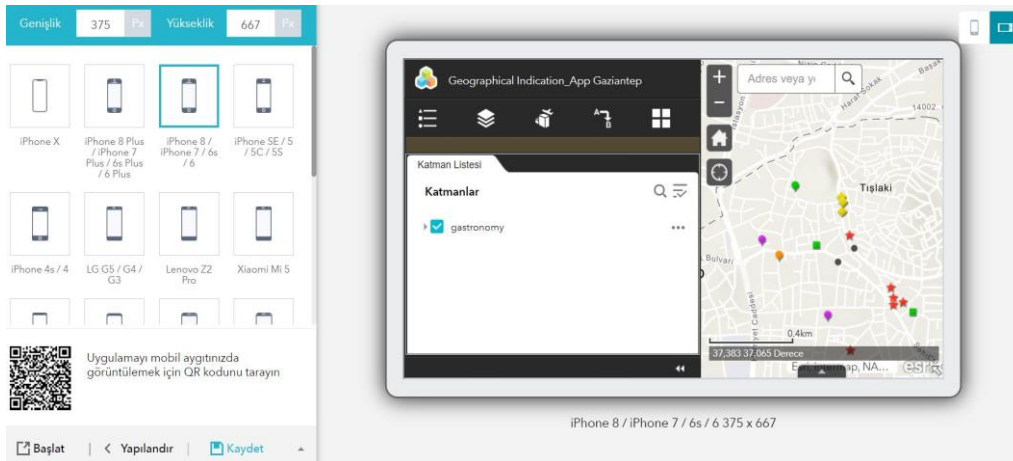
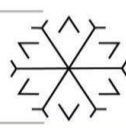
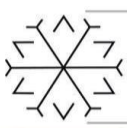


Figure 5: Mobile compatible application design for geographic indications

4. Results and Conclusion

Studies have shown that using cloud based GIS systems provide efficiency and elasticity for tourism informing activities. Digital maps are essential components for tourists. Paper maps are also useful but they have limited and generally old information. Otherwise digital maps may have huge information and hypermedia sets with the help of cloud storage support. Researches about gastronomy and geographical indication have shown that these attractions are very important for tourism activities. However many tourists are searching how to find local geo-indicated foods while they travel a local zone and sometimes it is hard to find quality foods or other products. With this app, users can easily ask related attribute files of a geo-indicated product or location selling that product. Social media integration of created app (especially Instagram) enables users to get informed about suggested locations in a dynamical way.

References



- Akinola, T. Odeyemi F. and Suru P. (2014). (Nigeria) Maps: an Essential Instrument in Tourism Industry Development FIG Congress 2014 Engaging the Challenges – Enhancing the Relevance Kuala Lumpur, Malaysia 16-21 June 2014
- Armbrust, M. et al., (2010). A View of Cloud Computing, 2010, Association for Computing Machinery
- Bedirođlu, Ő. (2013). Web haritalarının bulut biliŐim ile yayımlanması: Trabzon ili orneđi. Karadeniz Teknik Üniversitesi. Fen Bilimleri Enstitüsü.
- Eboy, O. (2017). Tourism Mapping: An Overview of Cartography and the Use of Gis, BIMP-EAGA Journal for Sustainable Tourism Development, 6, pp. 61–67.
- Han, C. M. (1989). Country Image: Halo or Summary Construct?, Journal of Marketing Research, 26(2), pp. 222–229. doi: 10.1177/002224378902600208.
- Kızilirmak, I.Ofluođlu, M. and ŐiŐik, L. (2016). Türkiye'de Uygulanan Gastronomi Turları Rotalarının Web Tabanlı Analizi ve Deđerlendirmesi. Journal of Tourism and Gastronomy Studies. Cilt: 4Sayı: Sayfa: 258 – 269
- Pamukçu, H. et al., (2021). The Effects of Local Food and Local Products with Geographical Indication on the Development of Tourism Gastronomy, Sustainability, MDPI, Open Access Journal, vol. 13(12), pages 1-13, June.
- Richards, G. (2002). Gastronomy: an essential ingredient in tourism production and consumption?', Book: Tourism and Gastronomy, 1st Edition, First Published 2002, Pages 18
- Seal, P. and Piramanayagam, S. (2018). Branding Geographical Indication (Gi) of Food and Its Implications on Gastronomic Tourism: An Indian Perspective 8th Advances In Hospitality and Tourism Marketing and Management (Ahtmm) Conference, June 25 – 29, 2018, Bangkok, Thailand
- Toker, B. and Kalıpcı, M. B. (2019). Happiness İn Tourism Students: A Study On The Effect Of Demographic Variables On Happiness.
- Wahab, I. N., and Soonthodu, S. (2018). Geographical Information System in Eco-Tourism. In S. Chaudhuri, & N. Ray (Ed.), GIS Applications in the Tourism and Hospitality Industry (pp. 61-75). IGI Global.
- Wang, C. et al. (2018). Cloud Platform for the Management of Tourism Resources', in 2018 26th International Conference on Geoinformatics, pp. 1–9. doi: 10.1109/GEOINFORMATICS.2018.8557190.
- Yıkımsı, S. and Ünal, A. (2016). The importance of geographical indication in gastronomy tourism: Turkey, International Journal of Agricultural and Life Sciences, 2, pp. 73–79. doi: 10.22573/spg.ijals.016.s12200069.
- Zerihun, M. (2017). Web Based GIS for Tourism Development Using Effective Free and Open Source Software Case Study: Gondor Town and Its Surrounding Area, Ethiopia, Journal of Geographic Information System, 09, pp. 47–58. doi: 10.4236/jgis.2017.91004.

A Novel Most Probable Path Computation of Stochastic Hidden Systems with Updated Parameters by using 1-Step Optimization Discrete Control Algorithm

Mete Özbaltan ¹[0000-0002-3215-6363] and Mehmet Kurucan ²[0000-0003-4359-3726]

¹mete.ozbaltan@erzurum.edu.tr, Erzurum Technical University

²mehmetkurucan@ardahan.edu.tr, Ardahan University

Abstract

We extend our existing work and propose a novel most probable path computation of stochastic hidden systems with updated parameters by using 1-step optimization discrete control algorithm. We experimentally evaluate and validate our framework with an implementation of a stochastic hidden system, the Hidden Markov Model, where a given system a priori learns and then updates its parameters. In our implementations, we use the artificial dataset we created, where the data is randomly generated on each implementation. Our approach relies on formal control techniques; where the given system behavior is encoded as a discrete controller synthesis problem by means of modeling synchronous data-flow equations; and solving the problem synthesizes a controller that will lead us to the result of the most probable path. The main advantage of the discrete controller technique work as model checking so has formal correctness.

The Hidden Markov Model is an undetectable Markov chain in which the latent state generates a yielding symbol, which can be depicted in arbitrary structure. The generation of an output symbol and transitions between hidden states have a likelihood value in this model. These likelihood values are held in matrices called emission and transition, respectively. In any case, it ought to likewise be considered that since the genuine model is not known, that is, it is a black box, the emission, and transition matrices should be updated to be near the boundaries of original parameters. To solve this present circumstance, the most convenient and iterative Baum-Welch algorithm is utilized.

Stochastic hidden systems consist of a hidden state sequence and finding it is the task and there are several methods available for the find the most probable path as model verification, heuristics, machine learning, and some standard control techniques. The Viterbi algorithm among them is one of the most common and accurate solving method, where the algorithm finds the maximum value of the transition probability in the Markov graph to obtain the most probable path. We show that in terms of the experimental evaluation by means of a comparison of the Viterbi and our method, our method can be a good candidate in order to find the most probable path, especially for hidden systems with updated parameters.

Keywords. Discrete Controller Synthesis, Optimal Control, Hidden Systems, Viterbi Algorithm, Baum-Welch Algorithm

Covid-19 Detection with Deep Learning Methods from X-Ray Images

Hafize Arduç ^{1*}[0000-0002-2231-3580] and Yaşar Daşdemir ²[0000-0002-9141-0229]

¹hafize.arduc46@erzurum.edu.tr, Erzurum Technical University, Computer Engineering

²yasar.dasdemir@erzurum.edu.tr, Erzurum Technical University, Computer Engineering

Abstract

COVID-19 is a new virus that emerged in Wuhan, China in December 2019, causing infection in both the upper respiratory tract and lungs. It is very important to prevent the spread of the disease with rapid diagnosis methods and to detect positive cases as early as possible. The most common testing technique used to diagnose COVID-19 is RT-PCR, which is a real-time reverse testing technique. However, the long duration of pathological laboratory tests and inaccurate test results have led researchers to different areas. Radiological imaging has begun to be used to monitor COVID-19 disease as well as being useful in detecting various lung diseases. The application of deep learning techniques together with radiological imaging has a very important place in the correct detection of this disease.

In this study, the differentiation performance of 125 COVID-19 data from each other was investigated with an ensemble deep learning system based on the Maximum Voting scheme consisting of 5 different deep convolutional neural network (CNN) based ResNet-50, ResNet-34, VGG-19, MobileNetV2 and DenseNet201 models. In addition, the transfer learning method was applied to eliminate the problems of insufficient data and training time. A total of 1125 X-Ray images, 125 COVID-19, 500 Pneumonia and 500 Normal, were used to develop the model. X-Ray images were used 80% for training and 20% for verification. The performance of the proposed model was evaluated using the 5-fold cross-validation procedure for triple classification. The three-class classification performance of the model was evaluated for each Fold and the average classification performance was calculated. Among all models, DenseNet201 model achieved the highest performance with 82% accuracy. Also, taking into account all other metrics, DenseNet201 has a precision of 100%, a sensitivity of 80%, and an F1-Score of 88%.

Performance accuracy from combining these 5 models using the maximum voting scheme is 83% on average. The values of 83%, 79%, 82%, 83% and 87% were calculated for Fold-1, Fold-2, Fold-3, Fold-4 and Fold-5, respectively.

Keywords. Coronavirus, COVID-19, Deep learning, Chest X-ray images, DenseNet201

Can Machines Talk? Turkish Voice Assistant and Chatbot Design with Artificial Intelligence in Erzurum Technical University

Emre Çintas 1,2*[0000-0002-4954-5816] , Emrah Şimşek 1,2[0000-0002-1652-9553] and Barış Özyer 2[0000-0003-0117-6983]

¹Department of Computer Engineering, Atatürk University, Erzurum, Turkey

²Department of Computer Engineering, Erzurum Technical University, Erzurum, Turkey

{emrecintas, emrah.simsek, baris.ozyer} @atauni.edu.tr

Abstract

Chatbots are interactive virtual assistants in which users communicate with a human or, more, machines via text or voice messaging in the digital environment and use them for various purposes such as taking action on a subject and obtaining information. These assistants help complete a variety of tasks, from answering a person's questions to solving problems and to playing their favorite songs. In addition, thanks to the developments in artificial intelligence methods, especially deep learning algorithms, it can provide a more accurate and relevant answer to the user by better imitating human dialogue. However, these algorithms require high-capacity data and lead to prestige- and time-wasting problems when they are not made efficient to perform many tasks. In this study, a hybrid chatbot model was designed to respond to the students at Erzurum Technical University in written and audio formats. This model consists of two main stages. In the first stage, more efficient work (normalization) was carried out with less computer memory by using natural language processing (NLP) techniques. Deep learning model (DNN) was used for real-time classification of normalized data. In the study, a new dataset was created with different support requests, frequently asked questions and some traditional conversations started by the University Information and Management System (UBYS) users used within the university. When the experimental results were examined, it was determined that the proposed chatbot showed 88% accuracy with high performance.

Keywords. Chatbot, artificial intelligence, deep learning, NLP, Turkish voice assistant

1. Introduction

Chatbots are applications that can chat with users through voice or written methods within an algorithm. Voice assistants are generally used interchangeably with the concept of chatbot, but voice assistants serve in a wider area. These assistants/bots can interact with the user in writing or speaking (Ho et al. 2018). These bots, developed mostly based on rules, are now being improved on the basis of NLP and artificial intelligence with the developing technology. Alan Turing, who sought an answer to the question "Can machines think" in the 1950s, conceptualized chatbots for the first time. Later, with the development of artificial intelligence algorithms day by day, chatbots continued to be the subject of research and took their current form. The use of these bots is especially preferred by Apple, Samsung, Facebook, Skype, and Telegram (Tekin & Köymen 2020).

Chatbots are generally applied for banking, healthcare, e-commerce, customer service, or information purposes (Işık & Yağcı 2020). Frequently used chatbots are basically divided into two stage; rule-based and artificial intelligence-based. The first rule-based chatbots were traditional programmed chatbots. This type of chatbot basically works according to predefined if-else rules. In these developed bot applications, question and answer sequences are predefined and the answer to the n. question is searched in the same index in the answer sequence. Such developed chatbots usually ask the user to use more specific expressions. This causes users not to use these bots. Artificial Intelligence-based chatbots are more advanced applications utilizing up-to-date technologies. The success rates of these applications can be increased by combining them with NLP techniques. Which is a subcategory of artificial intelligence and linguistics. Chatbots developed based on artificial intelligence are basically divided into two stage. These can be listed as those developed with classification (machine learning) algorithms and deep learning algorithms. Bots based on classification algorithms have lower success rates than chatbots developed with



deep learning algorithms. Chatbots depending on deep learning algorithms, on the other hand, can respond more appropriately to users based on the information they have learned before (Işık & Yağcı 2020). These algorithms operate by finding similar sentences with high probability in answer selection (Sutskever, Le & Vinyals 2014; Bonilla & Ugalde 2019).

Since it is current technology, the number of studies in the field of chatbots is highly limited in the relevant literature. In his study dated 1966, Joseph Weizenbaum imitated a psychotherapist who looked for keywords in users' input and gave response feedback. This study, which is not considered very intelligent, has nevertheless been quite successful in influencing people (Anonymous 2021). In the study by Ming-Hsiang Su et al., a chatbot for elderly care was developed using the LSTM architecture. For the study, daily conversations with the elderly were used. The proposed model worked with 79.96 percent of accuracy (Su et al. 2017). Another study proposed an academic counseling chatbot that is designed by recording student grades of all the courses (Latorre-Navarro & Harris 2015). The chatbot algorithm was not initially used by users. However, the system, which showed an accuracy rate of 80%, was later welcomed. A recent study has been conducted to combine IoT and chatbot for employees to facilitate their connection to machines with smart devices (Muslih et al. 2018).

Our aim in this study is to design a hybrid chatbot that can answer the frequently asked questions of the students at Erzurum Technical University (ETU) by using rule-based and artificial intelligence-based algorithms by speaking and in writing. It is also to propose a chatbot in order to test its usability as a student support service. The proposed chatbot includes a combination of natural language processing techniques (Utkan & Kınasakal 2018), deep learning algorithm (Povinsky, Melicherik & Siladi 2019), and traditional programming. Therefore, in this study, we propose a hybrid chatbot capable of real-time voiced and written responses with collected datasets. For the remainder of the paper, a brief overview of the basic architecture of the system, natural language processing processes, and deep learning algorithm is given in Chapter 2. Chapter 3 contains the experiments and results. Finally, the paper ends in Chapter 4.

2. Methodology

In this study, a hybrid approach model was applied and a chatbot was developed to provide real-time answers to frequently asked questions by ETU students. For this purpose, tokenization, stemming, and stop words, which are natural language processing (NLP) techniques in the literature, were used together in data preprocessing, Bag of words was applied in feature extraction, and finally, deep neural network (DNN) was performed (Povinsky, Melicherik & Siladi 2019). In addition, for the training and testing of the deep neural network, a data set was created, consisting of different questions including different support requests, frequently asked questions, and some traditional conversations started by the users of the University Information and Management System (UBYS) used within ETU.

2.1. Data Preprocessing

Natural Language Processing has recently been used to computationally represent and analyze human language (Khurana et al. 2017). Data preprocessing is the first operation in any dataset and consists of all operations (removal of deficiencies, correctness of data, normalization) before the actual data processing begins. With this process, it is possible to understand the nature of the data, to analyze and to extract meaningful information (Kontuk & Turan 2020).

For this purpose, before training the DNN, firstly, a preprocessing step was applied for efficient training with less data. In the created dataset, some symbols, links and wrong words were cleaned (normalized) with the NLTK library, and then all the words were converted to lowercase and all words were dedifferentiated.

Then, the dataset was split into words using tokenization with the NLTK library. In addition, each word obtained was stemmed and simplified, and again normalized. Finally, stop ones among the obtained words were removed and every word that did not express anything was removed from the data list.

2.2. Deep Neural Network

A DNN model with one dropout, one hidden layers and 32 hidden units was chosen for the proposed chatbot model of this study as its classification algorithm. For this purpose, DNN was used to train and test the dataset. The parameters used for the training of the data collected as a result of the experiments are presented in Table 1 below. The number of input units of the DNN is consistent with the chatbot-input feature vector size. It uses a softmax activation whose size is set to the number of possible answers. In addition, the DNN architecture created is given in Figure 1.

Table 1: Our DNN Parameters.

Dense	Dropout	Shuffling	Optimization	Activation Function	Loss Function	Epoch	Batch Size
32	0.2	Yes	Adam	Relu and Softmax	categorical_crossentropy	100	8

As given in Table 1, 1 hidden layer (32 dense), 1 dropout (0.2), 100 epoch, 8 batch size and relu/softmax activation functions and Adam optimization were used. The number of hidden layers and the hidden units are chosen from cross-validation.

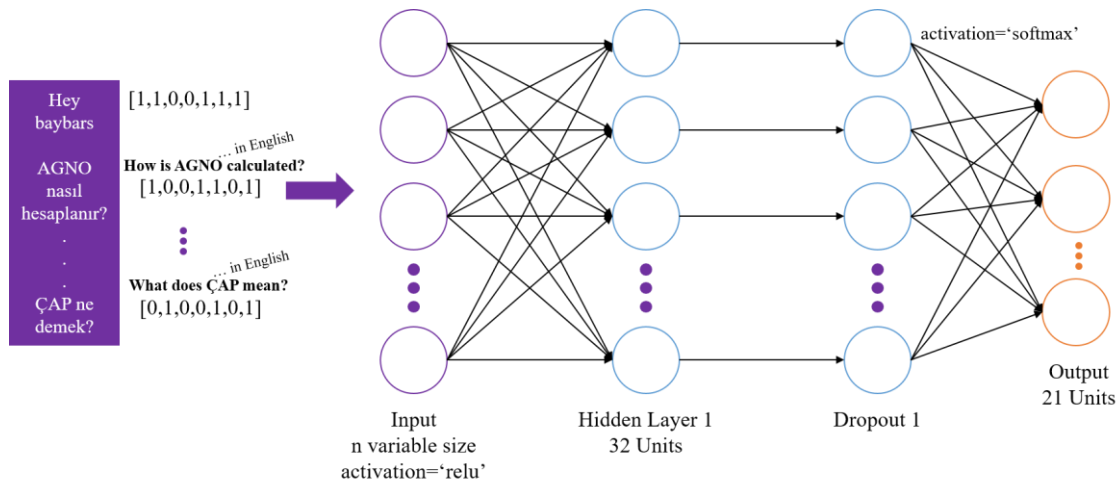


Figure 1: Our DNN Architecture.

As given in Figure 1, the input vectors were trained based on deep learning and taught to the model to which class they belong. In addition, the model has 21 classes as output values. Some of these 21 classes can be shown as “etubaybarsacilis, ogrenciAgno1, ogrenciDersKayitlari3, ogrenciCAPCiftAnaDall, ogrenciYazOkulu, ubys”.

2.3. Feature Extraction

Bag of Words has been translated into Turkish as "Kelime çantası modeli". BoW is a word representation method used when modeling text. It has also been successful in problems such as language modeling and text classification (Mittendorf & Winiwarter 2001; Aydoğan & Karci 2019). For this purpose, the BoW method was applied to the dataset and was used for the testing phase after deep neural network (DNN) training in order to achieve better results.

2.4. Proposed Chatbot Architecture: Baybars

The proposed chatbot block diagram is shown in Figure 2. NLP techniques were used for data normalization while DNN network proposed for training data. For this reason, with the Flask integration in the study, a chatbot that combined rule-based and artificial intelligence-based, could also respond to students in voice and text was designed and this bot was named Baybars.

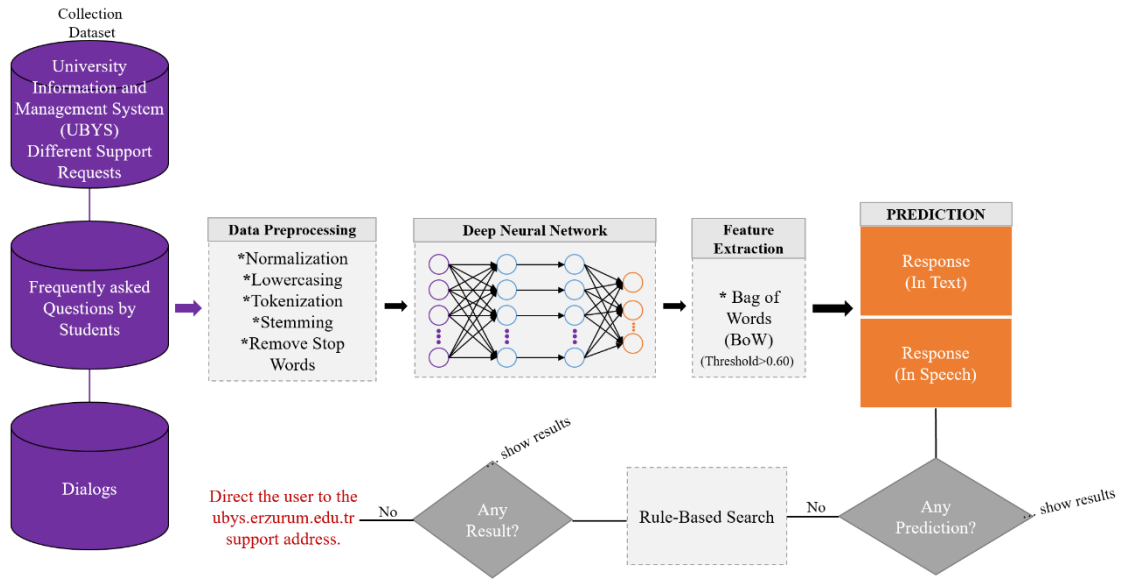


Figure 2: Chatbot Architecture.

As given in Figure 2, the threshold value was chosen as 0.60. When the deep learning model found 60 percent or less results, the rule-based search process was started. If a rule-based result cannot be produced, the user is directed to the support address of UBYs (ubys.erdurum.edu.tr).

2.5. Dataset Collection

The study was carried out with a new dataset consisting of different support requests, frequently asked questions and some traditional speeches started by students to the University Information and Management System (UBYS) used within ETU. In the dataset used to train and test the chatbot, there are dialogs based on many topics such as weighted grade point average, double major, course registrations, and summer school. Examples from the generated dataset are given in Table 2.

Table 2: A Small Portion of Collection Dataset.

```

{"dialogs": [
  {"class": "etubaybarsacilis",
   "inputs": ["Hey baybars","Hey sen","Baybars","hey merhaba","açıl"],
   "answers": ["Efendim","Buyrun","Hey, Selam","Merhaba, sana nasıl yardımcı olabilirim?","Hey, Merhaba","Devam et"]
  },
  {"class": "ogrenciAgno1",
   "inputs": ["Ağırlıklı genel not ortalaması nedir?", "AGNO nedir?","Agno nedir","Agno ne demektir?","Ağırlıklı genel not ortalaması ne demek?"],
   "answers": ["Öğrencinin öğrenime başladığı andan itibaren, tamamlamış olduğu yarıyıl da dahil olmak üzere almış olduğu tüm derslerin katılmışıyla elde edilen ve başarısını belirleyen not ortalamasıdır."]
  },
  {"class": "ogrenciAgno2",
   "inputs": ["AGNO nasıl hesaplanır?","Ağırlıklı genel not ortalaması nasıl hesaplanır?","Agno nasıl hesaplanıyor"],
   "answers": ["Öğrencinin tamamlamış olduğu yarıyıl da dahil olmak üzere, o güne kadar kayıt yaptırdığı her dersin AKTS kredisi ile dersin başarı notunun ağırlık katsayısı ile çarpılması ile elde edilen sayıların toplamının, almış olduğu tüm derslerin AKTS kredi toplamına bölünmesi ile hesaplanır."]
  },
  {"class": "ogrenciAgno3",
   "inputs": ["Tekrar aldığım derslerin notları AGNO'ya nasıl etki ediyor?","Tekrar aldığım derslerin notları Ağırlıklı genel not ortalamasına nasıl etki ediyor?","Agno tekrar aldığım derslerin ortalamasına nasıl etki ediyor"],
   "answers": ["Yarıyıl tamamlandığında AGNO değeri artık sabitlenir. Dolayısıyla herhangi bir dersi daha"]
  },
  {"class": "ogrenciDersKayitlari2",
   "inputs": ["Ders kayıt işlemi nasıl yapılır?","Ders kayıt işlemi nasıl yapabilirim?","Derse kayıt olmak için ne yapmak gerekiyor?","Derse kaydolmak için ne yapmak gerekiyor?","Ders kaydı nasıl yapılır?"],
   "answers": ["Öğrenci bilgi sistemi üzerinden, kayıt yenileme-ders seçme işlemleri menüsüne girip sayfada açılan derslerden seçimlerinizi yaparak danışman onayına göndermeniz gerekmektedir."]
  },
  {"class": "ogrenciCAPCiftAnaDal1",
   "inputs": ["Çift ana dal nedir?","ÇAP nedir?","ÇAP ne demek?"],
   "answers": ["Başarı şartını ve diğer koşulları sağlayan öğrencilerin aynı yükseköğretim kurumunun iki diploma programından eş zamanlı olarak ders alıp, iki ayrı diploma alabilmesini sağlayan programdır."]
  }
]
}

```

3. Experiments and Results

Experiments were conducted for the DNN network only. While training and testing the model, Google Colab was utilized and NVIDIA Tesla P100 graphics card was used. As training data, 90% of the dataset was used for training and the remaining 10% of the dataset was reserved for testing. While calculating the success score, the overlap between the answers produced by the method for the sentences detected and the ground-truth of the target sentences manually determined by people was taken into account. In addition, the test data were created with data that the model had not seen before. Overfitting was prevented by shuffling the data set. The training success rate of the model was 96.25%. Figure 3 shows the performance and loss rates of the data set in 100 iterations, and Figure 4 shows the confusion matrix created for the model.

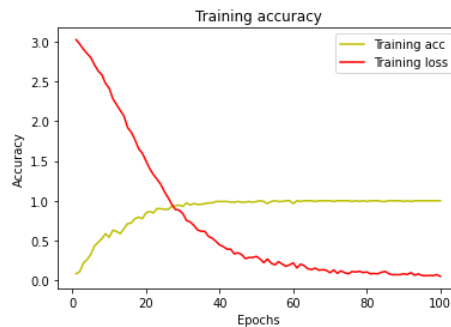


Figure 3: Loss and Accuracy Graph for Model.

As shown in Figure 4, the Threshold value is 0.60. This value was set as the threshold value to eliminate irrelevant questions.

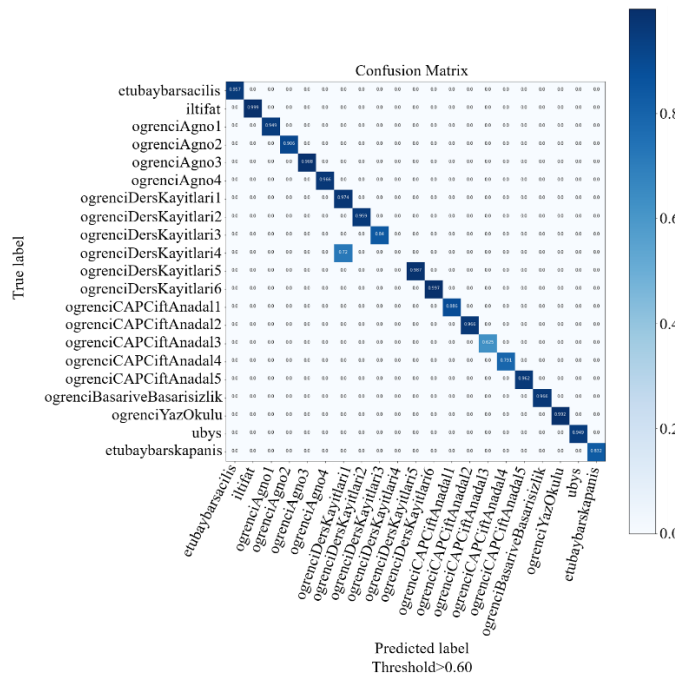
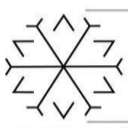


Figure 4: Confusion Matrix for the DNN Model.

The performance scores of the DNN network are given in Table 3. While creating the performance score, 5-fold cross-validation was calculated.

Table 3: The Performance of the DNN Method on Collective Dataset.

Method	Epoch	Accuracy
Deep Neural Network	100	88.05%



When the model was evaluated, it was determined that the model showed an accuracy rate of 88.05% on the test dataset that it had not seen before. Evaluation results are calculated only according to the data collected in ETU. Rule-based dialogues were not included in the evaluation results. In addition, a user-friendly interface with flask connection has been designed and sample voice and written speeches are given in Figure 5.

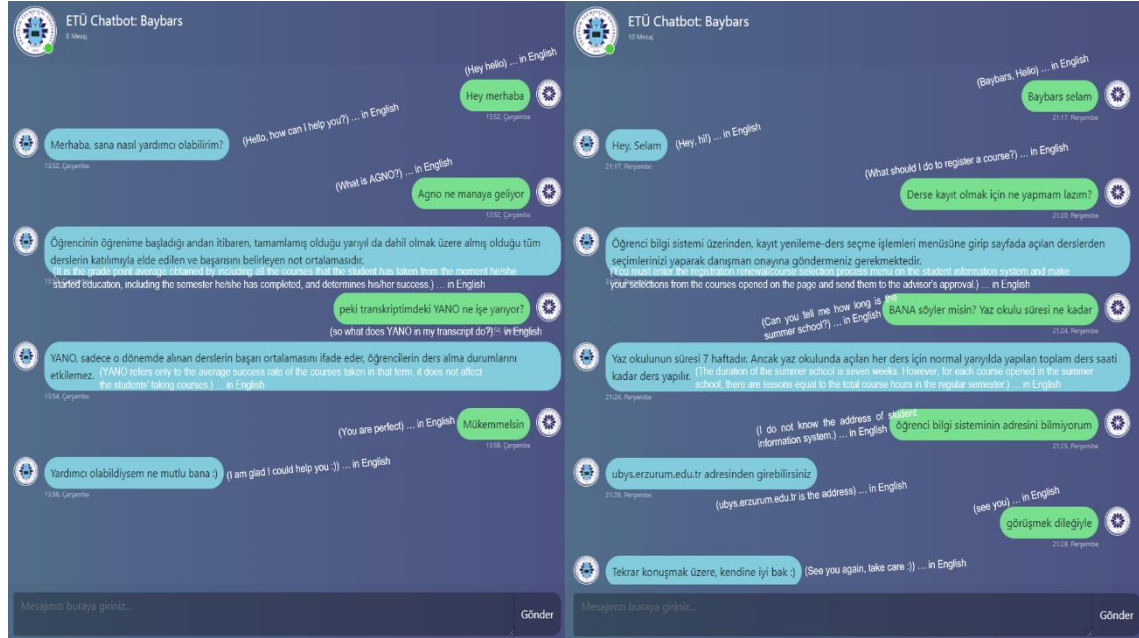


Figure 5: Sample Dialogues from Baybars Chatbot.

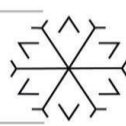
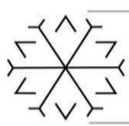
4. Conclusion

In this study, a chatbot that can respond in voice and text has been developed using NLP techniques, DNN model, Python programming language, and Flask application. It is planned to use the study as an example in order to answer the frequently asked questions of ETU students. In the study, a dataset with 21 classes consisting of frequently asked questions was collected and used. With the study, a non-repetitive chatbot has been designed that gives appropriate answers to the questions asked by the user with the data taken from the created dataset. The study is trained for the 100-step epoch with the categorical_crossentropy loss function. The obtained accuracy rate was detected to be 88.05%. According to the results, the accuracy rate increases as the training data increases.

It is thought that with more data, using LSTM, BERT algorithms, and integrating with telegram and rest api, the rate of use in the real environment will increase, comprehensive answers can be produced and higher accuracy results can be obtained.

Acknowledgements

The authors are very grateful to Erzurum Technical University Registrar's Office for frequently asked questions data used in the study.



References

- Anonymous, <https://web.njit.edu/~ronkowit/eliza.html> [Online] (Accessed: 18 October 2021)
- Aydoğan, M. and Karci, A. (2019) 'Turkish Text Classification with Machine Learning and Transfer Learning', *2019 International Artificial Intelligence and Data Processing Symposium (IDAP)*, pp. 1-6. doi: 10.1109/IDAP.2019.8875919.
- Bonilla, F. and Ugalde, F. (2019) 'Automatic Translation of Spanish Natural Language Commands to Control Robot Comands based on LSTM neural network', *Third IEEE International Conference on Robotic Computing (IRC)*, Naples, Italy, pp. 125-131.
- Ho, C. C. Lee, H. L. Lo, W. K. and Lui, K. F. A. (2018) 'Developing a Chatbot for College Student Programme Advisement', *International Symposium on Educational Technology (ISET)*, pp. 52-56. doi: 10.1109/ISET.2018.00021.
- Işık, A. and Yağcı, A. (2020) 'Telegram Bot Application with Sequence to Sequence LSTM Model', *Gazi Journal of Engineering Sciences*, 6(1), pp. 32-39. doi: 10.30855/gmbd.2020.01.03.
- Kontuk, R. and Turan, M. (2020) 'Classification of News according to Age Groups Using NLP', *Gazi University Journal of Science*, 8(2), pp. 372-382.
- Khurana, D. Koli, A. Khatter, K. and Singh, S. (2017) 'Natural Language Processing: State of The Art', *Current Trends and Challenges*, ArXiv abs/1708.05148.
- Latorre-Navarro, E. M. and Harris, J. G. (2015) 'An Intelligent Natural Language Conversational System for Academic Advising', *International Journal of Advanced Computer Science and Applications*, 6(1), doi: 10.14569/IJACSA.2015.060116.
- Mittendorfer, M. and Winiwarter, W. (2001) 'A simple way of improving traditional IR methods by structuring queries', *2001 IEEE International Conference on Systems*, Tucson, AZ, USA, pp. 951-953.
- Muslih, M. Supardi, D. Multipli, E. Nyaman, Y. M. and Rismawan, A. (2018) 'Developing Smart Workspace Based IOT with Artificial Intelligence Using Telegram Chatbot', *In 2018 International Conference on Computing, Engineering, and Design (ICCED)*, Bangkok, Thailand, pp. 230-234.
- Povinský, M. Melicherčík, M. and Siládi, V. (2019) 'A Chatbot based on Deep Neural Network and Public Cloud Services with TJBOT Interface', *2019 IEEE 15th International Scientific Conference on Informatics*, pp. 000101-000106. doi: 10.1109/Informatics47936.2019.9119304.
- Su, M. H. Wu, C. H. Huang, K. Y. Hong, Q. B. and Wang, H. M. (2017) 'A chatbot using LSTM-based multi-layer embedding for elderly care', *In 2017 International Conference on Orange Technologies (ICOT)*, pp. 70-74.
- Sutskever, I. Le, Q. and Vinyals, O. (2014) 'Sequence to Sequence Learning with Neural Networks', *In Advances in neural information processing systems*, pp. 3104-3112.
- Tekin, M. and Köymen, E. (2020) 'Use of Voice Command Technology in Architecture', *Al-Jazari Journal of Science and Engineering*, 7(3), pp. 1362-1370. doi: 10.31202/ecjse.776858.
- Utkan, E. and Kınasakal O. A. (2018) 'Turkish Chatbot For Administrative Inquiries in Bogazici University', *CMPE 492 Final Report*.

Sentiment analysis in Persian using discourse and external semantic information

Rahim Dehkharghani¹*[0000-0002-9619-8247] and HojjatEmami²[0000-0002-5280-4620]

¹rahim.dehkharghani@isikun.edu.tr, Computer engineering department, Faculty of Engineering, Isik University, Istanbul, Turkey

²emami@ubonab.ac.ir, Computer engineering department, Faculty of Engineering, University of Bonab, Bonab, Iran

Abstract

Many approaches have been proposed to extract the sentiment of individuals from documents written in natural languages in recent years. The majority of these approaches have focused on English, while resource-lean languages such as Persian suffer from the lack of research work and language resources. Due to this gap in Persian, the current work is accomplished to propose a hybrid method for sentiment analysis which has been applied in Persian. His method takes advantage of local discourse information and external knowledge bases, and also covers several language issues such as negation and intensification, and addresses different granularity levels, namely word, aspect, sentence, phrase, and document-levels. In order to evaluate the performance of the proposed approach, a Persian dataset is collected from Persian hotel reviews referred to as *hotel reviews*. The experimental results approve the effectiveness of the proposed approach when compared to related works.

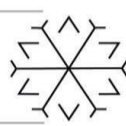
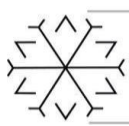
Keywords. Sentiment analysis, semantic relations, classifier combination, Persian

1. Introduction

Sentiment analysis identifies and extracts polarities toward entities such as topics, events, individuals, issues, services, products, organizations, and their attributes (Yue *et al.*, 2018). Sentiment analysis is a domain and language-dependent task. Words or phrases may carry different polarities in different domains. For example, the word "big" has positive polarity for the "room size" in the hotel domain, while it has negative polarity for the "battery size" in the camera domain. The issues mentioned above indicate that no general sentiment analysis system can work well for all natural languages. There exist a big deal of research on sentiment analysis in some languages; however, Persian is one of the less-studied languages in this field (Emami, Shirazi and Barforoush, 2016). Persian is a member of the Indo-European languages. Over 110 million people speak Persian in different countries such as Iran, Afghanistan, Tajikistan, and Uzbekistan, which constitute 1.5% of the world's population (Emami, Shirazi, and Barforoush, 2016). This large number of people produces the bulk of Persian content on the Web and social media. In this paper, we investigate sentiment analysis in Persian and propose an approach that covers different granularity levels and language issues.

Sentiment analysis can be examined in different granularity levels: document-level (Pang, Lee and Vaithyanathan., 2002), sentence-level (Meena and Prabhakar, no date), phrase level (Wilson, Wiebe and Hoffmann, 2009), aspect level (Singh *et al.*, no date), and word-level (Dehkharghani *et al.*, 2016). On the other hand, the sentiment analysis methods can be grouped into three main categories (Yue *et al.*, 2018): machine learning methods, lexicon-based methods, and hybrid methods.

Machine learning methods are more popular as they achieve encouraging results on sentiment analysis. Liu *et al.* (Liu, Bi and Fan, 2017) proposed a supervised multi-class sentiment classification method based on SVM and an improved one-vs.-one strategy. Tang *et al.* (Tang, Qin and Liu, 2015) proposed Neural Network models including Conv-GRNN and LSTM-GRNN for document-level sentiment classification. The model first learns sentence representation with a convolution neural network. Then, the semantic of sentences and their relations are adaptively encoded in document representation with gated Recurrent Neural Network. Parlar *et al.* (Parlar, Özel and Song, 2018) introduce a new feature selection method, called query expansion ranking (QER) for sentiment analysis from review texts. QER is based on query expansion term weighting methods. The main drawback of the supervised methods is that they require a relatively large training set. To overcome this problem, unsupervised methods are devised. Riz *et al.* (Riaz *et al.*, 2019) proposed a phrase-level sentiment analysis method to identify customer preferences by



analyzing subjective reviews. Suresh and Gladston (Suresh and Gladston, 2016) presented a novel fuzzy clustering method to analyze tweets regarding the sentiments of a particular brand.

In lexicon-based methods, polarity lexicons contain a (generally large) set of words/ phrases, which express individuals' feelings and opinions towards an issue by using quantitative values. The approach of lexicon-based techniques towards sentiment analysis is unsupervised because they do not require a prior training phase to classify data. Turney (Turney, 2002) employed a set of patterns of tags for extracting two-word phrases from reviews. Agarwal et al. (Agarwal et al., 2015) performed a polarity classification of Tweets. The authors employed five different combinations of features on unigrams, senti-features, and tree kernels. They evaluated the proposed method with 11,875 manually annotated tweets.

Most research interest has focused on the English language. Only a few studies have been performed on sentiment analysis for resource-lean languages such as Persian (Bagheri, A., M. Saraee, no date; Takhshid and A. Rahimi, no date; Saraee and Bagheri., 2013; Amiri, Scerri and Khodashahi, 2015; Golpar-Rabooki, E. and J. Rezaenour, 2015; Roshanfekar, Khadivi and Rahmati, 2017; Dashtipour et al., 2018, 2020; Basiri et al., 2019). Since English and Persian have different characteristics, in order to apply proposed approaches for English on Persian, they need to be modified first. Therefore, the majority of proposed approaches for Persian have been specialized for this language. The contribution of this paper is not to use the state of the art classifiers such as deep neural networks but to prepare Persian texts for sentiment analysis by analyzing language issues such as negation and intensification and also covering co-reference resolution.

2. Proposed approach

The proposed approach is composed of four main steps: pre-processing, feature extraction, feature integration, and grouping. Pre-processing consists of the co-reference resolution, sentence segmentation, tokenization, and partial normalization.

2.1. Pre-processing

In the co-reference resolution phase, pronouns and entity mentions are replaced by their corresponding representative mentions in the text. To resolve co-references, first, coarse-grained entity types, including person, location, and organization, are annotated using a multi-lingual named entity recognizer (Al-Rfou et al., 2015). Then, annotated documents are passed to a rule-based co-reference resolution module (Fallahi and Shamsfard, 2011) to resolve co-referent mentions. This module identifies co-reference chains for all the entities mentioned in the document. The mentions within every co-reference chain are replaced with their referent mention. For example, in the following sentences,

هتل استقلال، خیلی زیبا است. آن را خیلی دوست دارم.

The Esteghlal hotel is very beautiful. I like it so much.

The pronoun "it/آن" is replaced with mention "هتل استقلال/ the Esteghlal hotel" which results in the following sentence:

هتل استقلال، خیلی زیبا است. هتل استقلال را خیلی دوست دارم.

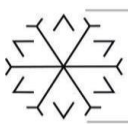
The Esteghlal hotel is very beautiful. I like the Esteghlal hotel so much.

This step contributes to the sentiment analysis task due to replacing a pronoun-which is neutral- by a noun –which might be polar.

In sentence segmentation, each document $d_i \in D$ is segmented into m sentences using the separators such as period, exclamation mark, and question mark. In the next step, tokenization is used to split a sentence into words, phrases, symbols or other meaningful tokens. Each sentence $s_i \in S$ is tokenized using the Hazm tokenizer tool (Dashtipour, et al., 2020). Finally, partial normalization transforms plural forms to the singular and removes stop words and postfixes from words. Prefixes are not removed as they usually indicate the polarity of Persian words. For example, in the Persian word “بی‌دقت/careless”, the prefix “بی/less” should be kept on the word to indicate its polarity.

In order to accomplish this phase, we used Hazm morphology analyzer. As an example, given the following sentence,

میهمانان از این هتل خیییییییی لذت می برند.



Guests enjoy this hotel verrrrrrry much”.

The result would be

میهمان هتل خیلی لذت بردن

Guest enjoy hotel very much.

2.2. Feature Extraction

This phase takes as input the pre-processed text and extracts features, which are required for the grouping phase. These features are listed in Table 1, which can be classified into two groups: sentence-level and document-level. Note that all features except F15 and F16 are used in both sentence and document-level sentiment analysis tasks. Features F15 and F16 are used only at document-level.

Table 1: List of features extracted from reviews, S: Sentence, D: document.

Feature id	Name	Level
F1	Avg. positive polarity of words in SentiFars	S, D
F2	Avg. negative polarity of words in SentiFars	S, D
F3	Avg. polarity of Positive words in Persent	S, D
F4	Avg. polarity of negative words in Persent	S, D
F5	Avg. polarity of positive words in LexiPers	S, D
F6	Avg. polarity of negative words in LexiPers	S, D
F7	Accumulative Prob. of Pos. and Neg. words	S, D
F8	Accumulative Prob. of Pos. and Neg. words	S, D
F9	Existence of exclamation mark	S, D
F10	Existence of question mark	S, D
F11	Existence of positive emoticons	S, D
F12	Existence of negative emoticons	S, D
F13	Domain-dependent positive indicative keywords	S, D
F14	Domain-dependent negative indicative keywords	S, D
F15	Polarity of the first sentence	D
F16	Polarity of the last sentence	D
F17	Length of document/sentence	S, D

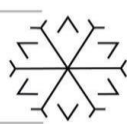
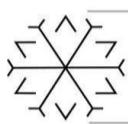
Features F1, F2 compute the average positive/negative scores of all unigrams and bigrams based on SentiFars (Dehkharghani, 2020), a Persian polarity lexicon. Features F3, F4 compute the average polarity of positive and negative words based on PerSent (Dashtipour *et al.*, 2016) -another Persian polarity lexicon. Features F5, F6 are used to compute the number of positive and negative words based on LexiPers (Sabeti, B. *et al.*, 2016)-another Persian polarity lexicon, a Persian polarity lexicon. Features F7, F8: To compute these features, we defined the following equation.

$$Prob(i) = i \times P(i) \quad (1)$$

where i is the number of positive/negative words in a review and $P(i)$ is the probability of seeing i positive/negative words in positive/negative reviews. Features F9, F10 check the existence of exclamation and question marks in reviews. Features F11, F12 check the existence of positive and negative emotions. Emoticons carry positive or negative emotions; therefore, they are good polarity indicators in reviews. Features F13, F14 focus on domain-dependent keywords. These keywords are those words or phrases which can explicitly express the polarity of a review, in which they appear. For example, the word "کوچک" (small) usually carries negative polarity, e.g., for *room size* in hotel domain, while it has positive polarity for *battery size* in the camera domain. Features F15 and F16 are used only in the document-level sentiment analysis. In these features, the average polarity of all words in the first and last sentences of a document is computed based on the scores of SentiFars and PerSent. Feature 17 is simply the length of a review. In the feature integration phase, we prune the features in order to prepare them for the classification phase. Feature integration focuses on two challenges: handling language issues and also different granularity levels.

2.2.1. Handling language issues

The polarity scores of words and consequently reviews are used as features for classification; however, polarity shifters such as negation or intensification marks can modify these polarity scores. In order to handle negation, we used the following approach (Wilson, *et al.*, 2009): if the verb is negated in a sentence, all words in that sentence will be negated, but if an adjective or noun is negated, only the



polarity of that word will be negated. When a polar word is negated, its polarity score is shifted, meaning that this score is decreased or increased by a constant value.

On the other hand, if an adjective is intensified, only the polarity of this adjective is modified. A subset of negation marks and intensifiers are listed in Table 2. Negation and intensification handling depend on the format of polarity scores or tags assigned to each polar word/phrase. The assigned polarity might be a tag (as in LexiPers) or a float number (as in SentiFars). In the case of using polarity tags, the polarity of words preceding the negation mark is switched from positive to negative or from negative to neutral.

Table 2: A subset of negators and intensifiers

Negator	نیست، نمی باشد، نبود، نباشد، نمی شود، نخواهد بود (was/ is/ will not) بدون، بی / without
Intensifier	خیلی، بسیار، زیاد (additive) (very) کمی، یکم، یک ذره (reducer) (a little)

2.2.2. Handling different granularities

Besides the word-level, we also cover other granularity levels such as the phrase, aspect, Sentence and document levels.

Phrase level SA. We generate phrases using a syntactic and semantic analysis module. The syntactic analysis phase uses the Hazm dependency parser¹ and generates a dependency syntactic graph G_d for each sentence of the text. Figure 1 displays the dependency graph for a sample sentence. In the dependency graph G_d, every single word is represented as a node and word-word dependencies are represented as directed edges between nodes. In other words, dependency graph G_d represents binary relations between words of a sentence, in which words are connected with their parent words with a unique edge labeled with a syntactic function (Emami, Shirazi and Barforoush, 2016). The sample sentence in Figure 1 is given below.

هتل استقلال تهران منظره بسیار خوبی دارد.

Tehran's Esteghlal Hotel has a great view.

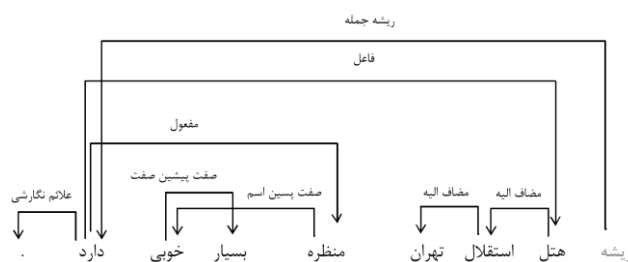


Figure 1: The dependency graph for a sample sentence

The semantic analysis phase takes as input the dependency graph generated by the syntactic analysis phase and augments the dependency graph with semantic information. The semantic analysis phase provides a sense mapping from surface words and named entity mentions in a dependency graph to the unique entries of ontology. In this phase, we first disambiguate the word senses using Babelify (Moro, Raganato and Navigli, 2014), i.e., the correct sense of a word is extracted according to its context. We then filter the resulting senses by pruning the senses corresponding short tail mentions that are covered by other long-tail mentions. We map surface textual words and mentions to word senses and named entities in BabelNet ontology (Moro, Raganato, and Navigli, 2014). Figure 2 shows the result of semantic analysis for a sample sentence. In Figure 2, notation bn:i refers to the i-th BabelNet sense for the given word. As different senses of a word/phrase might have different polarity scores, word sense disambiguation can contribute to the sentiment analysis task at different granularity levels.

¹ <http://www.sobhe.ir/hazm>

دارد	بسیار خوبی	منظره	هتل استقلال تهران
-	bn:00114215r	bn:00625423n	bn:17230067n

Figure 2: Semantic analysis for a sample sentence

To map the dependency graph's nodes to ontology entries and create a syntactic-semantic graph, we start from the dependency graph G_{dof} sentence *s*, and a set of disambiguated senses for *s*. If a disambiguated sense is a single token and covers a single node in G_d, it is assigned to the corresponding dependency node. If a disambiguated sense is a multi-word expression and covers more than one node in G_d, we merge the sub-graph referring to the same concept or entity to a single semantic node. Figure 3 shows the sense mapping and the result of the dependency graph summarization for the graph G_d given in Figure 1.

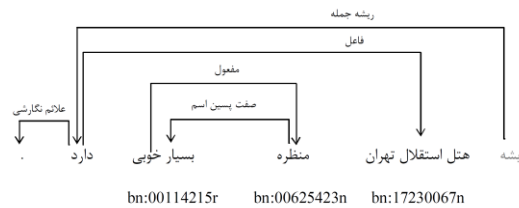


Figure 3: Syntactic-semantic analysis for a sample sentence

In order to compute the polarity of a phrase, the average polarity of all words appearing in the phrase, extracted from the dependency tree, is computed by Equation (2).

$$Pol(phrase) = \frac{\sum_{w_i \in phrase} pol(w_i)}{n} \quad (2)$$

Aspect-level SA. In the aspect-level phase, we used Equation (3) to estimate the polarity of an aspect that appeared in a sentence.

$$Pol(A) = \frac{\sum pol(w_i)}{n} \quad (3)$$

P(A) is the average polarity of the aspect word A; *n* is the number of words following the aspect A and *w_i* are those words preceding A in the same sentence. In other words, the polarity of an aspect in a sentence is equal to the average polarity of words preceding that aspect in the sentence. The intuition behind this method is that the polarity of an aspect is usually expressed by adjective(s) and a verb appearing after the aspect in the same sentence.

As an example, in the following sentence, the polarity of aspect word “غذا” (food) is expressed by the adjective “خوشمزه”(delicious) and the verb “دوست دارم” (like) following the aspect.

من در این هتل فقط غذای خوشمزه آن را دوست دارم.

I like only the delicious food of this hotel.

Table 3: A subset of aspect keywords in the hotel domain

Persian	English
غذا	Food
قیمت	Price
منظره	View
سرویس	Service
حمل و نقل	Transportation
نور	Light
فضا	Space

The list of aspects have been manually extracted from reviews in the hotel domain includes explicit aspects, which have been listed in Table 3. SentiFars is used to extract positive and negative scores of words in aspect-level sentiment analysis.

Sentence and document level SA. Almost the same set of features are used in the sentence and document levels. Features 15 and 16 (in Table 1) are used only for the document-level. We approach a document as a bag of sentences and each sentence as a bag of words, which have been extracted from the

sentences of that document. Note that the first and last sentences are processed differently compared to sentences in the middle of the document.

2.3. Classification

Two ternary classification tasks for classifying the sentences and documents in Persian hotel reviews have been separately accomplished. Three classifiers, namely, multilayer perceptron, Logistic classifier, and SMO are separately trained on 60% of data and tested on the remaining 40%. After this phase, the confidence values of these three classifiers together are used as features for training another classifier. In other words, by using the confidence values of each classifier for each class, we trained another Logistic classifier with nine feature values (3*3=9). The logistic classifier is chosen due to its higher generalization accuracy. The tool used for classification is WEKA.

3. Evaluation

In this section, dataset, performance measures, obtained results, and discussion on results are presented.

Dataset. We used 761 documents and 3613 sentences included in these documents, as Persian hotel reviews, a subset of which is available in the first author’s homepage². These documents and sentences have been manually labelled as positive, negative, or neutral by three (plus one) native speakers. The distribution of different classes in sentences and documents are respectively (neg, obj, pos) = (27%, 13%, 60%) and (neg, obj, pos) = (22%, 7%, 71%). The number of objective (neutral) reviews is lower than subjective ones probably because only those people write their ideas about their stay in hotels that would like to express a subjective idea.

Performance measures. The proposed method is evaluated using four metrics: precision (*P*), recall (*R*), accuracy (*A*) and F1 measure (Parlar, Özel and Song, 2018). Precision (*P*) is the number of correctly classified documents over the total number of classified documents with respect to a class. Recall (*R*) is the number of correctly classified documents over the total number of items that belong to a given class. Accuracy is the portion of number of correctly classified data over the number of all data. F1-measure is a composite score of precision and recall, computed as follows.

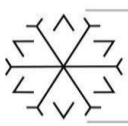
Results. Table 4 shows the accuracy of the proposed methodology for classifier combination approach when using different subsets of features for ternary classification. The best pair of features in isolation is polarity scores extracted from SentiFars in sentence-level and polarity scores extracted from PerSent at the document level. The combination of SentiFars and PerSent gives higher accuracy and the set of all features achieves the highest accuracy. The performance of features F15 and F16 is shown only at document-level. Moreover, as emoticons, exclamation and question marks are rarely used in reviews, features F9 to F12 are not separately evaluated.

Table 4: Ternary classification accuracy in the sentence- and document-level sentiment analysis on test data (40%)

Document-level		Sentence-level	
Feature subset	Accuracy (%)	Feature subset	Accuracy (%)
F1-F2	80.28	F1-F2	69.24
F3-F4	80.48	F3-F4	68.47
F1-F4	81.86	F1-F4	69.52
F5-F6	77.66	F5-F6	67.45
F1-F6	80.48	F1-F6	69.31
F7-F8	76.43	F7-F8	67.1
F1-F8	80.77	F1-F8	70.11
F9-F14	74.66	F9-F14	65.21
F15-F16	77.56	All features	70.81
All features	80.98		

Table 5 reports Precision and Recall values for each class. This table illustrates the performance of the combined classifier separately for each class. As can be seen, the classifier is more successful in estimating the polarity of positive reviews, probably because people generally express their positive ideas more clearly, while they use indirect polarities or sarcasm in their negative reviews.

² <http://myweb.sabanciuniv.edu/rdehkharghani/files/2018/11/Labelled-Persian-Reviews.txt>

**Table 5:** Precision and Recall values for each class in ternary classification evaluated by test data.

	Class	Precision (%)	Recall (%)	F1(%)
Doc-level	Negative	82.99	73.05	77.70
	Objective	37.73	40.0	38.83
	Positive	94.44	92.22	93.31
Sent- level	Negative	89.33	71.52	79.43
	Objective	33.48	59.45	42.83
	Positive	77.67	89.23	83.04

According to obtained results in Table 4, it can be concluded that using three polarity lexicons (SentiFars, PerSent, and LexiPers) achieves much higher accuracy than using features F9 to F14. As emoticons, exclamation and question marks, and domain-dependent indicative keywords are rarely used in reviews, these features achieve the lowest accuracy in isolation compared to other feature subsets. The difference between using all features and only three polarity lexicons is almost 1%. This low difference emphasizes the impact of the polarity lexicons on the proposed approach.

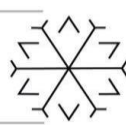
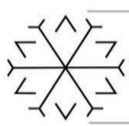
The difference of the current work with the existing ones in the literature is that the current work covers three classes (including the objective class) while the literature mostly focuses on the binary classification of reviews considering only the positive and negative classes. Moreover, reference resolution is usually omitted in the related works, while it plays an important role in accurately extracting the sentiment from Persian documents. Furthermore, language issues such as negation and intensification and also different granularity levels, including phrase and aspect levels, have not been deeply investigated in the literature.

4. Conclusion

In this paper, we investigated sentiment analysis in Persian and proposed a hybrid approach based on classifier combination that covers some language issues and different granularity levels. The proposed approach benefits from different features and classifier combination to classify Persian reviews into opinion classes. Although the proposed approach has experimented on Persian, it can be applied to other languages with some modifications, such as updating pre-processing phase. The application of the current work includes extracting public opinion regarding an issue or product based on the reviews written by the customers or predicting the elections by analyzing the comments of internet users in social media. As future work, we will apply other newer approaches such as deep neural networks on our dataset and will compare it with the proposed approach. The goal of this work is solely to prepare the text in terms of co-reference resolution and handling language issues for sentiment analysis.

References

- Agarwal, B. *et al.* (2015) 'Concept-Level Sentiment Analysis with Dependency-Based Semantic Parsing: A Novel Approach', *Cognitive Computation*, 7(4), pp. 487–499.
- Al-Rfou, R. *et al.* (2015) 'Polyglot-NER: Massive Multilingual Named Entity Recognition', in *Proceedings of the 2015 SIAM International Conference on Data Mining, Vancouver, British Columbia, Canada*, pp. 586–594.
- Amiri, F., Scerri, S. and Khodashahi, M. (2015) 'Lexicon-based sentiment analysis for Persian Text', *Proceedings of the International Conference Recent Advances in Natural Language Processing*.
- Bagheri, A., M. Saraei, and F. de J. (no date) 'Sentiment classification in Persian: Introducing a mutual information-based method for feature selection', in *Electrical Engineering (ICEE), 2013 21st Iranian Conference on. 2013. IEEE*.
- Basiri, M. E. *et al.* (2019) 'The effect of aggregation methods on sentiment classification in Persian reviews', *Enterprise Information Systems*. Taylor & Francis, 0(0), pp. 1–28. doi: 10.1080/17517575.2019.1669829.
- Dashtipour, K. *et al.* (2018) 'Exploiting Deep Learning for Persian Sentiment Analysis', *Lecture Notes in Computer Science (including subseries Lecture Notes in Artificial Intelligence and Lecture Notes in Bioinformatics)*, 10989 LNAI, pp. 597–604. doi: 10.1007/978-3-030-00563-4_58.
- Dashtipour, K. *et al.* (2020) 'A hybrid Persian sentiment analysis framework: Integrating dependency grammar based rules and deep neural networks', *Neurocomputing*. Elsevier B.V., 380, pp. 1–10. doi:



10.1016/j.neucom.2019.10.009.

Dehkharghani, R. *et al.* (2016) 'SentiTurkNet: a Turkish polarity lexicon for sentiment analysis', *Language Resources and Evaluation*, 50(3), pp. 667–685.

Dehkharghani, R. (2020) 'SentiFars: a Persian polarity lexicon for sentiment analysis', *ACM Transactions on Asian and Low-Resource Language Information Processing*, 19(2), pp. 1–12.

Emami, H., Shirazi, H. and Barforoush, A. A. (2016) 'A Semantic approach to person profile extraction from Farsi documents', *Journal of Information Systems and Telecommunication*, 4(4), pp. 232–243.

Fallahi, F. and Shamsfard, M. (2011) 'Recognizing Anaphora Reference in Persian Sentences', *International Journal of Computer Science Issues*, 8(2), pp. 324–329.

Golpar-Rabooki, E., S. Z. and J. Rezaenour (2015) 'Feature extraction in opinion mining through Persian reviews.', *Journal of AI and Data Mining*, 3(2), pp. 169–179.

Liu, Y., Bi, J. W. and Fan, Z. P. (2017) 'A method for multi-class sentiment classification based on an improved one-vs-one (OVO) strategy and the support vector machine (SVM) algorithm', *Information Sciences*. Elsevier Inc., 394–395, pp. 38–52. doi: 10.1016/j.ins.2017.02.016.

Meena, A. and Prabhakar, T. (no date) 'Sentence level sentiment analysis in the presence of conjuncts using linguistic analysis', in *European Conference on Information Retrieval. 2007. Springer*.

Moro, A., Raganato, A. and Navigli, R. (2014) 'Entity linking meets word sense disambiguation: a unified approach', *Transactions of the Association for Computational Linguistics*, 2, pp. 231–244.

Pang, B., Lee, L. and Vaithyanathan, S. (2002) 'Thumbs up?: sentiment classification using machine learning techniques', in *Proceedings of the ACL-02 conference on Empirical methods in natural language processing. Association for Computational Linguistics*.

Parlar, T., Özel, S. A. and Song, F. (2018) 'QER: a new feature selection method for sentiment analysis', *Human-centric Computing and Information Sciences*. Springer Berlin Heidelberg, 8(1), pp. 1–19. doi: 10.1186/s13673-018-0135-8.

Riaz, S. *et al.* (2019) 'Opinion mining on large scale data using sentiment analysis and k-means clustering', *Cluster Computing*. Springer US, 22, pp. 7149–7164. doi: 10.1007/s10586-017-1077-z.

Roshanfekar, B., Khadivi, S. and Rahmati, M. (2017) 'Sentiment analysis using deep learning on Persian texts', *2017 25th Iranian Conference on Electrical Engineering, ICEE 2017, (ICEE20 17)*, pp. 1503–1508. doi: 10.1109/IranianCEE.2017.7985281.

Saraee, M. and Bagheri, A. (2013) 'Feature selection methods in Persian sentiment analysis', in *International Conference on Application of Natural Language to Information Systems, Springer*.

Singh, V. K. *et al.* (no date) 'Sentiment analysis of movie reviews: A new feature-based heuristic for aspect-level sentiment classification.', in *Automation, computing, communication, control and compressed sensing (iMac4s), 2013 international multi-conference on*.

Suresh, H. and Gladston, R. S. (2016) 'An unsupervised fuzzy clustering method for twitter sentiment analysis', *2016 International Conference on Computation System and Information Technology for Sustainable Solutions, CSITSS 2016*, pp. 80–85. doi: 10.1109/CSITSS.2016.7779444.

Takhshid, R. and A. Rahimi (no date) 'A rule based algorithm for detecting negative words in Persian', *arXiv preprint arXiv:1708.06708, 2017*.

Tang, D., Qin, B. and Liu, T. (2015) 'Document modeling with gated recurrent neural network for sentiment classification', *Conference Proceedings - EMNLP 2015: Conference on Empirical Methods in Natural Language Processing, (September)*, pp. 1422–1432. doi: 10.18653/v1/d15-1167.

Turney, P. D. (2002) 'Thumbs up or thumbs down?', in *Proceedings of the 40th Annual Meeting of the Association for Computational Linguistics (ACL)*. Philadelphia, Pennsylvania, USA, pp. 417–424. doi: 10.3115/1073083.1073153.

Wilson, T., Wiebe, J. and Hoffmann, P. (2009) 'Recognizing contextual polarity: An exploration of features for phrase-level sentiment analysis', *Computational linguistics*, 35(3), pp. 399–433.

Yue, L. *et al.* (2018) 'A survey of sentiment analysis in social media', *Knowledge and Information Systems*. Springer London, pp. 1–47. doi: 10.1007/s10115-018-1236-4.

BCI-based Game Design Promoting Our Cultural Heritage

Taha Rıdvan Baran^{1*}[0000-0003-2063-3713], İbrahim Şengün^{2*}[0000-0002-9210-8259],
and Yaşar Daşdemir³[0000-0002-9141-0229]

¹taha.baran18@erzurum.edu.tr, Erzurum Technical University, Computer Engineering

²ibrahim.sengun72@erzurum.edu.tr, Erzurum Technical University, Computer Engineering

³yasar.dasdemir@erzurum.edu.tr, Erzurum Technical University, Computer Engineering

Abstract

Nowadays, Human-Computer Interaction (HCI) systems e.g. keyboard, mouse, Virtual Reality (VR) controller, and joystick are frequently used by anyone. However, those ways to interact with computers maybe not be suitable for disabled persons. Brain-Computer Interface (BCI) is an HCI system that can be used as an alternative for these persons. This approach allows playing a computer game using only the brain signals, for instance, imagine a situation where a participant only needs to think about action to make it happen: to move, to select an object, to open the door, or to control the movements of their virtual body, by “thought” alone.

Playing with the mind is no longer science fiction. BCIs have started to enter our daily lives with portable and low-cost brain signal sensors. BCI systems are used in the fields of communication, rehabilitation, control, diagnosis and play. Serious Game, on the other hand, is used to denote video games used in fields such as education, defense, health, simulation, and engineering, as opposed to entertainment.

The purpose of this study is to implementation via serious games to create awareness and facilitate general awareness of cultural heritage. For this purpose, a serious game design was realized in the Twin Minaret Madrasa (The Çifte Minareli Medrese), which has an important place in Erzurum cultural heritage, offering cultural and historical educational content.

The lack of adequate training examples and noisy high-dimensional features are the main challenges faced by mental instruction decoding algorithms for electroencephalogram (EEG)-based Brain-Computer Interface (BCI). For this reason, Filter Bank Convolution Network (FBCNet), which provides acceptable performance in benchmark datasets, is used in our study. The Cross-Validation analysis was conducted in a 10 fold setting, with the 9 folds being used for training and 1 fold for testing. The performance of mental commands (opening the door and turning on the lights) including binary classification was 76.20%. These mental commands have been successfully tested in real-time experimental scene design.

Keywords. Serious Game, Brain-Computer Interface, Electroencephalography, Virtual Reality

Voice Spoofing Countermeasure to Detect Replay Attacks Using Spectral Features and BiLSTM

Rahman Ullah¹, Saima Zareen², Farman Hassan^{3*}, Auliya Ur Rahman⁴

¹arahmanullah95@gmail.com, Software Engineering Department, University of Engineering and Technology, Taxila, Punjab, Pakistan.

²saima.zareen@uettaxila.edu.pk, Software Engineering Department, University of Engineering and Technology, Taxila, Punjab, Pakistan.

³farmanhassan555@gmail.com, Software Engineering Department, University of Engineering and Technology, Taxila, Punjab, Pakistan.

⁴auliyaurrahman555@gmail.com, Computer Science Department, University of Engineering and Technology, Peshawar, KPK, Pakistan.

Abstract

Automatic speaker verification (ASV) system validates user based on the voice provided to it. Most ASVs are vulnerable to numerous voice spoofing attacks such as Physical Access (PA) and Logical access (LA) attacks. Recently, there have been significant improvements in the detection of voice spoofing attacks. However, intruders use enhanced recording devices, which record voices remarkably similar to the original speakers and play to ASV systems to grant access for malicious purposes. In this paper, we proposed a voice replay spoof detection system, which is capable of capturing the alterations in the spoof audio signal that are generated due to environmental noise, microphone distortions, recording and replay devices. More specifically, we proposed a novel set of fused spectral features i.e., Linear frequency cepstral coefficients (LFCC), gammatone cepstral coefficients (GTCC), and spectral centroid (SC) to effectively detect PA attacks. Later, we employed BiLSTM for classification purposes to discriminate spoof and genuine audio. We used the ASVspoof2019 PA dataset for experimentation purposes. The proposed method (LFCC-GTCC-SC-BiLSTM) achieved an equal error rate (EER) of 4.98%, which is 6.06% and 8.56% smaller than the baseline methods such as Constant Q cepstral coefficients (CQCC) and LFCC using gaussian mixture model (GMM) as backend classifier. Experimental results and comparative analysis with existing state-of-the-art methods show that the proposed system is robust and can reliably be used to detect voice spoofing replay attacks.

Keywords. ASVspoof2019, Deep learning, machine learning, spoofing, voice replay.

1. Introduction

In recent years, numerous biometric technologies i.e., iris recognition, facial recognition, and fingerprint recognition have been employed in different security systems. Products based on voice verification systems have grown exponentially as compared with other biometrics technologies. It brings much accessibility to people's lives, but it carries risks. The intruders may use spoofed speech to grant unauthorized access to ASV systems, for example, ASV systems can be fooled by an artificial speech sample [1,2]. ASV systems are vulnerable to spoofing attacks and are categorized into four types i.e., voice replay attacks, impersonation, speech synthesis (SS), and voice conversion (VC) [3,4]. Voice replay attacks pose a significant threat to ASV systems [5] and its detection is a tricky task. Moreover, a voice replay attack is simple to fool ASV systems as it required only two devices i.e., recording and replay devices. Replay attacks can be carried out without any advanced or high price device, nor require professional knowledge. So, in this paper, our main focus is to detect voice replay attacks. The baseline methods of the ASVspoof2019 challenge, which are based on (CQCC-GMM) and (LFCC-GMM) achieved an equal error rate (EER) of 11.04% and 13.54%, respectively.

Initially, in the features extraction process, features from speech signals are extracted. There are various techniques used for the feature extraction from speech fragments i.e., Mel-frequency cepstral coefficients (MFCC), GTCC, LFCC, CQCC, and Constant Q transform (CQT). In [6], spoofing countermeasure was designed to detect voice replay attacks, which combined the training and development set for training purposes and achieved an EER of 19.77%. The MFCC is widely used in speech recognition [7,8]. CQCC



is based on CQT and is well known in music analysis processing techniques [9,10]. Researchers used raw data of speeches [11] or synthesize the speech by employing a short-time Fourier transform (STFT) into a full spectrum and later used the technique of image recognition and classification for the detection of spoofing attacks [12]. In the second step, extracted features are classified using machine learning or deep learning classifiers. Traditional classifier such as GMM [13] is simple and widely used classifier for the classification purpose of authentic and spoofed voice. The baseline of ASVspoof2015 and ASVspoof2017 also employed GMM. Support vector machine (SVM) [14,15], linear discriminant analysis (LDA) [16], [17], and deep neural networks (DNN) [18] are also used as efficient classifiers. The research community believed that the deep learning methods Convolutional neural network (CNN), recurrent neural network (RNN), CNN-RNN, long short-term memory (LSTM), or BiLSTM [19] have made significant improvements in classification tasks.

For the task of audio spoofing detection, many new features were proposed, such as CQCC [22], CFCCIF [20,21], and the band energy difference (BED) descriptor [23]. Among these approaches, the authors insisted that the features are more important than the classifiers or complex models. However, there are some different ideas. The authors in [11] showed that a deep learning model with the raw wave can get promising performance. In [24], the system with score fusion leads to better overall performance compared to the parallel scheme. In [39], a system based on the fusion of spectral features i.e., MFCC, CQCC, and Perceptual linear predictive were used to detect voice replay attacks. Ensemble classifiers comprising of different variants of GMM were employed to discriminate authentic and spoofed samples. In [38,40], high-frequency-based selectivity was discussed to address the detection of voice replay attacks. In [38], Two features i.e., frequency modulation and transmission line cochlea amplitude modulation were used to train the GMM for the classification of genuine and spoof speech. However, compared to frequency modulation the amplitude modulation feature has a high computational cost because it takes much time to modulate the signal. Similarly, in [40], three spectral features i.e., inverted-MFCC, LPCCres, LFCC were utilized for capturing the high-frequency features along with CQCC, MFCC, and cepstrum. GMM was employed for classification purposes. However, due to higher features' computational complexity, these techniques are not suitable to deploy in real-time applications. Few works [41,42,43] have highlighted reverberation and channel information, recording as well as playback device characteristics that need to be examined for the detection of voice replay attacks. In [41], linear prediction residual signals were used to analyze the characteristics of recording and playback devices. Two features i.e., Residual-MFCC and residual inverse MFCC were used and GMM was employed for the classification purpose of replay speech and authentic speech. In [42], three spectral features i.e., MFCC, CQCC, and Mel-Filterbank-Slope were used for training the GMM model to detect voice replay attacks. The authors also investigated channel information and reverberation from non-voice segments. Similarly, in [43] scheme named low-frequency frame-wise normalization was designed to detect voice replay attacks as well as to capture the artifacts from the replay speech.

The research community has also explored various deep learning-based approaches [25-33,36,37] for voice replay spoofing detection. This [26] method performed data augmentation to show that it enhances the performance of the ASVspoof2019 baseline [25]. A deep residual network was employed for feature extraction, but this method has some shortcomings i.e., manual data augmentation was required, using STFT based spectrogram degrades the performance results. In [27], spoofing countermeasures based on the fusion of two spectral features i.e., CQCC and MFCC were designed to detect voice replay attacks. DNNs, ResNet, and GMM were employed for classification purposes. However, a fusion of MFCC-ResNet, CQCCResNet, and CQCC-GMM yielded the lowest EER. In [28], high-frequency cepstral coefficients and CQCC were used to generate the embeddings by employing a DNN. SVM was used for classification purposes to discriminate audio as spoof or bonafide. In [36], long-term average spectrum and MFCC were used to detect voice replay attacks. DNN was employed for classification purposes. Few works [32,33] have utilized machine-learned features instead of extracting certain features i.e., MFCC, CQCC, etc., which are then fed to DL models for classification purposes. In [32], spoofing countermeasure based on both machine-learned and extracted features was designed to detect voice replay attacks. GMM-Universal Background Model (UBM) was employed to classify audio as bonafide or spoof. In [29], maximum feature-map (MFM) activation was used to train lightweight deep learning frameworks for the detection of a voice replay attack. MFM can reduce the dimension by selecting the most related features to do classification. This technique [29] was extended in [31] to analyze the effectiveness of an angular margin-based softmax activation function. Light CNN was employed to classify replay and bonafide audio. The authors of [37] also employed light CNN to detect voice replay attacks.

Even if the literature discussed above illustrates that considerable progress has been made in the detection of voice replay attacks, the problem is far from being solved, ASV systems are still vulnerable to voice replay attacks [2] and spoofing countermeasures have maximum EER values. In this paper, we proposed a novel approach that successfully detects voice replay attacks with the lowest EER values than existing state-

of-the-art methods. In the first step, we use the fusion of spectral features to extract the maximum possible information from the voice samples. Next, we use a deep learning network architecture as a classifier, that is BiLSTM for classifying bonafide and spoof samples. The major contributions of this paper are as follows,

- We proposed a novel set of features for audio representation comprising of LFCC, GTCC, and SC that better captures the discriminative traits of bonafide and spoof samples.
- Our proposed feature descriptor (LFCC-GTCC-SC) is able to capture non-redundant microphone-induced traits from audio signals to better distinguish replay and authentic speech.
- To validate our approach, we conducted rigorous experiments on the ASVspoof2019 PA dataset to detect voice replay attacks.
- Experimental results and comparative analysis show that our method has superior performance and can reliably be used for voice replay attacks detection.

The remaining paper is organized as follows, Section II provides the proposed working mechanism, section III has details of the experimental setup and results in discussion. Finally, section IV concludes our work.

2. Proposed System

This section presents the detailed working mechanism of the proposed system. The main objective of the proposed voice spoofing countermeasure is to detect voice replay attacks. The proposed system comprises of three steps i.e., feature extraction from audio, classification, and validation. In the initial step, we extracted 14-dim LFCC, 14-dim GTCC, and 1-dim SC features. Next, these 29-dim features are fed into the BiLSTM network for classification purposes. Subsequently, the proposed system predicts bonafide and spoof speech. The details of the proposed voice spoofing countermeasure for voice replay attacks are given in Figure 1.

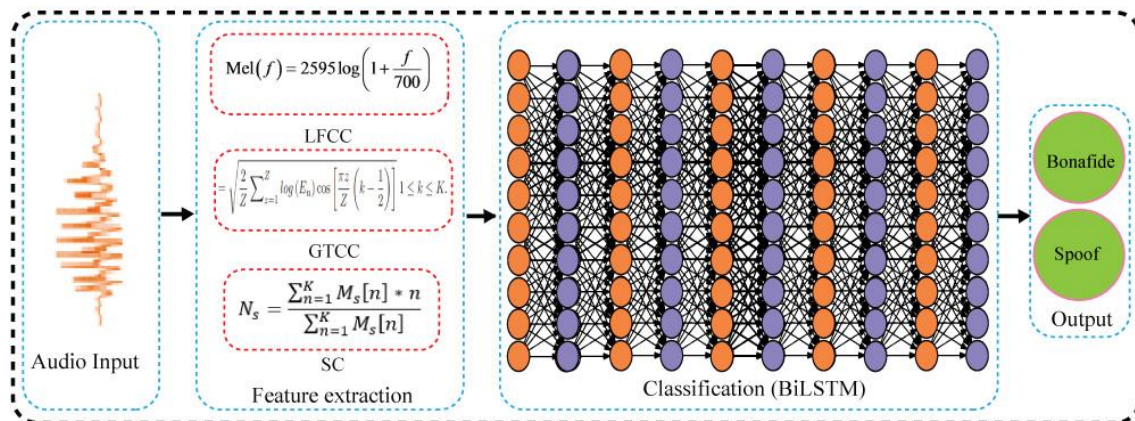


Figure 1: Proposed System.

2.1. Feature Extraction

Effective feature extraction is a crucial part to develop a reliable spoofing countermeasure. The extraction of the best parametric representation of audio signals is important to get improved performance results. For this purpose, we used a fusion of spectral features comprising of LFCC, GTCC, and spectral centroid to better capture the microphone, recording, and playback device distortions present in spoof samples. The proposed set of fused features is capable to extract informative, non-redundant, and discriminative features from the ASVspoof2019 PA dataset.

2.2. LFCC

We extracted 14-dimensional LFCC features. In the LFCC feature extraction process, audio is divided into multiple segments comprising a fixed number of frames. MFCC and LFCC have the same feature extraction process [44]. MFCC used a Mel filter-bank while LFCC uses a linear filter-bank. The linear filter-bank of LFCC can extract features from a high-frequency area. The detailed LFCC features extraction process is shown in Figure 2.

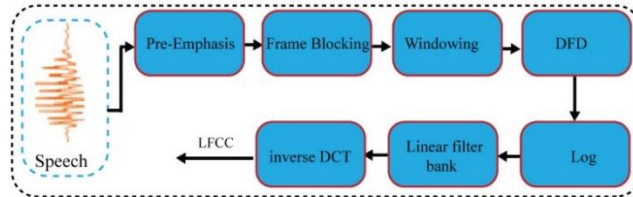
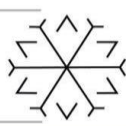


Figure 2: LFCC Computation Process.

2.3. GTCC

We extracted 14-dimensional GTCC features. Initially, we employed Fast Fourier Transform (FFT) on every speech window followed by applying gammatone filter-bank comprising of 48 filters to FFT of audio signals. The energy of every sub-band is computed. In the next step, we computed the logarithm of each sub-band followed by applying DCT. The detailed GTCC features computation process is shown in figure 3.

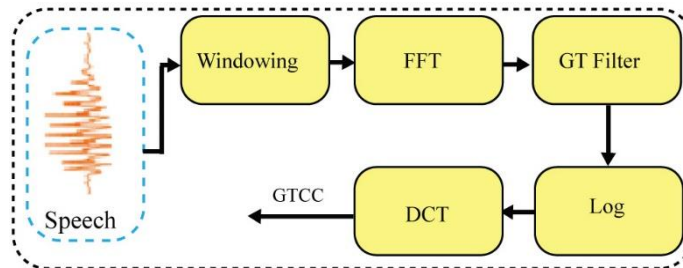


Figure 3: GTCC Computation Process.

2.4. Spectral Centroid

We extracted the 1-dim SC feature. SC represents the center of gravity of all the power spectrum as well as the energy distribution of high and low-frequency bands. We computed the SC as below,

$$N_s = \frac{\sum_{n=1}^K M_s[n] * n}{\sum_{n=1}^K M_s[n]} \quad (1)$$

Where M_s is the magnitude of FT at current window s of the audio signal and frequency bin n .

2.5. Classification

BiLSTM is well suited for the classification of time series data. Therefore, we also employed BiLSTM for classification purposes using a 29-dim proposed set of features and tuned some input parameters to train the network. We used an adam optimizer, a maximum number of epochs equals 50, a mini-batch size of 64 observations for each iteration, a Gradient threshold value of 1, 100 hidden units, 10 hidden layers, and a fully connected layer followed by SoftMax and classification layer. The details of the BiLSTM network are shown in Figure 4.

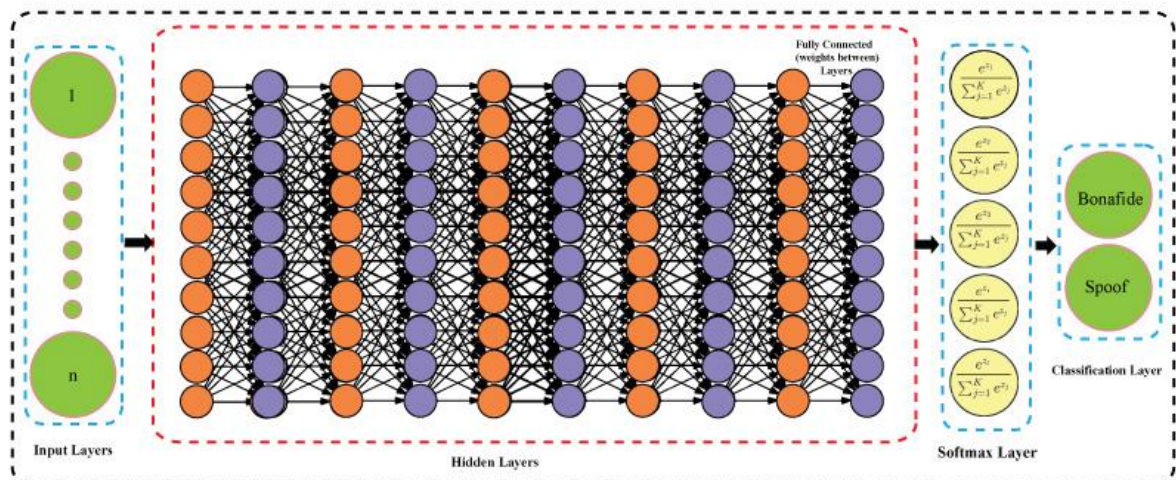
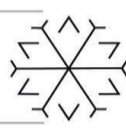
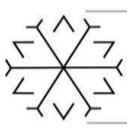


Figure 4: Classification.



3. Experimental Setup and Results Discussion

The proposed voice anti-spoofing method has allocated scores to spoof and genuine voice samples. We consider False Negative, False Positive, True Negative, True Positive based on these assigned scores we calculated equal error rate (EER), accuracy recall, precision, and F1-score.

3.1. Dataset

ASVspoof2019 comprises two sub-datasets i.e., PA and LA datasets. ASVspoof2019 dataset focuses on major three types of voice spoofing attacks i.e., voice conversion, speech synthesis, and voice replay attacks. PA dataset contains voice replay attack samples while the LA dataset has voice conversion and synthetic speech samples. We evaluated the performance of our proposed method on the ASVspoof2019 PA dataset to detect voice replay attacks. Each sub-dataset is further divided into three partitions i.e., training set, development set, and evaluation set. The details of the ASVspoof2019 dataset are given in below Table 1.

Table 1: Details of the ASVspoof2019 PA Dataset.

Subset	Bonafide	Spoof	No of speakers
Training	5400	48600	20
Evaluation	5400	24300	48
Total	28890	18954	78

3.2. Performance Evaluation of the Proposed System

The purpose of this experiment is to evaluate the performance of the proposed system to detect voice replay attacks. For this purpose, we extracted 14-dim LFCC, 14-dim GTCC, and 1-dim SC from the training and evaluation set of the ASVspoof2019 PA dataset. We employed BiLSTM architecture to discriminate between bonafide and spoof audio. We used 19,000 samples of the training set for training the BiLSTM network, and 20,000 samples of the evaluation set for the testing purpose. From Figure 5, we can observe that our system achieved an accuracy of 95%, precision of 81.68%, recall of 100%, F1-score of 89.91%, and an EER of 4.98%. The baseline methods (CQCC-GMM) [25] and (LFCC-GMM) [25] achieved an EER of 11.04% and 13.54%, respectively. From these results, we observe a drop of an EER value of 6.06% and 8.56% by our method than (CQCC-GMM) [25] and (LFCC-GMM) [25], respectively. We observe significant improvement in detecting the voice replay attacks by our method. Experimental results illustrate that our method better captures the distortions produced by replay and recording devices. More specifically, the lower EER value of our system than baseline methods indicates that our method is reliable to be used for the detection of voice replay attacks.

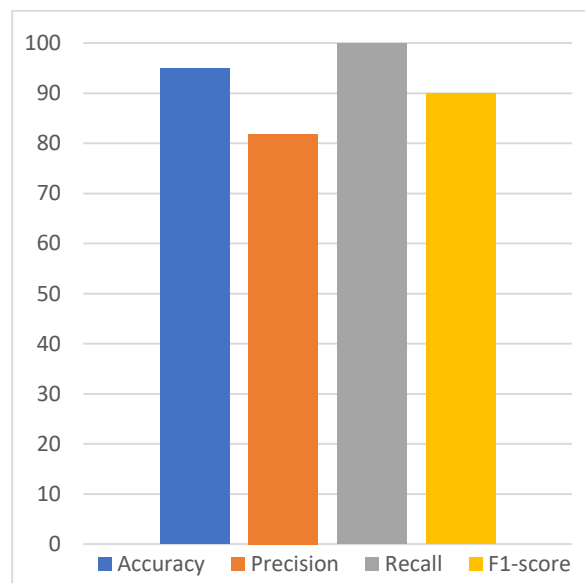


Figure 5: Performance Evaluation on ASVspoof2019 PA Dataset.

3.3. Performance Evaluation on Machine Learning Methods

The purpose of this experiment is to show the superiority of the proposed method against the machine learning methods. For this purpose, we extracted 29-dim LFCC, GTCC, and SC to train four different



machine learning algorithms such as ensemble, SVM, KNN, and decision tree (DT). We compared these methods based on the EER values. From the results reported in Table 2, we can observe that (LFCC-GTCC-SC-DT) performs worst and achieved an accuracy of 82.99%, precision of 63.24%, recall of 71.08%, F1-score of 66.93%, and an EER of 17%. (LFCC-GTCC-SC-KNN) performs second best and achieved an accuracy of 74.83%, precision of 85.24%, recall of 85.24%, F1-score of 85.24%, and an EER of 8.03% while our method performs best and achieved an accuracy of 95%, precision of 81.68%, recall of 100%, F1-score of 89.81%, and an EER of 4.98%. We observe a gain of accuracy by our method of 8.68%, 7.84%, 20.17%, and 12.01% than ensemble, SVM, KNN, and DT, respectively. This substantial increase in accuracy demonstrates that the proposed method has superior performance over the traditional machine learning algorithms. More specifically, our method is effective to capture the variations present in the audio signals and can reliably be used to detect voice replay attacks.

Table 2: Performance Evaluation on Machine Learning Algorithms.

Feature	EER %	Accuracy %	Precision %	Recall %	F1-score%
Ensemble	13.68	86.32	71.53	76.63	73.99
SVM	12.83	87.16	68.27	81.53	74.31
CNN	8.03	74.83	85.24	85.24	85.24
DT	17	82.99	63.24	71.08	66.93
Proposed (BiLSTM)	4.98	95	81.68	100	89.91

3.4. Comparison with Other Methods

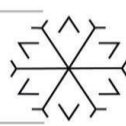
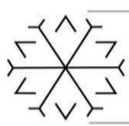
The purpose of this experiment is to compare the proposed method with other existing state-of-the-art methods to detect voice replay attacks. For this purpose, we compared our method with existing state-of-the-art methods [25,45,46,47] to show the superiority and effectiveness of our method against other methods. From the results listed in Table 3, we can observe that Yamagishi, Junichi, et al. [25] performs worst and yielded an EER of 11.04% on (CQCC-GMM) and 13.54% on (LFCC-GMM), respectively. Das, Rohan Kumar, et al. [46] performs second best and yielded an EER of 7.99% using (CQSPIC-DNN) while our method (LFCC-GTCC-SC-BiLSTM) performs best and yielded an EER of 4.98%. Moreover, we observe that the proposed system yielded smaller EER value of 6.06%, 8.56%, 6.46%, 3.01%, and 5.82% than [25,45,46,47], respectively. This lower EER value indicates that our method is effective to detect voice replay attacks. Experimental results and comparative analysis illustrate that our method better captures the most discriminatory traits from the voice replay attacks samples. These results signify that our method is robust and reliable to be used for the detection of voice replay spoofing attacks.

Table 3: Performance Comparison with Existing Methods.

Authors	EER%
Yamagishi, Junichi, et al. (Baseline) [25]	11.04
Yamagishi, Junichi, et al. (Baseline) [25]	13.54
Yang, Jichen, et al. [45]	11.44
Das, Rohan Kumar, et al. [46]	7.99
Sarkar, Achintya Kumar, et al. [47]	10.80
Proposed (LFCC-GTCC-SC-BiLSTM)	4.98

4. Conclusion

This paper has presented a novel voice spoofing countermeasure to detect voice replay attacks. Fraudsters use advanced recording devices to record the voices of genuine users and replay the recorded voices in front of ASVs to grant access for fraudulent purposes. This is a significant threat to the security of ASVs. To improve the security of ASVs, we proposed a novel voice spoofing countermeasure to detect voice replay attacks. We used a fusion of three features such as LFCC, GTCC, and SC to train the BiLSTM network. Our method yielded the lowest EER value of 4.98%. Experimental results, comparative analysis with the existing state-of-the-art methods, and traditional machine learning classifiers show that our method is robust to detect voice replay attacks. In the future, we aim to work on logical access attacks and deep fakes.



References

- [1] S. K. Ergunay, E. Khoury, A. Lazaridis, and S. Marcel, "On the vulnerability of speaker verification to realistic voice spoofing," in *Biometrics Theory, Applications and Systems (BTAS), 2015 IEEE 7th International Conference on*. IEEE, 2015, pp. 1–6.
- [2] M. Sahidullah, H. Delgado, M. Todisco, H. Yu, T. Kinnunen, N. Evans, and Z.-H. Tan, "Integrated spoofing countermeasures and automatic speaker verification: An evaluation on asvspoof 2015," 2016.
- [3] A. Sizov, E. Khoury, T. Kinnunen, Z. Wu, and S. Marcel, "Joint speaker verification and antispoofing in the i-vector space," *IEEE Transactions on Information Forensics and Security*, vol. 10, no. 4, pp. 821–832, 2015.
- [4] N. W. Evans, T. Kinnunen, and J. Yamagishi, "Spoofing and countermeasures for automatic speaker verification." in *Interspeech, 2013*, pp. 925–929.
- [5] Z. Wu, N. Evans, T. Kinnunen, J. Yamagishi, F. Alegre, and H. Li, "Spoofing and countermeasures for speaker verification: A survey," *speech communication*, vol. 66, pp. 130–153, 2015.
- [6] B. S. M. Rafi, K. S. R. Murty, and S. Nayak, "A new approach for robust replay spoof detection in asv systems," in *Signal and Information Processing (GlobalSIP), 2017 IEEE Global Conference on*. IEEE, 2017, pp. 51–55.
- [7] C. Ittichaichareon, S. Suksri, and T. Yingthawornsuk, "Speech recognition using mfcc," in *International Conference on Computer Graphics, Simulation and Modeling (ICGSM'2012) July 2012*, pp. 28–29.
- [8] R. Vergin, D. O'shaughnessy, and A. Farhat, "Generalized mel frequency cepstral coefficients for large-vocabulary speaker-independent continuous-speech recognition," *IEEE Transactions on speech and audio processing*, vol. 7, no. 5, pp. 525–532, 1999.
- [9] B. Zhu, F. Wu, K. Li, Y. Wu, F. Huang, and Y. Wu, "Fusing transcription results from polyphonic and monophonic audio for singing melody transcription in polyphonic music," in *Acoustics, Speech and Signal Processing (ICASSP), 2017 IEEE International Conference on*. IEEE, 2017, pp. 296–300.
- [10] L. Lu, M. Wang, and H.-J. Zhang, "Repeating pattern discovery and structure analysis from acoustic music data," in *Proceedings of the 6th ACM SIGMM international workshop on Multimedia information retrieval*. ACM, 2004, pp. 275–282.
- [11] H. Dinkel, Y. Qian, and K. Yu, "Investigating raw wave deep neural networks for end-to-end speaker spoofing detection," *IEEE/ACM Transactions on Audio, Speech, and Language Processing*, vol. 26, no 11, pp. 2002–2014, 2018.
- [12] P. L. D. Leon, B. Stewart, and J. Yamagishi, "Synthetic speech discrimination using pitch pattern statistics derived from image analysis," in *Thirteenth Annual Conference of the International Speech Communication Association*, 2012.
- [13] D. A. Reynolds, T. F. Quatieri, and R. B. Dunn, "Speaker verification using adapted gaussian mixture models," *Digital signal processing*, vol. 10, no. 1-3, pp. 19–41, 2000.
- [14] F. Alegre, R. Vipperla, and N. Evans, "Spoofing countermeasures for the protection of automatic speaker recognition systems against attacks with artificial signals," in *INTERSPEECH 2012, 13th Annual Conference of the International Speech Communication Association*, 2012.
- [15] Y. Liu, Y. Tian, L. He, J. Liu, and M. T. Johnson, "Simultaneous utilization of spectral magnitude and phase information to extract super vectors for speaker verification anti-spoofing," in *Sixteenth Annual Conference of the International Speech Communication Association*, 2015.
- [16] N. Chen, Y. Qian, H. Dinkel, B. Chen, and K. Yu, "Robust deep feature for spoofing detection—the sjtu system for asvspoof 2015 challenge," in *Sixteenth Annual Conference of the International Speech Communication Association*, 2015.
- [17] Y. Qian, N. Chen, and K. Yu, "Deep features for automatic spoofing detection," *Speech Communication*, vol. 85, pp. 43–52, 2016.
- [18] M. J. Alam, P. Kenny, V. Gupta, and T. Stafylakis, "Spoofing detection on the asvspoof2015 challenge corpus employing deep neural networks," in *Proc. Odyssey, 2016*, pp. 270–276.
- [19] J. Salamon and J. P. Bello, "Deep convolutional neural networks and data augmentation for environmental sound classification," *IEEE Signal Processing Letters*, vol. 24, no. 3, pp. 279–283, 2017.
- [20] T. B. Patel and H. A. Patil, "Combining evidences from mel cepstral, cochlear filter cepstral and instantaneous frequency features for detection of natural vs. spoofed speech," in *Sixteenth Annual Conference of the International Speech Communication Association*, 2015.
- [21] T. B. Patel and H. A. Patil, "Cochlear filter and instantaneous frequency based features for spoofed speech detection," *IEEE Journal of Selected Topics in Signal Processing*, vol. 11, no. 4, pp. 618–631, 2017.
- [22] M. Todisco, H. Delgado, and N. Evans, "A new feature for automatic speaker verification anti-spoofing: Constant q cepstral coefficients," in *Speaker Odyssey Workshop, Bilbao, Spain*, vol. 25, 2016, pp. 249–252.



- [23] D. Luo, P. Korus, and J. Huang, "Band energy difference for source attribution in audio forensics," *IEEE Transactions on Information Forensics and Security*, vol. 13, no. 9, pp. 2179–2189, 2018.
- [24] P. Korshunov and S. Marcel, "Impact of score fusion on voice biometrics and presentation attack detection in cross-database evaluations," *IEEE Journal of Selected Topics in Signal Processing*, vol. 11, no. 4, pp. 695–705, 2017.
- [25] Yamagishi J, Todisco M, Sahidullah M, Delgado H, Wang X, Evans N., et al. ASVspoof 2019: The 3rd Automatic Speaker Verification Spoofing and Countermeasures Challenge database, 2019.
- [26] Z. Chen, Z. Xie, W. Zhang, and X. Xu. "ResNet and model fusion for automatic spoofing detection," in *Proc. Inter Speech*, 2017, pp. 102–106.
- [27] P. Nagarsheth, E. Khoury, K. Patil, and M. Garland, "Replay attack detection using DNN for channel discrimination," in *Proc. Inter Speech*, 2017, pp. 97–101.
- [28] G. Lavrentyeva, S. Novoselov, E. Malykh, A. Kozlov, O. Kudashev, and V. Shchemelinin, "Audio replay attack detection with deep learning frameworks," in *Proc. Inter Speech*, 2017, pp. 82–86.
- [29] X. Wu, R. He, Z. Sun, and T. Tan, "A light CNN for deep face representation with noisy labels," *IEEE Trans. Inf. Forensics Secur.*, vol. 13, no. 11, pp. 2884–2896, Nov. 2018.
- [30] G. Lavrentyeva, S. Novoselov, A. Tseren, M. Volkova, A. Gorlanov, and A. Kozlov, "STC antispoofing systems for the ASVspoof 2019 challenge," 2019, arXiv:190405576.
- [31] B. T. Balamurali, K. W. E. Lin, S. Lui, J. Chen, and D. Herremans, "Towards robust audio spoofing detection: a detailed comparison of traditional and learned features," 2019, arXiv:1905.12439.
- [32] A. K. Sarkar, Z. Tan, H. Tang, and J. Glass, "Time-contrastive learning based deep bottleneck features for text-dependent speaker verification," in *Proc. IEEE/ACM Trans. Audio, Speech, Lang. Process.*, 2019.
- [33] Y. Gong, J. Yang, J. Huber, M. MacKnight, and C. Poellabauer, "ReMASC: Realistic replay attack corpus for voice controlled systems," 2019, arXiv:1904.03365.
- [34] B. Bakar and C. Haniçli, "Replay spoofing attack detection using deep neural networks," in *Proc. 26th Signal Process. Commun. Appl. Conf.*, 2018, pp. 1–4.
- [35] ASVspoof Challenge. [Online]. Available: "<https://www.asvspoof.org>," Accessed on Jul. 25, 2019.
- [36] V. Tiwari, M. F. Hashmi, A. Keskar, and N. C. Shivaprakash, "Virtual home assistant for voice-based controlling and scheduling with short speech speaker identification," *Multimedia Tools Appl.*, pp. 1–26, 2018.
- [37] D. Cooper, "Speech detection using gammatone features and one-class support vector machine," M.S. Thesis, Dept. Elec. Eng. & Comp. Sci., Univ. of Central Florida, Orlando, FL, USA, 2013.
- [38] T. Gunendradasan, S. Irtza, E. Ambikairajah, and J. Epps, "Transmission line cochlear model based AM-FM features for replay attack detection," in *Proc. IEEE Int. Conf. Acoust., Speech Signal Process.*, 2019, pp. 6136–6140.
- [39] Z. Ji et al., "Ensemble learning for countermeasure of audio replay spoofing attack in ASVspoof2017," in *Proc. Inter Speech*, 2017, pp. 87–91.
- [40] M. Witkowski, S. Kacprzak, P. Zelasko, K. Kowalczyk, and J. Galka, "Audio replay attack detection using high-frequency features," in *Proc. Inter Speech*, 2017, pp. 27–31.
- [41] J. Mishra, M. Singh, and D. Pati, "Processing linear prediction residual signal to counter replay attacks," in *Proc. Int. Conf. Signal Process. Commun.*, 2018, pp. 95–99.
- [42] J. Yang and R. K. Das, "Low frequency frame-wise normalization over constant-Q transform for playback speech detection," *Digit. Signal Process.*, vol. 89, pp. 30–39, 2019.
- [43] A. P. Tapkir and H. A. Patil, "Significance of teager energy operator phase for replay spoof detection," in *Proc. Asia-Pacific Signal Inf. Process. Assoc. Annu. Summit Conf.*, 2018, pp. 1951–1956.
- [44] [10] M. J. Alam, P. Kenny, and V. Gupta, "Tandem Features For Text Dependent Speaker Verification On The Reddotts Corpus," *Proc. Annu. Conf. Int. Speech Commun. Assoc. Interspeech*, Vol. 08–12–Sept, Pp. 420–424, 2016.
- [45] Yang, Jichen, et al. "Discriminative features based on modified log magnitude spectrum for playback speech detection." *EURASIP Journal on Audio, Speech, and Music Processing* 2020.1 (2020): 1-14.
- [46] Das, Rohan Kumar, Jichen Yang, and Haizhou Li. "Assessing the scope of generalized countermeasures for anti-spoofing." *ICASSP 2020-2020 IEEE International Conference on Acoustics, Speech and Signal Processing (ICASSP)*. IEEE, 2020.
- [47] Sarkar, Achintya Kumar, et al. "Time-contrastive learning based deep bottleneck features for text-dependent speaker verification." *Ieee/acm Transactions on Audio, Speech, and Language Processing* 27.8 (2019): 1267-1279.

An Overview of Ransomware Attacks and Mitigation Techniques

Merve Yildirim ¹*[0000-0001-6834-3470]

¹merve.yildirim@erzurum.edu.tr, Erzurum Technical University

Abstract

With the development of computer systems and the spread of Internet services, there has been a serious increase in the number of malicious software that threatens these systems. Ransomware is one of these malicious software that provides the fastest profit to cyber attackers, especially in recent years. Using ransomware, cyber attackers encrypt users' files using different techniques, including cryptography, and then demand a ransom payment to decrypt them. Ransomware is a type of cyber attack that targets not only individuals but also large companies, institutions and even government agencies. It is expected that ransomware will increase even more in the coming period by increasing its threat level and impact. Recent developments; shows that individual users and companies are not sufficiently aware of falling into ransomware traps. There are many examples of lagging behind in catching up with the methods developed by cyber attackers and taking the necessary precautions. Especially in recent years, ransomware that has been successfully completed has caused individuals, companies and public institutions to suffer serious financial losses and lack of reputation. It is essential to create the necessary level of awareness to prevent attackers from continuing to make money in this way. In this research paper, ransomware types have been examined, methods used to detect ransomware attacks have been researched, and mitigation techniques to reduce the damage to information systems have been presented. With this study, it is aimed to raise awareness about ransomware for organizational systems.

Keywords. Ransomware, cyber security, cyber attacks, security awareness, information security

1. Introduction

The concept of ransom which has been a common tactic used by attackers in cyber domains in today's world is an actually ancient phenomenon. Cyber attackers have started to apply this tactic in the cyber world by using encryption technologies used to secure systems.

The term Ransomware, formed by combining the words "Ransom" and "Ware", belongs to the malicious software (Humayun et al., 2020) family, which refers to ransom payment. Attackers can use ransomware attacks very effectively and easily to profit themselves. Ransomware is a type of malicious malware that can encrypt user files and lock users systems, and then demand a ransom to decrypt the file or unlock the system. Apart from that, a ransomware attack can cause service interruption, data loss, reputational damage for companies and government agencies, and data breach. As the rate of use of Internet services and digital assets of businesses increase, they also become the target of cyber attackers (Alshaiikh et al., 2020). These malicious software can easily infect users' computers through various methods such as advertisements, spam mails and social engineering attacks. Ransomware generates private keys by encrypting files on infected systems with encryption algorithms that are difficult to decipher, and these keys are kept separately on a private server. (Luo and Liao, 2007).

Ransomware is any type of malware in which cybercriminals hold electronic data on mobile phones, computers, and other connected devices for ransom and demand money to regain access to those files. Simply put, ransomware is malicious software that restricts access to computer systems or files and obliges the data subject to pay a ransom for restored access. Examples of ransomware that have been widely used in the recent past include CryptoLocker and WannaCry.

Ransomware attacks have increased tremendously in recent years. In 2017, the number of blocked WannaCry attacks reached more than 5 billion. Ransomware has now begun to target new architectures such as the Internet of Things (IoT), cloud computing (Azmoodeh et al., 2017). Some attacks, such as Jigsaw, Locky, Bat Rabbit, Cerber, Petya, CryptorBit, Nemucod, CryptoDefense,



NotPetya, CryptoLocker, CryptoWall, TeslaCrypt, Torrentlocker, Gerber, VaultCrypt, which emerged later, used ransomware as a trap to cause interruption of services (Eset, 2018).

Attackers that carry out ransomware usually give a screen warning that the user will see on the systems they have infected with the malware, stating that they have encrypted the user's files and that the ransom must be paid in order to be given the key to unlock the password and to reopen the system they have restricted access to. Since the attackers had problems because the payment they requested was made in traditional currencies and could be traced naturally, they have started to use payment systems such as Bitcoin today. With the payment request made through these systems, it has become difficult for the attackers to be detected by the cyber defense teams.

In addition, ransomware continues to be one of the most important cyber threats worldwide; It has been determined that ransomware attacks have increased especially against public institutions, finance, health, telecommunications and educational institutions especially during the Covid 19 pandemic. Worse still, the source code of some ransomware can be hacked with basic software knowledge, and the aid of Bitcoin use makes some ransomware attacks easier.

When the recent ransomware attacks, which have caused great harm to individuals and institutions, are examined, it is revealed that adequate measures are not taken against these attacks. In this article, what needs to be done for a more effective fight against ransomware is tried to be explained from a theoretical point of view. Considering the evolution of ransomware from the first years of its existence to the present, possible measures to be taken regarding how to combat these software in the future have been suggested.

2. Types of Ransomware

There are four types of ransomware, namely Crypto ransomware, Locker ransomware, Leakware, and Scareware (Moussaileb et al., 2018, Almashhadani et al., 2019 and Kaspersky, 2021). **Crypto ransomware** attacks users' devices using different attack vectors and encrypts especially valuable files. These files become inaccessible to the users, the attacker demands the user to pay the ransom to decrypt the file. Instead of accessing files, **Locker ransomware** (Jelen, 2021) directly locks user devices and makes them inaccessible and demands a ransom to unlock the devices. This type of ransomware does not encrypt the file. **Leakware** (Doxware) (Anghel and Racatuanu, 2019) only collects sensitive information from the victim's device and then blackmails the victim for ransom. Finally, **Scareware** is a less dangerous form of ransomware that notifies users that their files are encrypted or locked and demands ransom, and in fact only uses scare tactics (Simoiu et al., 2019).

Among the ransomware types, crypto ransomware is the most harmful, destructive, and the most numerous. Figure 1 shows the market share of the most famous crypto ransomware such as WannaCry, Locky, and CryptoLocker (Kumar and Ramlie, 2021; Eric, 2021).

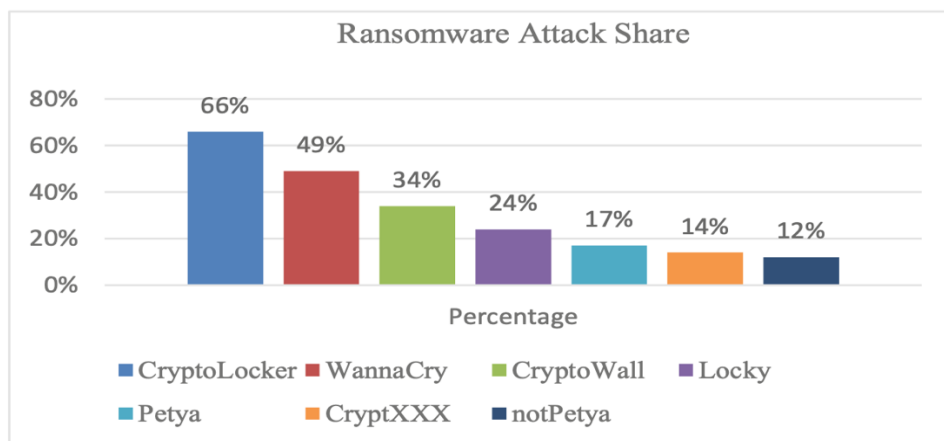
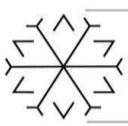


Figure 1: Crypto Ransomware Market Share (Kumar and Ramlie, 2021)



3. Detection of Ransomware Attacks

Ransomware attack detection methods aim to implement different mechanisms to detect when the attacks occur, immediately or afterward. By not detecting intrusions, the intent is to identify end devices and then detect any suspicious events. In this way, possible damage to the system is minimized as it is prevented at the initial stage of the attack. Intrusion detection can include both proactive and reactive solutions to protect the system.

Ransomware using the latest technologies can be combated using different methods. Some of the methods that can be used for ransomware detection are listed below: (Newtec, 2021 and McCormac, 2021)

- Monitoring and scanning network traffic and the entire system for anomalies
- Using Intrusion and Prevention Detection Systems (IDS, IPS)
- Use sandbox technique to dynamically detect new or advanced ransomware
- Using machine learning techniques to detect anomalies in the file system and network traffic
- Use home call detection method used to detect communication between infected computer and server

4. Mitigation Techniques

With the spread of the Internet and the rise of different types of malware in particular, concerns about information security have also increased. Knowing the ransomware lifecycle and payment methods is essential to prevent or mitigate cyber threats. Figure 1 shows the life cycle of ransomware.



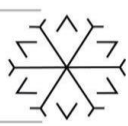
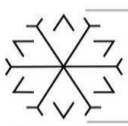
Figure 2: Ransomware Life Cycle (Silva et al., 2019)



The methods used to combat malicious software such as existing anti-virus software and sandbox solutions are largely unsuccessful against new generation attacks. This is because new generation malicious software has the ability to constantly change their digital signatures and can no longer be recognized by signature-based and static analysis. Cyber attackers using ransomware can easily circumvent intuitive and behavior-based automatic analysis mechanisms with the methods they have developed. Sometimes, these defense methods seem to be late in detecting new malware. Therefore, understanding how ransomware attacks have evolved allows us to better understand why cybercriminals may or may not use certain tactics or methods and how to defend against them (Celik and Celiktas, 2018).

Some mitigation methods to reduce the damage done by ransomware is listed below:

- 1- Backing Up:** One of the best and easiest defenses against ransomware attacks is backup and data recovery. If backups of the files encrypted by the attacker can be recovered, the organization will have survived the ransomware attack harmlessly. Since it can also target backup systems from attackers, it should be kept out of reach of malware. Also, testing the recovery process of files from backup is just as important as the backup. If the recovery process has not been tested, it will be difficult to ensure the security of backups. Backup policies and procedures of critical systems should be prepared seriously by organizations. In the event of an attack, when the system is out of use, it should be ensured that the system can be restarted without losing any data. In addition, the management system should ensure that the backup process is performed at regular intervals and that it can report the termination status and errors of the processes.
- 2- Avoiding Phishing and Social Engineering Attacks:** Phishing and social engineering attacks are the most common ways to spread ransomware. To protect against these attacks, end users should not click on links or open attachments of unknown origin in spam e-mails. Cybercriminals also use compromised ads to spread ransomware. These attacks targeting trusted websites can be blocked with ad blockers. Employees should also be trained to avoid spam, and the organization's IT unit should consider standardizing ad-blocking software.
- 3- Patching and Updating:** Systems that are missing updates and patches are always more vulnerable to ransomware attacks. For this reason, the operating system, browsers and security software should always be kept patched and up to date. If plug-ins such as Java and Flash are allowed, they must also be kept patched. In addition, methods such as whitelisting and limiting user rights can be used to reduce the possibility of ransomware infection. Since antivirus software is often not sufficient to deal with ransomware, combined solutions may be required to prevent such attacks.
- 4- Network Configuration and Management:** Against a ransomware attack, organizations must ensure that their network design requirements are met. For this, it is necessary to monitor the network structures, complete the configurations and manage the network systems correctly. The current network topology should be removed as soon as possible and this work should be monitored periodically.
- 5- Security Awareness Training:** The human element is generally the weakest link in terms of security of the information systems of any institution or organization. For this reason, institutions and organizations should provide users with the necessary expertise to realize their cyber security strategies and ensure that they gain awareness against ransomware attacks. Examining the most harmful malware attacks known, it becomes clear that the problems of information breaches are usually the lack of information security awareness of the employees. In order to increase the awareness level of the employees, regular training and awareness tests should be applied. The training given for current attack methods and



the measures that can be taken against them has an important effect on increasing the awareness level of the employees against the attacks.

- 6- Adopting Security Procedures:** Ransomware poses a threat to both the security of the data and the survival of the organization. Organizations first need to understand the extent of the threat ransomware poses to the organization. They can then make the right decisions about preventing these threats and taking the necessary precautions. Organizations must implement an effective security procedure to protect their information systems and employees. These procedures should include the steps of taking the necessary technical measures on many issues, especially the control of foreign devices connected to the network. Ransomware policies, protection and response procedures should be structured to cover the entire network.

5. Conclusion and Future Research

Ransomware attacks, which have increased rapidly in the past few years, have hit most institutions or organizations, from large companies to government organizations; has caused serious damage to users and information systems. It has been revealed that these institutions and organizations cannot completely protect themselves from the latest threats and smart cyber attackers. Attackers target users, who are the weakest link in the security chain, so they can access the data they want. Mostly at the source of the attacks, basic system vulnerabilities; stolen or abused privileges, a system that has not been installed and updated with security patches, or a careless user.

After being successful in a blackmail attack, cyber attackers can easily steal valuable data belonging to other institutions and organizations. From this point of view, information sharing between institutions and organizations, which is an indispensable element in the acquisition and analysis of cyber threat intelligence, emerges as a subject that needs to be emphasized. Within the scope of combating ransomware attacks, institutions and organizations can cooperate more effectively in detecting and controlling cyber attacks by using effective security intelligence technologies. The WannaCry example has proven that traditional security procedures are not sufficient to create an effective cyber defense strategy in terms of ensuring the security of states. (Darcılı, 2017).

The attack points and impact volumes of new ransomware, such as CryptoLocker, WannaCry, Petya, are directly related to the methods used in the attacks. It is of great importance to carry out theoretical and practical researches and to create combat teams to combat cyber threats in order to determine in advance what kind of vulnerabilities these attacks can exploit in systems. It is very important to create machine learning-based attack detection systems, in order not to be aware of vulnerabilities when they create attacks that only damage critical infrastructures, and to take precautions beforehand.

In addition, institutions need to identify a unique method of action to identify what went wrong with their systems and how to prevent it in the future. Precautions such as vulnerability and patch management, software update procedure, security awareness training, strict e-mail and file scanning measures, and a comprehensive backup plan must be included in the security strategy of institutions and organizations.

As a result; as stated in this study, it is possible to be protected from many attacks and to be prepared to be harmed at the minimum level by using effective fighting methods and applying the basic security measures regarding ransomware attacks. At this point, it is important to increase the security awareness of users and to develop new software and hardware-based solutions.

References

Anghel, M., Racautanu, A., (2019) A note on different types of ransomware attacks. IACRCryptol, ePrint Arch. <https://eprint.iacr.org/2019/605.pdf>, Accessed 17 Nov 2021



- Almashhadani, A.O., Kaiiali, M., Sezer, S., O'kane, P. (2019) A multi-classifier network-based crypto ransomware detection system: a case study of locky ransomware. *IEEE Access* **7**, 47053–47067. <https://doi.org/10.1109/ACCESS.2019.2907485>
- Alshaikh, H., Ramadan, N., Hefny, H.A., (2020) Ransomware detection and mitigation techniques. *Int. J. Comput. Appl.* **177**(40), 31–39
- Azmoodeh, A.; Dehghantanha, A.; Conti, M.; Choo, K.K.R. (2017) Detecting Crypto-ransomware in IoT Networks based on Energy Consumption Footprint. *J. Ambient Intell. Hum. Comput.* **9**, 1141–1152. [CrossRef]
- Çelik, S., & Çeliktas, B. (2018). Güncel Siber Güvenlik Tehditleri: Fidyeye Yazılımlar. *CyberPolitik Journal*, *3*(5), 105-132.
- Darıncı, A.B. (2017). Siber Uzay ve Siber Güvenlik Nedir? Bursa, Dora Yayınları, s. 233-234.
- Eric,C.; Ransomware Facts, Trends & Statistics for 2021. <https://www.safetymagazine.com/blog/ransomware-statistics/>, Accessed 20 Nov 2021
- Eset, E. *ESET Security* (2018); Technical Report; ESET: Bratislava, Slovakia, 2018.
- Herrera Silva, J. A., Barona López, L. I., Valdivieso Caraguay, Á. L., & Hernández-Álvarez, M. (2019). A survey on situational awareness of ransomware attacks—detection and prevention parameters. *Remote Sensing*, *11*(10), 1168.
- Humayun, M., Jhanjhi, N.Z., Alsayat, A., Ponnusamy, V. (2020) Internet of things and ransomware: evolution, mitigation and prevention. *Egypt. Inf. J.* <https://doi.org/10.1016/j.eij.2020.05.003>, 1-13
- Jelen, S. Ransomware Attacks: What They are, Common Types and How to Protect Yourself. <https://securitytrails.com/blog/ransomware-attacks>, Accessed 28 Nov 2021
- Kaspersky: What are the different types of ransomware? <https://www.kaspersky.com/resource-center/threats/ransomware-examples>, Accessed 15 Nov 2021
- Kumar, P. R., & Ramlie, R. E. B. H. (2021). Anatomy of Ransomware: Attack Stages, Patterns and Handling Techniques. In *International Conference on Computational Intelligence in Information System* (pp. 205-214). Springer, Cham
- Luo, X., Liao, Q. (2007). Awareness Education as the Key to Ransomware Prevention. *Information Systems Security*, s.195-202.
- McCormac, C.: Five Stages of a Malware Attack. <https://www.sophos.com/en-us/medialibrary/Gated%20Assets/white%20papers/sophos-five-stages-of-a-web-malware-attack.pdf>, Accessed 20 Nov 2021
- Moussaileb, R., Bouget, B., Palisse, A., Le Boudher, H., Cuppens, N., Lanet, J.L. (2018) Ransomware's early mitigation mechanisms. In: 13th International Conference on Availability, Reliability and Security, Hamburg, Germany, 27–30 August 2018, pp. 1–10
- Newtec: Malware and Attacks Explained. <https://newtecservices.ie/malware-exploit-attacks-explained/>, Accessed 20 Nov 2021
- Simoiu, C., Gates, C., Bonneau, J., Goel, S. (2019) "I was told to buy a software or lose my computer. I ignored it", a study of ransomware. In: 15th International USENIX Conference on Usable Privacy and Security, Santa Clara, CA, USA, 11–13 August 2019, pp. 155–174

Deep Computerized System For Lung Based Diagnostic Problems In CT Scans

Dr. Ali Berkan URAL ¹[0000-0001-5176-9280]

¹PhD, Department of Electrical Electronics Engineering, Circuit and Systems/Biomedical, Kafkas University, Kars, TURKEY

Abstract

This paper presents diagnosis and evaluation of early stage lung based diagnostic problems (lung cancer/nodule and COVID-19) with using a specific Computer Aided Diagnosis (CAD) system from chest computed tomography (CT) images. According to the statistics, the time factor is crucial to discover the disease/cancer in the patient as possible as early and fast. Especially, there were some misdiagnosis problems in the detection stage between lung cancer and COVID-19 disease and these two problems have been generally confused by physicians/doctors in radiology. In this study, a novel computer based algorithm is developed using Image Processing, Data Mining and Deep Learning methods to detect and classify the problems at early stage with more accuracy. Firstly, the decision support system works with Image Processing methods (Image acquisition, Noise removal, Region Growing Segmentation, Morphological Operations, Outlining, Lung Border Extraction, Segmentation etc.). Secondly, the system works with Data Mining methods (classification, prediction, pattern matching and clustering). Then, the system segments the area of interest of lungs (ROI-lungs) and then analyzes the separately obtained area for cancer detection or COVID-19 in order to diagnosis the problem. After segmentation, with using the Spectrogram/STFT inspired/based RGB images, the specific deep learning based method (customized Convolutional Neural Network (CNN)) is applied to classify the lung based problems.

Keywords. COVID-19, Lung cancer, Region Growing, Segmentation, Deep Learning

A Performance Monitoring System with the Capability of Detecting Anomalies for Corporate Business Intelligence Reporting Systems

Serap Yalçın ^{1*}[0000-0001-8225-700X] and Mustafa Ağaoğlu ^{2*}[0000-0002-7678-6316]

¹serap.budak@hotmail.com, Marmara University and Kuveyt Turk Participation Bank, R&D Center, Kocaeli, Turkey

²agaoglu@marmara.edu.tr, Marmara University

Abstract

Business Intelligence plays a key role in corporate companies to make managerial decisions. Especially for larger ones, Business Intelligence reporting systems get more complex with their large amount of data. When the number of reports increased, the performance of the reporting system might be a more important issue. Failures that may arise in reporting systems may disrupt the decision-making processes of corporate companies. Therefore, it is necessary to understand better the Business Intelligence reporting system to capture the problems quickly. In this study, a system is established to monitor the performance of the Business Intelligence reporting system of a Bank, with the capability of detecting anomalies. This system, it is aimed to facilitate the monitoring of the reporting environment and to detect and prevent problems that may arise in the environment. For anomaly detection, the data are collected from reporting environment and analyzed. The collected data are trained with different Machine Learning models. Then, AdaBoost Classifier algorithm is integrated into the performance monitoring system as the best fitted model with 89.76% recall rate. In this performance monitoring system, many indicators of the business intelligence reporting system are integrated into the established system and presented to the employees as a new report. With this system integrated into the bank, employees can follow the Business Intelligence reporting environment more easily. Thanks to the monitoring system, about half of the reports in the system were determined to be idle and removed from the system. Thus, the load on the system is reduced.

Keywords. Anomaly Detection, Business Intelligence, Data Mining, OLAP, Performance Monitoring

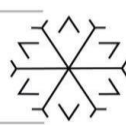
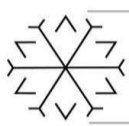
1. Introduction

Business Intelligence (BI) plays a key role in corporate companies while making managerial decisions. Especially for larger ones, BI reporting systems become more complex with their large amount of data. When the number of reports increased, the performance and health of the reporting system will be a more important issue. Therefore, we need to better understand the BI reporting system to catch problems quickly. In this work, a system with the capability of detecting anomalies to monitor the performance of the BI reporting system of a Bank is set up.

The work aims to establish a system to monitor the performance of the BI reporting systems in corporate companies and to detect anomalies in the system. This structure aims to enable the performance of the reporting system to be followed more easily and to be able to detect the problems that may arise in the system in advance. When the system experiences an error, it will speed up the solution of the problem by warning the relevant personnel or by intervening the system. With this structure, the works that tire the reporting system can be detected more easily and may be removed from the system by the personnel in charge. Hence, the load on the system can be reduced and performance can be increased. This will save both cost and time.

Although there are many studies in the literature on OnLine Analytical Processing (OLAP) structure, performance monitoring, and anomaly detection, there is no similar scientific work on the performance of corporate-wide reporting systems based on our research. This study will provide a solution structure applicable in corporate life as well as academic benefits.

Microsoft's business intelligence tools are used for reporting system implementation. For an exemplary corporate reporting system managed over OLAP cubes, a performance monitoring structure is created with Microsoft Power BI and Microsoft SQL Server Analysis Services tools, and each leg of the reporting system



is tracked from a single location. Again, to provide data to this structure, the Microsoft Server Integration Services tool and Extract Transform and Load (ETL) packages are used to transfer data to the system.

In order to detect anomalies in this reporting system, some Data Mining methods are applied and the results are compared. Details of the Data Mining methods used are explained in the following chapters. Then, the most successful alternative method is integrated into the performance monitoring system.

1.1. Business Intelligence

The main purpose of companies is to make a profit. With globalization, it has become very difficult to make a profit by providing a good balance of income and expenses, and it has increased the importance of business decisions. Business intelligence is the name given to software and services that are used to make data useable to help an organization for making strategic business decisions. BI tools analyze relevant data and present it in summary reports to give users detailed information about the state of the business.

Thanks to BI systems, users can get useful information from massive data and organizations can make more informed, smarter business decisions while collaborating with customers, suppliers, and competitors, as well as to adapt to a volatile environment and survive in the business world [1]. Hence, BI systems are costly to set up. Users in the system must be well trained. This is both time consuming and costly. In small companies, no personnel do not have complete knowledge about BI systems and can apply this area.

1.2. Database & Data Warehouse

Database refers to the collection of organized and manageable information stored in a computer environment. These data can be processed. Database management systems are used to create, store and manage data in the database. In databases, data are kept as systematic data with a certain structure and definitions. There are two types of databases as relational and non-relational. The relational databases are most preferred. In relational databases, data are stored in tables and these tables are related to each other. Besides relational databases, there are also non-relational databases. These are called as NoSQL databases. NoSQL is an alternative to relational database systems. In these systems, large amount of data can be processed more efficiently than relational databases.

A data warehouse is the collection and storage of data collected from various sources in order to contribute to the decision support system or to be used for different purposes. Data warehouses form the basis of business intelligence reporting systems and are used in many industries. The data warehouse is a warehouse where the relevant data can be queried and analyzed.

Databases use OnLine Transaction Processing (OLTP) as a processing method, while data warehouses use OLAP. In databases, data structures are normalized and do not contain redundant data, while data warehouses include denormalized data with repeated data. Therefore, databases have data that are more accurate but slow to retrieve data. Data analysis in databases is hard because of large number of table joins needed and the small time frame of data available. Data analysis is easy thanks to small number of table joins needed and extensive time frame of data available in data warehouses [2].

Microsoft SQL Server Analysis Services (SSAS) is a tool that enables us to handle large volumes of data and make analytical calculations. It is easy to collect data from different data sources and use the data for various aims such as analyzing it. Additionally, Data Analysis Expressions (DAX) is a part of SSAS as a formula expression language [3]. Microsoft SQL Server provides Data Quality Services, Integration Services, and Reporting Services too. SSIS is used as an ETL tool in the work to extract data from the system and load it to the database as usable data [4]. SSAS is used to prepare data for analysis.

OLAP is the name given to software that is used to perform multidimensional analysis at high speeds on large volumes of data in a data warehouse. While data are stored in two-dimensional structures in data warehouses, they are stored as multidimensional in the OLAP structure. This allows data to be processed and analyzed quickly. The data used within the scope of the business are often multidimensional. For bank customers, customers may have multiple dimensions such as personal, financial, and physical data. OLAP structure is very useful and provides convenience for such situations [5].

The application layer of the business intelligence architecture enables the analysis of integrated data. Trends, patterns, and exceptions are identified to query, report and analyze information. OLAP databases, predefined datasets, and users can be easily selected, extracted, and displayed. In the work, Microsoft SQL Server Analysis Services is used for creating and managing OLAP cubes as data sources for BI reports [6].



1.3. Data Mining & Machine Learning

Data Mining can be described as the extraction of hidden information from large databases. It is a technology with great potential and popularity to analyze important information in the data warehouse. Data mining looks for hidden patterns in databases. It can find predictive information that experts might overlook. Data mining tools can analyze large databases when applied with high performance servers. As a result of the analysis made, it can answer questions such as which customers are most likely to use the next promotion. This technology is increasing its popularity and usage areas continue to expand [7].

Machine Learning (ML) explores how computers can learn by feeding data. Its research interests are that computer programs automatically learn complex patterns and make smart decisions based on data. Machine Learning is growing rapidly and its importance in daily life is increasing. In our daily life, we use technologies that make use of machine learning in many areas. While data mining is used to make sense of large amounts of data, Machine Learning teaches systems how to learn repetitive patterns [8].

There are many similarities between data mining and machine learning. ML research generally focuses on accuracy for classification and clustering tasks. In addition, Data Mining research focuses on the efficiency, scalability, and ways in which mining methods handle large data sets.

Supervised learning is one of the learning methods and teaches the ML models some information about how inputs and outputs behave. It tries to explain the relation between inputs and outputs. There is also information about the groups that the values in the dataset belong to. The groups are called as “classes”. It means data tell that which inputs give which outputs. Then, the ML model will try to predict about new inputs. Unsupervised learning is another learning method in ML with unlabeled data. Opposite to supervised learning, there is no information about the behavior of inputs and outputs. It means data do not tell about that which inputs give which outputs. Semi-supervised learning is the last learning method in ML. In this learning method, there are both labelled and unlabeled data in the dataset. The labelled data are used to train the ML model. Unlabeled data is used to teach the model boundaries of classes.

1.4. Problem Definition

The purpose of this work is to set a structure to monitor the business intelligence reporting systems that are containing large amounts of data in corporate companies. In addition, the work aims to allow performance tracking and detect anomalies in the system.

The main goal of this structure is to enable the performance of the reporting system to be followed more easily and to be able to detect the problems that may arise in the system in advance. When the system experiences an error, it will speed up the solution of the problem by warning the relevant personnel or by intervening in the system. With this structure, the works that tire the reporting system can be detected more easily may be removed from the system by the personnel in charge. Hence, the load on the system can be reduced and performance can be increased. This will save both cost and time.

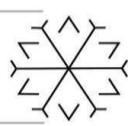
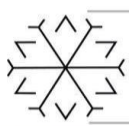
In corporate companies with high volume of data, BI reporting system might be overloaded and the RAM is swollen while the models (SSAS cube) were being processed (updating the data in the model). The server that is used for reports might be shut down automatically and access to all reports might be cut off. As the number of models increased, the problem will occur very often. In the bank, we had to monitor to reporting system to catch anomalies and see the causes of problems.

1.5. Literature Review

Most of the works begin with the test of the reports and their OLAP cubes. Harinath, Isaza, Mirchandani and Dumitru [9] mentions that testing is a key aspect of any software development and they explains the types of SSAS cube testing such as cube processing, dimension processing, single user query performance and multi-user query performance testing. The SSAS engine can be also tested for processing scalability as well as query performance. Then they focused on single user query performance testing.

Tasrif, Huda, Kurnia Saputra and Mubai [10] made a server performance monitoring application that is supported by the Script Shell to get information from the server. They used SNMP and SNORT to generate information and Sendemail and Gammu applications to report to the admin of the system. This monitoring application is able to monitor, recap and report server performance. They provide CPU, RAM, memory and average usage information in addition to warning messages and other threats.

The most similar work with our topic is “Monitoring and Profiling Solution for The BI System” by Bc. Matej Veselovský [11] which is written in the Czech language. It mainly focuses on monitoring and



profiling of SSAS cubes and POWER BI reports. In the project, MS Visual Studio 2015, MS SQL Management Studio and Power BI are used to accomplish the goal. He wanted to set a solution that should be a profiling and monitoring solution over business intelligence systems and should be applicable to any company and respective data warehouse.

Unlike these studies, the work will also focus on detection of anomalies on the reporting systems and try to implement some data mining techniques. There are variety of techniques for anomaly detection related studies in the literature. A dissertation, which is “Anomaly Detection in Real-World Temporal Networks” by Pablo Moriano Salazar [12], used Graph mining to show that surprising patterns about community structure and k-shell decomposition of graphs can be leveraged to detect classes of anomalies. Prarthana T. S. and N. D. Gangadhar studied user behavior anomaly detection (UBAD) based on OLAP based data analysis techniques [13].

In recent years, anomaly detection based on deep learning has become popular. Davis, Raina and Jagannathan developed an anomaly detection model based on deep learning for transportation networks. Then, they compared the model with some statistical, machine learning, and hybrid deep learning baselines [14]. Shriram and Sivasankar compared different unsupervised anomaly detection techniques using some performance metrics like precision, recall, F-score and area under the curve. They used One Class Support Vector Machine (One Class SVM), Local Outlier Factor (LOF), Isolation Forest (IF) and Elliptic Envelope (EE) as unsupervised learning techniques. Then, they compared the results with supervised learning techniques such as SVM and k-NN. They showed that unsupervised learning techniques are better for anomaly detection compared to supervised learning techniques for the shuttle and satellite datasets [15].

2. Material and Method

2.1. Methodology

In this work, a performance monitoring system is implemented in a bank to monitor the performance of the BI reporting system and to detect anomalies in it. The work aims to develop a monitoring system that can cover all legs of the reporting system. Additionally, anomalies in the reporting system can be detected as an output of the work. There are several methods to set a monitoring system and detect anomalies in a reporting system. In this work, different tools and methods are used. BI tools of Microsoft are used to develop a performance monitoring system. Then, some Machine Learning algorithms are applied and the results are compared to build an efficient anomaly detection model. In this part, these methodologies are explained.

The reporting system is constituted by several parts. To get data from all parts of BI reporting system, SSAS is selected as development tool. It is used to manage OLAP cubes and collect data from the business intelligence reporting system. OLAP gives the ability to make hard calculations and advanced data modeling. Thus, data model is developed and calculations are made in SSAS.

Some of the data is collected from databases via ETL processes and the Microsoft SQL Server Integration Services tool. ETL will be used for data collection, manipulation, and loading data to another place. Especially to collect historical data about the memory usage of data models in BI reporting system which is used for creating dashboards, ETL is a must to get current memory information from the server and write it to a table in database. Thanks to the ETL, memory usages of data models are stored as historical. When we need to use historical memory usage, it will be available in the database.

Additionally, same performance counters are collected from server machine such as memory, physical disk and processor related data. Besides these performance counters, SSIS job execution history is gathered from database engine. To be able to detect anomalies, Python is used to train and test some models and compare the results. The outlier executions are detected via outlier detection method depending on the job execution history. The number of outlier execution and the failure counts are collected. These data are used as new features in ML models that try to find anomaly situations in BI reporting system.

After ML model is created, current dataset that is prepared to detect anomalies is included in SSAS OLAP cube. Then, the new coming data is integrated into the system to feed the current ML model and to improve ML model. Details of data collection process are explained in the following sections. After data collection process is done, all prepared data is collected to an OLAP cube. Then, needed calculations are made here as measures to be able to use in visualization tool.

To visualize the performance monitoring system, Microsoft Power BI is used as a business intelligence visualization tool. A prepared OLAP cube is used as a data source in Power BI. A dashboard is developed depending on the needs of company to monitor all parts of BI reporting system at the same time. The



dashboard includes report server usage details, data model execution details, report usage details, SSIS job scheduling, memory usage of data models and total memory usage in the server historically.

In the literature, there are different methods to detect anomalies. In this work, different supervised anomaly detection techniques are used such as Random Forest, Support Vector Machine, and Bugging Classifier. These ML algorithms are implemented for the same dataset by using Python. Several ML algorithms are applied and their results are compared. Depending on the results, some of the algorithms are combined as hybrid algorithms to get better results. These processes are explained in detail in the following sections.

2.2. Data Collection

The reporting system has many legs. In order to be able to follow the whole system at the same time, we need to get data from all these legs. Since an OLAP cube is used for monitoring the reporting system, the data was collected via SSAS into the OLAP cube.

The first of these legs are OLAP cubes in the reporting system that were created by collecting data from different data sources to create BI dashboards. The information about these cubes must be gathered from Analysis Services. While collecting the data, statistical data belonging to the server that is used for maintaining the reporting system was collected. Some queries were created with Multidimensional Expressions (MDX) language because of the nature of Analysis Services. Sizes and other information about the OLAP cubes in the reporting system were collected from the Analysis Services data source by using MDX queries.

Some information about OLAP cubes in the reporting system were collected such as Object Cpu Time, Object Reads, Object Memory Shrinkable, Object Version, and Object Time Created. Some other technical details about OLAP cubes were gathered such as Description, Roles, Date Modified, Compatibility Level, and Version. To get these information, SSAS Dynamic Management View is used with some scripts like "select * from \$system.discover_object_activity".

Another leg of the BI reporting system is Power BI Report Server platform, which enables reports to be physically presented to the user. Some data can be collected from this platform. Power BI Report Server usage logs were also included in the reporting system monitoring model. The information about entries of users that are made to the reports in the reporting system from the main platform of the bank is also taken from databases to determine the usage frequency of the reports as an indicator of report importance.

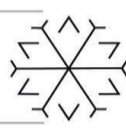
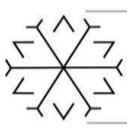
There is also some relation between documents in Power BI Report Server and main banking platform. The detailed information about BI reports in the reporting system are collected from databases and put into the reporting system monitoring system. All preprocessing and manipulation processes are done in the OLAP cube. Then, some performance counters are created.

For anomaly detection part, performance monitor logging has been set up on the server to detect abnormal situations. With this setup, certain metrics started to be collected periodically. To set it, Performance Monitor is used with user defined data collector sets. To track the performance of the server some performance counters are chosen. To see general server health, Processor Utilization, Disk Activity, Memory Usage and Network Usage are important. At the beginning of the selection process of performance counters, some of the CPU and performance-related ones were selected depending on their meanings.

Initially, data was not collected very often in order not to affect machine performance. In the following process, the frequency of data collection has been increased in a controlled manner. Various features were collected in this process and their changes were observed. According to the change in the collected fields, additions and subtractions were made into the data set and the current state was obtained.

The finalized labelled dataset includes 38 columns and 3283 rows in total. The data includes 3195 rows as normal data and 88 rows as anomaly data. The prepared dataset has 2.7% anomaly data. 2.7% is a quite low rate, but it is realistic at the same time when we consider anomaly situations. After the dataset is set, the dataset were prepared for modelling.

To get related features for the machine learning model, SQL Server Agent job history is collected and some features were derived from job history. Here, the number of jobs started in a dedicated period was also put on the dataset to be added as a feature to the model. Durations of jobs for each trigger are calculated and outlier analysis is made. Outliers are flagged as outlier occurrences and the total numbers per period are added to dataset as a new feature. These derived features are Failed Job Count, Outlier Job Count, Not Responding Job Count, and Day Time Label.



All these features are used for training ML algorithms. After training, the results are investigated and some of the features are removed from dataset because they are ineffective or correlated features. Additionally, some of the features are eliminated because of overfitting.

In the end, performance related data that were collected from the remote server is determined as the final dataset to be used in machine learning models. With the dataset, unsupervised and supervised learning methods were tried. To do this, the dataset had to be labelled.

Labelling data is a difficult task. While doing this, support was received from experts. Only situations that were sure to be anomalies were labelled as anomaly data. Likewise, only the situations that are sure to be normal are included in the data set as normal cases. This labelling process has been tried to be obtained as accurately as possible in line with the guidance of the experts. Thus, within the scope of the information we have, a labelled data set was formed.

In this study, we prepared a dataset without noisy data thanks to technical knowledge. In addition, the dataset has missing values. In the data cleaning step, missing values are filled with the mean of related features. The prepared dataset does not include categorical features. All features are numerical. In data transformation step, MinMax scaler is mainly used to scale data to a standard range to get better performance. With MinMax scaler, features are transformed into a range which is 0 to 1 as minimum and maximum values respectively.

Some produced features are tried but they are not used in final version of dataset. Additionally, some of the features were investigated as ineffective. Then, these features are not included in the final dataset. The whole dataset is split into train and test parts. While doing these, different test sizes and random states are used. The tried values are presented with model results in the following sections.

The prepared dataset will be used in anomaly detection with several machine learning algorithms. Then, all collected data and anomaly predictions will be visualized with Microsoft Power BI as a monitoring tool. As mentioned before, the main purpose of this study was to create a performance monitoring system with the capability of detecting anomalies for corporate business intelligence reporting systems.

2.3. Model Implementation & Training

After the data preprocessing step, relevant machine learning models were started to be applied to the prepared dataset. To detect anomalies, different learning models are used. With the originally gathered dataset, some unsupervised learning models are trained. These are K Means Clustering, Isolation Forest, Local Outlier Factor and One Class Support Vector Machine. With labelled dataset, some supervised learning models are trained. These are Logistic Regression, KNN, Random Forest, Decision Tree, Bagging Classifier, Ada Boost Classifier, SVC, Gradient Boosting Classifier, Hist Gradient Boosting Classifier, MLP Classifier, Stacking Classifier, XGBoost and CatBoost.

Then, a Deep Learning Model is trained with 2 hidden layers. First hidden layer has an activation function as Relu while second has Softmax. Additionally, Adam optimizer is used with loss function as `sparse_categorical_crossentropy`.

For modelling part, 100% of dataset without labels is used for training purpose with unsupervised learning models. After that, labels of same dataset is used to calculate performance measures of applied unsupervised models. Then, 66% of the dataset is used for training and remaining part is used for testing purposes with supervised learning models.

Recall and AUC scores are used as the main performance criteria. More than these performance criteria are calculated but these are used as main ones. For example, accuracy is an important performance criterion in Machine Learning but not for anomaly detection problems. Because there is low number of anomaly data, the accuracy is generally high for most of the applied models. Recall, AUC Score and Sensitivity are more realistic indicators for anomaly detection problems. Our success factor while creating the anomaly detection system is keeping the 80% precision and recall rate as desired value.

For unsupervised anomaly detection algorithms, there is no random sampling because the nature of unsupervised learning methods that do not need labels to predict. The whole dataset is used for training one time.

To build a K-Means clustering model, Sum of Squared Error (SSE) values are calculated with different K values. Depending on the changes in SSE values, 2 and 3 are tried to decide on K value. At the end, K values is used as 2. A value of 2 is suitable for being K value of an anomaly detection problem.



To build a LOF model, related parameters are determined by considering the article which is “LOF: Identifying Density-Based Local Outliers” by Breunig, Kriegel, Ng, and Sander. The results of the training part are shown in Table 1.

Table 1: The Average Results of Trained Unsupervised Models

	Accuracy	Precision	Recall	F1	AUC
K-Means	0.1709	0.0228	0.7159	0.0442	0.4359
Isolation Forest	0.9668	0.4444	0.9545	0.6065	0.9608
LOF	0.9555	0.0606	0.0455	0.0519	0.513
One Class SVM	0.5263	0.0536	1	0.1017	0.7567

Depending on these results, Isolation Forest is the best algorithm with highest performance scores for all metrics. Hence, precision value of the Isolation Forest are low for being a good anomaly detection model. After that, unsupervised anomaly detection algorithms are trained too. Performance scores are calculated in the same way as in unsupervised learning. In order to validate the results, the experiments are run 10 times with different random seed values. The results that are reported in the work are averages over 10 repetitions on same dataset with different random seeds. After a trial and error phase, 3 is selected for being K value of KNN model as an odd number with better results. The average of each training with supervised anomaly detection algorithms are shown in Table 2.

Table 2: The Average Results of Trained Supervised Models

	Accuracy	Precision	Recall	F1	AUC
Logistic Regression	0.9945	1	0.7778	0.874	0.8889
KNN	0.997	0.9927	0.886	0.9352	0.9429
Random Forest	0.9961	0.9922	0.8529	0.9163	0.9264
Decision Tree	0.9945	0.9132	0.8727	0.8887	0.9352
Bagging Classifier	0.9956	0.9962	0.8257	0.902	0.9128
AdaBoost Classifier	0.9972	0.9925	0.8976	0.9417	0.9487
SVC	0.9966	0.9728	0.8906	0.9285	0.945
Gradient Boosting Classifier	0.9926	0.8653	0.8403	0.8504	0.9184
Hist Gradient Boosting Classifier	0.9968	0.9909	0.8792	0.9305	0.9395
MLP Classifier	0.9958	0.9557	0.8744	0.9123	0.9367
Stacking Classifier	0.9951	0.973	0.824	0.8913	0.9117
XGBoost	0.9962	0.993	0.8586	0.9192	0.9292
CatBoost	0.9958	0.988	0.8411	0.9071	0.9204
Keras	0.9956	0.9592	0.8628	0.9058	0.9309

When all the applied algorithms are compared, it is seen that the Isolation Forest model gives the highest Recall value but the Accuracy and Precision values for this model are low compared to the others. Especially the Precision value is well below the desired value. This is not an acceptable value for the study. For this reason, Isolation Forest is not selected as the best algorithm. When supervised learning models are compared, it has been observed that the AdaBoost Classifier algorithm gives the best results on average. Besides that, other performance values give adequate results. The second candidate algorithm is the SVC model. Then, these models with good results were combined with Voting Classifier and different methods and calculated again but better results could not be obtained. For this reason, AdaBoost Classifier, which is the algorithm with the best results, is integrated into the monitoring system as an estimation algorithm. The most important features were determined according to the successful model. Feature importances depending on the results of selected algorithms are shown in Figure 1.

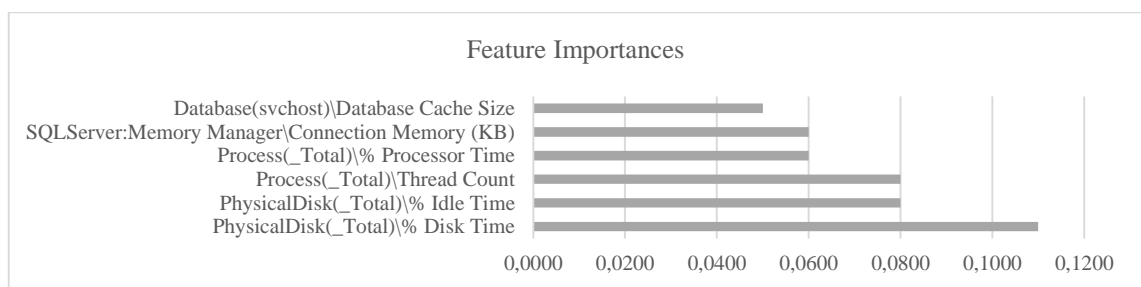
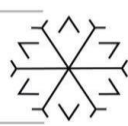
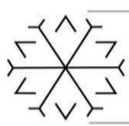


Figure 1: The Top 6 Feature Importances.



The most important feature is PhysicalDisk(_Total)\% Disk Time depending on Figure 1. Additionally, other features can be categorized as efficient and inefficient. With this type of categorized feature set, there may be set an alert mechanism with dedicated threshold values for each efficient feature.

2.4. Performance Monitoring Report

A report has been created where we can monitor every area touched by our business intelligence reporting system and see its performance. Thanks to this report, the reporting system, which has become difficult to manage and follow, has become easily followed. By adding an anomaly detection feature to the developed report, it is provided to alert users when abnormal situations occur.

A Performance Monitoring Report is created with Power BI. The report includes five main parts related to the BI reporting system in the bank. Reporting System Monitoring page includes information about the current situation of the reporting system such as memory usage in reporting server machine. Additionally, the page shows the usage and up-to-dateness of reports. There is a page which is called as Report Usage and it contains information about the usage details of report for the last 3 months. Another page is Job – Model Execution Details. It shows working jobs in the system with their results, execution time and error messages. Thanks to the page, any person from business department who is not able to monitor job details from SQL Database Engine can reach working details and errors related to their own jobs without the support of technical person.

Memory Monitoring page shows the memory details of production and preparation environment at the same time. Memory details for production environment is stored historically in weekly period. Thanks to the page, memory allocation details of each model can be observed and possible memory related problems can be detected in early stage. The last page is Reporting Machine Anomalies. The page includes the result of the Anomaly Detection Model. Some of the related features are added to the page to show the change during abnormal situations such as SQL Server Memory Manager Memory and Process(_Total)IO Data Bytes.

In the bank, we had a model of approximately 300 GB and this model was particularly tiring for the system. We had to improve the model or remove it from the system. Then we removed the model from the system and moved it to another machine. Thanks to the monitoring system we have created, the bank has been able to easily detect such problematic models. Besides that, the total memory usage of the whole models in the machine can be followed historically via the monitoring system.

In addition to the memory usage information of the models, the usage and up-to-dateness information of the reports fed by these models are also included in the monitoring system as different indicators that show the quality of the reports. With a KPI score created in the light of this information, it became easier to take actions to improve models that show poor performance or to remove them from the system if they are not used. In this way, reporting system performance has been improved. Thanks to this study, people from all departments became able to observe the health of the reports.

With the ability of anomaly detection, it has been tried to predict in which situations the system has problems in general and it has become possible to take precautions. In order to detect the problems in the system, some important indicators of the system were learned by applied machine learning algorithms. By monitoring these indicators, system users were warned without machine failures.

3. Conclusion

In this study, various machine learning methods have been tried. 15 algorithms from supervised and unsupervised learning methods have been tried. The most successful ones were AdaBoost Classifier and SVC algorithms. The results of these algorithms on the prepared dataset are explained in detail in the previous sections.

In the work, the detection success of anomaly detection systems developed with Machine and Deep Learning algorithms in anomaly-based attacks has been examined. Real data collected from a bank were used. When the results obtained with Machine Learning are examined, it is seen that the most successful algorithm is AdaBoost Classifier with 89.76% Recall rate. Then, the second was the SVC algorithm with 89.06%.

The work proposes a monitoring system that brings together business intelligence reporting structure and machine learning. The system also facilitates the management of business intelligence reporting systems. Thanks to the system, all employees will be able to follow the working status of the reports they use and are responsible for. In addition, checking the health of the business intelligence reporting systems has



become easier for BI developers and reporting system responsible. Furthermore, much information concerning the reporting system can be accessed at the same time via the monitoring system. In the light of this information, it has become possible to make system improvements and to detect problems beforehand. The interruptions in the system have been reduced with the precautions taken.

The outputs of this work will be used in a bank. The structure that will be used in a bank will facilitate the follow-up of the business intelligence reporting system in the bank and will save time for the employees that are responsible for managing business intelligence reporting system. It will allow errors in the reporting system to be quickly detected and corrected. The work we will propose can be useful in many areas, including corporate companies. It will also contribute to the academic literature on business intelligence and data mining. This work can be presented in an academic setting and can be an inspiration for those aiming to progress academically in the field of business intelligence. The study will be a reference for future studies that can compare their results with the results and performance of the study we have proposed. Corporate companies can benefit from this study as it applies to business life.

The dataset used in this study is limited to a bank's reporting system. In order not to increase the interruptions in the system, data has been collected without interfering with the reporting system. When the time constraints of the work study are considered, collecting more anomaly data will contribute to the development of the study. Although the anomaly data collected from the system is sufficient. Collecting more abnormal situation data and adding new features related to the system can be the next stages for this work. Since the data collected from the system is not large and the machine learning models used do not take a long time, the performance of the models is not considered in the work. The work can be improved by examining the running times of the models for structures with larger datasets and near real-time anomaly detection.

References

- [1] Olszak, C., Zurada, J. (2015) Information Technology Tools For Business Intelligence Development In Organizations, Polish Journal of Management Studies, 12, 132-142.
- [2] Panoply, Database vs. Data Warehouse Comparison, <https://panoply.io/data-warehouse-guide/the-difference-between-a-database-and-a-data-warehouse/>, January 2021.
- [3] https://www.tutorialspoint.com/power_bi/dax_basics_in_power_bi.htm, January 2021.
- [4] Harinath, S., Pihlgren, R., Lee, D. G.-Y., Sirmon, J., Bruckner, R. M. (2012) Professional Microsoft SQL Server 2012 Analysis Services with MDX and DAX, Wrox.
- [5] IBM, <https://www.ibm.com/cloud/learn/data-warehouse>, January 2021.
- [6] Přikrylová, I. D. (2016) Business Intelligence Models for Capturing and Analysis of Enterprise Marketing Data, Brno.
- [7] Pujari, A. K. (2001) Data Mining Techniques, Sangam Books Ltd.
- [8] Han, J., Kamber, A. K., Pei, J. (2011) Data Mining. Concepts and Techniques, Morgan Kaufmann.
- [9] Harinath, S., Isaza, G., Mirchandani, A. and Dumitru, M. (2008) Testing Microsoft SQL server analysis services. Proceedings of the 1st International Workshop on Testing Database Systems, 13 June, Vancouver, BC, Canada.
- [10] TASRIF, E. (2019) Design of Server Performance Monitoring Application Integrated Administration Service System in Electronic Engineering Department. Journal of Physics: Conference Series, 1387, 12-29.
- [11] VESELOVSKÝ, M. (2017) Vytvoření monitorovacího a profilovacího řešení nad BI systémem. Master Thesis, Brno University of Technology, Brno, Czech Republic, 1-20.
- [12] Salazar, P.M. (2019) Anomaly Detection in Real-World Temporal Networks. PhD Thesis, School of Informatics, Computing, and Engineering, Indiana University, Indiana, USA, 1-10.
- [13] Prarthana, T. S. and Gangadhar, N. D. (2017) User Behaviour Anomaly Detection in Multidimensional Data. 2017 IEEE International Conference on Cloud Computing in Emerging Markets (CCEM), 1-3 November, Bangalore, India.
- [14] Davis, N., Raina, G., and Jagannathan, K. (2019) A Framework for End-to-End Deep Learning-Based Anomaly Detection in Transportation Networks. Transportation Research Interdisciplinary Perspectives, 5, 100-112.
- [15] Shriram, S. and Sivasankar, E. (2019) Anomaly Detection on Shuttle data using Unsupervised Learning Techniques. 2019 International Conference on Computational Intelligence and Knowledge Economy (ICCIKE), 11-12 December, Dubai, United Arab Emirates.

Sentiment Analysis of Turkish Tweets on Covid-19 Using Word Embedding vectors and Bidirectional Long Short Term Memory Networks

Emine akmakc₁ ¹ [0000-0000-0000-00000], Saeid Agahian ^{2*} [0000-0003-2462-6166] and İrfan Yıldırım ³ [0000-0002-5635-2991]

¹emine.cakmakci36@erzurum.edu.tr, Erzurum Technical University

²saeid.agahian@erzurum.edu.tr, Erzurum Technical University

³irfan.yildirim@erzurum.edu.tr, Erzurum Technical University

Abstract

Sentiment analysis attempts to extract the polarity from data. This field has gained growing popularity in recent decades. The data used for this task can be in different formats such as audio, video, image, or text. We chose to work on textual data to extract its polarity. Covid-19, as a pandemic issue in all countries, has dedicated a significant portion of discussions in social media such as Twitter. Turkish tweets are not an exception in this field; Turkish people discuss this universal issue on Twitter every day. Moreover, as most non-English languages such as Turkish suffer from the lack of research in sentiment analysis, we decided to analyze Turkish tweets. The current study focuses on the sentiment analysis of Turkish tweets on Covid-19 using the word embedding vectors and deep neural networks. For this aim, we collected a dataset of 11,000 tweets posted on Twitter between December 2020 and April 2021. After manually labeling each tweet as positive, negative, or neutral, we achieved 4000 positive, 5000 negative, and 2,000 neutral tweets in the dataset. The proposed method uses the Word2vec model for numerical representation of tweets' text. These numerical vectors are then fed to a deep neural network model. The model used in this work is Bidirectional Long-short Term Memory (BiLSTM) networks. Finally, after adding a Dense and a Softmax layer to the BiLSTM model, a ternary classification (positive, negative, objective) task is performed on the labeled tweets. Experimental evaluation using 10-fold cross-validation on the designed deep neural model could achieve 75.34% accuracy in the ternary classification of tweets.

Keywords. Sentiment Analysis, Covid-19, NLP, Word2vec, LSTM

Recognition of Electronic Circuit Components Using a Modern Convolutional Object Detector

Uğur KILIÇ ¹*[0000-0003-4092-3785], Yasin DEMİR ¹*[0000-0002-0834-2780], Nur Hüseyin KAPLAN ¹*[0000-0002-4740-3259] and Gülşah TÜMÜKLÜ ÖZYER ²[0000-0002-0596-0065]

¹ugur.kilic@erzurum.edu.tr, Dept. of Computer Engineering, Erzurum Technical University

²yasin.demir@erzurum.edu.tr, Dept. of Electrical-Electronics Engineering, Erzurum Technical University

²huseyin.kapl@erzurum.edu.tr, Dept. of Electrical-Electronics Engineering, Erzurum Technical University

²gulsah.ozyer@atauni.edu.tr, Dept. of Computer Engineering, Ataturk University

Abstract

In the electronics industry environment, fast and accurate recognition of electronic circuit elements is a requirement for visual guidance of intelligent robots. Low recall and accuracy values are produced in the recognition of electronic circuit elements with traditional image recognition technologies. In deep learning-based rapid recognition methods, when trained with sufficient data, high recall and accuracy values are achieved because they can learn high-level features about the objects in the images. For this reason, rapid recognition methods based on deep learning have become the focus of researchers in object recognition.

In this paper, YOLOv4 algorithm is used for fast and accurate detection of electronic circuit elements. Recently, the YOLOv4 algorithm has been one of the modern convolutional object detectors that has attracted attention by producing successful results in real-time applications. Firstly, the most frequently used electronic circuit elements are examined and divided into 12 classes. A new image dataset is generated for electronic circuit elements by creating a separate image set for each class. The dataset is randomly divided into three parts: testing, validation and training. Secondly, a model is created on the training dataset by using the YOLOv4 algorithm, which is one of the modern convolutional object detectors. Finally, the model has been examined on the test dataset in real time, and the effectiveness of the model is observed. As a result, the value of accuracy is reached to 94% in the created test set.

Keywords. Rapid recognition, Vision-based method, YOLOv4, Electronic circuit components dataset

1. Introduction

Intelligent systems need real-time object recognition for target detection. For instance, unmanned aerial vehicle navigation to make maneuvering decisions, it is necessary to recognize targets in remote sensing images in real time. On the other hand, real-time recognition for road signs, traffic lights and pedestrians is required for safe autonomous driving in land vehicles (Guo et al., 2021). Real-time recognition of targets like as electronic components has great importance for concept actions of intelligent robots in industrial production (Xu et al., 2020).

The aim of target object recognition, in the field of computer vision, is quickly and accurately determining the class and location of a particular object in digital images. Since the traditional image recognition methods produce low recall and accuracy values, machine learning based algorithms have been of interest, recently. Fast object recognition methods based on deep learning, when trained with sufficient data, high recall and accuracy values are obtained because they can learn high-level features about the objects in the images. Object recognition methods based on deep learning can be classified as one-stage and two-stage detection algorithms. Since two-stage deep learning algorithms achieve object recognition in two stages, they have low performance in real-time applications in terms of speed and efficiency. Single-stage deep learning algorithms achieve higher performance in terms of speed with a close accuracy rate compared to two-stage algorithms in real-time applications (Guo et al., 2021; Huang et al., 2019).

In this paper, one of the modern one-stage convolutional object detector, YOLOv4 algorithm is used. Recently, YOLOv4 algorithm has been attracted researchers by producing successful results in real-time applications. A new

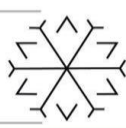


image dataset is created for the most frequently used electronic circuit elements. The 12 classes of electronic circuit elements are given in Figure 1.

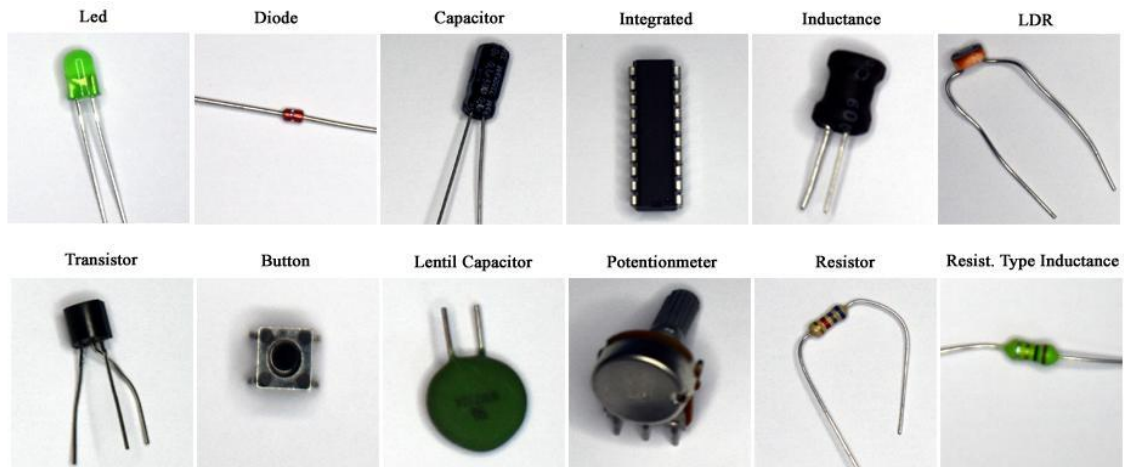


Figure 1: Electronic circuit elements used in the dataset

The rest of the paper is organized as follows. In Section 2, studies related to rapid recognition methods based on deep learning are included. In Section 3, the dataset, labeling and training methods are explained and the YOLOv4 method used in the recognition of electronic circuit elements is explained. The performance evaluation of the created model is explained in Section 4. General conclusions are given in Section 5.

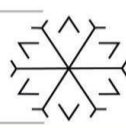
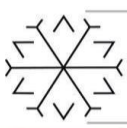
2. Related Work

The existing image recognition methods in the literature are divided into two categories. The methods in the first category classify images according to their spatial and transform domains. The methods in the second category perform recognition on images with deep learning architectures such as convolutional neural networks (CNNs) that automatically learn image properties. (Hu et al., 2020).

Traditional image recognition methods have been developed by researchers for many years. In traditional image recognition methods, image features are extracted by applying a preprocessing step such as morphological transformations to the image. The recognition process is performed according to these extracted features. Conventional methods cannot process large amounts of images due to computational complexity. In addition, the recognition performance of these methods reduce if there are more than one object class to be determined. Due to these problems experienced in traditional methods, object recognition methods based on deep learning architectures have been developed. Deep learning algorithms have been brought object recognition through convolutional neural networks (CNN) to a point where it can be used in real-time industrial applications (Xu et al., 2020).

The first time two-stage algorithm using CNN structures for object recognition is the R-CNN (Region Based Convolutional Neural Networks) algorithm proposed by Girshick et al (2014). In the R-CNN structure that used the selective search algorithm, candidate regions that can contain about 2000 target objects are determined. Then, features are extracted for each candidate region by using CNNs (2000 CNNs for 2000 regions). With the use of the features, the class of the object from the SVM models and the bounding boxes from the regression models are determined (Girshick et al., 2014). Fast R-CNN has been developed to reduce the cost caused by the excessive processing complexity of R-CNN structures in the training process (Girshick, 2015). Ren et al. (2016) propose the use of Faster R-CNN algorithm by using RPN (Region Proposal Network) instead of selective search, which is costly. Mask R-CNN is developed by adding a second network branch that produces segmentation results on an object basis to increase the object detection performance of Faster R-CNN (He et al., 2017).

Although two-stage algorithms have high detection accuracy, candidate frame generation requires a large amount of computation, resulting in low detection efficiency. Therefore, many YOLO (You only look once) (Redmon et al., 2016), SSM (Single Shot MultiBox) (Liu et al., 2016), RefineDet, etc.) (Zhang et al., 2018), EfficientDet (Tan et al., 2020)) one-step algorithms are developed. The single-stage algorithms, the YOLO algorithm has been



achieved superior speed and accuracy compared to other algorithms in real-time application. As a result of various optimizations made by the researchers in the YOLO algorithm to YOLOv2 and YOLOv5 has been developed. In this paper, YOLOv4 version is used that optimized by Bochkovskiy et al (2020).

3. Proposed Method

3.1. YOLOv4 Architecture

R-CNN (Girshick et al., 2014), Fast R-CNN (Girshick, 2015) and Faster R-CNN (Ren, 2015) object recognition algorithms perform the object recognition process in two stages. In the first stage, regional suggestions are made for the regions that objects can be found. In the second stage, the softmax and regressor layers are run for the suggested regions. The Softmax layer is responsible for finding the class of the object in the region, and the Regressor layer is responsible for drawing the bounding box of the detected object. Since the object recognition process is done in two stages, the processing time is longer than single stage algorithms. A completely different approach is used in the YOLO algorithm developed by Redmon et al. (2016). The YOLO is a one-step object recognition algorithm based on convolutional neural networks. The YOLO algorithm divides the input image into a $S \times S$ grid by passing it through the convolutional neural network in a single step. Each grid cell checks whether there is an object in it. In case of there is an object in the grid cell, it checks whether the object's center point is inside the grid cell. In the event of the center point is inside the grid cell, the grid cell is responsible for detecting the attribute information (bounding box information, confidence score, class) of the object. The confidence score is created according to the detection probability of the object. The YOLO algorithm estimates the bounding box information and class probabilities from the entire image. In case of collision or coverage operation occurs in the bounding boxes, the nonmaximum suppression algorithm is run. Making predictions with a single convolutional neural network evaluation for a single image makes YOLO extremely fast (Redmon et al., 2016; Redmon and Farhadi, 2017). One of the versions of YOLO, YOLOv4 algorithm is published by Bochkovskiy et al. (2020). Bochkovskiy et al. (2020), have created an algorithm that can be trained quickly on a single graphics processing unit (GPU) and produces more accurate results in the YOLOv4 algorithm. The architecture of YOLOv4 is given in Figure 2.

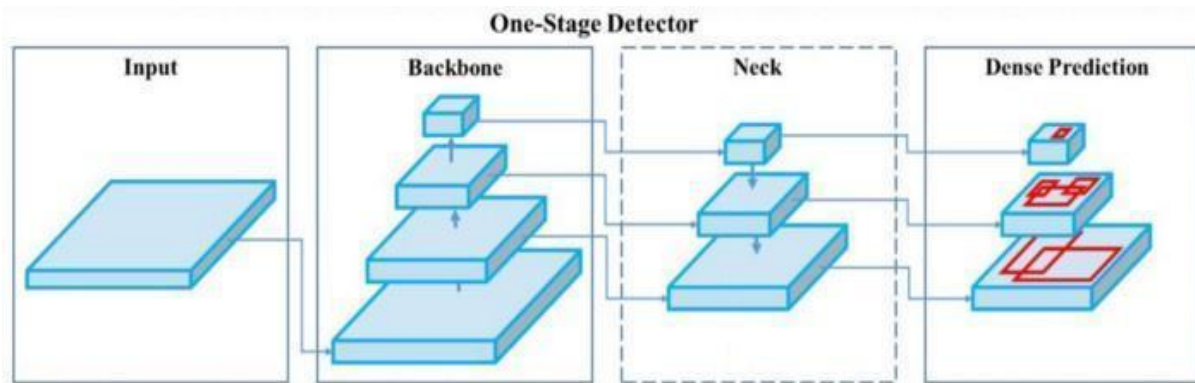


Figure 2: YOLOv4 Architecture (Wang et al., 2020)

The YOLOv4 model consists of three parts: Backbone network, Neck and Head (Dense Prediction). In the YOLOv4 model, the CSPDarknet53 (Wang et al., 2020) neural network is used as the backbone network to collect features over different image particles. In order to provide more gradient flow from the network, CSPDarknet53 performs splitting and merging operations on the attribute map. The Neck section consists of bottom-up, top-down ways to collect and combine the parameters of the network in different layers to provide more accurate display characteristics for the Head section. Some techniques used in the neck section of the YOLOv4 model are FPN, SPP (He et al., 2015), PAN (Liu et al., 2018). In addition, Bag of freebies and Bag of specials packages are used for dataset enrichment and optimization processes. The Dense Prediction layer, which is the head section, has the same structure as YOLOv3. The head section is responsible for creating a vector containing the object's coordinates, confidence score, and label. Compared to the previous version, YOLOv4 has increased AP by 10% and FPS by 12%. In this paper, the YOLOv4 algorithm is used because of the fact that it is widely used in real-time object detection applications due to its speed.



3.2. Dataset

Within the scope of this study, first of all, the most frequently used electronic circuit elements are examined and 12 classes are generated. A new dataset is created for each class by taking pictures with the NIKON D3500 camera. Since the lack of diversity in the dataset will cause over learning, Since the lack of diversity in the dataset will cause over learning, has been cared to ensure diversity while creating the dataset. With the aim of ensure diversity, images have been taken different distances and views. There are 388 images in the dataset, and a total of 857 electronic circuit elements within the images. The dataset is made publicly available at (<https://github.com/ugrkilc/Recognition-of-electronic-circuit-components>). The dataset is randomly divided into two parts, 90% training and 10% testing. In order to increase the success of the training, the training dataset is divided into two parts as 90% training 10% validation.

Table 1: Numerical information of electronic circuit elements dataset

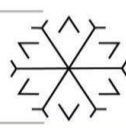
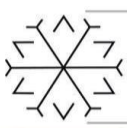
Type of electronic circuit element	number of images in the class	Total number of elements in images
Button	30	52
Capacitor	39	111
Diode	39	88
Inductance	27	45
Integrated	34	96
LDR	30	55
Led	23	86
Lentil Capacitor	33	89
Potentiometer	37	57
Resistance Type Inductance	32	54
Resistor	29	49
Transistor	35	75
Total	388	857

3.3. Dataset Labeling

YOLO architecture needs "<image_name>.txt" files that contain the coordinate information of the objects to be trained in the images, along with the images of the objects to be trained during the training process. For this reason, all images in the training and validation datasets are labeled and recorded in YOLO format using LabelImg program.

3.4. Training

In order to perform training with the darknet backbone in the YOLO architecture, the "yolov4-custom.cfg" files containing the configuration information have to be edited. The "yolov4-custom.cfg" configuration file is the file containing the network structure of the YOLO architecture. The number of classes to be trained in the "yolov4-custom.cfg" configuration file located in the root directory of the darknet backbone and the values of the last layer of the network model are arranged according to the created dataset. Class names of electronic circuit elements in the dataset need to be given to the darknet backbone. Therefore, the class names are recorded in the "obj.names" file and placed in the darknet root directory. The file paths of the training and verification images are created by



recording the "obj.data" file and placed in the darknet root directory. After editing the "yolov4-custom.cfg" file and creating the "obj.names", "obj.data" files, the training process can be carried on. However, since the initial weight values are chosen randomly, the training may be longer than necessary. In order to shorten the training time and to provide transfer learning, the training is started by using "yolov4.conv.137" weight values as initial weights. The training process has been carried out on the GPU on a computer with Intel(R) Core(TM) i5-7400 CPU 3.00 GHz processor, Nvidia Geforce RTX 2080 8gb GPU. Model training has been carried out in 34 hours as 10000 iterations. The visual of the change in mean average precision (mAP) and Loss function values of the model created during the training process is shown in Figure 4.

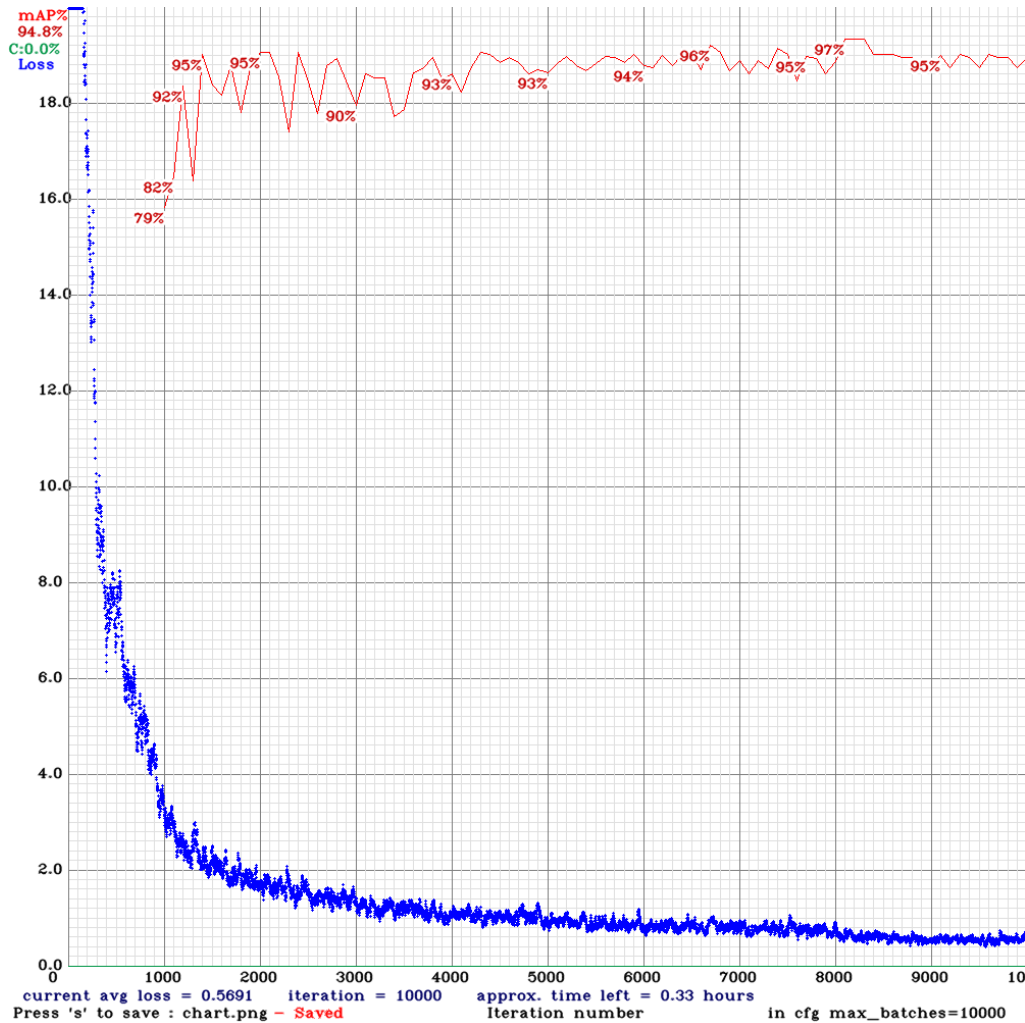
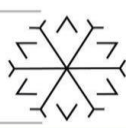


Figure 4: Evaluation of mAP and loss values (red curve: mAP value, blue curve: Loss function) by training iterations.

The mAP value is a metric that indicates the accuracy of the object detection prediction. The mAP value shows how much the bounding box of the predicted object overlaps with the actual bounding box of the object. The Loss function calculates how much the prediction made by the model differs from the ground truth. In other words, the Loss function is a function that calculates the error rate of the created model. In a successful model, the loss value is expected to be low.

4. Experimental results

Performance evaluation of the model created during the training phase is made on the test set consisting of 37 images (94 electronic circuit elements in total). The IoU (Intersection over Union) metric known as the Jaccard index is used as the threshold value to measure the accuracy of the model in the test set. The IoU value is calculated by dividing the intersection area of the bounding box of the object predicted by the model and the actual bounding



box of the object by the junction area of these two bounding boxes. In case of the IoU has a value of greater than 0.5 is meant to be a good estimate and conversion to classification is used generally accept. In contrast with, the IoU has lower value than 0.5 is meant to be bad estimation. If the IoU value of an electronic circuit element detected by the model is greater than 0.5 it is classified as true positive (TP), otherwise it is classified as false positive (FP). In case of there is an electronic circuit element in the test image, but the model cannot detect this circuit element, it is classified as false negative (FN). As a result of these classifications, the confusion matrix of the model is given in Figure 5.

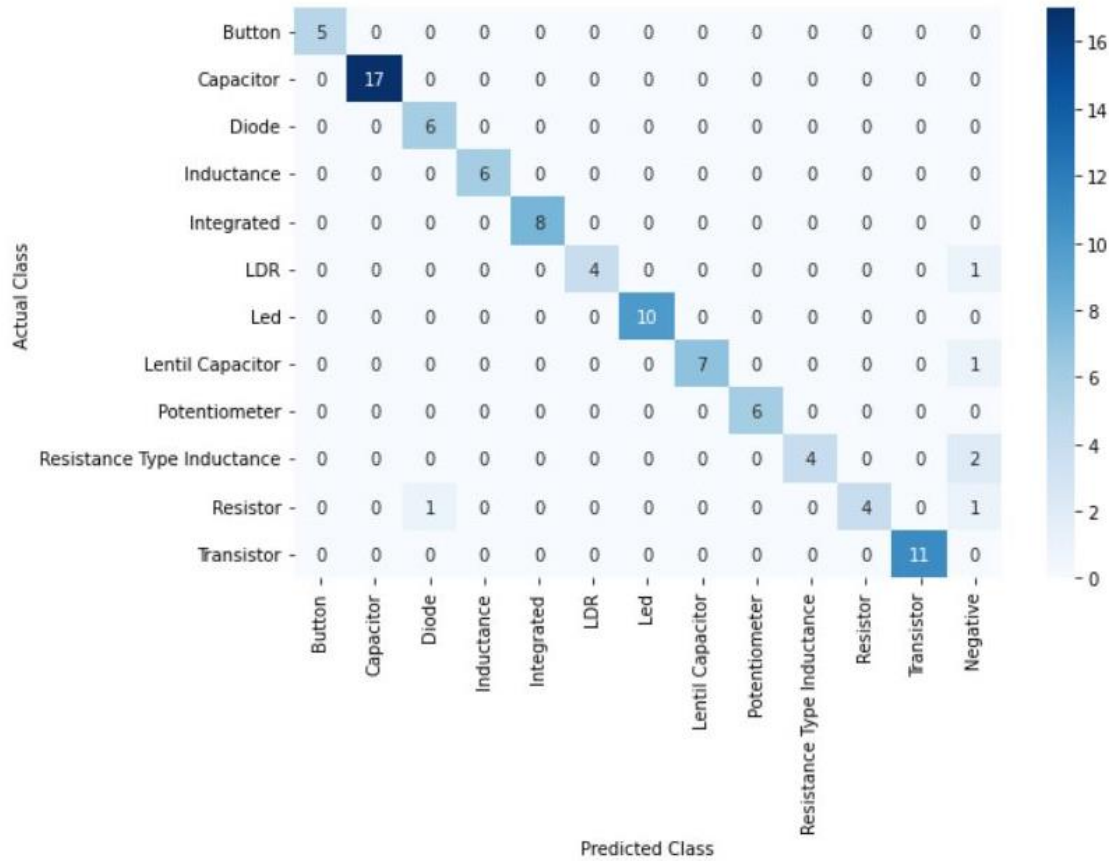


Figure 5: Confusion Matrix for the model

In experimental studies, there is actually an electronic circuit element in the test image, but it has been seen that the model can not classify this electronic circuit element (False Negative). In order to show these situations, a column named "Negative" has been added to the Confusion matrix as the last column. One of the most popular evaluation metrics in multiclass classification is accuracy. Accuracy can be calculated directly from the confusion matrix. Using the equation given below, the accuracy of the model is calculated as %94.

$$Accuracy = \frac{TP+TN}{TP+TN+FP+FN} \tag{1}$$

In Figure 6, image of the results produced by the model created for the six images in the test set are shared. On the other hand, in Figure 7, image of the results produced by the model in the images with multiple classes that are not in the dataset are shared.

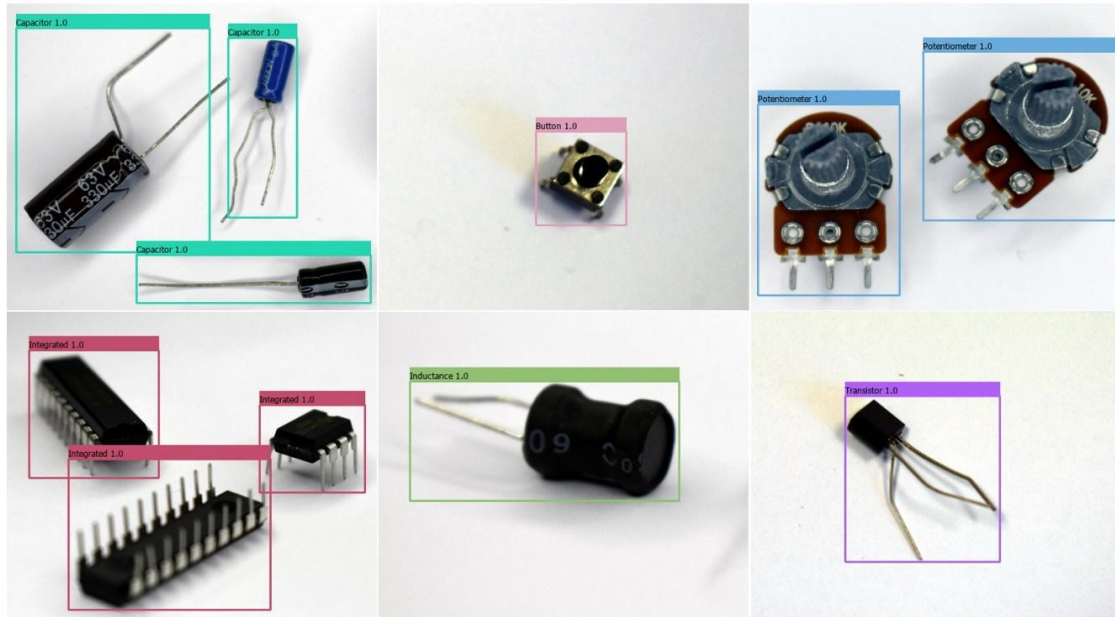


Figure 6: Experimental results of the model on test dataset

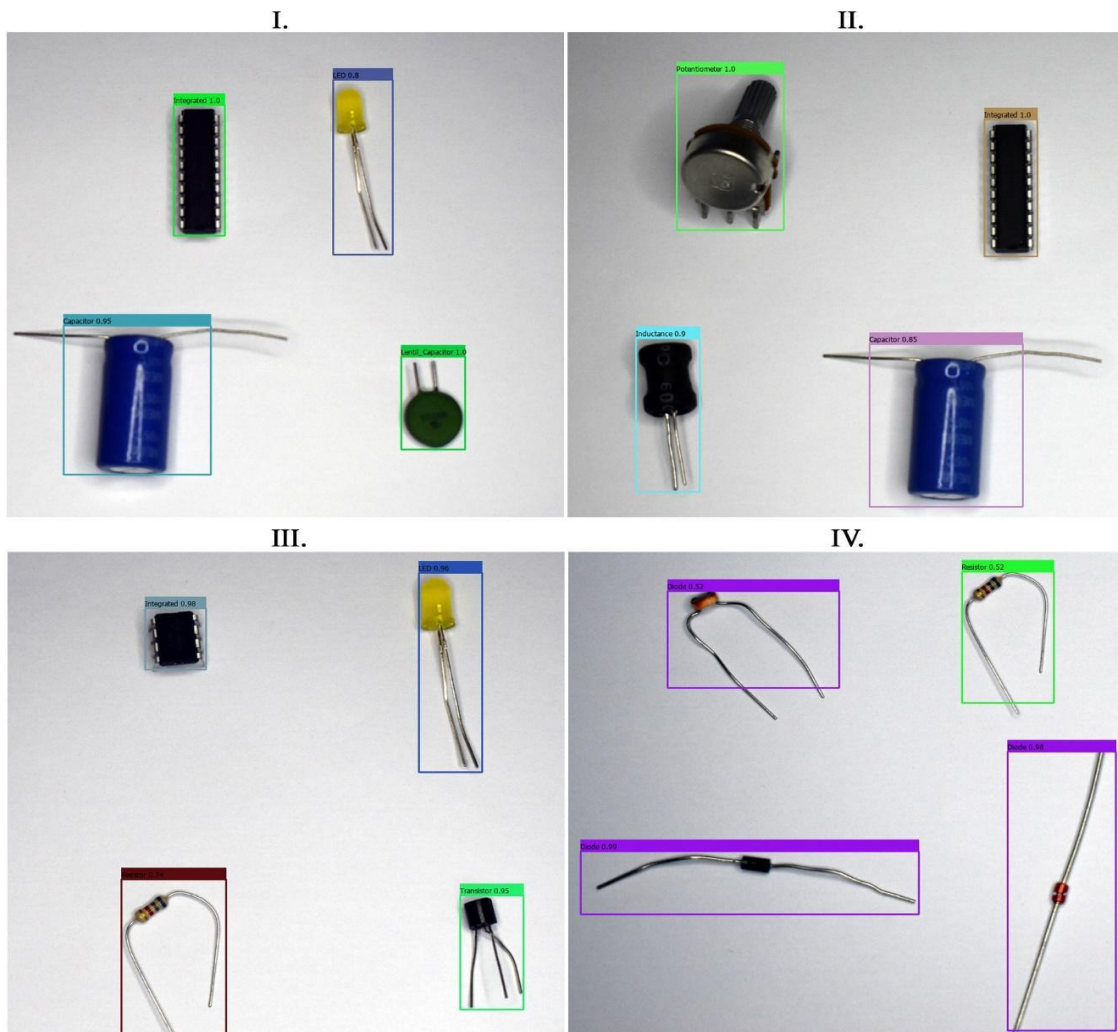


Figure 7: Experimental results of the model does not exist on test dataset



5. Conclusion

In this paper, a model based on YOLOv4 algorithm, one of the modern convolutional object detectors, is created to recognize electronic circuit elements quickly and accurately. First, a new dataset is created for electronic circuit elements. Then, labeling is performed on the dataset. After the labeling process, the dataset is divided into two parts as training and testing. The training process is carried out using the YOLOv4 algorithm on the training dataset. The confusion matrix is created by testing the model created as a result of the training process on the test dataset. Model accuracy is calculated as %94. The confusion matrix is examined, it is seen that the "Resistance Type Inductance" and "Resistor" classes reduce the success of the model. In future studies, the size of the dataset will be increased. The classification success of the model in the "Resistance Type Inductance" and "Resistor" classes will increase with the enlargement of the dataset is thought. After increasing the success of the model by enlarging the dataset, the performance of the model will be studied in real-time applications. In addition, on the recognition of the types and values of circuit elements for industrial applications will be studied.

References

- Bochkovskiy, A., Wang, C.Y. and Liao, H.Y.M., 2020. Yolov4: Optimal speed and accuracy of object detection. arXiv preprint arXiv:2004.10934.
- Girshick, R., 2015. Fast r-cnn. In Proceedings of the IEEE international conference on computer vision (pp. 1440-1448).
- Girshick, R., Donahue, J., Darrell, T. and Malik, J., 2014. Rich feature hierarchies for accurate object detection and semantic segmentation. In Proceedings of the IEEE conference on computer vision and pattern recognition (pp. 580-587).
- Guo, C., Lv, X.L., Zhang, Y. and Zhang, M.L., 2021. Improved YOLOv4-tiny network for real-time electronic component detection. Scientific reports, 11(1), pp.1-13.
- He, K., Gkioxari, G., Dollár, P. and Girshick, R., 2017. Mask r-cnn. In Proceedings of the IEEE international conference on computer vision (pp. 2961-2969).
- He, K., Zhang, X., Ren, S. and Sun, J., 2015. Spatial pyramid pooling in deep convolutional networks for visual recognition. IEEE transactions on pattern analysis and machine intelligence, 37(9), pp.1904-1916.
- Huang, R., Gu, J., Sun, X., Hou, Y. and Uddin, S., 2019. A rapid recognition method for electronic components based on the improved YOLO-V3 network. Electronics, 8(8), p.825.
- Hu, X., Xu, J. and Wu, J., 2020, April. A Novel Electronic Component Classification Algorithm Based on Hierarchical Convolution Neural Network. In IOP Conference Series: Earth and Environmental Science (Vol. 474, No. 5, p. 052081). IOP Publishing.
- Liu, S., Qi, L., Qin, H., Shi, J. and Jia, J., 2018. Path aggregation network for instance segmentation. In Proceedings of the IEEE conference on computer vision and pattern recognition (pp. 8759-8768).
- Liu, W., Anguelov, D., Erhan, D., Szegedy, C., Reed, S., Fu, C.Y. and Berg, A.C., 2016, October. Ssd: Single shot multibox detector. In European conference on computer vision (pp. 21-37). Springer, Cham.
- Ren, S., He, K., Girshick, R. and Sun, J., 2015. Faster r-cnn: Towards real-time object detection with region proposal networks. Advances in neural information processing systems, 28, pp.91-99.
- Redmon, J., Divvala, S., Girshick, R. and Farhadi, A., 2016. You only look once: Unified, real-time object detection. In Proceedings of the IEEE conference on computer vision and pattern recognition (pp. 779-788).
- Tan, M., Pang, R. and Le, Q.V., 2020. Efficientdet: Scalable and efficient object detection. In Proceedings of the IEEE/CVF conference on computer vision and pattern recognition (pp. 10781-10790).
- Wang, C.Y., Liao, H.Y.M., Wu, Y.H., Chen, P.Y., Hsieh, J.W. and Yeh, I.H., 2020. CSPNet: A new backbone that can enhance learning capability of CNN. In Proceedings of the IEEE/CVF conference on computer vision and pattern recognition workshops (pp. 390-391).
- Xu, Y., Yang, G., Luo, J. and He, J., 2020. n Electronic Component Recognition Algorithm Based on Deep Learning with a Faster SqueezeNet. Mathematical Problems in Engineering, 2020.
- Zhang, S., Wen, L., Bian, X., Lei, Z. and Li, S.Z., 2018. Single-shot refinement neural network for object detection. In Proceedings of the IEEE conference on computer vision and pattern recognition (pp. 4203-4212).

Detection of Distributed Denial of Service (DDoS) Attacks with Machine Learning Methods

Merve YILDIRIM¹[0000-0001-6834-3470], Muhammed YÜCEL² and Duygu ÇALIK³

¹merve.yildirim@erzurum.edu.tr , Erzurum Technical University

²muhammed.yuce113@erzurum.edu.tr, Erzurum Technical University

³duygu.calik31@erzurum.edu.tr, Erzurum Technical University

Abstract

While the use of the Internet provides convenience and advantages in all areas of our daily life, it also poses a risk in terms of being vulnerable to cyber threats. With the efficient operation of Internet-based systems, DDoS attacks targeting these systems and growing rapidly today became one of the cyber attack methods that threaten institutions and organizations significantly. Its main purpose is to prevent users from accessing systems by sending intense requests to the servers or resources of the website and exhausting network resources. Today, many defense systems have been developed against these attacks. Intrusion detection system, which is one of the most important processes in most defense systems, is the first processing step. Defense systems aim to take action quickly and inform the personnel in order to reduce the damages that may occur as a result of these attacks. In this study, it is aimed to detect DDoS attacks using machine learning algorithms and to classify these attacks according to their types. In the study, CICDDoS 2019 dataset, which is one of the most up-to-date datasets and pulled from normal network data traffic, was used to train the system. In the literature, there are many methods developed to detect DDoS attacks. In this study, it is aimed to detect abnormal behaviors and prevent possible dangers by suggesting an alternative method with the use of supervised machine learning algorithms. Different models will be developed by using KNN (K-Nearest Neighbor), SVM (Support Vector Machine), logistic regression, decision trees method to compare the datasets with the original size dataset. Based on the models obtained, it will make the assumption that how harmful the incoming data is or how harmless it is. In the study, it is aimed to determine the models with the highest performance for test data and to detect and classify DDoS attacks by using the specified algorithms and feature selection methods.

Key Words: DDoS Attacks, Cyber Threats, Machine Learning

Wi-Fi Fingerprint-based Indoor Localization in Different Environments

Zümrüt SATILMAZ¹, Yaren Deniz KAYA², Gökür BÜLBÜL³, İlknur NACAĞ⁴ and Işıl KARABEY AKSAĞALLI⁵ [0000-0002-4156-9098]

¹zumrut.satilmaz28@erzurum.edu.tr, Department of Computer Engineering, Erzurum Technical University

²yaren.kaya29@erzurum.edu.tr, Department of Computer Engineering, Erzurum Technical University

³goknur.bulbul64@erzurum.edu.tr, Department of Computer Engineering, Erzurum Technical University

⁴ilknur.nacak75@erzurum.edu.tr, Department of Computer Engineering, Erzurum Technical University

⁵isil.karabey@erzurum.edu.tr, Department of Computer Engineering, Erzurum Technical University

Abstract

Nowadays, GPS (global positioning system) systems are widely used for locating and tracking processes, and these systems can be used effectively in outdoor environments. On the other hand, GPS cannot be performed correctly in indoor environments due to the weakening of signal strength. Indoor localization systems include various applications used for locating and tracking indoor environments such as large buildings, homes, campuses, hospitals, schools, shopping malls, etc. Some technologies that are not used in the existing in-building infrastructure, such as Wi-Fi, Bluetooth, Femtocell, and cellular-based systems, are used as existing equipment for the system. Among these Technologies, Wi-Fi technology is widely used in indoor localization systems because it is faster and more effective in frequency spreading and data transfer than other technologies such as Bluetooth, infrared, and femtocell. To create a successful localization system, some metrics must be precisely defined in terms of cost, accuracy and precision, scalability, coverage, and limitations. This study presents a mobile indoor positioning application that does not require extra hardware for positioning. The application creates a dataset collecting the Wi-Fi signal strength from the access points in the environment. After the data collection process in a home environment, the accuracy of the methods is compared with each other by applying various machine learning methods such as kNN (k-Nearest Neighbor), SVM (Support Vector Machine), Random Forest, Naive Bayes. In addition, the datasets created from the university environment and the home environment are compared with each other. Thus, we evaluate whether the accuracy of the Wi-Fi fingerprint-based system is environment-independent or not.

Keywords. Fingerprint-based technology, indoor localization using Wi-Fi, machine learning in indoor localization

Using Deep Learning Models with Pre Process for Classification Hyperspectral Data

Ömer Faruk Yıldırım ^{1*}[0000-0002-4789-9522]

omerfaruk.yildirim@erzurum.edu.tr, Department of Computer Engineering, Erzurum Technical
University

Abstract

Hyperspectral imaging is concerned with measuring and analyzing a specific area, at close or far distance, basically all spectra using aircraft or satellite sensors and obtained with these sensors. Hyperspectral image (HSI) classification labels pixels to accurately distinguish different objects using this rich spectral information. The main problem in classification problems in which these data are used, for example, in rural area mapping, is that different tree species cross each other in images taken from far away, neighboring pixels may belong to different classes, and it is difficult to make this distinction. Another difficulty is the small number of labeled data. Although traditional machine learning techniques and artificial neural network models showed specific performances, at one point, they could not provide sufficient accuracy due to unbalanced data. The shortcoming of this data set problem has been trying to be researched and developed for a long time based on machine learning. In recent years, the point reached in deep learning techniques has produced alternative and efficient solutions for many problems. Data classification in remote sensing has made tremendous progress in recent years, with recent studies using deep learning for image processing and pattern recognition. Especially for standard images (RGB), deep convolutional neural networks (CNN) for tasks such as classification, object detection, or semantic segmentation are used in almost every field. This imbalance mentioned in the data sets poses severe classification problems in deep learning approaches. HSI uses Convolutional Neural Networks (CNN) with different convolutional, pooling, and fully connected layers to classify its data. To test the performance of CNN models, experiments are usually performed with two key HSI datasets, such as Indian Pines, University of Pavia. In classification problems, successful results were obtained since these data sets were correctly labeled based on location by descending into the field. However, for data sets that do not have sufficient label data, algorithmic approaches will be studied to verify the neighboring pixel information, generate data synthetically, and make this irregular data more regular. The creation of these data will increase the accuracy of deep learning models and reduce the long training times of hyperspectral data.

Keywords. Hyperspectral Image, CNN, Deep Learning, Pre-Process

A New Mathematical Model for Private Car Sharing

Zeliha Ergul Aydin ^{1*}[0000-0002-7108-8930] and Banu Icmen Erdem ²[0000-0002-2734-3471], Zeynep Idil Erzurum Cicek ³[0000-0001-9641-8935]

¹zergul@eskisehir.edu.tr, Eskisehir Technical University

²bicmen@eskisehir.edu.tr, Eskisehir Technical University

³zierzurum@eskisehir.edu.tr, Eskisehir Technical University

Abstract

In Turkey, some of the teachers live in the city center, and they travel to the village school which they work almost every working day. To get to school, some of them drive their own cars, while others take public transportation. The waiting time for teachers using public transport is quite long due to the mismatched public transport timetable and teachers course schedules. Public transportation services are very infrequent in villages far from the center. For this reason, some teachers have to reach the village one day before their courses and pay for accommodation. Besides, teachers who use their private cars struggle to afford transportation costs. Another aspect of using private cars is the environmental pollution problem. The fact that private car ownership is the only passenger in the car increases the carbon dioxide emissions in the world. The unoccupied seats of private cars are an opportunity to address the reduction of carbon dioxide emission. The sharing economy concept based on sharing of resources is applied to this problem as car-sharing in this study. This car-sharing case can be handled as an optimization problem. This study presents a new mixed-integer car-sharing mathematical model that aims to reduce teachers' total transportation distance. The novelty of this model comes from using the vehicle routing model considering sharing economy concept. We aim to save teachers money on transportation and accommodation and reduce carbon dioxide emissions with this model. The output of this model is minimum distance routes that ensure every teacher reaches village school according to course schedules and which teachers' cars to use.

Keywords. car-sharing, transportation, vehicle routing

A Two-Step Method Based on Local Search for Two-Dimensional Two-stage Cutting Stock Problem

Banu İçmen Erdem ^{1*}[0000-0002-2734-3471] and Refail Kasimbeyli ²[0000-0002-7339-9409]

¹bicmen@eskisehir.edu.tr, Eskisehir Technical University

²rkasimbeyli@eskisehir.edu.tr, Eskisehir Technical University

Abstract

This work uses a metaheuristic solution approach to investigate a two-dimensional two-phased guillotine cutting stock problem, which includes determining how we cut stock panels in an optimally. This method is a two-stage technique to solving the problem. The items assigned to each stock material are decided at random in the first stage. In the second stage, these items are cut from corresponding stock under the guillotine constraint assumption by considering length and width constraints. The goal of this solution approach is to use local search metaheuristic at two separate places to discover feasible solutions to the problem in a short amount of time. We proposed a new placement heuristic in the metaheuristic and compared the solution performances with different iteration numbers.

Keywords. Cutting stock problem, Local search, Metaheuristic, Guillotine cutting

1. Introduction

Cutting smaller items from more oversized stock materials by limiting the number of used stocks or the trim loss is described as a cutting stock problem, according to the predetermined demand list. The dimensionality of such problems is one of the essential features used to classify them. The dimensionality is the minimal number of real-number dimensions required to describe the patterns' geometry (Dyckhoff, 1990). The one-dimensional cutting stock problem is a trim loss minimization problem in which a certain number of rolls of varying widths and diameters are to be cut from stock rolls of a standard width (Delorme, Lori and Martello, 2016; Dyckhoff, 1981; Furini, Malaguti and Yagiura, 2013; Gilmore and Gomory, 1961; Kasimbeyli, Sarac and Kasimbeyli, 2011; Martello and Toth, 1990).

In cases when a sheet of paper, metal, glass, or wood must be separated into smaller rectangular items, two-dimensional problems arise (Cofmann et al., 2013; Furini and Malaguti, 2013; Gilmore and Gomory, 1965; Lodi, Martello and Vigo, 2002; Lodi, Martello and Monaci, 2002; Lodi, Martello and Vigo, 2004; Lodi et al., 2014; Martello and Monaci, 2015). The one-and-a-half-dimensional (1.5-dimensional) cutting stock problem is a variant of the two-dimensional problem in which the length of a sheet is large enough (practically limitless) (Gasimov, 2007). The three-dimensional cutting stock problem is also known as the container loading problem. It involves determining the best number of containers to pack a set of rectangular cartons of various sizes (Chen, 1995).

We investigated two-dimensional cutting stock problems (2DCSP) with the following assumptions:

- Items should not overlap since this creates an infeasible cutting pattern. Every item should cover its area.
- Items should be cut in an orthogonal pattern; this means all the cutting processes are parallel to the edges. Since every item is rectangular, this assumption provides a feasible solution.
- The cutting processes' width will be ignored since it is too narrow to affect the solution.

Many alternative strategies are used to classify two-dimensional cutting stock problems. The most fundamental classification is based on the cutting technology utilized. The cutting technology employed in manufacturing items from stock materials is divided into two categories.

- Guillotine cutting begins at one edge of the stock material and proceeds parallel to the other two edges perpendicular to this edge. The cutting continues indefinitely until the stock material's endpoint is reached (see Figure 1(a)).
- Cutting technology that allows ninety-degree rotation at any point of the stock material is known as non-guillotine cutting (see Figure 1(b)).

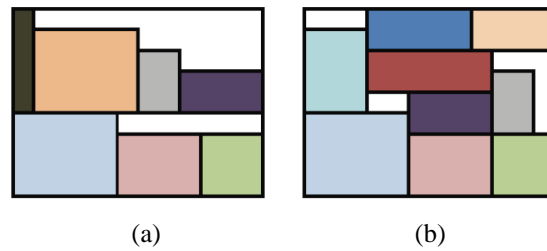


Figure 1: Guillotine (a) and Non-Guillotine Cutting (b).

Additional differentiation develops for procedures that only use guillotine cutting technology, a cutting stage number. If an item is cut from stock in most two-stages, then no more than two cuts should be conducted to obtain an item (see Figure 2(a)). Trim loss can only be removed with a third-stage cut. If a third cut is made to acquire an item that is not a trim loss, this is referred to as a three-stage cut (see Figure 2(b)).

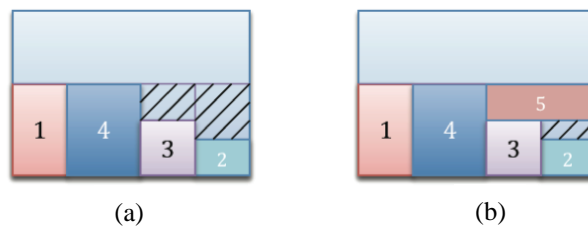


Figure 2: Two-stage (a) and Three-stage Cutting (b).

Two-dimensional cutting stock problems were investigated in this paper using the guillotine cut constraint and the two-stage cutting procedure.

The remainder of the paper is structured as follows: Section 2 describes the two-step method based on local search developed for the two-dimensional two-stage guillotine cutting stock problem. We describe the placement heuristic proposed in this method in Section 2.1, along with examples. Section 2.2 utilizes the developed method to solve test problems from the literature and the results are given. Section 3 concludes the paper with a brief conclusion.

2. Two-Step Method Based on Local Search

For the solution of the two-dimensional two-stage guillotine cutting stock problem (2D2GCSP), we develop a two-step solution strategy. Local search is employed in this method to create neighbor solutions and scan the search space. The suggested algorithm is divided into two steps. The first step is establishing item lists called sub-lists assigned to stock materials. The sub-lists generated in the first phase are achieved by considering the items' area limits and employing the fewest number of stock materials. The items are then assigned to the appropriate stock materials in the second step, considering the guillotine and size limits.

A Local search is a heuristic approach used to solve computationally challenging optimization issues. Local search can solve problems described as maximizing or minimizing of an objective function among a set of feasible solutions. Local search algorithms make local adjustments to go from solution to solution in the search space until a feasible or optimal solution is found or a time limit is met.

The representation of possible solutions is the first step in the algorithm. We represent the possible solutions with the numerical sequence of the items in this study.

Table 1: Data of the Example.



ITEM NO	LENGTH	WIDTH	DEMAND
1	21	13	3
2	36	17	1
3	54	20	2
4	20	21	2
STOCK MATERIAL	60	30	

Table 1 shows the item and stock material dimensions for an example problem. According to these data, four-item types with a total demand of eight items will be cut from the stock material, whose dimensions are specified so that the quantity of stock materials used is minimized. As a result, the possible solution developed for the example problem is as follows;

$$1 - 1 - 1 - 2 - 3 - 3 - 4 - 4$$

The provided sequence corresponds to the order in which the items are placed in the cutting process. We calculate the sum of the item's areas in this sequence and generate the sub-list by pausing at the point where it passes the main stock area. For the sake of illustration, Table 2 depicts this process.

Table 2: Sub-list Generation.

ITEMS	1	1	1	2	3	3	4	4
AREA	273	273	273	612	1080	1080	420	420
TOTAL AREA	273	546	819	1431	1080	1080	420	840
STOCK MATERIAL	1	1	1	1	2	3	4	4

Table 3 shows the sub-lists created using the sub-list generation technique illustrated in Table 2.

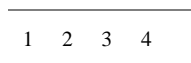
Table 3: Sub-lists for the example problem.

Sub-list 1	1	1	1	2
Sub-list 2	3			
Sub-list 3	3			
Sub-list 4	4	4		

The 2-opt exchange operator creates neighbor solutions that the local search heuristic will analyze. The 2-opt algorithm swaps two parts provided in the item sequence. A new candidate solution is obtained due to the relocation of the determining elements. The two-step method generates neighborhood solutions by applying 2-opt to lists generated at two different points. In the first phase, we use all ordered 2-opt modifications from the array of undivided items to construct the sub-lists used in the second step.

As shown in Figure 3, the total number of 2-opt changes in a 4-item array is 6. Equation (1) calculates the number of neighboring candidate solutions acquired due to all 2-opt changes, for example, with n pieces in the array of undivided items.

$$candidate\ solution\ number = \frac{(n-1)n}{2} \tag{1}$$





2	1	3	4
3	2	1	4
1	3	2	4
1	4	3	2
1	2	4	3

Figure 3: All 2-opt Changes of a 4-item List.

In the second step, we apply a 2-opt exchange to all sub-lists for a predetermined number of iterations. The selection of the items to be changed is made randomly. In this way, more solution candidates are examined by applying a 2-opt exchange at two points.

After obtaining the sub-lists that generate the candidate solutions, we calculate the objective function value of each candidate solution by applying the placement heuristic to these sub-lists following the constraints. The algorithm of the developed two-step method based on local search is given in Figure (4).

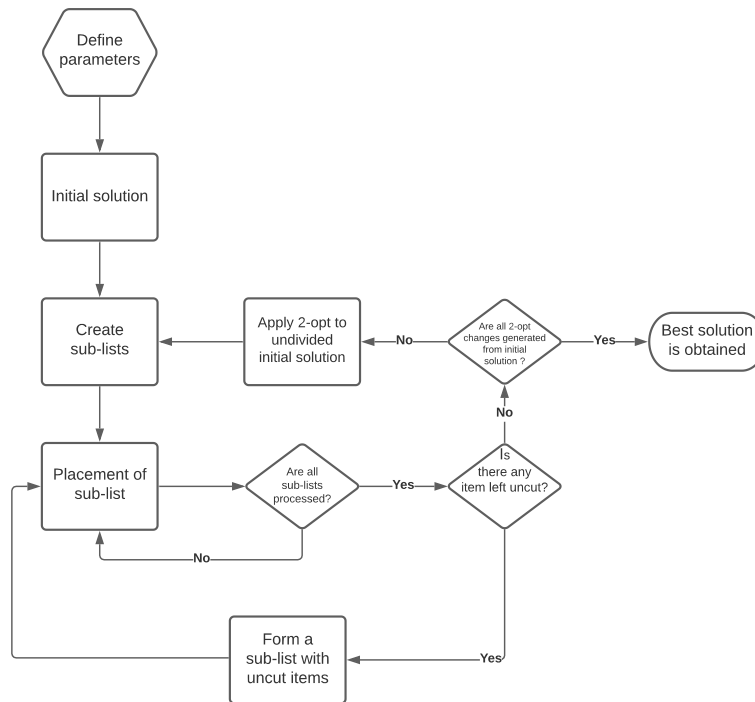


Figure 4: Algorithm of the Two-Step Method Based on Local Search.

2.1. Sequential Placement Heuristic

We establish a sequential placement heuristic for the two-step method based on the local search technique to position the formed sub-lists to the stock materials in line with guillotine and size limitations. This heuristic is based on the logic that the first item cut adjacent to the edge of the stock material in the y plane forms a level in two-dimensional stock cutting problems with guillotine cutting. The width of an item that can be cut must be equal to or less than the width of the leading item. It begins with the first unassigned item in the candidate solution array, which sets the breadth of the level it is located. The level is then filled by traveling through the array and determining the items whose width is less than the level's breadth and which can fit in length. When the length of the level becomes insufficient, either a new level is passed, or a new stock material is unlocked for use. The created placement heuristic's algorithm and definition of parameters are as follows;



- i, j : items
- q : Stocks
- W : Width of stock
- L : Length of stock
- w : Width of item
- l : Length of item
- L_s : Length of level

Algorithm of the Sequential Placement Heuristic

Step 1: Define parameters, $W = W_q$

Step 2: Generate candidate

Loop: Choose first unassigned item(i)

 If: $W \geq w_i$

 Item i is level starter and assigned

$L_s = L - l_i$

 Loop: Choose first unassigned item (j)

 If: $l_j \leq L_s$:

 Item j is assigned, $L_s = L_s - l_j, j = j + 1$

 Else:

$j = j + 1$

 Stop: All unassigned items j is processed

$W = W - w_i$

$i = i + 1$

 Else: $i = i + 1, q = q + 1, W = W_q$

Stop: All unassigned items i is processed

Output: Feasible cutting placement

2.2. Computational Results

We used a set of 30 instances of two-dimensional knapsack problems from (Hifi and Roucairol, 2001) to demonstrate the efficiency and performance of the suggested solution method. The two-step method based on local search is used to solve test problems. The studies are carried out on a PC equipped with an Apple MacBook Pro with a 2.8 GHz IntelCore i7 processor and 4 GB RAM. Table 4 contains information regarding exam issues. The data is presented using the notations shown below.

- Instance - denotes the name of test problems;
- n - is the number of item types;
- \tilde{n} - is the total number of items;
- L - is the length of the stock panel;
- W - is the width of the stock panel.

Table 5 shows the outcomes achieved. We give the optimal solutions derived for the test problems presented in the literature in the OPT column. The results corresponding to the number of iterations utilized for the sublists and the time required to obtain them are reported in the other columns. The number of 2-opt changes applied to the undivided stock material increases proportion to the number of items in the problem. As a result, alterations in durations were detected. As can be observed, despite the increase in iteration numbers, the solution timings remained below 1 second, demonstrating the method's success in providing feasible solutions in a relatively short time.

Table 4: Test Problems.

INSTANCE	n	\tilde{n}	W	L
HH	5	18	98	127



CW1	25	67	105	125
CW2	35	63	165	145
CW3	40	96	207	267
HCHL2	35	75	130	130
HCHL9	35	76	76	65
2S	10	23	70	40
3S	20	62	70	40
A1S	20	62	60	50
A2S	20	53	60	60
STS2S	30	78	85	55
STS4S	20	50	99	99
OF1	10	23	40	70
OF2	10	24	40	70
W	10	24	40	70
CHL1S	30	63	100	132
CHL2S	10	19	55	62
A3	20	46	80	70
A4	20	35	70	90
A5	20	45	100	132
CHL5	10	18	20	20
CHL6	30	65	130	130
CHL7	35	75	130	130
CU1	25	82	125	100
CU2	35	90	175	150
HCHL3S	10	51	98	127
HCHL4S	10	32	98	127
HCHL6S	22	60	244	253
HCHL7S	40	90	241	263
HCHL8S	10	18	20	49

Furthermore, when we increase the number of iterations to 500, the optimal solution is identified in 14 of the 30 test problems. We only use one more stock material in half of the remaining problems. We obtain the optimal solution for the case with 1000 iterations in 13 out of 30 problems. Therefore, we can conclude that increasing the number of iterations will not lead to more optimal solutions. Since we apply a random 2-opt operator to sublists, the increase of iterations is not reflected in obtaining the solutions. In order to overcome this problem, we will explore the application of different exchange operators to sublists.

3. Conclusion

This study investigated the two-dimensional cutting stock problem with guillotine and two-stage cutting limitations, and a unique two-stage heuristic technique based on local search was developed. In order to assign items to their slots for each stock material, a sequential placement algorithm that considers guillotine and two-stage cutting constraints is applied. The sequential placement heuristic is utilized in local search to generate feasible cutting patterns. Because the suggested technique employs local search in two places of the algorithm, it is referred to as a two-stepped method. We utilize different iteration numbers in local search and compare iterations' effects.

The heuristic method created for problem-solving ensures that feasible solutions are obtained in less than one second. As a result, it may be helpful to utilize in industrial systems where quick results are required. The technique also showed effectiveness and openness to refinement by yielding the best solution in 14 of 30 situations.

Table 5: Computational results.

OPT	ITERATION:100		ITERATION:500		ITERATION:1000	
	Number	Duration	Number	Duration	Number	Duration



HH	2	2	0,02	2	0,06	2	0,12
CW1	10	12	0,05	11	0,25	11	0,5
CW2	12	14	0,05	14	0,25	14	0,49
CW3	16	18	0,08	18	0,42	18	0,82
HCHL2	6	7	0,07	7	0,27	7	0,57
HCHL9	10	12	0,06	12	0,28	12	0,6
2S	2	2	0,01	2	0,08	2	0,15
3S	23	26	0,08	26	0,38	26	0,72
A1S	23	25	0,08	23	0,31	23	0,6
A2S	12	14	0,05	13	0,22	14	0,41
STS2S	12	14	0,06	14	0,33	14	0,64
STS4S	5	6	0,03	6	0,16	6	0,35
OF1	4	4	0,01	4	0,07	4	0,14
OF2	5	5	0,01	5	0,09	5	0,2
W	24	27	0,08	27	0,34	27	0,66
CHL1S	6	7	0,04	7	0,24	7	0,41
CHL2S	3	3	0,01	3	0,06	3	0,14
A3	8	9	0,04	8	0,17	8	0,32
A4	5	5	0,02	5	0,12	6	0,21
A5	5	5	0,03	5	0,15	5	0,3
CHL5	4	4	0,01	4	0,07	4	0,13
CHL6	6	7	0,06	6	0,22	6	0,43
CHL7	6	7	0,06	6	0,27	7	0,53
CU2	15	18	0,08	17	0,35	17	0,7
CU1	12	14	0,07	14	0,32	13	0,6
HCHL3S	3	4	0,03	4	0,16	4	0,31
HCHL4S	2	3	0,01	3	0,09	3	0,19
HCHL6S	5	6	0,04	5	0,2	5	0,39
HCHL7S	7	8	0,06	8	0,31	8	0,58
HCHL8S	2	2	0,01	2	0,05	2	0,1

Combining the two-stage technique with a genetic algorithm will be studied in future studies. In addition, the effect of various placement heuristics on issue solving will be examined. Finally, the method's adaption in the non-guillotine kind of the two-dimensional cutting stock problem will be investigated.

Acknowledgments

This study was supported by Eskisehir Technical University Scientific Research Projects Commission under grant no: 20DRP013.

References

- Chen, C., Lee, S. and Shen, Q., 1995. An analytical model for the container loading problem. *European Journal of Operational Research*, 80(1), pp.68-76.
- Coffman, E. G., Csirik, J., Galambos, G., Martello, S. and Vigo, D., 2013. *Handbook of combinatorial optimization*. Springer, New York, pp.455-531.
- Delorme, M., Lori, M. and Martello, S., 2016. Bin packing and cutting stock problems: Mathematical models and exact algorithms. *European Journal of Operational Research*, 255(1), pp.1-20.



Dyckhoff, H., 1981. A New Linear Programming Approach to the Cutting Stock Problem. *Operations Research*, 29(6), pp.1092-1104.

Dyckhoff, H., 1990. A typology of cutting and packing problems. *European Journal of Operational Research*, 44(2), pp.145-159.

Furini, F. and Malaguti, E., 2013. Models for the two-dimensional two-stage cutting stock problem with multiple stock size. *Computers & Operations Research*, 40(8), pp.1953-1962.

Furini, F., Lori, M., Martello, S. and Yagiura, M., 2015. Heuristic and Exact Algorithms for the Interval Min–Max Regret Knapsack Problem. *INFORMS Journal on Computing*, 27(2), pp.392-405.

Gasimov, R., Sipahioglu, A. and Saraç, T., 2007. A multi-objective programming approach to 1.5-dimensional assortment problem. *European Journal of Operational Research*, 179(1), pp.64-79.

Gilmore, P. and Gomory, R., 1961. A Linear Programming Approach to the Cutting-Stock Problem. *Operations Research*, 9(6), pp.849-859.

Gilmore, P. and Gomory, R., 1965. Multistage Cutting Stock Problems of Two and More Dimensions. *Operations Research*, 13(1), pp.94-120.

Hifi, M. and Roucairol, C., 2001. Approximate and exact algorithms for constrained (un) weighted two-dimensional two-staged cutting stock problems. *Journal of Combinatorial Optimization*, 5(1), pp.465-494.

Kasimbeyli, N., Sarac, T. and Kasimbeyli, R., 2011. A two-objective mathematical model without cutting patterns for one-dimensional assortment problems. *Journal of Computational and Applied Mathematics*, 235(16), pp.4663-4674.

Lodi, A., Martello, S. and Vigo, D., 2002. Recent advances on two-dimensional bin packing problems. *Discrete Applied Mathematics*, 123(1-3), pp.379-396.

Lodi, A., Martello, S. and Monaci, M., 2002. Two-dimensional packing problems: A survey. *European Journal of Operational Research*, 141(2), pp.241-252.

Lodi, A., Martello, S. and Vigo, D., 2004. Models and Bounds for Two-Dimensional Level Packing Problems. *Journal of Combinatorial Optimization*, 8(3), pp.363-379.

Lodi, A., Martello, S. and Vigo, D., 2004. Models and Bounds for Two-Dimensional Level Packing Problems. *Journal of Combinatorial Optimization*, 8(3), pp.363-379.

Martello, S. and Toth, P., 1990. Lower bounds and reduction procedures for the bin packing problem. *Discrete Applied Mathematics*, 28(1), pp.59-70.

Martello, S. and Monaci, M., 2015. Models and algorithms for packing rectangles into the smallest square. *Computers & Operations Research*, 63, pp.161-171.

A Discrete Differential Evolution Algorithm for Unidirectional Loop Layout Problem

Feristah Ozcelik ^{*[0000-0003-0329-203X]}

fdurmaz@ogu.edu.tr, Eskisehir Osmangazi University, Department of Industrial Engineering,
Eskisehir, Turkey

Abstract

The layout of the machines has a significant impact on the materials handling cost and time, on throughput, and on productivity of the facility. Amongst the different layout types, unidirectional loop layouts in which a material handling device moves in a closed-loop rail to transport parts among the machines are preferred to other configurations due to their relatively low initial investment costs and high degree of material handling flexibility. With these layouts, future introduction of new part types and process changes are easily accommodated. In unidirectional loop layout problem, objective is to assign each machine to one of the candidate locations such that the material handling cost is minimized. In this study, a discrete differential evolution algorithm is developed to solve the unidirectional loop layout problem which is very common in flexible manufacturing systems. Differential evolution (DE) is a floating point encoded evolutionary optimization algorithm for continuous optimization problems. The most distinct feature of DE is that it mutates vectors by adding weighted, random vector differentials to them. Like other evolutionary algorithms, it starts with a randomly generated initial population. In each generation, the operators of mutation, crossover and selection are applied on the entire population in order to produce new, 'better' populations with higher 'quality' individuals. The evolutionary process is repeated until a predefined termination criterion is reached. The basic DE algorithm cannot be used to directly generate discrete machine permutations since it is originally designed to solve continuous optimization problems where the individuals are represented by floating-point numbers. Therefore, in this paper, we used a discrete differential evolution algorithm for solving unidirectional loop layout problem. The proposed algorithm is tested on 150 test instances from the literature. Experimental results showed promising results.

Keywords. Facilities planning, flexible manufacturing systems, loop layout problem, metaheuristic algorithm

Improving Warehouse Operations by Radio Frequency Identification (RFID) Technology

Ozan ATEŞ ¹[0000-0003-4178-2603]

¹ozan.ates@outlook.com.tr, İstanbul Gedik Üniversitesi

Abstract

Stock and warehouse operations are of critical importance in that they are operations in all rings of the supply chain, and any disruption that may occur in these operations may adversely affect the supply chain in general, and any improvement that can be made in these operations will positively affect the supply chain in general. The increase in quality and quantity of stored products has made stock and warehouse management difficult. However, trying to continue the process with Bar Code and QR Code Technology has slowed down the processes, and the desired speed, flexibility and accuracy targets have not been achieved.

On the other hand, rapid development in technology forces businesses to be fast. For this reason, RFID (Radio Frequency Identification) Technology, which is a fast, flexible, accurate and human error-free technology, has entered the agenda of businesses. RFID Technology promises a fast and human-independent operation environment as much as possible. For this reason, businesses are aware of the necessity of effective warehouse operation and are investigating how RFID Technology can be used in these operations.

In the existing warehouse operation structures, Bar Code Technology is used only to determine the location of the products that have been ordered. The handling of the products in question by which transport device and in which order depends entirely on the knowledge and experience of the warehouse personnel. However, with RFID Technology, it is possible to carry out more complex operations such as determining the positions of the transport devices that will handle those products and in which order which products will be handled by which transport devices. In our study, this situation that RFID Technology promises is examined and presented concretely in the application example at the end of our study.

The most important point that distinguishes our study from similar studies is that the distances of the products that are stocked or the transport tools that carry out the handling operations are determined by the Clark & Wright savings algorithm instead of intuitive Euclidean calculations. Although heuristic Euclidean calculation methods are preferable because they are easy to apply, the biggest disadvantage is that they do not take into account the travel distances caused by obstacles such as shelves between products. For this reason, in our study, the Clark & Wright savings algorithm, which takes into account all circulating distances, was used in order to make a healthier distance measurement.

Keywords. Radio frequency identification, warehouse operations, Clark & Wright savings algorithm

1. Introduction

With the concept of Industry 4.0, the issue of digitalization, which finds more place in the business world, has included artificial intelligence and automation in the agenda of businesses. More and more businesses are using automation systems in warehouse operations. Businesses that produce their own products can implement automation in warehouse systems by providing a certain standardization in product and parcel sizes, therefore, they can build efficient, human error-free, fast and flexible structures by continuing to use Bar Code Technology.

However, since there are different types of products in 3PL (Third Party Logistics Providers) companies that serve many businesses, it is not possible to talk about the same product and parcel size standardization. However, digitalization forces 3PL businesses to establish automation structures as well as other businesses.



RFID Technology provides convenience to businesses that have difficulty in establishing automation structures because there is no specific product and parcel size standardization. Unlike Bar Code or QR Code Technology, RFID Technology is a series of complex and more warehouses such as determining the location of the products in the warehouse, as well as the location of the appropriate quality and quantity of transportation tools to handle these products in the warehouse, the diagnosis of the most suitable transport tool for the handling process, and the determination of the collection order. It has made the systems more suitable for automation by carrying out the operations based on the knowledge and experience of its personnel in an integrated and automatic manner.

The concept of automation, which entered our lives with Industry 4.0, has also found a place in warehouse management. While the standardizable products of the companies are stocked in their own warehouses, products of various standards from various customers can be stocked in the warehouses of the logistics service providers. While the companies can make the necessary preparations for warehouse automation easier by standardizing their products, it is more difficult for logistics service providers to provide such standardization. Our study presents an opinion on how the existing system can be made more automatic in an environment where product standards are very different and therefore automatic transport systems cannot be installed.

Our study differs from similar studies in terms of automating warehouse operations of logistics service providers. Unlike the warehouses of companies where standardized products are stocked, our study focuses on how to automate the operation of a warehouse with products of different standards. The use of the Clark & Wright savings algorithm is another unique aspect of our study. Contrary to the intuitive Euclidean distance calculations, which are more preferred in distance calculations in the warehouse environment, the Clark & Wright savings algorithm is used in our study and it is aimed to make the distance calculations more accurate.

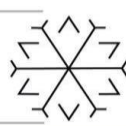
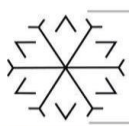
Bar Code Technology, one of the information technologies currently used in warehouse operations, has been preferred because it provides traceability and accuracy to warehouse operations and has reached an important position today. In recent years, QR Code Technology has been used frequently in industry circles and has found a wide area of use in the public sector due to its reliability. The fact that QR code technology can be read very quickly, can also read data with alphanumeric and binary characters apart from numerical data, has a low margin of error in reading and is more tolerant to negative situations such as erasure, contamination, tearing and wear has made this technology more advantageous than bar code technology. However, since these technologies cannot provide the speed, flexibility, accuracy and integration promised by RFID Technology, it is predicted that their usage areas will decrease with digitalization.

2. Stock and Warehouse Management

Stock; it briefly refers to stocked materials and stored capacity (Aydın, 2009). Stock; Material values such as goods, raw materials, semi-finished products, operating materials, auxiliary materials, finished goods, which are not out of the ownership and disposal of the enterprise on the valuation day, which are held by the enterprise to sell, produce or be used for business needs (Tüccarın El Kitabı Serisi VIII – Stok Yönetimi, 2007).

Warehouse; They are the intermediate points that play a strategic role in the realization of a whole series of activities from the raw material environment of the products to the production stage and from there to the consumption distribution centers. Warehouse management, on the other hand, covers the operations of unloading the goods correctly, sorting them, placing them on the shelves in a certain order, protecting them, then removing them from the shelves with the order, loading them and making them ready for shipment. Qualified human resources, warehouse information system (software, RFID, barcode, reader, etc.), warehouse floor, shelf systems, forklifts and pallets are the basic elements of warehouse management (Erdal, 2009).

When the raw materials and semi-finished products are ordered on time for the products that should be produced in accordance with the customer's needs in the sales department, these orders will be produced on time, sent to the company, stocked and used correctly, quickly and as needed, and ultimately, the products suitable for customer needs will be presented to the market as quickly as possible. The problem at any stage will affect the



whole operation as a chain, and as a result, it may be possible to introduce the product to the market late. The products presented to the market on time should be transferred to the warehouses on time, and the products stored according to the orders should be shipped on time. As can be seen, in all processes in the supply chain; From the procurement of the raw material to the delivery of the product to the end customer, stock and storage operations were mentioned everywhere. Therefore, an improvement in these operations will automatically improve the performance of the supply chain. Semi-finished products and raw materials will be supplied in the desired quantity and quality shortly after they are ordered, and accordingly, the production of the final product will be accelerated and can be transferred to the warehouses quickly.

Proper storage and fast delivery of orders will enable businesses to deliver their products earlier than usual, to offer their products to the market without missing various opportunities, and to deliver to their customers earlier, which will return the company as competitive advantage and customer satisfaction. Since the Supply Chain relates to all processes of a final product, a problem in a link affects the entire chain (Ko et al, 2011). Apart from this, thanks to the trust and cooperation to be established between the companies, a result that adds dynamism to the supply chain and provides an advantage against the competitors will be achieved by sharing the risks, increasing flexibility, and as a result, new products will be introduced to the market faster (Özdemir, 2004).

3. RFID (Radio Frequency Identification) Technology

RFID is the name given to technologies that use radio waves to automatically identify different materials. RFID allows tracking, analyzing and managing the movements of an object carrying a tag equipped with a microprocessor containing the data of the object and an antenna integrated into this microprocessor, with the information it carries on this tag; It is an automatic object identification and tracking technology that provides data exchange with radio frequencies (Yüksel and Zaim, 2009). Look at Figure 1 for a simple RFID System (Laudon and Price, 1998).

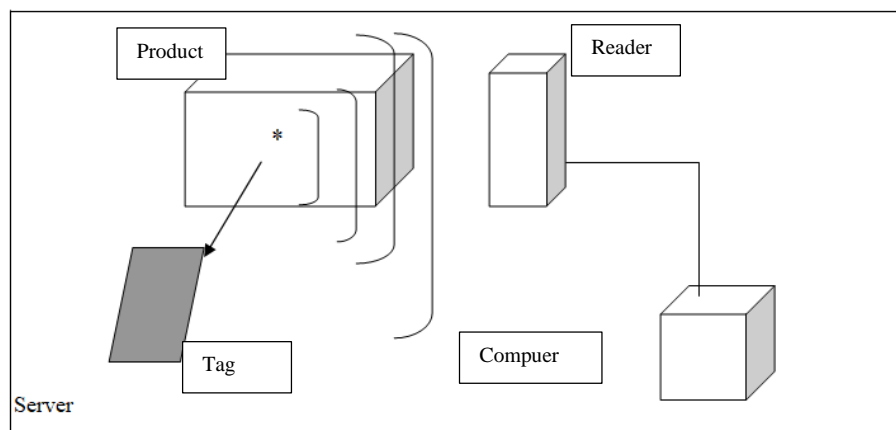


Figure 1: RFID System Components

The fact that RFID Technology provides many positive developments such as providing improvements in stock management, reducing labor costs, better revealing the causes of various losses, and more efficient use of storage and operation areas shows that this technology will be preferred more in the future (Bayrak Meydanoğlu, 2009).

4. Operating RFID Technology in Warehouse Operations

Bar Code Technology is mostly used in warehouse operations to monitor the expiration date and to determine the position of the products in the warehouse. Thus, the time to search for the product in the warehouse is saved. However, this improvement step is no longer sufficient in the face of today's increasing customer demands. In order to speed up the warehouse operations, besides determining the locations of the products, it is possible to determine the transport device that will perform the collection process, to direct it to the order and to collect the



products with the appropriate collection order and transfer them to the desired point with RFID Technology. The algorithm steps in Figure 2 are suggested for these processes (Poon et al, 2009).

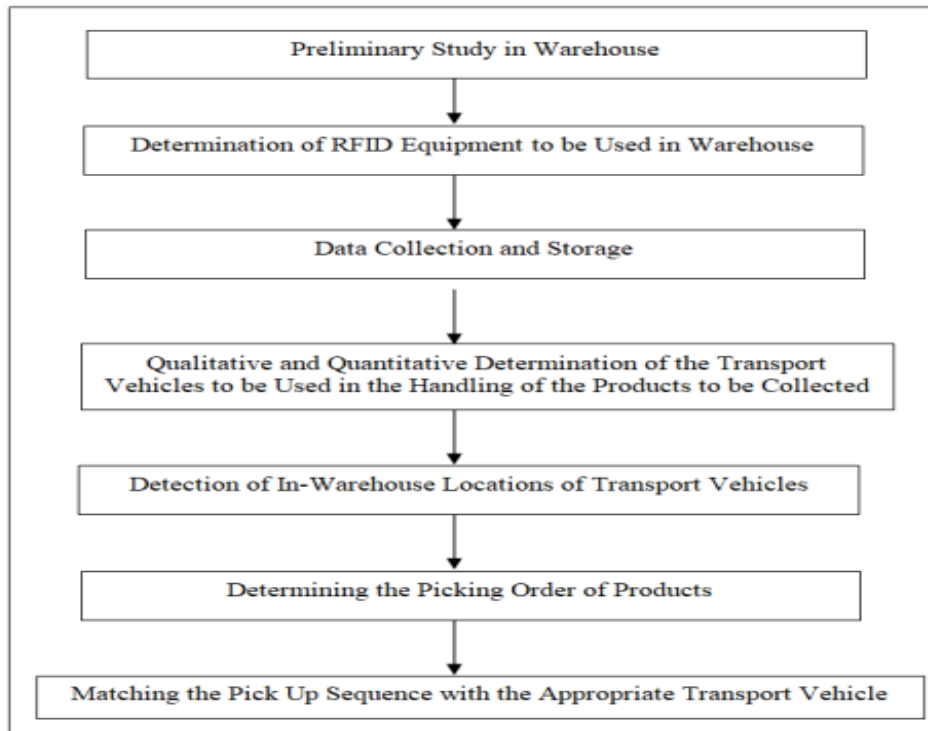


Figure 2: Operating RFID Technology in Warehouse Operations Steps

4. 1. Preliminary Study in Warehouse

The application study was carried out in the warehouse of a 3PL company operating in Turkey, in Istanbul. The warehouse in question consists of 3-storey shelves and its general features are as follows.

- Overall Rack Height: 5,5 Metres
- The Number of Floors Each Shelves Contains: 3 Floors
- Avarage Height of Each Floor: 1,4 Metres
- Aisle Width: 3,2 Metres
- Carrying Capacity of Each Shelves: 2,5 Tons

4. 2. Determination of RFID Equipment to be Used in Warehouse

RFID tags are divided into active and passive tags. While active RFID tags can provide detailed information about the chemical properties of the products, in addition to providing the product with tracking capability, passive tags only provide the product with tracking capability. While the cost of active tags can vary between \$20 – \$30 per tag, the cost of the reader that can detect active tags is between \$2000 – \$3000 per reader. The passive tag cost is between 5 cents – \$1 per tag and the reader cost is around \$1000 – \$2500. Since there are no chemical products or food products among the products stored, and it is aimed to only monitor the products and direct them to the appropriate transport device, it has been decided to use passive labels, taking into account the said costs.



			Upper Floors	
Transpalet	1 Ton	Human Speed	No	Human Power
Battery Powered Transpalet	2 Tons	5 km/h	No	Electrical Power (Up to x)
Forklift	1,5 Tons	5 km/h	Yes	Electrical Power (Up to 5x)

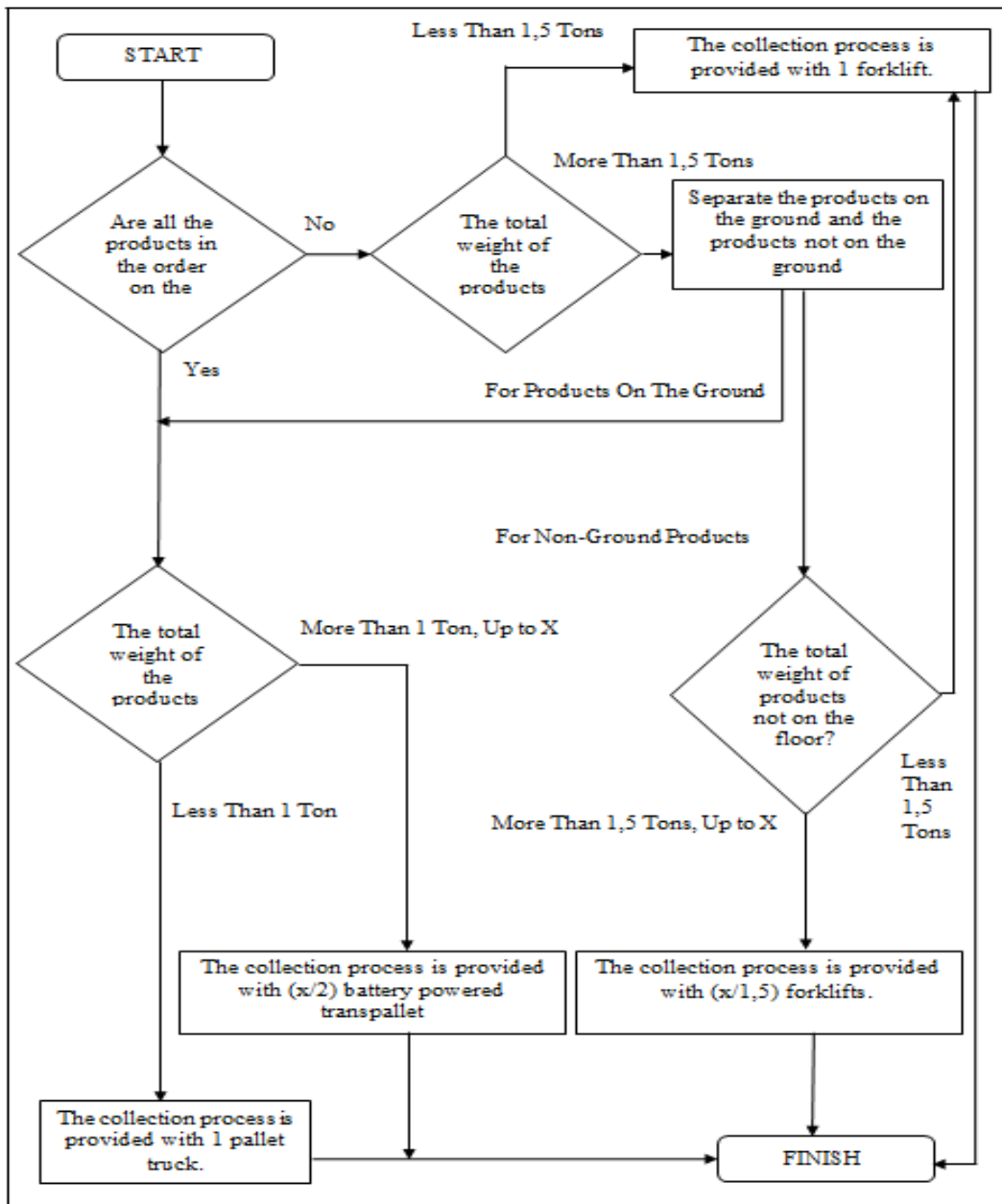
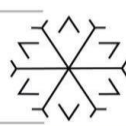
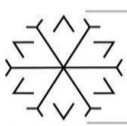


Figure 4. Qualitative and Quantitative Determination of the Transport Vehicles



4. 5. Detection of In-Warehouse Locations of Transport Vehicles

After determining the number and types of transport equipment that will carry out the collection process in the previous step, the positions of the transport equipment suitable for this type in the warehouse are determined in this step. Location detection begins with RFID readers placed at the beginning and end of each shelf detecting the transport devices within the coverage area and determining the distances of the readers from the transport devices according to the formula below.

$$d_{0001,A} = \frac{f_x \cdot V_x \cdot P_x}{2 \cdot C_x} \quad (1)$$

f_x : Frequency of Reader 001

V_x : Wavelength of Reader 001

P_x : Time for Reader to Detect A Transport Vehicle

C_x : Total Number of RFID Tags Detected During the Time That the Reader 001 Detects the A Transport Vehicle

Considering that the same transport device is detected by three different readers, the y coordinate of the transport device is determined by applying the following formula.

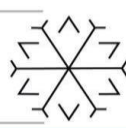
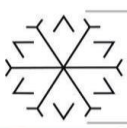
$$y^2 A = \frac{2(A \cdot x_{0003} D + CD + A^2 y_{0003}) \cdot y A}{A^2 + D^2} + \frac{C^2 + 2 \cdot A \cdot X_{0003} C - A^2 B}{A^2 + D^2} = 0 \quad (2)$$

$$A = 2(X_{0001} - X_{0002}) \quad B = d_{0003,A}^2 - y_{0003}^2 - x_{0003}^2$$

$$C = (d_{0001,A}^2 - d_{0002,A}^2) - (y_{0001}^2 - y_{0002}^2) \quad D = (y_{0001} - y_{0002})$$

When the y coordinate of the transport equipment is determined by applying the formula (2), the formula no (3) and the distance of the relevant transport vehicle to any of the self-sensing RFID Readers must be used to determine the x coordinate.

$$d_{0001,A} = \sqrt{(x_{0001} - x_A)^2 + (y_{0001} - y_A)^2} \quad (3)$$



4. 6. Determining the Picking Order of Products

In this step, the order in which the products included in an order and that need to be collected will be handled, that is, collected, is determined. The handling process starts by deciding which product the collection will start with and which product it will end with, taking into account the location (transfer point) where the products are to be collected by making calculations according to the location information of the products whose locations are determined and which are coded on the RFID tag on this information. Then, after deciding with which product the collection process will start and end, a suitable order is determined for the products in between. As a result, the order of the products to be collected is determined. The handling process consists of the following steps:

- Products to be Collected: i, j, k, l, m
- Transfer Point: D

The first step is to find the distances of each of the products to be collected separately from the D point, which is the transfer point. The distance calculation is made according to the formulas below, and the farthest point to the D point is determined as the starting point of the addition process, and the closest point is determined as the end point of the addition process. The order in which the products to be collected will be collected and transported to the D transfer point is calculated using the Clark & Wright savings algorithm.

The Clark & Wright savings algorithm is based on changing the set of laps to get a better set at each step. In the method, initially a separate route is created for each vehicle, that is, each demand point is served by a separate vehicle. Then, the two routes are combined according to the greatest savings and eligibility conditions. The savings expressed here are the cost reductions if nodes i and j are served with a single vehicle instead of two separate vehicles. There is a simple warehouse where all vehicles will leave and return. Customer demands and locations are known. The warehouse location is defined as 0 and the customer locations as 1,2,3,..n. The cost of going from the warehouse to each customer location is considered as follows (Kosif and Ekmekçi, 2012).

Parameters:

$S(i,j)$: Saving Values for i and j Pairs

$C(i,j)$: Distance Between i and j

$C(0,i)$: Path Taken From Origin to Point i

$C(0,j)$: Distance Taken From Origin to Point j

Algorithm Steps:

Step 1: Firstly savings values ($s(i,j)$) are calculated for all (i, j) pairs with $i \neq j$

Step 2: Calculated savings values are listed from largest to smallest

Step 3: For the CW heuristic application, the process has been started by considering the greatest saving value

Step 4: All route pairs were examined, respectively, and the procedures were continued

The order of the sum with these algorithm steps is determined as follows as an example:

$i \rightarrow k \rightarrow m \rightarrow l \rightarrow j$



4. 7. Matching the Pick Up Sequence with the Appropriate Transport Vehicle

In this step, the suitable transport device that will carry out the handling closest to the product where the collection will start is determined. The Clark & Wright savings algorithm is also used to determine the closest transport device.

5. Conclusions and Recommendations

Stock and warehousing operations have an important place in every part of the supply chain, and an improvement in the structure of these operations will positively affect the overall performance of the supply chain. Today, almost all of the storage operations are operated with Bar Code Technology and a small part with QR Code Technology. Although Bar Code and QR Code Technologies add traceability and accuracy to the operation, since the reading of the labels is generally done manually, it slows the operation down and makes human error possible. In addition, the usage areas of these technologies in warehouse operations are limited only to counting and location determination.

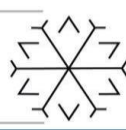
In RFID Technology, tags are read automatically when RFID readers enter the coverage area and the position of the product can be monitored continuously as it moves. Obtaining information on the chemical properties of the product is possible with active labels. Thanks to RFID Technology, it is possible to collect orders more automatically in warehouse operations.

In our study, this situation has been put forward in a concrete way. The positions of the ordered products in the warehouse are determined by the RFID tags in the products, the suitable transport device to handle these products is determined by the developed algorithm, and the location of the appropriate transportation device in the warehouse is determined by the RFID tags. Taking into account the desired location of the products, the picking order is determined by the Clark & Wright savings algorithm, and it is possible for the order picking process to be faster. The biggest advantage of this algorithm is that it offers the shortest solution by considering the travel distances between the shelves, so it is possible to obtain a solution suitable for the real site.

Since the product standards are more specific in the companies own property warehouses, it seems more possible to switch to automation in these warehouses. Therefore, it makes sense to choose Bar Code Technology, which is less costly than RFID Technology, since handling operations (goods receiving, product transfers between shelves and order picking) can be carried out in such warehouses by conveyors and automatic side forklifts (also known as reach trucks).

However, it is more difficult to implement a similar automation in the warehouses of logistics service providers that accept products of different standards from different customers. For this reason, it is possible to accelerate and partially automate the processes away from human error by using RFID Technology in the warehouses of logistics service providers where it is not possible to automate in this way.

Another issue to consider regarding the collection of orders is that the heavy products should be placed under the light ones in the same transport device. If heavy products are placed on top of light products, the packaging of the product or the product itself may be damaged. For this reason, it is necessary to determine a picking order, taking into account the weights of the products, while picking the orders. In future studies, it is recommended to consider product weights as a criterion when determining the order of collection.



References

- Aydın, C., (2009). Tedarik Zincirinde Müşteri Hizmet Düzeyi – Stok Optimizasyonu, Yüksek Lisans Tezi, Bahçeşehir Üniversitesi Fen Bilimleri Enstitüsü, İstanbul.
- BTSO, (2007). Tüccarın El Kitabı Serisi VIII – Stok Yönetimi, Yayın No:8, Bursa, 20 – 22.
- Erdal, M., (2009), Depo Yönetimi, <http://www.temesist.com/tr/depo-yonetimi.html>, 1 Kasım 2011.
- Ko, M., J., Kwak, C., Cho, Y. ve Kim, C. (2011), “Adaptive Product Tracking in RFID-Enabled Large-Scale Supply Chain” Expert System With Application” 38: 1583.
- Özdemir, A., (2004). “Tedarik Zinciri Yönetiminin Gelişimi, Süreçleri ve Yararları” Erciyes Üniversitesi İktisadi ve İdari Bilimler Fakültesi Dergisi, (23): 93.
- Yüksel, M. E. ve Zaim A. H. (2009) “Otomatik Nesne Tanımlama ve Takibinde, Veri Yönetimi ve Analiz Sistemlerinde RFID Üstünlükleri” 5. Uluslararası İleri Teknolojiler Sempozyumu, Karabük, 13 – 15 Mayıs 2009.
- Laudon K. ve Price J., (1998) “Managing the Digital Firm” Information Technology: Concepts and Issues, 2: 297 – 302
- Bayrak Meydanoğlu, S. E., (2009) “Perakandeci Piyasalarında RFID Sistemleri” Ege Akademik Bakış Dergisi, 9: 141.
- Poon, T. C., Choy, K. L., Harry Chow, K., H., Henry Lau, C., W., Felix Chan, T. S. ve Ho, K. C., (2009) “A RFID Case-Based Logistics Resource Management System for Managing Order-Picking Operations in Warehouses”, Expert Systems with Applications, 36: 8277.
- Kosif, B., Ekmekçi, İ. (2012) "Araç Rotalama Sistemleri ve Tasarruf Algoritması Uygulaması." İstanbul Ticaret Üniversitesi Fen Bilimleri Dergisi, cilt 11, sayı 21, s 41-51

Prediction of COVID-19 Death Rates with Artificial Neural Network Under Different Time Series Models Based on Moving Averages

Ömer Faruk Çaparoglu ^{1*}[0000-0001-7216-6198], Yeşim Ok ²[0000-0001-8349-7005] and

Mahmut Tutam ³[0000-0002-2018-5458]

¹ omer.caparoglu@erzurum.edu.tr, Department of Industrial Engineering, Erzurum Technical University

² yesim.ok@atauni.edu.tr, Department of Industrial Engineering, Atatürk University

³ mahmut.tutam@erzurum.edu.tr, Department of Industrial Engineering, Erzurum Technical University

Abstract

The novel corona virus disease (Covid-19), spreading more than 230 million people and causing nearly 5 million deaths as of October 2021, was declared as a global pandemic by the World Health Organization in March 2020. Accurate and consistent estimation of incidences is utmost importance for countries to combat the Covid-19 pandemic and its consequences. One of the most important indicators showing the effective fight against the Covid-19 is the number of deaths. In this study, different Artificial Neural Network designs and time series models are evaluated, and the best network design is suggested to predict the future death numbers with a high accuracy rate. We find that the best estimation of death numbers relies on historical data with 11 days of moving average model for the number of tests and cases, as well as 10-13 days of weighted moving average model for the number of seriously ill patients.

Keywords. Covid-19, Prediction, Time-Series, ANN, Death Numbers

1. Introduction

The appearance of a new coronavirus disease (Covid-19) that spreads rapidly from person to person has been reported in December 2019 in Wuhan, China. Since then, the number of cases has increased rapidly all over the world. Eventually, Covid-19 has been officially declared as a pandemic by the World Health Organization (WHO) on March 11, 2020 [1]. Unfortunately, as of October 10th of 2021, approximately 5 million deaths and 230 million cases have been confirmed worldwide [2]. In a reasonably short period of time, various types of vaccines have been found, produced and administrated by different countries and pharmaceutical companies. Moreover, approximately 35% of the world population has been vaccinated so far [3]. However, there are concerns about the effectiveness of vaccines on Covid-19 variants.

This pandemic disease also persists in seriousness, in Turkey as well as all over the world. On 11 March 2020, the Ministry of Health has confirmed the first case of Covid-19 in Turkey. However, the first death has been recorded on 17 March 2021. Since then, different measures have been implemented in Turkey to prevent the spread of the pandemic. As of October 10th 2021, approximately 7,5 million cases and 66 thousand deaths have been confirmed in Turkey [4]. Figure 1 demonstrates the number of cases, tests, seriously ill patients and deaths for 324 days. As expected, the number of cases and deaths are dramatically increasing in Turkey because most restrictions are eased by the government recently. Therefore, predicting the number of cases and/or deaths is very important in terms of the course of the epidemic. This study determines the best network design and times series models to estimate accurately the number of cases and deaths in Turkey.

This paper is organized as follows. Literature review section contains previously studied prediction models for the Artificial Neural Network (ANN) and Covid-19. The following section describes the research design and methodology used in this article. Moreover, data structure and data preprocessing are presented, as well as the architecture of the proposed ANN. In the last section, the best prediction model is determined by evaluating the performances of different combinations of network designs and time series models.

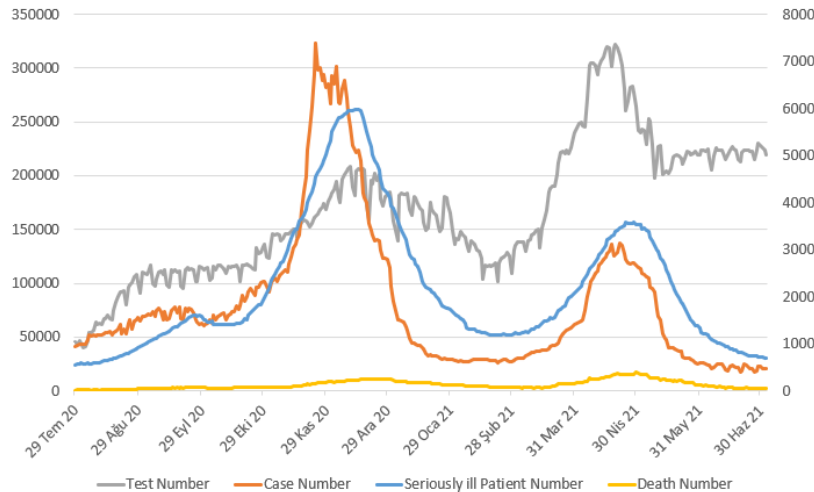


Figure 1: Daily Covid-19 data in Turkey

2. Literature Review

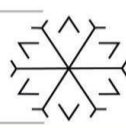
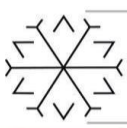
From the 20th century, the epidemics that affect people the most are Spanish flu, Hong Kong flu, Asian flu, HIV–AIDS and COVID-19, among others. The Spanish flu, known as the H1N1 virus, appeared in 1918 and 1919 and killed a total of 50 million people. Emerging in China in 1957, Asian flu caused over a million deaths worldwide [5]. Another epidemic experienced in the 20th century is the Hong Kong flu and approximately 4 million people died between 1968 and 1970 [6]. According to the report of the World Health Organization (WHO), 76 million people infected by HIV since the epidemic started in 1981 and caused 33 million deaths so far. As of today, 38 million people continue to live with HIV [7].

Studies are constantly being carried out to understand the epidemiological characteristics of pandemics, hence to minimize their impacts on human health. There are many predictive studies for the spread of pandemic diseases by using various statistical methods such as regression, correlation, time series analysis and machine learning methods etc. Recently, different methods are suggested to identify the number of daily or cumulative cases, deaths and recovers for Covid-19 [8–12]. Specifically, the cumulative number of confirmed cases for Covid-19 in UK, Italy and USA is estimated by using the fractional nonlinear gray Bernoulli model [13]. Moreover, Susceptible-Exposed-Infectious-Recovered (SEIR) approach is used to predict the infected Covid-19 cases in Delhi, India [14]. Six different machine learning methods are used to predict Covid-19 cumulative confirmed cases in Brazil [15].

ANN has a great ability to learn while training and generate future information what it has learned from the historical data. Therefore, ANN is frequently used to recognize patterns and forecast the future in different fields such as education, engineering, healthcare etc. [16]. Specifically, it is used for outbreak prediction, virus spread tracking, diagnosis and treatment process for Covid-19 [17]. An ANN model is proposed to estimate the amount of future cases in Pakistan [18]. The accuracy of the two prediction methods (ARIMA and ANN) were compared in [19]. They conclude the proposed ANN model has higher precision than the ARIMA model. [20] is employed a deep learning model to forecast the number of Covid-19 cases in Iran. [21] concludes ANN is quite successful in predicting the number of Covid-19 cases for the future. Using a feed-forward back propagation neural network having a single hidden layer with 15 neurons, [22] shows the fastest rise on cases occurs between 20 and 37 days in Turkey.

Apparently, there exists an enormous number of publications on the prediction of daily or cumulative case or death numbers for Covid-19. Different from earlier studies, we determine the best ANN model by considering different network designs in combination with different time series models. Specifically, our results reveal the death number can be predicted more accurately with 11 days of moving average for the number of tests and cases, and 10-13 days of weighted average for the number of seriously ill patients.

3. Materials and Method



Comparing with the alternative prediction methods, ANN provides an important advantage when working with nonlinear data sets [23]. Therefore, in this research, the ANN is used to predict the number of daily deaths. First, the characteristic of the data is explained. Then, data preprocessing is performed to make data well suitable for neural network training. Explaining the proposed ANN model, the performance of the trained model is presented.

3.1. Data Description and Gathering

The main dataset of this study is gathered from the WHO and Ministry of Health in Turkey [4,24]. The data includes date index (DI), the number of daily cases, tests, seriously ill patients and deaths for 324 days (from July 25, 2020 to July 3, 2021). Test and case numbers (TN and CN) are calculated based on moving average (MA) model. Moreover, a weighted moving average (WMA) model is calculated for the number of seriously ill patients (SIPN). Formulations used for the moving and weighted moving average models are given in Table 1.

Table 1: Formulations of MA and WMA models

N-days MA-TN	$TN_i = \frac{\sum_{k=i-n}^{k=i-1} TN_k}{n}$
N-days MA-CN	$CN_i = \frac{\sum_{k=i-n}^{k=i-1} CN_k}{n}$
N-days WMA-SIPN	$SIPN_i = \sum_{k=i-n}^{k=i-1} \frac{i-k}{n(n+1)/2} \times SIPN_k$

3.2. Data Preparation

The output of an ANN model is obtained by applying many numerical operations to input data. Therefore, working with long series decreases the success of the training period. As a result, data pre-processing has a significant impact on the model performance. Depending on the technique, normalization brings the attributes of the data within a common scale [25]. In this research, Z-Score and Adjusted Linear Max-Min normalization methods are used to compare ANN models:

$$\text{Adjusted Linear Max-Min: } z_i = 0.8 \left(\frac{x_i - \min[x]}{\max[x] - \min[x]} \right) + 0.1$$

$$\text{Z-Score: } z_i = \frac{(x_i - \mu)}{\sigma}$$

3.3. The Proposed Method

This section explains the proposed ANN model. In this study, a Feed Forward Neural Network consisting of an input layer, a hidden layer and an output layer is used (see Figure 2). After selecting some basic parameters for the ANN model (as default), the input parameters such as the numbers of neurons for hidden layer are determined. We used 75% of the data to train the model while the rest of data is used to measure the accuracy of the model. Three training algorithms are compared: Levenberg-Marquardt (trainlm), Bayesian Regularization (trainbr) and Scaled Conjugate Gradient (trainscg).

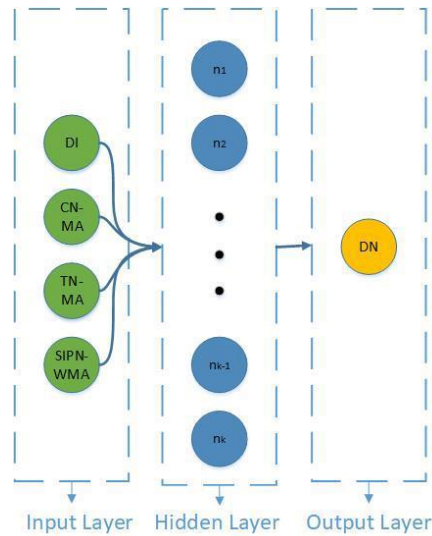


Figure 2: The network design

The number of neurons is one of the most important factors affecting the performance of the model [26] because it may result in over- or under-fitting the data. The model can perform well on training data but bad on test data (over-fitting) or it can perform well on test data but bad on training data (under-fitting). Defining n as the number of neurons in the hidden layer, n ranges between 1 and 20. Therefore, the number of neurons giving the best results for both test and training data is determined by using a trial and error approach. Obtaining the results and finding the best network design, the MATLAB Neural Network Toolbox is used [27].

3.4. Model Assessment Criteria

After training, the ANN model is generated outputs for the data allocated for testing. Then, predicted values are obtained from output values by applying a reverse transformation of the normalization method used in the data preprocessing. Evaluating the quality of the model, the error is calculated between the actual and predicted values. Moreover, Mean Absolute Percent Error (MAPE) is used to determine the prediction accuracy.

$$MAPE = \frac{1}{n} \sum_{t=1}^n \left| \frac{\hat{y}_t - y_t}{y_t} \right|$$

Where n is the number of observations, y_t , \underline{y}_t and \hat{y}_t represent the observed, average of the observed and predicted values at time t , respectively.

4. Results

This section presents results obtained by the best network designs for each time series model. Specifically, different ANN designs are trained for 70 different input data (14 MA models for TN and CN and 5 WMA models for SIPN). Moreover, all models are trained 50 times for each network design with 2 different normalization methods (Adj. LMM and Z-Score) and 3 different training algorithms (trainbr, trainscg and trainlm). Table 2 shows the MAPE values obtained by the best ANN design for each time series model.

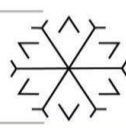
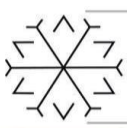


Table 2: Result of ANN models

	4**	7**	10**	13**	16**
	MAP E	MAP E	MAPE	MAPE	MAP E
1*	2,50 %	2,94 %	3,07 %	2,87 %	2,92 %
2*	2,79 %	2,80 %	2,94 %	2,74 %	3,18 %
3*	2,70 %	2,52 %	2,84 %	2,51 %	2,73 %
4*	2,35 %	2,63 %	2,66 %	2,90 %	2,59 %
5*	2,56 %	2,51 %	2,44 %	2,55 %	2,48 %
6*	2,36 %	2,36 %	2,14 %	2,37 %	2,31 %
7*	2,46 %	2,37 %	2,31 %	2,42 %	2,32 %
8*	2,34 %	2,58 %	2,52 %	2,45 %	2,54 %
9*	2,58 %	2,51 %	2,46 %	2,44 %	2,30 %
10*	2,23 %	2,43 %	2,34 %	2,45 %	2,52 %
11*	2,13 %	2,39 %	1,85 %	1,98 %	2,19 %
12*	2,48 %	2,40 %	2,22 %	2,55 %	2,28 %
13*	2,50 %	2,48 %	2,33 %	2,48 %	2,23 %
14*	2,30 %	2,14 %	2,13 %	2,32 %	2,29 %

* MA CN&TN and ** WMA SIPN

5. Discussion

The best design is obtained by using Z-Score normalization method and Bayesian Regularization training algorithm with 18 neurons in the hidden layer. Considering the results obtained, we observe the "trainbr" training algorithm gives a better MAPE value than those obtained from the "trainlm" and "trainscg" algorithms. Interestingly, the number of neurons in the hidden layer ranges from 13 to 19 for network designs with all the best MAPE values. As shown in Figure 3, the estimates obtained through the model were highly consistent with the actual values for all cases.

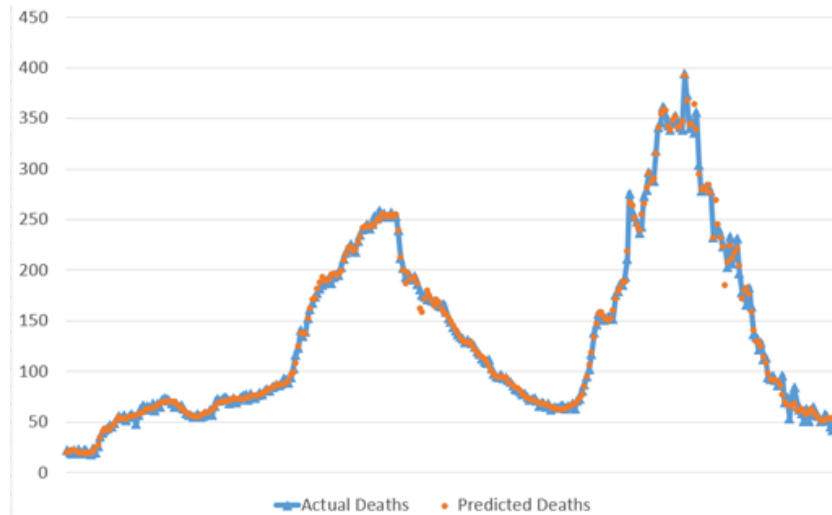


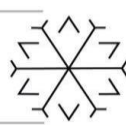
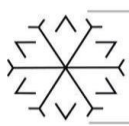
Figure 3: Result of training set

6. Conclusion

In this study, we determine the best ANN design and time series models to predict the number of deaths in Turkey. As expected, there is a powerful relationship between the number of deaths and the number of cases, tests; as well the number of seriously ill patients. Based on the results obtained, we conclude that the prediction of death numbers relies on the historical data. The best prediction results can be obtained by using 11 days of moving average model for the number of tests and cases, and 10-13 days of weighted moving average models for the number of seriously ill patients. Therefore, we can suggest taking more than ten days for moving average models.

References

- [1] (2021) WHO Director-General's opening remarks at the media briefing on COVID-19 [Online]. Available: <https://www.who.int/director-general/speeches/detail/who-director-general-s-opening-remarks-at-the-media-briefing-on-covid-19---11-march-2020>
- [2] (2021) WHO Coronavirus (COVID-19) Dashboard [Online]. Available: <https://www.who.int/emergencies/diseases/novel-coronavirus-2019>
- [3] (2021) Coronavirus (COVID-19) Vaccinations [Online]. Available: https://ourworldindata.org/explorers/coronavirus-data-explorer?zoomToSelection=true&facet=none&pickerSort=desc&pickerMetric=population&Interval=Cumulative&Relative+to+Population=true&Align+outbreaks=false&country=~OWID_WRL&Metric=People+fully+vaccinated
- [4] (2021) WHO Coronavirus (COVID-19) Dashboard [Online]. Available: <https://covid19.who.int/>
- [5] P. Farmer, "Ebola, the Spanish flu, and the memory of disease," *Critical Inquiry*, 2019;46:56–70. <https://doi.org/10.1086/705301>.
- [6] (2021) 1968 flu pandemic | History, Deaths, & Facts | Britannica [Online]. Available: <https://www.britannica.com/event/1968-flu-pandemic>
- [7] (2021) HIV/AIDS [Online]. Available: <https://www.who.int/data/gho/data/themes/hiv-aids>
- [8] D. Fanelli, F. Piazza, "Analysis and forecast of COVID-19 spreading in China, Italy and France," *Chaos Solitons & Fractals*, 2020;134. <https://doi.org/10.1016/j.chaos.2020.109761>.
- [9] V.K.R. Chimmula, L. Zhang, "Time series forecasting of COVID-19 transmission in Canada using LSTM networks," *Chaos Solitons & Fractals*, 2020;135. <https://doi.org/10.1016/j.chaos.2020.109864>.



- [10] C. Anastassopoulou, L. Russo, A. Tsakris, C. Siettos, "Data-based analysis, modelling and forecasting of the COVID-19 outbreak," *PLoS One*, 2020;15. <https://doi.org/10.1371/journal.pone.0230405>.
- [11] O.E. Owokotomo, S. Manda, A. Kasim, J. Claesen, Z. Shkedy, T. Reddy, "Modelling the positive testing rate of COVID-19 in South Africa Using A Semi-Parametric Smoother for Binomial Data," *MedRxiv*, 2020:2020.11.11.20230250. <https://doi.org/10.1101/2020.11.11.20230250>.
- [12] M.A.A. Al-qaness, A.I. Saba, A.H. Elsheikh, M.A. Elaziz, R.A. Ibrahim, S. Lu, "Efficient artificial intelligence forecasting models for COVID-19 outbreak in Russia and Brazil," *Process Saf Environ Prot*, 2021;149:399–409. <https://doi.org/10.1016/j.psep.2020.11.007>.
- [13] U. Sahin, T. Sahin, "Forecasting the cumulative number of confirmed cases of COVID-19 in Italy, UK and USA using fractional nonlinear grey Bernoulli model," *Chaos Solitons & Fractals*, 2020;138. <https://doi.org/10.1016/j.chaos.2020.109948>.
- [14] Y. Marimuthu, B. Nagappa, N. Sharma, S. Basu, K.K. Chopra, "COVID-19 and tuberculosis: A mathematical model based forecasting in Delhi, India," *Indian J Tuberc* 2020;67:177–81. <https://doi.org/10.1016/j.ijtb.2020.05.006>.
- [15] M.H.D.M. Ribeiro, R.G. da Silva, V.C. Mariani, L.D.S. Coelho, "Short-term forecasting COVID-19 cumulative confirmed cases: Perspectives for Brazil," *Chaos, Solitons and Fractals*, 2020;135:109853. <https://doi.org/10.1016/j.chaos.2020.109853>.
- [16] O.I. Abiodun, A. Jantan, A.E. Omolara, K.V. Dada, N.A. Mohamed, H. Arshad, "State-of-the-art in artificial neural network applications: A survey," *Heliyon* 2018;4. <https://doi.org/10.1016/j.heliyon.2018.e00938>.
- [17] Q.V. Pham, D.C. Nguyen, H.T. Thien, W.J. Hwang, P.N. Pathirana, "Artificial Intelligence (AI) and Big Data for Coronavirus (COVID-19) Pandemic: A Survey on the State-of-the-Arts," *Ieee Access*, 2020;8:130820–39. <https://doi.org/10.1109/access.2020.3009328>.
- [18] I. Ahmad, S.M. Asad, "Predictions of coronavirus COVID-19 distinct cases in Pakistan through an artificial neural network," *Epidemiol Infect*, 2020;148. <https://doi.org/10.1017/s0950268820002174>.
- [19] A.I. Saba, A.H. Elsheikh, "Forecasting the prevalence of COVID-19 outbreak in Egypt using nonlinear autoregressive artificial neural networks," *Process Saf Environ Prot*, 2020;141:1–8. <https://doi.org/10.1016/j.psep.2020.05.029>.
- [20] L. Moftakhar, M. Seif, M.S. Safe, "Exponentially Increasing Trend of Infected Patients with COVID-19 in Iran: A Comparison of Neural Network and ARIMA Forecasting Models," *Iran J Public Health* 2020;49:92–100.
- [21] S.K. Tamang, P.D. Singh, B. Datta, "Forecasting of Covid-19 cases based on prediction using artificial neural network curve fitting technique," *Glob J Environ Sci Manag*, 2020;6:53–64. <https://doi.org/10.22034/gjesm.2019.06.si.06>.
- [22] A.B. Çolak, "Prediction of infection and death ratio of CoVID-19 virus in Turkey by using artificial neural network (ANN)," *Coronaviruses* 2020;01. <https://doi.org/10.2174/2666796701999200915142539>.
- [23] G.P. Zhang, B.E. Patuwo, M.Y. Hu, "A simulation study of artificial neural networks for nonlinear time-series forecasting," *Comput Oper Res*, 2001;28:381–96. [https://doi.org/10.1016/S0305-0548\(99\)00123-9](https://doi.org/10.1016/S0305-0548(99)00123-9).
- [24] (2021) General Coronavirus Table [Online]. Available: <https://covid19.saglik.gov.tr/TR-66935/genel-koronavirus-tablosu.html>
- [25] G. Aksu, C.O. Güzeller, M.T. Eser, "The Effect of the Normalization Method Used in Different Sample Sizes on the Success of Artificial Neural Network Model," *Int J Assess Tools Educ*, 2019;6:170–92. <https://doi.org/10.21449/ijate.479404>.
- [26] A. Zamaniyan, F. Joda, A. Behroozsarand, H. Ebrahimi, "Application of artificial neural networks (ANN) for modeling of industrial hydrogen plant," *Int J Hydrogen Energy*, 2013;38:6289–97. <https://doi.org/10.1016/j.ijhydene.2013.02.136>.
- [27] (2021) Matlab [Online]. Available: <https://www.mathworks.com/help/deeplearning/ref/fitnet.html>

The Method of Modulated Fourier Series Expansion Applied to Hourly Electricity Consumption

E. Yükseltan^{1*}[0000000278532897], A. Yücekaya^{2*}[0000000232718418], A.H. Bilge^{3*}[0000000260430833],
E. Ağca Aktunç^{4*}[000000029597569X]

¹ergun.yukseltan@stu.khas.edu.tr, Department of Industrial Engineering, Kadir Has University

²ahmety@khas.edu.tr, Department of Industrial Engineering, Kadir Has University

³ayse.bilge@khas.edu.tr, Department of Industrial Engineering, Kadir Has University

⁴esra.agca@khas.edu.tr, Department of Industrial Engineering, Kadir Has University

Abstract

Hourly electricity consumption for European countries belonging to the ENTSO-E grid for the years 2006-2016 is modelled using a modulated Fourier Series Expansion. The scheme is used to determine the breakdown of the consumption into industrial and household components and to determine electricity usage for heating and cooling purposes. The model can be used to predict hourly consumption over a year, with an accuracy of around 3%, in cases where electricity usage for heating purposes is not dominant.

Keywords. ENTSO-E grid system, Fourier Series Expansion, Special Days Detection, Time Series Method

1. Introduction

Electricity consumption can be broadly classified as industrial and domestic usage, and household usage can be categorized as consumption for illumination, heating, and cooling purposes. These consumption patterns lead to daily, weekly and seasonal variations. Fourier Series Expansion (FSE) in terms of the harmonics of fundamental frequencies is a standard tool of time series analysis. However, it fails to reproduce the variations of the amplitudes of the daily and weekly variations during a year. This situation is similar to the “amplitude modulation” used to broadcast the high-frequency carrier signal with the low-frequency speech signal by modulating a high-frequency “carrier” signal. In mathematical terms, this amounts to the multiplication of these two periodic functions.

The modulated FSE method has been applied to the hourly electricity consumption of Turkey, using data provided by EPIAS, and hourly consumption has been predicted with an accuracy of about 5% over a year horizon in Yükseltan et al. (2017). The success of the forecast model is mainly due to the fact that in Turkey, electricity is rarely used for heating purposes; hence it follows a more or less deterministic pattern. The usage for cooling purposes is not negligible, but as it is confined to a shorter period, its effect on the performance of the model is acceptable. The effects of heating and cooling and other short-term changes in consumption are incorporated into the model by a feedback mechanism that improves the short-term prediction error (Yükseltan et al., 2020).

In Yükseltan et al. (2021), the Modulated Fourier Series model is applied to the hourly electricity consumption of European countries in the ENTSO-E electricity grid, covering the period 2006-2018. The method is applied to the hourly data of each country to obtain a model for electricity consumption. In this model, special events such as holidays, industrial shutdowns during summer, changes to/from daylight saving time appear as outliers, and they are removed from data as part of data pre-processing. The periods corresponding to industrial shutdowns are used to determine the ratio of the household to industrial consumption, and the difference between weekday and weekend consumption is further used to determine the ratio of industrial and office usage to household consumption as in Yükseltan et al. (2017). The modulated FSE, without any meteorological information, uses only mathematical functions as regressors and provides a reasonably satisfactory long-term prediction for hourly consumption. In Yükseltan et al. (2021), the goodness of the long-term fit of the predicted consumption to the data is used to determine the breakdown of the electricity consumption of a country into its industrial/household/heating/cooling components. Meteorological information and forecasts can be incorporated into the model for short-term forecasts.



Europe has an interconnected grid system in which countries can transmit or receive electricity from the grid. Hourly consumption data for each country have been released for the years 2006-2018 for 38 countries. The European Green Deal announced in December 2019 aims to decrease greenhouse gas emissions by 55% compared to 1990 by 2030 and become nature neutral by 2050 (European Court of Auditors, 2021). As renewable energy resources have a strong dependency on meteorological conditions, it is also important to assess the composition of electricity consumption for heating and cooling. A detailed analysis of the clustering of European countries with respect to the types of consumption is presented in Yukseltan et al. (2021). In the present work, we give a brief outline of the method used therein. We refer to Yukseltan et al. (2017) and Yukseltan et al. (2020) for a comprehensive survey of the literature on methods for modelling and prediction of electricity consumption.

2. Data Processing and Methodology

Members of the Internal Electricity Market (IEM) in the European Union founded ETSO in 1999 to create a shared network and cross-border electricity trade. With the success of ETSO in operation and compensation, in 2008, 36 European Transmission System Operator (TSO) signed a protocol to expand this shared network. At the end of that year, European Transmission System Operation for Electricity (ENTSO-E) was created. All ETSO activities were transferred to ENTSO-E in 2009. ENTSO-E consists of five Regional Security Coordinators (RSCs), Coreso, TSC, SCC, Nordic, and Baltic, and all members operate under these RSCs. Figure 1 shows the territory of the RSCs and adhered countries across Europe.

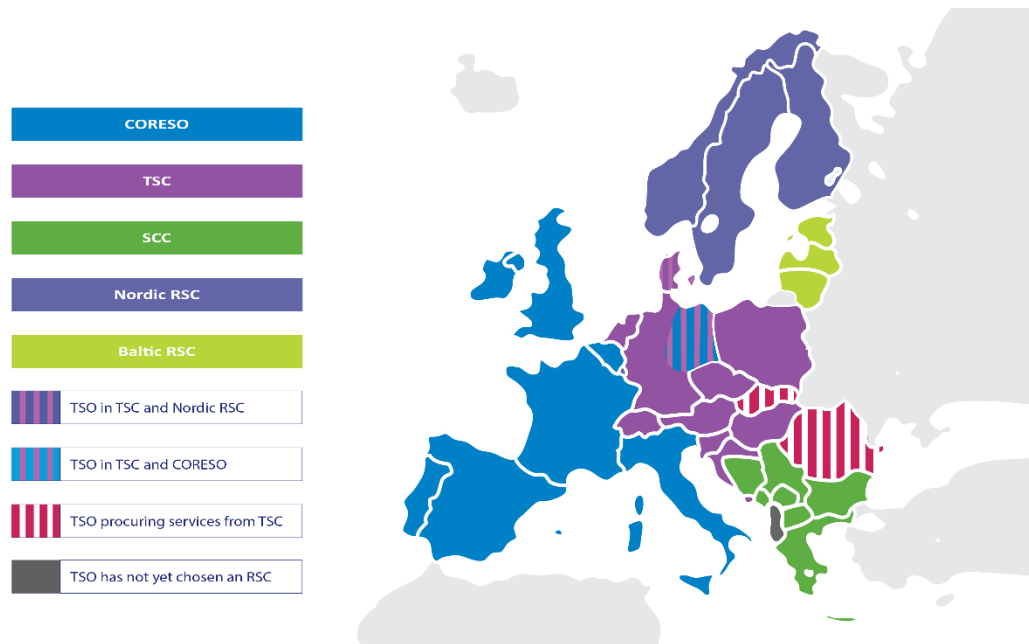


Figure 1: ENTSO-E RSCs and countries map (<https://www.entsoe.eu>)

The data consist of hourly consumption and covers the period 2006-2018 (Data source: <https://www.entsoe.eu/data/power-stats/>). Data quality was checked for each country, and in cases of extensive missing and inaccurate data, the whole year was excluded. After this step, missing hourly data was filled with the data of the same hour of the same day in the previous week.

In Figure 2, we give an overview of the data for the year 2018 in terms of aggregate consumption for all countries and consumption of countries with average hourly consumption between 1 GW and 5 GW. As the contribution of industrialized countries dominates, in Figure 2(a), we see a strong weekly variation reflecting the weekday/weekend effects. Based on Figure 2(b), we note that winter consumption is higher than summer and spring consumptions, indicating that, in addition to increased illumination needs, electricity is likely to be used for heating. In Figure 2(a), a low consumption period shows an industrial shutdown in summer.

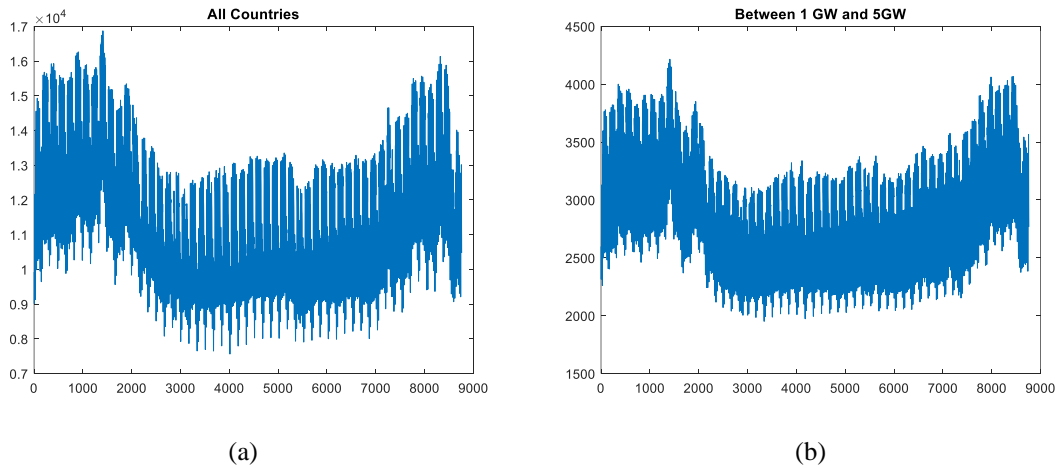
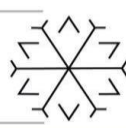
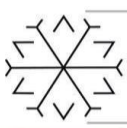


Figure 2: Yearly consumption classification for 2018 based on average daily consumption (a) for all countries and (b) for the countries with 1-5 GW hourly average consumption (Yukseltan et al., 2021).

When the electricity consumption data of all countries are examined, different consumption patterns are observed, as displayed in Figure 3 for Sweden, Croatia, Germany, and Poland. The consumption of Sweden is high and irregular in winter, indicating the use of electricity for heating. For Croatia, increased summer consumption indicates cooling needs, and summer and winter consumption is higher than in spring and autumn due to the same heating and cooling capacity. The seasonality of electricity consumption in Germany and Poland is less dominant, indicating a higher weight of industrial consumption. Strong weekly variations are also indicators of industrialization. The consumption patterns for Germany and Poland are at different scales but follow a similar pattern throughout the year.

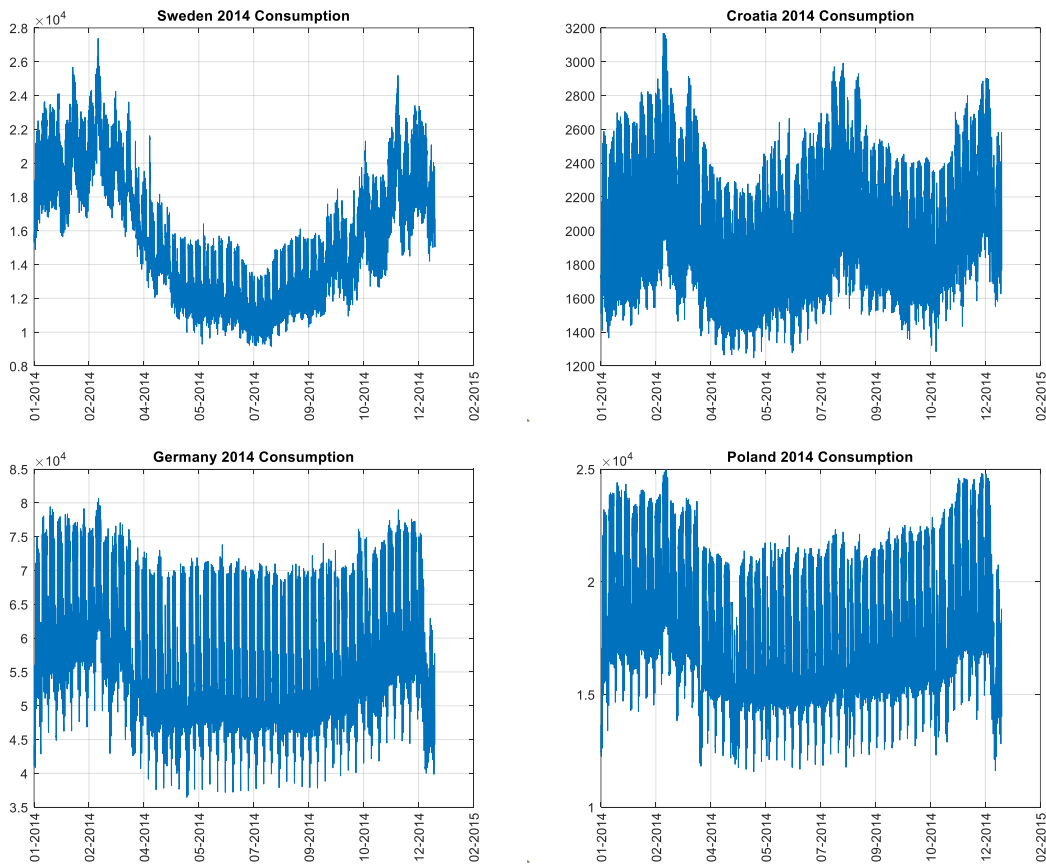


Figure 3: Comparison of consumption patterns for Sweden, Croatia, Germany, and Poland.

The proposed method, “Modulated Fourier Expansion,” is powerful in modelling periodic variations. Therefore, regular components of electricity consumption, like lighting, weekend-weekday effect, are appropriately predicted. On the other hand, irregular components such as heating and cooling are sensitive



to weather conditions. In Yukseltan et al. (2021), the properties of the modelling error are used to obtain a clustering of the countries with respect to the breakdown of electricity consumption into various components.

In the next section, we outline the method for detecting special events and their removal as part of pre-processing data.

2.1. Special Events and Holidays

Holidays and special events can be country-specific or regional, like New Year's Eve, Christmas holidays, or time changes for daylight savings throughout Europe. In Muslim countries, the dates of the religious holidays change each year, and they come to the fore every year because they are determined according to the lunar calendar. Also, the countries that have higher industrial activities have industrial shutdown periods in summer. In Figure 4, we display a close-up of the data for Turkey and Italy as typical examples.

In Figure 4(a), we display the low consumption period in Turkey, corresponding to religious holidays. The dates of these religious holidays are determined according to the lunar calendar, and they move back each year by ten days. In such cases, FSE fails to detect and predict these periods, and special treatment of these events is needed. Figure 4(b) corresponds to an industrial shutdown period in Italy.

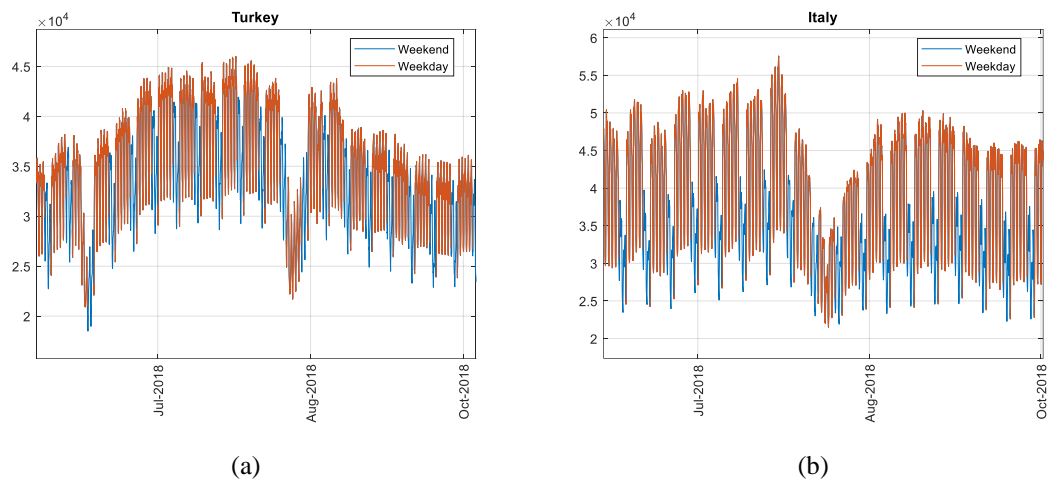


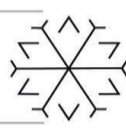
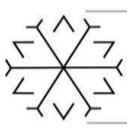
Figure 4: Holiday consumption changes. (a) Turkey, low consumption periods coincide with religious holidays; (b) Italy, low consumption period corresponds to the shutdown of industrial facilities in mid-summer.

2.2. Methodology

Electricity demand has an increasing trend component, climatic effects, and stochastic characteristics. A linear model of a modulated FSE was used to forecast hourly electricity demand over a 1-year horizon. This method is handy in cases where periodic variations are dominant, and electricity is used predominantly for illumination, i.e., heating and cooling-related demand is negligible. The method can be used not only for prediction but also to understand how electricity consumption is affected by external factors or changes (Yukseltan et al., 2017; Yukseltan et al., 2020).

The model based on modulated FSE can be summarized as follows. A periodic function $f(t)$ with period T can represent an infinite sum of cosine and sine functions with periods T/n . Those sinusoidal functions with periods T/n are called the “harmonics” of the main variation. In the time series for the hourly electricity demand, the dominant component is the daily variation with 24 hours. The harmonics of this variation have periods of 12, 8, 6, $24/n$ hours.

In addition to these “fast” variations, there are weekly and seasonal variations. The weekly variation reflects the weekend effect, i.e., industrial and office consumption shutdown. Seasonal variations have components arising from illumination, heating, and cooling needs. The change in the demand due to the changes in the daylight hours can be incorporated into the FSE by adding the “modulation” of the high-frequency variations (i.e., sinusoids with periods of $24/n$ hours, $n=1, 2, \dots$) and the low-frequency variations (i.e., the harmonics of the seasonal variation with periods of $365/n$ days, $n=1, 2, \dots$). This “modulation” considers the variations in the amplitude of the 24-hour variation throughout a year. It is obtained by adding the



products of high- and low-frequency harmonics as regressors. The demand arising from heating and cooling needs is modelled by adding the deviations from comfortable temperatures as a regressor to the linear model. In addition to these periodic components, overall trends are arising from demographics and economic growth. Finally, it should be noted that electricity demand on special days, such as holidays, has to be treated separately. Time-series methods, such as AR or ARMA, focus on short-term electricity consumption forecasts. However, the modulated FSE provides hourly forecasts over a long-term horizon such as a year, within good modelling and forecast errors, particularly in cases where illumination and industrial usage are dominant.

The number of regressors to be included in the modulated FSE is limited theoretically by the ‘‘Sampling Theorem,’’ stating that the shortest period that can be included in the expansion is twice the sampling interval, in this case, 2 hours. Hence, the number of regressors should be large enough to capture the essence of the data but should be moderate to avoid the inversion of matrices with high condition numbers.

In the model, the daily electricity demand is denoted by S . A constant vector (represented by 1) and a linear term (represented by t) are used for the linear trend in the data. Periodic variations consist of X_n (the n th harmonics of sinusoidal functions with a period of one year, i.e., $364/n$ days, $n=1, \dots, N$), Z_m (the m th harmonics of one week, i.e., $7/m$ days, $m=1, \dots, M$) and of Y_k (the k th harmonics of sinusoidal functions with a period of 24 hours, i.e., $24/k$ hours, $k=1, \dots, K$). The regressors that represent the modulation of the high-frequency variations (Z_m and Y_k) by the low-frequency variations (X_n) is included by the component-wise product of the corresponding vectors, denoted as $X_n Z_m$ and $X_n Y_k$. The number of this last group of regressors should be moderate to avoid over-learning. The effect of climatic conditions is represented by $T_\delta = \text{abs}(T_c - T)$, which measures the deviation from a threshold temperature T_c , that people start to use electricity for cooling or heating. The representation of the model is as follows.

$$F = [1, t, X_1, X_2, \dots, X_N, Z_1, Z_2, \dots, Z_m, Y_1, Y_2, \dots, Y_K, X_1 Z_1, \dots, X_i Z_j, \dots, X_1 Y_1, \dots, X_k Y_l, T_\delta] \quad (1)$$

Then, the coefficient vector a and model vector y can be calculated as below.

$$a = (F^t F)^{-1} F^t S \quad (2)$$

$$y = Fa \quad (3)$$

The model is adopted to the prediction as follows. Data is split into ‘‘training’’ and ‘‘test’’ periods. Recall that the regression coefficients are obtained from equation (2), where S is the data and F is the matrix, whose columns are the model functions, and the best fit to the data in the mean square sense is given by equation 3. The data splitting into training and test periods corresponds to the splitting of the matrix F and the vector S as, $F^t = [F_1^t, F_2^t]$, $S^t = [S_1^t, S_2^t]$, where F_1 and S_1 cover the training period. The model coefficients are computed in terms of F_1 and S_1 as follows.

$$a_1 = (F_1^t F_1)^{-1} F_1^t S_1 \quad (4)$$

The prediction for the test period is obtained from the equation below.

$$y_2 = F_2 a_1 \quad (5)$$

The prediction error is the norm of the difference between prediction for the test period, y_2 , and the data for the test period, S_2 , $|F_2 a_1 - S_2|$.

In the next section, we present the results of the proposed model in terms of detecting electricity consumption for heating and cooling at the country level and predicting future consumption.

3. Results

3.1. Detection of the electricity consumption for heating and cooling

Temperature is one of the primary external information that affects electricity consumption. The sensitivity of the consumption depends on countries' resource allocation for heating and cooling. If the electricity is used for heating, consumption during winter is high and irregular. Furthermore, weekend consumption can be higher in winter. If the electricity is used for cooling, summer consumption is high and irregular. In general, irregularity indicates electricity usage for heating and cooling purposes. In such cases, the data must be supplemented by metrological information to make a reliable model and forecast.

Figure 5 displays the weekday and weekend consumptions for Germany and Estonia from January-March 2018. For Germany, weekday consumption is considerably higher than weekend consumption. For Estonia,



weekend consumptions are comparable with weekday consumptions in January-February, while in subsequent months, weekend consumption decreases due to seasonality effects.

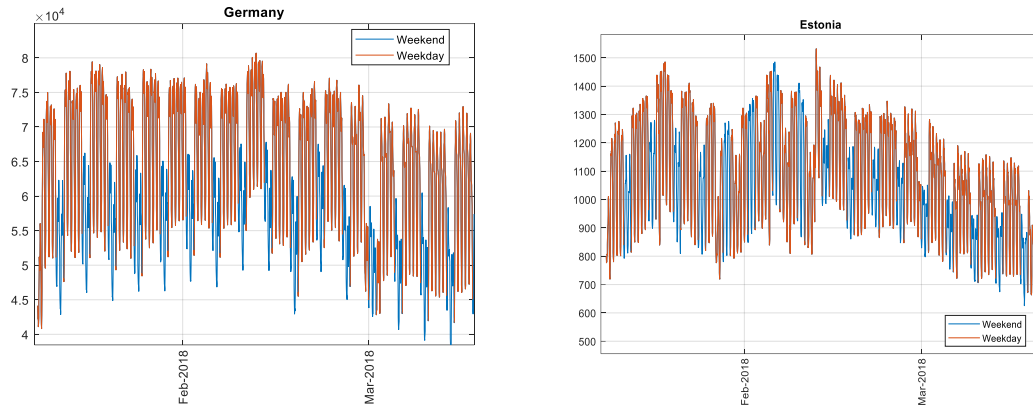


Figure 5: Weekday- weekend consumption pattern for Germany and Estonia in winter 2018.

Suppose electricity usage for heating and cooling is negligible compared to illumination and industrial consumption. In that case, the modulated FSE method is excellent as a reliable model to forecast electricity. The reason for that is, except heating-cooling, other variations in electricity consumption are strongly periodic and regular. Note that the changes in daylight saving time should be taken into consideration.

3.2. Prediction

In this section, the electricity consumption data of all countries were predicted annually using Fourier Methods presented in the previous sections. The model can predict consumption for different periods, but the annual prediction was consistent, comparing different consumption profiles. In order to make an annual prediction, the first two years (2006-2007) of the data set was used as a training set, and the following year (2008) was predicted according to this training set. The electricity consumption of 2008-2018 was predicted by shifting the training set on a yearly basis.

As mentioned previously, temperature is one of the critical factors affecting electricity consumption. However, adding temperature as a regression coefficient to the model does not significantly change the error rate in long-term predictions. The reason for that is, in long-term prediction, the effect of extreme temperatures is reduced. However, the error rates of the forecasts formed by the addition of temperature are essential in comparing the consumption profiles of each country. It can be said that countries with more remarkable error change in predictions with the addition of temperature have a higher portion of electricity usage for heating and cooling purposes because consumption is more sensitive to temperature changes. As seen in Figure 6 below, prediction error changes are not the same for all countries when external information, temperature, is added to the model.

Based on the prediction errors in Figure 6, although Sweden and Switzerland have the same climatic condition, their model response to using temperature as additional information is different. There is considerable improvement in Sweden's prediction with temperature, because their electricity usage for heating purposes is very high, like Finland. However, Germany and Switzerland have nearly no change in prediction error when the temperature is known. We can say that electricity is not a primary resource for heating and cooling purposes for both countries. Another reason can be the dominance of industrial usage.

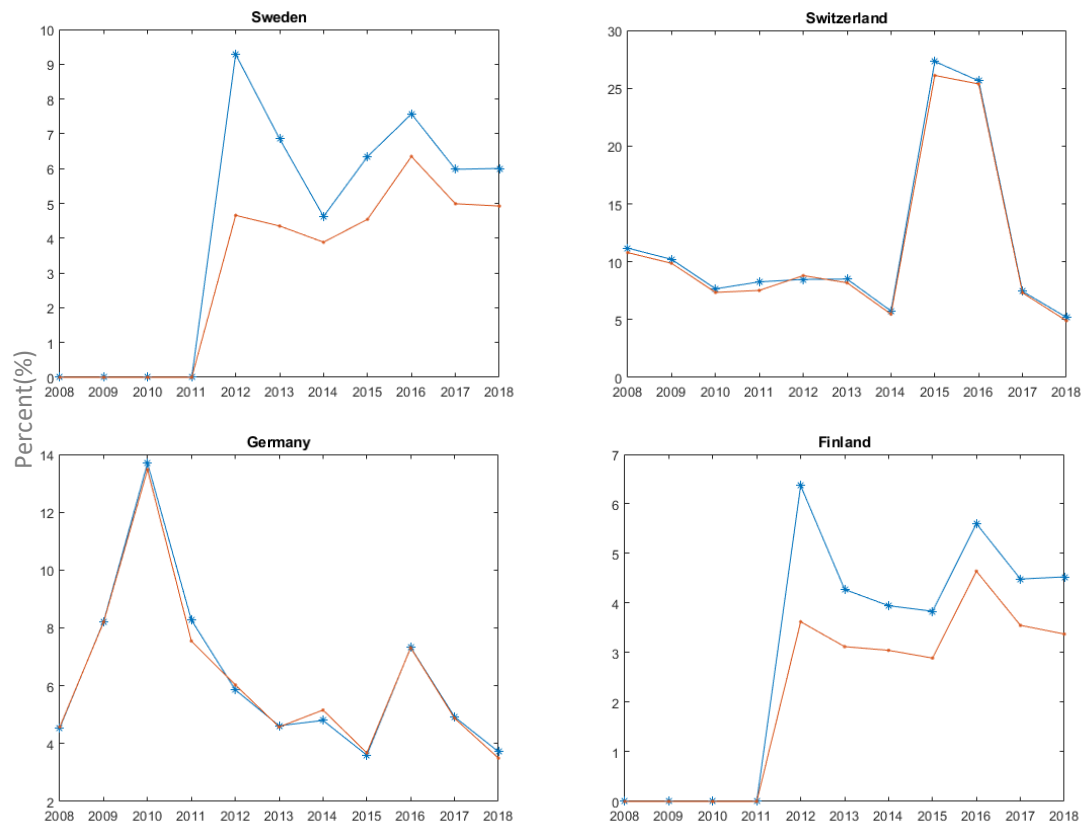
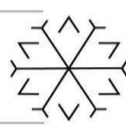
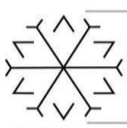


Figure 6: Prediction errors of selected countries with (in red) and without (in blue) temperature information.

To understand how temperature affects the model result and prediction quality, we analyze errors according to the countries' heating and cooling degree days. Heating and cooling degree days (HDD-CDD) are the data that shows how heating and cooling capacity are required to reach room or comfortable temperature. Data were obtained from Eurostat for each country. When the HDD-CDD numbers are compared with the model performance for each country, the distribution of the performance shows which country has a considerable amount of electricity consumption for heating and cooling. Similar to the above figures, even though countries have the same climatic conditions, their model performance is different due to differences in heating-cooling resources, and we refer the reader to Yukseltan et al. (2021) for a more detailed discussion.

4. Conclusion

In this study, the hourly electricity consumption of countries in the ENTSO-E electricity grid from 2006-2016 is analyzed and modelled using a modulated Fourier Series Expansion. The proposed model is used to determine the breakdown of consumption into industrial and household components as well as consumption for heating and cooling purposes. The model is also used to predict the annual hourly consumption for different countries, and the average prediction errors range from 3% to 11% for the selected countries with different consumption patterns. The model can be used to predict hourly consumption over a year, with an accuracy of around 3% in cases where the usage of electricity for heating purposes is not dominant.

References

- Yukseltan, E., Yucekaya, A., Bilge, A.H., Agca Aktunc, E. (2021) 'An Overview of the ENTSO-E Electricity grid', Preprint. Istanbul.
- European Court of Auditors. (2021) 'Infrastructure for charging electric vehicles: more charging stations but uneven deployment makes travel across the EU complicated', Special report No 05, 2021.
- Yukseltan, E., Yucekaya, A. and Bilge, A. H. (2017) 'Forecasting electricity demand for Turkey:



Modeling periodic variations and demand segregation', *Applied Energy*, 193, pp. 287–296. doi: 10.1016/j.apenergy.2017.02.054.

Yukseltan, E., Yucekaya, A. and Bilge, A. H. (2020) 'Hourly electricity demand forecasting using Fourier analysis with feedback', *Energy Strategy Reviews*, 31, p. 100524. doi: 10.1016/j.esr.2020.100524.

Jetty Optimization and An Application

Engin Başbüyük ^{1*}[0000-0003-4667-5508] and Cafer Çelik ²[0000-0002-7025-2647]

¹engin.basbuyuk12@ogr.atauni.edu.tr, Department of Industrial Engineering, Atatürk University

²ccelik@atauni.edu.tr, Department of Industrial Engineering, Atatürk University

Abstract

Port; can be defined as a place protected from waves, winds, and tides, providing specific dimensions to dock a ship safely. A port should also have berths where ships dock for loading and unloading. Ports are strategic logistics facilities of countries as they combine land and sea connections. Due to the importance of ports, port efficiency is also critical. However, port characteristics (width, draft, and tonnage limit) and the collected data (arrival times, processing times, cargo quantities, drafts) depend on several factors.

This study aims to optimize the docking program of oil tankers by using operations research methods. In this context, will be examined the port section of the İzmit Refinery of Turkish Petroleum Refineries Corporation (TÜPRAŞ), located in the İzmit district of Kocaeli province, for the study. Data set is collected from three hundred ships docking at the company's port in a period of approximately 4 months in order to solve the problem. The evaluated problem is known in the literature as the dynamic and discrete berth allocation problem (DDBAP). One of the main purposes of the berth allocation problem is to determine the docking sequence of ships by minimizing the waiting time of each ship in the dock. For this, an integer linear programming model is presented. Tonnage and draft constraints of the docking ships were also taken into consideration in the model.

DDBAP is referred to as the NP-Hard problem type in the literature. Therefore, it is tough to find the optimum solution for the number of large-sized ships. It is necessary to develop heuristic or metaheuristic methods to find solutions near the optimum. Hence, a metaheuristic algorithm, which converges the result to the most plausible solution, especially in large-scale problems, is desired to develop.

Keywords. Berth allocation problem, Integer linear programming, Metaheuristic methods

Review On: Construction Waste Minimization by Adopting Different Techniques

Abdul Raday Munawar^{1*}[0000-0000-0000-0000] and Usman Hussain* [0000-0000-0000-0000]

bce183014@cust.pk,

usman.hussain@cust.edu.pk,

Abstract

Waste management is an important part of sustainable construction. Waste management is avoiding waste where possible, decreasing waste where feasible, and recycling material that would otherwise be discarded, proper techniques will be used which required. Solid waste management strategies have highlighted waste reduction, recycling, and reuse as critical to resource sustainability. This paper presents the literature review of different techniques and factors of waste minimization keeping in the economy of project. By adopting all these techniques, we can decrease our solid waste annually and achieve sustainability. Site management is important to tackle all waste from its handling to dumping it at a safe site or reusing it. On the other hand, by reusing and recycling this waste economy can be achieved and we start following circular economy concept. In modern world BIMs is the platform which is being used for fast communication between stakeholders in order to do amendments in design or plan which helps in minimizing waste on site. In order to get betterment in our construction industry we need to adopt several policies for recycling industries for waste minimization.

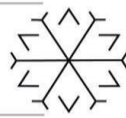
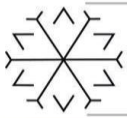
Keywords. Waste management, BIM, Waste minimizing, Techniques, Site waste

1. Introduction

The list of industries which generate the most revenue and job opportunities for the people ranging from illiterate to the highly educated is topped by the mighty 'Construction Industry'. Every person on the planet has been directly or indirectly involved in the Construction Industry. In the previous few years, development has evolved worldwide at a massive rate. As Pakistan is developing country the annual investment of construction in Pakistan is about US\$ 1 billion (approx.). The total revenue of construction industry of Pakistan is about \$19 billion with annual growth rate of 3.2% from time period of 2015-2019. As in present year the growth rate of Pakistan is about -0.05% and projected to at 4% in 2022.

Construction industry have a prominent role in development of a nation. A famous French stated that "If construction industry moves everything moves". As construction industry is the biggest industry all over the world, so it uses different materials to take forward their projects and production for smooth growth. These materials include concrete, glass, wood, bricks, steel, plastic etc. As construction industry have good impact on nation on the other hand it also has some type of bad effect on nation i.e., about 30-35% of the solid waste is generated by construction industry.

In order to minimize this construction waste, Industry stakeholders suggest several techniques and processes to take construction sites and projects toward sustainability. Faniran and Caban (1998, 182–183) stated that the key tactics for reducing construction waste include staying away from, destructing, or limiting waste at the source, as well as reusing waste materials to limit the amount of trash delivered into the environment. On the other hand, the over ordering of material is the main cause of construction waste in order to come over this flaw engineer should have to order proper.



2. Measures to Minimize Construction Waste

Construction waste means that the waste that is produced from construction activities i.e., concrete, glass, wood, bricks, steel, plastic etc. As construction waste have negative impact on project economy of project as well as environment like there is also the practice of not documenting construction waste dumped by the side of the road or on a vacant plot of land. These types of waste disposal practices are quite common in India, and they make trash assessment unfeasible (Bendi, 2010).

Doust k et al., (2020) stated that literature study compiled scholarly, expert, proficient, administrative and trade data on building waste management sustainability techniques. The researchers concluded that, based on the blend of information derived from the literature investigation, an examination in light of the blend of data got from the writing investigation, an assessment of the conceivable effective and proficient front-end construction waste plan would give ideal triple-main concern business, ecological, and local area advantages to partners subsequent to finishing the itemized writing survey and examination of the information obtaining data set.

2.1. Site Waste Management Plan

According to (Kolaventi SS et al., 2021) a typical SWMP comprises a thorough:

- Description of the project. (Location, size, waste generated information, and so on)
- Quantification of waste created by categories, and recommended WM alternatives.
- Waste Management cost estimates based on proper tracking and documenting of produced trash.
- Among other things, there is a record of reused materials.
- Building team training.

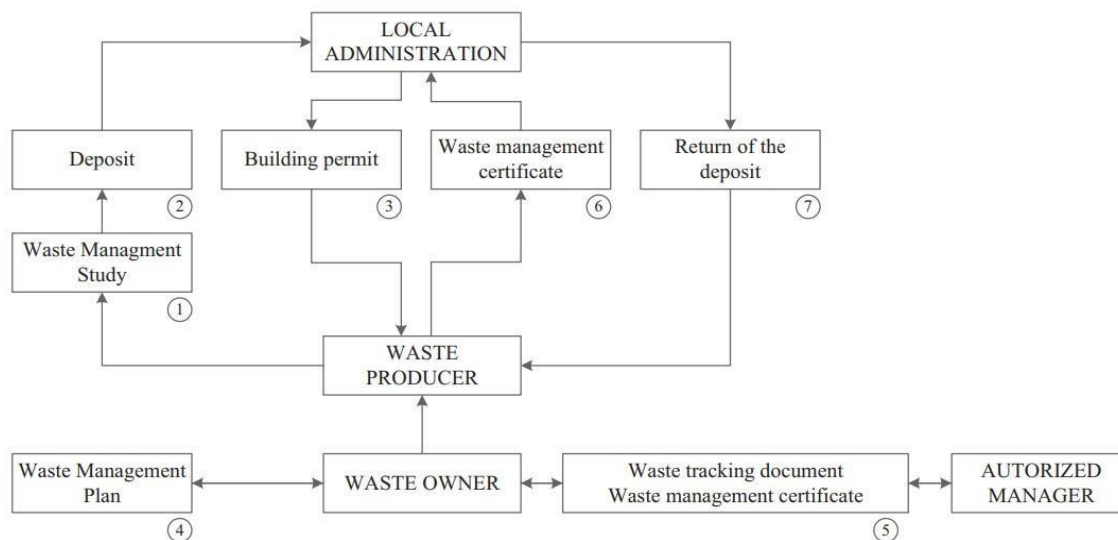


Figure 1: Construction waste management model (Marta G., 2014)

Figure-1 shows the waste production on site and management which includes a relation of waste owner and local administration. Further-more it describes the whole construction waste management process

2.2. Reuse, Reduce, Recycle

Reduce, reuse, and recycle are the three R's: Reduction is the prevention of waste creation at the source; reuse is the re-use of the same material (for the same or a different application); and recycling is the transformation of construction waste into new resources. The reduction principle is the most highly recommended of the three R principles since it minimizes waste creation from the start. It lowers material consumption, the difficulty of repurposing trash, and end-of-pipe treatment (e.g., recycling or landfilling). CWM has evolved into an interdisciplinary field as a result of increased attention from the worldwide scientific community.

The 6Rs, which complement the classic 3Rs with three more Rs: rethink, refuse, and repair, have emerged as a result of this evolution (Boon et al., 2020). Rethink means reconsidering one's actions before acting in order to find more effective methods to use materials; deny means refusing to buy anything superfluous or

worthless; and repair means seeking to repair broken products before replacing them with new ones (Kazancoglu et al., 2020; Morsetto, 2020).

Use of the same material in building more than once is referred to as reuse the same material for a different purpose (e.g., formwork in building) (Ling, Y.Y et al., 2000) as well as repurposing for a new function (e.g., shelves made of cut-corner steel bar; road made of stony fraction) (Duran, X et al., 2006) (basic material). After reduction, it is the most preferable choice since it requires the least amount of processing and a reduction in energy use. Recycling, according to (Tam, W.Y.V., 2008), may provide three benefits:(a) bringing down the interest for new assets. (b) bringing down transportation and assembling energy costs. (c) repurposing trash that would somehow or another end up in landfills.

The 3Rs can occur at any step of a construction project's life cycle throughout the whole project's life cycle Researchers from all around the globe have come up with a list of 11 methods that might aid with waste reduction. Normalization of design, stock control to decrease overordering, ecological instruction for workers, consideration of reusing and garbage removal organizations in the production network, on schedule/without a moment to spare conveyances, punishments for helpless waste administration, motivations and delicate charges for squander minimization, squander examining, expanded utilization of off-site procedures, utilization of on location compactors, reverse logistics. (Arif et al., 2010, 2009a; Dainty et al., 2010, 2009b).

2.3. Circular Economy Concept

The circular economy, or CE, is a business model that replaces the "end-of-life" concept—a stage of any product that does not receive continuing support, either because existing processes are terminated or because it has reached the end of its useful life with reducing or alternatively reusing, recycling, and recovering materials in the production/distribution and consumption processes. (Kirchherr, J. 2017)

The phrase "circular economy" is becoming more widely used. The phrase has been used in law in countries such as China and Germany, however the emphasis varies (Benton, 2015). Waste minimization and closed-loop recycling are key components (Bilitewski, 2012), whereas in Chinese policy, the term refers to eco-design, resource efficiency, and eco-industrial parks and networks to create a recycling-oriented society (Geng et al., 2012). Preconstruction, construction and building rehabilitation, collection and distribution, end-of-life, and material recovery and manufacturing are the five stages of the CE system in the construction and demolition sector (Ruiz, L et al., 2020).

There has been little study on how to apply circular economy ideas to the built environment in a whole system setting. The majority of research and activity in Europe has concentrated on waste generating end-of-pipe solutions (EC, 2011b; Yuan and Shen, 2011). This has resulted in an overall improvement in CDW management (Defra, 2015)

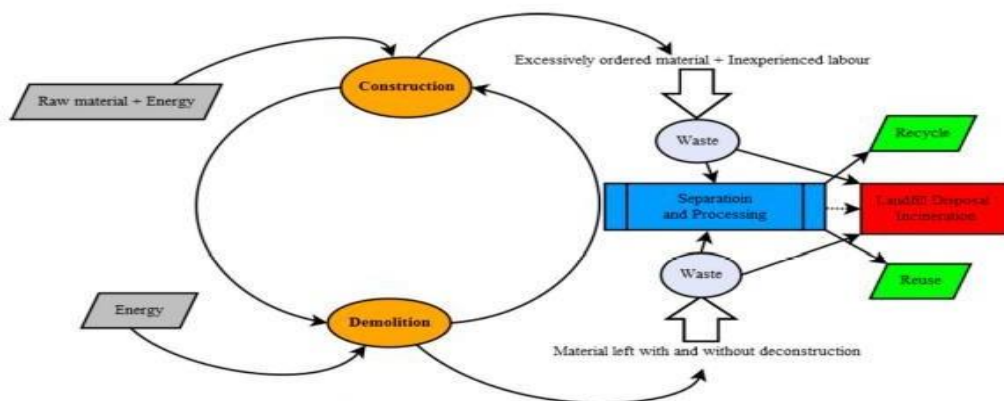
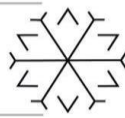
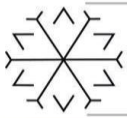


Figure 2: Whole process of Circular Economy Concept (Clarence P.,2020).

Figure-2 shows the whole process how construction waste can be reused and minimized. The purpose of a CE is to decrease, if not eliminate, the amount of CDW thrown in landfills and cremated, while simultaneously increasing the volume and quality of CDW recycling and reuse, as well as its potential for use in new construction (Ghaffar, S., 2020). Three tactics are required for an effective CE framework (Baldassarre, B., 2019): (a) narrowing resource loops—using less material in manufacturing to produce less trash at the conclusion of its life cycle. (b) slowing loops—this refers to the prolongation of the material's usage phase. (c) closing resource loops—this can also be referred to as material reusing.



3. BIM for Waste Management

Building Information Modelling (BIM) is a process that includes the creation and perpetuation of advanced portrayals of physical and utilitarian parts of spots and is upheld by an assortment of apparatuses, innovations, and agreements. Building Information models (BIMs) are PC documents that might be recovered, moved, or arranged to empower decision-production about a built resource (regularly however not generally in exclusive organizations and including restrictive information). People, associations, and government offices who plan, plan, develop, oversee, and keep up with structures and different actual frameworks use BIM software's.

BIM is a new technology that is reshaping the building industry throughout the world. Building Information Modelling (BIM) is quickly befitting the industry's standard design and duplication platform, with Industry Foundation Class (IFC) serving as an interchanging platform (Porter et al., 2014). Although there has been less work put towards incorporation waste condemnation into existing BIM tools and platforms like Revit, MicroStation, ArchiCAD, and Tekla, an effort has been made to construct BIM tools for waste estimates (Akinade et al., 2016; Bilal et al., 2016). Cheng and Ma (2013) created a BIM system that can extract construction materials and volume data for precise waste approximation and planning. Despite the study's restriction to BIM solutions for estimating waste disposal costs, it indicates a trend toward modifying the material ontology of current BIM tools or designing BIM compatible tools to perform waste reduction activities. As the wind of BIM adoptions keep on blowing across the industry, more research attention is likely to be directed toward the use of BIM technology for waste minimization.

BIM with 3D digital model visualisation and information management capabilities can also benefit with the collection, management, and utilization of a variety of data in Design for construction waste minimization (Osmani, Demian, & Baldwin, 2015; Lu, Webster, Chen, Zhang, & Chen, 2017a). It can provide a computational design for CWM if properly developed; anytime a design alternative is established, its CWM potential may be estimated for designers to evaluate. Furthermore, regenerative design, which is described as a process-oriented design approach that prioritizes the linked interaction between human and ecological systems (Cole, 2012), has the potential to increase Design for construction waste minimization performance and, in turn, establish a new paradigm in the industry.

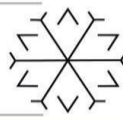
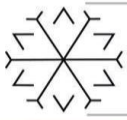
Porwal and Hewage (2012) created a tool for engineers to utilize to reduce the use of bar material in technical design as part of a research case study. For the structural engineer to utilize in the technical design phase, a BIM-assisted tool to decrease material wastage was created, with an emphasis on structural material reduction. According to (WRAP 2013), a case study based on implementing BIM to achieve resource efficiency, proposed the potential of BIM to assist in decreasing material wastage through its implementation at the early design stage. However, it lacked 48 instructions, which have been created for the BIM implementation on reducing material waste during design (WRAP 2013). A questionnaire survey conducted by (O'Reilly., 2012) states that BIM could assist architects with reducing material waste by the creation of informed design decisions during the concept and design stages. According to (WRAP 2013), a case study centered on adopting BIM to achieve resource efficiency, BIM has the potential to help reduce material waste by being implemented early in the design process. It did, however, miss 48 directions developed for BIM implementation on decreasing material waste during design (WRAP 2013). According to a questionnaire survey done by (O'Reilly 2012), BIM can help architects reduce material waste by allowing them to make more informed design decisions throughout the idea and design stages.

4. Factors of Generating Construction Waste

Not all of the faults which happens on site cause construction waste. Materials that are damaged or excess can frequently be recovered and repurposed, or simply resold to the materials' vendor. However, the wastes that are generated can be recycled. Typically, this is due to a lack of proficiency in one of the following areas:

4.1. Design Change

Mistakes and faults in design are the 1st leading cause of building waste. This backs up a conclusion by Wan et al., (2009), which revealed that "design flaws" are a primary cause of change orders and rework, resulting in a large amount of construction waste. Furthermore, Australian researchers found a similar effect in his study and classified common construction waste causes as design modification and design mistake (Faniran et al., 2007). Furthermore, study in China discovered that design flaws resulted in reworks. This



is another truth backed up by the research, as rework is a waste due to design flaws and errors (Zhao et al., 2003). As a result, a researcher in the United States noticed and grouped the causes of construction waste into design (Gavilan et al., 1994). A comparable survey found that typical construction waste causes are classified into two parts: design mistake and design change (Faniran et al., 2007). During the building period, a committee should be in charge of waste management and handling. Prior to the start of the project, the company should demand that all documentation and drawings be completed. This minimizes the need for next design changes (Arif M et al., 2012).

4.2. Improper Site Management

The top cause generating construction waste, according to the Mean Rank Value of 7.17, was poor site management and monitoring. This assertion is backed up by evidence as in Wang et al., (2008), Chinese research. They said that there was a lack of Management abilities and a lack of monitoring combine to create significant contributors to massive waste creation Furthermore, lack of monitoring was noted as a problem in Chile for generating waste (Serpell et al., 1995). In a recent study, it was also noted that poor construction also results in waste (Lu et al., 2011). In addition, pilot research was carried out in Sri Lanka, stating that a significant proportion of the majority of construction waste is caused by poor planning, site management and supervision (Jayawardane et al., 1998).

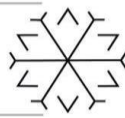
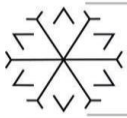
4.3. Immaturity of Waste Recycling Industry

The term "industrial life cycle" refers to the process by which each industry evolves from its creation through its decline (Li et al., 2018). Yongbyon Su (2020) stated that The CW recycling industry's life cycle is divided into four stages: beginning development, ongoing stages, mid-development, and mature development. As Pakistan is a developing country so the construction waste is normally dumped into open area as well as canals. In order to handle this situation Pakistan government agency has created waste recycling industry (WRI). As there is no check and balance so this industry is not working as much as they need to do, because of which we are far away from sustainability. As this industry don't have proper policies from government agencies on which they can work. On the other-hand they don't have good connections with contractors which cause it to move towards waste generation.

5. CONCLUSION:

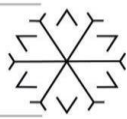
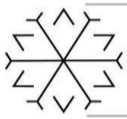
In this paper, we present different techniques which we can adopt for construction waste minimization and concluded that:

- Train construction team for waste handling and its minimization.
- Reuse Reduce and Recycle waste material by utilizing it in construction.
- Circular economy concept facilities in producing less trash and prolongation of material usage.
- Normalize using BIMs to get on-time update about any change in design.
- Develop different policies for waste recycling.



References

- Ajayi, S.O., Oyedele, L.O., Bilal, M., Akinade, O.O., Alaka, H.A. and Owolabi, H.A., 2017. Critical management practices influencing on-site waste minimization in construction projects. *Waste management*, 59, pp.330-339.
- Akinade, O.O., Oyedele, L.O., Munir, K., Bilal, M., Ajayi, S.O., Owolabi, H.A., Alaka, H.A. and Bello, S.A., 2016. Evaluation criteria for construction waste management tools: towards a holistic BIM framework. *International Journal of Sustainable Building Technology and Urban Development*, 7(1), pp.3-21.
- Arif, M., Bendi, D., Toma-Sabbagh, T. and Sutrisna, M., 2012. Construction waste management in India: an exploratory study. *Construction innovation*.
- Arif, M., Egbu, C., Alshawi, M., Srinivas, S. and Tariq, M., 2010. Promoting green construction in India through industry-academia collaboration. *Journal of Professional Issues in Engineering Education and Practice*, 136(3), pp.128-131.
- Arif, M., Egbu, C., Haleem, A., Ebohon, J., & Khalfan, M. M. (2009). Green construction in India: Gaining a deeper understanding. *Journal of architectural engineering*, 15(1), 10-13.
- Baldassarre, B., Schepers, M., Bocken, N., Cuppen, E., Korevaar, G. and Calabretta, G., 2019. Industrial Symbiosis: towards a design process for eco-industrial clusters by integrating Circular Economy and Industrial Ecology perspectives. *Journal of cleaner production*, 216, pp.446-460.
- Bendi, D., 2010. Challenges and the best practices of waste management in green building construction in India. *unpublished MSc thesis, University of Salford, Manchester*.
- Benton, D., 2015. Circular Economy Scotland. *Green Alliance*, pp.1-23.
- Benton D., Coats E., & Hazell J. 2015. A circular economy for smart devices. Green alliance, London, UK.
- Bilal, M., Oyedele, L.O., Qadir, J., Munir, K., Akinade, O.O., Ajayi, S.O., Alaka, H.A. and Owolabi, H.A., 2015. Analysis of critical features and evaluation of BIM software: towards a plug-in for construction waste minimization using big data. *International Journal of Sustainable Building Technology and Urban Development*, 6(4), pp.211-228.
- Bilitewski, B., 2012. The circular economy and its risks. *Waste management*, 1(32), pp.1-2.
- Boon, E.K. and Anuga, S.W., 2020. Circular economy and its relevance for improving food and nutrition security in Sub-Saharan Africa: The case of Ghana. *Materials Circular Economy*, 2(1), pp.1-14.
- Cheng, J.C. and Ma, L.Y., 2013. A BIM-based system for demolition and renovation waste estimation and planning. *Waste management*, 33(6), pp.1539-1551.
- Cole, R.J., 2012. Transitioning from green to regenerative design. *Building Research & Information*, 40(1), pp.39-53.
- Dainty, A.R. and Brooke, R.J., 2004. Towards improved construction waste minimisation: a need for improved supply chain integration?. *Structural Survey*.
- Defra., 2015 UK Statistics on Waste. Defra, London, UK
- Doust, K., Battista, G. and Rundle, P., 2021. Front-end construction waste minimization strategies. *Australian Journal of Civil Engineering*, 19(1), pp.1-11.
- Duran, X., Lenihan, H. and O'Regan, B., 2006. A model for assessing the economic viability of construction and demolition waste recycling—the case of Ireland. *Resources, Conservation and Recycling*, 46(3), pp.302-320.
- Faniran, O.O. and Caban, G., 1998. Minimizing waste on construction project sites. *Engineering, construction and architectural management*.
- Ginga, C.P., Ongpeng, J.M.C., Daly, M. and Klarissa, M., 2020. Circular economy on construction and demolition waste: A literature review on material recovery and production. *Materials*, 13(13), p.2970.
- Ginga, C.P., Ongpeng, J.M.C., Daly, M. and Klarissa, M., 2020. Circular economy on construction and demolition waste: A literature review on material recovery and production. *Materials*, 13(13), p.2970.
- Geng, Y., Fu, J., Sarkis, J. and Xue, B., 2012. Towards a national circular economy indicator system in China: an evaluation and critical analysis. *Journal of cleaner production*, 23(1), pp.216-224.
- Ghaffar, S.H., Burman, M. and Braimah, N., 2020. Pathways to circular construction: An integrated management of construction and demolition waste for resource recovery. *Journal of cleaner production*, 244, p.118710.
- Jayawardane, A.K.W., 1998. Material and labour wastage on Sri Lankan construction sites. *Journal of Construction Management*, 13, pp.221-239.



- Kirchherr, J., Reike, D. and Hekkert, M., 2017. Conceptualizing the circular economy: An analysis of 114 definitions. *Resources, conservation and recycling*, 127, pp.221-232.
- Kolaventi, S.S., Momand, H., Tadepalli, T. and Siva Kumar, M.V.N., 2020, February. Construction waste in India: a structural equation model for identification of causes. In *Proceedings of the Institution of Civil Engineers-Engineering Sustainability* (Vol. 173, No. 6, pp. 303-314). Thomas Telford Ltd.
- Li, X., Alam, K.M. and Wang, S., 2018. Trend analysis of Pakistan railways based on industry life cycle theory. *Journal of Advanced Transportation*, 2018.
- Ling, Y.Y. and Leo, K.C., 2000. Reusing timber formwork: importance of workmen's efficiency and attitude. *Building and Environment*, 35(2), pp.135-143.
- Lu, W., Webster, C., Chen, K., Zhang, X. and Chen, X., 2017. Computational Building Information Modelling for construction waste management: Moving from rhetoric to reality. *Renewable and Sustainable Energy Reviews*, 68, pp.587-595.
- Morseletto, P., 2020. Targets for a circular economy. *Resources, Conservation and Recycling*, 153, p.104553.
- Osmani, M., 2015. *Integration of waste minimisation strategies into the design process of buildings* (Doctoral dissertation, Loughborough University).
- Porter, S., Tan, T., Tan, T. and West, G., 2014. Breaking into BIM: Performing static and dynamic security analysis with the aid of BIM. *Automation in Construction*, 40, pp.84-95.
- Tam, V.W., 2008. On the effectiveness in implementing a waste-management-plan method in construction. *Waste management*, 28(6), pp.1072-1080.
- Porwal, A. and Hewage, K.N., 2012. Building information modeling-based analysis to minimize waste rate of structural reinforcement. *Journal of construction engineering and management*, 138(8), pp.943-954.
- Serpell, A., Venturi, A. and Contreras, J., 1995. Characterization of waste in building construction projects. *Lean construction*, pp.67-77.
- Su, Y., 2020. Multi-agent evolutionary game in the recycling utilization of construction waste. *Science of The Total Environment*, 738, p.139826.
- Wan, S.K., Kumaraswamy, M.M. and Liu, D.T., 2009. Contributors to construction debris from electrical and mechanical work in Hong Kong infrastructure projects. *Journal of Construction Engineering and Management*, 135(7), pp.637-646.
- WRAP., 2013a. BIM (Building Information Modelling) utilization to achieve resource efficiency in construction: Leeds Arena
- Yuan, H. and Shen, L., 2011. Trend of the research on construction and demolition waste management. *Waste management*, 31(4), pp.670-679.
- Zhao, Y. and Chua, D.K., 2003, July. Relationship between productivity and non-value-adding activities. In Proceeding of the 11th annual conference of the international group for lean construction, Blacksburg, Virginia, USA.

TYPES OF CONSTRUCTION WASTE, THEIR CONTRIBUTIONS TO THE ECONOMY AND SUSTAINABILITY OF THE PROJECT

Ali Hassan Nasir ¹*[0000-0000-0000-0000] and Usman Hussain ²[0000-0000-0000-0000]

¹bce183051@cust.pk, BS Student

²Usman.hussain@cust.edu.pk, Associate lecturer

ABSTRACT:

Construction materials are very vital to the whole process of building, demolishing, reshaping, and providing the foundations for the basics of a civilization. A structural member owes its value and strength to a combination of construction materials. These materials are transported on to the construction sites in quite sizeable quantities as they are a fundamental part of the construction industry. These materials are needed during different phases of the construction cycle. Often those involved in the construction industry are faced with a problem where materials that are initially intended to become useful become a part of group which is neither economical nor environmentally sustainable. This fact can be realized during and after the construction. In order to address this issue in a more effective manner, identification of the issue by tracing back sources and causes of the various materials is important. The weightage of each waste material and its impact on the environment also needs to be known. This has been the purpose of this study. After the appropriate information was gathered, a review on how these materials can be managed in a way that they are in coherence with the sustainability pillars was done. This work has been done with an aim to be able to portray a better and clearer picture of the issue of the construction materials that eventually go on to become waste materials. By providing a picture that facilitates the understanding of the issue, the readers can also correlate the environmentally sustainable goals of the modern society which can enable them to deal with several other issues.

Keywords: Construction waste management, Environmental Sustainability, Waste management, Construction Industry

1. Introduction

While the construction is underway there are several materials that are being used at a time or with a particular order. Some materials are used in their original form while are others are mixed and a combination of number of materials is created in order to attain an independent homogenous product. For example, bricks are used in their original form and are used in brick masonry. While cement, sand and aggregate are added together to get concrete which is an independent homogenous material. The aforementioned materials are some of the various materials that are used on a construction site. There are several other materials that are a vital part of construction industry depending upon the type of construction work that is being carried out. The materials ordered or prepared on a construction site vary over a wide range. Although, the construction that is being carried out has specific objectives that need to be fulfilled. So, in order to meet those objectives, a variety of materials are present on a construction site (Boussink et al, 1997).

For instance, the construction of a building that is objected to provide residence to hundreds of people say, a building consisting of residential apartments is to be constructed. The building of this sort would need basic as well as the secondary necessities in order to accommodate the future inhabitants of this building. For this purpose there will be a wide range of materials that will be ordered and present on site during and even after most of the construction is done. (Liu et al, 2020)

As Civil Engineers we have witnessed that the materials that are used during the construction works are either in excess or are not treated or managed in a way that can be regarded as sustainable. In fact, waste generated on the construction site constitutes of a greater part of the solid waste that is generated worldwide. Either it is overordering of the virgin materials or the disposing off of the materials that are made on the



construction sites, the generation of waste is an inevitable issue. But efforts could be made to minimize the waste generation.

2. Sources of Construction Waste

Construction Industry accounts for the 35% of the industrial waste generated all over the world (Osmani et al, 2008). Waste materials such as rubbles etc arise from construction practices. Whether they are demolition, renovation or an entirely new construction. The construction industry is traditionally environment friendly. But, the traditional construction practices contribute to waste generation when trade contractors are rewarded for speed rather than their environmental impact of their work.

Every year, the building sector utilises 40% of raw stone, sand, and gravel, as well as 25% of virgin wood. According to a survey on construction in the United Kingdom, labour is only employed to half of its potential, and at least 10% of building materials are squandered. According to Osmani et al., project design accounts for roughly 33% of waste. This study opted to analyse the identified sources of construction waste in terms of their waste contributions and impacts after identifying the sources of construction waste. Gavilan and Bernold classified construction waste into six categories in the United States: (1) design; (2) procurement; (3) material handling; (4) operations; (5) residuals; and (6) others. Ekanayake and Ofori backed these six and categorised them into four categories: design, operations, material handling, and procurement. According to Navon and Berkovich (2012), a common problem on major building projects is a lack of up-to-date information on on-site supplies; due to a lack of knowledge about supply and placement of materials on site, the same items are ordered again, resulting in waste. Furthermore, waste can accumulate at any stage of development due to a variety of variables, including building operations as well as external factors such as theft and vandalism.

The above mentioned categories have been further sub divided so that the actual source of each category can be traced. Basic construction practices are coherent all across the globe. Keeping this perspective, this study has kept a parity between the results obtained that are shown in the table below and the results of our own results.

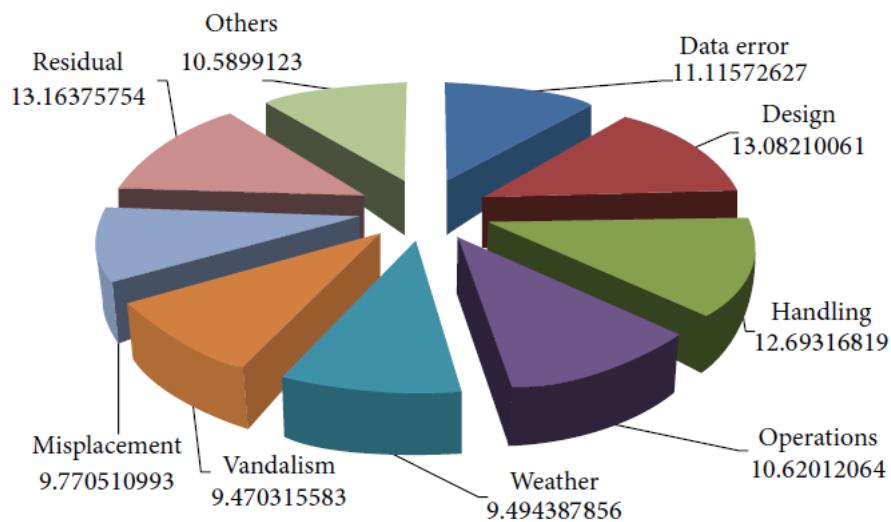
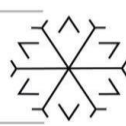
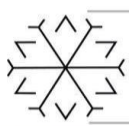


Figure: Rate of contribution of different waste materials

Table 1: Sources of Construction waste



Sources of waste	Causes
Procurement	Errors in ordering, resulting in disposal of waste on sites
Design	Design Changes, faulty documentation
Material Handling	Inappropriate storage, transportation and offloading
Operations	Installing the wrong materials and having to remove them is an example of a tradesperson's blunder.
Weather	Temperature, weather conditions
Vandalism	Inadequate security
Misplacement	Abandoning of materials
Residual	Cutting of materials
Others	Absence of waste management plan

Despite the fact that considerable research efforts have been done for the identification of the sources of construction waste, there is a need for research targeting the analysis of the identified sources in terms of their waste contribution rates and impacts.

There are a number of waste materials that can be seen on various construction sites:

- Concrete
- Bricks
- Ceramic and Tiles
- Wood
- Insulation Materials
- Glass
- Plastic
- Ferrous/Non-Ferrous Metals
- Stone and Clay
- Soil
- Paint

Some of these materials have been explained below.

1.1 Bricks

Bricks are essential in almost every aspect of construction industry. Although, they also account for a decent part of the waste generated at the construction sites. Bricks could either be from pre-existing structures on the site. But the bricks that become a part of construction waste material are usually the broken off pieces or the overordered bricks. Bricks obtained from demolition of old buildings need proper care for them to stay usable in near or far future. This might reduce our construction speed but, that is not the scope of our study.

The quality of bricks also matters to how many ordered bricks will be a part of the project and what percentage of them will become a part of the construction waste. Lower quality bricks will break into pieces that are almost unusable. These bricks will most probably be a part of the construction waste. Although, if the project is planned in a way that the bricks that are unusable directly in the brick masonry, can be used as fill material for foundations.

1.2 Concrete



Concrete is the most frequent type of construction trash, accounting for approximately 67.5 percent of all building and demolition waste by weight. As a recyclable material, crushed reinforced concrete is in high demand. Crushed concrete aggregate, often known as sand and gravel in the industry, can be used to replace new material in new concrete. (Boussink et al. 1997). Faulty calculations of the concrete to be used is also a cause of concrete contributing to the overall construction waste generation.

Especially in Pakistan, where an error in design is usually covered up by excessive concreting also leads to the problem of concrete going to waste. This not only causes the reordering of the constituents of the concrete but also an overall add on to the waste generated on construction site. Moreover, the transport of the materials required for the preparation of concrete also have an impact on the environment which make the construction practice unsustainable. (Bakchana et al. 2019)

1.3 Glass

Glass is often seen as a waste material on construction sites. Whether it is generated from demolition works or from the mishandling of the newly ordered glass, it is one of the most important waste materials that needs to be managed in a way that it does not create any safety issues for the on-site workers. (Butler et al. 2019)

1.4 Wood

Wood, often from roof beams, wall supports, and torn-up hardwood floors, makes up a significant portion of construction debris. After a new building project is completed, it may leave behind leftover wood or generate wood shavings and waste. (Udoeyo et al. 2004)

1.5 Metals

Ferrous metal, iron and its alloys, such as steel — often comes from old pipes in demolition projects. It has a high value for reuse and recycling.

Other than iron, nonferrous metals have a high recyclability and reuse value. Ferrous metals like aluminum, copper, lead and zinc are common in pipes and components like nails and rebar. Electrical wiring also contains valuable recyclable metals like copper and aluminum. (Man et al. 2010)

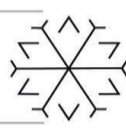
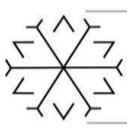
2. Benefits of minimizing Construction Waste

Because materials can account for up to half of a project's cost (Kong et al. 2001), a construction project's success and profitability are mainly determined by how well its materials buy is managed. This means that not only is excellent material acquisition coordination necessary for waste mitigation, but it is also critical for the project's overall success. Tam (2008), on the other hand, recognised procurement management as a useful tool for decreasing waste in building projects. Other research have shown a number of ways in which materials purchases might be effectively used to reduce waste. Before ordering supplies, it is critical to address actions that could lead to incorrect purchases (Bernold et al. 1991; Muhwezi et al., 2012).

The findings show that the most important procurement and materials logistics technique for minimising waste is the take back programme, which is a mutual agreement between the project team and suppliers to return unwanted goods at the end of building operations. As a result of this collaboration, waste from wasted materials would be significantly reduced. Materials leftover account for a large amount of overall waste generated by construction activities, according to Osmani et al. (2008) and Oyedele et al. (2013). As a result, the promise to take back scheme is capable of reducing the volume of waste landfilled by the construction industry in addition to returning reusable goods to the market.

Another top logistical technique for diverting waste from landfill is to utilise minimal packaging for construction supplies. Materials suppliers are expected to support procurement techniques that reduce packaging waste because packaging waste accounts for a large amount of construction garbage (Yeheyis et al., 2013; Saez et al., 2011). This will help you avoid one of the most prevalent sources of waste in construction projects. Nonetheless, it is expected that a balance will be achieved between minimal and insufficient packing, the latter of which might lead to material breakdown.

2.1 Cost Reduction



After reviewing the literature, it has been found out that waste minimization has several benefits. Under this heading, its economic aspect will be discussed. Ordering material in a manner where it does not affect the overall speed of the project and it also does not create a problem to manage materials in a way where they eventually go on to become a part of on-site construction waste. (Ann et al. 2017)

If the waste minimization is given the appropriate method, it can also lead to the lower construction costs. This will reduce the revenues allocated for any project. The amount of money spent on materials can be reduced by evaluating the need of the material during a specific phase of construction. This will reduce the material going on to become waste.

An efficient waste management plan does not only make our project sustainable and environment friendly but also it makes it economical.

2.2 Environmental Sustainability

Weak waste management policies have created an issue that have severe impacts on our environment. Their effects are rather long lasting and create problems that can alter the future of earth for us and for the generations to come. Identification of the waste materials is a primary step to creating a framework for the better management of construction waste on sites. Once we have determined the sources and the effects of each source on our environment, the work done in order to mitigate the issue will be a lot more effective. (Hasmori et al. 2020)

Once a decent amount of information has been gathered regarding the issue, efforts can be done to counter it. As it has been discussed on how to assess and mitigate those issues, here only the environment sustainability of the work discussed before will be discussed. Dealing with the issue in an effective manner can increase the probability of the construction projects being more eco friendly and sustainable. If we manage to identify the exact root cause and trace back the sources of about 85% of the materials available on the construction sites, we can develop a framework to make our project be more sustainable and less damaging to the environment. (Somrat et al. 2017)

3. Implementation of Construction waste management in Pakistan

Weak waste management policies have created an issue that have severe impacts on our environment. Their effects are rather long lasting and create problems that can alter the future of earth for us and for the generations to come. Identification of the waste materials is a primary step to creating a framework for the better management of construction waste on sites. Once we have determined the sources and the effects of each source on our environment, the work done in order to mitigate the issue will be a lot more effective. (Hasmori et al. 2020)

Once a decent amount of information has been gathered regarding the issue, efforts can be done to counter it. As it has been discussed on how to assess and mitigate those issues, here only the environment sustainability of the work discussed before will be discussed. Dealing with the issue in an effective manner can increase the probability of the construction projects being more eco friendly and sustainable. If we manage to identify the exact root cause and trace back the sources of about 85% of the materials available on the construction sites, we can develop a framework to make our project be more sustainable and less damaging to the environment. (Somrat et al. 2017)

4. Discussion

On construction sites, enormous amounts of garbage are generated. And, in order to address the problem, a number of eminent authors have conducted study that helps us better grasp the situation. This work has gone in the same direction, with distinctiveness playing an important role. Waste generated on construction sites can never be completely prevented. However, efforts can be taken to reduce it to the point that it has no substantial impact on the project's economic viability or the environment's long-term sustainability. This work's main objective has been to assist people better grasp the problem, address it, and then solve it.

5. Conclusion

It has been concluded from this work after reviewing the literature published on the respective topic that:



- Identification of the Waste generation and their sources need to be addressed
- Contribution of each waste material needs to be analyzed, and their effect on the cost of the project before and after.
- Concrete being the major waste material should be minimized going to waste and the inevitable waste needs to be reused.
- Waste management execution in an effective manner so as to ensure sustainable construction.

6. References

Ajayi, S.O., Oyedele, L.O., Akinade, O.O., Bilal, M., Alaka, H.A., Owolabi, H.A. and Kadiri, K.O., 2017. Attributes of design for construction waste minimization: A case study of waste-to-energy project. *Renewable and Sustainable Energy Reviews*, 73, pp.1333-1341.

Ajayi, S.O., Oyedele, L.O., Akinade, O.O., Bilal, M., Owolabi, H.O. and Alaka, H.A., 2014, December. Ineffectiveness of construction waste management strategies: Knowledge gap analysis. In Okeil, M.(2014). *Smart, sustainable and healthy city, Proceedings of the First International Conference of the CIB Middle East and North Africa Research Network (CIB-MENA 2014)* (pp. 261-280).

Ajayi, S.O., Oyedele, L.O., Akinade, O.O., Bilal, M., Alaka, H.A. and Owolabi, H.A., 2017. Optimising material procurement for construction waste minimization: An exploration of success factors. *Sustainable materials and technologies*, 11, pp.38-46.

Bakchan, A., Faust, K.M. and Leite, F., 2019. Seven-dimensional automated construction waste quantification and management framework: Integration with project and site planning. *Resources, Conservation and Recycling*, 146, pp.462-474.

Bossink, B.A.G. and Brouwers, H.J.H., 1996. Construction waste: quantification and source evaluation. *Journal of construction engineering and management*, 122(1), pp.55-60.

Butler, J.H. and Hooper, P.D., 2019, January. Glass waste. In *Waste* (pp. 307-322). Academic Press.

Cha, H.S., Kim, J. and Han, J.Y., 2009. Identifying and assessing influence factors on improving waste management performance for building construction projects. *Journal of construction engineering and management*, 135(7), pp.647-656.

Fadiya, O.O., Georgakis, P. and Chinyio, E., 2014. Quantitative analysis of the sources of construction waste. *Journal of Construction Engineering*, 2014, p.9.

Hasmori, M.F., Zin, A.F.M., Nagapan, S., Deraman, R., Abas, N., Yunus, R. and Klufallah, M., 2020. The on-site waste minimization practices for construction waste. In *IOP Conference Series: Materials Science and Engineering* (Vol. 713, No. 1, p. 012038). IOP Publishing.

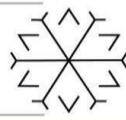
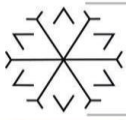
Kerdsuwan, S., Laohalidanond, K. and Jangsawang, W., 2015. Sustainable development and eco-friendly waste disposal technology for the local community. *Energy Procedia*, 79, pp.119-124.

Liu, J., Yi, Y. and Wang, X., 2020. Exploring factors influencing construction waste reduction: A structural equation modeling approach. *Journal of Cleaner Production*, 276, p.123185.

Osmani, M., Glass, J. and Price, A.D., 2008. Architects' perspectives on construction waste reduction by design. *Waste management*, 28(7), pp.1147-1158.

Man, Y.B., Sun, X.L., Zhao, Y.G., Lopez, B.N., Chung, S.S., Wu, S.C., Cheung, K.C. and Wong, M.H., 2010. Health risk assessment of abandoned agricultural soils based on heavy metal contents in Hong Kong, the world's most populated city. *Environment international*, 36(6), pp.570-576.

Gavilan, R.M. and Bernold, L.E., 1994. Source evaluation of solid waste in building construction. *Journal of construction engineering and management*, 120(3), pp.536-552.



Navon, R. and Berkovich, O., 2006. An automated model for materials management and control. *Construction Management and Economics*, 24(6), pp.635-646.

Udoeyo, F.F., Inyang, H., Young, D.T. and Oparadu, E.E., 2006. Potential of wood waste ash as an additive in concrete. *Journal of materials in civil engineering*, 18(4), pp.605-611.

Wang, J., Li, Z. and Tam, V.W., 2015. Identifying best design strategies for construction waste minimization. *Journal of Cleaner Production*, 92, pp.237-247.

Wang, J., Li, Z. and Tam, V.W., 2014. Critical factors in effective construction waste minimization at the design stage: a Shenzhen case study, China. *Resources, Conservation and Recycling*, 82, pp.1-7.

Yeheyis, M., Hewage, K., Alam, M.S., Eskicioglu, C. and Sadiq, R., 2013. An overview of construction and demolition waste management in Canada: a lifecycle analysis approach to sustainability. *Clean Technologies and Environmental Policy*, 15(1), pp.81-91.

Modeling of COVID-19 Pandemic with Artificial Neural Network: A Case Study for Turkey and the USA

Ömer Faruk Çaparoglu ¹[0000-0001-7216-6198], Nadide Çağlayan ²[0000-0001-7847-3439],

Merve Kayacı Çodur ²[0000-0003-1459-9678] and Mahmut Tutam ³[0000-0002-2018-5458]

¹omer.caparoglu@erzurum.edu, Department of Industrial Engineering, Erzurum Technical University

²nadide.caglayan@erzurum.edu, Department of Industrial Engineering, Erzurum Technical University

³merve.codur@erzurum.edu.tr, Department of Industrial Engineering, Erzurum Technical University

⁴mahmut.tutam@erzurum.edu.tr, Department of Industrial Engineering, Erzurum Technical University

Abstract

Throughout history, human beings faced and suffered from serious outbreaks and epidemics over different geographical regions. As a result of urbanization and globalization, the entire world started grappling with the deadliest pandemics over the last century. Hence, the improvement of governance in countries to control pandemics became more important than ever before in human history. Recently, the increasing number of Covid-19 variants revealed the importance of compatibility and synchronization of non-pharmaceutical interventions or vaccination strategies across countries even though unique country-specific implementations. In this study, the ANN-based models are utilized to identify relationships between input and output data. Five input datasets (date, daily test number, reproduction number, vaccination rate, stringency index) are used to accurately predict the output dataset (positive rate) for the time period from April 1, 2020 to November 15, 2021. Mean Absolute Percentage Error (MAPE) and Determination Coefficient (R²) are employed to evaluate performances of different network designs. Hence, the best Artificial Neural Network designs of two countries, namely Turkey and the USA, are determined.

Keywords. Covid-19, Machine Learning, ANN

Effect of Elastic Foundation on The Vibration of Non-Homogeneous Orthotropic Shell Geometry

Raafat Sameer Sadeq¹*[0000-0002-4209-3423], Prof. Dr. Mustafa Ozakca²[0000-0003-1544-8126]

and Esra E. Karatas³[0000-0003-1396-2463]

¹raafatmady2021@gmail.com, Ministry of Higher Education, Iraq

²ozakca@gantep.edu.tr, Civil Engineering Department, Gaziantep University, Gaziantep, Turkey,

³ekaratas@gantep.edu.tr, Civil Engineering Department, Gaziantep University, Gaziantep, Turkey

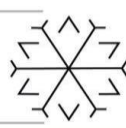
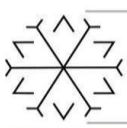
Abstract

A shell is a structure element which is characterized by its geometry. Its used in many engineering structure fields due to its thin thickness compared to its length and width. the present research studies the free vibration characteristics of non-homogeneous orthotropic thin circular cylindrical shells resting on elastic foundation. The study is divided into four groups, the first group analyzes the circular cylindrical shells, the second group analyzes the orthotropic cylindrical shells and the third group analyzes the cylindrical shells on elastic foundation and the fourth group analyzes the different cylindrical shells geometry. All the groups are tested by using ANSYS software as a tool for finite element investigation. The results show that when the value of foundation modulus increases, the frequency values increase. Also, when the shell thickness increases, the values of natural frequency increase; in addition to the layer's increase which changes the frequency based on the layer's design conditions. Moreover, when the length of circular cylindrical shells increase, the frequency decrease.

Keywords: cylindrical shells, elastic foundation, natural frequency, orthotropic material.

1. Introduction

Circular shells represent one of the principal elements in engineering, particularly in civil, mechanical, architectural, aeronautical, and marine engineering. Examples of the shell structures in civil and architectural engineering are large-span roofs, liquid-retaining structures and water tanks, containment shells of nuclear power plants, and concrete arch domes (Rawat, et al., 2016). The curved geometry of shells presents a high structural efficiency and allows them to be very thin. The forces induced through dynamic actions are considered relatively low because of direct proportional to the mass of the shell. The overall shape geometry is the most important factor of the design parameters. For instance, support conditions, thickness, type of material, and overall shape can determine the shell in terms of stability, safety and stiffness due to space of span and without intermediate supports (Michiels and Adriaenssens, 2017). In the present study, the non-homogeneous materials considered as the material properties that vary as a function when subjected in specific body position. The used non-homogeneous function position correlated with the orthotropic material properties. The orthotropic materials mean that the materials have different properties along three perpendicular axes. In shell structural behavior, the subjected load produces a basic displacement with basic stress. This disturb the elastic equilibrium of the shell structure by imposing a small additional deformation and lateral deflection. For that, the main objective in shell design is to find a form that can present a specific properties of the material and the design conditions (Tomas & Marti, 2010). The main shell design conditions are considered the material properties. There are two types of shell structure materials, the homogeneous materials and non-homogeneous materials. The non-homogeneous materials are of considerable interest to design engineers in various technological situations (Sofiyeld et al., 2014). Their design requires an accurate analysis for their stability characteristics. The non-homogeneity of material properties across the thickness of shells introduces additional difficulties and thus draws additional attention. Massalas et al. (1981) have studied the dynamic instability of truncated conical shells under periodic compressive forces with the elasticity modulus as a linear function of thickness coordinate. Recently, Sofiyev & coworkers (2004) proposed a model in which, the Young's moduli and density of the orthotropic materials of the shells are assumed to vary continuously and piecewise continuously in the thickness coordinate and have solved the dynamic and static stability problems of single-layer and laminated orthotropic cylindrical and conical shells with simple or freely supported edges. The mechanical response of shell structure is affected by martial choice and constituents. Nevertheless, the shape shell structure plays an important role in shell structure design. The state of the art researches aim to achieve desired structural requirements by finding optimal geometry. For this purpose, it is



possible to change the bending response, modify the buckling behavior, and influence the vibration characteristics by varying the shape of a shell structure. The assignment of a variable thickness of the shell allows to modify the shell structure stiffness by redistributing the materials within the reference domain. Variable thickness can improve the properties of shell structure by increasing the stiffness where the stresses are high. Efraim and Eisenberger in 2010 studied the natural frequencies of thick spherical shell panels based on variable thickness with various boundary conditions (Efraim and Eisenberger, 2010.) Jiang and Redekop in 2003 also studied the free vibrations of orthotropic shells by means of a semi-analytical differential quadrature method. In this study, the variable thickness profile is defined by a sinusoidal variation and the results are obtained for different geometric configurations (Jiang and Redekop, 2003.)

In the practical application of (Psotny and Havran, 2017), the circular shells were subjected to various loads such as radial and axial loads. These loads affected the circular shell foundation. The relatively crude mechanical representation of soil foundation was firstly introduced by Winkler, in 1867 (Teodoru, 2015). Theoretically, the main characteristic of the Winkler model is that the underlying foundations are assumed to be simulated as a series of independent linear springs rested by the beam (Liu and Ma, 2013). Elastic foundation model is the elastic layer of infinite extent resting on a rigid base and composed by an infinite sequence of elastic column. The foundation is rather a complex medium such as rubber-like fuel binder, or a fluid boundary layer or a granular solid. The response of the foundation at the contact area was provided at the end of the 19th century (Winkler, 1867). One of the most important deficiencies of the Winkler model is that a displacement discontinuity appears between the loaded and the unloaded part of the foundation surface. In reality, the soil surface does not show any discontinuity (Teodoru, 2015). In the most situations, the influences of normal force, shear force, distributed moment and temperature can be neglected (or the beam is not exposed to them) as stated by Aleali (2010) and Frydrýšek and Gondek (2013). For that reason, this research investigates and discusses the free vibration characteristics of non-homogeneous orthotropic thin circular cylindrical shells resting on elastic foundation. The experimental program presents thirty-two simulation test that involves deformation modes, different orthotropic cylindrical shells and different cylindrical shells geometry. The tests take into consideration the effect of Winkler and Pasternak foundation.

2. Formulation of the Problem

The free vibration response of any system can be obtained by analyzing the governing equation of motion for the system. This can be obtained from the equations below (Chen, 2014):

$$[M]\{\ddot{U}\} + [K]\{U\} = \{0\} \quad (1)$$

In which [M] and [K] are the mass and stiffness matrices of the system, respectively; and {U} is the displacement vector. Therefore, the natural frequencies (ω) and the mode shapes $\{\phi\}$ of any system governed by Equation (1) are the solutions of the eigenvalue problem represented by the equation:

$$[[K] - \omega^2[M]]\{\phi\} = \{0\} \quad (2)$$

For non-trivial solution of Equation (Rensburg et al, 2006):

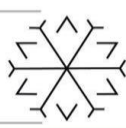
$$[[K] - \omega^2[M]] = 0 \quad (3)$$

Equation (3) is called the frequency equation of the system. Expanding the determinant will give an algebraic equation on the m degree in the frequency parameter ω^2 for a system having m degrees of freedom. The mth roots of this equation ($\omega_1^2, \omega_2^2, \omega_3^2, \dots, \omega_m^2$) represent the frequencies of m modes of vibration which are possible in the system. The axes of orthotropic in all layers are parallel to x and y axes. The equations of motion of circular cylindrical thin shells resting on an elastic foundation are as follows (Sofiyev et al, 2014):

$$N_{11,x} + N_{12,y} = \rho_1 h_{1u_u} \quad (4)$$

$$N_{21,x} + N_{22,y} = \rho_1 h_{1v_u} \quad (5)$$

In which when $h_l = 2h$, a comma denotes partial differentiation with respect to the corresponding coordinates. N_{11}, N_{12} and N_{22} are, respectively, the axial and circumferential normal forces and the accompanying shear force; M_{11}, M_{22} and M_{12} are, respectively, the bending moments in axial and circumferential directions and the accompanying twisting moment, u, v and w are, respectively, the displacements on the reference surface in the



directions of x, y and z axes. I represent time coordinate, ko is foundation modulus and the following definitions apply (Sofiyev et al,2014):

$$\rho_1 = \sum_{k=1}^N \frac{\rho_o^k}{N} \tag{6}$$

In which p(k)o are the densities of the homogeneous materials in the kth layer. The Kirchhoff hypothesis on non-deformable normal element and Karman type geometric non-linearity are taken into account. In that case, in large deformation the stress-strain relations for a thin laminated layer, which has non-uniform Young's moduli with respect to the thickness coordinate are given as follows (Sofiyev et al,2014):

$$\begin{pmatrix} \sigma_{11}^{(k)} & \sigma_{22}^{(k)} & \sigma_{12}^{(k)} \end{pmatrix} = \begin{bmatrix} Q_{11}^{(K)} & Q_{12}^{(K)} & 0 & Q_{12}^{(K)} & Q_{22}^{(K)} & 0 & 0 & 0 & Q_{66}^{(K)} \end{bmatrix} \begin{bmatrix} u_x + 0.5(w_x)^2 - zw_{xx} & v_y - \frac{w}{R} + 0.5(w_y)^2 - zw_{yy} & 0.5(u_y + v_x) + w_x w_y - zw_{xy} \end{bmatrix} \tag{7}$$

In which σ(k)₁₁, σ(k)₂₂ and σ(k)₁₂ are the stresses in the layers. The quantities Q(k) ij , i, j = 1, 2, 6 for orthotropic lamina are (Sofiyev et al,2014)::

$$Q_{11} = V_{21} \times Q_{11} = V_{12} \times Q_{22} \tag{8}$$

$$Q_{66} = G_o \times \varphi \times Z - h + (k - 1)\delta \leq z \leq -h + k\delta z = \frac{z}{h} \tag{9}$$

$$k = 1,2,3, \dots, N, \delta = 2hN^{-1} \tag{10}$$

In which the superscript k denotes the kth layer. The quantity E(k) 01 and E(k) 02 are Young's modulus of the homogeneous material in the x and y directions for the layer k G(k) 0 are the shear modulus of the homogeneous material in the x-y plane of the layer k, ν (k) 12 and ν(k) 21 are the Poisson's ratio for contraction in the y and x directions due to tension in the x and y directions for the layer k, respectively. For compatibility and dynamic stability equations of laminated circular cylindrical shells resting on an elastic foundation and after some mathematical operations, the Equation goes as follows:

$$L(w) + L(\phi) - \frac{\phi_{xx}}{R} = L(\phi, w) \tag{11}$$

In which L is the length of the cylinder and the amplitude-frequency relation for the finite deformations of laminated non-homogeneous orthotropic cylindrical thin shells resting on elastic foundation is obtained in the following form:

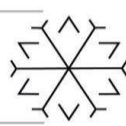
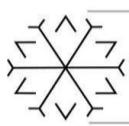
$$\frac{wNL}{wL} = \left[1 + \frac{8A\lambda}{3\pi h\lambda} + 0.75 \left(\frac{A}{h} \right)^{0.5} \left(\frac{\lambda_3}{\lambda_1} \right) \right]^2 \tag{12}$$

And natural frequency is taken into consideration in the form:

$$\underline{WL} = \frac{wL}{2\pi} \tag{13}$$

In which ωo Frequency parameter ωL, ωL, Linear frequency and natural frequency (Hz), respectively ωNL non-linear frequency of free vibrations. Also, Ap, Ap/hl represent the amplitude and dimensionless or relative amplitude of motion, respectively. The coefficients λ2 = λ3 = 0, k1= 0 yields the amplitude-frequency relation for the geometric linear free vibration analysis of a laminated nonhomogeneous orthotropic cylindrical thin shell as a special case.

3. Results and Discussion



This section is intended to present the collected experimental load and displacement based on multi-layered composite shells using ANSYS software. This research studies the free vibration characteristics of laminated non-homogeneous orthotropic thin circular cylindrical shells resting on elastic foundation. The results of the free vibration for the parallelepiped cylindrical beam are provided in addition to the linear and nonlinear results involving the frequencies and mode shapes. The validation of the model is derived from the previous studies. The following Tables 1 and 2 show the material properties and dimension of shell, respectively. The used material properties are; $E=2 \times 105$ (MPa), $\rho=7.8 \times 103$ kg/m³, $\nu= 0.3$ and the shell dimensions $h=2.29 \times 10^{-4}$ m, $R=0.337$ m, $L= 0.234$ m. The researcher uses the results of previous experiments which is developed by previous studies as a validation model and the results have been performed by finding the natural frequency of thin circular shell. To validate the analysis, for simply supported one layered orthotropic cylindrical shells, the values of relative frequency are compared with the analytical results obtained from previous studies by using ANSYS software using one layered isotropic cylindrical shells. This can be done by taking the effect of foundation into consideration and the values of dimensionless frequency parameter are compared with the analytical results of the other studies as shown in Table 1 and plotted in Figure 1.

Table 1: Comparison of natural frequencies

Mode no.	Lakis et al.	Lindholm et al.	Sofiyev et al.	Present study
5	942	995	1012	1194.5
6	1353	1430	1429	1323.4
7	1853	1938	1935	1948.2

The simulation results observe a comparison between independent data of previous numerical results and ANSYS tests based on the same conditions. The results show the variation in values of natural frequency magnitudes. There is an agreement between these results and the results obtained in this study in which they when compared, it is found that the minimum differences values of natural frequencies are in deformation 7. Also a similarity frequency values in all cases results which indicate that the model is valid is observed.

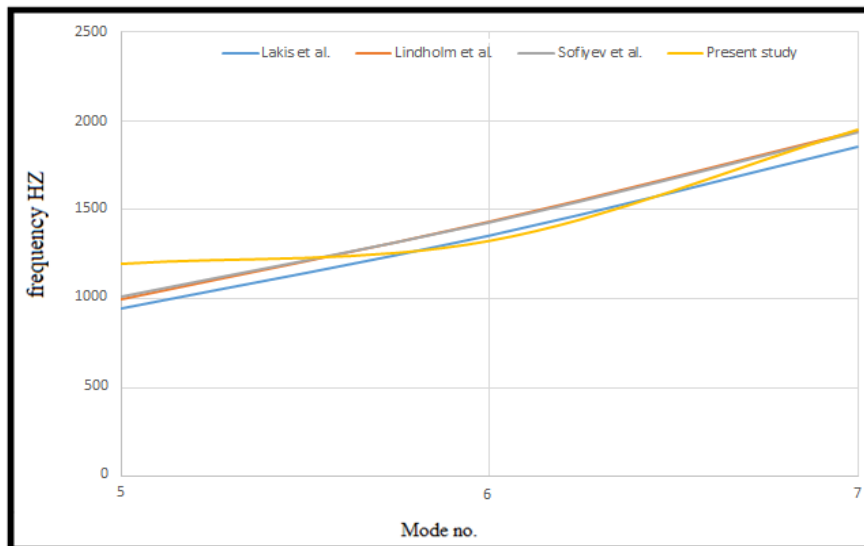
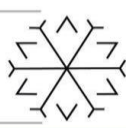


Figure 1: Comparison plot of natural frequencies

4. Modal Analysis for orthotropic cylindrical shells

Orthotropic materials have material properties that differ in three mutually-orthogonal axes, where each axis has a twofold rotational symmetry. These directional differences in strength can be quantified by using ANSYS software. To study the effect of orthotropic materials on the natural frequencies, three different stacking sequences are used to get numerical results for the laminated composite circular cylindrical shells which has the geometrical, material and laminate properties given as $E1= 1.3237 \times 105$ (MPa), $E2= 1.0755 \times 104$ (MPa), $\rho=1.308 \times$



103kg/m³, $G = 5.6537 \times 10^3$ (MPa), $\nu_1 = 0.24$, $\nu_2 = 0.0195$. Three different stacking sequences are used and in each of them 0° and 90° fiber orientations are utilized for each ply. The calculations presented in Table 2 show are done by considering the cases of cross-ply laminated orthotropic cylindrical shells up to four layers, in all layers of cross-ply cylindrical shell.

Table 2: Variation of the natural frequencies and deformation with respect to number and of layers

No. of layers	Stacking of layers	frequency	deformation
2	(0,90)	794.6	6.35
2	(90,0)	794.6	6.35
3	(0,90,0)	774.23	5.92
3	(90,0,90)	814.22	6.3
4	(0,90,90,0)	753.82	5.85
4	(90,0,90,0)	794.59	5.86
4	(90,0,0,90)	821.68	5.93

5. Modal Analysis of circular cylindrical shells

Modal analysis is the study of the dynamic properties of systems in the frequency domain. It helps to determine the vibration characteristics (natural frequencies and mode shapes) of a mechanical structure or component, showing the movement of different parts of the structure under dynamic loading conditions, such as those due to the lateral force generated by the electrostatic actuators. The natural frequencies and mode shapes are important parameters in the design of a structure for dynamic loading conditions. Modal analysis, or the mode-superposition method, is a linear dynamic-response procedure that evaluates and superimposes free-vibration mode shapes to characterize displacement patterns (Ustundag, 2011). Mode shapes describe the configurations into which a structure will naturally displace. Typically, lateral displacement patterns are of primary concern the structure with N degrees of freedom will have N corresponding mode shapes. Each mode shape is an independent and normalized displacement pattern which may be amplified and superimposed to create a resultant displacement pattern. The modal domain is one perspective for understanding structural vibrations. Structures vibrate or deform in particular shapes called mode shapes when being excited at their natural frequencies. Under typical operation conditions a structure will vibrate in a complex combination which consists of all mode shapes. Modal analysis also transfers a complex structure that is not easy to perceive, into a set of decoupled single degree of freedom systems that are simple to understand.

6. Modal Analysis for cylindrical shells on elastic foundation

In order to study how the influence of the boundary condition by increasing the elastic foundation modulus in the shell, it is known that, response of elastic media can be presented by using Winkler & Pasternak foundation models. In this study, the response of elastic media is given by Winkler foundation model.

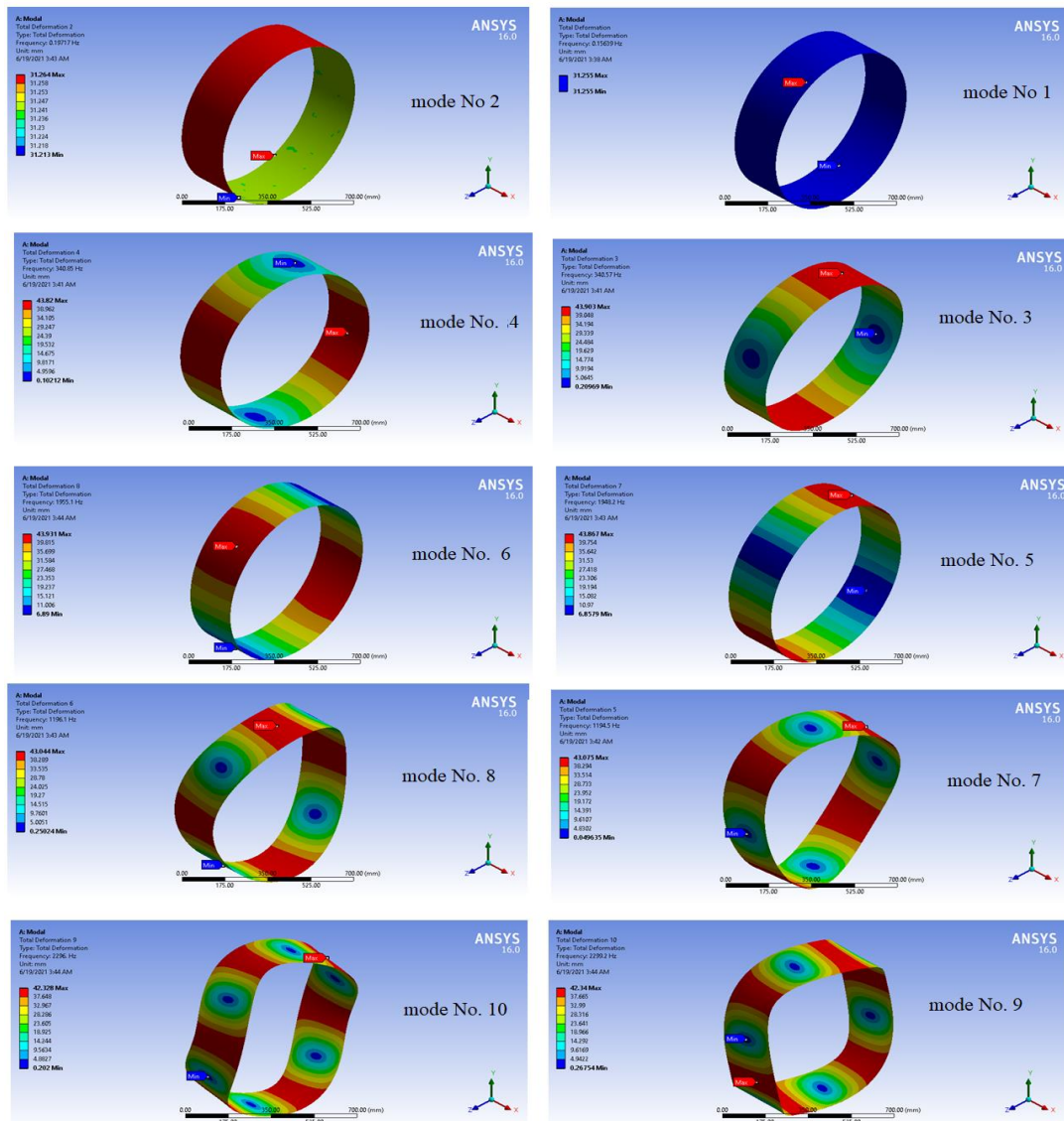
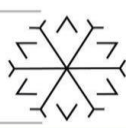


Figure 2: modal deformation mode of cylindrical shell

It is known that Winkler represented an elastic foundation by a set of closely spaced, independent linear springs. The results are simply a supported beam on Winkler elastic foundation as it is presented in Table 3. The Table represents variation of the natural frequencies with respect to different dimensional foundation modulus.

Table 3: Variation of the natural frequencies with respect to different non-dimensional foundation modulus

Mode	k=0	k=0.01	k=0.1
1	0	0	0
2	0	0.026974	0.024595
3	2.08E-02	65.223	182.29
4	2.40E-02	65.523	183.29
5	6.86E-02	210.17	611.48
6	0.12413	216.17	613.49



7	1.0484	264.44	806.46
8	1.0495	267.44	807.45
9	2.2535	307.59	948.72
10	2.2538	308.59	949.92

It can be seen that the increase of foundation modulus value will increase the frequency in the shell.

7. Modal Analysis for different cylindrical shells geometry

In this section, the mode vibration of circular cylindrical shells is discussed. The mode of vibration of cylindrical shells corresponds to the different modes. The natural frequency of cylindrical shells is computed, with a fixed mode and fixed free boundary conditions using ANSYS. The comparison of frequencies of the mode of circular cylindrical shells obtained from beam and shell theories is shown in Figure 3 and Table 4.

Table 4: The comparison results of the natural frequency for the circular cylindrical shell with different length using fixed and fixed-free boundary conditions

length	Frequency of not fixed sample	Frequency of fixed sample
5	855.1415	2808.835
10	542.3457	1631.995
20	229.5499	455.1539
30	114.7749	227.577
40	57.38747	113.7885
50	34.18053	108.1839

Figure 3 shows the variation of the natural frequency to (Hz) with the various thickness and length for cylindrical shell with the simply supported boundary condition at the edge and without supported. It is observed that for shell, the natural frequency parameter rapidly decreases and the shell length increases. On the other hand, as the thickness of the shell increases, the natural frequency parameter slightly increases. The results observe that the length of cylindrical shell effect on the deformation shape. Due to that, as the length increases, the stiffness of the shell increases and as stiffness increases, the frequency parameters of the shell decreases.

The results observed that the elastic behavior of orthotropic materials observed four engineering constants: the shear stiffness, the Young's modulus and the contraction coefficient. the effect of geometry on frequency values increases based on the effect of the number of layers' variation and material thickness. When the effect of elastic foundation considered in the problem situation, there is an effect in variation of number of layers on the frequency values.

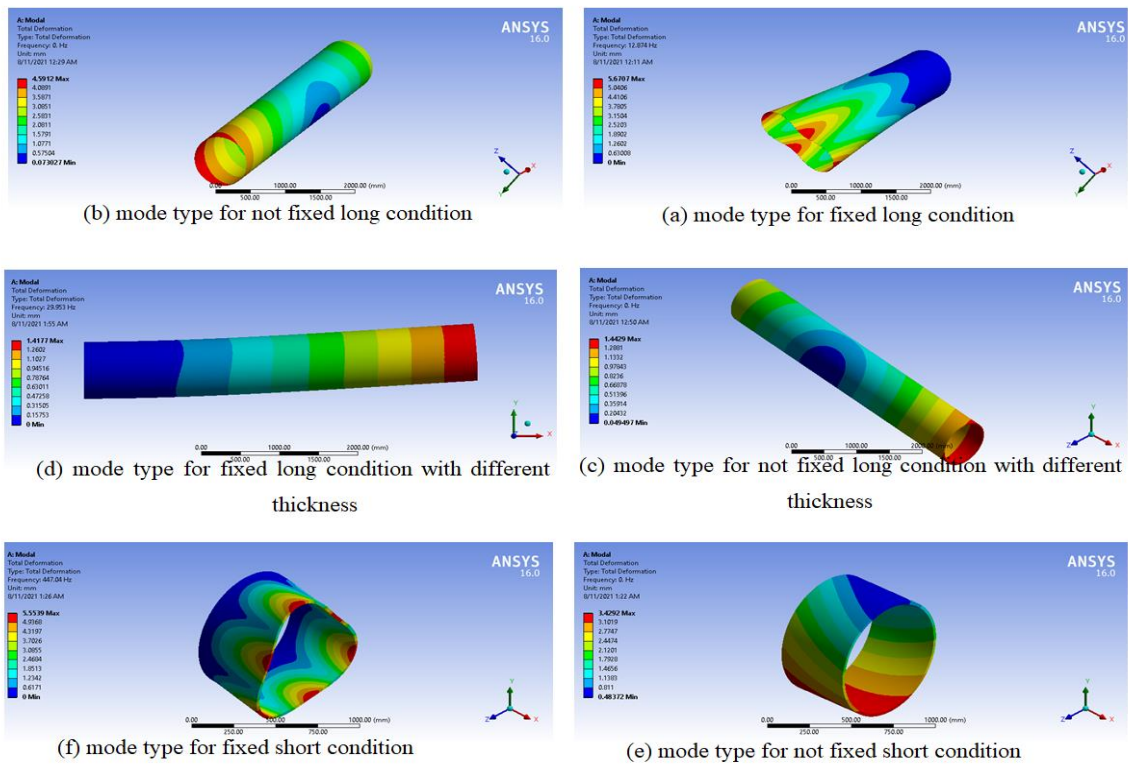


Figure 3: the variation of the natural frequency ω (Hz) with the various thickness and length

8. Conclusion

In this study, the response of cylindrical shell in different models was subjected to elastic foundation. The current work included finite element models by using ANSYS program. The effect of non-linearity on natural frequency and relative frequency values decreases. In order to establish an analytical relation between length and frequency, the following conclusions have been drawn from the numerical analysis carried out using the ANSYS program: a) When the effect of elastic foundation is not taken into consideration, the effects of geometrical and ordering of layers are very important on frequency values. b) When the value of foundation modulus increases, the frequency values increase and these factors do not have effects on frequency values in larger values of foundation modulus. c) When the shell thickness increases, the values of natural frequency increase d) When the layer increases, the deformation values decrease while the frequency change based on the layer's design. e) When the length increase, the frequency decrease and the deformation values also decrease.

It is also found that, the natural frequency is proportional to the wall thickness and length. This behavior is related to the fact that the dynamic stiffness of shell cylinder is a function of its wall thickness.

Acknowledgements

The researchers gratefully acknowledge the support by Faculty of Civil Engineering, University of Gaziantep.

References

- Ahad F., D. Shi, and Z. Hina, "2296. Computational approaches to vibration analysis of shells under different boundary conditions – a literature review," pp. 14–27, 2017, doi: 10.21595/jve.2016.16884.
- Akour, S. 2014 'Dynamics of Nonlinear Beam on Elastic Foundation', (July).
- Bacon B. J. and Gregory I. M., 2007. "General equations of motion for a damaged asymmetric aircraft," AIAA Atmos. Flight Mech. Conf., vol. 1, no. August 2007, pp. 63–75, 2007, doi: 10.2514/6.2007-6306.
- Chen, G.S., 2014. *Handbook of friction-vibration interactions*. Elsevier.



- Dubyk Y., Orynyak I., and. Ishchenko O, 2015. "An exact series solution for free vibration of cylindrical shell with arbitrary boundary conditions AN EXACT SERIES
- Efraim, E. and Eisenberger, M., 2010. Dynamic stiffness vibration analysis of thick spherical shell segments with variable thickness. *Journal of mechanics of materials and structures*, 5(5), pp.821-835.
- Farshidianfar A. and Oliazadeh P., 2012. "Free Vibration Analysis of Circular Cylindrical Shells: Comparison of Different Shell Theories," *Int. J. Mech. Appl.*, vol. 2, no. 5, pp. 74–80, 2012, doi: 10.5923/j.mechanics.20120205.04.
- Frydryšek, K. and Gondek, H. 2013 'Solutions of Beams, Frames and 3D Structures on Elastic Foundation Using FEM'.
- Jiang, W. and Redekop, D., 2003. Static and vibration analysis of orthotropic toroidal shells of variable thickness by differential quadrature. *Thin-walled structures*, 41(5), pp.461-478.
- Khalifa M., 2019. "Effects of non-uniform Winkler foundation and non-homogeneity on the free vibration of an orthotropic elliptical cylindrical shell European Journal of Mechanics A / Solids Effects of non-uniform Winkler foundation and non-homogeneity on the free vibration," *Eur. J. Mech. / A Solids*, vol. 49, no. February 2015, pp. 570–581, , doi: 10.1016/j.euromechsol.2014.09.009.
- Khan and Z. Mustansar 2016, "Reliability of Using Elastic Modulus for Non-Homogeneous Materials Reliability of Using Elastic Modulus for Non- Homogeneous Materials," no. September, 2016, doi: 10.1051/mateconf/20164909001.
- Liu, Q. and Ma, J. 2013 'Analytical Model for Beams on Elastic Foundations Considering the Coupling of Horizontal and Vertical Displacements', (December), pp. 1757–1768. doi: 10.1061/(ASCE)EM.1943-7889.0000635.
- Massalas, C., Dalamangas, A. and Tzivanidis, G., 1981. Dynamic instability of truncated conical shells, with variable modulus of elasticity, under periodic compressive forces. *Journal of Sound and Vibration*, 79(4), pp.519-528.
- Michiels, T. and Adriaenssens, S. 2017 'Identification of key design parameters for earthquake resistance of reinforced concrete shell structures', *Engineering Structures*, 153(February 2018), pp. 411–420. doi: 10.1016/j.engstruct.2017.10.043.
- Psotny, M. and Havran, J. 2017 'Stability analysis of an open shallow cylindrical shell with imperfection under external pressure', *MATEC Web of Conferences*, 107. doi: 10.1051/mateconf/201710700052.
- Pulicherla Y. and R. Kesana, 2017. "Experimental and Numerical Study of Orthotropic Materials," vol. Independen,, Available: <http://bth.diva-portal.org/smash/get/diva2:1170340/F.pdf%0Ahttp://urn.kb.se/resolve?urn=urn:nbn:se:bth-15710>.
- Rawat, A., Matsagar, V. and Nagpal, A. K. 2016 'Finite element analysis of thin circular cylindrical shells', *Proceedings of the Indian National Science Academy*, 82(2), pp. 349–355. doi: 10.16943/ptinsa/2016/48426.
- Sofiyev, A. H. et al. 2014 'Stability analysis of clamped nonhomogeneous shells on the elastic foundation', *Acta Physica Polonica A*, 125(2), pp. 459–461. doi: 10.12693/APhysPolA.125.459.
- Teodoru, I. 2015. 'Beams on Elastic Foundation . The Simplified Continuum Approach', (November).
- Tomás, A. and Martí, P. 2010. 'Shape and size optimisation of concrete shells', *Engineering Structures*, 32(6), pp. 1650–1658. doi: 10.1016/j.engstruct.2010.02.013.
- Tomás, A. and Martí, P., 2010. Shape and size optimization of concrete shells. *Engineering Structures*, 32(6), pp.1650-1658.
- Udwadia F. and Schutte, 2010. "Equations of motion for general constrained systems in lagrangian mechanics," *Acta Mech.*, vol. 213, no. 1–2, pp. 111–129, 2010, doi: 10.1007/s00707-009-0272-2.
- Ustundag, B., 2011. On the free vibration behavior of cylindrical shell structures (Doctoral dissertation, Massachusetts Institute of Technology).
- Van Rensburg, N.F.J. and Van der Merwe, A.J., 2006. Natural frequencies and modes of a Timoshenko beam. *Wave motion*, 44(1), pp.58-69.

Deep Learning Based Intelligent Traffic Volume Measurement

Burak Çelik ¹*[0000-0003-1562-6615], Ahmet Tortum ²[0000-0002-5770-766X],

¹burak.celik, Department of Civil Engineering, Atatürk University, Erzurum, Turkey

²atortum@atauni.edu.tr, Department of Civil Engineering, Atatürk University, Erzurum, Turkey

Abstract

With the development of Computer Vision technology in recent years, this technology has started to be used in Intelligent Transportation Systems as well as in many different fields. With the use of Computer Vision in Intelligent Transportation Systems, the necessary infrastructure can be provided for real-time intelligent control of traffic signaling times, elimination of traffic delays, and more effective and more dynamic control of traffic conditions. Therefore, in this paper, a traffic volume measurement software system that can detect and count selected vehicle classes is proposed in order to calculate real-time traffic signal intervals. Thus, it is aimed to eliminate time and energy losses caused by traffic conditions. In this study, a software system that can detect two different vehicle classes and perform unique counting according to vehicle class has been established by combining YOLOv3 (You Only Look Once) and SORT (Simple Online and Realtime Tracking) algorithms. The training and testing of the algorithm were carried out with a dataset of 84499 labels in 12652 images. Traffic surveillance videos with different conditions were used to validate the proposed method. When the experimental results were examined, it was determined that the proposed method showed a 92.8% count accuracy rate with high performance.

Keywords. Intelligent transportation systems, computer vision, traffic counting, transportation planning, traffic signal systems

1. Introduction

Intelligent Transportation Systems are all technologies developed for the effective management of transportation. Thanks to new products and technologies developed day by day, the transportation sector is developing and becoming more human-oriented. Developments in communication technologies in the mid-80s accelerated the development of Intelligent Transportation Systems, and with the implementation of various applications such as electronic toll collection systems, smart intersection control systems, and passenger and driver information systems, Intelligent Transportation Systems have begun to be seen as a separate field of study and a separate discipline [1].

The first International Intelligent Transportation Systems Congress was held in 1994, and it has continued to be held regularly every year since that date. Countries have established their own Intelligent Transportation Systems organizations in line with the knowledge and existing needs that have emerged with these activities, as well as academic studies in the field of Intelligent Transportation Systems [1]. In our country, the Ministry of Transport and Infrastructure and AUSDER play a leading role in realizing and developing applications in this field.

Vehicle detection and counting play a vital role in the accurate determination of traffic density. In particular, the collection of accurate and detailed traffic flow data makes traffic control systems more effective and valuable. Many developed countries (USA, Japan, Germany, etc.) have started to develop Intelligent Transportation Systems to effectively control traffic conditions and to solve problems such as traffic jams and traffic accidents. Intelligent Transportation Systems is a way of combining systems such as navigation, traffic signaling control systems, and automatic license plate recognition into a single transportation management and control system [2]. One of the basics for these technologies is to define the traffic flow, that is, to count the vehicles passing through the pre-determined sections. Besides, counting the number of passing vehicles according to vehicle classes (car, minibus, bus, truck, etc.) will allow more consistent traffic analysis.

Until recent years, most of the methods used for counting and classifying vehicles in traffic volume measurements adopted manual counting methods or hardware counting methods. Manual methods [3] operate the manual counting stage by people through paper form, mechanical/electronic counters, or special software by transferring the image to the computer. Automatic counting methods [4] are roughly divided into hardware (using various counting equipment) methods and software methods. Compared to manual methods, the time and resource usage rates of automatic counting methods that adopt this approach are quite low. However, hardware methods, which are among the automatic counting methods, are more costly than software methods and road surfaces can be



damaged during their placement [4] and hardware methods also require manpower. Again, placing some hardware counting equipment on the road surfaces may affect the drivers' behavior, causing them to pass out of the lane, and accordingly, leading to wrong counting results.

Today, with the development of computer vision, software methods that give high-performance scores in object detection in dynamic images are deep learning-based algorithms. In these algorithms [5]-[6], large CNN (Convolutional Neural Network) architectures are required and the last layers of these architectures are successful in inferring. However, these architectures are insufficient in capturing details in objects. For this reason, small CNN networks are often used for object detection, as the first layers in the CNN network are more sensitive to changes in the appearance of objects, which will be more effective in determining their target location. In computer-visioned traffic volume measurement studies, Zhang et al. [7] have developed deep Spatio-temporal neural networks to count vehicles on low-quality city camera images. To overcome the limitations of existing methods and to include temporal information of traffic images, a new FCN -rLSTM network has been designed for estimating vehicle density and number of vehicles together by connecting Fully Convolutional Networks with Long/Short Term Memory Networks. The aim of their work was to extract vehicle numbers from the real-time video stream captured by city cameras. In another study, Lin and Sun [2] have proposed a system that can count traffic flow using the YOLO (You Only Look Once) [8] algorithm. This system classifier consists of a buffer and a counter that stores the vehicle coordinates. In the study, to better understand the traffic situation at National Central University, a system that can calculate the traffic flow in real-time through the cameras placed at the entrance and exit of the campus was proposed. The pre-trained YOLO algorithm was used as the basic architecture of the classifier in the system. By default, the YOLO algorithm was trained with the ready-made COCO [9] dataset and can recognize cars, buses, and trucks as vehicle types. In a recent study, Dai et al. [10] have proposed a traffic counting system consisting of 3 components (object detection, object tracking, and trajectory processing). The traditional tracking method was combined with a matching algorithm to perform tracking after object detection. Vehicles were counted by dividing into 3 categories: cars, buses, and trucks. Since the system can work in real-time, its usability in intelligent traffic control and dynamic signal duration determination has been demonstrated. A unique dataset named VDD (Vehicle Detection Dataset) was used for training the YOLOv3 [11] algorithm.

Based on the motivation mentioned above, this study proposes a method that can accurately detect and count car and truck classes over real-time and streaming video images. The proposed method includes a combination of deep learning-based YOLO object detection algorithm, Kalman Filter [12], and SORT [13] algorithms, as well as computer interface software. For this reason, a traffic volume measurement system working in computer systems has been proposed by combining the data set collected in this study and the data set from a reference study in the literature [14].

For the rest of the paper, a brief overview of the basic architecture of the system, the object detection algorithm, and the established counting system will be given in Chapter 2. Chapter 3 contains the experiments and results. Finally, the paper ends in Chapter 4.

2. Method

In this study, a new approach model was applied for traffic volume measurements and an algorithm was developed. For this purpose, You Only Look Once (YOLOv3) [11], which is one of the algorithms that give the highest and fastest results in the object detection and recognition process in the literature, Kalman Filter [12] to estimate the location of the object in the next frame, and finally, the Simple Online and Realtime Tracking (SORT) [13] algorithm to obtain the unique identification number of the object after the detection and estimation phase were used together. In addition, for the training and testing of the YOLOv3 algorithm, the dataset [14], which has been originally collected from different images containing cars and trucks and referenced from a study in the literature, was combined and used.

2.1. YOLO Algorithm

The YOLO [8] algorithm has been a state-of-the-art algorithm in object detection in recent years. The reason why this algorithm is state of the art is that it provides a high hit rate while detecting objects in real-time. The reason why the YOLO algorithm is much faster than the others is that it can predict the class and coordinates of all objects in the image by passing the image through the neural network at once. Comparison results of the YOLOv3 algorithm and other algorithms are given in Figure 1.

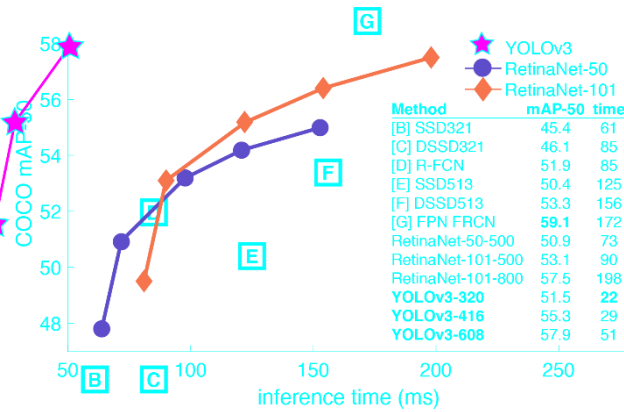


Figure 1: Comparison of YOLOv3 [8] and Other Algorithms for COCO Dataset [9].

2.2. SORT Algorithm

SORT algorithm is one of the simplest algorithms used in object tracking. It is used for multi-object tracking in real-time applications. Where an object detected in the current frame will be in the next frame is predicted by using the Kalman Filter [11]-[13]-[15]. IoU score is used for associating objects in consecutive frames [11]. The larger the intersection area, the higher the IoU score. The SORT algorithm produces better results in terms of speed and performance than many real-time multi-object tracking algorithms, but it may not give successful results in cases where the object does not appear or disappear in the next frame.

2.3. Kalman Filter

The Kalman Filter [12] has been introduced by Rudolf Emil Kalman in 1960. It is a filter that predicts the states of the systems from the input and output information together with the information of the previous states of the systems and it is very powerful in estimating the unmeasured states of the systems [16]. The Kalman Filter is a method used to predict the state and values of systems in many different areas. It is used to predict the states of mathematically linear systems. It is a very useful filter in practice and its theoretical aspect is also strong [16]-[17]. Block diagram of Kalman Filter is given in Figure 2.

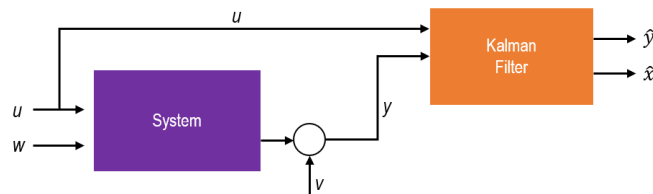


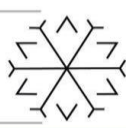
Figure 2: Block Diagram of Kalman Filter.

The Kalman Filter tries to predict the actual output (\hat{y}) and state (\hat{x}) of the system by looking at the input (u) entered to the system and the measured noise output (y). In this study, thanks to the Kalman Filter, it is estimated where the object detected in the current frame and enclosed in the bounding box by the YOLOv3 [8] algorithm will be located in the next frame and thus, it is ensured that the counting process is done correctly by preventing the reassignment of a new identity number to the object.

2.4. Proposed Method

The block diagram of the proposed method is shown in Figure 3. First of all, the test video is selected from the system interface and the ROI is placed in an appropriate position on the video. Object classification and positioning is done by the YOLO detector for the ROI area in each frame when the video is played. Objects detected with the SORT algorithm are associated and sorted. The Kalman Filter, which works with the SORT algorithm, also predicts where the objects will be in the next frame. With the help of this estimation, the counting process is performed pursuant to the association and assigning a unique ID number made by the SORT algorithm. The counted vehicles are entered in the user interface.

The hit rate is obtained by comparing the system results with the manual counting results. Therefore, the hit rate is given in Equation 1. The total number of errors is taken as the sum of missing and multiple counts.



$$\text{Counting Accuracy} = \frac{\text{Ground Truth} - \text{Total Number of Error}}{\text{Ground Truth}} \quad (1)$$

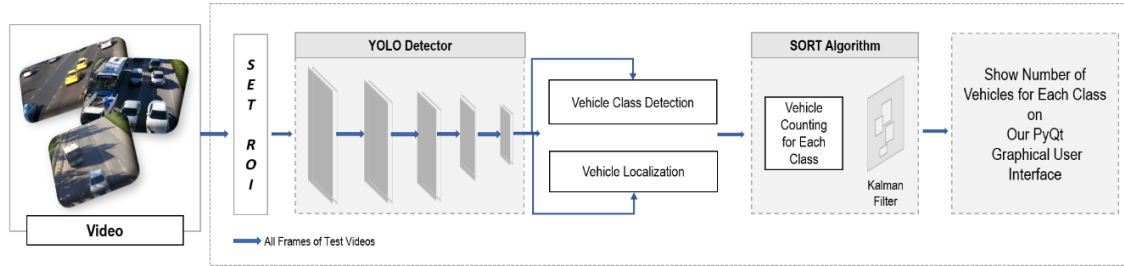


Figure 3: Block Diagram of Proposed Method.

As a result, while the proposed algorithm takes the advantage of accurate object detection and dynamic positioning from YOLO, the SORT algorithm is used for counting detected objects with unique identification numbers.

2.5. Dataset Collection

One-third of the labels in all the images in the dataset used in this study were taken from the reference [14] study, the other images were collected originally, and the remaining two-thirds of these labels in the dataset were originally prepared. There were a total of 12652 images in the dataset, and a total of 84499 labels were made for car and truck vehicle classes. There was an average of 4.2 labeled items in each image in the dataset. 80% of the dataset was reserved for training the YOLOv3 network and 20% for testing. Image samples from the collected data set are given in Figure 4.

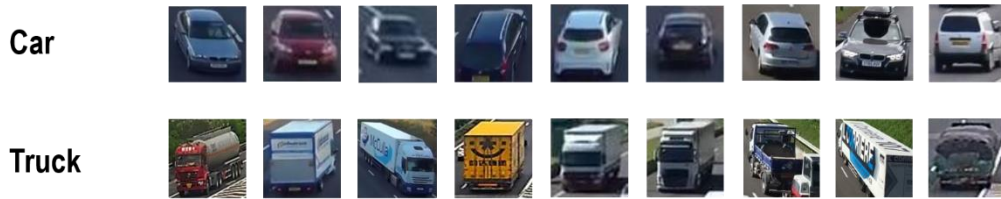


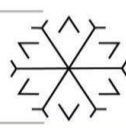
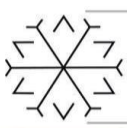
Figure 4: Sample Frames from Collection Dataset.

3. Experiments and Results

After the training process had been completed, the experiments were performed for the YOLOv3 network in the first step. Google Colab was used during the training of the model. While interpreting the results Nvidia Geforce RTX 3070 8 GB GDDR graphics card, 16 GB DDR4 memory card, and Intel Core i7-10870H 2.20 GHZ processor were used. Table 1 shows the metric scores of the different iterations in the dataset. F1 score and mAP value were taken into account in the evaluation of metric scores. The higher the F1 score, the more robust the classification model. Therefore, as given in Table 1, the model trained with 8000 iterations was suitable for use.

Table 1: Scores of the Trained Model with Collected Dataset.

Model	Iteration	AP (Car) (%)	AP (Truck) (%)	F1- Score	mAP (%)
YOLOv3 832*832	5000	95.21	96.31	0.86	95.76
YOLOv3 832*832	6000	94.69	96.53	0.86	95.61
YOLOv3 832*832	7000	96.29	97.23	0.90	96.76



YOLOv3 832*832	8000	95.69	97.17	0.90	96.43
-------------------	------	-------	-------	------	-------

The robust model obtained in the second step was tested with video images taken from different countries and belonging to different scenarios (light intensity, weather conditions, different traffic flow directions, etc.). The test results had a success rate that could create an infrastructure for a traffic counting system to be established. The traffic video footage used for the test consisted of videos with different scenarios. These videos run at an average of 20-23 fps. The results of the system tests performed on 7 different videos are shown in Table 2. In videos 1, 3, 4, and 7 the traffic flow direction was towards the camera. In other videos, it was the opposite.

Table 2: Results of System Tests for 7 Different Videos.

Video	Vehicle Class	Number of passed vehicles	Number of detected vehicles	Missing/Multiple Detection/Error	Precision %	Recall %	F1-Score	Counting Accuracy %
1.mp4 (2 dk)	Car	154	150	4/0/4	0.97	1	0.98	0.97
	Truck	9	10	0/1/1	1	0.90	0,95	0.78
	Total/Avg.	163	160	4/1/5	0.99	0.95	0.97	0.88
2.mp4 (2 dk)	Car	115	115	0/0/0	1	1	1	1
	Truck	7	8	0/1/1	1	0.88	0.93	0.86
	Total/Avg.	122	123	0/1/1	1	0.94	0.97	0.93
3.mp4 (5 dk)	Car	237	257	20/0/20	1	0.92	0.96	0.92
	Truck	21	21	0/0/0	1	1	1	1
	Total/Avg.	258	278	20/0/20	1	0.96	0.98	0.96
4.mp4 (5 dk)	Car	272	277	0/5/5	1	0.98	0.99	0.98
	Truck	5	6	0/1/1	1	0.83	0.91	0.8
	Total/Avg.	277	283	0/6/6	1	0.91	0.95	0.89
5.mp4 (4 dk)	Car	283	297	0/14/14	1	0.95	0.98	0.95
	Truck	17	17	0/0/0	1	1	1	1
	Total/Avg.	300	314	0/14/14	1	0.98	0.99	0.98
6.mp4 (6 dk)	Car	245	249	0/4/4	1	0.98	0.99	0.98
	Truck	13	16	0/3/3	1	0.81	0.90	0.77
	Total/Avg.	258	265	0/7/7	1	0.90	0.95	0.88
7.mp4 (14 dk)	Car	389	399	0/10/10	1	0.97	0.99	0.97
	Truck	48	47	1/0/1	0.98	1	0.99	0.98
	Total/Avg.	437	446	1/10/11	0.99	0.99	0.99	0.98

Accordingly, the images of our system, which was programmed with Python programming language and designed to have a user-friendly interface with PyQt, are given in Figure 5.

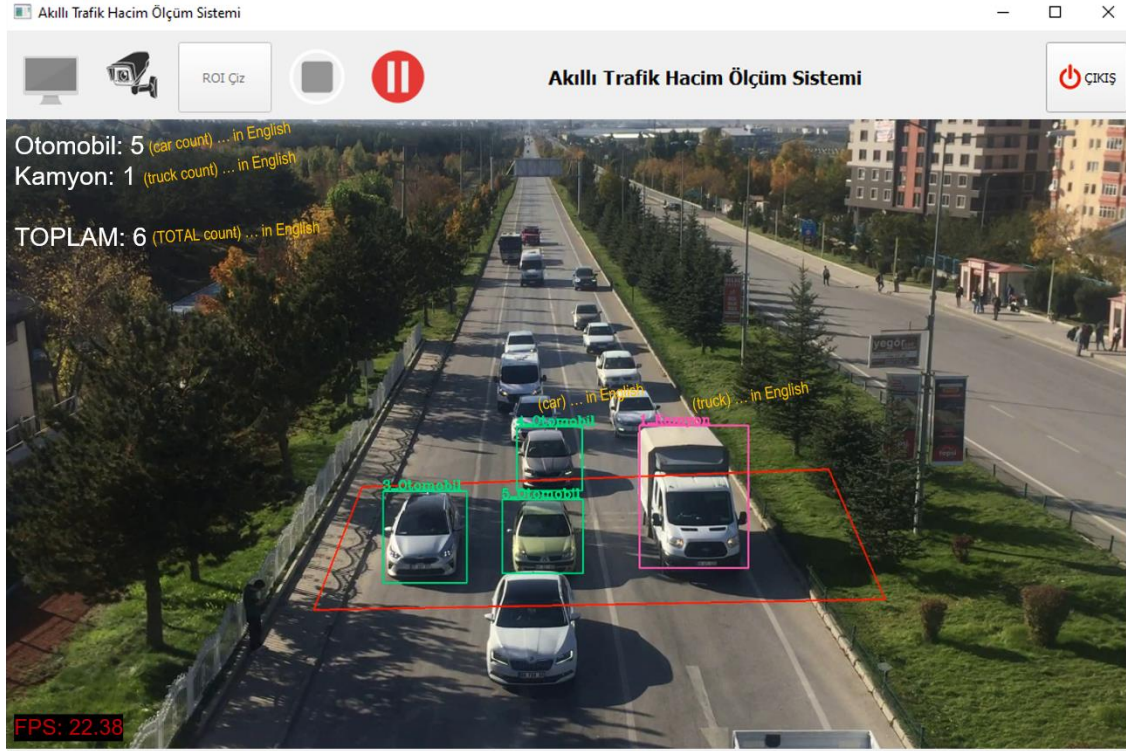
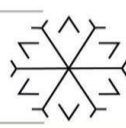
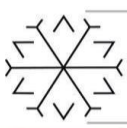


Figure 5: A Sample Screen from our Proposed System.

4. Conclusion and Future Work

In this study, a traffic volume measurement software was developed using YOLOv3 deep learning algorithm, SORT algorithm, and Python programming language. With the proposed method and system, a strong alternative to traffic counts made with various equipments or human power over video was presented. A dataset of car and truck classes was collected and used in the study. The average counting accuracy of the proposed method was 92.8% for the car and truck classes.

To increase the hit rate, it is recommended to enlarge the dataset and increase the number of vehicle classes. In addition, it is thought that by combining our proposed method with different algorithms (DeepSORT, CenterNet, etc.) in future studies, results with higher hit rates can be obtained.



References

- [1] Ulaştırma ve Altyapı Bakanlığı (2021). *Akıllı Ulaşım Sistemleri*, [Online]. Available at: <https://hgm.uab.gov.tr/akilli-ulasim-sistemler-aus> 23.10.2021 (Accessed: 22 Oct 2021).
- [2] Lin, J. P and Sun, M. T. (2018) 'A YOLO-based Traffic Counting System', *Conference on Technologies and Applications of Artificial Intelligence (Taai)*, p82-85.
- [3] Karaşahin, M. (2016) *Trafik Mühendisliği Ders Notları*, İstanbul, İstanbul Üniversitesi İnşaat Mühendisliği Bölümü.
- [4] Nkaro, A. (2004) *Traffic Data Collection and Analysis*, Botswana, Ministry of Works and Transport Roads Department Publishers.
- [5] Uzun et al (2019) 'Detection Based Tracking of Unmanned Aerial Vehicles', *27th Signal Processing and Communications Applications Conference (SIU)*, p1-4.
- [6] Karn, U. (2016) *An Intuitive Explanation of Convolutional Neural Networks* [Online]. Available at: <https://ujjwalkarn.me/2016/08/11/intuitive-explanation-convnets/> (Accessed: 27 Oct 2021).
- [7] Zhang et al (2017) 'FCN-rLSTM: Deep Spatio-Temporal Neural Networks for Vehicle Counting in City Cameras', *IEEE International Conference on Computer Vision (ICCV)*, p3687-3696.
- [8] Redmon, J. and Farhadi, A. (2018) *YOLOv3: An incremental improvement* [Online]. Available at: <http://arxiv.org/abs/1804.02767> (Accessed: 18 Oct 2021).
- [9] Lin et al (2014) 'Microsoft COCO: Common Objects in Context', *CoRR*, vol. abs/1405.0312, p740-755.
- [10] Dai et al (2019) 'Video-Based Vehicle Counting Framework', in *IEEE Access*, vol. 7, p64460-64470.
- [11] Çintaş, E. Özyer, B and Şimşek, E. (2020) 'Vision-Based Moving UAV Tracking by Another UAV on Low-Cost Hardware and a New Ground Control Station', in *IEEE Access*, vol. 8, p194601-194611.
- [12] Kalman, R. E. (1960) 'A New Approach to Linear Filtering and Prediction Problems', *Journal of Basic Engineering*, p35-45.
- [13] Bewley et al (2016) 'Simple online and realtime tracking', *2016 IEEE international conference on image processing (ICIP)*, p3464-3468.
- [14] Song et al (2019) 'Vision-based vehicle detection and counting system using deep learning in highway scenes', *European Transport Research Review*, 11(1).
- [15] Çakmak, D. (2020) 'SORT ve DeepSORT Algoritmaları' [Online]. Available at: <https://deryacakmak.medium.com/sort-ve-deep-sort-algoritmalar%C4%B1-7f50c246eac7> (Accessed: 26 Oct 2021)
- [16] Kocadağ, F. (2015) *Hareketli Araçlarda Kalman Filtresi Yardımıyla Uydu Takibi Gerçekleşmesi*, Sakarya: Sakarya Üniversitesi Fen Bilimleri Enstitüsü.
- [17] Çayiroğlu, İ. (2012). 'Kalman filtresi ve Programlama', *Fen ve Teknoloji Bilgi Paylaşımı*, 2012-1.

Parametric Analysis of a Box Girder Highway Bridge for Different Lead Rubber Bearing Properties Using API

Yersaiyn BEXULTAN ^{1*}[0000-0002-7867-5847] and Ali İhsan KARAKAŞ ²[0000-0001-7790-3345]

¹ersaiynb@gmail.com, Civil Engineering Department, Karadeniz Technical University, TURKEY

²aliihsan.karakas@ktu.edu.tr, Civil Engineering Department, Karadeniz Technical University, TURKEY

Abstract

A three-span box girder highway bridge seismically isolated with lead rubber bearings is investigated for changing properties of bearings. These properties are characteristic strength and post-elastic stiffness which determine the behavior of an elastomer bearing. The bridge is analyzed using horizontal and vertical design response spectra. The fundamental period of the bridge, maximum displacement of the superstructure and maximum internal forces of pier columns are compared for different characteristic values. A hand-made program is developed through the MATLAB programming language by utilizing the Application Programming Interface (API) feature of the CSiBridge commercial bridge program in order to be able to conduct a large number of structural analyses parametrically. All the required analyzes are performed automatically and quickly with the help of this program.

As a result of the conducted structural analyses it is seen that an increase in the characteristic strength and post-elastic stiffness reduces the horizontal displacements of the bridge superstructure while increases the internal forces generated at the bases of the bridge pier columns. Therefore, the importance of careful selection of the bearing characteristic strength and post-elastic stiffness values in the lead rubber bearing design is realized for decreasing the bridge responses by keeping the displacements at a reasonable value.

Keywords. Application programming interface, highway bridge, lead rubber bearing, seismic isolation

1. Introduction

Scientists have been working to find applicable methods to reduce the responses of various structures to earthquake ground movements for many years. As a result of these studies, various seismic isolation and energy absorbing methods have been developed. In recent years, among these methods, especially seismic isolation methods have come to the fore.

Seismic isolation separates the structure from the earthquake's horizontal ground motion and reduces the internal forces caused by the earthquake. For the separation process, various isolation devices with low horizontal rigidity are placed between the superstructure and its substructure. These devices are generally called seismic isolation bearings. Seismic isolation bearings are divided into two main classes as elastomer-based and friction-based. In this study, lead rubber elastomer bearing, which is one of the elastomer-based seismic isolation bearings frequently used in bridge structures, will be considered.

Elastomer bearings are a type of seismic isolation device obtained by bonding rubber layers to steel plates. The horizontal flexibility (low shear stiffness) of the elastomer bearing depends on the total thickness of the rubber, while its vertical stiffness depends on the distance between the steel plates. Another type of elastomer bearings is lead rubber bearings. These bearings are obtained by placing a lead core in the center of the elastomer bearing. The lead core provides energy dissipation of the seismic isolator (Warn & Whittaker, 2008).

Various studies are available in the literature to examine the effects of elastomer bearings on the seismic response of bridges ((Ghobarah, 1988), (Turkington, et al., 1989a), (Turkington, et al., 1989b), (Jangid, 2004), (Dai, et al., 2006), (Haque, et al., 2010)). In addition, various studies have been conducted to compare the mechanical properties and types of elastomer bearings ((Tubaldi, et al., 2016), (Tubaldi, et al., 2018)). Moreover, there are studies examining the structure-soil interaction and many environmental, material and geometric uncertainty parameters in elastomer supported bridges. For example, it has been concluded that more economical designs can be obtained by considering the soil-structure interaction in bridges with elastomer bearings (Neethu, 2019). Also, it has been shown that parameter uncertainty is an important issue for bridges with elastomer bearings and must be taken into account appropriately for pure



analysis (Frag, et al., 2019). Researches with different isolation devices together with elastomer bearings can also be mentioned. For instance, the dynamic properties of seismically isolated bridges with lead rubber elastomer bearings and steel limiters have been investigated (Quanani, et al., 2020). Also, the effects of different reinforcement devices in reducing the seismic response of bridges with high column lengths have been investigated (Chen & Li, 2020).

In this study, a three-span box girder highway bridge seismically isolated with lead rubber bearings with varying mechanical properties is investigated comprehensively. A hand-made computer program is developed using MATLAB programming language (MATLAB, 2021) since this parametric study requires a large number of structural analysis and iterative solutions. This program utilizes the application programming interface (API) feature of the CSiBridge finite element bridge analysis program (CsiBridge, 2019) to conduct structural analyses automatically and quickly.

2. Geometrical and Material Properties of the Bridge

Bridge components consist of cast-in-situ concrete box girders as the bridge superstructure, and the cap beam, piers and abutments as the bridge substructure. The longitudinal section of the bridge examined within the scope of the study is shown in Figure 1, the superstructure cross-section and the bridge section are shown in Figures 2 and 3, respectively. The superstructure box girder cross-section consists of 3 boxes in total and the related dimensional notations are shown in the Figure 2.

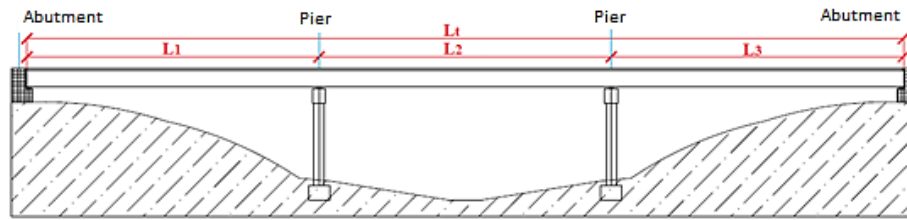


Figure 1: Bridge longitudinal cross section.

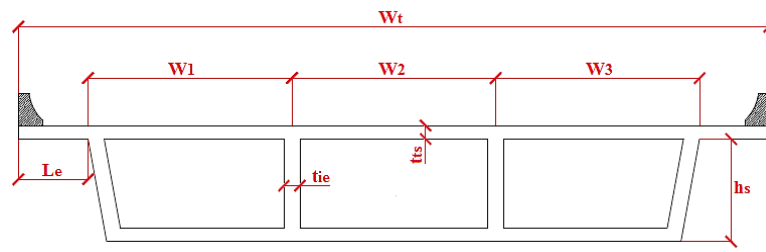


Figure 2: Bridge superstructure cross section.

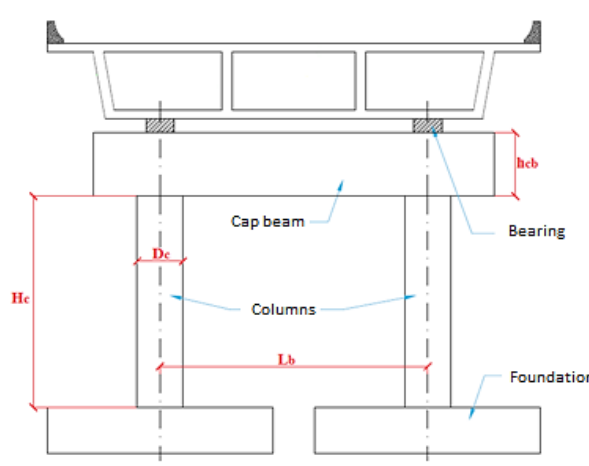


Figure 3: Bridge transverse cross section.

Bridge substructure consists of abutments at the ends of the bridge, cap beams, columns (mid-piers) and foundations. Within the scope of the study, foundations are taken into account as fixed supports. The bridge superstructure is supported by two abutments and two middle piers consisting of two columns each. The related substructure notations are shown in the Figure 3. Also, the dimensions and distances of the superstructure and substructure components of the bridge considered in this study are given in Table 1.

The properties of the concrete material used in the bridge superstructure and substructure components are given in Table 2. Concrete unit weight is taken as 25 kN/m³.

Table 1: Geometric properties of the bridge.

Bridge total length L_t , (m)	95
Bridge side-span lengths L_1, L_3 , (m)	30
Bridge mid-span length L_2 , (m)	35
Superstructure total width W_t , (m)	14
Superstructure box widths W_1, W_2, W_3 , (m)	3.8
Superstructure depth h_s , (m)	1.9
Deck thickness t_{ds} , (m)	0.25
Box inner thickness t_{ie} , (m)	0.30
The distance to the first box L_e , (m)	1.3
Column diameter D_c , (m)	1.3
Column height H_c , (m)	6
Cap beam depth h_{cb} , (m)	1.8
Center to center distance of the columns L_b , (m)	7.6

Table 2: Concrete classes and material properties.

Bridge Component	Concrete Class	Modulus of elasticity (MPa)
Box girder	C45	36057
Cap beam	C30	29440
Pier Columns	C30	29440

3. Mechanical and Geometrical Properties of the Bearings

A lead rubber elastomer bearing shows a bilinear hysteretic behavior as shown in Figure 4. The mechanical behavior of it can be expressed with characteristic strength Q_d , post-yield stiffness K_d and yield displacement D_y as shown in the figure (Naiem & Kelly, 1999). The total characteristic strength of the bearings (Q_d) in the zero-displacement state can be calculated by the following equation depending on the cross-sectional area of the lead core (A_L) and the shear yield strength (σ_L):

$$Q_d = \sum_{i=1}^n A_L \sigma_L = \sum_{i=1}^n \frac{\pi D_L^2}{4} \sigma_L \quad (1)$$

Here, D_L indicates the diameter of the lead core and n is the total number of bearings. The shear yield strength of the lead material is taken into account as 10 MPa. The total characteristic strength Q_d can be selected as a desired portion of the total superstructure weight (W). In this study, the required minimum lead core diameter is found by changing Q_d/W ratio between 0.05 and 0.2.

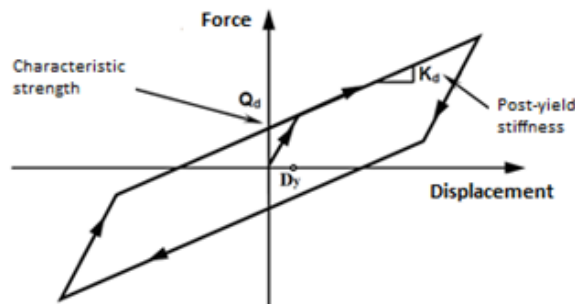


Figure 4: Hysteretic behavior of a lead rubber elastomer bearing.

The post-yield stiffness of the elastomer bearing K_d can be calculated with respect to the shear modulus G , the sum of the thickness of the elastomer layers T_r and the cross-sectional area A_r of the elastomer material as:

$$K_d = \sum_{i=1}^n \frac{GA_r}{T_r} \quad (2)$$

Here, the sum of the thicknesses of the elastomer layers is 200 mm and the shear modulus of the elastomer material is taken into account as 0.4 MPa. The elastomer area in Equation (2) is:

$$A_r = ((D_B + t_c)^2 - D_L^2)/4 \quad (3)$$

Here, D_B denotes the cross-sectional diameter of the elastomer material and t_c indicates the elastomer coating thickness. In this study, the coating thickness is considered as 30 mm. The diameter D_B is obtained by changing the period value T_d between 2 s and 4 s which is calculated with the following equation depending on the post-yield stiffness. In the equation, g stands for gravitational acceleration.

$$T_d = 2\pi\sqrt{W/(gK_d)} \quad (4)$$

The yield displacement is used to calculate the effective damping ratio of the elastomer bearing. The yield displacement is derived from the force displacement cycle of the bearing and generally varies between 6 mm and 25 mm. In this study, $D_y = 20$ mm is taken into account. The cross-sectional components of a lead rubber bearing are shown in Figure 5.

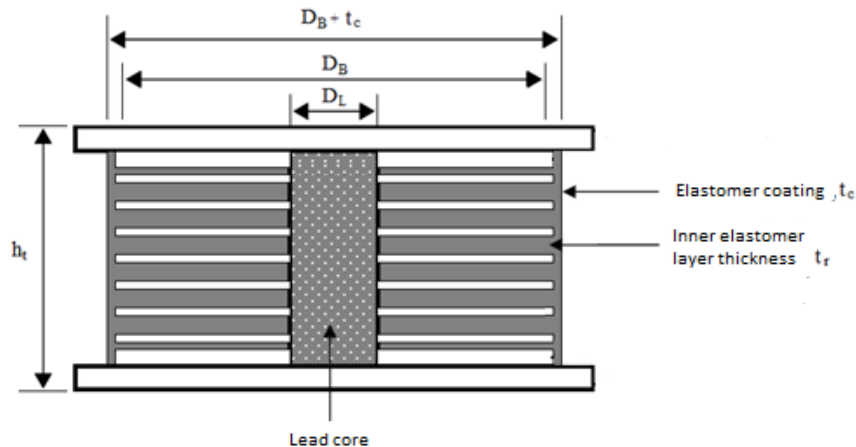


Figure 5: Cross section of a lead rubber bearing.

4. Finite Element Model of the Bridge

The bridge finite element model is obtained by using the CSiBridge commercial structural analysis program (CSI Bridge, 2017). In the finite element model, the bridge superstructure and substructure are represented by line elements. The line element has a total of 6 degrees of freedom with 3 rotations and 3 displacements at nodes. The bridge superstructure is assumed to be a continuous beam. The abutments are placed directly on the bearings. The bottom ends of the columns and abutments are assumed to be fixed and therefore the soil-structure interaction is not taken into account.

The connection between the bridge substructure and the superstructure is provided by means of lead rubber bearings. They are placed between the box girders and the cap beams. The lead rubber bearings are defined as “rubber isolator” link elements in the related finite element program. These link (spring) elements, like line elements, have a total of 6 freedoms, including 3 displacements and 3 rotations. Each freedom is expressed by the effective stiffness and damping ratio. However, in this study, elastomer bearings were modeled taking into account only the displacement freedoms in the vertical and two horizontal directions.

The effective stiffness of elastomer bearings (K_{eff}) in the transverse and longitudinal horizontal directions is obtained by the following equation and D_D is the design earthquake displacement.

$$K_{eff} = K_d + \frac{Q_d}{D_D} \quad (5)$$

The effective damping ratio of the bearings β_{eff} is obtained by the following equation:

$$\beta_{eff} = \frac{4Q_d(D_D - D_y)}{2\pi K_{eff} D_D^2} \quad (6)$$

The structural analyses are performed by an iterative method because the earthquake design displacement of the bridge is not known initially and the bridge properties (K_{eff} ve β_{eff}) depend on this displacement value. In the first step of this iterative method, an assumption is made for the design earthquake displacement value and it is changed until a convergence is achieved. The effective stiffness of the bearings in vertical direction K_V is calculated as:

$$K_V = \frac{A_r}{T_r} \left(\frac{1}{E_c} + \frac{4}{3K} \right)^{-1} \quad (7)$$

K is the bulk modulus of the elastomer material, and in this study its value is taken into account as 2000 MPa. The compressive elasticity modulus E_c is calculated as follows:

$$E_c = 6GS^2 \quad (8)$$

Here, S is the shape factor and it is calculated for circular sections as follows:

$$S = \frac{A_{ra}}{\pi D_B t_r} \quad (9)$$

A_{ra} is the cross-sectional area of the elastomer material without the thickness of the elastomer coating and it is calculated as:

$$A_{ra} = (D_B^2 - D_L^2)/4 \quad (10)$$

The three dimensional solid model and the simplified finite element model of the bridge are shown in Figures 5, respectively.

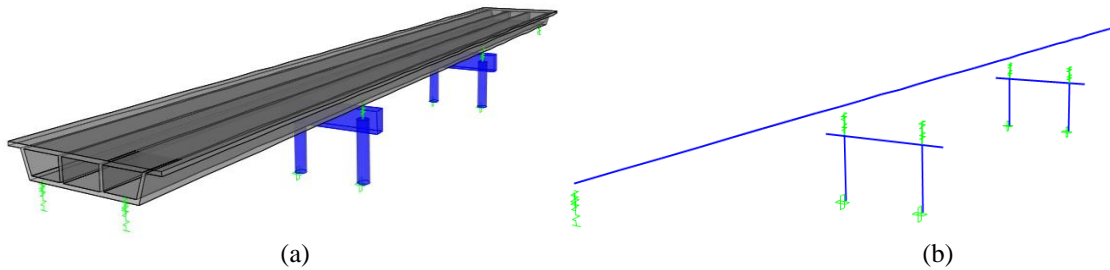


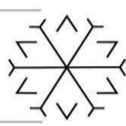
Figure 5: a) Three dimensional solid model and b) simplified finite element model of the bridge.

5. Design Earthquake Response Spectra

The horizontal and vertical design response spectra are determined according to the design earthquake level, local ground class, spectral acceleration coefficients and local ground effect coefficients given in Table 3 for latitude 39.746453 and longitude 39.49134. The parameters shown in Table 3 are obtained using the Earthquake Hazard Maps Interactive Web Application of Turkey (TDTH, 2021). The spectrum curves are scaled with spectrum reduction coefficients for different effective damping ratios and taken into account in the related response spectrum analyses.

Table 3: Design earthquake parameters.

Earthquake level	DD-2
Local ground type	ZB
Short period spectral acceleration coefficient S_s	1.051
1 sec period spectral acceleration coefficient S_1	0.776
Local ground effect coefficient for short period F_s	0.9
Local ground effect coefficient for 1 sec period F_1	0.8



6. CSiBridge Application Programming Interface (API)

CSiBridge API (Application Programming Interface) is a powerful programming tool that provides a great opportunity to automate most of the processes necessary for creating, analyzing and designing structural models and obtain analysis results. In order to achieve this goal, CSiBridge creates an external connection with another application. Thus, a two-way flow of information is provided between the programs.

One of the important features of the API is that there are several programming languages available to have a connection with CSiBridge. These are modern languages such as Visual C#, Python, MATLAB, Visual C++, Visual Fortran, and Visual Basic Applications (VBA). In this study, the MATLAB programming language is preferred to use the API feature of CSiBridge. A hand-made MATLAB program is developed in this study and it is used for the iterative calculation of earthquake design displacement of the bearings. Also, it is used for the consideration of different bearing characteristics automatically and quickly.

7. Effects of Lead Rubber Bearing Characteristics on the Responses

The most important characteristic parameters affecting the mechanical behavior of the lead rubber bearings are the characteristic strength value Q_d at zero displacement and the post-yield stiffness value K_d . In this part, the effects of these two elastomer bearing properties on bridge responses are examined. The normalized state of the characteristic strength at zero displacement divided by the weight of the superstructure Q_d/W is taken into account as the first characteristic of the bearing and its value is changed from 0.05 to 0.20. While changing this ratio, the value of K_d is kept constant.

As the second feature of the bearing, the value of the post-yield stiffness K_d is taken into account by changing the period value T_d calculated according to the post-yield stiffness given by Equation (4). According to this equation, an increase in the value of T_d is achieved by reducing the value of the post-yield stiffness. In addition, increasing the value of T_d also means reducing the diameter of the elastomer bearing. The effects of post-yield stiffness are studied by keeping the ratio Q_d/W constant and changing the value of T_d from 2 sec to 4 sec.

The bridge fundamental period values obtained from the free vibration analyses for different Q_d/W ratios and T_d values are shown in Figure 6. It is seen that the fundamental period value decreases with increasing Q_d/W ratio while decreases with increasing T_d value. The fundamental period values reach the maximum when the value of T_d is 4 sec and the ratio of Q_d/W is 0.05. The period value increases from 1.861 sec to 3.128 sec when the ratio of Q_d/W is 0.05, and from 1.239 sec to 1.590 sec when the ratio of Q_d/W is 0.20. This corresponds to an increase of 68% and 28%, respectively. Accordingly, an increase in T_d makes the bridge more flexible for a lower ratios of Q_d/W .

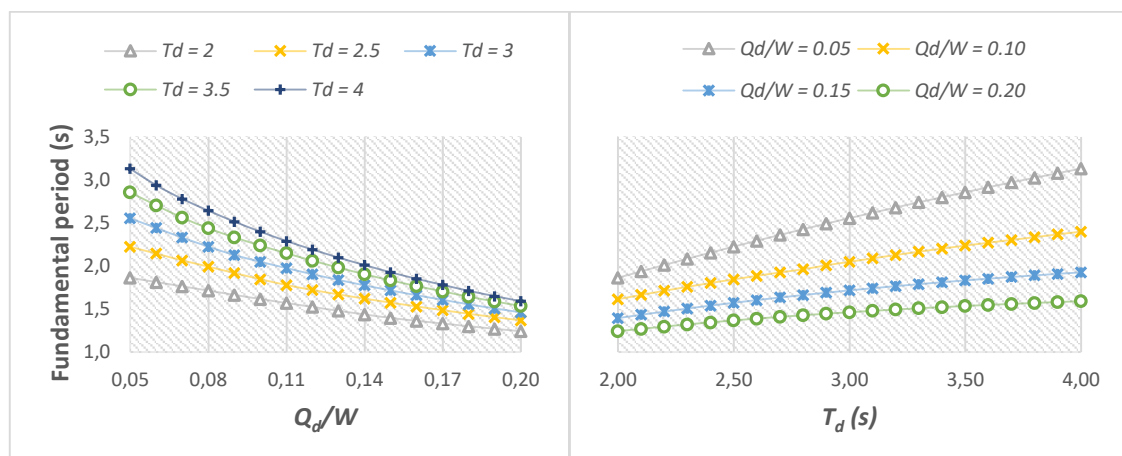
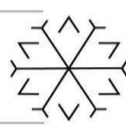
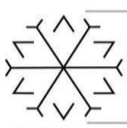


Figure 6: Fundamental periods for different values of Q_d/W and T_d .

The maximum horizontal displacements of the bridge superstructure obtained from the response spectrum analysis for different values of Q_d/W and T_d are given in Figure 7. The bridge horizontal displacements show similar behaviors of the bridge fundamental period values. The displacement value decreases from 230 mm to 113 mm with the increasing ratio Q_d/W for the minimum value of T_d . For the maximum value of T_d , the displacement value decreases from 301 to 144 mm. Accordingly, the reduction in displacement occurs by nearly 50% for each T_d value. For the case where the ratio Q_d/W is 0.05, the displacement value



increases from 230 to 301 mm with increasing value of T_d . It increases from 113 mm to 144 mm for $Q_d/W=0.2$. The increasing ratios are 30% and 27%, respectively. As a result, it can be concluded that the minimum displacement is obtained at the largest value of T_d and the smallest value of Q_d/W .

It can be seen from Figure 8 that the normal forces at the base of the pier columns decreases until a certain value of Q_d/W and then increase continuously. For example, the normal force value decreases from 1318 kN to 1149 kN, and then increases to 1268 kN at the constant value of $T_d=2$ s. The minimum value is reached at a value of 0.12 of the ratio Q_d/W . Similarly, it decreases from 588 kN to 586 kN and then increases to 915 kN for the constant value of $T_d=4$ sec. The minimum value is reached at a value of 0.06 of the ratio Q_d/W . Thus, it can be concluded that the normal forces reach the minimum values for the ratio of Q_d/W between 0.06 and 0.12 for varying values of T_d .

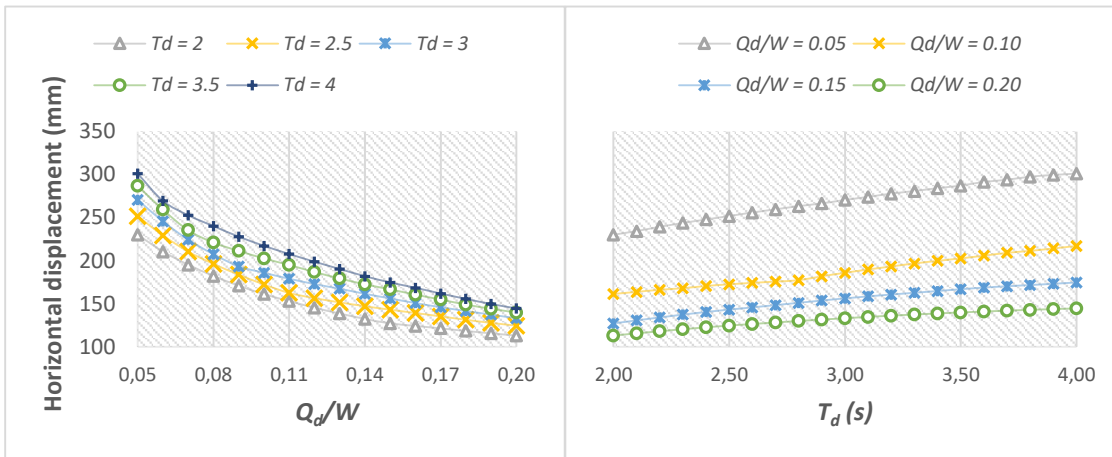


Figure 7: Horizontal displacements for different values of Q_d/W and T_d .

According to Figure 8, the normal forces generated at the base of the column tend to decrease with an increase in the period value T_d . The normal force value for the ratio $Q_d/W=0.05$ decreases from 1318 kN to 588 kN. This is a reduction ratio of about 55%. If the ratio Q_d/W is 0.10, 0.15 and 0.20, then these reduction ratios are 43%, 33% and 28%, respectively. Accordingly, it can be stated that the decrease in the normal force with an increased value of T_d decreases with an increasing ratio of Q_d/W .

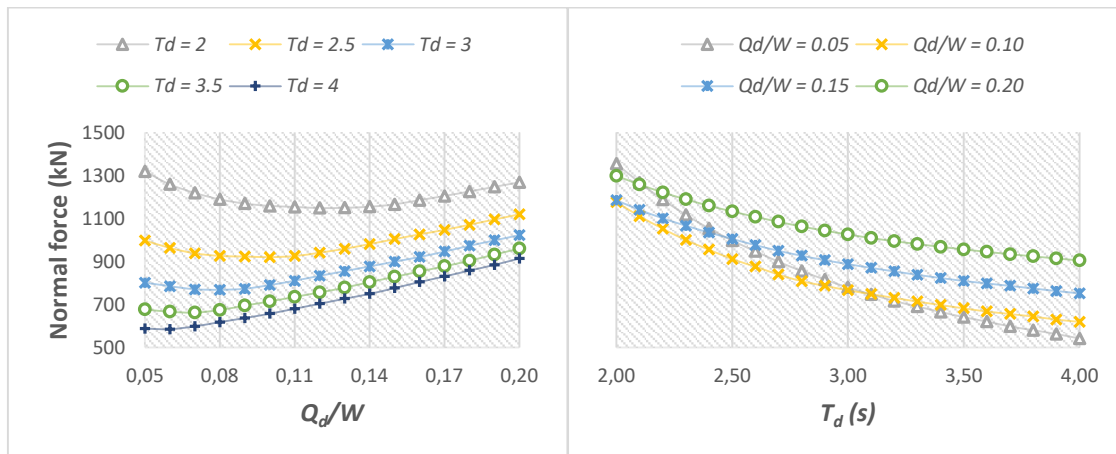
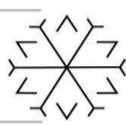


Figure 8: Pier column normal forces for different values of Q_d/W and T_d .

Shear forces and bending moments at pier column bases for different Q_d/W ratios and T_d values are shown in Figure 9 and 10, respectively. They behave in a manner similar to the normal forces. The minimum values for bending moments and shear forces are obtained for Q_d/W ratio between 0.06 and 0.14 for different T_d values .

The shear force decreases from 908 kN to 500 kN for the minimum and maximum values of T_d at the constant ratio of $Q_d/W =0.05$ and it is a decrease of about 45%. For cases where the ratio Q_d/W is 0.10, 0.15 and 0.20, these reduction ratios become 34%, 25% and 22%, respectively.



According to Figure 10, an increase in T_d leads to a decrease in the bending moments at the base of the column. The bending moments reach their largest and smallest values for the ratio of $Q_d/W = 0.05$. For this ratio, the values of the bending moment are 5670 kN.m for $T_d=2$ sec and 2912 kN.m for $T_d=4$ sec. So, the reduction ratio is 48% for $Q_d/W = 0.05$. But, it is 24% for $Q_d/W = 0.2$. Accordingly, increasing T_d value decreases the bending moment more when the the Q_d/W ratio is smaller.

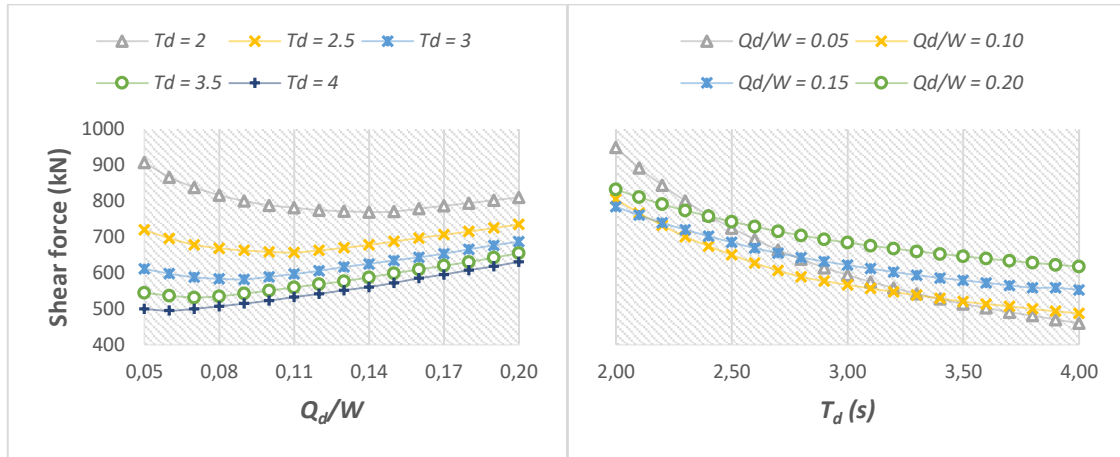


Figure 9: Pier column shear forces for different values of Q_d/W and T_d .

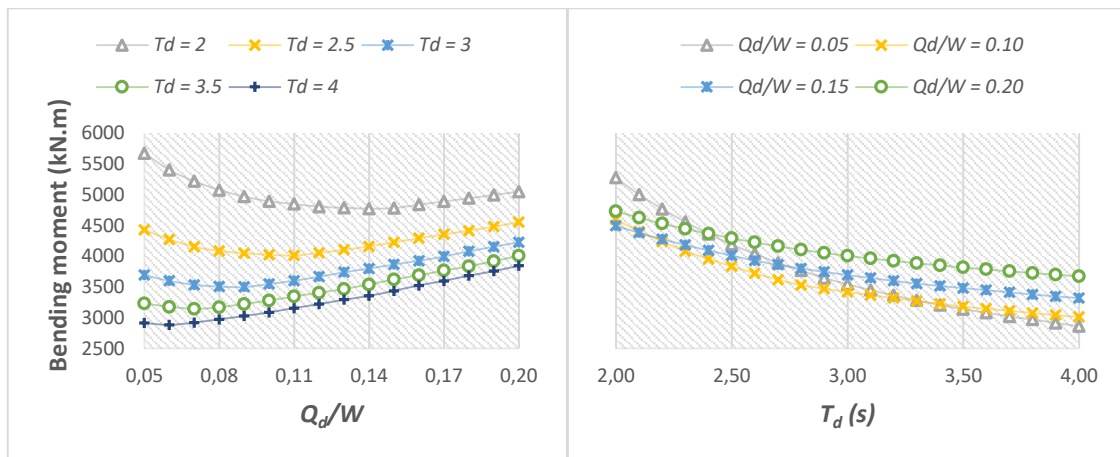


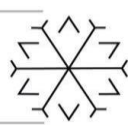
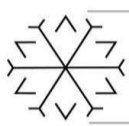
Figure 10: Pier column bending mments for different values of Q_d/W and T_d .

8. Conclusions

In this study, several structural analyses were performed by changing the ratio of the lead rubber bearing's characteristic strength at zero displacement to the weight of the superstructure and the period value calculated with respect to the post-yield stiffness in order to investigate the effects of these bearing properties on structural behavior.

These structural analyses performed within the scope of the study were performed quickly by using the API feature of the CSiBridge program and automated using a program developed with MATLAB programming language. The results obtained in this context are listed as follows:

- ❖ It is observed that the values of the fundamental period and horizontal displacement of the bridge decrease with an increase in the ratio of Q_d/W . It means that increasing the ratio Q_d/W adds additional rigidity to the bridge. The fundamental period and displacement values reduced by about 50% with increasing the ratio of Q_d/W from 0.05 to 0.20.
- ❖ It is observed that increasing the value of Q_d/W until a certain value reduces the values of normal force, shear force and bending moment formed at the base of the bridge columns, but they increase after this certain value. For different values of post-yield stiffness, the internal forces of the columns reach their minimum values between the values of 0.06 and 0.14 of the ratio Q_d/W .



- ❖ An increase in T_d significantly increases the values of the fundamental periods and horizontal displacements of the bridge. As an example, increasing the value of T_d from 2 sec to 4 sec for $Q_d/W = 0.05$ leads to increases of 68% and 30% in the fundamental period of the bridge and its horizontal displacement, respectively. Also, the normal force, shear force and bending moment values formed at the base of the bridge column decrease by 55%, 45% and 48%, respectively.

As a conclusion, in order to reduce the internal forces generated at the base of the columns in seismically isolated bridges, a lead rubber bearing with a small Q_d/W ratio can be designed by keeping the horizontal displacements at a reasonable value. Also, it is more suitable for the bearing design to select the T_d value between 2.5 s and 4 s in order to obtain small internal forces.

References

- Chen, X. & Li, C., 2020. Seismic performance of tall pier bridges retrofitted with lead rubber bearings and rocking foundation. *Engineering Structures*, Vol 212, pp. 1-15.
- CsiBridge, 2019. *Bridge Structural Analysis Program*. Berkeley, California: Computers and Structures Inc.
- Dai, W., Moroni, M., Roesset, J. & Sarrazin, M., 2006. Effect of isolation pads and their stiffness on the dynamic characteristics of bridges. *Engineering Structures*, 28(9), pp. 1298-1306.
- Farag, M. ve diğerleri, 2019. Precast beam bridges with a buffer-gap-elastomeric bearing system: uncertainty in design parameters and randomness in ground records. *Journal of Bridge Engineering*, 24(5), pp. 1-16.
- Ghobarah, A., 1988. Seismic behaviour of highway bridges with base isolation. *Journal of Civil Engineering*, 15(1), pp. 72-78.
- Haque, M., Bhuiyen, A. & Alam, M., 2010. *Seismic response analysis of base isolated highway bridges: effectiveness of using laminated rubber bearings*. Bangladesh, IABSE-JSCE Joint Conference on Advances in Bridge Engineering-II.
- Jangid, R., 2004. Seismic response of isolated bridges. *Journal of Bridge Engineering*, 9(2), pp. 56-166.
- MATLAB, 2021. *The language of technical computing*. ABD: Mathworks.
- Naiem, F. & Kelly, J., 1999. *Design of Seismic Isolated Structures From Theory To Practice*. New York: John Willey and SONS.
- Neethu, B., 2019. Effect of dynamic soil-structure interaction on the seismic response of bridges with elastomeric bearings. *Asian Journal of Civil Engineering*, Vol 20, pp. 197-207.
- Quanani, M., Sandjak, K. & Tiliouine, B., 2020. Dynamic analysis of multi-span simply supported prestressed concrete bridge with restrainer and seismic isolation devices. *Journal of Building Materials and Structures*, Vol 7, pp. 105-118.
- TDTH, 2021. *Turkey Earthquake Hazard Maps Interactive Web Application*. AFAD.
- Tubaldi, E., Mitoulis, S. & Ahmadi, H., 2018. Comparisin of different models for high damping rubber bearing in seismically isolated bridges. *Soil Dynamics and Earthquake Engineering*, Vol 104, pp. 329-345.
- Tubaldi, E., Mitoulis, S., Ahmadi, H. & Muhr, A., 2016. parametric study on the axial behaviour of elastomeric izolators in multi-span bridges subjected to horizontal seismic excitations. *Earthquake Engineering*, Vol 14, pp. 1285-1310.
- Turkington, D., Carr, A., Cooke, N. & Moss, P., 1989a. Design method for bridges on lead-rubber bearings. *Journal of Structural Engineering*, 115(12), pp. 3017-3030.
- Turkington, D., Carr, A., Cooke, N. & Moss, P., 1989b. Seismic design of bridges on lead-rubber bearings. *Journal of Structural Engineering*, 115(12), pp. 3000-3016.
- Warn, G. & Whittaker, A., 2008. Vertical earthquake lods on seismic isolation systems in bridges. *Journal of Structural Engineering*, 134(11), pp. 696-1704.

The Influence of the Horizontal Friction on the Internal Forces of the Slab on Ground Affected by Shrinkage

Dang-Bao Tran ^{1,2}[0000-0003-0367-9779]

¹dang.bao.tran@vsb.cz, Department of Structures, Faculty of Civil Engineering, VSB–Technical University of Ostrava, Ludvíka Poděšťě 1875/17, Ostrava, 70800, Czech Republic.

²baotd@tdmu.edu.vn, Department of Civil Engineering, Faculty of Architecture, Thu Dau Mot University, Tran Van On 06, Binh Duong Province, 75000, Vietnam.

Abstract

The horizontal strain can induce compression (by compressive strain) or extension (by tensile strain) on the slab foundation. The causes of horizontal strain are the foundation which is constructed in the mining area, the shrinkage, creep, and temperature changes of the concrete. The horizontal friction forces made by horizontal strain affect the internal forces of the slab foundation. Shrinkage is one of the causes of horizontal strain. ANSYS is a finite element software which is a reliable and effective technique to simulate the structure model. The concrete shrinkage as a phenomenon is usually considered as a structure subjected to initial strain. Such a type of loading is not available in the ANSYS. The objectives of this paper are i) to present how to simulate the shrinkage phenomenon of the slab on the elastic inhomogeneous isotropic half-space by ANSYS 2020 R1 software ii) to investigate the influence of the horizontal friction on the internal forces of the slab on the ground affected by shrinkage strain.

Keywords. ANSYS 2020 R1, horizontal friction, shrinkage

1. Introduction

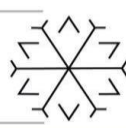
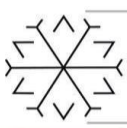
The horizontal strain can induce compression (by compressive strain) or extension (by tensile strain) on the slab foundation. The causes of horizontal strain are i) the foundation is constructed in the mining area ii) the shrinkage, creep, and temperature changes of the concrete.

Shrinkage of the concrete takes place when chemically free water evaporates from the capillaries of the cement paste. The formation of water menisci in the capillaries is accompanied by surface tensile stress (capillary stress) formation. This stress causes pressure on the solid phase-skeleton, the deformation of which manifests as shrinkage. The shrinkage of the concrete thus does not depend on whether the concrete is subjected to loading or not, but on concrete mixture proportions and material properties, method of curing, ambient temperature and humidity conditions, and geometry of the concrete element.

Stress and strain fields in the concrete slab on the ground considering the shrinkage phenomenon can be determined by using the analytical method (Zhang and Leng, 2004; Zhang and Li, 2001). Despite some numerical approaches (Reggia et al., 2015; Dere et al., 2006; Blanco et al., 2015; Bernardi, Cerioni and Michelini, 2013), the friction effects at the contact of the slab and the subsoil were still neglected.

The friction between the slab foundation and subsoil was considered in (Tomasovicova, 2016) when simulating in the three-dimension model. The industrial floor on the elastic inhomogeneous isotropic half-space with the effect of the volume changes of the concrete slabs on the ground was modeled by ANSYS 11 program with the element types: SHELL 43, SOLID 45, and CONTAC52. However, this paper did not describe how to determine the value of shrinkage strain and how to convert this value to input the ANSYS program.

This paper aims to investigate the influence of the horizontal friction on the internal forces of the slab on the ground affected shrinkage by the ANSYS 2020R1 software with the element types: SOLID186, CONTA 174 with the TARGE 170 to consider the influence of the friction. The shrinkage phenomenon



represented by converting the measured shrinkage strain to an equivalent temperature is also described in this paper.

2. Specification of analyzed structures

A slab on the ground (Labudkova and Cajka, 2015) was chosen to model and investigate the influence of horizontal friction on the internal forces of the foundation. The size of the ground plan chosen to examine is 6 x 6 m. The modulus of deformability at the bottom slab is $E_{def} = 23.7$ MPa. Poisson coefficient of the subsoil is $\mu = 0.35$. The dimension of the concrete slab was 2 x 2 x 0.17 m. Concrete C25/30 was used. Table 1 shows the cement type, ambient temperature, humidity conditions, the age of concrete at loading, the period of the end curing of the concrete element.

Table 1: Input parameter for shrinkage strain.

Age of concrete at loading t (days)	Ambient temperature $T(^{\circ}\text{C})$	Relative humidity of ambient environment RH (%)	Cement type	Age of concrete at end of curing t_s (days)
7	35	40	R	4

The subsoil is modeled by inhomogeneous space (Labudkova and Cajka, 2015; Rajapakse and Selvadurai, 1991; Stark and Booker, 1997; Doherty and Deeks, 2003), divided into five layers with a thickness of 0.4m. The boundary condition selected in this paper is fixed in the base of the subsoil. The modulus of deformability and the Poisson's ratio changed with the depth, which is calculated by the formulas (Pan, 1985)

$$E(z) = E_{def}(1 + m_1z), \quad (1)$$

$$\mu(z) = \mu(1 + m_2z), \quad (2)$$

where $m_1 = 0.5065$, $m_2 = 0.0123$

z is the depth of the soil (m)

Table 2: The modulus of deformability and the Poisson coefficient of the subsoil layers.

The depth of the subsoil (m)	The modulus of deformability of the subsoil layers E (MPa)	Poisson coefficient
0	23.7	0.350
0.4	28.5	0.352
0.8	33.3	0.353
1.2	38.1	0.355
1.6	42.9	0.357

3. Estimation of the shrinkage strain

The calculation of the shrinkage strain is based on the standard Eurocode 2 (CEN, 2004). Total shrinkage strain ε_{cs} is calculated as a sum of drying shrinkage strain ε_{cd} and the autogenous shrinkage strain ε_{ca}

$$\varepsilon_{cs} = \varepsilon_{cd} + \varepsilon_{ca}. \quad (3)$$

Drying shrinkage strain development in time is given by equation

$$\varepsilon_{cd}(t) = \beta_{ds}(t, t_s)k_h\varepsilon_{cd,0}, \quad (4)$$

in which



$$\beta_{ds}(t, t_s) = \frac{t-t_s}{t-t_s+0.04\sqrt{h_o^3}} \quad (5)$$

t -is the age of concrete of the analyzed moment, days

t_s is the age of concrete at the beginning of drying process; usually it is the time when curing is finished, days

h_o is the size of the member which is defined by

$$h_o = \frac{2A_c}{u}, \quad (6)$$

with A_c , u are the area and the perimeter of the cross-section subjected to drying, respectively

$\varepsilon_{cd,0}$ is the ultimate value of strain.

Autogenous shrinkage strain development is given by equation

$$\varepsilon_{ca}(t) = \beta_{as}(t)\varepsilon_{ca,\infty}, \quad (7)$$

where

$$\varepsilon_{ca,\infty} = 2.5(f_{ck} - 10)10^{-6}, \quad (8)$$

$$\beta_{as}(t) = 1 - \exp(-0.2t^{0.5}). \quad (9)$$

The total strain due to shrinkage defined by the above equations is $\varepsilon_{cs} = 71.31 \times 10^{-5}$.

4. Analysis model by ANSYS 2020 R1 software

ANSYS is a well-known finite element software using linear and nonlinear methods to analyze various engineering problems. In this paper, ANSYS 2020 R1 was used. However, the software will be adapted to simulate the shrinkage problem, which cannot be applied directly from the program.

4.1. Element Type

The ANSYS software is a general multi-purpose finite element program, so there are a lot of elements used in it. The SOLID186 element was chosen to model the concrete and the subsoil. This element has twenty nodes with three degrees of freedom at each node translations in the nodal x , y , and z directions. This element is capable of plastic deformation, cracking in three orthogonal directions, and crushing. Remarkably, SHELL 43 and SOLID 45 elements were used in (Tomasovicova, 2016) to model the concrete and the subsoil, respectively.

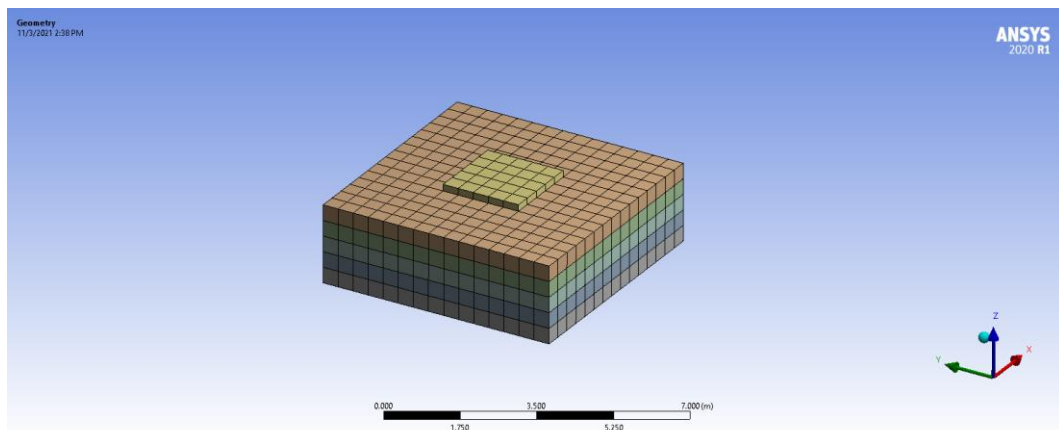
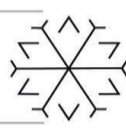
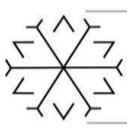


Figure 1: 3D numerical model of the foundation slabs and the inhomogeneous subsoil.

The element CONTA 174 with the TARGE 170 is used to model the interaction between the foundation and subsoil with the influence of friction. CONTA174 is applicable to 3-D structural and coupled-field contact analyses. It can be used for both pair-based contact and general contact. Fig. 1 shows the model of



the foundation slabs and the inhomogeneous subsoil performed in ANSYS 2020 R1. The mesh 400 x 400 mm is generated in this model.

4.2. Concrete stress-strain relationship

Fig. 2 shows the uniaxial stress-strain curve of the concrete. The compressive uniaxial stress-strain relationship for the concrete model was obtained by using the following equations suggested by (MacGregor et al., 1997; Wolanski, 2004)

$$f = \frac{E_c \varepsilon}{1 + \left(\frac{\varepsilon}{\varepsilon_0}\right)^2}, \quad (10)$$

$$\varepsilon_0 = 2 \frac{f'_c}{E_c}, \quad (11)$$

$$E_c = \frac{f}{\varepsilon}, \quad (12)$$

where f is the stress at any strain ε
 ε is strain at stress f .

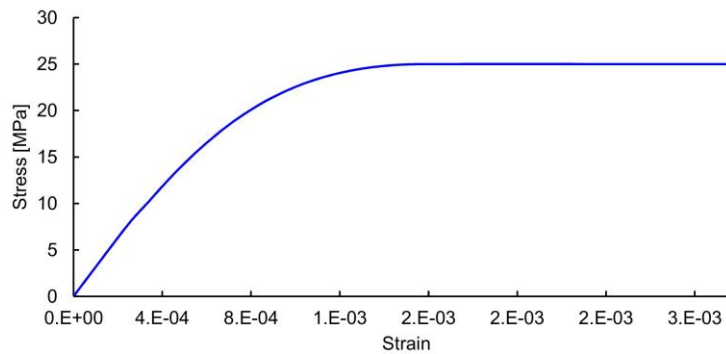


Figure 2: Uniaxial stress- strain curve.

4.3. Loads condition

The concrete shrinkage as a phenomenon is usually considered as a structure subjected to initial strain. Such a type of loading is not available in the ANSYS, so an approach is needed to simulate the shrinkage effect in this program. It is worthy to note that (Tomasovicova, 2016) did not mention how to determine the value of shrinkage strain and how to convert this value to input the ANSYS program. This paper uses the proposed method by (Kianoush, Acarcan and Ziari, 2008; Gao, Ma and Cai, 2006), which transformed the measured total shrinkage strain to an equivalent temperature change. The following calculations illustrate the conversion of shrinkage strains to an equivalent temperature change as

$$\Delta T = \frac{\varepsilon_{free}}{\alpha}, \quad (13)$$

where ΔT is the equivalent shrinkage
 ε_{free} is the total recorded free strain
 $\alpha = 10.10^{-6} K^{-1}$ is the coefficient of thermal expansion (CEN, 2004).

And according to this approach, the equivalent shrinkage temperature $\Delta T = 79.23^\circ C$ is applied at each node in the finite element model.

Thermal conductivity is not dealt with in EN 1992-1-1 (CEN, 2004). Three principal factors are influencing the thermal conductivity of concrete:

1. The aggregate type
2. The aggregate volume – aggregate has a higher thermal conductivity than both cement and water
3. The moisture content – as concrete hydrates and dries, the space previously occupied by water empties, and the conductivity reduces.



According to Bamforth, P. B. (CIRIA, 2007), the published thermal conductivity values vary considerably but are typically within the range of 1.0 – 2.5 W/m°C. The thermal conductivity value of the concrete used to investigate the change of the internal forces in this paper is 2.5 W/m°C.

Friction is the resistance against slip in the contact boundary between two materials, which results in a frictional force along the slip plane opposite the direction of the movement. When considering the friction between two materials, the coefficient of friction, μ_c , is typically used. The coefficient of friction of concrete and subsoil (MU) used to investigate the internal forces of the slab foundation in this paper is assumed to vary in the range of 0.3 - 0.8.

5. Results

Fig. 3a depicts the normal stress of concrete at the bottom slab without friction. It can be seen clearly that the slab foundation is subjected the compressive stress primary. The maximum tensile stress is on the edge of the slab.

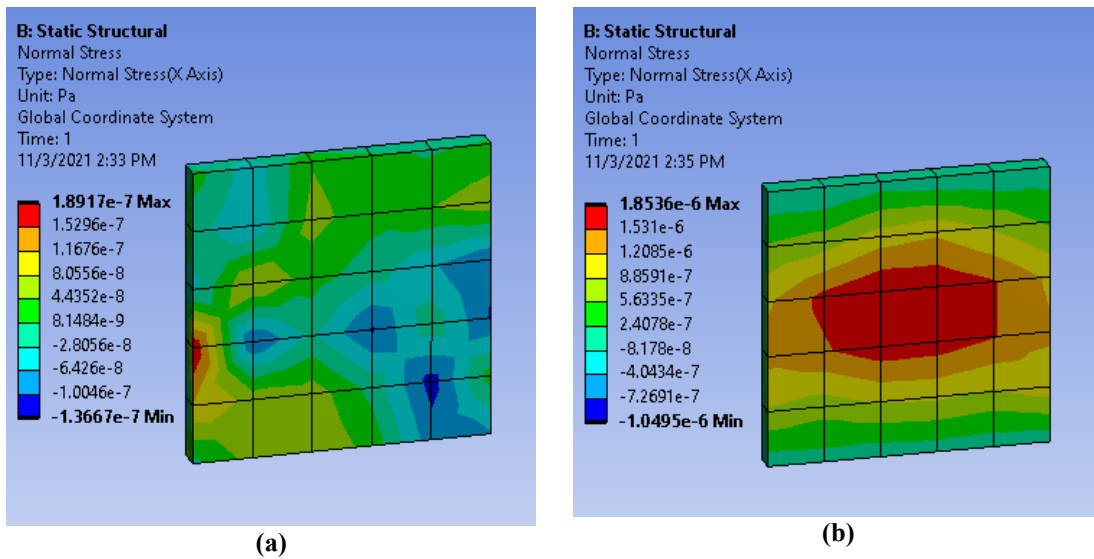


Figure 3: Normal stress in concrete at the bottom slab with (a) MU= 0; (b) MU= 0.3, unit [MPa].

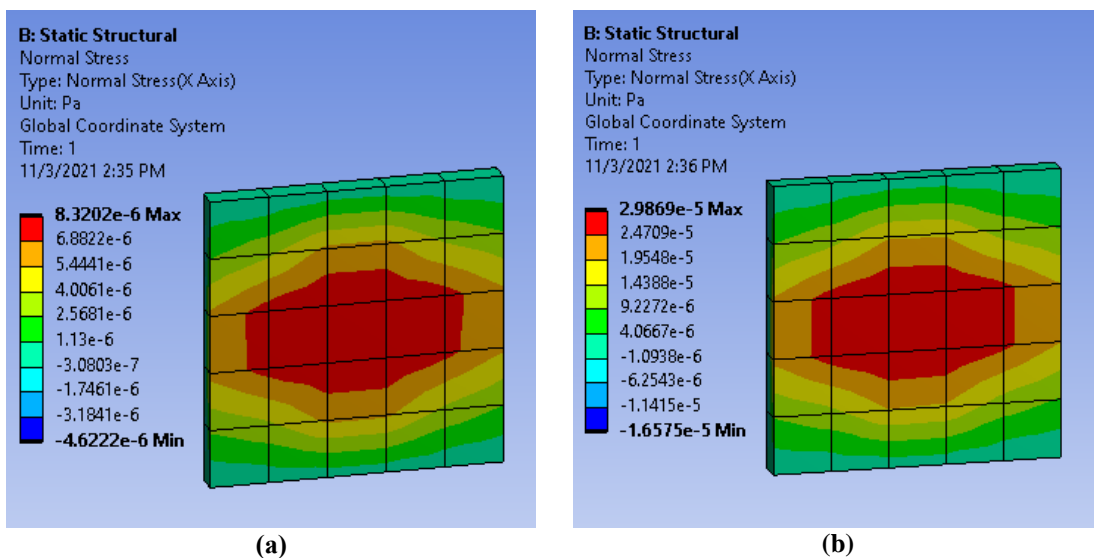
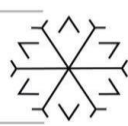
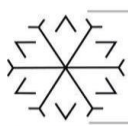


Figure 4: Normal stress in concrete at the bottom slab with (a) MU= 0.5; (b) MU= 0.8, unit [MPa].

Fig. 3b, Fig. 4a, Fig. 4b show the normal stress of concrete at the bottom slab with the variable coefficient friction MU = 0.3, MU = 0.5, MU = 0.8, respectively. The maximum compressive stress of the slab foundation is $1.6575 \cdot 10^{-5}$ MPa. The maximum tensile stress of the slab is distributed in the center of the slab. This value is $2.9869 \cdot 10^{-5}$ MPa, which is under the allowance tension stress. Therefore the crack will



not appear. It can be seen from Fig 3 and Fig.4 that the normal stress without considering the friction has the lowest value. The higher is the coefficient of friction; the bigger is the tensile stress of the concrete.

6. Conclusions

This study has shown i) to present how to simulate the shrinkage phenomenon of the slab on the elastic inhomogeneous isotropic half-space by ANSYS 2020 R1 software ii) to investigate the influence of the horizontal friction on the internal forces of the slab on the ground affected by shrinkage strain. It can be concluded that the horizontal friction will increase the stress in the slab foundation. Therefore the effect of the friction needs to be eliminated.

Acknowledgements

This article has been achieved with the financial support of the Ministry of Education, specifically by the Student Research Grant Competition of the Technical University of Ostrava under identification number SP2021/77.

References

- Zhang, J. and Leng, B. (2004) 'Analysis of shrinkage-induced stresses in concrete pavements', Magazine of Concrete Research, 56(10), pp. 585–595. doi: 10.1680/mac.2004.56.10.585.
- Zhang, J. and Li, V. C. (2001) 'Influence of supporting base characteristics on shrinkage-induced stresses in concrete pavements', Journal of Transportation Engineering, 127(6), pp. 455–462. doi: 10.1061/(ASCE)0733-947X(2001)127:6(455).
- Reggia, A. et al. (2015) 'Analysis of a jointless floor with calcium sulpho-aluminate and portland cement', American Concrete Institute, ACI Special Publication, 2015-Janua(SP 305), pp. 45.1-45.10.
- Dere, Y. et al. (2006) 'Failure prediction of skewed jointed plain concrete pavements using 3D FE analysis', Engineering Failure Analysis, 13(6), pp. 898–913. doi: 10.1016/j.engfailanal.2005.07.001.
- Blanco, A. et al. (2015) 'Application of FRC constitutive models to modelling of slabs', Materials and Structures/Materiaux et Constructions, 48(9), pp. 2943–2959. doi: 10.1617/s11527-014-0369-5.
- Bernardi, P., Cerioni, R. and Michelini, E. (2013) 'Analysis of post-cracking stage in SFRC elements through a non-linear numerical approach', Engineering Fracture Mechanics, 108, pp. 238–250. doi: 10.1016/j.engfracmech.2013.02.024.
- Tomasovicova, D. (2016) 'Analysis of Shear Interaction Between Industrial Floor Slab and Subsoil', 16th International Multidisciplinary Scientific GeoConference SGEM2016, Science and Technologies in Geology, Exploration and Mining, 3, pp. 35–42. doi: 10.5593/sgem2016/b13/s02.005.
- Labudkova, J. and Cajka, R. (2015) 'Comparison of the Results from Analysis of Nonlinear Homogeneous and Nonlinear Inhomogeneous Half-Space', Procedia Engineering, 114, pp. 522–529. doi: 10.1016/j.proeng.2015.08.101.
- Rajapakse, R. K. N. D. and Selvadurai, A. P. S. (1991) 'Response of circular footings and anchor plates in non-homogeneous elastic soils', International Journal for Numerical and Analytical Methods in Geomechanics, 15(7), pp. 457–470. doi: 10.1002/nag.1610150702.
- Stark, R. F. and Booker, J. R. (1997) 'Surface displacements of a non-homogeneous elastic half-space subjected to uniform surface tractions. Part II: Loading on rectangular shaped areas', International Journal for Numerical and Analytical Methods in Geomechanics, 21(6), pp. 379–395. doi: 10.1002/(sici)1096-9853(199706)21:6<379::aid-nag876>3.0.co;2-2.
- Doherty, J. P. and Deeks, A. J. (2003) 'Scaled boundary finite-element analysis of a non-homogeneous elastic half-space', International Journal for Numerical Methods in Engineering, 57(7), pp. 955–973. doi: 10.1002/nme.706.
- Pan, F. L. (1985) 'Effect of buried depth of soil layer on Poisson's ratio and lateral compressive stress to vertical compressive stress ratio', China Civil Engineering Journal, 18, pp. 53–60.
- CEN, T. (2004) 'EN 1992-1-1, Eurocode 2: Design of concrete structures--Par 1--1: General rules and rules



for buildings', European Committee for Standardization, Brussels.

MacGregor, J. G. et al. (1997) Reinforced concrete: Mechanics and design. Prentice Hall Upper Saddle River, NJ.

Wolanski, A. J. (2004) Flexural behavior of reinforced and prestressed concrete beams using finite element analysis. Citeseer.

Kianoush, M. R., Acarcan, M. and Ziari, A. (2008) 'Behavior of base restrained reinforced concrete walls under volumetric change', *Engineering Structures*, 30(6), pp. 1526–1534. doi: 10.1016/j.engstruct.2007.10.009.

Gao, Y., Ma, B. and Cai, M. (2006) 'Finite Element Analysis of Shrinkage in the Interface of Functionally Graded Concrete Segment Used in Shield Tunneling', *Journal of Wuhan University of Technology (Materials Science Edition)*, 21(z1), pp. 94–98. Available at: <http://d.wanfangdata.com.cn/Periodical/whgydxxb-e2006z1020>.

CIRIA, B. P. B. (2007) 'C660: Early-age thermal crack control in concrete', CIRIA, London, UK.

Impacts Of Climate Change On Water Resources Of Turkey

Ahmed Alyasin Alkhani ^{1*}[0000-0001-8481-2345], Asst. Prof. Ayşe Yeter Günel ^{2*}[0000-0002-4866-2914] and

Prof.Dr. Mustafa Günel ^{3*}[0000-0002-6787-2466]

¹a.alkhani@hotmail.com, Gaziantep University, Engineering Faculty, Gaziantep/Turkey

²agunal@gantep.edu.tr, Gaziantep University, Engineering Faculty, Gaziantep/Turkey

³gunal@gantep.edu.tr, Gaziantep University, Engineering Faculty, Gaziantep/Turkey

Abstract

One of the world's most important challenges is climate change. Global warming is out of control, endangering food, water, and energy security while also affecting temperature, precipitation, and evaporation patterns. Turkey is one of the Mediterranean macro-climatic zones that will be affected by many of these negative climate change effects, particularly in terms of water supply. This article examines the impact of climate change on Turkey's water resources, including case studies from throughout the country and strategies for dealing with the effects of climate change.

Keywords. : adaptation, climate change, Turkey, water resources

1. Introduction

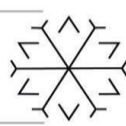
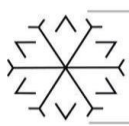
Scientific studies undertaken by the Intergovernmental Panel on Climate Change (IPCC) and other international organizations show that the climate is changing, and global warming is one of the most important concerns of our day. Climate change has had profound and life-threatening repercussions for all living and nonliving animals on the planet, including increased glacier melting, rising sea levels, extinction of plant and animal species, and freshwater scarcity. To combat global warming, the amount of greenhouse gas emissions in the atmosphere must be lowered. Drought, excessive rainfall, floods, erosion, water scarcity, and air pollution are all on the rise, according to the IPCC's 5th Assessment Report (AR5). The goal of this study is to assess Turkey's long-term water resource management in light of climate change, as well as the adaptation techniques that will be employed to mitigate the risks.

2. Methodology

The research approach used in this study is to obtain important points from linked sources and to compare and contrast the perspectives and findings of various authors. Various books, journals, papers, project reports, statistical data, and web-resources were evaluated as reference materials. In Turkey, studies and best practices on water resources and climate change adaptation were examined. There were three chapters to the paper. The first point of concern is the effects of climate change on water resources. Concerns over Turkey's water resources as a result of climate change were then acknowledged. Recent works on integrated water resource management and climate change adaptation in Turkey were investigated.

3. Impacts of climate change on water resources

Climate change, in addition to natural climate variability observed over comparable time periods, was defined as a change in climate caused by human activity that modifies the composition of the global atmosphere. Because it is driven by excessive human activity, climate change is now referred to as "anthropogenic" (IPCC 2013). According to the United Nations, the world's population has already surpassed 7 billion people (UN). Urban areas are home to around half of the population. This percentage will have climbed to 65 % by 2025. Cities are rapidly expanding, putting pressure on natural resources and the capacity of surrounding communities. According to UN Habitat estimates, cities account for nearly 75% of global energy consumption and 80% of global greenhouse gas emissions that contribute to climate change. As a result of migration from the village to the city and concentration of human activity in cities, environmental concerns, increasing population demand on water resources, the climate



change problem have reached a level that cannot be compared to the past. Water is a very important resource in terms of ecosystem services. The hydrological cycle and the climate system are inextricably intertwined, and every change has an impact on both. Increasingly concentrated greenhouse gases in the atmosphere generate the following effects in the hydrological cycle and water resources:

- Changes in the balance of snow and rain,
- Water loss has increased, and soil moisture has decreased,
- Decrease in agriculture and pasture areas exposed to droughts and floods,
- Water resources are being depleted in quantity and quality,
- Sea level rise has resulted in the loss of wetlands,

Long-term observations and measurements, as well as the identification of additional elements impacting climate change and water cycle processes, are necessary to illustrate all of these impacts for a specific location (EEA 2017). The number of individuals migrating as a result of climate change or other natural disasters is increasing by the day, making finding solutions even more difficult. In the face of climate change, it's important to explore for strategies to adapt and build integrated water management systems (Lehman 2009; Sipahi and Tekin 2016; IPCC 2014).

4. Water issues linked to climate change in Turkey

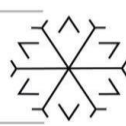
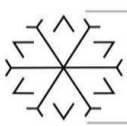
Turkey is located between 26° and 45° east longitudes and 36° and 42° north latitudes. Seas surround Turkey on three sides. Turkey's total area is 780.000 km² (Erolu 2007; SHW 2012b). According to figures from the Turkish Statistical Institute (TURKSTAT), Turkey's population grew from 56.47 million in 1990 to 80.81 million in 2017. (TURKSTAT 2018). Turkey is located in the climatic zones of mid-latitude and subtropical climate zones. Due to its geographical location, Turkey has numerous climate zones, however it is largely located within the Mediterranean macroclimatic zone (MoEU 2016).

Turkey's climate is semi-arid. Topographical factors, distance from the sea, and height fluctuations all contribute to climate variation over short distances.

Turkey was ranked 78th out of 147 countries in a study comparing water scarcity indexes (Lawrance; Meigh & Sullivan, 2002). (Table 1) (Lawrance; Meigh & Sullivan, 2002).

Table 1: Ranks of various countries with respect to water scarcity index

Country	Resource	Access	Capacity	Usage	Environment	Water scarcity index
Finland (1)	12.2	20.0	18.0	10.6	17.1	78.0
United Kingdom (11)	7.3	20.2	17.8	10.3	16.0	71.5
Germany (35)	6.5	20.2	18.0	6.2	13.7	64.5
Congo Republic (75)	17.1	10.3	11.8	7.3	10.9	57.3
Turkey (78)	7.8	14.8	13.1	10.7	10.1	56.5
Nigeria (129)	7.4	7.5	8.5	10.4	10.1	43.9

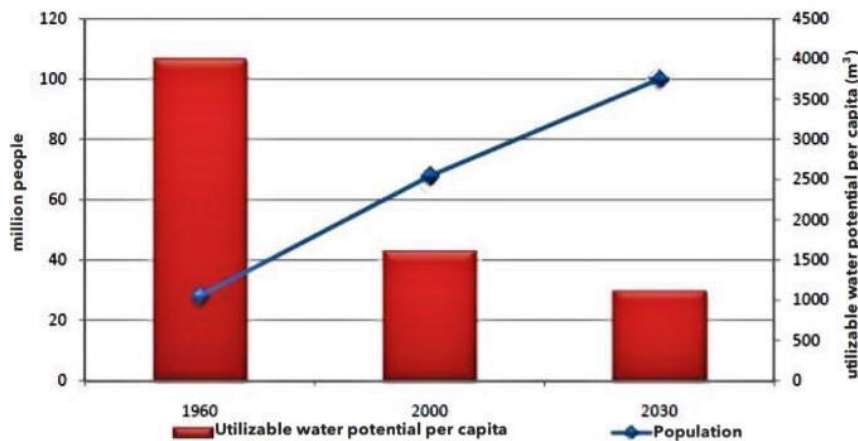


The Falkenmark index classifies Turkey as a "water-stressed country" based on per capita water use (Table 2). In 1960, Turkey's utilizable water potential per capita was 4000 m³. Due to the population rise, the water potential, which was reduced to 1600 m³ in 2000, is expected to be reduced to 1120 m³ in 2030. (Figure 1) (former Republic of Turkey Ministry of Forestry and Water Affairs, 2009).

Table 2: Water status of Turkey with respect to Falkenmark Index

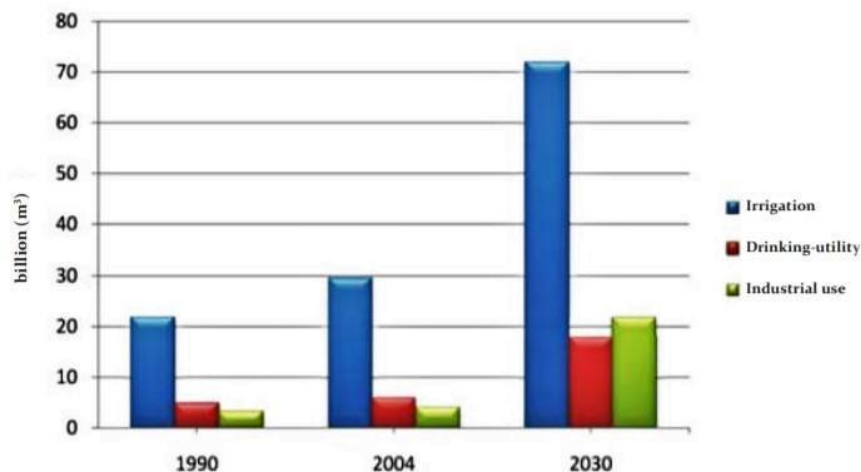
Amount of freshwater available for each person each year	Turkey
Less than 1.000 m ³	1120 m ³ /person/year (2030)
Less than 2.000 m ³	1519 m ³ /person/year (2008)
More than 8.000-10.000 m ³	4000 m ³ /person/year (1960)

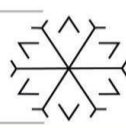
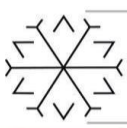
Figure 1: Water potential of Turkey per capita (former Republic of Turkey Ministry of Forestry and Water Affairs, 2009)



The following is the sectoral distribution of water uses in Turkey as of 2004: irrigation (74%), drinking (15%), and industrial (11%). These percentages will be 64%, 16%, and 20% in 2030, respectively (Figure 2). According to these figures, water use in agriculture will decrease proportionately while water use in industry will double.

Figure 2: Sectoral water use in Turkey





The world's water stress situation will rise if suitable water management measures are not taken while climate change continues at its current rate.

These numbers are crucial because they show that freshwater resources are in short supply across the world. The world's population more than doubled between 1950 and 1990, rising from 2.5 billion to 5.3 billion. The population is expected to reach 9 billion by 2050. (UN HABTAT 2016). The amount of water per capita is a common metric for determining there is enough water or there isn't. As a result, when assessing water potential, population is a critical factor to consider. The amount of water consumed per person can be calculated using a variety of methods. For example, according to the Falkenmark indicator, water stress differentiation proposed as shown in Table 3.

Table 3: Water stress differentiation proposed Falkenmark

Index (m ³ per capita)	Category/Condition
>1,700	No Stress
1,000-1,700	Stress
500-1,000	Scarcity
<500	Absolute Scarcity

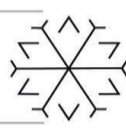
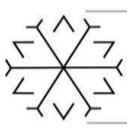
All of these forecasts assume that current water supplies and potential be passed down to future generations in the same way that they are now (SHW 2012b). All nations, not just Turkey, should manage their water resources properly for future generations. The geopolitical effects of climate change and their impact on water resources, as well as local political, social, and economic factors, as well as the level of climatic differentiation, should all be examined in water management research (Kibarolu 2008).

5. Water management studies in the context of adaptation to climate change in Turkey

Turkey is divided into 25 hydrological basins (Figure 3). Inland river basins with no coasts and river basins having coasts to the Black Sea, Mediterranean Sea, Aegean Sea, and Marmara Sea were grouped among Turkey's twenty-five river basins.

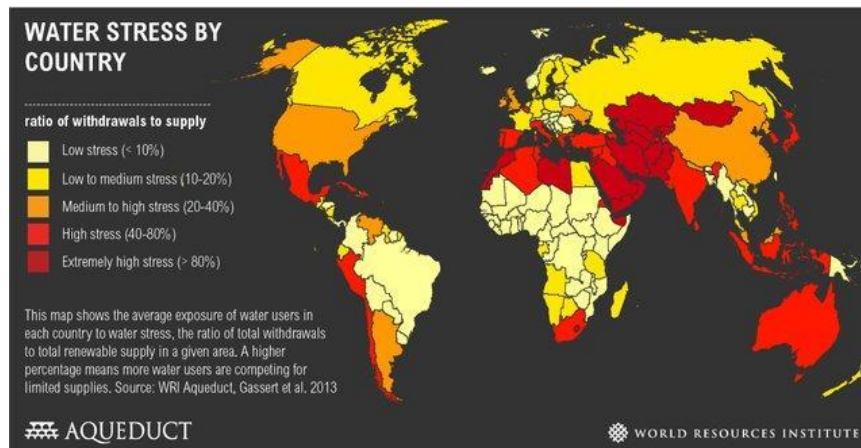
Figure 3: Hydrological Basins of Turkey





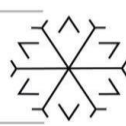
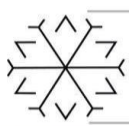
Turkey is bordered by sea on three sides, has a fractured terrain and orographic characteristics, and its water resources will be affected by climate change to various degrees. Turkey's water demand for drinking, agriculture, industry, and energy has increased considerably during the second half of the twentieth century (Kibarolu 2008). Turkey's current sustainable and useable water potential is 112 billion m³, comprising 98 billion m³ of surface water and 14 billion m³ of underground water. Water stress in Turkey's central and western areas is expected to reach 40% by 2030, according to study conducted by the European Environment Agency (EEA) to evaluate the amount of water stress in the European Union and Turkey between 2000 and 2030. This ratio is predicted to reach between 20 and 40% in the southeast and eastern areas. Turkey, according to study performed among European countries, is the country with the greatest risk of water contamination. Surface water levels in the basins are expected to drop by 20%, 35%, and 50% by 2030, 2050, and 2100, according to scientific estimations. It is conscience that expanding population and water demand will increase water stress in the coming years (MoEU 2016; SHW 2012a). Developing a basin-based strategy is the most appropriate scale for guaranteeing successful water management. River Basin Protection Action Plans (RBPAPs) should be prepared to enable coordinated and regulated water management (en 2009; MoEU 2016; climatechange.gov 2018; Gosling et al., 2011). Figure 4 shows the ratio of total withdrawals to total renewable supply in each area, indicating the countries' water stress levels.

Figure 4: Water Stress Level of the Countries – 2013 (Maddocks 2013)



Turkey is a developing country that is working to meet its socioeconomic development goals. In order to achieve these aims, Turkey has developed and implemented integrated basin management plans to preserve water resources. The data on water resources was gathered from the stations of the General Directorate of State Hydraulic Works (SHW). The hydrological and climatic variables gathered and monitored in this context include river flows, groundwater and lake water levels, sediment loads, water quality, precipitation, and evaporation (SHW 2012b). Turkey has a variety of state institutions and organizations aimed at developing the land and water resources in 25 river basins, in addition to SHW. Basin Management Plans are the most efficient method of resolving these problems and allowing the water cycle to resume.

Turkey and the European Union have begun conversations through the Environment Section, which was established on December 21, 2009. (EU). Studies were conducted to ensure that the EU acquis was adhered to, especially in the water sector. Basin Management Committees were established in compliance with the Water Framework Directive of the European Union (WFD). WFD also works on River Basin Management, Action Plans, and other environmental projects. The WFD made no specific mention of climate change or adaptation (OECD 2017). In response to the negative effects of climate change in Turkey, the Water Management Coordination Committee (WMCC) was established in 2012 with high-level participation from relevant ministries to coordinate and work on water issues. National water policy are decided by the Water Management Coordinating Committee (WMCC). In addition, a Basin Steering Committee was formed, with the presidency of Undersecretary of MoFWA. RBPAPs for 25 Turkish basins began in 2009 and were completed in 2013. Basin Management Committees, with the cooperation of the Water Management Coordination Committee and the Basin Management Central Committee at the national level, supervise the execution of RBPAPs and Provincial Water Management Committees at the local level (MoFWA, 2015). The NRBSM (National River Basin Management Strategy) (2014–



2023) was published in 2014. (Official Gazette dated 04.07.2014 and numbered 29050). Turkey's national water policy was laid out by the NRBMS (MoFWA 2015).

River Basin Management Plans, which were prepared between 2011 and 2013, take consideration water bodies and typology, categorization, target setting, and economic analysis, in addition to these studies (MoFWA, 2015). MoFWA launched the Climate Change Impacts on Water Resources Project (CCIWR) for 25 basins to find water resource adaptation techniques under climate change scenarios using a basin management framework. 138 adaptation efforts for Turkey were selected based on the findings of this research, and the ClimaHydro Database was created by collecting all of the project's outputs. Water stress would arise in both water resources and sectors in Turkey as a result of expected climate change impacts on water resources due to the predicted decrease in precipitation together with an increase in evaporation rate. These findings suggest that, considering climate change, the following three sectors are important for Turkey's water resources: drinking water, agriculture, and industrial. The adaptation activities under these titles were determined as shown in Table 4.

Table 4: Determined adaptation activities under CCIWR Project (MoFWA2016)

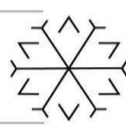
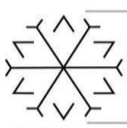
Water Intended for Human Consumption	Agriculture	Industry
Decreasing seepage loss (Non-Revenue Water) ratios	Product design compatible with climate change	Intra-facility control
Rainwater harvesting	Effective irrigation techniques	Clean production
Domestic wastewater recovery	Organic agriculture	Industry wastewater recovery

At the basin level, the development of effective agriculture techniques and the selection of climate-change-compatible items are important. More awareness of water resources should be produced in order to limit the population's usage of water. Economic sectors should establish water-friendly and long-term manufacturing strategies.

6. Discussion

The effects of climate change in the Mediterranean Basin, which includes Turkey, would be severe enough to affect the nations' long-term growth and national security, according to IPCC Assessment Reports and other national and international scientific research. Turkey will definitely be affected by global warming. Heat waves, forest fires, and floods are all expected to increase as a result of climate change in Turkey. As a result of these harmful effects of climate change, Turkey must develop basin-based water management systems. Water is primarily used for human use, agriculture, and industry in Turkey, according to scientific research. As a result, river basin scale water resource management should be considered as a starting point. Because the basin level comprises all sectors, all resource users, and all considered consequences that must be examined together, it is the most suitable scale. The quantity of water predicted to be utilized in 2023 will be similar to the amount of water available now if freshwater resources are moved without being lost. Water protection and wastewater reuse should be considered in a sustainable way to limit water losses. In Turkey, water resources must be managed responsibly, which require integrity of the hydrologic system. Turkey's worldwide water policy targets equitable and fair water usage while minimizing negative implications for downstream countries. In the areas of water, food, energy, and ecosystem security, national studies are being done in order to establish legal, scientific, and technological competence as well as expertise. For future generations, Turkey should maintain and increase its efforts in all fields.

7. Conclusion



Climate change is a challenge to national security and has a negative influence on the development of countries. Climate change has to be implemented immediately. Water should be recognized as an essential resource. Water is also essential for the economic development of a country as well as the survival of all living things. Water is important for food production, energy production, and environmental preservation. Climate change and water resource studies have been carried out not only to secure and effectively use present resources, but also to examine the possible implications of diverse activities on ecosystems in a cohesive way, as well as the possibility of climate change acceleration. It's important to remember that policies that are well-thought-out and consistently applied ensure a water-safe future.

References

- Albayrakođlu, E. (2011). Climate change and security: The case for Turkey, Gazi University Akademik Bakış Journal, 5 (9), 59-76.
- Brown, A. and Matlock, M., D. (2011). A review of water scarcity indices and methodologies. The Sustainability Consortium, White Paper 106, 20p.
- Climate Change Post (2018). Fresh Water Resources-Turkey. Retrieved from Climate Change Post website <https://www.climatechange.org/turkey/fresh-water-resources/>. Accessed 12 March 2018
- Demirci, M., (2015). Kentsel İklim Deđişikliği Yönetişimi, Journal of Erciyes University Faculty of Economics and Administrative Sciences, 46, 75-100. [In Turkish]
- Demirkesen, A., Evrendilek, F. and Berberođlu, S. (2008). Quantifying coastal inundation vulnerability of Turkey to sea-level rise, Environmental Monitoring and Assessment, 138(1-3), 101-106.
- SHW (2012a). Chapter II: land and water resources-Water and DSI. Retrieved from SHW website: <http://www2.dsi.gov.tr/english/water-and-dsi/files/assets/basic-html/page9.html>. Accessed 12 February 2018
- TURKSTAT (2018), Population projections, 2018-2080. Retrieved from website: <http://www.turkstat.gov.tr/PreHaberBultenleri.do?id=30567>. Accessed 21 February 2018
- Greenfacts (2008). Summary of United Nation water development report. Retrieved from Greenfacts website <https://www.greenfacts.org/tr/water-resources/water-resources-foldout-tr.pdf>. Accessed 28 January 2018
- Kıbarođlu, A. (2008). Küresel İklim Deđişikliğinin Sınırşan Su Kaynakları Politikasına Etkisi, pp.347-357. TMMOB (Eds.) TMMOB 2. Su Politikaları Kongresi, 20-22 March 2008, Ankara Turkey, 576p. [In Turkish]
- OECD (2017). OECD Environmental performance reviews: Turkey, Environment Policy Committee Working Party on Environmental Performance, Retrieved from OECD website: <http://www.oecd.org/env/epoc.htm>. Accessed 15 February 2018
- MoFWA (2015). General directorate of water management, Basin management department. Retrieved from MoFWA website: http://www.suyonetimi.gov.tr/Libraries/su/HAVZA_IC_ING.sflb.ashx. Accessed 15 February 2018

X-Ray Impermeability of Concretes Containing Celestite Aggregate Produced With Calcium Aluminate Cement

Furkan TÜRK ¹[0000-0002-8156-0354], Hayriye Nur NAYAN ²[0000-0002-6418-9442], Murat SAYDAN ³[0000-0003-3598-468X], Ülkü Sultan KESKİN ⁴[0000-0002-9517-9116]

¹fturk@ktun.edu.tr, Konya Technical Univesity, Konya, Turkey and Yalova University, Yalova, Turkey

²e218222001014@ktun.edu.tr, Konya Technical University, Konya, Turkey

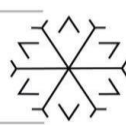
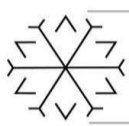
³msaydan@ktun.edu.tr, Konya Technical University, Konya, Turkey

⁴uskeskin@ktun.edu.tr, Konya Technical University, Konya, Turkey

Abstract

Nuclear power plants are complex structures of high importance in today's world and bring some dangers. The most important of these dangers is the possibility of radiation leakage of these structures, considering any adverse situation. Therefore, the strength and durability properties of concrete to be used in the construction of nuclear power plants should be designed with a good thought. This study aimed to produce a radiation barrier by using celestite, which is abundant in Turkey, in concrete mixtures at various rates. Moreover, calcium aluminate cement (CAC), which has high early strength, very high abrasion resistance and high resistant to chemical attacks, was used as a binder in the mixtures. Within the scope of this study, small rooms were created from concrete specimens, and the specimens were exposed to X-rays. X-rays passing over the specimens were detected with a hand detector placed inside the small rooms. As a result of X-ray impermeability tests, it has been observed that there is an increase in impermeability up to 34% when 80% celestite is used in the mixtures.

Keywords. Calcium aluminate cement, celestite, radiation



1. Introduction

Nuclear power plants built with sufficient radiation-absorbing elements are very advantageous in energy production in terms of both environment and efficiency. Heavy concretes with a unit weight of more than 3200-3500 kg/m³ are used to protect from gamma and X-rays in the construction of nuclear reactors and structures where radioactive sources are used (Makarious *et al.*, 1996). Concrete is increasingly used in packaging low and medium radioactive waste as an engineering barrier to keep radioactive waste harmless. However, current studies reveal that concrete designs that can be a barrier to radioactive damage from high-level waste can also be developed (Kořátková *et al.*, 2017). Heavy concrete produced with ordinary portland cement (OPC), which can be used in military facilities, medical units and dam bodies as well as nuclear power plants, differs from conventional concrete in that the unit volume weight of the aggregate used in the mixtures is higher than normal aggregates. As it is known, the unit volume weight of the aggregate, which is used at a rate of approximately 70-75% in concrete mixtures, affects many physical and mechanical properties of the concrete (Kharita, Yousef and AlNassar, 2009). It is known that natural aggregates such as barite, magnetite, limonite and hematite as well as artificial aggregates such as iron pieces are used in the production of concrete with high density and therefore high radiation absorption in order to be protected from possible damages of radiation (Şemsettin, Başıyigit and Akkurt, 2007; Sharifi, Bagheri and Shirmardi, 2013; Baradan, Yazici and Aydin, 2015; Özen *et al.*, 2016). However, it is essential to develop concrete with radiation absorption capability, instead of the radiation impermeability gained due to its high unit weight, to minimize the potential effects of radioactive waste.

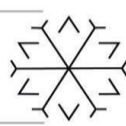
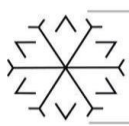
Celestite (strontium sulfate) is found in sedimentary rocks as a high density (min 3.75 g/cm³) mineral. Its high density, superior stability properties and most importantly, its high radiation absorption capacity show that this material can be used in shielding applications (Bhatti, 2012; Rushdi *et al.*, 2015). Cement-based materials have a high potential to absorb radioactive waste due to their high absorption and binding properties (Chen, Chen and Li, 2009). Choosing the suitable concrete matrix is closely related to the chemistry of the inactive and radioactive materials in the waste. For example, ionic exchanges of some radioactive wastes have been reported to have compatibility problems with OPC (Kořátková *et al.*, 2017). This incompatibility causes the waste to degrade the cement-based matrix over time. Calcium aluminate cement (CAC) is the cement that sets much faster compared to OPC, gains strength, especially at early ages, and is resistant to high temperature, chemical attack and abrasion (Scrivener, Cabiron and Letourneux, 1999; Scrivener and Capmas, 2003). Therefore, it is thought that it would be more advantageous to use CAC instead of OPC as a binder in heavy concrete production of structures that need to be constructed quickly, absorb radiation, be resistant to chemical attacks and provide high strength.

It is known that heavy concretes produced with OPC have radiation shielding ability (Şemsettin, Başıyigit and Akkurt, 2007; Akkurt *et al.*, 2011). In this study, celestite, which could replace heavy aggregate, was used, and CAC, which has superior properties than OPC, was used as a binder. Within the scope of this study, small rooms were created from concrete specimens, and the concrete rooms were exposed to X-rays. X-rays passing over the concrete were detected with a hand detector placed inside the small rooms.

2. Material and Method

2.1. Concrete Constituents and Preparing Mix

REFRO 40 CAC supplied from the CİMSA was used in the concrete designs prepared at a dosage of 400 kg/m³. The chemical components of cement are presented in Table 1. Limestone aggregate with a gradation of 0-4 mm and 4-12 mm was used in concrete mixtures. First of all, in order to determine the effectiveness of celestite, a control specimen containing 100% limestone aggregate was produced. After that, 20%, 40%, 60% and 80% of the fine limestone aggregate were replaced by fine celestite supplied from the Sivas mining quarry of Barit Maden Turk with 0-4mm granulometry. The water/cement ratio was determined as 0.45 in all prepared mixtures, and a polycarboxylate based plasticizer additive was used at the rate of 1% by weight of the binder. Prepared concrete mixes are presented in Table 2.

**Table 1:** Chemical composition of the cement

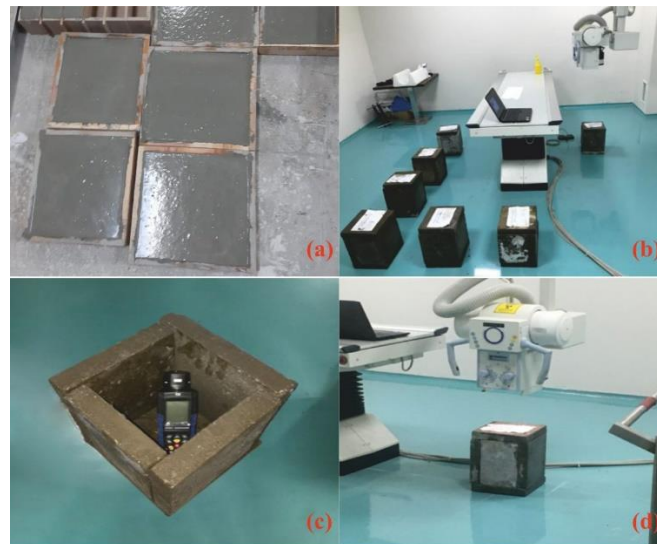
Component	Quantity (%)
SiO ₂	5
Al ₂ O ₃	38
Fe ₂ O ₃	19
CaO	38
MgO	1
SO ₃	0,2
TiO ₂	3
Na ₂ Eq	0,3

Table 2: Concrete mixing proportions

Mix.	Cement (kg/m ³)	Water (kg/m ³)	Coarse aggregate (%)	Fine aggregate (%)	Fine celestite (%)	Superplasticizer (kg/m ³)
Control	400	240	100	100	0	4
CSF20	400	240	100	80	20	4
CSF40	400	240	100	60	40	4
CSF60	400	240	100	40	60	4
CSF80	400	240	100	20	80	4

2.2. Method

The prepared mixtures were taken into moulds of different sizes in order to form small rooms with a thickness of 4 cm. After 24 hours, the specimens removed from the moulds were subjected to water curing for 27 days, and small rooms of 25x25x25 cm were formed by combining them with a thin layer of epoxy adhesive. X-ray shots were made three times from the X-ray device in the Selcuk University Faculty of Veterinary Medicine with 36 cm distance and 360 mA to the specimens. The intensity of X-rays passing through the specimens was determined by a portable handheld detector (PCE – RAM10) placed inside the rooms (Figure 1).

**Figure 1:** Molding of the mixture (a), moving the small rooms to the X-ray room (b), placing the hand detector inside the room (c), exposure of the specimen to X-ray (d)

3. Result and Discussion

As a result of X-ray impermeability tests, the X-ray intensity of the specimens is presented in Figure 2. While the mean values read in the control specimen for X-ray shots were 14.0 mR/h, it was determined as 9.51 mR/h in the %80 celestite containing the specimen. As could be seen from these results, the increase in the amount of celestite used in the concrete increased the X-ray impermeability. It is known that concrete could protect from rays such as alpha, beta, gamma and X, thanks to its high density and high crystalline water content (Creutz and Downes, 1949). However, in this study, instead of aggregates such as barite and limonite, which are used to increase the density of concrete, celestite with high density and stability ($> 3.75 \text{ gr/cm}^3$) (Zorađa, 2009; Rushdi *et al.*, 2015), which Turkey has about 20% of the world's reserves were used. Moreover, using CAC, which is known to increase the crystalline water content in concrete (Scrivener, Cabiron and Letourneux, 1999; Navarro-Blasco *et al.*, 2013), as a binder instead of OPC in mixtures is considered to be entirely accurate.

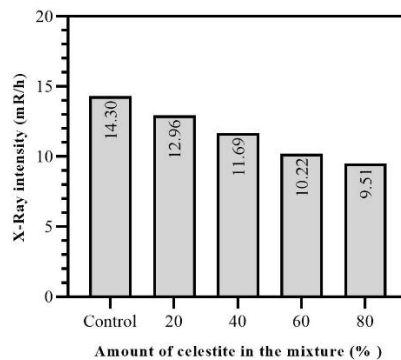


Figure 2: X-ray intensity of the specimens

The impermeability increase rates obtained according to the control specimen are presented in Figure 3. It was found that the concretes containing 20%, 40, 60, and 80 fine celestite minerals had an impermeability increase of 9.32%, 18.24, 28.51 and 33.49, respectively, compared to the control specimen without celestite. It is understood from this that even the use of low amounts ($<20\%$) of celestite increases the X-ray impermeability of the specimens significantly (about 10%).

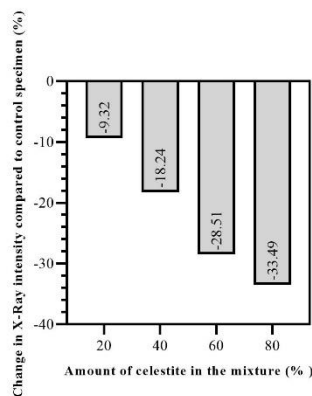
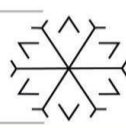
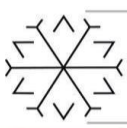


Figure 3: Change in X-ray intensity compared to control specimen



4. Conclusion

The following conclusions were reached in this study, which was carried out to provide X-ray impermeability improvement in hardened concrete by using celestite, which is Turkey has about 20% of the world's reserves.

- The use of fine celestite mineral as aggregate with CAC based mixtures increased the X-ray impermeability of concrete.
- It has been observed that there is an increase in impermeability up to 34% when 80% celestite is used in the mixtures.
- It is clear that the unit weight of concrete increases as a result of replacing the limestone aggregate with celestite. However, further experimental studies are required to determine whether the increase in X-ray impermeability obtained as a result of the experiments is due to the radiation absorbing ability of celestite or due to the increase in a unit weight of concrete.

Acknowledgements

The authors are grateful to Selcuk University for allowing its infrastructure to conduct the experiments, Cimsa Cement Factory and Barit Maden Turk for their support in the supply of materials.

References

- Akkurt, I. *et al.* (2011) 'Ağır agregaların radyasyon zırhlama özellikleri', *Engineering Sciences*, 6(4), pp. 1481–1485.
- Baradan, B., Yazici, H. and Aydin, S. (2015) *Beton (ikinci baskı)*, Dokuz Eylül Üniversitesi Mühendislik Fakültesi Yayınları, İzmir, Türkiye.
- Bhatti, K. P. (2012) 'Synthesis of strontium carbonate and strontium chromate from the celestite ore', *Journal of the Chemical Society of Pakistan*, 34(6).
- Chen, Liang, Chen, Li and Li, J. (2009) 'Aanalysis of Cementation Technology for Liquid Radioactive-Waste in PWR NPPs [J]', *Nuclear Power Engineering*, 2.
- Creutz, E. and Downes, K. (1949) 'Magnetite concrete for radiation shielding', *Journal of applied physics*, 20(12), pp. 1236–1240.
- Kharita, M. H., Yousef, S. and AlNassar, M. (2009) 'The effect of carbon powder addition on the properties of hematite radiation shielding concrete', *Progress in Nuclear Energy*, 51(2), pp. 388–392.
- Kořátková, J. *et al.* (2017) 'Concrete and cement composites used for radioactive waste deposition', *Journal of environmental radioactivity*, 178, pp. 147–155.
- Makarious, A. S. *et al.* (1996) 'On the utilization of heavy concrete for radiation shielding', *Annals of Nuclear Energy*, 23(3), pp. 195–206.
- Navarro-Blasco, I. *et al.* (2013) 'Solidification/stabilization of toxic metals in calcium aluminate cement matrices', *Journal of hazardous materials*, 260, pp. 89–103.
- Özen, S. *et al.* (2016) 'Properties of heavyweight concrete for structural and radiation shielding purposes', *Arabian Journal for Science and Engineering*, 41(4), pp. 1573–1584.
- Rushdi, M. A. H. *et al.* (2015) 'Strontium sulfate as an EPR dosimeter for radiation technology application', *Radiation Physics and Chemistry*, 106, pp. 130–135.
- Scrivener, K. and Capmas, A. (2003) 'Calcium aluminate cements', *Advanced concrete technology*, 3, pp. 1–31.
- Scrivener, K. L., Cabiron, J.-L. and Letourneux, R. (1999) 'High-performance concretes from calcium aluminate cements', *Cement and concrete research*, 29(8), pp. 1215–1223.
- Şemsettin, K., Başığit, C. and Akkurt, İ. (2007) 'Barit agregalı ağır betonların radyasyon zırhlama amacıyla kullanımının araştırılması', *Gazi Üniversitesi Mühendislik Mimarlık Fakültesi Dergisi*, 22(2), pp. 393–399.
- Sharifi, S., Bagheri, R. and Shirmardi, S. P. (2013) 'Comparison of shielding properties for ordinary,

Last name, First initial. (Year published). Chapter title. In: First initial. Last name, ed., Book Title, 1st ed.* City: Publisher, Page(s).

barite, serpentine and steel–magnetite concretes using MCNP-4C code and available experimental results', *Annals of Nuclear Energy*, 53, pp. 529–534.

Zorağa, M. (2009) *SrSO₄'(Selestit)'in Karbonatlı Çözeltide Çözündürülmesi*. İstanbul University.

Effect of Low Content of Hemp Fibre on Flexural Behavior of Mortar

Furkan TÜRK ¹[0000-0002-8156-0354], Murat SAYDAN ²[0000-0003-3598-468X], Ülkü Sultan KESKİN ³[0000-0002-9517-9116]

¹fturk@ktun.edu.tr, Konya Technical Univesity, Konya, Turkey and Yalova University, Yalova, Turkey

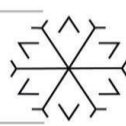
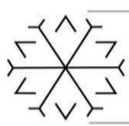
²msaydan@ktun.edu.tr, Konya Technical University, Konya, Turkey

³uskeskin@ktun.edu.tr, Konya Technical University, Konya, Turkey

Abstract

While the most common fibre types used as fibre reinforcement in cement-based materials are steel, synthetic or glass fibres, hemp fibres are the most common among natural fibres. Industrial hemp is used in construction, textiles, food, automobiles, biofuels and many other fields. Herein, the change in bending behaviour of beam specimens was investigated when natural hemp fibres were used in cement-based mortars. In the case of using 0.5% hemp fibre additive by cement weight in mortar mixtures, there was no change in flexural strength, while an increase of approximately 48% in maximum deflection. Moreover, it increased the strain corresponding to maximum stress by 30%. Therefore, it could be said that the use of a low rate of hemp fibre increases the ductility of mortar beams without affecting the flexural strength.

Keywords. Ductility, flexural strength, hemp fibre



1. Introduction

The use of products obtained from nature in building materials dates back to the past years. The idea of use, which started with the use of straw in adobe, appears as the use of natural fibres such as coconut, bamboo and sisal as reinforcement material in cement-based mixtures (Swift and Smith, 1979; Ramaswamy, Ahuja and Krishnamoorthy, 1983). However, the use of natural fibres as reinforcement material in concrete also brings some disadvantages. For example, natural fibres show a more significant variation in properties than steel or glass fibres. Such a situation may cause changes in concrete quality. In addition, there are no suitable mixing methods and estimation tools to predict the mechanical performance of the resulting concretes (Li, Wang and Wang, 2004). Therefore, in cases where natural fibres are used as reinforcement material to increase the performance of concrete, it does not seem possible to predict the changes in the final mechanical properties of concrete with any degree of accuracy. However, if the production conditions such as mixing ratios, curing conditions, mixing processes are kept constant, it is also possible to obtain a less variable concrete in terms of mechanical behaviour (Li, Wang and Wang, 2006).

The modern development of fibre-reinforced concrete dates from the 1960s to the present (Nibasumba and Liu, 2011). Steel, synthetic or glass fibre is the most common fibre used as fibre reinforcement in cementitious materials (Bentur and Mindess, 2006). Among the natural fibres examined in the literature, hemp fibres are the most common. Hemp is one of the oldest plants used in various applications and is, therefore, one of the most recognizable plants in the World (Netinger Grubeša *et al.*, 2018). Hemp fibre, which is frequently used in building materials, increases the flexural strength (Li, Wang and Wang, 2004) and ductility of the concrete (Awwad *et al.*, 2012), while negatively affecting the compressive strength when used in concrete mixtures (Li, Wang and Wang, 2006).

Moreover, it increases Marshall Stability when used in hot bituminous mixtures (Serin *et al.*, 2018). It has also been reported that although it does not directly affect the fire resistance of concrete, it can reduce crack propagation at high temperatures (Netinger Grubeša *et al.*, 2018). In this experimental study, the effects of hemp fibers used in low amount (0.5%) in mortar mixtures on flexural strength and ductility of mortars were investigated.

2. Material and Method

2.1. Mortar Constituents and Preparing Mix

In this study, natural sand with a sieve diameter of 0-4 mm and a specific gravity of 2.60 gr/cm³ was used. In the preparation of the mixtures, CEM I 42.5N Portland cement according to TS EN 197-1 was supplied by the Konya Cement Factory. The specific gravity of the cement used is 3.12 gr/cm³. Hemp, a woody and annual plant from the *Cannabaceae* family close to the nettle, has two subspecies as *cannabis sativa* and *cannabis indica*. *Cannabis sativa* is used for fibre production and has industrial importance. The length of the hemp fibres used in this study is approximately 50 mm and varies within itself. The fibres used in the study is presented in Figure 1.

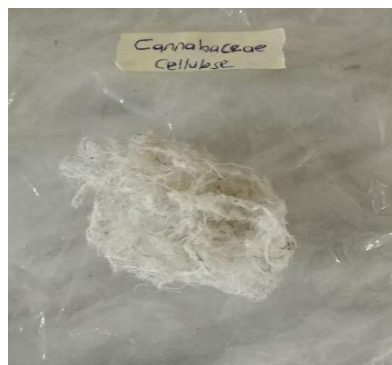
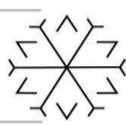


Figure 1: Hemp fibre

Cement dosage was chosen as 450 kg/m³ in the prepared mixtures, water/cement ratio was taken as 0.5 and kept constant in all mixtures. Specimens with dimensions of 45x75x360 mm, which do not contain fibers and contain 0.5% hemp fiber by weight of cement, were produced. Polycarboxylate-based superplasticizer was used at the rate of 1% by weight of cement in the reference mixture without fiber, and at the rate of 2%



in the mixture containing fiber, since the fibers absorb the mixing water. Mortar mixing proportions are given in Table 1.

Table 1: Mortar mixing proportions

Mix.	Cement (kg/m ³)	Water (kg/m ³)	Fine aggregate (kg/m ³)	Hemp fiber (% by weight of cement)	Superplasticizer (kg/m ³)
Control	450	225	1350	0	4.5
FC05	450	225	1350	0.5	9

2.2. Method

Beam specimens with dimensions of 45x75x360 mm were taken out of the mould after 24 hours and left to water cure. The flexural strength test was performed on specimens at the age of 28. Four-point bending tests were carried out in accordance with the TS EN 12390-5 standard to determine the bending strength. The test setup is shown in Figure 2. The load values applied to the specimen were read through the load cell, and the deflection values were read from the computer-aided system by the potentiometric ruler. The equation given in Equation 1. was used to calculate the stress, and the equation given in Equation 2 was used to calculate the strain.

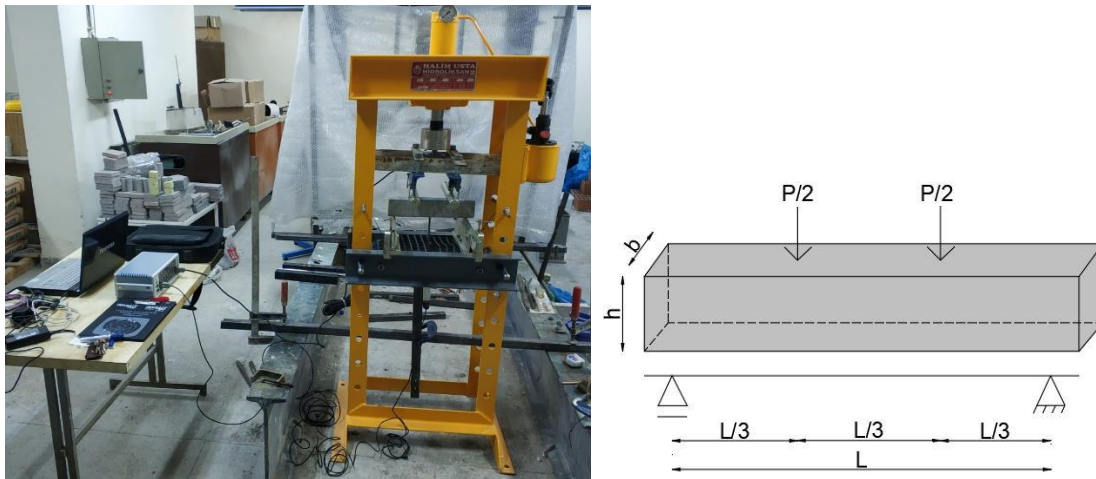


Figure 2: Four-point bending test

$$\sigma = \frac{PxL}{bxh^2} \tag{1}$$

$$\varepsilon = \frac{6xDxh}{L^2} \tag{2}$$

σ : Stress

ε : Strain

P: Load

L: Distance between supports

D: Deflection

b,h: Specimen dimensions

3. Result and Discussion

The stress-strain relations obtained from the four-point bending test of the specimens produced from the mixture with hemp fibre additive at the rate of 0.5% by weight of cement and without fibre are given in Figure 3.

While the control specimen showed a bending strength of 5.65 MPa and a deflection of about 0.31 mm, the fibrous specimen showed a bending strength of 5.75 MPa and a deflection of about 0.46 mm. In fact, the 2% difference in bending strengths is statistically negligible. However, there was a difference of approximately 48% between the maximum deflections. It is understood from this that when 0.5% hemp fibre additive by cement weight is used in mortar mixtures, there is almost no increase in the bending strength of the mortars, but it increases the flexibility of the beam by providing a significant increase in the maximum deflection capacity

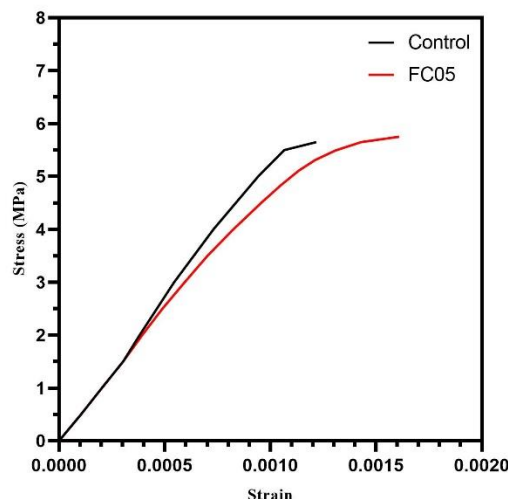


Figure 3: Stress-strain relations of beams

When the stress-strain relationship of the specimens was examined, the control specimen indicated 0.0012 strain against the maximum stress. The specimen containing hemp fibre, on the other hand, indicated 0.0016 strain in response to the maximum stress. While hemp fibre did not change the flexural strength of hardened mortars, it caused a significant increase in energy absorption capacity. Çomak, et al., 2018 reported that the flexural strength of the concrete could be increased up to 17%, and the ductility of the concrete could be increased with the help of using the hemp fibre in the mixtures at 2-3% rates. Ghalieh et al., 2017, on the other hand, put forward that ductility and thus energy absorption capacity could be increased in columns wrapped with hemp fibres. This experimental study reveals that even at meagre rates, hemp fibres could increase the energy absorption capacity of beam specimens.

4. Conclusions

The conclusions reached from the four-point bending test of mortars using 0.5% hemp fibre by weight of cement are as follows:

- When 50 mm long hemp fibres were used in mortar mixes, it did not affect bending strength.
- Although the flexural strength does not change, the maximum deflection increased by approximately 48%.
- The strain corresponding to the maximum stress increased by about 30%.



References

- Awwad, E. *et al.*, 2012. Studies on fiber-reinforced concrete using industrial hemp fibers, *Construction and Building Materials*, 35, pp. 710–717.
- Bentur, A. and Mindess, S., 2006. *Fibre reinforced cementitious composites*. Crc Press.
- Çomak, B., Bideci, A. and Salli Bideci, Ö., 2018. Effects of hemp fibers on characteristics of cement based mortar, *Construction and Building Materials*, 169, pp. 794–799. doi: 10.1016/J.CONBUILDMAT.2018.03.029.
- Ghalieh, L. *et al.*, 2017. Concrete Columns Wrapped with Hemp Fiber Reinforced Polymer – An Experimental Study, *Procedia Engineering*, 200, pp. 440–447. doi: 10.1016/J.PROENG.2017.07.062.
- Li, Z., Wang, L. and Wang, X., 2004. Compressive and flexural properties of hemp fiber reinforced concrete, *Fibers and Polymers*, 5(3), pp. 187–197.
- Li, Z., Wang, X. and Wang, L., 2006. Properties of hemp fibre reinforced concrete composites, *Composites Part A: Applied Science and Manufacturing*, 37(3), pp. 497–505. doi: 10.1016/j.compositesa.2005.01.032.
- Netinger Grubeša, I. *et al.*, 2018. Effect of hemp fibers on fire resistance of concrete, *Construction and Building Materials*, 184, pp. 473–484.
- Nibasumba, P. and Liu, X. L., 2011. Recent developments in fibre reinforced concrete and their effect on concrete columns analysis, *Construction and Building Materials*, 18(7), pp. 549–558.
- Ramaswamy, H. S., Ahuja, B. M. and Krishnamoorthy, S., 1983. Behaviour of concrete reinforced with jute, coir and bamboo fibres, *International Journal of Cement Composites and Lightweight Concrete*, 5(1), pp. 3–13.
- Serin, S. *et al.*, 2018. Doğal kenevir lifi kullanımının asfalt beton karışımlara etkisi, *Düzce Üniversitesi Bilim ve Teknoloji Dergisi*, 6(4), pp. 732–744.
- Swift, D. and Smith, R. B. L., 1979. The flexural strength of cement-based composites using low modulus (sisal) fibres, *Composites*. doi: [https://doi.org/10.1016/0010-4361\(79\)90288-X](https://doi.org/10.1016/0010-4361(79)90288-X).

Leveraging Clean and Advanced Technologies to Increase Health System Resilience in Conflict Areas

ALI MOHAMAD ¹[0000-0003-2496-6304], Asst. Prof. Dr. Ayşe Y. GÜNAL ²[0000-0002-4866-2914]

¹ eng.alimhm@gmail.com, Gaziantep University, Faculty of Engineering, Civil Engineering Department

² agunal@gantep.edu.tr, Gaziantep University, Faculty of Engineering, Civil Engineering Department

Abstract

To strengthen the health system resilience of the Primary Health Care Centers (PHCCs) and hospitals in fragile areas.

Due to increase in operational hours and case-loads have led to a rise in energy demand for in ongoing conflicts zones. The main obstacles in the Health Sector are: 1) High prices and unstable supply of fuel to operate diesel generators; 2) Fuel dependency for mobility; 3) Shortage and overload of qualified health professionals at all levels (especially after the speared of the COVID-19 Pandemic).

Using integration of 3 leveraging clean and advanced technologies to overcome the challenges thorough: 1) Solar Photovoltaic as alternative to fuel for diesel generators; 2) BEV for health transportation; 3) Streamlined TM to enable remote support.

Solar Photovoltaic System can help reduce the dependency on fuel, while ensuring that the critical department and services, like emergency departments and Intensive Care Units have electricity on 24/7 at hospital during diesel outages. Battery Electric Vehicles as alternative to conventional mobility for ambulance and vaccine transport via charging from powered Solar Photovoltaic Systems. Telemedicine Platform will allow for qualified medical professionals to effectively help deliver certain services in remote communities.

It's possible to transition health system to 100% renewables in health facilities, with BEV to reduce mobility expences – and reducing patient referral through advanced telecommunication systems – in the most difficult places – it's seen that the potential for the rest of the world to do same as logical and necessary – especially in light of the urgency of achieving climate goals.

Keywords. Energy, Battery Electric Vehicle (BEV), Telemedicine (TM), Sustainability, Climate Change

Dynamic Analysis of a Framed Machine Foundation with Vibration Isolation Materials

Kadir GÜR ^{1*}[0000-0001-7966-574X] and Şeref D. AKBAŞ ²[0000-0001-5327-3406]

¹kadir.gur82@gmail.com, Bursa Büyükşehir Belediyesi

²serefda@yahoo.com, Bursa Technical University, Department of Civil Engineering

Abstract

In this study, harmonic analysis and responses of a framed machine foundation under dynamically loads are investigated by considering with soil-structure interaction. The machine foundation is considered with different type of vibration isolation such as, rubber, silicone rubber, wood, cork. The considered problem is modelled by using ANSYS Workbench software program and finite element models are obtained. In the solution of the dynamic and soil-structure interaction problem, 3 dimensional finite element model is used. The machine, the foundation and the soil are modelled separately and connected with each other. The machine is considered as 3 dimensional solid and connect to the framed foundation with vibration isolation materials. Also, the soil is considered 3 dimensional finite element and the boundary and dimensions of the soil are selected enough large dimensions. In the finite element model of the soil, SOLID185 finite element type is used and SOLID65 finite element type is used in the modeling of the reinforced concrete foundation and the machine in ANSYS Workbench program. The dynamically machine load is considered as a harmonic property. In the results, effects of different isolation materials and load parameters on the dynamic responses of the framed machine foundation by using 3 dimensional finite element approach. In the results, displacements and vertical accelerations of the foundation and special points of the soil are obtained and discussed according to different types of isolation material and soil types. It is obtained from the dynamic results, the isolation materials are very effective on the absorption of the machine loads. Also, using the soil-structure interaction model gives more accuracy and realistic responses for design analysis of foundation machines.

Keywords. Framed Machine Foundation, Soil-Structure Interaction, Finite Element Method, Dynamic Analysis

Some Mechanical Properties of Polymer Modified Concrete

Haluk Görkem Alcan ¹[0000-0002-6696-4297], Barış Bayrak ²[0000-0002-7438-1227], Oğuzhan Çelebi ³[0000-0002-4409-4235],
Oğuzhan Akarsu ⁴[0000-0002-2662-1417], Abdulkadir Cüneyt Aydın ⁵*[0000-0002-6696-4297]

¹hgorkemalcan@kafkas.edu.tr, Department of Civil Engineering, Kafkas University

²baris.bayrak@atauni.edu.tr, Department of Civil Engineering, Atatürk University

³celebioguzhan@atauni.edu.tr, Department of Civil Engineering, Atatürk University

⁴oguzhan.akarsu14@ogr.atauni.edu.tr, Department of Civil Engineering, Atatürk University

⁵acaydin@atauni.edu.tr, Department of Civil Engineering, Atatürk University

Abstract

The effect of styrene acrylic rubber (SAR) and styrene butadiene rubber (SBR) latex on some mechanical properties of concrete such as compressive and flexural strength was investigated, throughout this study. The mixes were prepared with polymer/cement ratio of 5%, 10%, and 15%. In addition, the effect of water/cement ratio and curing conditions on the mechanical properties of the composite was studied. It has been observed that the addition of SAR and SBR latex in polymer modified concrete results an improvement of flexural strength, conversely a negative effect on compressive strength. On the other hand, it has been observed that the water/cement ratio increases to a certain level and water+air curing increases the mentioned mechanical properties of the composite. Although, for the high dosage of cement, it has been observed that the workability is decreased with the polymer ratio increase. Thus, the dosage of polymer latex needs to be adjusted, carefully. According to the results, it may be recommended to use polymer modified concrete with SAR latex for the conventional concrete structures and/or members within the affect of flexural loading(s).

Keywords. Styrene acrylic rubber, butadiene rubber (SBR) latex, flexural strength, compressive strength

1. Introduction

Concrete is composite building material that is often preferred because of its high compressive strength and economical. But also concrete and cement mortar have some disadvantages such as low tensile strength, drying shrinkage, low toughness and low chemical resistance (Hirde and Dudhal, 2016). To minimize these disadvantages, researchers have conducted variety of studies that concrete-polymer composite is one of these methods. Polymers are lower in compressive strength, but can have higher tensile strength, chemical resistance and good bonding (Islam et al., 2011). Polymer concretes are divided into three groups, these are polymer concrete (PC), polymer modified concrete (PMC) and polymer impregnated concrete (PIC). PC is a composite material its binder phase consists of different polymer, while the PMC is made of using different proportions of cement and polymer together as a binder. PIC is needed the polymer injection of hardened concrete followed by the different polymerization process (Kardon, 1997).

In PC, polymer matrix binds stronger to aggregate particles unlike cement concrete. But polymer matrix materials are more expensive than ordinary cement, and can generate heat and undergo shrinkage during curing. Also PC is sensitivity to high temperature so it's usually chosen for precast connection and repairs (Soni and Joshi, 2014). PIC is prepared by impregnated a polymer into the cracks and voids of hardened concrete. Polymer is polymerized after it's enter into the concrete by chemical activator or heat. PIC strength is depend on impregnation depth cause of limited porosity of concrete, the exposure time of polymer and pressure applied. Therefore PIC applications are limited to precast thin panels and highway surfaces (Sivakumar, 2011). PMC is made by the modifying Portland cement concrete with polymer additives such as latexes, polymer powders, water-soluble polymers and monomers also, the polymer material is added to the usual cement mortar or concrete in its fresh form during mixing. Styrene acrylic rubber (SAR), styrene butadiene rubber (SBR), natural rubber and polyvinyl acetate latexes are preferred types of polymers in PMC production. Latex is a polymer formed by the emulsion polymerization of monomers and it contains different solids by weight. After mixing latex, polymer particles suspended in the latex are dispersed throughout cement paste. During the cement hydration, voids and gel products are



covered by deposits of polymer particles. The polymer particles gradually concentrate in the capillary pores due to growth of hydration products since water is consumed in hydration process. The polymer particles on gel product and in voids come together to form continuous film or membrane due to withdrawal of water by hydration or drying. These membranes form a co matrix mix with hydrated cement paste and binding the hydrates with the aggregates (Ohama, 1995). In the resulting matrix phase, the hydrated cement elements and the polymer film form a space network structure that is intertwined with each other, and the aggregate grains are wrapped by a two-component continuous phase (Bideci et al.). These microstructural reactions increase the toughness, adherence, flexural strength and impermeability of PMC. Polymer modified concrete is preferred more than other types of polymer concrete because it is easier and cheaper to apply. Therefore it use bridge decks, roadways, flooring, pipes, repair for deteriorated structures, strengthening, insulation, etc (Assaad and Daou, 2017).

In this paper is presented the effect of different polymer latexes, different water/cement ratios, different latex ratios and different curing conditions on the mechanical performance of concrete.

2. Materials and Methods

The cement used was CEM I 42,5R (Committee, 2011) supplied by Erzurum Aşkale Çimento Manufacturing Company also the properties of cement are given in Table 1. River sand and crushed stone were used as fine (0-5 mm) and coarse (5-15mm) aggregates, respectively. The composition of the SAR and SBR latexes used as polymer is given in Table 2.

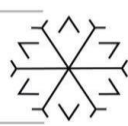
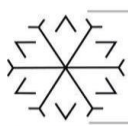
Table 1. The physical properties and chemical analysis of Portland cement (CEM I 42,5R)

Chemical Analysis		Physical and Mechanical Tests	
SiO ₂	18,32	Fineness (%)	<10
Al ₂ O ₃	4,51	Specific gravity (g/cm ³)	3,15
Fe ₂ O ₃	3,07	Specific surface (cm ² /g)	3562
CaO	63,75	Initial setting time (hour-min.)	160
MgO	1,6	Final setting time (hour-min.)	210
SO ₃	3,17	Volume expansion (mm)	1
Na ₂ O	0,37	Compressive early strength (MPa)	26,2
K ₂ O	0,85	Compressive standard strength (MPa)	48,1
Cl ⁻	0,007	Water requirement of cement (%)	30

In experimental study, 5%, 10%, 15% SAR, and SBR added by weight of cement. At the same time free water in polymer latex was considered in this study. Cylinder and prism samples were produced to test the compressive and flexural strength of polymer modified concrete. Cylinder specimens of 10x20 cm and beam specimen of 28x7x7 cm were cast. The 4-point loading was applied to determine the flexural strength (Figure 1). All mixes were prepared using a mechanical mixer also control and design group mixtures were given Table 3 and Table 4, respectively. The samples were demolded after 24 h casting, and then subjected to the following three different curing systems; natural dry curing, water curing and 3-day water curing / 4-day dry curing.

Table 2. Physical and chemical Properties of SAR and SBR Latex

	SAR	SBR
Form	Milky White Liquid	Milky White Liquid



Density (kg/lt)	1,08	1,02
Solid Content	%42	%35
pH	7-9	8-9,5

Table 3. Design of control group mixture

	Control 1	Control 2	Control 3	Control 4
Cement	400	400	400	400
Water	120	120	140	180
Coarse aggregate	1135	1135	1104	1042
Fine aggregate	757,2	757,2	736,3	694
Plasticizer	6	6	4	0
Cure condition	Air	Water	Water	Water + Air

*All units are (kg/m³)

Table 4. Design of mixture

	Group 1	Group 2	Group 3	Group 4	Group 5	Group 6	Group 7	Group 8	Group 9	Group 10	Group 11	Group 12
Cement	400	400	400	400	400	400	400	400	400	400	400	400
Water	120	120	120	120	120	120	140	180	180	180	180	180
Coarse aggregate	1066,3	1066,3	997	997	927,7	927,7	965,8	903,4	972,7	903,4	972,7	972,7
Fine aggregate	710,9	710,9	664,7	664,7	618,4	618,4	643,9	602,3	648,5	602,3	648,5	648,5
Latex	48 (SAR)	48 (SAR)	96 (SAR)	96 (SAR)	144 (SAR)	144 (SAR)	96 (SAR)	96 (SAR)	48 (SAR)	96 (SBR)	48 (SBR)	48 (SAR)
P/C Ratio*	5	5	10	10	15	15	10	10	5	10	5	5
Cure condition	Air	Water	Air	Water	Air	Water	Water	Water	Water	Water	Water	Water + Air

*All units are (kg/m³)

*The polymer/cement ratio was determined according to the solid content of the polymer

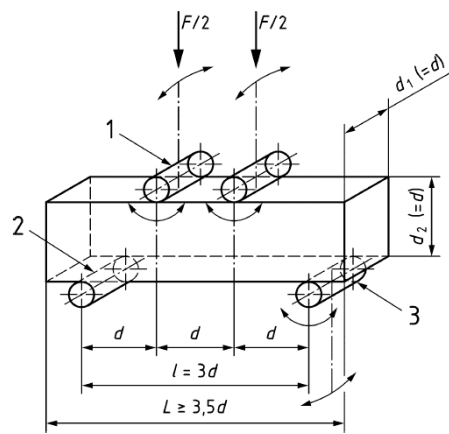


Figure 1. Four-point flexural test

3. Results and Discussion

The compressive strength test was conducted according to TS EN 12390-3 (CEN, 2009). The results of the compressive strength of the samples are shown in Figure 2 and Table 5. It is observed that compressive strength is decreased with the addition of latex at early age (7 days). The sample with the highest compressive strength is Group 12 with 22.4 MPa compressive strength. The group with the lowest compressive strength is Group 7 with a compressive strength of 7.9 MPa. It may be that the addition of latex does not penetrate sufficiently into the internal structure of concrete at an early age and does not fill the voids.

The flexural strength test was performed according to TS EN 12390-5 (de Normalisation, 2009) and the results are given in Figure 3 and Table 5. If the flexural strength results are examined, it is seen that the flexural strength values of PMC samples increase. The highest and lowest flexural strength are Group 12 and Group 5 with 5.1 MPa and 1.5 MPa values, respectively. It is believed that this result is due to the fact that the polymer film layer more powerful bridging between the aggregate grains with mortar.

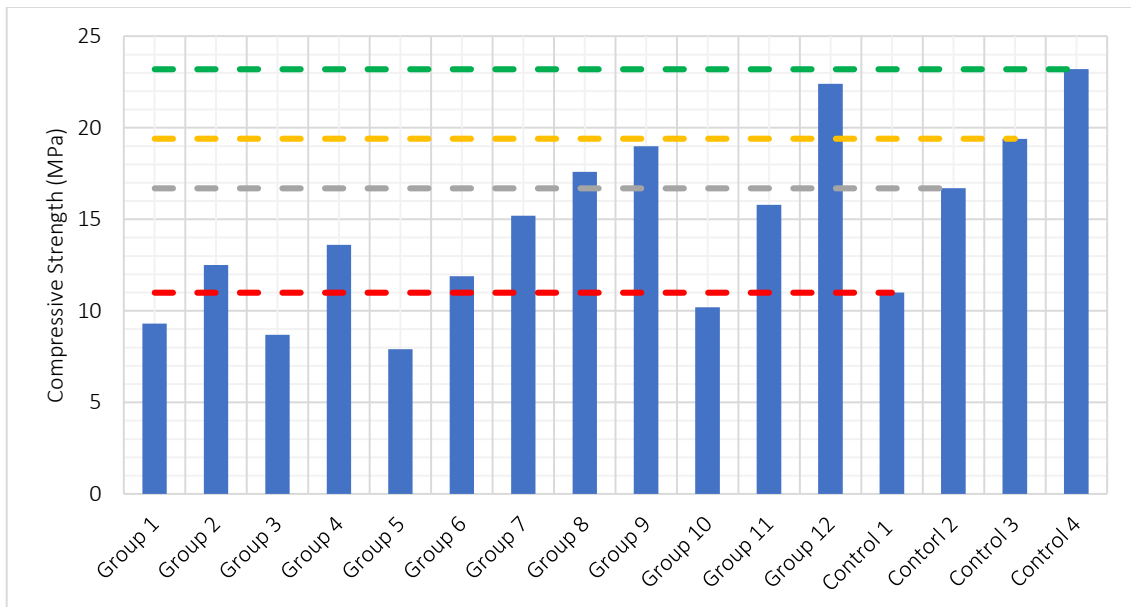


Figure 2. Compressive strength of samples

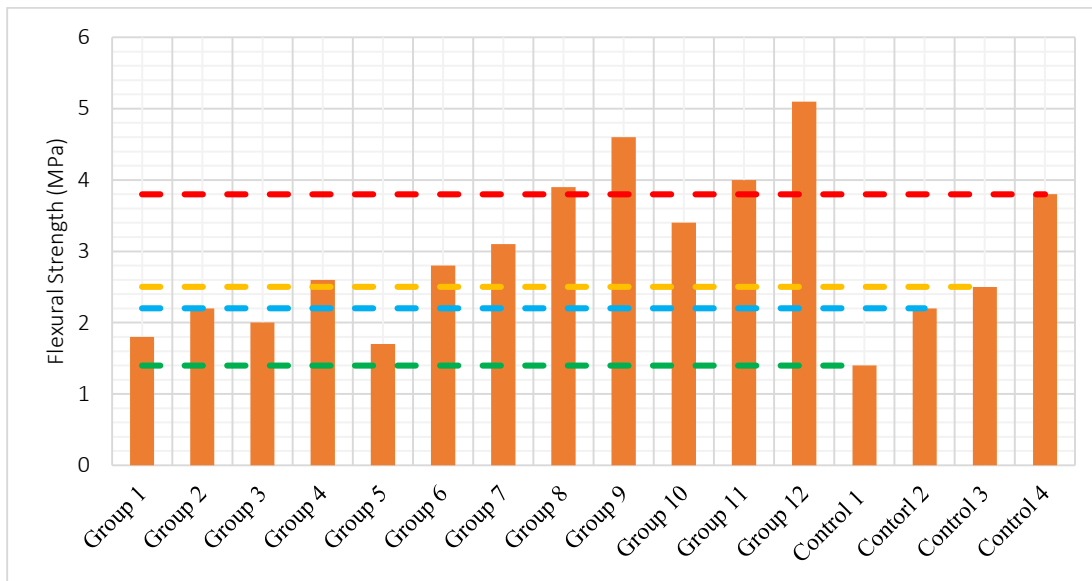
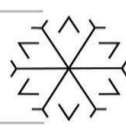
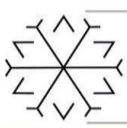


Figure 3. Flexural strength of samples

Table 5. Compressive strength and flexural strength of samples (MPa)

	Group 1	Group 2	Group 3	Group 4	Group 5	Group 6	Group 7	Group 8
Compressive Strength	9,3	12,5	8,7	13,6	7,9	11,9	15,2	17,6
Flexural Strength	1,8	2,2	2	2,6	1,7	2,8	3,1	3,9
	Group 9	Group 10	Group 11	Group 12	Control 1	Control 2	Control 3	Control 4
Compressive Strength	19	10,2	15,8	22,4	11	16,7	19,4	23,2
Flexural Strength	4,6	3,4	4	5,1	1,4	2,2	2,5	3,8

On the other hand, it seems that increasing the water-cement ratio to a certain level (from 0,3 to 0,45) and applying water-air cure leads to an increase in the compressive and flexural strength of the PMC. In Figure 4 and Figure 5, the percentage changes of the compressive and flexural strengths of the samples with admixture according to Control1, 2, 3 and 4 are shown. The negative side of the graphs means that the samples with admixture have less strength as a percentage, and the plus side of the graphs means that they have the higher strength.

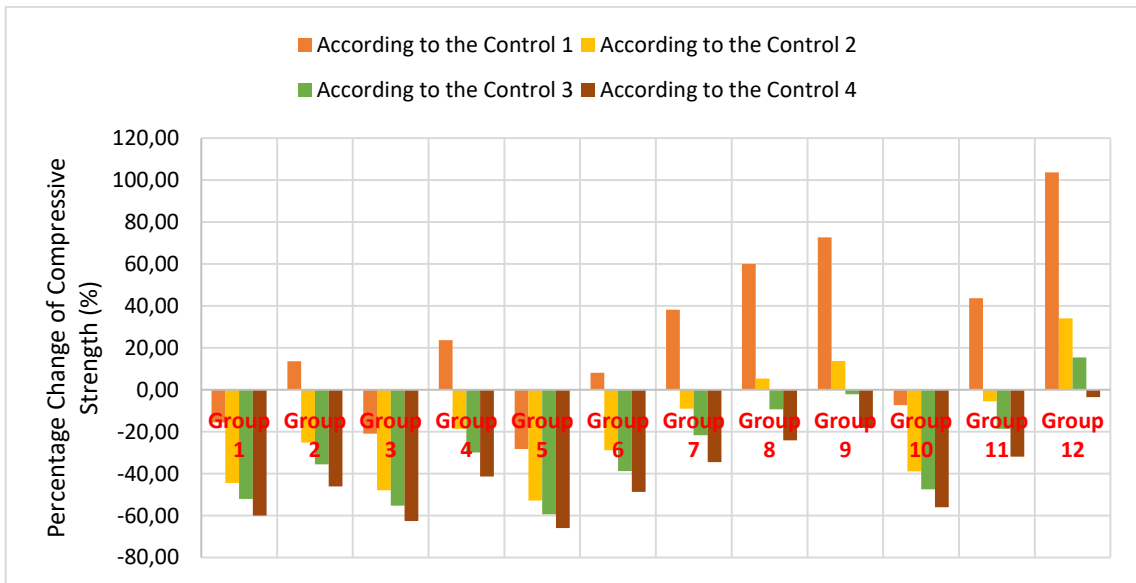
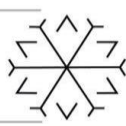


Figure 4. Percentage change of compressive strength of samples according to the control groups

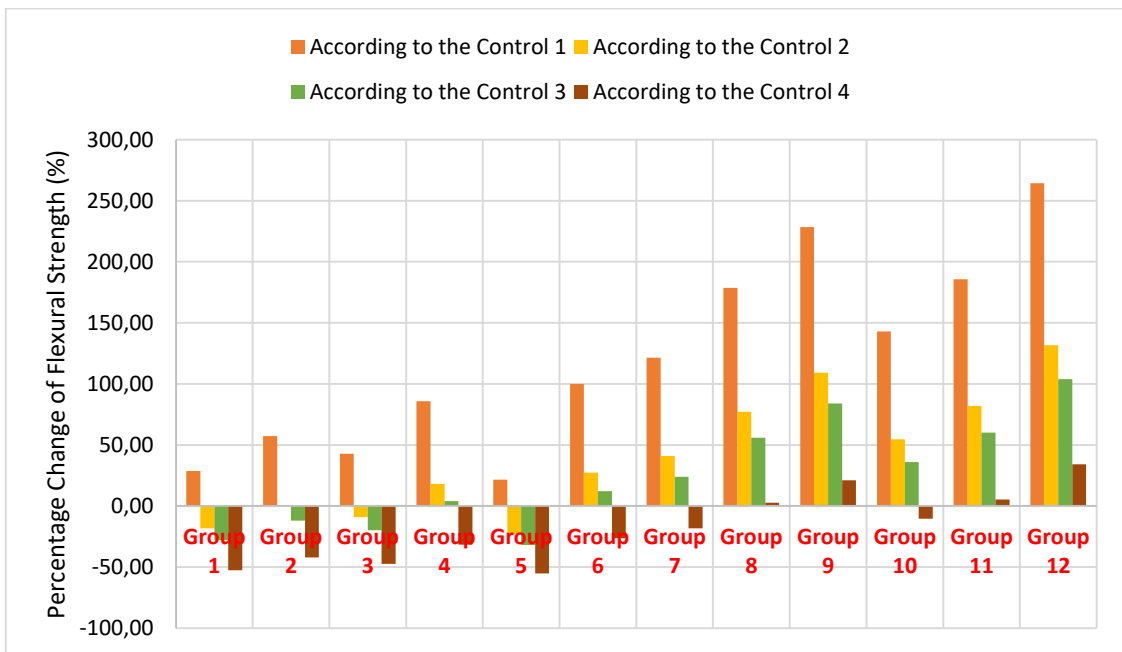


Figure 5. Percentage change of flexural strength of samples according to the control groups



Figure 6. Tested samples

Figure 6 shows the condition of polymer modified concrete samples after bending and compression tests. The latex additives formed a polymer film layer between the aggregate and the cement paste surface after hydration. Therefore, PMC samples are more ductile than control samples. It also reduced the interface zone of the latex additives.

4. Conclusion

In this paper is presented the effect of different polymer latexes, different water/cement ratios, different latex ratios and different curing conditions on the mechanical performance of concrete. According to the results of the study, it was observed that the flexural strength of concrete increased with the addition of latex polymers to concrete. These results showed similarities with the literature studies. It has been interpreted that the reason for the decrease in compressive strength is due to the early age of the concrete. It has been showed that 5% – 1% polymer ratio gives better results. In addition, increasing the water/cement ratio to 0.4-0.45 and mixed type curing (water+air) had a positive effect on the mechanical properties of PMC.

Disclosure Statement

The authors declare that there is no conflict of interest.

REFERENCES

- Assaad, J., and Daou, Y., 2017. Behavior of structural polymer-modified concrete containing recycled aggregates. *Journal of adhesion science and Technology*, 31, 874-896.
- Bideci, A., Doğan, M., Çomak, B., Bideci, Ö.S., and Besli, E., 2016. Stiren-Bütadien Kopolimer Katkısının Çimento Harçlarına Etkisi. *Düzce Üniversitesi Bilim ve Teknoloji Dergisi*, 4.
- Cen, E., 2009. Testing hardened concrete—part 3: compressive strength of test specimens. European Committee for Standardization, Brussels.
- Committee, E., 2011. EN 197-1: 2011. Cement—Part 1: Composition, Specifications and Conformity Criteria for Common Cements. European Committee, Brussels, Belgium.
- De Normalisation, CE., 2009. EN 12390-5: Testing Hardened Concrete—Part 5: Flexural Strength of Test Specimens. CEN: Brussels, Belgium.
- Hirde, S., and Dudhal, OS., 2016. Review on polymer modified concrete and its application to concrete structures. *International Journal of Engineering Research*, ISSN, 3.
- Islam, M., Rahman, M. and Ahmed, M., 2011. Polymer-modified concrete: world experience and potential for Bangladesh. *The Indian Concrete Journal*, 22, 55-63.
- Kardon, JB., 1997. Polymer-modified concrete. *Journal of Materials in Civil Engineering*, 9, 85-92.
- Ohama, Y., 1995. *Handbook of polymer-modified concrete and mortars: properties and process technology*, William Andrew.



Sivakumar, M., 2011. Effect of polymer modification on mechanical and structural properties of concrete–an experimental investigation. *International Journal of Civil & Structural Engineering*, 1, 732-740.

Soni, E. K. and Joshi, Y., 2014. Performance analysis of styrene butadiene rubber-latex on cement concrete mixes. *Journal of Engineering Research and Applications*, 3, 838-44.

Effect of Antifreeze Additives on The Properties of Mortars Containing Silica Fume Exposed to Frost in Fresh State

Ali Öz^{1*}[0000-0002-6590-3775], Fatma Karagöl²[0000-0003-1760-1972] and Rıza Polat³[0000-0002-8990-035X]

¹alioz@atauni.edu.tr, Atatürk University, Narman Vocational School, Construction Dept., Erzurum,
Turkey

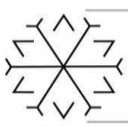
²fatma.karagol@atauni.edu.tr, Atatürk University, Engineering Faculty, Civil Engineering Dept.,
Erzurum, Turkey

²rizapolat@atauni.edu.tr, Atatürk University, Engineering Faculty, Civil Engineering Dept., Erzurum,
Turkey

Abstract

Mineral and chemical additives in cement-based materials are routinely used for the purposes like the evaluation of wastes, protection against adverse climatic conditions and extension of construction seasons. However, the literature on the interaction of mineral additives and antifreeze additives is not sufficient. In this study, mortar samples containing silica fume were produced with the single and dual-use of two different antifreeze additives and exposed to frost in the fresh state. Silica fume and antifreeze admixtures (calcium nitrate and sodium thiocyanate) were used at 8% and 6% of binder weight, respectively. The samples produced were exposed to cold air at -5°C and -10°C in fresh condition for 12 hours and then subjected to standard water curing until the experiment times. Water absorption, capillary water absorption, UPV (Ultrasonic Pulse Velocity) and compressive strength tests were performed on the mortar samples and compared with the reference samples. As a result, in both early and later ages, it was determined that antifreeze additives reduce the water absorption rate of the mixtures containing silica fume approximately 10% more compared to the reference samples and decrease the capillary water absorption coefficients in dual-use. In addition, it was determined that the use of antifreeze additives, especially in silica fume added samples, is more effective in terms of strength and void structure at -5°C and -10°C frost effect.

Keywords. Antifreeze additive, Calcium nitrate, Compressive strength, Cold weather concrete, Silica fume, Sodium thiocyanate.



1. Introduction

Improving the strength and durability properties of cement-based materials, expanding their use in different climatic conditions, using them as composite material components with other materials are always on the agenda of scientific research.

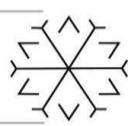
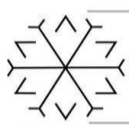
It is not completely suitable today to define concrete, which is the most commonly used cement-based material, as that consisting of aggregate, water and cement. Namely, when the types of cement produced are examined, it is seen that a significant majority consists of cement with mineral additives, in addition to this; chemical additives take their place as an indispensable component in the ready-mixed concrete sector due to economic or other reasons.

The additives used in the production of concrete, which are divided into two classes in their most basic form, are mineral and chemical additives. These additives can improve the properties of fresh and hardened concrete to a significant degree and generally be used while the concrete is fresh or after it has hardened if necessary. Hydration reactions between water and cement can be significantly altered by small amounts of chemicals. In short, additive materials are generally used to regulate the workability of fresh concrete, hydration heat, setting time of concrete and to improve pumping ability. They are used to reduce the water/cement ratio, the amount of cement and thus the cost. After the concrete hardens, it is generally used for purposes like to increase strength, improve durability and reduce maintenance costs during its service life, etc.

Mineral additive materials which are natural (volcanic ash, tuff, ignimbrite, baked clay, etc.), or waste materials (silica fume, fly ash, slag, etc.) generally contain amorphous SiO_2 and some amount of Al_2O_3 , Fe_2O_3 , CaO .

Chemical additives are briefly set accelerators (calcium formate, calcium acetate, nitrates, lactic acid, formaldehyde, chlorides...), plasticizers (lignosulphate salts and derivatives, hydroxyl and carboxylic acid derivatives, polymeric materials, naphthalene, melamine (super), polycarboxylic acid. (hyper)), setting retarders (lignosulphoric acid, hydroxyl-carboxylic acid, sugar, phosphate, borate, zinc, gypsum...), air-entraining additives (resin salts, petroleum acids, synthetic detergents, wood resin salts, proteinaceous substances, synthetic detergents, lignosulphonates...), antifreeze additives (NaCl , CaCl_2 , K_2CO_3 , NaNO_2 , $\text{CO}(\text{NH}_2)_2$, $\text{Ca}(\text{NO}_3)_2$, urea ($\text{CH}_4\text{N}_2\text{O}$), NaSCN , NaNO_3), activators (Na , K , LiOH , Na_2SiO_3 and K_2SiO_3), alkali aggregate reaction inhibitor additives (phosphate and nitrate anions, Mg , Li , Br cations), non-chloride additives (set accelerating additives except Cl), coloring additives (metal oxides, Fe Si Mn), expanding additives (ettringite, CaSO_4 , MgO and CaO), anti washout and underwater additives (polymers, water-soluble acrylic ether and cellulose ether), impermeability additives (soap derivatives, petroleum products, bituminous materials, cut back asphalt, mineral oils), viscosity additives (natural and synthetic polymers), anti-corrosion additives (Na and K benzoate, Na and K nitrate calcium nitrite) etc. (Baradan et al., 2012).

On the other hand, in cement-based materials, one or more additives with different properties are used together when necessary, depending on the desired performance/property. The chemical contents and physical properties of additives may vary and interact with each other. In this case, it is necessary to investigate the use of mineral and chemical additives in binary combinations, as they can affect the concrete properties positively or negatively or reduce the performance of the additives. The suitable period in a year for construction works gets shortened especially in the regions where the air temperature is low for a long time. According to ACI 306R-10, cold weather is defined as the average daily temperature below 4°C for longer than 3 days (Polat, 2016). In this case, the reactions of the cement slow down or almost stop at temperatures below 0°C . In addition, the fresh concrete which is saturated with water freezes easily and a significant volume change occurs and voids are formed. For this reason, it is necessary to protect the concrete until it gains strength of 3.5-5 MPa. Otherwise, it loses 30-40% of its strength (Polat, 2016). Especially in concrete production, this period can be extended by taking precautions with heating systems or additives so that the reactions of the cement continue. For this purpose, antifreeze additives are used to reduce the freezing temperature of the water and accelerate hydration so that the fresh concrete is not affected by frost, on the other hand, mineral additives such as silica fume and fly ash are used to improve concrete properties and performance. When the studies on the use of these two basic additives were considered, Justnes and Nygaard stated that the effectiveness of calcium nitrate as a setting accelerator depends on the type of cement (Justnes and Nygaard, 1995). Collepari and Franke investigated the effect of calcium nitrate on concretes with blended Portland cement (containing 70% blast furnace slag or 20% fly ash or 15% limestone dust) by comparing with concrete containing only Portland cement at temperatures of 5°C and 20°C (Collepari and Franke, 2015).



Kičaitė et al. investigated the effect of calcium nitrate on the setting and hardening rate of Portland cement concrete at temperatures of 5°C and 20°C (Kicaite et al., 2017). Chikh et al. studied the effects of calcium nitrate and triisopropanolamine on the setting time and the strength development of Portland cement pastes at standard curing temperatures (Chikh et al., 2008). Gök and Kılınç investigated the effect of antifreeze additives (calcium nitrate, triethanolamine and triisopropanolamine) in different contents at ambient temperature (Gök and Kılınç, 2015, Alkılıç, 2015). Skripkaunas et al. (Skripkiunas et al., 2021) researched the effect of calcium nitrate on the properties of low-temperature curing Portland-limestone cement-based concrete. Ogunbode and Hassan searched the effect of calcium nitrate in concretes containing volcanic ash under normal curing conditions (Ogunbode and Hassan, 2011). Karagöl et al. (Karagöl et al., 2011) investigated the effect of calcium nitrate in cold weather with normal Portland cement. Kičaitė et al. investigated the effect of calcium nitrate on the properties of Portland cement paste and fresh concrete for curing at low temperatures (Kicaite et al., 2020). They found that the most effective application of $\text{Ca}(\text{NO}_3)_2$ is achieved at -5°C and lower frost temperatures (-5°C, -10°C) require higher $\text{Ca}(\text{NO}_3)_2$ dosages (2-3%). Justnes (2007) found that a small amount of sodium thiocyanate (NaSCN) in combination with calcium nitrate can give approximately the same 1-day strength value as those found for samples with CaCl_2 (Justnes, 2007). In the study by Uyan and Yıldırım, authors produced concrete with 2, 3 and 4 % set accelerator additives (3 types of additives) by using PC 42.5, blended and trass cement (three types of cement). As a result, it was observed that the effectiveness of the additive increased as the percentage of mineral additive increased in cement. As the percentage of the setting accelerator increased, the compressive strength of all mixtures was observed to decrease at the rate of 15-20% (Uyan and Yıldırım, 1991).

Karagöl et al. (Karagöl et al., 2017) were studied the freeze-thaw resistance of the mortars produced by using silica fume, fly ash, and antifreeze additives and the change in the fresh state properties under cold weather. In this study, the mineral and antifreeze admixtures were selected 10% and 1% of the binder weight, respectively. After the freeze-thaw effects, the compressive strength of the fly ash added mixtures decreased, but it was stated that the compressive strength of the mixtures in which silica fume and antifreeze additives were used together increased. The studies by Ramachandran (Ramachandran, 1995), Polat (Polat, 2016), Karagöl et al. (Karagöl et al., 2013), Demirboğa et al. (Demirboga et al., 2014), Karagöl et al. (Karagöl et al., 2015) are on the use of antifreeze additives such as calcium nitrate and urea together with Portland cement.

When the studies in the literature were examined, no study was found to include the compatibility of single and dual-use calcium nitrate and sodium thiocyanate as antifreeze additives in mortars with silica fume. In this study, mortar samples containing silica fume were produced with the single and dual-use of two different antifreeze additives and exposed to cold weather in the fresh state. Silica fume and antifreeze admixtures (calcium nitrate and sodium thiocyanate as single and dual-use) were used at the rate of 8% and 6% of total binder weight. The samples produced were exposed to cold weather at -5°C and -10°C in fresh form for 12 hours and then subjected to standard water curing until the test times. Water absorption, capillary water absorption, UPV and compressive strength tests were performed on the mortar samples and compared with the reference samples.

2. Materials and Method

Portland Cement (CEM I 42.5R) produced by Aşkale Cement Industry and Trade inc. was used in the experiments, in accordance with TS EN 197-1. The chemical, physical and mechanical properties of the cement are given in Table 1. As the mineral additive, silica fume obtained from the facility producing Silico Ferrochrome in Antalya Electrometallurgy Enterprise was used and its properties are presented in Table 2 (TS EN 13263-1+A1). As convenient with TS EN 934-2: 2011+A1 standard, CHRYSO®XEL AH-3 (calcium nitrate) and CHRYSO®XEL AH 665 (sodium thiocyanate) supplied from Chryso-Additive-Materials-Industry and Trade inc. were used antifreeze additives which have setting accelerating properties (Table 3). 0-4 mm river sand with a gradation in accordance with TS EN 802 was used in the mixtures as aggregate and its specific gravity is 2.60. Fine aggregate was divided into 0-2 mm and 0-4 mm and used granulometrically at the rates of 68%-32%. Mortar samples of 5*5*5 cm³ were produced by taking the water/cement ratio of 0.46 and the cement/sand ratio of 1/2.75 in all groups in the study. In addition, in the mixtures containing silica fume, the additive ratio is constant and is 8% of the total binder weight. On the other hand, the calcium nitrate and sodium thiocyanate (3% + 3% in dual-use) are 6% of the total binder weight in mixtures with antifreeze additives. Mortar mixing ratios are given in Table 4.

**Table 1.** Chemical and physical properties of the cement

Chemical properties	Results (%)	Physical properties	Results
Total SiO ₂	18,99	Specific surface (Blaine) (cm ² /g)	3532
Insoluble residue	1,09	Specific weight (g/cm ³)	3,12
Al ₂ O ₃	4,62	Volume expansion (mm)	1
Fe ₂ O ₃	3,36		
CaO	63,04	Setting time (min.)	Start 155
MgO	1,83		Finish 215
SO ₃	2,80	Compressive strength (MPa) (2 nd day)	26,7
Loss of glow	3,70	Compressive strength (MPa) (28 th day)	55,1
Na ₂ O	0,27		
K ₂ O	0,86		
Cl-	0,0085		
Free CaO	1,05		

Table 2. Chemical properties of silica fume (%)

SiO ₂	Al ₂ O ₃	Fe ₂ O ₃	CaO	MgO	Cr ₂ O ₃	C	S
91,92	0,42	0,20	2,06	3,69	0,37	0,207	0,067

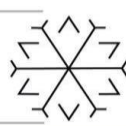
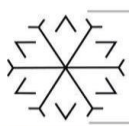
Table 3. The properties of antifreeze additives

	CHRYSO@XEL AH 665	CHRYSO@XEL AH-3
Appearance	Homogenous	Homogenous
Colour	Yellow	Brown
Density (gr/cm ³)(20°C)	1,321	1,150
pH	7,14	6,28
Water Soluble Chloride (%)	0,06	0,02
Solid Content (%)	41,57	19,66
Effective Component	Convenient	Convenient
Alkali Content	<%5	<%5

Table 4. Mortar mixture rates (gr)

Sample Code *	Cement	Water	Calcium nitrate	Sodium Thiocyanate	Fine sand (0-2)	Sand (0-4)	Silica fume
R	1170	540	-	-	220	3000	-
RC	1170	470	70	-	220	3000	-
RN	1170	470	-	70	220	3000	-
RCN	1170	470	35	35	220	3000	-
S	1075	470	-	-	220	3000	95
SC	1075	470	70	-	220	3000	95
SN	1075	470	-	70	220	3000	95
SCN	1075	470	35	35	220	3000	95

*The codes R, S, C, N and CN define the reference mixtures that do not contain silica fume, the mixtures containing silica fume, the dual use of calcium nitrate, sodium thiocyanate, and the dual use of antifreeze additives, respectively.



The samples produced from each mixture were divided into 3 groups. One group of samples were kept in the laboratory environment (20-23°C and 50% relative humidity) for 1 day and then their moulds were removed and subjected to standard water curing until the time of the experiment. In addition, one group of samples from each mixture were exposed to cold weather for 12 hours at -5°C and -10°C, respectively in fresh form. After they were kept in the laboratory for 12 hours, their moulds were removed and subjected to standard water curing until the time of the experiment (28 days) Figure 1.

Water absorption and capillary water absorption tests were conducted on samples at the end of the 28-day according to the method specified in the references of Sumer (Sümer, 1994) and Polat et al. (Polat et al., 2010). UPV tests and 7- and 28- day compressive strength tests were performed according to ASTM C 642, TS EN 13057, ASTM C597 and ASTM C109/C109M standards, respectively.



Figure 1: Samples in the deep freezer exposed to frost

3. Results and Discussion

3.1. Water absorption

The water absorption percent by weight of antifreeze and mineral added (silica fume) mortar samples produced in the scope of the study and exposed to different temperatures (water cure, -5 °C and -10 °C) are given in Figure 2. It was observed that the water absorption ratios of the mortar samples (R) without chemical (antifreeze additive) and mineral additive (silica fume) were the highest. It was determined that the water absorption rates of the silica fume added samples were lower when all mixtures were evaluated. The use of antifreeze additives, which generally have setting accelerating properties, has reduced water absorption rates. In reference samples (without silica fume), it was observed that water absorption rates were higher in water curing samples as a result of the dual-use of antifreeze additives, but the water absorption rates of the samples decreased at -5°C and -10°C with the use of antifreeze.

It was identified that the water absorption rates of the reference and silica fume added samples without antifreeze additives were lower than the antifreeze additive samples. Therefore, it was determined that water absorption rates decrease in all curing conditions in the case of using antifreeze additives. It is thought that silica fume fills the voids due to both its pozzolanic feature and filler function, and as a result, it reduces the water absorption rates. It was concluded that antifreeze additives reduce the water absorption rate by 10% more, especially in silica fume added samples and calcium nitrate is more effective in silica fume added mixes.

3.2. Capillary water absorption

Water impermeability of concrete in dams, water tanks, pipes, canals and building foundations is one of the basic properties desired. Undesirable particular conditions for the concretes are the formation of different colors and structures on the surface due to the evaporation of rising water from the surface through the capillary spaces and frost damage in water-saturated concrete. The capillary water absorption coefficients of the samples exposed to frost for 12 hours at an early age at -5°C and -10°C curing environments with standard water curing after 28 days are shown in Figure 3- Figure 4.

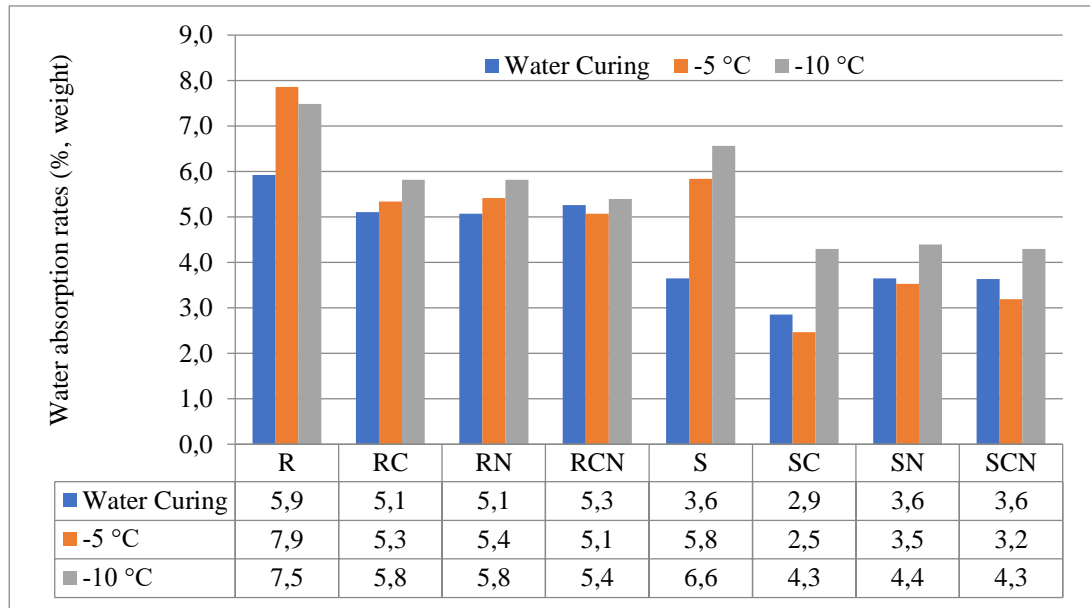
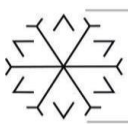


Figure 2. Water absorption rates (% weight)

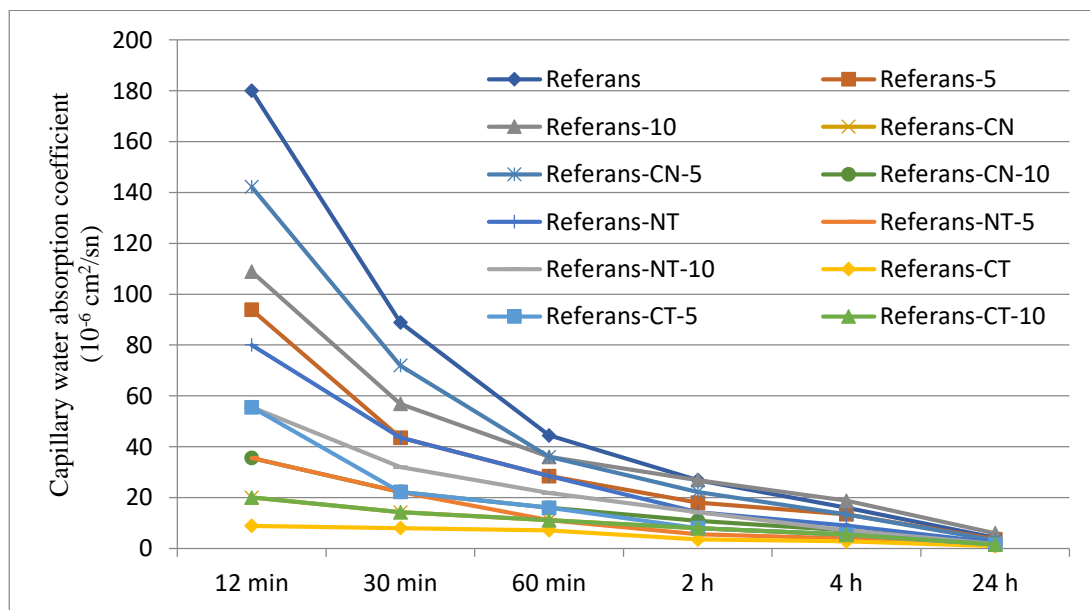


Figure 3. Comparison of capillary water absorption coefficients of reference samples

It is seen when Figure 3 is evaluated that the capillary water absorption coefficients in the reference samples are lower in the case of dual-use of antifreeze additives both in early and later times; the mixtures using sodium thiocyanate have a lower coefficient compared to those using calcium nitrate, and also the coefficient is relatively higher in mixtures without additives.

When Figure 4 is evaluated, it can be said that the coefficients are generally close to each other and especially the dual-use of antifreeze additives is effective. When evaluated in general, it is seen that this coefficient is lower than the reference samples in all mixtures with silica fume additives and the use of dual antifreeze additives is an effective method.

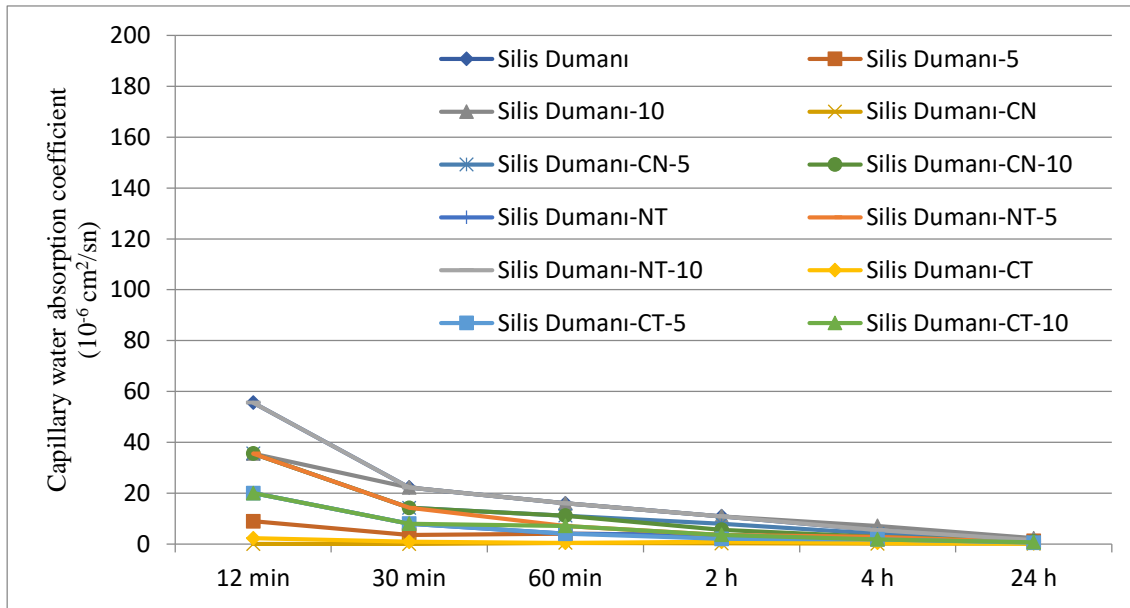
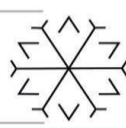
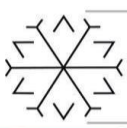


Figure 4. Comparison of capillary water absorption coefficients of samples containing silica fume

3.3. UPV

UPV method can supply information about the structure of voids in materials like concrete. In this study, measurements were made on 28-day-old samples to evaluate the void structure in the case of the use of mineral and chemical additives in the samples exposed to the effect of frost at an early age (12 hours of early age frost in -5°C and -10°C curing environments). The results are presented in Figure 5.

As can be clearly seen from Figure 5, the UPV values of the mixtures using silica fume are particularly high. In addition, it is seen that the values of all samples subjected to water cure are higher than the samples exposed to the effect of early age frost. It was determined when the single and dual uses of antifreeze additives are evaluated that although there is no significant difference, the use of antifreeze in the ambient conditions in the reference samples reduces the UPV values, but reduces the rate of decrease in the samples exposed to the -5°C and -10°C frost effects. It is clearly seen in Figure 5 that the use of antifreeze additives, especially in silica fume added samples, has a remarkable effect at -5°C and -10°C . According to the standard water cured samples, the UPV reduction amounts for S, SC, SN and SCN in mixtures containing silica fume were -5.4%, -0.9%, -0.8%, -1.4% and -7.3%, -1.7%, -3.0%, -4.3% for the samples exposed to -5°C and -10°C frost temperature, respectively (Figure 6).

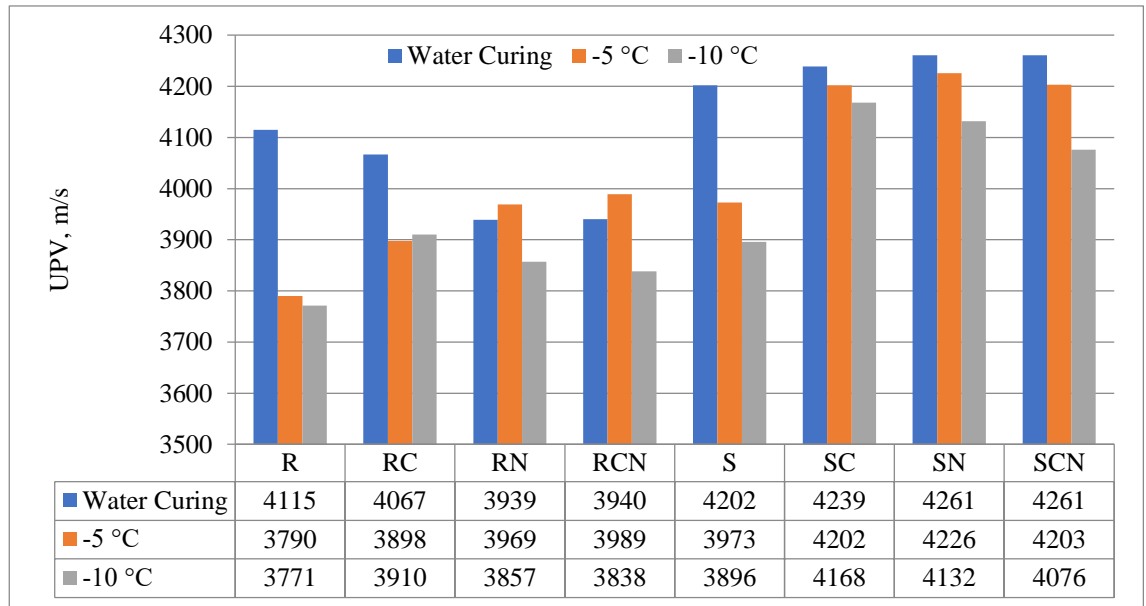
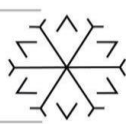
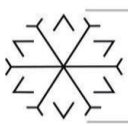


Figure 5. UPV results (m/s)

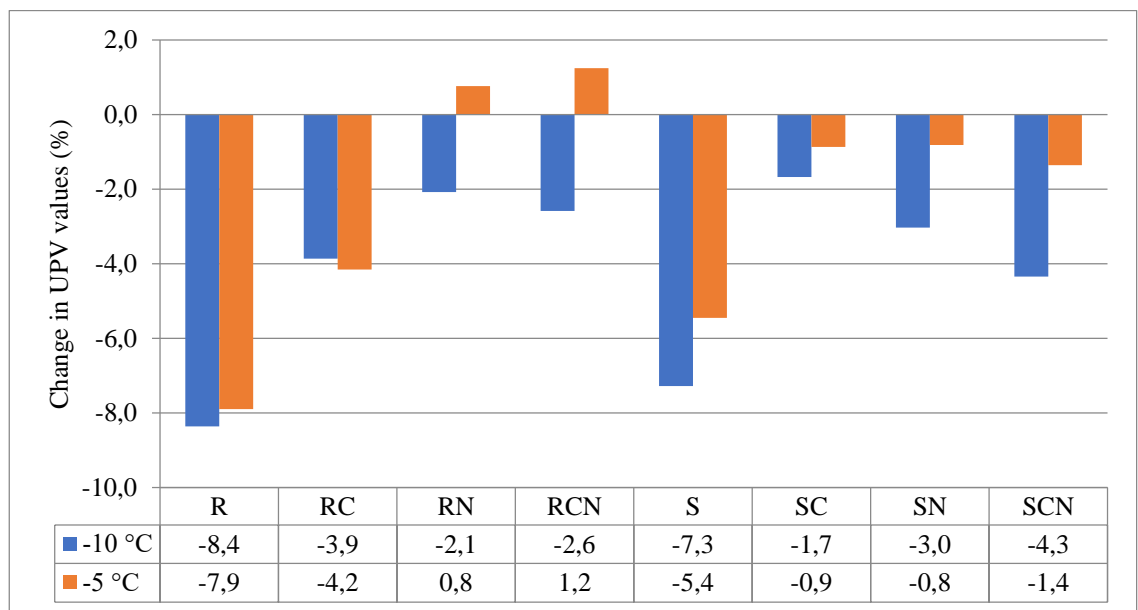


Figure 6. Change in UPV values the samples exposed to -5°C and -10°C frost temperature according to the standard water cured samples (%)

3.4. Compressive Strength

Determination of compressive strength is the most important research experiment in cement-based materials and in this study, it was carried out to determine how the single and dual use of antifreeze additives in mixtures containing mineral additives affect the mechanical properties of mortars under the effect of frost at different temperatures. The samples produced for this purpose were subjected to standard water curing until the test times after 12 hours of exposure to -5°C and -10°C frost effects, and their 7-day strengths are given in Figure 7.

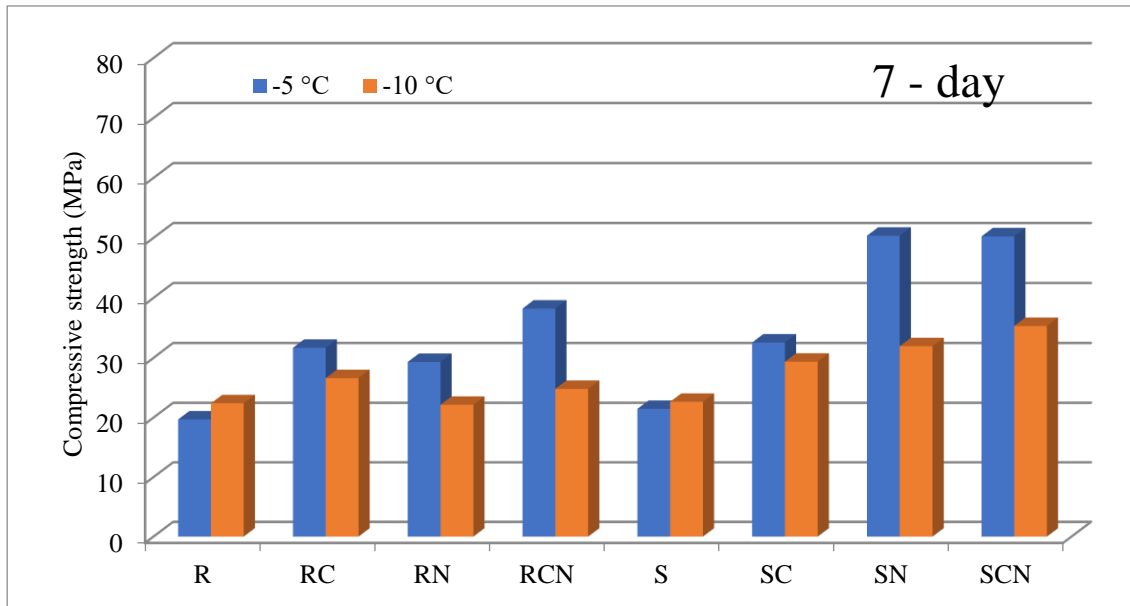
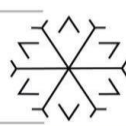
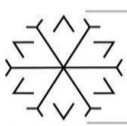


Figure 7. 7-day compressive strength of samples exposed to 5°C and -10°C frost effect (MPa)

According to the results of 28-day strength tests, it is seen that especially sodium thiocyanate additive is more effective in samples exposed to frost effect at -5°C in general and even at -10°C, there is no significant decrease in strength in antifreeze added samples. It can be seen from the figure that the dual use of antifreeze additives is at least as effective as its single-use. In addition, when Figure 8 is considered, it is observed that the frost resistance of mixtures containing silica fume is better at -5°C and the use of dual antifreeze additives at -10°C is more efficient (Figure 8).

A comparison of the 28-day strength changes of the samples exposed to different frost effects compared to the standard cured samples is given in Figure 9.

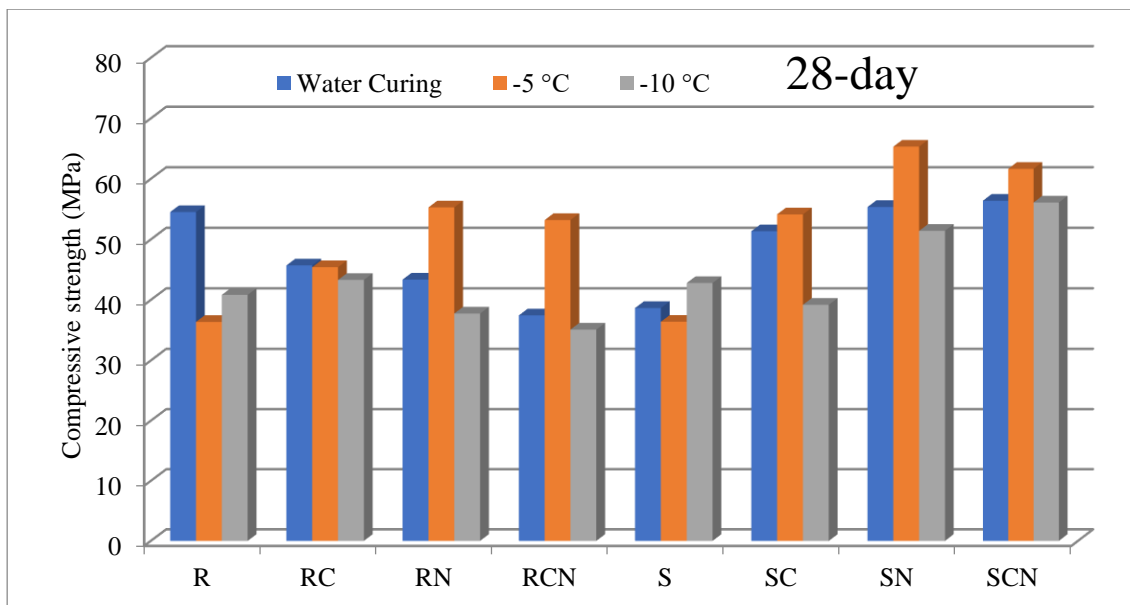


Figure 8. 28-day compressive strength (MPa) of standard cured specimens exposed to frost exposure at 5°C and -10°C (MPa)

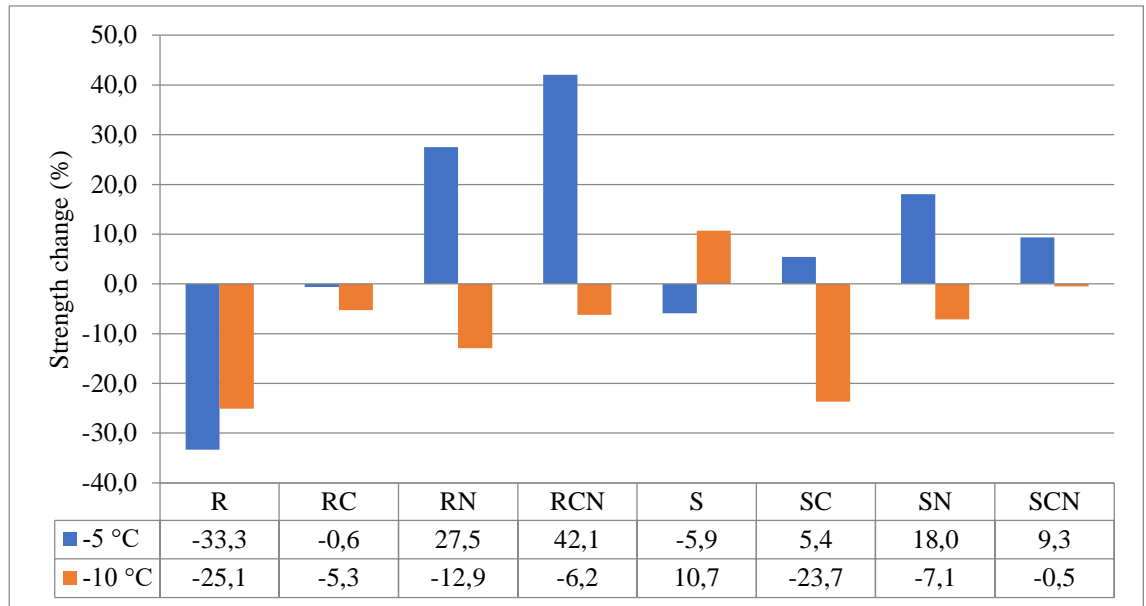
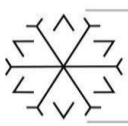


Figure 9. Change in 28-day strength values the samples exposed to -5°C and -10°C frost temperature according to the standard water cured samples (%)

4. Conclusion

Mortar samples with and without silica fume (produced only with Portland Cement) were produced with the single and dual-use of two different antifreeze additives and exposed to cold weather (5°C and -10°C frost effect for 12 hours) in fresh form. Calcium nitrate and sodium thiocyanate were used as antifreeze additives as single and dual-use 6% ratio of its binder weight. Water absorption, capillary water absorption, UPV and compressive strength tests were performed on the produced samples and compared with the reference samples.

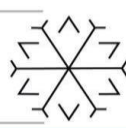
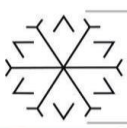
As a consequence, following results are found in the study.

— It was determined that the water absorption rates of the mortar samples (R) without antifreeze additives and silica fume were the highest, and the water absorption rates of the samples with silica fume additives were lower than the reference samples. In the case of the use of antifreeze additives, it has been observed that the water absorption rates decrease in all curing conditions. It was concluded that antifreeze additives reduce the water absorption rate by 10% more, especially in silica fume added samples, and calcium nitrate is more effective in silica fume added mixtures.

— It is seen that the capillary water absorption coefficients of the reference and the samples containing silica fume are generally lower both early and later in the case of dual use of antifreeze additives, and the coefficient is relatively higher in mixtures without antifreeze additives. When evaluated in general, it is seen that this coefficient is lower than the reference samples in all mixtures with silica fume additives and the use of dual antifreeze additives is an effective method.

— The UPV values of the samples using silica fume are particularly higher compared to those not using and the same condition is valid for the samples subjected to water cure compared to those exposed to frost. The use of antifreeze additives in silica fume added samples was particularly effective at -5°C and -10°C frost effect. In the mixtures containing silica fume, the UPV reduction amounts for S, SC, SN and SCN were -5.4%, -0.9%, -0.8% and -1.4% in the samples exposed to -5°C frost effect and -7.3%, -1.7%, -3.0% and -4.3% for those exposed to -10°C frost effect.

— It was determined that the effect of the use of especially dual antifreeze additives is larger at 7-day compressive strengths at both -5°C and -10°C compared to single-use. It was determined according to the 28-day compressive strength results that the frost resistance of the mixtures containing silica fume is better at -5°C and the use of dual antifreeze additives at -10°C is more effective.



References

- Alkılıç, M. O., 2015. Effect of Triisopropanol Amine and Calcium Nitrate on The Strength Development of Glass Fiber Reinforced Concrete. Master Thesis.
- Baradan, B., Yazıcı, H. and Aydın, S., 2012. Beton, Dokuz Eylül Üniversitesi Mühendislik Fakültesi Yayınları No:334.
- Chikh, N., Cheikh-Zouaoui, M., Aggoun, S. and Duval, R. 2008. Effects of calcium nitrate and triisopropanolamine on the setting and strength evolution of Portland cement pastes. *Materials and Structures*, 41, 31-36.
- Collepari, S., Collepari, M., Troli, R., and Franke, W., 2015. The Influence of Calcium Nitrate on Concrete with Portland Blended Cements. Eleventh International Conference on Superplasticizers and Other Chemical Admixtures in Concrete. Ottawa, Canada. .
- Demirboga, R., Karagol, F., Polat, R. and Kaygusuz, M. A., 2014. The effects of urea on strength gaining of fresh concrete under the cold weather conditions. *Construction and Building Materials*, 64, 114-120.
- Gök, S. G. and Kılınc, K., 2015. Effect of Calcium Nitrate, Triethanolamine And Triisopropanolamine on Compressive Strength of Mortars. *Kırklareli University Journal of Engineering and Science*, 1, 12-19.
- Justnes, H., 2007. Kalcijev nitrat kot mnogo-funkcionalni dodatek betonu ("Calcium Nitrate as Multifunctional Concrete Admixture" in Slovenian), . 14th Slovenian colloquium on Concrete. Ljubljana, Slovenia.
- Justnes, H. and Nygaard, E. C., 1995. Technical Calcium Nitrate as Set Accelerator for Cement at Low-Temperatures. *Cement and Concrete Research*, 25, 1766-1774.
- Karagol, F., Demirboga, R., Kaygusuz, M. A., Yadollahi, M. M. and Polat, R., 2013. The influence of calcium nitrate as antifreeze admixture on the compressive strength of concrete exposed to low temperatures. *Cold Regions Science and Technology*, 89, 30-35.
- Karagol, F., Demirboga, R. and Khushefati, W. H., 2015. Behavior of fresh and hardened concretes with antifreeze admixtures in deep-freeze low temperatures and exterior winter conditions. *Construction and Building Materials*, 76, 388-395.
- Karagöl, F., Demirboğa, R., Kaygusuz, M. A. and Yadollahi, M. M., 2011. The Influence of Calcium Nitrate on The Compressive Strength of Concrete Exposed to Freezing Weather. International Balkans Conference on Challenges of Civil Engineering, BCCCE. EPOKA University, Tirana, ALBANIA: .
- Karagöl, F., Polat, R. and Tosun, Y., 2017. Donma-Çözölmeye Maruz Kalan Mineral ve Antifriz Katkılı Harçların Özelliklerinin İncelenmesi. Uluslararası Yapılarda Kimyasal Katkılar Sempozyumu ve Serqisi Bildiriler Kitabı.
- Kicaite, A., Pundiene, I. and Skripkiunas, G., 2017. The influence of calcium nitrate on setting and hardening rate of Portland cement concrete at different temperatures. 3rd International Conference on Innovative Materials, Structures and Technologies (Imst 2017), 251.
- Kicaite, A., Skripkiunas, G. and Pundiene, I. 2020., The Effect of Calcium Nitrate on the Properties of Portland Cement Pastes and Concrete Hardening at Low Temperatures. *Ceramics-Silikaty*, 64, 263-270.
- Ogunbode, E. B. and Hassan, I. O., 2011. Effect of Addition of Calcium Nitrate on Selected Properties of Concrete Containing Volcanic Ash. *Leonardo Electronic Journal of Practices and Technologies*, 19, 29-38.
- Polat, R., 2016. The effect of antifreeze additives on fresh concrete subjected to freezing and thawing cycles. *Cold Regions Science and Technology*, 127, 10-17.
- Ramachandran, V. S., 1995. Concrete admixtures handbook, Properties, Science, and Technology (second ed.), Accelerators. Antifreezing Admixtures, , Noyes Publications, New Jersey.
- Skripkiunas, G., Kicaite, A., Justnes, H. and Pundiene, I., 2021. Effect of Calcium Nitrate on the Properties of Portland-Limestone Cement-Based Concrete Cured at Low Temperature. *Materials*, 14.
- Uyan, M. and Yıldırım, H., 1991. Effectiveness of Super Plasticizer Concrete Admixtures in High Strength Concrete Production, . TMMOB Chamber of Civil Engineers, 2nd National Concrete Congress, High Strength Concrete, May 27-30.

Optimization of urban bus stops for increasing the use of public transportation

Emre Kuşkanan^{1*}[0000-0003-0711-5567], Ömer Kaya²[0000-0003-1037-5546], Kadir Diler Alemdar³[0000-0002-8837-7640] and Muhammed Yasin Çodur⁴[0000-0001-7647-2424]

¹emre.kuskapan@erzurum.edu.tr, Erzurum Technical University, Engineering and Architecture Faculty, Erzurum/Turkey

²omer.kaya@erzurum.edu.tr, Erzurum Technical University, Engineering and Architecture Faculty, Erzurum/Turkey

³kadir.alemdar@erzurum.edu.tr, Erzurum Technical University, Engineering and Architecture Faculty, Erzurum/Turkey

⁴mycodur@erzurum.edu.tr, Erzurum Technical University, Engineering and Architecture Faculty, Erzurum/Turkey

Abstract

With the increase in the number of vehicles, traffic congestion is increasing. Traffic congestion causes delays, gas emission and fuel consumption increase. In order to reduce the number of vehicles in traffic, people should be directed to public transportation. It is necessary to make public transport more attractive in order to prevent all these negative situations and to provide more convenient transportation opportunities. Making public transportation more attractive is possible by ensuring the satisfaction of the passengers. In this context, surveys were conducted with passengers for the two bus lines with the longest route in the province of Erzurum. According to the results of the survey, dissatisfaction was determined and the number of stops were optimized according to the regulations of the bus stop location. Location analysis of the number of stops and passengers of the lines and stopped delay were made with Geographic Information Systems. Thanks to the optimization, a significant reduction in the number of bus stops has been achieved. As a result of this, CO₂ emission and fuel consumption have been reduced by reducing fuel consumption and environmental and economic advantages have been achieved. So the optimization process resulted in shorter travel times and minimization of delays.

Keywords. Bus stops, public transport, route optimization, traffic congestion, transportation network

1. Introduction

The number of registered motor vehicles in traffic in the province of Erzurum is approximately 119 000 (Turkish Statistical Institute, 2018). The continuously increasing number of vehicles has required development of the road infrastructure. In addition, roads faced many problems in terms of public transport service, urban planning and road pavement types. Despite the studies and improvements made in urban roads, Damage and deterioration have occurred in these roads due to heavy winter conditions. While the highway network structure is being constructed, the city center is considered as a priority, the growth and developments are tried to be supported with temporary solutions. There are 37 bus lines, 6 minibus lines and many stops on these routes in the city (Erzurum Metropolitan Municipality, 2018). Considering that there is also passenger lowering and loading apart from bus stops, the line times of public transportation vehicles increase significantly. Despite the fact that road construction, maintenance and repair processes are applied from time to time, the desired developments in public transportation have not been made. There are many traffic and environmental problems in the city center, such as traffic congestion, low traffic flow rates, traffic accidents and emissions. Since these problems are encountered in many cities of the world, there are many studies to improve public transportation.

Studies on this issue should be examined before providing solutions for the problem of length on current bus routes, inability to meet passenger needs and frequent loss of time. In this context, Zhang and Huang (2011) mentioned that bus route planning in Wuhan, China has become increasingly complex with railway transit construction. As a solution to this situation, they made GIS based optimization in order to alleviate or solve the problems arising from bus routes. A method is used for multimodal transit route design to the stops to restrict certain railway routes. A genetic algorithm has been applied to search for the optimal combination of candidate routes, and a scenario for the short-term situation has been developed on some lines. As a result of the study, a comparison was made between the existing and optimized results, and the idea is observed that the GIS based

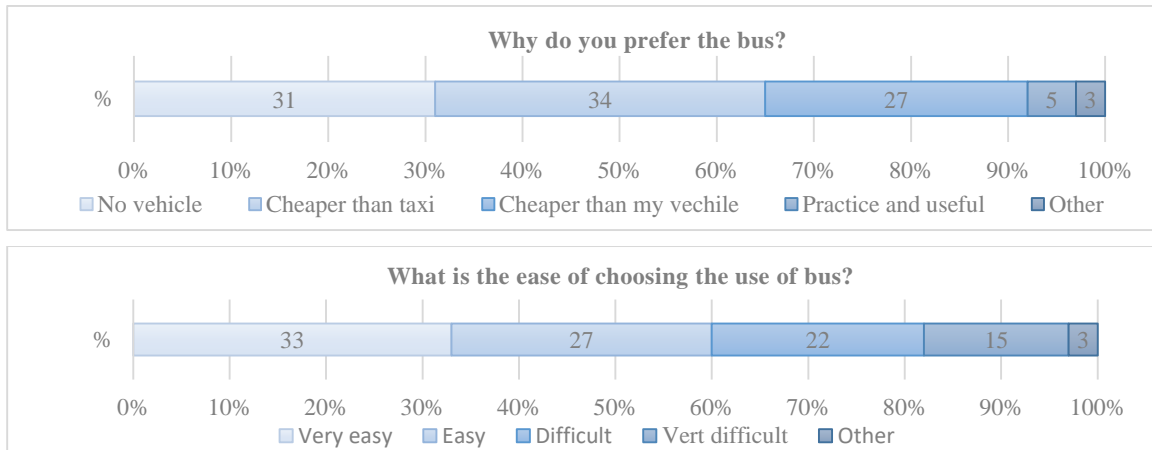
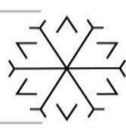


optimization approach could create a more suitable bus route network for Metropolitan. Pampal et al. (2009) compared the public transportation systems in the Dikimevi Beşevler line in Ankara in terms of the number of passengers, fuel economy, travel time, impact on the traffic problem, capacity and efficiency criteria. Considering the number of passengers and cost in the rail system, it is determined that it is much more advantageous than the bus. As a result, it was stated that bus lines that have the same route as the rail system are inefficient. In another study, Mandl (1980) mentioned that there are very few studies for the improvement of public transport networks and the improvements made cannot meet the needs of the users. For this purpose, it has conducted a study to increase the service quality level of public transportation systems and its performance. It has been shown how to calculate distances and routes for large networks by using an intuitive algorithm that improves the public transport network. It is explained how to evaluate the average transportation cost of passengers in a public transport network, using this algorithm. Wu (2009) made an optimization model to improve the accessibility of disabled people in daily life. The access of disabled people to bus stops is facilitated using this model. Emiliano et al. have presented a multi objective optimization model to find efficient bus fleet combinations taking into account greenhouse gas emissions, conventional air pollutant emissions and costs. The main goal of this study is to minimize, simultaneously, three objective functions, CO₂ emissions, other types of emissions, and total costs, for the bus fleet of a transit agency. An et al. have designed a refueling system for battery electric buses by applying battery-swapping technologies together with a local charging system. This study intends to answer four fundamental questions: How many battery-swapping stations should be installed? Where should they be? How to assign the depleted electric buses to battery-swapping stations? What is the service capability of the battery-swapping stations? With the study conducted to answer these questions, the locations of the battery exchange stations have been determined by testing on a real network in the southeast region of Melbourne, Australia.

Increasing the quality of public transportation and rate of use is possible with the satisfaction of the passengers. For this purpose, Gökaşar et al. (2018) examined the satisfaction surveys conducted by IETT on the internet to determine the service quality of the bus lines in Istanbul. The service quality of the buses has been modeled using the survey data and factor analysis. The results reveal that users care more about access to service than comfort. In another study to improve public transportation, they developed an integer linear programming model and determined the optimum number of buses for Kuwait. Using the Pareto analysis method, the five most important routes were determined and the optimum annual profit was calculated for each route using the Pareto analysis method. As a result of the study, it was determined which mark of vehicle to use is more economic. In this way, it is aimed to reduce the cost of public transportation (Alkheder, Alrukaibi, & Zaqzouq, 2018). Alrukaibi & Alkheder (2019) aimed to improve public bus services in Kuwait in terms of improving time, protecting the environment, reducing costs and traffic congestion. With the model they developed, bus stops on certain routes were arranged. Some bus stops were eliminated and the distance between the stops was optimized. In order to get better results, it has been mentioned that there is a need to implement practices at the country administration level to attract more passengers and reduce dependence on private vehicles.

Özcan (2018) has developed the Harmony Survey optimization model to improve the frequency of service and bus travel times in urban bus routes. As a result of the output of the model, it is stated that both operator and user benefits can be increased with the solution that delays the departure time and the solution of the frequency of service optimization problem. Shahraki (2015) designed transportation optimization modeling to minimize carbon monoxide emissions, traffic congestion and transportation costs. With the model results applied for Istanbul, suitable routes for capacity increase and public transportation lines to be added are shown. In another study, Geçer (2009) conducted a study to solve feeder bus route design problems using analytical approach and network approach methods. The feeder bus route design, tracking times on routes and access of feeder bus routes to railway stations are simultaneously improved with network models. Tran et al. (2015) addressed issues related to real-time control of public transport operations to minimize passenger waiting time. The uncertainty of the transit routes was examined using a dynamic Bayesian network. They implemented preventive strategies to prevent bus unreliability and to restore reliability using corrective strategies when unreliability was evident. Savsar et al. (2012) made an analysis to program and guide public buses. In the study, the road replanning system was considered by using the available data. The best routes were selected by modeling to determined potential areas for identified improvements and to investigate suitable solution approaches. The results show that there are significant improvements and cost savings for the public transport system.

When all these studies are examined; The necessity of planning to improve urban public transportation systems has come to the fore for sustainable transportation. Passenger satisfaction and environmental factors that affect this process should be taken into consideration. In case of increased passenger satisfaction, public transportation will be widespread and higher efficiency will be achieved. For this purpose, unlike previous studies; An optimization was made in the number of stops on the bus lines by considering both passenger satisfaction surveys



and geometrical conditions for Erzurum Province. In addition, spatial analysis of the stops, number of passengers and delays were made. Therefore, it is an important study in which both situations are evaluated together. As a result of the study, a comparison is made between the present and optimized results and the obtained gains are numerically revealed. With this study, it is aimed to reduce the traffic congestion and operating costs in urban public transportation services, as well as to improve environmental impacts and time use.

2. Materials and Methods

Erzurum is a province located in the Eastern Anatolia region and has an altitude of 1 890 meters. In addition, the province is located at the foot of the Palandöken mountain. Unlike plain cities, the residential areas are located at different altitude. For this reason, urban public transportation is provided by minibuses and buses and there is no urban rail system transportation. Since minibus lines operate on shorter routes, the minibuses make frequent services. However, as a result of the examinations made for bus lines, it was determined that some lines have very long routes and therefore delays are very high and the efficiency is low. In this context, two bus lines with the longest route for Erzurum Province were examined. First of all, surveys were conducted on the people traveling on the bus lines in order to identify the problems better. Then, the bus stops on the bus lines, how many passengers got on and off at the stop and the average fuel conditions of the vehicles were determined.

The G4/A and B2/A lines, the two lines with the longest route from the bus lines in Erzurum, have a length of 67.2 and 42.7 kilometers, respectively. Table 1 shows the starting, ending stops and routes of these bus lines. The G4/A bus line, the longest route, generally runs in the north and south directions of the city. The starting point on the departure route is " Station Area" and it passes through a total of 62 stops until reaching the end point "Erzurum Technical University", and 65 stops on the return route. The B2/A line, the second longest route, generally runs in the east and west directions of the city. The starting point on the departure route is "Dadaşkent" and it passes through a total of 60 stops until reaching the end point "Yoncalık", and 76 stops on the return route. Although the B2A line has shorter route lengths than the G4A line, the number of stops is larger. The locations of the departure and return routes and stops for both bus lines are shown in Figure 1-2.

Table 1: B2/A and G4/A bus route informations.

Bus Line Name	Starting Stops	Route	Ending Stops
B2/A	Dadaşkent	Center for Accessible Living - Deniz Feneri - Bora Park - A.Gazi Dorms - Erzurum Technical University – MNG Shopping Mall- City Tourism -Havuzbaşı – Gez Street - Gürcükapı - Yeşil Yakutiye	Tokiler
G4/A	Station Area	Mahallebaşı - Tokiler - Nalbantoğlu -Yunusemre - Kayakyolu - Police School – 2nd Markets - Regional Education Hospital - Ataturk University - MNG Shopping Mall - A.Gazi Dorms	Erzurum Technical University

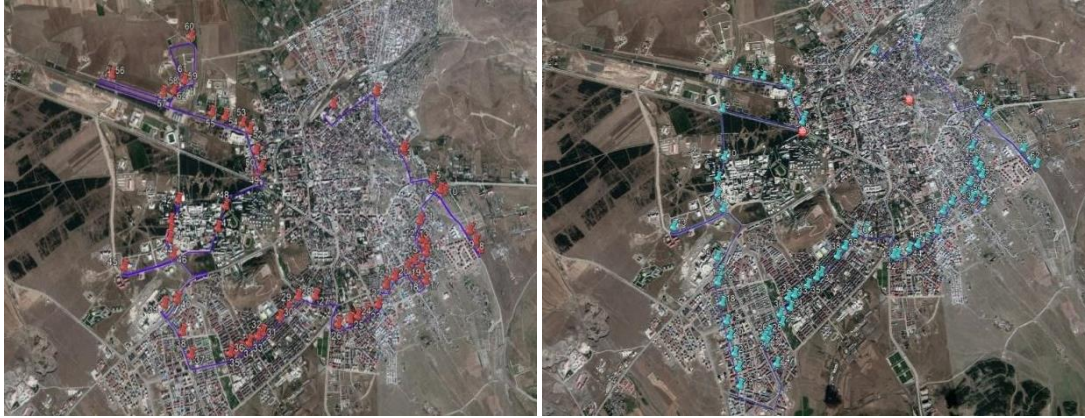


Figure 1: G4/A bus route departure, return and location of bus stops.

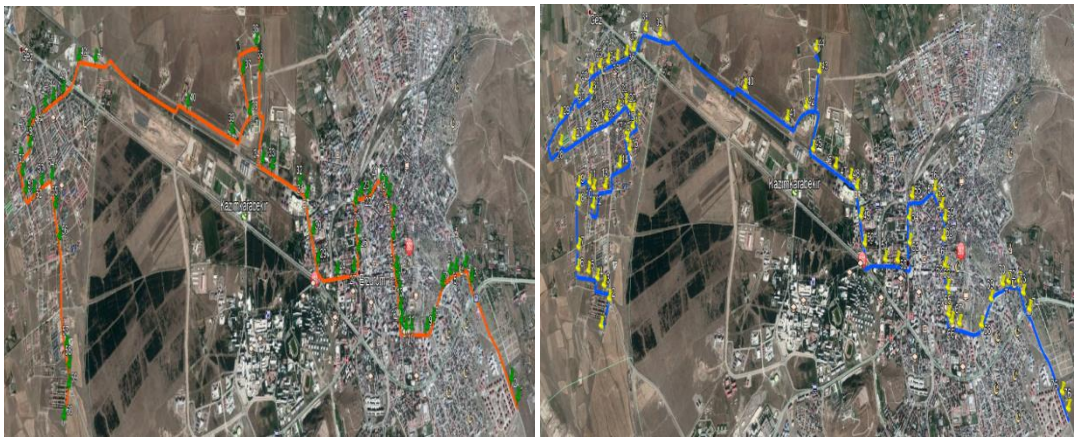
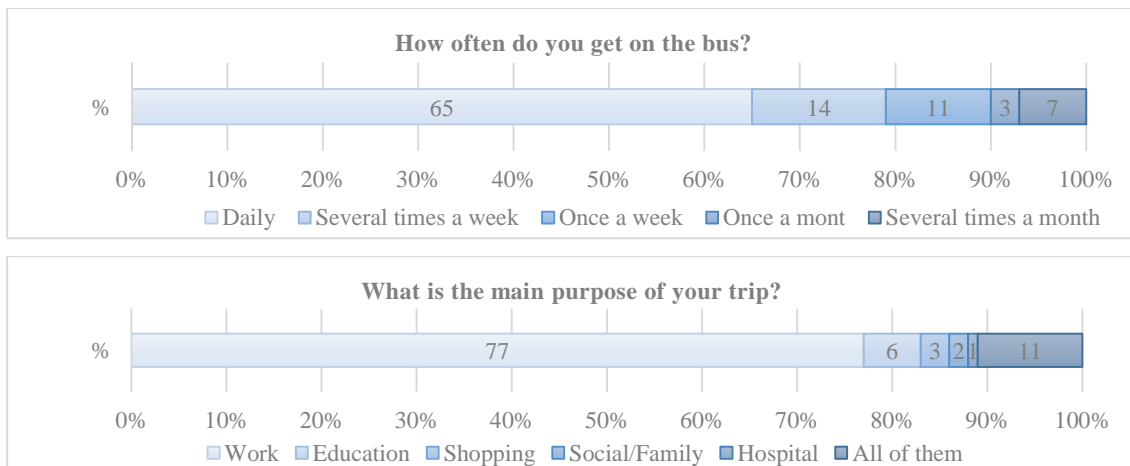


Figure 2: B2/A bus route departure, return and location of bus stops.

2.1. Data collection

Routes have been identified and numerical data have been analyzed to better identify transportation problems. For this purpose, bus use satisfaction survey was conducted in Erzurum for users. The survey was carried out in different days and hours in a 3-month period in 2019. In addition, the survey was controlled by using the data obtained from Erzurum Metropolitan Municipality. Figure 3 shows survey questions and answers. Question and answer evaluations for bus service satisfaction are shown in Figure 4. Finally, some questions were asked and the results were stated in order to learn the most important issues in the travel in Figure 5. In order to interpret the survey results better, the evaluations are shown in percent.



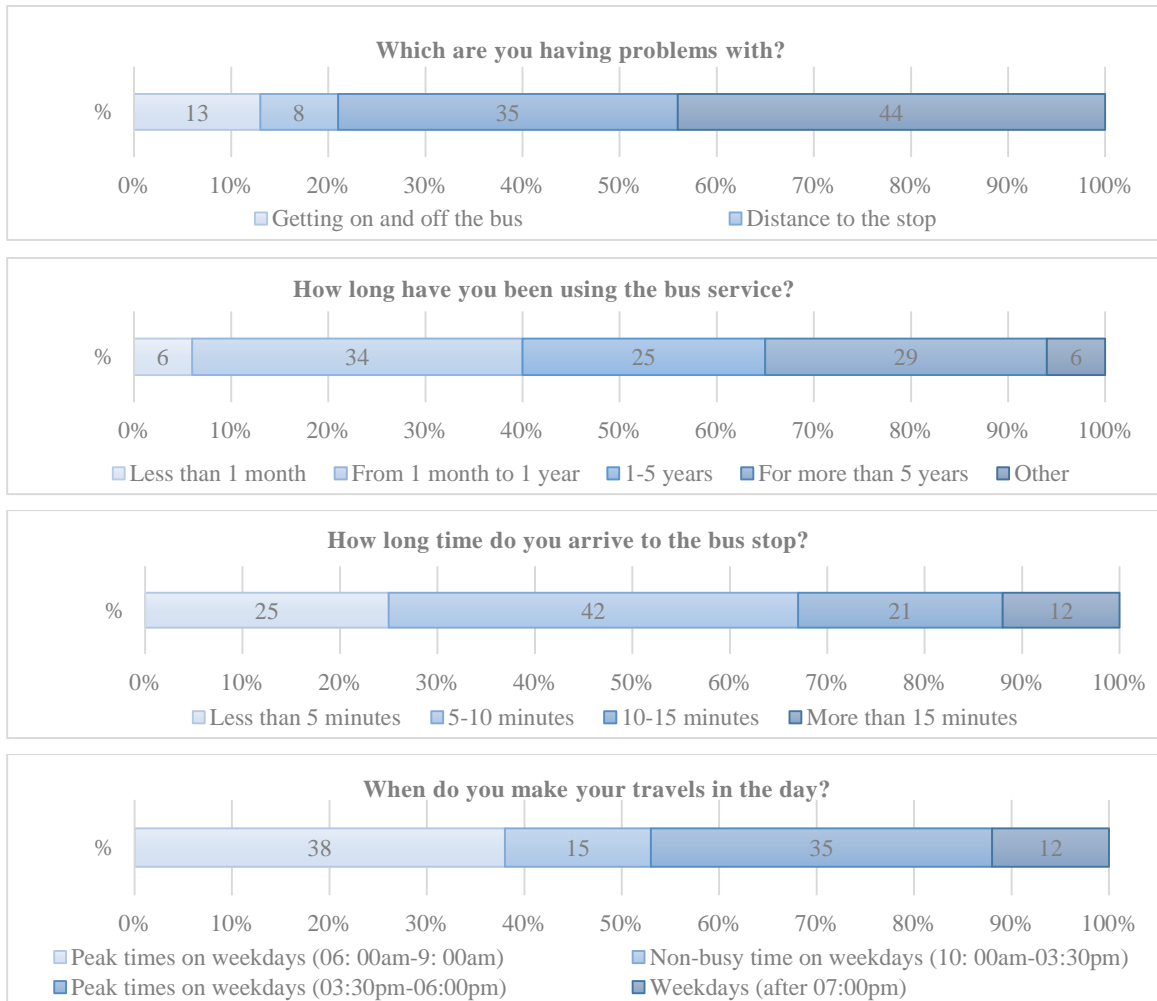
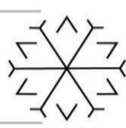


Figure 3: General information survey study of bus travel.

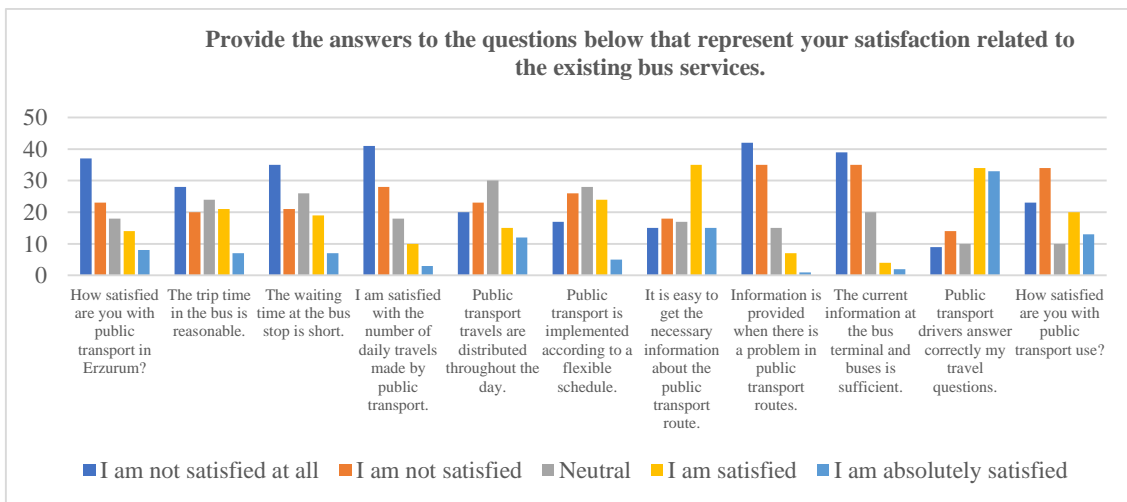


Figure 4: The survey for bus service satisfaction.

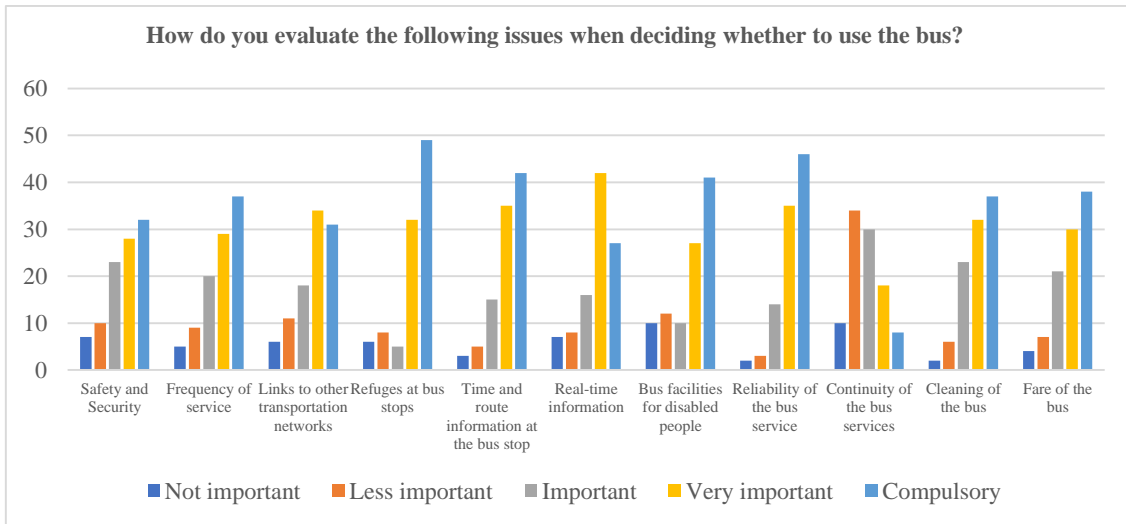


Figure 5: The survey on the issues that are most important in travel.

2.2. Optimization of Bus Stops

While performing the optimization process at the bus stops, it should not be contrary to the relevant regulations. For this purpose, the Turkish Standards Institute (2018) 11783 numbered city roads and bus stops location selection rules were examined. This regulation is which “The stop should be chosen at least 100 m from the intersections; Waiting vehicles at the intersection should be prevented to sag on the road section at the stop and the distance between the two stops should be at least 400 m in order not to decrease the flow speed of the traffic. On the first degree roads, this distance should be 600 m. In road sections with high passenger density, these distances can be reduced by 100 meter”. For this study, the minimum distance between Erzurum city bus stops is 500 meters. In the study, it is seen that the stops are located very close in some regions on both bus lines and do not meet the minimum distance rule between the stops. Similarly, the fact that some bus stops are closer to intersection points than 100 meters does not comply with the regulation. If the conditions determined in the regulation are restrictive, the equations 1,2 and 3 are obtained.

On the road, on average,

$$g_1(x) = m \geq 500 \text{ meter} \quad (1)$$

At stops near intersections,

$$g_2(x) = n - m \geq 100 \text{ meter} \quad (2)$$

Objective function,

$$\min f(x) = \sum_{i=1}^n (x_i) \quad (3)$$

2.3. Location Analysis of Bus Stops

In this study, spatial analyses as visuals of B2/A and G4/A were made. These analyses were done with ArcMap 10.5 version. Kernel density analysis was made by determining the locations of the stops, the number of passengers at the stops and the delay times due to the passengers. Density maps of G4/A are given as an example in Figure 6.

When the density maps obtained as a result of the analysis are examined, it is observed that the number of passengers in the south-east part of the city is high for the direction of the line and accordingly, the delays increase. Although the number of stops for the western part of the line is high, it is seen that there is not enough passenger demand. It is observed that the number of passengers in the western and southwestern part of the city is high for the direction of the return line and accordingly, the delays increase. Although the number of stops for the south and east part of the line is high, it is seen that there is not enough passenger demand. Therefore, the number and location of the stops should be arranged according to the optimization result in these regions.

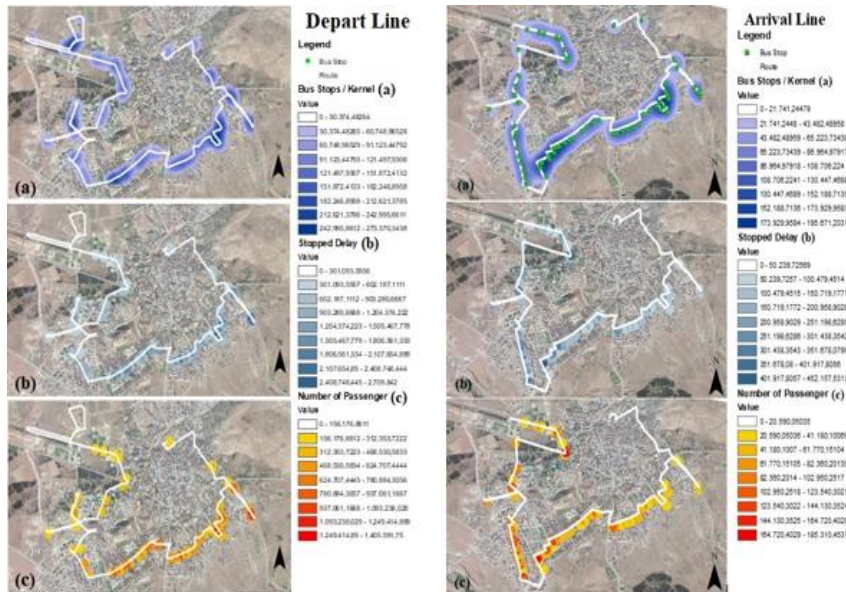
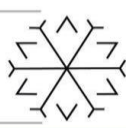


Figure 6: Departure and return line of G4/A (a) bus stops (b) stopped delay (c) number of passengers.

3. Results and Discussion

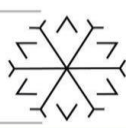
When the surveys conducted for individuals using public transportation and the regulations regarding the city roads and bus stops location selection rules are examined together; there is a need for optimization regarding stop locations and numbers. Thanks to the decrease in the number of stops and the change of some stop places, the number of stop-and-go buses will be reduced. On the other hand, delays and waiting at stops will be reduced as the journey times will be shorter. In addition, reducing the number of stop-and-go in buses will reduce fuel consumption, thereby providing economic gain and reducing air pollution. According to the information obtained from the drivers using public transportation vehicles, it was determined that the fuel consumption spent during the stop-and-go operation is approximately 2 times more than the normal conditions. Accordingly, fuel calculations were made by assuming that the fuel consumption at each stop was twice the fuel consumption in the normal course.

While optimizing the number of stops of the spatially analyzed lines, the stops where the landing and boarding situations were intense were applied in a way that would be a priority. Since the main criterion in the study is user satisfaction, using the stops frequented by the passengers are not changed. For this reason, the fact that some important stop points are close to intersections and the distance between other stops is close can be ignored. In Table 2 below shows the current situation for both bus lines and the number of stops after the improvement.

Table 2: Number of bus stops before and after optimization.

Number of Stops	Bus Lines			
	G4/A		B2/A	
	Departure	Return	Departure	Return
Current Situation	62	65	60	76
After Optimization	46	47	45	53
Decrease	16	18	15	23

In the table, it is seen that there is a serious decrease in the number of stops when optimization is applied at bus stops. As a result of the improvement, it is observed that there is a 26% decrease in the number of stops on the route of the G4/A line and a 28% decrease in the number of stops on the return route. In B2/A line, it has been determined that there is a 25% decrease in the departure route and 30% in the return route. Table 3 below shows the daily average fuel consumption values of the public transportation buses in the situation that occurred after the optimization and the daily costs resulting from these fuels. Since there are buses with CNG (compressed natural gas) and diesel fuel type for both lines, calculations are made separately.

**Table 3:** Fuel and cost condition before and after optimization.

Fuel Consumption and Cost		Current Situation		After Optimization	
		G4/A	B2/A	G4/A	B2/A
Daily Average Fuel Consumption	CNG Buses (bar)	210	190	165,4	139,3
	Diesel Buses (liter)	160	150	126,13	109,96
Daily Cost (Turkish Lira-TL)		1 485	1 375	1 170,28	1 008,01

*CNG price (bar): 2,5 TL, diesel price (liter): 6 TL as the calculation is made.

Thanks to the improvement in the number of stops on both bus lines, it has been determined that the daily average fuel consumption and the daily cost of vehicles working with natural gas and diesel fuel have decreased significantly. For the G4/A line; it is observed that approximately 315 TL per day, 9 450 TL per month will be saved, for the B2/A line; it will be saved approximately 367 TL per day and 11 010 TL per month. Although the savings achieved for both lines are considered to be low in the short term, they can provide significant gains in the long term. Considering that the fuels used in public transportation buses are consumable resources, these fuels should be used more economically. Similarly, the increase in fuel prices every year reveals the necessity to use these resources in a saving manner.

Although the journey times of the buses can change according to the days and traffic density, the average duration of the journey is 2 hours 25 minutes for the G4/A line and 2 hours for the B2/A line. During the journey, the waiting time for each stop and lost time for stop-and-go operation have been noted. After the optimization, the number of stops and the duration of the trips decreased. With the decrease in the number of stops, 38 minutes on the departure route and 40 minutes on the return route saved time for the G4/A bus line. For the B2/A bus line, 35 minutes on the departure route and 43 minutes on the return route were saved time. In the surveys conducted to the passengers, the biggest problem encountered was found to be waiting or standing for more than 10 minutes at the stops. As the number of stops decreases, delays will be minimized. So the waiting time of the passengers at the stops will decrease. On the other hand, the increase in the distance of passengers to the stops causes a negative situation. However, it is predicted that this situation will not be a major problem since most of the transportation to the bus stop distances are less than 10 minutes. Because, as a result of the surveys, it is seen that the passengers are disturbed not by the distance of the bus stops but by the waiting at the bus stops. In addition, since this situation increases the walking distances of the passengers, it creates a beneficial situation for individuals.

4. Conclusion

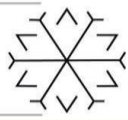
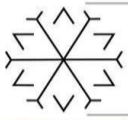
According to the quality of service provided by the public transport systems to the passengers in the cities, the satisfaction level increases. Increasing the satisfaction level of the passengers can also make public transportation more attractive. In case a public transport service is of high quality in a city, people can turn to public transport instead of traveling by individual vehicles. On the other hand, stop-and-go events cause traffic congestion in buses used in public transportation. Traffic congestion increases the average fuel consumption and emissions of the vehicles. In addition, traffic jams; it causes delays and increases bus times. Considering all these situations, when both passenger demands and bus routes and stop locations are evaluated together, it may be necessary to make some improvements. In this study made in this context; A number of examinations and passenger satisfaction surveys of 2 bus lines with the longest route were made among the bus lines in Erzurum. In these examinations; the number of passengers getting on and off at each bus stop and the waiting times of the buses at the stops were determined. Then, an optimization process was applied for the stops on the departure and return routes of both bus lines. In the optimization process; passenger satisfaction surveys and current regulations were decisive. As a result of the optimization process, the number of stops decreased by 27% for both bus lines. Thanks to this improvement, reductions in buses' trip times and fuel consumption have been identified. Thus, important results have been achieved in terms of reducing air pollution and increasing passenger satisfaction and contributing to the increase in public transportation use.

References

- Akay A. (2015). A minimum transfer focused solution approach to the route optimization problem on public transport networks. Doctoral thesis. Karadeniz Technical University, Trabzon.
- Alkheder, S., Alrukaibi, F., & Zaqzouq, A. (2018). Optimal bus frequency for Kuwait public transportation company: A cost view. *Sustainable Cities and Society*, 41, 312-319. doi: 10.1016/j.scs.2018.05.042



- Alrukaibi, F., & AlKheder, S. (2019). Optimization of bus stop stations in Kuwait. *Sustainable Cities and Society*, 44, 726-738. doi: 10.1016/j.scs.2018.10.037
- Emiliano, M. W., Costa, L., Carvalho, S. M., Telhada, J., & Lanzer, E. A. (2020). Multiobjective optimization of transit bus fleets with alternative fuel options: The case of Joinville, Brazil. *International Journal of Sustainable Transportation*, 14(1), 14-24. doi: 10.1080/15568318.2018.1518500
- Erzurum Metropolitan Municipality (2018). Urban bus and minibus lines. Retrieved from <https://ulasim.erzurum.bel.tr/bilgisi.aspx?mid=1005>
- Gecer D. (2009). Feeder bus routes design problem. Master thesis. Yıldız Technical University, Istanbul.
- Gokasar, I., Buran, B., & Dunder, S. (2018). Modelling the quality of bus services by using factor analysis on urban bus satisfaction survey data: Case of IETT. *Pamukkale University Journal of Engineering Sciences*, 24(6), 1079-1086. doi: 10.5505/pajes.2017.48278
- Jaramillo-Alvarez, P., Gonzalez-Calderon, C. A., & Gonzalez-Calderon, G. (2013). Route Optimization of Urban Public Transportation. *Dyna-Colombia*, 80(180), 41-49.
- Kızgın M.A. (2013). Analysis of urban transport in agri province and a planning study for public transport. Master thesis. Bahçeşehir University, Istanbul.
- Kun, A., Wentao, J., & Inhi K. (2019). Battery-swapping facility planning for electric buses with local charging systems. *International Journal of Sustainable Transportation*, DOI: 10.1080/15568318.2019.1573939
- Mandl, C. E. (1980). Evaluation and Optimization of Urban Public Transportation Networks. *European Journal of Operational Research*, 5(6), 396-404. doi: Doi 10.1016/0377-2217(80)90126-5
- Muti B.Ş. (2018). Bus assignment optimization in public transport planning. Master thesis. Yıldız Technical University, Istanbul.
- Nehir Y. (2009). A study on the efficient use of bus stops in Izmir. Master thesis. Dokuz Eylül University, Izmir.
- Ozcan T. (2018). Flight frequency optimization in urban public transportation systems. Master thesis. Pamukkale University, Denizli.
- Pampal, S., Avşar, N., & Özcan E.C. (2009). Comparison of the bus and rail system in Dikimevi – Beşevler route. *Journal of Faculty of Engineering and Architecture of Gazi University*, 24(2), 293-302.
- Paul, T., & Yamada, H. (2014). Operation and Charging Scheduling of Electric Buses in a City Bus Route Network. 2014 Ieee 17th International Conference on Intelligent Transportation Systems (Itsc), 2780-2786.
- Savsar, M., Alnaqi, J., & Atash M. (2012). Scheduling and routing of city buses at kuwait public transport company. *International Journal of Applied Operational Research*, 1(3), 11-32.
- Shahraki N. (2015). Urban transportation network design problem with sustainability considerations, Doctoral thesis. Koc University, Istanbul.
- Tran, V.T., Eklund, P., & Christopher, C. (2015). Toward real-time multi-criteria decision making for bus service reliability optimization, *Proceedings of the 22nd International Symposium on Methodologies for Intelligent Systems: Foundations of Intelligent Systems*, pp. 371-378.
- Turkish Statistical Institute. (2018). City roads - bus stops site selection rules in Turkey. Retrieved from http://www.ceidizleme.org/ekutuphaneresim/dosya/159_1.pdf
- Turkish Statistical Institute. (2018). Number of motor vehicles by provinces in Turkey. Retrieved from <http://www.tuik.gov.tr/PreHaberBultenleri.do?id=27647>
- Uludağ, N. (2010). Modeling of bus lines with fuzzy optimization and linear target programming approaches. Doctoral thesis. Pamukkale University, Denizli.



Wu, W. (2009). Optimization models for selecting bus stops for accessibility improvements for people with disabilities. Master thesis. Florida International University, Florida.

Zhang, N., & Zhengdong, H. Z. (2011). Evaluation and optimization of the bus route network in wuhan china. The Seventh Advanced Forum on Transportation Of China, 2011 International Conference, pp. 140-148.

Ultimate Drift Ratio Limit of Steel Plate Shear Walls

Muhammed Gürbüz ¹[0000-0001-6628-3363] and İlker Kazaz ^{2*}[0000-0002-3885-1885]

¹muhammed.gurbuz@erzurum.edu.tr, Erzurum Technical University, Civil Engineering Department,
Erzurum, Turkey

²ilkerkazaz@erzurum.edu.tr, Erzurum Technical University, Civil Engineering Department, Erzurum,
Turkey.

*Corresponding Author

Abstract

Steel plate shear walls (SPSW) are used as primary lateral load resisting systems of building structures. There is a wide range of studies on the main parameters, such as initial stiffness, frame stiffness, and infill plate geometry, affecting the seismic performance of the system for code-limited inter-story drift levels. Codes adopted inter-story drift limits commonly in a range between 1% and 2.5% of the story height. However, there is a lack of detailed investigation about the nonlinear structural behavior of SPSW at collapse level drift. A parametric study was performed to investigate the ultimate drift limits of steel plate shear wall systems under cyclic loading. The main design parameters of the investigation are column flexibility factor, infill plate aspect ratio, infill plate thickness, horizontal boundary element flexural stiffness, and axial load ratio. The finite element analyses results showed that there is a strong correlation between the design parameters and ultimate drift capacity of steel plate shear wall systems. A formula depending on the design parameters is proposed to predict the collapse drift ratio limit of steel plate shear walls.

Keywords. Steel plate shear walls, nonlinear behavior, cyclic loading, ultimate drift, finite element.

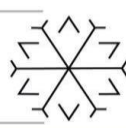
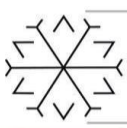
1. Introduction

Steel plate shear walls (SPSW) are structural components with high energy dissipation capacity, initial stiffness and ductility under lateral loads. Reduced seismic load due to reduced dead weight and thickness of the walls are some of the advantages of the steel plate shear walls. These characteristics make them attractive to resist seismic loading and dissipate seismic energy. A typical steel plate shear wall consists of vertical and horizontal boundary elements (VBE and HBE) and an infill steel plate.

The design equations and processes developed for SPSWs are based on well-established mechanical models. The shear strength of steel plate shear walls has been investigated by previous experimental research and accurately established by analytical research. Thorburn et al. (Thorburn, Montgomery and Kulak, 1983) proposed an analytical model of yielding infill steel plate known as strip model, where the inclined tension field was represented by a series of pin-ended strips. Timler and Kulak (Timler and Kulak, 1983) verified the strip model presented by Thorburn et al. (Thorburn, Montgomery and Kulak, 1983) by an experimental study on SPSWs.

The strip model enables the calculation of the shear capacity of SPSW. SPSW design requirements are given in AISC-341 (AISC, 2016), and practical low and high seismicity design processes are illustrated in AISC Design Guide 20 (Sabelli and Bruneau, 2006). The design story shear strength given in AISC-341 originates from the strip model representing the collapse mechanism of an SPSW with simple connections.

The stiffness of bounding columns significantly affects the overall performance of steel plate shear wall (SPSW) systems under lateral loading conditions. Wagner's (Wagner, 1931) analytical studies on diagonal tension fields provided the theoretical background on the flexibility coefficient of vertical boundary elements (ω_v). Wagner (Wagner, 1931) derived the flange flexibility parameter by considering the elastic deformations of a cantilever plate girder under transverse loading. Kuhn et al. (Kuhn, Peterson and Levin, 1952) simplified the flange flexibility parameter that is introduced by Wagner (Wagner, 1931). The simplified flexibility is used to specify the stiffness limits for the boundary frames. The given flexibility parameter is;



$$\omega_i \approx 0.7h_{st} \left(\frac{t_w}{(I_u + I_o)L} \right)^{0.25} \quad (1)$$

where h_{st} stands for the spacing between the neighboring stiffeners, I_u is the moment of inertia of bottom flange (corresponds to the tension column of SPSW), I_o is the moment of inertia of top flange (corresponds to the compression column of the SPSW), t_w is the infill plate thickness and L is the clear distance between flanges. Montgomery and Medhekar (Montgomery *et al.*, 2001) proposed that the column flexibility parameter ω_i should not exceed 2.5 to form a relatively uniform tension field on steel plate shear walls.

Steel plate shear wall design equations are accommodated in various provisions and standards (CAN, 2009; AISC, 2016). CAN\CSA 2009 (CAN, 2009) recommends that the infill plate of the SPSW is designed to resist the entire load and neglects the contribution of the surrounding boundary frame.

This study is a comprehensive comparative study covering SPSW preliminary design parameters and expounds on the correlation of the parameters with collapse drift ratio. For that purpose, a numerical parametric study is devised to investigate the effect of a wide range of parameters such as plate thickness, aspect ratio, axial load and relative stiffness of boundary elements on the behavior of SPSW models using finite element analysis. Both code-limited columns (flexibility parameter less than 2.5) and columns that violate requirements (column flexibility parameter above the limit 2.5) are considered. A wide range of aspect ratios are investigated.

2. Finite Element Model Verification

Four different steel plate shear wall specimens from four different research were chosen for finite element model validation. The first specimen, SPSW2, is a 1/4 scale model tested by Lubell *et al.* (Lubell *et al.*, 2000) representing a steel-framed office building core is displayed in Figure 1(a). Steel plate web thickness is 1.5 mm. The distance between two vertical boundary elements centerlines is 900 mm. The steel plate has a width-to-height aspect ratio of 1:1. S75x8 steel profiles were used as vertical and horizontal boundary elements. To develop a full internal tension field on the steel web panel, an additional S75x8 beam was welded onto the top horizontal boundary element. The model has rigid beam to column connections.

The second model is selected from the study of Wang *et al.* (Wang *et al.*, 2015). The selected specimen, TM2, is a 1/3 scale, three-story unstiffened steel plate shear wall as shown in Figure 1(b). In different stories, different plate thicknesses were used; 6 mm for the lower story plate and 4 mm for the top two-story plates. Behavior of the middle story was investigated in the experimental work. 450 kN vertical loads were applied on top of the columns. The TM2 frame was designed as a moment frame with welded connections.

Specimen F2 tested by Berman and Bruneau (Bruneau and Berman, 2005) is used as the third model. As seen in Figure 1(c), model F2 is a single-story structure with semi-rigid connections between beam and column. On both vertical boundary element bases, simple pin supports were used to provide the required foundation fixity. Steel plate web thickness of model F2 is 0.98 mm. The bay width and story height of specimen F2 are 3660 mm and 1830 mm, respectively.

The last model, 3SPSW was tested by Behbahanifard *et al.* (Behbahanifard, Grondin and Elwi, 2003). The specimen is a 1/2 scale SPSW as illustrated in Figure 1(d). The shear wall has moment-resisting beam-to-column connections and different loading conditions compared to other experimental models. Before applying lateral loads, a 400 kN gravity load was applied in the first three cycles and was increased to 540 kN and kept constant afterward. Equal lateral loads were applied at each floor level, so the effect of multipoint load application on steel plate shear wall was considered. Further details on the dimensions of the specimens and the test setup can be found in referenced papers.

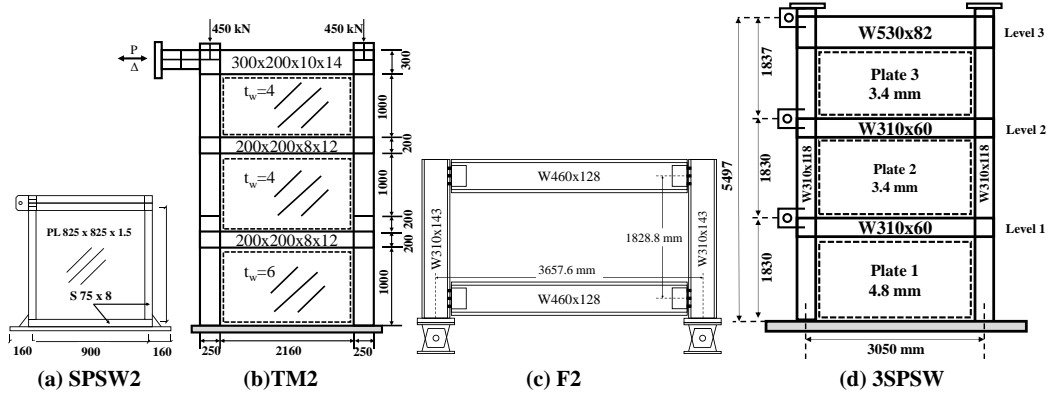


Figure 1: Geometry of the experimental specimens used for FE model validation.

All specimens were exposed to cyclic quasi-static loading in experimental studies. All test results indicated that steel plate shear walls show high ductility capability and desired energy dissipation. The results of monotonic and cyclic finite element analyses are plotted against the experimentally measured load-deformation curves in Figure 2.

Elastic stiffness and ultimate shear strength of the system are adequately predicted by monotonic static analysis as displayed in Figure 2(a). Cyclic analysis results predict the physical test results of SPSW2 successfully. Elastic stiffness, load-displacement behavior, pinching of hysteresis loop are obtained accurately in the FE model. It was reported that the SPSW2 cyclic test was terminated due to fracture propagating inwards through the outer flange at the loaded column at $6\delta_y$, which is approximately 48 mm (δ_y is the observed global yield displacement). Under monotonic loading, plastic hinges form at the column elements. At the end of the analysis significant inelastic deformations develop at the columns.

For the specimen TM2, the calculated load-deformation relationships display a good agreement with the test results as plotted in Figure 2(b). Comparing the hysteresis curve of cyclic test results with the numerical analysis, it is seen that the elastic stiffness and capacity of the structure are predicted well. In TM2, the first story steel web panel is thicker than the remaining stories and also there is a column cross-section change at the second story. Consequently, the structure's observed failure mode was the flange buckling of the second-story columns and tear failure of the middle panel. The pinched hysteresis behavior observed in the actual test is also captured in the cyclic response of the finite element analysis as shown in Figure 2(b). The finite element model subjected to cyclic loading displays a failure pattern similar to experimental behavior. The FE analysis captures the flange buckling at the second story column bottom and plate failure of the middle story.

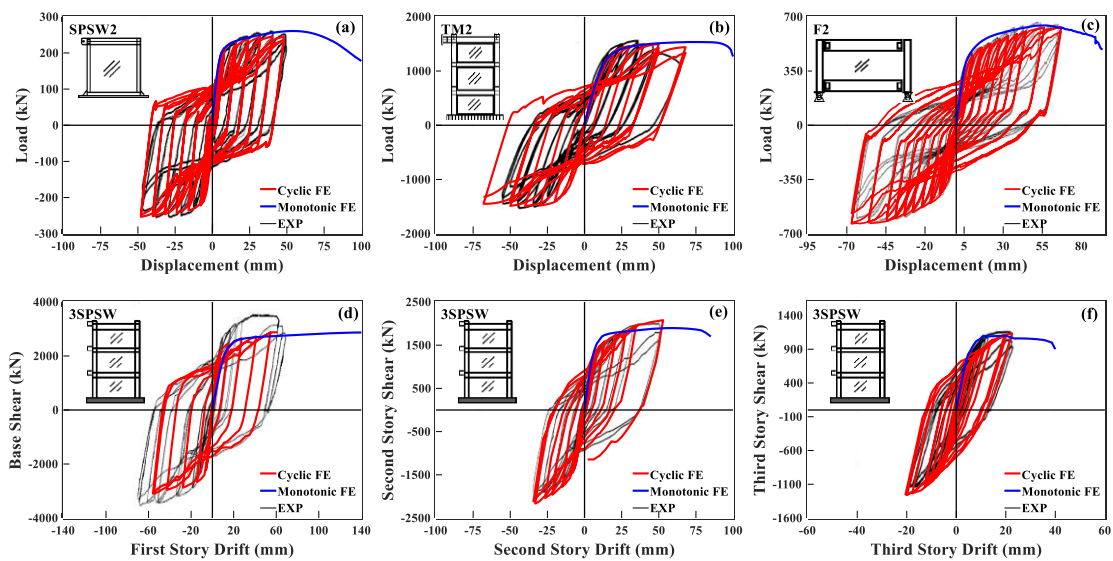
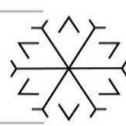
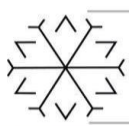


Figure 2: Comparison of experimental and numerical load-deformation curves.



Experimental cyclic response of specimen F2 and numerical cyclic and monotonic analyses results are presented in Figure 2(c). The semi-rigid connection is modeled as a plastic hinge using beam elements. Initial stiffness and total base shear capacity are in good agreement with the experimental data. Since the column bases are pin-connected and beam-to-column connections were designed as semi-rigid connections, the failure has occurred before the boundary elements exceed the elastic limits. The test was stopped because the hydraulic actuator had reached its stroke capacity. Before reaching the stroke capacity, fractures were observed at the corners of the infill plate. It was reported that the failure of the specimen was due to large fractures at the corners. The pinching behavior in the numerical cyclic response does not agree very well with the actual test results due to the simplified modelling of the beam-to-column connection.

For the 3-story model 3SPSW, cyclic and monotonic loading analysis results are shown in Figure 2(d-e-f). Monotonic loading analysis predicts the elastic stiffness well, but the load capacity of the specimen is underestimated in the first story. Cyclic analysis results have good agreement with the test results. The local buckling at the first story column flange was observed in the experiment. Elastic stiffness of the shear plate wall and hysteresis behavior of the cyclic response was predicted well in the analysis. Ultimate load capacity is also underestimated for the cyclic case. This situation is actually due to an intervention strengthening after the observed global yield in the actual test. Specimen 3SPSW is a re-used model from a prior experiment. Previously, Driver et al. (Driver *et al.*, 1997) tested a four-story steel plate shear wall where the damage mainly was concentrated in the bottom level of the frame at the end of the test. Behbahanifard et al. (Behbahanifard, Grondin and Elwi, 2003) removed the first story of the specimen and tested upper three stories. The authors stated that the strength increase after the significant yielding might be originating from the possible increase of initial stiffness of the materials during the prior testing. The material properties used for the finite element analysis are taken directly from Driver et al. (Driver *et al.*, 1997) without considering any of these pre-loading effects.

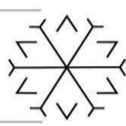
Considering the response of 3SPSW, the first two-story steel web plates are fully yielded. Afterward, global buckling of the left side first story column and global and local buckling at the first story right side column is observed. Comparing the FE analysis results with the experimental data, good agreement is observed especially for the second and third stories as plotted in Figure 2(e-f). Stiffness, displacement at the maximum story shear force and energy dissipation capacity in both directions are predicted well.

The agreement between numerical simulations and experimental results can be considered sufficient for all models. According to the analysis results of FE, especially the collapse mechanisms and the damage propagation reported in the experiments are closely estimated by cyclic loading analyses. Based on the results of this exercise, it is determined that the numerical simulation tool and methodology can be employed for a parametric study covering a wide variety of parameters.

3. Parametric Study

The investigated design parameters that affect the behavior of SPSWs are the infill plate thickness (t_w), infill plate aspect ratio (L_p/h_p), column flexibility parameter (ω_i), moment of inertia of the horizontal boundary element (I_b) and axial load ratio (P/P_{cr}) of the columns. 42 three-story finite element models are generated depending on different combinations of these parameters. A typical three-story SPSW model outlining the analysis parameters is shown in Figure 3(b). Geometric and member properties of the FE models are presented in Table 1.

To reinforce the top beam against the internal steel plate forces, an additional beam is connected to the top beam and they are assumed to be anchored along the flanges as displayed in Figures 3(a) and 3(b). The panel aspect ratio, which is specified as the ratio of infill plate length to height L_p/h_p , varying from 0.6 to 2 is considered. A constant plate height of 3000 mm is used in all models. Plate thicknesses t_w are selected as 3, 4, 5 and 6 mm. According to the AISC provision, past research was focused on walls with an L_p/t_w ratio ranging from 300 to 800 although no limits are specified on that ratio. The aspect ratios are chosen between 300 and 2000 to cover a wide range of the infill plate slenderness ratio. As the thickness of the plate in both stories is identical, the demand on the beam is negligible. Thus, the moment of inertia of the horizontal boundary elements is chosen by the ratio of I_o/I_b , which varies between 1 to 5. In the models, VBEs are exposed to axial load levels of 0.1, 0.2 and 0.3 times the critical axial load $P_{cr}=F_yA_g$. The selected values for axial load ratio cover the experimental database axial load ratio limits. The column flexibility factors (ω_i) of models vary from 1.58 to 2.68.

**Table 1:** Details of the models subjected to cyclic loading.

No	t_w (mm)	L_h (mm)	L_p (mm)	Column Section	Beam Section	ω_i	L_p/h_p	I_c/I_b	P/P_{cr}	L_p/t_w	DR_u
1	3	3000	3000	HD 360 x 162	HE 300 B	2.23	1.00	2.05	0.1	1000	0.056
2	3	3000	3000	HD 360 x 162	HE 280 A	2.21	1.00	3.77	0.1	1000	0.063
3	3	3000	3000	HD 360 x 162	HE 300 B	2.23	1.00	2.05	0.2	1000	0.043
4	3	3000	3000	HD 360 x 162	HE 280 A	2.21	1.00	3.77	0.2	1000	0.048
5	3	3000	3000	HD 360 x 162	HE 300 B	2.23	1.00	2.05	0.3	1000	0.033
6	3	3000	3000	HD 360 x 162	HE 280 A	2.21	1.00	3.77	0.3	1000	0.037
7	3	3000	6000	HD 400 x 262	HE 400 A	1.70	2.00	1.98	0.2	2000	0.100
8	3	3000	5000	HD 400 x 314	HE 500 AA	1.72	1.67	2.02	0.2	1670	0.099
9	3	3000	4000	HD 400 x 347	HE 400 B	1.72	1.33	2.17	0.2	1330	0.100
10	3	3000	3000	HD 400 x 421	HE 340 M	1.71	1.00	2.09	0.2	1000	0.120
11	3	3000	2000	HD 400 x 634	HE 550 B	1.70	0.67	2.01	0.2	670	0.110
12	3	3000	6000	HD 400 x 262	HE 400 A	1.70	2.00	1.98	0.3	2000	0.073
13	3	3000	4000	HD 260 x 114	HE 280 B	2.68	1.33	0.98	0.3	1330	0.015
14	5	3000	2000	HD 400 x 634	HE 550 B	1.94	0.67	2.01	0.2	402	0.083
15	6	3000	5000	HD 360 x 147	HD 360 x 147	2.47	1.67	1.00	0.3	1002	0.008
16	6	3000	6000	HD 320 x 127	HE 340 A	2.60	2.00	1.11	0.3	1000	0.007
17	4	3000	5000	HD 360 x 196	HE 320 A	2.03	1.67	2.77	0.1	1252.5	0.078
18	6	3000	5000	HD 320 x 158	HE 280 A	2.50	1.67	2.90	0.1	835	0.018
19	5	3000	5000	HD 320 x 158	HE 300 B	2.41	1.67	1.57	0.1	1002	0.029
20	4	3000	4000	HD 320 x 158	HE 240 M	2.38	1.33	1.63	0.1	997.5	0.050
21	4	3000	4000	HD 400 x 382	HE 500 AA	1.83	1.33	2.59	0.1	997.5	0.116
22	5	3000	6000	HD 320 x 300	HE 340 A	1.91	2.00	3.14	0.1	1200	0.070
23	6	3000	2000	HD 400 x 551	HE 340 M	2.03	0.67	2.96	0.1	335	0.120
24	6	3000	2000	HD 400 x 509	HE 300 M	2.06	0.67	3.45	0.2	335	0.114
25	4	3000	2000	HD 400 x 287	HE 450 A	2.30	0.67	1.56	0.2	502.5	0.071
26	4	3000	6000	HD 320 x 158	HE 280 A	2.16	2.00	2.90	0.3	1500	0.020
27	5	3000	3000	HD 400 x 314	HE 400 A	2.14	1.00	2.45	0.3	600	0.060
28	5	3000	4000	HD 400 x 287	HE 280 M	2.01	1.33	2.52	0.2	798	0.070
29	4	3000	3000	HD 400 x 287	HE 450 B	2.12	1.00	1.25	0.2	750	0.061
30	5	3000	4000	HD 400 x 287	HE 450 B	2.10	1.33	1.25	0.3	798	0.042
31	6	3000	3000	HD 320 x 300	HE 320 A	2.33	1.00	3.79	0.3	500	0.061
32	6	3000	2000	HD 400 x 287	HE 320 A	2.45	0.67	4.35	0.3	335	0.053
33	4	3000	4000	HD 320 x 158	HE 260 AA	2.36	1.33	4.97	0.2	997.5	0.051
34	5	3000	6000	HD 400 x 237	HE 300 B	1.94	2.00	3.13	0.1	1200	0.087
35	4	3000	4000	HD 320 x 245	HE 320 AA	2.09	1.33	4.14	0.2	997.5	0.080
36	4	3000	2000	HD 360 x 147	HE 260 A	2.65	0.67	4.43	0.2	502.5	0.029
37	5	3000	5000	HD 400 x 237	HE 500 AA	2.13	1.67	1.44	0.2	1002	0.047
38	5	3000	6000	HD 260 x 142	HE 360 AA	2.64	2.00	1.06	0.2	1200	0.008
39	5	3000	3000	HD 400 x 382	HE 340 B	1.98	1.00	3.85	0.2	600	0.104
40	6	3000	5000	HD 360 x 196	HE 500 AA	2.35	1.67	1.16	0.3	835	0.014
41	4	3000	4000	HD 360 x 162	HE 450 AA	2.33	1.33	1.23	0.2	997.5	0.023
42	6	3000	6000	HD 400 x 744	HE 700 M	1.58	2.00	1.04	0.1	1000	0.118

In the design, the geometric properties, infill plate thickness (t_w) and infill plate aspect ratio (L_p/h_p), of the SPSW is determined first, then using Eq. (2) the column moment of inertia is calculated. The beam stiffness is selected via I_c/I_b ratio. European rolled wide-flange sections are used to design HBEs (HE sections) and VBEs (HD sections). Structural steel grades of S235 ($F_y=235$ MPa, $F_u=360$ MPa) and S355 ($F_y=355$ MPa, $F_u=510$ MPa) are used for steel infill panels and the boundary elements, respectively.

In this study, the ultimate drift ratio (DR_u) is defined as the drift ratio, where the maximum system strength is decreased by 15%. At this stage, it has been assumed that the model completed the failure mechanisms and reached the collapse level. Peak values of primary analyses results are also summarized in Table 1.

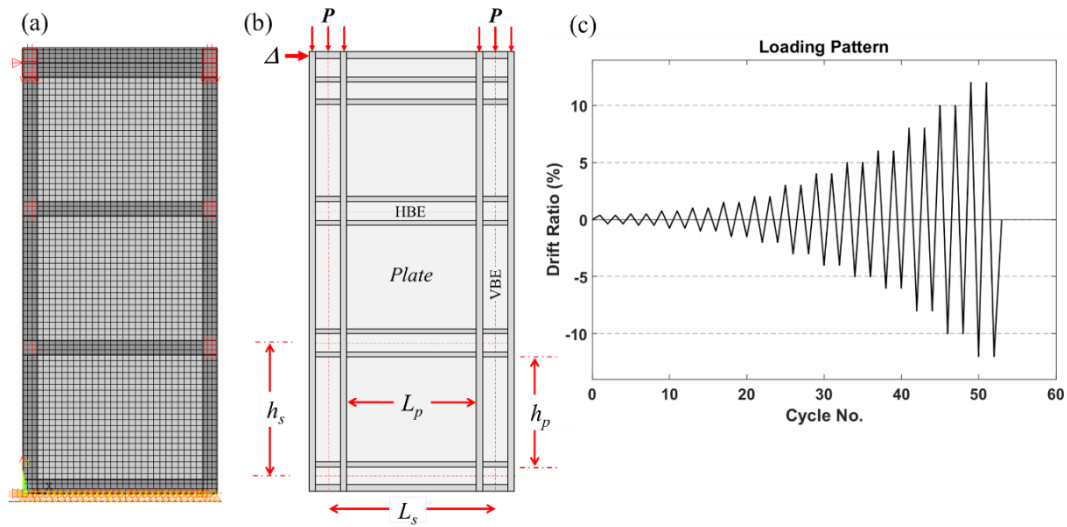


Figure 3: (a) A representative finite element model of SPSWs used in this study, (b) typical steel plate shear wall configuration, (c) Loading protocol.

4. Results of Analyses

The main response quantities, which are the load and displacement capacity are compared among monotonic and cyclic analyses. As previously illustrated in Figure 2 for the experimental specimens, the SPSW models under monotonic and cyclic loading nearly produce the same load capacity and closely match with the experimental results in terms of strength. It can be asserted that the finite element analysis method produces very close estimations of the load capacity of SPSWs for both loading cases.

Obviously under such a variety of parametric combinations, it should not be expected that all models will fail in a specific hierarchical order even the design is performed under code specifications. It is observed that the combination of some parameters over a certain critical range leads to unpredictable and undesirable failure patterns limiting the deformation capacity of SPSW. The strongest correlation with the ultimate drift ratio is displayed by the column flexibility factor as presented in Figure 4(a). As a general observation, models with a column flexibility factor below 2.1 follow the desired failure sequence and show high displacement capacity without exception. Even when the model has very high axial load ratio and high aspect ratio combination, which negatively affects the behavior, the models exhibit desirable behavior. SPSWs with a higher column flexibility factor should be designed more carefully in terms of aspect ratio, infill panel thickness, I_c/I_b ratio and axial load level.

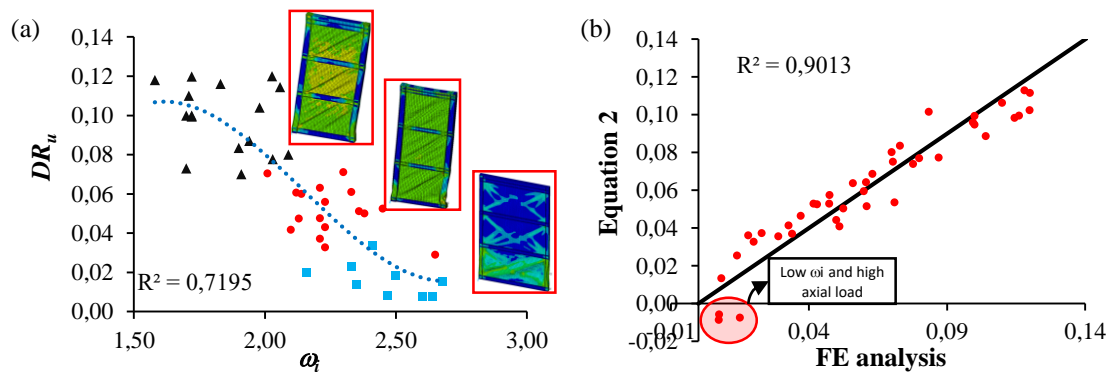


Figure 11: (a) The correlation of column flexibility parameter and ultimate drift ratio (b) the comparison of FE analyses results and Equation (2).

Considering the average values in Table 1, it is seen that the ultimate drift capacity increases while the axial load decreases. As the average value of ω_i increases, the drift capacity decreases. When SPSWs are designed with high ω_i , stiffer beams (in terms of moment of inertia close to column) lead to early failure.



As expected, with high axial load, deformation capacity decreases. Due to interaction of lateral load, infill plate induced loads and high axial load, $P-\Delta$ effect increases and an early failure occurs when compared to low axial load cases. When an SPSW has a high axial load, the system may have a reduced drift capacity even if the wall meets the code requirements.

For the ultimate drift ratio, a formula is developed using linear regression analysis and given as;

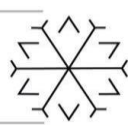
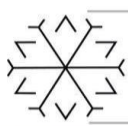
$$U_d = 0.3084 + 0.00474t_w - 0.10376\omega_i - 0.02342 \frac{L_p}{h_p} + 0.002324 \frac{L_c}{I_b} - 0.09961 \frac{P}{P_{cr}} \quad (2)$$

The predictions are compared with analysis results in Figure 4(b). The $R^2=0.90$ indicates that the proposed equation successfully predicts drift of SPSWs. Using the formula, the ultimate drift ratio and wall behavior might be predicted at the beginning of the preliminary design stage.

5. Conclusion

The finite element method is used to investigate the behavior of three-story steel plate shear wall models. The inelastic behavior of SPSW frames is investigated under monotonic and cyclic loads. The boundary elements should be rigid enough to ensure that the entire infill plate yield. The nonlinear behavior of SPSWs in this study demonstrates that if the column flexibility factor, ω_i is kept below 2.1, most undesired behaviors may be avoided. However, if the parameter combination is properly chosen, satisfactory behavior can be obtained with a greater column flexibility factor.

An equation that predicts the ultimate drift ratio is proposed. The proposed equation consists of the preliminary design parameters of steel plate shear walls. The findings of the finite element analysis and the equation results were compared. The formula accurately predicted the ultimate drift ratio limit of the steel plate shear walls.



References

- AISC (2016) 'Seismic Provisions for Structural Steel Buildings', *ANSI/AISC 341*, 16.
- ANSYS (2011) 'ANSYS Mechanical APDL', © ANSYS, Inc., (August), p. www.ansys.com. doi: www.ansys.com.
- Behbahanifard, M. R. ., Grondin, G. Y. and Elwi, A. E. (2003) *Experimental and Numerical Investigation of Steel Plate Shear Wall*. Edmonton.
- Bruneau, J. W. and Berman, M. (2005) 'Experimental Investigation of Light-Gauge Steel Plate Shear Walls', *Journal of Structural Engineering*, 131(2). doi: 10.1061/(ASCE)ST.1943-541X.0000531.
- CAN, C. S. A. (2009) 'CSA-S16-09 limit states design of steel structures', *Rexdale, ON: Canadian Standard Association*.
- Driver, R. G. *et al.* (1997) 'Seismic behaviour of steel plate shear walls', *Earthquake Engineering & Structural Dynamics*, 26(10). doi: 10.1002/(SICI)1096-9845(199710)26:10<1059::AID-EQE694>3.3.CO;2-D.
- Kuhn, P., Peterson, J. P. and Levin, L. R. (1952) 'A summary of diagonal tension Part I: methods of analysis'.
- Li, C. H. and Tsai, K. C. (2008) 'Experimental responses of four 2-story narrow steel plate shear walls', in *Proceedings of the 2008 Structures Congress*. Vancouver, Canada. doi: 10.1061/41016(314)101.
- Lubell, A. S. *et al.* (2000) 'Unstiffened Steel Plate Shear Wall Performance under Cyclic Loading', *Journal of Structural Engineering*, 126(4), pp. 453–460. doi: 10.1061/(ASCE)0733-9445(2000)126:4(453).
- Montgomery, C. J. *et al.* (2001) 'Unstiffened Steel Plate Shear Wall Performance under Cyclic Loading', *Journal of Structural Engineering*, 127(8), pp. 973–975. doi: 10.1061/(ASCE)0733-9445(2001)127:8(973).
- Sabelli, R. and Bruneau, M. (2006) 'Steel Plate Shear Walls (Steel Design Guide 20)', *American Institute of Steel Construction, Inc.*
- Thorburn, L. J., Montgomery, C. J. and Kulak, G. L. (1983) *Analysis of steel plate shear walls*. Edmonton, Canada.
- Timler, P. A. and Kulak, G. L. (1983) *Experimental Study of Steel Plate Shear Walls.*, *Structural Engineering Report*. doi: 10.7939/R3C24QV49.
- Wagner, H. (1931) *Flat sheet metal girder with very thin metal web: Part 1: General theories and assumptions*. National Advisory Committee for Aeronautics.
- Wang, M. *et al.* (2015) 'Experimental and numerical study of unstiffened steel plate shear wall structures', *Journal of Constructional Steel Research*, 112, pp. 373–386. doi: 10.1016/j.jcsr.2015.05.002.

Numerical Analysis of the Impact of Polypropylene Fiber on the Shear Strength of Hollow-Core Slabs

Moqdad Hemid ¹[0000-0003-4312-1526], Mustafa Ozakca ²[0000-0003-1544-8126], Esra E. Karatas ³[0000-0003-1396-2463] and Akrem S. Mahmoud ⁴[0000-0002-1956-0281]

¹moqdadhamdi7474@gmail.com, Department of Civil engineering, Engineering College, Gaziantab University

²ozakca@gantep.edu.tr, Department of Civil engineering, Engineering College, Gaziantab University

³ekaratas@gantep.edu.tr, Department of Civil engineering, Engineering College, Gaziantab University

⁴dr.akramsh1@uoanbr.edu.iq, Department of Civil engineering, Engineering College, Al -Aanbar University.

Abstract

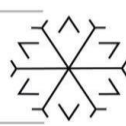
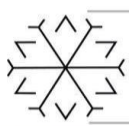
Many countries used the precast prestress hollow slabs due to their easy installation and reduced construction time and high-quality control. In recent years raised concerns that ACI318 code provisions may overestimate the web-shear capacity of thick precast prestressed hollow slab (PHCS) members exceeding 315 mm in member depth (h) as a result, the ACI318-08 code requires that minimum shear reinforcement be. Shear reinforcements are utilized to improve shear resistance and shift reinforced concrete's failure mode to a more ductile failure mode. Hollow-core slab (HCS) failure, caused by concrete brittleness, is one of the most hazardous failures in structure construction. Many Experimental and analytical research investigations have shown that the addition of fibers in the appropriate amounts improves the shear behavior of Reinforced Concrete (RC) elements, allowing them to completely or partially replace conventional web reinforcement. The objective of the current research is to study the effect of Polypropylene on the shear strength in the prestressed precast hollow slabs. Simulation model of HCS (42 cm high, 120 cm wide, and 600 cm long) were tested under shear loading. Two tests were performed on each model varying the shear-span-to-effective depth ratio ($a/d = 2.8$ according to EN1168 and $a/d = 3.5$). The test program was carried out to investigate the effect of Polypropylene fiber mix with concrete by varying content such as 0%, 0.5%, 0.8%, 1.15%, and 1.5% to find the optimum Polypropylene fiber content. All the groups were tested by using the ANSYS program as a tool for finite element investigation. The results showed improvement of up to 35% in the load capacity with 1.15% of fibres, moreover, the deflection decreased by 20% at the same load level.

Keywords. ANSYS, Hollow Slabs, Numerical Analysis, Polypropylene Fibers, Shear Strength.

1. Introduction

Hollow-Core Slabs (HCS) are precast components that are used mostly in residential, parking, and industrial buildings due to their excellent quality control, easy installation, and short construction time. It is a high-strength concrete product with pre-stressing strands of 9 mm and 16 mm diameters. These slabs are commonly manufactured by extrusion or slip-formworks using concrete with very low workability. The precast prestressed hollow slabs (PPHS) holes structure reduce the weight and improve several properties such as insulation, fire resistance, and voice. The PPHS are often produced with a width of 900 to 1250 mm and thickness of 100 mm to 400 mm (Haach et al, 2020). The maximum span length can be used up to 18 m (Mhalhal, 2017). Recently, much researchs improved the HCS by adding fibers to the concrete structures to overcome the concrete brittleness and tensile strength. The fibers' benefit is to enhance the resistance and rigidity behavior by improving their ability to transfer stresses across cracks of concrete. Fibers reinforcement involves glass, carbon, aramid, steel, etc. produced in the form of tendons, strands, bars, and grids, with a wide variety of characteristics and shapes (Li, et al, 2020).

The shear strength is required for the composite action; also, the vertical and horizontal shear strength of the joint has to be high enough to specify the forces based on load sharing of concentrated loads and horizontal diaphragm action (Meng, 2016). It is produced by the shear forces transfer mechanism and



occurs D-region discontinuity. These shear stresses are developed from unbalanced moments and gravity loads with movement during events; such as earthquakes and high winds. Through the years, thick units in between 200 and 265 mm, characterized by cross-sections based on circular voids, were replaced by deeper units (320, 370, 400 and 500 mm), and with non-circular voids cross-sections. Standardized cross-section shapes, mostly depending on the hollow core slab (HCS) thickness itself, were optimized increasingly. There are many deep HCS suffering shear cracks in most of the areas being exposed to heavy loads. Shear failure is caused by a diagonal crack at the web of HCS that appeared in the first quarter of the HCS span between the concentrated load and support. To avoid this critical failure, it had to be a suitable alternative to enhancement shear strength. Many experimental and numerical research studies proved effective in the addition of fibers in correct proportions finding alternatives of the conventional web reinforcement to improve mechanical behavior particularly the web shear strength. Fiber Reinforced Concrete (FRC) was shown to significantly improve the shear strength of Reinforced Concrete (RC) structures and prestressed elements (Vandewalle DD, L, Ortiz Navas F 2018). Fibers may typically replace the traditional web reinforcement required in these elements for both minimum shear reinforcement and equilibrium (Taerwe L2010, Bouverie, Thomas J206). [Paine et al 1998,1999] investigated the impact of steel fibers on the shear behavior of nine Hollow Cor Slabs (HCS) with a depth of 200 mm. The parameters were investigated: prestressing configuration, steel fiber type, fiber volume (0.5% and 1%), and shear span-to-effective depth ratio ($a/d = 2.0$ and 2.8). Authors found that steel fibers improved the element's shear capacity (between 4% and 31%) as well as its post-peak ductility when compared to a sample with conventional reinforcement (Cuenca et al 2013) achieved similar findings after testing in shear twenty-six hollow-core slabs (260 mm deep). The effects of the number of steel fibers (0, 50, and 70 kg/m³) and the a/d ratio (2.3–2.44 and 8.6) were studied. (Simasathien and Chao 2015) investigated the influence of steel fibers (0.50 percent and 0.75 percent volume fraction) on deeper slabs using eight HCS (458 mm depth with a/d ranging from 2.0 to 5.1). The results were that the addition of steel fibers increased shear strength significantly even in deep HCS. (Dudnik et al. in 2017) studied the behavior of ten HCS reinforced with different amounts of steel fibers (0.38 %, 0.50%, and 0.76%), finding similar results to previous tests but also highlighting that steel fibers volume fractions greater than 0.5 percent may cause concrete compaction problems in HCS, potentially affecting slab shear strength.

2. Background of Study

Shear reinforcements are used to increase shear resistance and alter the failure mode of reinforced concrete to a more ductile failure mode. One of the most dangerous failures in building construction is HCS failure, which is caused by concrete brittleness (Khayoun et al, 2020). Many methods have been presented to enhance the shear strength of flat HCS against shear failure (Brunesi et al,2015). (Mansour et al in 2015). Despite the fact that these studies are a significant step forward in understanding the shear behavior of Steel Fiber Reinforced Concrete (SFRC) members, many of them are characterized by tests on hollow slabs of special geometry with a limited range of critical parameters and conditions being investigated (concrete class, fibre geometry, content and composition, size, longitudinal and transverse reinforcing ratio). In addition, SFRC was used in the most of the studies. But, few investigations have been conducted on the shear behavior of components formed of synthetic fiber reinforced concrete. Among them were seventeen full-scale beams without stirrups tested with straight macro-synthetic fibers with considerable material properties (tensile strength (f_y) of 620 MPa and elastic modulus (E) of 9500 MPa) (Altoubat et al. 2009). When compared to reference samples, the increase in shear strength with a varying volume fraction of fibers ranging from 0.5% to 1.0 % was found to be in the 14–30% range (Antonio Comforti et al.2015). Fourteen Wide-Shallow Beams (WSBs) with two different width-to-effective depth ratios (b/d) ($b/d = 2$ and $b/d = 3$), fiber content, and also the minimum amount of classical shear reinforcement were tested. They found the resistance in shear of about 30– 40% (Antonio Comfortis et al.2017). Six full-scale prestressed double tees 6000 mm long, 500 mm high, and 2490 mm wide were manufactured and tested using a three-point loading method with a shear span-to-depth ratio (a/d) of 3.1. They found when the volume fraction (V_f) equal to 1.1 enhances the shear bearing capacity about 15%.

Concerning the usage of macro-synthetic fibers in HCS, which are particularly effective in shear during the previous decade only a very limited study is available in the literature (Antonio Comfortis et al.2019). Two 356 mm deep, HCS were used to assess the feasibility of employing copolymer/polypropylene fibers with volume fractions of 0.67 percent and 1% (Keith D.Palmer et al.in2011). Specimens were tested with $a/d = 3$ at their end zone. The authors emphasized that polypropylene fibers might improve the shear strength of HCS, even if the increase in shear strength was not quantified. (Antonio Comforti et al., 2020) they tested five full scales (1 RC and 4 PFRC) depth deep (420 mm) on each slab was conducted two testes depending on the shear-span-to-effective depth ratio ($a/d = 2.8$ according to EN1168 and $a/d = 3.5$) with the volume



fraction of polypropylene fibers 1.15 %. In addition, the authors observed an increase in post-cracking resistance led to increasing the shear strength by about 25%.

Furthermore, major efforts have been made in the last ten years to produce new forms of polypropylene (PP) fibers capable of adding significant toughness to concrete. As a result, polypropylene fibers have been extensively accessible on the market.

3. Equations for Web-Shear Computations

The Euro code (EC2), and American Concrete Institute (ACI) proposed that these members without transverse reinforcement, will be not feasible and fail in case of web-shear cracking at loads less than those designed by conventional methods (Elhashimy et al, 2020). As a result, ACI 318-08 now requires minimum shear reinforcement to be supplied in HCS units with depths greater than 12.5 in. (320 mm) if the factored shear force exceeds 50% of the design shear strength of the unit or the web-shear capacity must be reduced by half.

Web shear fractures form in high shear zones where the primary tensile stress in the web exceeds the concrete's tensile strength. These inclined cracks begin in the web of the PPHC slabs at the neutral axis, where the thickness of the web is thin, and then spread in diagonal directions when the load is raised. In this high shear zone, the web has a mixed state of stress that includes compressive stress caused by prestressing force and shear stress. Vertical tension can be ignored. Web shear cracking occurs when the primary tensile stress in a tiny element in this region exceeds the concrete's tensile strength (f_t). Tensile tension may be expressed using Mohr's circle as

$$f_t = \sqrt{v^2 + \left(\frac{f_{pc}}{2}\right)^2} - \left(\frac{f_{pc}}{2}\right) \quad (1)$$

Where:*

f_{pc} = the effective prestress at the centroid of the slab.

f_t = is the tensile strength of concrete

v = is the shear strength

The web shear cracking stress can be written from Eq.(1) as

$$v_{cw} = f_t \sqrt{1 + \frac{f_{pc}}{f_t}} \quad (2)$$

The web shear capacity (V_{cw}) of a hollow-core slab with prestressing steel is then given as

$$V_{cw} = \left(f_t \sqrt{1 + \frac{f_{pc}}{f_t}}\right) bwdp \quad (3)$$

Where

bw is net web-width of the slab.

dp is the effective depth of the slab.

Using a conservative value of v and simplifying the term under square root which gives close result, the web shear capacity for hollow-core slab with horizontal prestressing steel ($V_p = 0$) can be written as

$$V_{cw} = (0.3\sqrt{f'_c} + 0.3f_{pc}) bwdp \quad (4)$$

4. Description of Test Specimen

This section presents the collected simulation results using ANSYS software. In this study, the experimental work using a model of precast hollow core-slab based polypropylene fibers was carried out to study the behavior and characteristics using ANSYS software. The support mimics of the actual hollow slab were subjected to a three-point loading test orthogonally using different types of stressed bars in each direction with prestressed 1200 MPa under shear load were performed. Two tests were performed on each slab, each with a different shear-span-to-effective-depth ratio ($a/d = 2.8$ according to EN1168 and $a/d = 3.5$). Specimen

dimensions were (42 cm high, 120 cm wide and 600 cm long). Reinforcements were placed orthogonally at the tension face and compression face as a reinforcement layer with a clear upper cover of 43 mm and lower cover of 38 mm. The model has been drawn using the ANSYS software program as shown in Figure 1, Figure 2 and Figure 3.

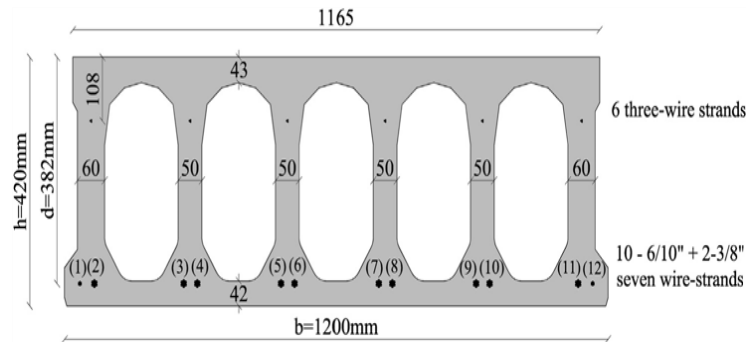


Figure 1: Actual Casting Mold (Conforti et al, 2020)

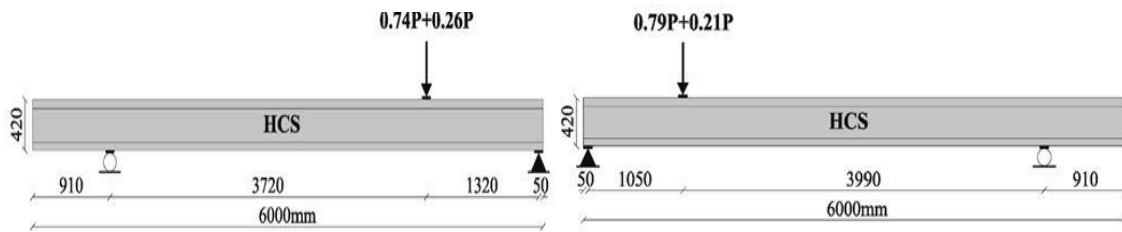


Figure 2: Side View of the Hollow Core Model (Conforti et al, 2020)

5. Finite Element Modeling and Material Properties:

The materials or hollow construction materials are the major requirements in the modern age of technology. There are many types of building materials used for different construction works. In this work the HCS was tested under shear load at the end zone; the model was generated with the three-dimensional finite hollow element. HCS was modeled using Solid65 brick elements with 33909 elements for concrete while the prestressing strands were modeled using LINK180. Solid185 elements of the steel plate have linear elastic properties. Figure 3 illustrates the generated finite element model for the HCS. Table 1 shows material properties and additional material parameters.

Table 1: Material Properties

Concrete C 45.1
Modulus of elasticity $E_c = 31607 \text{ MPa}^*$ Modulus of elasticity $E_c = 31607 \text{ MPa}^*$ Poisson's Ratio $\nu = 0.2$ Uniaxial Cracking Stress = 4.5 MPa Open Shear Transfer Coef. $\beta_t = 0.4$ Close Shear Transfer Coef. $\beta_{cc} = 0.8$
Concrete C40.6
Modulus of elasticity $E_c = 29725 \text{ MPa}^*$ Poisson's Ratio $\nu = 0.2$ Uniaxial Cracking Stress = 4MPa Open Shear Transfer Coef. $\beta_t = 0.4$ Close Shear Transfer Coef. $\beta_c = 0.8$
Steel reinforcement



Modulus of elasticity $ES = 200000$ MPa Poisson's Ratio $\nu = 0.3$ Yield Stress with diameters of 16 mm $f_y = 1819$ MPa Yield Stress with diameters of 9mm $f_y = 1734$ MPa Yield Stress with diameters of 3mm $f_y = 1854$ MPa Loud Plates Modulus of elasticity $ES = 2E10$ MPa Poisson's Ratio $\nu = 0.3$ Yield Stress $f_y = 400$ MPa
Loading Plates
Modulus of elasticity $ES = 2E10$ MPa Poisson's Ratio $\nu = 0.3$ Yield Stress $f_y = 400$ MPa
Polypropylene fibers
Modulus of elasticity $ES = 3.5$ Gpa Poisson's Ratio $\nu = 0.3$ Yield Stress $f_y = 400$ MPa

Table 1 (continued): Material Properties

6. Loading and Boundary Conditions:

Two steel plates with dimensions of 50 mm width, 1200 mm length and 50 mm thickness were used for supports and load placement at the top and bottom. The size of the plate mesh was set to correspond with the concrete mesh element to minimize stress concentration and ensure the most uniform distribution of stresses. SOLID185 components were used to simulate steel plates with three degrees of freedom for each node (the displacements in X, Y, and Z directions) as shown in Figure 3. The applied loads were modeled as a line load distributed on top nodes (13 nodes per plate) along the centerline of the plates.

The centerline of the steel plate of supports was constrained as a simple support to enable rotation of the support under the concrete nodes to apply the true boundary requirements. In order to ensure that the structural simulation model is built in the right conditions and will be solved in a good representation of reality, the validation technique is used by comparing the results based on a specific selected model. The researcher uses the results of laboratory experiments that is developed by (Conforti et al, in 2020) as a validation model and the experimental results have been performed by applying the multi loads on the center of the hollow slab in order to measure the deflection in the slab. The numerical results of HCS are compared with (Conforti et al, 2020).

a- $a/d = 3.5$						
NO	Specimen. PPHS	Pmax .Exp (KN)	$\delta(\max)$.Exp(mm)	Pmax. FEM(KN)	$\delta(\max)$.FEM(mm)	Error in PMax
1	($V_f = 0$)	346.64	4.31	356	5.23	3%
2	($V_f = 1.15\%$)	465.8	5.18	471.2	5.34	1%
b- $a/d = 2.8$						
1	($V_f = 0$)	316	3.4	322	3.37	2%
2	($V_f = 1.15\%$)	381.6	4.68	396	4.67	2%

Table 2: Verification of Numerical Results at Fibers Contain ($V_f = 0, V_f = 1.15\%$)

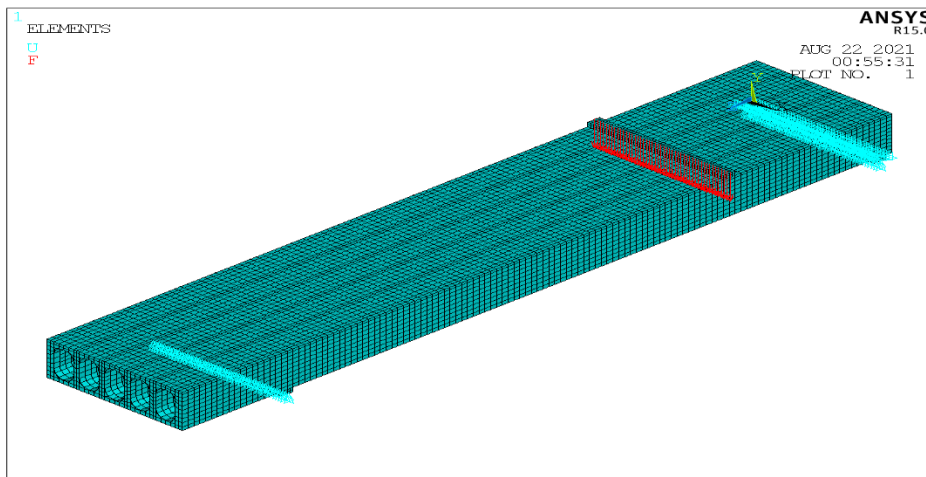


Figure 3: Geometry Mesh Process and Applied Loads.

7. Model Verification

The predicted ultimate shear strength under load from the numerical models accomplished by using ANSYS software is compared with the experimental results obtained from the experimental tests as shown in table 2. The numerical models' values for specimens are very well approved by the lab test results.

The typical load versus deflection behavior of Fiber Reinforcement Concrete (FRC) hollow slab is presented in this section. The vertical deflection is measured at the lower face of HCS. The results of the finite element model and the experimental were in good agreement as shown in the load-deflection curve figures 4 and 5. A comparison between experimental work and the numerical finite element analysis is presented in Figure 4 and Figure 5, it can be seen that all load-deflection curves have similar behavior. In comparison with the experimental results, the numerical models approximately display small deflection at the ultimate stage. Both Figures 4 and 5 show that the load-deflection curves from the numerical investigation models agree well with lab test data from experimental for the hollow slab model with varying shear-span-to-effective depth ratio ($a/d = 2.8$ and $a/d = 3.5$).

Contour plots are shown in Fig. (6). It shows the deformed model's minimum and maximum deflection values. The area colored in red shows the greatest value in concavity. On the other hand, the area colored in blue represent the highest value in the convexity. Between the two preceding zones, there is a gradient of zones shaded in different colors that depict the deformation that occurs throughout loading stages or ultimate loading for the HCS model. For the deformation model in the HCS, there is a clear difference between the specimens. The specimens with fibers reinforcement concrete have greater deformation than the normal reinforcement concrete hollow slab; this is seen from the high rate of load compared to the deflection ($\Delta P/\Delta \delta$).

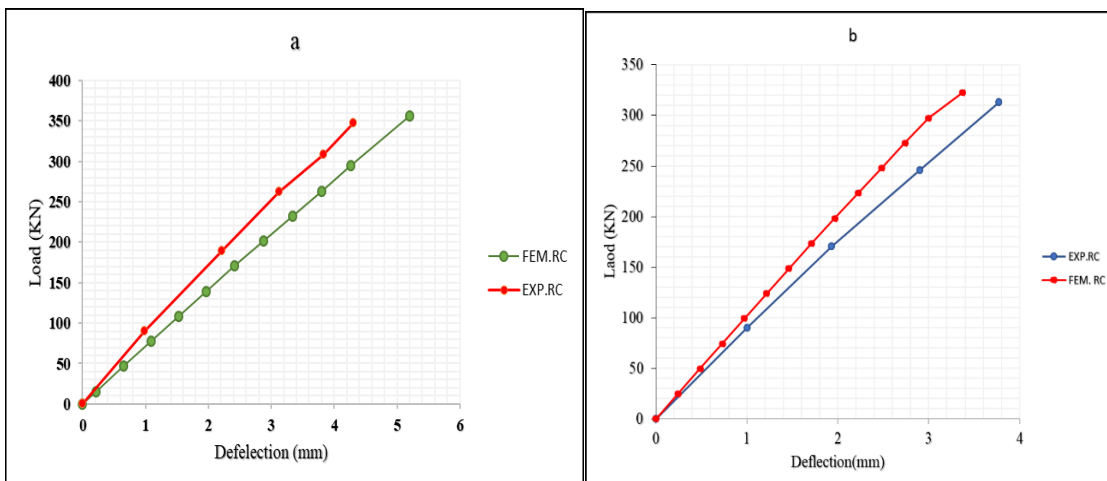


Figure 4^a. Load deflection of Experimental and Numerical Results for ($V_f=0$) at $a/d=3.5$



Figure 4^b. Load deflection of Experimental and Numerical Results for ($V_f=0$) at $a/d=2.8$

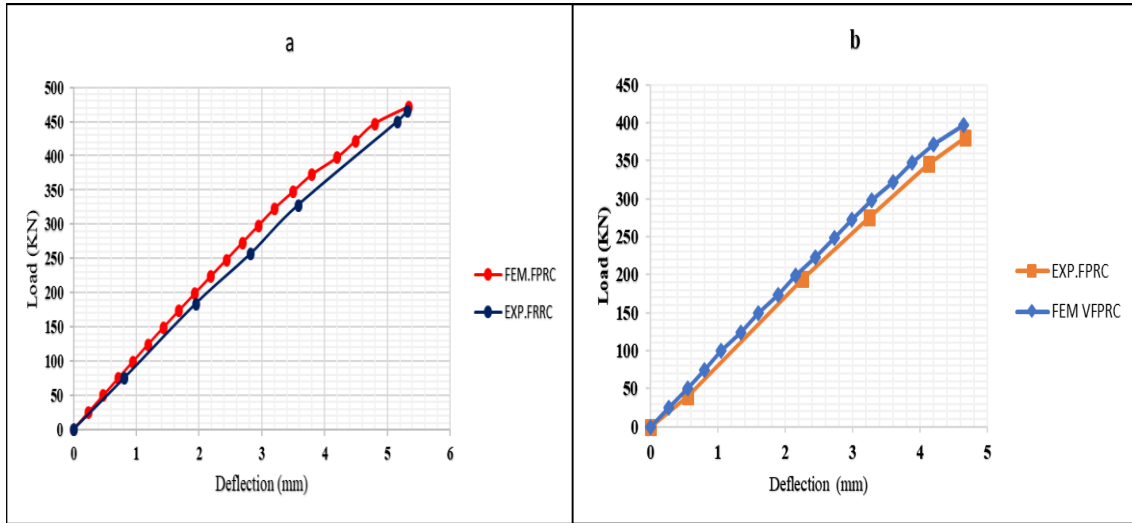


Figure 4^a. Load deflection of Experimental and Numerical Results for ($V_f=1.15$) at $a/d=3.5$

Figure 4^b. Load deflection of Experimental and Numerical Results for ($V_f=1.15$) at $a/d=2.8$

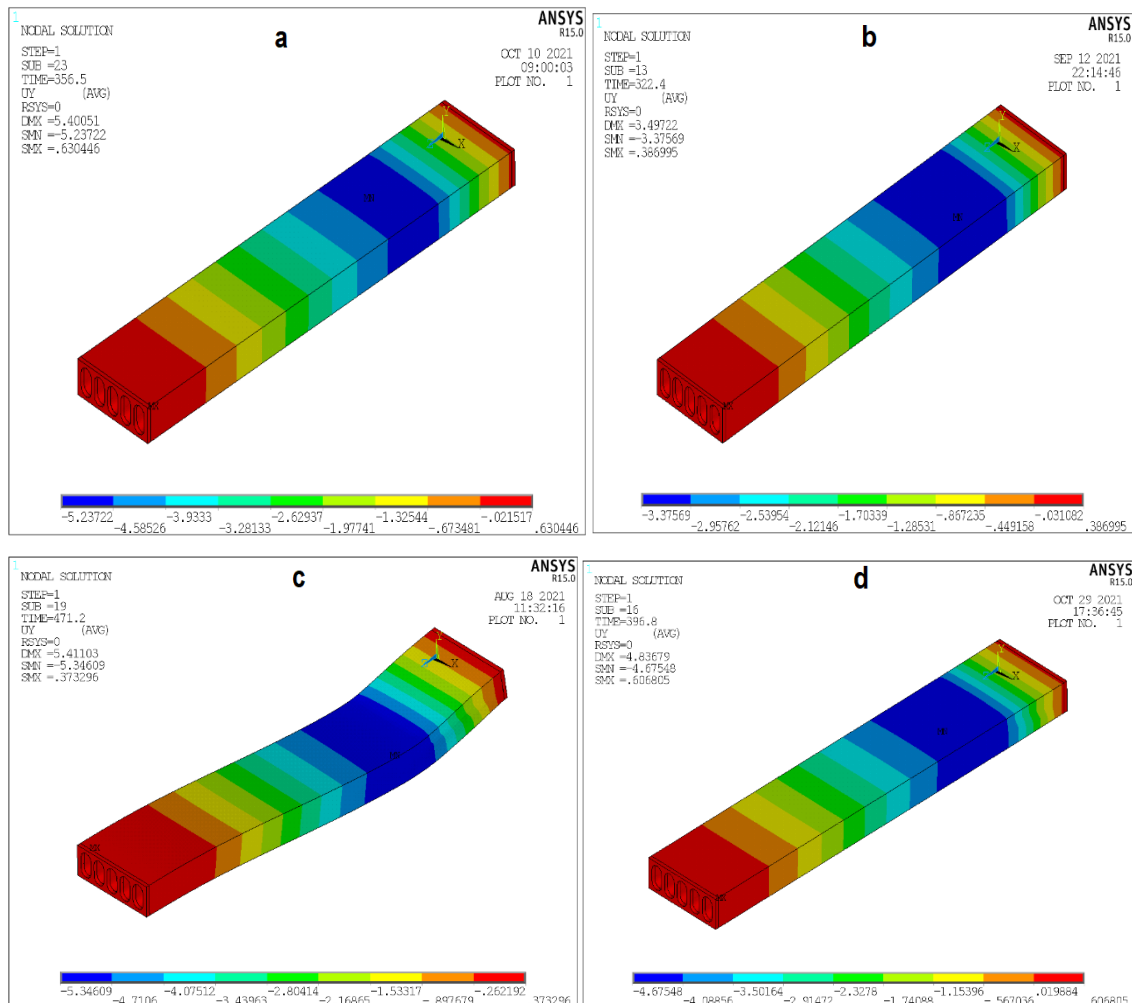
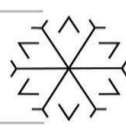
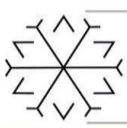


Figure 6^a: Contour Plots for Verification Results of HCS tests at ($a/d=3.5, V_f=0$)

Figure 6^b: Contour plots for verification results of HCS tests at ($a/d=2.8, V_f=0$)

Figure 6^c: Contour plots for verification results of HCS tests at ($a/d=3.5, V_f=1.15\%$)

**Figure 6^d:** Contour plots for verification results of HCS tests at ($a/d=2.8, V_f=1.15\%$)

8. Proposal Fiber Volume Fraction (V_f)

Three different fibers' volume fractions 0.5%, 0.8% and 1.5% have been employed to investigate the effect of fiber volume fractions on the behavior of fiber-reinforced concrete HCS. It is noteworthy that the geometrical properties of developed FE models are similar to those used in the experimental study (Antonio Comfortis et al. in 2020). Table 3 provides the deflection at the maximum load of the studied HCS. It is obvious from Figure 6 and Table 3 that there is a clear correlation between the volume fraction of the fibers and the maximum load capacity of these HCS. As expected, the maximum load capacity of each HCS tends to increase with using a higher volume fraction. The increase can be attributed to two reasons; first reason is the fiber reinforcement concrete improves the shear strength of hollow-core slab end zones primarily by enhancing the connection between tendons and concrete, leading to less tendon slippage. This improves the effectiveness of prestressing activities on shear strength even at higher loads, allowing fiber reinforcement concrete samples to achieve higher shear strength than reinforcement concrete hollow-core slabs (Antonio Comfortis et al. in 2020). The second reason can be attributed to the bridging action of the fibers across the cracks that restrained the propagation of microcracks at the inception only. The stress is transferred to the bridging fibers after the tensile crack, which contains the crack propagation for some time and thus tensile strength is enhanced could be concluded that using short fiber materials as internal reinforcement led to enhancing the ultimate shear strength of structural concrete members with high rigidity behavior (Jiang et al. in 2014).

Table 3: Numerical Results of Different Proposal V_f

a/d=3.5			
NO	V_f of PPHS model	P_{max} (KN)	δ (max).(mm)
1	$V_f=0.5\%$	421	3.85
2	$V_f=0.08\%$	446	4.16
3	$V_f=1.15\%$	471	5.34
4	$V_f=1.5\%$	493	6.20
a/d=2.8			
1	$V_f=0.5\%$	347.2	3.2
2	$V_f=0.08\%$	372	4.15
3	$V_f=1.15\%$	396.8	4.7
4	$V_f=1.5\%$	396.8	5.01

The ultimate shear strength is listed with its corresponding displacement in Table 3 for two cases, it shows that adding fibers significantly enhances the resistance of the hollow slab. In case ($a/d=3.5$) the addition



of 0.5%, 0.8% , 1.15% and 1.5%, of polypropylene fibers to the concrete, improved the ultimate shear strength by about 21%, 25%, 36% , and 42% respectively compared to the plain concrete. But In case ($a/d=2.8$) the addition of 0.5%,0.8% , 1.15% and 1.5%, of polypropylene fibers to the concrete, improved the ultimate shear strength by about 10%, 17%, 25% , and 25 % respectively compared to the plain concrete. Based on these findings an increase in concrete tensile strength is best when the fiber V_f is between 1.15 and 1.5 percent.

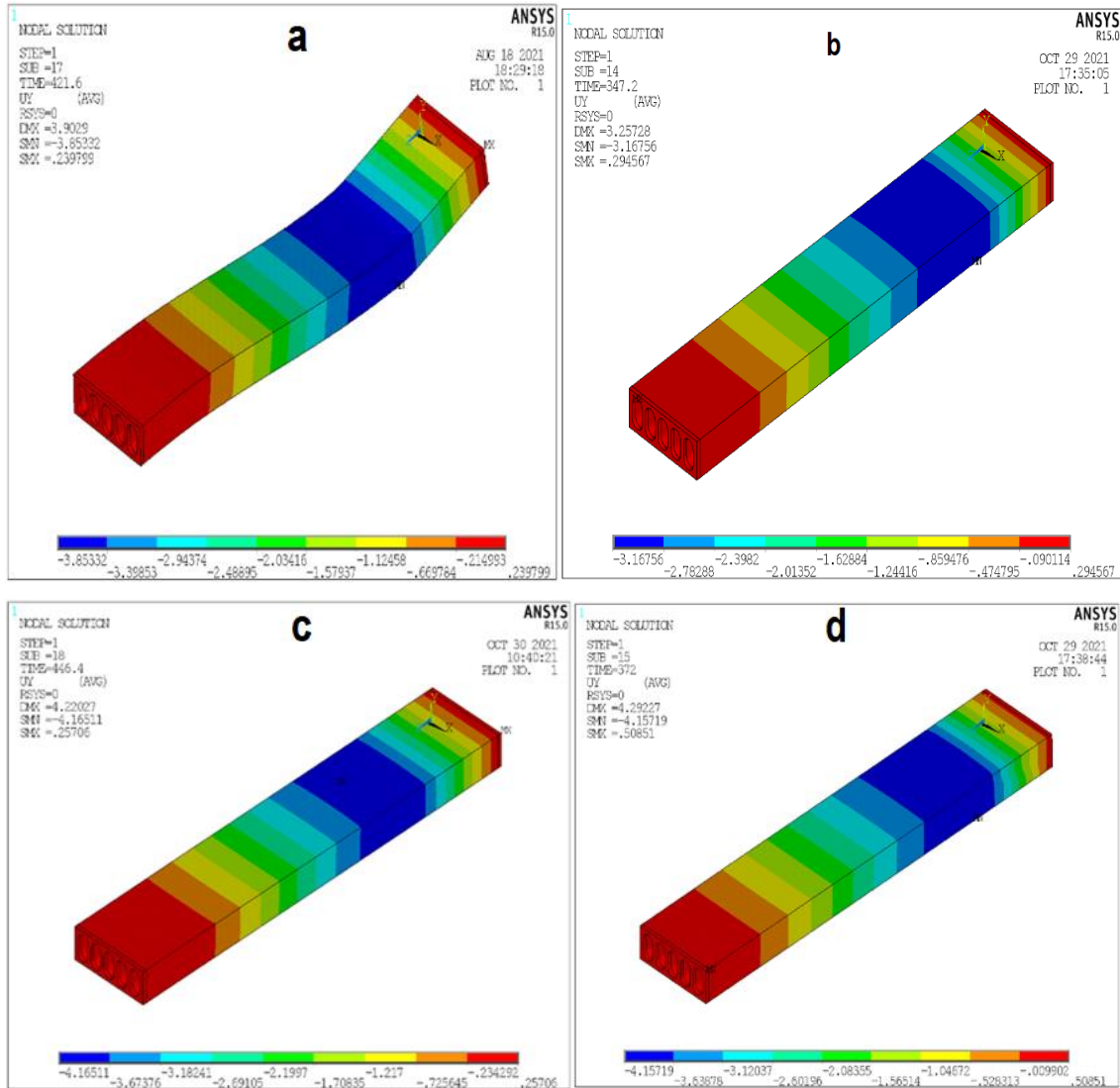


Figure 7^a: Contour plots of HCS tests at ($a/d=3.5$ $V_f=0.5\%$)

Figure 7^b: Contour plots of HCS tests at ($a/d=2.8$ $V_f=0.5\%$)

Figure 7^c: Contour plots of HCS tests at ($a/d=3.5$ $V_f=0.8\%$)

Figure 7^d: Contour plots of HCS tests at ($a/d=2.8$ $V_f=0.8\%$)

Fig. 7 shows Contour plots for the deflection at ultimate load capacity, it can be seen a clear difference between the specimens that have different V_f . Deformation increases when the amount of the polypropylene fiber reinforcement increases due to improvement in concrete stiffness of the hollow slab model, this is clearly seen from the high rate of load compared to the deflection ($\Delta P/\Delta \delta$).

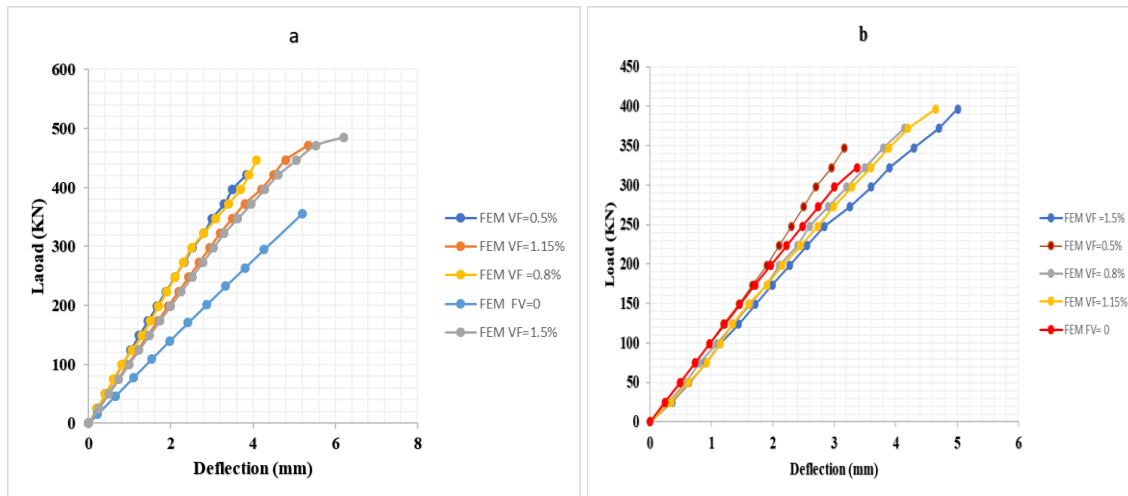
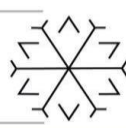
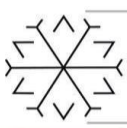


Figure 8: Load-deflection Relationship of Numerical Results

It is evident from the study that fiber addition had a beneficial effect on the shear strength of fiber-reinforced concrete HCS when compared with plain concrete and is in harmony with the finding of other researchers. Furthermore, the rigidity behavior of the HCS specimens reinforced with higher fiber volume fraction was increased as indicated in Figure 7, 8, and Table 3. It could be concluded that using polypropylene fibers as internal reinforcement led to enhance the shear strength of structural concrete members with high rigidity behavior.

9. Conclusion

The following conclusions can be drawn from the results obtained by the finite element model of the hollow slab model

1. Inclusion of the fibers in the concrete matrix increased the shear strength gradually as the fiber content increased. Optimization reaches the best state when using a fiber content of 1.15% to 1.5% the highest shear resistance can be obtained
2. The addition of fibers leads to a decrease in deformations at all stages of loading due to the stiffness change of the material.
3. The relationship between the applied load and deflection of hollow-core slabs was linear during the early stages of loading up to the maximum load capacity.
4. Increasing the proportion of polypropylene added enhances the experimental conclusion reliability that adding fibers to concrete increases the efficiency of prestressing by increasing the bonding between the ropes and concrete.

References

- Brunesi, E., Bolognini, D. and Nascimbene, R. (2015) 'Evaluation of the shear capacity of precast-prestressed hollow core slabs: numerical and experimental comparisons', *Materials and Structures/Materiaux et Constructions*, 48(5), pp. 1503–1521.
- Bothma, J. (2013) 'ISI2013-15. Literature Review on Macro Synthetic Fibres in Concrete', University of Stellenbosch, Institute of Structural Engineering, p. 20.
- Brunesi, E., Bolognini, D. and Nascimbene, R. (2015) 'Evaluation of the shear capacity of precast-prestressed hollow core slabs: numerical and experimental comparisons', *Materials and Structures/Materiaux et Constructions*, 48(5), pp. 1503–1521.
- Chaitanya, J. D. et al. (2016) 'Experimental Studies on Glass Fiber Concrete, American Journal of Engineering Research (AJER)', *American Journal of Engineering Research*, 5(5), pp. 100–104.



- Chowdhury, M. A. and Hossain, S. (2020) 'A Review on Tensile and Flexural Properties of Fiber-Reinforced Polymer A Review on Tensile and Flexural Properties of Fiber-Reinforced Polymer Composites', Iosr-Jpte, (November).
- Ezz El-Arab, I. M. (2017) 'Web Shear Strengthening Technique of Deep Precast Prestressed Hollow Core Slabs under Truck Loads', Journal of Building Construction and Planning Research, 05(04), pp. 129–145.
- Conforti et al, in 2020. Enhancing the shear strength of hollow-core slabs by using polypropylene fibres.
- Elhashimy, A. M., Tawhed, W. F. and Agamy, M. H. (2020) 'Behavior of Hollow Core Slabs Reinforced with GFRP Prestressing Bars', International Journal of Engineering and Advanced Technology, 9(3), pp. 1796–1803..
- Haach, V. G. and Paiva, M. A. do C. (2020) 'Application of the rebound test for the technological control of concrete hollow-core slabs', Revista IBRACON de Estruturas e Materiais, 13(4).
- Vandewalle DD, L. Shear Capacity of Concrete Beams Containing Longitudinal Reinforcement and Steel Fibers. Spec Publ n.d.;216.
- Ortiz Navas F, Navarro-Gregori J, Leiva Herdocia G, Serna P, Cuenca E. An experimental study on the shear behaviour of reinforced concrete beams with macrosynthetic fibres. Constr Build Mater 2018;169:888–99.
- Taerwe L, Boverie N, Moerman W, De Pauw P. Replacement of shear reinforcement by steel fibres in pretensioned concrete beams. Tailor Made Concr Struct 2010:104.
- Thomas J, Ramaswamy A. Shear strength of prestressed concrete T-beams with steel fibre reinforced concrete for prestressed hollow-core slabs, University of Nottingham; 1998
- Cuenca E, Serna P. Failure modes and shear design of prestressed hollow core slabs made of fiber-reinforced concrete. Compos Part B Eng 2013;45:952–64.
- Dudnik VS, Milliman LR, Parra-Montesinos GJ. Shear behavior of prestressed steel-fiber-reinforced concrete. PCI J 2015;60:85–101.
- Palmer, KD & Schultz, AE 2010, 'Factors affecting web-shear capacity of deep hollow-core units', PCI Journal, vol. 55, no. 2, pp. 123-146.
- Vandewalle DD, L. Shear Capacity of Concrete Beams Containing Longitudinal Reinforcement and Steel Fibers. Spec Publ n.d.;216.
- Khayoun, Z. I., Kamal, H. M. and Ibrahim, Y. K. (2020) 'The Effect of Hybrid Fibers Reinforcement on the Mechanical and Physical Properties of Concrete', The Open Civil Engineering Journal, 14(1), pp. 207–216.
- Li, Z. et al. (2020) 'Steel Fibre Reinforced Concrete Meso-Scale Numerical Analysis', Advances in Civil Engineering, 2020(2017).
- Nguyen, H. T. N. and Tan, K. H. (2020) 'Effect of steel fibers on fire endurance of extruded hollow-core slabs', pp. 353–362.
- Conforti A, Minelli F, Plizzari GA. Shear behaviour of prestressed double tees in selfcompacting polypropylene fibre reinforced concrete. Eng Struct 2017;146:93–104.
- Meng, X. (2016) 'Shear Strengthening of Prestressed Hollow Core Slabs Using Externally Bonded Carbon Fiber Reinforced Polymer Sheets', Available at: internal
- Conforti A, Minelli F, Tinini A, Plizzari GA. Influence of polypropylene fibre reinforcement and width-to-effective depth ratio in wide-shallow beams. Eng Struct 2015;88:12–21.
- Mhalhal, J. M. (2017) 'Prestressed Precast Hollow-Core Slabs with Different Shear Span to Effective Depth Ratio', Wasit Journal of Engineering Sciences, 5(2), pp. 1–11
- Jiang, C., Fan, K., Wu, F., Chen, D. (2014). Experimental study on the mechanical properties and microstructure of chopped basalt fibre reinforced concrete. Materials & Design, 58, 187-193.
- Altoubat S, Yazdanbakhsh A, Rieder KA. Shear behavior of macro-synthetic fiber-reinforced concrete beams without stirrups. ACI Mater J 2009;106:38–389

Numerical Analysis on Spiral Heat Exchanger; Effects of Using Nanofluid and Ball Turbulators

Faraz Afshari ^{1*}[0000-0001-9192-5604], Burak Muratçobanoğlu ²[0000-0003-0671-2861]

¹E-mail: faraz.afshari@erzurum.edu.tr, Affiliation: Erzurum Technical University, Department of Mechanical Engineering, Erzurum, Turkey.

²E-mail: burakmuratcobanoglu1@gmail.com, Erciyes University, Department of Mechanical Engineering, Kayseri, Turkey

Abstract

In this study, a numerical study was carried out on a spiral exchanger using Computational Fluid Dynamics methods. For the designed heat exchanger, two different cold and hot fluids have been used and heat transfer between the fluids arose due to the temperature difference. The effects of nanofluid and ball type turbulator were examined separately and the related important results were compared. In calculations, the Al₂O₃ nanoparticle with particle size of 50nm were used in 2% Vol. for preparing water-based nanofluid. Pressure drop, heat transfer rate and PEC (performance evaluation criteria) and other values were achieved and obtained results have been discussed on diagrams. Temperature and velocity distribution have been presented on contours to show the flow structure and temperature values in different locations inside heat exchanger. In the present study, ANSYS/Fluent (version 19) program was used as a CFD software and the necessary domain, mesh and boundary conditions were applied in the software and detailed solutions and results were obtained. The use of the turbulator showed a higher performance than the nanofluid in terms of heat transfer. According to the numerical results, heat transfer was increased approximately 7.71% and 6.85% by using ball type turbulator and nanofluid respectively at 0.1 m/s fluid velocity. These heat transfer values were 14.05% and 5.93%, where the fluid velocity was 0.5 m/s. The pressure drop for both parameters was compared and it was shown that the use of a turbulator caused a greater increase in pressure drop.

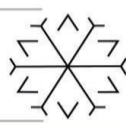
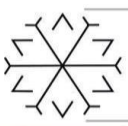
Keywords. Heat Exchanger, CFD, Numerical Analysis, Heat transfer, Nanofluid, Turbulator

1. Introduction

Heat exchangers can be considered as thermodynamic devices that provide two or several fluids at various temperatures to have heat transfer without any contact between the fluids. Developments in technology and industrial modifications have led researchers to examine different kinds of exchangers including shell and tube, double tube, spiral and plate type exchangers. Considering the advantages of nanofluids and the enhancement of the thermal performance of base liquids such as pure water in the exchangers, utilizing of nanofluids as heat transfer fluid has become common and has been widely researched.

Due to high thermal conductivity of solid materials compared to liquids, nanofluids can be employed as a solution for used base fluids with low thermal performance, which are achieved by mixing nano-sized particles in the fluid. Nano fluids have the mentioned advantages, but on the other hand, they also have some disadvantages when are used as heat transfer fluids. Increasing pressure drop, clogging in the channel, sedimentation and erosion inside the system are some of the main disadvantages of nanofluids. In this regard, new technological methods have been presented to decrease the effects of these problems by minimizing the nanoparticle size smaller than 100 nm (Selbaş et al. 2006, Pantzali et al. 2009 and Farajollahi et al. 2010).

Rajeshkumar et al. (2021) studied on heat transfer characteristics of finned tube heat exchanger using numerical method. For the solution of the model computational fluid dynamics method was used and thermal performance was evaluated. Vivekanandan et al. (2021) conducted a research to evaluate efficiency of spiral tube heat exchangers both experimental and CFD methods were utilized and heat transfer characteristics were discussed. In other study, CFD simulations were perform to experiment heat transfer characteristics with aqueous Al₂O₃ nanofluid as heat transfer fluid in a heat exchanger. Temperature distribution flow characteristics were discussed and obtained results were compared (Kim et al. 2018). Tiwari et al. (2014) studied on plate heat exchanger and used nanofluids as heat transfer fluid in the heat exchanger. Numerical methods were employed to analyze heat transfer performance and fluid flow structure



inside exchanger. CFD simulation and also experimental work were carried out for have a comparison of heat transfer characteristics in the plate type heat exchangers. In the mentioned study, TiO_2 /water nanofluid was used and results were compared (Khanlari et al. 2019). Khorshidi et al. (2016) designed a spiral type heat exchanger and heat transfer performance of the heat exchanger was discussed. Heat transfer rate as a main parameter in all heat exchanger have been considered and obtained results were compared when exchangers are operated in different working conditions.

2. CFD Simulation

2.1. Geometry

Initially a spiral exchanger was designed using Fluent-geometry section. In the next step, mesh generation was applied and the problem was solved numerically. To increase heat transfer rate and exchanger performance, ball type turbulators were settled in the path of both fluids inside. In Fig. 1, the geometry and boundary condition of the spiral type heat exchanger is shown. Both fluids inlet and outlet field, turbulators and walls are given in the figure.

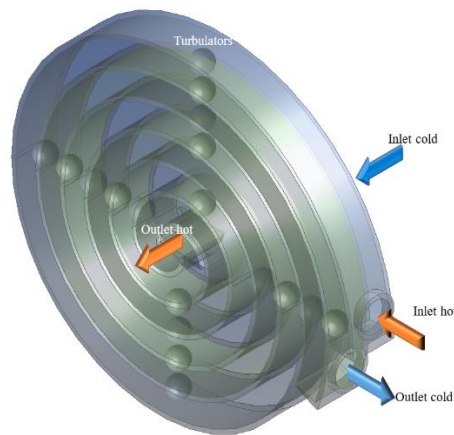
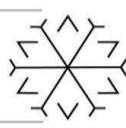


Figure 1: Geometry and boundary conditions of the used spiral heat exchangers

2.2. Boundary Condition

In this section boundary conditions have been defined and numerical analysis on the simulated domain was performed to evaluate thermal performance of the spiral heat exchanger in different operated conditions. Additionally, related data and information about dimensions of the exchanger, nanoparticles and the test conditions have been provided. The inlet hot and outlet cold fluid were both defined as 153.94 mm^2 . The inlet cold and the outlet hot sections area are 169.1 mm^2 . For the experiment with the turbulator, 9 ball type turbulators were installed in each channel. The diameter of balls turbulators was defined as 9 mm. Lengths of the hot and cold channels are 905.3 and 687.3 mm, respectively and their width is the same as 10 mm and a height of 20 mm. Aluminum material was used for exchanger block and ball turbulators. Two different heat transfer fluids were selected; pure water and water- Al_2O_3 nanofluid prepared with particle size of 50 nm at volume concentration ratio of 2%. The problem was solved in two different inlet velocities as 0.1 m/s and 0.5 m/s.

Equations



In this section, practical equations required to solve the problem have been presented. Heat transfer and thermophysical properties have been evaluated using related formula. Heat transfer rate at both cold and hot fluids can be calculated by Eqs. 1 and 2, where $\dot{Q}_h = \dot{Q}_c$ As follows,

$$\dot{Q}_h = \dot{m}_h C_{p,h}(T_{in,h} - T_{out,h}) \quad (1)$$

$$\dot{Q}_c = \dot{m}_c C_{p,c}(T_{out,c} - T_{in,c}) \quad (2)$$

Nanofluid properties including thermal conductivity, viscosity and density have been calculated using following equations considering particle diameter and average temperature. Thermal conductivity can be calculated by following equations (Vajjha et al. 2009),

$$k_{nf} = \frac{k_p + 2k_{bf} - 2(k_{bf} - k_p)\phi}{k_p + 2k_{bf} + (k_{bf} - k_p)\phi} k_{bf} + 5 \times 10^4 \beta \rho_{bf} C_{p,bf} \sqrt{\frac{\kappa T}{\rho_p d_p}} f(T, \phi) \quad (3)$$

$$f(T, \phi) = (2.8217 \times 10^{-2} \phi) \left(\frac{T}{T_0}\right) + (-3.0669 \times 10^{-2} \phi - 3.91123 \times 10^{-3}) \quad (4)$$

$$\beta = 8.4407(100\phi)^{-1.07304} \quad 1\% \leq \phi \leq 10\% \quad 298K \leq T \leq 363K \quad (5)$$

Viscosity of nanofluid has been proposed as follows (Khanafar et al. 2017),

$$\begin{aligned} \mu_{nf} = & -0.4491 + \frac{28.837}{T} + 0.574\phi - 0.1634\phi^2 + 23.053 \frac{\phi^2}{T^2} + 0.0132\phi^3 - 2354.735 \frac{\phi}{T^3} \\ & + 23.498 \frac{\phi^2}{d_p^2} - 3.0185 \frac{\phi^3}{d_p^2} \end{aligned} \quad (6)$$

$$1\% \leq \phi \leq 9\%, 20 \leq T \leq 70, 13 \text{ nm} \leq d_p \leq 130 \text{ nm}$$

Having the density of base fluid and particle, density of the nanofluid can be obtained,

$$\rho_{nf} = (1 - \phi)\rho_{bf} + \phi\rho_p \quad (7)$$

one of the main factors involved in calculating heat transfer of a nanofluid is specific heat capacity, which is quite different from that of the base fluid. For the synthesized nanofluid, C_p can be expressed as (Xuan et al. 2000),

$$C_{p,nf} = \frac{(1-\phi)\rho_{bf}C_{p,bf} + \phi\rho_p C_{p,p}}{(1-\phi)\rho_{bf} + \phi\rho_p} \quad (8)$$

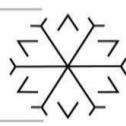
Performance Evaluation Criteria (PEC) can be expressed as follows,

$$PEC = \frac{Nu/Nu_0}{(f/f_0)^{1/3}} \quad (9)$$

Thermophysical properties of nanofluid water/ Al_2O_3 2% have been calculated for particles with 50 nm diameter.

3. Simulation Results

The heat transfer rates between the two fluids for two different inlet velocities obtained as a result of the analysis performed have been presented in Figure 2. It was aimed to show the effect of nanofluid and turbulator on thermal performance. As can be seen from the diagram, the turbulator effect was more than the nanofluid in terms of heat transfer rate. The nanofluid was compared with pure water and achieved



higher heat transfer rate from water at both inlet velocities. The enhancement made by the nanofluid on the heat transfer was obtained as 6.85% and 5.93% at 0.1 and 0.5 m/s, respectively. It is clearly seen in the diagram that the improvement made by the use of the turbulator is more than the nanofluid. In the analyses made under the same conditions, by adding a turbulator to the heat exchanger, an increase of 7.71% at 0.1 m/s and 14.05% at 0.5 m/s was obtained.

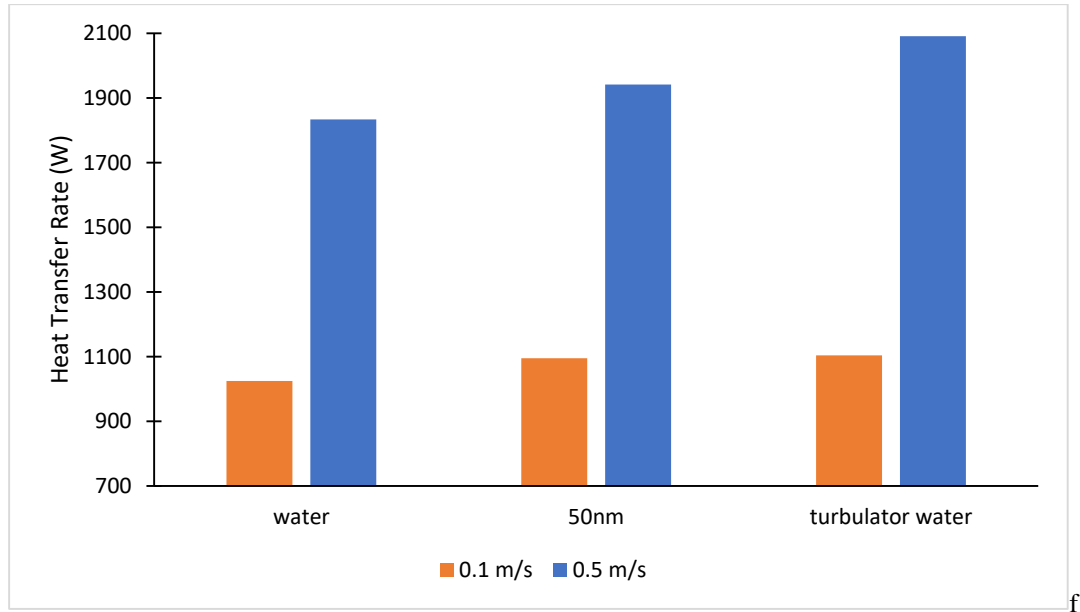


Figure 2: Heat transfer rate of pure water, using nanofluid and using ball turbulator with pure water

One of the important parameters in terms of heat transfer performance is the heat transfer coefficient. Comparison of nanofluid and turbulator with the results of analysis performed with water in without turbulator heat exchanger have been given in Figure 3. It was observed that the use of nanofluids and turbulators increased the heat transfer coefficient in both cases. In addition, as demonstrated in the figure, the nanofluid increased the thermal performance and heat transfer coefficient more at low velocities, while the turbulator exhibited higher performance at high fluid velocities. On the heat transfer coefficient, nanofluid revealed an improvement of 18.66% and 5.34% at 0.1 and 0.5 m/s velocities. By using turbulator heat transfer coefficient increased by 16.36% and 24.87%, respectively, under the same conditions.

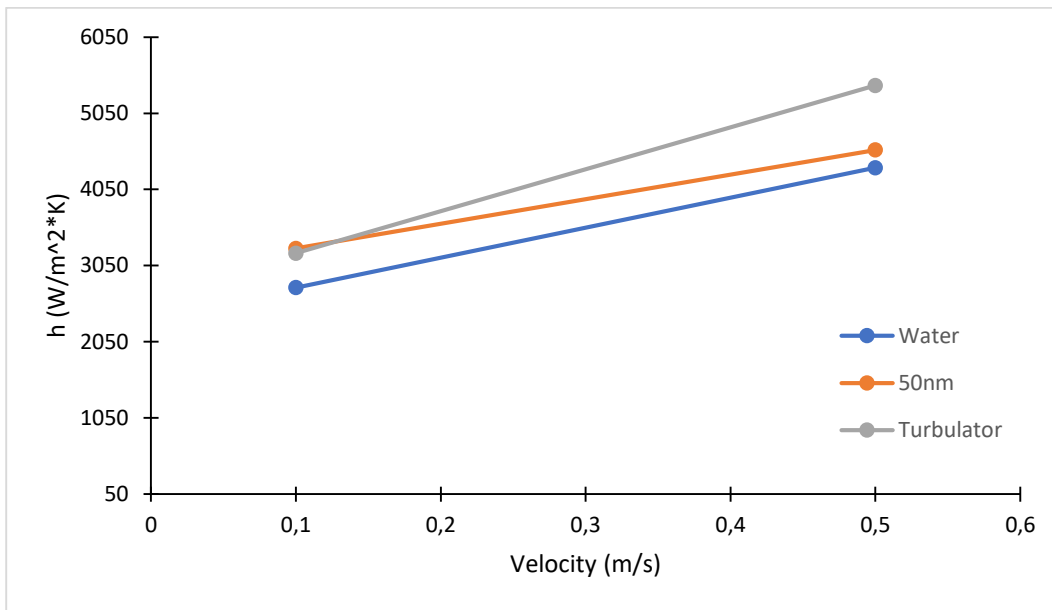
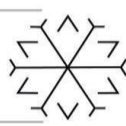
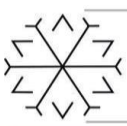


Figure 3: Variation of heat transfer coefficient with inlet velocity using pure water, nanofluid and ball turbulator with pure water

The Nusselt number, which is considered as the ratio of convective heat transfer to conduction heat transfer, is an important number for thermal analysis. In the Figure 4, the variation of the Nusselt number with the inlet velocity in all three cases (using pure water, nanofluid and ball turbulator) have been given. If the Nusselt numbers of water and nanofluid are compared, it can be discerned that the Nusselt number of water is higher than the nanofluid for both velocity values. The reason for this is that the high conductivity Al₂O₃ nanoparticles dispersed in the water increased considerably the conductivity coefficient of the water. However, since the same rate of increase did not occur in the heat transfer coefficient, Nusselt number values were lower than water. Since the thermal conductivity of water remains constant and the convection heat transfer coefficient increases in the use of the turbulator, it can be determined that the turbulator was quite effective on the Nusselt number in the comparison of the heat exchanger with and without turbulators.

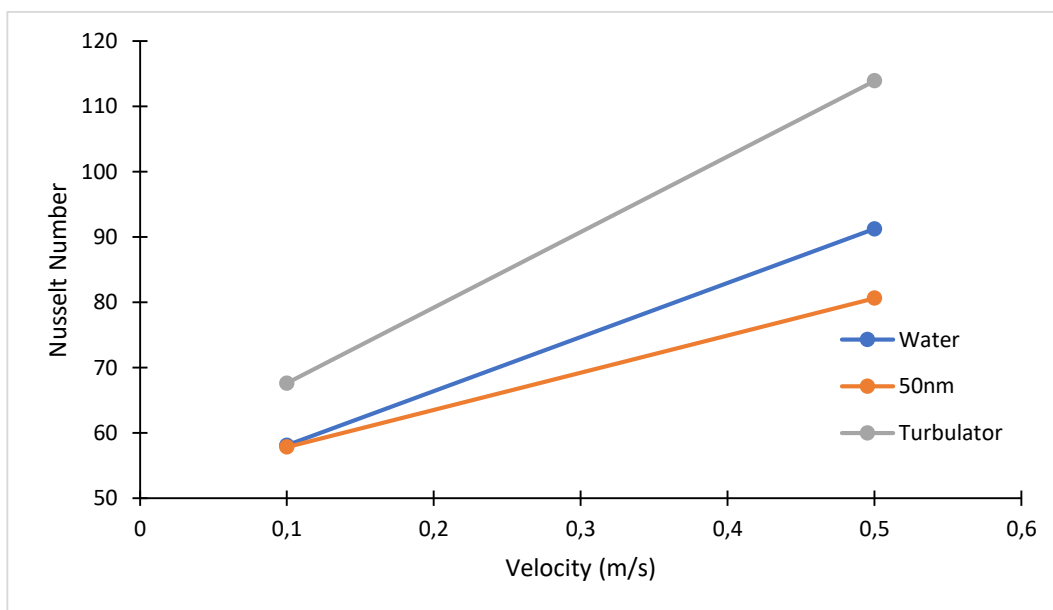
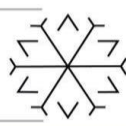
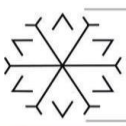


Figure 4: Variation of Nusselt number with inlet velocity using pure water, nanofluid and ball turbulator with pure water



Although nanoparticles positively affect the heat transfer and thermal properties of the base fluid in which they are dispersed, they rise the pressure drop due to the increase in viscosity. This influences the power required to procure the nanofluid flow under the same conditions with the base fluid. In the Figure 5, the pressure drop for water, nanofluid and heat exchanger with turbulators has been illustrated. The turbulator works as an obstacle in front of the flow, and therefore the pressure increased compared to the water. This increase was found to be as 57.74% and 39.71% at 0.1 and 0.5 m/s input velocities, respectively. Due to the reason mentioned above, a pressure increase was observed in the nanofluid which was lower than that of turbulator. The pressure drop increase for the nanofluid is 18.82% and 10.48% at 0.1 and 0.5 m/s inlet velocities, respectively.

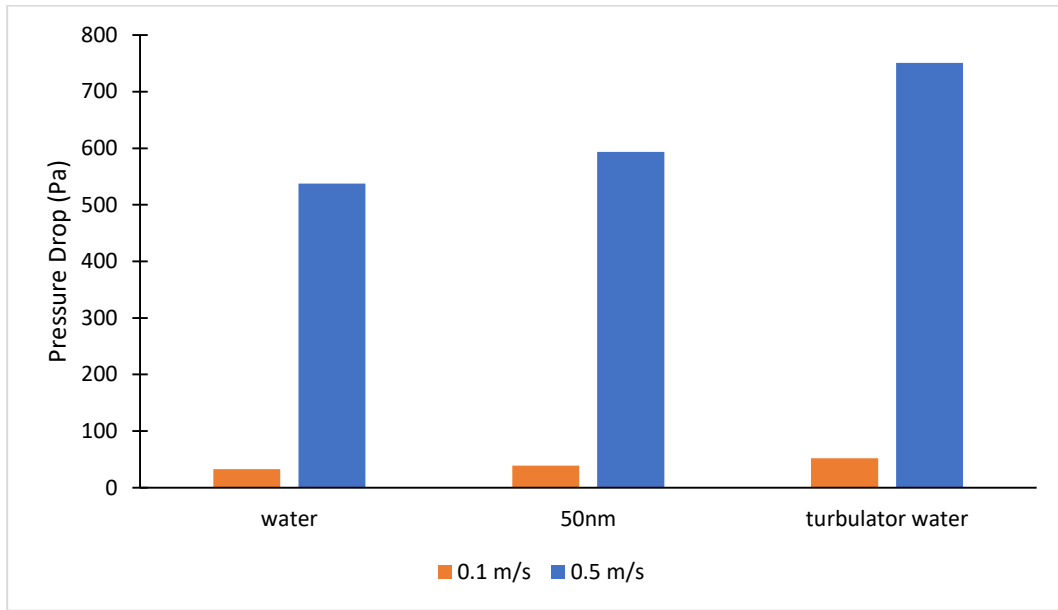


Figure 5: Pressure drop variation of pure water, using nanofluid and using ball turbulator with pure water

Performance evaluation criteria were calculated according to 0.1 and 0.5 m/s velocity values. These calculated values were evaluated for turbulator and nanofluid. As a reference, the Nusselt number and friction factor for water were calculated at velocity of 0.1 m/s and PEC values were obtained accordingly as presented in figure 6. Approximately the same PEC values were achieved in nanofluid and turbulator for 0.1 m/s inlet velocity. However, since the effect of the turbulator is more pronounced as the velocity increases, the PEC value of the turbulator at 0.5 m/s velocity was 7.45% higher than the PEC value of the nanofluid.

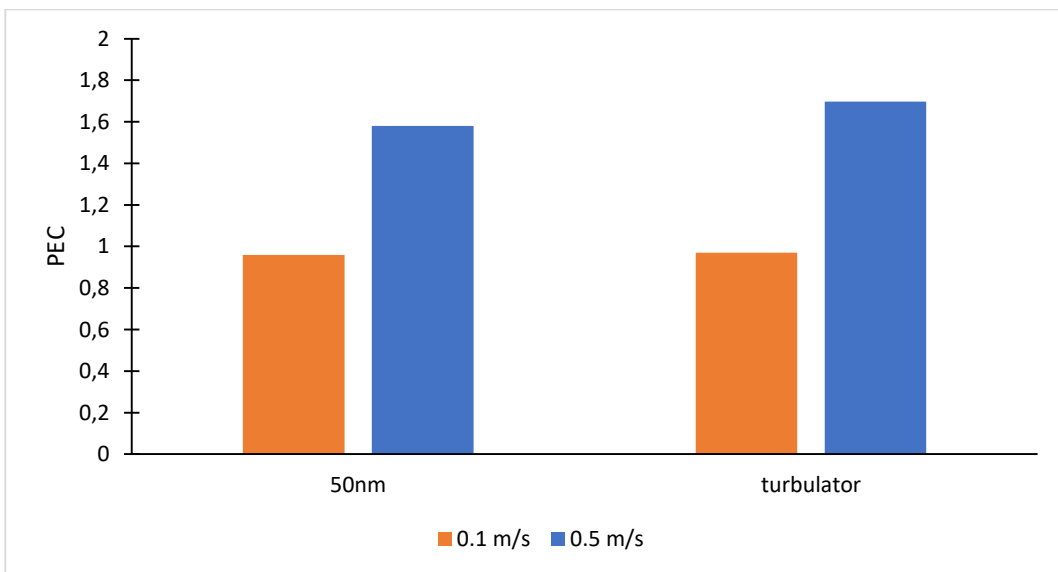
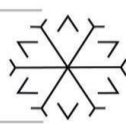
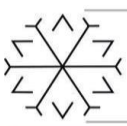


Figure 6: A comparison of Performance evaluation criteria obtained for nanofluid and ball turbulator



In the Figure 7, temperature contours for ball type turbulator heat exchanger with velocity of 0.1 m/s have been given. The temperature profiles that occur after the heat transfer between the hot and cold fluids in the counterflow heat exchanger are demonstrated. It can be seen that the hot fluid entering the heat exchanger at 70°C leaves the heat exchanger at about 50 °C, and the cold fluid entering at 20 °C leaves the heat exchanger at about 35 °C. In Figure 8, velocity contours of the water are given for the heat exchanger examined. Fluid makes enter both the hot and cold sides with an inlet velocity of 0.5 m/s and there are regional changes in its velocity with the effect of turbulators. These velocity changes create vortexes and fluctuations in the fluid, and as a result, have a positive effect on heat transfer. However, due to the turbulators that obstruct the flow, heat exchangers require more energy than the heat exchanger without turbulator to provide the flow under these conditions.

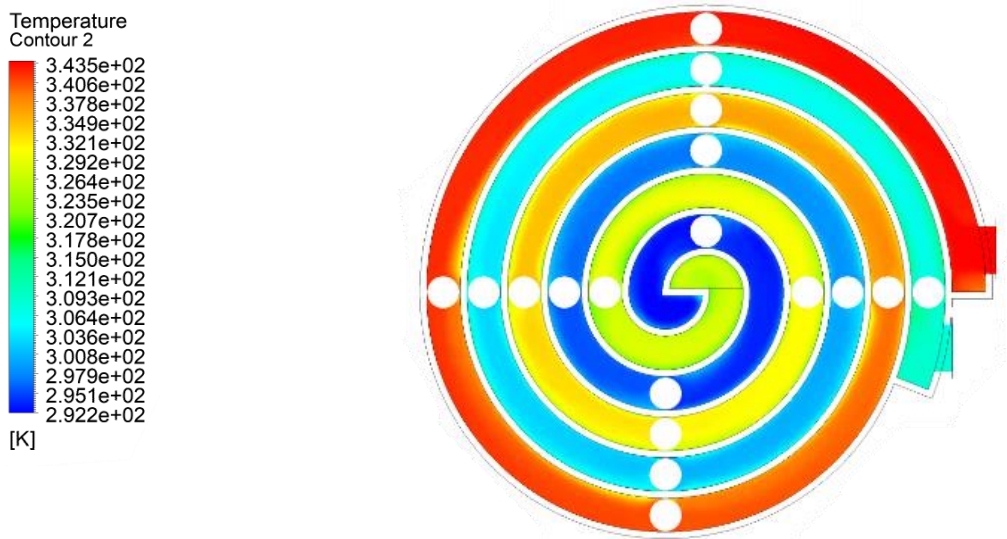


Figure 7: Ball type turbulator effects on temperature contour where heat transfer fluid is water at 0.1 m/s

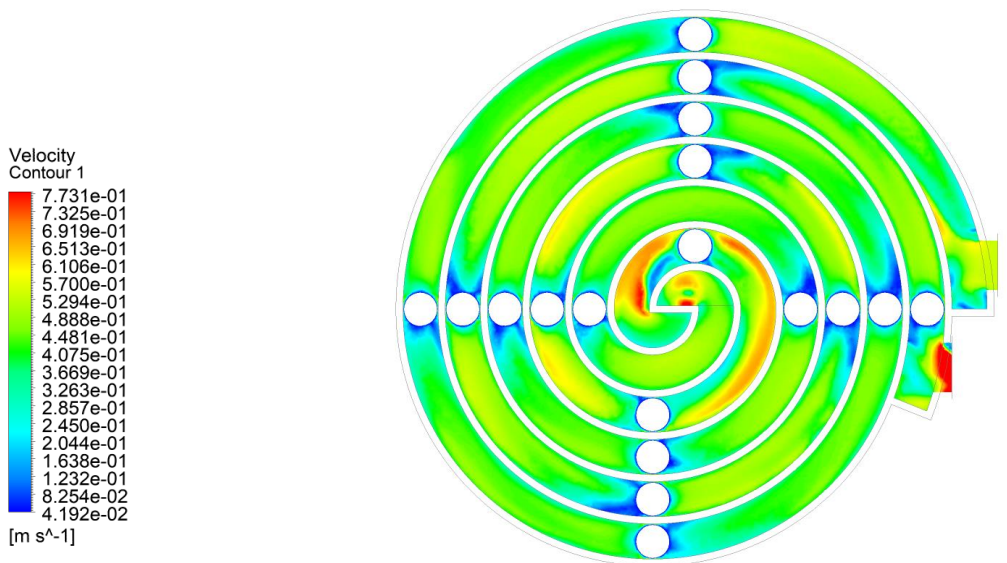
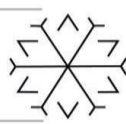
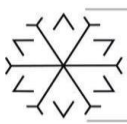


Figure 8: Ball type turbulator effects on velocity contour where heat transfer fluid is water at 0.5 m/s



4. Conclusion

In the literature different heat transfer augmentation methods have been presented including, porous material, fins in different geometry, various prepared nanofluids, vortex turbulators phase-change devices and high thermal conductivity composite materials. In this study, a numerical analysis was made and the results on the heat exchanger were obtained and compared to evaluate two above mentioned factors; nanofluids and turbulator. In this context, the contribution and effect of nanofluid and turbulator factors on thermal performance of spiral type heat exchanger were investigated. According to the results obtained, the use of nanofluids together with the use of turbulators can be considered and even recommended. The employing turbulators can remarkably improve heat exchanger operated with nanofluids. Obtained results were presented in the form of diagrams and contours to compare concluded numerical results and evaluate flow structure and temperature distribution inside heat exchanger.

Acknowledgements

This present CFD simulation work was carried out in line with the joint project supported by the Scientific and Technological Research Council of Turkey (TÜBİTAK, Project No. 119N727) and University of Tabriz and Iran Ministry of Science, Research and Technology (MSRT, Project No. 99-24-800). The authors gratefully acknowledge the support of the project.

References

- Selbaş, R., Kızılkın, Ö., Reppich, M. (2006). A new design approach for shell-and-tube heat exchangers using genetic algorithms from economic point of view. *Chemical Engineering and Processing: Process Intensification*, 45(4), 268-275.
- Pantzali, M. N., Mouza, A. A., Paras, S. V. (2009). Investigating the efficacy of nanofluids as coolants in plate heat exchangers (PHE). *Chemical Engineering Science*, 64(14), 3290-3300.
- Farajollahi, B., Etemad, S. G., Hojjat, M. (2010). Heat transfer of nanofluids in a shell and tube heat exchanger. *International Journal of Heat and Mass Transfer*, 53(1-3), 12-17.
- Rajeshkumar, M., Logesh, K., Thangaraj, M., Govindan, S. (2021). Heat transfer study on finned tube heat exchanger using CFD. *International Journal of Ambient Energy*, 42(3), 239-243.
- Vivekanandan, M., Saravanan, G., Vijayan, V., Gopalakrishnan, K., & Krishna, J. P. (2021). Experimental and CFD investigation of spiral tube heat exchanger. *Materials Today: Proceedings*, 37, 3689-3696.
- Kim, S., Song, H., Yu, K., Tserengombo, B., Choi, S. H., Chung, H., Jeong, H. (2018). Comparison of CFD simulations to experiment for heat transfer characteristics with aqueous Al₂O₃ nanofluid in heat exchanger tube. *International Communications in Heat and Mass Transfer*, 95, 123-131.
- Tiwari, A. K., Ghosh, P., Sarkar, J., Dahiya, H., Parekh, J. (2014). Numerical investigation of heat transfer and fluid flow in plate heat exchanger using nanofluids. *International Journal of Thermal Sciences*, 85, 93-103.
- Khanlari, A., Sözen, A., Variyenli, H. İ. (2019). Simulation and experimental analysis of heat transfer characteristics in the plate type heat exchangers using TiO₂/water nanofluid. *International Journal of Numerical Methods for Heat & Fluid Flow*.
- Khorshidi, J., Heidari, S. (2016). Design and construction of a spiral heat exchanger. *Advances in Chemical Engineering and Science*, 6(02), 201.
- Vajjha, R. S., Das, D. K. (2009). Experimental determination of thermal conductivity of three nanofluids and development of new correlations. *International Journal of Heat and Mass Transfer*, 52(21-22), 4675-4682.
- Khanafar, K., Vafai, K. (2017). A critical synthesis of thermophysical characteristics of nanofluids. *Nanotechnology and Energy*, 279-332.



Xuan, Y., Roetzel, W. (2000). Conceptions for heat transfer correlation of nanofluids. *International Journal of Heat and Mass Transfer*, 43(19), 3701-3707.

Geopolymers in Soil Stabilization from Past to Present

Asena KARSLIOĞLU ^{1*}[0000-0001-5178-4069] and Mehmet İnanç ONUR ²[0000-0002-2421-4471]

¹asenakarsliloglu@eskisehir.edu.tr, Department of Civil Engineering, Eskisehir Technical University

²mionur@eskisehir.edu.tr, Department of Civil Engineering, Eskisehir Technical University

Abstract

Civil engineers are studying to find safe and economical solutions in design and construction steps. The soil conditions of the project site have a great effect on the design and construction methods in civil engineering applications. Problematic soil conditions can cause important problems therefore; soil conditions should be improved. Soil stabilization is the improvement of certain properties of soils by using several mechanical, chemical or biological methods. The main objectives in soil stabilization are reducing the compressibility, and maximizing its strength. When the literature is examined, although there are many different methods in soil stabilization, the easiest and most practical one is to improve the soil by adding additives to the soil. Materials such as cement, lime, bitumen, fly ash are some of the additives used in soil stabilization. It is possible to use geopolymers instead of cement, which is often used in soil improvement. For years, the behaviour of geopolymer has been studied by researchers and geopolymers showed well performs in soil stabilization. In this study, researches from the past to the present on the use of geopolymers in the field of soil improvement are presented. The present study results show that waste materials can be disposed of with minimal harm to the environment and the geopolymer can be used in an environmentally friendly way. In addition, future research needs to focus on long-term durability as well as mechanical property.

Keywords. Alkaline activator, Geopolymer, Soil stabilizer.

1. Introduction

The name of the geopolymer was given to the structures formed by inorganic molecules in 1978 by the French materials scientist Joseph Davidovits, who is also known as the father of geopolymer. Geopolymer's raw materials contain silica and aluminum, which are natural materials that are usually heat activated and formed. These resources consist of waste materials such as fly ash, metakaoline and blast furnace slag. The waste stocks of factories and thermal power plants are regulated thanks to the use of geopolymer. Among the main reasons for the increasing interest in geopolymer recently can be listed as; low cost, contribution to the country's economy, environmental friendliness, resistance to environmental effects, fire resistance, mechanical properties, rheological properties.

The productivity of geopolymer has been investigated by researchers in several fields. At the same time, it is possible to use geopolymers in the field of soil improvement in geotechnical engineering applications. Soil stabilization is the process of improving soils that are considered unsuitable for geotechnical engineering. General soil stabilization methods are given in Figure 1. The two main methods of soil stabilization are mechanical and chemical stabilization used depending on the construction process. While mechanical stabilization aims to reduce voids in the soil, chemical stabilization increases strength, reduced permeability, etc. For this purpose, additives such as lime and cement are added to the weak soil. The most important problem with conventionally used soil stabilizers is the overuse of energy in the production processes and the emission of large amounts of carbon dioxide (CO₂). According to the studies, producing one ton of cement causes almost one ton of CO₂ released into the atmosphere, and it is also stated that ready-made raw materials are consumed excessively to produce cement today. In cement stabilization, mechanism is related to hydration and pozzolanic reactions (Yao et al., 2009; Disu and Kolay, 2021). One of the alternatives to these methods is usage of geopolymers. In recent years, the usage of environmentally friendly and sustainable geopolymers for soil stabilization has been researched. This article examines the using of geopolymer application for soil stabilization.

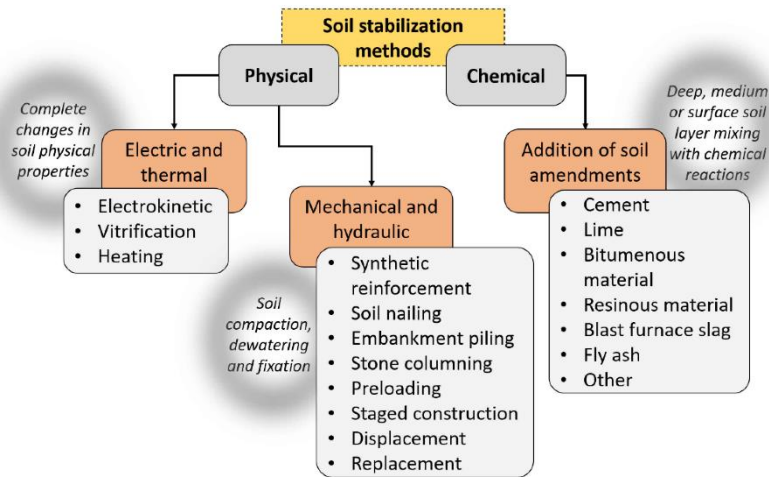
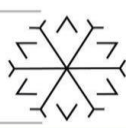
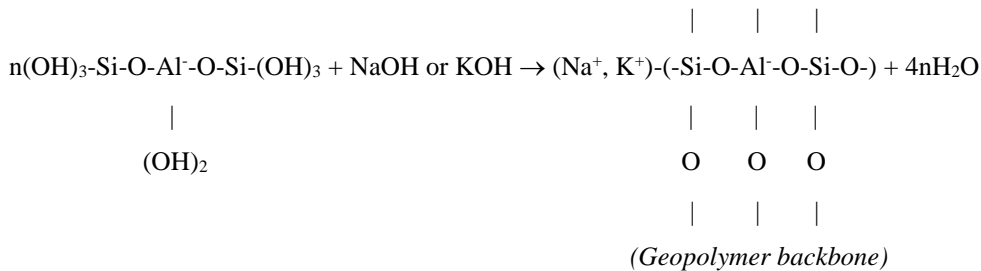
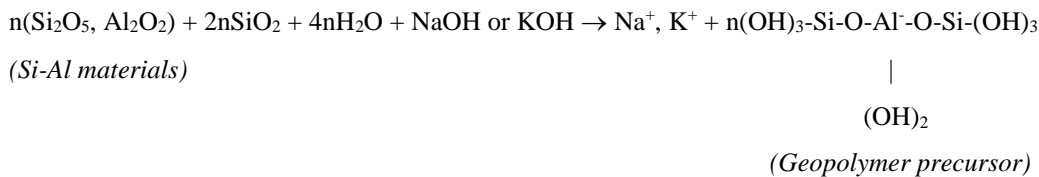


Figure 1: General soil stabilization methods (Vincevica-Gaile et al., 2021)

2. Geopolymerization

Matters with an amorphous and semi-crystalline 3-dimensional alumina-silicate network improved by Joseph Davidovits in 1978 are called geopolymers (Davidovits, 1991). Davidovits explained chemical reactions with alumina-silicate oxides under high alkaline conditions with the following reactions (Xu, 2000). These two reactions show that geopolymerization can occur with any two aluminosilicate materials (Jaarsveld et al., 1997).



Geopolymer can be synthesized by using alkaline medium or acidic medium. In the alkaline medium, the process of geopolymerization occurs when the oxides of silicon and aluminum minerals or aluminosilicates react with the alkaline solution to form polymeric silicate bonds (Ng et al., 2018). Figure 2 shows that structure of polysialate. Sialate is an acronym used to represent silicon-oxo-aluminate (Si-O-Al).

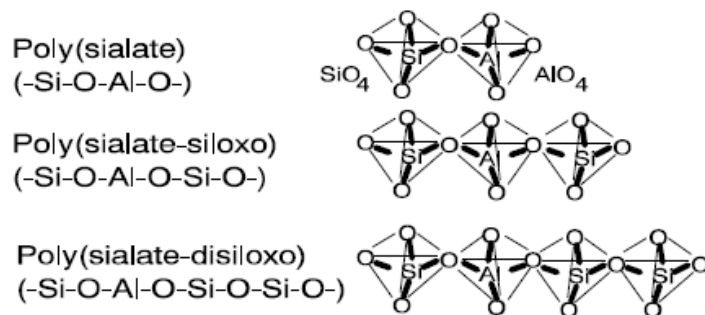


Figure 2: Structure of Poly(sialate) (Davidovits, 1994).



3. Review of Literature

In the geopolymerization process, first step is choosing carefully the raw material such as fly ash, metakaolin or ground granulated blast furnace slag (GGBS). It has been noted that raw material and processing conditions are determinative in affecting the setting behavior, workability, chemical and physical properties of geopolymeric products (Duxson et al., 2007). Different types of resource material give various strengths to the geopolymer, as they have different effects on chemical bonding (Abdullah et al., 2015). The geopolymer production with room or high temperature curing with three main components which are soil, alumina silica resources and alkali activator is given in Figure 3.

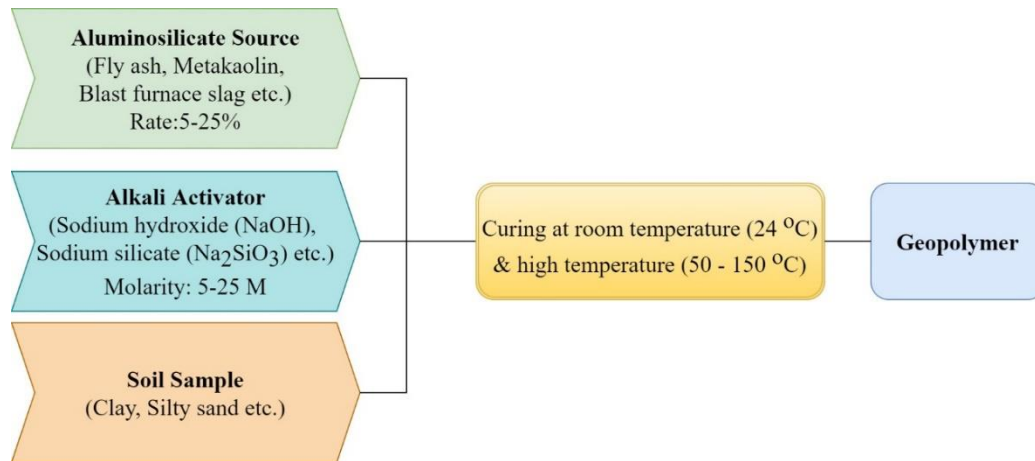


Figure 3: Production of geopolymer.

Clay soil has the improving potential by adding sodium silicate (Na₂SiO₃). Moayedi et al. (2011) applied Na₂SiO₃ to kaolinite clay for stabilization. As a result of the study, the use of 5 mol/L Na₂SiO₃ gave the highest unconfined compressive strength (UCS) results.

Cristelo et al. (2011) examined the use of alkaline activation of fly ash as a source of aluminasilica for the stabilization of soft soils. It was observed that the use of fly ash and alkaline activator increased soil strength up to 11.4, 16.7 and 43.4 MPa at 28, 90 and 365-day cure, respectively, with the experimental results. Also, increasing the activator concentration up to 15 M did not show any benefit because similar results could be obtained using 12.5 M is more economical.

Mozumder and Laskar (2015) investigated the effect of geopolymerization on the UCS of clayey soil. The amount of binder was used as a percentage of the dry weight of the soil sample, 4-50% for GGBS, 4-20% for FA and GGBS + FA mixture. Also, the molar concentration of the alkali solution (sodium silicate, Na₂SiO₃, and sodium hydroxide, NaOH) was used as 4 M, 8 M, 10 M, 12 M and 14.5 M.

Singh et al. (2016) researched the soil-geopolymer containing slag, fly ash and a mixture of slag and fly ash as raw material. It has been determined that the molar concentration of the alkali activator, the aluminasilicate source material ratio and the percent content of the raw material are effective on the UCS of the soil. Also, UCS of the soil-geopolymer system increases with the binder material content.

Phetchuay et al. (2016) examined the evolution of clay strength and carbon footprint by forming a geopolymer based on calcium carbide residue and fly ash with clay soil. A mixture of Na₂SiO₃ solution and NaOH was used as alkali activator. It has been found that the strength of the clay soil depends on the fly ash content and the NaOH concentration. The carbon footprints of the geopolymer-applied soils are lower 22-43% than the cement-stabilized soils.

Ayyappan et al. (2017), used different concentrations (2% and 4%) of metakaolin-based geopolymer to examine the stabilizing property of geopolymer in soft clay and sand mixtures with. UCS test and standard proctor compression test were performed. UCS increased in clayey soil samples stabilized with metakaolin-based geopolymer and it has been shown that this method can be an effective soil improvement method.

Yu et al. (2020) examined GGBS to develop the strength properties of soft clay and the use of anhydrous sodium metasilicate (ASM) powder as an alkali activator in soil stabilization. As a result of the study, it has been shown that ASM powder can be used instead of NaOH for practical applications in soil stabilization.

Eskişar and Aksu (2020) investigated the effects of the activator content and ratios (Activator 1: 90% Na₂SiO₃ + 10% NaOH (8M) and Activator 2: 70% Na₂SiO₃ + 30% NaOH (8M)) of the geopolymerization method on the



strength for clay, clayey sand and sandy soils. In the geopolymerization process, two different methods were tried with variable temperatures (Method 1: 38 °C and Method 2: 80 °C at 24 hours + 20 °C). It has been concluded that the use of liquid activator as much as the optimum water content in sand and clayey sand samples provide improvement, while the use of liquid activator approximately twice of the optimum water content increases the strength in clay soil samples.

Gadir et al. (2021) determined the effect of geopolymer produced by using 0-15% volcanic ash for soil stabilization on shear strength behaviors. It has been stated that increasing volcanic species content changes the structure of clayey soil through flocculation and thus develops shear resistance.

4. Conclusion

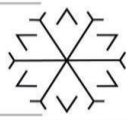
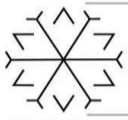
Studies showed that various additives and chemicals can be used to enhance and stabilize the geotechnical properties of the soil. The widespread binders such as cement gives high stabilization potential, but they are uneconomical and may contribute to environmental problem. In recent years, many studies have been carried out to develop a new material without high CO₂ emissions. Geopolymers offer cost-effective solutions to the problems associated with hazardous wastes that needs store. Alkaline activation of aluminosilicate sourced materials are seen as a suitable substitute for cement as it can overcome many of the known disadvantages of cement that is commonly used for soil stabilization. The use of industrial wastes in the production of geopolymer binders that can be used to increase the strength of the soils with environmentally friendly and low carbon footprint. The literature shows that geopolymers will play an important role in the future of soil stabilization with its high strength, low cost, low energy consumption and low CO₂ emissions. Therefore, more research is required to evaluate the potential of geopolymers in field application rather than experimental studies. In addition, researches focused on long-term durability as well as mechanical property are suggested to optimum solutions.

Acknowledgements

The author Asena KARSLIOĞLU would like to thank those concerned for their support with Tübitak Bideb 2211-A General Domestic Doctoral Scholarship and YÖK 100/2000 Doctoral Scholarship.

References

- Abdullah, M. S., Ahmad, F., & Mustafa Al Bakri, A. M., 2015. Geopolymer application in soil: a short review. In *Applied Mechanics and Materials* (Vol. 754, pp. 378-381). Trans Tech Publications Ltd.
- Ayyappan, A., Palanikumar, S., Kumar, D. D., & Vinoth, M., 2017. Influence of Geopolymers in the Stabilization of Clay Soil. *International Journal of Emerging Technologies in Engineering Research (IJETER)* Volume, 5.
- Cristelo, N., Glendinning, S., & Teixeira Pinto, A., 2011. Deep soft soil improvement by alkaline activation. *Proceedings of the Institution of Civil Engineers-Ground Improvement*, 164(2), 73-82.
- Davidovits, J., 1991. Geopolymers: inorganic polymeric new materials. *Journal of Thermal Analysis and calorimetry*, 37(8), 1633-1656.
- Davidovits, J., 1994, October. Properties of Geopolymer Cements. In *First International Conference On Alkaline Cements and Concretes* (Vol. 1, Pp. 131-149). Kiev State Technical University, Ukraine: Scientific Research Institute On Binders and Materials.
- Disu, A. A., & Kolay, P. K., 2021. A Critical Appraisal of Soil Stabilization Using Geopolymers: The Past, Present and Future. *International Journal of Geosynthetics and Ground Engineering*, 7(2), 1-16.
- Duxson, P., Fernández-Jiménez, A., Provis, J. L., Lukey, G. C., Palomo, A., & van Deventer, J. S., 2007. Geopolymer technology: the current state of the art. *Journal of materials science*, 42(9), 2917-2933.
- Eskisar, T. & Aksu, G., 2020. Zeminlerde tek fazlı geopolimerizasyon uygulaması ve geopolimerizasyonun serbest basınç mukavemeti üzerindeki etkisi. *Konya Mühendislik Bilimleri Dergisi*, 8 (3), 466-478. DOI: 10.36306/konjes.611595.
- Ghadir, P., Zamanian, M., Mahbubi-Motlagh, N., Saberian, M., Li, J., & Ranjbar, N., 2021. Shear strength and life cycle assessment of volcanic ash-based geopolymer and cement stabilized soil: A comparative study. *Transportation Geotechnics*, 31, 100639.
- Moayedi, H., Huat, B. B., Moayedi, F., Asadi, A., & Parsaie, A., 2011. Effect of sodium silicate on unconfined compressive strength of soft clay. *Electronic Journal of Geotechnical Engineering*, 16, 289-295.



- Mozumder, R. A., & Laskar, A. I., 2015. Prediction of unconfined compressive strength of geopolymer stabilized clayey soil using artificial neural network. *Computers and Geotechnics*, 69, 291-300.
- Ng, C., Alengaram, U. J., Wong, L. S., Mo, K. H., Jumaat, M. Z., & Ramesh, S., 2018. A review on microstructural study and compressive strength of geopolymer mortar, paste and concrete. *Construction and Building Materials*, 186, 550-576.
- Phetchuay, C., Horpibulsuk, S., Arulrajah, A., Suksiripattanapong, C., & Udomchai, A., 2016. Strength development in soft marine clay stabilized by fly ash and calcium carbide residue based geopolymer. *Applied clay science*, 127, 134-142.
- Singhi, B., Laskar, A. I., & Ahmed, M. A., 2016. Investigation on soil-geopolymer with slag, fly ash and their blending. *Arabian Journal for science and engineering*, 41(2), 393-400.
- Van Jaarsveld, J. G. S., Van Deventer, J. S. J., & Lorenzen, L., 1997. The potential use of geopolymeric materials to immobilise toxic metals: Part I. Theory and applications. *Minerals engineering*, 10(7), 659-669.
- Vincevica-Gaile, Z., Teppand, T., Kriipsalu, M., Krievans, M., Jani, Y., Klavins, M., ... & Burlakovs, J., 2021. Towards Sustainable Soil Stabilization in Peatlands: Secondary Raw Materials as an Alternative. *Sustainability*, 13(12), 6726.
- Xu, H., & Van Deventer, J. S. J., 2000. The geopolymerisation of alumino-silicate minerals. *International journal of mineral processing*, 59(3), 247-266.
- Yao, X., Zhang, Z., Zhu, H., & Chen, Y., 2009. Geopolymerization process of alkali-metakaolinite characterized by isothermal calorimetry. *Thermochimica Acta*, 493(1-2), 49-54.
- Yu, J., Chen, Y., Chen, G., & Wang, L., 2020. Experimental study of the feasibility of using anhydrous sodium metasilicate as a geopolymer activator for soil stabilization. *Engineering Geology*, 264, 105316.

Modal Analysis of Industrial Steel Stacks with Soil-Structure Interaction

Achmet KALIN ¹{0000-0002-1529-5329} and Şeref D. AKBAŞ ²{0000-0001-5327-3406}

¹ahmet.kalin@hotmail.com, Bursa Technical University, Department of Civil Engineering

²serefd@yadoo.com, Bursa Technical University, Department of Civil Engineering

Abstract

In the purpose of this study, modal analysis of and vibration responses of industrial steel stacks are investigated by considering with soil-structure interaction. The steel stacks are designed according to Steel Structures Code - 2016 and Turkish Building Seismic Code – 2018 with different geometry parameters. The industrial steel stacks are modelled as 3 dimensional solids in ANSYS Workbench software. In order to investigate the soil-structure interaction on the industrial steel stacks, the different soil types are modelled in ANSYS Workbench software and connected with steel stacks. In the modal analysis, 3 dimensional finite element analysis is used and vibration responses are obtained for different vibration modes. The steel stack and the soil are modelled separately and connected with each other. In order to get realistic results from soil-structure interaction analysis, the soils is considered 3 dimensional finite element and the boundary and dimensions of the soil are selected enough large dimensions, and the boundary conditions of the soils are considered in viscoelastic spring. In the finite element model of the soil, SOLID185 finite element type is used and SOLID65 finite element type is used in the modeling of the industrial steel stacks in ANSYS Workbench program. In the results, the effects of geometry parameters of steel stacks and different soil types on the vibration responses of industrial steel stacks are investigated with considering soil-structure interaction. In the results, vibration periods and vibration modes of the industrial steel stacks presented and discussed according to different types of soil and geometry parameters of the steel stacks. The results show that the soil effects can be an important role on the dynamic responses of industrial steel stacks, especially high rising steel stacks.

Keywords. Industrial Steel Stacks, Soil-Structure Interaction, Modal Analysis, Finite Element Method

Numerical Investigation of the Solute Dispersion Phenomenon Based on the Advection–Diffusion Equation

Amin GHAREHBAGHI¹

¹amin.gharehbaghi@hku.edu.tr, Hasan Kalyoncu University, Faculty of Engineering, Department of Civil Engineering, Şahinbey, Gaziantep, Turkey

Abstract

In this work, we have suggested a one-dimensional time-dependent numerical model for the advection-diffusion equation with variable coefficients in the semi-infinite domain to simulate the solute dispersion phenomena in porous media. For this purpose, the upwind and central schemes of the finite volume method are employed. The field's inhomogeneity is achieved by the spatially dependent flow. The problem domain is divided by uniform node distribution. To examine the numerical predictions, two analytical solutions are implemented and acceptable precision was observed. The results approve that the used solution techniques are suitable for implementing a wide range of problems in various engineering and science areas.

Keywords. Solute Dispersion Phenomenon, Advection–Diffusion Equation, Finite Volume Method, Central Scheme, Upwind Scheme

1. Introduction

The widespread use of the Advection–Diffusion Equation (ADE) including, but not limited to, transport of heat, sediment, ground water and surface flow pollutant is fully sufficient for researchers to handle this question frequently (Gharehbaghi 2016, 2017). Although various analytical models have been established based on ADE, with the remarkable progress in computer science, many researchers have tried to apply numerical methods to solve ADE. Using an analytical solution has limitations in application. For instance, enforcing an analytical model is heavily influenced by boundary and/or initial conditions and several troubles can emerge in dealing with complex geometries. Fortunately, numerical methods provide us an environment that can handle complex problems and geometries. Among the various numerical techniques for discretizing the equations, three traditional and powerful computational methods can classify as the Finite Element Method (FEM), the Finite Difference Method (FDM), and the Finite Volume Method (FVM) (Gharehbaghi et al., 2017). Because of some advantages of FVM in fluid mechanics we selected this method to discretize the equations (Versteeg and Malalasekera, 2007).

As mentioned earlier, due to the important role ADE plays in science and engineering, over the years, many researchers have taken an interest in it. According to our best knowledge, the overwhelming majority of scholars have preferred to apply this equation with constant coefficients. Besides, mostly they focused on homogeneous and finite area. To fill this gap and simulate the nature of dispersion problems more realistically, we have introduced a numerical model for ADE with variable coefficients in one-dimensional (1D) form and in the semi-infinite area. The aforesaid equation is addressed with two FVM approaches (i.e., Central and Upwind) for two dispersion problems.

2. Numerical Solutions of ADE

The 1D form of ADE is given as follows (Kumar et al. 2010):

$$\frac{\partial c(x,t)}{\partial t} = \frac{\partial}{\partial x} \left(D(x,t) \frac{\partial c(x,t)}{\partial x} \right) - \frac{\partial u(x,t)c(x,t)}{\partial x} \quad (1)$$

Where c is the dispersing solute concentration, x is the longitudinal axis, and t is the time. In the case of presuming D and u as constant values, these values can call as dispersion coefficient and uniform velocity of the flow field, respectively. In this paper Eq. (1) is used as follows:

$$\frac{\partial c(x,t)}{\partial t} = \frac{\partial}{\partial x} \left(D_0 \cdot f_1(x,t) \frac{\partial c(x,t)}{\partial x} \right) - \frac{\partial u_0 f_2(x,t) c(x,t)}{\partial x} \quad (2)$$

where D_0 and u_0 are constant whose dimensions depend upon the expressions $f_1(x,t)$ and $f_2(x,t)$. The analytical expressions of ADE for two hydrodynamic dispersion problems have been suggested by Kumar

et al. (2010). The uniform node distribution has implemented in the domain. In the meantime, the initially solute-free condition has presumed for each problem.

2.1. Dispersion Through Inhomogeneous Domain

The main influence of the inhomogeneity on problem domain is alteration in the velocity of the flow through it. Jaiswal et al. (2009) investigated on this alteration. To satisfy the required circumstances for speed factor in the ADE the alteration in speed is presumed as small order. Furthermore, as the second hypothesis, dispersion factor is considered relative to the square of the velocity (Scheidegger, 1957). Hence, the values of $f_1(x,t)$ and $f_2(x,t)$ for Eq. (2) are presumed as below (Kumar et al. 2010):

$$f_1(x,t) = (1 + ax)^2 \quad \text{and} \quad f_2(x,t) = (1 + ax) \quad (3)$$

where a describes the inhomogeneity of the area and dimension is $(\text{length})^{-1}$. Also, the boundary and initial conditions are hired as:

$$c(x,0) = 0, \quad c(0,t) = c_0, \quad c(1,t) = 0 \quad (4)$$

Kumar et al. (2010) announced the following analytical expression for this case.

$$c = \frac{c_0}{2} \left[(1 + ax)^{-1} \operatorname{erfc} \left(\frac{\ln(1+ax)}{2a\sqrt{D_0 t}} - \beta\sqrt{t} \right) + (1 + ax)^\delta \operatorname{erfc} \left(\frac{\ln(1+ax)}{2a\sqrt{D_0 t}} + \beta\sqrt{t} \right) \right] \quad (5)$$

Where $\beta = \sqrt{\frac{\omega_0^2}{4a^2 D_0} + au_0} = \frac{u_0 + aD_0}{2\sqrt{D_0}}$, $\delta = \frac{u_0}{aD_0}$.

2.2. Dispersion Along Unsteady Flow Through Inhomogeneous Domain

To determine the behavior of concentration, in this case it is presumed that the inhomogeneity causes a linear rise in speed given in Eq. (3), and the relation between dispersion and velocity can define as dispersion is proportional to the square of the velocity. (Scheidegger, 1957). Additionally, the flow is time dependent and alter with it, hence, dispersion displays similar manners too.

So, the following phrases can apply in Eq. (2) (Kumar et al.2010):

$$f_1(x,t) = f(mt)(1 + ax)^2 \quad f_2(x,t) = f(mt)(1 + ax) \quad (6)$$

Because of the boundary and initial conditions presented in Equation (4) and its application with a uniform input condition, the solution looks like Equation (5). The only difference is related to the time as follows:

$$T = \int_0^t f(mt) dt \quad (7)$$

3. Numerical Study

As mentioned earlier, in this article, two approaches of FVM, which are named upwind (UFVM) and central (CFVM) approaches, are applied to discretize the ADE. The illustration of 1D discretization based on the FVM is presented in Fig.1.

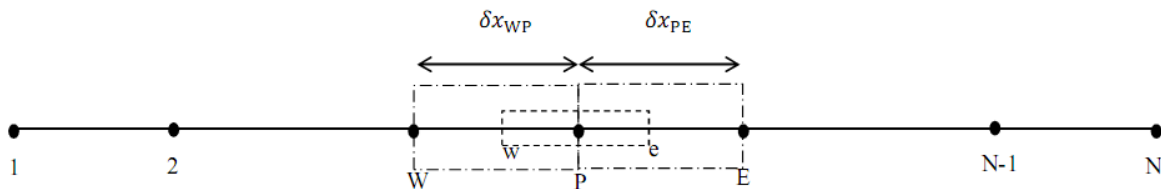


Figure 1: 1D discretization of FVM (Gharehbaghi, 2017)

In this figure, P , E , W , e , and w are the target node point, the east side neighbor point, the west side neighbor point, the face of the control volume on the east side, and the face of the control volume on the west side, respectively. Moreover, δx displays space between the nodes. In the initial stage for numerical evaluation, Eq. (2) rearranged as follows:

$$\frac{\partial c(x,t)}{\partial t} = \left(D_0 \cdot \frac{\partial f_1(x,t)}{\partial x} - u_0 f_2(x,t) \right) \frac{\partial c(x,t)}{\partial x} + D_0 \cdot f_1(x,t) \frac{\partial^2 c(x,t)}{\partial x^2} - u_0 c(x,t) \frac{\partial f_2(x,t)}{\partial x} \quad (8)$$

3.1 Numerical Study of Dispersion Through Inhomogeneous Domain



In this case study, a solute dispersion through a semi-infinite and inhomogeneous domain, with the boundary and initial conditions yielded in Eq. (4), and initially solute-free condition yielded in Eq. (3), are applied. Hence, by some manipulations and substitutions, the integral of Eq. (8) is rewritten as:

$$\int_t^{t+\Delta t} \int_{CV} \frac{\partial c(x,t)}{\partial t} \cdot dV \cdot dt = \int_t^{t+\Delta t} \int_{CV} ((1+ax)(2 \cdot a \cdot D_0 - u_0) \frac{\partial c(x,t)}{\partial x}) \cdot dV \cdot dt + \int_t^{t+\Delta t} \int_{CV} D_0 \cdot (1+ax)^2 \frac{\partial^2 c(x,t)}{\partial x^2} \cdot dV \cdot dt - \int_t^{t+\Delta t} \int_{CV} u_0 a c(x,t) \cdot dV \cdot dt \quad (9)$$

The integration of Eq. (9) over the control volume and over a time interval (i.e., t to $t + \Delta t$) is expressed as:

$$(c_p - c_p^0) \Delta V = (1+ax)(2 \cdot a \cdot D_0 - u_0)(A_e c_e - A_w c_w) \cdot \Delta t + D_0 \cdot (1+ax)^2 \left(A \frac{\partial c}{\partial x} \right)_e - \left(A \frac{\partial c}{\partial x} \right)_w \cdot \Delta t - u_0 a c \cdot \Delta V \cdot \Delta t \quad (10)$$

In Eq. (10), ΔV refers to the volume of the control volume and is equal to $A \cdot \Delta x$. In this relation, A and Δx are the face area of the control volume and the width of the control volume, respectively.

To obtain the useful forms of the discretized equations, the gradient $\partial c / \partial x$ at east and west sides, and the amounts of interface coefficients c_e and c_w are necessary. Scientists developed several numbers of approximations for this purpose. In this research, two well established and popular approximations are implemented as:

$$\text{Central scheme} \quad c_e = \frac{c_P + c_E}{2}, \quad c_w = \frac{c_P + c_W}{2} \quad (11)$$

$$\text{Upwind scheme} \quad c_e = c_P, \quad c_w = c_W \quad (12)$$

Also, for east and west cell faces, these relations are applied.

$$\left(\frac{\partial c}{\partial x} \right)_e = \frac{c_E - c_P}{\Delta x_{PE}}, \quad \left(\frac{\partial c}{\partial x} \right)_w = \frac{c_P - c_W}{\Delta x_{PW}} \quad (13)$$

By applying the above-mentioned equations and some operations, the solution of Eq. (10) as CFVM and UFVM, are given as follows

$$\text{CFVM} \quad c_p = \frac{Y_1}{2} (c_E^0 - c_W^0) + G_1 (c_E^0 - 2c_P^0 + c_W^0) + K_1 c_p^0 \quad (14)$$

$$\text{UFVM} \quad c_p = Y_1 (c_P^0 - c_W^0) + G_1 (c_E^0 - 2c_P^0 + c_W^0) + K_1 c_p^0 \quad (15)$$

Where $Y_1 = (1+ax)(2 \cdot a \cdot D_0 - u_0) \frac{\Delta t}{\Delta x}$, $G_1 = D_0 \cdot (1+ax)^2 \frac{\Delta t}{\Delta x^2}$, and $K_1 = (1 - u_0 a \cdot \Delta t)$.

It is important to note that, the ADE is solved in explicit form. Hence, in Eq. (14-15) superscript '0' shows the values at the old-time (i.e., time t). Nevertheless, values at new-time (i.e., time level $t + \Delta t$) are without any superscript. Because of the explicit approach, these methods must be able to satisfy the stability condition. In this paper, the authors used Courant number for testing the stability condition.

$$C_{adv} = \frac{\delta t \times |u_0 f_2(x,t)|}{\delta x} \leq 1, \quad C_{dif} = \frac{\delta t \times |D_0 \cdot f_1(x,t)|}{\delta x^2} \leq 1 \quad (16)$$

where C_{adv} is the advection parameters Courant number, and C_{dif} is the diffusion parameters Courant number.

3.2 Numerical Study of Dispersion Along Unsteady Flow Through Inhomogeneous Domain

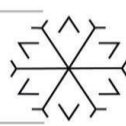
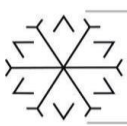
In this case, an unsteady flux through an inhomogeneous area which is the function of the time is presumed. For $f_1(x,t)$ and $f_2(x,t)$, the expressions given in Eq. (9) are employed. Additionally, in this case for $f(mt)$, Kumar et al. (2010) recommended $(1 - \sin(mt))$. By replacing this relation, implementing the integration of FVM, and a few manipulations, Eq. (2) is given as:

$$\int_t^{t+\Delta t} \int_{CV} \frac{\partial c}{\partial t} \cdot dV \cdot dt = \int_t^{t+\Delta t} \int_{CV} D_0 \cdot (1 - \sin(mt)) (1+ax)^2 \frac{\partial^2 c(x,t)}{\partial x^2} \cdot dV \cdot dt + \int_t^{t+\Delta t} \int_{CV} (1+ax) (1 - \sin(mt)) (2 \cdot a \cdot D_0 - u_0) \frac{\partial c(x,t)}{\partial x} \cdot dV \cdot dt - \int_t^{t+\Delta t} \int_{CV} u_0 a c \cdot (1 - \sin(mt)) dV \cdot dt \quad (17)$$

By using the boundary and initial conditions, given in Eq. (4), the eventual solutions for CFVM and UFVM are presented as below:

$$\text{CFVM} \quad c_p = \frac{Y_3}{2} (c_E^0 - c_P^0) + G_3 (c_E^0 - 2c_P^0 + c_W^0) + K_3 c_p^0 \quad (18)$$

$$\text{UFVM} \quad c_p = Y_3 (c_P^0 - c_W^0) + G_3 (c_E^0 - 2c_P^0 + c_W^0) + K_3 c_p^0 \quad (19)$$



where $Y_3 = (1 + ax)(1 - \sin(mt))(2 \cdot a \cdot D_0 - u_0) \frac{\Delta t}{\Delta x}$, $G_3 = D_0 \cdot (1 - \sin(mt))(1 + ax)^2 \frac{\Delta t}{\Delta x^2}$, and $K_3 = 1 - u_0 a \cdot (1 - \sin(mt)) \Delta t$.

4. Results and discussion

As mentioned earlier, this paper proposed a numerical model to simulate the solute dispersion phenomena in porous media. For this reason, FVM and ADE with variable coefficients in the semi-infinite domain are used. Two problems with exact solutions picked. The details of these cases are given in Table (1). In the aforesaid table, the first, and second cases are referred to as dispersion through inhomogeneous domain, and dispersion along unsteady flow through inhomogeneous domain, respectively. Additionally, the outcomes of these case studies are given in Tables (2-3). Besides, in these tables, x refers to the distance (km), t the time (year), *Exact* the results of analytical solutions, *CFVM* the results of the central finite volume method, and *UFVM* the results of the upwind finite volume method. In both of the cases execution duration and distance were selected as one year and one km, respectively. Both of the cases have solved with 4 separate Δt and Δx . To evaluate the numerical outcomes, the root-mean-square-errors (RMSE), are calculated by the following relations.

$$RMSE = \sqrt{\frac{\sum_{i=1}^N (C_{Exact\ Solution} - C_{Numerical\ Solution})^2}{N}} \tag{20}$$

In Fact, the offered model can obtain accurate outcomes for greater values of the aforementioned duration and distance. Nevertheless, because the computation time and grid size impacted with the amount of duration and distance, thus, we have decided to employ the duration and distance used by Kumar et al. (2010). Anyway, only to prove the statement, the outcome of dispersion through the inhomogeneous domain (first case) for 1.3 years and 3 km with $\Delta t=0.0000065$ and $\Delta x=0.0769$ is shown in Fig. (2). This figure shows that both the implemented schemes can predict acceptable results in several time intervals (0.1, 0.5, 0.7, 1, and 1.3 years). Based on the results of RMSE have presented in tables (2-3), the CFVM has predicted more accurate results.

Table 1: Table of coefficients

	a(km ⁻¹)	c ₀	D ₀ (km ² /year)	u ₀ (km/year)	m(year ⁻¹)	f(mt)
First case	1	1	0.71	0.6	-	-
Second case	1	1	0.71	0.6	10	1-sin(mt)

Table 2: Table of RMSE for the first case

	Δt	Δx	0.1	0.2	0.3	0.4	0.5	0.6	0.7	0.8	0.9	1
UFVM	0.00033333	0.1	0.0214	0.018	0.0137	0.0112	0.0098	0.0089	0.0084	0.008	0.0078	0.0076
CFVM	0.00033333	0.1	0.0025	0.0004	0.0002	0.0002	0.0003	0.0003	0.0003	0.0003	0.0004	0.0004
UFVM	0.00033333	0.05	0.0156	0.0126	0.0097	0.008	0.007	0.0065	0.0061	0.0059	0.0057	0.0055
CFVM	0.00033333	0.05	0.0018	0.0005	0.0002	0.0002	0.0001	0.0001	0.0001	0.0001	0.0001	0.0001
UFVM	0.0002	0.1	0.0218	0.0181	0.0137	0.0112	0.0098	0.0089	0.0084	0.008	0.0078	0.0076
CFVM	0.0002	0.1	0.0022	0.0002	0.0001	0.0002	0.0003	0.0003	0.0003	0.0003	0.0003	0.0004
UFVM	0.0001	0.025	0.0117	0.0091	0.0069	0.0057	0.005	0.0046	0.0044	0.0042	0.0041	0.004
CFVM	0.0001	0.025	0.0007	0.0002	0.0001	0.0001	0.0001	0.0001	4.94E-05	4.90E-05	4.89E-05	4.88E-05

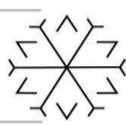


Table 3. Table of RMSE for the second case

	Δt	Δx	0.1	0.2	0.3	0.4	0.5	0.6	0.7	0.8	0.9	1
UFVM	0.00033333	0.1	0.0171	0.0182	0.0218	0.0161	0.0106	0.009	0.0085	0.0085	0.0084	0.008
CFVM	0.00033333	0.1	0.005	0.0044	0.0021	0.0004	0.0003	0.0003	0.0003	0.0003	0.0003	0.0004
UFVM	0.00016667	0.1	0.0169	0.018	0.022	0.0163	0.0107	0.009	0.0085	0.0085	0.0084	0.008
CFVM	0.00016667	0.1	0.0052	0.0046	0.0018	0.0002	0.0002	0.0003	0.0003	0.0003	0.0003	0.0003
UFVM	0.00016667	0.05	0.0146	0.0152	0.0165	0.0115	0.0077	0.0062	0.0062	0.0061	0.0061	0.0058
CFVM	0.00016667	0.05	0.0016	0.0014	0.0009	0.0003	0.0001	0.0001	0.0001	0.0001	0.0001	0.0001
UFVM	0.00005	0.025	0.0111	0.0114	0.012	0.0082	0.0055	0.0047	0.0045	0.0044	0.0044	0.0042
CFVM	0.00005	0.025	0.0006	0.0005	0.0003	0.0001	0.0001	0.000041	3.37E-05	3.00E-05	4.24E-05	5.16E-05

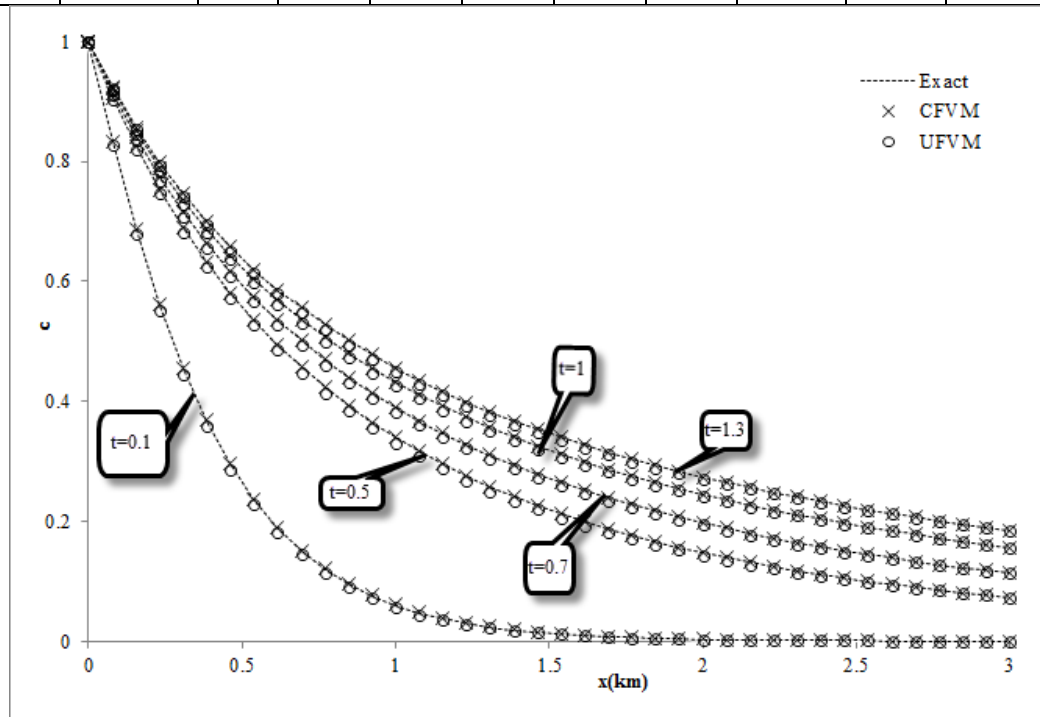


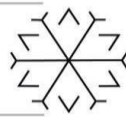
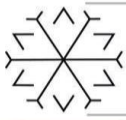
Figure2: Illustration of results for several time intervals for 3 km

5. Conclusion

In this paper, the ADE with variable coefficients in semi-infinite domain is discretized with two approaches of FVM, namely the central and upwind approaches. To assess the established model two solute dispersion problems are employed as follows: (i) solute dispersion along steady flow through inhomogeneous domain, and (ii) solute dispersion along temporally dependent unsteady flow through the inhomogeneous domain. The numerical results have compared by using the RMSE. Both of the implemented schemes calculated precise results and showed good overlap with analytical solutions. But by considering numerical outcomes of tables (2-3) it is possible to say that the outcomes of the CFVM are more accurate and reliable.

References

Gharehbaghi, A., Kaya, B., and Saadatnejadgharahassanlou, H., 2017. Two dimensional bed variation models under non-equilibrium conditions in turbulent streams. Arabian Journal for Science and Engineering, 42, pp.999-1001, DOI: DOI 10.1007/s13369-016-2258-4



Gharehbaghi, A., 2016. Explicit and Implicit Forms of Differential Quadrature Method for Advection–Diffusion Equation with Variable Coefficients in Semi-infinite Domain. *Journal of Hydrology*, 541(B), pp.935-940, DOI: 10.1016/j.jhydrol.2016.08.002

Gharehbaghi, A., 2017. Third- and fifth-order finite volume schemes for advection–diffusion equation with variable coefficients in semi-infinite domain. *Water and Environment Journal*, 31(2), pp.184-193, doi:10.1111/wej.12233

Jaiswal, D.K., Kumar, A., Kumar, N., and Yadav, R.R., 2009. Analytical solutions for temporally and spatially dependent solute dispersion of pulse type input concentration in one-dimensional semi-infinite media. *Journal of Hydro-environmental Research*, 2, pp.254–263.

Kumar, A., Kumar, D., and Kumar, J.N., 2010. Analytical solutions to one-dimensional advection–diffusion equation with variable coefficients in semi-infinite media. *J. Hydrol.*, 380, pp.330–337.

Scheidegger, A.E., 1957. *The Physics of Flow through Porous Media*, University of Toronto Press, Toronto.

Versteeg, H.K, and Malalasekera, W., 2007. *An introduction to computational fluid dynamics the finite volume method*, 2th Ed., Longman scientific & technical. New York, USA.

The Effect of Using Various Reinforcement Mesh on Fire Performance of Composite Flooring System

Burak Kaan Cirpici ^{1*}[0000-0002-4310-2782] and Melih Ermancik ²[0000-0000-0000-00000]

¹burak.cirpici@erzurum.edu.tr, Erzurum Technical University

²melih.ermancik34@erzurum.edu.tr, Erzurum Technical University

Abstract

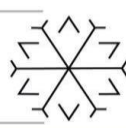
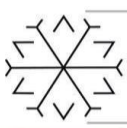
Composite floors, which have been increasingly popular in recent years, are chosen in multi-story office buildings because they provide vast volumes. They are widely used in structures with high building important coefficients because of the benefits it brings to the structure, such as fire resistance and heat insulation (school, hospital, etc.). The use of different reinforcing mesh (i.e. A142 - Ø6, A252 - Ø8 and A393 - Ø10) which is one of the potential parameters that will affect the performance of composite floors in the event of a fire, was chosen in this study, and it was determined how much the performance of a composite floor under the Standard (ISO 834) fire impact was adversely affected. While conducting the analyses, a new mathematical model is developed using Eurocode design equations and the Excel (Macros) program. The temperatures of the reinforcements (meshes) used herein the study at different depths in the concrete were obtained with vertical displacements of each mesh. Due to deflection of the floor slab, tensile membrane action develops and causes an increase in load carrying capacity. This situation was observed in this study. When A393 reinforcement mesh was used, it deflected very little for 70 minutes, and, it had a deflection of roughly 37.5 mm at the end of 90 minutes. When compared to other meshes, the usage of A393 reinforcing mesh considerably improved the fire performance of composite flooring in the applied fire over the design duration of 90 minutes considered in the mathematical model.

Keywords. Composite slab, fire performance, reinforcement mesh, tensile membrane action

1. Introduction

Since the 1920s, steel sheets have been utilized as formwork in typical reinforced concrete floors, and from the 1950s, the usage of composite floor structural elements with concrete as tension reinforcement became popular. The grooves and protrusions generated in the aforementioned steel sheets were the earliest examples of modern composite flooring in the 1960s. The construction elements are lighter and more cost effective because to advancements in the materials that make up the composite flooring system over time, as well as modifications in design standards.

Steel sheet was initially used as a permanent concrete formwork for floors of reinforced concrete structures, thus the first examples of composite floors emerged. These elements were used as different elements at different times. With the emergence of different sheet types, each country started to establish its own standards. For example, the Iron and Steel Institute of America started research on mixed records in 1967. These researches formed the basis of American, British and European standards ((ASCE), 1994, (BSI), 1990, CEN, 2005a) related to composite design systems (Yorgun, 2005). Application of fatigue loads greater than the bond load between the steel beam and shear studs in composite floors often results in shear bond rupture (Mahachi, 1994, Mahachi, 1995). Bailey and Moore (2000) investigated a new method for the design of steel-framed structures with fire-exposed composite floor slabs. Within the scope of the study, fire tests were carried out in a full-scale steel framed building. Tests have shown that the existing design procedures for the fire boundary situation are underutilized for the performance of composite flooring systems. Üstündağ and Çelik (2006) gave information about composite flooring systems used in multi-storey steel structures in their study. In the study, new systems are explained and suggestions are made according to 2006's technological advances. Yılmaz (2008) examined the positive moment carrying capacity of composite flooring elements in his MSc study. In the study, trapezoidal sheet metal elements were used in the slab, and 6 simple beam composite slab samples with a similar sheet thickness and slab height of 4.10 m were tested under the effect of vertical loads. Obtained theoretical and experimental data were compared. In the study of Cordeiro and Silva (2016), three methods to design a composite steel-concrete slab were considered and applied in a metro station. The mezzanine floor in the subway was exposed to fire for 90 minutes. Steel beams provided protection against fire. Using the results obtained, the



membrane effect was modeled using VULCAN software and the simplified Bailey method. In the experimental study of Selamet and Yolaçan (2017), they used a symmetrical joint mechanism on both sides of the composite floor designed for a high-rise steel structure, and provided a larger floor area test opportunity than the experimental area (furnace). It was determined that the concrete slab, which was subjected to the test, showed membrane behavior during fire and loading and continued its load-bearing property throughout the fire, and they suggested that the secondary (secondary) steel beams in composite floor slabs remain uninsulated. A simplified approach based on the critical temperature for the fire resistance of steel-concrete composite beams by Li and Wang (2013) was developed based on the load-bearing limit state method, by determining the critical temperature and fire protection values of the composite beams, already included in the Chinese Technical Standard for fire safety of steel structures. an approach has been proposed. The temperature on the exposed top surface of the steel sheet is particularly important when the fire is not directly exposed to the sheet (Nguyen et al., 2015, Cirpici et al., 2019a, Cirpici et al., 2019b, Cirpici et al., 2019c). However, when for some reason the fire hits the top surface of the concrete, the top of the concrete may become more important, causing cracks to form in the concrete block and spreading the fire to steel parts, including the slab and steel. This issue was discussed by Wang et al. (2021), it is still in the area of interest of researchers. Nguyen et al. (2015) developed a small-scale partially shielded composite floor with unprotected secondary and interior beams and shielded edge beams to understand slab behavior in terms of deflection and load bearing capacity with fire testing and numerical models. They concluded that the inner beams could be left unprotected as no structural deterioration could be obtained and rotational restriction along the protected edge beams caused intense stress concentration on these beams in the slab. Nguyen and Tan (2017) investigated the effect of bending stiffness of protected edge beams based on fire test and loaded numerical studies including the relationship between element temperatures and mid-span deflections. It has been determined that the slab deflection can be reduced by increasing the rigidity of the protected main beams and the composite movement between the beams plays a key role in this beneficial effect. In order to discreetly discuss the Eurocode design method and determine the capacity of the shear joint and propose a new design formula, the behavior of transverse trapezoidal sheet metal and head shear nails attached to the flooring was investigated in both ambient and fire conditions. The rotational capacity of steel I-section beams at increasing temperatures was investigated by running numerical three-dimensional models to capture the non-linear behavior of steel beams regardless of the slab type with shear studs (Pantousa and Mistakidis, 2017). Alam et al. (2018) aimed at a finite element analysis approach to model the fire behavior of unprotected and protected thin slabs. Their results reveal that shielded thin floors offer a higher fire resistance as the steel temperature remains within 400°C after 60 minutes of standard fire exposure. Jiang et al. (2018) concluded in their study that welded wire mesh reinforcement is not always necessary in composite flooring elements, but it helps to control cracking. In addition, the separation of the steel sheet from the concrete with the effect of loading at high temperatures and the pouring of the concrete due to the heat penetration due to the cracks formed and the buckling of the sheet exposed to the direct fire were stated in the test study conducted by Lim and Wade (2002). After 20 minutes of fire testing in this study, cracks propagated upwards at an angle of approximately 45 degrees from the intersection between the top of the slit and the concrete slab. Cirpici et al. (2020) performed heat transfer analyzes on the slab by affecting the Fast and Standard (ISO 834) fires from the concrete part (from the top) for 1 hour without loading the composite slab. In the numerical model they developed, they applied fire protection to the steel profile and sheet metal and obtained the temperature distributions in the structural elements of the flooring.

2. Material and Method

2.1. Temperature Predictions in Steel Beams

Unprotected Steel

$$\Delta T_{st} = k_{sh} \frac{A_m/V}{\rho_{st} C_{st}} \frac{A_s}{V} h_{net} \Delta t \quad (1)$$

k_{sh} - Correction factor for shading effect

A_m/V - Section factor (1/m)

A_m - Surface area of a unit length element (m²/m)

V - Volume of structural element unit length (m³/m)

C_{st} - Specific heat of steel (J/kgK)



ρ_{st} – unit volume mass of steel

h_{net} – Design value of net heat axis per unit area (W/m²)

Δt – Time step (sec)

- Correction factor for shadow effect in I – sections under the influence of standard fire (ISO 834);
 $k_{sh} = 0.9[A_m/V]_b/[A_m/V]$
- In all other cases; $k_{sh} = [A_m/V]_b/[A_m/V]$
- $h_{net} = \varepsilon_f \varepsilon_m$ where $\varepsilon_f = 1.0$ and ε_m should be taken from EN 1991-1-2 (CEN, 2002)

Protected Steel

According to EN 1993-1-2, the temperature of a protected steel section is calculated using Equation below.

$$\Delta T_{st} = \frac{\lambda_p A_p / V}{d_p c_{st} \rho_{st} \left(1 + \frac{\phi}{3}\right)} \frac{T_f - T_{st}}{\Delta t} - (e^{\phi/10} - 1) \Delta T_f \quad (2)$$

$$\text{with } \phi = \frac{c_p \rho_p}{c_{st} \rho_{st}} d_p \frac{A_p}{V}$$

where λ_p (W/mK) is the thermal conductivity of the fire protection material, A_p/V (m⁻¹) is the section factor of the protected steel section based on the diameter, d_p (m) is the fire protection thickness, c_p (J/kgK) and ρ_p (kg/m³) are specific heat and density of the protection material, T_f (°C) and T_{st} (°C) is the exposed fire temperature (ISO) and steel temperature respectively, Δt (s) is the time interval in seconds.

2.2. Material Thermal Properties

Steel Properties

The thermal conductivity, specific heat and density of steel structural steel has been obtained from Eurocode 3 Part 1.2 (CEN, 2005b).

- The thermal conductivity of steel is:
If steel temperature T_{st} (K) is lower than 800°C;

$$\lambda_{st} = 54 - 3.33 \times 10^{-2} T_{st} \quad (3)$$

If steel temperature is higher than 800°C;

$$\lambda_{st} = 27.3 \quad (4)$$

where λ_{st} is the steel thermal conductivity (W/mK). Figure 1 presents the thermal conductivity of steel-temperature relationship based on EN 1993-1-2.

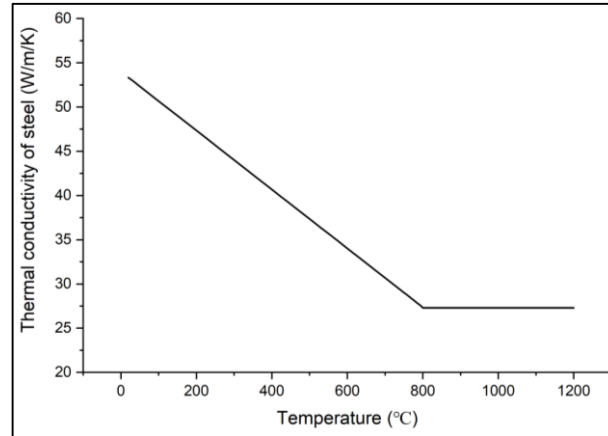
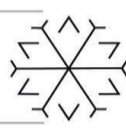
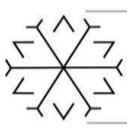


Figure 1: The change of thermal conductivity steel with temperature

- The specific heat-temperature relation is:

If $20^{\circ}\text{C} \leq T_{st} < 600^{\circ}\text{C}$;

$$C_{st} = 425 + 7.73 \times 10^{-1}T_{st} - 1.69 \times 10^{-3}T_{st}^2 + 2.22 \times 10^{-6}T_{st}^3 \quad (5)$$

If $600^{\circ}\text{C} \leq T_{st} < 735^{\circ}\text{C}$;

$$C_{st} = 666 + \frac{13002}{738 - T_{st}} \quad (6)$$

If $735^{\circ}\text{C} \leq T_{st} < 900^{\circ}\text{C}$;

$$C_{st} = 545 + \frac{17820}{T_{st} - 731} \quad (7)$$

If $900^{\circ}\text{C} \leq T_{st} < 1200^{\circ}\text{C}$;

$$C_{st} = 650 \quad (8)$$

where C_{st} is the specific heat $\left(\frac{\text{J}}{\text{kg}} \cdot \text{K}\right)$

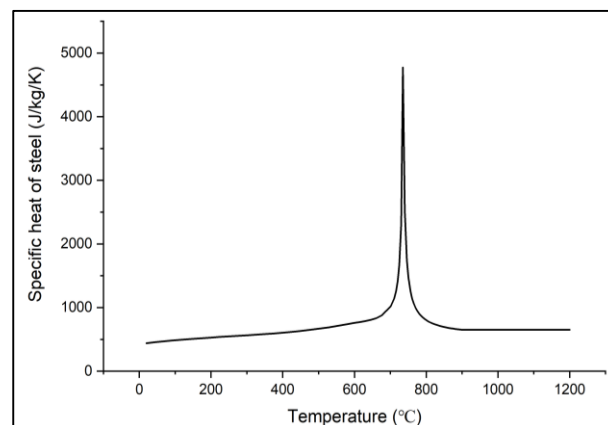


Figure 2: Specific heat of steel with the change of temperature

2.3. Theoretical Model Properties

In all analyses, 5.2 kN/m² as dead load (3.5 kN/m² + 1 kN/m² partitions + 0.7 kN/m² headlining, service spaces and flooring material) and 4 kN/m² as live load It is based on and 1,35G_k + 1,5Q_k according to Eurocode is applied for the load combination.



The properties of ATAPANEL Composite Flooring Panel (See. Figure 3) are used in the model for the sheet metal to be used in composite flooring.

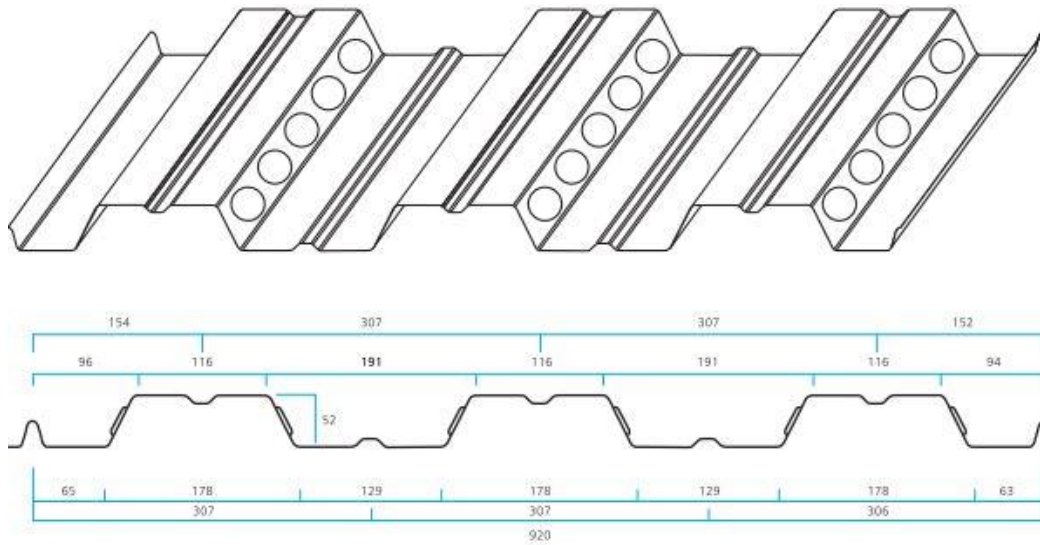


Figure 3: Features of ATAPANEL Composite Flooring Sheet

The concrete material used in the flooring is light-weight concrete and its compressive strength is C30/37 ($f_{ck} = 30 \text{ N/mm}^2$).

As a result of the structural analysis, the main beams of the steel beams used under the flooring system are IPE 360 and the secondary beams are HE 340 B, and temperature calculations for the above-mentioned variable parameters will be made over these beams. The yield strength used in the model is $f_y = 255 \text{ N/mm}^2$ for both beam profiles and reinforcement.

Fire Standard (ISO 834) applied in all developed mathematical models is the fire curve and 90 min. applied throughout. The results obtained (temperature calculations, etc.) are the results up to this time.

The rate of fire load applied in all developed models was taken as 90% (PD 6688-1-2:2007, Table A.2.) (CEN 2002).

Microsoft Excel - Macros were used to make structural calculations and make the developed mathematical model applicable.

Intumescent paint, which is one of the passive protective systems and which swells (inflates) when exposed to heat, is used as a fire protection material. The main reasons for choosing this material are; It is aesthetic, can be applied quickly, and most importantly, it can be easily applied to complex surfaces (for example, column-beam joint areas or the area between sheet metal and steel beam in composite flooring systems).

3. Results

In long span slabs considered in the mathematical model, the length of the main beam is 7.5 m and the length of the secondary beam is 7.5 m. In short span flooring systems, the length of the main beam is 7.5 m and the length of the secondary beam is 3.75 m. One secondary beam is unprotected and all main beams are fireproofed. The properties of these used reinforcements are given in Table 1 according to BS 4483 (BSI, 2005). The main difference between the them is the reinforcement sizes used.

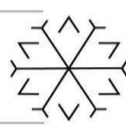
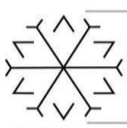


Table 1: Properties of meshes used in the composite floor model

	Mesh sizes nominal wire spacing		Wire sizes		Cross-sectional area per meter width (m ²)		Weight (1/m ²)
	Main (mm)	Cross (mm)	Main (mm)	Cross (mm)	Main (mm)	Cross (mm)	kg
A142 (Ø6)	200	200	6	6	142	142	2,22
A252 (Ø8)	200	200	8	8	252	252	3,95
A393 (Ø10)	200	200	10	10	393	393	6,16

3.1. A142 (Ø6) Reinforcement Mesh Results

The average depth temperature is usually taken as the basis, and the temperature value for short span analysis is 397.1°C for A252. According to Eurocode 4 Part 1.2 Table 3.4, the strength drop coefficient at this temperature is 0.942. Compared to the this results of the reinforcement temperature at different depths in the long span section, lower temperatures were obtained when A142 rebar mesh was used after 90 minutes (Figure 4(b) and Table 2). This shows that the reinforcement mesh has a positive effect on the fire performance of the composite flooring in this case. Higher temperatures were obtained when A393 reinforcing mesh was used ((Figure 4(c) and Table 2) due to the cross-sectional area.

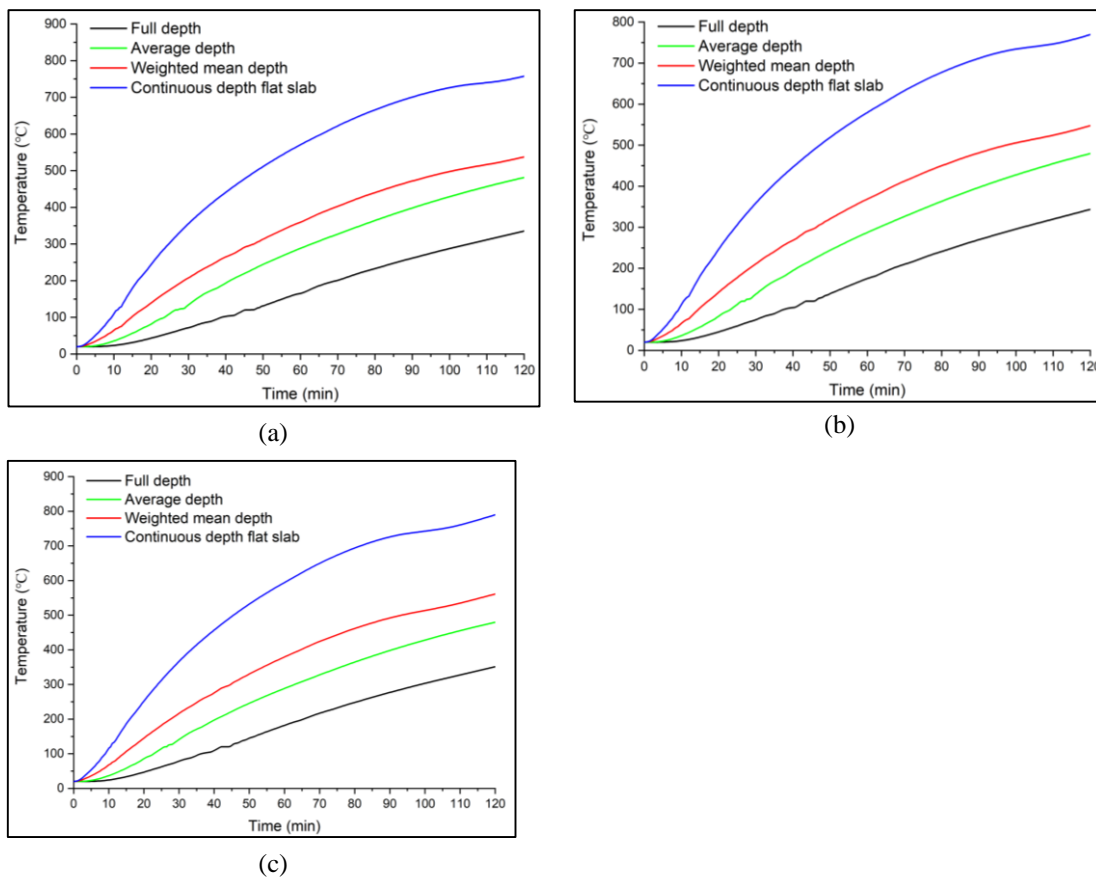
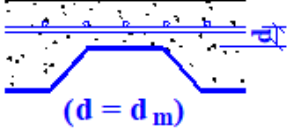
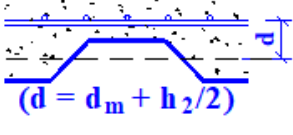
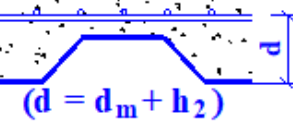
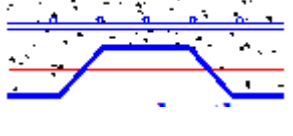


Figure 4: Temperatures of reinforcements (meshes) at different depths in concrete (a) A142 (b) A252 (c) A393

**Table 2:** Reinforcements (mesh) temperatures after 90 minutes at different heights in A142 (Ø6), A252 (Ø8) and A393 (Ø10) reinforced composite flooring

	A142	A252	A393	
Span	Temperature (°C)	Temperature (°C)	Temperature (°C)	Depth Locations
Continuous depth	697.4	711.6	725,9	 (d = d _m)
Average depth	396.1	397.1	398,1	 (d = d _m + h ₂ /2)
Full depth	237.6	269.6	277,0	 (d = d _m + h ₂)
Weighted mean depth	457.7	481.3	492,0	

TSlab deflection calculation was also done according to the study of Newman et al. (2006). In this calculation, the lowest surface temperature and the upper surface temperature of the flooring and its dimensional properties are considered.

$$v = \frac{\alpha(T_2 - T_1)l^2}{19.2h} + \sqrt{\frac{0.5f_y}{E_{t=20^\circ\text{C}}} \times \frac{3}{8}L^2} \quad (9)$$

According to the vertical displacement shown in Figure 5(a), the use of small diameter reinforcement (A142 - Ø6) caused a displacement of approximately 480 mm at the end of 90 minutes. This, of course, is an undesirable situation for the composite flooring system. The flooring was able to protect itself in the applied fire for an average of 50 minutes. The displacement resulting from the 90-minute design was 181.4 mm and exceeded the allowable displacement amount (160.9 mm) for A252 – Ø8 (Figure 5(b)). According to the vertical displacement shown in Figure 5(c), the use of large diameter reinforcement (A393-Ø10) caused a very little deflection for approximately 70 minutes, resulting in a displacement of approximately 37.5 mm at the end of 90 minutes. Of course, this is a very positive result and a desirable situation for the composite flooring system. As long as the duration of the applied fire, that is, 90 minutes, the flooring was able to protect itself in the applied fire and even 120 minutes. did not reach the permissible amount of deflection at the end. The use of A393 reinforcement mesh as fire performance significantly increased the performance of composite flooring.

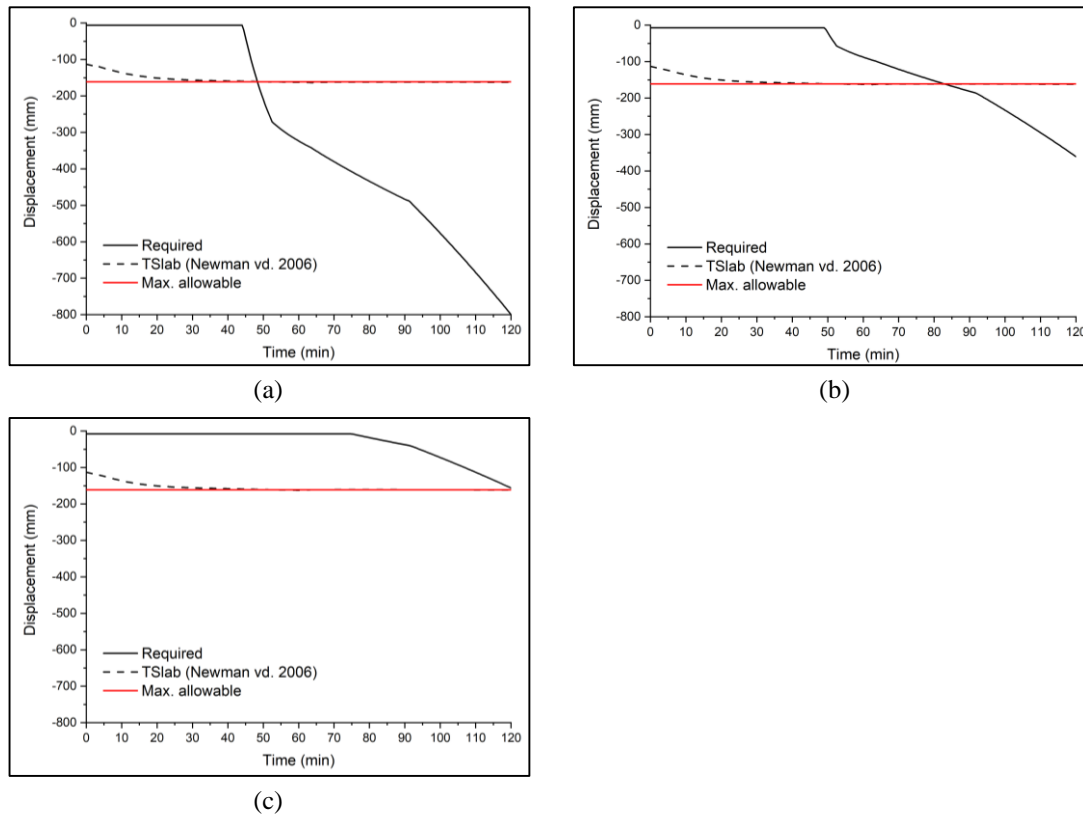
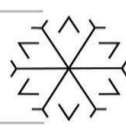
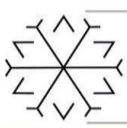


Figure 5: Vertical displacement of slab over time (a) A142 mesh (b) A252 mesh and (c) A393 mesh

4. Conclusion

Different reinforcement meshes and sizes (A142, A252 and A393) are used within the concrete block at the top of the composite flooring system. When both are compared, it is concluded that the use of A393 reinforcing mesh contributes significantly to the load carrying capacity of the flooring. In addition, higher temperatures were obtained when larger reinforcement diameters were used at different depths (full depth, average depth, weighted average depth and continuous depth) in the concrete. This shows that the fire performance of the flooring increases well. When A393 reinforcement mesh is preferred, it deflected very little for 70 minutes, and this value made a deflection of approximately 37.5 mm at the end of 90 minutes. During the design period of 90 minutes considered in the mathematical model, the flooring was able to protect itself in the applied fire. It was concluded that the use of A393 reinforcement mesh significantly increased the fire performance of composite flooring compared to other meshes.

References

- (ASCE), A. S. O. C. E. 1994. Standard for the Structural Design of Composite Slabs and Standard Practice for Construction and Inspection of Composite Slabs.
- (BSI), B. S. I. 1990. British Standard BS 5950, Structural Use of Steelwork in Buildings, Part 8: Code of Practice for Fire Resistant Design. London.
- (BSI), B. S. I. 2005. British Standard BS 4483:2005, Steel fabric for the reinforcement of concrete - Specification. London.
- Alam, N., Nadjai, A., ALI, F. and NADJAI, W., 2018. Structural response of unprotected and protected slim floors in fire. *Journal of Constructional Steel Research*, 142, 44-54.
- Bailey, C. and Moore, D. B., 2000. The structural behaviour of steel frames with composite floorslabs subject to fire: Part 1: Theory. *The Structural engineer*, 78, 19-27.
- CEN 2002. EN 1991-1-2:2002 Eurocode 1: Actions on structures. Part 1.2: General actions - Actions on structures exposed to fire. BSI: London.



- CEN 2005a. EN 1993-1-1: Eurocode 3. Design of Steel Structures. Part 1-1: General rules and rules for buildings. BSI: London.
- CEN 2005b. EN 1993-1-2: Eurocode 3. Design of Steel Structures. Part 1.2: General Rules - Structural fire design. BSI: London.
- Cırpıcı, B. K., Orhan, S. N. and Kotan, T., 2019a. Numerical Modelling of Heat Transfer Through Protected Composite Structural Members. International Civil Engineering and Architecture Conference 2019 (ICEARC 2019). Trabzon-Turkey.
- Cırpıcı, B. K., Orhan, S. N. and Kotan, T., 2019b. Numerical modelling of heat transfer through protected composite structural members. Challenge Journal of Structural Mechanics, 5, 96-107.
- Cırpıcı, B. K., Orhan, S. N. and Kotan, T., 2019c. Thermal performance of protected composite slab-beam systems exposed to fire. 3rd International Conference on Advanced Engineering Technologies, 2019c Bayburt-Turkey.
- Cırpıcı, B. K., Orhan, S. N. and Kotan, T., 2020. Finite element study on composite slab-beam systems under various fire exposures. Steel and Composite Structures, 37.
- Cordeiro, L. C. S. and Silva, V. P., 2016. Sobre o dimensionamento de laje mista de aço e concreto em situação de incêndio. Revista da Estrutura de Aço, 5, 39-58.
- Jiang, J., Mam, J. A., Weigand, J. M. and Sadek, F. H., 2018. Thermal performance of composite slabs with profiled steel decking exposed to fire effects. Fire Safety Journal, 95, 25-41.
- Li, G.-Q. and Wang, W.-Y., 2013. A simplified approach for fire-resistance design of steel-concrete composite beams. Steel and Composite Structures, 14, 295-312.
- Lim, L. and Wade, C., 2002. Experimental Fire Tests of Two-Way Concrete Slabs. In: LIMITED, B. (ed.) Fire Engineering Research Report 02/12. Porirua City, New Zealand: University of Canterbury.
- Mahachı, J., 1994. Response of composite bond-deck slabs to fatigue load. 5th International Conference on Steel Structures, Indonesia. 177-182.
- Mahachı, J., 1995. A comparison of two decking profiles subjected to fatigue load. RILEM International Conference on Dynamic Behaviour of Concrete Structures, Slovakia. 210-211.
- Newman, G. M., Robinson, J. T. and Bailey, C. G., 2006. Fire safe design: A new approach to multi-storey steel-framed buildings. UK: The Steel Construction Institute.
- Nguyen, T. T. and Tan, K. H., 2017. Behaviour of composite floors with different sizes of edge beams in fire. Journal of Constructional Steel Research, 129, 28-41.
- Nguyen, T. T., Tan, K. H. and Burgess, I. W., 2015. Behaviour of composite slab-beam systems at elevated temperatures: Experimental and numerical investigation. Engineering Structures, 82, 199-213.
- Pantousa, D. and Mistakıdı, E., 2017. Rotational capacity of pre-damaged I-section steel beams at elevated temperatures. Steel and Composite Structures, 23, 53-66.
- Selamet, S. and Yolaçan, T. F., 2017. Çelik-Beton Kompozit Kat Döşemesi Yangın Dayanım Deneyi. Teknik Dergi, 8007-8022.
- Üstündağ, C. and Çelık, O. C., 2006. Çok Katlı Çelik Yapılarda Kullanılan Kompozit Döşeme Sistemleri. Yapı Dergisi, 293, 88-92.
- Wang, Y., Jiang, Y., Huang, Z., Li, L., Huang, Y., Zhang, Y., Zhang, G., Zhang, X. and Duan, Y., 2021. Post-fire behaviour of continuous reinforced concrete slabs under different fire conditions. Engineering Structures, 226.
- Yılmaz, S., 2008. Kompozit Döşeme Elemanlarda Pozitif Moment Taşıma Kapasitesinin İrdelenmesi. MSc, İstanbul Teknik Üniversitesi.
- Yorgun, C., 2005. Çelik Sac-Beton Kompozit Döşeme Sistemlerinin Uygulamalarına Yönelik Değerlendirmeler. TÜRKİYE MÜHENDİSLİK HABERLERİ, 435, 60-64.

Clays and Polymer/Clay Nanocomposites and Their Application in Engineering

Babak KARIMI GHALEHJOUGH ^{1*}[0000-0001-7897-9085] and Hayrettin EROĞLU ²[0000-0001-8197-4162]

¹karimi.babak@gmail.com, Civil Engineering Department, Erzurum Technical University

²hayrettin.eroглу@erzurum.edu.tr, Chemical Engineering Department, Erzurum Technical University

Abstract

Clays as one the cheap and accessible materials is used at different sectors such as civil, geology, geotechnical engineering, industry and health sectors. Usage of clays and clay nanocomposites (CNPs) are developing every day. Nano material obtained from clays and polymer in nano dimension have significant improved properties that are different from main materials. Different kinds of polymers are using with clay for preparing new kinds of CNPs. Different properties can be characterized as properties of clay minerals such as: plasticity, hardening on firing or drying, layered structure of particle, anisotropic particles or layers. Existence of several types of surfaces and easy modification of external and internal surface by methods like adsorption or ion exchange are some other properties of clay minerals. These properties can be changed by use of different types of polymers. These polymers are categorized in groups of vinyl polymers, condensation polymers and rubbers, polyolefins, specialty polymers and biodegradable polymers. Each of above-mentioned group has its own subgroup of polymers with different properties. Final characteristics of CNPs like mechanical, dynamic, swelling, plasticity, heat resistance and strength, gas permeability and moduli can be improved according to final purpose of CNPs preparation.

Keywords. Clay, clay nanocomposites, polymer, CNP

1. Introduction (Heading 1)

Clay as one the accessible and cheap materials is used at different sectors such as geology, geotechnical engineering, industry, health and etc. Up to recent years the main focus of clay researches was on geotechnical, geological and mineralogical aspects of this material. On past few decades, clay science is focusing on physico-chemical orientation and rapid development of this area has sown its effect on different sectors. New properties of clay and clay nanocomposites and its interaction with different materials at different condition lead to clay getting enough attention that scientists at different fields of science start working on it. The results of researches and new studies are publishing at different national and international journals or conferences. On this way, getting information about new properties of clay or clay minerals is necessary for anyone who is in contact with this material. Civil engineers, specially geology, geotechnical and material engineers are the groups that are facing with clay in lots of their projects. So, having enough information about clay such as types, properties, modification methods and its application at different condition is undeniable. Clays have two main properties that made them interesting. 1: their availability and 2: their different extraordinary properties that made them can be used for different purposes. This paper is going to present some general and new properties of clay that can be used at field of civil engineering.

It seems that Georgius Agricola who is known as founder of geology was the first one who presented a formalized definition to clay. Other most famous definition was made by nomenclature committees (JNCs) of the Association Internationale pour l'Etude des Argiles (AIPEA) and the Clay Minerals Society (CMS). Regarding to JNCs definition clay is a natural material made of very fine-grained minerals that has plastic properties at appropriated water content and will be harden while firing or drying (Guggenheim and Martin, 1995).

At unified soil classification system (USCS), materials with particle size less than $2\mu\text{m}$ ($<2\mu\text{m}$) is defined as clay. Although size of the particles is the key parameter in all definitions of clay but according to JNCs definition, clays should have plasticity and hardening properties during drying or firing and materials with just particle size smaller than $2\mu\text{m}$ or clay-like materials without above properties will not defined as clay.

Ability to change into a special or certain shape without rupturing during applying stress and retaining ruptured shape after removing the stress is defined as plasticity of clay and can be affected by different factors such as particle aggregation and chemical composition. Plasticity can be measured is different ways



in different industries. For examples in engineering it is expressed in terms of plasticity index that is the different between liquid and plastic limits ($PI=LL-PL$), while in ceramics industry it is commonly measured as liquid and plastic limits (water of plasticity).

Different properties can be characterized as properties of clay minerals such as:

1. Plasticity
2. Hardening on firing or drying
3. Layered structure of particles (It is one dimension between 0.7nm to 1nm)
4. Anisotropic particles or layers
5. Existence of several types of surfaces
6. Easy modification of external and internal surface by methods like adsorption or ion exchange

At the same time, it should be mentioned that there are some types of solids like alkali silicates, crystalline, phosphates and silicic acids, that have similar properties of phyllosilicates such as interaction potential, charge characteristics and structure of layers but they are not clays (Lagaly and Beneke, 1991; Schwieger and Lagaly, 2004). Another point that should be mentioned is that, because of sharing many attributes, clay minerals can be confused with zeolites. Both of them can be modified, synthesized and tailored by physical, chemical and thermal treatments. Not only clay that its interaction with extraneous substance is interesting. This interaction can be influenced by different factors such as ionic strength, pH, temperature or pressure that can be occur at different states of plasma, gas, liquid, melted solid or solid (Dixon and Schulze, 2002).

2. Structure of Clay Minerals

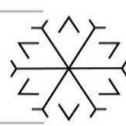
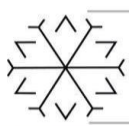
Depending on clays mining source, large number of clays with different properties can be formed. Clay are part of hydrous phyllosilicate group of minerals that have silica, alumina and water. At the same time there are variable number of inorganic ions like Mg^{2+} , Na^+ , Ca^{2+} in clay minerals too. These particles contain metal cations and anionic layered silicates. These minerals can be described by presence of two-dimensional sheets, octahedral (Al_2O_3) and tetrahedral (SiO_4). The silicon–oxygen tetrahedron consists of silicon surrounding by four oxygen atoms and unite to form the silica sheet. Aluminum or magnesium octahedron consists of aluminum surrounding by six hydroxyl units and combine to form gibbsite sheet (If aluminum is main dominating atom) or brucite sheet (If magnesium is main dominating atom) (Guggenheim and Martin, 1995). Some cation exchange capacity and specific area of clay minerals has been shown in Table.1.

Different clay minerals can be gained and categorized based on presence of tetrahedral and octahedral layer in clay structure. There are 4 main groups of clay as below (Kumari and Mohan, 2021).

- 1- **Kaolinite Group**
- 2- **Montmorillonite/Smectite Group**
- 3- **Illite Group**
- 4- **Chlorite Group**

The distinctive crystal structure of clays and very small size of clay minerals lead to unique properties of clays such as swelling behavior, high cation exchange capacity, adsorption capacity and specific surface area and etc. Even most chemical and physical properties of the soils are because of presence of clay minerals in the soil (Klein and Hurlbut, 1985).

Kaolinite or China clay is one the clay minerals with $Si_4Al_4O_{10}(OH)_8$ chemical formula. Generally, it is white and soft kind of clay minerals and there is no charge in ideal form of kaolinite. Due to the hydrogen bonding the structure of Kaolinite is fixed. So there is low shrink-swell capacity and no expansion between the layers when it contacts with water. At the same time this kind of clay mineral has low cation exchange capacity (< 1 centimole/kg), surface areas and capacity to adsorb the ions. The other rare forms of kaolinite are dickite and nacrite that chemically are similar to kaolinite [Perry, 2011; Layerd Silica Clays, 2020].

**Table 1:** Cation exchange capacity and specific area of clay minerals (Kumari and Chandra, 2021)

Cation Exchange Capacities (CEC) and Specific Surface Areas of Clay Minerals		
Mineral	Cation-Exchange Capacity at pH 7 (milliequivalents per 100 grams)	Specific Surface Area (square meters per gram)
Kaolinite	3-15	5-40
Halloysite	40-50	1,100
Illite	10-40	10-100
Chlorite	10-40	10-55
Vermiculite	100-150	760
Smectite	80-120	40-800
Palygorskite-Sepiolite	3-20	40-180
Allophane	30-135	2,200
Imogolite	20-30	1,540

Smectite group of clays with general structural formula of $(\text{Na}, \text{Ca})_{0.33} (\text{Al}, \text{Mg})_2 \text{Si}_4 \text{O}_{10} (\text{OH})_2 \cdot (\text{H}_2\text{O})_n$ are mainly based on dioctahedral (Montmorillonite) or trioctahedral (Saponites) structure. High surface area, cation exchange capacity (CEC), adsorption, swelling and shrinkage capacity are some main properties of this group. For example, the CEC for Montmorillonite changes from 80 to 100 milliequivalent per 100 grams and it has very poor thermal stability. Bentonite clay is one the most important types of smectite group that consisting 98% of montmorillonite and is divided to different types based on its respective dominant element such as aluminum, calcium sodium and potassium. So, there are three types or classes of calcium, sodium and potassium bentonite [Guggenheim and Martin, 1995; Murray, 2006]. Because of excellent colloidal properties, sodium bentonite expands during contacting with water by absorbing the water several times of its dry mass. It is known as drilling mud and used in boreholes for geotechnical investigations [Odom, 1984]. Calcium bentonite is a useful adsorbent for fats, ions, and oils [Theng, 1979]. It can be converted to sodium bentonite by ion exchange process (Adding 5–10% of a soluble sodium salt (Sodium carbonate is an example) to wet bentonite and mixing for a certain time the ion exchange will take place) that lead to showing many properties of sodium bentonite. Properties of converted calcium bentonite may not be fully comparable with natural sodium bentonite [Odom, 1984; Lagaly, 1995]. Potassium bentonite is known as K-bentonite or potash bentonite that is considered as potassium-rich illitic clay and formed from alteration of volcanic ash.

3. Characteristics of Clay Minerals

Different properties can be mentioned as characteristics of clay minerals. They can be listed as below:

- **Cation Exchange Capacity (CEC):** is the ability of adsorbing certain anions/cations that depends on negative or positive charge deficiency in clay mineral structure.
- **Swelling Capacity:** is the capacity of adsorbing water in controlled environment that lead to water to be added into interlayer space of clay mineral. This water cause expansion or swelling of interlayers. Swelling capacity depends on hydration energy forces associated with the particle's interaction [Karpinski and Szkodo, 2015].
- **Surface Charge Properties:** Affects different chemical properties of clay by changing the quantity of surface and electrical charge density [Karak et al., 2005].



- **Adsorptive Properties:** Clay mineral shows noncovalent in 3 different ways of physical adsorption, ion exchanges and addition of small molecules in pore and partial elimination [Aboudi Mana, 2017].
- **Specific Surface Area (SSA):** is the surface area of clay particles per unit volume or mass of dry clay that shown in m^2/m^3 or m^2/gr units. Clay minerals have high SSA [Gunal and Ransom, 2006].
- **Plasticity:** is the deformation of shape of clay under a finite loading or force. This property is affected by type of clay minerals, specific surface, particle size distribution and characters of water such as surface tension and viscosity [Andrade et al., 2011].
- **Dispersion/Flocculation:** that is defined as a system that liquid/solid particles are dispersed into the continuous phase of liquid/solid/gas [Rengasamy and Olsson, 1991].

4. Clay Nanocomposites

Organic and inorganic hybrid materials was one the most interesting topics in last decade that research activities in complex system of atomic and nanometer (molecular) scale specially based on silicates and silica are still continuing. The application of molecular engineering that new kinds of materials with new properties can be obtained [Ruiz-Hitzky, 1981]. Composite material are solid materials gain from combination of few simple materials that have properties different from properties of components taken separately [Ruiz-Hitzky, 2003; 2004]. Clay nanocomposites are polymer/clay nanocomposites (PCNs) that are new category or class of materials that have new interesting and excellent properties such as less gas permeability, high dimensional stability and enhanced mechanical properties in comparison with clay or pure polymer [Manias et al., 2001; LeBaron et al., 1999].

There are different ways to developing PCNs by use of different combination of matrix polymers and organoclays like polybenzoxazine, polypropylene (PP), polystyrene, epoxy polymer resin, polystyrene (PS) and liquid crystalline polymers (LCP). There are three technologies to gain PCNs.

- 4.1. **Intercalation of Polymer or Prepolymer from Solution:** that based on soluble pre-polymer or polymer and swellable silicate layers. First the silicate swollen in a solvent and then mixed with polymer. The polymer chains intercalate and displace the solvent and by removing the solvent PCNs will be resulted.
- 4.2. **In-situ Intercalative Polymerization Method:** an organoclay will be swollen in a liquid monomer and polymer will form between intercalated sheets. Polymerization can be started by cation exchange by help of heat or radiation before the swelling step by the monomer.
- 4.3. **Melt Intercalation Method:** that involves annealing, under shear or statically, a mixture of the organoclay and polymer above the softening point of the polymer [Polymer/Clay Nanocomposites, Masami Okamoto, Toyota Technological Institute].

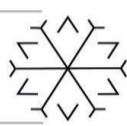
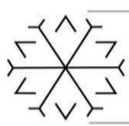
5. Types of Polymers Used for Polymer/Clay Nanocomposite Preparation

5.1. Vinyl Polymers

- 5.1.1. Poly methyl methacrylate (PMMA)/Clay Nanocomposites
- 5.1.2. Polystyrene (PS)/Clay Nanocomposites
- 5.1.3. Poly styrene-co-acrylonitrile (SAN) /Clay Nanocomposites
- 5.1.4. Poly vinyl alcohol (PVA) /Clay Nanocomposites
- 5.1.5. Block Copolymer/Clay Nanocomposites

5.2. Condensation Polymers and Rubbers

- 5.2.1. Nylon/Clay Nanocomposites
- 5.2.2. Poly ϵ -caprolactone (PCL)/Clay Nanocomposites
- 5.2.3. Poly ethylene terephthalate (PET)/Clay Nanocomposites
- 5.2.4. Poly butylene terephthalate (PBT)/Clay Nanocomposites
- 5.2.5. Poly ethylene oxide (PEO)/Clay Nanocomposites
- 5.2.6. Polycarbonate (PC)/Clay Nanocomposites
- 5.2.7. Liquid crystalline polymers (LCP)/Clay Nanocomposites
- 5.2.8. Polybenzoxazole (PBO)/Clay Nanocomposites
- 5.2.9. Thermoset Epoxy/Clay Nanocomposites
- 5.2.10. Poly dimethyl siloxane (PDMS)/Clay Nanocomposites



5.2.11. Polyurethanes (PU)/Clay Nanocomposites

5.2.12. Polyimide/Clay Nanocomposites

5.3. Polyolefins

5.3.1. Polypropylene (PP)/Clay Nanocomposites

5.3.2. Polyethylene (PE)/Clay Nanocomposites

5.4. Specialty Polymers

5.4.1. Poly N -vinylcarbazole (PNVC)/Clay Nanocomposites

5.4.2. Polyaniline (PANI)/Clay and Polypyrrole (PPY)/Clay Nanocomposites

5.4.3. Hyperbranch polymers (HBP)/Clay Nanocomposites

5.5. Biodegradable Polymers

5.5.1. Polylactide (PLA)/Clay Nanocomposites

5.5.2. Poly butylene succinate (PBS)/Clay Nanocomposites

Detailed information about above PNCs is presented at clay nanocomposites reported by Toyota technological institute.

6. Properties of Polymer/Clay Nanocomposites

Generally, because of interfacial interaction between matrix and layered silicate, PNCs consist of clay and polymers have remarkable improved material and mechanical properties in comparison with polymers or layered silicates. These improved properties can include increased heat resistance and strength, less gas permeability and high moduli.

Remarkable improved mechanical properties of NPC are dynamic mechanical property that is a response of materials to cyclic loading or deformation (tension–torsion). In dynamic mechanical analysis three main parameters are important. (a) elastic response to the deformation (G') that is known as storage module, (b) plastic response to the deformation (G'') that is known as loss modulus and (c) (G''/G') ratio that is using for determining of occurrence of molecular mobility transitions.

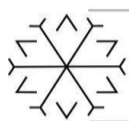
The other mechanical property is tensile modulus of PNCs. For example, because of strong interaction between matrix and silicate layers via formation of hydrogen bonds, Nylon 6 matrix and various nanocomposites (N6CNs) has remarkable tensile strength. Another property of polylactide (PLA) and PLACNs is their flexural properties that reported by Ray et al (2003). Heat distortion temperature (HDT) is an index of heat resistance toward applied load. HTD of PCNs can be increased significantly. PCNs have improved thermal stability in comparison with normal polymers or clays. Other improved properties of MMT based nanocomposites is reduction in flammability. Nano-clays and PCNs can have effect on gas barrier property, ionic conductivity, optical transparency, increasing scratch resistance, dimensional stability and solvent resistance [Sinha, 2003].

7. Conclusion

Clay as one the accessible and cheap materials in the world can be used for different goals in civil engineering. Preparing various types of PCNs by use of different kinds of polymers give new significant properties to the final nanomaterial. Nanocomposites can be used separately or with other materials as additives. Dependent on purpose of improvement different properties can be obtain by use of different kinds of polymers. Although there are lots of studies have been done at this field, but there is still new methods or properties can be studied. In engineering, by working on the properties of materials used in civil engineering, better properties or even new kinds of materials can be reached.

References

- Aboudi Mana, S.C., Hanafiah, M.M. and Chowdhury, A.J., 2017. Environmental characteristics of clay and clay-based minerals. *Geology Ecology and landscape*, 1,p155-161. DOI: <https://doi.org/10.1080/24749508.2017.1361128>
- Andrade, F.A., Al-Qureshi, H.A. and Hotza, D., 2011. Measuring the plasticity of clays: A review. *Applied Clay Science*, 51, p1-7. DOI: <https://doi.org/10.1016/j.clay.2010.10.028>
- Dixon, J.B. and Schulze, D.G. (Eds.), 2002. *Soil Mineralogy with Environmental Applications*. Soil Science Society of America, Madison, WI.
- Guggenheim, S. 'Introduction to the properties of clay mineral. Available', from http://www.minsocam.org/msa/Monographs/Mngrph_03/MG003_371-388.pdf
- Guggenheim, S. 'Introduction to the properties of clay mineral'. Available from http://www.minsocam.org/msa/Monographs/Mngrph_03/MG003_371-388.pdf



- Guggenheim, S. and Martin, R.T., 1995. Definition of clay and clay mineral: joint report of the AIPEA nomenclature and CMS nomenclature committees. *Clays and Clay Minerals*, 43, p255–256 and *Clay Minerals* 30, p257–259.
- Gunal, H. and Ransom, M.D., 2006. Clay mineralogy, specific surface area and micromorphology of polygenetic soils from eastern Kansas. *Archives of Agronomy and Soil Science*, 51, p459-468. DOI: <https://doi.org/10.1080/03650340500186439>
- Karak, T., Das D.K., Singh, U.K. and Maiti, D., 2005. Influence of pH on soil charge characteristics and Cadmium sorption in some noncontaminated soil of indian subtropics. *Scientific World Journal*, 5, p183–194. doi: 10.1100/tsw.2005.26
- Karpinski, B. and Szkodo, M., 2015. Clay minerals – Mineralogy and phenomenon of clay swelling in oil and gas industry. *Advanced in material science*, 15,p37-55. DOI: <https://doi.org/10.1515/adms-2015-0006>
- Klein, C. and Hurlbut, C., 1985. *Systematic Mineralogy Part IV: Silicates*. Manual of Mineralogy, 20th Ed. John Wiley and Sons: New York, p366-467
- Kumari, N and Mohan, C., 2021. Basics of Clay Minerals and Their Characteristic Properties. IntechOpen, DOI: 10.5772/intechopen.97672. Available from: <https://www.intechopen.com/online-first/76780>
- Lagaly, G., 1995. Surface and interlayer reactions: bentonites as adsorbents. Churchman, GJ, Fitzpatrick RW, Eggleton RA (ed). *Clays Controlling the Environment*. Proceedings of the 10th International Clay Conference, Adelaide, Australia, p137-144
- Lagaly, G. and Beneke, K., 1991. Intercalation and exchange reactions of clay minerals and non-clay layer compounds. *Colloid and Polymer Science*, 269, p1198–1211.
- Layer silicate clays – Genesis and classification. Available from <http://ecoursesonline.iasri.res.in/Courses/Introduction%20to%20Soil%20Science/SSAC121/Data%20Files/lec15.pdf> , (Accessed on 2020-07-30)
- LeBaron, P.C., Wang, Z. and Pinnavaia, T., 1999. *J. Appl. Clay Sci.* 15, p11.
- Manias, E., Touny, A., Wu, L., Strawhecker, K., Lu, B. and Chung, T. C., 2001. *Chem. Mater.* 13, p3561.
- Murray, H.H., 2006. Structure and composition of clay minerals and their physical and chemical properties. *Applied clay mineralogy – occurrence, processing and applications of Kaoline, Bentonite, Polygonskite-Sepiolite and common clays*. Haydn H Murray.p7-31. Doi:10.1016/s1572-4352(06)02002-2
- Odom, I.E., 1984. Smectite clay minerals: Properties and uses. *Philosophical transactions of the Royal Society. Mathematical, physical and Engineering Sciences*, p311:391. doi:10.1098/rsta.1984.0036. JSTOR 37332
- Perry, D.L., 2011. *Handbook of Inorganic Compounds*. 2nd ed. Boca Raton: Taylor & Francis.
- Masami Okamoto. *Polymer/Clay Nanocomposites*. Toyota Technological Institute, Tempaku, Nagoya, Japan
- Rengasamy, P. and Olsson, K.A., 1991. Sodicity and soil structure. *Australian journal of soil research*, 29, p935-952. DOI: <https://doi.org/10.1071/SR9910935>
- Ruiz-Hitzky, E., 1988. Génie cristalline dans les solides organo-minéraux. *Molecular Crystals and Liquid Crystals*, 161, p433–452.
- Ruiz-Hitzky, E., 2003. Functionalizing inorganic solids: towards organic-inorganic nanostructured materials for intelligent and bio-inspired systems. *The Chemical Records* 3, p88–100.
- Ruiz-Hitzky, E., 2004. Organic-inorganic materials: from intercalations to devices. In: Gómez-Romero, P., Sánchez, C. (Eds.), *Functional Hybrid Materials*, Chapter 2. Wiley-VCH, Weinheim, p15–49.
- S. Sinha Ray, S., Yamada, K., Okamoto, M. and Ueda, K., 2003. *Polymer* 44, p857.
- Schwieger, W. and Lagaly, G., 2004. Alkali silicates and crystalline silicic acids. In: Auerbach, S.M., Carrado, K.A., Dutta, P.K. (Eds.). *Handbook of Layered Materials*, Marcel Dekker, New York, p.541–629.
- Theng, B.K.G., 1979. *Formation and properties of clay polymer complexes*. Elsevier.

Experimental Behaviour of Screw Beam-to-Column Connections in Cold-Formed Steel Under Cyclic Loading - A review

Mustafa Ensar TAVLAŞOĞLU ^{1*}, Merve SAĞIROĞLU MAALI^[0000-0001-8717-0800] and Mahyar MAALI ¹
[10000-0002-6398-1139]

^{1*}mustafa.ensar.tavlasoglu@gmail.com, Erzurum Technical University, Faculty of Engineering and Architecture, Civil
Engineering Department, Erzurum, Turkey

¹merve.sagiroglu@erzurum.edu.tr, Erzurum Technical University, Faculty of Engineering and Architecture, Civil
Engineering Department, Erzurum, Turkey

¹mahyar.maali@erzurum.edu.tr, Erzurum Technical University, Faculty of Engineering and Architecture, Civil Engineering
Department, Erzurum, Turkey

Abstract

The Cold formed steel sections, they are light construction materials that are formed by rolling or pressing steel plates at ambient temperature. Cold-formed steel (CFS) materials have been widely used due to their good mechanical and seismic performance, high corrosion resistance and aesthetic appearance. However, due to the early buckling behavior of the elements, it is generally used in low-rise structures today. In this paper, experimental and theoretical studies to investigate the behavior of screw beam-to-column connections in cold-formed steel under cyclic and seismic loadings are reviewed. The moment-rotation behavior of the connections are investigated under these loadings, the information was contributed to the high strength and ductility of the CFS connections has been examined. In general, there is a lack of knowledge about the structural behavior of cold-formed steel connections. So, there are still some knowledge gaps that need to be examined by future comprehensive research. The presented articles and research can help to better understand and improve connection behaviours of CFS structures.

Keywords. Cold-formed steel, steel connection, cyclic loading behaviours, loading protocol, moment-rotation

1. Introduction

Steel construction materials are divided into two as hot-formed steel and cold-formed steel according to the forming methods in the manufacturing processes. Producing of hot formed steel sections, roller hearth furnaces are used. However, the production of cold-formed steel sections is done at ambient temperature. In cold forming, the desired sections are obtained because of plastic deformation of the steel. Pressing methods or roller forming are used to create profile of sections. The most commonly used profiles are C, U, Z and L section profiles. In need, new sections can be created by combining different profiles. The thickness of cold-formed steel sections generally varies between 0.5 mm and 10 mm. The preferred length in the production of cold formed steel sections varies between 6 meters and 12 meters. It is usually galvanized, so that, it becomes more resistant to corrosion. Cold-formed steel reduces the dead weight of the building because it is lighter than traditional building materials. It is less affected by seismic forces than other structural elements. Therefore, it is also used in regions that have high earthquake risk. In the forming process, the hardening that occurs due to cold forming increases the yield strength of the steel. Therefore, the strength of cold-formed steel per unit weight is higher than that of hot rolled steel.

In cold forming, significant changes occur in the mechanical structure of the material, especially for the corner regions of the material. It is the fact that the corner regions of the material are more affected by plastic deformation than the flat regions.

After any load is applied and removed on the material, the residual stresses on this material have a high importance in cold steel profiles. When compared, cold formed steel profiles that is under the no-load and the after the loading of CFS, residual stresses occurring in the cold-formed material, especially in the corner



regions, provide an increase in the yield strength of these regions. The representation of bending residual stresses as a percentage of yield strength in a cold-formed profile is shown in Figure 1.

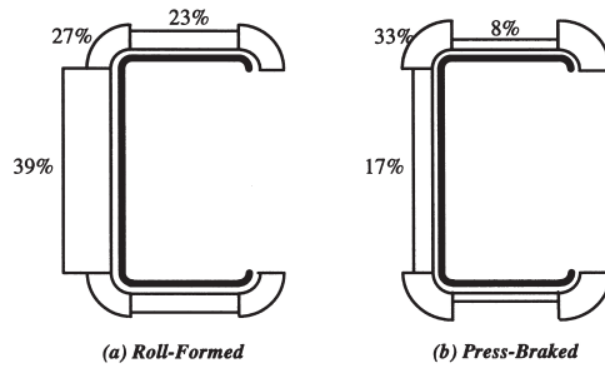


Figure 1. The representation of bending residual stresses as a percentage of yield strength in a cold-formed profile

This increase is the result of a good incorporation of the cold formed process into the hardening range. With the effect of cold forming process, the average yield stress increases by 15% to 30%. For use in the design parameters, it can be assumed that the yield stress is increased by a minimum of 15% (Yu & LaBoue, 2010).

Cold formed steel profiles are useful due to their high ductility and production under the continuous control action. Since there are no formwork materials in reinforced concrete construction, dead materials are not used in manufacturing. They are easy to transport and building-up. They also provide a sustainable and environmentally friendly construction as they are completely recyclable. It is possible to produce economically and quickly different cross-section shapes that are very high load carrying capacity to weight ratio by forming in cold. In addition, when the hot rolled and cold formed channel type sections with the same mechanical cross-sectional area are compared, it is seen that the cold-formed sections have a large moment of inertia because their wall thicknesses are thinner. In fact that, they have larger bending moment values (Narayanan, Kalyanaraman, Santhakumar, Seetharaman, & Kumar, 2011).

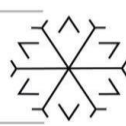
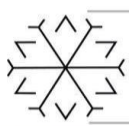
Moreover, the following point should not be overlooked. The strength-to-weight ratios obtained by using thin materials are significantly higher. However, it is necessary to fulfill the appropriate design conditions to consider the expected buckling problems (Tunca, Erdal, Sağsöz, & Çarbaş, 2018).

In the last two decades, cold-formed steel has started to be used more in the construction industry. There are so many researches about the steel construction to increase stability and reliability of the steel structures. Detailed design procedures are not common due to the wide variety of cold-formed steel connections. Most designs are made according to experimental results. This article aims to compile and review research on cold-formed steel connections. The review focused on cold-formed steel screw beam to column connections and their behavior under cyclic loading.

2. Cold Formed Steel Connections

The connection is defined as the physical component that mechanically fixes the structural elements. It is essential to transfer the force and moment from the structural element to the load-bearing elements in the connections. Traditional connecting methods such as screwing, riveting, bolting and welding can be used in cold-formed steel structure connections. While designing the connection, bending, buckling, tensile behavior of the elements should be considered and additional information should be informed from the tests about the durability of the connections. AISI specifies as a general rule that all connections should be designed to transfer the maximum design force in accordance with the eccentricity (Yu & LaBoue, 2010).

2.1. Screw Connections



Screw connection is a type of connection commonly used in the connections of cold-formed steel structural members. Due to the thinness of the cold-formed steel, the screw connection provides the advantage of fast assembly.

When the size and type suitable for the characteristics of the elements to be joined are selected, the screws can provide the combination of two or more elements. Since the screw size must be longer than the sum of the thicknesses of the connecting parts, it is important to know the thickness of the connecting parts (Nasfa, 2000).

(Tartar A, 2002) stated that as a result of her study, at least two screws should be used in joining cold-formed steel elements, and that the head of the screw should be on the side of the thinner part to be joined.

Screw connections transfer the shear force and tensile force acting on them to the other structural element. Forces create stresses by acting on the connection points of the elements from different directions and different axes. It can be said that if the direction of the forces is perpendicular to the screw length, shear force is applied, and if it is parallel, tensile force is applied.

Pre-drilled and drilled-in-place screws are the most commonly used screw types for connecting cold formed profiles. Self tapping screws connect the elements to be connected by drilling with their own threads without the need to drill holes beforehand. Self-tapping screws are used to join 0.84 mm or thicker steels. These screws are applied by opening their own holes and screw pitches without breaking or deformation during assembly (Siyahhan, 2005). Self-tapping screws are produced with carbon steel and galvanized with zinc to protect against corrosion (Baehre, Tomà, & T., 1993). Self-tapping screws have better moment capacity compared to conventional screws.

(Serrette & Peyton, 2009), in their study, they investigated the strength of screwed joints in steel structures. They compared the self-tapping screw behavior of a profile with a low ductility value and a profile with a high ductility value. They stated that it is important to use the material safety factor during the detail design phase.

(Stone & LaBoubeb, 2005), in their study, they are researched experimental studies to examine the behavior of cold-formed steel profiles. Self-trapping screws were placed at specified intervals in all of the test samples. As a result of the experimental studies, it has been seen that the current design requirements are safe.

(Tahir, Hamid, Tan, & Mahendran, 2011), investigated screw connections experimentally in their study. They examined 12 different column-beam combinations and compared them with the Eurocode standard. As a result of the experimental study, they stated that the strength of the joints increased as the depth of the beam increased.

(Maali, Sagioglu, & Solak, 2017), in their study, experimentally investigated the behavior of self-tapping beam-column joints in cold-formed steel structures. They used the beam thickness as a variable in their experiments. They explained the test results with moment-rotation curves. As a result, they stated that as the thickness increases, the maximum moment and plastic deformation capacity increase and the maximum deformation decreases.

2.2. Loading Protocols and Behaviour of Cyclic Loading

(Jiao, Kishiki, & Yamada, 2012) examined the loading protocols used in beam experiments to evaluate the seismic behavior of steel structures. Generally, they stated that most countries have their own standard loading protocols for beam testing, but they have doubts about whether existing loading protocols are sufficient to represent true beam behavior during earthquakes. The examined loading protocols are shown in Figure-2.

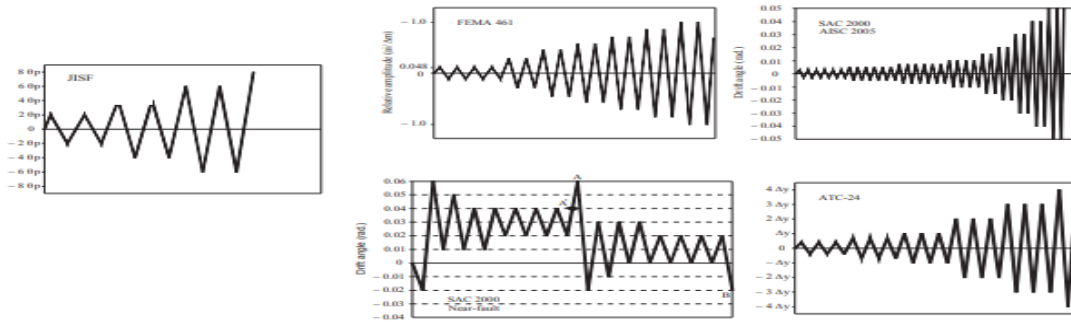
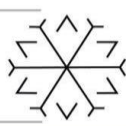


Figure 2: The examined loading protocols

Atc-24 is one of the first mini-protocols used to evaluate the performance of steel structure components using cyclic loading. This loading protocol works with elastic deformation control. Jisf 2002 is the loading protocol recommended by the Japan Iron and Steel Federation. In this loading protocol, it is requested to conduct an experiment by applying 2 loadings in each cycle, starting with $\pm 2\theta_p$ value of the frames, increasing as $\pm 2\theta_p$. θ_p is the plastic rotation value when the moment of the cantilever end of the beam is equal to the plastic moment (M_p). Fema 461 protocol was developed for testing drift-based structural components. However, it can also be used in structural components sensitive to drift, such as beams in general. According to this loading protocol, there should be two cycles per load. The amplitude starts from $a_1=0.048 \Delta m$.

Fema 350 protocol has been recommended by the American Institute of Steel Construction for beam to column connections in steel structures. Cyclic loading protocols are in terms of interstory drift angle. the deformations of the steps and the number of cycles are given in Table 1.

Table 1: Fema 350 Loading Protocol Steps

Load Step #	Peak deformation θ	Number of cycles, n
1	0.00375	6
2	0.005	6
3	0.0075	6
4	0.01	4
5	0.015	2
6	0.02	2
7	0.03	2

After the 7th step, until assembly damage occurs at the connections θ will continue to increase in 0.01 radians, and two cycles are performed at each step. Damage will be considered to occur when the peak loading in a cycle drops to 20% of that achieved at maximum load, to a state where stability under gravity load becomes uncertain.

Sac-2000 includes two types of loading protocols. The first is typically the same as the fema 350. Contains smaller elastic cycles. The second is the loading protocol with irregular amplitudes and loading numbers.

(Krawinkler, 2009) presented information about the purposes of using cyclic loading protocols in his study. He stated that all structural elements have limited strength and deformation capacities for connection security and damage control values, and we need to have information about their load and deformation histories to evaluate these capacities. He stated that it is necessary to consider the effects of cyclic loading and cumulative damage in the design of structures and also stated that the concept of deformation history should be used in order to estimate the damage situation. He explained that there is no unique and perfect loading history, earthquakes are not similar to each other and connections can have very different structural components, so different loading protocols should be developed. He emphasized that while creating the

loading protocols, the number and amplitudes of the cycles should be determined by taking into account the ground motion and the components of the structure.

(Shen & Astaneh-Asl, 1999) experimentally investigated the inelastic behavior of bolted beam to column connections under cyclic deformation, their failure modes under cyclic loading, and the energy dissipation capacity of bolted connections. To compare with bolted connections and welded connections, many bolted connections are much more flexible than welded connections. However, welded connections are stiffness, complex behavior and ductility, as well as cost of construction. They stated that the inelastic behavior of a bolted connection is more complex than that of a welded joint, which complicates the design and analysis of the bolted connection. But also, when properly designed, a bolted joint can have high ductility and cyclic energy dissipation capacity as it eliminates brittleness. Therefore, under ground motion, bolted semi-rigid frames may have less stress concentrations. They used in their experiments the displacement controlled in loading history is shown in Figure 4. They applied the same displacement of cycle twice. Displacement, global and local response of the samples were measured with Lvdts.

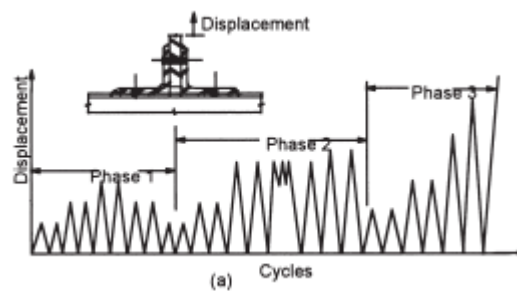


Figure 4: Shen and Astaneh Loading Protocol

As a result of the experiments, they reported that the bolted connections showed stable cyclic responses and reliable energy dissipation capacity under cycled loading. They also stated that the ductility value is small in the low-to-high-amplitude loading type compared to monotonic loading.

(Uang, Sato, Hong, & Wood, 2010) in their studies, they experimentally investigated the bolted connection of C-section beam and column under the effects of cyclic load to support the development of seismic design parameters of cold-formed steel structural systems.

The hydraulic actuator is attached to the end of the beam and the cyclic load is applied from this point. It used lateral bracing to prevent beam buckling. According to the results of the experiment, they reported that the connections initially responded elastically, and the bolted connections showed a rigid behavior. They stated that as a result of the widening of the bearing deformation with the effect of cyclic load, the sliding gap enlarged and a significant increase in strength occurred until the bolt holes were broken. They emphasized that bolt slippage is one of the design parameters that should be considered when designing steel frames. As a result of this study, they developed a model for the sliding movements of bolt connections.

(Serror, Hassan, & Mourad, 2016) investigated the rotational capacities of cold-formed steel beams in their study. They used different profiles in their experiments. They stated that buckling occurs earlier without out-of-plane reinforcements and reinforcements are used to obtain high moment strength. They compared experimental results and numerical results using the ANSYS program. They stated that the experimental results and numerical results were in good agreement. They concluded that C-section beams need reinforcements for ductility and greater moment capacity.

In their study, (Ghassemieh & Rahimzadeh, 2018) investigated the deformation capacities of steel connections by using different loading protocols and compared the results of this research. As a result of this study, it has been revealed that the loading histories have a great influence on the performance and capacity parameters of the connections, and the seismic behavior of the connection can understand better if an appropriate loading protocol is selected. They explained that radiated energy, elastic strain, deformation capacity, and failure are sensitive to the loading protocol. They stated that the ATC-24, one of the loading protocols they examined, consists of cycles with large amplitudes, therefore the demands



imposed by the loading protocol on the connection are not realistic and another loading protocol which is called as FEMA 350 has less damaging cycles. Moreover, with SAC-2000 loading protocol, they stated that all loaded connections can easily reach $\pm 6\%0p$, and larger rotation values are obtained from this protocol. In addition, a new loading protocol was developed and proposed in the study. Compared to the SAC-2000, loading protocol, the amplitude and loading steps have a greater effect on the connection behavior, and these loaded connections achieved more ductile deformation and strength capacity. The developed loading protocol has smaller cycles. The deformation values and the number of cycles are shown in Table.2.

Table 2: Ghassemieh and Rahimzadeh Loading Protocol

Loading step	Maximum deformation amplitude	Number of the cycles in the step
1	0.00375	6
2	0.005	6
3	0.00625	4
4	0.0075	4
5	0.01	2
6	0.0125	2
7	0.015	2
8	0.02	2
9	0.03	1
10	0.04	1
11	0.05	1
12	0.06	1
13	0.07	1
14	0.08	1

(Pachoumis, Galoussis, Kalfas, & Christitsas., 2009) experimentally investigated the moment strength under cyclic loading by reducing beam section used HEA profiles in their study. They created a theoretical model with the finite element method and compared the experimental results with the results obtained from the finite element method. They used HE 240A profiles as beams and HE 300B profiles as columns in the experiment. The ductility plates, whose thickness was chosen to be equal to the flange thickness of the beam, were used to form a strong panel in the column. They used the ABAQUS program to model with the finite element method. The analysis was carried out by applying cyclic variable amplitude displacements on the beam at a distance of 1 m from the column surface. The loading protocol is shown in Table 3 and the amplitude graph of the number of cycles according to the loading protocol in Figure-5.

Table 3: Loading Protocol

Load step	Peak deformation, δ_y	Number of cycles, n
1	0.375	6
2	0.50	6
3	0.75	6
4	1.00	4
5	1.50	2
6	2.00	2
7	3.00	2

Continue with increments in δ_y of 1.00 δ_y , and perform two cycles at each step

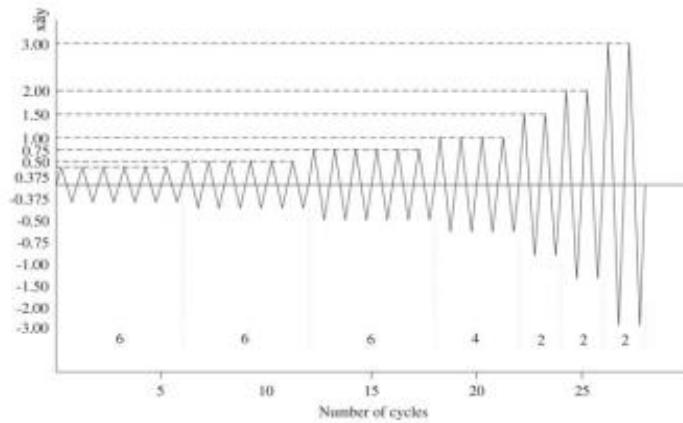
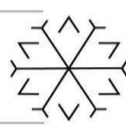
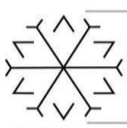


Figure 5: Number Of Cycles Graph

They produced several full loading cycles for each sample with displacement amplitudes in multiples of Δy . As a result of their studies, based on both experiments and numerical results, they stated that the connection moment strength increases when a plastic connection is formed in the weakened section.

(Azizinamini & Radziminski, 1989) conducted experimental and analytical studies to examine the behavior of semi-rigid steel beam to column connections under static and cyclic loading. They stated that one of the important parameters that affect the torque-rotation behavior is the geometric properties, and in the experiments they applied static displacement values, they obtained the moment-rotation curves for connections with different geometrical properties. In the static displacement experiments, the moment-rotation curves showed a non-linear behavior in the early period during loading, due to the local yielding in the tension flange and the final plastic hinge formation, and the moments increased continuously throughout the full rotation range applied during the experiments. Three different protocols were applied in cyclical experiments. They were applied as low to high, high to low and constant amplitude displacement. Experiments were performed by applying constant amplitude or variable amplitude displacement values shown in Figure 6.

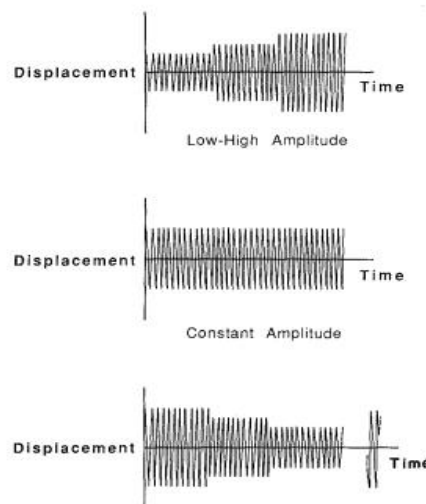


Figure 6: Experiments were performed by applying constant amplitude or variable amplitude displacement values

They stated that the crack expansion rate increased by expanding in displacement amplitude in the samples that tested under low to high amplitude loadings. They observed that cracking started earlier at high-to-low amplitude loadings, but in some cases, crack growth stopped temporarily due to the gradual increase in displacement amplitudes. Under random or seismic loading, displacement and load amplitude are important for the behavior of the structure.



3. Conclusion

In this paper, experimental and theoretical studies to investigate the behavior of screw beam-to-column connections in cold-formed steel under cyclic and seismic loadings are reviewed. The moment-rotation behavior of the connections are investigated under these loadings, the information was contributed to the high strength and ductility of the CFS connections has been examined. In general, there is a lack of knowledge about the structural behavior of cold-formed steel connections. So, there are still some knowledge gaps that need to be examined by future comprehensive research. The presented articles and research can help to better understand and improve connection behaviours of CFS structures.

References

- Azizinamini, A. and Radzimirski, J. B., 1989. Static and cyclic performance of semirigid steel beam-to-column connections. *Journal Of Structural Engineering*, 2979-2999.
- Bachre, Tomà, R. v. and T., 1993. *Cold-Formed Steel in Tall Buildings*. New York: McGraw-Hill .
- Ghassemieh, M. and Rahimzadeh, A., 2018. Impact of loading protocol on the performance of the steel moment frame connections. *Journal of Rehabilitation in Civil Engineering*, 115-138.
- Jiao, Y., Kishiki, S. and Yamada, S., 2012. Loading protocols employed in evaluation of seismic behavior of steel beams in weak-beam moment frames. In *Proceeding of 15th World Conference on Earthquake Engineering*. Lisbon.
- Krawinkler, H., 2009. Loading histories for cyclic tests in support of performance assessment of structural components. In *The 3rd International Conference On Advances In Experimental Structural Engineering*. San Francisco.
- Maali, M., Sagioglu, M. and Solak, M., 2017. Experimental Behavior of Screwed Beam-to-Column Connections in Cold-formed Steel Frames. *Kuala Lumpur*.
- Narayanan, R., Kalyanaraman, V., Santhakumar, A., Seetharaman, S. and Kumar, S., 2011. *Teaching Material*. Institute for Steel .
- Nasfa., 2000. *Prescriptive Method – For Residential Cold-Formed Steel Framing*. North American Steel Framing Alliance.
- Pachoumis, D. T., Galoussis, E. G., Kalfas, C. N. and Christitsas, A. D., 2009. Reduced beam section moment connections subjected to cyclic loading. *Engineering Structures*, 216-223.
- Serrette, R. and Peyton, D., 2009. Strength of screw connections in cold-formed steel . *Journal of Structural Engineering*, 951-958.
- Serror, M. H., Hassan, E. M. and Mourad, S. A., 2016. Experimental study on the rotation capacity of cold-formed steel beams. *Journal of Constructional Steel Research*, 216-228.
- Shen, J. and Astaneh-Asl, A., 1999. Hysteretic behavior of bolted-angle connections. *Journal of Constructional Steel Research*, 201-218.
- Siyahhan, R., 2005. *Hafif Çelik Sistemler*. İstanbul: Y.T.Ü. Fen Bilimleri.
- Stone, T. and LaBoube, R., 2005. Behavior of cold-formed steel built-up I-sections.
- Tahir, M. M., Hamid, H. A., Tan, C. S. and Mahendran, M., 2011. Structural behavior of screwed beam-to-column moment connections with cold-formed steel members. *Proceedings of the 6th International Symposium on Steel Structures*, (s. 503-510). Seoul, Republic of Korea.
- Tartar A., 2002. *Light Steel Construction Technology and Design Possibilities*. İstanbul: İTÜ Fen Bilimleri Enstitüsü.
- Tunca, O., Erdal, F., Sağsöz, A. E. and Çarbaş, S., 2018. Structural features of cold-formed steel profiles. *Challenge Journal of Structural Mechanics*, 77-81.
- Uang, C. M., Sato, A., Hong, J. K. and Wood, K., 2010. Cyclic testing and modeling of cold-formed steel special bolted moment frame connections. *Journal of Structural Engineering*, 953-960.
- Yu, and LaBoue., 2010. *Cold-Formed Steel Design (4rd Edition)*. Missori: Rolla.

Sustainable Aviation Fuels: Policy and Production

Olja Čokorilo ^{1*}[0000-0002-3871-504X], Marija Todorović ² and Srdjan Čokorilo ³

¹ o.cokorilo@sf.bg.ac.rs, Full Professor, University of Belgrade, Faculty of Transport and Traffic Engineering, Vojvode Stepe 305, Belgrade, Serbia

² m.todorovic1998@gmail.com, Student, University of Belgrade, Faculty of Transport and Traffic Engineering, Vojvode Stepe 305, Belgrade, Serbia

³ cokorilo.s@vakademija.edu.rs, Lecturer, Aviation College, Bulevar Vojvode Bojovića 2, Belgrade, Serbia and Assistant Director, Aviation Academy Belgrade, Bulevar Vojvode Bojovića 2, Belgrade, Serbia

Abstract

In recent years, renewable energy resources have become more critical due to the limited number of regions to produce petroleum-based fuels, which are continuously depleting. The aviation sector has an increasing need for conventional and alternative fuels in terms of commercial and cargo transportation. Derivatives of petroleum fuels used in aviation have negative impacts on air quality. Factors causing greenhouse gas emissions (GHG) in the aviation sector must be reduced. However, such fuels used in the aviation sector are not sustainable. Biofuels, which can replace petroleum fuels and help with emissions, are heavily investigated in developed countries for independence, creating a better environment and sustainability. Biofuels already used for ground vehicles could also be implemented in the aviation sector to reduce fuel costs and emissions. Overall, aviation fuels made of sustainable resources would also support social and economic development. Numerous industrial initiatives have emerged to find alternative ways to attain bio-aviation fuels. Therefore, there has been increasing research regarding alternative aviation fuels made of biomass in recent years. This paper analyses policies and measures for environmentally sustainable aviation sector, which would cause minimal pollution to air and water, and contribute to high-quality human life.

Some policy actions are already ongoing at the EU and global levels that aim to create incentives to increase SAF uptake. The carbon offsetting and reduction scheme for international aviation (CORSIA) designed by the ICAO to target neutral carbon growth in aviation and to be implemented as of 2021 includes the possibility of reducing emissions from international aviation through SAF. ICAO is in the process of finalizing the procedures that would allow producers to demonstrate that fuel is CORSIA-eligible and aircraft operators to claim a reduction in their offsetting requirements. According to the revised EU Renewable Energy Directive (RED II), SAF can be counted towards achieving the renewable energy targets provided for in the directive in the EU Member States, on the condition that they comply with the sustainability criteria listed in the order. Renewable energy directive from 2009 predicted at least 20 % of EU's total energy to be filled with renewables by 2020, mainly to be achieved through the national targets of the member states. All EU countries must also ensure that at least 10 % of their transport fuels come from renewables by 2020. These directives qualify biofuels as renewable energy sources only if they achieve a 65% greater reduction in emissions against a fossil fuel baseline of 94 g CO₂/MJ. However, it has been noted that the economic incentive to switch to the use of SAF under the CORSIA mechanism is estimated to be small. A few EU countries, including the Netherlands, France, Finland, Sweden, and Portugal, have already implemented or are planning policy support measures, such as SAF supply obligations. The final conclusion outlines the flightpath for future investments in aviation sustainable fuels, research and production.

Keywords. Aircraft, Aviation, Biofuels, Sustainability

Carbon Negative Buildings

Ergin Özkök

erginozkok74@gmail.com

Abstract

The construction industry has significant greenhouse gas emissions, and concrete alone accounts for around 8% of global CO₂ emissions. But it's hard to imagine that we'll be building less in the coming years and finding a material as versatile as concrete. Therefore, we must find more environmentally friendly solutions that make the world more livable for future generations, and the construction industry must be a part of this green change. Biochar is a charcoal-like substance that is produced by heating bio-based raw materials in the absence of oxygen, i.e. by pyrolysis. Biochar has the property of sequestering carbon - for example from biomass - for centuries, thereby combating climate change. Biochar has numerous applications. For example, it removes heavy metals from water and air when used as an active carbon filter because of its extremely high adsorption capacity. Biochar can be used to improve the compactness of the cementitious matrix composed of cement, fine and coarse aggregates. This leads to 'filling' of the voids in the cementitious matrix resulting in greater hydration and improved strength from an early age. Depending on the biomass, biochar can improve the strength of concrete by 10% – 20%. Moreover, depending on the quality of the concrete, biochar can reduce the water absorption and penetration in the concrete by 30-60%. This means a significant improvement in the durability of structural and non-structural building components.

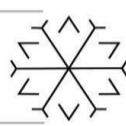
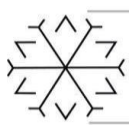
Biochar improves the properties of concrete and cementitious composites and also addresses the problem of premature shrinkage cracking in cementitious building materials. The internal curing effect of biochar leads to better hydration and redistribution of moisture, resulting in a lower probability of shrinkage cracking. Innovations in material design and processing can help to achieve higher carbon sequestration in cementitious building materials through carbonation curing. Using this technique, CO₂ emissions from industries can be captured in concrete through mineralization (calcium carbonate crystals) and this provides low carbon cement, and increases the strength and durability of cementitious materials.

Keywords. Biochar, waste management, climate change, Sustainability, pyrolysis

Introduction (Could pyrolysis save the planet?)

Concrete, but most importantly the cement in concrete, is responsible for about 8% of global greenhouse gas emissions. Infrastructure and housing are key issues for the next few years. The developments we'll obtain will determine whether concrete will go down in history as a climate protector or a climate killer. In any case, climate clay can make a significant contribution to achieving climate goals.

Sand and gravel alternatives are already used for concrete production. The replacement of cement using blast furnace slag and similar facilities is followed and optimized with great effort. This will also help further reduce the current footprint of around 521 kg CO₂ / t cement ! In the face of rising CO₂, there are even ways to capture the CO₂ emitted in the chimney of the cement plant using CCS (Carbon Capture and Storage) technology. The prices are high and it will certainly be used in the next few decades, however,



major changes are needed to create positive climate impacts with concrete. The use of sustainably sourced technical carbon, which will make concrete a noticeable carbon sink in the long run!

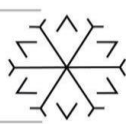
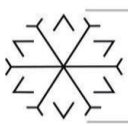
Biochar is combined in such a way that the positive effect of the concrete in terms of the general climate is achieved. The properties of the concrete are significantly improved. It is in no way inferior to its traditional counterparts, both in terms of compressive strength and surface properties. Biochar is not only positive in terms of climate, but also has a significant value compared to the traditional concrete product. Carbon Storage Concrete Technology is a sensitive, sustainable and permanent carbon sink, a true NET, Negative Emission Technology.

It consists of Biochar with 80%-95% carbon content. This biochar is a byproduct of climate-positive energy systems. In addition to the carbon from residual forest wood, these systems also provide sustainable, regional electricity and heat and are therefore among the most modern wood-fired power plants.

As mentioned earlier in this section, biochar has the potential to reduce the net greenhouse gas emissions by sequestering atmospheric carbon. A life cycle analysis performed by Roberts et al. (2009), found that biochar has the potential to reduce net greenhouse gas emissions by up to 870 kg CO₂ per dry ton of feedstock (Roberts et al., 2010). In addition, the biochar can be saturated with CO₂ before it is added to the concrete for additional biochar sequestration, at up to 300 kg CO₂ per tone of dry feedstock (Wei et al., 2012). As with the other applications, biochar also has several characteristics that can improve the quality of cementitious composites. Firstly, as particles within the size range of nano to micro scale can have a large impact on the mechanical properties of concrete, the first improvements would come from the effect of the small particle size that biochar can present. The use of carbon-based nano-particles has been found to offset the brittle behaviour of cement that is associated with an increase in strength by improving the ductility of the composite (Restuccia & Ferro, 2016). The size of sand used in concrete can play a large role in the fracture toughness of a cement composite, where reducing the size or loading level can increase the fracture strength to ideal levels. Due to this, modifying loading levels or particle size could allow for biochar to be used to tailor the brittle behaviour of concrete without compromising mechanical strength (Shin et al., 2015). In addition to the effects of particle size, the absorptive and adsorptive properties of biochar play an important role as well. The water retention of biochar allows it to absorb the water used in the initial mixing, which means that the evaporation loss of water can be reduced with the addition of biochar (Choi et al., 2012). More importantly, the water retained by biochar during initial mixing is released during the hardening of the concrete, promoting secondary 22 hydration reactions, thereby having a positive effect on the mechanical properties of the concrete (Choi et al., 2012; Gupta & Kua, 2017). In addition, the use of nano-particles can increase the hydration process speed (Restuccia & Ferro, 2016). While other nano- or microparticles may also improve the mechanical properties of concrete, the lightweight nature of biochar can allow for decreases in the overall density of concrete, which will have advantages in transportation costs.

Outside of the mechanical properties of the cement composites, some of the favourable properties of biochar such as low thermal conductivity, high chemical stability, and low flammability can be transferred to the matrix which support the material (Gupta & Kua, 2017). The low thermal conductivity of biochar is due to the presence of various pores throughout the particle (Brewer et al., 2009), which break thermal bridging within concrete. This is key for increasing insulation and therefore heating and cooling energy requirements within buildings (Gupta & Kua, 2017). In addition to heat insulation, biochar provides excellent humidity insulation when used in walls and buildings. The pores in biochar allow it to store moisture in the air, regulating the humidity levels within 40- 75 % (Schmidt, 2013). This has large health implications, as it can prevent asthma and other respiratory illnesses brought on by dry air, as well as mould growth caused by damp air (Gupta & Kua, 2017; Schmidt, 2013). While biochar may have properties similar to charcoal, in that it is combustible in the presence of oxygen, studies have found that biochar itself is not a flammable material. In a study on the combustion front propagation of biochar, biochar produced through slow pyrolysis showed no combustion front propagation, whereas fast pyrolysis chars showed slightly higher propagation, though not enough to be considered flammable. Through this, it was found that the level of volatiles and fixed carbon influence the combustion properties, and a low H/C ratio is important for reducing flammability (Zhao et al., 2014).

Concrete itself is not a flammable material, and is generally considered to perform well in the presence of fire or extreme heat. However, in the presence of high temperatures, concrete can still undergo a loss of strength as well as spalling (Cather, 2003). Spalling is the structural deformation and breaking up of layers of concrete as it is exposed to fire, and is caused by several factors such as aggregate fracturing, particles expanding, and evaporation of trapped water (Hertz, 2003). Due to this, biochar may have



positive effects by maintaining structure in the presence of high temperatures, and retaining free water to prevent evaporation.

Lastly, biochar offers chemical stability within concrete. Stability is an important factor when applying additives to concrete and asphalt, as they are susceptible to degradation reactions and oxidation. Since these reactions can compromise the quality of the building material and result in harmful products, it is important to know that these reactions will not be triggered by additives, to result in durable materials (Gupta & Kua, 2017). Similar to the application in soil, the stability of biochar depends largely on the fixed carbon level of the material, and the lack of reactive surface groups on the biochar. As discussed previously, the surface functional groups of biochar largely depend on the feedstock that is chosen, and the pyrolysis temperature as these groups will disappear with higher treatment temperatures (Kloss et al., 2011). Due to this, a biochar with a low O/C ratio will have lower reactivity, and as a result will be less likely to cause or promote reactions within concrete and asphalt (Gupta & Kua, 2017).

There is only one technology that we know of that can reliably suck carbon dioxide out of the atmosphere and sequester it. Photosynthesis. It is what every plant on the planet does every day. Humans have been great at releasing CO₂ to the atmosphere and singularly useless at capturing it again. But could we harness the power of plants at a big enough scale to offset our growing emissions profile?

The answer is yes and the technology could be pyrolysis combined with plant photosynthesis.

To recap, we have been very efficient at finding and burning “old” carbon (coal, oil and gas) in the form of fossil fuels that was created by plants eons past and laid down in sedimentary layers. We have dug up and burned that carbon and by doing so added it to the “new” carbon cycle or the biosphere where we and all other life live.

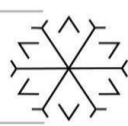
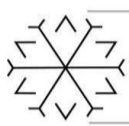
By replacing 15% cement with 15% Biochar, it is possible to produce climate-positive concrete whose properties are at least equal to or even exceeding the corresponding reference concrete (C25 / 30). It is ideally workable and therefore offers a wide variety of application options. In addition to the climate-positive properties of concrete with the use of Biochar, the technical conditions of the concrete also have a positive effect. High compressive strengths are as much an effect as improved internal finishing, improved sound insulation or more optimal thermal insulation behavior. And of course not forgetting the significantly better moisture-regulating properties.

Biochar is prepared from a wide variety of biomass feedstocks, including wood waste, agricultural and food waste that are processed and pyrolyzed under a range of finely tuned production conditions. Engineered biochar can be used to reduce cement demand by 2 – 5%, resulting in improved concrete strength and durability. Concrete made with blended biochar has superior workability, lower air content, lower permeability and higher strength than conventional concrete.

Conclusion

It has been proposed to use biochar as an additive for concrete, due to its ability to sequester atmospheric CO₂ (Gupta & Kua, 2017). A life cycle analysis performed on biochar showed that biochar can potentially reduce greenhouse gas emissions by 870 kg CO₂ per ton of dry feedstock (Roberts et al., 2010). In addition, biochar has several characteristics that can lead to increased performance of concrete. As a material with a low bulk density, biochar has the potential to drastically decrease the density of hardened concrete (Schmidt, 2013). Additionally, the porosity and high pH of biochar results in it having high water retention, which can lead to it absorbing free water while mixing. This water is released as the hydration reaction continues and the available moisture decreases, which leads to secondary hydration and additional curing of the concrete (Choi et al., 2012). Consequently, this can reduce the workability of the fresh concrete mixture.

Recently, a few studies have been conducted to investigate the addition of biochar to cement mix and mortar (cement and sand). A study showed that 5% hardwood biochar added mortar provided improvements in compressive strength, with the strength decreasing at higher levels (Choi et al., 2012). In addition, it was discovered that the addition of hazelnut and peanut shell biochar improved both the compressive strength as well as the flexibility of the concrete (Restuccia & Ferro, 2016). This goes against typical concrete behaviour, where an increase in compressive strength results in more brittle material, with lower tension resistance and fracture toughness. Carbonized bamboo fibers were also added to cement, which resulted in a more tortuous crack path being shown through the concrete leading to a



higher amount of energy being required to fracture the material (Ahmad et al., 2015). Both these studies have shown that these small particles act similarly to fine aggregate, forcing crack paths to either go around the particles, or through the particle, which leads to strong concrete with more ductility and durability (Ahmad et al., 2015; Restuccia & Ferro, 2016).

It has also been suggested that biochar can have positive effects in terms of electrical, acoustic, and thermal properties of biochar. Porous concrete containing voids and interconnected pores is very effective in sound absorption. Acoustic waves that enter these pores are dissipated by having their acoustic energy converted to heat through refraction and interference (C. Zhao et al., 2014). Porous concrete developed with other recycled material has been investigated thoroughly, where studies have shown that using coal bottom ash created a highway noise barrier concrete meeting the same standards as the traditional concrete used in these applications (Arenas et al., 2015). The high quantity of pores present in biochar may assist in the absorption and dissipation of sound waves, meaning biochar/ concrete (charcrete) composites could be used in sound reduction applications.

Lastly, low thermal conductivity and flammability of biochar present different advantages for insulation or in case of fire. The low thermal conductivity is due to the presence of various sized pores throughout the material. When used in materials, the pores help to break up thermal bridging within the material, and help to provide insulation, which could result in lower energy costs for charcrete used in buildings (Gupta & Kua, 2017). For example, in 2010, buildings accounted for 32% of total global final energy usage, with space heating accounting for 32% of total building energy consumption (Berardi & Naldi, 2017). There are several effective insulating materials on the market, such as polystyrene and polyisocyanurate, with some of them even being made of recycled materials like fiberglass and cellulose (United States Department of Energy, n.d.). Despite the abundance of effective materials present in industry, the ability to increase the effective thermal capacity of a building through the addition of carbon-sequestering biochar would help lead to reduced energy usage and GHG emissions. The low flammability of biochar can help to reduce the risks of damage done to concrete in the case of fire and extreme temperature. While concrete is not a flammable material, and is generally considered to perform well when exposed to fire, concrete can still undergo strength loss and spalling under heat (Cather, 2003). Spalling is the breaking up of layers of concrete when exposed to fire, and is down to several factors such as aggregate breaking, particle expansion, and water vaporization leading to pressure build-up (Hertz, 2003). The excellent behaviour of biochar when exposed to high temperature can help to reduce the damage done to concrete, by maintaining particle structure and retaining free water to prevent evaporation. Despite the research being done on using biochar in cement mixtures, there is little research having been done on adding biochar to industrial concrete (cement, sand, and aggregate). This chapter aims to determine the effects of using biochar at various loading levels in concrete, to determine its performance in terms of mechanical, thermal, and acoustic properties.

References

WWF climate protection in the concrete and cement industry; February 2019, contact person Dr. Erika Bellmann (ClimateProtectionandEnergyPolicyWWFGermany; [WWF_Klimaschutz_in_der_concrete_and_Zementindustrie_WEB.pdf](#))

According to the 2018/19 annual report of the cement industry, the footprint of cement produced in Austria; Austrian Cement Industry Association (VÖZ), Science Center TU Wien, Franz-Grill-Straße 9, O 21; www.zement.at Recarbonization of concrete: CO₂ containing cement

Workability of Concrete Having Hybrid Natural Fibers of Different Lengths for Easy Pouring

Muhammad Abrar ^{1*}[0000-0002-3738-017x] and Majid Ali ²[0000-0002-3690-2183]

¹enr.m.abrar@outlook.com, Capital University of Science & Technology Islamabad

²professor.drmaid@gmail.com, Capital University of Science & Technology Islamabad

Abstract

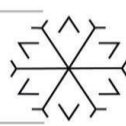
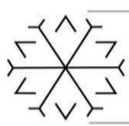
Fiber reinforced concrete having agricultural wastes is getting popular as construction material due to its better properties as compared with conventional concrete. These agricultural wastes include natural fibers which have low density, light weight and have less ecological effects on environment. Hybridization of these natural fibers with varying lengths is done to take their combined effect. As fresh properties of concrete are directly related with the mechanical and dynamic properties of concrete. It is necessary to determine the workability of fresh concrete for ease of handling and pouring. The aim of this study is to determine the effect of hybrid natural fibers on the workability of fresh concrete. The purpose of this research is to check the influence of jute and wheat straw hybrid natural fibers of varying lengths. For this work, jute fibers of 25 mm, 50 mm and 75 mm are hybridized with 12.5mm and 25 mm long wheat straw fibers. Five combinations are made by keeping the fixed percentage i.e. 4.5% for jute fibers (JF) and 0.5% wheat straw (WS) fibers by mass of cement in each. Slump cone test is performed to determine the workability of hybrid natural fibers reinforced concrete (HNFRC) and plain concrete and results are compared with plain concrete (PC). The results revealed that by the addition of hybrid natural fibers (HNFs) the value of slump decreased. PC, HNFRC₁, HNFRC₂, HNFRC₃, HNFRC₄ and HNFRC₅ showed slump of 100 mm, 0 mm, 26 mm, 0 mm, 74 mm, 0 mm respectively.

Keywords. Agricultural waste, Hybrid natural fibers, workability, Slump cone test

1. Introduction

Concrete is the most widely used construction material and it is the backbone of construction industry (Tian et al., 2020). With the growing age, the utilization of concrete is growing day by day. This can be due to the increase of urbanization rate in many developing countries and even developed countries. Besides its abundant utilization, concrete has adverse ecological effects and there is always need to reduce the impacts of concrete on environment. Sustainable material is always needed to reduce the cement content of concrete resulting in reduction of air pollution due to less emission of carbon dioxide (CO₂) in air. Concrete is brittle in nature; it is stronger in compression phase and weaker in tension (Aslani and Samali, 2014, Khan and Ali, 2019). Natural fibers gained popularity due to their less cost, eco-friendly nature and light weight. They also have good physical properties. The use of agricultural waste natural fibers lead towards the reduction of workability of concrete (Ali and Chouh, 2009). Workability of fresh concrete is directly related to the strength parameters of concrete. By the incorporation of short discrete fibers in concrete, workability is minimized up to some extent as compared with conventional concrete (Huang et al., 2021). Jute and wheat straw are also the agricultural waste natural fibers and they lead to reduce workability of concrete. This reduction is due to water absorption property of both natural fibers (Song et al., 2021).

Therefore, by the utilization of all agricultural waste natural fibers, the workability may reduce (Wongsa et al., 2020). With the increment of quantity of additive fibers the workability of fresh concrete decreased (Guler et al., 2021, Ahmad et al., 2020, Faris et al., 2021). Slump cone test is performed at both i.e. construction site and laboratory for the determination of workability of fresh concrete (Yeh, 2006, Yeh, 2007). Workability is related to the slump value. The material with high slump value is considered as more workable and vice versa. The additive natural fibers and raw material has great influence on the workability of concrete. So, workability is controlled by these substituents of concrete and by water to cement ration (W/C). Reduction in water to cement ratio caused reduction of workability. To meet the flaw, different plasticizers and super-plasticizers are used (Nematzadeh et al., 2021). These admixtures help to increase workability. Many researchers reported the effect of agricultural waste like wheat straw fibers on the properties of concrete (Tong et al., 2021, Jiang et al., 2021, Farooqi and Ali, 2018). Jute fiber is a natural fiber which can be used to enhance the mechanical as well as dynamic properties of concrete. It was



observed that by the usage of jute fibers, the resistance against impact loading can be enhanced (Hussain and Ali, 2019, Ahmed and Ali, 2020). By the hybridization of fibers the combined effect of both fibers may produce better performance in concrete as compared to sole natural fiber. Numerous studies are being conducted by researchers on the combined effect of hybrid fibers of different lengths and their effects towards to fresh and hardened properties of concrete (Li et al., 2021, Balea et al., 2021, Vishaul et al., 2021).

There is a wide range of studies available on the workability of artificial hybrid fiber reinforced concrete (Gao et al., 2021). But the literature on the workability of agricultural waste hybrid natural fibers with different lengths is very less. Workability plays an important role in the hardened properties of concrete. So, there is need to explore the effect of assorted lengths hybrid natural fibers on the workability of concrete. For this purpose, HNFRC is casted which contains different lengths combinations of jute and wheat straw fibers. Fibers content is kept fixed i.e. 4.5% and 0.5% by mass of cement for wheat straw and jute fibers respectively as recommended by (Arooj, 2021). Slump cone test is performed to check the workability of HNFRCs and PC. Lower value of slump may cause difficulty in handling and pouring. It may also tends to deviate from required strength properties. This study may help to understand the workability of PC and HNFRCs. It may also help to explore the behavior of agricultural waste hybrid natural fibers when used with concrete and their effect towards workability of fresh concrete.

2. Methodology

2.1. Raw Ingredients

Ordinary Portland cement (OPC), Margalla crush and locally available sand were used to prepare PC. For the preparation of HNFRCs jute fibers of 25 mm, 50 mm, 75 mm lengths are used along with wheat straw of 12.5 mm and 25 mm lengths. The percentage of fibers is kept fixed as 4.5% and 0.5% by mass of cement for wheat straw and jute fibers respectively. Tap water is used to prepare PC and HNFRCs. PC is prepared with a water to cement ratio (W/C) of 0.6 and HNFRCs are prepared with W/C 0.7. The wheat straw and jute fibers used in experimental work are shown in Figure 1. The varying length combinations of wheat straw and jute fibers are shown in Table 1.



Figure 1: a) Jute fibers b) wheat straw fibers.

Table 1: HNFRCs lengths combination and mix design ratio

Concrete Mix	Concrete Ratio	Jute Fibers Lengths (mm)	Wheat Straw Fibers Lengths (mm)
HNFRC ₁	1:2:3	25	25
HNFRC ₂	1:2:3	25	12.5
HNFRC ₃	1:2:3	50	25
HNFRC ₄	1:2:3	75	12.5
HNFRC ₅	1:2:3	75	25



2.2. Mix Design and Concrete Preparation

For the preparation of plain concrete a mix design ratio for cement, sand and aggregates was kept as 1, 2 and 3 respectively. W/C for PC was taken as 0.6. Same mix design was used for all HNFRCs. To the best of the author's knowledge there is no standard method present for mixing of HNFRC. So, method of mixing of ingredients was adopted as layer method. The W/C ratio for HNFRCs was adopted as 0.7, due to presence of natural fibers like wheat straw and jute fibers. This increment of W/C was for good compaction and to make it workable. Less compaction may lead to reduce strength. A step-wise increment of water was adopted to avoid bleeding. For the preparation of PC, all ingredients were added in concrete mixer and mixer was allowed to rotate for three minutes. All materials were added in mixer in such a way that they may mix efficiently. To prepare HNFRCs, one third of the aggregate was spread in mixer in a layer followed by the one third of jute fiber and wheat straw. Then one third of sand was poured and spread by the help of spade followed by one third of the cement. All layers were thoroughly spread to attain homogeneous mix. Same procedure was adopted for whole ingredients in each HNFRC. One third of the water was added in mixer and then mixer was allowed to mix. Rest of the water was added in increments during the rotation of concrete mixer to make HNFRCs workable.

2.3. Workability Test

Slump cone test is performed to determine the workability of concrete. This test is adopted at both laboratory and construction site before pouring of concrete into molds. ASTM standard C143/C143M-15a states that slump test is the method which provides a procedure to investigate the slump of plastic hydraulic concrete. The slump cone used in test had upper top diameter 100 mm and bottom diameter as 200 mm. Tempering rod with hemispherical ends of diameter 16 mm and having length of 100 mm is used for compaction of concrete. One third of the cone is filled with concrete and compacted by tamping rod; dropping at random places from a height of 25 mm. Same procedure is adopted for rest of two layers. By rolling and screeding, surface can be made smooth. Cone is lifted up and placed besides the molded concrete. Tamping rod is placed over the molded concrete in such a way that it may cover the molded concrete and cone. A ruler is used to measure the slump value as shown in Figure 2.

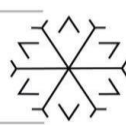
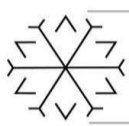


Figure 2: Measuring slump of HNFRC.

3. Results and Analysis

3.1. Slump of Fresh Concrete

The slump of PC and HNFRCs is provided in Table 2. The value of slump for PC is 100 mm. It can be noted that HNFRC₁, HNFRC₃ and HNFRC₅ have zero slump. The common thing is that all these three fiber reinforced concretes (FRCs) have wheat straw of 25 mm lengths but different lengths of jute fibers. There is a 100% decrease in slump value for HNFRC₁, HNFRC₃ and HNFRC₅. But on the other hand HNFRC₂ and HNFRC₄ showed 74% and 26% decrease as compared to PC. Whereas, HNFRC₂ and HNFRC₄ have lengths of wheat straw 12.5 mm and jute fibers of 25mm and 75 mm lengths respectively. It can be clearly observed that when jute fibers and wheat straw fibers have same lengths i.e 25 mm, slump is zero. This may be due to the water adsorption of both natural fibers. By reducing the length of wheat straw from 25mm to 12.5 mm in HNFRC₂ the slump value is increased. When jute fibers length is increased from 25 mm to 50 mm and wheat straw fiber length is kept same as 25 mm in HNFRC₃ the value of slump decreased



from 26mm (HNFRC₂) to 0 mm. Again increasing the length of jute fibers from 50 mm to 75 mm and reducing the wheat straw length to 12.5 mm the value of slump becomes 74 mm. The increment of wheat straw length to 25 mm and keeping jute fibers length as HNFRC₄ the slump is obtained as zero.

Table 2: Slump and W/C for PC and HNFRCs

Mix	JF addition (%)	WS addition (%)	W/C (ratio)	Slump (mm)
PC	-	-	0.6	100
HNFRC ₁	0.5	4.5	0.7	0
HNFRC ₂	0.5	4.5	0.7	26
HNFRC ₃	0.5	4.5	0.7	0
HNFRC ₄	0.5	4.5	0.7	74
HNFRC ₅	0.5	4.5	0.7	0

3.2. Ease of Concrete Handling

The concrete pouring and transporting depends upon the workability of fresh concrete. In this regard, water to cement ratio plays an important role. If the concrete does not meet the required W/C, it may cause in reduction of slump value. Less slump value is less workability of concrete and vice versa. All HNFRCs are less workable than PC because all HNFRCs have less value of slump as compared with PC. Less value of slump is due to the incorporation of hybrid natural fibers in concrete. HNFRC₁, HNFRC₃ and HNFRC₅ have zero slump so they are more difficult to handle and transport as compared with other HNFRCs. Natural fibers present in the concrete mix may absorb water. Due to this reason, the other ingredients get less water, concrete become harder and workability is reduced. All HNFRCs has less workability so these are difficult to pour in molds and compact as compared with PC.

4. Conclusion

The effect of agricultural waste hybrid natural fibers of different lengths is determined in terms of workability of fresh concrete. For this purpose, slump cone test is performed on PC and HNFRCs. The wheat straw fiber content is taken as 4.5% and jute fiber content is taken as 0.5% by mass of cement. Jute fiber of 25 mm, 50 mm and 75 mm is used with wheat straw fibers of 12.5 mm and 25 mm lengths. After conducting this study following conclusions are made.

- Addition of varying lengths hybrid natural fibers tends to decrease the workability of fresh concrete.
- The hybrid natural fibers combinations that contain wheat straw of 25 mm length have zero slump.
- There is decrease of 100%, 74%, 100%, 26% and 100% for HNFRC₁, HNFRC₂, HNFRC₃, HNFRC₄ and HNFRC₅ as compared with PC.
- HNFRC₂ and HNFRC₄ has same wheat straw lengths but with the increment of jute fibers length in HNFRC₄ the workability is increased by 184% as compared with HNFRC₂.
- PC is more workable so it is more convenient to handle and transport
- HNFRC₁, HNFRC₃ and HNFRC₅ are much difficult to pour and handle as compared with other HNFRCs.

These above mentioned conclusions indicate that jute fiber and wheat straw natural fibers have draw-back towards the workability of concrete. The workability can be enhanced by revising the water cement ratio up to some extent or by introducing plasticizers and super plasticizers in concrete.

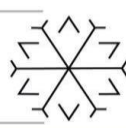
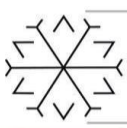
Acknowledgement

The authors would like to acknowledge every person who has helped throughout this research work.



References

- Caliskan, A. and Gurkan, G., 2021, August. Design and Realization of an Automatic Optical Inspection System for PCB Solder Joints. In 2021 International Conference on INnovations in Intelligent SysTems and Applications (INISTA) (pp. 1-6). IEEE.
- ahmad, W., Farooq, S. H., Usman, M., Khan, M., Ahmad, A., Aslam, F., Yousef, R. A., Abduljabbar, H. A. & Sufian, M. 2020. Effect of coconut fiber length and content on properties of high strength concrete. *Materials*, 13, 1075.
- Ahmed, S. & Ali, M. 2020. Use of agriculture waste as short discrete fibers and glass-fiber-reinforced-polymer rebars in concrete walls for enhancing impact resistance. *Journal of Cleaner Production*, 268, 122211.
- Ali, M. & Chouw, N. Coir fibre and rope reinforced concrete beams under dynamic loading. Annual Australian Earthquake Engineering Society Conference, "Newcastle Earthquake—20 years on, 2009.
- Arooj, K. 2021. Mechanical, Dynamic and Absorption Properties of Hybrid Fiber Reinforced Concrete for Rigid Pavements Application. Masters in Civil Engineering, Capital University of Science & technology.
- Aslani, F. & Samali, B. 2014. High strength polypropylene fibre reinforcement concrete at high temperature. *Fire Technology*, 50, 1229-1247.
- Balea, A., Monte, M. C., Blanco, A. & Negro, C. 2021. Recycled Fibers for Sustainable Hybrid Fiber Cement Based Material: A Review. *Materials*, 14, 2408.
- Faris, M. A., Abdullah, M. M. A. B., Muniandy, R., Abu Hashim, M. F., Bloch, K., Jež, B., Garus, S., Palutkiewicz, P., Mohd Mortar, N. A. & Ghazali, M. F. 2021. Comparison of Hook and Straight Steel Fibers Addition on Malaysian Fly Ash-Based Geopolymer Concrete on the Slump, Density, Water Absorption and Mechanical Properties. *Materials*, 14, 1310.
- Farooqi, M. U. & Ali, M. 2018. Contribution of plant fibers in improving the behavior and capacity of reinforced concrete for structural applications. *Construction and Building Materials*, 182, 94-107.
- Gao, D., Gu, Z., Pang, Y. & Yang, L. 2021. Mechanical properties of recycled fine aggregate concrete incorporating different types of fibers. *Construction and Building Materials*, 298, 123732.
- Guler, S., Öker, B. & Akbulut, Z. F. Workability, strength and toughness properties of different types of fiber-reinforced wet-mix shotcrete. *Structures*, 2021. Elsevier, 781-791.
- Huang, W., Quan, W. & Ge, P. 2021. Orthogonal tests investigation into hybrid fiber-reinforce recycled aggregate concrete and convolutional neural network prediction. *Journal of Asian Architecture and Building Engineering*, 1-16.
- Hussain, T. & Ali, M. 2019. Improving the impact resistance and dynamic properties of jute fiber reinforced concrete for rebars design by considering tension zone of FRC. *Construction and Building Materials*, 213, 592-607.
- Jiang, D., Jiang, D., Lv, S., Cui, S., Sun, S., Song, X., He, S. & Zhang, J. 2021. Effect of modified wheat straw fiber on properties of fiber cement-based composites at high temperatures. *Journal of Materials Research and Technology*, 14, 2039-2060.
- Khan, M. & Ali, M. 2019. Improvement in concrete behavior with fly ash, silica-fume and coconut fibres. *Construction and Building Materials*, 203, 174-187.
- Li, K., Yang, C., Huang, W., Zhao, Y., Wang, Y., Pan, Y. & Xu, F. 2021. Effects of hybrid fibers on workability, mechanical, and time-dependent properties of high strength fiber-reinforced self-consolidating concrete. *Construction and Building Materials*, 277, 122325.



- Nematzadeh, M., Maghferat, A. & Herozi, M. R. Z. 2021. Mechanical Properties and Durability of Compressed Nylon Aggregate Concrete Reinforced with Forta-Ferro Fiber: Experiments and Optimization. *Journal of Building Engineering*, 102771.
- Song, H., Liu, J., He, K. & Ahmad, W. 2021. A comprehensive overview of jute fiber reinforced cementitious composites. *Case Studies in Construction Materials*, e00724.
- Tian, H., Zhou, Z., Zhang, Y. & Wei, Y. 2020. Axial behavior of reinforced concrete column with ultra-high performance concrete stay-in-place formwork. *Engineering Structures*, 210, 110403.
- Tong, J., Wang, X., Kuai, B., Gao, J., Zhang, Y., Huang, Z. & Cai, L. 2021. Development of transparent composites using wheat straw fibers for light-transmitting building applications. *Industrial Crops and Products*, 170, 113685.
- Vishaul, K., Manikandaprabhu, S. & Radhakrishnan, R. 2021. Structural behavior of hybrid fiber reinforced concrete—An experimental study. *Materials Today: Proceedings*, 39, 818-822.
- Wongsa, A., Kunthawatwong, R., Naenudon, S., Sata, V. & Chindaprasirt, P. 2020. Natural fiber reinforced high calcium fly ash geopolymer mortar. *Construction and Building Materials*, 241, 118143.
- Yeh, I.-C. 2006. Exploring concrete slump model using artificial neural networks. *Journal of Computing in Civil Engineering*, 20, 217-221.
- Yeh, I.-C. 2007. Modeling slump flow of concrete using second-order regressions and artificial neural networks. *Cement and concrete composites*, 29, 474-480.

Review On Potential Of Waste Materials As Fire-Resistant Materials

Muhammad Saad Hassan ¹[0000-0002-1602-6999], Saqib Khalid ²[0000-0002-0266-6741], Wasif Ali ³[0000-0002-0725-712X], Mehran Sudheer ⁴[0000-0003-1703-842X] and Majid Ali ⁵[0000-0002-3690-2183]

¹saadrajapeace@gmail.com, BS Student, Capital University of Science and Technology, Islamabad

²saqibkhalid@gmail.com, BS Student, Capital University of Science and Technology, Islamabad

³h.wasifali@gmail.com, BS Student, Capital University of Science and Technology, Islamabad

⁴mehran.sudheer@cust.edu.pk, Lecturer, Capital University of Science and Technology, Islamabad

⁵majid.ali@cust.edu.pk, Professor, Capital University of Science and Technology, Islamabad

Abstract

With an increase in world population, the extent and kind of waste substances have accelerated accordingly. Most of the non-decayable debris substances will continue to be in the surroundings for decades, possibly heaps over years. The non-decayable waste substances purpose a waste disposal crisis, thereby contributing to the environmental problems. Modern lifestyle, along with technological advancements, has increased the amount and variety of garbage generated, resulting in a waste disposal dilemma. Reusing also helps in conserving natural resources, but it also aids in the resolution of a rising waste disposal challenge. Many constructing additives may be recycled wherein markets exist. Asphalt, concrete, and rubble are regularly recycled into the mixture of new asphalt and urban construction products. This paper emphasizes the study of waste materials and their application as fire-resistant materials. The potential of waste materials in the construction industry was reviewed to provide an alternative to the disposal of waste materials in landfills. In addition, characteristics of these waste materials were also reviewed to analyze their fire-resistant properties. Afterwards, waste materials were short-listed based on their ability to resist fire.

Keywords. Waste materials, fire-resistant, concrete, spalling, compressive strength

1. Introduction

Waste materials have enormous potential in the construction industry. For instance, Glass trash has a lot of potential for use in mortar and concrete as a partial replacement for pricey ingredients like silica fume, fly ash, and cement (Pereira-de-Oliveira, Castro-Gomes, and Santos, 2012). Non-recyclable waste glass is a challenge for solid waste disposal in Portugal's many local districts. The bottling business has traditionally provided the majority of non-recyclable mixed-color shattered glass. The current waste management method is still being used. The majority of non-recyclable glass is disposed of in landfills. Waste materials from agriculture and industry are utilized to make Waste Composed Bricks (WCB). WCB manufactured from diverse industrial solid wastes has high compressive strength. Water is absorbed by WCB, which is made from various industrial solid wastes. The compressive strength of WCB comprising waste paper pulp and paper industry residue is found to be the greatest among all other waste-based bricks with considerably higher water absorption values (Raut, Ralegaonkar, and Mandavgane, 2011). This waste (glass, plastics, and demolished concrete) cannot be eliminated in large amounts. Yet, the environmental impact can be reduced by making more sustainable use of this waste. Yet, the effect on the ecosystem can be reduced by making more sustainable use of this landfill. The "Waste Hierarchy" is what it's called. Its goal is to minimize, reuse, or recycle garbage, with recycling being the preferable waste disposal alternative. Figure 1 is a diagram of the waste hierarchy. The utilization of hammered glass particles in place of fine aggregates improved the strength of concrete mixes. The use of crushed glass particles in place of fine aggregates improved the strength of concrete mixes (Batayneh, Marie, and Asi, 2007).

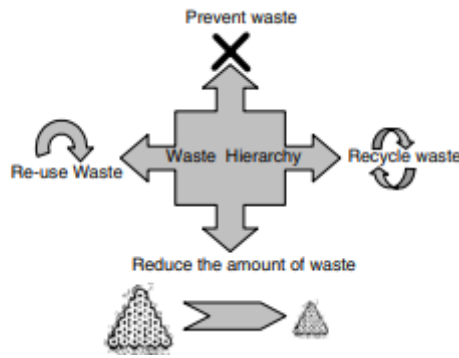


Figure 1: Waste Hierarchy (Batayneh, Marie and Asi, 2007:1871)

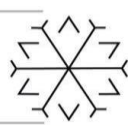
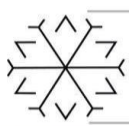
Characteristics of fire-resistant materials is a very essential step in the scope. Steel fibers are manufactured from ASTM 820 type 1 requirements tough low carbon high - strength steel wire that is continuously deformed. Fibrecon operates since, unlike mesh reinforcement, it is a solid material., the steel fibers support the concrete matrix in three dimensions. Fiber-reinforced concrete, with a 1.5 percent higher overall residual strength and fracture resistance than non-fiber concrete, has a higher overall residual strength and crack resistance. The carbonation process for concrete with steel fiber is somewhat impacted by temperature when compared to concrete without steel fiber. Concrete with 1.5 percent steel fiber obtained the highest compressive and modulus of elasticity values at 600°C (Nurchasanah, Masoud, and Solikin, 2016). Comparison of two fire-resistant materials: the essential components that caused No Fire A to beat Firex RX-2390 were its expansive fabric extension and no fabric compression. The moo warm conductivity of the char No Fire A as compared to the Firex RX-2390 fabric may be the moment calculate in its success. Fire-safe materials were classified concurring to their physical roots and assessed in terms of the elemental perspectives of chemical energy, mass misfortune, and warm transport (Koo, 1997). Substantial's shading changes, while concrete's compressive strength, modulus of flexibility, substantial thickness, and the presence of its surface become fundamentally impacted by high temperatures. Concrete made with block industry squander shows agreeable mechanical properties at room temperature, preferable imperviousness to fire over the one made with stream totals, and just marginally lower imperviousness to fire than the one made with dolomite (Netinger, Kesegic, and Guljas, 2011).

Materials which include metal fiber, Coconut shell, Glass granulated blast furnace slag, Fly ash, Ceramic waste, and a few different business wastes proved to be enormously powerful beneath the impact of accelerated temperatures. Next in sequence comes the shortlisting of waste materials as fire-resistant materials. The presence of polymeric fiber support in cement can build the compressive strength up to 20% With a consuming temperature of 800°C, it is advised that for concrete without fiber support, a proportion of 0.8 percent fiber to concrete is used with a consuming temperature of 800°C, it is advised that for concrete without fiber support, a proportion of 0.8 percent fiber to concrete is used (Bassam Z. Mahasneh, 2005). Then the more robust crosslinked alumina-silicate polymer structure, BAG concrete displayed superior structural stability than OPC concrete following exposure to elevated temperatures. Hairline cracks formed in BAG concrete between 600 and 800 degrees Celsius, whereas they appeared on the top of OPC concrete at 200 degrees Celsius. The BAG concrete had the best results, with an average strength decline of 16 percent compared to 50 percent for the OPC concrete. The strength of BAG concrete increased with increasing temperature, peaking at 600 °C, but the OPC concrete only reached peak strength at 200 °C. (Hussin et al., 2014). Squander glass powder with molecule measure extend of 100–850 lm can be utilized as an appropriate and proficient dormant powder in HSC, Tall quality concrete which is uncovered to terminating at tall temperature.HSC (High strength concrete) made by silica smolder is spalled prior to the HSC which contains squander glass powder beneath the impact of expanding in temperature (Ali, Dinkha, and Haido, 2017).

2. Fire Resistant Waste Materials

2.1. Potential Of Waste Materials In Construction Industry

In the building business, waste materials have a lot of upsides is key to providing an alternative for landfills. The utilization of these materials in the construction industry will produce a cyclic mechanism for these waste materials and reduce the burden on manufacturing industries. According to the most recent numbers on asphalt concrete manufacturing in Europe, 276.4 Mt was created in 2012, with 47 Mt (or 17%) made of reclaimed asphalt pavement (RAP) (indicating the significant possibility of employing the proposed municipal waste materials) (Poulikakos et al., 2017). Soil stabilization with HDPE and glass is reducing waste and promoting sustainability in highway



building. HDPE and Glass have been proven to be appropriate for use as stabilizers in subgrade stabilization for road structures, taking into account environmental and economic factors (Fauzi, Rahman, and Jauhari, 2013). Soda-lime glass has several advantages, including the use of crushed waste glass as a cement substitute in mortar, enhanced resistance to ASR and chloride penetration with replacement dosage, and significantly improved sulfate resistance without compromising strength. As a result, this waste material can successfully improve durability and contribute to the sustainability of buildings (Matos and Sousa-Coutinho, 2012).

The most common building and construction material is concrete, and it is produced in large quantities all over the world. As a result, from an engineering standpoint, it is required to increase the mechanical qualities of the concrete utilized in such constructions. Because of resource depletion, high green gas emissions, and high energy consumption, using virgin materials for concrete manufacturing has been a huge environmental burden. Over the last decade, a variety of waste materials have been tested around the world in the hopes of replacing virgin ingredients in concrete. According to the study's findings, natural zeolite and various industrial waste materials can be used as an alternative material to cement. Concrete tests were performed on several types of materials that used cement substitution as a percentage of weight. influence on concrete by utilizing past research's material-number of concrete curing days (Iswarya and Beulah, 2020). All waste products, Plastic containers, and tire material, which are employed here, are abundant in the environment and can be obtained for nearly no cost. Reusing such components in concrete appears to be an excellent choice for contributing to a cleaner environment and cheaper insulating costs. The influence of waste injection on the physical properties of concrete is also an important consideration for extending its use. (Yesilata, Isiker, and Turgut, 2009).

Concrete is a suitable material under normal conditions but needs enhancements or additives to perform in the desired manner under adverse conditions. The water-to-binder proportion was a key component in reducing the damage caused by sulfate assault on concrete. When exposed to sodium sulfate, increasing the water-to-binder ratio tends to boost the growth and energy shortage of concrete. Ettringite and gypsum were the primary degradation products of chemical attacks discovered by SEM methods and XRD analyses. The incorporation of solid waste materials may help to slow the deterioration of sulfate attack in concrete. (Figure 1) Tricalcium aluminate hydrate is reduced, CH is heated, and the matrix is densified to 30% of Portland cement could be substituted with solid waste materials in the production of sustainable concrete with cost-effective energy improvement and increased sulfate resistance. This would lessen the demand for Portland cement while also relieving the strain on solid waste management. (Tang et al., 2019).

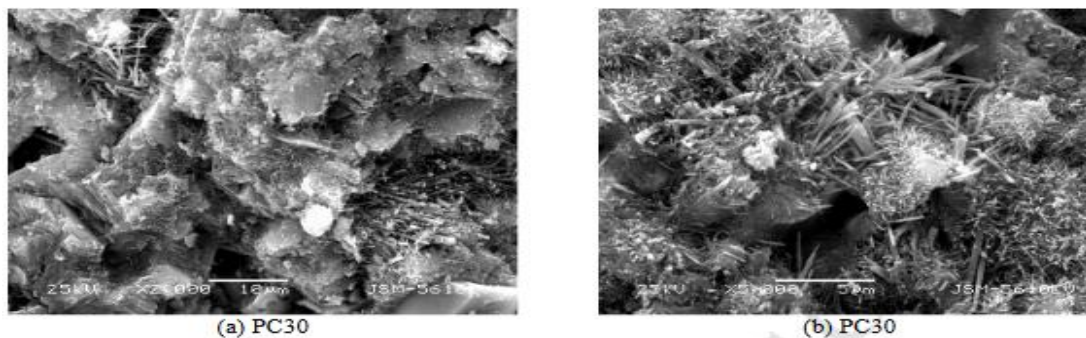
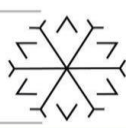


Figure 2: Microstructure of different concrete after exposure to sulfate solution (Tang et al., 2019:665)

2.2. Characteristics of Fire-Resistant Materials

To study the properties and composition of fire-resistant materials, it should be known the effects of fire on construction materials. This can help us distinguish fire-resistant materials and what damages these fire materials prevent. The behavior of concrete in a fire is governed by the amounts and ingredients employed in the concrete mix, as well as complex physicochemical transformations that occur during heating. At temperatures beyond 550–600 °C, however, the load-bearing capability of all Portland-cement-based concretes degrades. The fire's nature, the loading system, and the type of structure exposed to the fire all have an impact on structural concrete collapse. Concrete structure performance may deteriorate over time owing to concrete aging and environmental exposure. Concrete spalling is related to the age of the concrete, and the risk of spalling grows as the concrete's service life increases. The ability of aged concrete structures to withstand structural loadings as well as the impact of fire must be assessed using a structural and fire safety assessment process to determine whether additional fire safety measures are required, taking into account the risk of concrete spalling in a fire. Concrete spalling is a common issue. (Wang et al., 2013).



The comparison of a fire-resistant material with standard concrete will be helpful for us to understand the characteristics of fire-resistant materials. The presence of polymeric fiber reinforcement in concrete can boost compressive strength by up to 20% compared to concrete without fiber reinforcement. Based on a burning temperature of 600°C, the tensile strength increases by up to 44% when polymeric fiber reinforcement is used. As the temperature of the fire rises, the above value decreases. Regarding pullout, it is obvious that the influence of fiber reinforcing on pullout force decreases the pullout force by 7.1 percent at room temperature. When the temperature is raised to 600°C, the pullout force of reinforced concrete increases by 18.2 percent when compared to that of unreinforced concrete. The presence of fiber in concrete affects the pullout force as the temperature approaches 600°C, according to the result. This study was undertaken on unprotected concrete since it offered similar signs to prior studies on protected concrete, which could lead to the conclusion that such development will be less expensive in the long term (Bassam Z. Mahasneh, 2005). Although OPC dissolved totally at 800 °C, most GPC specimens had some residual binding strength even after 1200 °C contact. It thus demonstrated that GPC paste had outstanding bond performance even at extremely high temperatures (Figure 1). When the temperature was raised to 800°C, the color of GPC changed. GPC specimens had less visible cracks and no spalling phenomenon at exceptionally high temperatures (800°C, 1000°C, and 1200°C) when compared to OPC, showing that GPC has greater fire resistance (Jiang et al., 2020).

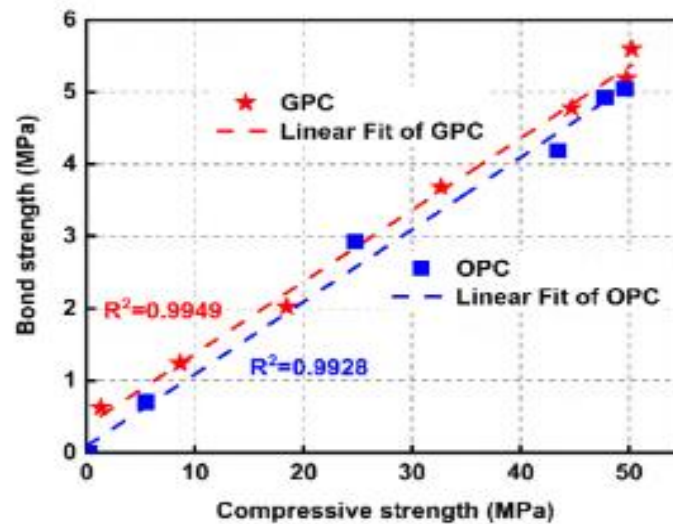
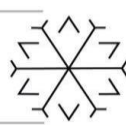
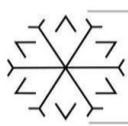


Figure 3: Difference of bond strength w.r.t compressive strength (Jiang et al., 2020:7)

After understanding the damages and comparison of fire-resistant with standard materials moving forward to the characteristics of fire which make them resist fire. Geopolymers are inorganic polymers having three-dimensional framework structures that have excellent mechanical and physical properties. Regarding the physical properties of concrete exposed to elevated temperatures, one of the factors is the aggregate's specific heat that has the greatest effect on the thermal conductivity, so this difference is thought to be due to the difference in the heat conduction of the lightweight aggregate. It is believed that the pore water pressure was released to the outside through the micro-cracks formed when the fibers melted, suppressing the explosive delamination that may accompany the formation of cracks. In addition, as seen in the experiments to evaluate the thermal conductivity (Table 1), it is thought that the difference in the thermal conductivity of the lightweight aggregate caused the difference in the increase in the internal temperature (Won et al., 2011). It has been found that the chemical composition of the raw material has a substantial influence on geo-orientated polymer response patterns, physical and mechanical qualities, and fire resistance. The compressive strength was found to be much higher in the presence of silica fume. Geopolymer mortar made from all raw materials was highly refractory up to 600°C but then declined (Saxena, Kumar and Singh, 2017).

Table 1: Properties Of Fire Resistant Materials (Saxena, Kumar and Singh, 2017:3812)

	SiO ₂ (%)	Al ₂ O ₃ (%)	K ₂ O (%)	Na ₂ O (%)	Fe ₂ O ₃ (%)	CaO (%)	MgO (%)	Specific gravity	Porosity %	Thermal conductivity (kcal/mh °C)
Perlite	70-75	12-16	1-4	2.5-5	0.15-1.5	0.1-2	0.2-0.5	0.15	90	0.03-0.05
Pyrophyllite	70-75	15-21	0.25-0.5	0.1-0.5	0.1-0.5	0.05-0.15	0.15-3	2.3	-	1.26-1.60



Vermiculite	36-46	6-16	1-6	-	6-13	1-5	16-35	2	90	0.02-0.05
-------------	-------	------	-----	---	------	-----	-------	---	----	-----------

2.3. Short-Listing Of Waste Materials As Fire Resistant

The shortlisting had been done through the review of papers. Materials which include metal fiber, Coconut shell, Glass granulated blast furnace slag, Fly ash, Ceramic waste, and a few different business wastes proved to be enormously powerful beneath the impact of accelerated temperatures. At high temperatures, the impact of 2 binding-oriented categories and 2 fiber-orientated categories on the physical behavior and spall liners of waste porcelain ceramics concrete were investigated. The mechanical properties, after 400 and 800 ° C exposure, cylindrical samples' mass flow rate, geometrical parameters, and gradual deterioration were measured. At 400°C, compressive strength losses were substantially lower for the specimens. The results obtained with Portland cement were better than those obtained with refractory cement, demonstrating that Portland cement performs well at this temperature. However, above 800°C, the temperature rises. The compressive strengths of the specimens were measured. Those recorded in specimens with refractory cement than those measured in specimens with this exposes the more stable microstructure of Portland cement. When steel fibers were added to the concrete mixes, the compressive strength of the control specimens was improved by 20% and 30% at 400 and 800 degrees Celsius, respectively. Carbon alloyed iron fiber, as a thermal conductor, distributes energy throughout the specimen, reducing thermal stresses and cracking, and preventing strength loss. Control specimens containing Portland cement underwent explosive spalling, whereas those containing refractory cement did not. Concrete examples with polypropylene and steel fibers were shown to be less prone to spalling. Despite much research concluding that only polypropylene fibers can prevent or significantly reduce concrete spalling at high temperatures, the outcomes showed that the expansion of steel strands additionally could forestall spalling contrasted with without-fiber examples with OPC. The aftereffects of fractal aspect investigation of the examples uncovered that they encountered fractional or no breaking at 400°C and that adjustments of their fractal aspects were zero percent, showing that the examples were not seriously harmed. Besides, fractal aspect investigation at 800°C uncovered that the utilization of steel strands in cement would lessen break inception and spread as well as harm to concrete. At long last, the examples containing both obstinate concrete and steel strands had minimal changes in their fractal aspects (Figure 3) (Talaei and Mostofinejad, 2021).

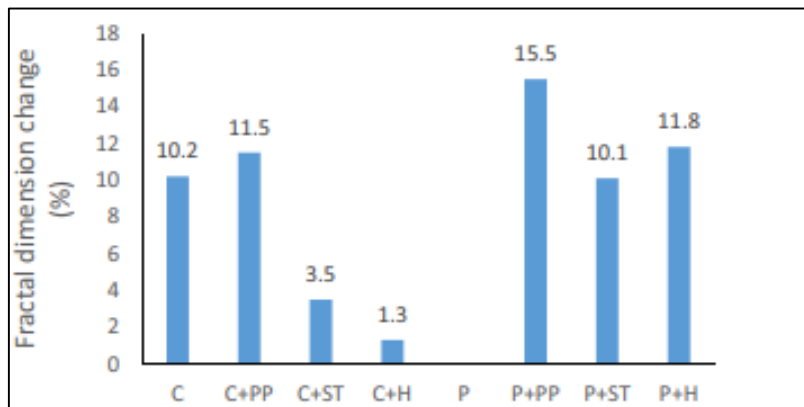
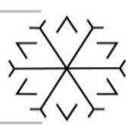
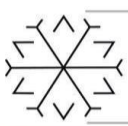


Figure 4: Percentage change in fractal dimension (Talaei and Mostofinejad, 2021:11)

Although When loading a concrete with heat (1000°C), refractory ceramic aggregates and heat resistant cement are used, heat spalling may happen because of a rise in water vapor pressure within the material's structure. For concretes with very low humidity, Oxygenation and a modification of the concrete that includes reused tile aggregate made of fiber reinforcement give efficient spalling prevention (dry). The chance of spalling increases as the humidity of the concrete rises. The use of hybrid composites as a concrete additive to prevent spalling in high moisture circumstances is ineffective circulation or the insertion of pores into the structure of the concrete building with ceramic aggregate and hence aluminum cement is an effective means of protecting the fabric against spalling even in conditions of high humidity. Moistened concrete based on aluminum cement and sanitary ceramics that has been amended with an aeration additive keep shape, cohesiveness, and thus the average compressive capacity of 18.78 MPa after heating at 1000°C (Zegardło, Szeląg, and Ogrodnik, 2018).

Since the tempered glass debris gravel had a smaller surface area than the broken stone dust., the slump values of fresh concrete increased by up to 20% as the consistency at constant water increased. Since the unstructured waste of unglazed aggregates, the creation of minor holes occurred internally during the concrete pouring. As a result, UPV and weights fell. The twenty-eight-day compression capacity of concretes made using twenty-five percent



waste ceramic aggregates enhanced by thirty-five percent. The stability of concrete with ceramic recycled aggregate was decreased by 40% when compared to control concretes. The impact of discarded ceramic gravel on concrete characteristics at temperatures up to 900 degrees Celsius was explored. The unit weight of concrete was reduced by 30%, while the UPV of the concrete was reduced by 50%. You're sick of the influence of escalating heat. The compression capacity of concrete specimens, in addition to the concrete containing 100 percent waste ceramic aggregate, was reduced to half an hour. The temperature had no impact on compression capacity in concrete made entirely of waste ceramic aggregate. The bending strength of the reference concretes was reduced by fifty percent as a result of the heat impact. Heat treatment of leftover ceramic aggregate concrete improved its strength (Canbaz, 2016).

It is seen that by raising the KOH concentration, the fire resistance properties can be increased. The same fire resistance experiments were carried out with various quantities of metakaolinite and silicate of sodium. When the amount of metakaolinite added is increased, the fire gets hotter. It is possible to improve resistance qualities. However, fire is another story. The quantity of resistance does not seem to be related to the amount of resistance. A silicate of sodium has been added. The temperatures on the other side of the coin. After each trial, the temperature of the test panels was less than 350°C, after 35 min. It showed that a geopolymer based on granulated blast furnace slag is a good fire-resistant material that may be employed in engineering applications (Cheng and Chiu, 2003). Heat resistant and waterproof properties of geopolymer-type coatings made with industrially available soluble glass differ from those prepared with synthetically prepared soluble glass. To use a polymer-type compound in conjunction with moisture: When compared to samples with a water: cement ratio of 0.41, samples with a cement ratio of 0.41 had greater stability. After seventy-two hours, the cement ratio was 0.5, and it had lost 34 percent of its volume.

SEM micrographs of the MK-0.41 and MK-0.5 samples were peeled off the metal substrate after 30 minutes of exposure to a gas torch at about 1100°C. Although the developed polymer-type coatings had poor moisture stability, their adhesion to metal substrates and thermal resistance were excellent (Temuujin et al., 2011). Data gained indicates that CHB with coconut shells and fiber can withstand fire, implying that CHB with coconut shells and fiber can withstand high temperatures. On the 28th day, the findings achieved a mean load capacity of 64.15 KN and three 3.175 MPa for average stress (Table 2). SEM micrographs of the MK-0.41 (b and d) and MK-0.5 (a and c) test after 30 minutes of exposure to a gas burner at about 1100°C and subsequently being peeled from the metal substrate. (Ganiron Jr, 2013).

Table 2: Fire resistances of CHB with coconut shell and fiber (Ganiron Jr, 2013:12)

Speicmen	Weight (Kg)	Load (KN)	Stress (MPa)
1	9.8	68.32	3.38
2	9.4	59.98	2.97

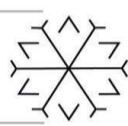
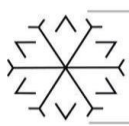
3. Conclusion And Recommendations

The review done in this study is primarily intended to show the relative benefits of using various building wastes such as broken concrete debris, plastics, and glass as a fire resistant material in construction products. This would provide a view of the construction industry's reutilization of construction debris.

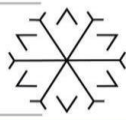
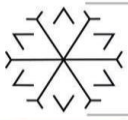
- There is a significant potential for waste material in the construction industry. It not only counters the problem of the landfill but also enhances the mechanical properties of concrete under various conditions. One of those conditions which were highly emphasized in this review was their behavior under elevated temperature.
- Characteristics of waste materials under elevated temperature were proved to be reliable, properties such as porosity, resistance to spalling, mass loss, residual compressive strength were altered to their desired standard by using these waste materials.
- Materials such as steel fiber, coconut shell, class granulated blast furnace slag, fly ash, ceramic waste, and some other industrial wastes proved to be highly effective under the effect of elevated temperatures.

Future studies in the utilization of waste materials as fire-resistant can lead to more safe and sustainable production in the construction industry. Effects of fire on different concrete structures can be analyzed based on their functionality.

References



- Caliskan, A. and Gurkan, G., 2021, August. Design and Realization of an Automatic Optical Inspection System for PCB Solder Joints. In 2021 International Conference on INnovations in Intelligent SysTems and Applications (INISTA) (pp. 1-6). IEEE.
- Pereira-de-Oliveira, L.A., Castro-Gomes, J.P. and Santos, P.M.S. 2012. The potential pozzolanic activity of glass and red-clay ceramic waste as cement mortars components. *Construction and Building Materials*, 31, pp.197–203.
- Raut, S.P., Ralegaonkar, R.V. and Mandavgane, S.A. 2011. Development of sustainable construction material using industrial and agricultural solid waste: A review of waste-create bricks. *Construction and Building Materials*, 25(10), pp.4037–4042.
- Batayneh, M., Marie, I. and Asi, I. 2007. Use of selected waste materials in concrete mixes. *Waste Management*, 27(12), pp.1870–1876.
- Nurchasanah, Y., Masoud, M.A. and Solikin, M. 2016. Steel Fiber Reinforced Concrete to Improve the Characteristics of Fire-Resistant Concrete. *Applied Mechanics and Materials*, 845, pp.220–225.
- Netinger, I., Kesegic, I. and Guljas, I. (2011). The effect of high temperatures on the mechanical properties of concrete made with different types of aggregates. *Fire Safety Journal*, 46(7), pp.425–430.
- Koo, J.H. (1997). Thermal Characteristics Comparison of Two Fire Resistant Materials. *Journal of Fire Sciences*, 15(3), pp.203–221.
- Ali, M.H., Dinkha, Y.Z. and Haido, J.H. 2017. Mechanical properties and spalling at elevated temperature of high-performance concrete made with reactive and waste inert powders. *Engineering Science and Technology, an International Journal*, 20(2), pp.536–541.
- Bassam Z. Mahasneh 2005. The Effect of Addition of Fiber Reinforcement on Fire Resistant Composite Concrete Material. *Journal of Applied Sciences*, 5(2), pp.373–379.
- Hussin, M.W., Bhutta, M.A.R., Azreen, M., Ramadhansyah, P.J. and Mirza, J. 2014. Performance of blended ash geopolymer concrete at elevated temperatures. *Materials and Structures*, 48(3), pp.709–720.
- Khoury, G.A. 2000. Effect of fire on concrete and concrete structures. *Progress in Structural Engineering and Materials*, 2(4), pp.429–447.
- Wang, G., Barber, D., Johnson, P. and Hui, M.-C. 2013. Fire Safety Provisions for Aged Concrete Building Structures. *Procedia Engineering*, 62, pp.629–638.
- Jiang, X., Xiao, R., Zhang, M., Hu, W., Bai, Y., and Huang, B. 2020. A laboratory investigation of steel to fly ash-based geopolymer paste bonding behavior after exposure to elevated temperatures. *Construction and Building Materials*, 254, p.119267.
- Won, J.-P., Kang, H.-B., Lee, S.-J., Lee, S.-W. and Kang, J.-W. 2011. Thermal characteristics of high-strength polymer–cement composites with lightweight aggregates and polypropylene fiber. *Construction and Building Materials*, 25(10), pp.3810–3819.
- Saxena, S.K., Kumar, M., and Singh, N.B. (2017). Fire Resistant Properties of Alumino Silicate Geopolymer Cement Mortars. *Materials Today: Proceedings*, 4(4), pp.5605–5612.
- Fauzi, A., Rahman, W.M.N.W.A. and Jauhari, Z. (2013). Utilization Waste Material as Stabilizer on Kuantan Clayey Soil Stabilization. *Procedia Engineering*, 53, pp.42–47.
- Poulikakos, L.D., Papadaskalopoulou, C., Hofko, B., Gschösser, F., Cannone Falchetto, A., Bueno, M., Arraigada, M., Sousa, J., Ruiz, R., Petit, C., Loizidou, M. and Partl, M.N. (2017). Harvesting the unexplored potential of European waste materials for road construction. *Resources, Conservation and Recycling*, [online] 116, pp.32–44. Available at: https://publik.tuwien.ac.at/files/PubDat_251234.pdf [Accessed 15 Sep. 2021].
- Matos, A.M. and Sousa-Coutinho, J. 2012. Durability of mortar using waste glass powder as cement replacement. *Construction and Building Materials*, [online] 36, pp.205–215. Available at: <https://www.sciencedirect.com/science/article/pii/S0950061812002292> [Accessed 16 Dec. 2019].
- Iswarya, G. and Beulah, M. 2020. Use of zeolite and industrial waste materials in high strength concrete – A review. *Materials Today: Proceedings*.
- Tang, Z., Li, W., Ke, G., Zhou, J.L. and Tam, V.W.Y. 2019. Sulfate attack resistance of sustainable concrete incorporating various industrial solid wastes. *Journal of Cleaner Production*, 218, pp.810–822.



Cheng, T.W. and Chiu, J.P. 2003. Fire-resistant geopolymer produced by granulated blast furnace slag. *Minerals Engineering*, 16(3), pp.205–210.

Talaei, M. and Mostofinejad, D. 2021. Mechanical properties of fiber-reinforced concrete containing waste porcelain aggregates under elevated temperatures. *Construction and Building Materials*, 289, p.122854.

Zegardło, B., Szeląg, M. and Ogródnik, P. 2018. Concrete resistant to spalling made with recycled aggregate from sanitary ceramic wastes – The effect of moisture and porosity on destructive processes occurring in fire conditions. *Construction and Building Materials*, 173, pp.58–68.

Canbaz, M. 2016. The Effect of High Temperature on Concrete with Waste Ceramic Aggregate. *Iranian Journal of Science and Technology, Transactions of Civil Engineering*, 40(1), pp.41–48.

Temuujin, J., Rickard, W., Lee, M. and van Riessen, A. 2011. Preparation and thermal properties of fire-resistant metakaolin-based geopolymer-type coatings. *Journal of Non-Crystalline Solids*, 357(5), pp.1399–1404.

Ganiron Jr, T.U. 2013. Sustainable Management of Waste Coconut Shells as Aggregates in Concrete Mixture. *Journal of Engineering Science and Technology Review*, 6(5), pp.7–14.

Yesilata, B., Isıker, Y. and Turgut, P. 2009. Thermal insulation enhancement in concretes by adding waste PET and rubber pieces. *Construction and Building Materials*, 23(5), pp.1878–1882.

Potential Of Used-Diesel-Engine-Oil As An Admixture In Cement Composites: A Detailed Review

Zain Ul Abideen ¹ and Majid Ali²

¹E-mail address: xain.noor02@gmail.com, Department of Civil Engineering Capital University of Science and Technology Islamabad

²E-mail address: professor.drmaid@gmail.com, Department of Civil Engineering Capital University of Science and Technology Islamabad

Abstract

Used Diesel engine oil (UDEO) is some of the poisonous wastes that have an effect on surroundings and human lives. Modern construction practice involves the use of industrial waste or by-products as raw materials for cement and concrete. These offer many advantages for the environment and have economic effects, since the disposal costs are constantly rising due to strict environmental regulations. Introduction of superplasticizer (SP) diesel engine oil as an additive. One of the most essential properties of concrete is its excellent flowability, which makes it easier to handle and place while also allowing for the removal of unwanted air gaps. With the increased use of concrete, new types of cost-effective admixtures may have a wide range of economic and technological implications for the construction industry as well as global concrete usage. Meanwhile, the number of vehicles on the road worldwide is increasing, resulting in a growth in the production of spent diesel engine oil (UDEO). The purpose of this study is to find out the flaws and innovative items for concrete. This paper includes the state of the art review that addition of UDEO to concrete under different checks. It was similar to adding air entraining admixture to concrete. UDEO has also been reported to improve some concrete properties, so it may result in higher SP costs and the elimination of UDEO problems and hardened concrete. The optimal percentage of adding UDEO to concrete has been found in the literature. Flexural strength, load bending behavior, crack pattern, crack width and ductility factor were checked. As a result, UDEO is a viable alternative to SP, addressing the issues of SP's greater cost and the efficient use of hazardous waste such as UDEO, both of which have major environmental consequences. It may be concluded that UEO outperformed super plasticizer in terms of durability improvement.

Keywords. Used Diesel engine oil, SP-super-plasticizer, Concrete-admixture, Environment.

1. Introduction

Rapid population growth and industrialization have resulted in massive amounts of trash. Current landfill and landfill methods have proven to be harmful due to the environment and the water contamination. Recently, interest in using greener technologies has increased. Many wastes are used to replace commercially accessible materials. Industrial, agricultural, and other higher-denomination trash or by-products or other methods which have no economic demand must be disposed off properly. Concrete business has thought of utilization industrial waste to be used as concrete admixtures so as to provide higher quality and additional durable building material. Water reducers are perhaps the most common additives used in the concrete industry, their use being particularly common in ready-mixed concrete. The influence and outcomes of using admixtures are determined by the type of cement used, the total amount of cement used, the grading of the combination, the proportions of the mix, and the mix's richness. Industrial waste and by-products, both solid and liquid, primarily of chemical origin, are widely available around the world. It had been reportable that below 45% of the used motor oil is collected all around the world, whereas the opposite 55% our ecosystem eventually comes to an end [1].

Sometimes the admixture affects on a specific piece of land. Generally more than one additive is used in the same mixture and sometimes the addition has a negative impact on concrete's desirable qualities. The choice of additives must therefore be made wisely. Concrete's outstanding flowability is one of its most important characteristics, which makes it easier to handle and install and allows for the removal of undesirable air spaces by using a superplasticizer. (SP Superf Plasticizers are a type of plasticizer that has been enhanced Super-plasticizers can lower



water content by up to 30% while still preserving workability [2]. The inclusion of superplasticizer results in a concrete that is homogeneous and cohesive, with little tendency for segregation or bleeding. whereas the previous researchers have mentioned the powerful operate of super plasticizer, another admixture to exchange it's one thing new be explored. As the use of concrete increases, new types of economical additives could have different economic and technical impacts on development activities in addition to the use of concrete around the worldIt is claimed that one gallon of Used engine oil is enough when incorrectly disposed of, it can pollute a million gallons of water [2].

In addition, industries turn out really injurious and extensive amount of waste. These wastes are widely used in modifying the properties of concrete [3]. The workability of modern self-consolidating concrete was unaffected by the marble mud. They claim that scrap marble will improve certain qualities of fresh and hardened self-consolidating concrete in a cost-effective manner [4]. Gencil O replaced the mixture with marble waste to form pavers, The paver's physical and mechanical qualities were then examined utilising specimens. Adding marble scraps reduced enhanced compressive strength frost as well as abrasion resistance They came to the conclusion that the type of cement is a vital preservative. that the production of pavement covering blocks that waste marble is desirable for the same old mix used in the production of concrete pavement covering blocks [5]. Steel powder concrete blocks have been demonstrated to boost compressive and tensile strength by 41% and 40%, respectively, according to research. The results of metal waste, such as processing waste, garbage cans, drinkable bottle caps, and steel dust waste, in an indeterminate amount of 1% of the total weight of concrete as fibres were researched by the authors. The concrete flexural strength of bottle cap reinforced blocks increased by 26%. [6]. According to Okoye F's findings, increasing the SF content improves the compressive, tensile, and flexural strength of made geopolymer concrete. SF has been given absolute to minimize workability. They used NaOH / sodium silicate and hardened the concrete at 100 ° C to make concrete from ash-based geopolymers with radically different SF concentrations. Alkaline activators included sodium hydroxide (14 M) and sodium silicate. Geopolymer concrete was also tested in the presence of 2 percent H₂SO₄, 5 percent Na₂SO₄, and 5 percent NaCl, according to the authors. [7].

Regarding the utilization of motor oil, concrete immersed in an oil solution or a water/oil combination had a reduced compression rate and strength, according to the researchers, however, when immersed in water, it has a stronger corrosion resistance. The concrete samples were subjected to a concentrated crude solution as well as a simulated crude oil/water mixture and cured for 3, 7, 28, and 56 days at different temperatures. The corrosion rate in pure crude oil was higher than in the crude oil/water mix, according to the study [8]. Regarding the utilization of motor oil, the researchers reportable the concrete was immersed in an oil solution and a water/oil mixture had a lower compression rate and strength, however, when not immersed in water, it has a stronger corrosion resistanc. Authors conjointly declared that UEO failed to considerably have an effect on the ultimate load or deflection of structural members. Chin declared Slump ratio increased by 18 to 38 percent, and air content increased by 26 to 58 percent, because to UEO [9]. Later, (Shafiq et al. 2011) says that by adding used motor oil to concrete increased concrete collapse by 18 to 38 percent and air content by 26 to 58 percent. To prolong initial sag and air content while reducing slump rate and initial set, the consistency and porosity were lowered, and the compressive strength was close to that of the same motor oil used in OPC concrete. Another study based on experimental data looked at the impact of used motor oil on the qualities of cslump test and hardened concrete using three different types of concrete: 100% OPC cement, 60% OPC cement + 40% ash, and 80% OPC cement + 20% rice husk ash. Each cluster had a mixing effect, with 0.15 % unspecified used engine oil mixed in. The review conclude that a small dose of used engine oil accumulated the concrete collapse. This, they claim, is due to the presence of 37 percent SO₃ in used engine oil, which generated a 20 percent difference in compressive strength when compared to the control combination. The review jointly shows that an indefinite small amount of used engine oil increased long term durability by reducing the oxygen porosity constant and porosity of all concrete mixes. [10].

Previous research has shown that the properties of concrete have been changed with UDEO. As we seen the physical apperance of used diesel engine oil in figure 1. Slump test, porosity, air entraining, and compressive strength are among these qualities. The chemical makeup of modern diesel engine oil, as well as the processes it undergoes, are considerably different.. Furthermore, no examination of the influence of UDEO on concrete has been reported. As a result, the effectiveness of UDEO on OPC concrete is examined in this study.

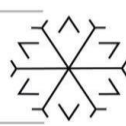
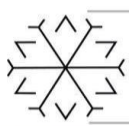


Figure 1: Used diesel engine oil physical appearance (Okashah et al., 2020)

2. Different liquid admixtures for cement composites

Different types of liquid accelerators supported by Na(sodium) aluminate; liquid accelerator supported aluminium sulphate; liquid accelerator based on fluoroaluminate) and As a result of the findings, the setting times of the initial and final cement pastes with 10% and 5% oxide fumes are 0.67 and 1.47 minutes, respectively, in the presence of 7.0 percent. The mortar with 10% silica fume achieves the best value of 16.8 MPa in the presence of 4.0 percent. Also, once the silica and fume dosages are 7.0% and 10%, the value of the primary exothermic peak of the pulp is 87.79 mW [11]. The compressive strength, modulus of elasticity, water absorption capacity, abrasion resistance and drying shrinkage of concrete mixes were completely affected by the addition of Dryshake surface hardener. However, the application of Dryshake surface hardener was found to have no vital impact on water absorption, depth of penetration of stressed water, and freezing and thawing performance [12].

The reinforcing effects of a large number of additives on styrene-acrylic emulsion-based cement compositions' tensile properties (SECC), note that the samples is in the order coalescing agent> nanometer aluminum oxide> plasticizer> adhesion promoter silane and also the optimal addition amounts are 4%, 1, 5%, 1% and 2%, respectively. The addition of acceptable amounts of coalescing agent and nanometric alumina improves the tensile strength, deformation and energy consumption properties of the samples; Meanwhile, adding the right amount of plasticizer to the test samples enhances the tensile set and energy-consuming qualities.[13]. The effects of a nanotube-containing pre-dispersed liquid additive (CNT) on the actual and cured performance of CNT-reinforced concrete (CNTRC). Carbon nanotube reinforced concrete is made with CNT's patented pre-dispersed additive. CNT-reinforced concrete with a longer mix time has significantly higher compressive strength. With dosage, fresh qualities improved, workability improved, and bleed was greatly reduced. At 1 day, CNT-reinforced concrete had a 46 percent higher strength, and at 28 days, it had a 37 percent higher strength. [14].

Liquid Additives Glucose retarder, calcium chloride accelerator, chloride free blowing agent, lingsulfonated plasticizer, shrinkage reducing additive (SRA), polycarboxylate ether superplasticizer (PCE) and sulfonated melamine formaldehyde (SMF). shrinkage cracking. Reducing the surface tension of the porous fluid in fresh concrete is one of the mechanisms. Superplasticizers showed a more pronounced reduction in PSC in high flow rate mixes. Additive dosages affect plastic removal mechanisms in a related way [15].

Table 1: Different Admixtures and their usage [11].

Admixture	Usage
Sodium Aluminate	To Accelerate Hardening And Increase Early Strength
Aluminum Sulphate	Shorten The Setting Time Of Cement
Fluoro Aluminate	Liquid Accelerator
Pre-Dispersed Carbon Nanotube	Mixing Time Significantly Improved

3. Used-diesel-engine-oil potential

The potential of engine oil as an additive for concrete has been discovered by completely different research. Second, in older grinding units, the loss of oil in the cement resulted in concrete that was more resistant to freezing and thawing, implying that adding used motor oil to the new combine could be equivalent to adding a



chemical air release additive to improve some of the durability properties of concrete while also serving as an alternative technique. Concrete disposal [10]. It has been jointly mentioned that used engine oil has similar superplasticizing properties due to the SO₃ content. we have see seen the chemical composition of used and new engine oil table 2. This summary document also addresses the search for a response to the growing concern about environmental problems resulting from the production of superplasticizers (SP) and used diesel fuel (UDEO). The objective of this review document is to identify the consequences of used motor oil with a force of relevance, the reflection required in the style and construction of new structures, and also once the condition of existing structures has been evaluated [16]. In OPC concrete, using UEO to lengthen the initial slump and air content while slowing slump loss and initial set. There was alittle decrease in 28 day compression, density, and degree of association. [17]. The introduction of UDEO to OPC concrete improved the quality of fresh concrete while lowering the strength properties due to the higher UDEO concentration. [18The qualities of recent and cured concrete as a function of the engine oil utilised. In comparison to the control concrete collapse, the concrete collapse rose from 18% to 38% and the air content increased from 26% to 58% with the introduction of used motor oil [19]. As a water-reducing additive, UEO, like SP, has the ability to boost the strength of concrete. The compressive strength increased from 0.15 to 0.3% used engine oil, which was added to the concrete. however, the additional addition decreased the compressive strength. 58% improved compressive strength in concrete with the addition of UEO compared to concrete with the addition of superplasticizers [20]. The compressive strength values of certain soil affected with diesel oil in mortar (w / c 0.4 and 0.5) enhanced, and the optimum amount of soil contaminated with oil is approximately 5%. With the addition of diesel-contaminated soil, the compressive and flexural strength of mortars was tested [21]. Reinforced concrete girders examined by alternative researchers and described in the literature. According to the literature, used motor oil has the potential to be used as a superplasticizer without losing the static and technical behavior of concrete [22].

Table 2: Used Engine Oil and New Engine Oil have different chemical structures. (Shafiq et al., 2018)

Chemical Composition	Used Engine oil (%)	New Engine oil (%)
SiO ₂	-	0.85
Fe ₂ O ₃	0.43	0.18
CaO	15.9	21.0
SO ₃	37.0	36.3
P ₂ O ₅	8.95	13.4
ZnO	17.7	25.6
CL ⁻	15.9	-

4. Expected gain and loss with used-diesel-engine-oil in cement composites

The setting times times were shortened by 15.2 percent and 5.6 percent, respectively, with the addition of 0.3 percent by weight UDEO to the cement. The addition of UDEO to OPC concrete lowered these setting times, but they still stayed within the acceptable minimum periods and most of the setting times, and it also improved the workability of the concrete while decreasing the compressive strength, whereby the proportion of UDEO decreased. With the addition of silica dust, the compaction problem of OPC concrete with excellent UDEO rose slightly, but the compressive ability was significantly changed. With a 10% alteration, the compressive strength of OPC concrete with UDEO improved by 13.6 percent, and with a 15% modification, it increased by 33.8 percent. When 15 percent and 10% SF, respectively, were added, the compressive strength increased by 36.9% and 17.6%, respectively. It's worth noting that adding different admixtures to concrete with UDEOs resulted in differing compressive strengths. [18]. Oil-contaminated soils do not always have a negative impact on the performance of cement-bound products. As shown in Fig 2, soil contaminated with diesel fuel produces a variety of cement-based compounds. This showed that soil-like solid waste contaminated with used diesel engine oil can be utilized in cement-based materials to increase performance such as consistency and strength while also improving environmental protection and benefits. At the start of development, diesel oil contaminating fine aggregate improved the total heat of hydration of bulk cement and the rate of heat release from a unit mass of cement.

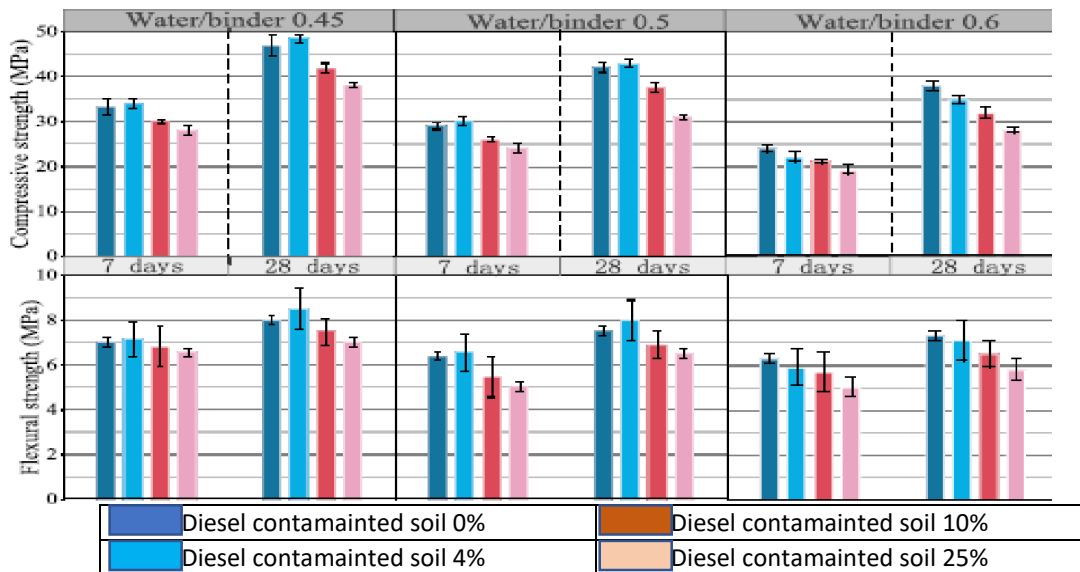
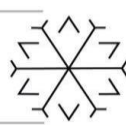
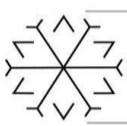


Figure 2: Contaminated diesel oil compressive and flexural strength soil (Li et al., 2020)

Soil contaminated with diesel fuel improved the yield strength and plastic consistence of cement paste and reduced the collapse values of cement mortars. The influence of petroleum-contaminated soils on cementitious material performance isn't always unfavourable. [21].

5. Conclusion

The following conclusions can be extracted from the study carried out:

- Used diesel engine oil has been shown to have the properties of a water reducing agent and an air-entraining agent. The increased air content explains admixing UEO has the opposite effect on concrete qualities (excluding setting time) because of UEO which is found to delay the initial setting time whereas not affecting the ultimate setting time.
- Used diesel motor oil will behave as a chemical plasticiser, similar to super plasticizer, to improve OPC concrete's flowability, air voids, and durability. When another additive, such as silica fume, is added to OPC concrete with the best used diesel oil, the compacting issue is increased
- Used diesel engine oil has the potential to improve the strength of concrete as a water-reducing admixture and increased the air content of the fresh concrete as compared to the air content of the control combine.
- It's also clear from expected gain and loss that no new hydration product generate and physical protection is that the mechanism of solidify diesel oils contaminated soil by cement based mostly materials.

It is concluded that used diesel oil can be used as free chemical plasticiser to boost concrete performance therefore opens the door for new approaches to standard construction to create concrete structure additional sustainable.

Acknowledgements

The authors would like to thank every person/department who helped thorough out the paper. Especially Engr Muhammad Abrar and Engr Blawal hasan.

References

- Gulum, M. and Bilgin, A., 2019. Measurement and prediction of density and viscosity of different diesel-vegetable oil binary blends. *Scientific Journal of Riga Technical University. Environmental and Climate Technologies*, 23(1), pp.214-228.
- Zhang K., Cao Q., Jin LE., Li P., Zhang X., 2017. A novel route to utilize waste engine oil by blending it with water and coal. *Journal of hazardous materials*:332:51–58. <https://doi.org/10.1016/j.jhazmat.2017.02.052>.
- Delveve I., Iltina M., Shanbayev M., Abildayeva A., Kuzhamberdieva S., Blumberga D. 2019: :23(1):168–187 Evaluation of Polymer Matrix Composite Waste Recycling Methods. *Environmental and Climate Technologies*. <https://doi.org/10.2478/rtuct-2019-0012>.



- Alyamaç, K.E. and Ince, R., 2009. A preliminary concrete mix design for SCC with marble powders. *Construction and Building Materials*, 23(3), pp.1201-1210.
- Gencil, O., Ozel, C., Koksall, F., Erdogmus, E., Martínez-Barrera, G. and Brostow, W., 2012. Properties of concrete paving blocks made with waste marble. *Journal of cleaner production*, 21(1), pp.62-70.
- Murali, G., Vardhan, C.V., Prabu, R., Khan, Z.M.S.A., Mohamed, T.A. and Suresh, T., 2012. Experimental investigation on fibre reinforced concrete using waste materials. *International Journal of Engineering Research and Applications (IJERA) ISSN, 2248(9622)*, pp.278-283.
- Okoye, F.N., Durgaprasad, J. and Singh, N.B., 2016. Effect of silica fume on the mechanical properties of fly ash based-geopolymer concrete. *Ceramics International*, 42(2), pp.3000-3006.
- Ejeh, S.P. and Uche, O.A.U., 2009. Effect of crude oil spill on compressive strength of concrete materials. *Journal of Applied Sciences Research*, 5(10), pp.1756-1761.
- Chin, S.C., Shafiq, N. and Nuruddin, F., 2012. Effects of used engine oil in reinforced concrete beams: the structural behaviour. *International Journal of Civil and Geological Engineering*, 6, pp.83-90.
- Shafiq, N., Choo, C.S. and Isa, M.H., 2018. Effects of used engine oil on slump, compressive strength and oxygen permeability of normal and blended cement concrete. *Construction and Building Materials*, 187, pp.178-184.
- Yang, R. and He, T., 2021. Influence of liquid accelerators combined with mineral admixtures on early hydration of cement pastes. *Construction and Building Materials*, 295, p.123659..
- Mardani-Aghabaglou, A., Karakuzu, K., Kobya, V. and Hatungimana, D., 2021. Durability performance and dimensional stability of road concrete containing dry-shake surface hardener admixture. *Construction and Building Materials*, 274, p.121789Hamad B. S., Rteil A. A., El-Fadel M. Effect of used engine oil on properties of fresh and hardened concrete. *Construction and Building materials* 2003:17(5):311-318. [https://doi.org/10.1016/S0950-0618\(03\)00002-3](https://doi.org/10.1016/S0950-0618(03)00002-3)
- Wang, T., Xu, J., Zhu, C. and Ren, W., 2020. Comparative study on the effects of various modified admixtures on the mechanical properties of styrene-acrylic emulsion-based cement composite materials. *Materials*, 13(1), p.8DeDene, C.D. and You, Z., 2014. The Performance of Aged Asphalt Materials Rejuvenated with Waste Engine Oil. *International Journal of Pavement Research & Technology*, 7(2).
- MacLeod, A.J., Fehervari, A., Gates, W.P., Garcez, E.O., Aldridge, L.P. and Collins, F., 2020. Enhancing fresh properties and strength of concrete with a pre-dispersed carbon nanotube liquid admixture. *Construction and Building Materials*, 247, p.118524.
- Combrinck, R., Kayondo, M., Le Roux, B.D., De Villiers, W.I. and Boshoff, W.P., 2019. Effect of various liquid admixtures on cracking of plastic concrete. *Construction and Building Materials*, 202, pp.139-153.
- DeDene, C.D. and You, Z., 2014. The Performance of Aged Asphalt Materials Rejuvenated with Waste Engine Oil. *International Journal of Pavement Research & Technology*, 7(2).
- Svintsov, A.P., 2019. Effect of petroleum products on physical and mechanical properties of concrete and the reliability of load-bearing structures. *Arabian Journal for Science and Engineering*, 44(5), pp.4277-4287.
- Okashah, A.M., Abdulkareem, M., Ali, A.Z., Ayeronfe, F. and Majid, M.Z., 2020. Application of automobile used engine oils and silica fume to improve concrete properties for eco-friendly construction. *Environmental and Climate Technologies*, 24(1), pp.123-142.
- Yaphary, Y.L., Lam, R.H. and Lau, D., 2020. Reduction in cement content of normal strength concrete with used engine oil (UEO) as chemical admixture. *Construction and Building Materials*, 261, p.119967.
- Varghese, R.G. and Sakaria, P.E., 2017. Experimental investigation on the properties of fresh and hardened concrete with used engine oil as super plasticizer. *Int. Res. J. Eng. Technol.*, 5(4), pp.2230-2236.
- Li, Y., Zeng, X., Zhou, J., Liu, H., Gu, Y., Pan, Z., Zeng, Y. and Zeng, Y., 2020. Incorporation of disposed oil-contaminated soil in cement-based materials. *Resources, Conservation and Recycling*, 160, p.104838.
- Chin, S.C., Shafiq, N. and Nuruddin, F., 2012. Effects of used engine oil in reinforced concrete beams: the structural behaviour. *International Journal of Civil and Geological Engineering*, 6, pp.83-90.
- Abdelaziz, G.E., 2011. Utilization of used-engine oil in concrete as a chemical admixture. Benha University, Egypt.

An Overview on Different Corrugated Sheets from Manufacturing to Housing Element

Aaroon Joshua Das^{1*}[0000-0003-3228-9075] and Majid Ali²[0000-0002-3690-2183]

¹E-mail address: ajodas@yahoo.com, Ph.D. student, Department of Civil Engineering, Capital University of Science and Technology, Islamabad, Pakistan

²E-mail address: professor.drmaid@gmail.com, Professor, Department of Civil Engineering, Capital University of Science and Technology, Islamabad, Pakistan

Abstract

The corrugated sheets are covering element which are quiet useful in the low cost construction. The corrugated sheets allow stressess to distributed in the corrugation and making the member efficient for long term. Usually the corrugated sheets are made up of steel and in some places concrete. Steel is vulnerable to corrosion and is expensive. Galvanization and other techniques are used which are expensive and used to protect the sheets from corrosion. Other materials are still limited in competing for steel. The shape and geometry of the corrugated sheets have much significance. These sheets were initially not regarded aesthetically and the use was limited to warehouses and stores etc. The construction industry out of all this enormous use of Corrugated sheets is requiring a sustainable solutions and low-cost solutions. This study intends to overview the materials available for corrugated sheets. Further exploration is required to provide a substitute for corrugated sheets through recycling of waste plastic or other means.

Keywords. Corrugated sheets, waste plastic, roofing sheets

1. Introduction

The corrugation was first employed by Henry Robinson Palmer in 1820s. The intention was to develop low cost roofing which were fixed on timber with masonry footings (Thomson and Banfill, 2005). The corrugated sheet were coated with zinc galvaniation to minimize corrossion. The sheets develop from different materials are efficient and used in parking areas, low cost construction and warehouses. These sheets have problems in service life and produce cracks and water leakages for which only remedy is to either replace the sheets of redo the joints in the arrangement. The corrugated sheets are recommended for low cost construction and can provide large supported pannels over arrangements of beams, trusses etc. The geometry available is mostly rectangular and circular in some places.

Ludwig Hatschek, provided a technique to produce the aesbestos – cement roof in 1907. The technique employees vacuum foaming. An attempt was made to produce the corrugated sheets from fique fibre which showed staisfatorry results (Delvasto *et al.*, 2010). In the conclusion it was recommended that the use of different fibres shall complement the corrugated sheet manufacturing. These aesbestos sheets have been regard as a health hazard in some countries. Different materials are commercially available which are discribed in details. The portland cement based corrugated sheets which are produced from the process of Hatschek process produce cracking at the edges, lining damages at corrugations which are mechanical, selling at some spots, damages in stock piling, damages due to transport and assembling, shrinkage and others (de Mello Innocentini *et al.*, 2019). These are best cleared by other materials such as steel.

The corrugated sheets are differentiated through relative comparisons. Comercially the comparisons exists for preexisting sheets which are of thickness, bending, galvanizing, resistance towards different external conditions such as heat, noise, wind. The uses of the sheets diversify from hangars, warehouses, houses in extreme cold weathers, stores, parking areas, wall claddings, etc. (Wakeland, 1954).

The purpose of this study is to overview different geometries and different materials for corrugated sheet for intended replacement of steel and concrete from recycled waste plastic corrugated sheets. The option to recycle waste plastic is currently being demanded all over the World as only 9% of the disposal is being recycled (Geyer, Jambeck and Law, 2017). The construction industry can employ waste plastic as a plausible material which is not only cheaper but is resistant to corrosion. The waste plastic needs pre-sorting

prior to be used in recycling and manufacturing process of corrugated sheets this can produce better product to be used commercially (Das and Ali, 2021).

2. Geometry of corrugated sheets

The geometry is widely available in rectangular shapes and can be reshaped by cutting to sizes. The geometry and intended use extends to wall claddings and shades. The modelling is complex due to shell elements being uncertain and indeterminate to transfer loads. Due to lesser thickness the malleability of the material is required. The commercially available materials are usually not more variant in material for corrugated sheets. A study was conducted wherein two numerical models were assessed for distribution of stresses, the stresses were distributed heterogeneously and it was concluded that the behaviour of the sheets can be modelled using FEM based softwares (Molina *et al.*, 2018). The corrugation is also found structurally efficient and also is better for torsional and bending stiffness (Malek and Williams, 2017). Figure 1 shows a typical geometry of a corrugated sheet commercially available. The upper portion are usual crests and the bottom of corrugation is the trough. The corrugation pitch is the distance between to crests or troughs and the corrugation depth is the linear distance between crest and trough.

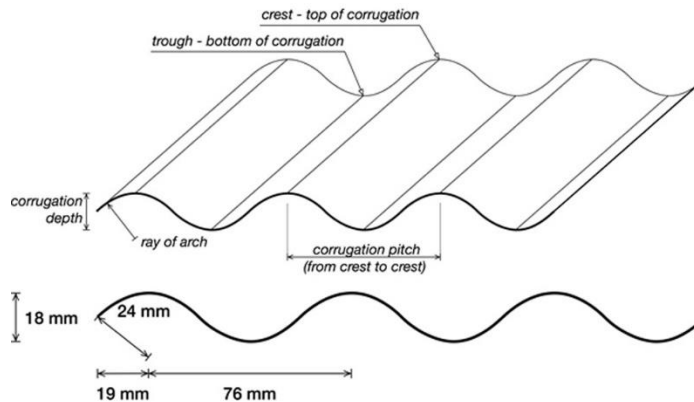


Figure 1: typical geometry of a corrugated sheet

Another study was conducted, wherein, it was deliberated that the wind imparts load which can lift the corrugated sheets, a set of structural solutions have been provided to cater the issues which were already provided in the codes. The implementation of the codes are required at individual level especially at the coastal areas where there are immense wind pressures (Alam *et al.*, 2017). A study was conducted to assess the flexural properties of the corrugated sheet and were recorded to behave more efficiently than flat roofs (Wakeland, 1954). The geometry and material do not cause high failure problems but are found to be effective for decades if the galvanization is proper.

3. Corrugated sheets of different materials

Steel sheets are widely being as roofing materials (Henderson and Ginger, 2011). The corrugated sheets made of cementitious materials have an issue of water absorption and air permeability (de Mello Innocentini *et al.*, 2019). Testing methods were developed to monitor the permeability of the corrugated sheets. Other materials commercially available for sheeting are bituminous, fibre cement, polycarbonate etc. FRP sheet have also been tested and results were compared with mathematical model to relate to modelling of the shell element, being indeterminate the sheets were evaluated for different boundary conditions (Gautam and Pathak, 1998).

The recycled polymer sheets, to date, have not been developed from plastic. Although, PVC roofing sheets from fresh resins have been developed and are being used in the construction industry. These sheets are properly designed and are sought to perform better than steel (Setyanto, 2019). Polycarbonate and other well-designed sheets of polymeric materials are also available which have been observed to have a respectable level of performance

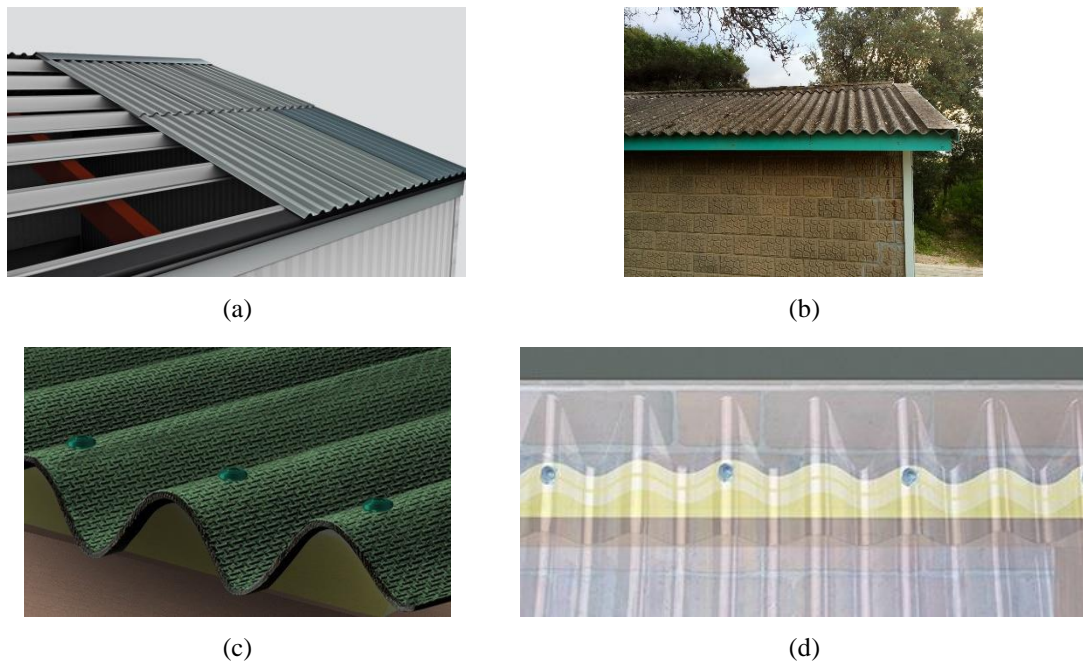


Figure 2: Different roofing material (a) steel corrugated roof over steel frame (b) Aesbestos roofing (c) bitumenous roofing sheet (d) PVC roofing sheet

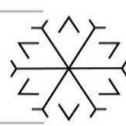
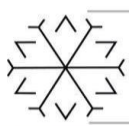
Figure 2 shows corrugated roofs of different materials of steel, asbestos, bitumenous, PVC collected from different sources. These materials have been found having different service life and having different cost in terms of manufacturing and repair.

Drawing laminates from the sheet extrusion process have been around for a considerable time an example of which is a fabric made from Polypropylene resin with Kevlar (Lin *et al.*, 2020). This process can be employed for preparing corrugated roof sheets (Du *et al.*, 2017). The sheet extrusion process is sensitive to the properties of a polymer. The production unit maintains a designed temperature to get desired properties. A substantial amount of sustainability can be achieved through developing proper green roofing (Besir and Cuce, 2018). The material used to produce roof should have a green component as 20-25% of the area in urban civilization is occupied by houses, buildings, and parking having roofs and should provide eco-system related benefits (Guzmán-Sánchez *et al.*, 2018). A mix of different plastic obtained from waste should require a better synthesis before remolding through extrusion.

4. Corrugated sheets as housing element

The corrugated sheet have problems of connectivity over laps the assessment of the same is under research and this causes water penetration and intense breakage (Mohammed and Kennedy, 2009). The use of corrugated sheets in the elements under loads have also been assessed which produces the same problems of connectivity (Mohammed, Kennedy and Smith, 2002). This is termed as fatigue failue which needs repair after certain service life depending upon the wind culture and external weather culture of the area.

Different roofing material are being used for housing. Table 1 presents different sheets commercially available and being used for construction with their advantages and disadvantages also their fixing modes are described in various sources. Much work has not been recorded in the past regarding the corrugated sheet elements and material for the corrugated sheets. Plausible studies are required like other structural elements to develop more appropriate materials for the corrugated sheets. The tests to relate to corrosion resistant is not available, even no standards exist to test the thermal conductivity, noisy or acoustic balances. The issues highlighted in the tables are compiled by observance of use in the housing or industrial use.

**Table 1:** Advantages and disadvantages of different corrugated sheets and there fixing method (IFRC, 2016)(Japan Stainless Steel Association, 1989)

Material used in construction	Advantages	Disadvantages	Fixing method
Corrugated Galvanized steel with coating of zinc	<ul style="list-style-type: none"> ▪ These are light weight ▪ Comes in different thickness and largely available and used ▪ Commercially available easily and at a very low cost 	<ul style="list-style-type: none"> ▪ The durability is limited to climatic conditions and expects corrosion depends upon the coating ▪ Gets heated in thermal conditions ▪ Noisy during rain and have low acoustics 	<ul style="list-style-type: none"> ▪ Rubber washers with screws bolts and with sealing materials
Corrugated aluminium with coating of zinc	<ul style="list-style-type: none"> ▪ These are lightweight ▪ Comes in different thickness and largely available and used ▪ Commercially available easily and at a very low cost ▪ Have resistance to corrosion ▪ Recommended for industrial use 	<ul style="list-style-type: none"> ▪ Are expensive than CGI ▪ Better than CGI in thermal conductivity ▪ Gets reacted with copper sulphate lead bronze etc ▪ Noisy during rain and have low acoustics 	<ul style="list-style-type: none"> ▪ Same as CGI Rubber washers with screws bolts and with sealing materials
Corrugated aluminium sheets	<ul style="list-style-type: none"> ▪ These are lightweight ▪ Comes in different thickness and largely available and used ▪ Commercially available easily and at a very low cost ▪ Have resistance to corrosion ▪ Recommended for industrial use 	<ul style="list-style-type: none"> ▪ Expensive than CGI ▪ Better than CGI in thermal conductivity ▪ Gets reacted with copper sulphate lead bronze etc ▪ Noisy during rain and have low acoustics 	<ul style="list-style-type: none"> ▪ Same as CGI Rubber washers with screws bolts and with sealing materials
Bitumen sheets having corrugations	<ul style="list-style-type: none"> ▪ High resistant and do not rust ▪ Thermally insulated ▪ Less noisy in weather like rain etc ▪ Lesser in cost ▪ Recommended for marine urban environments 	<ul style="list-style-type: none"> ▪ Only one size as that of the manufacturing limitations ▪ Are not easily commercially available ▪ Are heavy and can catch fire 	<ul style="list-style-type: none"> ▪ Rubber washers with galvanized screws bolts and with sealing materials
Fibre glass sheets with corrugations	<ul style="list-style-type: none"> ▪ Comes in transparent colours ▪ Comes in light weight and good aesthetical colours 	<ul style="list-style-type: none"> ▪ Only one size as that of the manufacturing limitations ▪ Brittle and break due to fatigue or shocks ▪ Expensive than other sheets 	<ul style="list-style-type: none"> ▪ Rubber washers with galvanized screws bolts and with sealing materials
Fibro cement sheets with corrugations	<ul style="list-style-type: none"> ▪ Good resistance against rust ▪ Bear heavy load and donot deform 	<ul style="list-style-type: none"> ▪ Only one size as that of the manufacturing limitations ▪ Brittle and break due to fatigue or shocks ▪ Expensive to make and tranport ▪ Acoustically low 	<ul style="list-style-type: none"> ▪ Proper washers of galvanized steel with bolts and sealing materials
plastic sheets with corrugation	<ul style="list-style-type: none"> ▪ High resistant and do not rust ▪ Comes in light weight and good aesthetical colours 	<ul style="list-style-type: none"> ▪ Brittle and break due to fatigue or shocks ▪ Expensive than other sheets 	<ul style="list-style-type: none"> ▪ Rubber washers with galvanized screws bolts and with sealing materials
Corrugated asbestos sheets	<ul style="list-style-type: none"> ▪ Do not rust and is in lighter weight 	<ul style="list-style-type: none"> ▪ Have health hazards and is prohibited in some countries. ▪ Not recommended for commercial or domestic uses 	<ul style="list-style-type: none"> ▪ Rubber washers with galvanized screws bolts and with sealing materials

5. Conclusion

The corrugated sheets are members which are used for roofing and are available in different materials and diverse in providing sheet solutions for walls and roofs. The following conclusions can be drawn from the above ideas

- The corrugation distributes the loads and provide better torsional and bending stiffness
- The corrugated sheets of different materials are used other than steel the variants of sheets can variably be developed from recycled waste plastic.
- The corrugated sheets due to low aesthetic are used for ware houses and stores. The corrugated sheets can be used for low cost housing

The future studies can be employed to convert recycled waste plastic to be used in corrugated sheet. The mechanical properties need to be assessed to be used in construction industry. The plausible recycled waste material sheets can prove a sustainable solution for low cost housing.

Acknowledgements



The authors would like to thank all persons/organizations who helped during this research.

References

- Alam, M. R. *et al.*, 2017. Vulnerability assessment and construction recommendations of local houses in the cyclone prone coastal areas of Bangladesh, *International Journal of Disaster Risk Reduction*, 21, pp. 118–130. doi: 10.1016/j.ijdr.2016.10.010.
- Besir, A. B. and Cuce, E., 2018. Green roofs and facades: A comprehensive review, *Renewable and Sustainable Energy Reviews*, 82(September 2017), pp. 915–939. doi: 10.1016/j.rser.2017.09.106.
- Das, A. J. and Ali, M., 2021. Recycling of waste plastic with least effect to environment : A review, pp. 1–4.
- Delvasto, S. *et al.*, 2010. An appropriate vacuum technology for manufacture of corrugated fique fiber reinforced cementitious sheets, *Construction and Building Materials*, 24(2), pp. 187–192. doi: 10.1016/j.conbuildmat.2009.01.010.
- Du, B. *et al.*, 2017. Fabrication and Flatwise Compression Property of Glass Fiber-Reinforced Polypropylene Corrugated Sandwich Panel, *International Journal of Applied Mechanics*. doi: 10.1142/S1758825117501101.
- Gautam, C. K. and Pathak, R. C., 1998. C.K. Gautam and R.C. Pathak Research & Development Establishment (Engrs), Pune-41 015', 113(1), pp. 105–113.
- Geyer, R., Jambeck, J. R. and Law, K. L., 2017. Production, use, and fate of all plastics ever made, *Science Advances*, 3(7), pp. 25–29. doi: 10.1126/sciadv.1700782.
- Guzmán-Sánchez, S. *et al.*, 2018. Assessment of the contributions of different flat roof types to achieving sustainable development, *Building and Environment*, 141(May), pp. 182–192. doi: 10.1016/j.buildenv.2018.05.063.
- Henderson, D. J. and Ginger, J. D., 2011. Response of pierced fixed corrugated steel roofing systems subjected to wind loads, *Engineering Structures*, 33(12), pp. 3290–3298. doi: 10.1016/j.engstruct.2011.08.020.
- IFRC, 2016. How to build safe roofs with corrugated galvanized iron (CGI) sheeting, p. 238.
- Japan Stainless Steel Association, 1989. For the DESIGN AND CONSTRUCTION of ROOFS OF STAINLESS STEEL SHEET For Publication of the English Edition'.
- Lin, M. C. *et al.*, 2020. Fabrication, properties, and failure of composite sandwiches made with sheet extrusion method, *Journal of Sandwich Structures and Materials*, 22(3), pp. 689–701. doi: 10.1177/1099636218766230.
- Malek, S. and Williams, C., 2017. The Equilibrium of Corrugated Plates and Shells, *Nexus Network Journal*, 19(3), pp. 619–627. doi: 10.1007/s00004-017-0347-7.
- de Mello Innocentini, M. D. *et al.*, 2019. Air permeability assessment of corrugated fiber-cement roofing sheets, *Cement and Concrete Composites*, 97(October 2018), pp. 259–267. doi: 10.1016/j.cemconcomp.2019.01.004.
- Mohammed, H. and Kennedy, J. B., 2009. Fatigue Resistance of Corrugated Steel Sheets Bolted Lap Joints under Flexure, *Practice Periodical on Structural Design and Construction*, 14(4), pp. 242–245. doi: 10.1061/(asce)sc.1943-5576.0000021.
- Mohammed, H., Kennedy, J. B. and Smith, P., 2002. Improving the Response of Soil-Metal Structures during Construction, *Journal of Bridge Engineering*, 7(1), pp. 6–13. doi: 10.1061/(asce)1084-0702(2002)7:1(6).
- Molina, J. C. *et al.*, 2018. Behavior of corrugated fibre cement sheets subjected to suction loads, *Ingeniare. Revista chilena de ingeniería*, 26(1), pp. 106–113. doi: 10.4067/s0718-33052018000100106.
- Setyanto, D., 2019. Design and FE Modeling of UPVC Corrugated Hollow Roofing Sheet, *MATEC Web of Conferences*, 258, p. 01017. doi: 10.1051/mateconf/201925801017.
- Thomson, N. and Banfill, P., 2005. Corrugated-Iron Buildings: An Endangered Resource within the Built Heritage, *Journal of Architectural Conservation*, 11(1), pp. 71–87. doi: 10.1080/13556207.2005.10784936.
- Wakeland, H. L., 1954. Flexural properties of corrugated metal roofing.

Determination of Changes in Precipitation and Snowpack Using Innovative Trend Analysis in Sinirbaşı Basin

M.Cansaran Ertas ¹*[0000-0002-6376-5516] and Hülya Bakır ²

¹cansaran.ertas@erzurum.edu.tr, Erzurum Technical University

²hulya.bakir@tarimorman.gov.tr, East Anatolian Agricultural Research Institute

Abstract

Water resources are one of the most crucial issues on which climate change has a lasting and major impact. Especially in recent years, repeated drought and heavy rainfall events have led to significant unknowns and problems regarding snow hydrology. These problems directly affect human life as well as indirectly affect agriculture, tourism, transportation and energy production. Considering these reasons, it is very important to monitor the annual amount of precipitation and snow cover during the seasons in the regions where a significant part of the precipitation falls in the form of snow, such as the mountainous eastern regions of Turkey. The main focus of this study is to determine the trend of precipitation and snow data for the 1997-2021 period in the Sinirbaşı Basin, which is a subbasin of the Euphrates Basin has grand snow potential in Turkey. Snow and meteorological observation network have been developed and sustained with projects carried out in the test basin. In the Innovative Trend Analysis (ITA) method, the time series is divided into two equal parts, the parts are sorted from small to large in themselves, then in the scatter chart, the first part is placed on the horizontal axis, and the second part is placed mutually on the vertical axis. The points in the upper part of the 1:1 line tend to increase, while the remaining points in the lower part show the decreasing trend. According to the preliminary findings indicate decreasing amount of 18 mm and 10 mm in summer and autumn precipitation, respectively.

Keywords. Climate change, precipitation, snow measurement, innovative trend analysis, sinirbaşı basin

Numerical Analysis of Embankment Slopes Reinforced by Different Methods Using Plaxis 2D Program

Cenk Cuma Çadır ¹{0000-0002-6031-2028}, and Yücel Güney ¹{0000-0001-9246-706X}

¹cenk.cadir@bozok.edu.tr, Yozgat Bozok University

¹yucel.guney@bozok.edu.tr, Yozgat Bozok University

Abstract

One of the most important topics in geotechnical engineering is slopes. Soft clay slopes, in particular, may lose their stability as they are loaded. Slopes that lose their stability can cause particularly great material damage. Considering this situation, it is necessary to improve the soft soils under the fill slope. Recently, many methods (bored pile, mini pile, jet grout, deep mix, stone column, etc.) based on the formation of columns in the soil are widely used. These methods each have advantages and disadvantages. When the previous studies are examined, it is found that the comparative analysis of the behavior of slopes of soft soils under embankment using different methods is limited.

From this point of view, this study used the Plaxis 2D program to investigate the effect of reinforcing the slope, which consists of a soft clay layer under the embankment, using four different methods (bored pile, jet grout, deep mix and stone column) on the stability of the slope. In the study, a soft clay layer ($c:5 \text{ kN/m}^2$; $\phi; 20^\circ$; $\gamma_k; 18 \text{ kN/m}^3$ etc.) of 8 m height and 20 m width is located under the embankment slope ($c:1 \text{ kN/m}^2$; $\phi; 40^\circ$; $\gamma_k; 19 \text{ kN/m}^3$ etc.) with a height of 4 m, a width of 15 m and a slope angle of 45° . First, the safety analysis of the embankment slope was performed without any improvement of the soft clay soil. Then, stability analysis was carried out by reinforcing the soft clay soil under the embankment in the same geometric model using four different methods (bored pile, jet grout, deep mix and stone column) with a diameter of $D: 60 \text{ cm}$, a column spacing of $S/D: 2.0$ and an application depth of $L: 8 \text{ m}$.

As a result of the analysis, the safety factor of unreinforced slope, 0.758, the safety factor of bored pile reinforced slope, 2.22, the safety factor of jet grout reinforced slope, 1.75, the safety factor of deep mix reinforced slope and the safety factor of stone column reinforced slope were found to be 1.64 and 1.31 respectively. When the numerical results were evaluated, it was found that the four different types of columns placed in the soft clay soil under the backfill increased the stability of the slope. It can be said that the bored pile method is the most effective method for the stability of the backfilled slope, the jet grout method gives very similar safety figures to the deep mix method, and the stone column method is slightly less ineffective than other methods. From here, it can be said that the bored pile method comes into prominence depending on the column stiffness, while the stone column method loses performance due to the lateral spread of the column material in the soil depending on the free compressive strength value of the soft clay soil. Consequently, the methods mentioned here can be used for the stability of soft clay soils under backfill. However, it can be considered that it would be more accurate to determine the method considering the lateral loads, the strength parameters of the soil as well as the desired stability values.

Keywords: Slope stability, bored pile, jet grout, deep mixing, stone columns

The Examination of the Effect of Rock Salt on The Setting Time of The Grout by Utilizing The Taguchi Method

A. Şahin Zamioğlu ^{1*}[0000-0001-5245-0212] and Elif Ayık Kılıç ²[0000-0001-5540-8247] and Fatih Artuk ³[0000-0003-4798-9277]

¹ zaimoglu@atauni.edu.tr, Atatürk University

² elif.ayik@erzurum.edu.tr, Erzurum Technical University

³ fatih.artuk@atauni.edu.tr, Atatürk University

Abstract

One of the soil improvement methods used in geotechnical applications today is grouting. Injection is a soil improvement method used during tunnel construction to stabilize soil and rocks, to fill existing cracks in rocks, to fix anchor rods and to prevent settlements on soils. In the areas where the injection process is applied, different formations (rock salt, etc.) can be encountered and the success of the process is affected by various parameters. One of these parameters is the setting time. For this reason, tunnels, anchorages, etc., which are hardly studied in the literature. The effects of the rock salt formation encountered in the applications on the setting time of the injection fluid were investigated.

In the study, 3-parameter, 4-level L16 experimental design was used according to the Taguchi Optimization Method. In the Taguchi Optimization Method, water/cement ratio (S/C), sand percentage (KY) and rock salt saturation percentage (KTDY) were selected as parameters and their levels were determined as 0,8-1,0-1,2-1,4, 0%-25%-50%-100% and 0%-25%-50%-100%, respectively. Setting time was determined by the Vicat Needle test.

According to the test results, the lowest setting time was 693 minutes, the water/cement ratio was 0.8 (1st level), the sand percentage was 25% (2nd level) and the saturation percentage with rock salt was 25% (2nd level). The highest setting time was determined in experiment with 2751 min, where S/C ratio was 1.4 (4th level), KY (0%) (1st level) and KTDY was 100% (4th level). In addition, S/N analyzes of each experiment were made by using the test results of the setting times. In the Taguchi Optimization Method, S/N values were calculated considering the situation where the shortest setting time is the best.

The lowest S/N value and the highest S/N value were obtained at the fourth and first levels of the S/C ratio as -68.79 and -56.81, respectively. In order to determine the effects of water/cement ratio, sand and rock salt saturation on the setting time, variance (ANOVA) analysis was performed and according to the results of the analysis, the most effective and least effective parameters on the setting time were determined as KTDY (45.91%), KY (%) 2.25) As a result, it was seen that the optimum mixing ratio for the setting time was 0.8, S/C ratio was 0.8, KY was 100%, and KTDY was 25%.

Keywords. Grout, rock salt, setting time, Taguchi Optimization Method

Acknowledgment: The study was supported by the BAP Coordinatorship at Atatürk University under the project number FYL-2020-8223.

Evaluation of The Importance of Geomorphic Indices on River Basins Located on Different Slopes, Case Study: Sivas Province, Koyulhisar, Turkey

Redvan Ghasemlounia ^{1*}[0000-0003-1796-4562] and Mustafa Utlu ²[0000-0002-7508-4478]

¹redvan.ghasemlounia@gedik.edu.tr, Department of Civil Engineering, Faculty of Engineering, Istanbul Gedik University, Istanbul, Turkey

²mutlu@bingol.edu.tr, Faculty of Science and Letter, Department of Geography, Bingöl University, Bingöl, Turkey

Abstract

This paper aims to evaluate the different aspect characteristics of basins. In this respect, 2 north-facing basins and 2 south-facing basins were selected as the study area from Sivas Province Koyulhisar, Turkey. 19 different geomorphic indices were used depending on the linear, areal and relief morphometry in the quantitative explanation and comparison of the development of the river basins located on different slopes in the study area. The ArcGIS pro, ArcGIS 10.x and some statistical programs were used. The Digital Elevation Model (DEM) with a resolution of $\pm 10 \times 10$ meters obtained as a result of digitizing the 1/25.000 scaled H38b2-b3, H39a1-a4 maps was prepared from the General Command of Mapping. Depending on the results obtained, the aspect effect was clearly seen on these basins. It is understood from the indices of Rl, Rb, Fs and Dd that in these basins, which have similar features in terms of shape and area, especially the river drainage network has higher values in the basins facing south. From the values obtained on the north-facing slopes, it was observed that the basin shape was more circular, while the south-facing basins had a more elongated geometry. Other indices for the selected basins were also calculated and the results were compared each other in this work.

Keywords. Basin, Geomorphic indices, Relief parameters, Linear parameters, Areal parameters

1. Introduction (Heading 1)

Nowadays, lots of researches are being done on different basins in order to prevent floods, to benefit from water and many other purposes in the term of protection and having benefits from the water in the basins by several researchers. Morphometry science is the measurement of the world surface quantitatively. This measurement helps to understand different aspects (Pidwirny, 2006; Mahmood and Gloaguen, 2012). So, it is crucial to solving and understanding the drainage basin characteristics (Singh, 2017). Based on the mentioned information, morphometric studies have gained importance today, which measure various river drainage watershed properties using several indices concerning linear, areal, and relief parameters (Youssef et al., 2011; Patel et al., 2012; Kumar, 2016). These indices facilitate understanding hydrologic properties and drainage watershed properties concerning flood potential (Bhat et al., 2019). By using these indices and applying up to dated analysis on them, it is possible to rank the basins base on their flood risk. Ghasemlounia and Utlu (2021) have an study on flood prioritization of basins using principal component analysis, morphometric analysis and Redvan's priority methods in Harşit River basin, based on geomorphometric properties and using of theses indices. Many other researchers have some studies on many basins such as El Tahan and Elhanafy (2016); Gunjan et al. (2020); Abdelkarim et al. (2020); Utlu and Ghasemlounia (2021); Sezer (2019); Archer et al. (2018); Costache et al. (2019); El-Fakharany and Mansour (2021); Farhan et al. (2017); Luu et al. (2021); Singh and Singh (2017); Baltacı (2018); Aydin and Raja (2020); etc.

The main aim of the current paper is to study on the morphometric characterization and comparison of the results of selected four Basins in Sivas Province Koyulhisar, Turkey.

2. Material and Method



2.1. Study Area

The sub-basins chosen for the study area pour their waters into the Kelkit Stream Basin. In this study, in which different aspect characteristics were evaluated, 2 north-facing basins and 2 south-facing basins were selected as the study area (Fig 1). These basins are located within the borders of Sivas province Koyulhisar in Turkey and have different characteristics. Among these differences, there are both lithological units and land use cover/usage characteristics as well as climatic characteristics. North-facing basins vary between 13.69 and 18.05 km², while south-facing basins vary between 12.38 and 36.25 km². Again, the basin no. K1 facing north varies between 534.19-1879.46 m, while the basin no. K2 varies between 520.85-1640.1 m. Among the south-facing basins, G1 is between 534.71-2183.1, while the G2 basin has elevations varying between 522.43-1806.3 m.

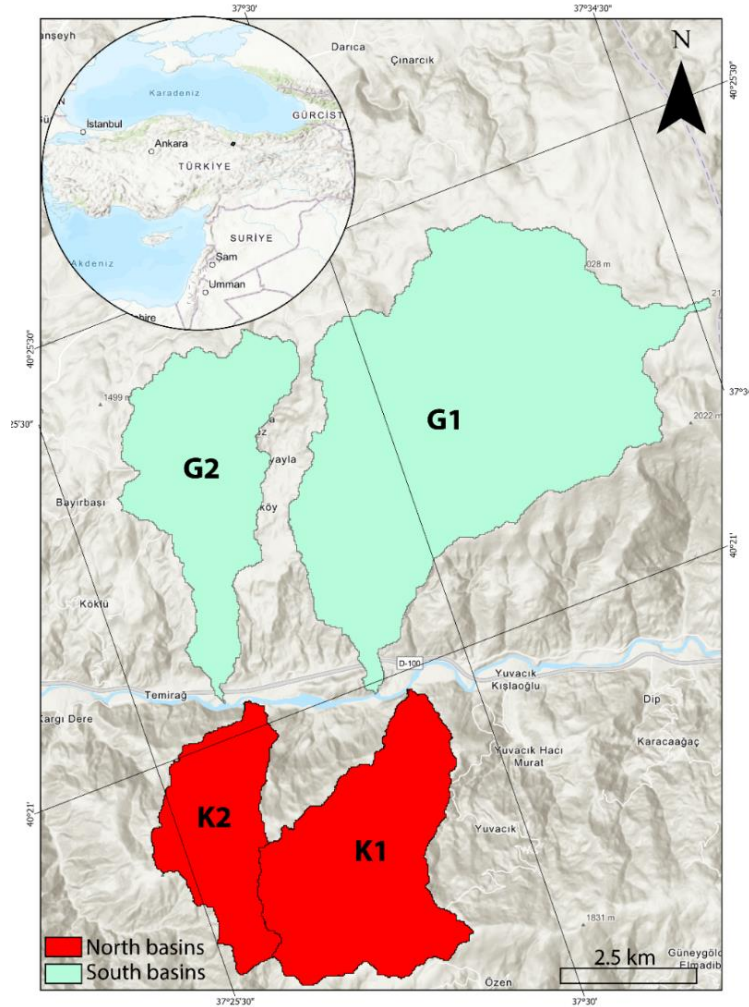


Figure 1: The location of the study area.

There are also differences in the distribution of lithologic units obtained from the 1/500000 scaled geological map of the study area (Fig 2a). While there are agglomerate, andesite and tuff, basalt and schist units in the basins facing north, limestone, basalt, sandstone and mudstone units are observed in the basins facing south. In addition, there are differences in the basins facing different slopes due to their location, where there are also different types of land use characteristics (Fig 2b). Agricultural areas occupy more space on south-facing slopes due to the more favorable temperature values, while they occupy less space in north-facing areas. On the other hand, mixed forests, are located on the north-facing slopes, and are not seen at all on the south-facing slopes. The temperature and precipitation characteristics of the basin are also under the influence of Filyos Stream, apart from the aspect effect. It can be said that the temperature values are felt more intensely in the Filyos brook valley and its immediate surroundings, and in the lower parts and valleys of the south-facing G1-G2 basins. In the total precipitation values, it is around 632 mm at a high rate in the Filyos Stream valley and its close surroundings.

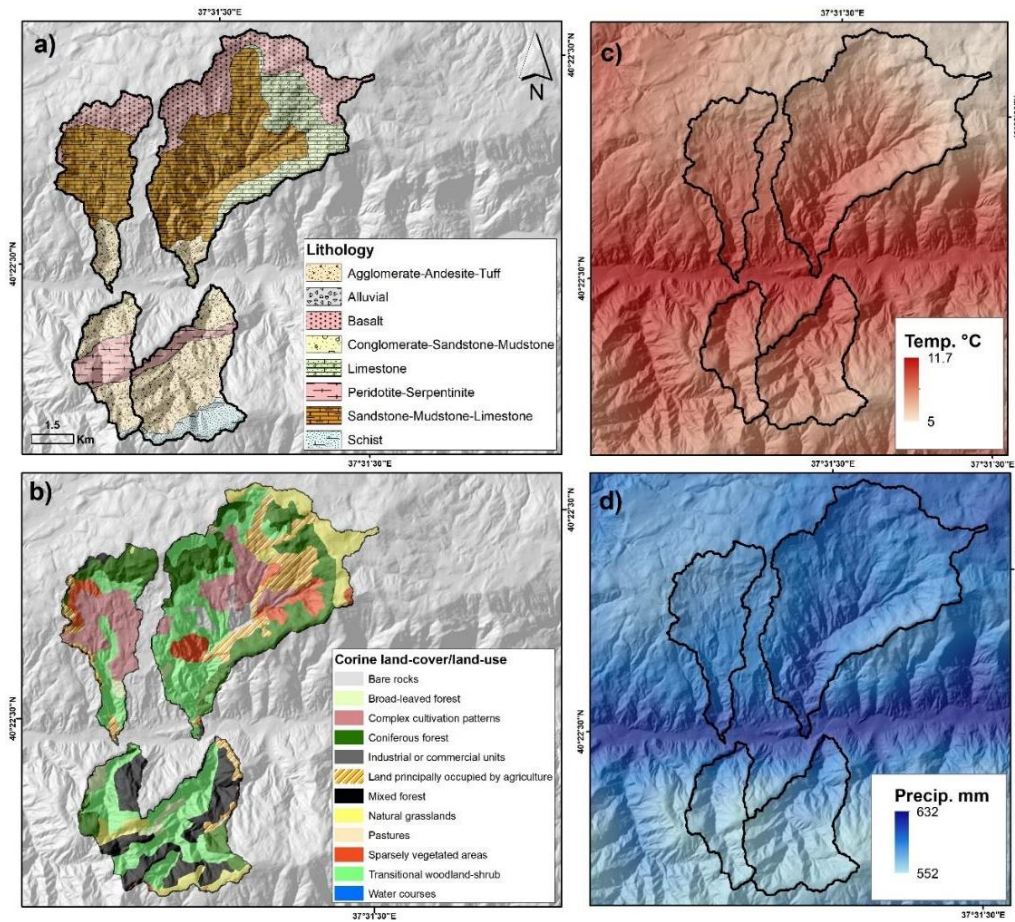
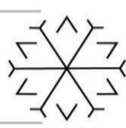


Figure 2: a) The lithological units (modified from Şenel 2002), b) land cover of the study area (Url-1), c) the distribution of the average temperature (Url-2), and d) the distribution of the total precipitation (Url-2 and Ficj and Hijmans, 2017).

2.2. Data

All of the quantitative data in the study were based on geographic information systems and statistics. In this context, ArcGIS pro, ArcGIS 10.x and some statistical programs were used. Apart from this, the Digital Elevation Model (DEM) with a resolution of $\pm 10 \times 10$ meters obtained as a result of digitizing the 1/25.000 scaled H38b2-b3, H39a1-a4 maps produced by the General Command of Mapping was used. The creation of the basins was carried out using the ArcGIS Spatial Analyst Hydrology tool. The threshold value of 500 was used to produce the stream network. WGS84 37th Zone reference system was used as a basis for mapping and performing spatial analysis.

2.3. Methodology

In the current study, geomorphic indices were used to explain the development of 4 river basins with different aspects. These indices contribute to the quantitative explanation of the development of the basins by taking into account the linear, areal and relief characteristics. In this context, 19 different geomorphic indices were used and these used indices are given in Table 1. Six indices are used in linear parameters, 7 indices in spatial parameters, and 6 indices in relief parameters.

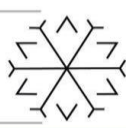


Table 1: The morphometric parameters and formula which were used in the study.

Morphometric parameters	Nu	Unit	Mathematical expression	Reference
Basic param.				
	1	Area (A)		Horton(1945)
	2	Stream order (u)		Strahler(1964)
	3	Total number of stream (N)		Strahler(1958)
	4	Total number of each order Nu(1,2,3,..)		Horton(1945)
	5	Total length of stream (L)		Horton(1945)
	6	Total length of each order Lu(1,2,3,...)		
	7	Maximum elavation (H _{max})		
	8	Minimum elevation (H _{min})		
	9	Mean elevation (H _{mean})		
Linear param.				
	10	Bifurcation ratio (R _b)	$N_u=N_{u+1}/N_u$	Horton(1945)
	11	Stream length ratio (R _l)	$R_l=L_u/(L_{u+1})$	Strahler(1964)
	12	Rho coefficient (R _{ho})	$\beta=R_b/R_l$	Horton(1945)
	13	Length of overland flow (L _o)	$L_o=1/2D_d$	Horton(1945)
	14	Texture ratio (T)	$T=N_1/P$	Smith(1950)
	15	Drainage texture ratio (Dt)	$Dt= N_u/P$	Smith (1950)
Areal param.				
	16	Shape index (B _s)	$B_s=1/R_f$	Horton(1932)
	17	Drainage density (D _d)	$D_d=L/A$	Horton(1945)
	18	Stream frequency (F _s)	$F_s=N/A$	Horton(1945)
	19	Form factor (R _f)	$R_f=A/Lb^2$	Horton(1932)
	20	Elongation ratio (R _e)	$R_e=(2/L_b)*(A/\pi)^{0.5}$	Schumm(1956)
	21	Constant of channel maintenance (C _{cm})	$C_{cm}=1/D_d$	Schumm(1956)
	22	Compactness coefficient (C _c)	$0.2841P/A^{0.5}$	Gravelius(1914)
Relief param.				
	23	Basin relief (B _h)	$B_h=H_{max}-H_{min}$	Schumm(1956)
	24	Relief ratio (R _h)	$R_h=H/L$	Schumm(1956)
	25	Relative relief ratio (R _r)	$R_r=H/P*100$	Melton(1957)
	26	Ruggedness number (R _n)	$R_n=B_h*D_d$	Melton(1957)
	27	Melton ruggedness number (M _r)	$M_r=(H/1000)A^{0.5}$	Melton(1965)
	28	Hysometric integral (H _i)	$H_i=(H_{mean}-H_{min})/H_{max}-H_{min}$	Pike and Wilson(1971), Mayer (1990)

3. Results and Discussion

19 different geomorphic indices were used depending on the linear, areal and relief morphometry in the quantitative explanation and comparison of the development of the river basins located on different slopes. It is seen that the basin height values are higher in the south-facing basins, and the basin area and perimeter lengths are similar. On the south-facing slopes, only the G1 basin area is approximately 36.25 km² and the perimeter is 40.8 km. The number of river banks and their lengths are of great importance for linear morphometry in terms of understanding the dynamics of river basins, especially the transported sediment ratio, the presence of erosive power, and the degree of rupture of the basins (Karabulut and Özdemir 2019). While the number of indexes belonging to the basins facing north and south is 6 in the G1 basin, this ratio is 5 in other basins. In the basin G1, where the basin area covers a large area, the river and drainage network is higher, the total length of the river sequences reaches up to 300 km. This rate is equal to 97.66 km on the K1, 54.52 km on the K2, and 98.96 km on the G2. The total number order value is 1914 in the G1 basin. In other basins, it is 753 in K1 and 386 in K2 and 625 in G2. The basic descriptor values are higher on south-facing slopes and lower on north-facing slopes.

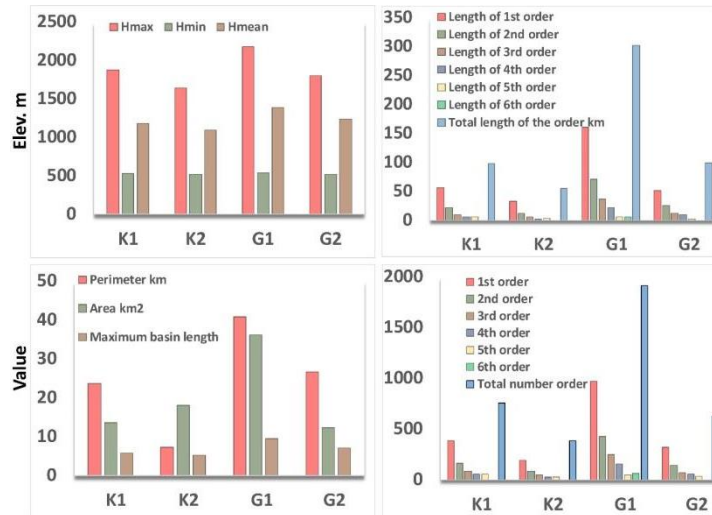
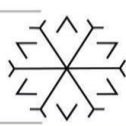
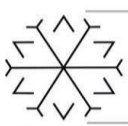


Figure 3: The general description of the basic morphometric parameters in the basins.

3.1. Linear parameters

Stream length ratio (rl), bifurcation ratio (Rb), length of overland flow (lo), drainage texture (Dt), texture ratio (T), rho coefficient (Rho) indices were used to understand the effect of aspect in linear morphometry. According to this, although there are not great differences, it is seen that the values are higher on the south-facing slopes. Stream length ratio (Rl) is between 1.9 and 2.2 on north-facing slopes, and 2.2 on south-facing slopes. The bifurcation rate (Rb) is between 1.68-1.7 in north-facing basins and between 1.8-1.9 in south-facing basins. The stream length (lo) value varies between 0.063-0.166. Low values are seen in south-facing basins, while high values are in north-facing basins. While the drainage texture ratio (Dt) is between 23.4-46.9 in the southern basins, this ratio varies between 31.7-52.4 in the north-facing basins. Again, the texture ratio (T) shows parallelism with Dt. The Rho value is 0.884-0.772 in the southern basins and 0.819-0.62 in the northern basins (Fig 4).

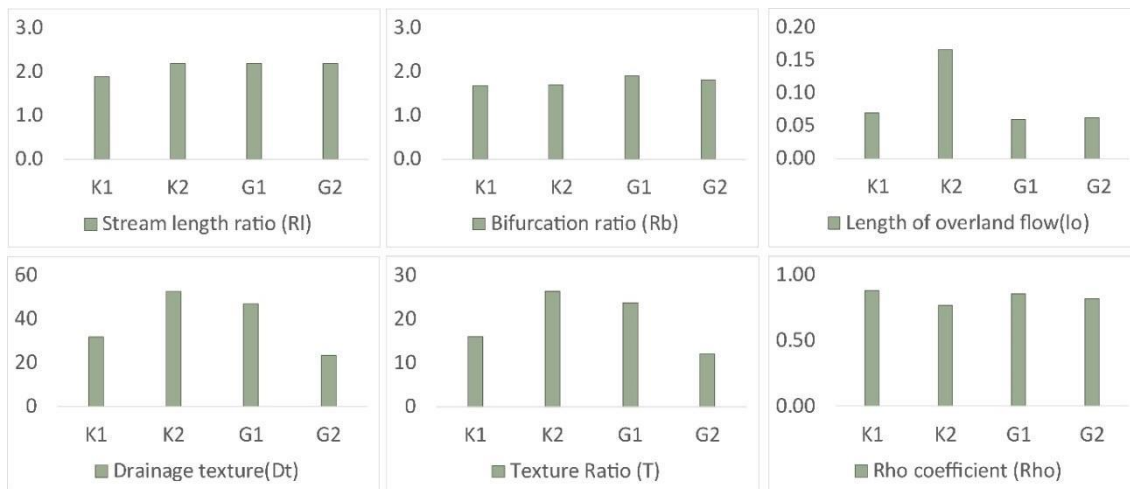
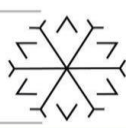


Figure 4: The linear morphometric results of the basins.

3.2. Areal parameters

Geometric features of the basins, areal parameters such as the area they cover and the length of the perimeter have a great importance in explaining the situations such as basin development and erosive activities. In addition, these features are also used in understanding and calculating indices such as the drainage network of the basins and the frequency of the streams. Drainage density (Dd), stream frequency (Fs), compactness coefficient (Cc), form factor, shape index (Bs), elongation ratio (Re), channel constant maintenance (Ccm) indices were used as a result of evaluating the aspect of the basins based on spatial parameters. Accordingly, Dd, Fs and Ccm values showed higher results than basin-areal morphometric parameters. Accordingly, Dd, Fs and Ccm values have higher results compared to basin areal morphometric parameters, especially low permeability and high surface flow potential,



while the Northern basins have a more circular shape based on Re, Rf, Cc and Bs values, only Re and Rf values in the basin no. G1 were close to the basin no. K1 from the northern basins. (Fig.5).

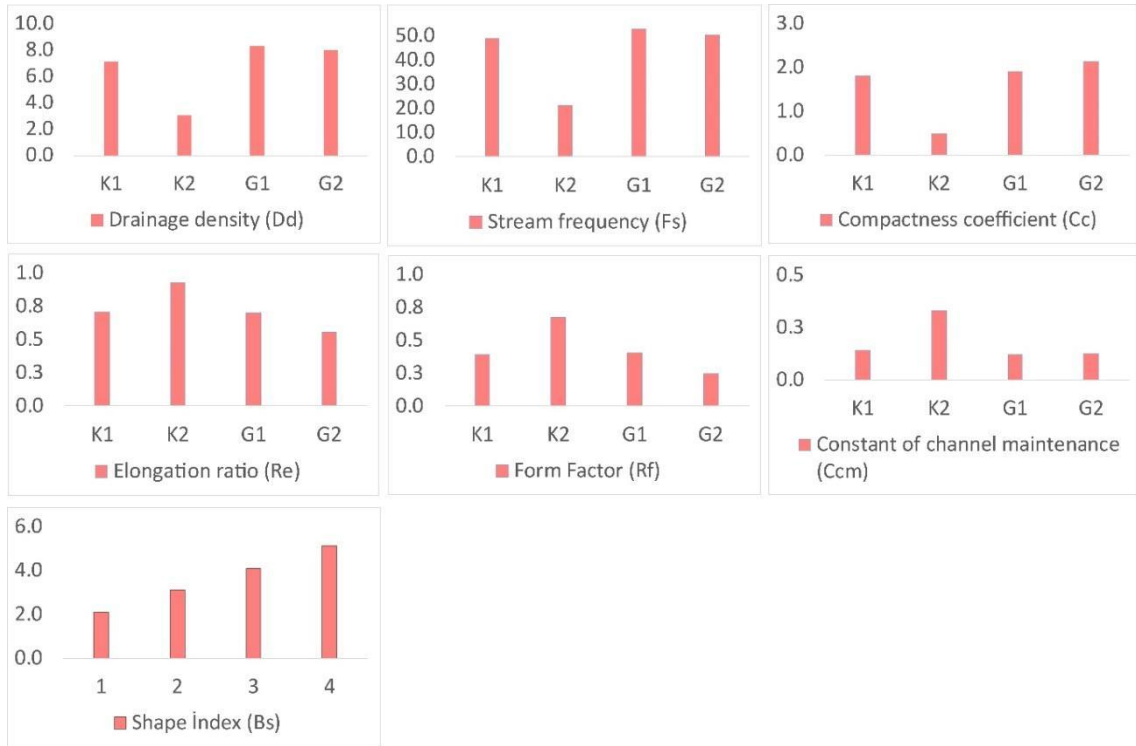


Figure 5: The areal morphometric results of the basins

3.3. Relief parameters

Relief parameters take into account the properties of the basins such as maximum, minimum and average elevation and geometric values of the basins that helps to understand erosional process, infiltration capacity and relief characteristics on the basins (Kaur et al. 2014, Islam and Deb Barman 2020, Valkanou et al. 2020, Abdelkarim et al. 2020). Basin relief (Bh), relief ratio (Rh) relative relief ratio (Rrf), Ruggedness number (Rn), Melton ruggedness number (Mrn) and Hypsometric integral (Hi) indices were evaluated within the scope of relief parameter. Accordingly, Bh values are between 1.65-1.28 in the southern basins and 1.35-.1.12 in the northern basins. Rh and Rrf values are higher in northern basins in these indices calculated according to the height values of the basins. In the Rn, Mrn and Hi indices, these values are mostly seen in the southern basins (Fig.6).

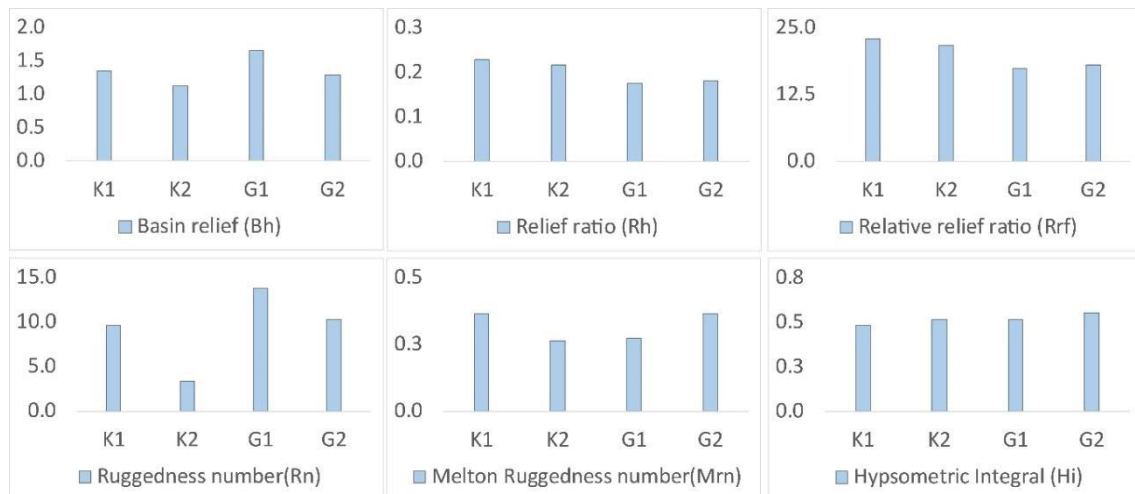


Figure 6: The relief morphometric results of the basins.

4. Conclusion



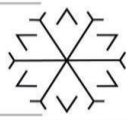
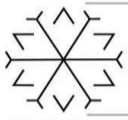
Four north and south oriented basins, which are the same in terms of location and very similar in terms of climatic characteristics, which are under the influence of different aspects, were examined using 19 different indices in terms of geomorphometrics. Especially in the lithological units, which are of great importance in the establishment and development of drainage, there are units with low permeability in the south-facing basins in the study area, where it is quite different, while there are more permeable units in the north-facing basins. In the study area, where the lithological units are quite different, there are units with low permeability in the south-facing basins, while there are more permeable units in the north-facing basins. Depending on the results obtained, the aspect effect was clearly seen on these basins. It is understood from the indices of Rl, Rb, Fs and Dd that in these basins, which have similar features in terms of shape and area, especially the river drainage network has higher values in the basins facing south. Again, it was observed that the roughness values were partially higher in south-facing basins depending on the Rn and Mrn indices and especially compared to the Hi value. The fact that these values are high, it is possible to say that the river erosion factor processes continue more actively in the south-facing basins, and that the basins are at a stage between maturity and old age, but the Hi values are quite close. From the values obtained on the north-facing slopes, it was observed that the basin shape was more circular, while the south-facing basins had a more elongated geometry. The fact that the texture and drainage texture ratios are also higher in the north-facing basins, according to the basin sizes, proves that these high values are especially high in the river indexes carrying water to the main branch.

References

- Abdelkarim, A., S. S. Al-Alola, H. M. Alogayell, S. A. Mohamed, I. I. Alkadi, and I. Y. Youssef. 2020. Mapping of GIS-Flood Hazard Using the Geomorphometric-Hazard Model: Case Study of the Al-Shamal Train Pathway in the City of Qurayyat, Kingdom of Saudi Arabia. *Geosciences* 10:333.
- Archer, L., Neal, J.C., Bates, P.D., House, J.I., 2018. Comparing TanDEM-X data with frequently used DEMs for flood inundation modeling. *Water Resour. Res.* 54, 205–222. <https://doi.org/10.1029/2018WR023688>.
- Aydin, O., Raja, N.B., 2020. Spatial-temporal analysis of precipitation characteristics in Artvin. Turkey. *Theor. Appl. Climatol.* 142, 729–741. <https://doi.org/10.1007/s00704-020-03346-6>.
- Baltacı, H., 2017. Meteorological analysis of flash floods in Artvin (NE Turkey) on 24 August 2015. *Nat. Hazards Earth Syst. Sci.* 17, 1221–1230.
- Baltacı, H., 2018. 18 temmuz 2017 tarihinde İstanbul 'da meydana gelen sel olayının meteorolojik analizi. *Marmara Fen Bilimleri. Dergisi* I, 55–60.
- Bhat, M.S., Alam, A., Ahmad, S., Farooq, H., Ahmad, B., 2019. Flood hazard assessment of upper Jhelum basin using morphometric parameters. *Environ. Earth Sci.* 78, 1–17. <https://doi.org/10.1007/s12665-019-8046-1>.
- Costache, R., Pham, Q.B., Sharifi, E., Linh, N.T.T., Abba, S.I., Vojtek, M., Vojteková, J., Nhi, P.T.T., Khoi, D.N., 2019. Flash-flood susceptibility assessment using multicriteria decision making and machine learning supported by remote sensing and GIS techniques. *Remote Sens.* 12, 106. <https://doi.org/10.3390/rs12010106>.
- El-Fakharany, M.A., Mansour, N.M., 2021. Morphometric analysis and flash floods hazards assessment for Wadi Al Aawag drainage Basins, southwest Sinai. Egypt. *Environ. Earth Sci.* 80, 1–17. <https://doi.org/10.1007/s12665-021-09457-1>.
- El Tahan, A.H.M.H., Elhanafy, H.E.M., 2016. Statistical analysis of morphometric and hydrologic parameters in arid regions, case study of Wadi Hadramaut. *Arab. J. Geosci.* 9, 1–10. <https://doi.org/10.1007/s12517-015-2195-7>.
- Farhan, Y., Anbar, A., Al-Shaikh, N., Mousa, R., 2017. Prioritization of Semi-Arid Agricultural Watershed Using Morphometric and Principal Component Analysis, Remote Sensing, and GIS Techniques, the Zerqa River Watershed, Northern Jordan. *Agric. Sci.* 08, 113–148. <https://doi.org/10.4236/as.2017.81009>.
- Fick, S.E. and R.J. Hijmans, 2017. WorldClim 2: new 1km spatial resolution climate surfaces for global land areas. *International Journal of Climatology* 37 (12): 4302-4315.
- Şenel, M., (2002). 1/500000 scaled geology map of Turkey, Samsun sheet. Ankara, Turkey: General Directorate of Mineral Research and Exploration.
- Ghasemlounia, R., Utlu, M. 2021. Flood prioritization of basins based on geomorphometric properties using principal component analysis, morphometric analysis and Redvan's priority methods: A case study of Harşit River basin. *Journal of Hydrology*, Doi: 10.1016/j.jhydrol.2021.127061.



- Gunjan, P., Mishra, S.K., Lohani, A.K., Chandniha, S.K., 2020. The Study of Morphological Characteristics for Best Management Practices Over the Rampur Watershed of Mahanadi River Basin Using Prioritization. *J. Indian Soc. Remote Sens.* 48, 35–45. <https://doi.org/10.1007/s12524-019-01061-y>.
- Horton, R.E., 1945. Erosional development of streams and their drainage basins: hydrophysical approach to quantitative morphology. *The Geological Society of America* 56, 275–370. (5).
- Islam, A., and S. Deb Barman. 2020. Drainage basin morphometry and evaluating its role on flood-inducing capacity of tributary basins of Mayurakshi River, India. *SN Applied Sciences* 2:1087.
- Kaur, M., S. Singh, V. K. Verma, and B. Pateriya. 2014. Quantitative Geomorphological Analysis & Land Use/ Land Cover Change Detection of Two Sub-Watersheds in NE region of Punjab, India. *ISPRS - International Archives of the Photogrammetry, Remote Sensing and Spatial Information Sciences* XL–8:371–375.
- Karabulut, M. S., & Özdemir, H. 2019. Comparison of basin morphometry analyses derived from different DEMs on two drainage basins in Turkey. *Environmental Earth Sciences*, 78(18), 1-14. <https://doi.org/10.1007/s12665-019-8585-5>
- Kumar, S., Chaudhary, B.S., 2016. GIS applications in morphometric analysis of Koshalya-Jhajhara watershed in northwestern India. *J. Geol. Soc. India* 88, 585–592. <https://doi.org/10.1007/s12594-016-0524-4>.
- Kumar Rai, P., Narayan Mishra, V., Mohan, K., 2017. A study of morphometric evaluation of the Son basin, India using geospatial approach. *Remote Sens. Appl.: Soc. Environ.* 7, 9–20. <https://doi.org/10.1016/j.rsase.2017.05.001>.
- Luu, C., Pham, B.T., Phong, T. Van, Costache, R., Nguyen, H.D., Amiri, M., Bui, Q.D., Nguyen, L.T., Le, H. Van, Prakash, I., Trinh, P.T., 2021. GIS-based ensemble computational models for flood susceptibility prediction in the Quang Binh Province. Vietnam. *J. Hydrol.* 599, 126500 <https://doi.org/10.1016/j.jhydrol.2021.126500>.
- Mahmood, S.A., Gloaguen, R., 2012. Appraisal of active tectonics in Hindu Kush: Insights from DEM derived geomorphic indices and drainage analysis. *Geosci. Front.* 3, 407–428. <https://doi.org/10.1016/j.gsf.2011.12.002>
- Melton, M.A., 1957. An analysis of the relations among elements of climate, surface properties and geomorphology (Project NR 389042. In: Tech. Rep., 11 Columbia University, New York, NY.
- Patel, D.P., Srivastava, P.K., Gupta, M., Nandhakumar, N., 2015. Decision support system integrated with geographic information system to target restoration actions in watersheds of arid environment: A case study of Hathmati watershed, Sabarkantha District. Gujarat. *J. Earth Syst. Sci.* 124 <https://doi.org/10.1007/s12040-014-0515->
- Pidwirny, M., 2006. The Drainage Basin Concept. *Fundamentals of Physical Geography*, second ed. <http://www.physicalgeography.net/fundamentals/10aa.html>.
- Schumm, S.A., 1956. Evolution of drainage systems and slopes in Badlands at Perth Amboy. New Jersey: *Bull. Geol. Soc. Am.* 67, 597–646.
- Sezer, I., 2019. Sezer, 2019.pdf. *Turkish Stud. Soc. Sci.* 14, 2463–2500.
- Singh, N., Singh, K.K., 2017. Geomorphological analysis and prioritization of subwatersheds using Snyder's synthetic unit hydrograph method. *Appl. Water Sci.* 7, 275–283. <https://doi.org/10.1007/s13201-014-0243-1>.
- Singh, N., Jha, M., Tignath, S., Singh, B.N., 2020. Morphometric analysis of a badland affected portion of the Mandakini River sub-watershed, central India. *Arab. J. Geosci.* 13, 423. <https://doi.org/10.1007/s12517-020-05405-8>.
- Sreedevi, P.D., Subrahmanyam, K., Ahmed, S., 2005. The significance of morphometric analysis for obtaining groundwater potential zones in a structurally controlled terrain. *Environ. Geol.* 47, 412–420. <https://doi.org/10.1007/s00254-004-1166-1>.
- Sreedevi, P.D., Owais, S., Khan, H.H., Ahmed, S., 2009. Morphometric analysis of a watershed of South India using SRTM data and GIS. *J. Geol. Soc. India* 73, 543–552. <https://doi.org/10.1007/s12594-009-0038-4>.
- Strahler, A.N., 1957. Quantitative analysis of watershed geomorphology. *Trans. Am. Geophys. Union* 38, 913. <https://doi.org/10.1029/TR038i006p00913>.
- Strahler, A.N., 1952. Hypsometric (area-altitude) analysis of erosional topography. *Geol. Soc. Am. Bull.* 63 (11), 1117–1142.
- Utlu, M., Ghasemlonia, R., 2020. Jeomorfometrik Özelliklere Göre Aras Nehri Havzalarının Taşkın Önceliklendirilmesi: İğdır İli Örneği. *Jeomorfol. Araştırmalar Derg.* 10.46453/jader.781152.



Valkanou, K., E. Karymbalis, D. Papanastassiou, M. Soldati, C. Chalkias, and K. Gaki-Papanastassiou. 2020. Morphometric Analysis for the Assessment of Relative Tectonic Activity in Evia Island, Greece. *Geosciences* 10:264.

Youssef, A.M., Pradhan, B., Hassan, A.M., 2011. Flash flood risk estimation along the St. Katherine road, southern Sinai, Egypt using GIS based morphometry and satellite imagery. *Environ. Earth Sci.* 62, 611–623. <https://doi.org/10.1007/s12665-010-0551-1>

Url-1: <https://land.copernicus.eu/pan-european/corine-land-cover>

Url-2: <https://www.worldclim.org/data/worldclim21.html>

A View of Historic Structures Survived in 1859 Erzurum Earthquake

Dursun Burak ÖZDOĞAN ¹*[0000-0003-4390-2955] and Dilek OKUYUCU ²[0000-0001-7694-9405]

¹*bozdoganitu@gmail.com, Department of Civil Engineering, Erzurum Technical University, Erzurum, Türkiye

²okuyucu@erzurum.edu.tr, Department of Civil Engineering, Erzurum Technical University, Erzurum, Türkiye

Abstract

The Anatolian peninsula is one of the most active seismic zones of the earth. Two major active fault zones exist within the boundaries of the land, *the North Anatolian Fault Zone and East Anatolian Fault Zone*, both of which created several destructive earthquakes in the past. Erzurum city is located in the vicinity of the connection point of the aforementioned fault lines. Historic memory of the city provides some documental information about highly destructive earthquakes that occurred in the last two centuries. Hence, these ground motions are from the pre-instrumentational time of seismology and researchers can only comment about the intensity of the earthquake from various reports. However, today's technical and technological possibilities enable stochastic modelling of past earthquakes and the creation of synthetic acceleration records of the selected ground motion of pre-instrumentational time. This study can help for a better understanding of the seismicity of the region and can create more reliable information to be used for seismic design in the future. Considering these issues, the 1859 Great Erzurum Earthquake was selected for synthetic acceleration record creation work. This study requires a variety of data collection from soil and fault properties to damage levels of the constructions. Among them; existing historic structures are of great importance for verification of the created earthquake records being as the living witnesses.

June 2, 1859, Erzurum Earthquake is considered to be the most severe earthquake in the history of Erzurum. The earthquake was the last and most destructive of an earthquake ring that started at midnight on June 1st. Although the first earthquake was non-violent felt from the west of the city, it turned into a great earthquake in the north and south directions of the city at around 4 pm on the night of June 2, and the city was razed to the ground with the second earthquake that occurred 15 minutes later. Even the earthquake lasted for a short time like 15 seconds, it was a very strong earthquake with its devastating effect. According to the Mercalli intensity measurement (MMI) unit, the intensity of the earthquake is at the 9 intensity level. The damage caused by the earthquake in the city is frightening. Although the numbers are not certain, it is stated that 360 people died in the reports written to the capital Istanbul. In terms of damage, 1462 houses were destroyed, about 3500 houses were heavily damaged, 6 mosques were destroyed, nearly 20 mosques and masjids were partially destroyed. In addition, a group of historic structures still existing today like *Lala Mustapha Pasha Mosque, Pervizoğlu Mosque and Erzurum Castle* were also suffered from the earthquake by various levels of damages.

It should be mentioned that comprehensive archive research has been carried out to collect damage information of historic structures. Finite element models of the related existing historic structures calibrated by operational modal analysis will be analyzed with the created synthetic acceleration data to evaluate damage levels stated in historic records. General information about the 1859 Erzurum Earthquake will be summarized and damages of the earthquake to some of the existing/lost historic structures will be presented in the oral presentation.

Keywords. Erzurum, Damage, Historic structures, Intensity, 1859 Earthquake.

An Application of Cold Weather Concreting in Erzurum

Burak GEDİK¹[0000-0001-8355-3839], Muhammet ŞAHİN²[0000-0003-1319-074], Burak ŞAHİN³[0000-0002-9418-6496],
Zabiullah FAKOURİ⁴, Muhammet TAŞÇI⁵, Muhammed Enes ÇELEBİ⁶[0000-0003-0403-8279], Memduh Şenol
ÇAVDAR⁷, Sabri AYDEMİR⁸[0000-0002-9270-0770], Dursun Burak ÖZDOĞAN⁹[0000-0003-4390-2955], Dilek
OKUYUCU¹⁰[0000-0001-7694-9405]

¹burak.gedik@erzurum.edu.tr, Department of Civil Engineering, Erzurum Technical University, Erzurum, Türkiye

²muhammetsahin48@gmail.com, Department of Civil Engineering, Erzurum Technical University, Erzurum, Türkiye

³burak.sahin74@erzurum.edu.tr, Department of Civil Engineering, Erzurum Technical University, Erzurum, Türkiye

⁴zabih.safari@gmail.com, Department of Civil Engineering, Erzurum Technical University, Erzurum, Türkiye

⁵muhammet.tasci54@erzurum.edu.tr, Department of Civil Engineering, Erzurum Technical University, Erzurum, Türkiye

⁶muhammed.celebi52@erzurum.edu.tr, Department of Civil Engineering, Erzurum Technical University, Erzurum, Türkiye

⁷msenolcavdar@hotmail.com, Department of Civil Engineering, Erzurum Technical University, Erzurum, Türkiye

⁸sabri.aydemir60@erzurum.edu.tr, Department of Civil Engineering, Erzurum Technical University, Erzurum, Türkiye

⁹bozdoganitu@gmail.com, Department of Civil Engineering, Erzurum Technical University, Erzurum, Türkiye

¹⁰okuyucu@erzurum.edu.tr@erzurum.edu.tr, Department of Civil Engineering, Erzurum Technical University, Erzurum, Türkiye

Abstract

Erzurum is a city located in East Anatolian Region of Türkiye that experiences long, cold and snowy winters. During winter time construction industry, *especially reinforced concrete applications*, almost stops. Main reason for this compulsory stop is associated with that of the technical problems in concrete casting in cold weather. Many people of the region earn their living from construction work. Hence, this situation creates lots of financial and sociological problems. Starting from this point, a research project which focuses on technical success of cold weather concreting for reinforced concrete applications has been prepared and submitted to The Scientific and Technological Research Council of Turkey for funding. The proposal has been accepted (*TÜBİTAK1001-219M403: Experimental Evaluation of Flexural Behaviour of Reinforced Concrete Beams Cast- in Cold (Winter) Weather*) and funded for 20 months of research. Within the scope of the project, full scale reinforced concrete beams have been proposed to cast in different cold weather conditions with two different concrete mixes and to be tested for flexural behaviour evaluation.

While the project works were continuing, a slipping occurred on the ground where the textile factory structures built on the sloping land in Erzurum province 2nd Organized Industrial Zone, and the single-storey textile factory structures were damaged and some of them became unusable. This event, which caused the halt of factory production, occurred in January 2021, during a period dominated by the winter season. In order not to stop the factory production for a long time and not to experience greater economic losses, the summer period was not waited for the soil strengthening works with the application of reinforced concrete bored piles and then the damaged factory repairs. Hence, construction works have been started on the field since February 2020. During this study, technical support was requested from our TÜBİTAK1001-219M403 project team by the competent authority for concrete pouring in winter.

In this context, a joint study was conducted with Memişoğlu Erzurum Concrete Incorporated Company. At the first stage fresh concrete temperature was monitored between the concrete plant and the bored pile casting area (transportation distance ~23 km). The aim of this study was to follow the difference between the temperature at the exit of the plant and the temperature at the time of pouring of the concrete transported in the metal bowl mixer in cold weather conditions. After the bored pile castings at a height of ~25 m in the ground, bored pile cap beams were manufactured on the ground in an environment open to the cold atmosphere. TÜBİTAK1001-219M403 project team actively worked at the site and a cold weather concreting application was realized. The details of the fresh concrete temperature monitoring study between the plant and the construction site in cold weather and the details of the bored pile cap beam manufacturing study will be shared in the oral presentation.

Keywords. Cold weather, Concreting, Erzurum, Reinforced concrete beam, Site application

Titanium-Zinc as an Architectural Material: ETU Campus Gate Project

Ekrem Bahadır Çalışkan ^{1*}[0000-0002-5258-2976] and Filiz Karakuş ²[0000-0002-7562-3435]

¹bahadir.caliskan@gmail.com, Department of Architecture, Ankara Yıldırım Beyazıt University

²fkarakus@ybu.edu.tr, Department of Architecture, Ankara Yıldırım Beyazıt University

Abstract

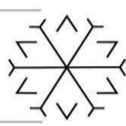
Designers and stakeholders of the construction industry have disposition to use the materials of which features can meet the requirement, function, aesthetic and budget criteria for the building projects. In recent years, the use of new construction materials has come to the fore with the developments in the material and construction industry. Titanium- Zinc, which is the subject of this study, as an architectural material offers some outcomes for building's roof and exterior claddings with its durability and almost zero maintenance need during life time. Within the scope of this article, primarily through literature review, the important features of Titanium-Zinc material with presenting alloy descriptions, material behavior, general system detail and varieties are explored. Afterwards, Erzurum Technical University Campus Gate Project is presented in which Titanium-Zinc was used to both consolidate the knowledge about the material and assembly detail on a particular example and state a record for evaluating the features of material depend on time at further studies. With this examination, it has been determined that the Titanium-Zinc material has not damaged since 2018, when the application was made, and that no maintenance was carried out during this time. With this study, it has also seen that basic behavior of the zinc material against weather conditions in terms of corrosion activity come with protective layer at the surface of material. Besides this, when it is decided to use material, miscellaneous features of alloy and details of the assembly system considering the high level of manufacturing and labor work precision should be taken into consideration.

Keywords. Campus Gate, Metal Material, Titanium-Zinc

1. Introduction

The diversity of materials and systems used for building finishes brings to designers and constructors many possibilities and alternatives. Besides the conventional and pre known materials, new materials and different usage of existing materials make building finishes having more functional and durable solutions against climatic conditions against time. Climatic background, economic aspects and requirements are the most important factors over the general factors affecting the choice of materials (Duggal, 2008). Owner and investor of the buildings desire the solutions for exterior claddings that have much durability against weather conditions, low maintenance cost and an intended design output. By taking account of the fact that a designer can have various decision for finishing and cladding materials upon design intentions, an alloy metal titanium-zinc brings important capabilities the system design for whom prefers the visual appearance of this specific material.

The titanium-zinc as an architectural material is not a new or new used material. It has been used over 180 years with their different alloys for roof, wall cladding and ornaments all over the world (Zahner, 2021). Although usage frequency of this material at buildings may be thought as not much in comparison to other materials, the construction industry, mainly material industry, works to make project stakeholders have more recognition to properties and capabilities of materials. This paper tries to present the material in terms of general background, properties and character, and a finished project for Erzurum Technical University Campus Gate which is dominated by the titanium-zinc rolled panels for exterior cladding. It is also aimed to note and take record of situation of the building to evaluate it after 3-5 years period.



2. Titanium-Zinc Material

2.1. Alloying Description

Titanium, zinc, copper and aluminum are non-ferrous metal and production and usage of non-ferrous metals is small in comparison to iron (Duggal, 2008). Based on 2020, Iron was mined 2.5 billion metric tons, whereas zinc was 13 million, copper was 20 million and aluminum was 64 million (USGS, 2020). These metals and their alloys are used in various industries because of their properties. The material “Titanium-Zinc” called in the construction industry is an alloy of Zinc, copper, titanium and aluminum. This architectural metal is manufactured by various brand as an alloy with the zinc purity grade of 99.995% according to European Standard EN 998 (*Rheinzink*, 2021; *Vmzinc*, 2021).

Various companies produce alloy with some differences with respect to range limit of standard. By the slight change of compound, companies offer properties and prices to be effective at the market. All metals in the alloy have purposes to contribute to material regarding the price per unit. The alloy is manufactured by melting and mixing of metals with determined ratio in accordance with the specifications of production. Main production process is master alloy, melting, rolling, coiling and stretching (*Rheinzink*, 2021). The formula of alloy according to EN 998 standard is given at Table 1.

Table 1: Titanium-Zinc Alloy

Titanium-Zinc	EN 988
Zinc	Z1
Copper	0,08-1,0%
Titanium	0,06-0,2%
Aluminum	≤0,015%

2.2. Material Properties

Zinc is the main body of this alloy. It is used for an important behavior of metal in corrosion concept. Corrosion is the degradation of a material’s properties or mass over time which makes materials lose their intended properties over time (Schweitzer, 2007). Corrosion is formation of oxides and sulfides for most metallic materials. Zinc has the ability to form a protective layer made up of basic carbonates, oxides, hydrated sulfates in time which reduce the rate of corrosion after the formation of layer (Schweitzer, 2007). The protective layered called patina, and it is formed between 6 months-2 years according the climatic conditions (*Vmzinc*, 2021). The layer is fixed to main body and protecting the material against weather conditions. If there is penetration to main body with a harder object, again zinc faces up to atmosphere and the same formation of this protective layer occurs. Because of this specific property of zinc, it is used for the prevention of different metals against corrosion (Figure 1). Besides, the runoff rate of zinc is low in comparison to other metals (Faller and Reiss, 2005). This means nearly zero mass reduction and no flow of materials to ground that may be harmful to surroundings. Zinc can be rolled and given shaped in wide range of geometries with is flexible nature. The alloying elements is used for improving the properties of alloy in different manners.

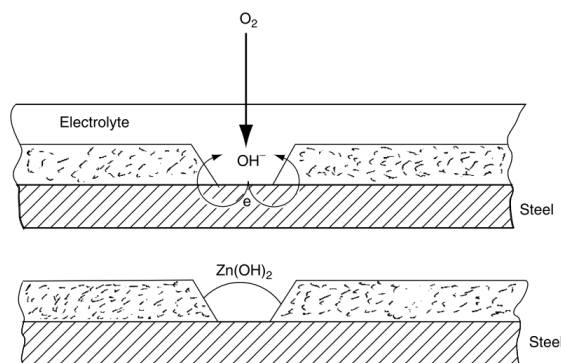
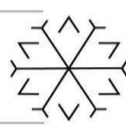
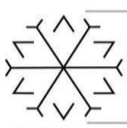


Figure 1: Action on a zinc metallic coating (Schweitzer, 2007)



Aluminum is added to zinc alloy to increase strength and reduce grain size, to improve cast ability and fluidity of the casting (Zahner, 2021). Copper increases the hardness, strength(tensile) and life time, titanium reduce the expand ratio and increase the resistance to deformation.

2.3. Properties Titanium-Zinc as an Architectural Material

Zinc Plate, zinc sheet and titanium-zinc plate are some of the names used in the industry for the specifies alloy described in this paper. The material is used for roof coverings, exterior wall cladding, interior finishes and ornaments because the properties coming from its alloying elements. Production companies presents this material in various form, details and visual appearance; however, the common features can be listed to underline usage advantages for designer and construction companies. Table 2 presents the physical and chemical properties of the alloy (Vmzinc, 2021; Rheinzink, 2021).

Table 2: Physical and Chemical Properties

Density	7.2 g/cm ³	Elasticity Modulus	≥80.000 N/ mm ²
Melting Point	420 °C	Thermal Conductivity	110 W / m. K
Coefficient of expansion in longitudinal	2.2mm/m x 100 K	Magnetic	Non
Coefficient of expansion in transverse	1.7mm/m x 100 K	Fire	A1 Class non-flammable
Recrystallization limit	300 °C	Electrical conductivity	17 m/Ω mm ²

The designers, investors and constructors decide for a material to use according their functional, application, maintenance properties. The features of the titanium-zinc alloy materials as a result of literature survey and companies documents are listed below (Adamus, 2014; Cheng, 2014; Alemdağ and Nohut, 2016; Vmzinc, 2021; Rheinzink, 2021; Zahner, 2021):

- Durable and weather resistant
- Creep Resistance
- Long service life (80-100 years)
- No maintenance, it can recover the surface scratches with its corrosion activity by reproducing a protective layer.
- Pre weathering process before applying to face for formation of patina layer.
- Slight visual differences on color according construction time, orientation and climatic conditions
- For natural zinc (non pre weathered) need for 6 months to 2 years period for patina
- No pollution both in life cycle and after life. Over 90% of material is recyclable
- Higher in price for initial purchase and apply
- Variable architectural shapes like straight and curved faces. Easy to give shape
- Thickness ranges from 0.65 mm to 1.00 mm
- Roll size width 50-65 cm, length up to 40 m
- Needs a metallic structure for cladding
- Various color options than patina surface layer(silver) with pigment application at production. Recovery also is present, but it turns to silver (patina layer) not applied color.
- The production process corresponds the Leed and Bream criteria
- Sound isolation performance for exterior sound sources
- Water isolation performance with connection details
- Need higher labor quality and control
- Need higher level of attention in sizing according to surface location of building

The natural zinc needs time from 6 month to 2 years to complete its chemical reaction over surface to get silver color. Generally the materials is not applied in natural state, pre-weathering process is done by manufacturer (Zahner, 2021). When the natural stated zinc (non-pre-weathered) is determined to apply, there must be attention to locate the panel according to orientation against climatic conditions. Because the



patina period differences, various visual appearances exist through the time. Figure 2 present some examples of surface color for titanium-zinc. With some manufacturing processes, diverse surface colors are offered. Except natural zinc (non-pre-weathered), all of them is at the final visual appearance. The rest is pre-weathered at the production process and form patina layer as protection. Natural Zinc(pre-weathered) shows the state after patina formation is finished whether in environment or production line. So, it can be stated that every titanium-zinc plate has tend to transform into this after recovery of surface if there is deformation on the surface by penetration of a harder object. For example; in a facade that red plate is applied, and a scratch which is deeper than patina layer becomes there will be recovery layer like natural zinc silver because of the chemical reaction of zinc and atmosphere. The metal will continue its life by not losing its mass and properties, however there will be a silver line on the red surface.



Figure 2: Surface Color Examples (Vmzinc, 2021; Rheinzink, 2021)

2.4. Application Systems

For different requirements, project decisions and application surfaces there are several application systems and details of titanium-zinc rolls and plate offered by industry. These different details are tried to solve problems and improve the durability of whole system with the material considering material consumption ratio, budget, labor and visual appearance. Classification according to location of surfaces can be done as; facade systems (vertical surfaces) and roof systems (horizontal surfaces). The affecting loads, weather conditions and needed water isolation are different (rain, snow, wind, sun), thus the connecting and application structure are different. Classification according to sub-structure of system can be stated as; assembly to wood decking (Figure 3) and assembly to metal structure directly (Figure 3). These details are considering the strength of the plate (thickness, size of panel) and offered the tested and certified solution by industry.

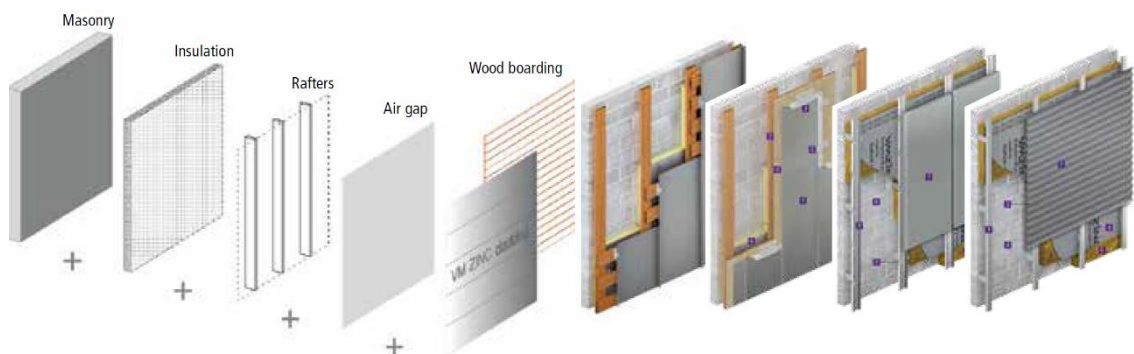


Figure 3: Assembly to Wood Decking(left), Assembly to metal structure(right) (Vmzinc, 2021)

Individuals' system examples vary according to functional and dimensional requirement with slight difference on manufacturing firms. They both offer the systems to the specific project environment and context, and develop solutions by their technical office for the project. The project stage and assembly details and labor are important in terms of needing precise and detailed approach for the usage of material. It is possible to have technical services from the manufacturing companies which have marketing and technical solutions offices at the region from the earlier phases of project. Decision of selecting to this material to use, elaborate the details and system and controlling the execution of the system on a building are recommended to do by participation of project stakeholders. Some examples of application systems are given in Figure 4.

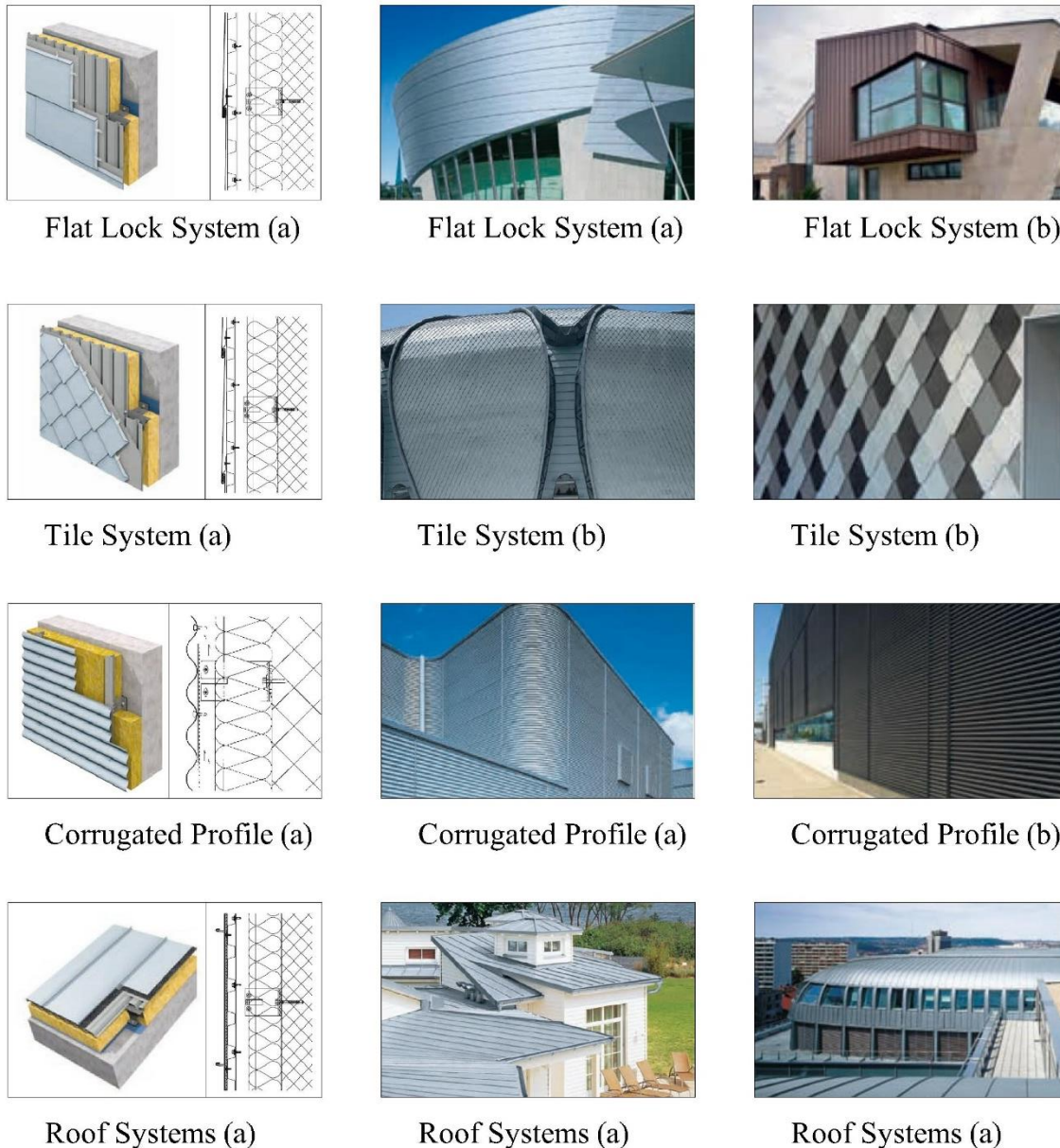


Figure 4: Examples of systems. a((Rheinzink, 2021), b((Vmzinc, 2021)

3. ETU Campus Gate Project

The gate project was completed from the author and it was constructed at two different campus entrance location. The main idea of the geometry is originated from formerly made conceptual studies by Gönül Evyapan and the author Çalışkan. The geometry of gate is elaborated with the interpretation of The Seljukian geometry of eight corner star. It is decided that the ground is mirror plane, thus the half of the



geometry is existing on the ground to sky and other half is thought as existing virtually below the ground (mirror plane). With this main and geometrically basic decision the following two situations are ensured. For functional requirements; the pedestrian and vehicle traffic transition are provided through gate. For conceptual decision; entering to and exiting from the campus are made by middle of 8 corner star which has various valuable meaning. The figure 5 and 6 are representing the location of the campus gate the design concept of the project.



Figure 5: Location of ETU Campus Gates (*Google Earth, 2021*),



Figure 6: Visual of the Project

It can be seen from the figure 6 and 7 that there are horizontal-vertical geometries and angular geometries which are shaping the half star shape. To underline these items, two different cladding materials and depending system are used. Considering the weather conditions of the region, the natural stone cladding on reinforce concrete structure, which is also main structure system of the building, is used for horizontal and vertical items, and also facade of the security office. The titanium-zinc plates are used with flat lock system (0.8 mm) for angular items on steel structures which is connected to R.C. structural systems (Figure 8). The titanium-zinc plate is durable and have recovery property resulting from corrosion behaviors with climatic conditions. Thus, by not needing any maintenance, it will have long life as an architectural material. A space definition for gate is tried to design by using this section twice in the plan direction. Figure 8 shows the system details of the system; cassette mesh detail at the left and flat lock system at the right.

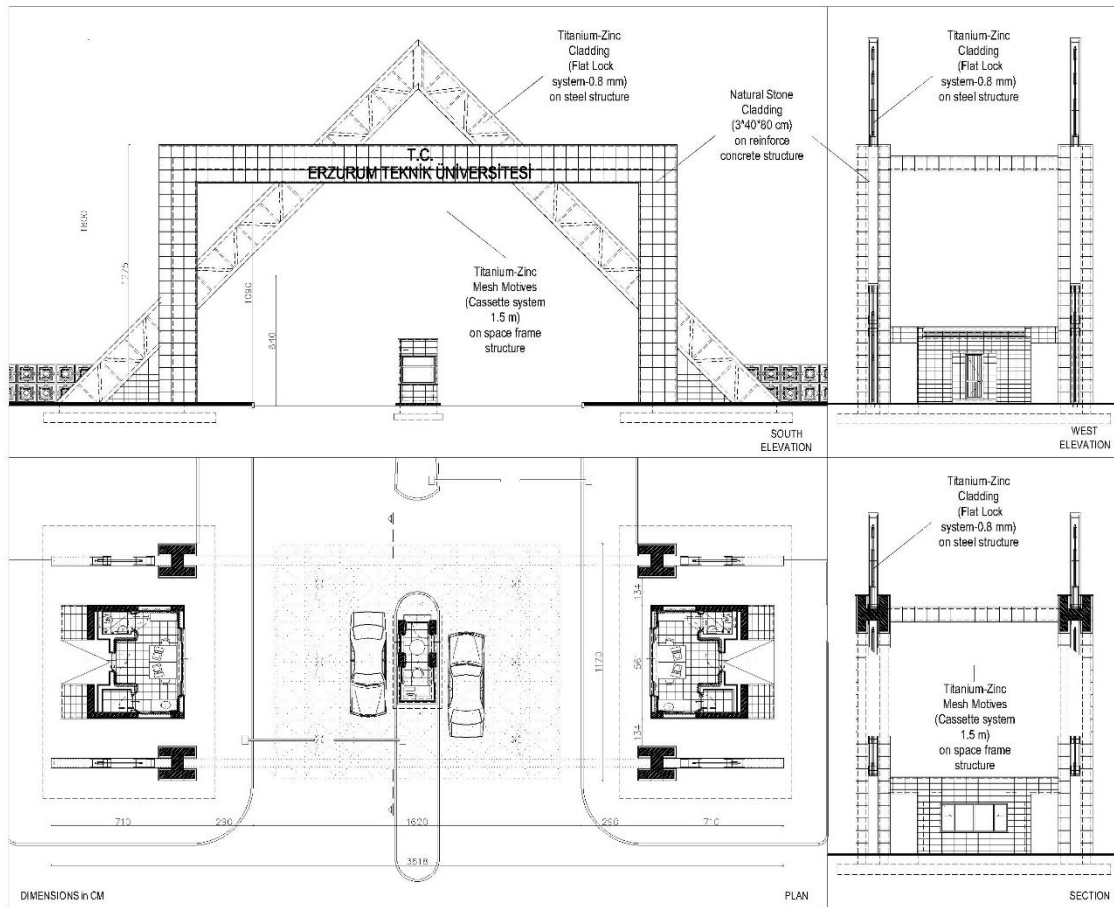


Figure 7: Technical Drawings

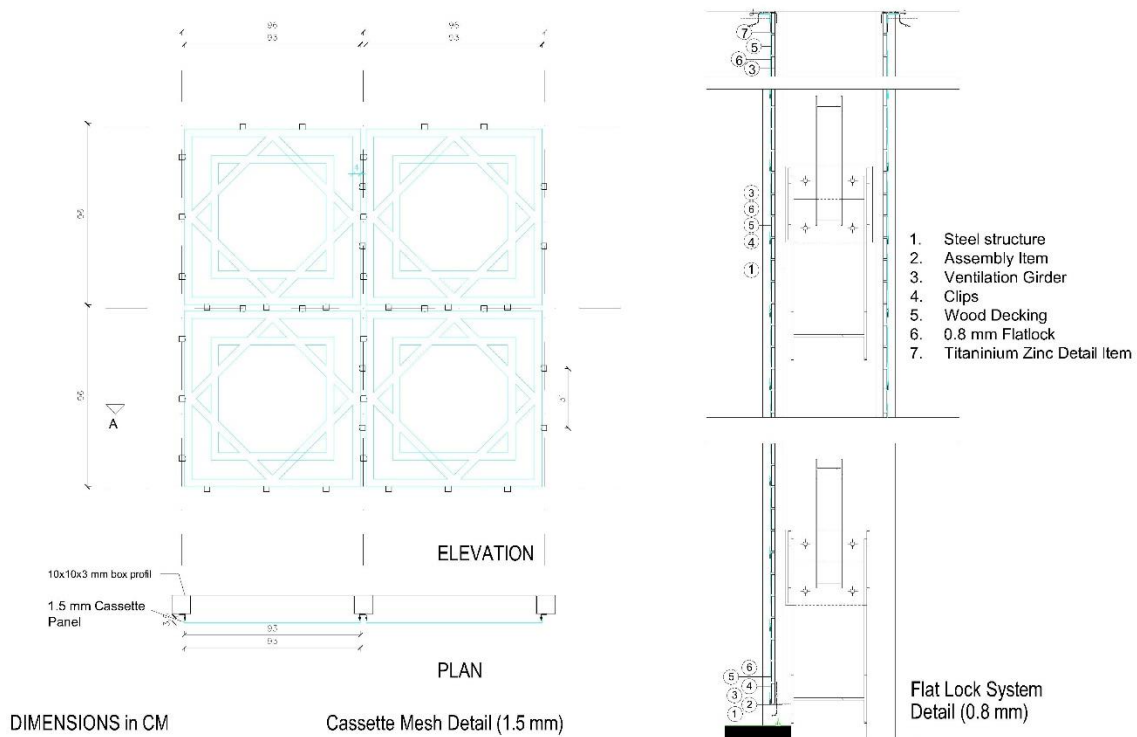


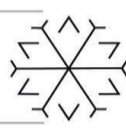
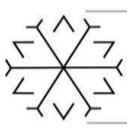
Figure 8: System Details



The designed outdoor area established the security check zone for both pedestrian and vehicles. Because of the weather conditions, it is important to prevent roof collecting the snow over it. First way is to construct a roof that is covering this huge space and discharge the snow out of the space. This is neglected, because it is not suitable for the design approach and there would be big amount snow to carry. The second and selected approach is the design a roof that is not exactly working as a roof in terms of protecting the under space from climatic conditions, that is defining the space at the top and letting the snow and rain fall. Thus, there would not be a mass snow which may be dangerous to fall on vehicle and pedestrian. The roof structure and near security wall are good architectural items to reflect the main design geometry. The same motives with different scale are developed for the applications. Because of the sizes and having enough strength and hardness, 1.5 mm cassette system is used. Every unit of motives is produced and installed after in the site. The two-campus gate construction were completed and begun to serve from the last days of 2018. As stated before at the paper, one of the objectives of this evaluation to track the material behaviors under the weather conditions throughout the long period. Thus, the photographs of the building which was taken by construction firm and controllers after the completion is presented at figure 9.



Figure 9: Photographs of The Campus Gate



4. Conclusion

Titanium-Zinc as an architectural material is an important material alternative specially for roofs and façade cladding which should have resistance to weather conditions. As seen in the example of Erzurum Technical University Campus Entrance Gate, which is covered within the scope of the study, in the cases that the budget and design expectations are convenient for decision makers, the material presents a long-life time with low (zero) maintenance and a qualified visual appearance. Principally the material may be remarkable selection for the structures or buildings that are facing to weather conditions from entire directions like presented example. The paper underlines this particular material for construction industry with its important features and application details, and present the constructed project to interpret the usage and start an evaluation within time. The evaluation will be handled by both being informed for any particular damage resulting from any impact and tracking the repairment in time after, recording the general situation of material against weather conditions in 2- and 4-years period. For this purpose, Directorate of Construction and Technical Works is asked to inform about. As a result of the examination on the sample, it has seen that the precision in the project, production and construction phase has critical importance in terms of suitability of the material for its intended usage, and as a result of the evaluation in time material behavior and situation will be presented in the future.

Acknowledgements

The project of Erzurum Technical University Campus Gate was completed at 2018. The construction started at 19.07.2018 and finished at 18.12.2018 under the control and supervision of Directorate of Construction and Technical Works, ETU.

References

- Adamus, J. (2014) "Applications of titanium sheets in modern building construction," *Advanced Materials Research*, 1020, pp. 9–14.
- Alemdağ, E. L. and Nohut, D. Öz. (2016) "Bina Cephelerinde Titanyum Çinko Levha Uygulamaları," in *8. Ulusal Çatı & Cephe Sempozyumu*. İstanbul: Mimar Sinan Güzel Sanatlar Üniversitesi.
- Cheng, Y. Y. (2014) "Architectural language function of zinc plate in the architectural surface design," *Advanced Materials Research*, 1030–1032, pp. 1096–1099.
- Duggal, S. K. (2008) *Building Materials*. New Age International.
- Faller, M. and Reiss, D. (2005) "Runoff behaviour of metallic materials used for roofs and facades: 5-year field exposure study in Switzerland," *Materials and Corrosion*, 56(4), pp. 244–249.
- Google Earth (2021). Available at: <https://earth.google.com> (Accessed: October 22, 2021).
- Rheinzink (2021). Available at: <https://www.rheinzink.com/> (Accessed: September 30, 2021).
- Schweitzer, P. A. (2007) *Fundamentals of Metallic Corrosion: Atmospheric and Media Corrosion of Metals*. 2nd ed. CRC Press.
- USGS (2020) *Mineral Commodity Summaries-U.S. Geological Survey*.
- Vmzinc (2021). Available at: <https://www.vmzinc.com.tr/> (Accessed: September 30, 2021).
- Zahner, L. W. (2021) *Zinc Surfaces: A Guide to Alloys, Finishes, Fabrication and Maintenance in Architecture and Art*. New Jersey: Wiley.

A Model for Visualization of Customer's Attention That Occurs on the Furniture by Using Eye-Tracking Technology and Determination Its Effect on New Product Design

Osman GÖKTAŞ ¹[0000-0001-7459-1104], Engin ERGİN ²[0000-0001-5146-5914], Fatma KÖMÜRÇÜOĞLU SOYTÜRK ³[0000-0002-6271-459X], Hatice Hicret ÖZKOÇ ⁴[0000-0003-0037-4603], Aytekin FIRAT ⁵[0000-0002-5599-5063], Gürcan ÇETİN ⁶[0000-0003-3186-2781], Gamze GÜLSUNAR GAZEL ⁷[0000-0003-3712-3613]

¹ogoktas@mu.edu.tr, Muğla Sitki Kocman University; ²enginergin@posta.mu.edu.tr, Muğla Sitki Kocman University; ³f.komurcuoglu@iku.edu.tr, İstanbul Kültür University; ⁴hatice.ozkoc@mu.edu.tr, Muğla Sitki Kocman University; ⁵aytekinfirat@mu.edu.tr, Muğla Sitki Kocman University; ⁶gucetin@mu.edu.tr, Muğla Sitki Kocman University; ⁷gamzegulsunargazel@lineadecor.com.tr, Dekor Ahşap A.Ş.

Abstract

Produced every furniture is not in demand as expected by the customers, and therefore production cannot turn into sales. However, it is important both economically and environmentally that every furniture to be produced is as preferable as possible, that is, it can be purchased by customers. The model proposal mentioned here has been developed for furniture design that can gain more attraction of customers for purchasing. The basis of this model is to mapping where the customers' attention is concentrated on when they look at a piece of furniture? In the model, which is planned to be carried out in two stages with a total of 120 participants, data will be collected by the eye tracking device and questionnaire. In the first stage, 60 participants (30 women +30 men) will be invited to observing 10 groups (90 modules) of kitchen for mapping attention customer on the furniture. These data will be used as a “decision support” for new designing and production for 4 groups (36 moduls). In the second stage, new groups furniture will be mixed in the first stage furniture and observed by different 60 participants and data collection will be repeated again. All obtained data will be analyzed with graphics and various statistical analyzes. Our hypothesis that, new designed and produced furniture should take more attention of customers. As a result, it is thought that this model will contribute to the realization of effective furniture designs and will provide benefits for sales.

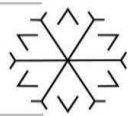
Keywords. Eye-tracking, furniture design, neuromarketing.

1. Introduction

With the developing technology, the product variety in the furniture sector is increasing day by day. It is difficult for consumers to choose, and many products cannot achieve sales success in such an environment. This situation brings along problems such as an increase in the amount of products that are not in demand in the stores. This situation creates the need for high attractive designed furniture.

One of today's marketing realities is to develop products that capture customer attention. Because “products that do not attract the attention of the customer cannot be sold”. It is possible to attract the attention of the customer only by creating and increasing the visual interest for that product. It has been demonstrated by scientific researches that the visual interest shown to a product significantly affects the decision process of choosing that product (Wastlund et al., 2018).

When talking about visual interest, the concept of “visual attention” should also be mentioned. Visual attention is determined by the number of eye looks at an object and the total duration of the gaze. The view that the higher the number and duration of views on a product, the higher the visual interest shown to that product (Van der Laan et al., 2015) and the view that high interest most likely results in preference is dominant in the literature (Lohse, 1997; Janiszewski, 1998). After a quick eye scan of a product, at the first stage, attention focuses on its color, shape and size, which are its visual characteristics, and in the second stage whether this product makes sense to itself. It is known that the resulting visual interest consists of



stimuli that make the product attractive at first, and then needs, goals and desires. In the third stage, irrelevant stimuli are eliminated in accordance with the selective filtering theory, and a final decision is made based on only relevant stimuli. This model, which is roughly stated in three stages, forms the basis of the customer selection process (Wastlund et al., 2018). It is possible to explain this process as a whole as “visual interest”. For this reason, since the measurement of visual interest level provides manufacturers and marketers with clearer and more refined data on the formation of decision processes (Paré and Doris 2011), studies in this direction are increasing.

1.1. Eye-Tracking Technology

Eye tracking is a sensor technology that makes it possible for a computer or other device to know where a person is looking. An eye tracker can detect the presence, attention and focus of the user. It allows for unique insights into human behavior and facilitates natural user interfaces in a broad range of devices. The ability to control a computer using the eyes is also vital for people who are unable to speak or use their hands (Tobii, 2021). The usage areas of eye tracking technology are not limited to usability tests, but the results of this technology continue to be used in many fields such as market research and psychological examinations.

Zimprich (2013) used eye tracking technology to determine the effect of the layout of supermarket aisles on consumer behavior. In the research conducted by showing photographs to 101 participants, according to the results obtained with the eye tracking device data, it was determined that the shelf layout affects the user behavior, which layout is more effective, which parts of the shelf users focus more on, and which layout helps the users more.

A blog by Maughan (2007) focuses on the usability and effectiveness of eye tracking technologies in advertising and marketing. Eye tracking data has been used to help advertisers and designers better run their ad campaigns to attract more consumers and customers to the products they are promoting.

Rebollar et al. (2015) conducted a research on identifying the imaging patterns of chocolate snack packages using the eye tracking technique. Experiments were carried out with 123 participants. In the experiments, 4 different layouts were used. According to the results obtained; It was found that the visual interest was mostly concentrated on the name of the product with 89.4%.

In a study on furniture, how the classical type of Chinese style furniture and the new type of modern Chinese style furniture attracted attention was determined using the eye tracking technique, through the furniture pictures shown to the subjects (Wan et al. 2018). The study was carried out with an eye tracking device on 28 subjects. In this study, the product or the part of the product that took the most observation time was evaluated as the most preferable. As a result, it was determined that the new Chinese-style furniture received more attention than the old types, and the female subjects looked at the products (details) more than the male subjects in total.

The most important features of the eye tracking device are that it does not limit the movements of the users and offers the opportunity to be used comfortably in any area. In this way, the diversity of research conducted with eye tracking method increases.

Eye tracking technology is based on the recording of image reflections with the help of infrared rays. Figure 1 shows the parts of an eye tracker and how it works. The infrared beam from the illuminator is directed into the eye to produce strong reflections on target eye areas and facilitate viewing. The beam enters the retina and is largely reflected back from the retina, making the pupil appear bright. Meanwhile, the image processing software determines the center of the pupil and the position of the corneal reflection. By measuring the vector between these two, the attention point of the eye is determined by various mathematical calculations. The basic components of an eye tracking device are; It is the processing unit that includes illuminators, cameras and image detection, 3D eye model and gaze mapping algorithms.

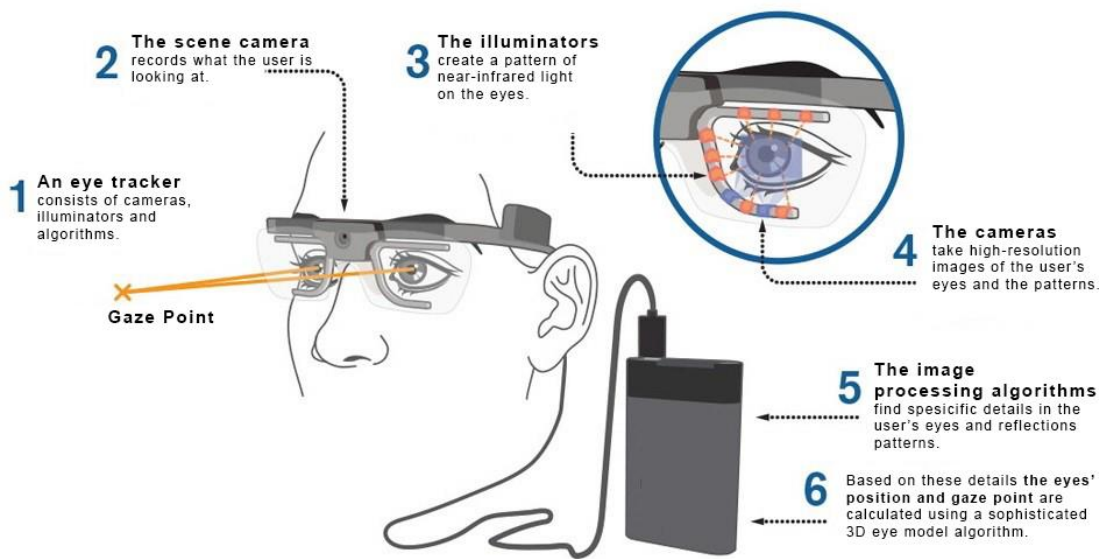
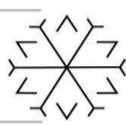


Figure 1. How the eye-tracking device works? (Tobii Pro, 2021)

The basic concepts of eye tracking technology are listed below as they provide information about the measurement data and features provided by this technology.

Gaze Point: It shows which elements of the stimulus the eyes are looking at.

Area of Interest (AOI): A tool for selecting subregions of displayed alerts and extracting custom metrics for those regions.

Heat map: It is a visual chart that grades from light green (the shortest/least) to red (the longest/most) according to the number and duration of fixed gazes.

Time to first fixation (TTFF): Shows the time it takes for a participant (or all participants) to look at a particular AOI since the start of the alert.

Standby time: The total amount of time spent in the area of interest (AOI).

Fixation sequences: Depending on where the subjects look and how much time they spend, their first, second, third, etc. It serves to provide information about the order of attention by telling them where they look.

2. Model Proposal

This model proposal aims to identify where and for what time potential customers' interest is concentrated on when they look at a piece of furniture, by using an eye tracking device in the furniture industry, and to transform this information into heat maps and visualize it. Thus, it will be ensured that the research results obtained through the interpretation of the graphics obtained, the statistical analysis of the data, as well as the evaluation of the questionnaires filled by the customers regarding their demographic information and furniture preferences, will be used as "decision support" in "design" and "marketing" strategies for product improvement/development.

2.1. Method

This model, which is recommended to be used as a "decision support" for the new product development process by determining the focus of attention on the furniture, that will be performed in two stages. The process between start and finish is generally shown in Figure 2.

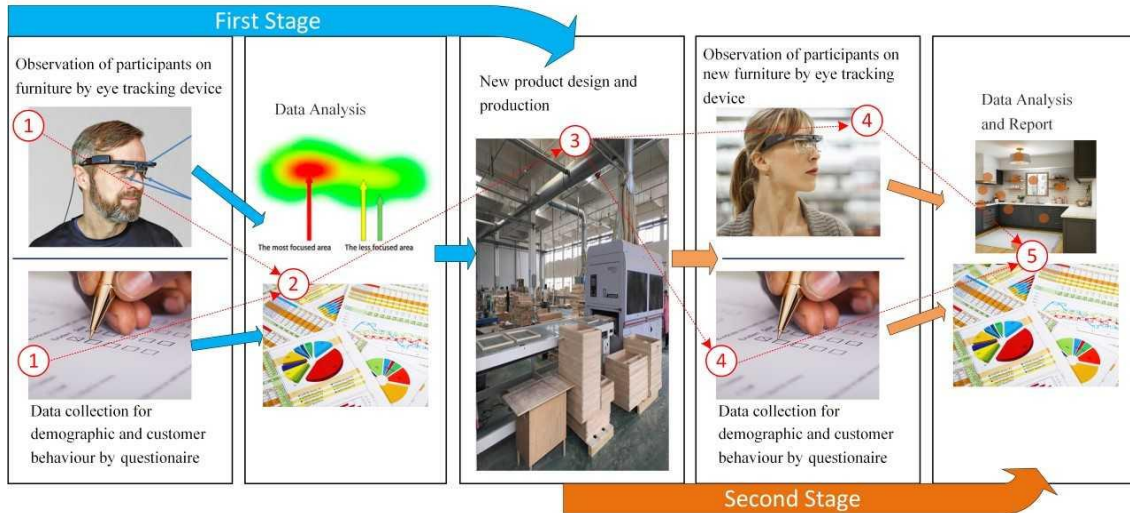
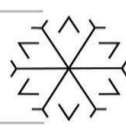
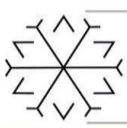


Figure 2. Process diagram

First stage: 60 participants, 30 women and 30 men, will examine the furniture in the real sales environment using an eye-tracking device, and then fill out the questionnaire on demographic characteristics and the reasons for purchasing and choosing furniture. Here, 10 grouped (approximately 90 modules) kitchen furniture consisting of different designs, materials and production types, each of which is brought together from an average of 9 modules, will be observed by the participants with the help of an eye tracking device. In order to prevent the participants from being affected psychologically, no information about the main purpose of the study will be given to the participants at the beginning of the process, and detailed information will be given after the process is completed. At the end of the first stage, answers to the questions listed below will be sought during the analysis of the data:

- Is there a change in the time and number of investigations of a point of interest based on gender? (with Mann Whitney U test)
- Is there a relationship between the data from the eye tracker and the demographic characteristics of the participants? (with Chi-Square test)
- Is there a change in the number and duration of examination of a point of interest in terms of education, income and marital status, and occupation? (with Kruskal-Wallis test)

In the first stage, obtained data will be used as "decision support" for the "new design" and "product development" process. Then 4 (36 modules) grouped new products will be designed and produced.

Second Stage: At this stage, a process similar to the first stage will be experienced. The 4 newly produced kitchen furniture groups will be mixed in the another 10 kitchen furniture groups (old) that are exhibited in the first stage. The new participant group of 60 people, 30 women and 30 men, will not be informed about which products are new and which products are old. Meanwhile, the aim of working with two different groups of participants is to ensure that all products are seen for the first time by the participants during the observation. Again, in this stage the demographic information and the observing data of the participants will be obtained through the questionnaire and eye tracking device.

The first and second stages observation data will be analyzed statistically for determining to difference between two stages. Thus, it will be evaluated whether there is an increasing in interest of participants in the products that redesigned and produced with the help of eye tracking technology.



Figure 3 shows the formation of attention focus in kitchen furniture with eye tracking device and the general functioning of the model.

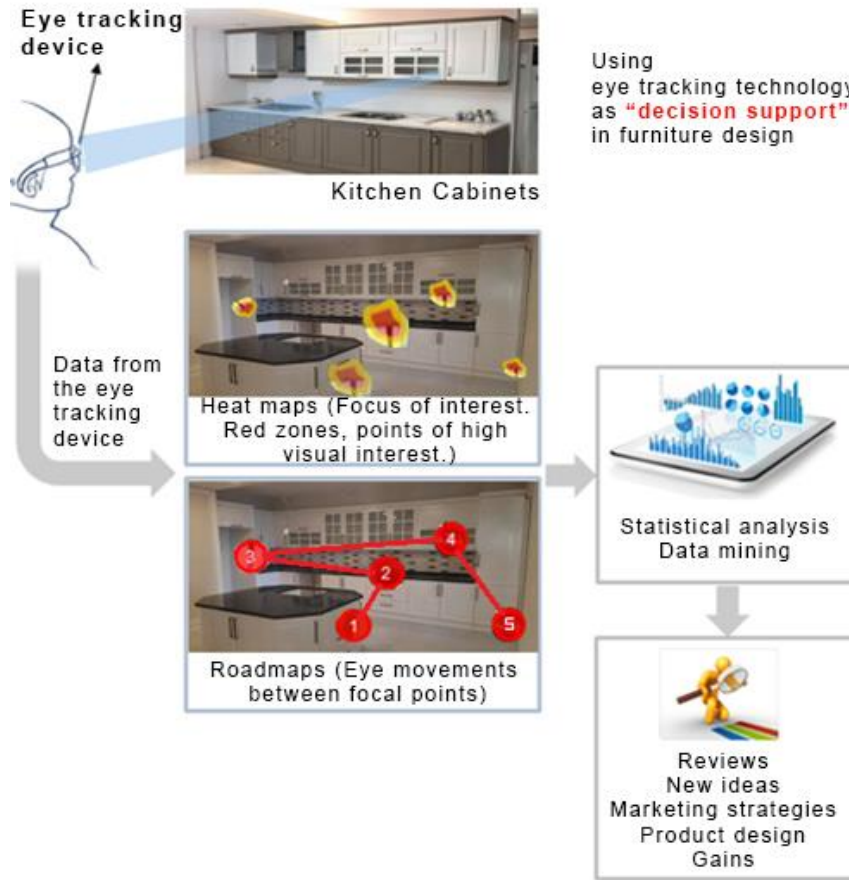


Figure 3. An application example of an eye-tracking device

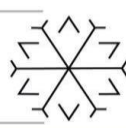
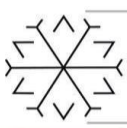
Table 1. shows the number of participants and kitchen groups and the number of observations expected to be measured in the model.

Table 1. Total number of observations

Stage	Participant	Kitchen Group	Number of Modules in a Group	Number of Observations of a Participant	Total Number of Observations
First Stage	30 Men 30 Women	10 groups	9 modules	1 x 10 x 9 = 90	60 x 90 = 5400
Second Stage	30 Men 30 Women	10 + 4 = 14 groups (4 new design)	9 modules	1 x 14 x 9 = 126	60 x 126 = 7560
Total	120 People	14 groups	-	-	12960

As can be seen in Table 1, in the "person x kitchen group x module" approach, approximately 5400 observations for the first stage and approximately 7560 observations for the second stage are expected by the participants. Within the scope of the study, it is calculated that a total of approximately 12960 observations will be made by 120 different participants.

It is possible for the observing participants to be affected by the striking objects around the product and by environmental factors such as refrigerators, dishwashers, ovens, flowers, kitchen utensils, and decoration



of the room. Therefore, while evaluating the total interest time on the product, the time spent looking at the objects around the furniture will not be taken into account. In other words, a "purification" process will be made between the furniture and the objects in terms of the duration of interest and the interest values of the furniture will be clearly revealed.

3. Conclusion

Furniture, which is one of the most used product types by people, is produced by many businesses. For more preference of customers, the eye tracking technology can be used in furniture sector. By the proposed model, observed and mapped information that obtained by eye tracking device can be used as "decision support" for attractive design. Thus, by providing more efficient use of production inputs, it will contribute to the realization of smarter designs in today's world where the consumption of resources, climate change and environmental pollution are frequently discussed. In addition, this model will be a pioneering research that will set an important example for the usability of neuromarketing, one of the popular topics of the era, in the furniture industry.

Acknowledgements

This model is prepared from the project titled "Visualization of customer's attention that occurs on the furniture by using eye-tracking technology and determination its effect on new product design." This project is supported by **The Scientific and Technological Research Council of Turkey (TÜBİTAK)-221O112**.

References

- Janiszewski, C., (1998). The Influence of Display Characteristics on Visual Exploratory Search Behavior. *J.Consum.Res.*25(3), 290–301.
- Lohse, G.L. (1997) Consumer Eye Movement Patterns On Yellowpages Advertising. *J. Advert.* 26(1), 61-73.
- Maughan L. Sergei G. Stevens, R. (2007) "Like More Look More Look More Like More: The Evidence From Eye Tracking". *Brand Management*, Sayı: 14, 4, 335-342.
- Paré, E, M., and Dorris, M. C. (2011). The Role of Posterior Parietal Cortex in the Regulation of Saccadic Eye Movements. In S. P. Liversedge, I. D. Gilchrist, & S. Everling (Eds.), *The Oxford Handbook of Eye Movements* (Pp. 257-278). New York: Oxford University Press.
- Rebollar, R., Lidón, I., Martín, J., & Puebla, M. (2015). "The identification of viewing patterns of chocolate snack packages using eye-tracking techniques". *Food quality and preference*,39, 251-258.
- Tobii (2021) *This is Eye Tracking*, <https://www.tobii.com/group/about/this-is-eye-tracking/>, [Accessed date: 20 October 2021]
- Tobii Pro (2021) *How do Tobii Eye Trackers work?*, <https://www.tobii.com/learn-and-support/learn/eye-tracking-essentials/how-do-tobii-eye-trackers-work> [Accessed date: 24 October 2021]
- Van Der Laan, L. N., Hooge, I. T., De Ridder, D. T., Viergever, M. A., and Smeets, P. A. (2015). Do You Like What You See? The Role of First Fixation and Total Fixation Duration in Consumer Choice. *Food Quality and Preference*, 39, 46-55.
- Wan Qian, Ge Ge Wang, Ya Chi Zhang, Sha Sha Song (2018) "Cognitive processing toward traditional and new Chinese style furniture: evidence from eye-tracking technology" *Wood research* vol. 63 (4):
- Wastlund, E. Shams, P. & Otterbring, T. (2018) Unsold is Unseen or is it? Examining The Role of Peripheral Vision in The Consumer Choice Process Using Eye-Tracking Methodology. *Appetite* 120, 49-56.
- Zimprich, M. (2013). The Layout of the Supermarket Shelf and its Influence on Consumer Behavior, *Yüksek Lisans Tezi*, Viyana Üniversitesi.

Erzurum Surp Minas Church

Firdevs Kulak Torun¹*[0000-0003-0133-4216] and Alper Torun²[0000-0002-6069-6551]

¹firdevskulaktorun@hotmail.com, Department of Interior Architecture, Atatürk University

²alpertorun@hotmail.com, Department of Interior Architecture, Atatürk University

Abstract

Erzurum and its surroundings have been home to many societies since the past. These societies have built many religious buildings. Some of these religious buildings still exist today. Many of the historical religious buildings that have preserved their existence have been protected. But there are also small religious buildings, of which there are not so many known. Surp Minas Church, located in Aziziye district, is also one of these small religious buildings. This church, which belongs to the Armenian community, belongs to a person today. The church, which is unusable, is in a position where urbanization is increasing. The Surp Minas Church, which was considered within the scope of the study, was examined within the scope of Armenian Churches. First, the history and characteristics of Armenian Churches were investigated. Then, the Surp Minas Church was observed and photographed on site. The data obtained from the literature information and the characteristics of the structure were examined. The purpose of the study is to increase the recognition of the structure. The number of people using the church has decreased in the region. For this reason, it is important to make a change in the function of the church and bring it to society. It is believed that the structure given to the community by this change will bring positive results for both the people of the region and the owner.

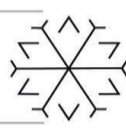
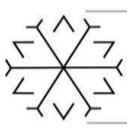
Keywords. Surp Minas Church, Historical Church, Historical Religious Building, Historical Interior

1. Introduction

Erzurum city is an entrance gate from the east and north directions. For this reason, its political and military position has been an important feature. Thanks to this feature, it has hosted many civilizations. The first settlement in the city dates back to BC. When the archaeological excavations, historical sources and surviving artifacts are examined, it has been revealed that the city hosts Arab, Byzantine, Roman, Iranian, Armenian and Turkish assets (Üstüner Çelik 2011).

In the Byzantine period, during the reign of Constantine V Copronymus, the Armenian population was settled in the Erzurum region and the eastern region (Garsoian 1997). The event that affected the ethnic character of the city was the Battle of Malazgirt in 1071. After the war, the Turks who entered Anatolia and the Orthodox Christian population began to be replaced by Turkish and Muslim populations. The Turks, who were outnumbered, dominated the region, and the minorities recognized this dominance. However, despite this increasing Muslim population, the Great Seljuks and Anatolian Seljuks treated non-Muslims fairly and tolerantly (Ismailhakkioğlu 2007). When the Turks came to the city, there were seven hundred churches (Simbat, 1946; Üstüner Çelik, 2011). However, while Turkish domination continued, churches continued to be used. Non-Muslim people have formed their own settlements around these churches (Erayşar, 2002). It is known that the churches continued to exist during the Seljuks and principalities. Different beliefs were not interfered with in Erzurum and he was released. For this reason, non-Muslim people did not leave the city and lived with the Turks for many years (Üstüner Çelik 2011). In the Ottoman period, which was lived after the Seljuk and Principalities periods, non-Muslims were granted important rights in all areas of life. For this reason, non-Muslims were free in their own communities on matters such as religion, administration, etc. With this freedom, they freely expressed themselves. Each minority also had a spiritual assembly made up of clergy. Each community was able to perform their religious worship and rituals according to their own beliefs (Tozlu 2014).

It is known that Georgian and Armenian communities come first among the non-Muslim population in Erzurum. This information is understood by the existence of religious buildings in the region (Üstüner Çelik 2011). Öşvank Church is the best known of the churches in this region. However, apart from this church, it is possible to come across Christian religious buildings in different parts of the city. Surp Minas Church, located in the Saltuklu neighborhood, is one of them. However, it is not as well known as the Öşvank church. Within the scope of the study, Surp Minas Church was discussed. The data obtained about the



church in the literature reviews about this building are very limited. It is aimed to introduce the Surp Minas Church and bring it into the literature. In the study, firstly, on-site observation was made and the building was photographed. Afterwards, a literature review was conducted. Then, in line with the data obtained from the researches, the building was introduced within the scope of religious buildings.

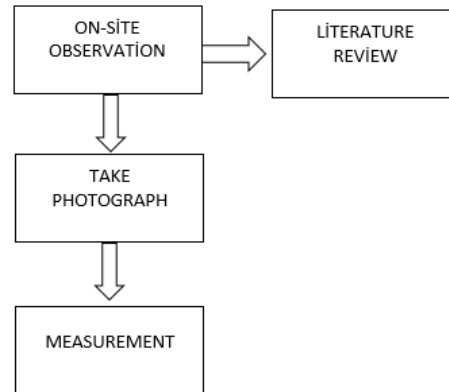


Figure 1: Method of Study

The research first started with the research of the churches in the region. In general, other religious structures in the region were mentioned. In the next section, general information and Armenian Churches are given. In the same section, information about Surp Minas Church is given. In addition, the plan scheme of the church, facade planes, interior features are also given.

1. Armenian Churches

According to the statements of Armenian historians, Armenians are the first nation to accept Christianity and they became the first Christian state in 301. IV. At the beginning of the century, under the leadership of Surp Gregory the Illuminator, Armenians collectively accepted Christianity. In this period, when Armenians accepted Christianity, religious debates continued in Rome. Then, with the efforts of Surp Krikor, the Armenian Churches were detached and separated from the main church (Kilic 1997). They destroyed pagan temples and built Christian temples (Seyfeli 2004; Hillez Halifeoğlu 2016).

Churches are very important to the Armenian community. Gürün (2005) stated in his book that it would be correct to talk about the Armenian churches, not the Armenian nation or state, and that the Armenian Churches gave birth to the idea of the Armenian state. He also stated that there are too many Armenian churches in Eastern Anatolia and that there are currently 109 churches in Erzurum and Van (İsmailhakkıoğlu 2007).

History of Armenian Churches It begins with the discovery of the temple ruins of the 2nd century (Ahunbay 1997; Hillez Halifeoğlu 2016). Armenians, who were the target of Greek, Iranian and Arab attacks throughout history, continued to build monumental churches (Maranci 2006). At the beginning of the 7th century, a style of church architecture of their own began to emerge. Armenian churches were not large structures as in other Christian societies. A large number of church architectural types have developed. This situation also increased diversity (Kouymijan 1992). Despite the different architectures seen in the first churches, they also have common features. These can be listed as follows (Hillez Halifeoğlu 2016):

- Stone was used as a material in churches.
- The ceilings are generally vaulted.
- The use of domes started from very early times. There was no use of a church without a dome in the 6th century. Such buildings are small, but perceptible with their solid mass.
- Ceilings are considered as multi-piece, as they have to cover the vaults and domes of the symmetrical interior organization in the mess.



Kouymjian (1992) classified Armenian church forms. In the classification he made, he named the forms as basilica and single nave, domed basilica and domed single nave church, central plan, square plan with niche, hripsime type, circular plan and jamatun.

The Basilica and the Single Nave Church were worshiped for parish churches in early architecture. Examples belong to the 5th and 6th centuries. Many are vaulted buildings in basilica form, without a dome. Churches of this plan type are more common in Mesopotamia and Asia Minor (Nersessian 1945; Hillez Halifeoğlu 2016). Most have three naves, but there are also variants with a single nave. Between the 4th and 6th centuries, a large number of single-nave buildings were built (Kouymjian 1992). The Domed Basilica and the Domed Single-nave Church are the products of the widespread use of the dome by the Armenians. This plan type replaced the vaulted and domeless basilicas in the historical process (Nersessian 1945; Hillez Halifeoğlu 2016). The Central Plan emerged in the 6th and 7th centuries. These churches are in the form of trefoil and have the appearance of a Greek Cross from the outside. They have four apses in a square plan buttressed with a niche. The apses protruding from the middle of all four square-shaped walls are covered by a centrally placed dome. There are two rooms in these churches. The basic plan of the hripsime type is clover inside, that is, the inner apses are combined to form a four-leaf clover. At the intersection of these apses, there are deep circular (three quarter cylinder) niches in each of the corners. These niches, together with the four apses, form an octagonal base which supports a high cylindrical drum. The symmetrical plan allows for the creation of a proportionally larger interior space without being hindered by columns or piers. Circular Plan The final design in the central plan is the perfectly circular church. VII. It has started to be seen since the 19th century (Kouymjian 1992).

Jamatun emerged in the middle of the 7th century as a different unit from other typologies. On the western façades of the monastic churches, there are the tombs of the clergy, the rich and the nobles, which were added later. Sometimes used for educational purposes, the place has a semi-religious, semi-civil function (Karaca 2006).

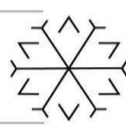
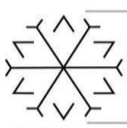
2. Surp Minas Church

Surp Minas Church, located in the Saltuklu neighborhood of the Aziziye district of Erzurum, is located on the 18th. it has been dated to the yy. It is an Armenian church. (Url-6 2021). Some sources say that it was built in 1790. However, it is believed that the church was built on the site of an old structure. Because an inscription dated 1740 was found on the wall of the church (Parsegian 1990). The church is not in use today. It is in a state of ruin. The structure belongs to one person. The authorities have met with the owner, a Turk living in Germany, for the restoration of the structure, but the owner has not taken a positive attitude to this issue (Url-7 2021).

The structure is built of masonry stone. It has one floor. The decommissioned building is currently located among the new settlements.



Photograph 1: General View (Personel Archieve 2021)



When viewed from the outside, the church is rectangular in shape. The general masonry in the stone structure is irregular. However, cut stone was used in the corners and openings such as window-entrance. All wall surfaces have openings. There are large window openings on the two wall surfaces. There are arches above the window openings. These arches are also made of molded stone.



Photograph 2,3: Wall Surfaces From Outside (Personel Archieve 2021)

The west wall of the building has an entrance centered on the plane. The entrance has an arch made of molded stone. However, this door is now closed. Currently, there is a door on the west side of the building that was opened later.



Photograph 3,4: Door General Photo (Personel Archieve 2021)

It is mentioned in the old records that the church had a lower narthex and a wooden bell tower (Persegian 1990). The roof section is inclined, but now there is no material left on the roof. The length of the structure is 15.4 meters and the width is 12.3 meters. The church has three naves. With the original entrance door, the entrance to the interior is made from the middle nave. There is an apse wall just opposite the entrance door. The structure has barrel vaults with transverse ribs supported by four columns that divide the space into nine compartments. The columns in the interior are made of a single piece of stone. They have very simple titles.

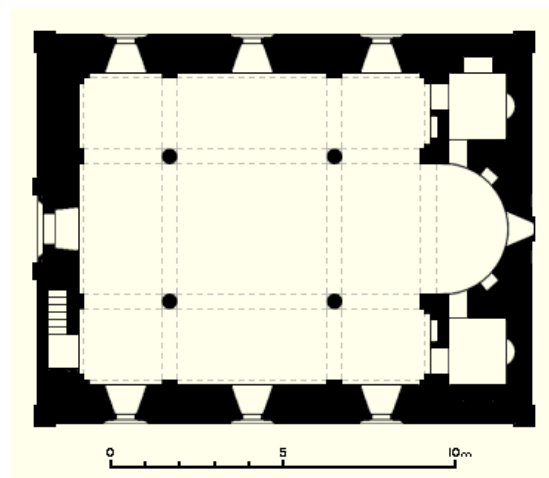


Figure 2: Surp Minas Church Plan Chart (Persegian 1990)

The columns in the interior are made of a single piece of stone. They have very simple titles.



Photograph 5: Column (Personel Archieve 2021)

In the upper part of the apse of the church, there is a circular window passing through the semi-dome of the vault. There are rooms on both sides of the apse.



Photograph 6: The Apse And The Two Rooms Next To İt (Personel Archieve 2021)

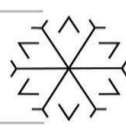
It is accessed through the doors on the eastern walls of the north and south naves and also through openings from the apse. There are small circular windows on the east wall.



Photograph 7: Small Circular Windows (Personel Archieve 2021)

3. Conclusion

Erzurum and its surroundings have hosted many societies in its history. These societies, which it hosted, have built many religious buildings in this geography. Some of these religious structures have survived until today. Many of these historical religious structures that have preserved their existence have been taken under protection. It is open to foreign tourists. However, there are still small historical religious buildings that are not well known by the society. Surp Minas Church, located in Saltuklu neighborhood in Aziziye district, is not in use today. Since it belongs to a person, it could not be included in any restoration project. New settlements are being built in the region where it is located. The church, on the other hand, remained among the new settlements in a dilapidated state.



In this study, which was carried out in order to increase the recognition of the building, the characteristics of the church were determined. In the literature review, it was found that the church was dated 1740. Although it is a structure built in the 18th century, it has been determined that it also has the characteristics of the Early Armenian Churches with the examinations made. The use of stone material and tone and vaults the symmetrical interior solution are common with Early features. It is known that the use of domes became widespread in Armenian churches after the 6th century. However, there is no use of a dome in this structure. Although there is no use of a dome, it is a small structure and can be perceived with its solid mass, which is compatible with the characteristics of the same period. Considering the classification of Armenian churches within the scope of plan typologies, the building is under the title of basilica and single nave. It is known that such churches often have three-nave examples. There are also three naves in the building. The church is a structure with a basilica plan typology, showing the characteristics of the Early Armenian Church. It is not as big a structure as other churches in the region. Because it is a more local church that has served a small congregation. However, it is an important issue to make the building usable again, since its historical value has survived until this time.

It is important that this church, which is included in daily life, turns into a living structure. Due to the fact that there are not many people from the church community in the region, it is thought that the restoration by changing the function will bring a positive result for the users and the owner. In addition, it is an important structure that should be adapted to daily life and brought to the society.

Referances

- Ahunbay, M. 1997., *Ermeni Mimarlığı ve Sanatı*. İstanbul: Yem Yayıncılık.
- Eravşar, O. 2002., *Ortaçağ Anadolu Kentler, Türkler, VII*, Ankara.
- Gürün, K. 2005., *Ermeni Meselesi*. İstanbul: Remzi Kitapevi.
- Hillez Halifeoğlu, S. 2016., *Güneydoğu Anadolu Bölgesinde Bulunan Ermeni Kiliseleri Koruma ve Kullanım Durumları*, Master's Thesis, Dicle University, Diyarbakır, Türkiye.
- İsmailhakkıoğlu, Z. 2007., *1908 – 1914 Yılları Arasında Erzurum'daki Ermeniler*, Master's Thesis, Balıkesir Üniversitesi, Balıkesir, Türkiye.
- Karaca, Z. 2006., *İstanbulda Osmanlı Dönemi Rum Kiliseleri*. İstanbul: YKY Yayınları.
- Kılıç, D. 1997., *Selçuklulara Kadar Anadolu'da Grogeryan Ermeni Kiliseleri (M 452-1100)*, *Türk Kültürünü Araştırma Enstitüsü Dergisi*, no.452, pp. 752-760.
- Kouymjian, D. 1992., *The Arts of Armenia. Chemins d'Arménie*.
- Maranci, C. 2006, *Building Churches In Armenia: Art At The Borders Of Empire And The Edge Of The Canon*, *The Art Bulletin*, 88(4), pp. 656-675.
- Parsegian, V.L., 1990, *Armenian architecture: A Documented photo-archival collection on microfiche for study of Armenian architecture of Transcaucasia and the Near and Middle-East, from the medieval period onwards*, Switzerland.
- Seyfeli, C., 2004, May, *Osmanlıya Kadar Diyarbakır Ve Çevresinde Ermenilerin Dini Durumlar. I. Uluslar Arası Oğuzlardan Osmanlıya Diyarbakır Sempozyumu'nda Sunulan Bildiri*. Diyarbakır Valiliği, (pp. 763-771).
- Üstüner Çelik, H. 2011. *Türkiye Selçukluları ve Beylikler Döneminde Erzurum'da Sosyal ve Kültürel Hayat*, Master's Thesis, Sakarya Üniversitesi, Sakarya, Türkiye.
- Url-1, viewed: 07.11.2021, <https://www.kulturportali.gov.tr/turkiye/erzurum/osvank-kilisesi>.
- Url-5, viewed: 07.11.2021, <https://www.kulturportali.gov.tr/repoKulturPortali/large/19022013/d913b6f9-6441-4e0f-9bab-423363926491.jpg?format=jpg&quality=50>.
- Url-6, viewed: 08.11.2021, <https://kulturenvanteri.com/yer/surp-minas-kilisesierzurum/#15.41/39.922427/41.181132>.
- Url-7 viewed: 10.11.2021, https://www.ntv.com.tr/galeri/sanat/surp-minas-kilisesi-kentsel-donusum-un-ortasinda-kal-di,38MjGWd2LE2P1XldCTWD2w/qiJXT0m_8EKznpa5lxQePA.

Evaluation of the Components of Design Thinking in Terms of Design Education

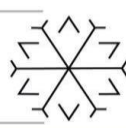
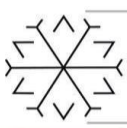
Özlem Kurt Çavuş ^{1*}[0000-0002-9992-2472]

¹ozlemkurt@eskisehir.edu.tr, Eskişehir Technical University

Abstract

The definition of “creative problem-solving process” is frequently encountered in the literature on design thinking. This process includes creative problem solving stages, which include values, principles and methods, the use of which has become widespread in more than one field, especially in recent years. Design thinking principles are frequently encountered in the content of design education, which is based on the creative problem-solving process. The “design thinking components” discussed in this study include the characteristics such as the attitude, principle, value, and perspective adopted by the individual during the application of design thinking as a problem-solving approach. These components express the mindset of individuals towards creative problem solving using design thinking. In this study, it is aimed to determine the basic components that make up the concept of design thinking through the classification of qualitative data obtained from literature reviews. As a result, according to the evaluation of the accessible and qualified resources in the design thinking literature by document analysis, the design thinking components extracted from these sources were brought together and the design thinking components were discussed within the framework of design education. It is predicted that these components brought together will contribute to design education conceptually. It is considered significant to transfer the concepts of design thinking to the students, especially in design education, which is very important to update itself in a dynamic structure. In this respect, it is expected that the study will have a widespread impact on the design education literature.

Keywords. design education, design-focused thinking, design learning, design pedagogy, design thinking



1. Introduction

Design education includes methods that aim to teach the design process, including problem-solving approaches based on creativity. Design education generally includes education models that prepare competent individuals for creative sectors. Undoubtedly, the competence and up-to-dateness of the training programs are important for the design industry to raise competent individuals. In the twenty-first century we live in, creative problem solving is frequently encountered as one of the priority topics that should be included in education programs (Carmeli, Gelbard and Reiter-Palmon, 2013; Funke, Fischer, and Holt, 2018; Öno1, 2013; Özkök, 2005; Şener, 2006). For this reason, in recent years, the concept of "design thinking", which is defined as "creative problem-solving approach", is frequently used in different fields. However, design thinking is closely related to the essence of design and design action, which has been conceptualized for many years and includes creative attitudes and methods towards problem-solving, which is one of the basic values of design education. In order to know how to use design thinking as a method in education programs or the face of any problem, first of all, it is necessary to know the whole values and principles that make up it. This article aims to contribute to the field of design theory and to associate it with the content of design education by bringing together the components of design thinking in the way they find their place in the relevant literature. In this regard, the research questions of the study were determined as follows:

“What are the components that build design thinking?”

“What can be the contributions of design thinking components to design education?”

In this direction, it is aimed to identify the components of design thinking, which has become more important in recent years, by scanning the sources that have high impact and quality in the international literature, and also to associate them with the professional qualifications that make up the content of design education. The data obtained as a result of the application of content analysis/document analysis with the qualitative research perspective of the relevant documents in the design thinking literature were transferred with the tables created.

2. The Structure of Design Education

Design education, which is intertwined with abstract concepts, has a complex and contradictory structure that is comprehensive, not too obvious, difficult to define, understand, classify and form (Yürekli and Yürekli, 2004, p. 53-62). When the historical development of design education is examined, one encounters the Bauhaus school, which is the source of the educational model foundations of many design schools today. The developments in industry and technology at the beginning of the twentieth century and the mass production that followed have led to the need for aesthetic shaping. Bauhaus, an institution that deeply affected art education at the beginning of this century, was established in Germany while the stages of reconstructing the union of art, technical knowledge and technology/production, which were separated by the effect of industrialization, were continuing (Ackermann, 2000, p. 8). The Bauhaus approach aimed to create an environment suitable for the mutual interaction of both fields by removing the border between applied design fields and fine arts (Erkmen, 2009, p. 17). In Bauhaus, the aim of meeting industry needs to be emerged and designs were prepared in workshop environments, prototypes were made in textile, glass, metal, printing and ceramic workshops and production was carried out in factories (Bulat, et al. 2014, p. 106). The fact that besides art, technological production based on scientific and technical knowledge is carried out at the Bauhaus, this shows that there is art, science and technology in the education program.

Design is also described as a problem-solving process. “Design is a multidisciplinary creative problem-solving and planning activity (Cooper and Press, 1995)”. The stages in the realization of the design action, which is defined as creative problem solving and planning activity, constitute the design process. Figure 1 shows the “Decision-based design process” diagram defined by Simon (1960).

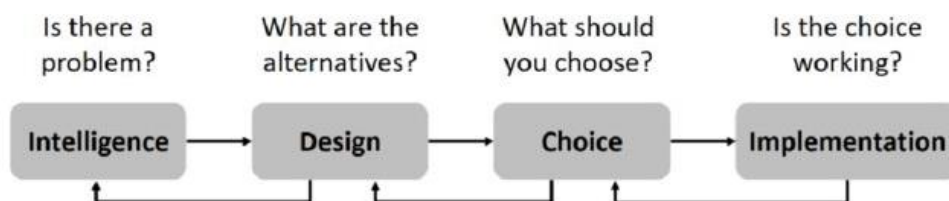


Figure 1: Decision-based Design Process Diagram (Simon, 1960)



The product or information produced by design actions gains original value at the end of this process. The solutions, works, products or spaces produced in the design process are directly related to the user.

3. The Concept of Design Thinking

The term thinking, which is an important concept in design education, is increasingly used to mean the human-centered and open problem-solving process that decision-makers use to solve complex real-world problems. (Melles, Howard and Thompson-Whitesidec, 2012). Dorst (2011) stated that “Design thinking” has been part of the collective consciousness of design researchers since Rowe used the concept of design thinking as the title of her book in 1987. The importance of the concepts of “design” and “design thinking” has recently been widely emphasized in more than one field. Today, “design thinking” is defined as an exciting new paradigm for dealing with problems in many professions, especially information technology (IT) and business (Dorst, 2011, p. 521). Johansson and Woodilla (2010) observed two different discourses on design thinking: one being the design-based thinking in the scientific literature, and the other being the thinking style in the widely accessible business media. In this context, “design thinking” is distinguished from the practice of “design focused thinking” used in the field of professional design (Johansson-Sköldberg et al. 2013, p. 122). Design thinking differs from traditional analytical user-centered design methods by focusing on expansion in the early stages of design (Baeck and Gremett, 2011). It is known that design-focused thinking is used by leading innovative companies such as Apple, Google, Samsung, GE by adopting design-focused thinking methods. In engineering, which is an area where design thinking is widely used, design is accepted as the central or distinctive activity of engineering (Simon, 1996). In addition, it is emphasized that engineering programs should graduate engineers who can design effective solutions to meet social needs (Evans, McNeill and Beakley, 1990). Razzouk and Shute (2012) stated that helping students think design-focused can better prepare them to cope with difficult situations and to solve complex problems at school, in their careers and life in general (Razzouk and Shute, 2012, p. 343).

The usage stages of design thinking are described in the most common form defined by Stanford d.school as in Figure 2.

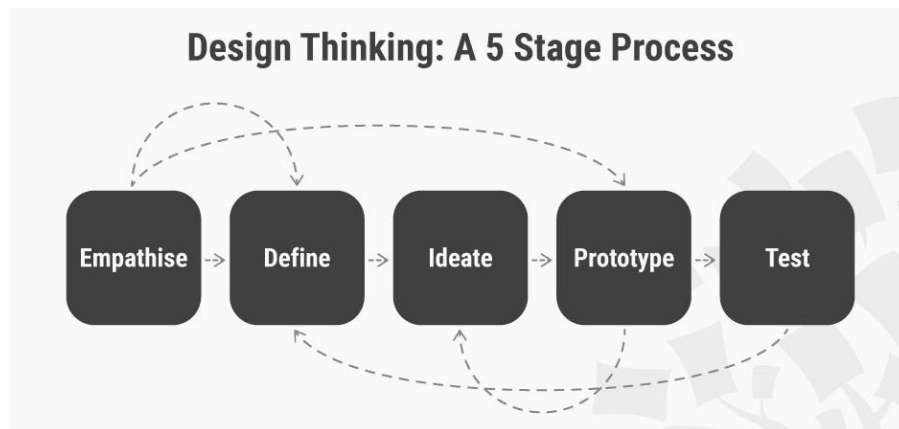


Figure 2: Five stages of design thinking process (Stanford d.school)

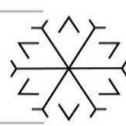
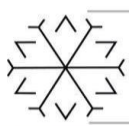
The diagram above describes the most commonly known process steps to explain the workings of design thinking.

4. Methodology

In the study, it was aimed to create knowledge by using an inductive perspective and a qualitative research approach. The knowledge obtained by document analysis, one of the content analysis methods based on the literature review, was synthesized. Coding method was used to analyze by Nvivo12 software and all the codes collected according to the frequency of occurrence in the sources. The findings were obtained by synthesizing based on creating a meaningful body of knowledge.

4.1. Collection of Data

The documents used in the study consist of online articles and reports that can be accessed from the internet. In this respect, the literature data related to the study were obtained as a result of the search. Basically, the studies that stand out with their quality are frequently cited in the design thinking literature have been



reached, and it has been tried to reach the concepts, attitudes, perspectives, principles and values for creating design thinking components from these publications.

5. Findings

Concepts, attitudes, perspectives, principles and values obtained as a result of analyzing the contents of scientific articles and report documents reached in the literature review on design thinking were brought together and "design thinking components" were formed.

The structure, which is defined as the components of design thinking, includes features such as values, principles, perspectives, and skills that a person can use in the creative solution of design problems and that he or she should have individually, in the process defined as design thinking in the literature. In short, it refers to the set of features required to solve a problem creatively. The most comprehensive scientific studies reached in the literature and found suitable for this study: Dosi, Rosati and Vignoli (2018), Schweitzer, et al., (2016), Razzouk and Shute (2012) and Howard et al. (2011, 2015) studies are given. The design thinking mind-structure features, which form the design thinking components determined by these studies, in other words, have been compiled in the table below within the scope of the study. For each component, the study to which the content analyzed in the formation of the component belongs is marked in Table 2. All headings must be numbered consecutively and hierarchically.

Table 1: Design Thinking Components (Created as part of the Study)

Design Thinking Components	Dosi, et al., 2018	Schweitzer , et al., 2016	Razzouk and Shute, 2012	Howard et al., 2011, 2015
1. Human-focused	X	X	X	X
2. Skill of visualization			X	X
3. Multifunctionality			X	X
4. Learning-focused	X	X		
5. Openness to interdisciplinary/ multidisciplinary collaborations	X	X	X	X
6. Openness to different perspectives and diversity	X	X		
7. Tendency to teamwork	X	X		
8. Critical thinking	X	X		
10. Empathy	X	X		
11. Reframing the problems	X			
12. Desire to make a difference	X	X		
13. Holistic perspective	X	X	X	X
14. Avoiding the need to choose			X	X
15. Risk-taking	X	X		
16. Ambition for innovation	X	X		
17. Experimental learning/learning by doing	X	X		
18. Learning from mistakes	X	X		
19. Ability and self-confidence of creative thinking	X	X		



20. Using language as a tool			X	X
21. Optimism	X	X		
22. Tolerance to ambiguity	X	X		

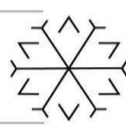
In Table 2, the sources that are considered important in terms of the theoretical literature on design thought in the world and the expressions taken from the relevant source are shown. As can be seen in the table, some concepts are components that have been included in several of the reviewed sources. These are the most common components; “human-focused”, “openness to interdisciplinary/multi-disciplinary collaborations” and “empathy”. “Critical thinking” is also an extremely important feature in the creative problem-solving process with design thinking. The “holistic perspective” is used in the sense of being able to manage knowledge and skills specific to more than one discipline with a holistic perspective and approaching problems from this framework. The ability to visualize has also been a common feature encountered in many document reviews. The “multifunctionality” component can be explained as being flexible and adapting to different disciplines and fields. “Learning-focused” means that the person has the motivation to learn and is always open to learning. The component of “openness to different perspectives and diversity” expresses being open to diversity and different views in cultural and social contexts. The component of “tendency to teamwork” is that the person is compatible with teamwork, as it is understood directly. The component defined as “critical thinking” is also referred to as “inquiring” in the sources. “Empathy” is a design thinking concept encountered in many sources. It is also referred to as “being an empathetic individual” or “empathy skill” in the sources. “Reframing the problems” means reframing, reconsidering and defining the problems encountered in the relevant field with all their dimensions. “The desire to make a difference” can be evaluated as the desire to seek the new and achieve extraordinary results, which can be associated with innovation. The “avoiding the need to choose” component is concerned with the attitude of designers when they look for other alternatives before moving on to choosing or making a decision. In this process, they look for ways to find new alternatives. “Risk-taking” means that the person should not be prejudiced against risks and avoid risk when necessary. “Ambition for innovation” refers to a person's ability to follow innovations, as well as the desire to make a difference. The component defined as “experimental learning/learning by doing” is related to the visualization skill, but basically means that the person has a structure that learns from experiences. The component defined as “learning from mistakes” expresses the tendency to learn through experiences, but this component emphasizes the individual characteristic of seeing mistakes and failures as learning tools. “Ability and self-confidence of creative thinking” refer to an individual's ability to use their creative thinking skills and their self-confidence based on previous experiences in this regard. “Using language as a tool” refers to the basic communication skill required for problem-solving in every field. The “optimism” component expresses the optimism towards making an impact. The last component, “tolerance to ambiguity”, describes the individual's ability to act tolerantly and flexibly against uncertain and unclear situations in the problem-solving process.

6. Conclusion

As a result of the analysis and evaluation of the contents of the documents examined at the end of the study, twenty-two items defined as design thinking components were determined. The content of each of the items is explained in the findings section. In this study, the content of design thought was defined with the components revealed through the data obtained from the literature, and its detailed and comprehensive theoretical framework was determined.

At the final of the research evaluations within the scope of the study, increasing the awareness of the concept of design thinking by collecting the components of design thinking into items and increasing the possibility of its application in many fields, especially in the field of design education, is one of the important results aimed to be achieved in this study.

There is a similarity between the design process and design thinking as a process and they are used interchangeably. After the designer identifies the design problem, the process that includes the stages of empathy, thinking, idea generation, decision making and testing, and is usually completed with the final product, constitutes the design thinking process. Similarly in the design process; A process is developing in the form of understanding, designing, choosing and applying the problem. Although the design process diagrams show slight differences in different sources, it basically proceeds in line with the same principles as the diagram (Figure 1 and Figure 2). The main purpose of the design studios and the pedagogy used in the studios is to provide the design student with skills that include creative problem solving techniques, and to make these skills an application experience through repetition and use in the design processes. In all



these respects, design thinking and design education are in harmony and very similar in terms of almost all principles and components.

For the use of design thinking as a method in design education as a creative problem-solving method, transferring the components and process operation to the students through the education program can contribute positively to the quality of education. For this reason, it would be more beneficial to include the theory and practice of design thinking in the program contents in design undergraduate programs, more intensively in the first year of education, in terms of awareness and use of design thinking.

References

- Ackermann, U. (2000) Bauhaus. in J. Fiedler, and P. Feierabend. (eds.) Cologne: Könemann.
- Baeck, A., Gremett P. (2011) Design thinking. In UX best practices - How to achieve more impact with user experience. H. Degen and X. Yuan. (eds.) New York: McGraw-Hill Osborne Media.
- Bulat, S., Bulat, M. and Aydın, B. (2014) 'Bauhaus tasarım okulu', Atatürk Üniversitesi Sosyal Bilimler Enstitüsü Dergisi, 18 (1).
- Carmeli, A., Gelbard, R., and Reiter-Palmon, R. (2013) 'Leadership, creative problem-solving capacity, and creative performance: The importance of knowledge sharing.', *Human Resource Management*, 52(1), p95-121.
- Cooper, R. ve Press, M. (1995) The design agenda: a guide to successful design management. John Wiley and Sons.
- Dorst, K. (2011) 'The core of 'design thinking' and its application', *Design Studies*, 32(6). p521-532.
- Dosi, C., Rosati, F. and Vignoli, M. (2018). 'Measuring design thinking mindset', *Proceedings of International Design Conference, DESIGN*.
- Erkmen, N. (2009) Bauhaus, Modernleşmenin Tasarımı. 50. Yıl Etkinlikleri, Bauhaus Ekolu Işığında Devlet Tatbiki Güzel Sanatlar Yüksek Okulu ve Marmara Üniversitesi GSF'nin Dünü-Bugünü. İstanbul: İletişim Yayınları.
- Evans, D.L., McNeill, B.W. and Beakley, G.C. (1990) 'Design in engineering education: past views of future directions', *Journal of Engineering Education*, 79(4).
- Funke, J., Fischer, A. and Holt, D. V. (2018) 'Competencies for complexity: problem solving in the twenty-first century', In *Assessment and teaching of 21st century*. Cham: Springer. p41-53.
- Howard, Z. (2013) Guest lecture to first year Bachelor of IT students at Queensland University of Technology in unit INB103 Industry insights. Lecture Notes. <https://www.slideshare.net/zaana/introducing-design-thinking>
- Johansson, U. and Woodilla, J. (2010) 'How to avoid throwing the baby out with the bathwater: an ironic perspective on design thinking', *European group for organization studies colloquium*. Lisbon, Portugal.
- Melles, G., Howard, Z. ve Thompson-Whiteside, S. (2012) 'Teaching design thinking: Expanding horizons in design education', *Procedia-Social and Behavioral Sciences*, 31. p162-166.
- Önol, M. (2013) Yaratıcı problem çözme etkinliklerinin bilimsel süreç becerilerine ve başarıya etkisi. Master Thesis. Balıkesir: Balıkesir Üniversitesi, Fen Bilimleri Enstitüsü.
- Özkök, A. (2005) 'Disiplinler arası yaklaşıma dayalı yaratıcı problem çözme öğretim programının yaratıcı problem çözme becerisine etkisi', *Hacettepe Üniversitesi Eğitim Fakültesi Dergisi*, 28(28). p159-167.
- Razzouk, R. and Shute, V. (2012) 'What is design thinking and why is it important?', *Review of Educational Research*, 82(3). p330-348.
- Schweitzer, J., Groeger, L. and Sobel, L. (2016) 'The design thinking mindset: An assessment of what we know and what we see in practice', *Journal of Design, Business & Society*, 2 (1). 71-94.
- Simon, H. A. (1996) The sciences of the artificial. Cambridge, MA: MIT Press.
- Şener, S. D. (2006) 'Triz: yaratıcı problem çözme teorisi ve diğer problem çözme yöntemleriyle karşılaştırma.', Master Thesis. İstanbul: İstanbul Teknik Üniversitesi Fen Bilimleri Enstitüsü.
- Yürekli, İ. and Yürekli, H. (2004) 'Mimari tasarım eğitiminde enformellik', *İTÜ Mimarlık Planlama Tasarım Dergisi*, 3 (1). p53-62.

Understanding the Meanings of Sustainability: Historical Roots, Current Perspectives, Future Directions¹

Seyda Emekci ^{1*}[0000-0002-5470-6485]

¹semekci@ybu.edu.tr, Ankara Yıldırım Beyazıt University

Abstract

Sustainability as a concept can be defined as development that meets the needs of the present without compromising the ability of future generations to meet their own needs. Although its origins are based on the 1987 Brundtland Report, it has survived since ancient times. Throughout history, human civilization has evolved and integrated into the environment to "live". Nowadays, this situation continues, and in the 21st century, most architects are sensitive to sustainability issues. The article aims to take a holistic approach to sustainability and to clarify its meaning by making use of historical milestones, current perspectives, and future directions.

Keywords. Sustainability, climate change, energy consumption, greenhouse gas emission

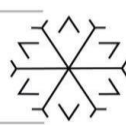
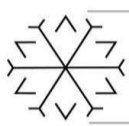
1. Introduction

People all across the world are becoming increasingly conscious of the significance of sustainability. The combination of human-induced climate change and population growth has resulted in significant environmental degradation. It is critical that all processes be carried out "sustainably" in order to protect both the global environment and human existence. However, it is a continuous obstacle in the literature because the concept of sustainability is not well defined and understood. The ambiguity and lack of definitions around sustainability in recent decades have been attributed to the concept's broad use, many and often conflicting interpretations, and a huge number of definitions that change according to the field or political situation in which it is utilized (Ciegis, Ramanauskienė, and Martinkus, 2009; Balaceanu and Apostol, 2014). However, the term 'sustainability' appears to be confusing and trite due to misperceptions and different descriptions. Heinen (1994) said that there is no universally accepted definition of "sustainability" owing to the diversity of scopes associated with various kinds of protection programs and communities and organizations. As a result, a large number of books, chapters, and articles with "sustainable" and "sustainability" in their names but no definitions of the idea have emerged, according to Spedding (1996). The study carried out by Mebratu (1998) states that there are more than 80 possible interpretations of the term "sustainability," while the research of Jacobs (1994) indicates that there are more than 350 definitions only in economics; however, neither research provides an explanation for these definitions. As a result, according to Pierantoni (2004), it should be mindful of the fact that the notion of sustainability may be difficult to grasp and that it may have varied meanings depending on the literature on the subject in which it is employed that has been evaluated. For this reason, the purpose of this article is to take a holistic approach to sustainability and to elucidate its meaning via the use of historical precedents, current perspectives, and future directions.

2. Emergence of Sustainability

Sustainability or Sustainable Development has been widely characterized as ensuring a higher quality of life for current and future generations, as well as a more environmentally friendly and sustainable planet for future generations to experience (WCED, 1987). There have been several significant turning points in the development of sustainability on a global scale: (a) Progress prior to the United Nations Conference on the Human Environment, (b) from the United Nations Conference on the Human Environment to World

¹ This article is produced from the master thesis titled "An Assessment on the Link Between Sustainability and Urban Form: The Case of Gaziantep".



Commission on Environment and Development, (c) Progress Following the World Commission on Environment and Development.

2.1. Progress prior to the United Nations Conference on the Human Environment

Beliefs in ancient times have taught humans throughout history to see and act on non-human nature in terms of specific human goals, beliefs, and social structures, rather than in terms of universal human nature. Throughout history, spiritual traditions have recognized and sanctified our connections with the nonhuman world, reminding us of the delicate and unavoidable nature of our relationship with the elements of air, land, water, and other living things (Mebratu, 1998). Therefore, it would not be wrong to look for the first foundations of sustainability there. Then, Thomas Malthus said in his essay on the theory of population in 1798 that growth in the global population placed a strain on natural resources. He also observed that the global population grew exponentially while available resources grew arithmetically. At this rate, famines, plagues, and wars would occur as population expansion outpaced the food supply. Maximum Sustainable Yield (MSY) became popular after World War II. The concept of MSY is based on production exists that can be harvested in permanency without altering the population (Vehkamäki, 2005). In the following years, Hardin (1968) developed an economic theory known as the tragedy of the commons. In his theory, Hardin highlighted human population increase, the utilization of the Earth's natural resources, and the welfare state, and natural resources were shared by many persons, according to the theory. If natural resources stay steady, the population will continue to grow, and limited resources will ultimately deplete. In the same year, Ehrlich (1968) wrote *The Population Bomb*, a book that analyzes population and environmental concerns, pointing out that population growth puts strain on economies and resources.

Table 1: Sustainability Initiatives

Date	Event	Description
1798	Thomas Malthus- An essay on the principle of population	Populations grew exponentially, but accessible resources grew arithmetically, according to this essay. Malthus prophesied that this would ultimately result in famine, pestilence, and war because population increase would outstrip food supply.
	Maximum Sustainable Yield (MSY)	Widely used after the second world war to restrict fishing
1936	The United States Flood Control Act	This Act brought welfare economics into the realm of practical decision-making. It was the catalyst for the concept of CBA. Projects could be evaluated by calculating their net benefit and then evaluating that net benefit in the context of the whole societal evaluation of that net benefit.
1962	Rachel Carsens-Origins of spring	The article examined the negative effects of pesticides on the environment, particularly on birds, and was significant in the final prohibition of DDT.
1968	Garret Hardin-Tragedy of the commons	Hardin stressed that the population would continue to rise if natural resources remain constant, and finite resources will eventually run out.
1968	Paul R. Ehrlich-The population Bomb	In 'the population bomb,' Ehrlich prophesied calamity for mankind as a result of overpopulation and population expansion.
1971	Polluter pays the principle	In order to bring the environment and the economy together, the OECD advises that those who pollute pay the consequences.

2.2. From the United Nations Conference on the Human Environment to WCED

Stockholm Conference on the Human Environment, which was the first major conference at which international environmental issues and the development of environmental politics were specified, is widely regarded as the starting point for the concept of sustainable development.

Rising populations and limiting resources became more of a challenge in the 1970s. As early as 1972, a book called *The Limits to Growth* demonstrated that the world has been heading the wrong way at an accelerating pace. Growing populations, limited resources, and increasing pollution were among the topics addressed in this book.

Sustainability was proposed as a solution during the 1976 United Nations Habitat Gathering on Human Settlements, known as Habitat I at the time and the biggest conference on human concerns. This was the first time that the global community had the opportunity to debate urban issues such as clean water, sanitation, and poverty and homelessness at the summit. The political relevance of the environment decreased from the 1970s to the 1980s. Several factors are to blame, according to Munds (1992), such as



the economic slump of the mid-1970s and the absence of complete integration of environmental consciousness into the economic planning system.

In 1980, the International Union for Conservation of Nature (IUCN) issued the World Conservation Strategy, a landmark document in the history of sustainable development. As part of this approach, environmental and development goals are integrated. For the first time, the term “sustainable development” has been used.

Table 2: Sustainability Initiatives

Date	Event	Description
1972	United Nations Conference on the Human Environment	Conference held in Stockholm in 1972. The conference theme was “Only one Earth”.
1972	Limits to growth paper	Emphasizing that the state of global equilibrium could be designed so that the basic material needs of each person on earth are satisfied and each person has an equal opportunity to realize his individual human potential.
1973	OPEC oil crisis	This fuels the limits to growth debate.
1974	CFC crisis	Rowland and Molina publish in the journal Nature that continued use of CFC gases at an unaltered rate would critically deplete the ozone layer
1976	HABITAT	First global meeting to link the environment and human settlement
1980	World Conservation strategy	The phrase ‘Sustainable development was first used Or rather ‘development that is sustainable’
1984	International Conference on Environment and Economics (OECD) in London	This conference concluded that environment and economics should be mutually reinforcing. This conference led to the Brundtland report

2.3. Progress Following the World Commission on Environment and Development

In 1987, the World Commission on Environment and Development issued Our Common Future, which introduced the phrase "sustainable development." The Brundtland report's principles were then included in the Common Inheritance: Britain's Environmental Strategy, a key document in British policymaking. Proposals were made for the convergence of economic development with environmental improvement.

After then, the inaugural UN Conference on Environment and Development (UNCED), often known as "the Earth Summit," was convened in Rio de Janeiro in June 1992. The conference is a major step forward in the fight for environmental sustainability. In this approach, human, natural, and social, and environmental pillars were woven together. A major shift was made during Habitat II in Istanbul in 1996 when the United Nations conducted its second conference on human settlements. An urbanization guide is needed to ensure that the world's cities, towns, and villages can grow sustainably in the 21st century, according to the report.

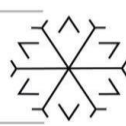
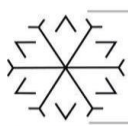
For urban areas, sustainable development policies started to gain relevance in the early 1990s, which necessitated an urban transformation. In the mid-1990s, the phrase "sustainable urban development" first appeared. Hong Kong's Declaration on Sustainable Development was a significant milestone for the city and regional planning in 2004.

In 2009, the United Nations hosted a series of climate change summits. One of today's biggest concerns, according to the conference participants, is climate change and the need to develop measures for lowering carbon emissions and employing sustainable energy. Then, The G20 Summit was held in Toronto, Canada, on June 26-27, 2010. The summit provided a foundation for robust, long-term, and balanced economic development (G-20 Toronto Summit, 2010). Rio+20 Corporate Sustainability Forum: Innovation and Collaboration for the Future We Want was the most recent effort. Rio de Janeiro hosted the forum in June of 2012. It intended to scale up and improve the quality of business sustainability practices in order to achieve holistic, harmonic, and long-term development.

In 2019, The IPCC Special Report on the Ocean and Cryosphere in a Changing Climate, adopted by the 195 IPCC member nations, presents additional evidence supporting the advantages of keeping global warming to the lowest feasible level- the target established by governments in the 2015 Paris Agreement.

Table 3: Sustainability Initiatives

Date	Event	Description
1987	Our Common Future/Brundtland Report World Commission on Environment and Development (WCED)	Brundtland Commission published a seminal report, Our Common Future, which coined and defined the term "sustainable development," fusing environmental and economic sensibilities.



1987	Montreal Protocol	International agreement to adopt measures for tackling a global environment problem
1988	Intergovernmental Panel on Climate Change (IPCC)	It was set up to assess the technical issues that were being raised. Its first report stated that global warming should be taken seriously
1989	Lynam and Herdt definition of sustainability	The capacity of the system to maintain output at a level approximately equal to or greater than its historical average, with the approximation determined by the historical level of variability
1990	This common inheritance: Britain's Environmental Strategy	The ideas from the Bruntland report 'Our Common Future' were taken up in the UK's first comprehensive strategy, the White Paper on the Environment This Common Inheritance.
1990	Definition of sustainability	Pearce and Turner (1990) ... maximizing the net benefits of economic development, subject to maintaining the services and quality of natural resources over time.
1991	Definition of sustainable development	ICUN (1991) Development that improves the quality of human life while living within the carrying capacity of supporting ecosystems.
1992	Rio Earth Summit	Between 1990 and 1992 Agenda 21 was developed to stand as a blueprint for sustainable development in the world
1992/ 1993	United National framework on Climate change (UNFCCC)	Introduced to fight global warning at Rio in which it was adopted.
1992	European Communities Green paper	Green Paper on the Impact of Transport on the Environment - A Community Strategy for "Sustainable Mobility". COM (92) 46, 20 February 1992
1993	Hardins 3 laws of human ecology	1 - 'we can never do merely one thing' (interconnectedness of society). 2 - 'there's no way to throw to' (an affluent society) 3 - The impact of any group or nation on the environment is represented qualitatively by the relation: $I = P A T$ (I = Impact, P = size of the population, A is the per capita affluence (measured by per capita consumption) and T is the measure of the damage done by the technologies that are supplying the consumption.
1994	Aalborg Charter	Charter of European Cities & Towns Towards Sustainability
1995	Creation of the World business council for sustainable development (WBCSD)	It was formed in 1995 from the world international conference on environmental management (WICEM) and the Business Council on sustainable development (BCSD)
1995	World summit for social development	This summit expressed a commitment to eradicate poverty
1995	The first conference of the parties (cop 1) to the FCCC (UNFCCC)	The first conference for all the countries who ratified the convention from the Rio Summit
1997	Kyoto Climate change Protocol	At Kyoto, a new set of targets for the reduction of greenhouse gases was agreed upon.
1998	The EU White paper Developing the citizens' network	Communication of 10 July 1998 from the Commission to the Council, the European Parliament, the Economic and Social Committee and the Committee of the Regions: "Developing the citizens' network - Why local and regional passenger transport is important and how the European Commission is helping to bring it about".
2001	Mobility 2001 World mobility at the end of the twentieth century and its sustainability	World Business Council for Sustainable development publication. This report considered current mobility patterns in the world at the start of the 21st century and then identified those factors that were threatening future sustainable mobility
2002	Johannesburg World Summit on Sustainable Development	
2003	Sustainable Communities: building for the future ODPM (2003)	Emphasizing that a wider vision of strong and sustainable communities is needed to underpin this plan, flowing from the Government's strong commitment to sustainable development.
2004	Mobility 2030 meeting the challenges to Sustainability	It produced 12 indicators for sustainable development. This report used the 3 pillars of sustainability as a guide for producing its indicators
2009	United Nations Environment Programme Report of the Governing Council Twenty-fifth session	Discussing issues about Globalization and the environment in the Forum.
2010	The G-20 Toronto Summit Declaration	The summit aims to create strong, sustainable, and balanced global growth
2010	United Nations Economic and Social Commission for Asia and the Pacific (UNESCAP)	Committee discussed social issues; environment and sustainable development; information, communication, and space technology; poverty reduction and development; statistics; trade and investment; and transport and tourism.
2011	United Nations Economic Commission for Europe	The committee promotes economic cooperation among its member states. it provides collective policy direction in the area of environment and sustainable development
2012	United Nations conference on climate change	The conferences stated that climate change is one of the greatest challenges of today's world and countries must provide plans for reducing carbon emission and using clean energy.



2012	Rio+20 Corporate Sustainability Forum	The forum aimed to bring greater scale and quality to corporate sustainability practices and achieve comprehensive, harmonious, and sustainable development.
2015	Paris Agreement	Its objective is to keep global warming considerably below 2 degrees Celsius, ideally 1.5 degrees Celsius, relative to pre-industrial levels.
2019	The IPCC Special Report on the Ocean and Cryosphere in a Changing Climate	supporting the advantages of keeping global warming to the lowest feasible level - the target established by governments in the 2015 Paris Agreement.
2021	AR6 Climate Change 2021	The IPCC creates comprehensive Assessment Reports on climate change knowledge, causes, probable consequences, and response choices.

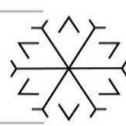
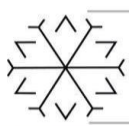
3. Future Context

The sustainability concept has been influenced by a variety of issues, including population growth, climate change, and resource consumption patterns. These considerations all play a role in setting current R&D objectives and strategies. As the world's population grows, so does the need for food, water, energy, and land. Many environmental issues stem from it. The world population is expected to grow by more than 20 percent even under the United Nations' low-fertility scenario (UN, 2021). In addition to that, global surface temperature will rise throughout the next century, according to the Fifth Assessment Report of the Intergovernmental Panel on Climate Change, regardless of whether or not anthropogenic greenhouse gas emissions are totally eliminated. In the future, it is expected that heat waves would get longer and more powerful, that cold winter extreme will become more frequent and severe, and that precipitation in dry areas will decrease (IPCC, 2014). Furthermore, energy consumption and economic development are inextricably intertwined (Bercu, Paraschiv, and Lupu, 2019). Since the Industrial Revolution, the cities' energy consumption has risen (OECD, 2020). As a result, the ecosystem was severely harmed. Eco-crisis is a phrase that some experts use to characterize the newly created economic-ecological link (Kay and Skolnikoff, 1972). It seems that the issues that humankind will encounter in the future will be similar to those that humanity has been already experiencing. Therefore, these issues will inexorably have an impact on how we define sustainability.

4. How to Define Sustainability

Sustainability has been defined in a variety of ways in the past, and it is clear that a definition has been formed based on the situation at hand. The present situation is still the same. Each problem has produced its definition of sustainability. For example, for the design of chemical products and processes, according to Boriani et al (2013), sustainability is the reduction or elimination of the usage of harmful chemicals, such as carbon dioxide emissions. Çalışkan et al (2013) discuss the utilization of renewable energy sources that do not emit greenhouse gas emissions in order to define sustainability in the production of energy. Pergola et al (2013) define sustainability as having the least amount of negative environmental effect while also being economically viable and generating social benefits for the agricultural production. As described by Perez (2013), sustainability is defined as making the best possible use of natural resources while also respecting cultural authenticity and ensuring economic viability for tourism. Similarly, future generations will confront many of the same challenges that we face now, therefore it's not hard to predict that sustainability will be characterized by factors like climate change, energy consumption, and rising population. However, the problem with the definition of the sustainability concept is that the definition of sustainability is to be limited to the problem for which a solution is sought.

The uncertainty of WCED's definition of sustainability, which was put forward in 1987, has led to the formation of various definitions over time. As can be seen from historical analysis, much of the effort to interpret the concept has been heavily influenced by the particular problems encountered. This resulted in an overarching, narrow interpretation framework that did not capture the whole picture. However, sustainability should be defined with a holistic perspective that considers the historical roots, current perspectives and future expectations, not only by responding to the problem encountered, but by overcoming the effects of these problems, strengthening the logical consistency within the concept, and improving the understanding of the concept.



5. Conclusion

There is a contemporary difficulty in sustainability research that stems from a lack of clarity regarding the notion of sustainability, which is due to the fact that there are many, different, and confusing definitions and interpretations for it. It is possible that this misconception is caused by the fact that the idea of sustainability has traditionally been researched in the context of a problem that has been encountered. Sustainability, on the other hand, should be defined from a holistic perspective that takes into account the historical roots as well as current perspectives and future expectations. This means that sustainability should be defined not only in terms of responding to problems, but also in terms of mitigating their consequences, strengthening the logical consistency of the concept, and improving the understanding of it. Aside from that, definitions are not always the best approach to convey a meaning of the idea rather, the meanings, the context in which they are utilized by society, make the concept more understandable.

References

- Balaceanu, C. and Apostol, D. (2014) 'The Perspective of Concept Sustainability', *Procedia - Social and Behavioral Sciences*, 116, pp. 2257–2261. doi:10.1016/j.sbspro.2014.01.555.
- Bercu, A.-M., Paraschiv, G. and Lupu, D. (2019) 'Investigating the Energy–Economic Growth–Governance Nexus: Evidence from Central and Eastern European Countries', *Sustainability*, 11(12). doi:10.3390/su11123355.
- Boriani, E. et al. (2013) 'Application of ERICA index to the evaluation of soil ecosystem health according to sustainability threshold for chemical impact', *Science of The Total Environment*, 443, pp. 134–142. doi:10.1016/j.scitotenv.2012.10.025.
- Caliskan, H., Dincer, I. and Hepbasli, A. (2013) 'Energy, exergy, and sustainability analyses of hybrid renewable energy-based hydrogen and electricity production and storage systems: Modeling and case study', *Applied Thermal Engineering*, 61, pp. 784–798.
- Ciegis, R., Ramanauskiene, J. and Martinkus, B. (2009) 'The Concept of Sustainable Development and its Use for Sustainability Scenarios', *Engineering Economics*, 2.
- Ehrlich, P.R. (1968) *The Population Bomb*. Newyork: Buccaneer Books Inc.
- Hardin, G. (1968) 'The Tragedy of the Commons', *Nature*, 162, pp. 1243–1248.
- Heinen, J.T. (1994) 'Emerging, diverging and converging paradigms on sustainable development', *International Journal of Sustainable Development & World Ecology*, 1(1), pp. 22–33. doi:10.1080/13504509409469857.
- IPCC (2014) *Climate Change 2014: Synthesis Report. Contribution of Working Groups I, II, and III to the Fifth Assessment Report of the Intergovernmental Panel on Climate Change*. Geneva, Switzerland: IPCC, p. 169.
- Jacobs, M. (1994) 'Sustainable Development – From Broad Rhetoric to local Reality', in *Conference Proceedings from Agenda 21 in Cheshire*. Chesire County Council (19).
- Kay, D.A. and Skolnikoff, E.B. (1972) *World Eco-Crisis*. Madison, WI, USA: University of Wisconsin Press.
- Mebratu, D. (1998) 'Sustainability and Sustainable Development: Historical and Conceptual Review', *Environmental Impact Assessment Review*, (18), pp. 493–520.
- OECD (2020) *Building energy efficiency in cities and regions - OECD*. Available at: <http://www.oecd.org/cfe/cities/energy-efficiency-cities.htm> (Accessed: 23 March 2021).
- Pérez, V.L. et al. (2013) 'Composite indicator for the assessment of sustainability: The case of Cuban nature-based tourism destinations', *Ecological Indicators*, 29, pp. 316–324. doi:10.1016/j.ecolind.2012.12.027.
- Pergola, M. et al. (2013) 'Sustainability evaluation of Sicily's lemon and orange production: An energy, economic and environmental analysis', *Journal of Environmental Management*, 128, pp. 674–682. doi:10.1016/j.jenvman.2013.06.007.
- Pierantoni, I. (2004) *A Few Remarks on Methodological Aspects Related to Sustainable Development*. doi:<https://doi.org/https://doi.org/10.1787/9789264020139-8-en>.



Spedding, C.R.W. (1996) *Agriculture and the Citizen*. Chapman & Hall.

UN (2021) *World Urbanization Prospects - Population Division - United Nations*. Available at: <https://population.un.org/wup/> (Accessed: 25 November 2021).

Vehkamäki, S. (2005) '2.2. The concept of sustainability in modern times, in Jalkanen, A., and Nygren, P., *Sustainable use of renewable natural resources — from principles to practices*, pp. 1–13.

WCED (1987) *Report of the World Commission on Environment and Development: Our Common Future*. Available at: <http://www.un-documents.net/A372BC4E-993E-4C10-B368-9E75816E59DB/FinalDownload/DownloadId-1990161B7AFC5CB358F7280210D7A48F/A372BC4E-993E-4C10-B368-9E75816E59DB/our-common-future.pdf> (Accessed: 28 July 2016).

Rural Studies in a Disaster Region – Obruk Plateau

Aziz Cumhur Kocalar ^{1*}{0000-0003-0580-9530}

¹ azizcumhurkocalar@gmail.com, Asst. Prof.Dr.

Abstract

The sinkholes (potholes, dolines) formed in the Central Anatolia Region in recent years have been increasing. In this sense, Konya Closed Basin constitutes an interdisciplinary problem area in terms of sinkholes whose numbers are increasing rapidly. The name of the place studied in this multi-layered complex region is “Konya Obruk Plateau”. No serious measures have yet been taken to prevent disaster risks in the region. Although the geological character of the region is known from previous studies, the precautions to be taken are still delayed.

Comprehensive alternative planning is needed, especially for villages in such risky areas with complex geological problems. However, up-to-date field data should also be provided prior to planning. In order to provide reliable data, it is expected that the determinations in the field will be carried out in coordination with different interdisciplinary working groups. There may be villages that need to be moved urgently, as there have been increasing risks of collapse and collapse type disasters in the region for a long time.

The subject has been examined with some photographs and maps from the relevant literature in different disciplines such as geology and remote sensing. In the last 3 years, some excursions have been made in the field, and the people of the settlement have been interviewed.

On the other hand, villages with settled population continue to live. The study proposes sustainable solutions using data on the area that needs urgent rural settlement solutions. Findings were gathered under six sub-headings, their details are included in the main text. A model was proposed for further studies; the model short name is CIDHRM with the 6 different steps. The proposed advanced study model has different professional components and topics.

Keywords. Disaster risky rural areas, Sustainability, Rural settlements, Regional planning.

1. Introduction

The sinkholes (potholes, dolines) formed in the Central Anatolia Region in recent years have been increasing. In this sense, Konya Closed Basin constitutes an interdisciplinary problem area in terms of sinkholes whose numbers are increasing rapidly. The name of the place studied in this multi-layered complex region is “Konya Obruk Plateau”.

No serious measures have yet been taken to prevent disaster risks in the region. Although the geological character of the region is known from previous studies, the precautions to be taken are still delayed.

Comprehensive alternative planning is needed, especially for villages in such risky areas with complex geological problems. However, up-to-date field data should also be provided prior to planning.

In order to provide reliable data, it is expected that the determinations in the field will be carried out in coordination with different interdisciplinary working groups. There may be villages that need to be moved urgently, as there have been increasing risks of collapse and collapse type disasters in the region for a long time.

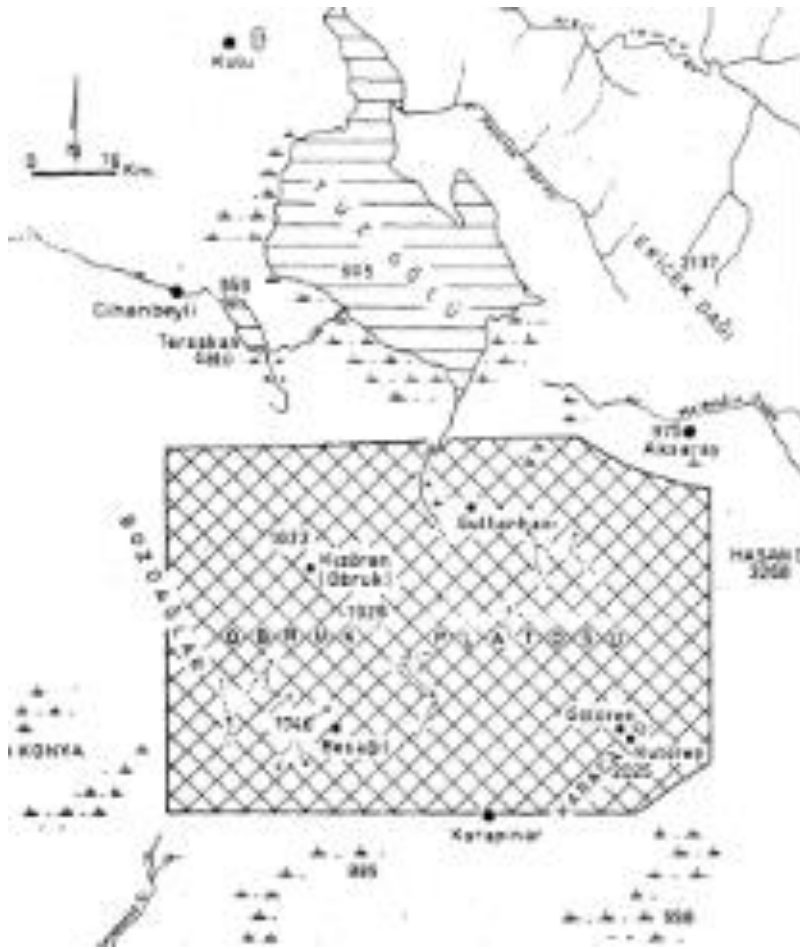


Figure 1: Obruk Plateau, Karapınar, Konya, Turkey (Biricik, A.S. 1992).

2. Material ve Method

The works to be done in the findings section are given in order and under sub-headings. Some definitions of some important concepts are also provided with details. Therefore, there are frequent references to studies in the sources of different disciplines.

There are also some photos and maps in the related-literature in the different disciplines, such as geology, remote sensing. The developing conditions of the sinkholes in the selected-region has been used by the remote sensing methods.

Risk assessment has to be carried out continuously under the conditions that can be called instantaneous, especially in the region.

In the last 3 years, some trips were made along the highway from time to time in the field.

3. Findings

In the Konya Closed Basin, the karstic formations, which have been rapidly increasing after 2000, occur due to geological, climatic and anthropogenic effects. Kızılören and Çıralı Obruk photos (closed-up) are also given by same authors in their paper. There appears to be a small amount of water in them. However, due to the drought in the region in recent years, many sinkholes are without water.

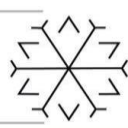
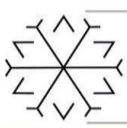


Figure 2: Dolines, Karapınar, Konya, Turkey (Günay, G., Çörekçioğlu, İ., Övül, G. (2011).

The works to be done below are given in order and under sub-headings with the definitions of some important concepts.

3.1. Interdisciplinary Coordinated Studies

In order to provide reliable data, it is expected that the determinations in the field will be carried out in coordination with different interdisciplinary working groups. There may be villages that need to be moved urgently, as there have been increasing risks of collapse and collapse type disasters in the region for a long time.

3.2. Pothole inventory information system

The developing conditions of the sinkholes in the selected-region, which names “Obruk Plateau”, should be monitored remotely by the remote sensing methods.

In a study on the establishment of the Konya closed basin pothole inventory information system is carried out to reduce the material / spiritual losses caused by sinkhole formation and to better understand the environmental factors controlling the spatial distribution of sinkhole (Orhan, Kırtıloğlu, Yakar, 2020).

3.3. Disaster Early Warning System

The alignment of the sinkholes can create a risk chain. Therefore, sinkhole alignment lines should be precisely determined and the related-settlements should be evacuated (Figure 2).

A region-specific Disaster Early Warning System (DEWS) is important and can be designed. Hazard mapping will also provide the basic data to this system. The disaster must be brought under control.

3.4. Hazard Mapping

A hazard mapping can be prepared with updated data. Because there are many sinkholes in the region. The data on this map cover is many important information about sinkholes. The sinkholes are generally arranged in the northwest-northeast direction. In general, the arrangement of the sinkholes on the plateau corresponds to the flow direction of the groundwater (Ersoy, 2015). The sinkholes can be grouped according to the direction of their arrangement (Table 1).

**Table 1.** Sinkholes (names) grouped according to the alignment direction.

Sink series #	The sinkholes in the northwest-southeast direction (1,2,3. series) The sinkholes in the southwest-northeast direction (4. series) Sinkholes that are not in a certain direction (5. series)					
1.series:	Kuru	Meyil	Ak			
2.series:	Karain	Hamam	Kızıl	Yeni Opan	Yarım	Çıralı
	Derin	Fincan	Potur	Kangallı	Zincancı	
3.series:	Kuru	Kayalı				
4.series:	Çifteler 1	Çifteler 2	Cehennem deresi	Dikmen		
5.series:	Kızılören	Karkın	Güvercinli			

Authors are also given many regional geological details by a geological map for Konya Closed Basin in their paper (Günay, G., Çörekçioğlu, İ., Övül, G. (2011). This map cover also risks areas in the regional planning. The alignment of the sinkholes creates a distinct risk chain. Therefore, sinkhole alignment lines should be precisely determined and the related-settlements should be evacuated. The risk interactions can occur.

3.5. Risk Analysis and Management

Risk analysis is an activity that covers risk identification, determination of danger locations and probabilities, identification of vulnerabilities, and measurement of loss probabilities. Technically, risk management is the process of determining the priorities of risks and risk reduction methods after the risk identification and assessment stages (Balamir, 2018).

The alignment of the sinkholes may have occurred in parallel with the settlement in order to find water in their villages, which may create a distinct risk chain. There may also be a possibility of such an increase in disaster risks in the region.

On the other hand, risks have to be constantly evaluated under conditions that can be called instantaneous developments specific to the region. Rought and natural resource shortages cause regression risks in economic development. The different risk interactions must be reviewed, because they are also can be triggered in some conditions.

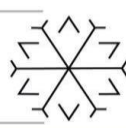
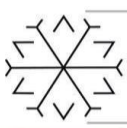
Therefore, it is essential to provide reliable data, it is clear that the determinations in the field require different interdisciplinary studies. In addition, these groups are expected to work in coordination.

3.6. Mitigation planning and sustainability with new rural architectural solutions

Comprehensive alternative planning is also needed, especially for villages in such risky areas with the complex geological problems. Mitigation planning for villages should be resolved urgently. Sustainable development opportunities can thus be re-established by taking measures for the future.

On the other hand, rural architecture should be re-evaluated according to current conditions. Perhaps different and more flexible solutions can be developed for those who have to stay or be temporarily in existing settlements, much more suitable for ground conditions. For settled living areas that need to be moved, places with reliable floors should be preferred.

4. Field Studies



Some field trips and rural studies were made along the highway from time to time in the region in the last 3 years. Some photos were taken during these trips, although it was not possible to go near the sinkholes, it was understood that the water holding conditions changed over time.

The social problems observed in the region require other field studies to be carried out without delay within the scope of regional sociology and rural sociology study subjects. Studies in the field and publications on this subject are still in progress.

5. Conclusion and Recommendations

Villages with settled population continue to live in the region. The mitigation planning is urgently needed for these villages. Sustainable development opportunities can thus be re-established by taking measures for the future. Therefore, solutions have been tried to be handled with a holistic approach through approaches belonging to different disciplines, such as geology, remote sensing, rural studies, etc.

Findings were gathered under 6 headings; their details are included in the main text. A model was proposed for further studies; the model short name is CİDHRM with the 6 different steps. The model proposed below has different professional components and topics below (Figure 3):

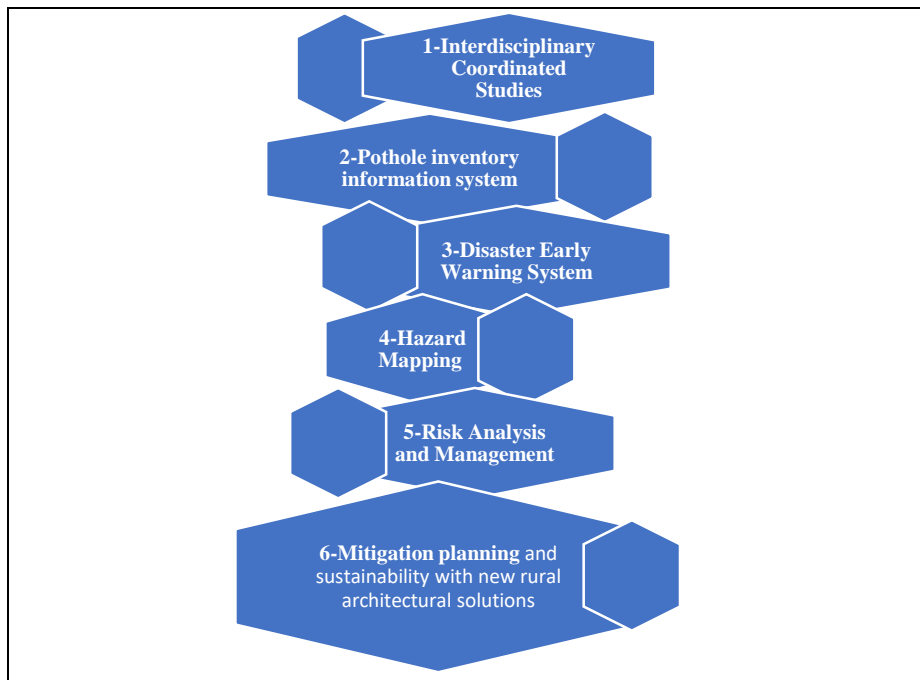


Figure 3. The different professional components and topics for the related-disciplines in the 6 steps a model (CİDHRM).

Future recommendations are concretely summarized below:

1. The developing conditions of the sinkholes should be monitored remotely by the remote sensing methods.
2. Rural architecture can be re-evaluated with relocation.
3. The study proposes also sustainability using data on the area that needs urgent rural settlement solutions.
4. The drought and desertification action plan specific to Konya and Karaman should be implemented effectively.
5. Risk assessment has to be carried out continuously under the conditions that can be called instantaneous, especially in the region.



Studies in the field are still continuing with the unique approaches of different projects and new publication studies on this subject.

Acknowledgements

Thank you to ICA_EAST 2021 organization and also the different engineering departments. The study is an output produced specifically for the scope of three different projects and new publications is coming:

- Urban Design-Planning-Conservation in Forestry-Wetland-Natural-Agricultural with Recreation/Recreative-Games and Sports Areas (RGSA), (01.01.2009-).
- Archaeological-Natural-Geological-Historical-Cultural Environment (Rivers-Basins-Lakes) Conservation Issues and Solution Proposals: "Bafa Lake Natural Park", (01.01.2010-01.12.2018).
- Urban Studies with Spatially Oriented Studies, (01.09.2019-).

References

Balamir, M. (2018). Disasters, Risk Management and Mitigation Planning - Explained Concepts and Terms, TMMOB Urban Planner Chamber, Ankara.

Biricik, A.S. (1992). Obruk Platosu ve Çevresinin Jeomorfolojisi. Marmara Üniversitesi Yayınları, İstanbul (1992).

Ersoy, B. (2015). Obruk Platosu örneğinde karstik yapıların morfometrik incelenmesi. Tübitak Çalışması.

Günay, G., Çörekçioğlu, İ., Övül, G. (2011). Geologic and hydrogeologic factors affecting sinkhole (obruk) development in Central Turkey. Carbonates Evaporites (2011) 26:3–9.

Orhan, O., Kırtıoğlu, O.S., Yakar, M. (2020). 'Konya Kapalı Havzası Obruk Envanter Bilgi Sisteminin Oluşturulması', Geomatik Dergisi Journal of Geomatics, 2020; 5(1); pp. 92-104. DOI: 10.29128/geomatik.577167

Urban Regeneration: Construction Of Factor Model

Sumana Jayaprakash,¹ and Dr. Vimala Swamy,²

Email: sj@mcehassan.ac.in , Asst Professor, Malnad College of Engineering, Hassan

Email: vimalaswamy@reva.edu.in, Professor, School of Architecture, REVA University, Bengaluru

Abstract:

Urban regeneration decision-making is a complex process, as it involves a wide range of decision-makers, public-private partnerships in finance and implementation, including the inevitable considerable amount of risk on a long-term basis. There are a multitude of stakeholders, the citizens being the key stakeholders. It is necessary to involve the citizens in the planning process. Such involvement allows the communities to express their needs and aspirations, which is useful in the policymaking, delivery of planning programs, and in the monitoring process. In such a context, Factor analysis was the statistical technique used (1) Carry out factor analysis based on the principal component analysis method using the software XLSTAT 2021.4.1.1205 - (2) Construct a factor model of Urban Regeneration. (3) Interpret and label the factor dimensions. The results of the analysis indicated that the first two principal components accounted for 60.04% of the total variance of the original dataset. All variables seemed to be, positively correlated to each other and contributed similarly to principal components PC1 & PC2. The observations were well clustered; except for very few outliers. The limitation of the work was that the perceptions of the citizens were limited to the variables derived by the researcher.

Keywords: citizens' perception, dimensionality reduction, factor model, variables, urban regeneration, variables.

1. Introduction:

Urban Regeneration is defined as the “comprehensive and integrated vision and action which leads to the resolution of urban problems and which seeks to bring about a lasting improvement in the economic, physical, social and environmental condition of an area that has been subject to change.” (Roberts, 2000) Urban regeneration rather than a discipline-based on a solid body of theory; is an empirical field of policy and practices. It operates in a complex environment with multiple actors and inherent conflicting issues. The urban problems and opportunities from historical phases of urban development portray the relationship between physical conditions and social, economic, and environmental response and the need for restructuring of the cities as the basis of Urban Regeneration. (Regenerating Urban Land, n.d.). Current regeneration practice goes beyond physical redevelopment, to stimulation of economic growth, together with the increase in community cohesion. Environmental sustainability and climate change issues have considerable prominence as objectives of regeneration policy. Urban Regeneration Intervention is based on a detailed analysis of the physical, social, economic, and environmental conditions of the area. (Blake, 1997) (Childers et al., 2014) The integrated strategy of planning and implementation is developed by making the best use of the existing features on-site and clear quantifiable objectives. The components of the physical factor include buildings, land and sites, urban spaces, open spaces and water, utilities and services, communications, infrastructure, and transport. Economic regeneration aims to attract and stimulate investment, create employment opportunities, and improve the environment of cities to make the best possible use of urban land and to avoid unnecessary sprawl. (Garau & Pavan, 2018) The use of Public-private partnerships in urban regeneration is associated with diverse contractual models, which require a wide range of institutions to support them. (De Magalhaes, 2015) (Shenvi & Slangen, 2018) It involves partnerships created from national and local government, the private and voluntary sectors, and members



of local communities. The policy framework, the institutional structure, the financial and regulatory mechanisms, and the political forces shape the context of Intervention. These are powerful tools for advancing an Urban Regeneration Intervention. Community participation in the planning of development projects is fundamental for project success and sustainability. It allows the communities to express their needs and aspirations and is useful in the policymaking, delivery, and monitoring process. (Ruá et al., 2019) (Martí et al., 2019) The preference of the citizens needs to be represented by the limited number of characteristics or a reduced number of variables if they have to be efficiently integrated into the planning process. (Dr. Vimala Swamy, 2020)

2. Methodology:

Large datasets are increasingly widespread in a comprehensive questionnaire survey in attempting to understand citizens' point of view in urban matters. To interpret such large datasets, methods are required to drastically reduce their dimensionality in an interpretable way, such that most of the information in the data is preserved. Many techniques have been developed for this purpose, but principal component analysis (PCA) is one of the oldest and most widely used. (Jorge, 2016). In the present work, a total of 45 variables were derived from nine Urban regenerations parameters, namely image and identity, Land use, open spaces and building form, transportation and movement network, activity support, environment, social, economic factors, financial and regulatory mechanisms. These parameters were based on a literature review. To organize this large database and construct a factor model, the principal component analysis was applied to each level to reduce the dimensions of the sample and derive the results of the analysis. The steps included: 1. Derivation of variables from the Urban Regeneration parameters. 2. Citizen questionnaire survey. 3. Dimensionality reduction by application of the principal component method. 4. Derivation of the factor dimensions. 5. Construction of the five-factor model of Urban Regeneration.

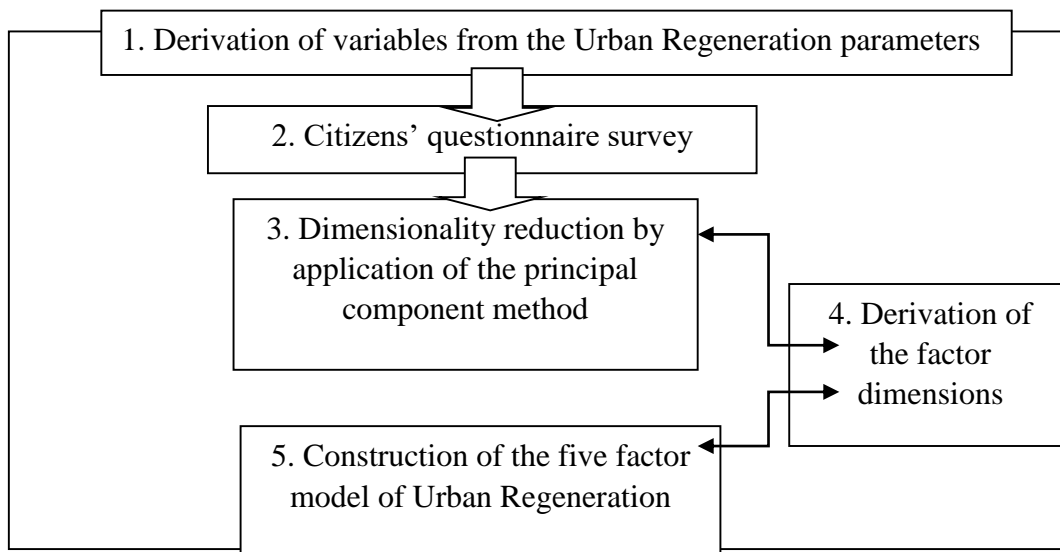
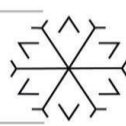
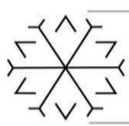


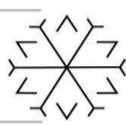
Fig 1: Flow chart of the methodology

2.1: Derivation of 45 variables from Urban Regeneration Parameters:

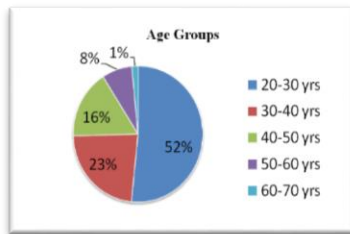
**Table 1:** List of Urban Regeneration Parameters and Variables

Parameters	Variables	
1. Identity and Image	1. City Image / visual appeal.	
	2. Historical monuments and buildings are important.	
	3. Old Temples are important.	
	4. Historical Tourist places of attraction	
	5. Preservation of old valuable buildings and areas	
	2. Land-use	6. Houses close to workplaces.
		7. Parks near residences.
		8. Industries located away from the city
		9. Markets and shopping centers close to homes.
		10. Preservation of water bodies etc.
3. Open Spaces and Building Form		11. Landmarks like the clock tower, fountains, etc
	12. Wide walking footpath spaces along the roads.	
	13. Character of the area like temple zone etc.	
	14. Availability of shopping, recreation and food courts	
	15. Uniform building fronts	
4. Transport & Movement Network	16. No wastage of urban land area	
	17. Less travel time to office	
	18. Well connected local buses within the city.	
	19. Private car /scooter services for travel in the city.	
	20. Vacant land use for parking etc.	
5. Activity Support	21. Street vendors appropriately accommodated	
	22. Walk able pedestrian zones within the city	
	23. Efficient waste management and garbage disposal	
	24. Efficient use of Renewable energy sources (solar)	
	25. Private owned publicly used spaces.	
6. Environmental Factors	26. Good quality of air and water	
	27. Open spaces and gardens	
	28. Eco-friendly buildings	
	29. Walking and cycling paths within the city	
	30. Pollution free environment within the city	
7. Social Factors	31. Citizen participation in planning	
	32. Places for people of all age groups	
	33. Gender equality	
	34. Appropriate /accessible social infrastructure like schools & hospitals.	
	35. People friendly places within the city	
8. Economic Factors	36. Financial investment for city development	
	37. Economic viability Profitability	
	38. Varied Sources of funding	
	39. Citizen's investment in city development and regeneration	
9. Financial &Regulatory Mechanism	40. Financial sustainability	
	41. Government role	
	42. Importance of Building Byelaws	
	43. Public Private partnerships	
	44. Political leadership	
	45. Planning and Implementation	

2.2. Citizens' Questionnaire survey:



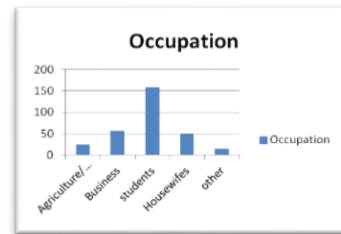
The Citizens' questionnaire survey was carried out on 430 citizens of Hassan. A total of 30 responses were discarded as the persons who responded were not from Hassan district. Hence a total of 400 respondents were considered for the research project. The respondents were to score the variables given in the form of a question, on a scale ranging from 1-10. A score of 10 meant a very important or preferred variable. The lowest score of 1 meant the least important variable. Google forms were used for this purpose. Following was the composition of the respondents in terms of age, occupation, and educational qualification.



Graph 1: Age groups (Source: Primary data)



Graph 2: Educational Qualification (Source: Primary data)



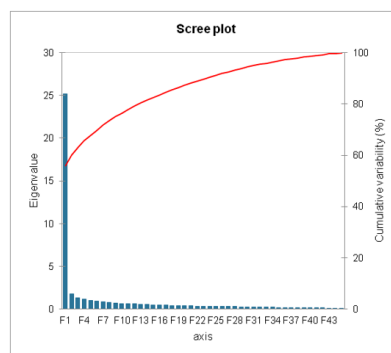
Graph 3: Occupation (Source: Primary data)

2.3: Dimensionality reduction by application of the principal component Analysis

Table 2: Total Variance explained by the 5-factor Matrix

	Initial Eigen values	The extracted sum of squared loadings			The rotated sum of squared loadings				
		Total	variability%	Cumulative %	Total	variability%	Cumulative %	Total	variability%
F1	25.209	56.019	56.019	25.209	56.019	56.019	15.543	14.511	14.511
F2	1.808	4.019	60.038	1.808	4.019	60.038	15.634	14.246	28.756
F3	1.327	2.949	62.987	1.327	2.949	62.987	14.468	12.707	41.464
F4	1.159	2.575	65.562	1.159	2.575	65.562	17.054	17.128	58.592
F5	0.999	2.219	67.781	0.999	2.219	67.781	11.888	9.189	67.781

XLSTAT 2021.4.1.1205 - Principal Component Analysis (PCA) - PCA type: Correlation, Filter factors Maximum number = 5, Standardisation: (n) Rotation: Varimax (Kaiser normalization) / Number of factors=5

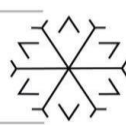
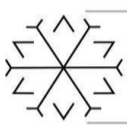


Graph 4: The Scree Plot

Table 3: Principal Component Analysis:

2.4: Principal Component Analysis:

	F1	F2	F3	F4	F5	F6	F7	F8	F9
--	----	----	----	----	----	----	----	----	----



Eigenvalue	25.209	1.808	1.327	1.159	0.999	0.913	0.866	0.773	0.693
Variability (%)	56.019	4.019	2.949	2.575	2.219	2.028	1.924	1.718	1.539
Cumulative %	56.019	60.038	62.987	65.562	67.781	69.809	71.733	73.451	74.990

Table 3: XLSTAT 2021.4.1.1205 - Principal Component Analysis (PCA) - PCA type: Correlation, Filter factors Maximum number = 5, Standardisation: (n) Rotation: Varimax (Kaiser normalization) / Number of factors = 5

2.4: Derivation of factor dimensions:

Table 4: Factor Dimension 1 Source: Research Survey Data

FACTOR D1	VARIABLES	FACTOR LOADINGS	COMMUNALITY %
	22.Walkable pedestrian zones within the city	0.682	75.9%
	23.Efficient waste management and garbage disposal	0.658	64.0%
	21.Street vendors appropriately accommodated	0.652	75.4%
	24.Efficient Renewable energy sources like solar	0.641	72.6%
	20.Vacant land use for parking etc.	0.622	74%
	26.Good quality of air and water	0.555	71.4%
	18. Well connected local buses within the city.	0.545	65.6%
	25. Private owned publicly used spaces.	0.508	62.5%
	12. Wide walking footpath spaces along the roads.	0.491	73.3%
	variability		14.511
	Cumulative %		14.511%

XLSTAT 2021.4.1.1205 - Principal Component Analysis (PCA) - PCA type: Correlation, Filter factors Maximum number = 5, Standardisation: (n) Rotation: Varimax (Kaiser normalization) / Number of factors= 5

Factor Dimension 1:

A total of 9 variables out of 45 are found loaded on the factor. Out of 67.781% of communality, this factor represents 14.511%.

Label: Qualitative public spaces. (Well managed, environmentally friendly, pedestrian zones with open spaces)

Table 5: Factor Dimension 2 Source: Research Survey Data

FACTOR D 2	VARIABLES	FACTOR LOADINGS	COMMUNALITY %
	9. Markets and shopping centres close to homes.	0.677	65.4%
	14.Availability of shopping, recreation and food courts	0.649	68.7%
	15.Uniform building fronts	0.643	64.6%
	13.Character of area like temple zone etc.	0.571	72.7%
	6. Houses close to work places.	0.552	58%
	7. Parks near to residences.	0.539	57.8%
	19.Private car /scooter services like ola for travel	0.507	54.7%
	16. No wastage of urban land area	0.503	59.9%
	17.Less travel time to office	0.466	61.7%
	8.Industries located away from city	0.439	47.6%
	variability		14.346
	Cumulative %		28.756%

XLSTAT 2021.4.1.1205 - Principal Component Analysis (PCA) - PCA type: Correlation, Filter factors Maximum number = 5, Standardisation: (n) Rotation: Varimax (Kaiser normalization) / Number of factors= 5

Factor Dimension 2:

A total of 10 variables out of 45 are found loaded on the factor. Out of 67.781% of communality, this factor represents 14.346%.



Label: Qualitative Individual spaces with the neighbourhood character (Convenient, utilitarian, recreational, ease of movement, inherent character)

Table 6: Factor Dimension 3 Source: Research Survey Data

FACTOR D3	VARIABLES	FACTOR LOADINGS	COMMUNALITY %
	34.Appropriate /accessible social infrastructure like schools and hospitals.	0.669	71.6%
	33. Gender equality	0.646	75.0%
	31. Citizen participation in planning	0.628	77.5%
	32. Places for people of all age groups	0.612	76.7%
	30. Pollution free environment within the city	0.607	72.7%
	35.People friendly places within the city	0.587	71.5%
	29. Walking and cycling paths within the city	0.466	67.8%
	28.Eco-friendly buildings	0.437	59.9%
	10. Preservation of water bodies etc.	0.427	68.0%
	variability		12.707
	Cumulative %		41.464

XLSTAT 2021.4.1.1205 - Principal Component Analysis (PCA) - PCA type: Correlation, Filter factors Maximum number = 5, Standardisation: (n) Rotation: Varimax (Kaiser normalization) / Number of factors= 5

Factor Dimension 3:

A total of 9 variables out of 45 are found loaded on the factor. Out of 67.781% of communality, this factor represents 12.707%.

Label: People-Friendly environmentally healthy places and accessible social functions (Participatory, accessible to all, pollution-free, pedestrian-friendly places and associated activities)

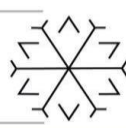
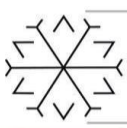
Table 7: Factor Dimension 4 Source: Research Survey Data

FACTOR D4	VARIABLES	FACTOR LOADINGS	COMMUNALITY %
	38.Varied Sources of funding	0.741	79.2%
	40. Financial sustainability	0.729	73.1%
	39. Citizen's investment in city regeneration	0.721	70.2%
	37.Economic viability Profitability	0.661	67.5%
	36. Financial investment for city development	0.640	71.9%
	44.Political leadership	0.637	62.2%
	45.Planning and Implementation	0.619	63.1%
	42.Importance of Building Byelaws	0.617	69.4%
	43.Public Private partnerships	0.603	72.1%
	41.Government role	0.596	68.5%
	variability		17.128%
	Cumulative %		58.592%

XLSTAT 2021.4.1.1205 - Principal Component Analysis (PCA) - PCA type: Correlation, Filter factors Maximum number = 5, Standardisation: (n) Rotation: Varimax (Kaiser normalization) / Number of factors =5

Factor Dimension 4:

A total of 10 variables out of 45 are found loaded on the factor. Out of 67.781% of communality, this factor represents 17.128%.



Label: Varied Sources of funding (Sustained financial management, public-private partnerships, conducive political climate, economically viable context, appropriate policies, citizen participation, planning, and implementation)

Table 8: Factor Dimension 5 Source: Research Survey Data

FACTOR D5	VARIABLES	FACTOR LOADINGS	COMMUNALITY %
	3.Old Temples are important.	0.790	45.2%
	2. Historical monuments and buildings are important.	0.692	70.4%
	4. Historical Tourist places of attraction	0.653	79.7%
	5.Preservation of old valuable buildings and areas	0.509	73.3%
	1.City Image / visual appeal.	0.437	62.2%
	variability		9.189%
	Cumulative %		67.781%

XLSTAT 2021.4.1.1205 - Principal Component Analysis (PCA) - PCA type: Correlation, Filter factors Maximum number = 5, Standardisation: (n) Rotation: Varimax (Kaiser normalization) / Number of factors= 5

Factor Dimension 5:

A total of 5 variables out of 45 are found loaded on this factor. Out of 67.781% of communality, this factor represents 17.128%.

Label: Historical conservation and tourism potential (Preservation and appropriate use, exploration of tourism potential, and city image building)

2.5. Five-factor model of Urban Regeneration.

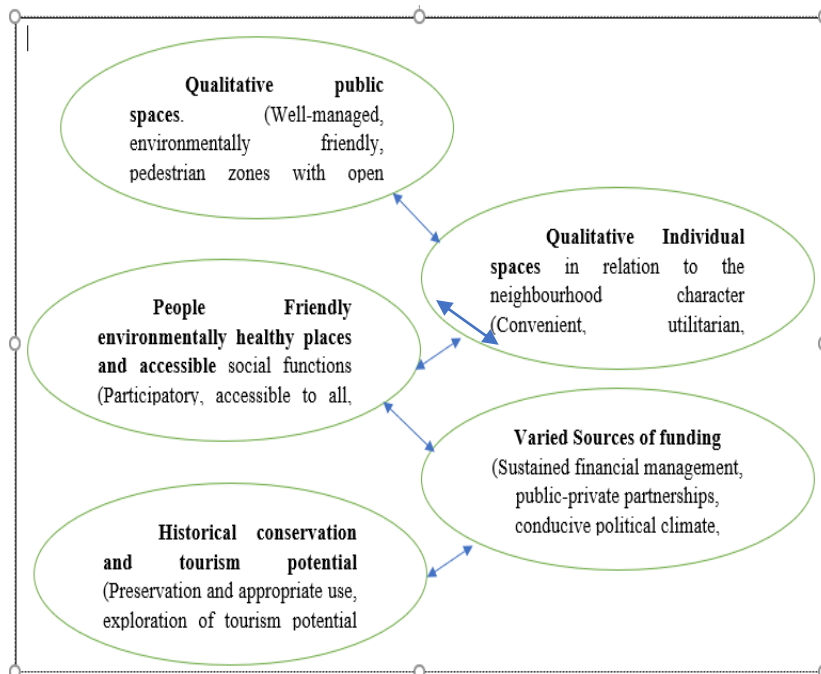


Figure 3: Five-factor model of Urban Regeneration.

3.Discussions and Conclusions:

Factor Dimension 1:



A total of 9 variables out of 45 are found loaded on the factor. Out of 67.781% of communality, this factor represents 14.511%.

Label: Qualitative public spaces. (Well managed, environmentally friendly, pedestrian zones with open spaces)

Factor Dimension 2:

A total of 10 variables out of 45 are found loaded on the factor. Out of 67.781% of communality, this factor represents 14.346%.

Label: Qualitative Individual spaces with the neighbourhood character (Convenient, utilitarian, recreational, ease of movement, inherent character)

Factor Dimension 3:

A total of 9 variables out of 45 are found loaded on the factor. Out of 67.781% of communality, this factor represents 12.707%.

Label: People-Friendly environmentally healthy places and accessible social functions (Participatory, accessible to all, pollution-free, pedestrian-friendly places and associated activities)

Factor Dimension 4:

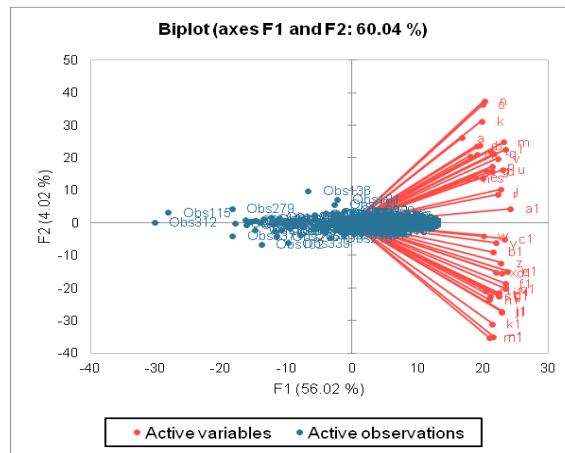
A total of 10 variables out of 45 are found loaded on the factor. Out of 67.781% of communality, this factor represents 17.128%.

Label: Varied Sources of funding (Sustained financial management, public-private partnerships, conducive political climate, economically viable context, appropriate policies, citizen participation, planning, and implementation)

Factor Dimension 5:

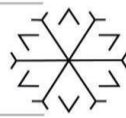
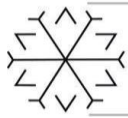
A total of 5 variables out of 45 are found loaded on this factor. Out of 67.781% of communality, this factor represents 17.128%.

Label: Historical conservation and tourism potential (Preservation and appropriate use, exploration of tourism potential, and city image building)



Graph5: The Biplot (XLSTAT 2021.4.1.1205 - Principal Component Analysis (PCA) - PCA type: Correlation, Filter factors Maximum number = 5, Standardisation: (n) Rotation: Varimax (Kaiser Normalization) / Number of factors = 5)

All variables have positive values on the PC1 axis. In the PC2 axis half, the number of variables is negative. Since all variables are positive in PC1, the ones that restrain the system in PC2 lie in the opposite quadrant. Blue dots are PC scores, orange lines correspond to eigenvectors; data were standardized; the first two PCs account for 60.04% of the total variance of the original dataset. In the PC2 axis, the two sets of variables have opposite effects on the system. All variables seem to be, positively correlated between each other and contributing similarly to PC1/PC2. The observation scores are well clustered; thus they all respond to the system quite uniformly, except some outsiders. The limitation of the work was that the perceptions of the citizens were limited to the variables derived by the researcher. Students were involved in collecting responses from the citizens. Therefore the in the age groups involved, student number seems to be in excess. Hence the responses may have been partial to that age group. Some students from places other than Hassan, presently living in Hassan have responded to the questionnaire survey. Their understanding of the city of Hassan may be partial. This factor may have affected the results obtained. Overcoming these limitations in further work can bring out more accurate results and analysis.



References:

- Blake, R. (1997). Nottingham City Challenge : Policies and Programmes, 1992-1997. In: Hommes et Terres du Nord, 1997/1. Les politiques urbaines en France et au Royaume-Uni. <https://doi.org/https://doi.org/10.3406/htn.1997.2573>
- Childers, D. L., Pickett, S. T. A., Grove, J. M., Ogden, L., & Whitmer, A. (2014). Advancing urban sustainability theory and action: Challenges and opportunities. *Landscape and Urban Planning*, 125, 320–328. <https://doi.org/10.1016/j.landurbplan.2014.01.022>
- De Magalhaes. (2015). https://www.researchgate.net/profile/Claudio_De_Magalhaes/publication/304194249_Urban_Regeneration/links/5811da0608ae205f8102540b/Urban-Regeneration
- Dr. Vimala Swamy. (2020). Smart Keys for smart eco-friendly cities. BUUKS. <https://www.amazon.in/Smart-Keys-Eco-friendly-Cities/dp/9390507642>
- Garau, C., & Pavan, V. M. (2018). Evaluating urban quality: Indicators and assessment tools for smart sustainable cities. *Sustainability (Switzerland)*, 10(3). <https://doi.org/10.3390/su10030575>
- Jorge, J. I. T. and C. (2016). No Title. *Principal Component Analysis: A Review and Recent Developments* Phil. Trans. R. Soc. A.3742015020220150202.
- Martí, P., García-Mayor, C., & Serrano-Estrada, L. (2019). Identifying opportunity places for urban regeneration through LBSNs. *Cities*, 90(February), 191–206. <https://doi.org/10.1016/j.cities.2019.02.001>
- Regenerating Urban Land. (n.d.). <https://openknowledge.worldbank.org/handle/10986/2174>
- Roberts, P. (2000). The evolution, definition and purpose of urban regeneration. *Urban Regeneration*, 9–36.
- Ruá, M. J., Huedo, P., Cordani, L., Cabeza, M., Saez, B., & Agost-Felip, R. (2019). Strategies of urban regeneration in vulnerable areas: A case study in Castellón, Spain. *WIT Transactions on Ecology and the Environment*, 238, 481–492. <https://doi.org/10.2495/SC190421>
- Shenvi, A., & Slangen, R. H. (2018). Enabling Smart Urban Redevelopment in India through Floor Area Ration Incentives. *ADB South Asia Working Paper Series*, 58(58). <http://dx.doi.org/10.22617/WPS189452-2>

Using Digital Technology in Architectural Design Education and Its Effect on Creativity

Masoumeh Khanzadeh ¹*[0000-0003-4606-0490]

¹khanzadeh@sakarya.edu.tr, Assist Prof.

Abstract

Digital technologies are one of the contemporary challenges in the application and education of in architectural design. Creative power of architecture and architect; it refers to many things that have been created as complexity, originality, rigor of execution and many things created during the design and apply process. Although the computer and its related design programs offer many design possibilities, it does not mean that manual sketches are eliminated. Understanding architectural design tools and their place in the design process requires knowing their features and components. Although design tools are mostly used to describe a specific action, they contain features closely related to architectural design. In addition, according to its functional nature, it serves the design by having certain abilities in the process in question. Digital technologies; as an auxiliary tool for human studies that used in architectural applications, preparation of basic ideas, experimental designs, two/three dimensional views and material layers, light, etc. These detailed features allow it to be created in a virtual environment according to the mentality of the architect.

In addition, the presence of researchers in the design workshops and observation, survey, document review, etc. It is field research in terms of collecting information in various ways and survey method. The research questions aim at a quasi-experimental study of the effectiveness of design tools in promoting creativity in the architectural design process in design workshops. Thus, it has been tried to offer solutions to close the gap by identifying the existing gaps in this field and creating/reinforcing the reasons that affect the success rate. The results of this research can be used in architectural design workshops, especially in architectural education.

Keywords: Architectural Design, Architectural Education, Creativity, Digital Technology.

Impact of Climate Change on Building Energy Consumption

Kübra SÜMER HAYDARASLAN ¹*[0000-0003-0663-6141] and Yalçın YAŞAR ² [0000-0003-1899-750X]

¹ kubrahaydaraslan@sdu.edu.tr, Suleyman Demirel University

² yyasar@ktu.edu.tr, Karadeniz Technical University

Abstract

Climate change is one of the most important issues affecting the environment. Due to the use of fossil fuels as an energy source, the amount of greenhouse gas emissions are increasing. The increase in greenhouse gas emissions accelerates climate change. In this study, the effect of climate change on building energy consumption was investigated. In the study, firstly, information about climate change and how Turkey will be affected by climate change was given. Afterwards, suggestions for the preparation of buildings for the effects of climate change were mentioned. In addition, suggestions were given to reduce the increase in energy consumption due to climate change.

Keywords. Climate change, building energy consumption, greenhouse gas emissions.

1. Introduction

The increase in the comfort conditions of the building occupants has increased the building energy consumption. The energy consumption of buildings has doubled compared to 2010 due to the increased need for heating and cooling (Global Energy CO₂ Status Report 2018). Increasing energy consumption increases greenhouse gas emissions mostly due to the use of fossil resources. The increase in greenhouse gas emissions causes climate change. CO₂ has the highest rate among greenhouse gases (Mgm 2018). The rate of CO₂ emissions increased by 1.7% from 2010 to 2018. This increase corresponds to 33.1 Gt of CO₂ emissions. This amount of emission reached is the historical record level in CO₂ emission (Tracking Clean Energy Progress 2018).

Countries are working to reduce the effects of climate change. Studies have concluded that the effects of climate change will be felt more in some countries. Since Turkey is located in the Eastern Mediterranean Basin, it is in the high risk group for climate change. For this reason, in this study, Turkey's studies on climate change were included. Then, information about reducing the energy consumption of buildings was given. In addition, suggestions were given on the preparation of buildings for the effects of climate change.

2. Climate Change and Buildings

Climate is the weather that occurs in a region over large time intervals (TCPCCNS 2015). Over time, natural climate changes occur due to reasons such as the sun and volcanic eruptions. However, today, the range of changes in the climate has decreased due to the high amount of greenhouse gas emissions. The reason for the increase in the amount of greenhouse gas emissions is human-induced. Especially the use of fossil fuels as an energy source is the biggest cause of climate change (Mgm 2018). Despite the IPCC and Paris Climate Agreement commitments, the use of fossil fuels is increasing. This is due to the increase in temperatures caused by climate change, and the increase in the need for energy with economic developments (WEF 2020). Efforts have been made to expand the use of renewable energy sources in order to reduce the effects of climate change. In this direction, the use of renewable energy sources has increased in recent years. However, since the demand for all fuel types has increased more in recent years, the amount of greenhouse gas emissions continues to increase (Figure 1) (Global Energy CO₂ Status Report 2018).

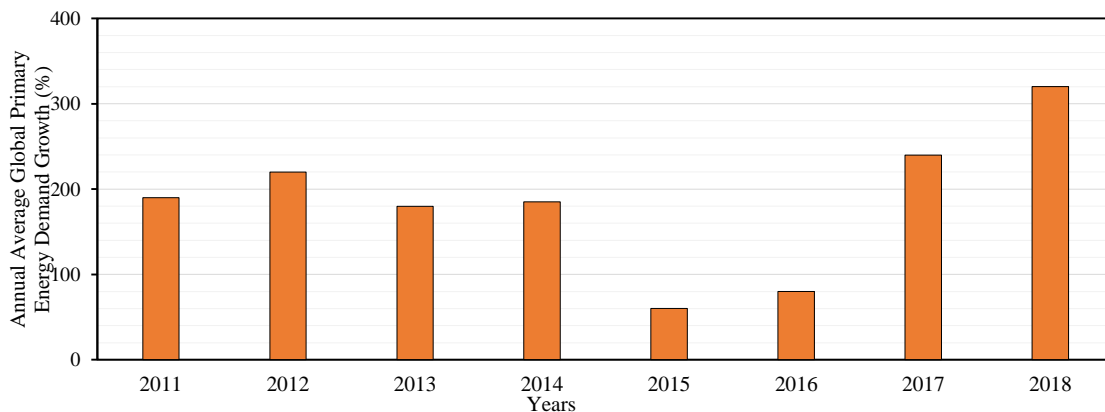


Figure 1: Increase in primary energy demand over the years

2.1. Studies on Climate Change and the Situation in Turkey

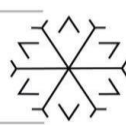
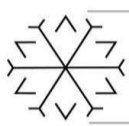
Climate change is an important issue affecting all countries. One of the important studies that bring countries together in this regard is the preparation of the climate change environmental contract. In 1990, the United Nations General Assembly decided to prepare the United Nations Framework Convention on Climate Change (UNFCCC). In 1992, the Climate Change Framework Convention was prepared. This convention has been accepted by 154 countries (UNFCCC 1994). Turkey adopted UNFCCC in 2004 (TCPCCNS 2015). With this contract, countries have committed to carry out work in all areas that cause greenhouse gas emissions and to fulfill the obligations of the contract (Climate change 2019). Another study on reducing the effects of climate change was the establishment of the Intergovernmental Panel on Climate Change (IPCC) in 1988. The IPCC has published reports on the effects of climate change in 1990, 1995, 2001, 2007 and 2013. Another annual study on climate change is the Conference of the Parties (COP). The first conference was held in 1995 and is held regularly every year. In addition, the Kyoto Protocol was prepared in 1997 within the scope of UNFCCC. This protocol entered into force in 2005. The protocol includes reducing the amount of greenhouse gas emissions. Turkey signed the Kyoto Protocol in 2009 (UNFCCC 1994).

Turkey has also signed the Vienna Convention and the Montreal Protocol, the UNFCCC, and the Paris Agreement within the scope of mitigating the effects of climate change. Turkey has committed to fulfilling its responsibilities on climate change with the agreements it has signed. In this direction, it is aimed to work in all areas that cause greenhouse gas emissions. Turkey Climate Change Strategy Document was published in 2010 (Turkey Climate Change Strategy Document 2019). In this document, the issue of greenhouse gas emission control was discussed. Targets were set under the headings of energy, transportation, industry, waste and land use, agriculture, and forestry. These targets are; limiting the amount of greenhouse gas emissions, cooperating with other countries to reduce the effects of climate change, raising awareness about the effects of climate change, creating a greenhouse gas emission inventory.

In the strategy document, greenhouse gas emission control is under five headings as energy, transportation, industry, waste and land use, agriculture, and forestry. Increasing the energy efficiency of buildings is among the targets planned to be realized in the short term under the energy heading. It also includes the development of projects for building materials technologies in cooperation with industry. Another target related to buildings is the preparation of an Energy Performance Certificate for existing buildings. Within the scope of greenhouse gas emission control, increasing electricity production from solar energy is another target (Turkey Climate Change Strategy Document 2019).

2.2. Climate Change and Energy Consumption of Buildings

Buildings still mostly use fossil fuels as an energy source. There are many studies on this subject by developed and developing countries such as Turkey. When these studies are examined, the orientation towards renewable energy sources has increased compared to ten years ago. In addition, the most important of these steps are for buildings. Strategies, plans, and legal regulations have been prepared to reduce the energy consumption of buildings. Efficient use of energy in buildings provides savings. These savings further increase the importance of the studies.



The increase in the share of energy consumption originating from buildings in total energy consumption has increased the number of studies on this subject. Studies have focused on reducing energy consumption in both new buildings and existing buildings. In addition, studies have been carried out that draw attention to the need for long-term energy plans to reduce the effects of climate change. In these studies, the necessity of reducing energy consumption in buildings as well as reducing CO₂ emissions is mentioned. For this, building envelope elements, mechanical systems, the form of buildings and the effect of climate change on energy consumption are examined. Since these parameters affect the energy consumption and CO₂ emissions of buildings at different rates, optimization studies have been carried out to reach the most appropriate solution.

With the development of technology, buildings have been built more resistant to the external environment. In this way, the life of the buildings is extended. It is estimated that 75-90% of existing buildings constructed in the northern hemisphere will continue to be used in 2050 (Huang & Hwang 2016; IEA Topics 2020). In the energy directive published by the EU, it is stated that the energy consumption of existing buildings should be reduced. In this context, it is aimed to reduce primary energy consumption by renewing 3% of existing buildings with optimum solutions every year (EED 2012). It is aimed to reduce primary energy consumption by 14% every year in Turkey. Reducing the energy consumption of existing buildings is included in the recommendations made to achieve this goal (National Energy Efficiency Action Plan 2019). The energy consumption of existing buildings can be reduced by 25-40% with the improvements made (Chowdhury et al. 2008). In the literature, many studies have been carried out on the reduction of energy consumption and CO₂ emissions of existing buildings (Kou et al. 2019; Martin Palma et al. 1998; Solovyev et al. 2015; Tokuç et al. 2015; Wijesuriya 2020; Amirkhani et al. 2019; Lerch et al. 2015; Chargui et al. 2014; Mustafaraj et al 2014; Becchio et al. 2016).

Climate change studies include changing building envelope elements (Huang & Hwang 2016; Domínguez Amarillo et al. 2019; Ferrara & Fabrizio 2017; Fontanini et al. 2016), how electrical energy consumption will change (Nik et al. 2015), renewing mechanical systems according to climate change (Asimakopoulos et al. 2012), increasing building energy performance by adapting to climate change (Dirks et al. 2015; Berger et al. 2014; Wang & Chen 2014). In addition, studies examining the effect of temperature increase due to climate change on energy consumption cost have been carried out at the regional scale (Rosenthal et al. 1995; Amato et al. 2005).

3. Conclusion

Fossil fuels are used as an energy sources in buildings. Due to the use of fossil fuels as an energy source, the amount of greenhouse gas emissions are increasing. The increase in the amount of greenhouse gases is shown among the most important causes of climate change. Among the greenhouse gases released, the most important parameter that triggers climate change is CO₂ emission. With the increase in greenhouse gas emissions in the international climate change panel, it is estimated that temperatures will rise in the range of 1.1 °C- 6.4 °C until the end of the 21st century. Climate change affects the entire earth. However, it is predicted that countries in the Eastern Mediterranean Basin, such as Turkey, will feel the effects of climate change as a high-risk group. For this reason, Turkey carries out studies on this subject and has determined to prevent the increase in the amount of CO₂ emissions as the most comprehensive target. The studies carried out include the target of reducing the primary energy consumption and CO₂ emissions of existing and new buildings. However, these targets are not targets that can be implemented quickly due to the high stock of existing buildings, costs, and long building life spans. On the other hand, the use of the measures taken for a long time and the change in temperatures due to climate change day by day is not as important as the first day. In addition to the long-term and gradual handling of measures in buildings, comprehensive planning is required.

Acknowledgements

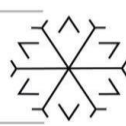
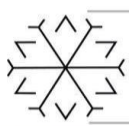
This study was supported by Karadeniz Technical University through Scientific Research Projects Coordination Unit (BAP Proje ID: 8564).

References

Amato, AD., Ruth, M, Kirshen, P and Horwitz, J 2005, Regional Energy Demand Responses to Climate Change: Methodology and Application to The Commonwealth of Massachusetts, Climatic Change, Vol. 71, pp. 175-201.



- Amirkhani S, Bahadori-Jahromi, A, Mylona, A, Godfrey, P and Cook, D 2019, 'Impact of Low-E Window Films on Energy Consumption and CO₂ Emissions of an Existing UK Hotel Building', *Sustainability*, Vol. 11, pp. 42-65.
- Asimakopoulos, DA, Santamouris, M, Farrou, I, Laskari, M, Saliari, M, Zanis, G and Giannakidis, G 2012, 'Modelling The Energy Demand Projection of The Building Sector in Greece in The 21st Century', *Energy and Buildings*, Vol. 49, pp. 488-498.
- Becchio, C, Corgnati, SP, Delmastro, C, Fabi, V and Lombardi P 2016, 'The role of nearly-zero energy buildings in the transition towards Post-Carbon Cities', *Sustainable Cities and Society*, Vol. 27, pp. 324-337.
- Berger, T, Amann, C, Formayer, H, Korjenic, A, Pospischal, B, Neururer, C and Smutny, R 2014, 'Impacts of Climate Change Upon Cooling and Heating Energy Demand of Office Buildings in Vienna, Austria', *Energy and Buildings*, Vol. 80, pp 517-530.
- Chargui, R and Sammouda, H 2014, 'Modeling of a residential house coupled with a dual source heat pump using TRNSYS software', *Energy Conversion and Management*, Vol. 81, pp. 384-399.
- Chowdhury, AA, Rasul, MG and Khan, MMK 2008, 'Thermal-Comfort Analysis and Simulation for Various Low-Energy Cooling-Technologies Applied to an Office Building in a Subtropical Climate', *Applied Energy*, Vol. 85, pp. 449-462.
- Dirks, JA, Gorrissen, WJ, Hathaway, JH, Skorski, DC, Scott, MJ, Pulsipher, TC, Huang, M, Liu, Y and Rice, JS 2015, 'Impacts of Climate Change on Energy Consumption and Peak Demand in Buildings: A Detailed Regional Approach', *Energy*, Vol. 79, pp. 20-32.
- Domínguez Amarillo, S, Fernández-Agüera, J, Sendra, JJ and Roafi S 2019, 'The Performance of Mediterranean Low-Income Housing In Scenarios Involving Climate Change', *Energy and Buildings*, Vol. 202, pp. 109374.
- EED 2012, Directive 2012/27/EU of The European Parliament and of The Council of 25 Ekim 2012 on Energy Efficiency.
- European Commission, United Nations Framework Convention on Climate Change 1994, Rio de Janeiro, Brezilya.
- Ferrara, M and Fabrizio, E 2017, 'Cost Optimal nZEBs in Future Climate Scenarios', *Energy Procedia*, Vol. 122, pp. 877-882.
- Fontanini, AD, Pr'Out, KM, Kosny, J and Ganapathysubramanian, B 2016, 'Exploring Future Climate Trends on The Thermal Performance of Attics: Part 1 – Standard Roofs', *Energy and Buildings*, Vol. 129, pp. 32-45.
- General Directorate of Meteorology, Climate Change, View 10 December 2018, <www.mgm.gov.tr>.
- Huang, K and Hwang, R 2016, 'Future Trends of Residential Building Cooling Energy and Passive Adaptation Measures to Counteract Climate Change: The Case of Taiwan', *Applied Energy*, Vol. 184 pp. 1230-1240.
- International Energy Agency (IEA) Global Energy CO₂ Status Report, View 2 March 2018, <www.webstore.iea.org>.
- International Energy Agency, Topics, View 05 July 2020, <www.iea.org>.
- Kou, R, Zhong, Y, Kim, J, Wang, Q, Wang, M, Chen, R and Qiao, Y 2019, 'Elevating low-emissivity film for lower thermal transmittance', *Energy and Buildings*, Vol. 193, pp. 69-77.
- Lerch, W, Heinz, A and Heimrath, R 2015, 'Direct Use of Solar Energy As Heat Source for A Heat Pump in Comparison to A Conventional Parallel Solar Air Heat Pump System', *Energy and Buildings*, Vol. 100, pp. 34-42.
- Martin-Palma, RJ., Vazquez, L, Martinez-Duart, JM and Malats, R 1998, 'Silver-Based Low-Emissivity Coatings for Archi-Tectural Windows: Optical and Structural Properties', *Solar Energy Materials and Solar Cells*, Vol. 53, pp. 55-66.
- Ministry of Energy and Natural Resources, National Energy Efficiency Action Plan 2017-2023, View 2 January 2019, <www.enerji.gov.tr>.



Ministry of Environment and Urbanization, Climate Change, View 20 February 2019, <www.iklim.csb.gov.tr>.

Ministry of Environment and Urbanization, Turkey Climate Change Strategy Document, View 15 January 2019, <www.csb.gov.tr/strateji-belgeleri>.

Mustafaraj, G, Marini, D, Costa, A and Keane, M 2014, 'Model Calibration for Building Energy Efficiency Simulation', Applied Energy, Vol. 130, pp. 72-85.

Nik, VM, Mata, E and Kalagasidis, AS 2015, 'A Statistical Method for Assessing Retrofitting Measures of Buildings and Ranking Their Robustness Against Climate Change', Energy and Buildings, Vol. 88, pp. 262-275.

Rosenthal, DH, Gruenspecht, HK and Moran, EA 1995, Effects of Global Warming on Energy Use for Space Heating and Cooling in The United States, The Energy Journal, Vol. 16, pp. 77-96.

Solovyev AA, Rabotkin, SV and Kovsharov NF 2015, 'Polymer Films with Multilayer Low-e Coatings', Materials Science in Semiconductor Processing, Vol. 38, pp. 373-380.

Tokuç A, Başaran, T and Cengiz Yesügey, S 2015, 'An Experimental and Numerical Investigation on The Use of Phase Change Materials in Building Elements: The Case of A Flat Roof in Istanbul', Energy and Buildings, Vol. 102, pp. 91-104.

Tokuç, A, Başaran, T and Cengiz Yesügey, S 2017, 'An evaluation methodology proposal for building envelopes containing phase change materials: the case of a flat roof in Turkey's climate zones', Architectural Science Review, Vol. 60, no. 5, pp. 408-423.

Turkey Climate Projections and Climate Change with New Scenarios, Research Department Climatology Branch Directorate, View 3 March 2018, <www.mgm.gov.tr>.

Wang, H and Chen, Q 2014, 'Impact of Climate Change Heating and Cooling Energy Use in Buildings in The United States', Energy and Buildings, Vol. 82, pp. 428-436.

Wijesuriya, WASI 2020, 'Experimental Analysis and Validation of A Numerical PCM Model for Building Energy Programs', PhD thesis, Colorado School of Mines, Colorado.

World Economic Forum (WEF), Renewable Energy, View 04 March 2020, <www.weforum.org>.

World Energy Outlook, Tracking Clean Energy Progress, View 2 September 2018, <www.iea.org>.

Study on Adsorption Performance of MIL-101(Cr) for Ibuprofen Uptake from Aqueous Media

Maryam Faisal^{1*}, H. Buket Engel², G. Gülenay Hacıosmanoğlu³, Serdar Şam⁴, Bercem Kıran Yıldırım⁵,
Seval Genç⁶, S. Zehra Can⁷

¹maryam.heibk@gmail.com, Environmental Engineering Department, Marmara University, Istanbul,
Turkey

²buketengel@gmail.com, Environmental Engineering Department, Marmara University, Istanbul,
Turkey

³g.haciosmanoglu@gmail.com, Environmental Engineering Department, Marmara University, Istanbul,
Turkey,

⁴serdar.sam@marmara.edu.tr, Environmental Engineering Department, Marmara University, Istanbul,
Turkey,

⁵bercem.kiran@marmara.edu.tr, Chemical Engineering Department, Marmara University, Istanbul,
Turkey,

⁶sgenc@marmara.edu.tr, Department of Metallurgical and Materials Engineering, Marmara University,
Istanbul, Turkey,

⁷zehra.can@marmara.edu.tr, Environmental Engineering Department, Marmara University, Istanbul,
Turkey,

Abstract

Metal–organic frameworks (MOFs) are a class of crystalline materials produced by metal ions linked with organic molecules to form three dimensional frameworks. They have interesting properties such as large surface area and pore volume. MOFs rely on making the best of the properties of both organics and inorganics. MOFs have attracted tremendous research interest as one of the most promising porous adsorbents. MIL-101(Cr) is a specific group of MOF, and it has the chemical composition $\{Cr_3F(H_2O)_2O(BDC)_3.nH_2O\}$ ($n \sim 25$; 1,4-benzenedicarboxylate (TPA)). MIL stands for Material of Institute Lavoisier where it was originally synthesized. Recently, it attracted considerable attention of several researchers due to its high pore volume, larger pore size, and high thermal and chemical stability. Ibuprofen with the formula ($C_{13}H_{18}O_2$) is a drug discovered during the mid-decades of last century and has been used since then as a pain killer and as a medicine to treat some diseases with risks related to its toxicity.

In this study, we investigated the adsorption of Ibuprofen (IBP) on chromium metal-organic framework MIL-101(Cr) in water. The adsorption mechanism was investigated using FTIR analysis.

The adsorption experiments were carried out in batch mode using a temperature controlled shaker (IKA, Germany) at a constant speed of 200 rpm. 10 ml aqueous IBP samples were prepared in 40 ml glass vials. The adsorbent dose was 10 g/L and the adsorption temperature was 25 °C. The amount of IBP adsorbed on unit weight of adsorbent at any time, t, is calculated using Eq (1):

$$q_t = \frac{(C_0 - C_t)V}{m} \dots\dots\dots(1)$$

Where q_t is the amount of IBP adsorbed (mg/g) at time t; C_0 is the initial IBP concentration (mg/L); C_t is IBP concentration at time t (mg/L); V is the volume of IBP solution (L) and m is the weight of adsorbent used (g). IBP concentrations in the samples before and after adsorption were measured by a gas chromatograph-mass spectrometer (GCMS-QP2010, Shimadzu, Japan). The detection limit of the method used was 0.5 nanogram ibuprofen injected.

Keywords. Adsorption, Ibuprofen (IBP), Metal-organic framework (MOF), Micropollutants.

Mechanochemical Synthesis and Characterization of Mn-B Phases

Amir Akbari ¹[0000-0003-4083-124X], İlayda Süzer ²[0000-0003-1825-7253], Esin Aysel ³[0000-0003-0422-9649], Sıddıka Mertdinc ⁴[0000-0002-2376-2062], M. Lütfi Öveçoğlu ⁵[0000-0002-1536-4961], Duygu Ağaoğulları ⁶[0000-0002-0623-5586]

¹akbari18@itu.edu.tr, Department of Metallurgical and Materials Engineering, Istanbul Technical University, Istanbul, Turkey

²suzeri@itu.edu.tr, Department of Metallurgical and Materials Engineering, Istanbul Technical University, Istanbul, Turkey

³aysele@itu.edu.tr, Department of Metallurgical and Materials Engineering, Istanbul Technical University, Istanbul, Turkey

⁴mertdinc@itu.edu.tr, Department of Metallurgical and Materials Engineering, Istanbul Technical University, Istanbul, Turkey

⁵ovecoglu@itu.edu.tr, Department of Metallurgical and Materials Engineering, Istanbul Technical University, Istanbul, Turkey

⁶bozkurtdu@itu.edu.tr, Department of Metallurgical and Materials Engineering, Istanbul Technical University, Istanbul, Turkey

Abstract

This investigation reports on the synthesis and characterization of manganese boride compounds, MnO, MnO₂ and Mn₂O₃ were used separately as starting powders respectively with native boron oxide (B₂O₃) and Mg as reducing agent. The powders were mixed in stoichiometric ratios, and the effect of milling durations (3, 5, 7 and 10 h) were investigated by using Spex 8000D mixer / mill device (1200 rpm) to carry out mechanochemical milling process. In addition, the effect of using raw materials in excess ratios were examined as well. Besides, the leaching process was carried out with different molarities of HCl to find optimum molarity to leach milled powders to get rid of by-products and manganese oxides. Rietveld analysis was conducted to investigate the amount of remaining materials in leached product. X-ray diffractometry (XRD), scanning electron microscopy/energy dispersion spectroscopy (SEM/EDS), transmission electron microscopy (TEM), vibrating-sample magnetometry (VSM) and particle size measurement were conducted for the characterization of the milled and leached powders. Consequently, the optimal result was obtained at 10 h of mechanochemical synthesis by using 100% and 50% excess amounts of B₂O₃ and Mg respectively.

Keywords. Manganese borides, mechanochemical synthesis, acid leaching.

Acknowledgment: This study was supported by the "TENMAK Boron Research Institute (BOREN)" with project number 2019-31-07-15-001.

Investigation of Photocatalytic Activity of Calcium Aluminate Spinel Ceramics Synthesized by Microwave Assisted Combustion Method

İbrahim Hakki Karakaş^{a,*}, Zeynep Karcıoğlu Karakaş^b

^a Chemical Engineering Department, Engineering Faculty, Bayburt University ,69100, Bayburt,TURKEY

^b Environmental Engineering Department, Engineering Faculty, Ataturk University ,25240, Erzurum,TURKEY

(*Corresponding Author : ihkarakas@bayburt.edu.tr)

Abstract

Calcium aluminate spinel ceramics is a chemical material of commercial importance. It is widely used for different purposes in many different industries. In this study, calcium aluminates were used for a different purpose than traditional usage areas and were used as a photocatalyst for the removal of organic pollutants from wastewater. Accordingly, calcium aluminate spinel ceramics were first synthesized by microwave assisted combustion method and characterized by techniques such as XRD, SEM, FT-IR and TEM. Later, these particles were used as photocatalysts in the removal of organic matter from wastewater containing organic dyestuffs and their photocatalytic activities were investigated. For this purpose, experiments were carried out with catalyst dosages of 0.01 g/L, 0.25 g/L, 0.50 g/L and 0.1 g/L, respectively. The obtained results show that calcium aluminate nanoparticles exhibit quite good photocatalytic activity. In experiments with catalyst dosages of 0.25 g/L and above, the dye in the solution was almost completely removed.

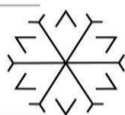
Keywords : CaAl₂O₄, Spinel, Photocatalysis, Removal

1. Introduction

Calcium aluminate spinel ceramics are important commercial chemical compounds that are widely used in industries such as cement and metallurgy, with unique properties such as low density, hardness, high strength, and high temperature resistance. In recent years, calcium aluminate-based materials, find use in a wide variety of fields such as the production of advanced ceramics, catalyst support, binders, optical ceramics, flame detectors, dental restorers and the production of structural ceramics. (Shiri et al., 2014, Ranjbar and Rezaei, 2014, Ranjbar and Rezaei, 2012, Rodríguez et al., 2012, Zawrah and Khalil, 2007, Zawrah et al., 2011)

Calcium aluminates (CaAl₂O₄) find use in a wide variety of medical applications with their unique physical properties such as high mechanical, chemical and thermal stability, bioactivity and biocompatibility. In addition, calcium aluminate-based glasses have a great importance in the production of many high-tech optical materials. Calcium aluminate-based nanomaterials are constantly finding new application areas with their unique properties. (Shiri et al., 2014, Ranjbar and Rezaei, 2014)

There are many various synthesis methods for the production of spinel calcium aluminates. The commercial production of the calcium aluminates are performed with solid phase reactions based on the reaction of calcium oxide (CaO) or calcium carbonate (CaCO₃) with alumina (Al₂O₃) powders, at temperatures exceeding 1400°C. The most important disadvantages of this method are clumping, inhomogeneous size distribution, wide variety of morphology, poor sinterability, high temperature requirement and presence of multiple and undesirable phases in the final product (Ranjbar and Rezaei, 2012). In addition, long processing times are required to produce single-phase calcium aluminate with these methods. Because of these disadvantages is needed new, effective, and environmentally friendly production methods for the production of CaAl₂O₄ spinels.



In the literature, different methods for the production of calcium aluminate spinels such as sol–gel (Vishista et al., 2005), reverse micelle process (Chandradass et al., 2009), high temperature combustion method (Rodríguez et al., 2012, Yi et al., 2002, Burkes* and Moore, 2007), precipitation method (Ranjbar and Rezaei, 2014) ve high energy ball milling (Shiri et al., 2014) is recommended. Compared to conventional methods, these methods offer significant advantages such as significantly reducing lower processing temperatures and homogeneous size and shape distribution of high purity products.(Rivas Mercury et al., 2005) But they also have significant disadvantages, such as high processing times and low production volumes, and expensive and complex production processes and expensive starting chemicals. However, the combustion method is an important chemical synthesis method that allows the rapid and safe production of various metal oxide nanoparticles and ferrites at laboratory scale and even at pilot scale, without the need for sophisticated equipment. In the combustion method, unlike other methods, a substance used as fuel is added to the system in addition to the starting reagents. Organic compounds such as glycine, urea, citric acid, alanine are used as fuel in the combustion method to increase the efficiency of the synthesis process. Among these organic compounds, urea is the most widely used. Because urea has important advantages such as low cost, abundant and easy to find, being safe and not showing toxic properties. (Mimani and Patil, 2001, Abu-Zied, 2002)

In this study, CaAl₂O₄ nanoparticles produced by microwave assisted combustion were used as photocatalysts in the process of removing the dye content by photocatalytic oxidation from synthetic wastewater containing astrazon red textile dye.

2. Results and Discussion

2.1. Synthesis and Characterization of Calcium Aluminate Photocatalyst

The CaAl₂O₄ nanoparticles used as photocatalyst in the study were synthesized by microwave assisted combustion method. Urea was used as fuel in the combustion reaction. Accordingly, nitrate salts of Calcium and Aluminum metals and certain amounts of urea were effectively mixed in a beaker and then the mixture was placed in a microwave oven. The amounts of reagents in the mixture were determined according to the reaction given below with Equation.



The reagent mixture was exposed to microwave irradiation for a certain period of time. At the end of this process, a black powder is obtained. Then, this powder is heat treated at 700°C for 2 hours and bright white colored CaAl₂O₄ nanoparticles are obtained. The X-Ray diffractogram of calcium aluminate powder obtained with this procedure is presented in Figure 2.

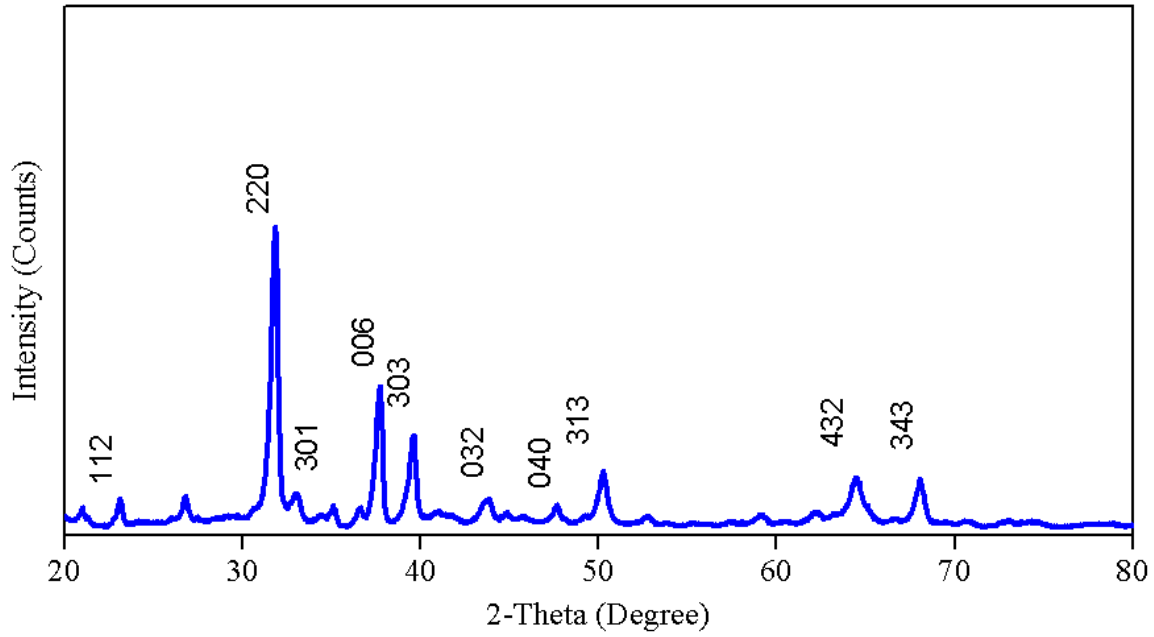
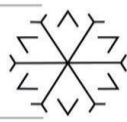
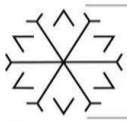
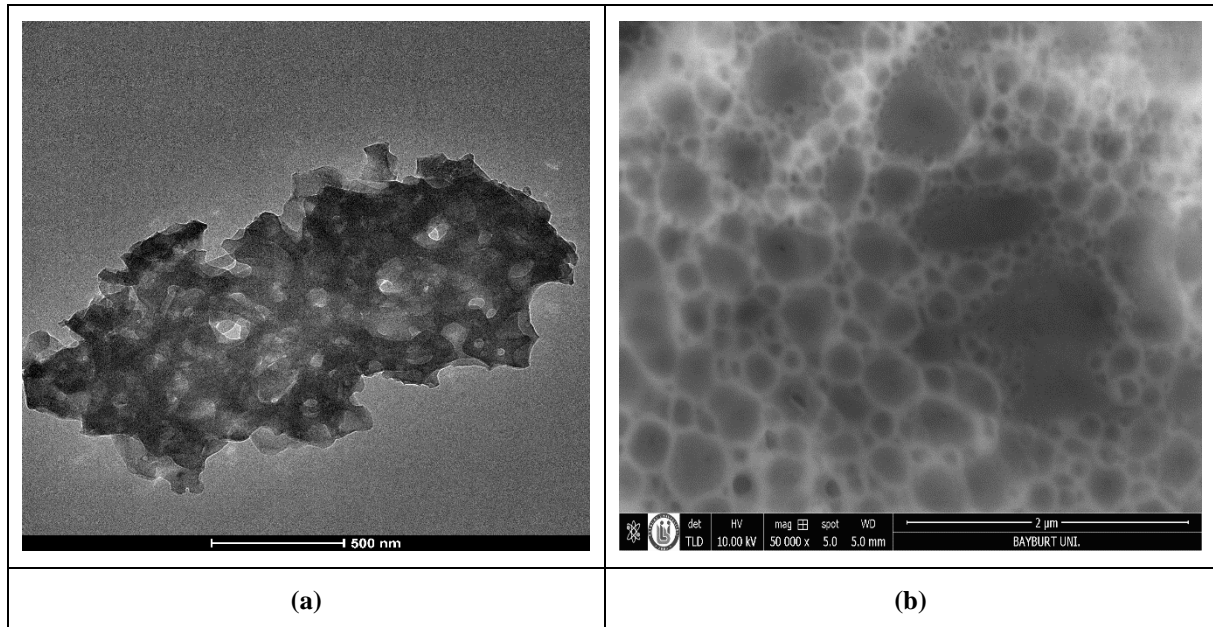
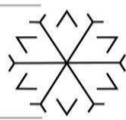
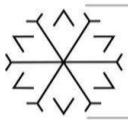


Figure 2. X-ray diffractogram of the Calcium Aluminate nanoparticles produced via Microwave Assisted Combustion Method

It is seen that the X-ray diffractogram given in Figure 1 is fully compatible with the standard diffraction pattern (JCPDS# 53-0191) defined for spinel calcium aluminate. This result indicates that the synthesized sample consists of single-phase calcium aluminate. SEM (Scanning Electron Microscopy) and TEM (Transmission Electron Microscopy) analyzes were performed to characterize the morphological features of the synthesized samples. Accordingly, the obtained SEM and TEM images are shown in Figure 3.



Şekil 2. The SEM and TEM images of the Calcium Aluminate nanoparticles produced via Microwave Assisted Combustion Method; (a) TEM image ; (b) SEM image



The SEM and TEM images presented in Figure 3 confirm that the synthesized calcium aluminate nanoparticles are nanosized. More detailed information on CaAl_2O_4 synthesis by microwave assisted combustion can be obtained from previous studies about this subject. (Karakas, 2019)

Investigation of the Photocatalytic Activity of CaAl_2O_4 nanoparticles

To examine the photocatalytic activity of the synthesized samples, simulated wastewater containing 50 mg/L astrazon red textil dye was prepared and then a certain amount of catalyst particles and 2 mL of H_2O_2 (w/w, 30%) solution were added. In order to determine the efficiency of the catalyst, trials were conducted with a total of four different catalyst dosages, 0.010 g/L, 0.025 g/L, 0.050 g/L and 0.10 g/L, respectively. In these experiments, the change in the concentration of the pollutant in the solution was followed by measuring the color change spectrophotometrically at certain time intervals. According to this; graphs showing the variations in absorbance values measured at regular intervals for experiments with various catalyst dosages are presented in Figure 4.

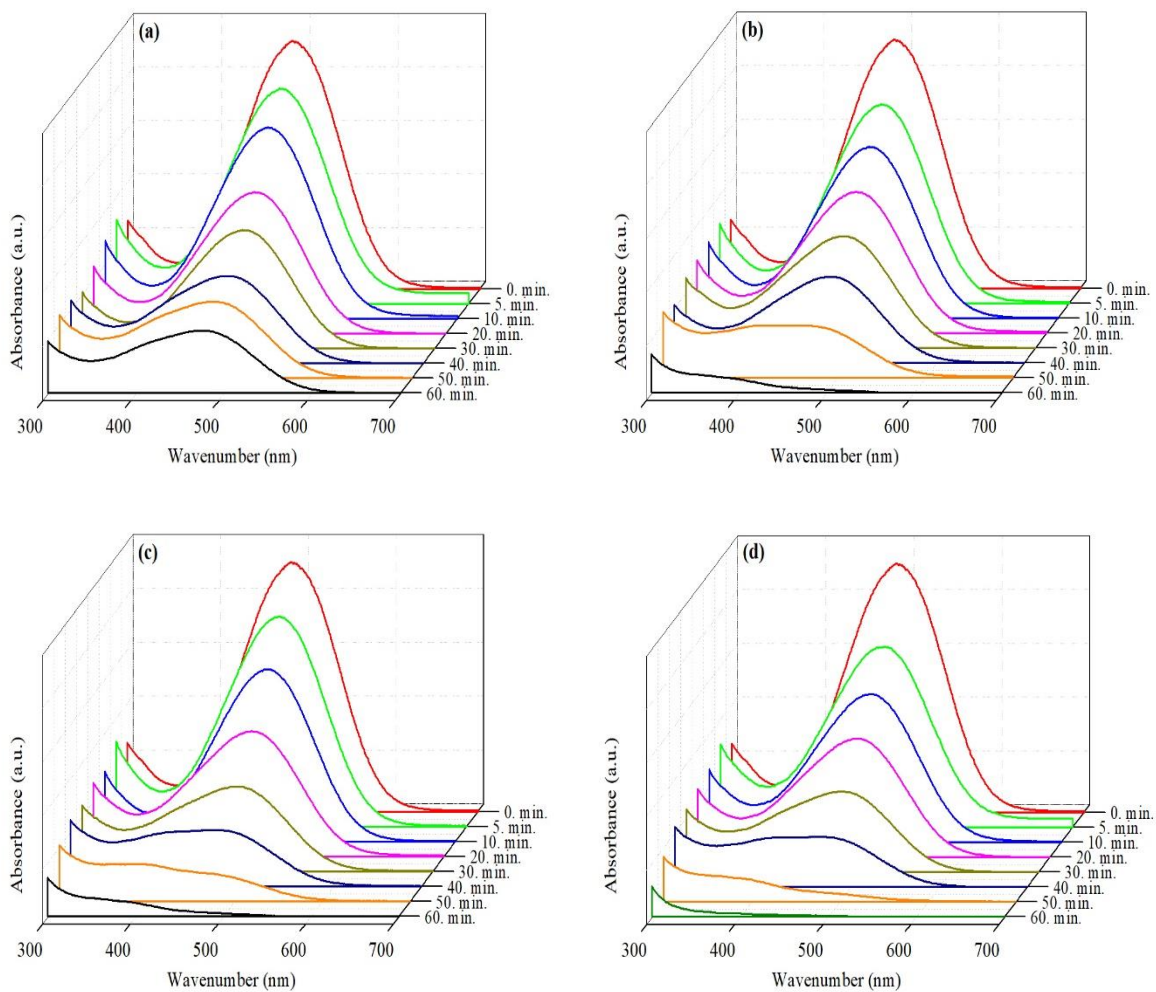


Figure 4. The variations in absorbance values measured versus time for experiments with various catalyst dosages (a) 0,010 g/L, (b) 0,025 g/L, (c) 0,050 g/L and (d) 0,10 g/L

According to the graphs presented in Figure 4, it is seen that the synthesized CaAl_2O_4 nanoparticles exhibited an impressive photocatalytic activity in almost all experiments and the measured absorbance values decreased drastically. The graph showing the removal efficiencies against time created for these trials is presented in Figure 5.

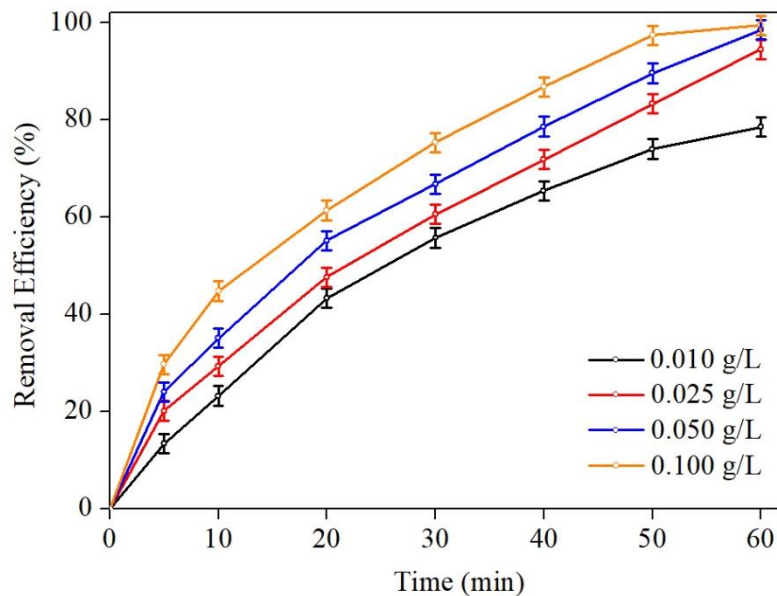
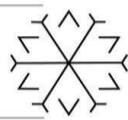
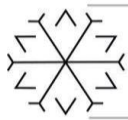


Figure 5. The removal efficiencies observed in experiments performed with different catalyst dosages

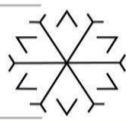
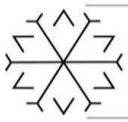
According to the graph presented in Figure 5, it is clearly seen that there is a significant removal in trials with all catalyst dosages. It is seen that the dyestuff in the solution has been completely removed at the end of the test period of 50 minutes in the experiments carried out with 0.050 g/L and 0.1 g/L catalyst dosages. There was no complete removal in the experiment with a catalyst dose of 0.01 g/L. It is thought that this is due to the fact that the applied light radiation time is limited to 60 minutes. It may be possible to achieve higher removal efficiencies when longer UV irradiation times are applied.

Conclusions

The data obtained from the study show that the microwave assisted combustion method is a good alternative for the synthesis of CaAl_2O_4 nanoparticles. In addition, it is seen that the nanoparticles synthesized by this method exhibit a very good photocatalytic activity. For the catalyst dosage levels studied, 0.050 g/L was evaluated as the optimum operating condition. However, more experimental studies are needed to determine the optimum operating parameters for the whole process.

References

- ABU-ZIED, B. 2002. Preparation of cadmium chromite spinel: A combustion approach. *Colloids and Surfaces A-physicochemical and Engineering Aspects - COLLOID SURFACE A*, 211, 27-42.
- BURKES, D. E. & MOORE, J. J. 2007. Auto-Ignition Combustion Synthesis of Calcium Aluminate Ceramic Powders. *Combustion Science and Technology*, 180, 143-155.
- CHANDRADASS, J., BAE, D. S. & KIM, K. H. 2009. Synthesis of calcium hexaaluminate (CaAl_2O_4) via reverse micelle process. *Journal of Non-Crystalline Solids*, 355, 2429-2432.
- MIMANI, T. & PATIL, K. 2001. Solution Combustion Synthesis of Nanoscale Oxides and Their Composites. *Mater. Phys. Mech.*, 4.
- RANJBAR, A. & REZAEI, M. 2012. Dry reforming reaction over nickel catalysts supported on nanocrystalline calcium aluminates with different $\text{CaO}/\text{Al}_2\text{O}_3$ ratios. *Journal of Natural Gas Chemistry*, 21, 178-183.
- RANJBAR, A. & REZAEI, M. 2014. Low temperature synthesis of nanocrystalline calcium aluminate compounds with surfactant-assisted precipitation method. *Advanced Powder Technology*, 25, 467-471.
- RIVAS MERCURY, J. M., DE AZA, A. H. & PENA, P. 2005. Synthesis of CaAl_2O_4 from powders: Particle size effect. *Journal of the European Ceramic Society*, 25, 3269-3279.
- RODRÍGUEZ, M. A., AGUILAR, C. L. & AGHAYAN, M. A. 2012. Solution combustion synthesis and sintering behavior of CaAl_2O_4 . *Ceramics International*, 38, 395-399.
- SHIRI, S., ABBASI, M., MONSHI, A. & KARIMZADEH, F. 2014. Synthesis of the CaAl_2O_4 nanoceramic compound using high-energy ball milling with subsequent annealing. *Advanced Powder Technology*, 25, 338-341.



- VISHISTA, K., GNANAM, F. & AWAJI, H. 2005. Sol–Gel Synthesis and Characterization of Alumina–Calcium Hexaaluminate Composites. *Journal of the American Ceramic Society*, 88, 1175-1179.
- YI, H., GUIGNÉ, J., MOORE, J., SCHOWENGERDT, F., ROBINSON, L. & MANERBINO, A. 2002. Preparation of Calcium Aluminate Matrix Composites by Combustion Synthesis. *Journal of Materials Science*, 37, 4537-4543.
- ZAWRAH, M. F. & KHALIL, N. M. 2007. Synthesis and characterization of calcium aluminate nanoceramics for new applications. *Ceramics International*, 33, 1419-1425.
- ZAWRAH, M. F., SHEHATA, A. B., KISHAR, E. A. & YAMANI, R. N. 2011. Synthesis, hydration and sintering of calcium aluminate nanopowder for advanced applications. *Comptes Rendus Chimie*, 14, 611-618.
- KARAKAS, İ. H. 2019. Mikrodalga Destekli Yakma Metoduyla Kalsiyum Aluminat (CaAl_2O_4) Spinel Seramiklerin Sentezi ve Karakterizasyonu . *Düzce Üniversitesi Bilim ve Teknoloji Dergisi* , 7 (3) , 1658-1670

Cannabis Production and State Policy in Turkey

Onur Namaldı ¹[0000-0002-5225-6441]

¹onurnamaldi@gmail.com, Environmental Engineering Department, Erciyes University, Kayseri, Turkey

Abstract

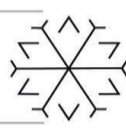
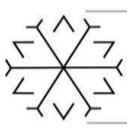
Cannabis is a herbaceous, annual, dioecious and flowering plant in the Cannabinaceae family. The most common use of hemp is the production of fiber and pharmaceutical raw materials. Cannabis sativa, one of the species of hemp, is used for fiber production, while Cannabis indica, another species, is used for the production of pharmaceutical raw materials. Cannabis is grown under supervision in many countries, including our country. The reason for this control is the presence of compounds containing narcotic properties in all cannabis strains and psychoactive substances derived from female cannabis. However, cannabis also has many positive effects. In the area where hemp is cultivated, its radiation decreases and it releases oxygen at high rates. Cannabis has been used in many areas and these areas have been included in various academic studies. There are studies on its use in many different sectors, such as the treatment of diseases in the health sector, its use in bakery products, its use as an energy source, its use in the textile industry, its use in asphalt concrete sectors, its use in paper production. It is possible for each part of hemp to be evaluated differently. The cannabis policy in Turkey has undergone many changes over the years. The main reason for this situation is that hemp is seen as a raw material for drugs and a financial source for terrorism rather than being a very useful plant. Today, there are 19 different points where cannabis production is allowed. In line with all these financial and official opportunities, studies should be carried out in order to grow domestic cannabis seeds in Turkey and to increase their yield and quality with studies. However, our country is a stakeholder in many international agreements in cannabis cultivation and trade. It is also thought that this partnership will limit and prevent the abuse of cannabis.

Keywords. Cannabis, cannabis policy, Turkey

1. Introduction

Cannabis which first appeared in the Asian and Indian regions of the World, is a herbaceous, annual, flowering and dioic (male and female flowers on different plants) plant belonging to the Cannabinaceae family (Yıldırım and Çalışkan, 2020; Akpınar and Nizamoğlu, 2019). The most common use of hemp is the production of fiber and pharmaceutical raw materials. One type of hemp Cannabis sativa is used for fiber production, in other species of Cannabis indicaIt is used for the production of pharmaceutical raw materials (Hayıt & Gül, 2020). Cannabis, which can be used in many different fields apart from fiber production and pharmaceutical raw material production, is grown under supervision in many countries, including our country. The main reason for this control is the narcotic properties found in the nature of cannabis. In fact, there are compounds containing narcotic properties in all cannabis species, but the presence of psychoactive substances obtained from female cannabis and high amounts of narcotic components, especially in Cannabis indica species, cause the cultivation of these plant species to be carried out under control (Pınarkara, 2007). However, cannabis also has many positive effects. Cannabis reduces radiation in the area where it is cultivated and releases oxygen at high rate

As in many countries, our country has focused on the production and operation of cannabis within the sustainability policies. Recently, steps have been taken within the framework of “Industrial Cannabis Cultivation and Action Plan” in Turkey. The aim of this study is to examine the



revisions made in the cannabis policy in Turkey in recent years, to describe the uses of cannabis and to present a new cannabis policy model.

This study was carried out via the document analysis method, one of the qualitative research methods. Document analysis includes finding, selecting, interpreting, evaluating and synthesizing data on the relevant subject (Kıral, 2020). In the present study, the recent cannabis policies in Turkey are discussed based on research and national reports.

In addition to hemp, fiber production and pharmaceutical raw material production, he has been integrated into many different fields and has been involved in academic studies. In the study conducted by Hayıt and Gül in 2020, the use of hemp in bakery products was examined and as a result of the study, it was stated that the natural content of hemp has positive effects on health. In the study carried out by Çalışkan and Yıldırım in 2020, the effect of cannabis on various diseases in the field of health was examined and it was stated that it has a therapeutic effect in many diseases. In the study conducted by Acar and Dönmez in 2019, the use of hemp as an alternative energy source was investigated. Another study in a different field was conducted by Serin et al. in 2018. In the research, it has been observed that hemp fibers have the effect of improving the mechanical properties of hot bituminous mixtures and it has been suggested that hemp fibers can be used among asphalt concrete mixtures in line with this effect. It is possible for each part of hemp to be evaluated differently. For example, while the seeds of hemp are used as flour and food material, oil is obtained as a result of pressing the seeds. This oil is widely used in the foodstuffs, biofuels, paints and cosmetics industries. In addition, substances such as animal feed, beer and protein powder can be produced from the pulp of hemp. According to the quality of the fiber part of hemp, products such as fabric, cellulose and paper can be obtained (Baser and Bozoğlu, 2020). In general, hemp has a sustainable circularity within itself. The products that can be produced from parts of the cannabis plant are shown in Figure 1.

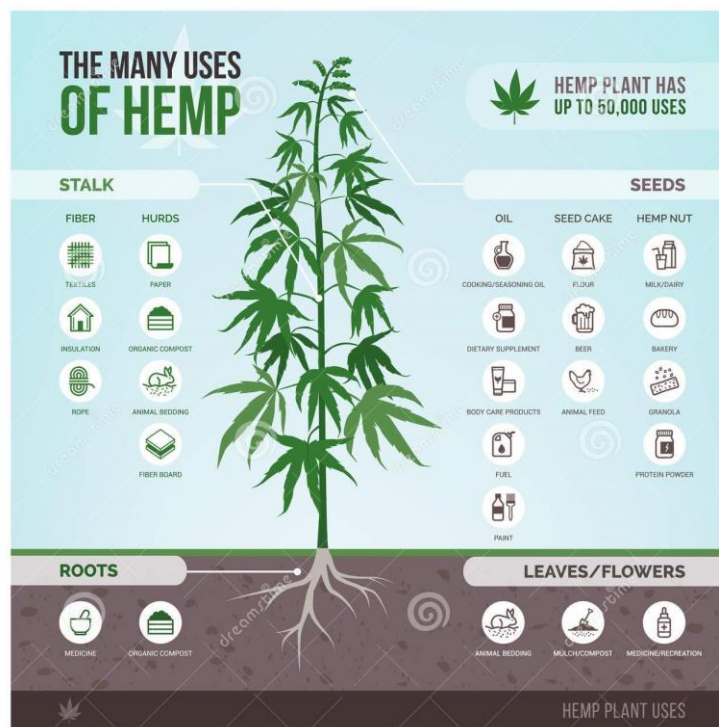


Figure 1: Products that can be produced from parts of the cannabis plant



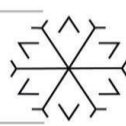
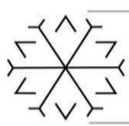
The cannabis policy of governments in Turkey has undergone many changes over the years. These policy changes have been reflected in the amount of hemp seed and hemp fiber cultivation areas and production amounts in our country. Table 1 and Table 2 show the change in hemp seed and hemp fiber cultivation areas and production amounts over the years.

Table 1: Cannabis seed cultivation area, production amount and yield change table in Turkey

	Cultivation Area (da)	Production Amount (tons)	Yield (kg/da)
2004	3750	30	8
2005	650	13	20
2006	645	13	20
2007	559	24	43
2008	294	12	41
2009	66	3	45
2010	221	7	32
2011	140	8	57
2012	64	4	63
2013	7	1	143
2014	10	1	100
2015	10	1	100
2016	25	1	50
2017	24	1	42
2018	59	3	51
2019	536	20	42

Table 2: Hemp fiber cultivation area, production amount and yield change table in Turkey

	Cultivation Area (da)	Production Amount (tons)	Yield (kg/da)
2004	3750	600	160
2005	650	55	85
2006	645	60	93
2007	559	38	68
2008	294	21	71
2009	66	4	61
2010	221	10	45
2011	157	16	102
2012	63	6	95
2013	12	1	83
2014	10	1	100
2015	10	1	100
2016	45	7	156
2017	46	7	152
2018	55	7	127
2019	160	19	126



The main reason for these changes in cannabis policy stems from the fact that cannabis is seen as a drug raw material and a finance source for terrorism rather than a very useful plant. It is very difficult to argue that this opinion is wrong because the most common drug used in Turkey is cannabis derived from cannabis. The data published by the TR Ministry of Interior in 2019 supports this view. According to the data of the Ministry, 65172 cannabis and skank incidents, a type of cannabis, took place in 2018, and 80707 kg of cannabis and skank were seized in these incidents.

However, very positive revisions have been made in recent years on the cannabis policy in Turkey. On January 11, 2019, “Industrial Cannabis Cultivation Report and Action Plan in Turkey” was prepared with the participation of the Ministry of Agriculture and Forestry, the Ministry of Industry and Technology, the Ministry of Health, TÜBİTAK and Samsun Ondokuz Mayıs University. In the prepared action plan, there are many action steps, especially increasing the local population of cannabis production in our country, increasing the population of the local Narlısay species grown in our country, and transitioning to the use of certified seeds through studies to obtain local seeds. In line with this action plan, Hemp Research Institutes were established at Samsun Ondokuz Mayıs University in 2019 and at Yozgat Bozok University in 2020 for research and development studies in cannabis production. The most important revision made within the scope of the action plan is related to the provinces that are allowed for cannabis cultivation in our country. Until 2004, only supervised cannabis cultivation was allowed in the provinces of Samsun, Kütahya, Çorum and Kastamonu. The hemp seed and hemp fiber production of the provinces within the permit between 2004-2017 are shown in Table 3.

Table 3: Hemp seed production and hemp fiber production amounts for Kastamonu, Kütahya, Samsun and Çorum between 2004-2007

Cities	2004	2005	2006	2007	2008	2009	2010	2011	2012	2013	2014	2015	2016	2017
Cannabis Seed Production (tonnes)														
Kastamonu	9	3	2	2	2									
Kütahya	1	1												
Samsun	20	9	11	22	10	3	7	8	4	1	1	1	1	1
Çorum	0	0												
Total	30	13	13	24	12	3	7	8	4	1	1	1	1	1
Hemp Fiber Production (tonnes)														
Kastamonu	508	6	8	5	4									
Kütahya	1	1												
Samsun	9	47	52	33	17	10	10	16	6	1	1	1	7	7
Çorum	1	1												
Total	600	55	60	38	21	4	10	16	6	1	1	1	7	7

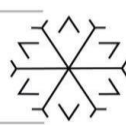
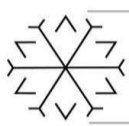


With the revisions in the cannabis policy, this number has been increased to 19. Today, permission has been granted for supervised cannabis cultivation in 19 different provinces. The provinces that are allowed for controlled cannabis cultivation in Turkey are shown in Figure 2.



Figure 2: Provinces authorized for controlled cannabis cultivation in Turkey

Today, the "Regulation on Cannabis Cultivation and Control" published in the Official Gazette No. 28942 is in force. The legal process of cannabis was expressed at the "Local Administrations Symposium in the Presidential Government System" held on January 9, 2019, and subsequently, "Report and Action Plan on Industrial Hemp Growing in Turkey" was prepared on January 11, 2019, together with the relevant stakeholders. In 2020, 700 TL support was provided per decare, provided that there are 19 different points where cannabis production is allowed. In line with all these financial and official opportunities, studies should be carried out in order to grow domestic cannabis seeds in Turkey and to increase their yield and quality with studies.



Conclusion and Suggestions

When the academic studies of hemp are examined, there are studies on its use in many different sectors such as the treatment of diseases in the health sector, its use in bakery products, its use as an energy source, its use in the textile sector, its use in the asphalt concrete sector, its use in paper production. In line with the studies carried out, the fact that hemp is a raw material open to wide sectoral use reveals the functionality of hemp and is an extremely strategic product for developing countries, including our country.

Against many environmental problems such as global climate change, air pollution, decrease in existing water resources and water pollution, which affect the whole world, hemp meets the EU Sustainability Goals with its low biodegradation process, the fact that it absorbs radiation due to its natural structure and releases oxygen, and contains cyclical sustainability within itself. It points out the key points for

In the light of the documents examined, it is seen that hemp production in Turkey is not stable and does not show any progress in production and processing amounts. It is thought that this situation is caused by the cannabis policies that have changed over the years.

An increase is expected in the planting and production amounts of cannabis seeds and hemp fiber in 19 different provinces, which were determined by the "Report and Action Plan on Industrial Cannabis Cultivation in Turkey" prepared in 2019 within the scope of the "Regulation on Cannabis Cultivation and Control" published in the Official Gazette No. 28942.

As a result of the studies to be carried out in 19 provinces determined within the scope of the "Report and Action Plan on Industrial Cannabis Breeding in Turkey", studies will be carried out to increase the yield of domestic cannabis seeds and it is planned to produce registered domestic cannabis seeds as a result of these studies. In order to ensure that the local and registered seeds obtained are not limited to only 19 provinces, and most importantly, considering the possibility of growing cannabis in almost every province of our country, it is considered to propose "Hemp Garden in Every Province" projects.

With the implementation of the "Hemp Garden in Every Province" project, it is thought that product costs will decrease as alternatives to raw materials used in many sectors will be offered. For the Turkish industry, which includes many sectors, this situation is important for the country's economy.

As a result, considering the parameters such as the use and effect of cannabis in many areas, its ability to be grown in almost every part of our country, its biological solubility and cyclicity and its sustainability, it is thought that the number of provinces allowed for supervised cultivation should be increased. In fact, it is recommended to implement "Cannabis Gardens in Every Province" policies in cooperation with many public and private institutions and universities, especially the Ministry of Interior. However, our country is a stakeholder in many international agreements in cannabis cultivation and trade. It is also thought that this partnership will limit and prevent the abuse of cannabis.

This study is limited to data up to 2020. Future studies may provide information on the progress of cannabis policy in Turkey with a broader perspective.



References

- Acar, M., Dönmez A., 2019. A different perspective on hemp. Black Sea Agricultural Research Institute, Samsun.
- Akpınar, D., & Nizamoğlu, A., (2019). Cannabis production from Ottoman to Republic. Social sciences, 14 (4): 1223-1236.
- Başer, U., & Bozoğlu, M. (2020). An overview on hemp (cannabis) policy and market of Turkey, TEAD, 6 (2), 127-135.
- Caliskan, UK, & Yıldırım, S. (2020). Hemp and its use in health. J.Fac. Pharm. Ankara, 44 (1), 112-136.
- Fike J (2016). Industrial hemp: renewed opportunities for an ancient crop. Critical Reviews in Plant Sciences 35 (5-6): 406-424
- Hayıt, F., Gul, H., 2020. The importance of cannabis and its use in bakery products. Electronic letters on science and engineering, 16(1): 17-25.
- King, B. (2020). Document analysis as a qualitative data analysis method. Siirt University Journal of Social Sciences Institute, 15, 170-189.
- Pınarkara, E., 2007. Characterization of drug type cannabis genotypes by rapd-pcr method and evaluation of statistical methods used. Selcuk University, Institute of Science, Department of Animal Science, Master's thesis, Konya, 103.
- Schultes RE (1970) Random Thoughts and Queries on Botany of Cannabis. J. & A. Churchill.
- Serin, S., Macit, ME, Çınar, EC, Çelik, S., 2018. The effect of using natural hemp fiber on asphalt concrete mixes. Düzce University Journal of Science and Technology, 6(4): 732-744.
- Singh M, Sardesai MM (2016). Cannabis sativa (Cannabaceae) in ancient clay plaster of Ellora caves, India. Current Science. Indian Academic Sciences. 110(5):884.
- TR Ministry of Interior, 2019. Ministry of Interior Turkey Drug Report. Ankara. EGM Publication Catalog No: 703
- TUIK, 2020. Turkish statistical institute. <http://www.tuik.gov.tr/Start.do>

Bio-Catalytic Conversion of CO₂ to Solid Carbonate

Fatima Neslisah Ulus ^{1*}[0000-0002-5348-0314] and Ozge Yuksel Orhan ²[0000-0003-0135-0363]

¹neslisahcihan@hacettepe.edu.tr, Department of Chemical Engineering, Hacettepe University, Ankara, Turkey

²oyuksel@hacettepe.edu.tr, Department of Chemical Engineering, Hacettepe University, Ankara, Turkey

Abstract

CO₂ emissions, which reached 414.8 ppm in November 2021, are considered to be largely responsible for global warming. If the use of fossil fuels as an energy source is not reduced, the amount of CO₂ emission is expected to reach 500 ppm in 2050. Although many methods have been studied for CO₂ capture systems, the most commercially-ready technology is solvent-based carbon capture. Chemical absorption is used to separate CO₂ from a gas mixture into conventional amine solvents with a reversible reaction for economically and sustainably reaching carbon emission reduction. 30 wt% monoethanolamine (MEA) aqueous solution is typically used for CO₂ capture from flue gas. However, the low CO₂ loading capacity and high energy demand of aqueous MEA system has been resulted in searching new liquid absorption processes. Studies on the use of catalysts or activators become the popular topic in world's agenda to increase the reaction rate, loading capacity by enrichment of sorbent surfaces with amine solutions. The design of hybrid solvent systems are carried out to achieve high CO₂ capacity, fast absorption and stripping rates, low volatility, low corrosivity, and low heat of absorption. Sterically hindered form of amines reduces carbamate stability. They are characterized by high CO₂ absorption rates and high CO₂ loading capacities, selectivity, and degradation resistance.

In this study, the use of carbonic anhydrase (CA) was inspired by the natural biocatalyst of the CO₂ metabolic process in humans. Aqueous solutions of sterically hindered amines (2-Amino-2-methyl-1,3-propanediol (AMPD) and 2-amino-2-methyl-1-propanol (AEPD)) were selected for the CO₂ process. Gas-liquid contact stirred reactor system was used to examine the CO₂ absorption-desorption performances of aqueous amine solutions in the absence and presence of CA. The absorption experiments were performed at 2 bar CO₂ pressure, in the temperature range of 303 K and amine concentration range of 0.1-0.5M AMPD (or AEPD). The CO₂ loadings and initial absorption rates were calculated in the absence and presence of 0.1 g/L CA. The desorption performances were investigated at 333 K and 1 bar N₂ pressure. The reusability of the aqueous amine solvents and the enzyme deactivation were also examined by performing 5 absorption-desorption cycle and were analyzed by Fourier transform infrared spectrometry (FTIR).

Furthermore, besides the biocatalytic CO₂ capture by CA, conversion of CO₂ into solid CaCO₃ using CA was studied in gas-liquid stirred cell contact reactor. Equal volumes of aqueous SHA and calcium chloride solution were mixed with 0.1 g/L CA. The precipitation formed after 30 min was recovered by centrifugation. The surface morphology and compositions of the precipitated solid crystals were studied using scanning electron microscopy (SEM) and X-ray diffraction (XRD), respectively. Chemical bonds and functional groups in the precipitates were analysed by Fourier transform infrared (FTIR). CaCO₃ production from CO₂ was observed by using a green biocatalyst CA.

Keywords. Carbonic anhydrase, CO₂ capture and utilization, equilibrium solubility, global warming, steric hindered amines

Determination of Geographical Origin in Alcoholic Beverages Using Vibrational Spectroscopy and Chemometrics

Didem Peren Aykas Çinkiliç¹

¹didem.cinkilic@adu.edu.tr, Department of Food Engineering, Faculty of Engineering, Aydın Adnan Menderes University, Aydın, Turkey

Abstract

The alcoholic beverages industry is an economically important and continuously growing area. However, determining the geographical origin, alcohol content, and purity are the main problems in this industry, and the price of an alcoholic beverage directly correlates with those factors. The geographical origin (indications) of an alcoholic beverage identifies the origin in the territory of a country or the region or locality in that territory. There are around 240 registered geographical indications for alcoholic beverages in the European Union. Traditional methods, including gas chromatography (GC), mass spectrometry (MS), MS coupled with GC or high-pressure liquid chromatography (HPLC), nuclear magnetic resonance spectroscopy (NMR) with the electronic nose (e-nose), electronic tongue (e-tongue), colorimetric sensor array, fluorescence, and UV-vis spectroscopy, are widely used techniques to determine the geographical origin of the alcoholic beverages. However, being time-consuming, expensive, requiring a large amount of solvent or gas, and requiring a well-trained analyst make these techniques less appealing and do not satisfy the global industry to meet the growing demand of alcoholic beverage production. To respond to the changes in the market demands quickly, it is crucial to find a quick, easy-to-use, sensitive, robust, and relatively cheap analysis technique that authenticates the samples in real-time and allows field-based applications. Vibrational spectroscopy (near-infrared, mid-infrared, and Raman) combined with chemometrics show excellent potential for real-time surveillance of alcoholic beverage authentication for geographical origin. Furthermore, with the developments in micro-electro-mechanical systems, semiconductor detectors, optical fibers, solid-state lasers, and microprocessors, miniaturized portable and handheld units were manufactured, and it is possible to analyze the samples on the field, in the production lines, or even in the markets.

Keywords. Alcoholic beverages, Chemometrics, Geographical origin, Vibrational spectroscopy

Determination of Some Quality Parameters of Cheese by Portable FT-NIR Combined with PLSR

Ahmed Menevseoglu ^{1*}{0000-0003-2454-7898}

¹amenevseoglu@gumushane.edu.tr Department of Food Engineering, Faculty of Engineering and Natural Sciences, Gümüşhane University, Gümüşhane, Turkey

Abstract

Quality control analysis of cheese and derivatives require high-cost instrumentation, lengthy and detailed sample preparation, and high skilled personnel. Therefore, rapid, cost-effective, and more convenient analytical technologies are needed in the quality control analysis. NIR spectroscopy have been frequently used in the dairy industry as an alternative to traditional methods. NIR spectroscopy techniques are easy to operate, non-invasive, and rapid for real-time assessments as well as cheaper alternatives to traditional methods. With the development of technology, handheld and portable FT-NIR spectrometers are available in the market. Portable vibrational spectrometers can be used not only for the detection of adulterated cheese but also determination of quality parameters. These units provide sensitive, high throughput, and rapid information of the cheese and their possible adulteration. NIR spectra was very accurate for protein, fat, salt, dry matter, moisture, and ash content of cheeses. PLSR models developed for textural parameters, nitrogen fractions, and ripening index coefficients did not show a good correlation between NIR spectra and reference results. Still, NIR spectroscopy techniques show great potential for real time surveillance to determine the quality parameters of cheeses.

Keywords. FT-NIR, Cheese, Quality parameters, Rapid determination, PLSR

Investigation of Properties of Renewable Films Prepared With Aloe Vera Gel

Ulku Soydal¹(0000-0001-8894-3940), Murat Yıldırım¹(0000-0002-4541-3752), Merve Ceren Okcuoglu^{1*} (0000-0001-8217-6306)
and Gulnare Ahmetli²(0000-0002-9381-4139)

¹ usoydal@selcuk.edu.tr, Selcuk University, Department of Biotechnology, Konya/Turkey,

¹ muratyildirim@selcuk.com.tr, Department of Biotechnology, Selcuk University, Konya/Turkey,

¹cerenokcuoglu@gmail.com, Department of Biotechnology, Selcuk University, Konya/Turkey,

²gahmetli@ktun.edu.tr, Konya Technical University, Department of Chemical Engineering,
Konya/Turkey

Aloe vera plant, known as yellow patience in Turkey, is a plant known for centuries in many ancient civilizations and used in various diseases and skin problems due to its healing power. Among its many health benefits, wound healing mainly, hypoglycemic or antidiabetic, hepatoprotective, anti-inflammatory, immune-boosting and gastroprotective, antioxidant, antimicrobial, antiviral and antifungal properties have also been reported. On the other hand, most of the monomers of polymer films produced in the industrial field are of petroleum origin. The fact that the depleting petroleum resources are both expensive and bring environmental problems such as waste problems lead scientists to seek cheaper and renewable resources. Therefore, synthesis studies of bio - based polymeric materials from different renewable sources such as oil - based sources are becoming increasingly important. In this study, aloe vera plant gel (AV), was used as a modifier for the preparation of film materials in biobased acrylated epoxidized soybean oil (AESO) resin matrix. Films were formed by adding aloe vera gel at different ratios (0 %, 10 %, 20 %, 30 %, 40 %, 50 % by weight). The effect of AV amount on pH change, swelling – solubility - water content, antibacterial and mechanical properties of the films were investigated. The prepared AV / AESO films were effective against Gram - positive (*Staphylococcus aureus* and *Enterococcus faecalis*) and Gram - negative (*Escherichia coli* and *Klebsiella pneumoniae*) bacteria. Finally, from the pH tests performed on the films, values between 7.23 and 7.35 were obtained. Accordingly, it showed that the films were compatible with the skin.

Keywords: Aloe Vera Gel, Antibacterial Activity, Biobased Film

An Experimental and Simulation Analysis of A Single-Cylinder Diesel Engine Fuelled by C2 Alcohol and Nano-Sized Materials

Ümit Ağbulut ^{1*} [0000-0002-6635-6494]

¹ umitagbulut@duzce.edu.tr, Department of Mechanical Engineering, Faculty of Engineering, Düzce University, 81620, Düzce, Turkey.

Abstract

In this study, it is aimed to reach the performance and emission data obtained from a single-cylinder, direct-injection, 4-stroke diesel engine by using the simulation software. With this framework, three different fuels were formed in the study. First, the experiments were carried out with conventional diesel fuel (DF) without any additives, then 10% by volume of 2-carbon alcohol was blended into the DF fuel (DF+C2). Finally, in the same tests, 100 ppm titanium oxide nanoparticles were doped into DF+C2 fuel (DF+C2+TiO₂). The experiments were carried out under varying engine loads and at a constant engine speed. In the results, the difference between the simulation software and the recorded BSFC values are found to be 4.83% for DF, 10.07% for DF+C2, and 6.04% for DF+C2+TiO₂ test fuel. On the other hand, the difference for NO_x emission is calculated to be 5.73% for DF, 3.74% for DF+C2, and 2.59% for DF+C2+TiO₂ test fuel. Overall, it is seen that the costly and time-consuming experimental results can be achieved within acceptable limits in the simulation environment.

Keywords. Engine performance, nanofuel, NO_x emission, fuel consumption, C2 alcohol

1. Introduction

Fossil fuels have finite reserves and are in danger of being completely depleted over time. However, 86% of the world's primary energy needs are met from fossil fuels (Abas et al., 2015). This situation makes one think about how the energy demand of all systems driven by fossil fuels can be met globally in the near future and forces policymakers to adopt some strict rules on this issue. In addition to the effects of fossil fuels on the country's economies, their effects on the environment are also very noticeable today and fossil fuels are not among the clean/environmental energy sources (Zhou et al., 2019, Dada et al., 2018, Rana et al., 2017). It is also known that when fossil fuels are burned in internal combustion engines, many harmful exhaust emissions are released into the atmosphere and cause air pollution. Changing and tightening emission norms and increasing concerns with negative environmental impacts in recent years encourage researchers to look for new and renewable energy sources. In this context, researchers have recently tested many fuel types as alternatives to conventional fuels in internal combustion engines (Bae et al., 2017, Ardebili et al., 2020, Verhelst et al., 2019, Leach et al., 2020).

Undoubtedly, biofuels are the most widely accepted fuel type in the literature as an alternative to conventional diesel fuel. However, there are some important disadvantages of using biofuels. For example, the viscosities of biodiesels are quite high compared to conventional diesel fuels. High viscosity adversely affects the fuel's injection characteristics and atomization stage, resulting in negative effects on engine performance. In addition, the energy contents of biodiesels are lower compared to conventional diesel fuels and the unit costs of biodiesels are higher than conventional fuels today (Firoz S., 2017, Lawan et al., 2020, Priyadarshi et al., 2019, Pham et al., 2018). These negativities have led researchers working on fuel to look for different fuel additives.

In recent years, with the developing technology, the production of materials in very small sizes (such as nano and micro) has become easier. It is stated in many studies that nanomaterial additives can have a good catalyst effect in the recovery of combustion thanks to the increased surface area/volume ratio, increased radiation / mass transfer properties, and good ignition properties (Leach et al., 2021, Karagöz et al., 2020, Ağbulut et al., 2020, Chen et al., 2018, Mei et al., 2019). Although it has been stated in many studies that nanoparticles significantly improve the fuel properties and combustion process, thanks to their superior properties, there is an issue that should not be ignored, which is that nanoparticles are very expensive materials and therefore researchers have difficulties in experimental studies. In order to solve this problem,



various software has been started to be used and developed by researchers recently. One of the most important of these software is Diesel RK software specially designed to simulate and optimize the working processes of one, two, and four-stroke internal combustion engines (Al-Dawody et al., 2019, Rajak et al., 2019, Raju et al., 2020). In this study, 3 types of fuel are modeled in Diesel RK software. The tests were conducted under a constant engine speed of 2400 rpm and at the different engine loads (3, 6, 9, and 12 Nm).

2. Material Method

In this study three different test fuels were designed. These are conventional diesel fuel (DF), alcohol added test fuel (DF+C2) obtained by adding 10% alcohol to diesel fuel volumetrically, and TiO₂ added test fuel (DF+C2+TiO₂) obtained by adding 100 ppm titanium oxide to alcohol added test fuel with mass fraction. Due to the precipitation problem of nanoparticles, the homogeneity of the prepared test fuels was ensured first with a mechanical stirrer and then with the help of an ultrasonic bath. Table 1 shows some characteristics of the fuels used and Table 2 shows the specific characteristics of the test engine.

Table 1: Test Fuels and Some Specific Properties.

Property	DF	DF+C2	DF+C2+TiO ₂
Density (g/L; @15°C)	825	821.5	821.6
Cetane number	54.12	52.44	53.24
Viscosity, (cSt @40°C)	2.5	2.7	2.8
Calorific value (MJ/kg)	43.2	41.7	42.3

Table 2: Technical Specifications of The Test Engine.

Model	Lombardini 15 LD 350
Engine type	Naturally-aspirated, air-cooled, DI diesel engine
Number of cylinders	1
Maximum power	7.5 HP/3600 rpm
Maximum torque	16.6 Nm/2400 rpm
Displacement	349 cm ³
Compression ratio	20.3/1
Bore*stroke	82 mm*66mm
Injection nozzle	0.22*4 holes*160°
Nozzle opening pressure	207 bar

In the experimental side of the study, the brake specific fuel consumption is calculated by using the Equations 1 and 2.

$$P_e = \frac{2\pi \cdot \omega \cdot T}{1000} \quad (1)$$

$$BSFC = \frac{\dot{m}_f \cdot 10^6}{P_e} \quad (2)$$

In Equation 1, P_e is the brake power (kW), ω is the angular velocity (s⁻¹), and T refers to torque value (Nm). On the other hand, In Equation 2, \dot{m}_f shows the fuel flow consumption (g.s⁻¹). While creating the simulation model, first of all, the general characteristics and structural features of the engine are defined. Afterward, fuel modeling is done by entering the required properties (viscosity, calorific value, cetane number, density, etc.) of the fuel or fuels to be used in the test. Finally, the simulation model is created by selecting the PM emission model, NO_x emission model, heat release model, fuel evaporation model, and fuel beam model. Figure 1 shows the ways to create a project by entering the structural features of the engine.

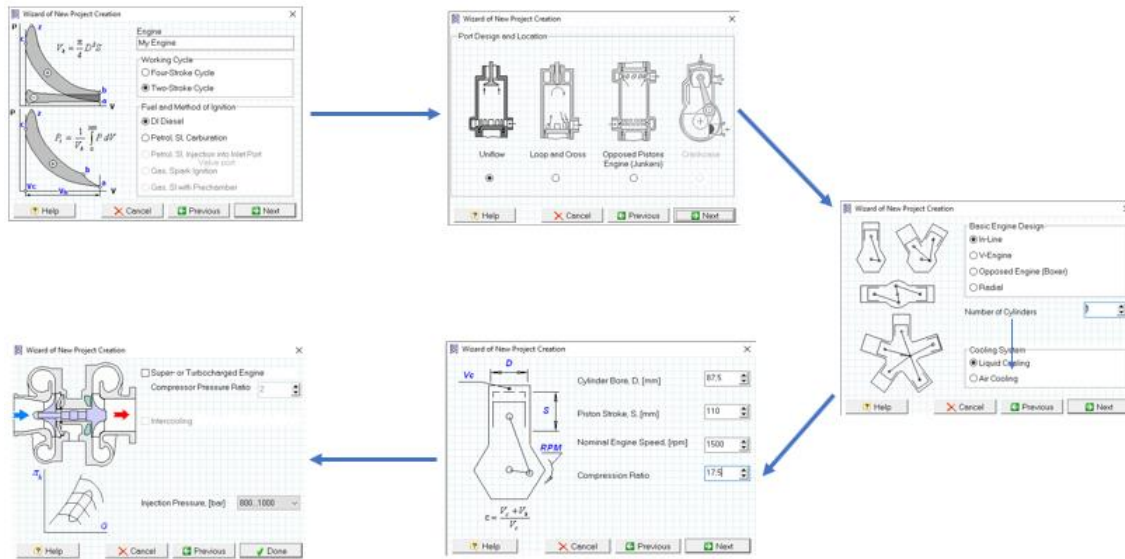


Figure 1: Project Creation Steps with Diesel RK Software.

3. Result and Discussion

Change on brake specific fuel consumption (BSFC) of each test fuel is illustrated in Figure 2 according to varying engine load. BSFC refers to the rate of mass fuel consumption to the brake power in tested fuel (Gumus et al., 2012; Sayin et al., 2010). From the figure, it is seen that there is an opposite trend between BSFC and engine load for each test fuel. That is, the BSFC value for each test fuel starts to be decreased with an increase in the engine load, and it reaches its minimum value of 12 Nm for each test fuel. Accordingly, the BSFC value in that engine load is found to be 266 g/kWh, 280 g/kWh, and 264 g/kWh. As can be seen from the figure, the BSFC value increases with the addition of C2 alcohol to the conventional diesel fuel. The reason behind it can be explained by the calorific value of the C2 alcohol. From Table 1, it is seen that the calorific value of C2 alcohol is lower than that of DF. In this case, more fuel should be sprayed into the combustion chamber for the achievement of the same engine response, leading to an increment in BSFC with the C2 alcohol. However, the addition of titanium dioxide nanoparticles into the C2+DF binary fuel pulls back the BSFC value. This is also due to the high energy density and high catalytic role of nanoparticles. Furthermore, a large surface area to volume ratio, as well as superior thermal properties of nanoparticles, leads to the reduction of BSFC. Accordingly, it can be seen in Figure 2, the lowest BSFC value in any engine load is obtained for TiO₂+C2+DF test fuel, while the lowest one is obtained for C2+DF test fuel.

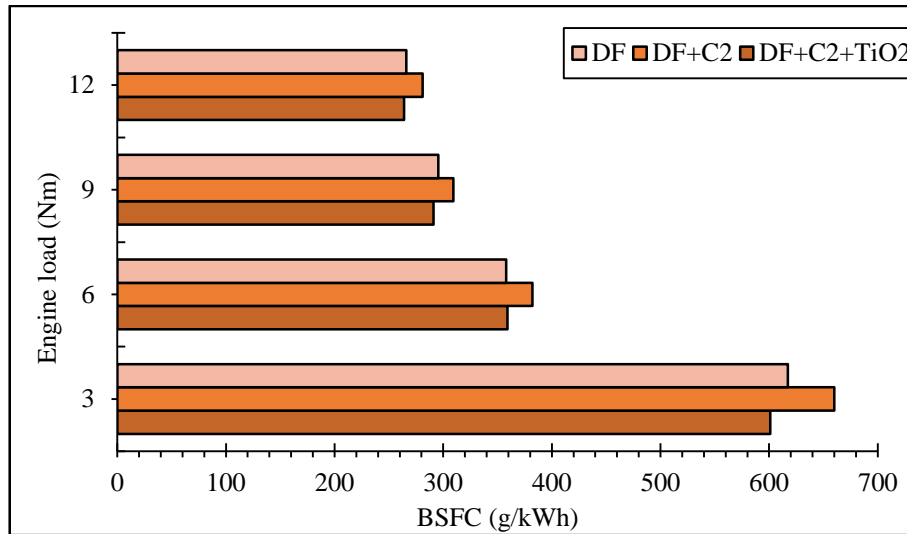


Figure 2: Brake Specific Fuel Consumption of Test Fuel According to Engine Load.

In the study, the BSFC value is calculated from the recorded values from the experimental side of the paper. Then the combustion chamber and test fuel properties are simulated on the simulation software with the aid of Diesel-RK software. Accordingly, Figure 3 gives the simulation and experimental BSFC results of DF test fuel together.

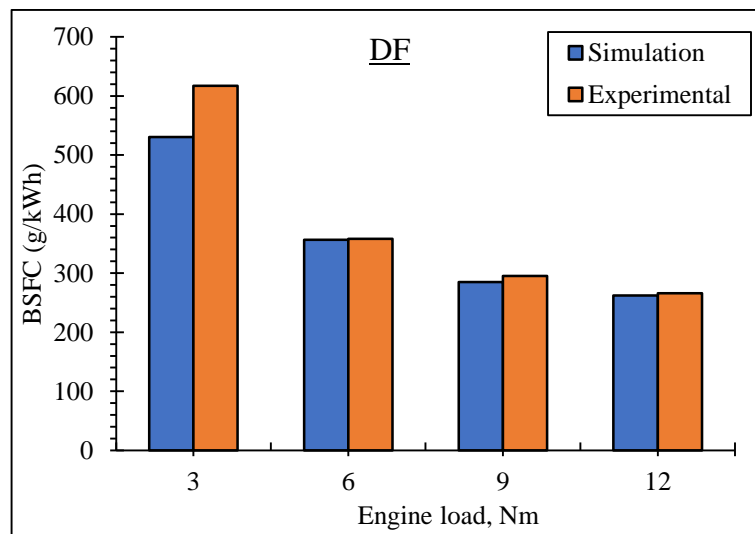
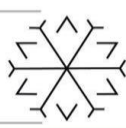


Figure 3: Simulation and Experimental BSFC Results for DF Test Fuel at Varying Engine Loads.

As can be seen in Figure 3, the simulation results for DF test fuel closely follow the experimental results, and have exhibited a very high R^2 value of 0.9905. The biggest difference between the simulation and experimental results is noticed in 3 Nm, and the error magnitudes between the simulation and experimental results considerably decrease as the engine load increases. This may be due to the numerical value of BSFC in 3 Nm. In that engine load, the numerical value of BSFC receives its highest value, and therefore the error magnitudes are relatively higher than that of remaining engine loads. Another reason can be attributable to the complex, non-linear combustion behavior, particularly at low engine loads. Accordingly, the error percentage of simulation results according to the experimental results are calculated to be 14.06%, -0.42%, -3.49%, and -1.36% at 3, 6, 9, and 12 Nm, respectively. Given that all engine loads together, the absolute average error percentage for DF test fuel is equal to 4.83%.

Figure 4 illustrates the simulation and experimental BSFC results for DF+C2 test fuel at varying engine loads. As can be seen in Figure 4, the simulation and experimental results have good fitting curves, and the R^2 value between the simulation and experimental result is calculated to be 0.9830. Similar to that of DF test fuel, the biggest error magnitude is obtained in 3 Nm. In this engine load, the error magnitude is



calculated to be 90.22 g/kWh. The error magnitudes in 6, 9, and 12 Nm are, on the other hand, calculated to be 39.1 g/kWh, 48.16 g/kWh, and -2.22 g/kWh. Given that the simulation and experimental results in all engine load together, the absolute average error percentage for DF+C2 test fuel is equal to 10.07%.

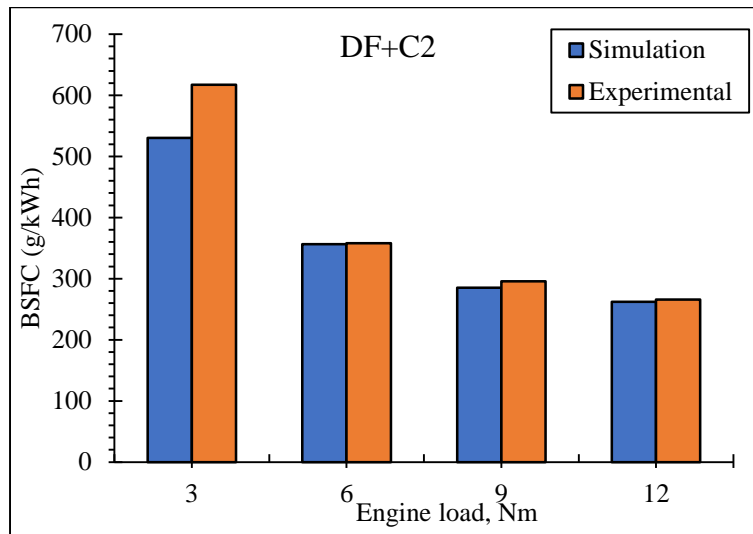


Figure 4: Simulation and Experimental BSFC Results for DF+C2 Test Fuel at Varying Engine Loads.

In Figure 5, the BSFC results from simulation and experiments are given according to the varying engine loads. The R^2 value between experimental and simulation BSFC results test fuel is calculated to be 0.9984 for DF+C2+TiO₂ test fuel. The error magnitude of simulation results is found to be 69 g/kWh at 3 Nm, 8 g/kWh at 6 Nm, -17 g/kWh at 9 Nm, and -13 g/kWh at 12 Nm. Considering the simulation and experimental results in all engine loads together, the absolute average error percentage for DF+C2+TiO₂ test fuel is equal to 6.04%.

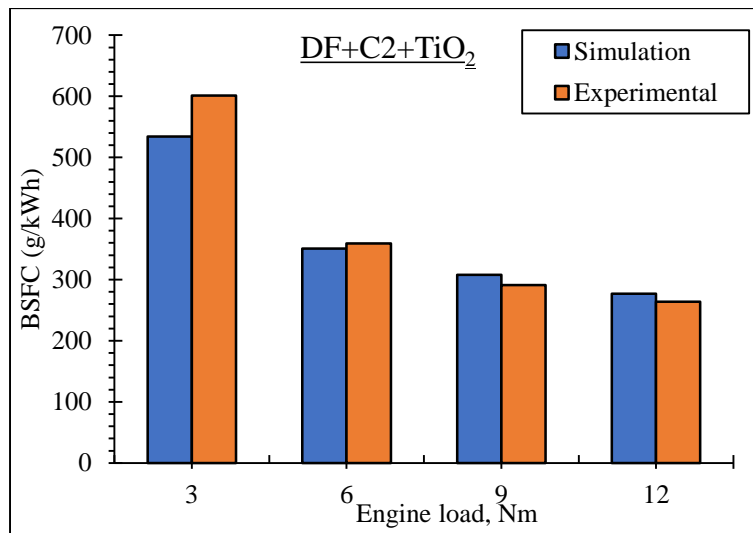


Figure 5: Simulation and Experimental BSFC Results for DF+C2+TiO₂ Test Fuel at Varying Engine Loads.

Another assessed engine response in the present research is nitrogen oxide (NO_x) emissions. Variation of simulation and experimental NO_x emissions is shown in Figure 6 with respect to varying engine load. NO_x emission is one of the biggest contributors to greenhouse gases, climate change as well as ozone depletion, and a respectable share of NO_x in the atmosphere is due to the burning of fossil fuels in diesel engines (Balasubramanian et al., 2021; Clairotte et al., 2020; Reşitoğlu, 2018; Yang et al., 2020). The main reasons which trigger to form the NO_x emissions are the fuel properties, in-cylinder temperature, the presence of oxygen in the fuel, higher excess air ratios, the time for the complete reaction, etc (Nabi et al., 2019; Ge et al., 2020; Appavu et al., 2019; Sezer, 2018; Manigandan et al., 2020; Verma et al., 2018). As can be seen from the relevant figure, the NO_x emission gradually increases with the parallel to the increment in the engine load. Probably, the reason behind the increment in NO_x emission can be attributable to the



increasing fuel consumption at elevated engine loads. As the engine load increases, the fuel consumption also increases. As a consequence of high fuel consumption, the in-cylinder temperature at high engine loads increases. This case results in a high chemical reaction activity for nitrogen and oxygen atoms and increases the NO_x levels in high engine loads. Similar results were also reported by the previous papers (Chen et al., 2018; Shameer and Ramesh, 2017; Zhang et al., 2017; Zare et al., 2021). As the nanoparticle is present in the test fuel, the NO_x emission pulls back. Probably, this case can be attributable to the lowered fuel consumption, leading to decreasing cylinder temperature. Another reason why NO_x reduces with the presence of nanoparticles can be due to the high thermal properties of nanoparticles, and large surface area to volume ratio, resulting in rapid heat transfer from the combustion chamber. All these may contribute to the reduction of NO_x emissions with the presence of nanoparticles in test fuels. Similar results were also reported by the fuel researcher (Tosun et al., 2017; Venu et al., 2019; Vigneswaran et al., 2021; Praveen et al., 2018; Nanthagopal et al., 2021).

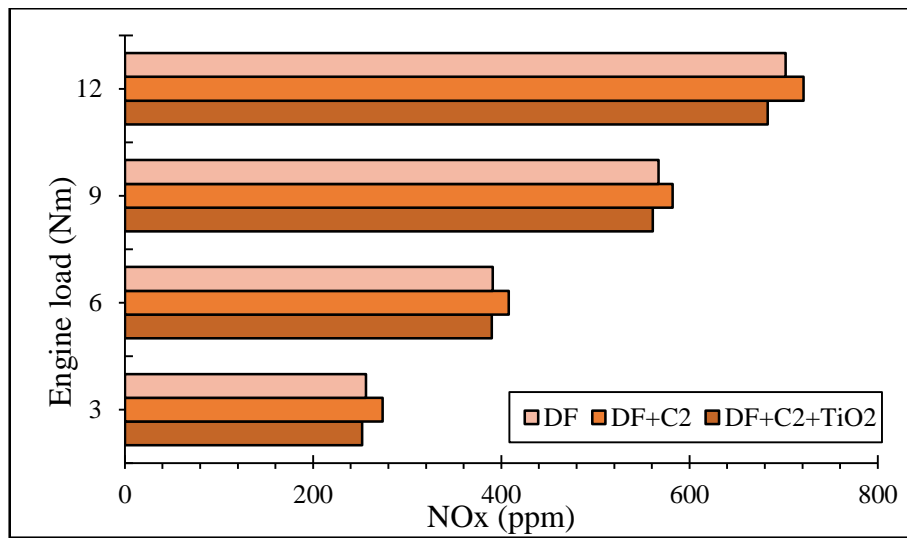


Figure 6: Recorded NO_x Emission of Test Fuels According to Engine Load.

In Figure 7, the NO_x emission levels gathered from the experiments and simulation software are illustrated for DF test fuel according to the varying engine load. Simulation software presents satisfying results and has a very high R² value of 0.9803. The error magnitudes in 3, 6, 9, and 12 Nm are equal to 17.68 ppm, -9.46 ppm, 26.78 ppm, and -62.18 ppm, respectively. Accordingly, given that the simulation and experimental results in all engine loads together, the absolute average error percentage for DF test fuel is equal to 5.73%.

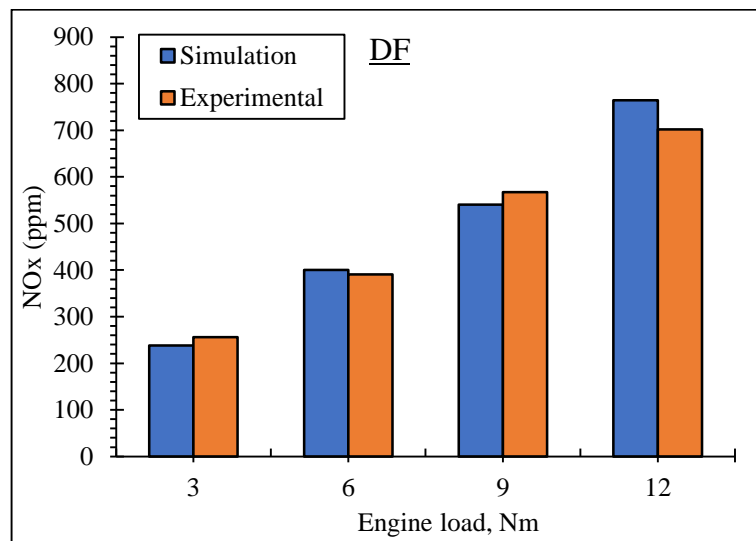


Figure 7: Simulation and Experimental NO_x Emissions for DF Test Fuel at Varying Engine Loads.

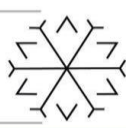


Figure 8 illustrates the simulation and experimental NOx emissions at varying engine loads. As can be seen in Figure 8, the simulation and experimental results have good fitting curves, and the R^2 value between the simulation and experimental result is calculated to be 0.9959. Just as the results for DF test fuel, The biggest error magnitudes are also obtained in the 12 Nm where recorded the highest NOx emission. Error magnitudes of DF+C2 test fuel in terms of NOx emission are equal to 13.58 ppm in 3 Nm, 29.47 ppm in 6 Nm, -12.43 ppm in 9 Nm, and -4.78 ppm in 12 Nm. On the other hand, considering all NOx emission results in all engine loads together, the absolute error percentage is calculated to be 3.74%.

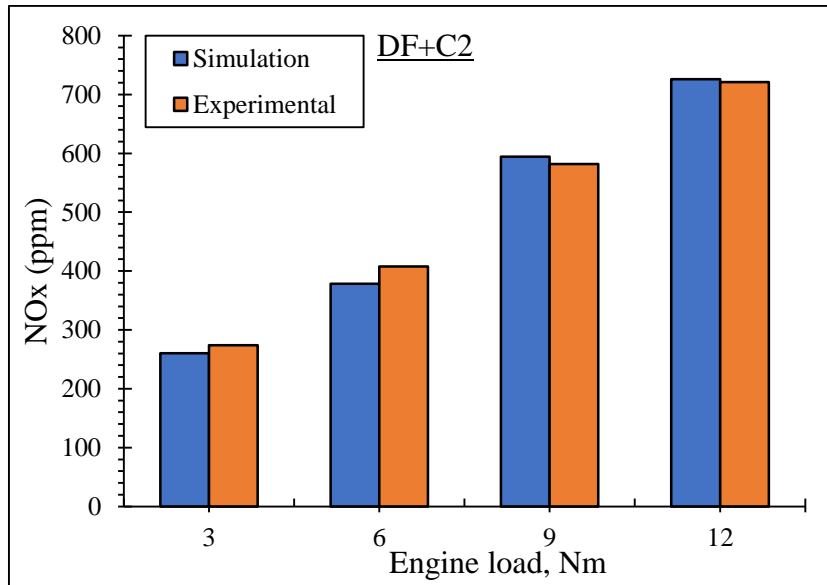


Figure 8: Simulation and Experimental NOx Emissions for DF+C2 Test Fuel at Varying Engine Loads.

Finally, the simulation and experimental NOx emission results are illustrated in Figure 9 for DF+C2+TiO₂ test fuel at varying engine loads. The R^2 value between the experimental and simulation results is 0.9898 for this test fuel. For nanoparticle added test fuel, the lowest error percentage in each engine load is generally achieved among all test fuels. Accordingly, the error magnitude of this test fuel is equal to 4 ppm in 3 Nm, 5 ppm in 6 Nm, -28 ppm, and 17 ppm in 12 Nm. Considering the results in all engine loads together, the absolute error percentage for DF+C2+TiO₂ test fuel is equal to 2.59%.

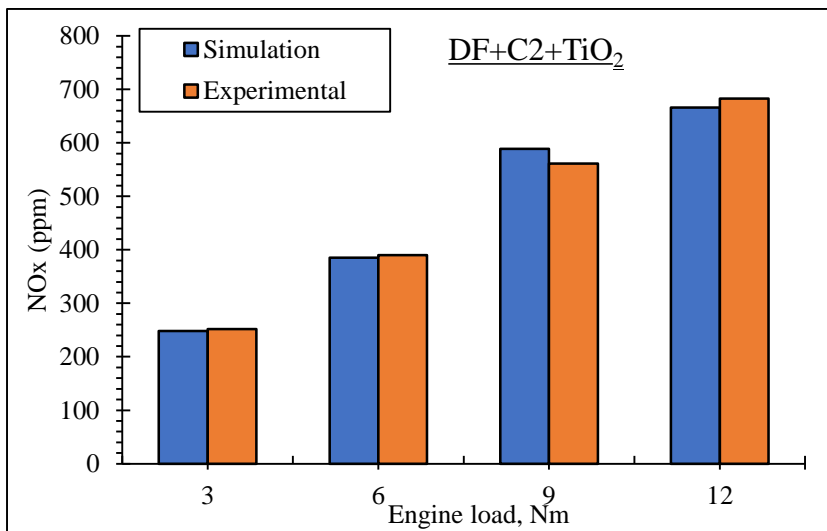


Figure 9: Simulation and Experimental NOx Emissions for DF+C2+TiO₂ Test Fuel at Varying Engine Loads.

4. Conclusion

In this study, brake-specific fuel consumption and nitrogen oxide emissions were recorded for different fuel types in a single-cylinder, direct-injection engine. The tests were conducted at varying engine load and a



constant engine speed. The present study aimed to achieve experimental results in a simulation environment by integrating engine specification and fuel properties into Diesel-RK software. In this framework, the results achieved from the study are briefly given below.

- It is noticed that there is an opposite trend between the BSFC and NO_x emissions. As the engine load increases, the BSFC value decreases, whilst the NO_x emission gradually increases. Probably, the fundamental reason behind the increment of NO_x emission can be associated with the increasing cylinder temperature in high engine load. As the fuel consumption increases, the in-cylinder temperature also increases, leading to high chemical activity for nitrogen and oxygen reaction.
- With the presence of alcohol in the DF test fuel, the BSFC increases. That is because the lower heating value of alcohol is lower than that of DF test fuel. Another reason may be attributable to the high viscosity value of alcohols as compared to that of DF, leading to poor atomization of fuel droplets as well as worsening combustion efficiency.
- As the nanoparticles dope to the alcohol added test fuel, the BSFC starts to improve. This case can be explained by the high energy density of nanoparticles, high catalytic roles, and large surface area to volume ratio.
- Given that the results obtained from the simulation software and the experiments, very satisfactory results were achieved particularly in terms of NO_x emission. The difference between experimental and simulation NO_x emissions is equal to 5.73% for DF, 3.74% for DF+C2, and 2.59% for DF+C2+TiO₂ test fuel.
- Considering the BSFC results in all engine loads together, the difference between experimental and simulation results is equal to 4.83% for DF, 10.07% for DF+C2, and 6.04% for DF+C2+TiO₂ test fuel.

As a result, in light of the data obtained from the study, it is possible to say that the experimental results can be reached with a very low error in the simulation environment. In today's technology, especially considering the high costs of nanoparticles and the time-consuming experimental applications, fuel consumption and exhaust emissions can be successfully obtained in a computer environment by designing the experiment with Diesel-RK software.

References

- Abas, N., Kalair, A., and Khan, N., 2015. Review of fossil fuels and future energy technologies. *Futures*, 69, (pp. 31-49).
- Ağbulut, Ü., Karagöz, M., Sarıdemir, S., and Öztürk, A., 2020. Impact of various metal-oxide based nanoparticles and biodiesel blends on the combustion, performance, emission, vibration and noise characteristics of a CI engine. *Fuel*, 270, 117521.
- Al-Dawody, M. F., Jazie, A. A., and Abbas, H. A., 2019. Experimental and simulation study for the effect of waste cooking oil methyl ester blended with diesel fuel on the performance and emissions of diesel engine. *Alexandria Engineering Journal*, 58(1), pp. 9-17.
- Appavu, P., Jayaraman, J., and Venu, H., 2019. NO_x emission reduction techniques in biodiesel-fuelled CI engine: a review. *Australian Journal of Mechanical Engineering*, 19(2), pp. 210-220.
- Ardebili, S. M. S., Solmaz, H., İpci, D., Calam, A., and Mostafaei, M., 2020. A review on higher alcohol of fusel oil as a renewable fuel for internal combustion engines: Applications, challenges, and global potential. *Fuel*, 279, 118516.
- Bae, C., and Kim, J., 2017. Alternative fuels for internal combustion engines. *Proceedings of the Combustion Institute*, 36(3), pp.3389-3413.
- Balasubramanian, D., Hoang, A. T., Venugopal, I. P., Shanmugam, A., Gao, J., and Wongwuttanasatian, T., 2021. Numerical and experimental evaluation on the pooled effect of waste cooking oil biodiesel/diesel blends and exhaust gas recirculation in a twin-cylinder diesel engine. *Fuel*, 287, 119815.
- Balasubramanian, D., Hoang, A. T., Venugopal, I. P., Shanmugam, A., Gao, J., and Wongwuttanasatian, T., 2021. Numerical and experimental evaluation on the pooled effect of waste cooking oil biodiesel/diesel blends and exhaust gas recirculation in a twin-cylinder diesel engine. *Fuel*, 287, 119815.
- Chen, A. F., Adzmi, M. A., Adam, A., Othman, M. F., Kamaruzzaman, M. K., and Mrwan, A. G., 2018. Combustion characteristics, engine performances and emissions of a diesel engine using nanoparticle-diesel



fuel blends with aluminium oxide, carbon nanotubes and silicon oxide. *Energy Conversion and Management*, 171, pp. 461-477.

Chen, H., Xie, B., Ma, J., and Chen, Y., 2018. NO_x emission of biodiesel compared to diesel: Higher or lower?. *Applied Thermal Engineering*, 137, pp. 584-593.

Clairotte, M., Suarez-Bertoa, R., Zardini, A. A., Giechaskiel, B., Pavlovic, J., Valverde, V., ... and Astorga, C. (2020). Exhaust emission factors of greenhouse gases (GHGs) from European road vehicles. *Environmental Sciences Europe*, 32(1), pp. 1-20.

Dada, O., and Mbohwa, C., 2018. Energy from waste: A possible way of meeting goal 7 of the sustainable development goals. *Materials Today: Proceedings*, 5(4), pp. 10577-10584.

Firoz, S., 2017. A review: advantages and disadvantages of biodiesel. *International Research Journal of Engineering and Technology*, 4(11), pp. 530-533.

Ge, J. C., Kim, H. Y., Yoon, S. K., and Choi, N. J., 2020. Optimization of palm oil biodiesel blends and engine operating parameters to improve performance and PM morphology in a common rail direct injection diesel engine. *Fuel*, 260, 116326.

Gumus, M., Sayin, C., and Canakci, M., 2012. The impact of fuel injection pressure on the exhaust emissions of a direct injection diesel engine fueled with biodiesel–diesel fuel blends. *Fuel*, 95, pp. 486-494.

Karagöz, M., Ağbulut, Ü., and Sarıdemir, S., 2020. Waste to energy: Production of waste tire pyrolysis oil and comprehensive analysis of its usability in diesel engines. *Fuel*, 275, 117844.

Lawan, I., Zhou, W., Idris, A. L., Jiang, Y., Zhang, M., Wang, L., and Yuan, Z., 2020. Synthesis, properties and effects of a multi-functional biodiesel fuel additive. *Fuel Processing Technology*, 198, 106228.

Leach, F. C., Davy, M., and Terry, B., 2021. Combustion and emissions from cerium oxide nanoparticle dosed diesel fuel in a high speed diesel research engine under low temperature combustion (LTC) conditions. *Fuel*, 288, 119636.

Leach, F., Kalghatgi, G., Stone, R., and Miles, P., 2020. The scope for improving the efficiency and environmental impact of internal combustion engines. *Transportation Engineering*, 1, 100005.

Manigandan, S., Atabani, A. E., Ponnusamy, V. K., Pugazhendhi, A., Gunasekar, P., and Prakash, S., 2020. Effect of hydrogen and multiwall carbon nanotubes blends on combustion performance and emission of diesel engine using Taguchi approach. *Fuel*, 276, 118120.

Mei, D., Zuo, L., Adu-Mensah, D., Li, X., and Yuan, Y., 2019. Combustion characteristics and emissions of a common rail diesel engine using nanoparticle-diesel blends with carbon nanotube and molybdenum trioxide. *Applied Thermal Engineering*, 162, 114238.

Nabi, M. N., Rasul, M. G., Anwar, M., and Mullins, B. J., 2019. Energy, exergy, performance, emission and combustion characteristics of diesel engine using new series of non-edible biodiesels. *Renewable energy*, 140, pp. 647-657.

Nanthagopal, K., Ashok, B., Tamilarasu, A., Johny, A., and Mohan, A., 2017. Influence on the effect of zinc oxide and titanium dioxide nanoparticles as an additive with Calophyllum inophyllum methyl ester in a CI engine. *Energy Conversion and Management*, 146, pp. 8-19.

Pham, M. T., Hoang, A. T., Le, A. T., Al-Tawaha, A. R. M. S., Dong, V. H., and Le, V. V., 2018. Measurement and prediction of the density and viscosity of biodiesel blends. *Int. J. Technol*, 9(5), pp. 1015-1026.

Praveen, A., Rao, G. L. N., and Balakrishna, B., 2018. Performance and emission characteristics of a diesel engine using Calophyllum inophyllum biodiesel blends with TiO₂ nanoadditives and EGR. *Egyptian journal of petroleum*, 27(4), pp. 731-738.

Priyadarshi, D., Paul, K. K., and Pradhan, S., 2019. Impacts of biodiesel, fuel additive, and injection pressure on engine emission and performance. *Journal of Energy Engineering*, 145(3), 04019006.

Rajak, U., Nashine, P., Verma, T. N., and Pugazhendhi, A., 2019. Performance, combustion and emission analysis of microalgae Spirulina in a common rail direct injection diesel engine. *Fuel*, 255, 115855.

Raju, V. D., Venu, H., Subramani, L., Kishore, P. S., Prasanna, P. L., and Kumar, D. V., 2020. An experimental assessment of prospective oxygenated additives on the diverse characteristics of diesel engine powered with waste tamarind biodiesel. *Energy*, 203, 117821.



- Rana, M. S., Vinoba, M., and AlHumaidan, F. S., 2017. Sustainability challenges in oil and gas development in the Middle East and North Africa. *Current Sustainable/Renewable Energy Reports*, 4(4), pp. 232-244.
- Reşitoğlu, İ. A., 2018. NO_x Pollutants from Diesel Vehicles and Trends in the Control Technologies. In *Diesel and Gasoline Engines*. pp. 161-176. IntechOpen.
- Sayin, C., Ozsezen, A. N., and Canakci, M., 2010. The influence of operating parameters on the performance and emissions of a DI diesel engine using methanol-blended-diesel fuel. *Fuel*, 89(7), pp. 1407-1414.
- Sezer, İ., 2018. A review study on the using of diethyl ether in diesel engines: Effects on NO_x emissions. *International Journal of Automotive Engineering and Technologies*, 7(4), pp. 164-183.
- Shameer, P. M., and Ramesh, K., 2017. Experimental evaluation on performance, combustion behavior and influence of in-cylinder temperature on NO_x emission in a DI diesel engine using thermal imager for various alternate fuel blends. *Energy*, 118, pp. 1334-1344.
- Tosun, E., Ozgur, T., Ozgur, C., Ozcanli, M., Serin, H., and Aydin, K., 2017. Comparative analysis of various modelling techniques for emission prediction of diesel engine fueled by diesel fuel with nanoparticle additives. *European Mechanical Science*, 1(1), pp. 15-23.
- Venu, H., Subramani, L., and Raju, V. D., 2019. Emission reduction in a DI diesel engine using exhaust gas recirculation (EGR) of palm biodiesel blended with TiO₂ nano additives. *Renewable energy*, 140, 245-263.
- Verhelst, S., Turner, J. W., Sileghem, L., and Vancoillie, J., 2019. Methanol as a fuel for internal combustion engines. *Progress in Energy and Combustion Science*, 70, pp. 43-88.
- Verma, P., Zare, A., Jafari, M., Bodisco, T. A., Rainey, T., Ristovski, Z. D., and Brown, R. J., 2018. Diesel engine performance and emissions with fuels derived from waste tyres. *Scientific reports*, 8(1), pp. 1-13.
- Vigneswaran, R., Balasubramanian, D., and Sastha, B. S., 2021. Performance, emission and combustion characteristics of unmodified diesel engine with titanium dioxide (TiO₂) nano particle along with water-in-diesel emulsion fuel. *Fuel*, 285, 119115.
- Yang, Z., Liu, Y., Wu, L., Martinet, S., Zhang, Y., Andre, M., and Mao, H., 2020. Real-world gaseous emission characteristics of Euro 6b light-duty gasoline-and diesel-fueled vehicles. *Transportation Research Part D: Transport and Environment*, 78, 102215.
- Zare, A., Bodisco, T. A., Jafari, M., Verma, P., Yang, L., Babaie, M., ... and Stevanovic, S., 2021. Cold-start NO_x emissions: Diesel and waste lubricating oil as a fuel additive. *Fuel*, 286, 119430.
- Zhang, C., Zhou, A., Shen, Y., Li, Y., and Shi, Q., 2017. Effects of combustion duration characteristic on the brake thermal efficiency and NO_x emission of a turbocharged diesel engine fueled with diesel-LNG dual-fuel. *Applied thermal engineering*, 127, pp. 312-318.
- Zhou, N., Price, L., Yande, D., Creyts, J., Khanna, N., Fridley, D., ... and Franconi, E., 2019. A roadmap for China to peak carbon dioxide emissions and achieve a 20% share of non-fossil fuels in primary energy by 2030. *Applied Energy*, 239, pp. 793-819.

Comparison of Experimental and Simulation Results for Alcohol and Nanofuels in CI Engines

Fikret POLAT ^{1*}[0000-0003-3767-3156]

¹fikretpolat@duzce.edu.tr, Mechanical Engineering Department, Duzce University, Duzce, Turkey

Abstract

In this paper, it is aimed to closely reach the experimental results with the Diesel-RK simulation software. For this purpose, the reference data is firstly gathered from the experimental rig. To observe the success of the simulation software in various test fuels, three test fuels are prepared in this study. The experiments are firstly done when the engine is fuelled by conventional diesel fuel. Then volumetrically 10% alcohol is blended into the conventional diesel fuel. In addition to these fuels, aluminum oxide nanoparticles at the mass fraction of 100 ppm also dope into the alcohol-blended test fuels. The tests are done at a constant crankshaft speed where the engine reaches its maximum load. Then the engine is loaded from 3 to 12 Nm with the 3 Nm intervals. In this study, there are two assessed parameters, and these are nitrogen oxide emissions (NO_x), and brake specific fuel consumption (BSFC). In the results, it is noticed that there is a reverse trend relation between these parameters. As the engine load increases from 3 Nm to 12 Nm, the NO_x emission gradually increases but the BSFC value decreases for each test fuel. Consequently, the absolute difference between the simulation and experimental results are found to be 5.73%, 3.74%, and 2.60% for NO_x emission and 4.83%, 10.07%, and 6.97% for reference fuel, alcohol-added test fuel, and Al₂O₃ nanoparticles added test fuel, respectively. In the conclusion, the present research clearly shows that the costly and time-consuming diesel engine experiments even for various based fuels can be achieved at a satisfying rate with the Diesel-RK software.

Keywords. Engine performance, exhaust emission, diesel-rk, simulation software

1. Introduction

For many years, internal combustion engines have played a dominant role as the main driving force in various sectors, especially in transport and industry (Zhao et al., 2020, Ghasemian et al., 2020, Kober et al., 2020). The rapid growth in urbanization has led to a sharp increase in the number of vehicles on urban roads, as well as the increase in the number of industrial plants and facilities in the world. Due to the twin problems of strict emission norms and depleting fossil fuel reserves, there is a natural need to search for suitable alternative fuel for the transportation sector (Yaqoob et al., 2021). The use of biodiesel, which is obtained from vegetable and animal oils, as an effective alternative fuel to petroleum-based diesel fuels in internal combustion engines has been a subject that fuel researchers and the engine community frequently dwell on (Unglert et al., 2020, Uzoh et al., 2021, Foo et al., 2021, Ge et al., 2017). It has been observed that the use of biofuels reduces CO₂, CO, SO₂, and HC emissions as it provides more complete combustion than diesel fuel due to the high oxygen content in its content (Leite et al., 2019). In addition, it is seen in the literature that the use of biofuels and their mixtures in internal combustion engines reduces engine power by approximately 5% compared to conventional diesel fuel, and increases fuel consumption and NO_x emissions (Sondors et al., 2019).

Fuel researchers have adopted various strategies to reduce NO_x emissions due to their environmental impact. Recently, the addition of nano additives to the base fuel has been one of the popular research topics. It has been observed in many experimental studies in the literature that nanoparticles significantly affect fuel properties and thus cause more efficient oxidation during combustion and therefore lower exhaust emissions (Gavhane et al., 2020, Hoseini et al., 2020, Wu et al., 2018). In addition to the many advantages, nanoparticles are still more costly products due to being a new technology and the situation makes it difficult for fuel researchers to conduct experimental studies.

Today, developments in the field of computer technology enable the numerical solution of many problems and significantly reduce costs by enabling fewer experiments. Various software continues to be used and developed by researchers. The most important of this software is the Diesel RK software, which is specially designed to imitate and optimize the working processes of one, two, and four-stroke internal combustion engines. In this study, 3 types of fuel are modeled in Diesel RK software. These are conventional diesel



fuel, alcohol added test fuel obtained by adding 10% biodiesel to diesel fuel, and Al₂O₃ added test fuel obtained by adding 100 ppm aluminum oxide to the alcohol added test fuel.

2. Material Method

Diesel fuel and alcohol were mixed volumetrically and then nanoparticles were added by mass using a precision balance. In addition, an ultrasonic bath was used for the homogeneous dispersion of nanoparticles. The processing time of this ultrasonic bath was maintained for 1 hour at a frequency of 40 kHz and a power of 160 Watt. Table 1 shows some specific properties of the fuels used and Table 2 shows the properties of the engine used in the experiments.

Table 1: Test Fuels and Some Specific Properties.

Property	Diesel Fuel	Alcohol Added Test Fuel	Al ₂ O ₃ Added Test Fuel	Standart
Density (g/L; @15°C)	825	821.5	821.6	TS EN ISO 12185
Cetane number	54.12	52.44	53.68	TS 10317 EN ISO 5165 TS EN 15195
Viscosity,(cSt @40°C)	2.5	2.7	2.8	TS 1451 EN ISO 3104
Lower heating value (MJ/kg)	43.2	41.7	42.5	-

Table 2: Technical Specifications of The Test Engine.

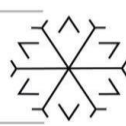
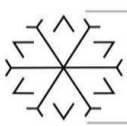
Model	Lombardini 15 LD 350
Engine type	Naturally-aspirated, air-cooled, DI diesel engine
Number of cylinders	1
Maximum power	7.5 HP/3600 rpm
Maximum torque	16.6 Nm/2400 rpm
Displacement	349 cm ³
Compression ratio	20.3/1
Bore*stroke	82 mm*66mm
Injection nozzle	0.22*4 holes*160°
Nozzle opening pressure	207 bar

2.1. Diesel RK Software

Modeling and simulation software Diesel RK, developed in the Department of Internal Combustion Engines (Piston Engines) at Bauman Moscow State Technical University in 1981-82, is mainly designed to simulate and optimize the working processes of all kinds of internal combustion engines. The main reason for using this software is to make a comparison between experimental and theoretical studies. A simulation model was created to display the experiments theoretically. This model takes into account the main equations defined by Fiveland and Assanis using Diesel RK software (Kuleshov, A.S., 2009, Kuleshov, A. and Mahkamov, K., 2008). Table 3 shows the main equations used in the Diesel RK software.

Table 3: Main Equations of Diesel-RK Software.

Name of equation	Governing equation for Diesel-RK model	Constants
Conservation of mass	$\frac{dm}{dt} = \sum_j \dot{m}_j$	m (total mass in kg)
Conservation of species	$Y_i = \frac{m_i}{m}$	m _i = Mass of the i th species (kg/s)
Species equations	$\frac{d(mY_i)}{dt} = \sum_j \dot{m}_j Y_i^j + \dot{S}_g$	\dot{S}_g = net generation rate of the i th species (kg/s)
Net generation of the i th species	$\dot{S}_g = \Omega_i W_{mw} v$	v = specific volume (kg/m ³), W _{mw} = Weight (kg/mol.)
Species conservation equation	$\dot{Y}_i = \sum_j \left(\frac{\dot{m}_j}{m}\right) (Y_i^j - Y_i^{cyl}) + \frac{\Omega W_{mw}}{\rho}$	$\rho = \text{kg/m}^3$
Conservation of energy	$\frac{d(mu)}{dt} = -P \frac{dv}{dt} + \frac{dQ_{ht}}{dt} + \sum_j \dot{m}_j h_j$	P = MPa



Air/fuel mixture equivalence ratio	$\alpha_1 = \frac{(A/F)}{(A/F)_s} = \frac{(\dot{m}_a/\dot{m}_f)}{(\dot{m}_a/\dot{m}_f)_s}$	\dot{m}_a = air mass flow (kg/s)
Frictional mean effective pressure	$FMEP = \alpha + \beta P_{max} + \gamma V_p$	$\alpha = \beta = \gamma = \text{constants}$, V_p = piston velocity (m/s)
Specific fuel consumption	$SFC = \frac{\dot{m}_f}{P_b}$	\dot{m}_f = fuel mass flow rate (kg/s), P_b = brake power (kW)
Zeldovich mechanism	$O_2 \leftrightarrow 2O$, $N_2 + O \leftrightarrow NO + O$, $N + O_2 \leftrightarrow NO + O$	
NO concentration during the combustion	$\frac{d[NO]}{d\theta} = \frac{P \times 2.333 \times 10^{-7} \cdot e^{-\frac{38020}{T_b}} [N_2]_e \cdot [O]_e \cdot \{1 - ([NO]/[NO]_e)^2\}}{R \cdot T_b \cdot \left(1 + \frac{2365}{T_b} \cdot e^{\frac{2365}{T_b}} \cdot \frac{[NO]}{[NO]_e}\right)} \cdot \frac{1}{\omega}$	ω = Angular velocity (rpm), R = Constant
NO concentration in a cylinder	$r_{NO_c} = r_{NO} r_{bc}$	
Specific NO emission	$e_{NO} = \frac{30 \times r_{NO} \times M_{bg}}{L_c \times \eta_M}$	

3. Result and Discussion

Figure 1 illustrates the brake specific fuel consumption values of experimental and simulation results together. Accordingly, it is seen that the BSFC value is declining as the engine load increases. As it is well-known, the in-cylinder temperature is lower in low engine loads, and it starts to increase as the engine load increases. That is because the fuel amount injected into the cylinder increases at elevated engine loads (Li et al., 2020; Uyumaz et al., 2019; Yousefi et al., 2018). This case leads to a rise in-cylinder temperature. Consequently, the atomization of fuel droplets at elevated engine load improves due to the high temperature in the combustion chamber, resulting in an increment in the combustion efficiency (Kumar et al., 2021; Saridemir et al., 2020; Ramesh et al., 2019). Therefore, as it is seen in Figure 1, the BSFC value gradually reduces as the engine load increases. Accordingly, the lowest fuel consumption is observed at the highest engine load (12 Nm) for each test fuel.

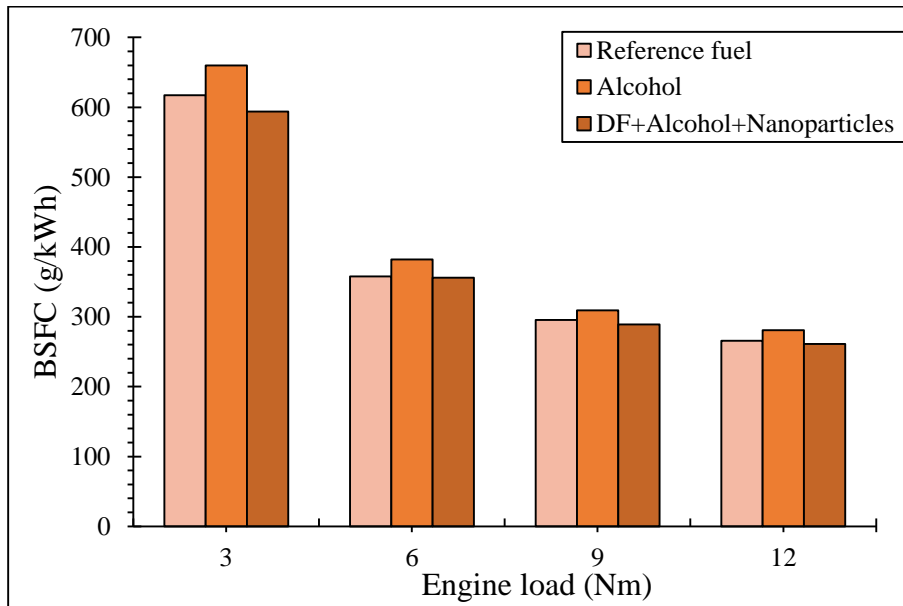


Figure 1: BSFC Variation of Test Fuels Against Engine Load.

As it is illustrated in Figure 1, the fuel consumption increases when the alcohol blends the reference test fuel (conventional diesel fuel). Probably, the fundamental reason behind the increment in fuel consumption with the presence of alcohol can be attributable to the lower energy content of alcohol as compared to that of conventional diesel fuel (Ustun, 2021; Örs et al., 2020; Yilmaz and Atmanli, 2017). The addition of alcohol into the reference fuel leads to more fuel consumption to reach the same engine load. In this case, the fuel consumption in 3 Nm is found to be 617 g/kWh for reference test fuel and 659 g/kWh for alcohol-added test fuel. In other words, the fuel consumption in this engine load increases by 6.8% for the alcohol-added test fuel. On the other hand, the addition of aluminum oxide nanoparticles into the alcohol-added test fuel pulls back the specific fuel consumption at a respectable rate, because the nanoparticles increase the



energy density of test fuels, and accelerate the chemical reactions during the combustion process due to their large surface to volume area ratio, catalytic role, and superior thermo-physical properties (Venu and Appavu, 2020; Devarajan et al., 2019; Sivakumar et al., 2018). In 3 Nm engine load, the fuel consumption for aluminum-added test fuel is found to be 550 g/kWh. BSFC values are achieved from the experimentally recorded values, and it is also obtained with the Diesel-RK software in the study. Figures 2, 3, and 4 show the BSFC values for reference fuel, alcohol-added test fuel, and alumina-added test fuel, respectively.

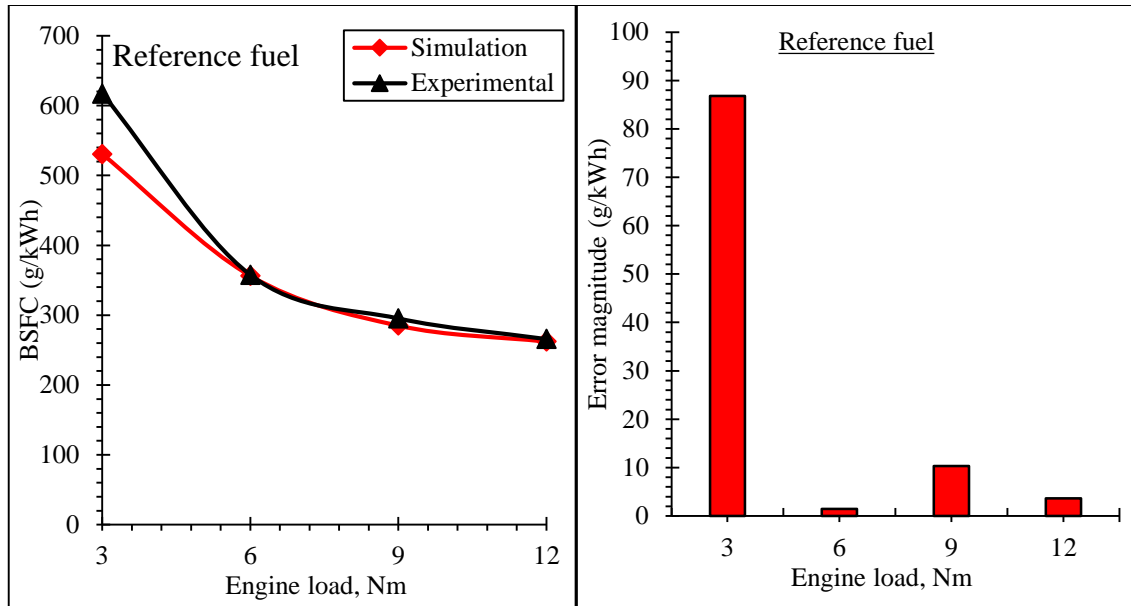


Figure 2: Simulation and Experimental Results of BSFC Values for Reference Test Fuel Against Engine Load (Left) and The Error Magnitudes Between The Numerical and Experimental Results (Right).

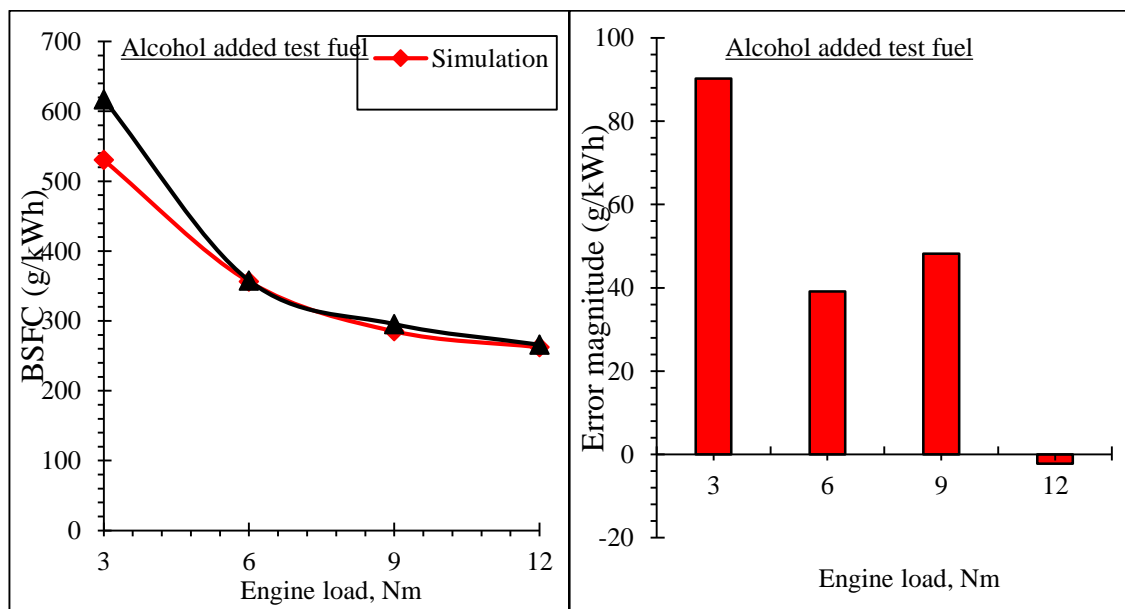


Figure 3: Simulation and Experimental Results of BSFC Values for Alcohol Added Test Fuel Against Engine Load (Left) and The Error Magnitudes Between The Numerical and Experimental Results (Right).

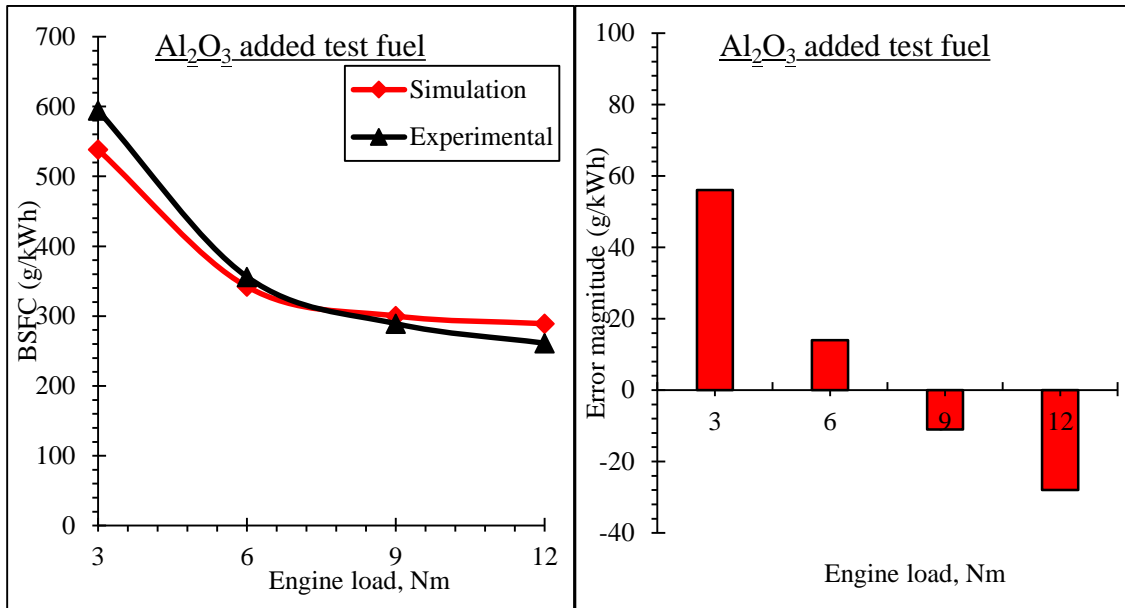


Figure 4: Simulation and Experimental Results of BSFC Values for Al_2O_3 Added Test Fuel Against Engine Load (Left) and The Error Magnitudes Between The Numerical and Experimental Results (Right).

As can be seen from Figures 2, 3, and 4, the simulation results closely follow the actual BSFC results and show a good fit indication. Accordingly, the coefficient of determination (R^2) is calculated to be 0.9905, 0.9830, and 0.9949 for reference fuel, alcohol-added test fuel, and Al_2O_3 added test fuel, respectively. From the figures, it is seen that the big error magnitudes between the simulated BSFC and experimental BSFC results are always found in 3 Nm. Probably, the complex and non-linear combustion behavior of test fuels due to the low cylinder temperature may be more effective on this big error magnitudes, particularly in low engine load. Considering all engine loads together, the average of absolute error magnitudes is calculated to be 25.55 g/kWh for reference test fuel, 43.81 g/kWh for alcohol added test fuel, and 27.75 g/kWh for alumina added test fuel. The absolute difference between the simulation and experimental results are found to be 4.83%, 10.07%, and 6.97% for reference fuel, alcohol-added test fuel, and Al_2O_3 nanoparticles added test fuel, respectively.

Another discussed result in this paper is the nitrogen oxide (NO_x) emission. Figure 5 gives the NO_x emission trends of experimental and simulation results together. As it is seen from the figure that the NO_x emission for each test fuel increases step by step as the engine load increases. The fundamental reason why the NO_x emission increases with the increment in the engine load can be explained by the increasing temperature value in the combustion chamber at elevated engine load (Qi et al., 2021; Aydın, 2020; Simsek, 2020). As it is well-known, the formation possibility of NO_x emission increases in high cylinder temperature (Hsueh et al., 2020; Serin and Yıldızhan, 2018). That is because the nitrogen and oxygen atoms can highly tend to react at high temperatures (Karagöz, 2020).

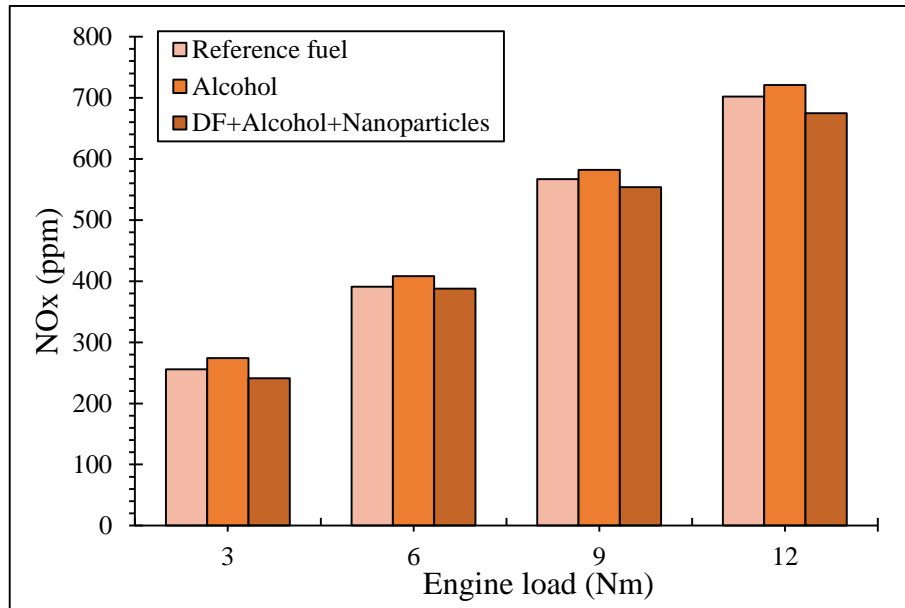


Figure 5: NOx Variation of Test Fuels Against Engine Load.

Given that the test fuels, it is noticed that the highest NOx emission in each engine load is recorded for alcohol added test fuel, while the lowest one is seen for nanoparticle-added test fuel. Probably, this case can be explained by the high oxygen content of alcohols. More oxygen in test fuels aids in supplying ample oxygen atoms in the combustion chamber, leading to more chances for the nitrogen and oxygen reaction (Goga et al., 2019). Consequently, the level of NOx emission increases more for alcohol added test fuel than that of other test fuel. On the other hand, as it is illustrated in Figure 5, the NOx emission reduces when the nanoparticles add to the test fuel. This case can be explained with less fuel consumption for this test fuel, resulting in the low in-cylinder temperature as well as low reaction chance for nitrogen and oxygen atoms. Similar results were also reported by the previous fuel researchers (Bunyan et al., 2021; Rastogi et al., 2020; Geng et al., 2021; Etefaghi et al., 2021). Figures 6, 7, and 8 show the NOx emissions for reference fuel, alcohol-added test fuel, and alumina-added test fuel, respectively.

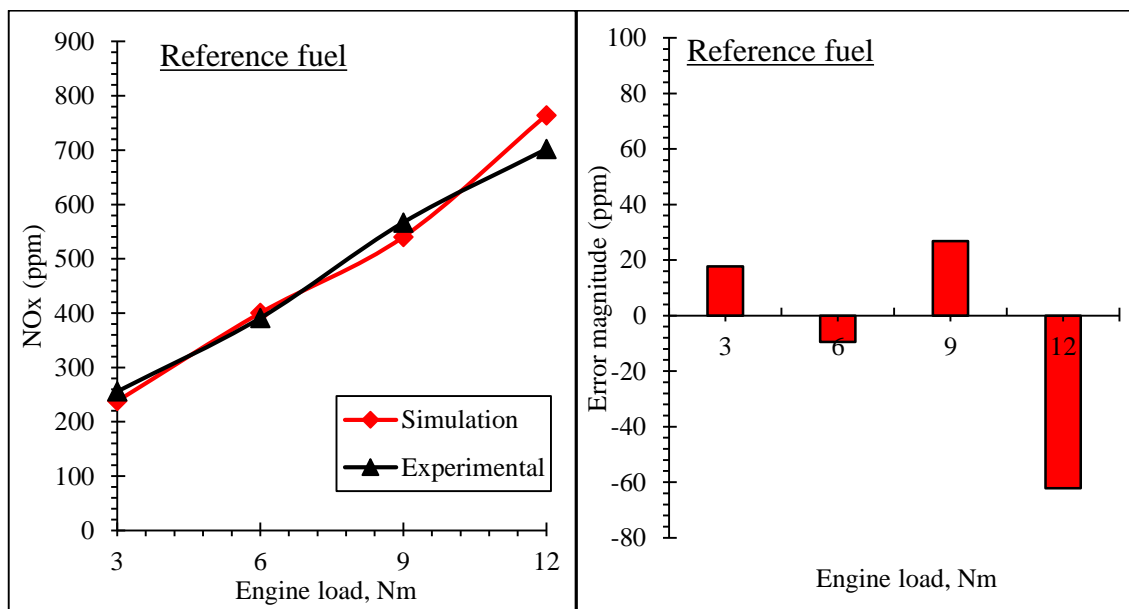


Figure 6: Simulation and Experimental Results of NOx Emissions for Reference Test Fuel Against Engine Load (Left) and The Error Magnitudes Between The Numerical and Experimental Results (Right).

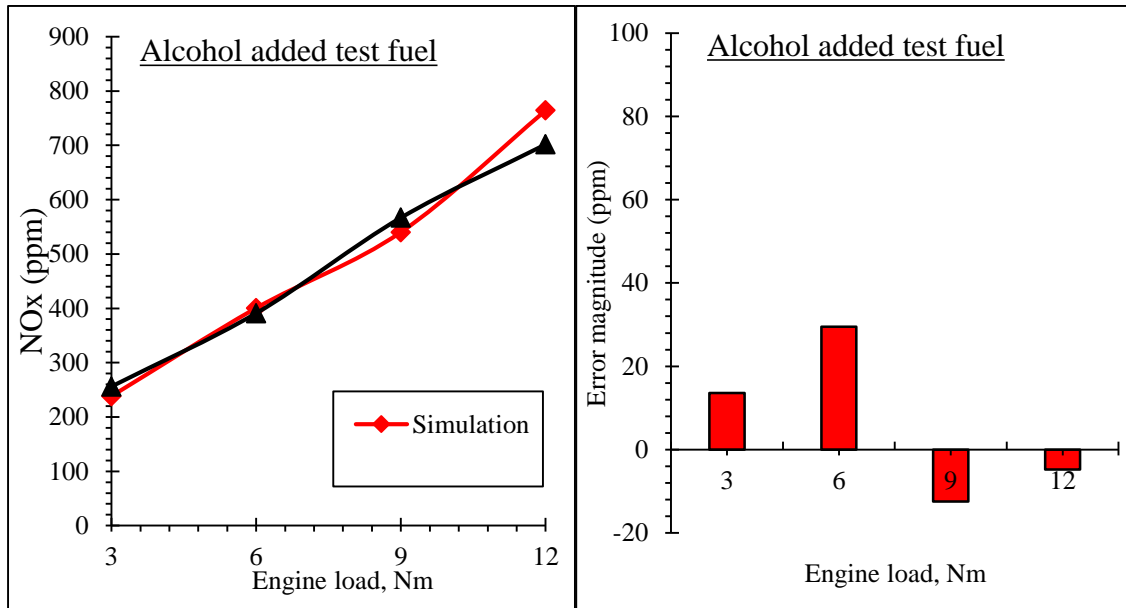
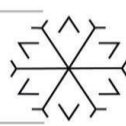
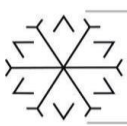


Figure 7: Simulation and Experimental Results of NOx Emissions for Alcohol Added Test Fuel Against Engine Load (Left) and The Error Magnitudes Between The Numerical and Experimental Results (Right).

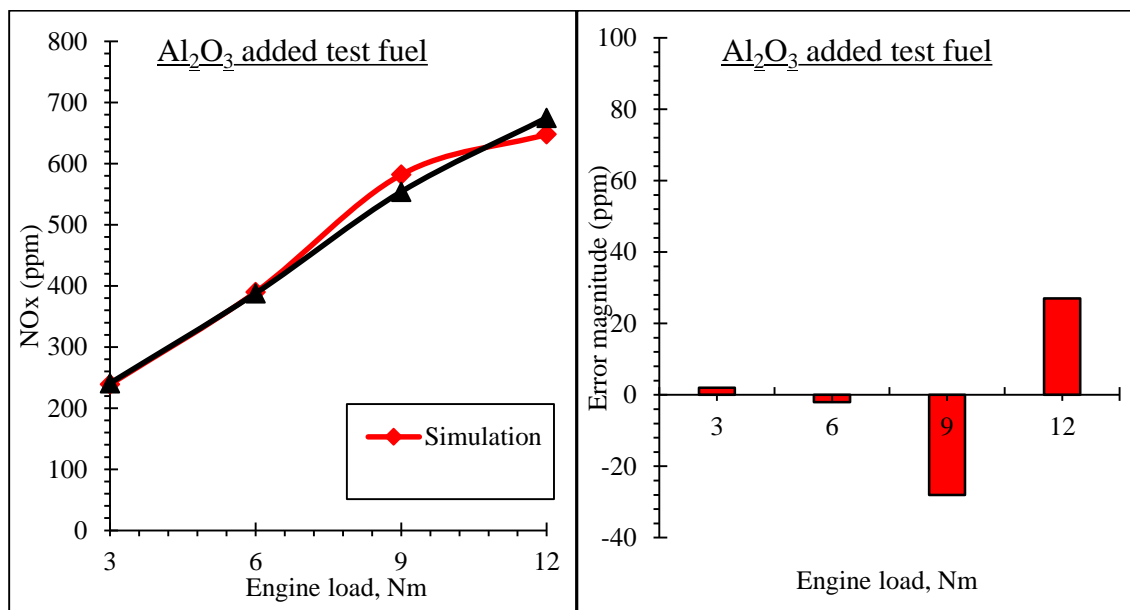


Figure 8: Simulation and Experimental Results of NOx Emissions for Al₂O₃ Added Test Fuel Against Engine Load (Left) and The Error Magnitudes Between The Numerical and Experimental Results (Right).

As it can be seen from the figures, the results gathered from the simulation software closely follow the experimental data, and exhibit a good fitting with the experimental results. The R^2 value of reference fuel, alcohol-added test fuel, and alumina-added test fuels are calculated to be 0.9802, 0.9959, and 0.9861, respectively. The absolute difference between the simulation and experimental results in terms of NOx emission is calculated to be 5.73%, 3.74%, and 2.60% for reference fuel, alcohol-added test fuel, and Al₂O₃ nanoparticles added test fuel, respectively. Accordingly, it is possible to say that the results obtained from the experimental side of the study can be highly reachable with the simulation software.

4. Conclusion

The core objective of the present research is to reach the experimental results with the simulation software. In this framework, three test fuels are formed in the study, and the experiments are conducted on a single-



cylinder diesel engine to gather the experimental results. Accordingly, the same operating conditions are created in the simulation environment and the results are gathered from the software. Then the following conclusion remarks are achieved from the present study.

- It is noticed that there is a reverse relation between the NO_x formation and fuel consumption. In other words, as the engine load increases, the NO_x emission also increases, but BSFC decreases step by step. This is probably due to the temperature value in the combustion chamber which is highly dependent on the engine load.

- The curves of simulation results have a very good fitting indication and closely follow that of experimental results. Each R² value between the simulation and experimental data has a very satisfactory result with a bigger than 0.98.

- The absolute difference between the simulation and experimental results is calculated to be 5.73%, 3.74%, and 2.60% for NO_x emission and 4.83%, 10.07%, and 6.97% for reference fuel, alcohol-added test fuel, and Al₂O₃ nanoparticles added test fuel, respectively.

Finally, it can be said that the experimental studies are both expensive and time-consuming applications. With this framework, this study proves that close results can be achieved by using such simulation software within satisfied percentages, and therefore it will be a benefit for the time and cost arising from the experimental trials.

References

Aydn, S. (2020). Comprehensive analysis of combustion, performance and emissions of power generator diesel engine fueled with different source of biodiesel blends. *Energy*, 205, 118074.

Bunyan, S. T., & Hasan, A. A. K. M. (2021). Experimental Study of the Influence of Nanoparticles Additive to Diesel Fuel on the Emission Characteristics. *Al-Khwarizmi Engineering Journal*, 17(1), 13-19.

Devarajan, Y., Nagappan, B., & Subbiah, G. (2019). A comprehensive study on emission and performance characteristics of a diesel engine fueled with nanoparticle-blended biodiesel. *Environmental Science and Pollution Research*, 26(11), 10662-10672.

Ettefaghi, E., Rashidi, A., Ghobadian, B., Najafi, G., Ghasemy, E., Khoshtaghaza, M. H., ... & Mazlan, M. (2021). Bio-nano emulsion fuel based on graphene quantum dot nanoparticles for reducing energy consumption and pollutants emission. *Energy*, 218, 119551.

Foo, W. H., Chia, W. Y., Tang, D. Y. Y., Koay, S. S. N., Lim, S. S., & Chew, K. W. (2021). The Conundrum of Waste Cooking Oil: Transforming Hazard into Energy. *Journal of Hazardous Materials*, 126129.

Ge, J. C., Yoon, S. K., & Choi, N. J. (2017). Using canola oil biodiesel as an alternative fuel in diesel engines: A review. *Applied Sciences*, 7(9), 881.

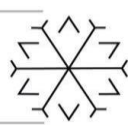
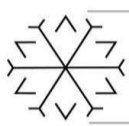
Geng, L., Li, S., Xiao, Y., Chen, H., Chen, X., & Ma, Y. (2021). Influence of the addition of titanium oxide nanoparticles to Fischer-Tropsch diesel synthesised from coal on the combustion characteristics and particulate emission of a diesel engine. *Process Safety and Environmental Protection*, 145, 411-424.

Ghasemian, S., Faridzad, A., Abbaszadeh, P., Taklif, A., Ghasemi, A., & Hafezi, R. (2020). An overview of global energy scenarios by 2040: identifying the driving forces using cross-impact analysis method. *International Journal of Environmental Science and Technology*, 1-24.

Goga, G., Chauhan, B. S., Mahla, S. K., & Cho, H. M. (2019). Performance and emission characteristics of diesel engine fueled with rice bran biodiesel and n-butanol. *Energy Reports*, 5, 78-83.

Hoseini, S. S., Najafi, G., Ghobadian, B., Ebadi, M. T., Mamat, R., & Yusaf, T. J. R. E. (2020). Biodiesels from three feedstock: The effect of graphene oxide (GO) nanoparticles diesel engine parameters fuelled with biodiesel. *Renewable energy*, 145, 190-201.

Hsueh, M. H., Wang, C. N., Hsieh, M. C., Lai, C. J., Wang, S. H., Hsieh, C. H., ... & Yu, J. H. (2020). An Analysis of Exhaust Emission of the Internal Combustion Engine Treated by the Non-Thermal Plasma. *Molecules*, 25(24), 6041.



İlker, Örs., Sayın, B., & Ciniviz, M. (2020). A comparative study of ethanol and methanol addition effects on engine performance, combustion and emissions in the si engine. *International Journal of Automotive Science and Technology*, 4(2), 59-69.

Karagöz, M. (2020). Investigation of performance and emission characteristics of an CI engine fuelled with diesel–waste tire oil–butanol blends. *Fuel*, 282, 118872.

Kober, T., Schiffer, H. W., Densing, M., & Panos, E. (2020). Global energy perspectives to 2060–WEC's World Energy Scenarios 2019. *Energy Strategy Reviews*, 31, 100523.

Kuleshov, A. S. (2009). Multi-zone DI diesel spray combustion model for thermodynamic simulation of engine with PCCI and high EGR level. *SAE International Journal of Engines*, 2(1), 1811-1834.

Kuleshov, A., & Mahkamov, K. (2008). Multi-zone diesel fuel spray combustion model for the simulation of a diesel engine running on biofuel. *Proceedings of the Institution of Mechanical Engineers, Part A: Journal of Power and Energy*, 222(3), 309-321.

Kumar, T. S., & Ashok, B. (2021). Critical review on combustion phenomena of low carbon alcohols in SI engine with its challenges and future directions. *Renewable and Sustainable Energy Reviews*, 152, 111702.

Leite, D., Santos, R. F., Bassegio, D., de Souza, S. N. M., Secco, D., Gurgacz, F., & da Silva, T. R. B. (2019). Emissions and performance of a diesel engine affected by soybean, linseed, and crambe biodiesel. *Industrial Crops and Products*, 130, 267-272.

Li, L., Yu, Y., & Lin, W. (2020). Numerical investigation on the effects of load conditions and hydrogen-air ratio on the combustion processes of a HSDI engine. *International Journal of Hydrogen Energy*, 45(17), 10602-10612.

Qi, D., Ma, L., Chen, R., Jin, X., & Xie, M. (2021). Effects of EGR rate on the combustion and emission characteristics of diesel-palm oil-ethanol ternary blends used in a CRDI diesel engine with double injection strategy. *Applied Thermal Engineering*, 199, 117530.

Ramesh, A., Ashok, B., Nanthagopal, K., Pathy, M. R., Tambare, A., Mali, P., ... & Subbarao, R. (2019). Influence of hexanol as additive with Calophyllum Inophyllum biodiesel for CI engine applications. *Fuel*, 249, 472-485.

Rastogi, P. M., Kumar, N., Sharma, A., Vyas, D., & Gajbhiye, A. (2020). Sustainability of Aluminium Oxide Nanoparticles Blended Mahua Biodiesel to the Direct Injection Diesel Engine Performance and Emission Analysis. *Pollution*, 6(1), 25-33.

S Gavhane, R., M Kate, A., Pawar, A., Safaei, M. R., M Soudagar, M. E., Mujtaba Abbas, M., ... & Shahapurkar, K. (2020). Effect of zinc oxide nano-additives and soybean biodiesel at varying loads and compression ratios on VCR diesel engine characteristics. *Symmetry*, 12(6), 1042.

Serin, H., & Yıldızhan, Ş. (2018). Hydrogen addition to tea seed oil biodiesel: Performance and emission characteristics. *International Journal of Hydrogen Energy*, 43(38), 18020-18027.

Simsek, S. (2020). Effects of biodiesel obtained from Canola, sefflower oils and waste oils on the engine performance and exhaust emissions. *Fuel*, 265, 117026.

Sivakumar, M., Sundaram, N. S., & Thasthagir, M. H. S. (2018). Effect of aluminium oxide nanoparticles blended pongamia methyl ester on performance, combustion and emission characteristics of diesel engine. *Renewable Energy*, 116, 518-526.

Sondors, K., Birkavs, A., Pirs, V., Birzietis, G., & Dukulis, I. (2019, May). Comparison of vehicle performance using fossil diesel fuel blends with biodiesel and HVO fuel. In *Proceedings of the 18th International Scientific Conference "Engineering for Rural Development", Jelgava, Latvia, 22-24 May 2019* (pp. 964-970). Latvia University of Life Sciences and Technologies.

Unglert, M., Bockey, D., Bofinger, C., Buchholz, B., Fisch, G., Luther, R., ... & Krahl, J. (2020). Action areas and the need for research in biofuels. *Fuel*, 268, 117227.

Ustun, S. (2021). Determination of optimum manganese amount by response surface methodology with alcohol–gasoline fuel blend in an SI engine. *International Journal of Environmental Science and Technology*, 1-14.



Uyumaz, A., Aydoğan, B., Solmaz, H., Yılmaz, E., Hopa, D. Y., Bahtli, T. A., ... & Aksoy, F. (2019). Production of waste tyre oil and experimental investigation on combustion, engine performance and exhaust emissions. *Journal of the Energy Institute*, 92(5), 1406-1418.

Uzoh, C. F., Nnuekwe, A., Onukwuli, O., Ofochebe, S., & Ezekannagha, C. (2021). Optimal route for effective conversion of rubber seed oil to biodiesel with desired key fuel properties. *Journal of Cleaner Production*, 280, 124563.

Venu, H., & Appavu, P. (2020). Al₂O₃ nano additives blended Polanga biodiesel as a potential alternative fuel for existing unmodified DI diesel engine. *Fuel*, 279, 118518.

Wu, Q., Xie, X., Wang, Y., & Roskilly, T. (2018). Effect of carbon coated aluminum nanoparticles as additive to biodiesel-diesel blends on performance and emission characteristics of diesel engine. *Applied Energy*, 221, 597-604.

Yaqoob, H., Teoh, Y. H., Sher, F., Jamil, M. A., Murtaza, D., Al Qubeissi, M., ... & Mujtaba, M. A. (2021). Current status and potential of tire pyrolysis oil production as an alternative fuel in developing countries. *Sustainability*, 13(6), 3214.

Yilmaz, N., & Atmanli, A. (2017). Experimental evaluation of a diesel engine running on the blends of diesel and pentanol as a next generation higher alcohol. *Fuel*, 210, 75-82.

Yousefi, A., Guo, H., & Birouk, M. (2018). An experimental and numerical study on diesel injection split of a natural gas/diesel dual-fuel engine at a low engine load. *Fuel*, 212, 332-346.

Zhao, F., Chen, K., Hao, H., & Liu, Z. (2020). Challenges, potential and opportunities for internal combustion engines in China. *Sustainability*, 12(12), 4955.

Frameless PMSM Position Control in Pan-Tilt System with 2-Axes

Mesud Yasin ÇELİK ¹[0000-0002-1801-8984], Mehmet Arif ADLI ²[0000-0002-3223-064X],
and Ali SAYGIN ³[0000-0003-1800-9655]

¹mesud.celik@tubitak.gov.tr, TÜBİTAK BİLGEM İLTAREN, Ankara, Turkey

²arif.adli@gazi.edu.tr, Department of Mechanical Engineering, Faculty of Engineering, Gazi University,
Ankara, Turkey

³asaygin@gazi.edu.tr, Department of Electrical and Electronics Engineering, Faculty of Technology, Gazi
University, Ankara, Turkey

Abstract

Rapid advancements in technology lead to changes in today's technology trends and discovery of methods and processes that are more advantageous in robotic technology. Especially in the military field, reaching the desired performance values becomes possible with less time, cost, and iteration. In previous robotics, pan-tilt systems, and seeker applications, DC motors, DC torque motors, and brushless DC motors have been widely used and researches have begun on the use of more efficient and high-performance alternative motors. In this study, frameless permanent magnet synchronous motors (PMSM) were used in a two-axis pan-tilt system, and the speed and position control performances of PMSM used in the pan-tilt system were investigated.

In this study, position control of the PMSMs directly coupled two-axis pan-tilt system were run in real-time using Matlab/Simulink package programs. In the application, DSP devices with code LAUNCHXL-F28379D and motor drivers with code BOOSTXL-DRV8305EVM were preferred. For the robotic motion of the system, kinematic equations were used. Motor parameters (Ld, Lq, etc.) and control parameters (PI) were applied in field oriented control (FOC). CAN protocol was applied for communication between DSPs and Biss-C protocol for position information from the encoders.

In conclusion, although the frameless structure of the PMSM and the faults of the system in mechanical production negatively affected the performance of the motors, the position controls of the PMSMs were completed successfully by using FOC, and the system was oriented to the desired position.

Keywords. Direct Drive, F28379D, Field Oriented Control, Frameless PMSM, Position Control

1. Introduction

Since the electric motor is one of the major components of the positioner pan-tilt systems, numerous researches have been conducted on motor control. According to the motor type, researchers have focused on physical and control algorithms to solve the problems encountered. When robotics, pan-tilt systems, and seeker studies in the literature are examined, it can be seen that DC motor, DC torque motor, and brushless DC motor have been extensively utilized. Motor drivers suitable for driving these types of motors have been designed, mechanical solutions have been derived, and control algorithms have been developed. Related to pan-tilt mechanisms in the literature; Haiyan Qiao et al. worked on solving the problem of weak dynamic variables related to the DC torque motor used in the seeker (Qiao *et al.*, 2020). Other examples in this field are reducing interference torque compensation (Liu, Zhao and Wang, 2019) in the pitch-roll seeker and optimization of parameters (Yang *et al.*, 2019) in the gimbal.

Permanent magnet synchronous motors consist of a fixed part called stator and a rotating part called rotor as in other motor types. Compared to DC motor types, PMSMs have less torque fluctuation, higher torque/weight ratio, and higher performance due to no copper loss in the rotor (Krishnan, 1991). Other advantages are that it can generate torque even at zero speed, does not spark, and has a wider speed range. Therefore, PMSMs have become more preferred motors, especially in industrial areas of application. At the same time, many studies have been carried out on the performance of PMSMs in the literature. Kazan and Bilgin conducted studies on modeling and simulation of PMSM at different speeds (KAZAN and BİLGİN, 2020). In other examinations, the effect of the PMSM control with an absolute encoder while encountering



disturbances was examined (Rudnicki, 2019). Experiments have also been performed with direct torque control (Luo, Tan and Su, 2019) and dynamic simulation (Lu *et al.*, 2017) based on sliding mode by using PMSM.

This research, it is aimed to control the position of frameless PMSMs in the pan-tilt system. For the movement of the system to the desired position, forward kinematic and inverse kinematic equations are used. Owing to inverse kinematic, the position reference input to be used in the control of motors has been obtained for both axes. Using the encoder feedback, the proposed field oriented control with PI controller is developed using Matlab/Simulink. Via the CAN protocol, communication between DSPs is completed.

In this paper, the parts of presenting the topology of the system, obtaining the kinematic equations of the system, Field Oriented Control, frameless PMSM, encoder, and CAN protocol are explained in detail.

Materials and Methods

1.1. 2-Axis Pan-Tilt System Topology

For each axis, hardware was built using DSPs as processors, absolute encoders as position information, three-phase motor driver module as motor driver, and computer as host. By choosing a field oriented control method, the parameterization of the motor and the controller parameterization were achieved, and they are aimed to be used in the microprocessor. The design architecture of the system is given in Figure 1.

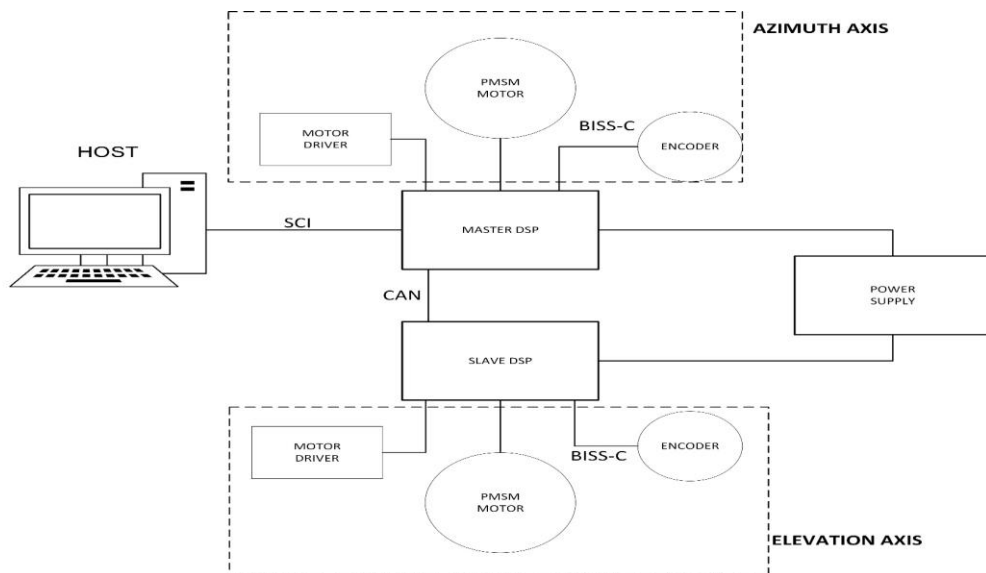


Figure 1: The System Architecture Schema

1.2. Kinematics of 2-Axis Pan-Tilt System

The system has two degrees of freedom and is capable of moving in azimuth and elevation. Both azimuth and elevation axes were so designed that they are driven directly by motors without requiring any transmission organs such as reducers, gears, belts etc. For the kinematic analysis, the coordinate system of the pan-tilt system in serial kinematic structure is shown in Figure 2.

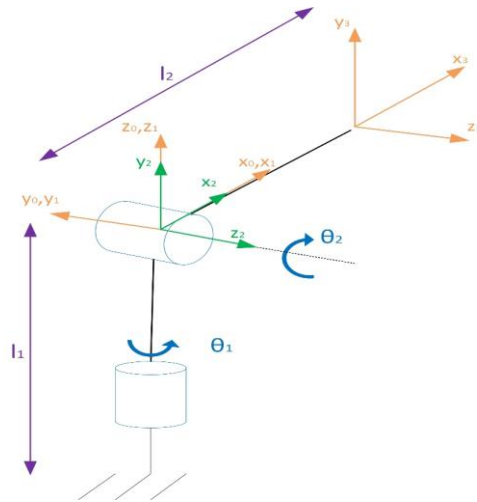
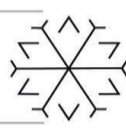
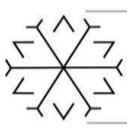


Figure 2: Link Frame Assignment for the Pan-Tilt System

Danevit-Hartenberg method was used to find the variable parameters needed for the robotic movements of the system. Forward kinematic values are given in the table below.

Table 1: Link Parameters of the Pan-Tilt System

Joint/Link <i>i</i>	α_i (rad)	a_i (m)	θ_i (rad)	d_i (m)	<i>R/P</i>
1	0	0	θ_1	0	R
2	$\pi/2$	0	θ_2	0	R
3	0	l_2	0	0	0

Using the table above, the homogeneous transformation matrix from the outer frame to the inner frame of the system can be written as follows:

$$T_3^0 = \begin{bmatrix} \cos\theta_1\cos\theta_2 & -\cos\theta_1\sin\theta_2 & \sin\theta_1 & \cos\theta_1\cos\theta_2l_2 \\ \sin\theta_1\cos\theta_2 & -\sin\theta_1\sin\theta_2 & -\cos\theta_1 & \sin\theta_1\cos\theta_2l_2 \\ \sin\theta_2 & \cos\theta_2 & 0 & \sin\theta_2l_2 \\ 0 & 0 & 0 & 1 \end{bmatrix} \quad (2)$$

Since the center of the two axes coincides with the center of mass of the system, a spherical coordinate system can be applied at the center of the mechanism as shown in Figure 3.

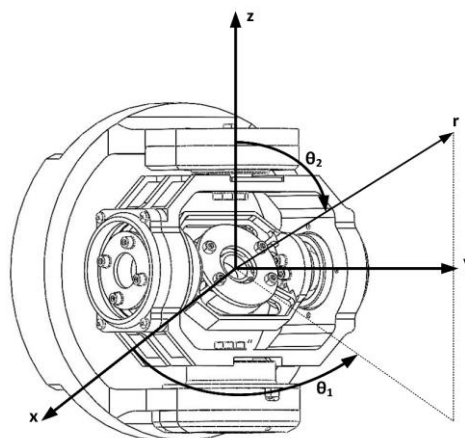


Figure 3: Spherical Coordinate System

The pan-tilt system coordinates based on the fixed frame are written as:

$$x = \cos\theta_1\cos\theta_2l_2 \quad (3)$$

$$y = \sin\theta_1\cos\theta_2l_2 \quad (4)$$

$$z = \cos\theta_2l_2 \quad (5)$$



Then, the axis joint variables of the system can be calculated easily as follows:

$$\theta_1 = \tan^{-1} \left(\frac{y}{x} \right) \tag{6}$$

$$\theta_2 = \tan^{-1} \left(\frac{\sqrt{x^2+y^2}}{z} \right) \tag{7}$$

$$l_2 = \frac{\sqrt{x^2+y^2}}{\cos \theta_2} \tag{8}$$

1.3. Field Oriented Control

Field oriented control (FOC) technique known as vector control is often used in high-performance AC motors. FOC method provides excellent control over full torque capability. In the FOC method, the stator currents are converted into flux from the rotor rotating in the **d-q** reference axis. The **q** component is directly proportional to the torque, and **d** is the component where the current is kept zero. Current, voltage, and angle of rotation play an important role in PMSM control. The current and voltage information read in the analog channel DSP are first transferred to the two-phase planes (**α,β**) and then to the stationary axis set (**d,q**). The transformations of the Clarke and Park are given in the equations, respectively (Samar *et al.*, 2012).

$$\begin{bmatrix} i_\alpha \\ i_\beta \end{bmatrix} = \frac{2}{3} \begin{bmatrix} 1 & -\frac{1}{2} & -\frac{1}{2} \\ 0 & \frac{\sqrt{3}}{2} & -\frac{\sqrt{3}}{2} \end{bmatrix} \begin{bmatrix} i_a \\ i_b \\ i_c \end{bmatrix} \tag{9}$$

$$\begin{bmatrix} i_d \\ i_q \end{bmatrix} = \begin{bmatrix} \cos(\theta) & \sin(\theta) \\ -\sin(\theta) & \cos(\theta) \end{bmatrix} \begin{bmatrix} i_\alpha \\ i_\beta \end{bmatrix} \tag{10}$$

The equations for inverse Park and Clarke transformation are given in equations, respectively.

$$\begin{bmatrix} v_\alpha \\ v_\beta \end{bmatrix} = \begin{bmatrix} \cos(\theta) & -\sin(\theta) \\ \sin(\theta) & \cos(\theta) \end{bmatrix} \begin{bmatrix} v_d \\ v_q \end{bmatrix} \tag{11}$$

$$\begin{bmatrix} v_a \\ v_b \\ v_c \end{bmatrix} = \begin{bmatrix} 1 & 0 \\ -\frac{1}{2} & \frac{\sqrt{3}}{2} \\ -\frac{1}{2} & -\frac{\sqrt{3}}{2} \end{bmatrix} \begin{bmatrix} v_\alpha \\ v_\beta \end{bmatrix} \tag{12}$$

In the experiment, the FOC method was used for position control. It contains the FOC method schematic in Figure 4 and simulink model in Figure 5 for one axis.

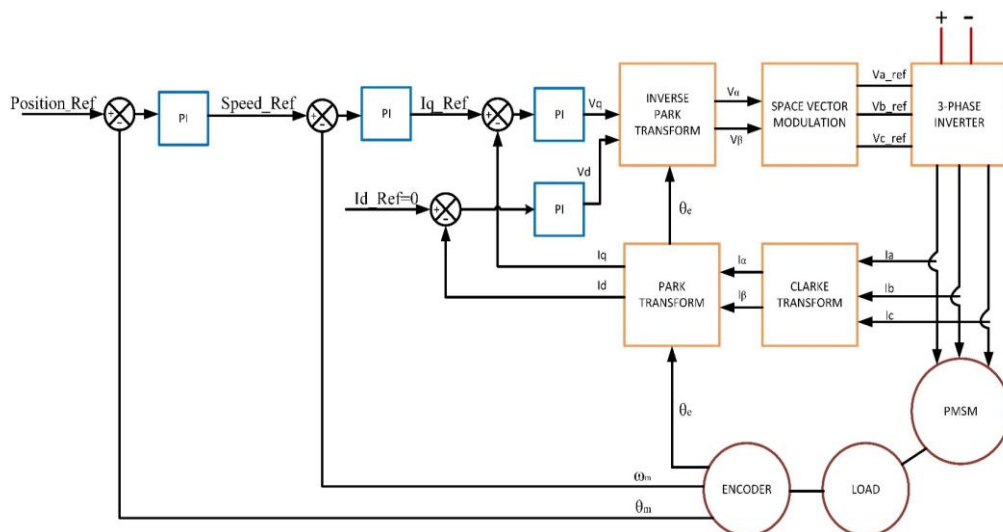


Figure 4: FOC Schema for one axis

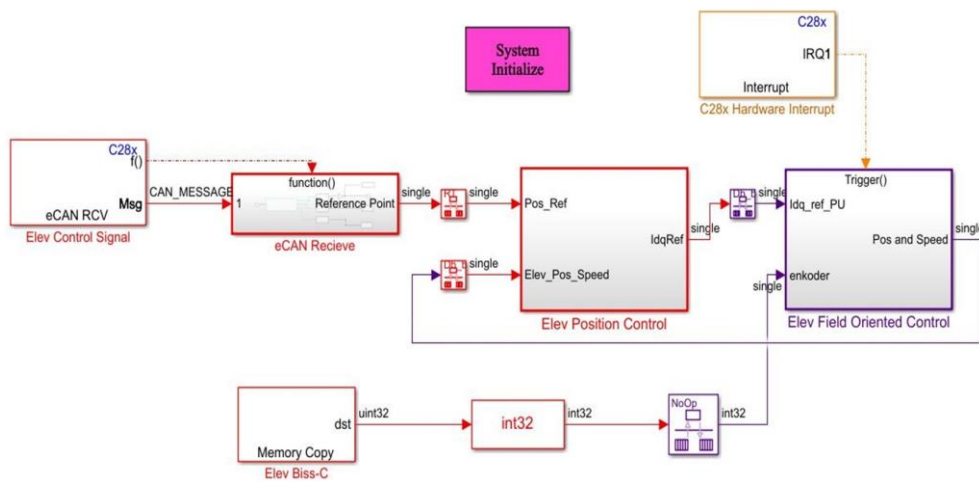


Figure 5: Simulink Model of Elevation Axis Position Control with FOC

1.4. Frameless PMSM

Three-phase permanent magnet synchronous motors have mainly two types. One of them uses rotor windings fed from stators and the other uses permanent magnets. In this study, a 16-pole, star-type winding motor with permanent magnets in the stator as frameless structure is utilized as shown in Figure 6.

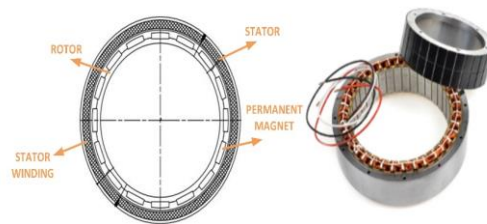


Figure 6: Structure of Frameless PMSM Example (Icpe, n. d.)

Thanks to sinusoidally distributed windings, the motor provides a smooth back emf. Due to its surface-mounted structure, it provides a compact structure in mechanical design, and owing to high performance, it provides many advantages in such structures. Other features of the motor used in both axes are its peak torque in operation 0.33 Nm, phase resistance 2.3 Ohm, and inductance 0.076 mH.

1.5. Encoder

One of the most crucial issues in motor position control is to accurately measure the position of the shaft to which the motor is connected directly. In this study, 17-bit absolute encoders with ± 0.01 precision were used to accurately measure the position of the system axis. Encoders were integrated with LAUNCHXL-F28379D by using the TIDM-1010 coded module. The communication between the module and the DSP was carried out with the Biss-C communication protocol. Using Matlab/Simulink package program, the algorithm that enables the position reading of the encoder written in C language was transferred to the Simulink environment as given in Figure 7.

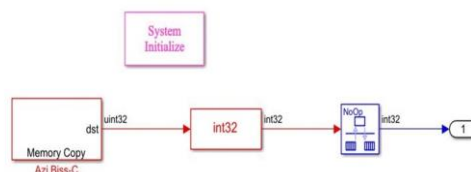


Figure 7: The Simulink Model of Captured Encoder Position



1.6. Controller Area Network

Controller Area Network (CAN) communication, which is a very secure protocol, was discovered for use in the automotive industry. Afterwards, CAN protocol started to be used in various sectors. In the proceed, communication between two DSPs was achieved by three cables, CAN-High, CAN-Low, and GND. The data in the protocol can be sent in discrete or pack form. In Matlab/Simulink program, thanks to CAN communication modules as pack form, the communication was established.

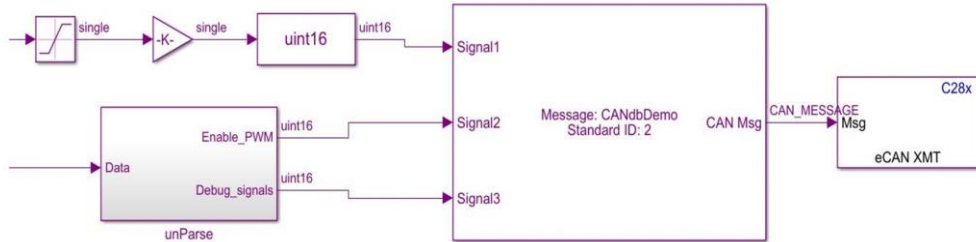


Figure 8: Sending The Control Signal using CAN Protocol in Simulink

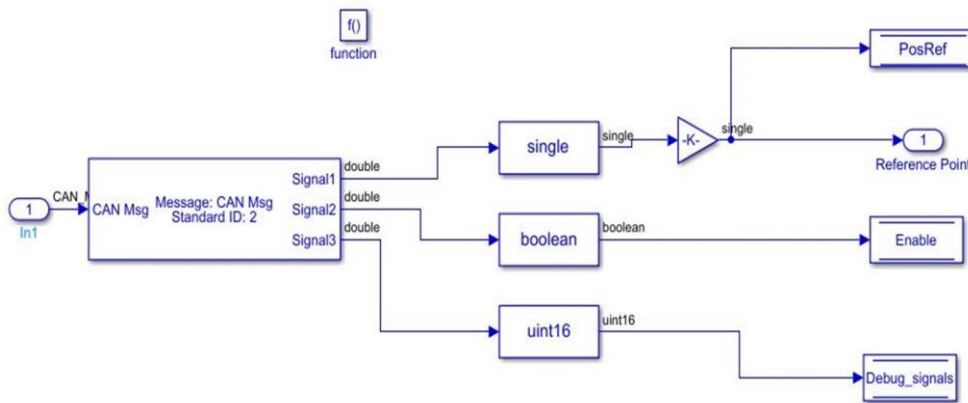


Figure 9: Receiving The Control Signal using CAN Protocol in Simulink

2. Experimental Studies

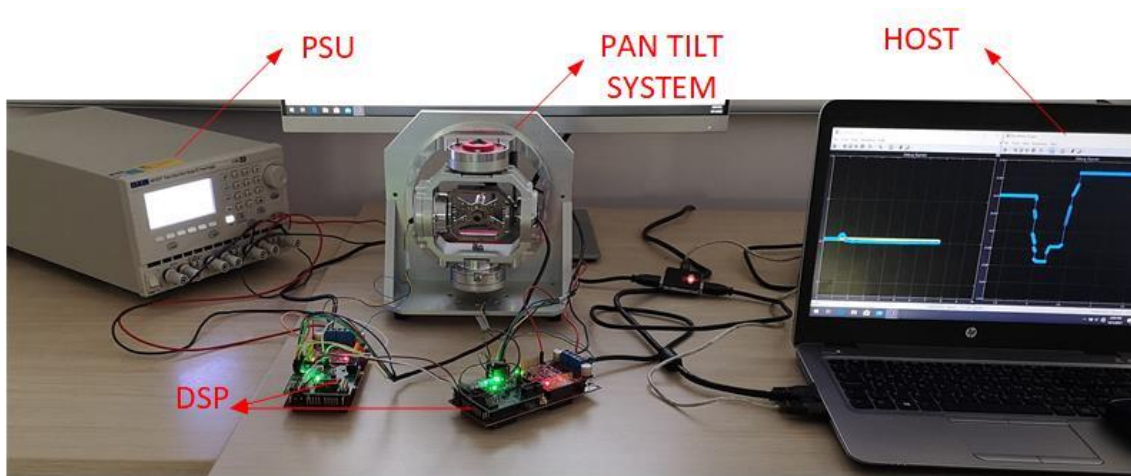


Figure 10: Experimental Set-up

The experimental set-up of the system is shown in Figure 10. Within the scope of experimental studies, the PMSMs in the azimuth and elevation axis were moved to different positions. In the azimuth axis, the mechanism was oriented from 0 degrees to +20 degrees, then to -20 degrees. As given in Figure 11, the comparison of the desired location and actual location data confirmed the expected accuracy of the system. When the graph is examined, it can be seen that the settling time of the motor from 0° to 20° was 0.28 s.

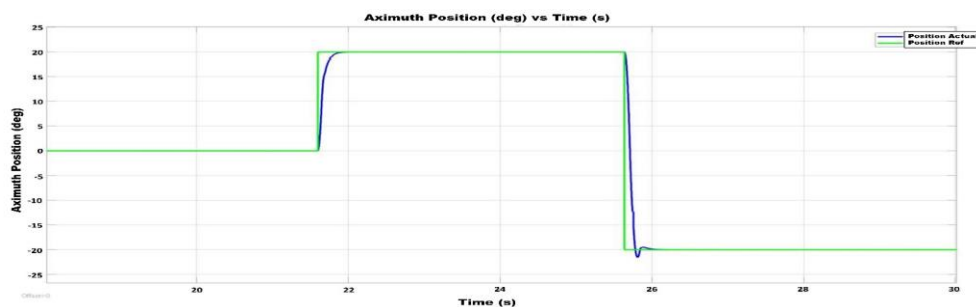


Figure 11: Azimuth Position

In Figure 12, the error curve related to angles of rotation in the azimuth axis is given. When the error between the desired position and the actual position is investigated, it can be observed that the error signal reached 20 degrees instantaneously since the ramp function in the reference position was not used while going from the first position to the second position. Within the system settling, the error was set to zero. A similar situation was observed in the second position change.

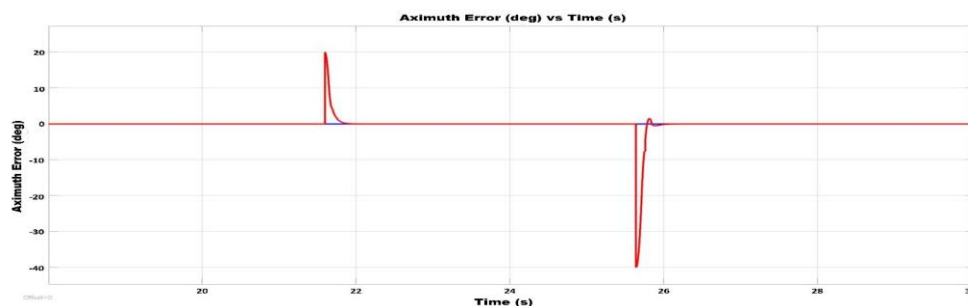


Figure 12: Azimuth Error

The speed curve of the motor in the azimuth axis is shown in figure 13. The speed magnitude is zero while the system maintains its position. While going from the starting position to the reference position, it went



up to approximately 60rpm in 0.28 seconds and came back to the stationary position. Within next position change, the speed reached 96.25 rpm.

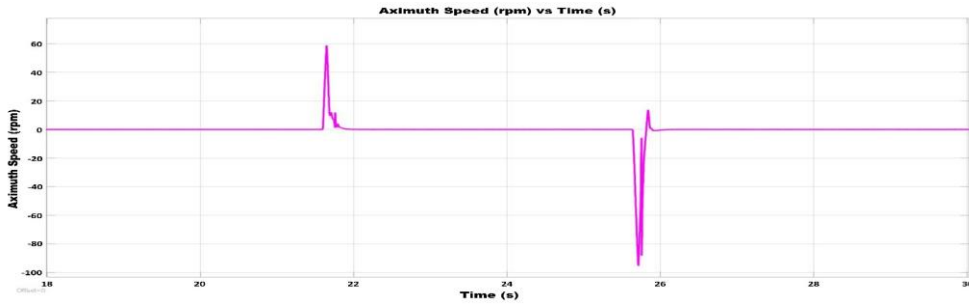


Figure 13: Azimuth Speed

On the elevation axis, the system was directed to $+20^\circ$ before the 0° position and then to the $+20^\circ$ position. In Figure 14, the desired position and actual position data are plotted with respect to time. The position settling time (4.2s) took longer in elevation axis than in azimuth axis.

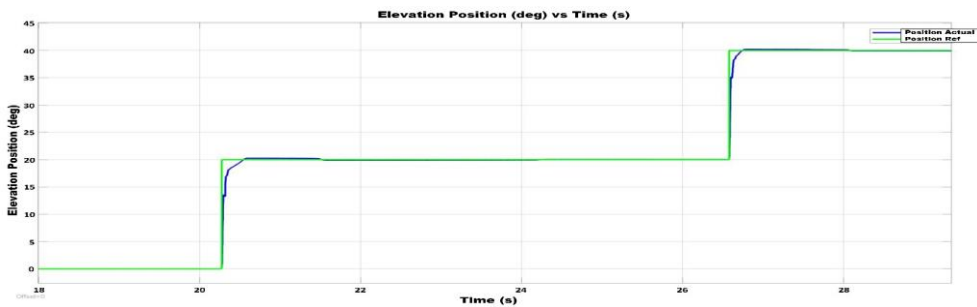


Figure 14: Elevation Position

The error curve related to angles of rotation in the elevation axis as shown in Figure 15. Since the ramp function was not utilized in the reference position, the instantaneous error values came out to be equal to the position change. Similar changes in the azimuth axis were observed in the error graph.

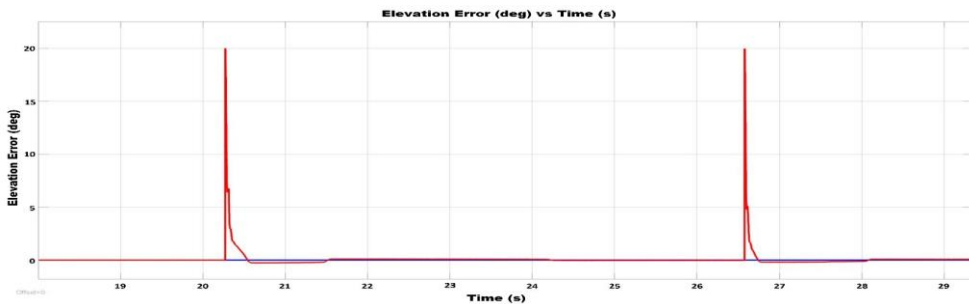


Figure 15: Elevation Error

In Figure 16, the speed curve of the PMSM in the elevation axis is given.

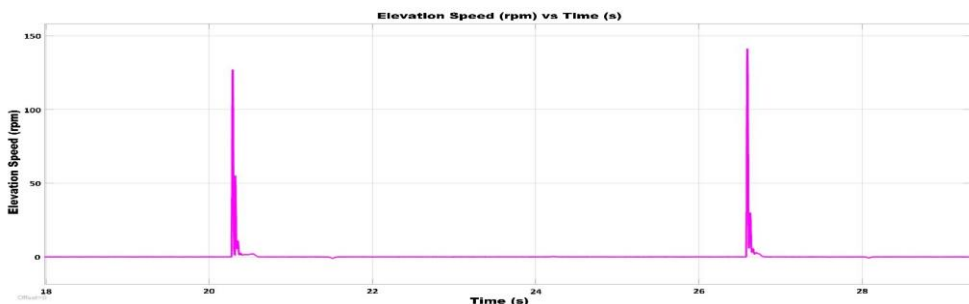
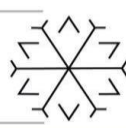
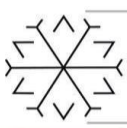


Figure 16: Elevation Speed



3. Conclusion

In this study, it was tried to achieve position control of frameless PMSM motor. Motor drivers and encoders were operated on each axis using DSP microcontrollers. Due to its mechanical design in the pan-tilt system, position control was carried out within the limits of ± 49 degrees on both axes. As an algorithm, field oriented control technique was used in DSPs with PI controller in motor position control. Optimizing the PI parameters was important for the system's fast response and settling time. By operating the encoders, motor drivers and motors in harmony, precise position control was realized as given in the experimental studies. CAN communication between the DSPs and serial communication with the computer has been operated in accordance with this purpose. The system was operated with the position precision of ± 0.01 . The speed of the motors was limited to ± 4500 rpm.

Due to the frameless structure of the PMSM, the stator and rotor parts of the motor had to be assembled delicately within a housing and the rotor had to be fitted with the bearing externally. However, it was very difficult to meet precision requirements due to mechanical tolerance build-up arising from mechanical production errors. These faults negatively affected the system's position precision and stability. Also, setting up time synchronization between components was a difficult task in the experiments.

References

- Icpe (no date) *Frameless Kit Motors*. Available at: <https://www.icpe.ro/special-electric-machines/frameless-kit-motors> (Accessed: December 20, 2021).
- KAZAN, F.A. and BİLGİN, O. (2020) "Farklı Hızlarda Çalışan PMSM'nin Simülasyonu ve PI Denetleyici Parametrelerinin Optimizasyonu," *Mehmet Akif Ersoy Üniversitesi Uygulamalı Bilimler Dergisi*, 4(1). doi:10.31200/makuubd.673400.
- Krishnan, R. (1991) "Application Characteristics of Permanent Magnet Synchronous and Brushless dc Motors for Servo Drives," *IEEE Transactions on Industry Applications*, 27(5). doi:10.1109/28.90357.
- Liu, Z., Zhao, Y. and Wang, Q. (2019) "Study on Compensation Strategy for Interference Torque in Roll-pitch Seeker," in *Proceedings of 2019 IEEE 4th Advanced Information Technology, Electronic and Automation Control Conference, IAEAC 2019*. doi:10.1109/IAEAC47372.2019.8997581.
- Lu, M. *et al.* (2017) "Composite controller design for PMSM direct drive SGCMG gimbal servo system," in *IEEE/ASME International Conference on Advanced Intelligent Mechatronics, AIM*. doi:10.1109/AIM.2017.8014003.
- Luo, Y., Tan, G. and Su, C. (2019) "Direct Torque Control of Permanent Magnet Synchronous Motor Based on Sliding Mode Variable Structure," *OALib*, 06(09). doi:10.4236/oalib.1105758.
- Qiao, H. *et al.* (2020) "Modeling and Simulation of Seeker Servo System," in *2020 IEEE International Conference on Mechatronics and Automation, ICMA 2020*. doi:10.1109/ICMA49215.2020.9233700.
- Rudnicki, T. (2019) "Measurement of the PMSM shaft position with an absolute encoder," *Electronics (Switzerland)*, 8(11). doi:10.3390/electronics8111229.
- Samar, A. *et al.* (2012) "The implementation of Field Oriented Control for PMSM drive based on TMS320F2808 DSP controller," in *Proceedings - 2012 IEEE International Conference on Control System, Computing and Engineering, ICCSCE 2012*. doi:10.1109/ICCSCE.2012.6487218.
- Yang, Y. *et al.* (2019) "Optimal Gimbal System Control Strategy for Error Prediction Compensation," in *Proceedings - 5th International Conference on Control Science and Systems Engineering, ICCSSE 2019*. doi:10.1109/ICCSSE.2019.00022.

Investigation of Tribological Properties of Ultra High Molecular Weight Polyethylene (UHMWPE) Bearings

Gökhan TAYLAN ¹[0000-0003-4939-6766], Yakup ARTUN ²[0000-0001-6044-1199] and C. Oktay AZELOĞLU ³[0000-0001-5283-9447]

¹gokhantaylan4@gmail.com, Yıldız Technical University

²yartun@yildiz.edu.tr, Yıldız Technical University

³azeloglu@yildiz.edu.tr, Yıldız Technical University

Abstract

Journal bearings are machine elements that provide rotational and oscillating motion between other machine elements with sliding motion. Journal bearings are frequently used in force transmission. Journal bearings, which are widely used especially in the machinery and automotive industries, are generally copper-based and tin-lead-based alloys. In recent years, it has been observed that the use of polymer-based materials for these bearings has increased significantly. Since polymer materials are good in tribological applications, there are numerous studies that investigated dry operation conditions of polymer-based bearings. In this study, tribological performances of ultra-high molecular weight polyethylene (UHMWPE) bearings with two different surface qualities under different loading and velocity conditions will be investigated.

Keywords. Journal bearings, tribology, UHMWPE

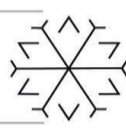
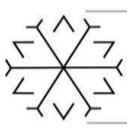
1. Introduction

Tribology is a science in which the friction, wear and lubrication properties of materials are studied for engineering applications. Some materials have superior tribological properties compared to other materials. These materials are called “tribo-materials” in the literature. It is expected that the tribological properties of the machine elements rubbing against each other in relative motion will be better. This has led to the search for new materials with better tribological characteristics.

It has been observed that polymer materials are frequently used in tribological applications. It is preferred in these applications due to its low thermal and electrical conductivity, wear and friction resistance, and corrosion resistance. Various methods are available to determine the tribological characteristics of materials. Pin-on-disc (PoD) testing is widely used to investigate the sliding behaviour of materials and relevant wear mechanisms under different tribological conditions (*Federici et al., 2017*). Its use and the fact that the experimental setup is not complicated provides convenience for these experiments. However, in order to determine the tribological properties of bearings and materials with similar geometries, different experimental setups, also seen in this study, are also used.

UHMWPE is a thermoplastic material with good chemical properties such as high molecular weight, as well as superior mechanical properties such as impact and abrasion resistance and good lubrication (*Ünal et al., 2014*). UHMWPE, which has a strength-to-weight ratio of approximately 8-15 times greater than steel, has also become a popular plastic for many industrial applications that require chemical resistance due to its high corrosion resistance.

Uzuner and Gediktaş (2004) investigated the changes in friction coefficient and contact surface temperature of radial journal plastic bearings with oscillating motion at 45 degree oscillation angle, depending on the sliding speed and surface pressure. Bearing bushes made of very high molecular weight UHMWPE and steel shaft were used in the experiments. Experiments were applied at 5 steps with oscillation frequency between 30 d/d-430 d/d ($v= 0.03-0.44$ m/s), load between 94.5-346.5 N. As a result of the experiments, they stated that the coefficient of friction increases with the sliding speed, decreases with the surface pressure, and the contact surface temperature increases with both the sliding speed and the pressure.



Ünal and Yetgin (2010) investigated the wear and friction behavior of UHMWPE and Polyamide-6 in a pin-disc wear device under dry conditions. The experiments were carried out with three different loads of 50, 100, and 150 N with a sliding speed of 0.5, 1.0, 1.5 and 2.0 m/s. As a result of their study, they determined that the friction coefficient of ÇYMAPE and PA 6 polymers decreased with the applied load, and the friction coefficient of UHMWPE and PA polymers increased with the increase of the sliding speed.

Sarı and Nteziyaremye (2006) tested Kestamid, Kestamid/HS, Kestoil, Kestlub, Ulpolen 1000 (UHMWPE) bearing materials in a radial journal bearing experimental setup using 316 stainless steel shaft. Three different loads, times and spindle speeds were used to determine the tribological properties of the bearing materials. Experimental parameters were determined according to Taguchi mixed type and friction coefficients were determined. The surface roughness of the polymer bed materials was compared before and after the experiment.

Quaglioni et al. (2009) investigated the optimum surface roughness for minimum friction of POM-H, PETP + PTFE, PA6 + wax(wax), PA66 + MoS2, UHMWPE, PTFE polymer bearing materials. As a result of the experiment, they stated that the modulus of elasticity of PTFE and UHMWPE polymers are low, the modulus of elasticity of PA66 + MoS2 and POM-H materials are high, the modulus of elasticity of PA6 + wax and PETP + PTFE materials are between 1000 and 3000 MPa. They also stated in their studies that the optimum surface roughness of the polymers for minimum friction is not the same.

Artun and Azeloğlu (2021) investigated the tribological performance of PTFE bearings on the same experimental device. The results showed that the friction coefficient of the materials increased as the sliding speed and sliding distance increased. It has been determined that increasing the pressure on the bearing also increases the friction coefficient values. It was also observed that the temperature values increased proportionally with the increase in pressure. However, it was observed that the material suffered a significant loss in terms of wear. Therefore, it is seen that it would be appropriate to add a certain amount of additives that will increase the wear resistance of the bearing to reduce the wear loss in pure PTFE bearings.

In this study, the tribological performances of “UHMWPE journal bearings in different operating scenarios were investigated. For this purpose, samples of different surface qualities were prepared from UHMWPE material and their parameters such as friction, wear and temperature were experimentally tested. In the project, first of all, journal bearing specimens were manufactured, then tribological and physical properties of all specimens were measured before the tests, and journal bearing tests were carried out according to predetermined scenarios. After the experiments, the tribological and physical properties of the samples were re-measured and compared with the pre-experimental conditions of the samples. This experimental study was completed using a radial journal bearing test setup. With this setup, coefficient of friction (μ), bearing temperature (T) and weight loss (%) values were obtained for different speed and load scenarios at 500m, 1000m, 1500m, 2000m sliding distances.

2. Experimental Studies

2.1. Experimental Setup and Scenarios

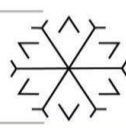
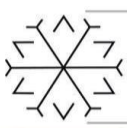
All experiments were performed with the radial journal bearing test which is shown below. Motor rotational speeds were adjusted according to experiment scenarios. Force values were obtained with a load scale. 10N and 20N loads were used in all experiments, which were added on load hanger. Friction coefficient values were obtained from this equation:

$$\mu = F_f / F_r \quad (1)$$

μ : Coefficient of friction

F_f : Frictional force

F_r : Radial force on bearing



Experiment setup is given in Figure 1 below.

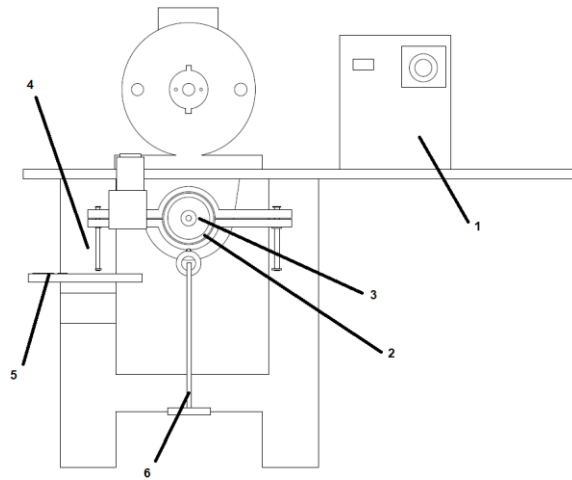


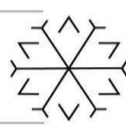
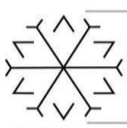
Figure 1. 1. Motor, 2. Bearing, 3. Shaft, 4. Pressure Bar, 5. Load scale, 6. Load Hanger.

The shaft surface roughness (R_a) was measured as $\sim 0.582 \mu\text{m}$ before and after the experiments. No wear occurred on the shaft after the experiments. The surface roughness of the journal bearing material with fine surface quality was measured as $3.438 \mu\text{m}$ and the journal bearing material with coarse surface quality was measured as $19.45 \mu\text{m}$ before the test. The surface roughness values on the materials after the tests will be given.

There were 8 scenarios for each journal bearing material with different surface quality. In the first scenario for each material, experiments were carried out at 0.5m/s speed and 10N loading in the journal bearing test device. Friction coefficient and temperature values were measured at 500m , 1000m , 1500m and 2000m sliding distances. In the second scenario for each material, friction coefficient and temperature measurements were made at 500m , 1000m , 1500m and 2000m sliding distances at 10N loading at 1m/s speed. In the third scenario for each material, friction coefficient and temperature measurements were made at 1.5m/s speed and 10N loading at 500m , 1000m , 1500m and 2000m distances. In the fourth scenario for each material, friction coefficient and temperature measurements were made at 2 m/s speed and 10N loading at 500m , 1000m , 1500m and 2000m sliding distances. In the fifth scenario for each material, experiments were carried out at a speed of 0.5m/s at 20N loading. Friction coefficient and temperature measurements were made at 500m , 1000m , 1500m and 2000m sliding distances. In the sixth scenario for each material, friction coefficient and temperature measurements were made at 1 m/s speed and 20N loading at 500m , 1000m , 1500m and 2000m distances. In the seventh scenario for each material, friction coefficient and temperature measurements were made at a speed of 1.5m/s at 20N loading at 500m , 1000m , 1500m and 2000m distances. In the eighth scenario for each material, friction coefficient and temperature values were measured at 2 m/s speed and 20N loading at 500m , 1000m , 1500m and 2000m distances.

In all scenarios, weight measurements of each sample were made before and after the test and the amount of wear was determined.

In all scenarios, surface roughness measurements of each sample were made before and after the experiment according to the scenarios.



2.2. Test Results

After our experiments, the data were graphed. Surface friction graph of bearings with fine surface quality is shown in Figure 2.

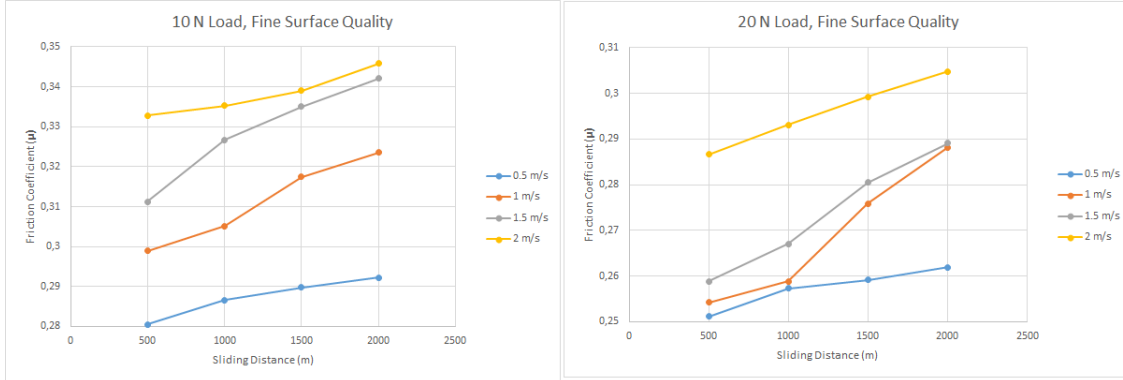


Figure 2. Friction coefficient values of bearings with coarse surface quality under 10N and 20N loads.

Surface friction graph of bearings with fine surface quality is shown in Figure 3.

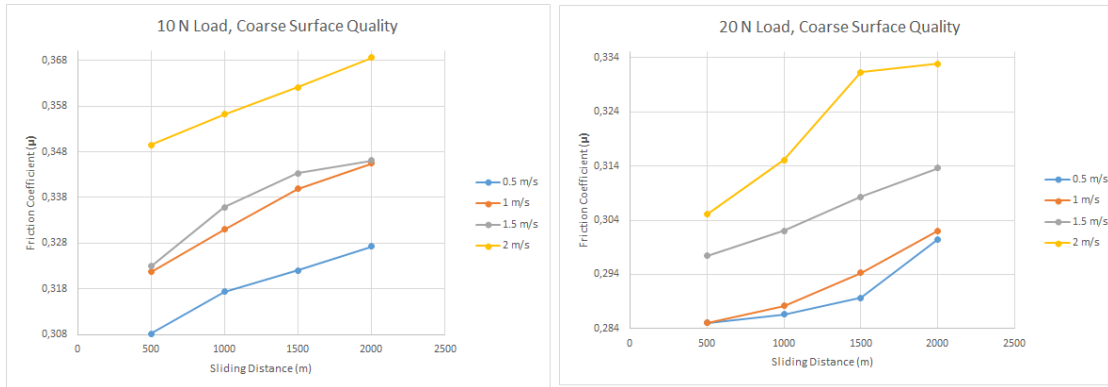
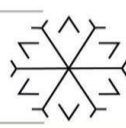
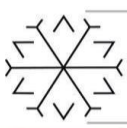


Figure 3. Friction coefficient values of bearings with coarse surface quality under 10N and 20N loads.

As it is seen, friction coefficient values increase as the sliding speed and sliding distance increases. For the bearings with fine surface quality, friction coefficient values are more stable. Also, it is seen that the friction coefficient values of the bearings with good surface quality were lower. When the load increases, we found that friction coefficient values decrease.



Temperature graph is shown in Figure 4 below. All temperature values were measured with infrared thermometer device.

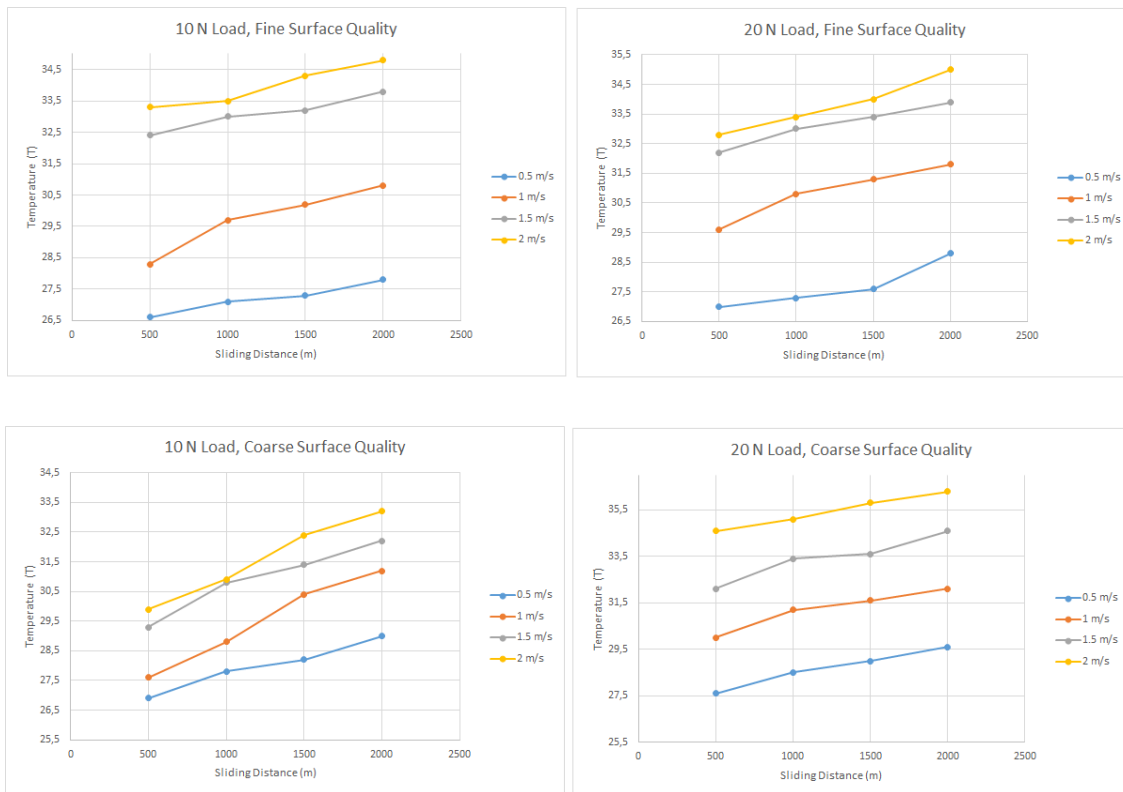


Figure 4. Temperature changes in each material under 10N and 20N loads.

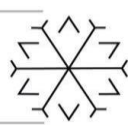
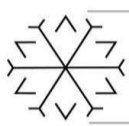
As it is seen, temperature rises as sliding speed increases in each scenario. It was observed that the temperature values increase with higher load.

Surface roughness values before the experiment (R_{a1}) are shown in table 1 below.

Table 1: Surface roughness values of bearings before the experiment.

Surface Quality	R_{a1} (μm)
Fine	3.438
Coarse	19.45

All values were measured more than once and possible errors were tried to be minimized.



Surface roughness values (R_{a2}) of bearings after the experiments (according to experiment scenarios) are shown in Table 2 below.

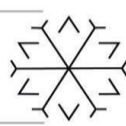
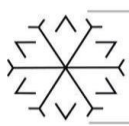
Table 2: Surface roughness results for speed and load scenarios.

Surface Quality	V (m/s)	P (N)	R_{a2} (μm)
Fine	0.5	10	2.87
Fine	1	10	2.518
Fine	1.5	10	2.394
Fine	2	10	2.269
Fine	0.5	20	3.161
Fine	1	20	2.998
Fine	1.5	20	2.813
Fine	2	20	2.559
Coarse	0.5	10	19.12
Coarse	1	10	19.03
Coarse	1.5	10	18.71
Coarse	2	10	18.44
Coarse	0.5	20	19.23
Coarse	1	20	18.68
Coarse	1.5	20	18.39
Coarse	2	20	18.26

Surface roughness values of the materials decreases as the sliding speed increases in each load cases. Values are shown in Table 3 and Table 3 (continued) below.

Table 3: Weight loss of bearings.

Surface Quality	Experiment Scenario	Weight Loss (%)
Fine	0.5 m/s speed, 10N load	0.076
Fine	1 m/s speed, 10N load	0.081
Fine	1.5 m/s speed, 10N load	0.085
Fine	2 m/s speed, 10N load	0.890
Fine	0.5 m/s speed, 20N load	0.072
Fine	1 m/s speed, 20N load	0.077

**Table 3 (continued):** Weight loss of bearings.

Surface Quality	Experiment Scenario	Weight Loss (%)
Fine	1.5 m/s speed, 20N load	0.083
Fine	2 m/s speed, 20N load	0.086
Coarse	0.5 m/s speed, 20N load	0.074
Coarse	1 m/s speed, 20N load	0.079
Coarse	1.5 m/s speed, 20N load	0.082
Coarse	2 m/s speed, 20N load	0.860
Coarse	0.5 m/s speed, 20N load	0.075
Coarse	1 m/s speed, 20N load	0.081
Coarse	1.5 m/s speed, 20N load	0.084
Coarse	2 m/s speed, 20N load	0.089

Table 2. Weight loss.

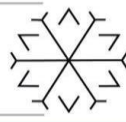
There is a slight loss of weight after the experiment. No visible wear was detected on the materials.

3. Conclusion

In this study, journal bearing specimens were manufactured. All specimens were tested under the same conditions (such as environment temperature etc.). Depending on our scenarios, it was found that the coefficient of friction increased according to the investigated parameters. The weight loss of the bearings were very low, which was predictable according to material properties. Also, the surface roughness values were also measured and the reductions were determined by comparing the values before and after the experiments. Temperature increases during the study were also investigated. Bearings with better surface quality gives less friction coefficient values. Also, less temperature rise was observed in bearings with better surface quality. It is clearly seen that surface quality has effect on friction coefficient values. These experiments give an idea of how the outputs will change according to the changing parameters. Thus, it will enlighten readers who will do experiments under similar materials and operating conditions. A comprehensive study will be carried out in order to obtain more detailed results.

References

- Artun, Y., Azeloğlu, C. O., (2021). Investigation of Tribological Properties of PTFE Journal Bearings, *International Conference on Advances in Mechanical Engineering (ICAME)*, 6
- Federici, M., Straffelini, Gialanella, S., (2017). Pin-on-Disc Testing of Low-Metallic Friction Material Sliding Against HVOF Coated Cast Iron: Modelling of the Contact Temperature Evolution, *Tribol Lett*, 65:12.
- Quaglioni, V., Dubini, P., Ferroni, D., Poggi, C., (2009). Influence of counterface roughness on friction properties of engineering plastics for bearing applications, *Materials and Design*, 30, 1650-1658.
- Sarı, A., Nteziyaremye, Ö. S., (2006). Polimer yatak malzemelerinin tribolojik özelliklerinin deneysel incelenmesi, *AKÜ FEMÜBİD*, 16, 446-453.



Unal, H., Yetgin, S. H., Findik, F., (2014). The effect of applied load and sliding speed on the tribological properties of Nylon 6 and ultra-high-molecular-weight polyethylene, *Industrial Lubrication and Tribology*, 66/3, 498-504.

Uzuner, F., Gediktaş, M., (2004). Salınım hareketi yapan radyal kaymalı plastik yataklarda sürtünme. *İstanbul Teknik Üniversitesi Dergisi/d Mühendislik*, 3, 91-98.

Ünal, H., Yetgin, S. H., (2010). ÇYMAPE ve PA-6 mühendislik polimerlerinin aşınma ve sürtünme davranışlarının incelenmesi, *Türk Bilim Araştırma Vakfı Bilim Dergisi*, 3, 145-152.

Design and Development of an Industrial Conveyor Line with Computerized Control

Fatih Akkoyun¹[0000-0002-1432-8926], Melisa Deniz²[0000-0003-3037-2182], Sena Sezen³[0000-0002-2584-2429],
Oğuzhan Karasu⁴[0000-0003-3037-2182], Gökçe Gül Günay⁵[0000-0003-1073-0616]

¹fatih.akkoyun@adu.edu.tr, Aydın Adnan Menderes University, Mechanical Engineering Department,
09010, Efeler, Aydın, Turkey

²denizmelisa3535@gmail.com, Aydın Adnan Menderes University, Mechanical Engineering
Department, 09010, Efeler, Aydın, Turkey

³eng.sena@outlook.com, Aydın Adnan Menderes University, Mechanical Engineering Department,
09010, Efeler, Aydın, Turkey

⁴oguzhankarasu78@gmail.com, Aydın Adnan Menderes University, Mechanical Engineering
Department, 09010, Efeler, Aydın, Turkey

⁵g.g.gunay@hotmail.com, Aydın Adnan Menderes University, Mechanical Engineering Department,
09010, Efeler, Aydın, Turkey

Abstract

Sorting and classification are indispensable processes in industrial mass production applications when competitive marketing and increasing the product value by reducing time and saving costs is in concern. Large-scale production ecosystems are connected to the most advanced technologies. Today, industrial production facilities require conveyor line mechanisms for carrying, moving, or rotating an object to achieve sorting, selecting, and grading duties. In this regard, an electrically driven conveyor system is a prominent technology, especially for automated industrial production flow lines. Most of the conveyor lines are used with the support of the labor force to achieve these goals. However, there are speed and cost limitations due to the limited capability of the labor force. A production line with a computer-controlled conveyor mechanism can handle many processes with more efficiency. It is a labor-saving solution that allows big-volume products to move rapidly through a process. In this study, a relatively low-cost and computer-controlled electrically driven conveyor line mechanism was developed. A computer model was designed and manufactured for the conveyor line using 3D drawing software. A combination of electronics units, mechanic components, and computer software was established. The speed and direction parameters are controlled via custom-written computer software. The electronic units are integrated to establish the communication between the computer unit, and the conveyor line mechanism. The speed of the conveyor line was adjusted according to the accepted signals by the computer software. The linear correlation was found over 0.99 (r^2) between user inputs and conveyor line speed. Thus, a computer controllable conveyor line mechanism with adjustable speed is developed to use for sorting, selecting, and grading duties in industrial applications.

Keywords. Computerized control, electrically driven conveyor system, feedforward control, speed, and direction control.

Tuned gyrostabilizer for control of vibrations in Two-wheeled Robot

Faruk Ünker ¹*[0000-0002-9709-321X]

¹farukunker@gumushane.edu.tr, Gümüşhane University

Abstract

In this study, the vibration performance of two gyroscopes mounted on a two-wheeled robot (inverted pendulum) was investigated. The frequency equations were derived and the required flywheel speed was obtained for vibration attenuation of the robot. As much as flywheel speed was increased, the amplitudes were reduced. This paper clearly showed that there is a relation between the gimbal amplitude and the flywheel speed of the gyroscope, in which the required flywheel speed can be decreased if the higher gimbal amplitude is used. A torque regulated by a gyroscopic controller was proposed as the control output to balance the roll angle of the gimbal, in which each gimbal gained the reverse inputs to eliminate the reaction torques on the body of a robot. The sinusoidal gimbal motion has resulted in a very small amplitude of sinusoidal motion in the upright position of the robot. Therefore, the gyroscopic control loop has maintained the balance of the robot with a stable continuous period. It can be concluded from the results that CMG (Control Moment Gyro) can convert the angular momentum to unidirectional thrust at the center of body mass along the forcing excitation axis, which has considerably attenuated the vibration at the target frequency. The vibration control moment gyroscope is more powerful and standalone than other conventional stabilizers by converting the angular momentum to unidirectional thrust. There was also a simulation model using RecurDyn software. The simulation results using RecurDyn software agreed well with the theoretical results of the Lagrangian mathematical model.

Keywords. Dynamic absorbers, gyroscope, gyrostabilizer, inverted pendulum, two-wheeled robot

Energy and carbon dioxide savings analysis for a single-family dwelling in Muğla region

Tolga Ural ^{1*}[0000-0002-1871-8569], Gülşah Karaca Dolgun²[0000-0002-6219-6016] and Reyhan Sena Güzelülke³[0000-0001-7435-8062]

^{1*}tolgaural@mu.edu.tr, Muğla Sıtkı Koçman University, Technology Faculty, Energy Systems Engineering Department, Muğla, Turkey.

²gulsahkaraca@mu.edu.tr, Muğla Sıtkı Koçman University, Technology Faculty, Energy Systems Engineering Department, Muğla, Turkey.

³reyhansenaguzelulke@gmail.com, Muğla Sıtkı Koçman University, Technology Faculty, Energy Systems Engineering Department, Muğla, Turkey.

Abstract

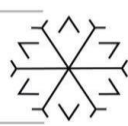
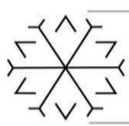
In recent years, there has been a trend towards renewable energy sources all over the world in order to prevent climate change and control global warming. The one of them is solar energy. In countries with high solar potential, the use of solar thermal collectors and photovoltaic panels is encouraged. Thus, fossil fuel consumption will be minimized and resource security will be ensured with the use of domestic resources. For this reason, solar collectors are used for purposes such as domestic hot water and building heating. Heat pumps are preferred in detached houses due to their high coefficient of performance and summer/winter operation. The use of heat pumps together with solar thermal collectors increases the coefficient of performance (COP) of the system and decreases the electricity consumption and carbon dioxide emissions. In this study, COP, energy and emissions saving parameters of the solar assisted air source heat pump was investigated according to different number of solar collectors. Three different models were created in the simulation program. Number of solar collectors were three in Model 1, four in Model 2 and five in Model 3. The COP values of the system were 6.5, 7.2 and 7.9 in Model 1, 2 and 3, respectively. The annual maximum energy savings were 5940.2 kWh, 5630 kWh and 5369.3 kWh in Model 1, 2 and 3, respectively. The annual maximum reductions of CO₂ emissions were 3186 kg, 3020 kg and 2880 kg in Model 1, 2 and 3, respectively.

Keywords. Heat pump, solar thermal collectors, COP, reductions of CO₂ emission.

1. Introduction

Heat pumps with a high coefficient of performance are used in remote areas where have not access to the natural gas. The advantages of heat pump are ease of use, automatic control, zero direct emission, both heating and cooling process, less maintenance and repair frequency, no dirt-rust and no need to store the fuel used. High initial investment cost is the negative side. If the electricity consumed by the heat pumps can be obtained from renewable energy sources such as wind, solar and hydroelectricity, carbon emissions of its will be zero. Therefore, heat pumps are promising technologies and it is thought that usage will become widespread. Heat pumps are divided into three as ground, water and air source. The use of air source heat pumps is more common due to the ease of installation and initial investment cost. Before choosing a heater for heating a house, the annual heating demand calculation should be made according to the months. In addition, if there is a need for domestic hot water demand in the house, the number of people should be determined. The heating system is decided by considering the existing resources in the region, the type of residence (apartment or villa), ease of use, initial investment cost and environmental factors. Examining the system with the simulation program before the installation plays an important role in the selection of the appropriate equipment. Standard of the TS 825 Thermal Insulation in Buildings was used to calculate the annual heating energy demand of the building.

Mohammed and Hamakhan (2021) compared solar water heating systems and electrical water heating systems for three cities in Iraq with Polysun simulation program. Solar fraction was between 34.2%-40.4% and annual CO₂ reduction values were between 771 and 824 kg. Nahavandinezhad and Zahedi (2022) compared four possible solar assisted ground source heat pump systems to supply aims of electricity



demand, domestic hot water, heating and cooling with Polysun simulation program. Maximum and minimum COP values of heat pumps were 3.87 and 4.39. Payback period of system according to optimal strategy was 7 years. Also, 5089 kg CO₂ emission was prevented (Nahavandinezhad and Zahedi, 2022). Jaber et al. (2021) simulated solar water heating systems for single family house in Iraq with Polysun simulation program. Artur et al. (2018) developed a hourly auxiliary heating model and compared with Polysun simulation program to analyse tank size and hot water consumption profiles in the solar thermal systems for 5 person family house in Mozambique. Ruesch and Haller (2017) compared direct cooling potential in low-temperature district heating and cooling (LTDHC) networks with combinations of heat sources for three different building as standard, low energy and passive. The measured data was compared with the borehole field model of Polysun and the results were similar under same loads. Cai et al. (2017) simulated PVT assisted ground source heat pump (GSHP) system for heating and cooling of building. PV was cooled with water to increase electrical efficiency and hot water was used as a heat source for heat pump to increase COP. Five different operation moods were used. Simulation results were verified with real data and optimized values of PV/T modules angle and tank volume were calculated as 45° and 8500 litres. It is also suggested to use two 40 kW heat pumps instead of using one 78 kW heat pump.

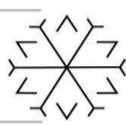
Özakın (2020) performed the performance analysis of the integrated photovoltaic – heat pump system. Experiments were carried out with a halogen solar simulator according to different radiation values. The effects of rectangular, cylindrical, delta and hexagonal fins of the heat pump evaporator on the energy and exergy efficiency of the system were investigated. In case the heat pump is used alone, the COP is calculated as 2.69 and the COP of the integrated system is calculated as 3.20. By using the heat pump together with photovoltaic panels, the energy efficiency has increased by 19%. Arpacı (2020) simulated greenhouse heating with a water source and solar assisted heat pump. Three different solar collectors were used for two greenhouse heating systems (cold and warm), these are flat plate, vacuum tube and parabolic solar collectors. Surface area is 20m². The solar fraction varies between 27.7% and 70%, depending on the type of solar collector used in the cold greenhouse system. The solar fraction in the warm greenhouse system varied between 24.2% and 53.4%. The highest solar fraction was observed in the use of parabolic solar collectors. Şensoy (2019) calculated the COP value of the photovoltaic thermal collector assisted heat pump as 4.65. In the heating season, 39.60% of the thermal energy demand was met by PVT collectors. Güteryüz (2019) performed the thermodynamic analysis of the solar assisted heat pump system. In the simulation, the COP value of the system varies between 2.9-4.3 in summer and between 2.0-3.7 in winter (Şensoy, 2019). Ergün (2019) designed a solar-assisted double-tank heat pump system and simulated it in the TRNSYS program. Water-to-water heat pump and PVT solar collectors are modeled for five different cities (Istanbul, Ankara, Izmir, Hakkari, Trabzon) for the restaurant's heating, cooling and domestic hot water needs. The minimum and maximum SPF values are 1.74 and 2.65, respectively. The system in İzmir worked 52% more efficiently than the system in Hakkari. Kuru (2019) compared existing central heating system and the hybrid heat pump with intelligent control system for heating or cooling a 500 m² greenhouse. In the hybrid system, solar energy and a waste heat recovery system were used. For this reason, with the hybrid heat pump system, the CO₂ emission was 14.55 tons/year and was reduced by 90%.

This is a case study for Muğla region. There have not been any study about this topic in the literature. In this study, solar assisted heat pump systems according to solar collector area were compared using the POLYSUN-Vela Solaris simulation program. The effect of the number of solar collectors on the seasonal performance coefficient of the system was investigated. In addition, the amounts of energy and CO₂ emissions saved with the use of heat pump and solar collector were examined.

2. Methodology

2.1. Description of the system

Three different models were built to supply heating and hot water demand of a single-family house. Location of the house is in the Gülağzı/Muğla with 37.145° latitude and 28.357° longitude. System consists of four parts as solar collectors, air to water heat pump, floor heating and hot water demand. Schematic diagram of heating system is given in Figure 1. Number of solar collectors were changed as three, four and five in Models and named as Model 1, Model 2 and Model 3, respectively. Thus, effect of solar collectors to the seasonal performance factor (SPF) of the heating system will be examined. Temperature of hot water was 40 °C, and daily domestic hot water demand (DHW) for four-person family was 200 litres. Minimum average outdoor temperature was -3 °C. Heating setpoint temperature of house was adjusted as 20 °C. Total heating energy demand excluding DHW was 8844 kWh. Heating capacity of air to water heat pump is 22 kW and COP value (A2/W35) was 4.2. Flat plate collector has a good quality. Orientation and tilt angle of collectors were set as 0° and 40°, respectively. Capacity of storage tank was 600 litres, and material was



steel. Tank was insulated with rigid PU foam (80mm). Heating element was floor heating and nominal inlet/return temperatures were 35/25 °C.

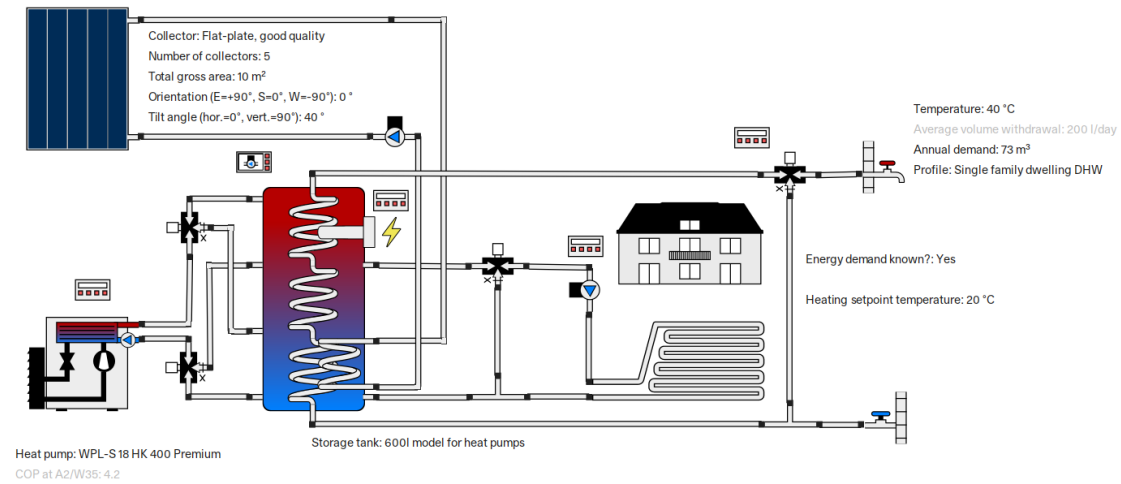


Figure 1. Schematic diagram of heating system.

2.2. Controlling of the system

Pump controller solar loop, auxiliary heating controller 1, auxiliary heating controller 2, heating/cooling controller and mixing valve controller were used. All data was recorded for one-minute intervals in simulation program.

2.3. Energy equations

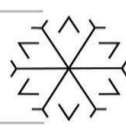
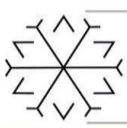
Q_{aux} is the amount of solar thermal energy. Q_{aux} is the amount of energy supplied from electrical air conditioning devices to fluid. E_{aux} is the amount of electrical power required by electrical air-conditioning devices. E_{tot} is the amount of electrical power required by fans, pumps, electrical air-conditioning devices, etc. Solar Fraction is calculated by Eq. (1) and SPF value of heat pump is determined by Eq. (3).

$$SF_n = \frac{\text{Solar energy to the system}}{\text{Solar energy to the system} + \text{Auxiliary energy to the system from HP}} \quad (1)$$

$$SF_n = \frac{Q_{sol}}{Q_{sol} + Q_{HP}} \quad (2)$$

$$SPF_{HP} = \frac{Q_{HP}}{E_{equipment}} \quad (3)$$

Storage tank is heated with solar water collectors and air to water heat pump. Thermal energy was used for domestic hot water usage and floor heating. Also, some energy was lost to the environment from the tank. The thermal energy balance of the tank at time t is expressed by Eq. 4. The amount of heat withdrawn from the tank for the domestic hot water requirement is given in Eq. 5. The thermal energy given to the system by the heat pump is equal to multiplying of the temperature change of water in the condenser, the mass flow rate and specific heat, and is given in Eq. 6. The thermal energy for the floor heating is found by multiplying the installation inlet and outlet water temperature difference, the mass flow rate and specific heat of water, and is given in Eq. 7. Heat loss from the storage tank is calculated by Eq. 8.



$$Q_{tank}(t) = Q_{solar}(t) + Q_{HP}(t) + Q_{tank}(t-1) - Q_{DHW}(t) - Q_{heating}(t) - Q_{loss}(t) \quad (4)$$

$$Q_{DHW}(t) = \rho \cdot c_p \cdot V_{DHW} (T_{outlet} - T_{inlet})_{DHW} \quad (5)$$

$$Q_{HP}(t) = \rho \cdot c_p \cdot V_{HP} (T_{outlet} - T_{inlet})_{HP} \quad (6)$$

$$Q_{heating}(t) = \rho \cdot c_p \cdot V_{heating} (T_{inlet} - T_{outlet})_{heating} \quad (7)$$

$$Q_{loss} = U \cdot (T_{max} - T_{amb}) \quad (8)$$

Carbon dioxide saving in solar thermal system is calculated by multiplying of amount of energy saving with CO₂ emission factor of fuel and is given in Equation 9. Carbon dioxide saving in heat pump system is calculated by multiplying of amount of energy saving with CO₂ emission factor of fuel and is given in Equation 10. CO₂ emission factor in the simulation program is taken from the ecoinvent centre (Schweizer Zentrum für Ökoinventare).

$$\begin{aligned} CO_2 \text{ savings solar thermal} & \quad (9) \\ & = \text{energy savings in solar thermal collector} \\ & * CO_2 \text{ emission of fuel} \end{aligned}$$

$$CO_2 \text{ savings heat pump} = \text{energy savings in heat pump} * CO_2 \text{ emission of fuel} \quad (10)$$

3. Result and Discussion

The simulation was repeated by changing the number of solar collectors. Data from Model 1, Model 2 and Model 3 were compared. In Model 1, when three collectors (6m²) were used in heating system, seasonal performance factor (SPF) and primary energy factor of the system were found as 6.5 and 0.29, respectively. Maximum energy savings was 1034.2 kWh and maximum reduction in CO₂ emissions was 555 kg with usage of solar collectors. Total energy savings was 4906 kWh and total reduction in CO₂ emissions was 2631 kg with usage of air to water heat pump. In Model 2, when four collectors (8m²) were used in heating system, seasonal performance factor (SPF) and primary energy factor of the system were found as 7.2 and 0.27, respectively. Maximum energy savings was 1187.9 kWh and maximum reduction in CO₂ emissions was 637 kg with usage of solar collectors. Total energy savings was 4442 kWh and total reduction in CO₂ emissions was 2383 kg with usage of air to water heat pump. In Model 3, when five collectors (10m²) were used in heating system, seasonal performance factor (SPF) and primary energy factor of the system were found as 7.9 and 0.24, respectively. Maximum energy savings was 1311.3 kWh and maximum reduction in CO₂ emissions was 703 kg with usage of solar collectors. Total energy savings was 4058 kWh and total reduction in CO₂ emissions was 2177 kg with usage of air to water heat pump.

With the increase of the solar collector area, the energy supplied to the system increased and the heat pump worked less. For this reason, electricity consumption of heat pump has decreased. Therefore, when the solar collector area increased, the CO₂ emission prevented by the collectors increased, and the CO₂ emission prevented by the use of heat pumps decreased.

The hot water requirement was met only by solar collectors for five months in all three systems. When the temperature difference between the two fluids is high, the heat transfer will be faster. Since the temperature difference was decrease after the tank was heated, no more thermal energy was transferred to the tank. For this reason, given solar thermal energy to the system was almost equal in all Models in Figure 2 for five months. However, the amount of heat supplied to the tank increased with the number of collectors, as heat was constantly drawn from the tank during the winter months. Amounts of solar thermal energy to the system (Q_{sol}) in whole year were 4517 kWh in Model 1, 5193 kWh in Model 2 and 5738 kWh in Model 3.

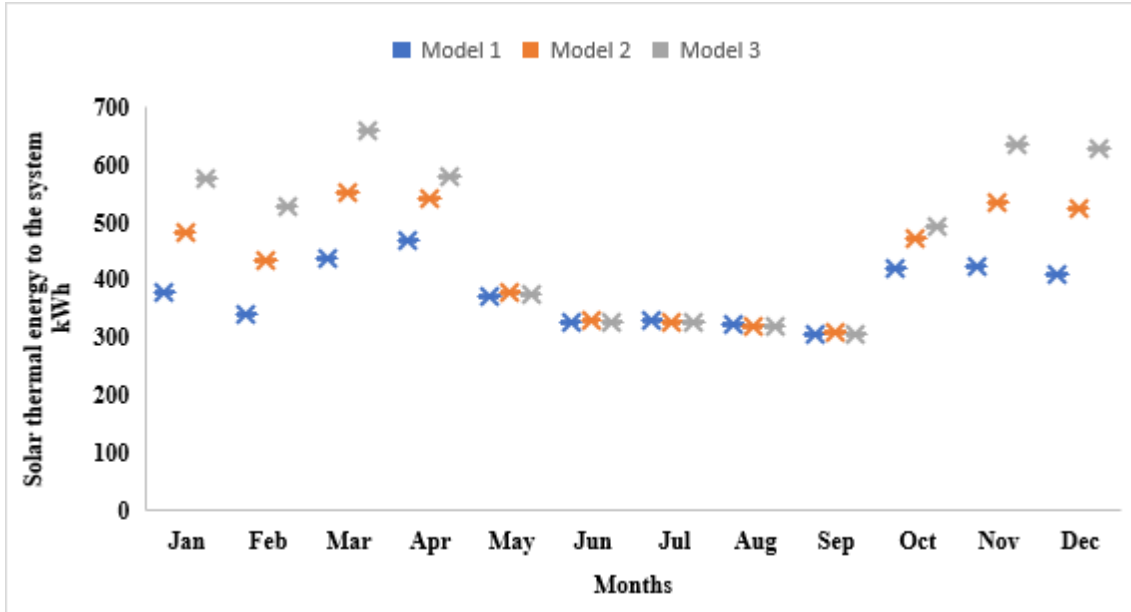


Figure 2. Solar thermal energy to the system according to models

Since all of the hot water needs in summer were met by solar collectors, it was seen that the solar fraction was 100%. The variation of the contribution of solar collectors to the heating system by months is given in Figure 3. Solar fraction hot water (SF_{nHw}) values were 64.3% in Model 1, 69.1% in Model 2 and 72.8% in Model 3. Solar fraction building (SF_{nBd}) values were 28.3% in Model 1, 35.1% in Model 2 and 40.8% in Model 3. Solar fraction (SF_n) values for a year were 41.5% in Model 1, 47.4% in Model 2 and 52.2% in Model 3.

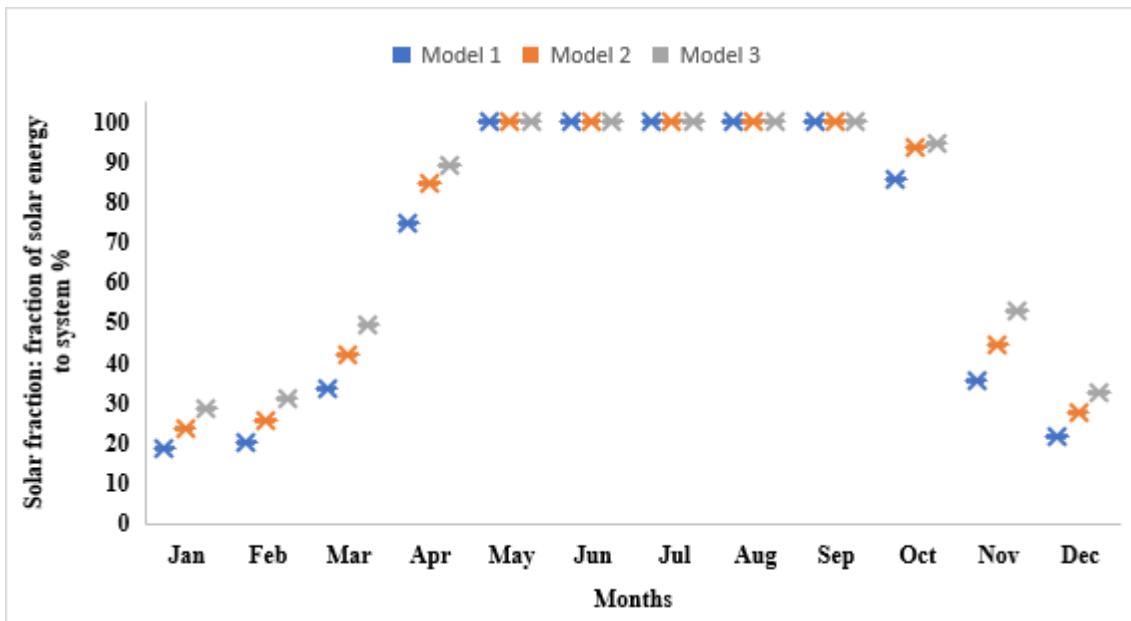


Figure 3. Fraction of solar energy to system according to models

Heat generator energy to the system according to models is given in Figure 4. Heat generator energy to the system (Q_{aux}) values in a year were 6362 kWh in Model 1, 5760 kWh in Model 2 and 5260 kWh in Model 3. Total electricity consumption of the system (E_{tot}) values in a year were 1551 kWh in Model 1, 1411 kWh in Model 2 and 1294 kWh in Model 3. With the increase in the number of solar collectors, operating time of the heat pump was shortened. For this reason, electricity consumption and the amount of thermal energy by the heat pump decreased. It was seen that there was not electricity consumption of the heat pump for five months, since all the existing hot water needs were met from the collectors in the summer months. Only, pumps consumed electricity for water circulation.

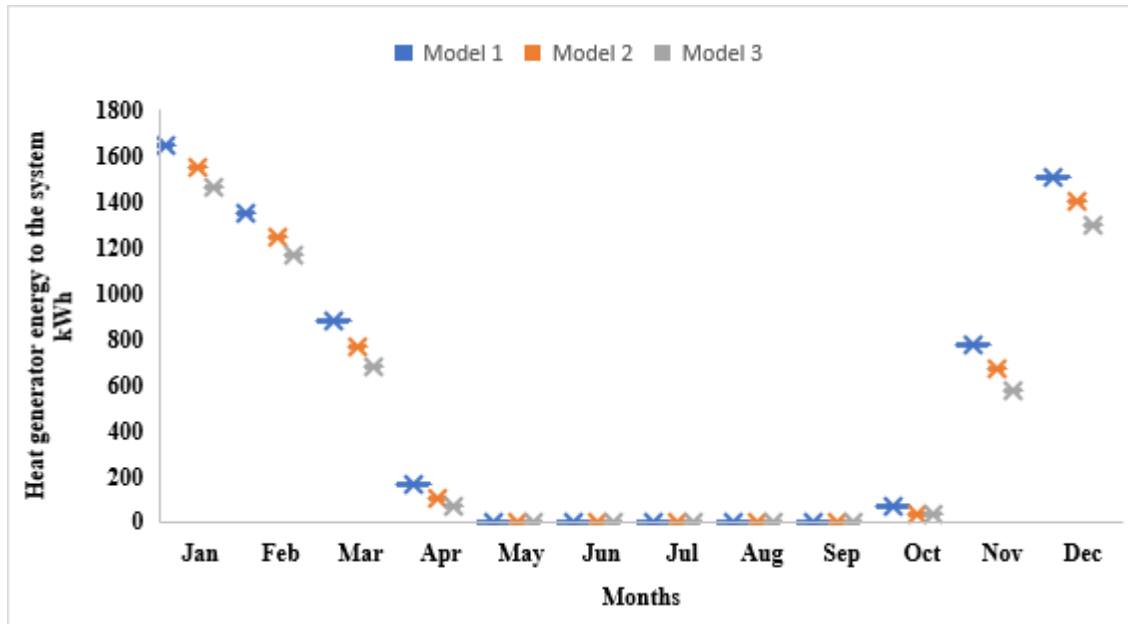
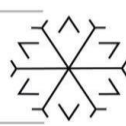
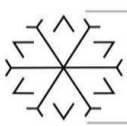


Figure 4. Heat generator energy to the system according to models

4. Conclusion

In this study, the coefficient of performance, maximum energy saving and maximum emission reduction of the heating system were investigated by changing the number of collectors. With the use of solar collectors, the electricity consumption of the heat pump has decreased and primary energy factor was also decreased. For a 4-person family, three collectors, 22 kW heat pump and a 600-liter tank were sufficient. Increasing the number of collectors does not contribute to hot water production in summer. However, the number of collectors has a role in reducing electricity consumption and CO₂ emissions. By adding PV panels to the system, some of the electricity consumption can be met from here. It is thought that this study will be an example for the use of solar assisted heat pumps in residences.

Acknowledgements

In this study, the POLYSUN simulation program was provided with the funding from the TUBITAK project numbered 1919B012006376.

References

- Arpaci, E. (2020) A greenhouse heating simulation in the cold climate with a water source heat pump assisted with solar energy. Van Yüzüncü Yıl University, Master Thesis.
- Artur, C. *et al.* (2018) 'Comparison of two dynamic approaches to modelling solar thermal systems for domestic hot water', *Sustainable Energy Technologies and Assessments*, 30, pp. 292–303. doi: 10.1016/j.seta.2018.10.012.
- Cai, J. *et al.* (2017) 'Performance study of a novel hybrid solar PV/T ground-source heat pump system', *Procedia Engineering*, 205, pp. 1642–1649. doi: 10.1016/j.proeng.2017.10.324.
- Ergün, E. H. (2019) Solar assisted dual tank heat pump application for a residential house. Uludağ University, Master Thesis.
- Güleryüz, B. (2019) Thermodynamic analysis of a solar assisted heat pump system. Kütahya Dumlupınar University, Master Thesis.
- Jaber, H. J. *et al.* (2021) 'Simulation Of Solar Water Heating System In Single Family House In Various Weather By Using Polysun Programs Simulation Of Solar Water Heating System In Single Family House In Various Weather By Using Polysun Programs', 12(11), pp. 313–317.



Kuru, M. (2019) The comparison of energy efficiency of natural gas heating system and solar assisted heat pump system. Karamanoğlu Mehmetbey University, Master Thesis.

Mohammed, A. K. and Hamakhan, I. A. (2021) 'Analysis of energy savings for residential electrical and solar water heating systems', *Case Studies in Thermal Engineering*, 27, p. 101347. doi: 10.1016/j.csite.2021.101347.

Nahavandinezhad, M. and Zahedi, A. (2022) 'Conceptual design of solar/geothermal hybrid system focusing on technical, economic and environmental parameters', *Renewable Energy*, 181, pp. 1110–1125. doi: 10.1016/j.renene.2021.09.110.

Özakın, A. N. (2020) Performance Analysis of Photovoltaic - Heat Pump Integrated System. Atatürk Üniversitesi.

Ruesch, F. and Haller, M. (2017) 'Potential and limitations of using low-Temperature district heating and cooling networks for direct cooling of buildings', *Energy Procedia*, 122, pp. 1099–1104. doi: 10.1016/j.egypro.2017.07.443.

Şensoy, B. (2019) Performance Analysis of Solar Energy Assisted Heat Pump Systems. Gazi University, Master Thesis.

Synthesis and Characterization of Magnetic Metal Organic Framework (MOF) for Methyl Orange Removal from Aqueous Solutions

Bengisu Karakaya^{1*} [0000-0002-7021-4851], Bercem Kiran Yildirim² [0000-0002-7504-0176], Zehra Semra Can³ [0000-0003-4447-3400], Gül Gülenay Hacıosmanoğlu³ [0000-0003-1674-0305], Serdar Şam³ [0000-0002-1019-8554], and Seval Genç¹ [0000-0002-0937-942X]

¹karakayabengisu@gmail.com, Marmara University, Engineering Faculty, Metallurgical and Materials Engineering Dept.

²bercem.kiran@marmara.edu.tr, Marmara University, Engineering Faculty, Chemical Engineering Dept.

³zehra.can@marmara.edu.tr, Marmara University, Engineering Faculty, Environmental Engineering Dept.

³gulenay.haciosmanoglu@marmara.edu.tr, Marmara University, Engineering Faculty, Environmental Engineering Dept.

³serdar.sam@marmara.edu.tr, Marmara University, Engineering Faculty, Environmental Engineering Dept.

¹sgenc@marmara.edu.tr, Marmara University, Engineering Faculty, Metallurgical and Materials Engineering Dept

Abstract

Water pollution has become a serious worldwide issue with the intensification of human activities and the rapid progress of modern industry even though water is one of the most valuable natural resources. Therefore, removal of pollutants from water is a considerable interest in the worldwide in the recent times. One of the important technique of this is adsorption which is the most preferred separation process due to its low cost, versatility and ease of operation. Traditional adsorbent materials have limitations in their application such as low adsorption capacity or difficulty in separation. Metal organic frameworks (MOFs), synthesised with metal ions and organic ligands, are important alternative as adsorbent based on their remarkable features such as large specific surface areas, higher porosity, *etc.* In addition to these features, MOF-based adsorbents combined with magnetic nanoparticles (NPs) can be separated easily with an external magnetic field. In this study, magnetic Co based MOF has (Co-MOF) been synthesised and the adsorption of methyl orange (MO) which is a widely used dye in various industrial processes has been investigated. Co-MOF was synthesized with CoCl₂·6H₂O. Terephthalic acid (1 mmol) was mixed with N,N dimethyl formamide (DMF) and ethanol solution (30 mL each), and then 0.5 mmol of CoCl₂·6H₂O was added into the solution. The solution was poured into a 25-mL Teflon-lined stainless steel autoclave and this was placed in an oven at 105 C for 20 h. The product was filtered and washed with DMF for three times to remove surplus reactants. The purple powder of Co-MOF was obtained by drying the product in an oven at 60 C for 12 h. The characterization of Co-MOF was performed by XRD, FT-IR, DTA/TGA, and SEM. The MOF particles was then dispersed in Fe+2 and Fe+3 salts and Fe₃O₄ was precipitated on MOF particles with the addition of NaOH (pH=10).

Adsorption experiments were carried out in a temperature controlled shaker at 250 rpm. Typically, Co-MOF with 1 g/L dose was added into a 10 mL aqueous solution containing an initial dye concentration of 500 mg/L and the adsorption temperature was 25 °C with various contact times. These typical conditions are applied for each adsorption experiment unless otherwise stated. The effect of contact time and the adsorbent amount on the MO adsorption have been determined and the results were evaluated to reveal the adsorption kinetics. As a conclusion, it can be suggested that Co-MOF can be an important alternative adsorbent for MO removal with its easy separation.

Keywords. Co-MOF, magnetic MOF, adsorption, , methyl orange

Parametric Analysis of Photovoltaic Module

Mustafa Asker^{1*}[0000-0001-5989-3366] Oguz Emrah Turgut²[0000-0003-3556-8889] Hadi Genceli³[0000-0002-9273-548X]

¹mustafa.aker@adu.edu.tr, Aydin Adnan Menderes University, 09010 Aydin, Turkey

²oguzemrah.turgut@bakircay.edu.tr, Izmir Bakırçay University, 35665 Izmir, Turkey

³hgenceli@yildiz.edu.tr, Yildiz Technical University, 34349 Istanbul, Turkey

Abstract

Estimating the intrinsic parameters of photovoltaic (PV) cells and modules is one of the significant challenges in the field of solar energy. A reliable predictive method enables the engineers to optimize the system performance. In this work, the five unknown parameter values are extracted at the standard test condition from the Monocrystalline SQ175-PC module. The nonlinear equations system is resolved by using Newton Raphson's technique coded in Matlab. The obtained I - V and P - V characteristics results of the PV module at general conditions for different temperatures as well as irradiance are demonstrated. The numerical model results are compared with published experimental data obtained from the literature and reasonable agreement is obtained. In addition, a parametric analysis is conducted to investigate the influence of solar radiation and cell temperature on the performance of PV modules. The results show that at the constant solar radiation of 1000 W/m^2 , the cell efficiency rates diminishes as the cell temperature increases. At the fixed cell temperature of 25°C , the efficiency values rise with the increment of solar irradiance.

Keywords., Monocrystalline, Photovoltaic, Single Diode Model

1. Introduction

Nowadays, several scientific efforts are made to improve the energy efficiency of renewable energy systems due to the increasing global energy consumption, the depletion of fossil fuels, and the increase in greenhouse gas emissions, which has led to environmental pollution and irreparable damage vital resources [1]. Today, photovoltaic (PV) systems are one of the most prevalent electricity generation technologies, among the advantages of which are: easy access, noiselessness, environmentally friendly and low maintenance costs [2]. Given the prevalence of using photovoltaic module cells, it is necessary to provide an accurate model of them; so that the characteristic curve of the simulated model is the same as the characteristic curve of the cell or module in different environmental conditions. In the past, the electrical properties of photovoltaic cells using different equivalent circuits have been modeled and in order to achieve the proposed model to be very accurate, the parameters of that model must be precisely estimated [3]. Various methods have been suggested to solve the problem of estimating the parameters of the electrical equivalent circuit model of the PV system. In general, these methods are divided into three main categories, the use of analytical, meta-heuristic optimization algorithms and combined methods (analytical-meta-heuristic). The use of meta-heuristic optimization algorithms is more popular than other methods because of its high accuracy in calculating the parameters of the PV system. This method turns the problem of estimating the parameter of photovoltaic cells into a problem of optimization and calculates the parameters, which result in the least error. Numerous detailed reviews related to classifying of the current equivalent electrical circuit [4], PV cell model parameter estimation problem [5] and the applications of hybrid PV-thermal systems [6] have been carried out by many researchers.

Several articles have been presented using different optimization algorithms. Orioli and Gangi [7] explained the algorithm in order to assess the parameters of a one-diode equivalent circuit capable of accurately displaying the electrical pattern of a PV cell through the set of technical information. Nassar-eddine et al. [8] compared the two estimation parameter techniques and assessed their influence on the solar cell I - V characteristics models. Lo Brano et al. [9] suggested an improved form of the five-parameter model capable of precisely show the electrical pattern of a PV panel based on the technical data frequently provided by manufacturers.

Chen et al. [10] proposed a novel hybrid teaching-learning-based artificial bee colony (TLABC) by combining the training-based optimization algorithm (TLBO) and the artificial bee cloning algorithm (ABC) in order to evaluate the parameters of the electrical equivalent circuit of the single-diode and two-diode models of the PV system with

this algorithm. The results obtained from the TLABC algorithm are compared with the results of the TLBO and ABC algorithms, and it is observed that this algorithm offers superior performance in terms of accuracy for various PV parameter estimation problems. . Derick et al. [11] proposed the wind Driven Optimization (WDO) method for identifying all the parameters of the PV module under different temperature and radiation conditions.

The objective of this study is to utilize the Newton Raphson approach, which is a powerful and suitable method for extracting the five unknown parameters for a single diode under STC. The simulation of I - V and P - V curves for different solar radiation and solar cell. In addition, the performance of PV module at various conditions are explored.

2. Mathematical Model

The present analysis will consider one diode of PV modules. The circuit of the model is displayed in Figure 1.

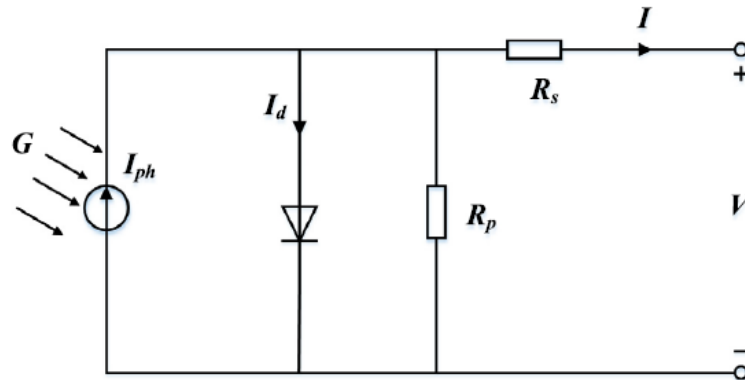


Figure 1: One Diode Model of Solar Cell

The mathematical equation that describes I - V characteristics is given as follows [8, 12]

$$I = I_{ph} - I_o \left[\exp\left(\frac{V + R_s I}{a N_s V_t}\right) - 1 \right] - \frac{V + R_s I}{R_p} \quad (1)$$

Where

$$V_t = \frac{K T}{q} \quad (2)$$

The five unknown parameters are I_{ph} : is photocurrent parameter, I_o : is diode reverse saturation current, a : is diode ideality factor. R_s :is series resistance and R_p :is parallel resistance. These parameters of equation (1) are calculated by developing a system of independent equations, which are solved using the Newton Raphson Method [8,13]. These equations are obtained from the I - V characteristic at standard test condition (STC) as follows

At open circuit point $I=0$, ($V_{oc},0$)

$$0 = I_{ph,ref} - I_{o,ref} \left[\exp\left(\frac{V_{oc,ref}}{a_{ref} N_s V_{t,ref}}\right) - 1 \right] - \frac{V_{oc,ref}}{R_{p,ref}} \quad (3)$$

At short circuit point $V=0$, ($0, I_{sc}$)

$$I_{sc,ref} = I_{ph,ref} - I_{o,ref} \left[\exp\left(\frac{R_{s,ref} I_{sc,ref}}{a_{ref} N_s V_{t,ref}}\right) - 1 \right] - \frac{R_{s,ref} I_{sc,ref}}{R_{p,ref}} \quad (4)$$

At $V=0$, $I=I_{sc}$

$$\frac{dI}{dV} = -\frac{1}{R_p} \quad (5)$$

At maximum power MP (V_{mp}, I_{mp}) equation (1) can be expressed as

$$I_{mp} = I_{ph,ref} - I_{o,ref} \left[\exp \left(\frac{V_{mp} + R_{s,ref} I_{mp}}{a_{ref} N_s V_{t,ref}} \right) - 1 \right] - \frac{V_{mp} + R_{s,ref} I_{mp}}{R_{p,ref}} \quad (6)$$

Besides at maximum power

$$\frac{dP}{dV} = \frac{d(IV)}{dV} = I + V \frac{dI}{dV} = 0 \quad (7)$$

$$\frac{dI}{dV} = -\frac{I_{mp}}{V_{mp}} \quad (8)$$

In this work, a Monocrystalline SQ175-PC type solar cell is used. The general properties of SQ175-PC type solar cell are given in Table 1 [14]

Table 1: Main Properties of PV Module [14]

Properties	SQ175-PC
Max. Power at STC	175 W
Open-Circuit Voltage at STC	44.6 V
Short-Circuit Current at STC	5.43 A
The voltage at maximum power point (STC)	35.4 V
Current at maximum power point at (STC)	4.95 A
Voltage temperature coefficient	-0.145 V/°C
Current temperature coefficient	-0.8×10 ⁻³ A/°C
Number of cells	72

By following the Newton Raphson Method procedure of Villalva et al. [13], the five unknown parameters under STC are obtained, and the general *I-V* characteristic is computed.

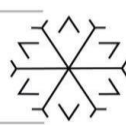
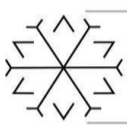
The efficiency of the solar cell is defined as

$$\eta = \frac{P_{max}}{G \times A} \quad (9)$$

3. Results and discussion

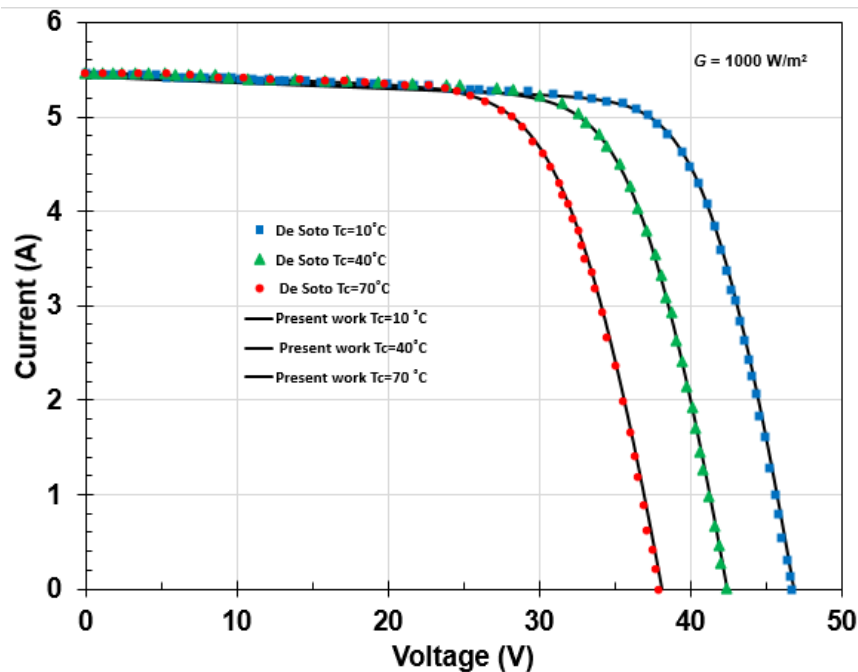
In this theoretical research study, the conventional Newton-Raphson method is employed to extract unknown parameters of monocrystalline silicon SQ175-PC from Solar cells. Technical specifications of the PV module based on standard test conditions are reported in Table 1. The following two issues should be precisely defined in order to solve the parameter identification problem of PV modules. (1) Defining the mathematical model whose unidentified parameters are extracted (2) Determining the mathematical tool used to estimate the unidentified model parameters. Five different parameters of the PV module are estimated by the Newton Raphson method for the single diode model at standard test conditions, which includes the light generated current (A) I_{ph} , reserve saturation current of the diode (A) I_o , diode ideality factor a , series resistance of the diode R_s (Ω), and parallel resistance of the diode R_p (Ω). Table 2 tabulates the estimated values of the single diode model parameters through the Newton-Raphson root-finding method for monocrystalline silicon SQ175-PC.

Table 2. Five Extracted Parameters at STC

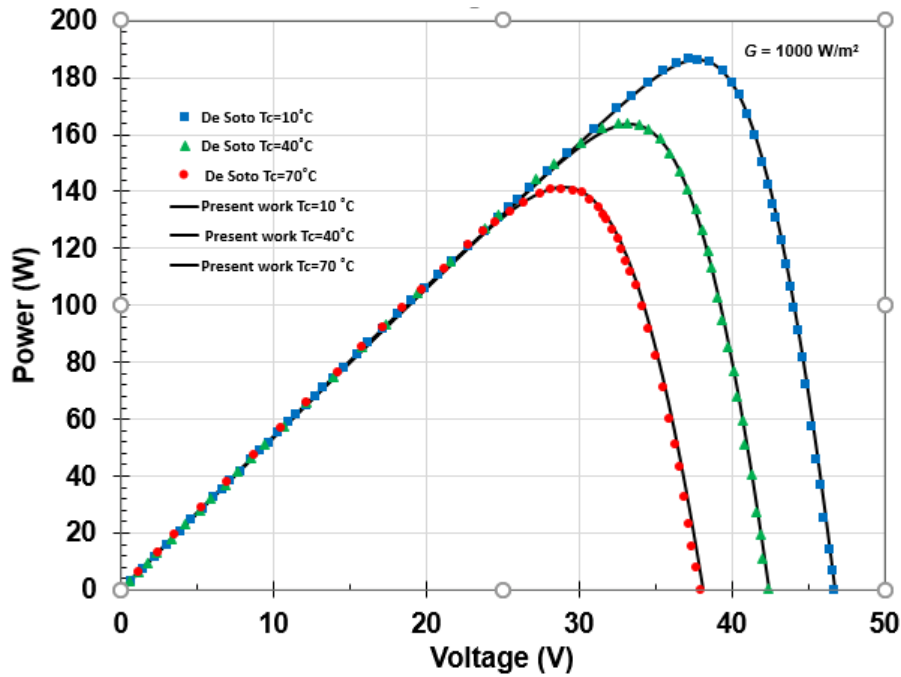
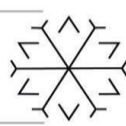
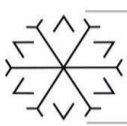


Properties	SQ175-PC
I_{ph}	5.45504 A
I_o	2.622×10^{-10} A
a	1.01706
R_s	0.73 Ω
R_p	158.61541 Ω

It is observed that the reverse saturation current of the diode takes a numerical value on the order of $2.622E-10$, which is negligibly small for the present data. Other parameters are respectively obtained as $I_{ph}=5.45505$ A, $a=1.01706$, $R_s=0.73 \Omega$, and $R_p=158.61541 \Omega$ for single diode model parameter identification case. Figure 2(a-b) shows the comparison between the different I - V curves obtained by the Newton-Raphson root-finding method and experimental data from De Soto [15] for different cell temperatures varying from 10 to 70°C while solar irradiation is fixed to $G=1000 \text{ W/m}^2$. A good agreement is evident between the experimental data and the proposed mathematical model for each I - V curve shown in Figure 2(a). Power versus Voltage curves for different cell temperatures are comparatively given in Figure 2(b). It is observed that the collected experimental data is well-matched with the Newton-Raphson based parameter estimation model at the constant solar irradiation $G=1000 \text{ W/m}^2$.



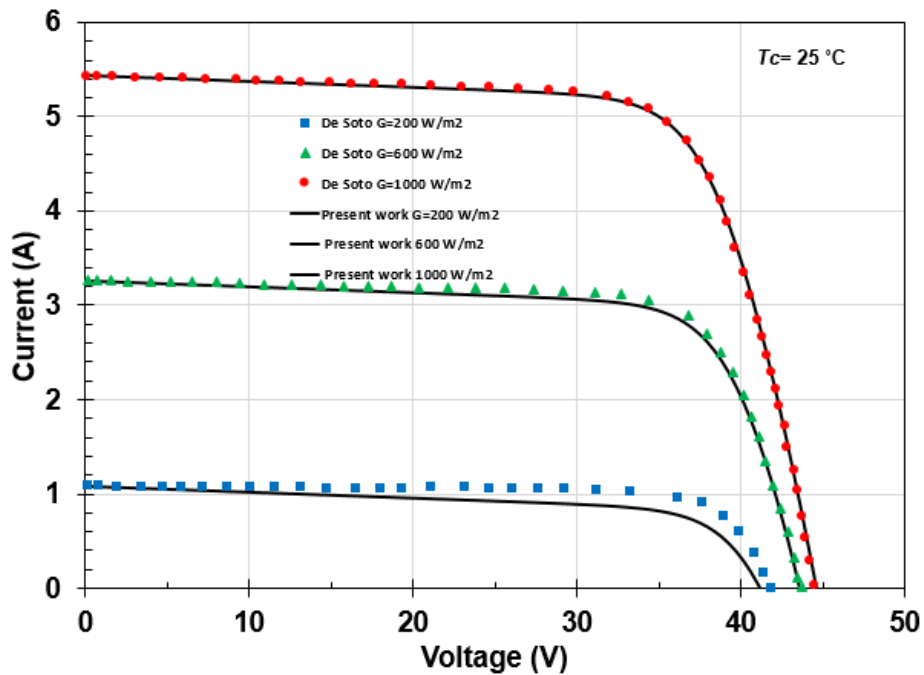
-a-



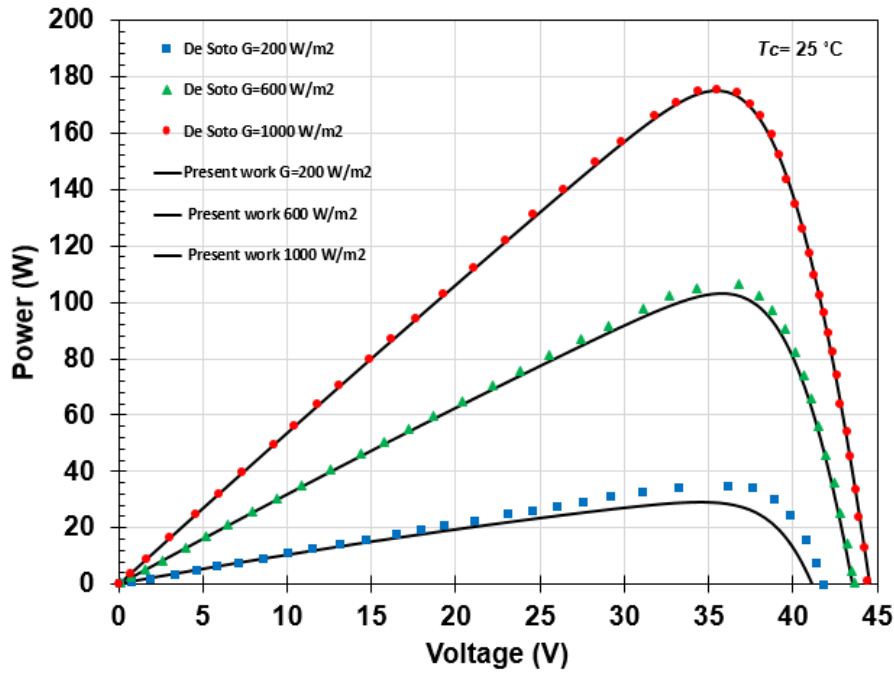
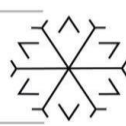
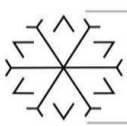
-b-

Figure 2: Comparison of the Present Model with Wxperimental Data Taken from De Soto et al. [15] at $G=1000$ W/m^2 (a) $I-V$ Characteristics (b) $P-V$ Characteristics

Figure 3(a-b) visualizes the $I-V$ and $P-V$ curves obtained by the proposed model and compares the predictive results with the experimental data for different solar irradiation levels varying from 200 to 1000 W/m^2 while cell temperature is fixed to 25 °C. At higher irradiation levels, experimental data coincides with the estimated model curves, which proves the superiority and the effectivity of the proposed conventional root solver method. However, when the solar irradiation rate is relatively lower, which is $G=200$ W/m^2 , predictions become jeopardized with increasing cell voltages on both $I-V$ and $P-V$ curves.



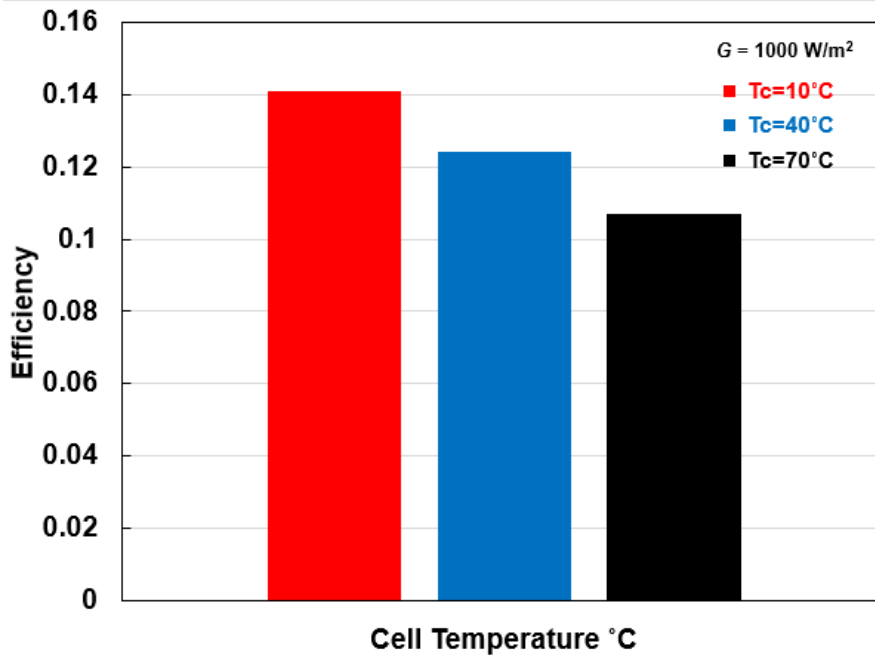
-a-



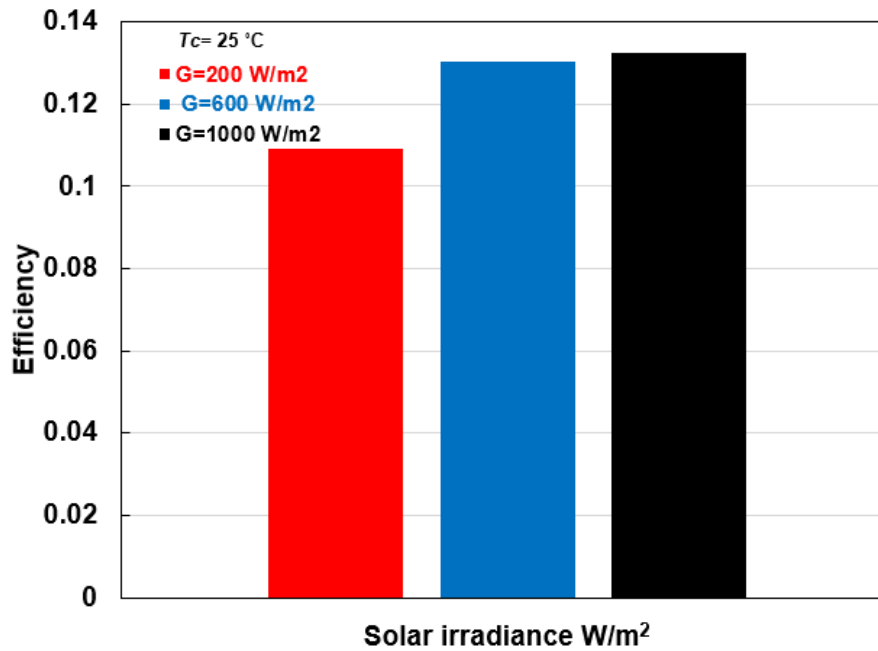
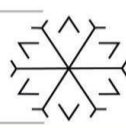
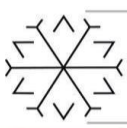
-b-

Figure 3. Comparison of the Present Model with Experimental Data Taken from De Soto et al. [15] at $T_c=25\text{ }^\circ\text{C}$
(a) *I-V* Characteristics (b) *P-V* Characteristics

Figure 4(a-b) compares the cell efficiencies for different cell temperatures and solar irradiance levels for the monocrystalline SQ175-PC cell module. As seen in Figure 4(a), cell efficiency rates decrease with increasing cell temperature at the constant radiation rate of 1000 W/m² while efficiency values incline to increase with increasing solar irradiance at the fixed cell temperature of 25°C



-a-



-b-

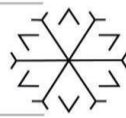
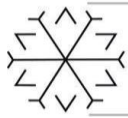
Figure 4. PV Module Efficiency (a) $G=1000 \text{ W/m}^2$ (b) at $T_c=25 \text{ }^\circ\text{C}$

4. Conclusion

In this research study, a mathematical model of PV cells is developed utilizing a computer program coded in Matlab. This model demonstrates a technique for estimating five unknown parameters for single diode PV cells with high accuracy. It can be seen that the collected experimental data is well-matched with the Newton-Raphson based parameter estimation. The I - V and P - V characteristics of a PV cell at any operating conditions can be modeled using the technical data sheet supplied by the manufacturer. The simulation result from the proposed model shows good agreement with published experimental data of PV modules. This method can be practical for engineers to specify the PV performance promptly.

References

- [1] Kanoğlu, M, Çengel, Y, & Dincer, I (2012), *Efficiency Evaluation of Energy Systems*, Springer.
- [2] Topcu, YI, & Ulengin, F (2004) 'Energy for the future: an integrated decision aid for the case of Turkey', *Energy*, vol. 29, pp. 137–154.
- [3] Allam, D, Yousri, DA, & Eteiba, M B (2016) 'Parameters extraction of the three diode model for the multi-crystalline solar cell/module using Moth-Flame Optimization Algorithm', *Energy Conversion and Management*, vol. 123, pp. 535–548.
- [4] Abbassi, R, Abbassi, A, Jemli, M, & Chebbi, S (2018) 'Identification of unknown parameters of solar cell models: A comprehensive overview of available approaches', *Renewable and Sustainable Energy Reviews*, vol. 90, pp. 453–474.
- [5] Jordehi, AR (2016) 'Parameter estimation of solar photovoltaic (PV) cells: A review', *Renewable and Sustainable Energy Reviews*, vol. 61, pp. 354–371.
- [6] Kandeal, AW, Thakur, AK, Elkadeem, MR, Elmorshedy, MF, Ullah, Z, Sathyamurthy, R, & Sharshir, SW (2020) 'Photovoltaics performance improvement using different cooling methodologies: A State-of-Art Review', *Journal of Cleaner Production*, 122772.



- [7] Orioli, A, & Di Gangi, A (2013) 'A procedure to calculate the five-parameter model of crystalline silicon photovoltaic modules on the basis of the tabular performance data', *Applied Energy*, vol. 102, pp. 1160–1177.
- [8] Nassar-eddine, I, Obbadi, A, Errami, Y, El fajri, A, & Agunaou, M (2016) 'Parameter estimation of photovoltaic modules using iterative method and the Lambert W function: A comparative study', *Energy Conversion and Management*, vol. 119, pp. 37–48.
- [9] Lo Brano, V, Orioli, A, Ciulla, G, & Di Gangi, A (2010) 'An improved five-parameter model for photovoltaic modules', *Solar Energy Materials and Solar Cells*, Vol. 94, No. 8, pp. 1358–1370.
- [10] Chen, X, Xu, B, Mei, C, Ding, Y, & Li, K (2018) 'Teaching–learning–based artificial bee colony for solar photovoltaic parameter estimation', *Applied Energy*, vol. 212, pp. 1578–1588.
- [11] Derick, M, Rani, C, Rajesh, M, Farrag, ME, Wang, Y, & Busawon, K (2017) 'An improved optimization technique for estimation of solar photovoltaic parameter', *Solar Energy*, vol. 157, pp. 116-124.
- [12] Ciulla, G., Lo Brano, V., Di Dio, V., & Cipriani, G. (2014) 'A comparison of different one-diode models for the representation of I–V characteristic of a PV cell', *Renewable and Sustainable Energy Reviews*, 32, 684–696.
- [13] Villalva MG, Gazoli JR, Filho ER. (2009) 'Comprehensive approach to modeling and simulation of photovoltaic arrays'. *IEEE Trans Power Electron*; 24, 5.
- [14] Ma, T., Gu, W., Shen, L., & Li, M. (2019) 'An improved and comprehensive mathematical model for solar photovoltaic modules under real operating conditions', *Solar Energy*, 184, 292–304.
- [15] De Soto, W., Klein, S. A., & Beckman, W. A. (2006) 'Improvement and validation of a model for photovoltaic array performance', *Solar Energy*, 80, 78-88.

NUMERICAL ANALYSES OF THE EFFECT OF REFLECTOR EMISSIVITY AT RADIANT TUBE HEATERS

Seyda Ozbektas ¹ [0000-0001-7399-733X] and Bilal Sungur ^{2*} [0000-0002-7320-1490]

¹seyda.ozbektas@omu.edu.tr, Department of Mechanical Engineering, Ondokuz Mayıs University, Samsun, Turkey

²bilal.sungur@samsun.edu.tr, Department of Mechanical Engineering, Samsun University, Samsun, Turkey

Abstract

Heating technology with radiation can generally be divided into two main groups as high-intensity and low-intensity radiant heaters. Heaters in which the air-gas mixture burns in a burner and the open bright flame is seen are called as high-intensity heaters. Heaters where combustion takes place in black tubes are called as low-intensity radiant heaters. Low-intensity radiant heaters radiated their energy over a wider area than high-intensity heaters because of larger surface area. However, low-intensity radiant heaters with the same capacity have lower surface temperatures than high-intensity radiant heaters which means lower heat transfer with radiation emitted from the unit surface. In low-intensity radiant heaters, reflectors placed on the tube have great importance in heat transfer by radiation. In this study, the emissivity values of the reflector above the low-density radiant heater placed in the room were changed and effect of this parameter on the temperature distribution in the room and the wall temperature of reflector was investigated numerically. The modelled radiant heater has 22 kW thermal power. Fluent package program was used as Computational Fluid Dynamic program. Calculations were made in three-dimensional conditions. The Standard k- ϵ model was used as turbulence model, the eddy dissipation model was used as combustion model, and the P1 model was used as radiation model. Conjugate heat transfer was considered in the radiant tube wall interfaces between the fluid and the solid zones. Results showed that increasing the emissivity ratio decreased the wall temperature of reflector. The effect of emissivity ratio on the temperature distribution in the room is negligible.

Keywords. Combustion, Radiant heating, Heat transfer, Reflector, Numerical modelling.

Quantification of Hemodynamic Parameters of Fetal Hearts Using Computational Fluid Dynamics

Huseyin Enes Salman ^{1[0000-0001-7572-9902]}

¹hsalman@etu.edu.tr, TOBB University of Economics and Technology, Mechanical Engineering Department,
Ankara, Turkey

Abstract

The cardiovascular system transports oxygen, nutrients, hormones, and other vital chemicals throughout the body's cells and organs. The proper functioning of the heart is critical for fetal development. Congenital heart defects (CHDs) occur in the early developmental stage and negatively affect the accurate functioning of the cardiovascular system. The incidence of CHDs is reported to be between 1.0 and 1.2 percent, indicating that CHDs impact a wide variety of society. The exact mechanism of CHD formation is still under debate. It is accepted that epigenetic factors play an important role in the formation of CHDs. However, only 2–4% of CHDs in infants are documented in families with a history of CHDs, suggesting that the majority of occurrences are observed without a family history of early cardiac abnormalities. This demonstrates that mechanobiological forces such as wall shear stresses (WSS) can also play a role in CHD formation. In this study, the healthy and underdeveloped hearts are analyzed and compared using computational fluid dynamics (CFD) simulations in order to investigate the mechanobiological forces. In the first step, two-dimensional heart geometries are generated using the ultrasound images of the fetal hearts. Then, the blood flow rates are measured in the heart valves using Doppler echocardiography and applied as realistic boundary conditions in the CFD simulations. The velocity contour plots, vorticity levels, and WSS amplitudes are determined for the healthy and underdeveloped hearts at different fetal developmental stages. It is observed that the formation of CHDs seriously alters the hemodynamics in the fetal hearts and results in a disturbed biomechanical environment.

Keywords. Biomechanics, Cardiovascular system, Computational fluid dynamics, Hemodynamics

Development of An Image Processing Tool for IVUS Images- Based Patient-Specific CFD Simulations

Abdussamet Subasi ¹[0000-0002-5919-9355]

¹subasiab@itu.edu.tr, Department of Mechanical Engineering, Istanbul Technical University, Istanbul, 34437,
Turkey

Abstract

Intravascular ultrasound (IVUS) is a catheter-based medical imaging technique used to visualize the inside of coronary arteries that supply the heart. It allows medical doctors to evaluate the characteristics of the plaques in the coronary arteries and the degree of stenosis in the vessels. IVUS sends sound waves and receives reflections that are different for interfaces between tissues or structures having different densities and creates a high-resolution cross-sectional image according to the amplitude of the reflected signal. On the other hand, advances in computer science and technology made the Computational Fluid Dynamics (CFD) technique available in biomedical researches such as investigation and assessment of coronary artery flows. For a patient-specific CFD simulation, the first step is to obtain a three-dimensional flow domain from the medical images. Therefore, the present study is dedicated to developing an image processing tool that creates a three-dimensional flow domain using high resolution cross-sectional intracoronary IVUS images for patient-specific CFD simulations. Firstly, an edge detection algorithm was applied in MATLAB to determine the boundaries of the lumen through which blood flows. However, the lumen dimensions on the y-z plane are in pixels. Therefore, they need to be converted to the real physical distance by defining a conversion factor. This conversion factor was determined by analyzing the scales on the IVUS images in mm/pixel and applied. This procedure was implemented for each successively taken high-resolution cross-sectional image. Then, the distance between the successive cross-sectional images which is known from the medical examination was applied to determine the real physical value of the x-coordinate. Finally, x, y, and z coordinates of each cross-sectional image in mm were imported to the SolidWorks and a three-dimensional patient-specific intracoronary flow domain which is ready for a CFD simulation was obtained. A representative CFD simulation was also reported within the content of this study. The developed tool can be used as an alternative to costly and commercial softwares for preliminary analysis.

Keywords. CFD, Coronary artery, IVUS, Image processing

Long-Term Stability Analysis of Surface-Modified Nanofluids

Faraz Afshari ^{1*}[0000-0001-9192-5604], Emre Mandev²[0000-0002-6791-4136], Bayram Şahin³, Eyüphan Manay⁴, Reza Teimuri-Mofrad⁵ and Shabnam Rahimpour⁶

¹faraz.afshari@erzurum.edu.tr, Affiliation: Erzurum Technical University, Department of Mechanical Engineering, Erzurum, Turkey.

²emre.mandev@erzurum.edu.tr, Affiliation: Erzurum Technical University, Department of Mechanical Engineering, Erzurum, Turkey.

³bayram.sahin@erzurum.edu.tr, Affiliation: Yildiz Technical University, Department of Mechanical Engineering, Istanbul, Turkey.

⁴emanay@erzurum.edu.tr, Affiliation: Erzurum Technical University, Department of Mechanical Engineering, Erzurum, Turkey.

⁵teymouri@tabrizu.ac.ir, Affiliation: University of Tabriz, Faculty of Chemistry, Department of Organic and Biochemistry, Tabriz, Iran

⁶k.rahimpour@tabrizu.ac.ir, Affiliation: University of Tabriz, Faculty of Chemistry, Department of Organic and Biochemistry, Tabriz, Iran

Abstract

Nanofluids can be defined as a suspension of nanoparticles in a conventional fluid having improved thermophysical characteristics, which are widely used in various industrial applications. In this context, instability of the prepared nanofluids is the main problem that causes a reduction in the thermal performance of heat exchangers and other energy conversion systems. Nanofluid stability has a notable role in its thermophysical characteristics which can highly affect the thermal performance of the energy systems. In this present study, Fe₃O₄ nanoparticles were synthesized by performing chemical surface modification methods. Three different methods were used for surface modification of nanoparticles including Fe₃O₄@SiO₂ (I1), Fe₃O₄@SiO₂@(CH₂)₃Cl NPs (II1), and Fe₃O₄@(CH₂)₃Cl NPs (I2). Water-based nanofluids were prepared with the obtained nanoparticles in a volume of 100 ml at 0.2% volume fraction. The two-step method was used for the preparation of these nanofluids. Scanning Electron Microscope (SEM) images and X-Ray Diffraction (XRD) method results were used for stability analysis of all prepared nanofluids. For the long-term stability assessment, 90 days were taken into account and the resulting analyses were obtained at the end of 90 days. In addition, modified novel nanofluid results were compared with the unmodified sample. During this specified time, a significant portion of the nanoparticles precipitated. The most stable nanofluid was chosen considering the ratio of suspended particles and their chemical structure. In addition, by incorporating the properties of suspended nanoparticles, a proposal has been made for the preparation of more stable and effective water-based Fe₃O₄ nanofluids.

Keywords. Nanofluid, Surface-Modification, Stability, Fe₃O₄

Investigation of The Effects of Different Corrosion Grades on Bending Strength of S235 Box Profiles

Kader DİKMEN¹, Mahyar MAALI², Zeynep YAMAN¹, Elif AĞCAKOCA¹, Muhammed MARAŞLI³

¹ Sakarya Üniversitesi, Mühendislik Fakültesi, İnşaat Müh. Bölüm, Sakarya / Türkiye

² Erzurum Teknik Üniversitesi, Mühendislik Mimarlık Fakültesi, İnşaat Müh., Erzurum/ Türkiye

³Fibrobeton Yapı Elemanları San. ve İnşaat A.Ş. Ar-Ge Merkezi, Düzce / Türkiye

Abstract

S235 steel, which is widely used in the industrial sector, is also frequently preferred in the structural field. As a result of contact with the environment in which metal elements are in, they may decompose by entering some reactions. The degradation of metals by reacting with the environment is called corrosion. With the corrosion mechanism, cross-sectional losses are seen in metals. With the corrosion damage of metal elements, there is a decrease in the carrying capacity. In low carbon steel alloys, the corrosion mechanism occurs rapidly and mass losses begin at the same time. In this study, the bearing capacity capacities of S 235 quality steel box profiles, which are frequently preferred in the structural and industry, were investigated at certain corrosion damage degrees. The steel box profiles used in the study were corroded by 10%, 20% and 40% by mass in 3.5% NaCl environment. With the accelerated corrosion mechanism prepared, anode and cathode regions were created and corrosion of the anode steel box profiles was ensured. The three-point bending strengths of the profiles reaching the desired corrosion damage were investigated. It has been observed that there is a decrease in the bending strength of the reference profiles that are not exposed to corrosion damage and the steel box profiles that are exposed to corrosion damage. Compared to the reference profiles, the flexural strength of the profiles, which lost 10%, 20% and 40% in mass, decreased by 20.91%, 25.27% and 52.82%, respectively.

Keywords. Corrosion, Flexural Strength, NaCl, Corrosion Damage by Mass, S235 Steel

Conformity in Theoretical and Experimental Analyses, Performance of Heat Pumps

Faraz Afshari ¹[0000-0001-9192-5604], Mehmet Akif Ceviz ²[0000-0001-6268-571X]

¹faraz.afshari@erzurum.edu.tr, Erzurum Technical University, Department of Mechanical Engineering,
Erzurum, Turkey.

²akif.ceviz@erzurum.edu.tr, Erzurum Technical University, Department of Mechanical Engineering,
Erzurum, Turkey.

Abstract

The conformity in theoretical and experimental analyses is an important issue to have reliable results in scientific investigations. In addition, numerical methods are also used widely to show the required agreement between obtained results. In this study, COP value of the vapor compression cooling system has been discussed and the conformity of the theoretically maximum coefficient of performance value (COP of Carnot cycle) has been compared with that of experimental performance. In this context, Carnot cycle has been proposed as a totally reversible ideal model with highest performance for heat engines operating between hot and cold ambient. Carnot refrigeration cycle can be obtained, in the condition where all process is reversed. By reviewing the proposed Carnot COP for heat pumps or cooling systems it can be stated that in the ideal cycle for heat pumps and refrigerators, the maximum performance can be achieved considering upper and lower temperatures regardless of the apparatus type and working principles and etc. In the laboratory and experimental conditions, the COP value of the heat pump is calculated as the ratio of the heat transferred to the work consumed by the compressor. In this context, the obtained experimental COP results have been compared with that of Carnot efficiency as reversible cycle and the possibility of corrections has been discussed. It is demonstrated that, there are some kinds of complexity to have a proper comparison between theoretical maximum COP and experimental COP values.

Keywords. Heat Pump, Thermal Performance, COP, Carnot Cycle

Investigation of The Static Strength of Porcelain Fused to Metal Dental Crowns with Surface Protrusions Produced by Selective Laser Melting by Finite Element

Merve Taftali ^{1*}[0000-0003-2455-9725], Kerem Turalioglu²[0000-0001-8769-1681], A.Fatih Yetim³[0000-0002-4314-6830], İrfan Kaymaz⁴[0000-0002-9391-7218], Yakup Uzun⁵[0000-0002-5134-7640], Salih Akpınar⁶[0000-0003-3247-991X] and Fatih Yildiz⁷[0000-0003-4475-5379]

¹merve.taftali53@erzurum.edu.tr, Erzurum Technical University, Faculty of Engineering and Architecture, Department of Mechanical Engineering, Erzurum, Turkey

²kerem.turalioglu@erzurum.edu.tr, Erzurum Technical University, High Technology Application and Research Center, Erzurum, Turkey

³fatih.yetim@erzurum.edu.tr, Erzurum Technical University, Faculty of Engineering and Architecture, Department of Mechanical Engineering, Erzurum, Turkey

⁴irfan.kaymaz@erzurum.edu.tr, Erzurum Technical University, Faculty of Engineering and Architecture, Department of Mechanical Engineering, Erzurum, Turkey

⁵yakup.uzun@atauni.edu.tr, Ataturk University, Faculty of Engineering, Department of Mechanical Engineering, Erzurum, Turkey

⁶salih.akpinar@erzurum.edu.tr, Erzurum Technical University, Faculty of Engineering and Architecture, Department of Mechanical Engineering, Erzurum, Turkey

⁷fatih.yildiz@erzurum.edu.tr, Erzurum Technical University, Faculty of Engineering and Architecture, Department of Mechanical Engineering, Erzurum, Turkey

Abstract

Implants, which have an important place on human health, are being improved day by day with the developing technology and increase the success rate with support biomaterials with superior properties. Porcelain fused to metal dental crowns (PFMDC) are frequently used in dental applications. Although dental crowns are mostly produced with conventional methods, it is possible to produce products that are difficult/impossible to produce with other production methods, with the unlimited geometry offered by additive manufacturing technology. It is possible to carry out production both easier and faster with the selective laser melting method, which is one of the additive manufacturing technologies. Additive manufacturing is also a very advantageous method in patient-specific dental designs. In addition, thanks to this method, it is possible to obtain products with geometries that cannot be obtained by classical methods. It is important to increase the lifetime of products in dental applications for lower costs and better patient psychology. By increasing the strength of metal-ceramic interfaces, the overall strength of dental crowns can be increased. Because of this reason, considering that dental crowns are produced with a thickness of 0.3 mm with traditional methods, 0.3 mm thick dental crowns were produced with the selective laser melting (SLM) method, which is one of the additive manufacturing methods. Surface protrusions have been designed and manufactured to increase metal-ceramic bonding to dental crowns. These crowns were tested under static loading conditions and their mechanical performance was compared with crowns produced using conventional methods. In addition, the behavior of dental crowns under static loading was also supported by using the finite element method. When the results were examined, it was seen that the metal-ceramic connection of dental crowns with surface protrusions was better both as a result of static loading and as a result of finite element analysis.

Keywords. Dental crown, Additive manufacturing, Fracture, Finite Element Method

Studies on Adhesively Bonded Layers under cyclic loading

Hasan Zandolu ¹ and Mehmet Yetmez ^{2*}

¹hasanzandolu3@gmail.com, Zonguldak Bulent Ecevit University

²yetmez@beun.edu.tr, Zonguldak Bulent Ecevit University

Abstract

In this study, stress analysis of adhesively bonded aluminum-ceramic composite beams under cycling loading is considered. General-purpose finite element code ANSYS (2020 R2) is used for the finite element beam models. Before understanding the cycling loading effect on the beam, dynamic characteristics of the models are compared with the experimental evaluations. All four types of materials namely aluminum, ceramic, adhesive type A and adhesive type B, are assumed to be linear elastic isotropic materials. Investigation of normal and shear stress behaviors of the beams with two different adhesives ($\rho=0.89$ g/cm³, $E=110$ kPa, $\nu=0.32$ for type A and $\rho=0.917$ g/cm³, $E=6$ kPa, $\nu=0.41$ for type B) under cycling loading in the range of 0-0.7 MPa is examined numerically. Results show that (i) there is a good correlation between experimental findings and numerical results of models proposed (ii) fundamental natural frequencies of untired composite beams are 1055 Hz for type A, 545 Hz for type 2, (iii) fundamental natural frequencies of fatigued (0.6 MPa) composite beams are 1054 Hz for type A, 450 Hz for type 2, (iv) fundamental natural frequencies of fatigued (0.7 MPa) composite beams are 694 Hz for type A, 230 Hz for type 2, (v) there is a 25% difference of major normal stress between the untired and fatigued of 0.6 MPa for type B, (vi) there is a 28% difference of major normal stress between the untired and fatigued of 0.7 MPa for type B, (vii) there is a 12% difference of major shear stress between the untired and fatigued of 0.6 MPa for type A, (viii) there is a 15% difference of major shear stress between the untired and fatigued of 0.7 MPa for type A.

Keywords. Aluminum layer, bonded ceramic layer, cycling loading, finite element model, vibration

An Experimental Study of Erosion Corrosion Behavior for Passive Metals

Yusuf Burak BOZKURT ^{1*}[0000-0003-3859-9322], Yeşim SEÇER KAVASOĞLU ²[0000-0003-4671-7384], Halim KOVACI ²[0000-0002-9053-3593], Ali Fatih YETİM ³[0000-0002-4314-6830], Ayhan ÇELİK ²[0000-0002-8096-0794]

¹yusuf.bozkurt@erzincan.edu.tr, Erzincan Binali Yıldırım University, Erzincan, Turkey

²yesim.secer@atauni.edu.tr, Atatürk University, Erzurum, Turkey

²halim.kovaci@atauni.edu.tr, Atatürk University, Erzurum, Turkey

³fatih.yetim@erzurum.edu.tr, Erzurum Technical University, Erzurum, Turkey

²ayhcelik@atauni.edu.tr, Atatürk University, Erzurum, Turkey

Abstract

316L stainless steel and commercial grade titanium (Cp-Ti) are two metallic materials that can be alternatives to each other in some application areas due to their similar corrosion behavior. They are widely preferred in very different disciplines such as space and aviation, automotive, medical equipment etc. Due to the oxygen-binding Cr and Ni elements in the chemical composition of 316L, its oxidation resistance is relatively high compared to other iron alloys. On the other hand, the natural oxide film layer formed on the surface of Cp-Ti during corrosion significantly increases the corrosion performance. These two materials with high corrosion resistance are generally not only exposed to corrosive effects under service conditions. In practice, the effect of the corrosive environment is only one component. Therefore, the analysis of the damage developed by the effects of systems such as flow-accelerated corrosion, erosion-corrosion and tribocorrosion depending on the service conditions is necessary to obtain more optimal results. In this perspective, the erosion-corrosion performance of 316L stainless steel and Cp-Ti was compared within the scope of the study. For this purpose, electrochemical corrosion tests were carried out under accelerated flow at different concentrations. SiC (silicon carbide) particles were added to distilled water at a rate of 0.25 gr/200 ml, 0.5 gr/200 ml, 0.75 gr/200 ml and 1 gr/200 ml to create an erosive effect on the sample surfaces. A peristaltic pump is integrated into the system for electrolyte flow. The experiment was carried out on a surface area of 2.54 cm² for each sample. Open circuit potential (OCP) and potentiodynamic polarization modules were used for electrochemical measurements. OCP scanning was performed for 5000 s. For potentiodynamic polarization, the scanning rate is 0.5 mV/s, and the scanning range is between -1 cathodic potential and +2 V anodic potential. According to the results of the measurements, the hard and abrasive particles in the solution damaged the passive oxide layers. Thus, oxidative resistance was weakened. Increasing concentration significantly changed the corrosion resistance. In addition, oxidation resistance was preserved more in titanium samples compared to 316L samples under the same conditions.

Keywords. 316L stainless steel, commercial pure titanium, erosion-corrosion, silicon carbide particle

Comparison of Electrochemical Corrosion Performances Using Variable Scan Rates on Surfaces with Different Layer Thicknesses

Yusuf Burak BOZKURT¹ [0000-0003-3859-9322], Burak ATİK^{2*} [0000-0003-2117-9284], Halim KOVACI² [0000-0002-9053-3593], Tuba YETİM³ [0000-0002-6237-6412], Ayhan ÇELİK² [0000-0002-8096-0794]

¹ yusuf.bozkurt@erzincan.edu.tr, Erzincan Binali Yıldırım University, Erzincan, Turkey

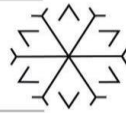
² burak.atik@atauni.edu.tr, halim.kovaci@atauni.edu.tr, ayhcelik@atauni.edu.tr, Atatürk University, Erzurum, Turkey

³ tuba.yetim@erzurum.edu.tr, Erzurum Technical University, Erzurum, Turkey

Abstract

The corrosion property of a material is one of the main subjects studied within the scope of surface engineering. When the literature is examined, it is seen that electrochemical methods are frequently used in the determination of corrosion properties. It offers very fast and accurate results, especially in the analysis of materials with improved corrosive properties by surface modifications. One of the most important modules of this method is potentiodynamic polarization experiments. This method, which provides information about the corrosion rate and amount of the material surface, gives very sensitive results with computer integrated package programs. The right selection of predetermined test parameters increases the degree of this sensitivity. In the potentiodynamic polarization experiment, the values entered into the system are respectively; scan rate, potential range, sample surface area, material density and equivalent weight. In this study, the effect of different scan rates on the measurement accuracy was investigated. Using two different parameters on the same base material (AISI 4140 steel), four different scan rates were applied (0.25 mVs^{-1} , 0.5 mVs^{-1} , 0.75 mVs^{-1} , 1 mVs^{-1}) for three different morphologies with the untreated surface. The plasma nitriding process was used as the surface modification technique. By using two different parameters, $400^\circ\text{C} - 1 \text{ hour}$ and $500^\circ\text{C} - 4 \text{ hours}$, different surfaces with different layer thicknesses were obtained. Thus, the layer thickness and corrosion behavior of diffusional coatings were associated with the scan rate. 3.5% NaCl was used as the electrolyte. In the triple galvanic cell arrangement, the reference electrode is Ag/AgCl and the counter electrode is graphite. Polarization values were chosen between -0.5 mV and $+1.5 \text{ mV}$. Before the potentiodynamic polarization measurements, the open circuit potential of each condition was monitoring for 3600 seconds. The anodic and cathodic arms of the obtained potentiodynamic polarization curves were examined in terms of quality and quantity. The effect of different scan rates on the result parameters obtained after the experiment was interpreted.

Keywords. Corrosion, scan rate, plasma nitriding



Effects of Connector Placement on The Biomechanical Performance of Spinal Implants Under Tension and Compression Loads

Kerem Turalioglu¹*[0000-0001-8769-1681], Merve Taftali²[0000-0003-2455-9725], A.Fatih Yetim³[0000-0002-4314-6830], Halim Kovaci⁴[0000-0002-9053-3593], Ayhan Çelik⁵[0000-0002-8096-0794]

¹kerem.turalioglu@erzurum.edu.tr, Erzurum Technical University, High Technology Application and Research Center, Erzurum, Turkey

²merve.taftali53@erzurum.edu.tr, Erzurum Technical University, Faculty of Engineering and Architecture, Department of Mechanical Engineering, Erzurum, Turkey

³fatih.yetim@erzurum.edu.tr, Erzurum Technical University, Faculty of Engineering and Architecture, Department of Mechanical Engineering, Erzurum, Turkey

⁴halim.kovaci@atauni.edu.tr, Ataturk University, Faculty of Engineering, Department of Mechanical Engineering, Erzurum, Turkey

⁵ayhcelik@atauni.edu.tr, Ataturk University, Faculty of Engineering, Department of Mechanical Engineering, Erzurum, Turkey

Abstract

Spinal implants are commonly used in spinal disorders and injuries. Pedicle screws, spinal rods, and connectors are the main components of a spinal implant construct. Pedicle screws are a type of bone screw applied into the vertebral pedicle. Spine rods are the elements that connect the pedicle screws to each other and connectors are the element that make the rods stand more rigid and they are used for the re-alignment of the vertebral. The connector is applied according to the type of injury and the treatment. In this study, the effect of connectors on the biomechanical performance of spinal implant constructs were investigated under compression or tension conditions. For this purpose, a spinal system constructs were created by mounting commercially purchased Ti6Al4V pedicle screws and spinal rods into the ultra-high molecular weight polyethylene (UHMWPE) blocks at certain torque values according to ASTM F1717-15. Connectors were mounted at the middle points of the rods and their screws were tightened according to a certain torque value. Then, static tension and compression tests were performed according to ASTM F1717-15 standard for spinal systems with and without connectors. Both tension and compression tests were repeated five times separately. According to the results, it was found that both the tensile and compressive strengths of the spinal implants with connectors increased in comparison to the ones without connectors.

Keywords. Biomechanics, Spinal rod, Pedicle screw, Spinal Connector

Triboperformance of Quenched and Single and Double Tempered AISI 4140 Steel

Engin Tan^{1*}[0000-0003-4441-3678], İsmail Ovalı²[0000-0002-8193-0060] and Rüçhan Yıldız³[0000-0002-5973-5496]

¹etan@pau.edu.tr, Pamukkale University, Faculty of Technology, Department of Metallurgical and Materials Engineering

²iovali@pau.edu.tr, Pamukkale University, Faculty of Technology, Department of Mechanical Engineering

³ruchanyildiz1540@hotmail.com, Pamukkale University, Faculty of Technology, Department of Metallurgical and Materials Engineering

Abstract

This study is concerned with investigating and also improving the wear behaviour of a commercially available AISI 4140 steel through conventional quenching and single tempering (QST) and alternative quenching and double tempering (QDT) heat treatments. For this purpose, after austenization at 850°C for 90 min, the specimens were quenched in oil and subjected to a two-stage (single and double) tempering process with three different temperatures for 60 min. Pin-on disc abrasive wear tests and hardness measurements were performed on the specimens. The results of this study showed the QDT process had the best combination of wear properties with hardness.

Keywords. AISI 4140, double tempering, wear, hardness, toughness.

1. Introduction

AISI 4140 steels are utilized in transportation and machine manufacturing industries with high strength, ductility and toughness properties. These steels gain this combination of superior properties with the alloying elements Cr, Ni and Mo in their content and with phase structures as ferrite, pearlite, bainite, martensite etc. obtained by the applied quenching and tempering heat treatments (Bandanadjaja et al. 2020, Balıkçı and Özbek 2016, ASM International Handbook Committee 1997). Although martensite generally increases mechanical properties such as strength and hardness, reduces the ductility of steel by causing brittleness due to its lath structure. Internal stresses occur during the transformation process further increase embrittlement. For this reason, these steels are generally not used in structural applications without tempering (Sanij et al. 2012). However, in general, quenching and tempering are common means to produce strength enhancement in steel, mainly by precipitation hardening, with a fine dispersion of alloy carbides in the microstructure during tempering (Chaouch, et al. 2018). Researches on quenching and tempering combinations for optimizing strength, ductility and toughness properties are important in this respect (Meysami et al. 2010). With the double heat treatment processes carried out, significant increases in toughness can be obtained with a small decrease in hardness (Chang et al. 1994).

In present study, the effects of single and double tempering processes applied after quenching on the hardness and wear behavior of AISI 4140 steel were investigated. The aim of the research is to improve the triboperformance of the selected material by obtaining the optimum double tempering parameters.

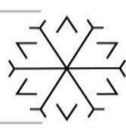
2. Materials and Method

2.1. Material Preparation

A commercially available low alloy steel (AISI 4140; Fe-0,42C-0,24Si-0,78Mn-1,02Cr-0,17Mo (mass%)) was used as experimental material. The hardnesses of base material is 229 HV. These base materials were machined to Ø10 x 20 mm cylindrical dimensions to produce wear tests and heat treatment process specimens.

2.2. Heat Treatment Processes

After austenitized at 850°C for 90 min and quenched into oil (O.Q), the specimens were single (QST) and double (QDT) tempered at various temperatures in a range of 350-550°C for 60 min constant tempering time in a chamber



furnace with air circulation. Finally samples were cooled by air (A.Q). Comparison of QST and QDT heat treatments processes are presented in Figure 1.

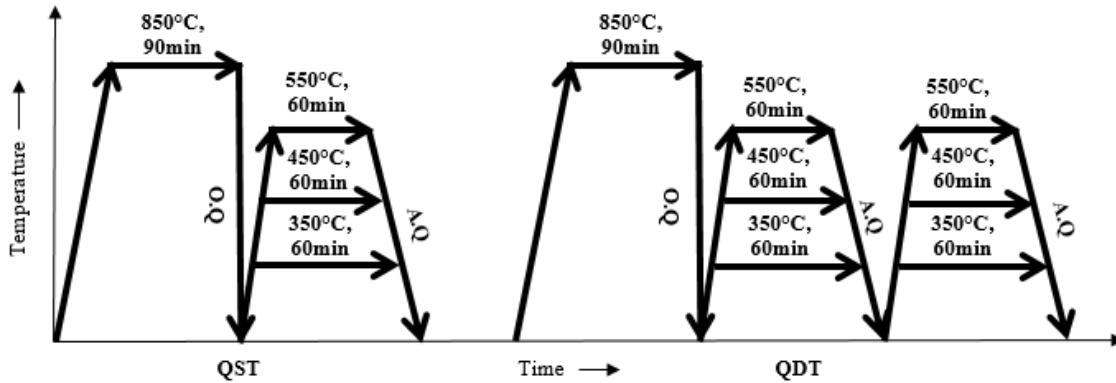


Figure 1: Comparison of Heat Treatment Processes: QST and QDT.

2.3. Test and Characterization Methods

After the heat treatment processes, the final wear test sample dimensions were prepared by machining in order to remove the oxide layers remaining on the surface of the samples. The mechanical properties including hardness and wear resistance in surface area, were determined for each heat treatment process. For obtaining the hardness of the samples, Rockwell HRC scale were used in accordance with ASTM E18 standards (ASTM Technical Committee, 2005). Wear tests were carried out based on the ASTM G99 standard using the test device in Figure 2. Worn surfaces were analysed according to ASTM E3 standard for revealing characterization of abrasion mechanism under optical microscopy.

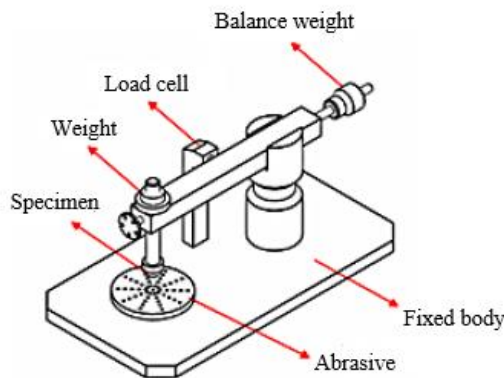


Figure 2: Schematic Representation of Wear Test Device (Ersöz and Ovalı, 2018)

The wear behavior of the samples was analyzed using weight loss and coefficient of friction parameters. The weight losses of the samples were determined with an accuracy of $\pm 10^{-3}$ g on an electronic balance. The friction coefficient was determined by force measurements using the load cell sensor. In the abrasive wear test, 5, 10 and 15 N loads were applied to the base, QST and QDT samples, the sliding speed was determined as 3 m/s and the sliding distance was determined as 100, 200 and 300 m. 180 grit sandpaper was used as abrasive.

The wear test diagrams giving the coefficient of friction were created using the Equation 1 (Kaplan 2020). The friction coefficient is

$$\mu = F/P \tag{1}$$

; where, F is the friction force and P is the normal load.

3. Results and Discussion

The hardness measurements results are given in Figure 3. From these results, it is evident that although the highest hardness was observed in quenched sample, while the lowest hardness value was obtained in QDT-550 sample. The hardness characteristics of QST and QDT specimens are similar after tempering process. While the hardness



of QDT specimens decreased gradually compared to QST for the equal tempering temperatures, decreasing tempering temperatures provided a regular increase in the hardness of QST and QDT specimens.

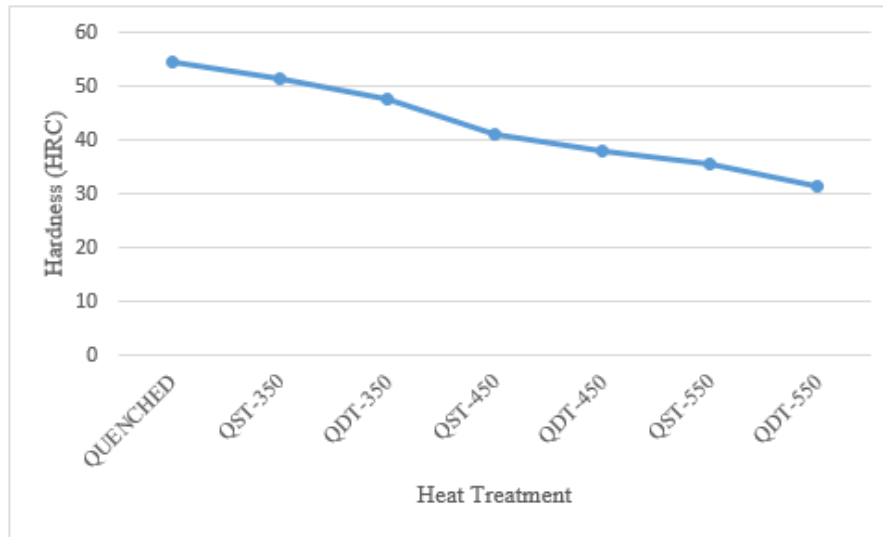


Figure 3: Hardness Distribution of Heat Treatment Specimens

The effect of tempering parameters on the weight loss as function of sliding distance and load are given in Figure 4. It can be seen clearly from Figure 4 that the wear resistance of AISI 4140 steel can be optimized with tempering and wear condition. The highest wear resistance was obtained at QST-350 sample (Figure 4-f). The result can be explained with highest hardness of QST-350 sample (Ali et al. 2019). Compared to tempered samples, the result can be concluded that lower tempering temperature show higher wear resistance. The result can be related with finer carbide size formed during tempering process [Sun et al. 2018]. Sliding distance and load are keys parameters affecting the weight loss of steel (Sales et al. 2009). All of weight loss graphics showed that weight loss increase with increasing normal loads and sliding distance. Increasing weight loss can be explained with higher interface temperature between sample and abrasive particles (Rooprai et al. 2021). The temperature of worn surface have critical role on abrasive wear resistance steel (Wang et al. 2018).

The weight loss of base sample as function of sliding distance and load are shown in Figure 5 because to compare wear resistance of base and tempered samples. Base samples show the lowest wear resistance because of their lowest hardness. The lower wear resistance are also related with absence of carbide in the microstructure (Kseer 2013).

Another important parameter for evaluation wear behavior of AISI 4140 steel is friction coefficient. Variation of friction coefficient as a function of sliding distance and material's heat treatment are given Figure 6. It can be clearly understood that tempering parameters significantly influence the wear resistance of AISI 4140 steel. The lowest friction coefficient values were obtained at 0.23 μm for QST-350 sample. The friction coefficient increase with increasing tempering temperatures. The higher friction coefficient values can be explained with lower hardness (Sohi et al. 2010).

Surface roughness have been widely used for characterization of steel as key parameter. The effects of tempering on the wear resistance of AISI 4140 samples are given in Figure 7. Surface roughness of tempered samples show similar trend with effects of tempering parameters on hardness and weight loss. The highest surface roughness value was obtained at 5.87 for base samples. The results can be related with lower hardness of base sample (Elbah et al. 2013). QST-350 samples showed the lowest surface roughness (2.27 μm).

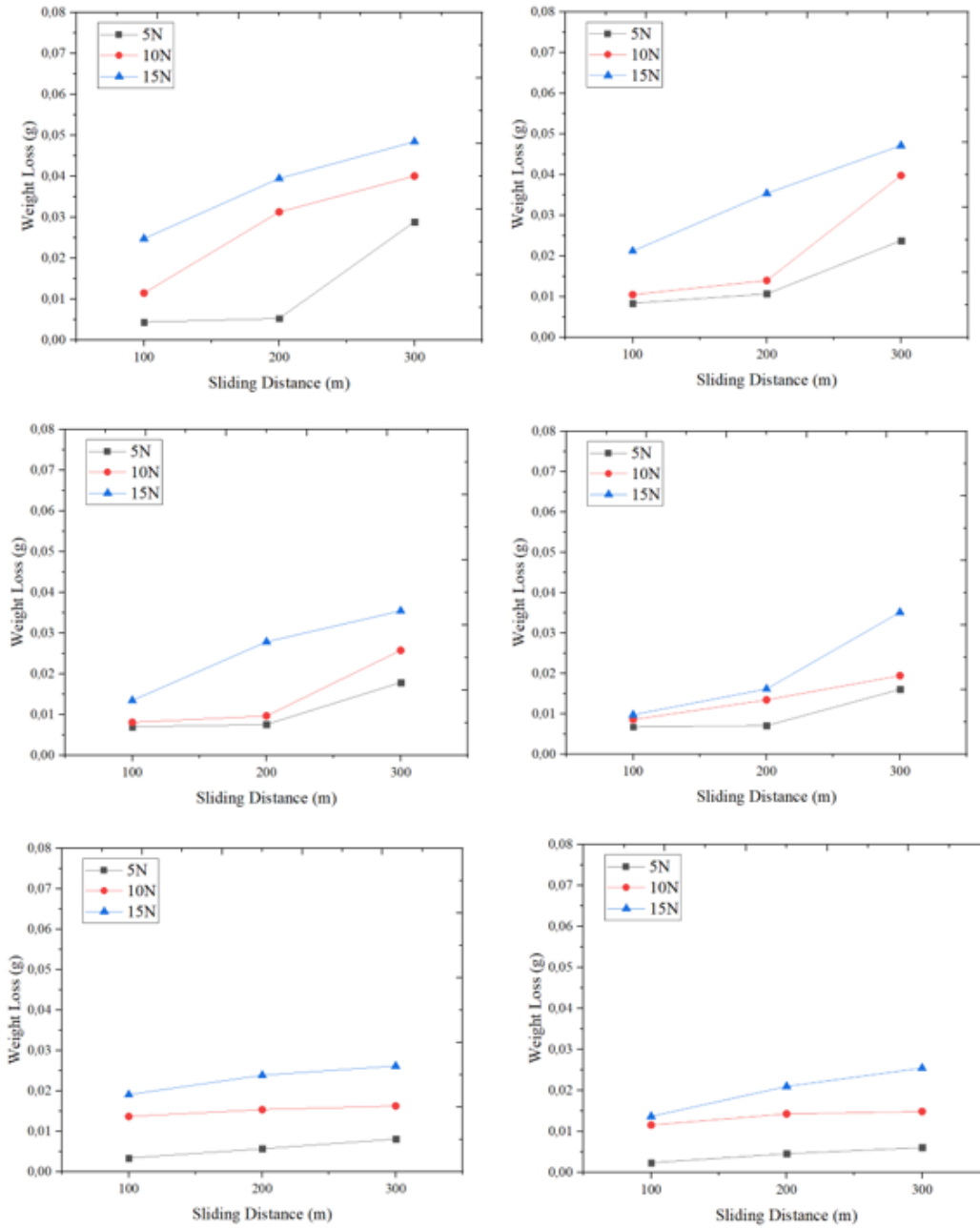
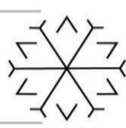


Figure 4. The effect of tempering parameters on the weight loss as function of sliding distance and load: (a) QDT-550; (b) QST-550; (c) QDT-450; (d) QST-450; (e) QDT-350, (f) QST-350

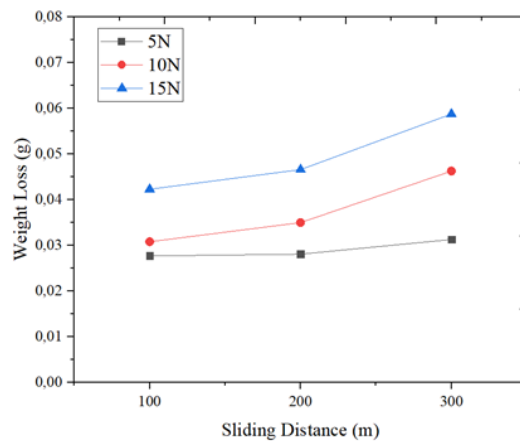




Figure 5: The weight loss of base sample as function of sliding distance and load

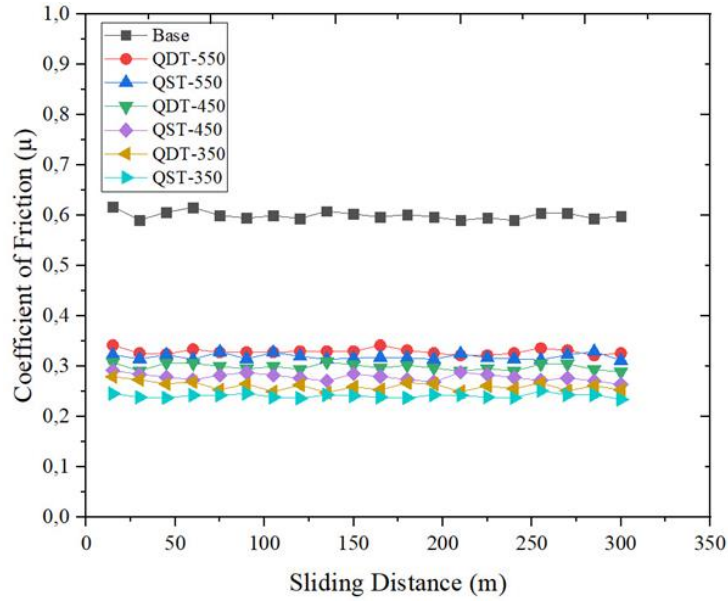


Figure 6: Variation of friction coefficient as a function of sliding distance and heat treatment process

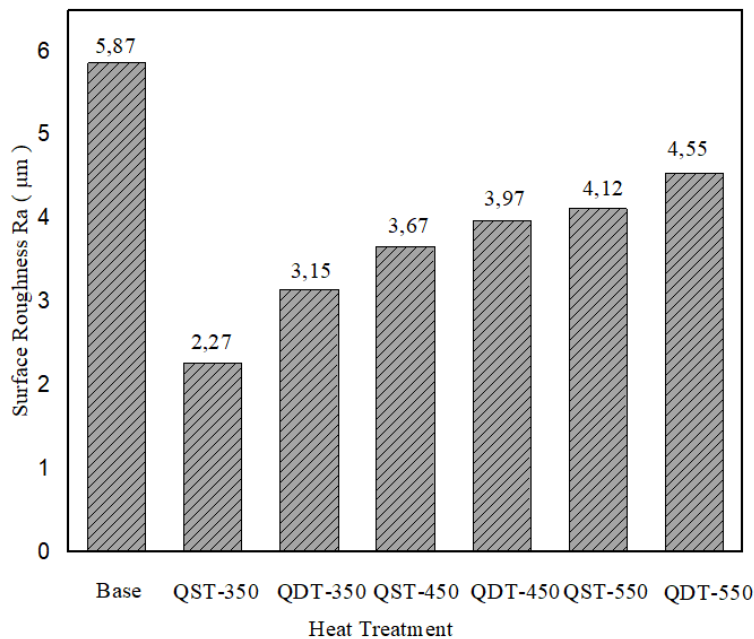


Figure 7: The effects of tempering on the wear resistance of AISI 4140 samples

4. Conclusion

The results of this study showed that the hardness and wear resistance of AISI 4140 steel can be optimized with tempering and wear condition. Among the tempered samples, the highest hardness was observed in the QST-350 sample with 51.6 HRC, and in accordance with this result, the highest abrasion resistance was also acquired in this sample. Base specimens had the lowest wear resistance due to their lowest hardness. The low wear resistance was also attributed to the absence of carbide in the microstructure.

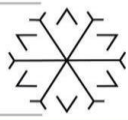
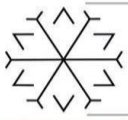
The lowest friction coefficient values for the QST-350 sample were obtained with 0.23 μm. QST-350 samples also had the lowest surface roughness of 2.27 μm.

Future work may include analysis of carbide structures and transformations of different main matrix phases by microscopic examination. By varying the quenching time and temperature, the effects of single and double tempering on toughness and strength properties can be determined.



References

- Bandanadjaja, B, Purwadi, W, Lilansa, N, Idamayanti, D & Putra, TRS. (2020). The effect of a single quenching double tempering process on the mechanical properties of NiCrMo alloyed steel casting, IOP Conf. Ser.: Materials Science and Engineering 850 012040.
- Balıkçı, G & Özbek, İ. (2016). Effect of austenitizing and tempering temperatures on the mechanical properties of hot forged AISI 4140 steel. In proceedings of 18th International Metallurgy & Materials Congress, UCTEA Chamber of Metallurgical & Materials Engineers, İstanbul, Türkiye, pp. 998-1001.
- American Society for Metals and ASM International. (1997). Metals Handbook. Materials Park, Ohio: ASM International.
- Callister, WD & Rethwisch, DG. (2011). Fundamentals of materials science and engineering, 5th edn, John Wiley & Sons NY.
- Sanij, MHK, Banadkouki, SSG, Mashreghi, AR & Moshrefifar, M. (2012). The effect of single and double quenching and tempering heat treatments on the microstructure and mechanical properties of AISI 4140 steel, Materials & Design, vol. 42, pp. 339–346.
- Chaouch, D, Sadok, A, Bendaoudi, SE & Chaouch, A. (2018). Effect of Charpy Impact Test on Microstructure Properties of AISI4140 Steel, Mechanics and Mechanical Engineering, vol. 22, no. 4, pp. 1463–1469.
- Meysami, AH, Ghasemzadeh, R, Seyedein, SH & Aboutalebi, MR. (2010). An investigation on the microstructure and mechanical properties of direct-quenched and tempered AISI 4140 steel. Materials & Design, vol. 31, pp. 1570–1575.
- Chang, E, Chang, CY & Liu, CD. (1994). The effects of double austenitization on the mechanical properties of a 0.34 C containing low-alloy Ni-Cr-Mo-V steel, Metallurgical and Materials Transactions A, vol. 25, pp. 545–555.
- Annual book of ASTM standards. (2005). ASTM E18, standard test method for Rockwell Hardness and Rockwell Superficial Hardness of metallic materials, vol. 03.01. ASTM Int, PA, www.astm.org.
- Annual book of ASTM standards. (2017). ASTM G99-17, standard test method for wear testing with a pin-on-disk apparatus, ASTM Int, West Conshohocken, PA, www.astm.org.
- Ersöz, E & Ovalı, İ. (2018). The effects of the industrial cryogenic process on the wear behaviours of AISI D2 cold work tool steels. Journal of Polytechnic, vol. 21(2), pp. 411-417.
- Annual book of ASTM standards. (2005). ASTM E3, standard practice for preparation of metallographic specimens, vol. 03.01. ASTM Int, PA, www.astm.org.
- Kaplan, Y. (2020). Role of reinforcement materials on mechanical and tribological properties of PTFE composites. Polymer Korea vol. 44(4), pp. 436-444.
- Ali, M, Porter, D, Kömi, J, Eissa, M & El faramawy, H. (2019). The effect of double austenitization and quenching on the microstructure and mechanical properties of CrNiMoWMnV ultrahigh-strength steels after low-temperature tempering, Materials Science & Engineering A, vol. 763, 138169.
- Sun C, Fu PX, Liu HW, Liu HH & Du, NY. (2018). Effect of Tempering Temperature on the Low Temperature Impact Toughness of 42CrMo4-V Steel, Metals, vol. 8, no. 4:232.
- Sales, W., Becker, M., Barcellos, CS., Landre, J. Jr., Bonney, J. & Ezugwu, EO. (2009). Tribological behaviour when face milling AISI 4140 steel with minimum quantity fluid application. Industrial Lubrication and Tribology, vol. 61, no. 2, pp. 84-90.
- Rooprai, RS, Singh, H, Singh, T & Singla, YK. (2021). Analysis of the wear properties of through hardened AISI-4140 alloy steel using Taguchi technique. Materials Today: Proceedings, in press.
- Wang, B, Liu, B, Zhang, X & Gu, J. (2018). Enhancing heavy load wear resistance of AISI 4140 steel through the formation of a severely deformed compound-free nitrided surface layer. Surface and Coatings Technology, vol 356, pp. 89-95.
- Kseer, KM. (2013). Effect of double quenching on wear behavior for low carbon dual phase steel. Al-Qadisiyah Journal for Engineering Sciences, vol. 6, no. 2, pp. 193-203.
- Sohi, MH, Ebrahimi, M, Raouf, AH & Mahboubi, F. (2010). Effect of plasma nitrocarburizing temperature on the wear behavior of AISI 4140 steel. Surface and Coatings Technology, vol. 205, supplement 1, pp. S84-S89.



Elbah, M, Yallese, MA, Aouici, H, Mabrouki, T & Rigal, JF. (2013). Comparative assessment of wiper and conventional ceramic tools on surface roughness in hard turning AISI 4140 steel. *Measurement*, vol. 46, no. 9, pp. 3041-3056.

Wave Dispersion Characteristics of Nanorods with Uniform Porosity

Mehmet N. Balci ^{1*}[0000-0002-4416-6761]

^{1*}mehmetbalci@hacettepe.edu.tr, Mechanical Engineering Department, Hacettepe University, Ankara, 06800, Turkey

Abstract

In nanotechnology, nanorods can be defined as one of the nanoscale structural elements having dimension interval from 1-100 nm. Nanorods may be produced based on direct chemical synthesis from metals or semiconducting materials (Hamzan et al., 2021). Nanorods have higher length when compared to their thickness which leads to get aspect ratios greater than one. Nanorods are future promising materials and they can be utilized in display technology and microelectromechanical systems (MEMS) (Ghodssi and Lin, 2011). Zinc oxide (ZnO) nanorods are widely used in the production of electronic nanodevices, such as ultrabright light emitting diode (LED) (Yi et al., 2005). Thus, mechanical and wave propagation properties of nanorods are significant. This study investigates the wave dispersion characteristics of nanorods possessing uniform porosity distribution. Wave propagation problem is derived according to the Eringen's nonlocal elasticity theory (Eringen and Edelen, 1972; Eringen, 1972; Eringen, 1983) and nonlocal stress gradient model is considered. Nanorod has even porosity distribution which provides uniform pores along the rod. Wave dispersion equation is solved, and wave number-wave frequency relation is obtained to examine the influences of small-scale coefficient and volume fraction of porosity. Wave characteristics of nanorod is acquired based on the Born-Karman model of Lattice Dynamics. Results obtained using classical (local) rod model, nonlocal rod model and Born-Karman model of Lattice Dynamics are compared. For classical (local) model, the wave numbers for the axial mode has a linear variation with the frequency which is in the terahertz (THz) range. While uniform porosity has no effect on wave dispersion at classical (local) theory, it becomes effective at nonlocal theory. The linear variation of the wave numbers at classical (local) theory denote that waves will propagate non-dispersively, i.e. the waves do not change their shapes as they propagate (Narendar, 2011). However, wave dispersion characteristics become nonlinear and quite different from that obtained at classical (local) rod model for larger values of small-scale coefficient, which implies the significance of the nonlocal theory in the examination of wave characteristics of porous nanorods.

Keywords. Nanorod, nonlocal elasticity theory, uniform porosity, wave dispersion

References

- Eringen, A.C. and Edelen, D.G.B. (1972) 'On nonlocal elasticity', *Int. J. Eng. Sci.*, 10(3), pp. 233-248.
- Eringen, A.C. (1972) 'Linear theory of nonlocal elasticity and dispersion of plane waves', *Int. J. Eng. Sci.*, 10(5), pp. 425-435.
- Eringen, A.C. (1983) 'On differential equations of nonlocal elasticity and solutions of screw dislocation and surface waves', *J. Appl. Phys.*, 54, 4703.
- Ghodssi, R. and Lin, P. (2011) *MEMS Materials and Processes Handbook*, vol. 1, New York, Springer Science & Business Media.
- Hamzan, N.b., Ng, C.Y.B., Sadri, R., Lee, M.K., Chang, L.-J., Tripathi, M., Dalton, A., Goh, B.T. (2021) 'Controlled physical properties and growth mechanism of manganese silicide nanorods', *J. Alloys Compd.*, 851, 156693.
- Narendar, S. (2011) 'Terahertz wave propagation in uniform nanorods: AA nonlocal continuum mechanics formulation including the effect of lateral inertia', *Physica E*, 43, pp. 1015-1020.
- Yi, G.-C., Wang, C. and Park, W.I. (2005) 'ZnO nanorods: Synthesis, characterization and applications', *Semicond. Sci. Technol.*, 20(4), pp. 22-34.

The Use of a Low-Cost Laser Scanning Range Finder Sensor to Estimate the Volume of an Object

Gokhan Bayar ¹*[0000-0002-6344-3621]

bayar@beun.edu.tr, Zonguldak Bulent Ecevit Unv., Mechanical Eng. Dept., Zonguldak/TURKEY

Abstract

Volume estimation is one of the methods used in robotics, mechatronics and control & automation applications to get an idea about the shape and volume of an object. In addition to estimating volume of an object, such information may be integrated into a control system as feedback to achieve a reference input control objective. The most common way to estimate the volume of an object is to use camera(s). An efficient image processing algorithm may provide sufficient data to estimate volume when the resolution of camera(s) is high and the computing platform is strong enough. This process generally needs computing time and high capacity of ram, processor, video card, etc. Therefore it can be said that this type of solution is not a low-cost method. In this study, a new perspective is proposed to estimate the volume of an object. The system is constructed based on a low-cost laser scanning rangefinder sensor. The laser sensor is mounted on a mechanism whose forward-backward motions are used to scan the object. While the mechanism makes motions, the required sensor data is collected and the volume of the object scanned is estimated using a geometrical approach proposed in this study.

Keywords. Laser scanner sensor, volume estimation, robotics, mechatronics, low-cost sensor.

1. Introduction

Recognition is important in robotics, mechatronics, automation and control applications since the required feedback can be generated according to this information. It can be achieved using different types of methods. The working environment or targeted object can be scanned via using a laser scanning system. The scanning may be performed using the other systems like lidar, sonar, etc. One or more cameras may be adapted into a system to see and recognize the surrounding, objects or structure. Close contact and close object recognition can be performed using IR or ultrasonic sensors. If a rotational motion in the third axis is given to these 2D sensors, a 3D scanning system is created and the three dimensional information could be collected from the surrounding. The information collected is then processed to estimate the volume of objects placed in the working environment. The volume estimation is commonly used in mobile robotics and unmanned ground vehicle tasks. The use of autonomous (driverless) forklifts in industrial tasks is one of the examples. When an autonomous forklift attends to grip a load/mass/package and carry it, its recognition system should be able to do following required processes; the first is whether the outer dimensions of the load are suitable for the gripper or not (in other words, the gripper's maximum opening should be smaller than the outer dimensions of the load so that the load can be gripped). The second process, which the recognition system should perform, is whether the forklift can be able to lift the load without tipping over (in this case the density of the load/mass is assumed to be known). The carrying possibility of the load by the forklift should also be decided via the computing system. This example is depicted in Figure 1. In this figure, an autonomous forklift plans to grip and carry some loads. It is suited with recognition sensors indicated by green-colored-rectangles. The sensors may be laser scanning rangefinder or cameras. The main objective in this case is to detect the outer dimensions of the loads and estimate the approximate volumes. If the volume is estimated and the density of the material inside the packages is introduced to the computing system, it is decided by the control system whether the loads can be safely gripped and carried or not. Note that in this example uniform-regular shaped objects are taken into account. In reality it is possible to face with non-uniform and irregular shaped objects.

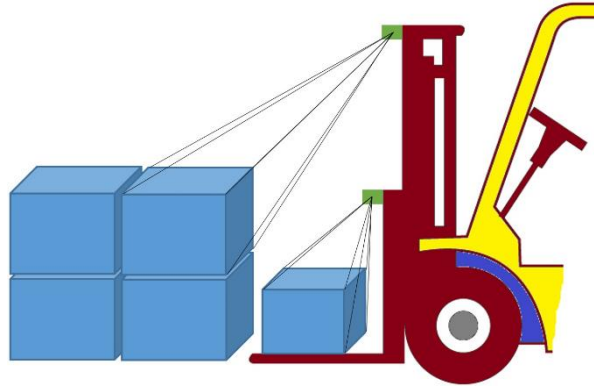


Figure 1: Presentation of an autonomous forklift and its recognition system.

In order to present the usage area and importance of shape and volume recognition of objects, an industrial case is depicted as given in Figure 2. In this case, a conveyor-belt system is shown. Objects having different shapes and dimensions flow through the conveyor-belt. A scanning sensor scans everything moving on the conveyor-belt. The sensor data is processed and detection / estimation tasks are performed by the algorithm running in the computing system. According to the responses of the estimation procedure, the robot is to be commanded to pick up some of the objects. The procedure makes volume estimation for each object (it is assumed that density is known), then the safe and allowable torque values for the actuators of the robot (T_1 , T_2 , T_3 and T_4) are calculated. In other words, the recognition system decides whether the object can be able to be picked up by the robot or not. Such a conveyor-belt system may need a labor as well (as presented in Figure 2). In this case, the volume estimation (hereby the weight estimation) of each object is performed so that the allowable weight that the labor can carry can be decided. This prevents the labor might have a slipped disc injury.

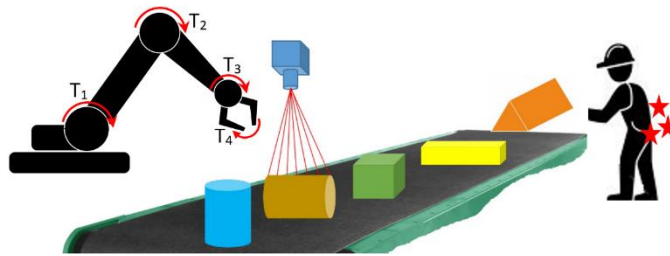


Figure 2: A conveyor system is scanned to get dimensions and volume information.

Another usage area of volume estimation is sand, coal dust, wheat, etc. pile. The measurement of weight of a huge pile is not an easy process. An example of such pile is shown in Figure 3. Huge coal dust pile is used in the thermal reactor located in the Catalagzi region of Zonguldak, Turkey. Four reactors use the coal dust stored in a giant store area as the energy source. The coal dust is transferred via ships to the port that has been specially designed. The weight of each pile pool is incredible and cannot be easily measured. However, the weight of coal dust is important since the energy that will be produced by each reactor should be able to be previously estimated. This estimation totally depends on the coal dust stored. One of the ways to get a weight measurement is to use an unmanned aerial vehicle (i.e., drone). The aerial vehicle is suited with some sensors and the pile pools are scanned. Then the data collected is processed and the approximate volumes of each pile pool can be calculated.



Figure 3: Coal dust pile used by the thermal reactor located in Catalagzi, Zonguldak, Turkey.



2. Related Studies

Generally speaking, the problem of reliable volume estimation for an object can be decomposed in various sub-problems: scanning of the object (the choice of the sensor type determines the accuracy in the estimation process); design of the scanning mechanism and its control strategy (the sensor is mounted on a robotized positioning system and its position is controlled); estimating to what extent the object resemble sphere, square, rectangular or triangular; and volume estimation algorithm (this is the mathematical model estimating the total volume of the object).

Artaso and Nicolas proposed a volume estimation method for merchandise by using multiple range cameras. The design of the volume estimation system was constructed to be adapted in the industrial applications. The verifications of the model were shown by the experimental results. Baldin and Reib proposed a mathematical model for volume estimation. The model focused on unbiased estimation of the volume of a convex body. Although the modelling structure is quite complex (in other words, the implementation of this model in real-time operations requires some extra efforts and computational units), it contributes to fill the gap in the volume estimation models. Cheein and Guivant introduced a slam based incremental convex hull processing approach for tree top volume estimation. The study focused on optimizing the computational cost associated with the mathematical processes doing estimation so that it could be adapted into real-time applications. Cheein et al. introduced a detection system used for agricultural applications. The system developed focused on precision mapping for agriculture fields. To construct the mapping of the working environment, the objects like trees on the reference trajectory were recognized via their body shape and volumes. The methodologies were experimentally tested and the results were presented. Bechar and Vigneault presented an autonomous agricultural robot application. The control system was developed by integrating the vision and RTK-GPS systems. The working environment of the robot was mapped both the objects' outer shapes and their volumes.

3. System Model

In industrial use and unmanned robotic applications, volume estimation is one of the referenced methods to achieve recognition of the working environment. This method has also been using in agricultural operations for different purposes in order to increase performance and processing speed in operations, accuracy and precision in results. It is a fact that performing volume estimation task is a sensor-based operation. The sensor data should be able to feed the mathematical model that reflects the reality. Considering the sensor-based solutions available in the literature, a flexible solution is proposed in this study to make an estimation for an object. The proposed solution also tends to find a way for increasing the accuracy in results. The principle of the strategy developed is depicted in Figure 4.

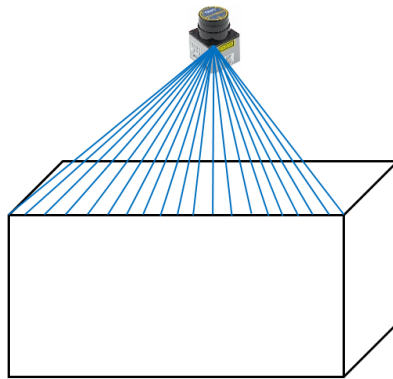


Figure 4: Representation of the scanning process of an object.

A laser scanning rangefinder sensor is located at the top of the object and scans from one end to the other end of the object. Then, many triangles are created by the use of these scanning information (Figure 5). After the scan is completed, the laser sensor is moved in the direction specified by a green-colored-arrow in Figure 5, then another scan is performed. The connection of the scan points between two moves generates many triangular or rectangular prisms which are used to make an estimation of the volume of the object.

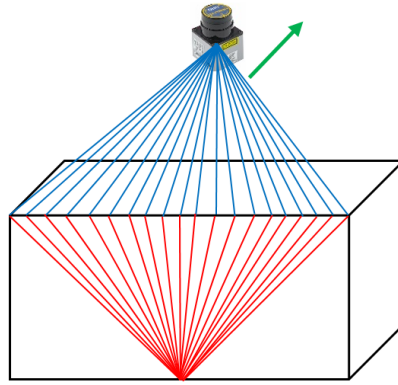


Figure 5: Laser scanner range finder sensor is moved to conduct scan processes from the surface.

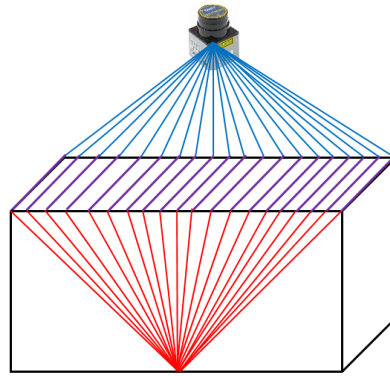


Figure 6: Scanning operation creates many triangles.

Mathematical modelling which aims to make and estimation of the volume of a 3D structure is constructed based on a methodology, triangular prism approach. The data points obtained from the scan processes are connected to form triangular prisms. In other words, triangular prisms are generated between the data points on the scanned surface (Figure 6). Each triangular prism is divided into infinite number of single triangles (Figure 7). The volume of each triangular prism is calculated and specified by Volume(i) ($i=1,2,3,\dots,n$). Then, the total volume of the object is obtained as the summation of each volume.

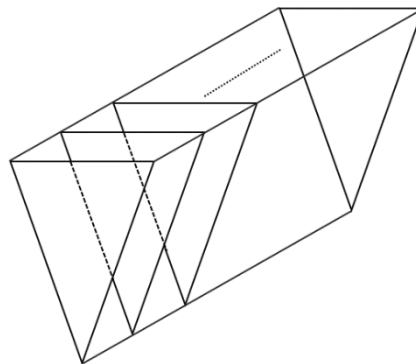
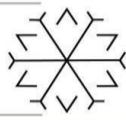


Figure 7: Each triangular prism is divided into infinite number of triangles.

4. Conclusion

Today, the methodologies, models and tools designed in the mechatronics researches have been using in almost everywhere in which enhancement in production and quality in the end product are required. It is a strong expectation that the use of them will enormously be increasing in the near future. The one, which focuses on the use of scanning systems and estimation algorithms, is a powerful feedback for the intelligent control systems used in autonomous systems and automation robots. It estimates the shape and the volume of an object. The information of volume of an object is used by a robotic system as a feedback. In this



study, it is aimed to design a volume estimation system for an object. The main strategy is to create an easy-to-use, easy-to-adapt and low-cost solution. The estimation system includes a laser scanning rangefinder sensor and an estimation model, entitled as the triangular prism approach for volume estimation.

References

Artaso, P. and Nicolas, G.L.,2016. Volume estimation of merchandise using multiple range cameras. *Measurement*, 89: 223-238.

Baldin, N. and Reib, M., 2016. Unbiased estimation of the volume of a convex body. *Stochastic Processes and their Applications*, 126: 3716-3732.

Cheein, F. A. and Guivant, J., 2014. SLAM-based incremental convex hull processing approach for treetop volume estimation. *Computers and Electronics in Agriculture*, 102: 19-30.

Cheein, F. A., Steiner, G., Paina, G. P. and Carelli, R. 2011. Optimized EIF-SLAM algorithm for precision agriculture mapping based on stems detection. *Computers and Electronics in Agriculture*, 78: 195-207.

Bechar, A. and Vigneault, C., 2017. Agricultural robots for field operations. Part 2: Operations and systems. *Biosystems Engineering*, 153: 110-128.

Chemical Properties of Metal Materials Used in Columns from the Hellenistic, Roman and Byzantine Periods in Stratonikeia and Lagina

Cem GÖK¹[0000-0002-8949-8129] and Bilal SÖĞÜT²[0000-0002-0171-318X], Evin CANER ÖZGEL³[0000-0003-0499-7517],
Sinan AKSÖZ¹[0000-0003-4324-5043], Yusuf ÖZCAN⁴[0000-0003-4355-5383]

¹ cemgok@pau.edu.tr, Pamukkale University, Department of Metallurgical and Materials Engineering

² Pamukkale University, Department of Archeology

³ Pamukkale University, Department of Conservation and Restoration of Cultural Heritage

⁴ Pamukkale University, Department of Biomedical Engineering

Abstract

Apart from the architectural and artistic aspects of the columns in ancient buildings, no detailed analysis has been made about the strength obtained due to their connections. Columns belonging to orders such as Doric, Ionic and Corinthian were mostly applied in a certain system in ancient times, and their aesthetic aspects and bearing features were taken into account. However, it has been observed that the physical or chemical properties of iron and lead materials, which directly affect their carrier properties and are used in the construction process, are not handled with their physical or chemical properties, and there are no experimental studies on this subject.

The aim of this study is to determine the use of binder materials (lead and iron) and the chemical properties of these materials, taking into account the characteristics of the columns divided into typologies according to their titles, such as Doric, Ionic and Corinthian, according to the load rate carried by the capital types. In the ancient period, each column capital was used in line with the load carried, and the usage intervals in the building were determined according to this situation. Although the load carried by each column type differs with the width of the body, it is thought that the ratios of the materials used in joining the columns also change.

For the study, the ancient city of Stratonikeia, where columns belonging to different periods and different uses are seen, was chosen. Apart from the ancient city, the examples in Lagina, which is the sanctuary of this place, are also included in the study. There are columns in the Doric, Ionic and Corinthian order in the ancient city of Stratonikeia. These are dated to the Roman, Imperial and Byzantine Periods. The columns in the Lagina Hecate Sanctuary are dated to the Hellenistic and Early Roman Imperial periods. Lagina Hecate Temple, which is among these, is the most monumental and famous structure of its period, dating back to 100 BC. In this structure, Corinthian and Ionic columns consisting of 5 drums were used together. There are 3 separate pegs at the junction of the columns. On the other hand, three or four drums were used in the Stoa columns of the Doric Order dating to the Early Imperial Period. In the ancient city of Stratonikeia, columns with 4 drums in Ionic order dating to the Early Imperial Period were preferred. On the North City Gate, there are 7 m high single-piece bodies dating to the Roman Imperial Period. There are also 3-drum columns dating to the Byzantine Period in the same area. The structures in both areas are examples of different orders and sizes, such as temples, stoa, columned streets, squares, city gates, fountain monuments. Thus, there are different and beautiful examples in terms of history and building diversity in Stratonikeia and Lagina.

In this study, for the samples taken from the Hellenistic, Roman and Byzantine period columns, the heights, diameters, tenon sizes, types, period characteristics of the columns in the area were taken into consideration. For this study, which will be carried out within the scope of the study, first of all, lead and iron materials used in the field were recorded, and experimental studies were carried out on the criteria to be considered for the study. EDS and TG, DTA, DCS analyzes and ICP-MS methods were used for the determination of the melting points and spectral analyzes were used for the compound analysis for the elemental analysis of lead and iron materials.

Keywords. Archaeometry, Metallurgy, Chemical Analysis, Material Analysis and Characterization

The Electrochemical Behaviour of Cp-Ti Coated by Ti-doped Al₂O₃ and Ni-doped Al₂O₃

Hilmi Tekdir¹[0000-0002-9141-9514], Merve Taftali²[0000-0003-2455-9725], Kerem Turalioglu³[0000-0001-8769-1681], Onur Çomaklı⁴[0000-0002-5792-5317], Mustafa Yazıcı⁵[0000-0002-8256-244X], Tuba Yetim⁶[0000-0002-6237-6412], Ali Fatih Yetim⁷[0000-0002-4314-6830], Halim Kovacı⁸[0000-0002-9053-3593], Ayhan Çelik⁹[0000-0002-8096-0794]

¹hilmi.tekdir@erzurum.edu.tr, Erzurum Technical University, Faculty of Engineering and Architecture, Department of Mechanical Engineering, Erzurum, Turkey

²merve.taftali53@erzurum.edu.tr, Erzurum Technical University, Faculty of Engineering and Architecture, Department of Mechanical Engineering, Erzurum, Turkey

³kerem.turalioglu@erzurum.edu.tr, Erzurum Technical University, High Technology Research Centre, Erzurum, Turkey

⁴onur.comakli@erzurum.edu.tr, Erzurum Technical University, Faculty of Engineering and Architecture, Department of Mechanical Engineering, Erzurum, Turkey

⁵mustafa.yazici@erzurum.edu.tr, Erzurum Technical University, High Technology Research Centre, Erzurum, Turkey

⁶tuba.yetim@erzurum.edu.tr, Erzurum Technical University, Faculty of Engineering and Architecture, Department of Chemical Engineering, Erzurum, Turkey

⁷fatih.yetim@erzurum.edu.tr, Erzurum Technical University, Faculty of Engineering and Architecture, Department of Mechanical Engineering, Erzurum, Turkey

⁸halim.kovaci@atauni.edu.tr, Ataturk University, Faculty of Engineering, Department of Mechanical Engineering, Erzurum, Turkey

⁹ayhcelik@atauni.edu.tr, Ataturk University, Faculty of Engineering, Department of Mechanical Engineering, Erzurum, Turkey

Abstract

In this study, the Al₂O₃, Ni-doped Al₂O₃, and Ti-doped Al₂O₃ nanocomposite ceramic coatings were prepared using a sol-gel method, and the Cp-Ti substrates were coated by dip-coating process. For both doping solutions, the same molar ratios of doped contents and Al₂O₃ were used for being able to compare the effect of the doped content as 0,5:1, for Ni: Al₂O₃ and Ti: Al₂O₃. The electrochemical behavior of these ceramic coatings was carried out using potentiodynamic polarization and electrochemical impedance spectroscopy (EIS). Surface characterizations before and after the corrosion, which occurred by the electrochemical process, were investigated by the scanning electron microscope (SEM) and X-ray diffraction (XRD) analysis. The results of corrosion tests exhibited that the corrosion of nanocomposite ceramic coatings became better than uncoated samples. Also, the corrosion of nanocomposite ceramic coatings was improved by the Ni and Ti doping on the Al₂O₃. When the corrosion behavior of the ceramic coatings was compared, the best corrosion resistance was obtained from the Ti-doped Al₂O₃ nanocomposite coating. Also, the uncoated substrate had the worst corrosion resistance. When the doped nanocomposite ceramic coatings were compared, the Ti-doped Al₂O₃ nanocomposite coating behaved less corrosion than the Ni-doped Al₂O₃ nanocomposite coating. Also, the corrosion resistance values of the doped nanocomposite coatings were approximately 4260 and 3100 Ω cm² for the Ti-doped Al₂O₃ nanocomposite coating and the Ni-doped Al₂O₃ nanocomposite coating respectively.

Keywords. Nanocomposite, Corrosion, Al₂O₃ Ceramic Coating, Sol-gel, Ni doping, Ti doping

Determination of Cutting Parameters for Peripheral Milling of S355J Sheet Metal with Aggressive-High-Performance Machining Method

Can TUNCER ¹[0000-0003-0539-1381], Sakıp TÜRKÖZ ²[0000-0001-7567-7743], Yunus Emre NEHRİ ³[0000-0003-2119-9031]
and Ali ORAL ⁴[0000-0002-9144-3821]

¹ can.tuncer@gri.com.es, GESBEY Enerji Türbini Kule Üretim San. ve Tic. A.Ş., Balıkesir, Turkey.

² sakip.turkoz@gri.com, GESBEY Enerji Türbini Kule Üretim San. ve Tic. A.Ş., Balıkesir, Turkey.

³ yunusnehri@balikesir.edu.tr, Balıkesir University Mechanical Engineering Department, Balıkesir, Turkey.

⁴ alioral@balikesir.edu.tr, Balıkesir University Mechanical Engineering Department, Balıkesir, Turkey.

Abstract

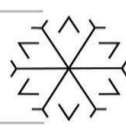
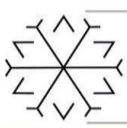
Milling operations are one of the most widely used machining methods in the industry. Efficiency in milling has direct effects on the cost, production time and quality of machined parts. Tool wear or breakage can also become a limitation, especially for heavy roughing operations. Higher material removal rates are required to reduce the machining time of the part, and high-performance machining is preferred in many heavy material removal operations. Compared to high-performance machining and traditional machining, it is possible to achieve lower machining time with high-performance machining. In this study, the cutting parameters were determined to open the beveling in one cutting depth with dry machining, all the edges of the sheet plates with 30 mm thickness S355J material used in the construction of the wind turbine tower. SNHX1406TN08-M12 MP2501 aluminum oxide coated cutting edge developed by Seco company was used. The cutting parameters related to the cutting tip were not declared by the manufacturer, and the study contributed to the determination of the cutting parameters of the material. At the end of the work, a total of 355 minutes of chipping was removed, and it was observed that the cutting tool was exposed to less wear when the cutting speed was increased and the feed value decreased.

Keywords. High performance milling, beveling machine, milling machine

1. Introduction

Machining is the process of breaking pieces from the stock material with the help of auxiliary elements (cutting tip, stone, etc.) in order to reach the desired material dimensions. It is one of the basic manufacturing processes and is widely used in industry (Durmaz, 2018). Studies in the field of metal processing have focused on economic and ecological production. Various technologies such as HSC (High Speed Cutting), HPC (High Performance Cutting), HFM (High Feed Milling) and dry machining are used to ensure these demands. The purpose of these technologies is to reduce production time while maintaining the quality and accuracy of the processed material (Fulemova *et al.*, 2015).

In this study, the cutting parameters were determined to open the weld beveling in one cutting depth with dry machining all the edges of the sheet plates with 30 mm thick S355J material used in the construction of the wind turbine tower. The weld beveling is opened in order to ensure sufficient penetration of the weld material on the edges of the two parts joined together (Oral *et al.*, 2017). Weld beveling is one of the processes that must be subjected to various machine parts and constructions, which are required to be manufactured with the welded manufacturing technique, before welding. The weld beveling formation process is based on the principle of performing deformation with or without chipping by using various methods on certain parts such as edges, corners, surfaces where the joint will take place in the workpieces to be subjected to the welded manufacturing process. Portable small weld beveling machines are traditionally used for machining large sheet metal sheets. Small portable machines, when placed on the sheet metal plate, remove chips along the edge and open the weld beveling. When these machines are placed on the sheet metal plate, they can start the chip removal process immediately. Portable weld beveling machines have a speed problem and it is not possible to bevel in thick sheet materials in one pass.



In this study, the weld beveling parameters were determined with the cutting tool specially designed for the beveling machine developed to bevel the thick sheet metal in one cutting depth.

In this study, a high volume machining method will be used in the beveling process. This method can be defined as aggressive machining process and HSC (High Speed Cutting), HPC (High Performance Cutting), HFM (High Feed Milling) terms are used in the literature. There are various studies in the literature regarding high performance machining. These studies are briefly mentioned below.

Oral et al. investigated the effects of conventional machining strategy and high performance machining strategies (iMachining) on tool life and machining times by milling AISI 1.2738 steels with a 4-flute HTG end mill. They concluded that the machining time is shorter than in conventional machining, since the depth of cut can be selected larger in the high-performance machining strategy. They observed that the cutting tool wears less in high performance when the same volume of chip is removed in both strategies (Oral *et al.*, 2017).

Tekeli and Budak milled aluminum parts with a 4-flute HSS end mill and made optimization studies for maximum metal removal rate and good surface quality. An analytical stability model was used to reduce vibration. With the model used, they determined the axial and radial depths of cut with less vibration. They concluded that machining time was reduced by about 40% with optimum parameters (Tekeli and Budak, 2005).

Fulemova et al. investigated the effects of cooling on tool life by milling S235JR steel with a 4-flute VHM end mill under air cooling and dry machining conditions. In their study with iMachining technology, they stated that air cooling is not suitable for rough milling (Fulemova *et al.*, 2015).

Li et al. investigated cutting performance and wear by milling nickel-based GH4169 super alloy with 4-fluted SiAlON-coated end mill under dry machining conditions. In experiments carried out at high cutting speed of 500 m/min, they observed flank wear and tool breakage due to material sticking on the insert (Li *et al.*, 2021).

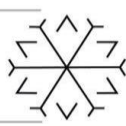
Prasath et al. investigated the tool wear and the temperature between tool and workpiece by machining special 465 steel with 3 different coating types (uncoated, TiCN and TiAlN) at high speed under dry machining conditions. They stated that the TiAlN coated insert gives the best performance for tool life and temperature (Prasath *et al.*, 2017).

2. Material Method

In the machine to be developed, weld beveling of the plate, the largest of which is 13000 x 3000 (mmxmm), by machining; It is aimed to complete the transport, preparation time and cutting time 40 minutes in total. For this purpose, a welding beveling machine with a 30 kW spindle motor, developed to open the weld beveling in one cutting depth, was developed, and a cutting tool with a total of 63 cutting inserts in 7 rows with a profile suitable for the weld beveling profile for chip removal was developed. The developed machine is given in Figure 1 and the specially designed cutting tool is given in Figure 2.



Şekil 1 : Sheet metal beveling machine



Şekil 2 : Beveling tool a-3D model, b-Tool photo c-position of sheet metal plate and cutters

It has been decided to use an aluminum oxide coated SNHX1406TN08-M12 MP2501 cutter as a cutting edge in the beveling process. The cutting parameters for the insert specified in the manufacturer's catalogs are not given, and it is stated by the country representatives that the tool life will be around 60 minutes. During the first trials, it was observed that the cutting data of the cutting edge were given in a very safe area, and therefore, it became necessary to determine the cutting parameters and tool life. Wear measurements were taken with a Dino-Lite AD4000 series digital microscope with 1/10000 mm sensitivity at 250 times magnification.

In the experimental study, the cutting speed value of 200-240 m/min and the feed rate per tooth $f_z=0.25-0.30$ mm/tooth were given by the company. As a result of the first trials made on the bench, it was seen that the desired productivity could not be achieved with these values, and it was decided to carry out a study to determine the cutting parameters that could provide the desired productivity values. In the cutting tool used for this purpose, different cutting speeds occur in each row of the cutting edges, which are arranged in 7 rows.

The test plate with dimensions of 2920X9270X30 mm, chips was removed at a height of 26 mm with an axial cutting depth of 2.5 mm (Figure 3). The cutting parameters used for the test runs on the test plate are given in Table 1. 1. The recommendations of the company were taken into for the cutting speed in the experimental parameters. The feed, on the other hand, was adapted according to the production speed, taking into account the first test results, and was taken higher than the recommended value.

Tablo 1 : Cutting speed and feed rate values used in the experiments

Tool Name	1. Experimental Parameters		2. Experimental Parameters	
	Cutting Speed m/min	Feed Rate mm/min	Cutting Speed m/min	Feed Rate mm/min
A	240	820	312	780
B	225	820	292	780
C	210	820	274	780
D	203	820	264	780

3. Experimental Study and Evaluation

Wear measurements were made after every 2 turns of chipping from all sides of the plate with the cutting tool. The wear criterion is based on the flank wear $VB=0.3$ mm defined in ISO 3685. Although the value declared by the company for tool life is 60 minutes, it has been evaluated that this life can be exceeded in the first trials. In the study, experiments were carried out with two different feed rates of 780mm/min and 820mm/min and two different cutting tool revolutions of 269rpm and 350rpm, in order to complete the beveling process on the largest plate in about 40 minutes. The cutting speeds corresponding to these revolutions are shown in Figure 2-c. Since each cutting tool is placed in different diameters, it causes the tool in each row to remove chips with different cutting speed (Table 1). No cutting fluid was used in the experiments, dry machining was performed.

In the experiments performed using the first experimental parameters, $VB=0.255$ mm remained even though it was processed for 355 minutes. Due to the high vibrations (value taken with the accelerometer $a=32$ m/s²) during the entry of the tool into the part, it was evaluated to machine at higher cutting speed and the study was carried out with the 2nd test parameters given in Table 1. By increasing the cutting speed, the vibrations were reduced (value taken with the accelerometer $a=22$ m/s²) and the processing time increased by only 2 minutes for the plate to be machined at maximum dimensions. The weld beveling and the chips obtained during the test studies are given in Figure 3. The wear results obtained in the experiments are given in Table 2, and the wear graphs are given in Figure 4 and Figure 5.

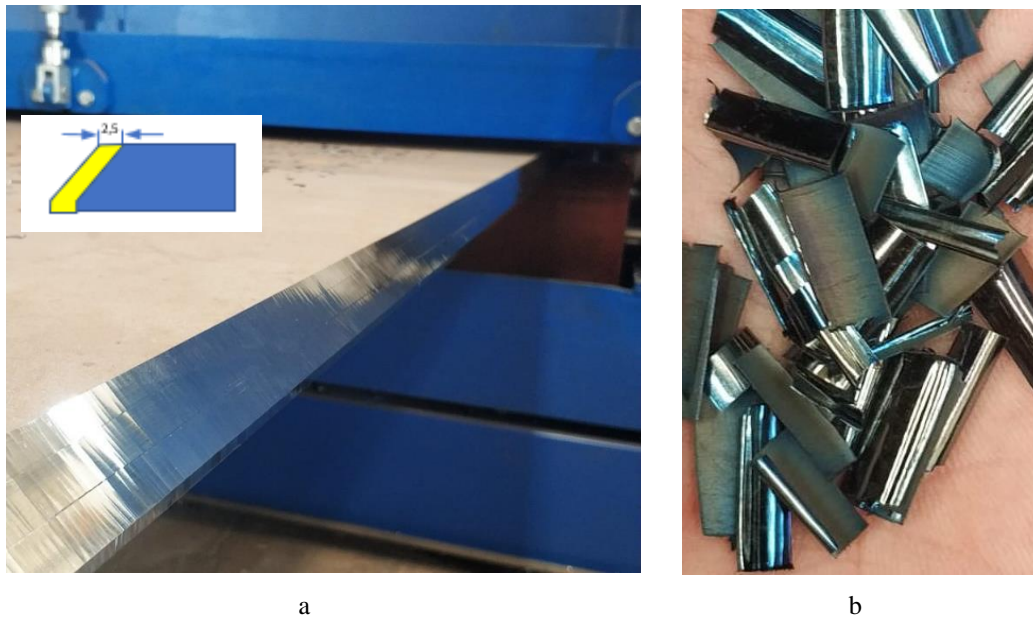


Figure 3 : a-Test plate, b-chip samples obtained at the end of the process

Table 2 : Wear measurements obtained at the end of the experiments

Vf=820 mm/min					Vf=780 mm/min				
Time	A (240)	B(225)	C(210)	D(203)	Time	A(312)	B(292)	C(274)	D(264)
60,0	0,084	0,059	0,054	0,072	63	0,063	0,049	0,046	0,056
119,0	0,095	0,075	0,094	0,111	125	0,070	0,059	0,063	0,076
178,0	0,105	0,13	0,108	0,176	176	0,087	0,078	0,067	0,087
237,0	0,157	0,151	0,125	0,207	248	0,118	0,110	0,077	0,127
296,0	0,22	0,205	0,136	0,236	310	0,135	0,127	0,097	0,145
355,0	0,23	0,236	0,168	0,255	371	0,157	0,156	0,123	0,189

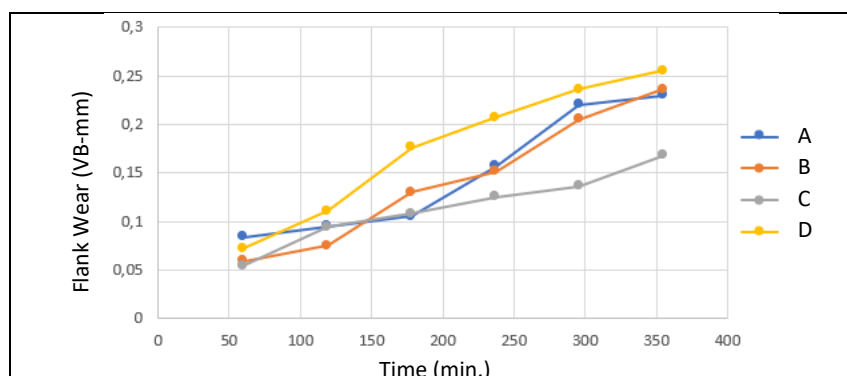


Figure 1: Wear development of cutting tools at a feed rate of Vf=820 mm/min

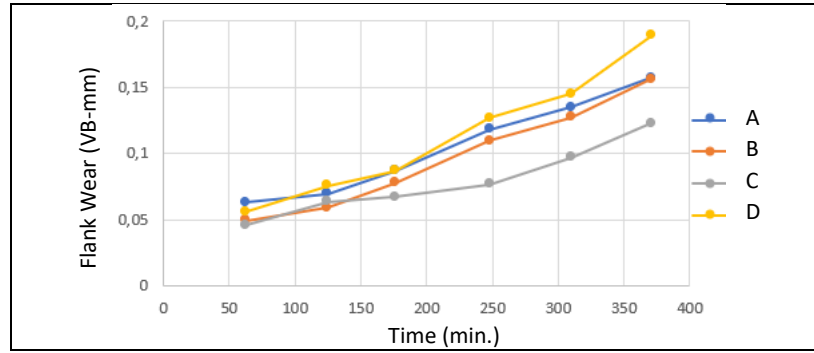


Figure 2 : Wear development of cutting tools at a feed rate of $V_f=780$ mm/min

4. Conclusion

A cutting speed of 200-240 m/min and a feed rate of 0.23-0.30 mm/tooth per tooth were recommended by the manufacturer, and it was stated that the tool life would be 60 minutes. In the preliminary studies, it was seen that the values recommended by the manufacturer were in a very safe zone and an experimental study was carried out to determine the appropriate cutting parameters for opening the weld beveling. At the end of the study, it was determined that the tool did not complete its life and was still in usable condition, although the 60-minute life targeted by the manufacturer was exceeded 6-7 times.

In both groups experiments, the highest wear was recorded despite the lowest cutting speed in the cutting tools that processed the vertical edge, and lower cutting speeds were recorded although the cutting speeds of the other tools were higher. In the cutting tool that processes the vertical edge, the approach angle is 90° and in other tools, the approach angle is 45° . This situation, which is seen as a contrary situation with the literature; It has been evaluated that the D tool, which cuts the vertical edges due to the approach angle, removes thicker chips and thus is exposed to higher cutting forces and is exposed to more wear. In the 1st group experiments, low cutting speed and high feed rate were used and after 355 minutes of chip removal, 0.255 mm flank wear was obtained. When the cutting speed was increased by 30% and the feed rate was decreased by 5%, the wear values decreased by approximately 35%.

In the continuation of this study, studies will be carried out to determine the optimum values by repeating the tests for different cutting speeds and feed rates without reducing the production speed.

References

Durmaz, Y. M., 2018. TiAlSiN, AlCrN ve TiAlN seramik filmleri ile kaplanmış karbür takımların yüksek hızlı frezeleme işleminde aşınma performansının incelenmesi. Erzurum Teknik Üniversitesi, Fen Bilimleri Enstitüsü, Erzurum.

Fulemova, J. et al., 2015. Influence of cooling methods on tool life during machining with imachining strategy, in Proceedings of the International Conference of DAAAM Baltic, pp. 15–20.

Li, Y. et al., 2021. Wear patterns and mechanisms of sialon ceramic end-milling tool during high speed machining of nickel-based superalloy, *Ceramics International*, 47(4), pp. 5690–5698. doi: 10.1016/j.ceramint.2020.10.155.

Oral, A. ,2017.Yüksek hacimli talaş kaldırma işleminin takım ömrüne etkisi, in 8th international symposium on machining. Available at: https://www.researchgate.net/publication/346914350_Yuksek_hacimli_talas_kaldirma_isleminin_takim_omrune_etkisi_The_effect_of_high_material_removal_rate_on_tool_life (Accessed: 24 November 2021).

Prasath, V. et al., 2017. Performance evaluation on high speed machining of custom 465 steel, *Materials Today: Proceedings*, 4(10), pp. 10810–10815. doi: <https://doi.org/10.1016/j.matpr.2017.08.032>.

Tekeli, A. and Budak, E., 2005. Maximization of chatter-free material removal rate in end milling using analytical methods, *Machining Science and Technology*, 9(2), pp. 147–167. doi: 10.1081/MST-200059036.

Mechanical and Tribological Properties of SLMed Silver Coated Copper Powder Material

Gürkan Kaya ¹[0000-0002-1696-3202], Onur Güler ²[0000-0002-9696-3287], Hüseyin Can Aksa ³[0000-0001-9086-6526], Serhatcan Berk Akçay ⁴[0000-0002-7492-4287], İlyas Hacısalihoğlu ⁵[0000-0002-5902-7203], Temel Varol ⁶[0000-0002-1159-5383], Fatih Yıldız ⁷[0000-0003-4475-5379]

¹gurkan.kaya@erzurum.edu.tr, Department of Mechanical Engineering, Erzurum Technical University, Erzurum/Turkey

²onurguler@ktu.edu.tr, Department of Metallurgical and Materials Engineering, Karadeniz Technical University, Trabzon/Turkey

³hcaksa@ktu.edu.tr, Department of Metallurgical and Materials Engineering, Karadeniz Technical University, Trabzon/Turkey

⁴serhatakay@ktu.edu.tr, Department of Metallurgical and Materials Engineering, Karadeniz Technical University, Trabzon/Turkey

⁵hacisalihoglu@erzurum.edu.tr, Department of Mechanical Engineering, Erzurum Technical University, Erzurum/Turkey

⁶tvarol@ktu.edu.tr, Department of Metallurgical and Materials Engineering, Karadeniz Technical University, Trabzon/Turkey

⁷fatih.yildiz@erzurum.edu.tr, Department of Mechanical Engineering, Erzurum Technical University, Erzurum/Turkey

Abstract

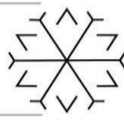
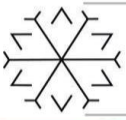
The mechanical and tribological properties of the parts produced by the Selective Laser Melting (SLM) method, which is one of the additive manufacturing methods, are highly affected by the parameters used in the manufacturing. For this reason, it is extremely important to know the effects of the parameters to be used in production on the mechanical and tribological properties of the material and to determine the optimum production parameters. In addition, post-processing (hot pressing, rolling and sintering) treatments greatly affects the tribological properties. In this study, the effect of different hatch spacing values on the mechanical properties of Ag coated Cu powder material (Cu-Ag) was investigated. Copper powders were coated with silver using the electroless coating method. Post treatments were applied to the sample with the best mechanical properties and its tribological properties were examined. The best mechanical properties were determined for the sample obtained with a scanning speed of 250mm/s and hatch spacing value of 45%. The lowest wear rate value was obtained in the sample, which was subjected to hot pressing at 750°C.

Keywords. Selective laser melting, silver coated copper powder, mechanical properties, wear properties, post-process

1. Introduction

Selective Laser Melting (SLM) method, which is one of the additive manufacturing methods, is a new generation production technology in which products with complex geometries can be produced. This method is in the form of melting the powdered material with a laser beam, connecting it layer by layer and forming the final product (Peleg, 2020).

Copper and silver metals are frequently used in electrical and electronic applications where electrical and thermal conductivity is of great importance (Chang *et al.*, 1999). Low oxidation resistance limits the use of long-lasting materials. For this reason, materials with higher electrical conductivity and oxidation resistance can be obtained at a lower cost than silver by using materials containing copper and silver (Hai *et al.*, 2006; Cao and Zhang, 2012; Liu, Yu and Zhao, 2021).



It is important to investigate the process parameters that directly affect the mechanical and wear properties of the processes performed with the SLM method (Kaya, Yildiz and Hacisalihoğlu, 2019; Xiong *et al.*, 2019). It has been determined that metals with high thermal conductivity and reflectivity, such as copper and silver, cause the formation of non-melted regions in the microstructure of the materials produced with SLM due to the low laser absorption (Wei *et al.*, 2019).

In the production method with SLM, many production parameters affect the mechanical, chemical, morphological and tribological properties of the final product. These production parameters are;

- Laser power,
- Laser scanning speed,
- Layer thickness,
- Scanning strategy,
- Build orientation,
- Laser pulse mode.

In the SLE method, the strength between the layers should be high and integrity should be ensured. This integrity is provided by the energy density (E), which is controlled by the change of laser power (P), layer thickness (t), laser scanning speed (V), hatch distance (h), known as production parameters. All these parameters affect the mechanical properties of the material (Thijs *et al.*, 2010). The relationship between production parameters and energy density is given in the formula below.

$$E = \frac{P}{V \cdot h \cdot t}$$

According to the literature study, the effect of production parameters made by SLM method using silver-coated copper powder material on mechanical and tribological properties was not yet investigated. For this reason, the mechanical and tribological properties of Cu-Ag materials in the production of SLM method were investigated in this study.

2. Material and Method

The copper powder material used in the production processes with the SLM method was coated with silver using the electroless coating method. The silver shell thickness obtained on the copper powders varied between 1 and 3 µm and was distributed homogeneously. Test samples from Cu-Ag powder material were produced by SLM method in order to examine the mechanical and tribological properties. In production with SLM, different production parameters were used with the Concept Laser M LabR SLM device. The SLM device shown in Figure 1 works with a 100 W Neodymium doped Yttrium Aluminum Garnet (Nd:YAG) laser system and has a 80x80x90 mm build platform. The productions made during this study were carried out using continuous laser pulse mode in the atmosphere of Argon (Ar) gas. Oxygen content was kept below 1% during production. STL file formats of the produced test samples were prepared with the help of AutoFab software. In order to examine the effect of the amount of hatch spacing on the mechanical properties, mechanical tests were carried out by producing tensile samples at different amounts of hatch spacing. Post processes were applied to the sample providing the best mechanical properties. After post-processing, wear tests were carried out to determine the best tribological values. Production parameters made from Cu-Ag powder material by SLM method were given in Table 1.



Figure 1: Concept Laser MLab R SLM device

Table 1: SLM Process Parameters

Sample	Laser Power (W)	Pre-exposure Power (W)	Layer Thickness (μm)	Hatch Spacing (%)	Scanning Speed (mm/s)
Cu-Ag	100	50	25	40-45-50	250

2.1. Mechanical Experiments

The dimensions of the tensile test specimens produced from silver-coated copper powder material were determined according to the ASTM E8 (Standard Test Methods for Tension Testing of Metallic Materials) standard, and the specimen dimensions were given in Figure 2. Tensile tests of Cu-Ag samples were carried out in the INSTRON 5982 static test device shown in Figure 3.

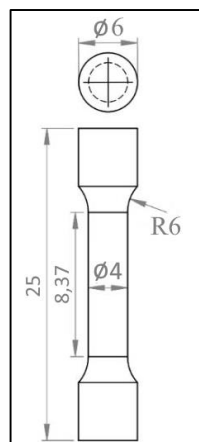


Figure 2: Tensile Test Sample



Figure 3: Static Test Device

2.2. Tribological Experiments

The wear tests of the samples produced from Cu-Ag powder material by SLM method and applied post-process were carried out in Bruker-UMT test device. The tribometer test device on which the wear tests were carried out was shown in Figure 4. The wear test parameters applied to the prismatic samples produced in 10x10x5 mm dimensions were shown in Table 2. The wear rates of the samples were calculated with the following formula. Hot pressing, sintering and rolling processes were applied to the samples as post processes.

$$Wear\ Rate\ \left(\frac{mm^3}{Nm}\right) = \frac{Wear\ volume\ (mm^3)}{Normal\ load\ (N) \times Wear\ distance\ (m)}$$

Table 2: Wear Test Parameters

<i>Test parameters</i>	<i>Values</i>
Test type	Reciprocating
Normal load (N)	5
Wear stroke (mm)	4
Velocity (mm/s)	8
Time(s)	3600
Ball type	Stainless steel
Temperature(°C)	Room temperature (23±2)
Ambient	Dry conditions

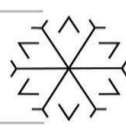
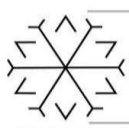


Figure 4: Tribometer Test Device

Bruker Contour-GT 3D optical profilometer device was used to determine the wear volumes of the samples after the wear tests. The wear volumes were obtained by multiplying the cross-sectional area of the wear trace, which was determined by taking an average of 10 measurements from each wear trace, by the trace length.

3. Results

3.1. Mechanical Test Results

One of the most basic deficiencies in the additive manufacturing process is insufficient elongation values that occur as a result of overcooling. It is of great importance to determine the optimum hatch spacing values by considering the tensile stress and elongation values obtained by the tensile test. The stress-elongation graph of the samples produced with the SLM method at different hatch spacing values was shown in Figure 5. Although the highest tensile stress values were quite close to each other, they were obtained for the sample produced at 45% hatch spacing values. Considering the % elongation amount, it was seen that the highest elongation value was obtained for 45% hatch spacing amount. It was seen that the elongation value remained quite low at the values below the hatch spacing value where the best elongation amount was obtained. This was due to the gas voids formed in the structure with excessive energy input (Hacısalıhoğlu *et al.* 2020).

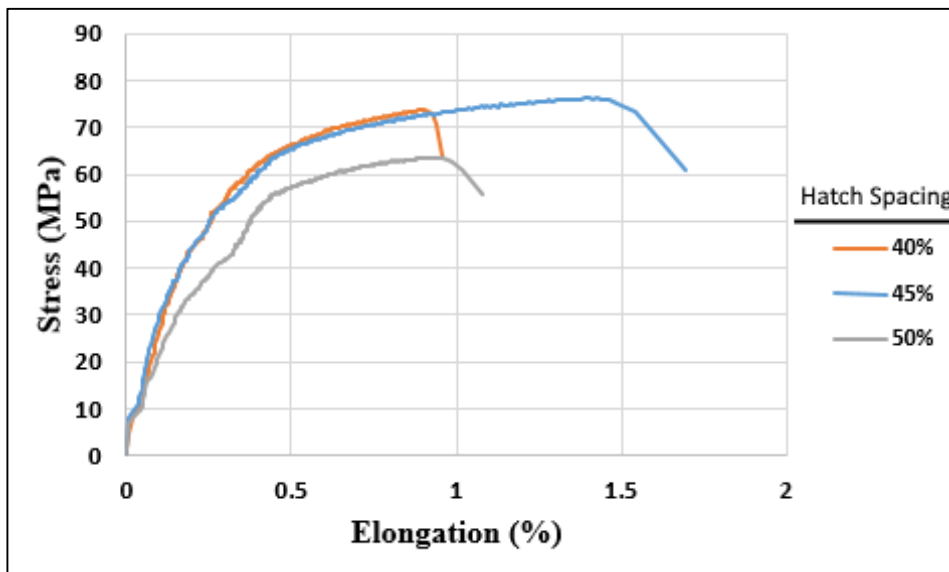


Figure 5: Tensile Test Results

3.2. Tribological Test Results

One of the problems encountered after production with SLM is the porosity in the microstructure. For this reason, post processes were applied to increase the density. Hot pressing, sintering and rolling processes were carried out at 750°C on the sample produced with 45% hatch spacing since it had the highest elongation and strength. Density values increased significantly after post-treatment of the Cu-Ag sample produced with SLM (Figure 6). Especially after the hot pressing and rolling processes, the increase in density was more effective than the sintering process. The highest density value was obtained by the hot pressing process at 750°C, and an increase of approximately 30% was obtained compared to the untreated Cu-Ag sample.

After post processing, wear tests were carried out to examine the tribological properties and the wear rates obtained were presented in Figure 7. 3D profilometer images of wear traces were given in Figure 8. Average friction coefficient values of the samples were presented in Table 3. The lowest friction coefficient values were obtained from the samples produced by the SLM with silver-coated copper powder materials. An increase was observed in the friction coefficient values due to the increased surface roughness values after the post processes applied at high temperature to the samples produced from silver-coated copper powder material. When the wear rates graph was examined, it was noteworthy that the wear rates of the hot pressed and rolled samples decreased significantly as the density increased. The lowest wear rate value among all samples was obtained for the sample in which the hot pressing process was applied at 750°C. Despite the increase in density after post-processing, the wear rate of the sample sintered at 750°C was higher than the untreated Cu-Ag sample. Because the highest surface roughness was obtained after the sintering process. Surface roughness (Ra) values are 0.075, 0.14, 0.3 and 0.16 μm for Cu-Ag, hot pressed, sintered and rolled samples, respectively.

Table 3: Average COF Values

Sample	Average friction coefficient values
Cu-Ag	0.59±0.071
750°C Hot pressing	0.62±0.063
750°C Sintering	0.95±0.091
750°C Rolling	0.78±0.074

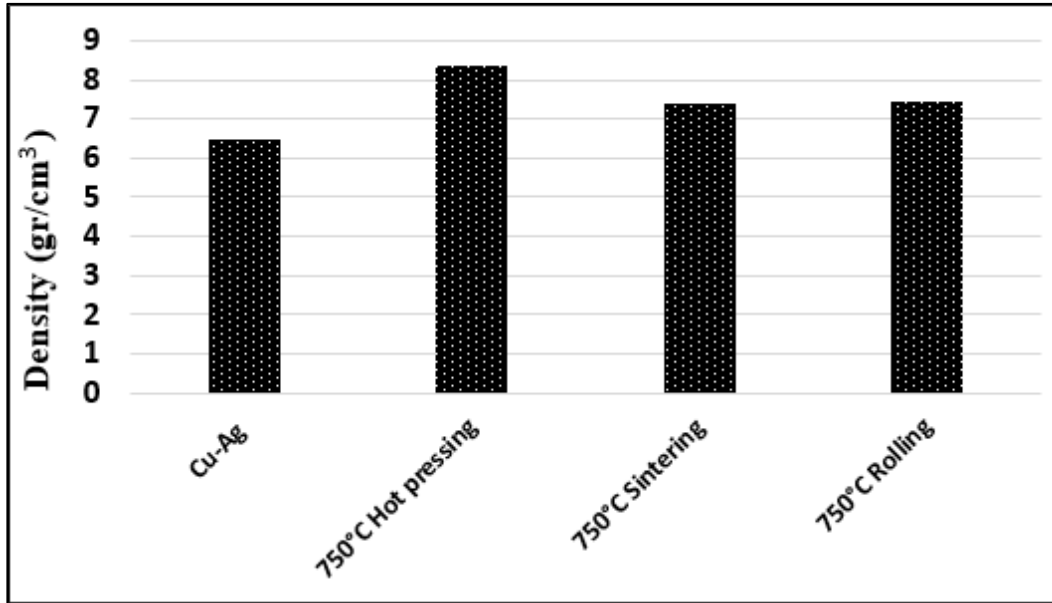
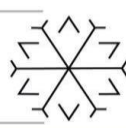
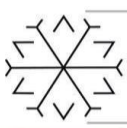


Figure 6: Density Graphs of Samples Produced by SLM Method and Post-processed

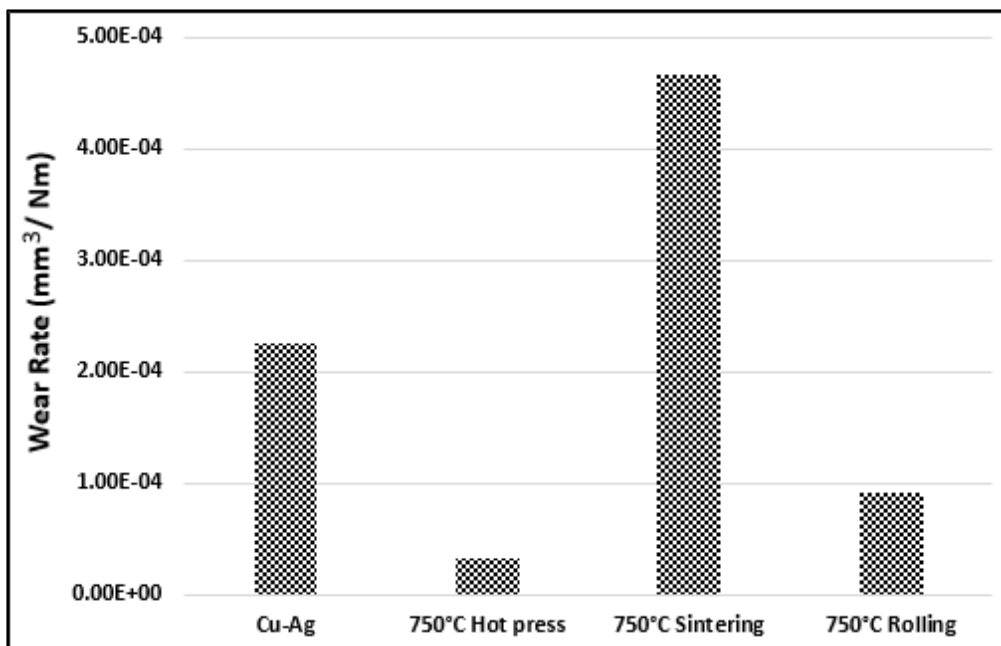


Figure 7: Wear Rate Graph of the Samples

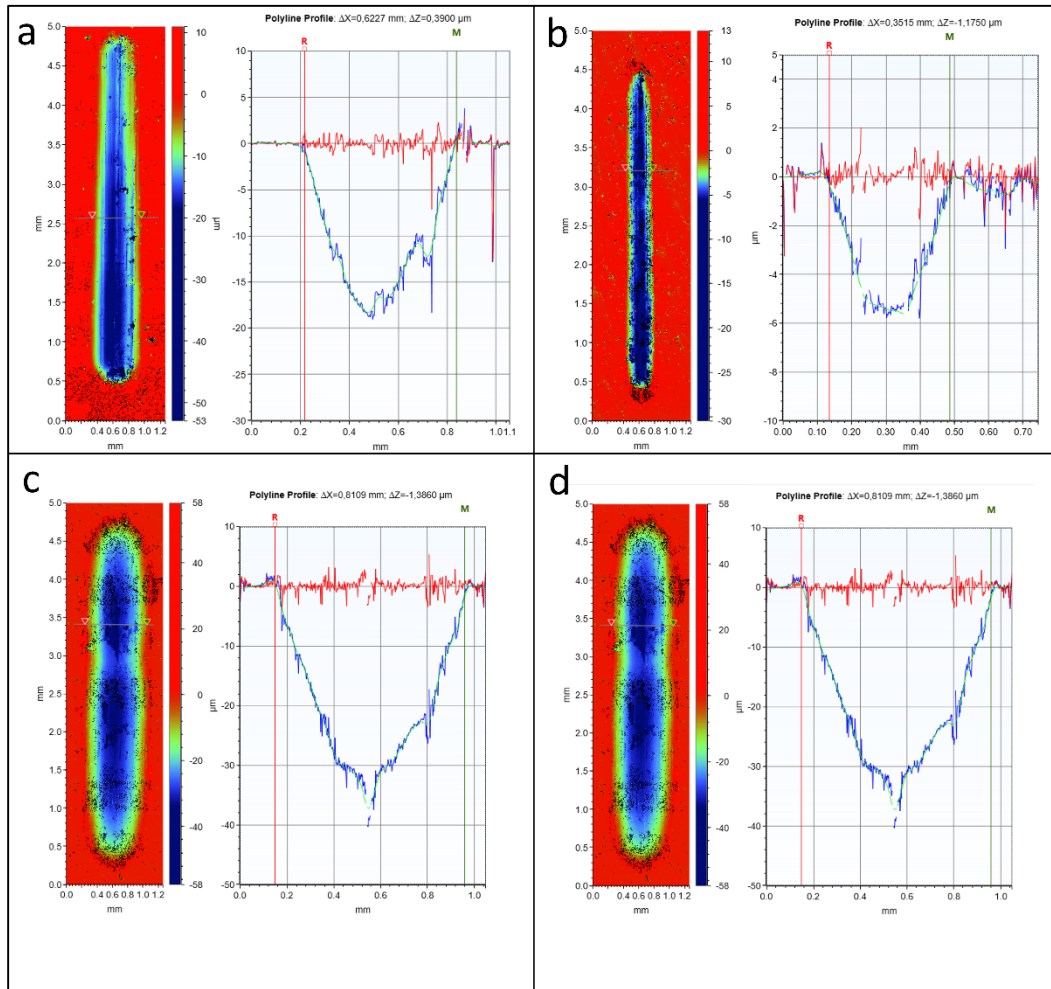


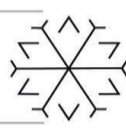
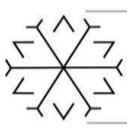
Figure 8: 3D Profilometer Images of Wear Traces (a) Cu-Ag, (b) 750°C Hot Pressing, (c) 750°C Sintering, (d) 750°C Rolling

4. Conclusions

In this study, it was determined that different hatch spacing values affect the mechanical and tribological properties as they changed the internal structure properties in SLM production. In order to obtain a stable melt pool in production with SLM, it was important to find the optimum hatch spacing value. The best mechanical properties were obtained for the sample produced with 45% hatch spacing in the productions using different hatch spacing range values. Hot pressing, rolling and sintering processes at 750°C were applied to this sample. After post processing, wear tests were carried out to examine the tribological properties. The lowest wear rate value was obtained for the sample applied to hot pressing at 750°C, where the highest density was obtained.

Acknowledgements

This study was financially supported by Scientific and Technological Research Council of Turkey (TÜBİTAK) through the Project no: 119M398. The authors would like to thank TÜBİTAK for its financial support in conducting this study. The authors also would like to thank Erzurum Technical University High Technology Research and Application Center (ETÜ-YÜTAM) for its support in experimental studies.



References

- Cao, X. G. and Zhang, H. Y. (2012) 'Preparation of silver-coated copper powder and its oxidation resistance research', *Powder Technology*. Elsevier B.V., 226, pp. 53–56. doi: 10.1016/j.powtec.2012.04.012.
- C. Wei, Z. Sun, Q. Chen, Z. Liu, L. Li. (2019) Additive Manufacturing of Horizontal and 3D Functionally Graded 316L/Cu10Sn Components via Multiple Material Selective Laser Melting, *J. Manuf. Sci. Eng. Trans. ASME*. 141. <https://doi.org/10.1115/1.4043983>.
- Chang, S. Y. *et al.* (1999) 'Processing copper and silver matrix composites by electroless plating and hot pressing', *Metallurgical and Materials Transactions A: Physical Metallurgy and Materials Science*, 30(4), pp. 1119–1136. doi: 10.1007/s11661-999-0164-z.
- Hai, H. T. *et al.* (2006) 'Developing process for coating copper particles with silver by electroless plating method', *Surface and Coatings Technology*. Elsevier B.V., 201(6), pp. 3788–3792. doi: 10.1016/j.surfcoat.2006.03.025.
- Hacısalıhoğlu, İ. *et al.* (2020) 'The effects of build orientation and hatch spacing on mechanical properties of medical Ti–6Al–4V alloy manufactured by selective laser melting', *Materials Science and Engineering: A*, 802, 140649. doi.org/10.1016/j.msea.2020.140649.
- Kaya, G., Yildiz, F. and Hacısalıhoğlu, A. (2019) 'Characterization of the Structural and Tribological Properties of Medical Ti6Al4V Alloy Produced in Different Production Parameters Using Selective Laser Melting', *3D Printing and Additive Manufacturing*, 6(5), pp. 253–261. doi: 10.1089/3dp.2019.0017.
- Liu, Y., Yu, Y. and Zhao, X. (2021) 'The influence of the ratio of graphite to silver-coated copper powders on the electromagnetic and mechanical properties of single-layer coated composites', *Journal of the Textile Institute*. Taylor & Francis, 112(11), pp. 1709–1716. doi: 10.1080/00405000.2020.1839218.
- Peleg, J. (2020) *Additive and Traditionally Manufactured Components A Comparative Analysis of Mechanical Properties, Additive and Traditionally Manufactured Components*. doi: 10.1016/c2019-0-04180-5.
- Thijs, L. *et al.* (2010) 'A study of the microstructural evolution during selective laser melting of Ti-6Al-4V', *Acta Materialia*. Acta Materialia Inc., 58(9), pp. 3303–3312. doi: 10.1016/j.actamat.2010.02.004.
- Xiong, W. *et al.* (2019) 'Effect of selective laser melting parameters on morphology, microstructure, densification and mechanical properties of supersaturated silver alloy', *Materials and Design*. The Authors, 170, p. 107697. doi: 10.1016/j.matdes.2019.107697.

The Effects of Selective Laser Melting Process Parameters on Thermal Conductivity of 316L Stainless Steel

Ufuk Gençoğlu^[0000-0003-2877-7957], Tevfik Oğuzhan Ergüder^{[0000-0002-8876-6152]*},

Gürkan Kaya^[0000-0002-1696-3202], İlyas Hacısalihoğlu^[0000-0002-5902-7203], Emre Mandev^[0000-0002-6791-4136],

Fatih Yıldız^[0000-0003-4475-5379]

Erzurum Technical University, Engineering and Architecture Faculty, Mechanical Engineering Department,
Erzurum/Turkey

*tevfik.erguder57@erzurum.edu.tr

Abstract

The thermal properties of the parts manufactured by the Selective Laser Melting (SLM) method, one of the additive manufacturing methods, are highly affected by the strategies and parameters used in manufacturing. Therefore, it is extremely important to know/control the effect of the parameters to be used in manufacturing on the thermal properties of the material and to determine the optimum production conditions. In this study, the effects of these production parameters on the thermal properties of 316L stainless steel were investigated. SLM processes were carried out at 3 different hatch spacing values and 3 different build orientations. Among the hatch spacing values, 70% hatch spacing value provided higher thermal conductivity values for all build orientations. The thermal conductivity values of the samples produced by the SLM method decreased with increasing build orientation angle values.

Keywords. Additive manufacturing, selective laser melting, hatch spacing, thermal conductivity, 316L stainless steel

1. Introduction

Due to its high corrosion resistance, stainless steels are widely used materials in many areas (Saeidi *et al.*, 2015; Alsalla, Smith and Hao, 2018; Tucho *et al.*, 2018; Liu *et al.*, 2020; Haghdaei *et al.*, 2021). One of the most widely used types of stainless steel is 316L stainless steel. Due to its superior properties, 316L stainless steel is widely used in the production of parts with functional and complex geometries in additive manufacturing. Selective Laser Melting (SLM) method, which is one of the additive manufacturing methods, is a new generation production technology in which products with complex geometries can be manufactured. In this method, the basis is to connect the powdered material together in layers by melting with laser and forming the final product (Peleg, 2020).

In the SLM process, the 3D design of the product that is aimed to be produced is transformed into a usable product without using cutting tools and molds. The structural, mechanical and tribological properties of the parts produced by the SLM method are greatly affected by the parameters and strategies used in production. All additive manufacturing machines commercialized to date use a layer-based approach, and the primary ways they differ are in the materials that can be used, how the layers are constructed, and how the layers are linked together. Such differences determine factors such as geometric accuracy and material properties of the final part (Gibson, Rosen and Stucker, 2015).

In the SLM method, many production parameters affect the mechanical, chemical, morphological and tribological properties of the final product. These production parameters are;

- Laser power,
- Laser scanning speed,
- Layer thickness,
- Scanning strategy,
- Build orientation,
- Laser pulse mode.



In the SLM method, the strength between the layers should be high and integrity should be ensured. This integrity is provided by the energy density (E), which is controlled by the change of laser power (P), layer thickness (t), laser scanning speed (V), hatch distance (h), known as production parameters. All these parameters affect the mechanical properties of the material (Thijs *et al.*, 2010; Kaya, 2019). The relationship between production parameters and energy density are given in the formula below.

$$E = \frac{P}{V \cdot h \cdot t}$$

In a study by Simmons *et al.*, the thermal conductivity of 316L stainless steel produced by selective laser melting was investigated as a function of production conditions and build orientation. Porosity and thermal conductivity were measured under different production conditions. They showed that the materials produced with SLM changed the microstructure compared to the conventionally produced materials and changed the thermal conductivity of the additively produced 316L stainless steel (Simmons *et al.*, 2020). In a study by Alkahari *et al.*, the thermal conductivity of metal powders with different particle diameters and their mixtures were analyzed. In addition, the thermal conductivity of the consolidated materials produced by the SLM process was also investigated. It has been observed that thermal conductivity decreases with the increase in porosity in these materials (Alkahari *et al.*, 2012).

In this study, the thermal conductivity coefficients were measured by using 10x10x5 mm prismatic samples produced from stainless steel powder in different parameters with the SLM method and compared with the stainless steel 316L produced by the conventional method. In the literature, studies have been carried out to determine the thermal conductivity coefficients of the samples produced with SLM. However, no study has been conducted on the effects of different hatch spacing values and different build orientations on the thermal conductivity coefficients of the samples produced with SLM. For this reason, the effects of these parameters on thermal conductivity were examined in this study.

2. Material and Method

2.1. SLM Process

Test samples used for thermal examinations were produced with Concept Laser M LabR SLM device using different production parameters. The SLM device shown in Figure 1 works with a 100W Neodymium doped Yttrium Aluminum Garnet (Nd:YAG) laser system and has a 80x80x90 mm build platform. The manufacturing processes were carried out using continuous laser pulse mode in the atmosphere of Nitrogen (N₂) gas. Oxygen content was kept below 1% during the production. STL file formats of the produced test samples were prepared with the AutoFab software. In order to examine the effect of hatch spacing, thermal conductivity tests were carried out by producing prismatic samples at different hatch spacing values. In addition to the hatch spacing values, the effect of different build orientations on thermal conductivity was investigated. SLM process parameters of thermal conductivity test samples were given in Table 1.



Fig. 1: Concept Laser M Lab R SLM device

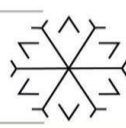
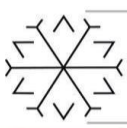


Table 1: SLM Process Parameters

Power (W)	Laser Scan Speed(mm/s)	Layer Thickness (µm)	Hatch Spacing (%)	Build Orientation(°)
100	600	25	60-70-80	0-45-90

In this study, it was tried to determine the optimum hatch spacing value for thermal conductivity by using different hatch spacing values. A schematic representation of the hatch spacing value was given in Figure 2. The hatch spacing can be defined as the separation between two consecutive laser beams. After single laser pulses using 100 W laser power, 600 mm/s laser scanning speed and 25 µm layer thickness, the laser trace width was obtained as approximately 100 µm. The production was carried out using the SLM method, with the hatch spacing values being 60, 70 and 80% of the laser trace width (100 µm) value.

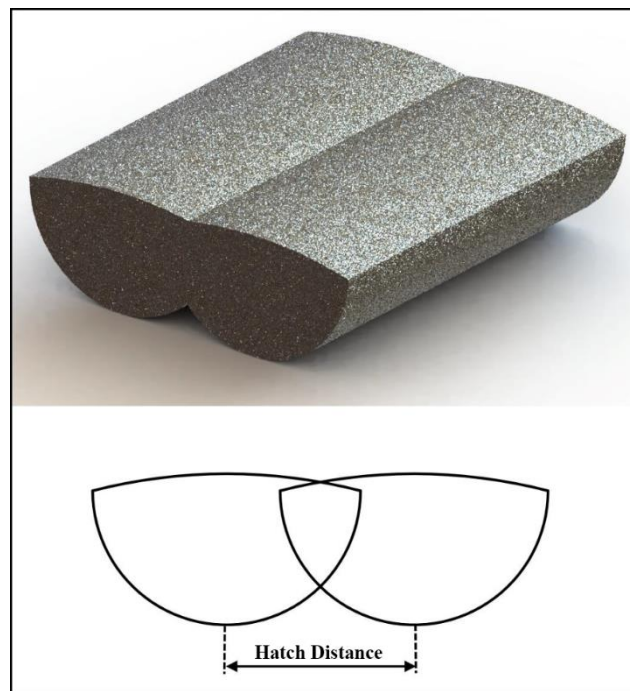


Fig. 2: A Schematic Representation of Hatch Spacing

In addition, besides the hatch spacing values, the effects of the build orientation on the thermal conductivity were investigated. A schematic representation of the build orientations was shown in Figure 3. Manufacturing in different build orientations affects the pore ratio in the structure and therefore affects the thermal conductivity values. For that reason, it was important to determine the optimum build orientation.

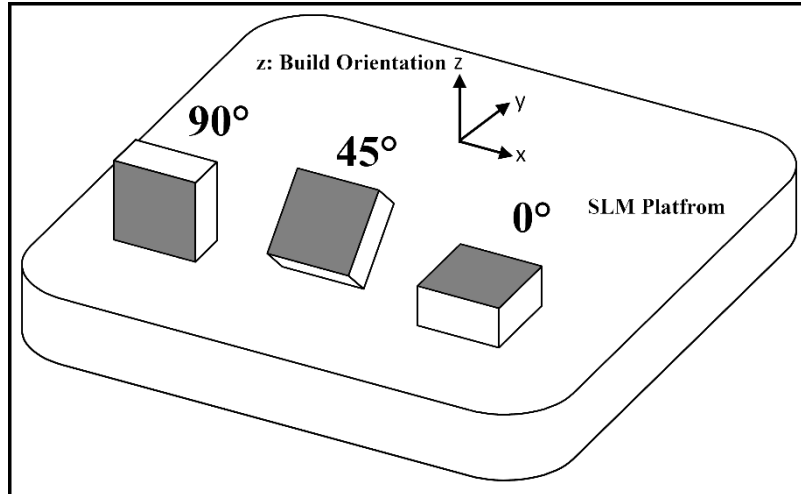


Fig. 3: Schematic Representation of Different Build Orientations

2.2 Thermal Conductivity Measurements

The thermal conductivity coefficients of the samples were measured with the GUNT WL372 thermal analyzer shown in Figure 4. The schematic view of the thermal analyzer used for thermal conductivity measurements were given in Figure 5. This device, which includes a heater, cooler and thermocouple, was in the form of a horizontal cylinder with a transmission line in the center, and the test sample was placed in the middle of the device while measuring. In addition, the device was completely thermally insulated. In the experiments, power, temperature and time measurements were taken from the thermal analyzer. The thermal conductivity values of the samples were obtained by the thermal resistance approach. For each sample, the experiment lasted 90 minutes and was repeated 3 times, and average results were obtained.



Fig. 4: Thermal Conductivity Device

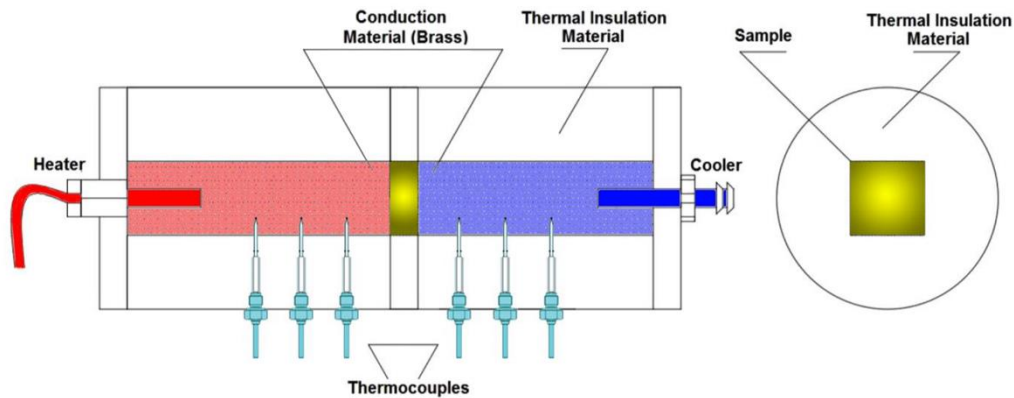
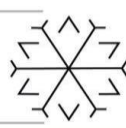
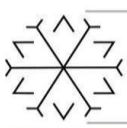


Fig. 5: A Schematic Representation of the Thermal Conductivity Device

3. Results

The thermal conductivity measurement results, which give important information about the amount of pores in the samples produced by using 3 different build orientations (0° , 45° and 90°) for different hatch spacing values, were presented in Figure 6. For comparison, the thermal conductivity result of 316L stainless steel produced by the conventional method was also added to the chart. When the graph was examined, it was seen that the highest thermal conductivity was obtained for the sample produced by the conventional method (forging). In the samples produced by the SLM method, the thermal conductivity values decreased as a result of the fact that the 100% density rate could not be reached as a result of the layer-by-layer production. In the evaluation made in terms of hatch spacing values, the 70% hatch spacing value gave higher thermal conductivity values for all three build orientations. The excessive thermal input caused by the low hatch gap value was thought to cause the formation of spherical gas voids in the microstructure. As a result of increasing the hatch spacing, the inadequate integration defects between the adjacent laser tracks that could not come into contact with each other and insufficient melting zones in the microstructure were thought to accelerate the decrease of the relative density values (Hacısalıhoğlu *et al.* 2020).

The thermal conductivity values of the samples produced by the SLM method decreased with increasing build orientation angle values. Due to the low number of layers and the lower heat input to the structure in the samples produced horizontally (0°) on the build platform, the thermal conductivity values were higher than the samples produced at 45° and 90° angles.

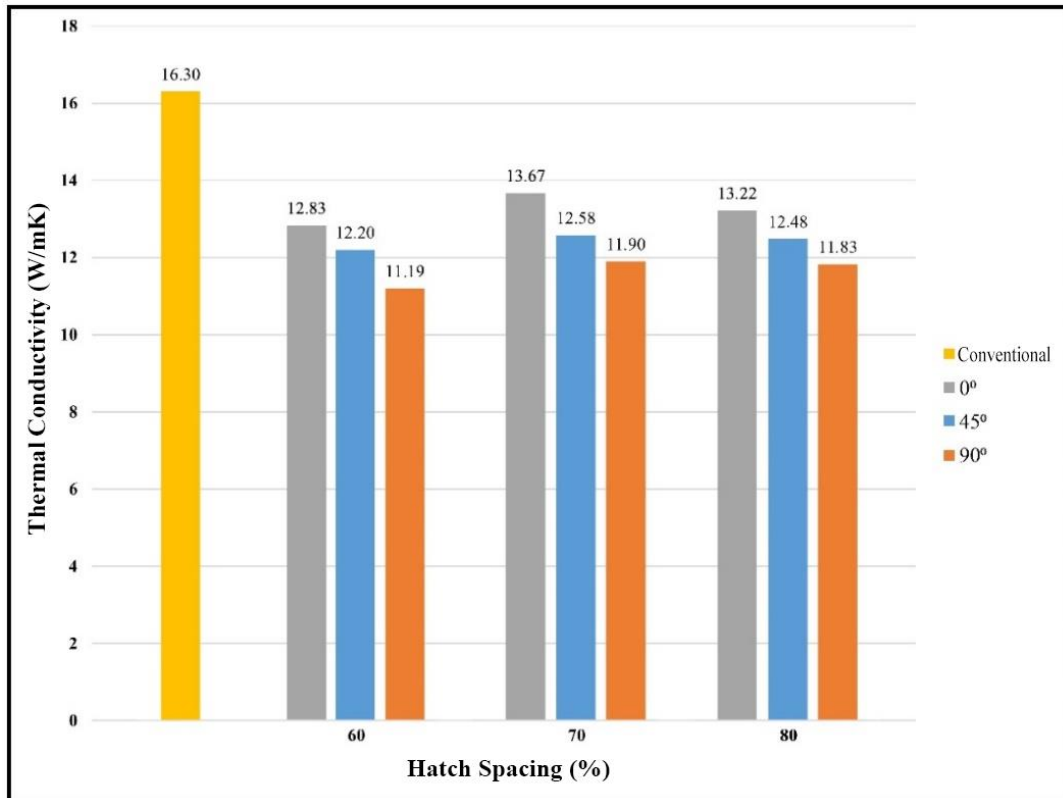


Fig. 6: Thermal Conductivity Values of Samples Produced Using the Conventional Method and SLM Method Using Different Hatch Spacing Values and Build Orientations

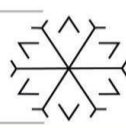
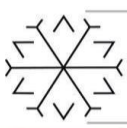
4. Conclusions

In this study, it was determined that different hatch spacing values and different build orientations affected the thermal conductivity of 316L stainless steel as they changed the internal structure properties in SLM production. In order to obtain a stable melt pool in production with SLM, it was important to find the optimum hatch spacing value and build orientation. The highest thermal conductivity value was obtained for the sample produced by the conventional method. Among the hatch spacing values, 70% hatch spacing value provided higher thermal conductivity values for all build orientations. The thermal conductivity values of the samples produced by the SLM method decreased with increasing build orientation angle values.

Acknowledgements

We would like to thank Erzurum Technical University High Technology Research and Application Center (ETÜ-YÜTAM) for its support in experimental studies. We would also like to thank the Higher Education Council of Turkey (YÖK) for providing scholarships within the scope of the 100/2000 program to Tevfik Oğuzhan Ergüder.

References



- Alkahari, M. R. *et al.* (2012) 'Thermal conductivity of metal powder and consolidated material fabricated via selective laser melting', *Key Engineering Materials*, 523–524, pp. 244–249. doi: 10.4028/www.scientific.net/KEM.523-524.244.
- Alsalla, H. H., Smith, C. and Hao, L. (2018) 'Effect of build orientation on the surface quality, microstructure and mechanical properties of selective laser melting 316L stainless steel', *Rapid Prototyping Journal*, 24(1), pp. 9–17. doi: 10.1108/RPJ-04-2016-0068.
- Gibson, I., Rosen, D. and Stucker, B. (2015) 'Additive manufacturing technologies: 3D printing, rapid prototyping, and direct digital manufacturing, second edition', *Additive Manufacturing Technologies: 3D Printing, Rapid Prototyping, and Direct Digital Manufacturing, Second Edition*, (3), pp. 1–498. doi: 10.1007/978-1-4939-2113-3.
- Hacısalıhoğlu, İ. *et al.* (2020) 'The effects of build orientation and hatch spacing on mechanical properties of medical Ti–6Al–4V alloy manufactured by selective laser melting', *Materials Science and Engineering: A*, 802, 140649. doi.org/10.1016/j.msea.2020.140649.
- Haghdadi, N. *et al.* (2021) 'Additive manufacturing of steels: a review of achievements and challenges', *Journal of Materials Science*, 56(1), pp. 64–107. doi: 10.1007/s10853-020-05109-0.
- Kaya, G. (2019) *Seçici Lazer Ergitme Yöntemi Kullanılarak Farklı Üretim Parametrelerinde Üretilen Ti6Al4V Alaşımının Yapısal Ve Tribolojik Özelliklerinin Karakterizasyonu*, MA Thesis, Erzurum Technical University, Erzurum.
- Liu, J. *et al.* (2020) 'Effect of scanning speed on the microstructure and mechanical behavior of 316L stainless steel fabricated by selective laser melting', *Materials and Design*, 186. doi: 10.1016/j.matdes.2019.108355.
- Peleg, J. (2020) *Additive and Traditionally Manufactured Components A Comparative Analysis of Mechanical Properties*, *Additive and Traditionally Manufactured Components*. doi: 10.1016/c2019-0-04180-5.
- Saeidi, K. *et al.* (2015) 'Hardened austenite steel with columnar sub-grain structure formed by laser melting', *Materials Science and Engineering A*, 625, pp. 221–229. doi: 10.1016/j.msea.2014.12.018.
- Simmons, J. C. *et al.* (2020) 'Influence of processing and microstructure on the local and bulk thermal conductivity of selective laser melted 316L stainless steel', *Additive Manufacturing*, 32(December 2019), p. 100996. doi: 10.1016/j.addma.2019.100996.
- Thijs, L. *et al.* (2010) 'A study of the microstructural evolution during selective laser melting of Ti-6Al-4V', *Acta Materialia*, 58(9), pp. 3303–3312. doi: 10.1016/j.actamat.2010.02.004.
- Tucho, W. M. *et al.* (2018) 'Investigation of effects of process parameters on microstructure and hardness of SLM manufactured SS316L', *Journal of Alloys and Compounds*, 740, pp. 910–925. doi: 10.1016/j.jallcom.2018.01.098.

Use of Phase-Changing Materials in Building Wall Blocks

Ersin HAYDARASLAN ¹[0000-0002-3142-9518], Burhan ÇUHADAROĞLU ² [0000-0002-9144-498X],

¹ Recep Tayyip Erdoğan University, Department of Electricity and Energy, 53100, Rize, Turkey

*Corresponding author, ersin.haydaraslan@erdogan.edu.tr

² Karadeniz Technical University, Department of Mechanical Engineering, 61080, Trabzon, Turkey

Abstract

This study investigates the effects of using phase-changing material (PCM) in-wall blocks to save energy in buildings. Firstly, the properties of wall blocks and phase-changing materials are discussed. Then, studies examining the effect of using phase-changing materials in wall blocks on energy-saving were compiled. At the end of the study, it has been reached that the use of phase-changing material, which is an innovative material in wall blocks, provides energy savings up to 80%.

Keywords: Hollow block form, thermal analysis, phase changing material, energy saving

1. Introduction

Today, fossil resources are generally used as an energy source. However, it is foreseen that these resources will be depleted soon. For this reason, studies are carried out to reduce energy consumption and increase conservation (Tomaz, 2018; IEA, 2020; EU, 2020; EPBD, 2018; BEP-TR, 2017). When the energy consumption rates in the world are examined, it is seen that 40% of the total energy consumption is based on buildings (E. Commission, 2012). When European energy consumption is examined; buildings in cities consume 60% of energy (IEA, 2020). In line with these rates, many studies have been carried out to reduce the energy consumption of buildings. The building envelope has an essential role in the studies on reducing the energy consumption of buildings. Improvements made in building envelopes, which directly interact with the external environment, reduce energy consumption. Wall blocks are widely used in building envelopes (Kant et al., 2017; Wang et al.; 2018). Wall blocks are produced in different forms and sizes. The blocks are also produced in different inner forms. Therefore, it is crucial to examine the differentiation of wall blocks from a thermal perspective (Coz et al., 2007; Sun and Fang, 2009; Al-Hazmy, 2006; Morales et al., 2011; Alghamdi et al., 2017; Zhang et al., 2019).

Innovation studies are carried out to reduce energy consumption in buildings. These studies include the use of building-integrated energy storage systems in buildings (IEA, 2020). It is recommended to expand the use of phase-changing materials in buildings. Studies show that 60-75% energy efficiency will be achieved with the widespread use of energy storage systems in buildings (SET Plan, 2017). In this study, it was aimed to examine the use of PCM in-wall blocks. Firstly, information about wall blocks and PCMs is given. Then, the studies on the effect of different inner forms of wall blocks on thermal performance are discussed. Finally, studies investigating the changes in thermal performance when PCM is added in blocks with different inner forms are examined.

2. Wall Blocks

Wall blocks are structural elements that are generally used as the raw material of clay, sand, gravel or pumice and are formed with quartz, cement, water, chemical binders etc (TS 3234; TS 2823; Yüksel, 2006). These blocks are named according to the raw material they are produced in the market and in the literature (brick, pumice, pumice block, pumice concrete etc.). In addition, these blocks are also named light concrete block, hollow wall block, briquette, light masonry unit, etc., regardless of the raw material (Uzun, 2008) (Gündüz, 2005). Wall blocks have a wide classification. They are classified firstly according to whether



they are empty or filled (solid). While solid blocks are divided into two as full-filled or half-filled blocks, hollow blocks are divided into four as single row, two-row and three-row blank (TS 2823). Wall blocks are mainly produced from pumice due to their hollow structure and lightweight. Thanks to this feature, pumice stands out compared to other raw materials in heat preservation and sound insulation. In addition, Turkey ranks third in the world in terms of pumice reserves. Thanks to this rank, wall blocks produced with pumice are widely used in Turkey. The production stages of the wall block with pumice are given in Figure 1 and the visual of the wall block produced from pumice is given in Figure 2.

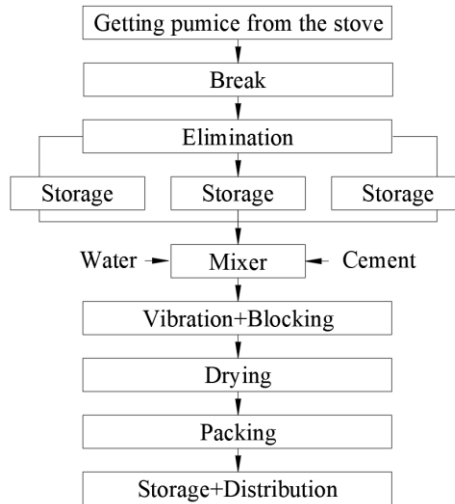


Figure 1. Wall block production stages with pumice



Figure 2. Wall blocks made of pumice

3. Phase-Changing Materials

The energy storage allows the energy obtained from renewable energy sources to be used without interruption (Pasupathy, 2008). Different storage methods such as chemical, thermal, electrical, and mechanical are used for energy storage. Among these methods, thermal energy storage includes thermal energy storage as hot or cold matter. This energy storage method is classified as sensible heat storage, thermochemical energy storage and latent heat storage (Gil et al., 2010; Kyung-Eun Min, 2019; Akeiber et al., 2016). Sensible heat storage; involves the release or storage of thermal energy by changing the temperature of a material (Abedin and Rosen, 2011; Zalba et al., 2003). Thermochemical energy storage is the storage or release of energy by chemical methods (Krese, 2018). Latent heat storage is the storage or release of thermal energy at a constant temperature (Figure 3) (Pielichowska and Pielichowski, 2014). It has been found that the amount of heat stored in a unit volume in materials with latent heat storage is 5-14 times more than other materials (Sharma et al., 2009). The most widely used materials in terms of latent heat storage are Phase-Changing Materials (Kyung-Eun Min, 2019).

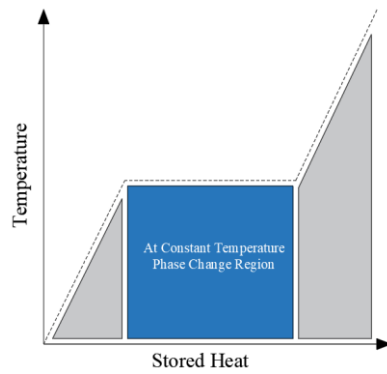
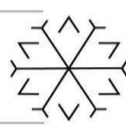
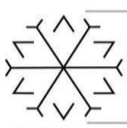


Figure 3. Latent heat storage

PCMs are materials that store or release heat during a phase change (liquid-solid, solid-liquid) in a fixed temperature range. Because of these properties, they are also called materials that store latent heat (Sharma et al., 2009). A diagram and graph showing the phase change of the PCM are shown in Figure 4 (Rami, 2018).

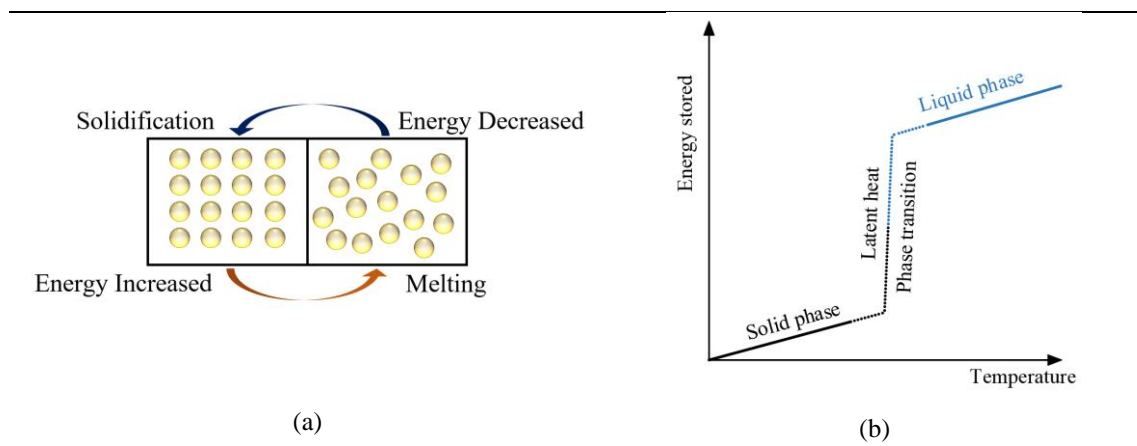


Figure 4. PCM process (a) diagram, (b) graph

PCMs can store the heat in the transition from solid to liquid state in case of heat transfer and release the stored heat to the outside in case of a change from liquid form to solid (Sharma et al., 2009). The high benefit of the heat storage properties of PCMs is related to the phase change of the PCM in a specific temperature range and high heat storage (Kyung, 2019; Zalba, 2003; Sharma, 2009). The energy storage of the PCM during phase change is shown in Figure 5 (Energyplus, 2020; Rami, 2018).

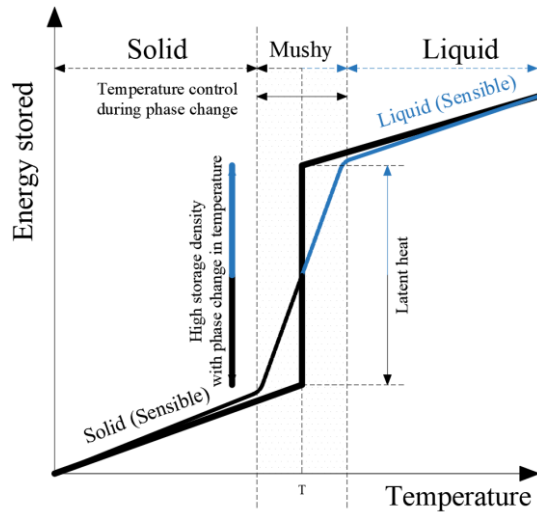


Figure 5. Energy stored change in PCM according to temperature

PCMs have different types in terms of physical and chemical properties. It is used in various areas such as air conditioning, food, medical, electronics, aviation and building materials (Pielichowska and Pielichowski, 2014; Kenisarin, 2010). PCMs are mostly classified as organic, inorganic and eutectic according to the sources from which they are obtained (Podara et al., 2021) (Figure 6). Advantages and disadvantages of organic, inorganic and eutectic PCMs are given in Table 1 (Podara, 2021; da Cunha, 2020; Kahwaji, 2019; Sharma et al., 2009).

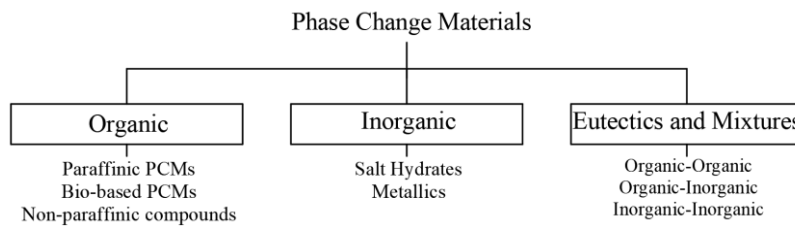
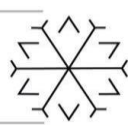
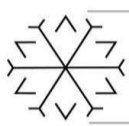


Figure 6. Classification of PCMs

Table 1. Advantages and disadvantages of organic, inorganic, and eutectic PCMs

	Advantages	Disadvantages
Organic PCM	Wide phase change temperature range Demonstrates stable thermal properties No phase separation in the melting process High latent heat Minimum volume change Recyclable Low cost	Low thermal conductivity Low density High flammability
Inorganic PCM	High thermal conductivity High energy efficiency (high enthalpy) Low volume change during phase Not flammable	Supercooling of the liquid phase To be toxic Limited compatibility High cost
Eutectic PCM	Specific phase change temperature The phase change temperature can be produced in accordance with the requirements. Thermally stable	High cost

PCMs are encapsulated using two techniques, microencapsulation, and macro-encapsulation, depending on the environment in which they are used and the size of the shell materials. (Lauck, 2013; Rathore and



Shukla, 2019). Macro encapsulation is the encapsulation method in which PCM is filled into containers and packages such as tubes, balls, spheres, bags, metal rods, panels. In its most general definition, this method refers to placing the PCM in a material larger than 5 mm (Rathore and Shukla, 2019; Milian et al., 2017). With macro encapsulation, a high amount of PCM can be used in buildings with macro encapsulation. Microencapsulation is the encapsulation of PCM at a size of a few micrometres. In this technique, encapsulation can be done by direct immersion into an acrylic polymer or membrane-derived material. This technique is more costly than macro encapsulation.

4. Studies on the Integration of Phase-Changing Materials in Wall Blocks

Wall blocks are produced in different sizes and forms. In addition, the internal cavity geometries also differ. The internal cavity geometries of the blocks play an important role in the thermal resistance of the blocks. Al-Hazmy examined the thermal analysis of a solid block and a block with three square spaces in a single row. At the end of the study, it has been reached that there is 63% less heat transfer in the block with an air gap and 73% less in the case of thermal insulation in the gaps, compared to the solid block (Al-Hazmy, 2006). Al-Tamimi et al. investigated the heat transfers of twelve different block forms experimentally and numerically. As a result of the study, it has been reached that the optimum design geometry determined from various forms has less heat transfer than conventional forms available in the market. (Al-Tamimi et al., 2020). Alhazmy numerically investigated the effect of cavity geometry on heat flux in hollow blocks. In the study, triangular cells were formed by putting layers folded in different numbers into the cavity. As the number of triangular cells increased, it was found that natural convection was inhibited, and the heat flux decreased. As a result of the study, it was reached that the heat flux decreased by 37-42% depending on the number and material of the partitions (Alhazmy, 2010). Sun and Fang performed a numerical thermal analysis for seventy-one hollow blocks. As a result of the study, increasing the number of gaps in the direction parallel to the heat transfer decreased the heat transfer, and thus the heat transfer decreased by approximately 25% (Sun and Fang, 2009). Alghamdi and Alharthi investigated the effect of void geometry on heat transfer in blocks with rectangular, diamond and hexagonal void geometry. At the end of the study, it was concluded that the form of the cavity did not affect the thermal conductivity of the block in the x and y directions much. However, the thermal conductivity in the z-direction decreased by 6% and 8% in the hexagonal and diamond cavity geometry, respectively (Alghamdi and Alharthi, 2017).

When the studies on PCM are examined; it is seen that PCM, which is used in building construction materials and elements, contributes to energy conservation. PCMs were first used in buildings in the 1980s. PCMs in buildings are used in building materials and building elements (Sharma et al., 2009; Zalba et al., 2003). Wang et al. used phase change material inside the wall to reduce the summer-day cooling load. In the study, the heat transfer from the external environment to the internal climate decreased as the PCM layer thickness increased. They stated that the optimal PCM layer location changes at each melting temperature. They concluded that of the six PCMs studied, the one with a melting temperature of 42 °C showed the best performance when it was 20 mm thick and on the outside of the wall. They stated that PCM with the best performance reduced the heat transfer up to 34.9% (Wang et al., 2018).

In the studies on filling the space inside the blocks with different materials, materials such as straw, perlite and PCM were filled into the briquette spaces, and the changes in the total heat transmission coefficient of the block and the energy storage capacities were investigated (Kant et al., 2017; Zhang et al., 2019). In these studies, it has been observed that the materials placed in the block cavities reduce the total heat transmission coefficient of the block compared to the presence of air in the cavities. Gao et al. investigated the heat flux in the block by placing PCM in a four-row five-cavity block. In the study, the optimum position of the PCM placed in different spaces was determined. As a result of the study, the maximum heat flux was reduced from 45.26 W/m² to 19.19 W/m² with the PCM placed in the optimum position. In addition, the use of PCM in the block gaps provides time delay, and sudden heat load fluctuations are prevented (Gao et al., 2020). Alawadhi filled PCM to the cavities of the block containing circular voids and made thermal analyzes. As a result of the study, the heat gain decreased with the filled with PCM to the cavities. The best performance in terms of heat gain is achieved with PCM placed in the central position of the blocks



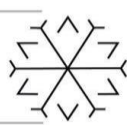
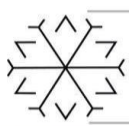
(Alawadhi, 2008). Zhang et al. carried out an experimental and numerical study by placing paraffin with a melting temperature of 48.3–57.8 °C into the hollow aluminium block. At the end of the study, it was found that there was a 2.5-fold difference in terms of time delay and temperature control with the use of paraffin in the blanks (Zhang et al., 2019). Saxena et al., in their study for a hot-humid climate, examined the time-dependent temperature change when PCM was added to the block. As a result of the experimental research, a temperature drops of 5–6 °C was observed with the addition of PCM. In addition, a 12% reduction in heat flux has been achieved. (Saxena et al., 2019). Kant et al. the case of filling hollow blocks with circular-shaped voids with PCMs of different properties has been numerically investigated. In the study, time-dependent temperature change and heat flux change were compared. As a result of the study, it was found that there was an 8.31% reduction in heat flux with the use of PCM (Kant et al., 2017). Vicente and Silva experimentally investigated the case of filled with PCM into hollow blocks. At the end of the study, it was reached that the heat transfer decreased by 50–80% (Vicente and Silva, 2014). Zhang et al. placed PCM at different locations inside the hollow blocks. In the study, the effect of PCM at various locations on indoor temperature was numerically investigated. They found that the addition of PCM showed thermal insulation properties and the sudden temperature change decreased (Zhang et al., 2011). Haghshenaskashani and Pasdarsahri numerically investigated the effect of using PCM inside hollow blocks on heat flux. As a result of the study, they reached a 32.8% decrease in heat flux filled with PCM (Haghshenaskashani and Pasdarsahri, 2009).

5. Conclusion

The foreseeing that fossil resources will be depleted soon has increased the importance of studies on reducing energy consumption and increasing conservation. The high share of energy consumption in buildings indicates that more focus should be placed on this area. In this context, studies prepared for the reduction of energy consumption in buildings are examined. In the studies examined, it has been seen that the building envelope has an important place. In addition, it has been stated that the blocks used in the building envelope and the innovative energy storage systems integrated into the blocks are effective in the energy consumption of the building. As a result, it has been seen that the inner form of the blocks and the PCMs to be used should be determined depending on the climate and the conditions in which they will be used. In addition, it is aimed to spread the more efficient use of energy with such studies.

References

- Abedin, AH and Rosen MA 2011, 'A critical review of thermochemical energy storage systems', *The Open Renewable Energy Journal*, Vol. 4, pp. 42-46.
- Akeiber, H, Nejat, P, Majid, MZA, Wahid, MA, Jomehzadeh, F, Zeynali Famileh, I, Calautit, JK, Hughes, BR, Zaki, SA 2016, 'A review on phase change material (PCM) for sustainable passive cooling in building envelopes', *Renew. Sustain. Energy Rev.*, Vol. 60, pp. 1470-1497.
- Alawadhi, EM 2008, 'Thermal analysis of a building brick containing phase change material', *Energy and Buildings*, Vol. 40, pp. 351-357.
- Alghamdi, AA, Alharthi HA 2017, 'Multiscale 3D finite-element modelling of the thermal conductivity of clay brick walls', *Construction and Building Materials*, Vol. 157, pp. 1-9.
- Al-Hazmy, MM 2006, 'Analysis of coupled natural convection-conduction effects on the heat transport through hollow building blocks', *Energy and Buildings*, Vol. 38, no.5, 515-521.
- Alhazmy, MM 2010, 'Numerical investigation on using inclined partitions to reduce natural convection inside the cavities of hollow bricks', *International Journal of Thermal Sciences*, Vol. 49, no.11, 2201-2210.
- Al-Tamimi, AS, Baghabra Al-Amoudi, OS, Al-Osta, MA, Ali, MR and Ahmad, A 2020, 'Effect of insulation materials and cavity layout on heat transfer of concrete masonry hollow blocks', *Construction and Building Materials*, Vol. 254, pp. 119300.
- da Cunha, SRL, de Aguiar, JLB 2020, 'Phase change materials and energy efficiency of buildings: A review of knowledge', *J. Energy Storage*, Vol. 27, pp. 101083.



del Coz Díaz, JJ, García Nieto, PJ, Betegón Biempica, C and Prendes Gero, MB 2007, 'Analysis and optimization of the heat-insulating light concrete hollow brick walls design by the finite element method', *Applied Thermal Engineering*, Vol. 27, pp. 1445-1456.

EnergyPlus Engineering Reference 2020, Viewed 20 December 2020, <www.energyplus.net/documentation>.

EPBD 2018, Directive 2010/31/EU of the European Parliament and of Council of 30 May 2018 on the energy performance of buildings (recast), EU Commission, Official Journal of the European Union.

European Commission 2012, Commission Delegated Regulation (EU) No.244/2012 of 16 January 2012 Supplementing Directive 2010/31/EU of the European Parliament and of the council on the energy performance of buildings by establishing a comparative methodology framework for calculating cost-optimal levels of minimum energy performance requirements for buildings and building elements, Official Journal of the European Union.

European Commission, Energy Efficiency 2019, Viewed 3 November 2020, <www.ec.europa.eu>.

Gao, Y, He, F, Meng, X, Wang, Z, Zhang, M, Yu, H, Gao, W 2020, 'Thermal behavior analysis of hollow bricks filled with phase-change material (PCM)', *Journal of Building Engineering*, Vol.31, pp. 101447.

Gil, A, Medrano, M, Martorell, I, Lázaro, A, Dolado, P, Zalba, B, Cabeza, L 2010, 'State Of The Art On High Temperature Thermal Energy Storage For Power Generation. Part 1 Concepts Materials And Modellization', *Renewable and Sustainable Energy Reviews*, Vol.14, pp.31-55.

Gündüz, L 2005, 'İnşaat Sektöründe Bimsblok', Süleyman Demirel Üniversitesi Pomza Arastırma ve Uygulama Merkezi, Isparta.

Haghshenaskashani S, Pasdarsahri H 2009, 'Simulation of Thermal Storage Phase Change Material in Buildings', *World Academy of Science, Engineering and Technology*, Vol.58, pp. 1020-1024.

International Energy Agency, Energy Technology Perspectives 2019, View 05 July 2020, <www.iea.org>.

International Energy Agency, World Energy Model, Sustainable Development Scenario 2020, View 15 March 2020, <www.iea.org/reports/world-energy-model>.

Jeffrey Stephen L 2013, 'Evaluation of Phase Change Materials for Cooling in a Super- Insulated Passive House', PhD thesis, Portland State University PDX-Scholar.

Kahwaji, S 2019, 'White, M.A. Edible Oils as Practical Phase Change Materials for Thermal Energy Storage', *Appl. Sci.*, Vol. 9, pp. 1627, 2019.

Kant K, Shukla A, Sharma A 2017, 'Heat transfer studies of building brick containing phase change materials', *Solar Energy*, Vol.155, pp. 1233-1242,.

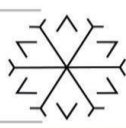
Kenisarin MM 2010, 'High temperature phase change materials for thermal energy storage', *Renewable and Sustainable Energy Reviews*, Vol. 14, pp. 955-970.

Krese G, Butala V, Stritih U 2018, 'Thermochemical seasonal solar Energy storage for heating and cooling of buildings', *Energy Build.*, Vol. 164, pp.239-253.

Kyung-Eun Min 2019, 'A Study of Thermal Energy Storage of Phase Change Materials: Thermophysical Properties and Numerical Simulations', PhD thesis, Portland State University, Portland.

Milian YE, Gutierrez A, Grageda M, Ushak S 2017, 'A review on encapsulation techniques for inorganic phase change materials and the influence on their thermophysical properties', *Renew. Sustain. Energy Rev.* Vol.73, pp. 983-999.

Morales, MP, Juárez, MC, Muñoz, P, Gómez, JA 2011, 'Study of the geometry of a voided clay brick using non-rectangular perforations to optimise its thermal properties', *Energy and Buildings*, Vol. 43, pp. 2494-2498.



- Pasupathy A, Velraj R, Seeniraj RV 2008, 'Phase change material-based building architecture for thermal management in residential and commercial establishments', *Renew Sustain Energy Rev.*, Vol 12, 39-64, 2008.
- Pielichowska K and Pielichowski K 2014, 'Phase change materials for thermal energy storage', *Progress in Materials Science*, Vol. 65, pp. 67-123.
- Podara, CV, Kartsonakis, IA, Charitidis, CA 2021, 'Towards Phase Change Materials for Thermal Energy Storage: Classification', *Improvements and Applications in the Building Sector. Appl. Sci.*, Vol. 11, pp. 1490.
- Rami Mohammad RS 2018, 'Advancement in Thermal Energy Storage Using Phase Change Materials', PhD thesis, Nuclear Engineering, Missouri University of Science and Technology, ABD.
- Rathore, PKS, Shukla, SK 2019, 'Potential of macroencapsulated PCM for thermal energy storage in buildings: A comprehensive review', *Construction and Building Materials*, Vol. 225, pp. 723-744.
- Saxena, R, Rakshit, D and Kaushik, SC 2019, 'Phase Change Material (PCM) Incorporated Bricks for Energy Conservation in Composite Climate: A Sustainable Building Solution', *Solar Energy*, Vol.183, 276-284.
- Sharma A, Tyagi VV, Chen CR and Buddhi D 2009, 'Review on thermal energy storage with phase change materials and application', *Renewable and Sustainable Energy Reviews*, Vol. 13, pp. 318-345.
- Sun, J, Fang, L 2009, 'Numerical simulation of concrete hollow bricks by the finite volume method', *International Journal of Heat and Mass Transfer*, Vol.52, pp. 5598-5607.
- T.C. Resmi Gazete, Binalarda Enerji Performansı Ulusal Hesaplama Yöntemine Dair Tebliğ. (30227), 01.10.2017.
- The Strategic Energy Technology (SET) Plan, 2017, Energy Research and Innovation in Europe, European Commission.
- Tomaž G 2018, 'The Adoption of the Kyoto Protocol of the United Nations Framework Convention on Climate Change', *Contributions to Contemporary History*, Vol.58, no.2, pp.160-188.
- TS 2823, 1986. Bimsbetondan mamul yapı elemanları, Türk Standartları Enstitüsü, Ankara.
- TS 3234, 1978. Bimsbeton yapım kuralları, Karışım hesabı ve deney metotları. Türk Standartları Enstitüsü, Ankara.
- Uzun, Ö 2008, Bimsblok ile Örülen Dış Duvarların Yapısal Performansının Değerlendirilmesi Üzerine Bir Alan Çalışması, Yüksek Lisans Tezi, İstanbul Teknik Üniversitesi, İstanbul.
- Vicente, R, Silva, T 2014, 'Brick masonry walls with PCM macrocapsules: An experimental approach', *Applied Thermal Engineering*, Vol. 67, pp. 24-34.
- Wang, J, Yu C, Pan W 2018, 'Life cycle energy of high-rise office buildings in Hong Kong', *Energy Build.* Vol. 167, pp. 152-164.
- Wang, Q, Wu, R, Wu, Y and Zhao, CY, 'Parametric Analysis of Using PCM Walls for Heating Loads Reduction', *Energy and Buildings*, Vol. 172, pp. 328-36.
- Yüksel İ, Özkan Ö and Bilir T 2006, 'Kazanaltı Külü ile Briket Üretimi', *Gazi Üniv. Müh. Mim. Fak. Der.*, Vol. 21, no. 3, pp. 527-532.
- Zalba B, Marin JM, Cabeza LF and Mehling H 2003, 'Review on thermal energy storage with phase change: Materials, heat transfer analysis and applications', *Applied Thermal Engineering*, Vol. 23, pp. 251-283.
- Zhang, JJ, Yang, CH, Zhang, JS 2019, 'Thermal characteristics of aluminum hollowed bricks filled with phase change materials: Experimental and numerical analyses', *Applied Thermal Engineering*, Vol.155, pp. 70-81.

Crack Path Prediction in Functionally Graded Materials Using a Local Criteria

Mohammed A. Bouchelarm ¹[0000-0001-9887-3149], Meriem Chafi ¹[0000-0002-3578-9625], and Abdelkader Boulenouar ¹[0000-0001-5116-2972]

¹ Laboratoire de Matériaux et Systèmes Réactifs LMSR. Djillali Liabes University of Sidi Bel Abbes.
22000 Sidi Bel Abbes, Algeria

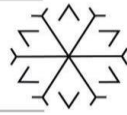
*m.bouchelarm@yahoo.com

Abstract

Functionally graded material (FGM) is a material solution and a material concept used for a new class of advanced composites characterized by gradual variation in composition, microstructure and material properties. These graded materials have emerged from the need to enhance material performance. Due to the variation of properties, predicting the fracture and crack propagation behavior in FGMs is very complicated. The presence of cracks in functionally graded materials can be problematic to predict numerically the crack path trajectory. When the loading or the geometry of the specimen are not symmetrical to the crack axis, the fracture occurs under mixed mode loading conditions. Therefore, it is necessary to use fracture criteria's to determine the crack growth direction.

In fracture mechanics, several numerical approaches have been used to study the mechanical behavior of cracked structures. However, for Functionally Graded Material (FGM), few studies have considered the effect of different fracture parameters on the crack propagation path. The main purpose of this study is to present a numerical prediction of crack propagation path in isotropic functionally graded materials under mixed-mode loading. The displacement correlation technique (DCT) is used to evaluate the mixed mode stress intensity factors and then the obtained values are used in a local criteria (MTS) to determine the new direction of the crack considering a small extension in FGM beam subjected to three points bending conditions. According to its formulations, the criteria assumes that the crack extension angle begins along the maximum value of the circumferential tensile stress. To this end, numerical programs are developed and integrated into a finite element code using the Ansys Parametric Design Language (APDL). The special quarter point finite elements are used to obtain a better approximation of the field near crack-tip. The mid-side node of the element in the crack-tip is moved to 1/4 of the length of the element. For the material, two applications are investigated using an initial crack perpendicular and parallel to material gradient.

Keywords. Functionally graded materials, Stress intensity factor, Displacement correlation technique, Crack propagation, Mixed mode.



Influence of the geometrical discontinuity on the mixed mode Crack Propagation in Functionally Graded Materials

Meriem Chafi ¹[0000-0002-3578-9625], Mohammed A. Bouchelarm ^{1*}[0000-0001-9887-3149] and Abdelkader Boulenouar ¹[0000-0001-5116-2972]

¹ Laboratoire de Matériaux et Systèmes Réactifs LMSR. Djillali Liabes University of Sidi Bel Abbes.
22000 Sidi Bel Abbes, Algeria

* m.bouchelarm@yahoo.com

Abstract

Functionally Graded Materials (FGMs) are inhomogeneous materials which are widely used in technological application. FGMs possess the distinguishing feature of nonhomogeneity with regard to thermomechanical and strength related properties including yield strength, fracture toughness, and fatigue and creep behavior. These multifunctional materials were introduced to take advantage of ideal behavior of its constituents, e.g. heat and corrosion resistance of ceramics together with mechanical strength and toughness of metals. In recent years, those materials have been especially studied its mechanical behaviors using different approaches. For the fracture of the FGMs, many studies have considered various crack problems in non-homogeneous materials. Knowledge of the behavior of cracks in FGMs is important for assessing and enhancing their structural integrity.

The presence of defects in structures weakens their mechanical strength, can lead to their ruin and be the cause of serious disasters. In order to avoid these, we must therefore be able to predict the behavior of cracked structures, and to guarantee their integrity. Therefore, in this work we have presented a numerical analysis of the effect of geometrical defects on the final path of crack propagation in FGM materials. This study is based on the use of the most efficient bifurcation criteria. Numerical calculations were carried out on several examples, using the ANSYS finite element calculation code. Examples of different cases are studied, these examples contain geometrical defects that can influence the propagation path of a crack, such as holes, cavities or inclusions or cavities. The obtained results are compared with results available in the literature in order to show that the numerical model used is able to reproduce with an excellent reliability the crack propagation path in the case of complex structures. The displacement extrapolation method (DET) is used to determine numerically the stress intensity factors and then the chosen criteria will determine the crack direction. The crack propagation model is characterized by successive propagation steps performed without user interaction. We concluded that a crack is always attracted to a geometric defect, which is attributed to the stress depression which will modify the maximum principal stress so that the crack orientates towards that defect. The presence of holes and inclusions in the plates disturbed the stress and strain fields providing interesting crack trajectories. The results indicated that FE analysis for fracture mechanics problems has been successfully employed for homogenous and FGM.

Keywords. Functionally graded materials, Stress intensity factor, Displacement extrapolation technique, Crack propagation, Mixed mode, inclusion, hole.